Transactions of the ASME

EDITORIAL STAFF
Editor, J. J. JAKLITSCH, JR.
Production Editor, RONNIE HEANEY
Prod. Asst., BETH DARCHI

APPLIED MECHANICS DIVISION
Chairman, R. S. RIVLIN
Secretary, R. M. CHRISTENSEN
Technical Editor, C. S. HSU
Associate Editors, S. T. ARIARATNAM
T. BELYTSCHKO
S. C. COWIN
R. C. DiPRIMA
J. DUNDURS
L. B. FREUND
D. S. GRIFFIN
M. HOLT
T. R. KANE
A. S. KOBAYASHI
T. L. LARDNER
S. LEIBOVICH
P. A. LIBBY
U. S. LINDHOLM
L. E. MALVERN
J. J. McCOY
M. S. PLESSET
R. PLUNKETT
R. T. SHIELD
C. R. STEELE
T. C. T. TING
G. A. WEMPNER

POLICY BOARD, COMMUNICATIONS
Chairman and Vice-President
I. BERMAN

Members-at-Large
M. J. RABINS
J. E. ORTLOFF
J. W. LOCKE
W. J. WARREN

Policy Board Representatives
Basic Engineering, F. LANDIS
General Engineering, A. A. SEIREG
Industry, R. K. HAMPTON
Power, R. E. REDER
Research, G. P. COOPER
Codes and Stds., L. L. ELDER
Computer Tech. Com., A. A. SEIREG
Nom. Com. Rep., S. P. ROGACKI

Business Staff
345 E. 47th St.
New York, N. Y. 10017
(212)644-7789

Mng. Dir., Pub., C. O. SANDERSON

OFFICERS OF THE ASME
President, DONALD N. ZWIEP
Exec. Dir. & Sec'y., ROGERS B. FINCH
Treasurer, ROBERT A. BENNETT

Journal of Applied Mechanics (ISSN 0021-8936) is edited and published quarterly at the offices of the American Society of Mechanical Engineers, United Engineering Center, 345 E. 47th St., New York, N. Y. 10017. ASME-TWX No. 710-581-5267, New York. Second Class postage paid at New York, N. Y., and at additional mailing offices.

CHANGES OF ADDRESS must be received at Society headquarters seven weeks before they are to be effective. Please send old label and new address.

PRICES: To members, $25.00, annually; to nonmembers, $50.00. Single copies, $15.00 each. Add $1.50 for postage to countries outside the United States and Canada.

STATEMENT from By-Laws. The Society shall not be responsible for statements or opinions advanced in papers or . . . printed in its publications (B13, Par. 4).

COPYRIGHT © 1980 by the American Society of Mechanical Engineers. Reprints from this publication may be made on condition that full credit be given the TRANSACTIONS OF THE ASME, JOURNAL OF APPLIED MECHANICS, and the author, and date of publication be stated.

INDEXED by the Engineering Index, Inc.

Journal of Applied Mechanics

Published Quarterly by The American Society of Mechanical Engineers

VOLUME 47 • NUMBER 2 • JUNE 1980

OBITUARY

225 William Prager

TECHNICAL PAPERS

227 Formation of Vortex Street in Laminar Boundary Layer
M. Kiya and M. Arie

234 Fluid Forces on Rods Vibrating in Finite Length Annular Regions
T. M. Mulcahy

241 Unsteady Incompressible Three-Dimensional Asymmetric Stagnation-Point Boundary Layers
M. Kumari and G. Nath

247 A Model of Pressure and Flow Distribution in Branching Networks
A. S. Popel

254 Transient and Residual Thermoviscoelastic Stresses in Glass
M. J. Crochet and A. Denayer

261 An Application of Mixture Theory to Particulate Sedimentation (80-WA/APM-1)
C. D. Hill, A. Bedford, and D. S. Drumheller

266 Constitutive Equations of Elastoplastic Materials With Elastic-Plastic Transition
K. Hashiguchi

273 Nonuniqueness in Contained Plastic Deformation
P. G. Hodge, Jr. and D. L. White

278 An Elastic-Plastic Stress Analysis of the Specimen Used in the Torsional Kolsky Bar
Eric K. C. Leung

283 Numerical Analysis of Elliptic-Hyperbolic Plastic Flow in Torsion
Y. K. Lee and J. L. Swedlow

291 Inelastic Analysis of Transverse Deflection of Plates by the Boundary Element Method
M. Morjaria and S. Mukherjee

297 A Generalized von Mises Criterion for Yield and Fracture
W. H. Yang

301 A Useful Theorem for Constructing Convex Yield Functions
W. H. Yang

304 Instability of a Layer on a Half Space
J. F. Dorris and S. Nemat-Nasser

313 On the Internal Stresses in a Half Plane and a Layer Containing Localized Inelastic Strains or Inclusions
Y. P. Chiu

319 Finite Thermoelastic Deformation of Sphere With Temperature-Dependent Properties
N. Kamiya

324 A Reinterpretation of the Palmgren-Miner Rule for Fatigue Life Prediction
Z. Hashin

329 Failure Criteria for Unidirectional Fiber Composites
Z. Hashin

335 A Mixed-Mode Crack Analysis of Isotropic Solids Using Conservation Laws of Elasticity
J. F. Yau, S. S. Wang, and H. T. Corten

342 Stress-Intensity Factors and Complex Path-Independent Integrals
P. S. Theocaris and N. I. Ioakimidis

347 A No-Slip Interface Crack
A. F. Mak, L. M. Keer, S. H. Chen, and J. L. Lewis

351 Normal and Shear Impact of Layered Composite With a Crack: Dynamic Stress Intensification
G. C. Sih and E. P. Chen

359 Diffraction of Antiplane Shear Waves by an Edge Crack
S. F. Stone, M. L. Ghosh, and A. K. Mal

363 Sanders' Energy-Release Rate Integral for Arbitrarily Loaded Shallow Shells and Its Asymptotic Evaluation for a Cracked Cylinder
J. W. Nicholson and J. G. Simmonds

370 Partitioned Transient Analysis Procedures for Coupled-Field Problems: Stability Analysis
K. C. Park

377 Finite-Element Analysis of Magnetoelastic Buckling of Ferromagnetic Beam Plate
K. Miya, T. Takagi, and Y. Ando

(Contents continued on Page 464)

Downloaded 04 May 2010 to 171.66.16.34. Redistribution subject to ASME license or copyright; see http://www.asme.org/terms/Terms_Use.cfm

CONTENTS (CONTINUED)

383 **Shear-Lag Effect in Sandwich Panels With Stiffeners Under Three-Point Bending**
K. Kemmochi, T. Akasaka, R. Hayaski, and K. Ishiwata

389 **The Effect of Initial Twist on the Torsional Rigidity of Beams—Another Point of View**
A. Rosen

393 **Torsion of Pretwisted Beams Due to Axial Loading**
D. H. Hodges

398 **In-Plane Vibration and Buckling of a Rotating Beam Clamped Off the Axis of Rotation**
D. A. Peters and D. H. Hodges

403 **Hoff's Problem in a Probabilistic Setting**
Isaac Elishakoff

409 **Nonlinear Resonances in a Column Subjected to a Constant End Force**
M. R. M. Crespo da Silva

415 **Controllability and Observability of Linear Matrix-Second-Order Systems**
P. C. Hughes and R. E. Skelton

421 **Theory of Index for Dynamical Systems of Order Higher Than Two**
C. S. Hsu

BRIEF NOTES

Vibrated Pendulum With a Mass Free to Move Radially — 428
B. A. Schmidt

On the Effect of a Small Circular Hole on States of Uniform Membrane Shear in Spherical Shells — 430
E. Reissner

Closed-Form Inversion of the Axisymmetric Integrated Photoelasticity Equations — 431
J. F. Doyle

Performance of the Axisymmetric Linear Shell Element for Vibration of Thin Circular Plates — 433
T. A. I. Akeju

Concerning the Solution of Elastic-Plastic Problems by the Finite-Element Method — 435
E. Zahavi

Thermal-Stress Singularities at the Ends of a Thin Elastic Stiffener Bonded to a Semi-Infinite Medium — 436
O. Tamate, H. Sekine, and T. Hanazawa

438 On Optimal Imperfect Columns Subjected to Linear Creep Buckling
R. Wojdanowska and M. Życzkowski

439 Constitutive Equations for Rate-Independent, Isotropic, Elastic-Plastic Solids Exhibiting Pressure-Sensitive Yielding and Plastic Dilatancy
L. Anand

441 On Stress-Intensity Factors for Circumferentially Cracked Circular Cylinders
Tsu-Tao Loo

444 The Response of Cracked Cylindrical Shells
H. J. Petroski and J. L. Glazik, Jr.

446 Analysis of a Cemented Tubular Joint
R. P. Nordgren

DISCUSSIONS

449–458 Discussions on previously published papers by **D. Krajcinovic; G. J. Weng; P. J. Torvik; T. Sarpkaya; F. H. Cornet; G. S. Bjorkman, Jr.,** and **R. Richards, Jr.; Maria Comninou** and **J. Dundurs**

BOOK REVIEWS

459 Theory of Thermoelasticity With Applications by **J. L. Nowinski** . . . Reviewed by **B. Boley**

Kinematics and Dynamics of Planar Machinery by **Burton Paul** . . . Reviewed by **R. L. Huston**

Introduction to the Mechanics of Plastic Forming of Metals by **W. Szczepinski** . . . Reviewed by **S. Kobayashi**

460 A Mathematical Introduction to Fluid Mechanics by **A. J. Chorin** and **J. E. Marsden** . . . Reviewed by **A. Leonard**

Mechanics of Composite Materials by **R. M. Christensen** . . . Reviewed by **J. J. McCoy**

461 Energy Methods in Finite Element Analysis edited by **R. Glowinski, E. Y. Rodin,** and **O. C. Zienkiewcz** . . . Reviewed by **T. H. H. Pian**

Formulas for Natural Frequency and Mode Shape by **Robert D. Blevins** . . . Reviewed by **R. Plunkett**

462 Local Loads in Plates and Shells by **Stanislaw Lukasiewicz** . . . Reviewed by **J. Lyell Sanders, Jr.**

(Contents continued on Inside Back Cover)

Downloaded 04 May 2010 to 171.66.16.34. Redistribution subject to ASME license or copyright; see http://www.asme.org/terms/Terms_Use.cfm

CONTENTS (CONTINUED)

ERRATUM

462 Erratum on "On the Stability of Steady Motions in Free and Restrained Dynamical Systems," by **P. Hagedorn,** published in the June, 1979, issue.

233	Announcement—Standard International Units
240, 272, 282, 290	Applied Mechanics Symposium Proceedings
303, 358, 397, 448, 458	Applied Mechanics Symposium Proceedings
300, 341, 346	Worldwide Mechanics Meetings Lists
427	Announcement—New Journal—Acta Mechanica Solida Sinica
OBC	Information for Authors

Downloaded 04 May 2010 to 171.66.16.34. Redistribution subject to ASME license or copyright; see http://www.asme.org/terms/Terms_Use.cfm

Provided by the Brown University Archives

WILLIAM PRAGER

1903–1980

William Prager was a man of the world. In his 76 years he lived and worked in Germany, Turkey, the United States, and Switzerland and held visiting positions in Sweden and the Netherlands. He wrote and spoke fluently in German, French, Turkish, and English, and his books were also translated into five other languages. Universities in seven countries have bestowed honorary doctorates and three countries have elected him to their National Academies.

William Prager was one of the giants of applied mechanics, and he represents a bridge in time between the giants of the past and those who are taking their place in the present and future. He was personally and professionally acquainted with such men as Prandtl (his thesis advisor), Hilbert, von Kármán, Lamb, Levi-Civitá, von Mises, and von Neumann. Indeed, many of these and others made the 1920's at Göttingen where Prager got his start a time and place that many consider the world's greatest in terms of mechanics and applied mathematics.

Two decades later Prager himself was instrumental in creating at Brown University what was certainly one of the greatest United States collection of applied mechanicians. Established international greats such as Bergman, Brillouin, von Mises, Synge, and Sokolnikoff were joined by young men and women who have since followed Prager's footsteps in chairing departments, editing journals, publishing papers, teaching students, and receiving awards.

But a great deal happened to William Prager between these two golden ages. He married Gertrude Ann Heyer in 1925 and their son Stephen was born in 1928. In 1933, at age 30, he returned to the city of his birth as Professor of Technical Mechanics at the Institute of Technology in Karlsruhe, the youngest full professor in Germany. However, that same year he was forced by Hitler to flee Germany. At this point in his career he had published a book and over 30 papers in plasticity and structural dynamics.

For the next eight years he was Professor of Theoretical Mechanics at the University of Istanbul and editor of the Revue de la Faculté des Science. During this period he published some 20 additional research papers in German, Turkish, and English, and textbooks on elementary mechanics and descriptive geometry written in Turkish—simultaneous evidence of his research, linguistic ability, and devotion to teaching. Also during this period he filed *and won* a law suit against the German government for violation of tenure. He accepted the year's back salary but declined the right to return to Germany.

In 1941 there was both a push and pull for the Pragers to move again. Hitler's troops were moving through the Balkans and threatening the mideast. Meanwhile, Brown University had established a new Program of Advanced Instruction and Research in Mechanics and wanted Prager to serve as its first director. The world situation, political considerations, and severe travel restrictions all made for complicated negotiations. Indeed, for weeks the Pragers were packed and ready to leave on 24 hours notice. Finally, the first week in October with the German army only 100 miles away, they started a 40-day trip by way of Baghdad, Karachi, and Capetown and arrived in New York just 3 weeks before Pearl Harbor.

Except for the five years from 1963 to 1968 which he spent at the IBM Research Laboratory in Zürich and the University of California, San Diego, Bill Prager stayed at Brown until his retirement in 1973

Copyright © 1980 by ASME
Downloaded 01 May 2010 to 171.66.16.243. Redistribution subject to ASME license or copyright; see http://www.asme.org/terms/Terms_Use.cfm

holding various titles of Professor of Applied Mechanics, Chairman of Division of Applied Mathematics, Chairman of Physical Sciences Council, L. Herbert Ballou University Professor, Director of the Computer Center, and University Professor of Engineering and Applied Mathematics. At the time of his retirement he had published over 230 papers (and the list was still growing) and a dozen books. Best known for his work in plasticity, he has also published extensively in general continuum mechanics, theory of flight, optimization problems, traffic flow, and computer programming. He has been the technical editor of six journals, including the JOURNAL OF APPLIED MECHANICS 1969–1971. His numerous honors are highlighted by three major awards from ASME: the Worcester Reed Warner medal in 1957, the Timoshenko Medal in 1966, and Honorary Membership in 1970; ASCE gave him the von Kármán medal in 1960 and made him an Honorary Member just a few months ago in October 1979; he is one of a very select group who have been elected to the National Academies of both Science and Engineering; abroad, he has given the James Clayton Lecture and received the Panetti prize, been awarded Honorary Membership in the Groupe Francais de Rhéologie and the Group pour l'Avancement des Méthodes Numériques de L'Ingénieur, and been elected to foreign membership in the Polish and French academies of science and the International Academy of Astronautics; he has received honorary doctorates from Liège, Poitiers, Case, Milan, Waterloo, Stuttgart, Hannover, Brown, Manchester, and Brussels.

The publications, the journals, and the honors are all part of the record. But above all of these, Bill Prager was a teacher. As a seminar speaker he was noted for his ability to illustrate complex theorems and techniques by analyzing structures as simple as a three-bar truss. His brilliant graduate lectures could lull the unwary listener into thinking "this stuff is easy," but woe betide the student who failed to study and search out the detail that lay behind the elegant presentation. And despite all of his administrative, research, and editorial responsibilities, his first love at the University was teaching undergraduates—preferably freshmen. In 1955, at a time of life when many are beginning to slow down, Prager bullied Brown into starting a computer center, served as its first director, organized and taught a freshmen course in computing, and wrote two elementary books on the subject.

This is the public Professor Prager whom everyone in Mechanics knows: researcher, editor, administrator, teacher. It was my good fortune to also call him friend. Bill was a quiet man. He was reserved, but he was not insensitive to the feelings of others. He knew his own worth, but he was never arrogant. His integrity was unquestioned, but he was more than generous in giving credit to others.

I have many private memories of Bill Prager—and they should remain private. But I must acknowledge that generosity. While a graduate student and research assistant at Brown in 1950, I was given the task of preparing a survey report on the then current status of plasticity. The result—a 400-page mimeographed report to the Office of Naval Research—was issued by Prager as "All-S2" with only my name on the cover. In fact, it was the typical student-professor collaboration: Prager's basic idea and rough outline, my first draft of writing, Prager's extensive criticisms and corrections, my second draft, his further changes, etc. Then Prager decided the time was ripe for a book on plasticity, negotiated with a publisher, completely rewrote "All-S2" with only minor additional input from me, and submitted a manuscript listing the two of us as equal co-authors. Indeed, his original submission listed my name first and it was only the publisher's insistence that reversed the order.

William Prager died last March. And yet, in a sense he lives forever. For all of his students, from Kurt Hohenemser at Göttingen in 1933 to Joop Nagtegaal in 1973 at Brown, his memory will never fade. None of us can hope to match his achievements, but we are all better for having known him. And if we can pass on to our students and our students' students something of the quality exemplified by Bill Prager, our lives, too, will not have been in vain.

Philip G. Hodge, Jr.
Minneapolis, 1980.

Downloaded 01 May 2010 to 171.66.16.243. Redistribution subject to ASME license or copyright; see http://www.asme.org/terms/Terms_Use.cfm

M. Kiya
Associate Professor.

M. Arie
Professor.

Department of Mechanical Engineering,
Hokkaido University,
Sapporo 060, Japan

Formation of Vortex Street in Laminar Boundary Layer

Main features of the formation of vortex street from free shear layers emanating from two-dimensional bluff bodies placed in uniform shear flow which is a model of a laminar boundary layer along a solid wall. This problem is concerned with the mechanism governing transition induced by small bluff bodies suspended in a laminar boundary layer. Calculations show that the background vorticity of shear flow promotes the rolling up of the vortex sheet of the same sign whereas it decelerates that of the vortex sheet of the opposite sign. The steady configuration of the conventional Karman vortex street is not possible in shear flow. Theoretical vortex patterns are experimentally examined by a flow-visualization technique.

1 Introduction

The present paper describes a theoretical investigation on the interaction of two parallel vortex sheets embedded in shear flow. In practice, such shear layers can be found in the wake of a long-span structure which is immersed in the turbulent planetary boundary layer. Another example of much smaller length scale is a two-dimensional bluff body suspended in a laminar boundary layer along a solid wall. The latter case is practically important because it is concerned with the mechanism governing laminar-turbulent transition induced by small bluff bodies suspended in a laminar boundary layer. Hall [1] demonstrated experimentally that the mechanism by which transition occurred was a local effect dependent upon the stability characteristics of the element wake rather than the stability characteristics of the boundary layer. That is, the transition of the boundary layer appeared to involve the direct seeding of turbulence into the boundary layer from the wake of the element, rather than amplification of wavelike disturbances as considered in the boundary-layer stability theory. The purpose of the present paper is thus to clarify some important features of the rolling up of two, parallel vortex layers in the presence of the background vorticity of the boundary layer.

A theoretical analysis of the rolling up of a single vortex sheet in shear flow was originally performed by Hama and Burke [2] in connection with the flow patterns associated with the laminar boundary-layer transition. They assumed a shear flow of constant vorticity, viz., a uniform shear flow which had a linearly varying velocity profile. It is a matter of great interest whether such a vortex sheet is unstable to small disturbances in the manner of the conventional Helmholtz instability. However, leaving the stability question open, they assumed that the vortex sheet would assume a sinusoidal distortion and calculated numerically the development of the vortex sheet by means of the discrete-vortex approximation of Rosenhead [3]. If the vortex sheet had a positive vorticity, the positive background vorticity was found to promote the rolling up of the vortex sheet, whereas the negative background vorticity decelerated it. They concluded that the vortex sheet did not roll up with a sufficiently large negative background vorticity. If an inviscid fluid is assumed, no diffusion of vorticity occurs so that the stability of the vortex sheet in uniform shear flow can be analyzed by the well-established method of small disturbances. Such an analysis was carried out by Kiya and Arie [4].

The wake of a two-dimensional body is formed by the interaction of two free shear layers which can combine to form a regular array of concentrated vorticity, namely, a Karman vortex street. Abernathy and Kronauer [5] showed that the formation of the vortex street in the wake could be explained by considering the nonlinear interaction of two, infinite, initially parallel vortex sheets in an inviscid incompressible fluid. In their analysis, the vortex sheets were represented by two rows of point vortices. Flow patterns based on the calculated motion of the point vortices indicated that the vortices tended to form clouds which reproduced some of the experimentally observed features of the Karman vortex street in the range of relatively low Reynolds number.

Kamemoto [6] analyzed, by this model, the rolling up of two pairs of initially parallel vortex sheets surrounded by uniform free stream in his investigation of the wakes of two bluff bodies displaced in a plane normal to the stream. Boldman, et al., [7], represented an extension of the Abernathy-Kronauer model to include the effect of unequal external velocities on vortex formation on the assumption that the strength of the two vortex sheets was different each other. The Abernathy-Kronauer model will also be utilized in the present investigation.

2 Flow Model

As were cogently discussed by Abernathy and Kronauer [5], viscosity is not essential to the formation of the vortex street provided

Contributed by the Applied Mechanics Division for publication in the JOURNAL OF APPLIED MECHANICS.

Discussion on this paper should be addressed to the Editorial Department, ASME, United Engineering Center, 345 East 47th Street, New York, N.Y. 10017, and will be accepted until September 1, 1980. Readers who need more time to prepare a discussion should request an extension from the Editorial Department. Manuscript received by ASME Applied Mechanics Division, February, 1979; final revision, September, 1979.

Copyright © 1980 by ASME
Downloaded 01 May 2010 to 171.66.16.243. Redistribution subject to ASME license or copyright; see http://www.asme.org/terms/Terms_Use.cfm

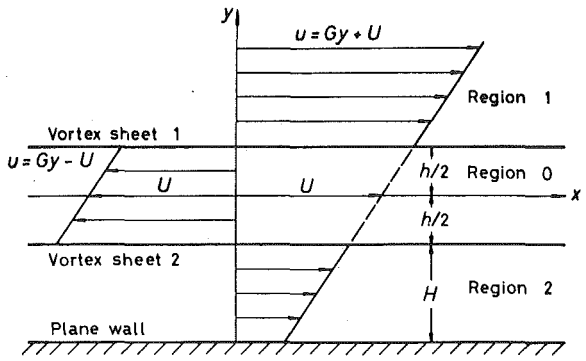

Fig. 1 Definition sketch of unperturbed vortex sheets

that the free vortex layers exist initially. It is also reasonable to disregard the finite thickness of the vortex layers which is usually an order of magnitude smaller than the wavelengths of the growing disturbances in the wake. Finally, the role of a bluff body in the formation of the vortex street can be neglected if the transition from the vortex sheets to the vortex street does not take place too abruptly. These features of the vortex-street formation may be assumed to be true even for the vortex layers immersed in shear flow in the neighborhood of a solid wall unless the distance between the vortex layers and the wall is too small.

Since the longitudinal velocity varies almost linearly over lower half of a laminar boundary layer along a solid wall, the flow in the boundary layer can be approximated by a uniform shear flow of constant vorticity. The authors are of the opinion that important features of the formation of vortex streets in boundary layers will not be destroyed by the assumption of uniform shear flow.

A general arrangement of two parallel vortex sheets in uniform shear flow is sketched in Fig. 1. A plane solid wall exists in the neighborhood of the vortex sheets. The x-axis coincides with the center line of the unperturbed vortex sheets and the y-axis is taken normal to the x-axis. The corresponding velocity components are written as u and v. The distance between the vortex sheets is denoted by h, the background vorticity by $-G$, and the velocity of the shear flow on the x-axis is expressed by U. The distance between the lower vortex sheet and the wall is written as H. The vortex sheets originally located at $y = h/2$ and $-h/2$, which will be called as vortex sheets 1 and 2, divide the region of flow into three regions, i.e., regions 0, 1, and 2, which are also shown in Fig. 1. If the velocity along the x-axis is tentatively designated by U^*, each vortex sheet has the same vorticity which is equal to $U - U^*$ per unit length. The temporal development of the flow patterns associated with the interaction of the vortex sheets will naturally have a different appearance corresponding to various combinations of the values of these parameters. However, an observer with the mean velocity $U_m[=(U + U^*)/2]$ will see a unique flow pattern which depends on the shear parameter $Gh/(U - U_m)$ and the ratio H/h, if the scales of length, velocity, and time are taken as h, $U - U_m$ and $h/(U - U_m)$. This follows from the reasoning which will be explained. On writing the vorticity per unit length of the vortex sheets as $2\Delta U$, one obtains $U = U_m + \Delta U$ and $U^* = U_m - \Delta U$. With reference to the coordinate system moving with the mean velocity U_m, ΔU is the only representative velocity relevant to the flow. Thus, in view of the assumption of an inviscid fluid, the development of the flow pattern nondimensionalized by the representative velocity ΔU-$(= U - U_m)$ and the representative length scale h will become unique for particular values of the shear parameter $Gh/\Delta U$ and the ratio H/h. Accordingly, one can put $U_m = 0$ to obtain $U^* = -U$ without any loss of generality.

From the foregoing discussion, it may be clear that the interaction of the vortex sheets in uniform shear flow can be described in terms of the shear parameter defined by

$$K = Gh/U \tag{1}$$

and the ratio

$$\delta = H/h \tag{2}$$

Although the parameters K and δ can be assigned independently, one considers, in what follows, the case of a uniform shear flow whose longitudinal velocity component vanishes on the solid wall. Then one has

$$\delta = \frac{1}{K} - \frac{1}{2} \tag{3}$$

This choice produces the longitudinal velocity profile similar to that in a laminar boundary layer along a solid wall. However, it should be noted that the longitudinal velocity associated with the distortion of the vortex sheets is not zero along the wall because of the inviscid nature of flow assumed in the theoretical part of this investigation.

An analysis of stability of the vortex sheets to small disturbances was performed on the basis of a linearlized form of Euler's equation of motion. Solutions of velocity components and pressure associated with the perturbed vortex sheets were obtained in regions 0, 1, and 2, and several constants included in them were determined from pertinent boundary conditions. The result is a fourth-order algebraic equation for the complex phase velocity whose imaginary part gives the growth rate of the disturbances. It was found, from numerical solutions of the equation, that the growth rate of antisymmetric disturbances is larger than that of symmetrical disturbances. The difference between the former and the latter becomes larger and larger as the shear parameter K is increased. In the case of uniform flow, the growth rates are the same for symmetric and antisymmetric disturbances. However, it is experimentally well established that a disturbance of the antisymmetric mode is actually amplified in uniform flow. Thus it may be reasonable to assume that an antisymmetric disturbance will also become dominant in shear flow and leads eventually to the rolling up of the vortex sheets.

Since the linearized analysis of the vortex sheets cannot predict the wave number of a disturbance to be selectively amplified, one must presume a plausible wave number in order to calculate the rolling up of the vortex sheets. In the present calculation, the wave number α will be selected as $1.762h^{-1}$, which corresponds to the Karman spacing ratio, although the authors are aware of the possibility that an appropriate value of the wave number may depend on the parameters K and δ. According to the authors' opinion, main features of the rolling up of the vortex sheets in shear flow will not be lost by the use of the single wave number.

In order to make the numerical calculation of the rolling up of the vortex sheets, one must also assign the value of K. Since the distortion of the vortex sheet 2 may be influenced by the effect of viscosity in the immediate neighborhood of the wall, the value of K will be taken in the range $0 \leqq K < 1$ by assuming rather arbitrarily that $\delta = 0.5$ is the critical location of vortex sheet 2, where the effect of viscosity becomes significant enough to invalidate the inviscid analysis.

3 Rolling Up of Vortex Sheets

The stages of the nonlinear growth of periodic disturbances in vortex wakes can be calculated by representing the vortex sheets by two rows of point vortices. The vortices in each row are of equal strength but the sense is opposite in two rows. The motion of the vortex sheets is then approximated by the evolution of the arrays of the point vortices.

In keeping with the discussion in Section 2, one now examines the growth of an antisymmetric sinusoidal disturbance of wavelength $a(=2\pi/\text{wave number})$ in two rows of vortices. Let the number of the vortex points per wavelength in each row be denoted by n. The strength of the vortices is $2Ua/n$ in vortex sheet 1 and $-2Ua/n$ in vortex sheet 2. The velocity components u and v induced at a point (x, y) by all the vortices are given by

Downloaded 01 May 2010 to 171.66.16.243. Redistribution subject to ASME license or copyright; see http://www.asme.org/terms/Terms_Use.cfm

$$u(x, y) = \frac{U}{n} \sum_{j=1}^{2} \sum_{k=1}^{n} (-1)^{j+1} \times \left(\frac{\sinh [\alpha(y - y_k^{(j)})]}{\cosh [\alpha(y - y_k^{(j)})] - \cos [\alpha(x - x_k^{(j)})]} - \frac{\sinh [\alpha(y + y_k^{(j)} + h + 2H)]}{\cosh [\alpha(y + y_k^{(j)} + h + 2H)] - \cos[\alpha(x - x_k^{(j)})]} \right) \quad (4a)$$

$$v(x, y) = -\frac{U}{n} \sum_{j=1}^{2} \sum_{k=1}^{n} (-1)^{j+1} \times \left(\frac{\sin [\alpha(x - x_k^{(j)})]}{\cosh [\alpha(y - y_k^{(j)})] - \cos [\alpha(x - x_k^{(j)})]} - \frac{\sin [\alpha(x - x_k^{(j)})]}{\cosh [\alpha(y + y_k^{(j)} + h + 2H)] - \cos [\alpha(x - x_k^{(j)})]} \right) \quad (4b)$$

where the coordinates $x_k^{(j)}$ and $y_k^{(j)}$ are referred to the kth point vortex in vortex sheet j(= 1 and 2). The differential equations which govern the motion of the centers of the individual vortices are

$$dx_i^{(l)}/dt = Gy_i^{(l)} + U + u(x_i^{(l)}, y_i^{(l)}) \quad (5a)$$

$$dy_i^{(l)}/dt = v(x_i^{(l)}, y_i^{(l)}) \quad (5b)$$

where t is the time, with $2n$ unknowns $x_i^{(l)}(t)$ and $y_i^{(l)}(t)$. An initial distribution of point vortices which is imposed at zero time is

$$x_i^{(l)}(0) = \frac{(i-1)a}{n} + \xi_l \left(\frac{2\pi(i-1)}{n} \right) \quad (6a)$$

$$y_i^{(l)}(0) = (-1)^{l+1} \frac{h}{2} + \eta_l \left(\frac{2\pi(i-1)}{n} \right) \quad (6b)$$

where $\xi_l(x)$ and $\eta_l(x)$ can be obtained from the linear analysis briefly described in Section 2. Both $\xi_l(x)$ and $\eta_l(x)$ contain an unknown constant, say A_0, as a multiplicative factor.

All of the calculations were performed for a wave number αh = 1.762, as noted in Section 2. The value of A_0 was so chosen that the initial amplitude of vortex sheet 1 in the x-direction was $0.0125a$ for each shear parameter K. The system of the differential equations (5) was solved by using the Runge-Kutta-Gill method with a constant time step $\delta t = 0.01a/U$. This time step was judged to be adequate because a half of this time step produced almost similar flow patterns. Time steps employed by the previous investigators who used the Abernathy-Kronauer model ranged from $0.004a/U$ (Abernathy and Kronauer [5]) to $0.028a/U$ (Boldman, et al., [7]).

The number of point vortices per wavelength in each row was selected to be $n = 24$ for all values of K. This value of n was judged to be appropriate to yield the correct overall feature of the rolling up of the vortex sheets in view of the results of the previous investigators (Kamemoto [6], Abernathy and Kronauer [5]). It may be remarked that the behavior of the vortex sheets is not necessarily better represented by simply increasing the number of vortices, owing to the instabilities in the movement of vortices associated with the singularity of each point vortex. In order to obtain a smooth rolling up of the vortex sheets, one must introduce some smoothening scheme of the motion of vortices, for example, such as suggested by Fink and Soh [8]. As just mentioned, the main purpose of the present investigation is to clarify the overall aspect of the formation of significant vortex clouds in shear flow. It may be reasonable to assume that the appearance of the vortex clouds will be influenced insignificantly by locally irregular motion of vortices. This is the reason why any smoothening procedure has not been employed in the present calculation.

The results of the calculations are shown in Figs. 2–5 as plots of the positions of the vortices at various nondimensional times Ut/a for the shear parameter K from 0 to 0.6. It should be noted that the actual rolling-up phenomena are represented by the various stages of development of the point-vortex patterns at increasing values of time, which can be seen progressively downward in each figure. The distribution of vortices for $K = 0$ (Fig. 2) are as a whole very similar to

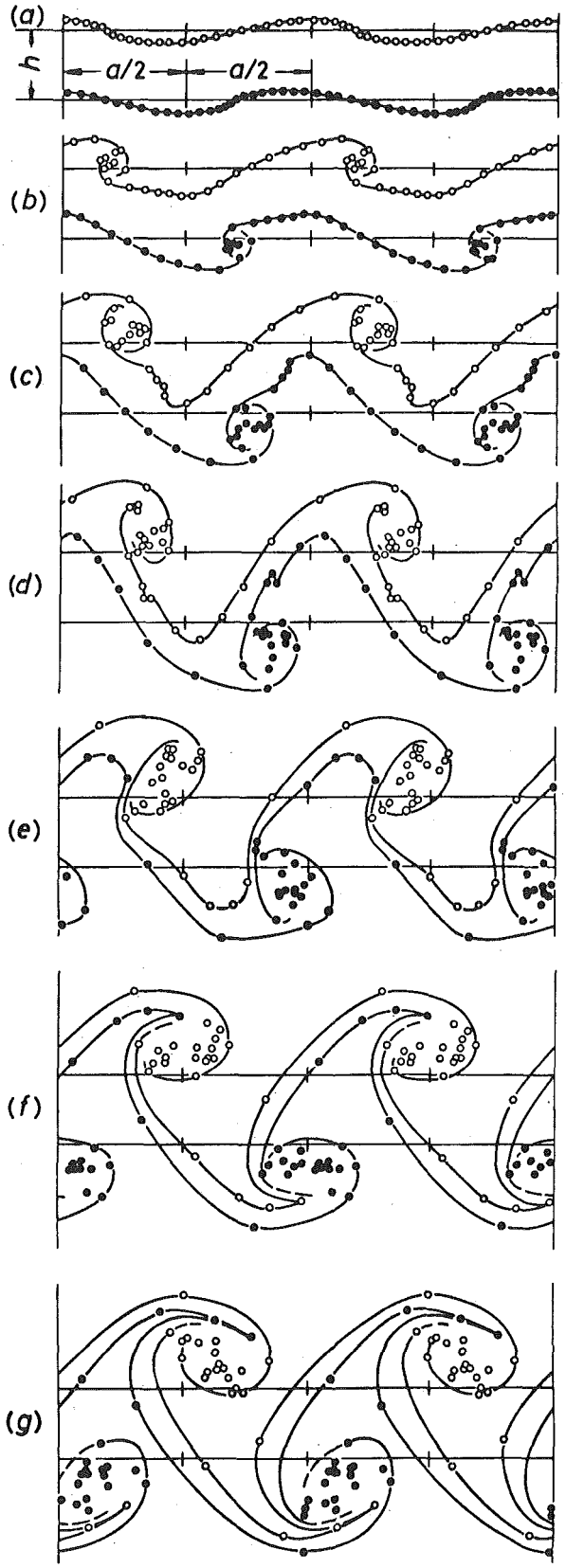

Fig. 2 Vortex patterns at shear parameter $K = 0$ and $\delta = \infty$. Initial amplitude of distortion of vortex sheet 1 in the x-direction is equal to $0.0125a$. $U\delta t/a = 0.01$, $n = 24$.

	(a)	(b)	(c)	(d)	(e)	(f)	(g)
Ut/a	0.2	0.4	0.6	0.8	1.0	1.2	1.4

Downloaded 01 May 2010 to 171.66.16.243. Redistribution subject to ASME license or copyright; see http://www.asme.org/terms/Terms_Use.cfm

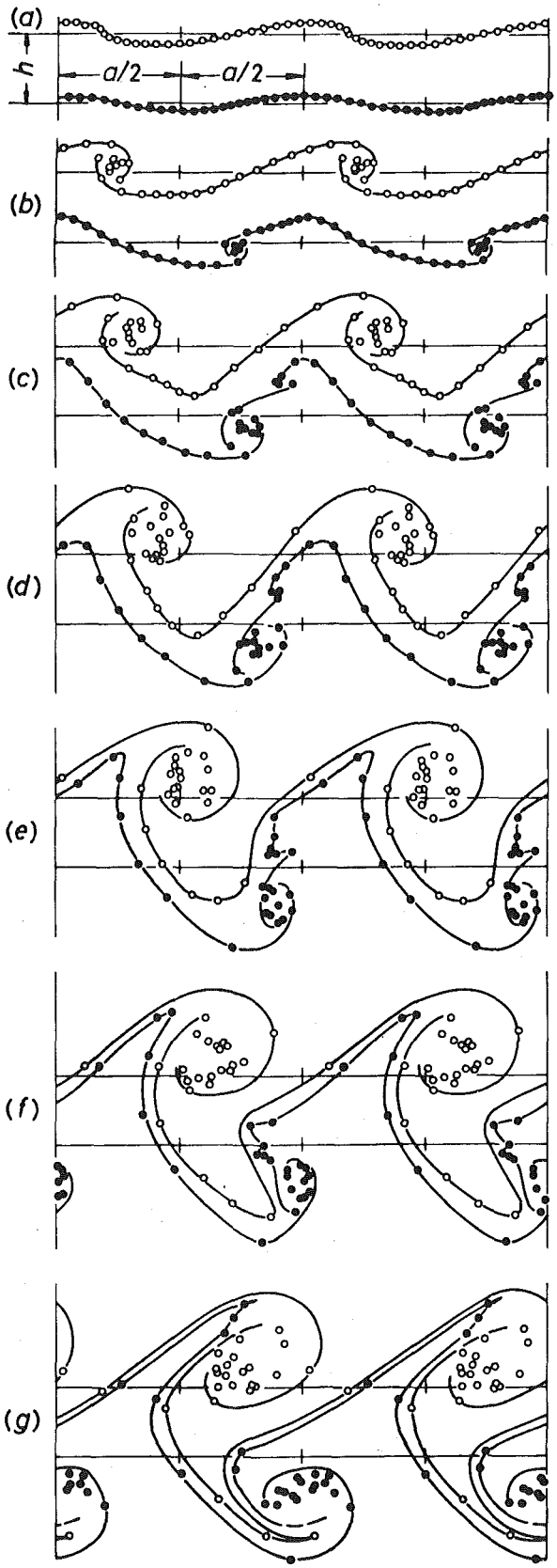

Fig. 3 Vortex patterns at shear parameter $K = 0.2$ and $\delta = 4.5$; values of other parameters are the same as in Fig. 2; (a)–(g) are also the same as in Fig. 2

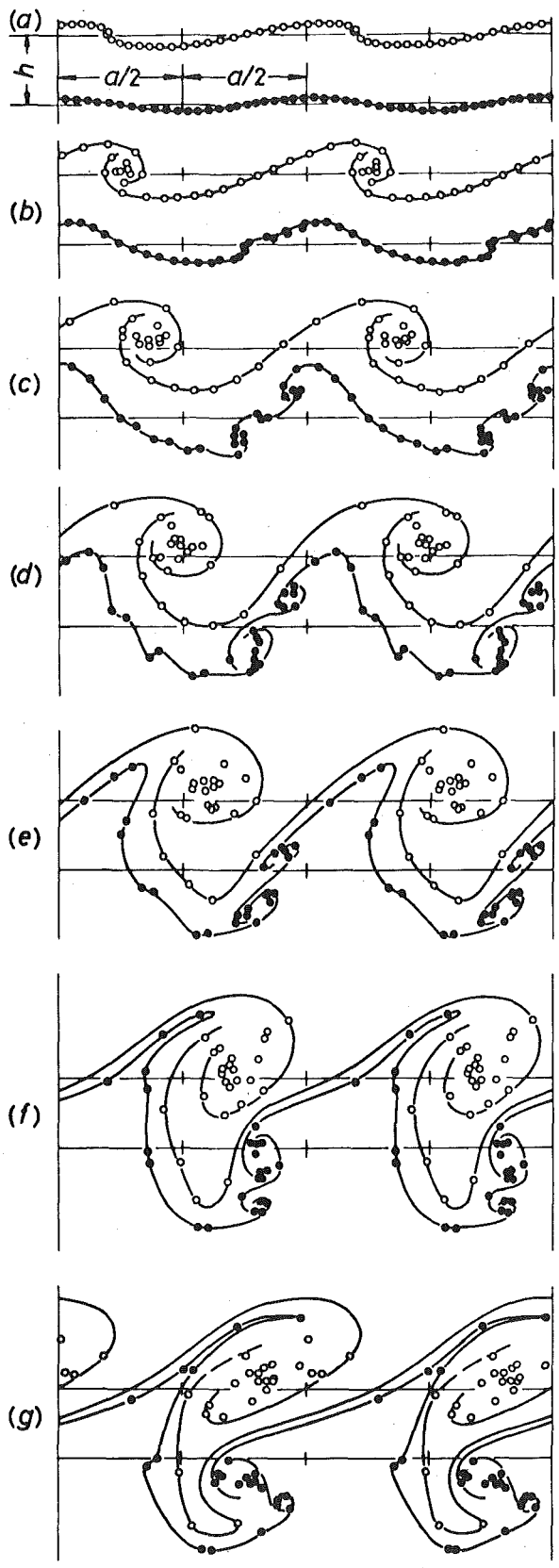

Fig. 4 Vortex patterns at shear parameter $K = 0.4$ and $\delta = 2.0$; values of other parameters are the same as in Fig. 2; (a)–(g) are also the same as in Fig. 2

Downloaded 01 May 2010 to 171.66.16.243. Redistribution subject to ASME license or copyright; see http://www.asme.org/terms/Terms_Use.cfm

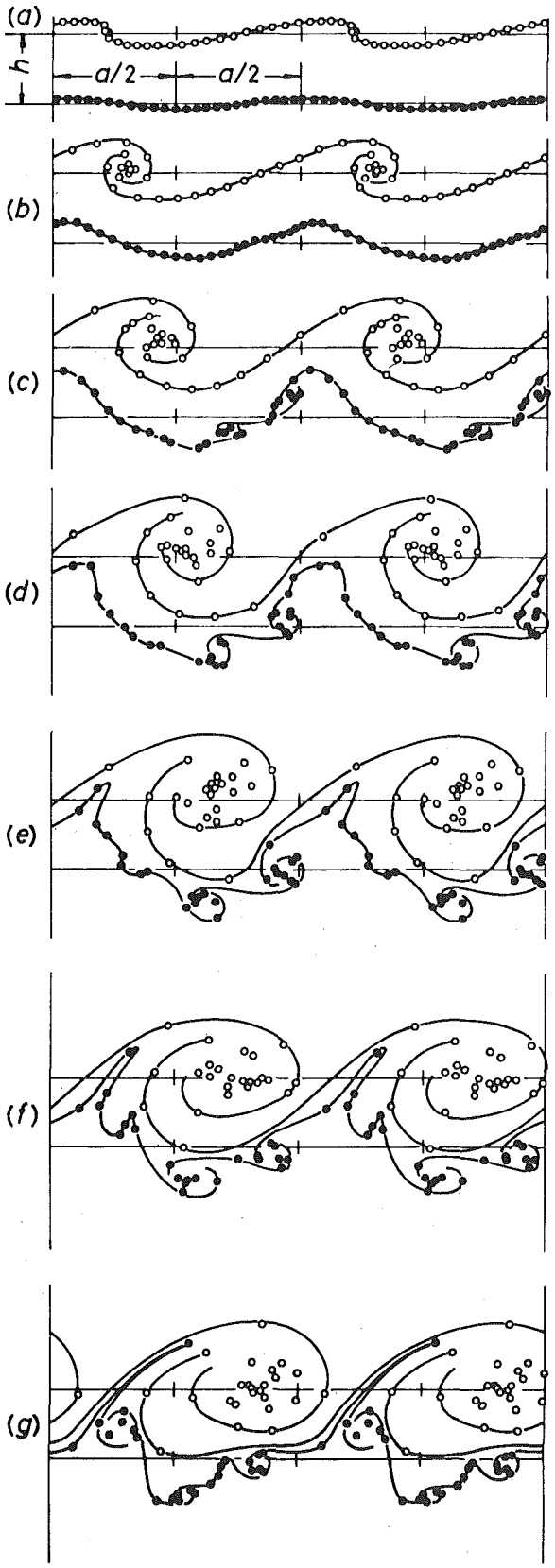

Fig. 5 Vortex patterns at shear parameter $K = 0.6$ and $\delta = 1.17$; values of other parameters are the same as in Fig. 2; (*a*)–(*g*) are also the same as in Fig. 2

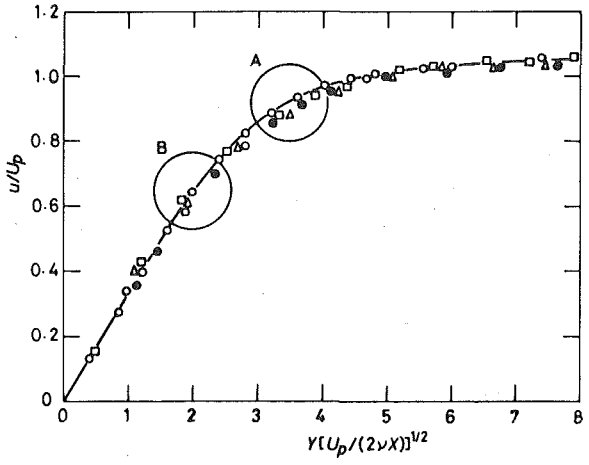

Fig. 6 Velocity profile in laminar boundary layer along flat plate. u = velocity component along plate, U_p = free-stream velocity extrapolated to the surface of plate, Y = distance measured normally from plate, X = distance along plate measured from effective origin, ν = kinematic viscosity of fluid. Solid line means theoretical velocity profile [9]. Data symbols are for different experimental runs. Two large circles show location and radius of circular cylinder. Finally, *A* corresponds to Fig. 7 and *B* to Figs. 8 and 9.

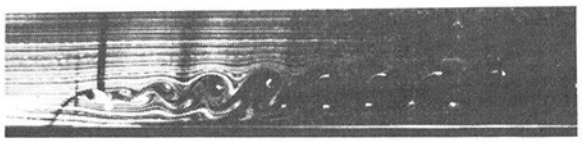

Fig. 7 Experimental vortex pattern behind circular cylinder in laminar boundary layer along flat plate; visualization by hydrogen bubbles and electrolytic dye production. $K = 0.14$, Re = 74, normal distance from plate = $3.46(2\nu X/U_p)^{1/2}$. It is clearly observed that lower vortices fall behind and are eventually overtaken by upper vortices.

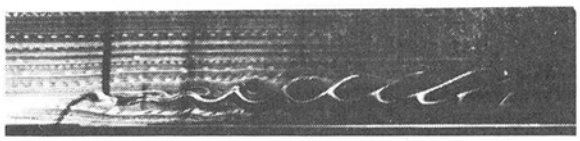

Fig. 8 Experimental flow pattern behind circular cylinder in laminar boundary layer along flat plate; visualization by hydrogen bubbles and electrolytic dye production. $K = 0.49$, Re = 52, normal distance from plate = $2.0(2\nu X/U_p)^{1/2}$. Note significant rolling up of upper shear layer in contrast to almost negligible rolling up of lower vortex sheet.

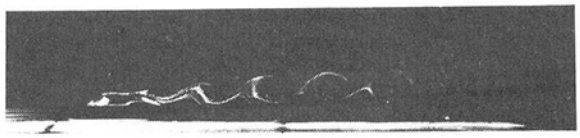

Fig. 9 Interaction of free shear layers shed from circular cylinder in laminar boundary layer along flat plate; visualization by electrolytic dye production. Values of the experimental parameters are almost the same as in Fig. 8.

those calculated by the previous investigators by the Abernathy-Kronauer model.

An examination of the theoretically computed vortex distributions as a function of time and the shear parameter shows several important trends which can be compared with experimental observations. First, when the shear parameter is increased, the rate of cloud formation in the lower row (vortex sheet 2) is reduced and the clouds which form in the upper row (vortex sheet 1) become more and more pronounced and diffused. This feature of the vortex-cloud formation is a main

Downloaded 01 May 2010 to 171.66.16.243. Redistribution subject to ASME license or copyright; see http://www.asme.org/terms/Terms_Use.cfm

result of the interaction between the background vorticity and the vorticity of the vortex sheets. Second, the calculated results exhibit an increasing tendency of the lower clouds to fall behind and eventually be overtaken by the upper clouds. Thus there is no equilibrium position of the lower clouds to the upper ones for the shear parameter other than zero, and the steady configuration of the conventional Karman vortex street is no longer possible. These features of the vortex clouds were also obtained by Boldman, et al., [7], in a theoretical investigation of the effect of unequal external velocities on the vortex formation. In their model, the strengths of two vortex sheets were adjusted to produce a required difference in the external velocities.

It should be emphasized that the strengths of the two vortex sheets are not same in the case considered by Boldman, et al., [7], while they are the same in the present case. Moreover, the background vorticity in the former is zero while that in the latter is a nonzero constant. The authors believe that the lower growth rate of a vortex sheet in Boldman, et al., [7], should be attributed to less strength of the vortex sheet concerned. In the present case, it is clear that lower growth rate of vortex sheet 2 is associated with the effect of the background vorticity of the opposite sign. This is the fundamental difference between Boldman, et al.'s case and the present one. However, the mechanism by which the lower clouds fall behind the upper clouds is common to both flows, i.e., the longitudinal velocity component of the surrounding fluid is higher for the upper vortex clouds than for the lower vortex clouds.

In order to examine the theoretical predictions just described, a flow-visualization experiment was conducted. The vortex sheets in shear flow were produced downstream of a circular cylinder 0.32 cm dia placed in the vicinity of a thin flat plate along which a laminar boundary layer developed. The flat plate and the circular cylinder were installed in a recirculating water channel with a rectangular test section 140 cm long, 60 cm wide and 8 cm high. The thickness of the laminar boundary layer at the location of the cylinder was about 1.34 cm at the free-stream velocity of 2.5 cm/s. The velocity distribution in the boundary layer measured by means of the hydrogen bubble technique was in good agreement with the theoretical velocity profile in a laminar boundary layer along a flat plate (Kiya, et al., [9]) as shown in Fig. 6, in which the location and diameter of the cylinder are also indicated. It may be remarked that the flow outside the boundary layer was a uniform shear flow in this experiment because the experimental apparatus had originally been constructed for the purpose of another investigation. Since there exists a rather wide range of fairly linear velocity distribution in this boundary layer, the flow inside the boundary layer can approximately be regarded as a uniform shear flow. The Reynolds number Re based on the diameter of the cylinder and the approaching velocity to the center of the cylinder ranged from 52 to 74. An approximate value of the shear parameter K was obtained by employing the diameter of the cylinder as the initial distance h between the shear layers. The parameter G was taken as the normal velocity gradient of the boundary layer at the center of the cylinder. The shear parameter realized in this experiment ranged from 0.05 to 0.49.

Typical results of the experiment are shown in Figs. 7–9 which clearly demonstrate the main features of the vortex clouds described in the foregoing. Flow pattern similar to Fig. 9 was also observed by Hall [1] (Fig. 13 of his paper). Although it may be argued that the agreement between theory and experiment is only qualitative, the important thing is that the seemingly complicated vortex patterns behind a two-dimensional bluff body placed in a laminar boundary layer can be understood in terms of the interaction of the vortex sheets with the background vorticity.

The convection velocities of the vortex clouds can be obtained by judging which point vortices belong to a cloud and then assigning an appropriate center of the cloud at each specified time. As noted previously, the temporal changes of vortex patterns are unique for particular values of $Gh/(U - U_m)$, δ, and h/a, provided that h, $U - U_m$, and $h/(U - U_m)$ are taken as the representative length, velocity, and time scales, respectively. Thus convection velocity U_v of a vortex cloud nondimensionalized in the form

$$(U_v - U_m)/(U - U_m) \equiv \beta \tag{7}$$

will become a function of the parameters $Gh/(U - U_m)$, δ, and h/a. The vortex patterns of the present calculations in which $U_m = 0$ and $h/a = 0.2805$ yield $U_v/U = 0.48$ for $G = 0$, while Boldman, et al., [7], obtained $U_v/U = 0.70$ for the same values of the parameters except U_m, which was taken as $U/2$. Accordingly, from equation (7), one obtains $\beta = 0.48$ and 0.4, respectively. The difference between these two values may be explained as errors in estimating the center of a vortex cloud and its convection velocity. It has been observed that the center of a vortex cloud is not exactly a linear function of time and the deviation from linearity is not small enough to yield a unique convection velocity. In fact, the value of $U_v/U = 0.48$ should be regarded as a mean convection velocity over the range of time $0.4 \leqq Ut/a \leqq 1.4$. On substituting $\beta = 0.48$ into equation (7), one has

$$\begin{aligned} U_v/U &= 0.48 + 0.52(U_m/U) \\ &= 0.74 + 0.26(U^*/U) \end{aligned} \tag{8}$$

which gives a relation between U_v/U and U^*/U, U^* being the velocity at the center of wake. Previous experimental investigations (Bearman [10], among others) suggest that the value $U_v/U = 0.8$ can be taken as a typical mean value of the convection velocity of concentrated vortices in the wake of two-dimensional bluff bodies placed in uniform flow. Hence, substitution of $U_v/U = 0.8$ into equation (8) yields $U^*/U = 0.23$. Under the assumption that this value of U^*/U can also be applied to the case of shear flow, one can estimate the convection velocity of concentrated vortices in shear flow by making use of the theoretical vortex patterns shown in Figs. 2–5. The results are summarized in Table 1 in which the suffixes 1 and 2 attached to β and U_v imply the upper and lower vortex clouds, respectively. It was not attempted to compare these results with the experiment because of the difficulty in the experimental determination of the velocities of concentrated vortices.

It has been well known for a long time that the total amount of

Table 1 Approximate convection velocity of vortex clouds estimated from theoretical vortex patterns under the assumption described in the text; Suffixes 1 and 2 refer to the upper and lower vortex clouds

K	H/h	β_1	β_2	U_{v1}/U	U_{v2}/U	U_{v2}/U_{v1}
0	∞	0.48	0.48	0.80	0.80	1.00
0.1	9.50	0.56	0.51	0.83	0.81	0.98
0.2	4.50	0.56	0.38	0.83	0.76	0.92
0.3	2.83	0.58	0.25	0.84	0.71	0.85
0.4	2.00	0.58	——	0.84	——	——
0.6	1.17	0.59	——	0.84	——	——
0.8	0.75	0.62	——	0.85	——	——

Table 2 Vorticity cancellation in the transition from vortex sheets to vortex clouds estimated from theoretical vortex patterns at time $Ut/a = 1.4$; n_1 = number of point vortices originally in upper vortex sheet, n_2 = number of point vortices originally in lower vortex sheet

		upper vortex clouds			lower vortex clouds		
K	H/h	n_1	n_2	Γ/Γ_0	n_1	n_2	Γ/Γ_0
0	∞	19	3	0.67	3	19	0.67
0.1	9.50	19	3	0.67	3	19	0.67
0.2	4.50	19	3	0.67	2	16	0.58
0.3	2.83	21	4	0.71	2	16	0.58
0.4	2.00	21	4	0.71	1	15	0.58
0.6	1.17	22	1	0.88	—	—	——
0.8	0.75	22	0	0.92	—	—	——

Downloaded 01 May 2010 to 171.66.16.243. Redistribution subject to ASME license or copyright; see http://www.asme.org/terms/Terms_Use.cfm

circulation (Γ_0) shed from one side of a bluff body during one cycle of the vortex formation is more than the amount of circulation (Γ) found in one fully formed vortex. Various investigators found that the ratio Γ/Γ_0 was between 0.3 and 0.66. Abernathy and Kronauer [5] obtained the value of $\Gamma/\Gamma_0 = 0.61$ by their model. In the case of uniform shear flow, the ratio Γ/Γ_0 becomes a function of the shear parameter. The results of the present calculation are shown in Table 2. It is clear that the background vorticity reduces the rate of vorticity cancellation in the vortex sheet of the same sign, whereas it increases that in the vortex sheet of the opposite sign. Since there are some vortices which are not included in any of particular vortex clouds at the specified time ($Ut/a = 1.4$), the total number of vortices in each line of Table 2 is not equal to 48, i.e., the number of point vortices in the upper and lower rows per wavelength.

4 Conclusions

In the present paper, some essential features of the formation of concentrated vortex streets from free shear layers emanating from two- dimensional bluff bodies in shear flow have been obtained by means of the Abernathy-Kronauer model. A uniform shear flow of constant vorticity was assumed in order to make the problem theoretically tractable. The vortex patterns in the wake of a circular cylinder placed in a laminar boundary layer along a flat plate were experimentally observed by a flow-visualization technique to examine some of the theoretical predictions. The main results of the present study may be summarized as follows.

1 The background vorticity of shear flow promotes the rolling up of the vortex sheet of the same sign, whereas it decelerates that of the vortex sheet of the opposite sign, thus yielding a larger and larger difference in the position of the upper and lower vortex clouds as the shear parameter increases. This feature of the vortex clouds was experimentally confirmed.

2 The vortex clouds in the low-velocity side of shear flow fall behind and are eventually overtaken by the vortex clouds in the high-velocity side. Thus the steady configuration of the conventional Karman vortex street is no longer possible in shear flow. This behavior was also verified by an experiment.

3 The background vorticity reduces the rate of vorticity cancellation in the vortex sheet of the same sign, whereas it increases that in the vortex sheet of the opposite sign.

Acknowledgments

The present study was supported by the Grant-In-Aid for Scientific Research from the Ministry of Education, Science and Culture (Japan). The photographs of flow shown as Figs. 7–9 were taken by Mr. M. Furukawa, a graduate student at the authors' Laboratory of Fluid Mechanics.

References

1 Hall, G. R., "Interaction of the Wake for Bluff Bodies With an Initially Laminar Boundary Layer," *AIAA Journal*, Vol. 5, No. 8, 1967, pp. 1386–1392.

2 Hama, F. R., and Burke, E. R., "On the Rolling Up of a Vortex Sheet," University of Maryland, Technical Note No. BN-220, 1960.

3 Rosenhead, L., "The Formation of Vortices From a Source of Discontinuity," *Proceedings of the Royal Society*, London, Series A, Vol. 134, No. 823, 1931, pp. 170–192.

4 Kiya, M., and Arie, M., "Helmholtz Instability of a Vortex Sheet in Uniform Shear Flow," *The Physics of Fluids*, Vol. 22, No. 2, 1979, pp. 378–379.

5 Abernathy, F. H., and Kronauer, R. E., "The Formation of Vortex Streets," *Journal of Fluid Mechanics*, Vol. 13, Pt. 1, 1962, pp. 1–20.

6 Kamemoto, K., "Formation and Interaction of Two Parallel Vortex Streets," *Bulletin of the JSME*, Vol. 19, No. 129, 1976, pp. 283–290.

7 Boldman, D. R., Brinich, P. E., and Goldstein, M. E., "Vortex Shedding From a Blunt Trailing Edge With Equal and Unequal External Mean Velocities," *Journal of Fluid Mechanics*, Vol. 75, Pt. 4, 1976, pp. 721–735.

8 Fink, P. T., and Soh, W. K., "A New Approach to Roll-Up Calculations of Vortex Sheets," *Proceedings of the Royal Society*, London, Vol. 362, No. 1709, 1978, pp. 195–209.

9 Kiya, M., Nishiyama, J., and Arie, M., "Laminar Boundary Layer Separation in a Uniform Shear Flow," *Bulletin of the JSME*, Vol. 16, No. 99, 1973, pp. 1289–1300.

10 Bearman, P. W., "On the Vortex Street Wakes," *Journal of Fluid Mechanics*, Vol. 28, Pt. 4, 1967, pp. 625–641.

Downloaded 01 May 2010 to 171.66.16.243. Redistribution subject to ASME license or copyright; see http://www.asme.org/terms/Terms_Use.cfm

T. M. Mulcahy

Components Technology Division,
Argonne National Laboratory,
Argonne, Ill. 60439
Mem. ASME

Fluid Forces on Rods Vibrating in Finite Length Annular Regions

Approximate expressions for the fluid forces acting on a central, rigid rod translating periodically in a finite length annular region of confined fluid are derived from the Navier-Stokes equations for a range of geometric and fluid parameters where viscous damping is significant. Based on the derived forces, lumped added mass, and linear dashpot modeling of an annular gap support typically found in nuclear reactors is employed to predict the fundamental frequency and modal damping of a single beam. Test methods and results for the same beam are presented which indicate the force expressions are applicable for small fluid motions.

Introduction

Many components found in nuclear reactors can be idealized for the purpose of flow-induced vibration analysis as circular cylindrical beams with axial variations in structural properties and multiple supports [1]. Invariably, one or more of the supports consists of a finite length of the cylindrical beam immersed in a dense fluid closely confined by a concentrically located cylindrical region which is part of another beam component or a relatively rigid boundary. Such supports meet design requirements for allowing component removal and/or relative thermal expansion of the structures during reactor thermal cycling; however they complicate designing to avoid flow-induced vibration failures since methods of modeling such supports for response analysis or scale model testing are difficult. A better understanding is required of the fluid forces and associated effective mass and damping provided by dense fluids in finite length annular gaps.

The rod-annular fluid filled gap support shown in Fig. 1 is a representation of many similar geometries found in reactor systems. Typically, fundamental structural frequencies occur from 2 to 50 Hz and the range of the dimensionless geometric parameters important to the dynamics of the structure and fluid in the gap are: $0.002 \leq h/R \leq 0.03$, $0.5 \leq L/R \leq 10$. These gap sizes are not all small enough to determine fluid forces with lubrication theory which neglects fluid inertia [2], nor are the gaps all large enough to employ ideal flow theory [3, 4] which neglects fluid viscosity. Essentially, potential flow occurs in a central region of the gap which is not large in comparison to the boundary layer region. In addition, the lengths of the gap are not always long enough for the flow in the gap to be idealized as two-dimensional, where information on the fluid forces is available [5, 6] for small fluid motions.

An alternate method of calculating fluid forces has been proposed [3, 7, 8], essentially an inverse procedure, where the energy associated with exact or approximate ideal flow solutions are first developed and then generalized forces are obtained via LaGrange's equations of motion. The method, although approximate, has the flexibility to be extended to large fluid motions, turbulent flow, and finite length annular gaps including estimates of damping based on pipe friction flow losses and averaged one-dimensional flow fields for the limiting cases of very short and very long annular regions. However, some arbitrariness exists in the predictions because of the uncertainty of what entrance and exit loss effects to assume.

Further characterization of the forces, added mass, and damping effects of the annular gap support shown in Fig. 1 is pursued for the parameter ranges previously defined where viscous damping is significant. The Navier-Stokes and continuity equations are formulated in dimensionless form, an approximate solution is obtained, and experimental results are presented which verify the approximate theory for the parameter range of interest.

Fluid Forces

To obtain an approximate solution to the governing equations, they were first formulated in dimensionless terms of the same order of magnitude. The appropriate parameters for nondimensionalizing the radial distance r, the radial gradient ∂r, and the axial distance z were chosen to be R, h, and L, respectively, based on the geometry of Fig. 1 for the condition $h/r \ll 1$. The velocity components were nondimensionalized with estimates of the maximum velocities expected in the annular region [9]. For the radial component, the maximum rod velocity ωh was used, based on the assumption that the maximum radial fluid velocity occurs on the rod surface. The estimates employed for the circumferential and axial components, ωR and ωL, respectively, were obtained from the continuity requirement for one-dimensional, nonviscous, circumferential or axial flow between the inside and outside walls of an annular region squeezing together with

Contributed by the Applied Mechanics Division for publication in the JOURNAL OF APPLIED MECHANICS.

Discussion on this paper should be addressed to the Editorial Department, ASME, United Engineering Center, 345 East 47th Street, New York, N. Y. 10017, and will be accepted until September 1, 1980. Readers who need more time to prepare a discussion should request an extension from the Editorial Department. Manuscript received by ASME Applied Mechanics Division, February, 1979; final revision, November, 1979.

Copyright © 1980 by ASME
Downloaded 01 May 2010 to 171.66.16.243. Redistribution subject to ASME license or copyright; see http://www.asme.org/terms/Terms_Use.cfm

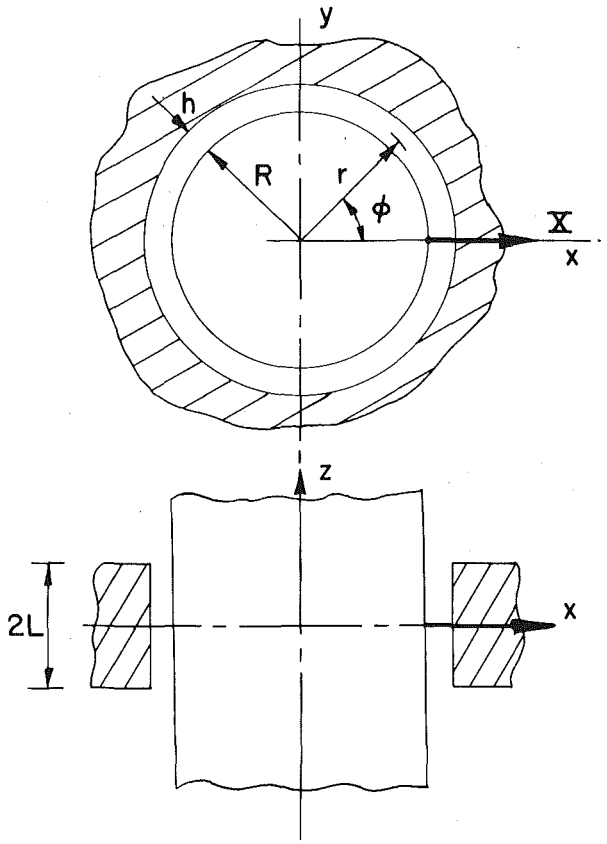

Fig. 1 Rod in fluid-filled annular region

relative velocity ωh. The pressure p was nondimensionalized by the dynamic pressure $(1/2)\,\rho(\omega L)(\omega R)$, a measure of the largest pressure drop in the annular region for a combination of circumferential and axial flow.

For the central rod of Fig. 1 translating periodically in the annular region according to

$$X = a\ \mathrm{Re}\,(e^{it}), \tag{1}$$

the Navier-Stokes equations [10] formulated in the dimensionless terms just discussed become

$$\frac{\partial u}{\partial t} = -\frac{\partial p}{\partial \alpha}\left(\frac{RL}{h^2}\right) + \frac{1}{2}\left(\frac{\delta_v}{h}\right)^2\left[\frac{\partial^2 u}{\partial \alpha^2} + \left(\frac{h}{R+\alpha h}\right)^2\frac{\partial^2 u}{\partial \phi^2} + \left(\frac{h}{L}\right)^2\frac{\partial^2 u}{\partial \beta^2} + \left(\frac{h}{R+\alpha h}\right)\frac{\partial u}{\partial \alpha} - \left(\frac{h}{R+\alpha h}\right)^2\left(\frac{2L}{h}\frac{\partial v}{\partial \phi} - u\right)\right],$$

$$\frac{\partial v}{\partial t} = -\left(\frac{L}{R+\alpha h}\right)\frac{\partial p}{\partial \phi} + \frac{1}{2}\left(\frac{\delta_v}{h}\right)^2\left[\frac{\partial^2 v}{\partial \alpha^2} + \left(\frac{h}{R+\alpha h}\right)^2\frac{\partial^2 v}{\partial \phi^2} + \left(\frac{h}{L}\right)^2\frac{\partial^2 v}{\partial \beta^2} + \left(\frac{h}{R+\alpha h}\right)\frac{\partial y}{\partial \alpha} + \frac{2h^3}{R(R+\alpha h)^2}\frac{\partial u}{\partial \phi} - \left(\frac{h}{R+\alpha h}\right)^2 v\right],$$

$$\frac{\partial w}{\partial t} = -\frac{R}{L}\frac{\partial p}{\partial \beta} + \frac{1}{2}\left(\frac{\delta_v}{h}\right)^2\left[\frac{\partial^2 w}{\partial \alpha^2} + \left(\frac{h}{R+\alpha h}\right)^2\frac{\partial^2 w}{\partial \phi^2} + \left(\frac{h}{L}\right)^2\frac{\partial^2 w}{\partial \beta^2} + \left(\frac{h}{R+\alpha h}\right)\frac{\partial w}{\partial \alpha}\right],$$

where nonlinear terms in velocity have been neglected. Thus a solution to these equations is expected to be valid only for small motions of the rod, $a/h \ll 1$. The δ_v is the viscous depth of penetration [10] into the fluid surrounding the vibrating rod. Damping is expected to be significant when (δ_v/h) is on the order of 1, which it is for many of the parameters of interest.

Utilizing the additional assumptions that $\delta_v/h = 0(1)$ and $h/r \ll 1$, the foregoing equations simplify to

$$\frac{\partial p}{\partial \alpha} = 0,$$
$$\frac{\partial v}{\partial t} = -\frac{L}{R}\frac{\partial p}{\partial \phi} + \frac{1}{2}\left(\frac{\delta_v}{h}\right)^2\frac{\partial^2 v}{\partial \alpha^2}, \tag{2}$$
$$\frac{\partial w}{\partial t} = -\frac{R}{L}\frac{\partial p}{\partial \beta} + \frac{1}{2}\left(\frac{\delta_v}{h}\right)^2\frac{\partial^2 w}{\partial \alpha^2}.$$

In the same dimensionless terms the continuity equation is

$$\frac{\partial u}{\partial \alpha} + \frac{\partial v}{\partial \phi} + \frac{\partial w}{\partial \beta} = 0. \tag{3}$$

The boundary conditions are

At $\alpha = 0$

$$u = \frac{a}{h}\cos\phi\ \mathrm{Re}\,(e^{it}) \tag{4}$$

$$v = -\frac{a}{R}\sin\phi\ \mathrm{Re}\,(e^{it}) \tag{5}$$

$$w = 0 \tag{6}$$

At $\alpha = 1$

$$u = 0 \tag{7}$$

$$v = 0 \tag{8}$$

$$w = 0 \tag{9}$$

and at $\beta = \pm 1$, $0 \le \alpha \le 1$, the constant ambient pressure is

$$p = p_a. \tag{10}$$

This approximation is strictly applicable only when entrance and exit effects are negligible, a condition approached as h/R diminishes.

Nomenclature

a = amplitude of central rod motion
d = outside diameter of beam
E = Young's elastic modulus
F_x = fluid force/length on central rod in x-direction
f_0 = fundamental beam frequency, Hz
h = thickness of annular gap
$i = \sqrt{-1}$
I = area moment of inertia of beam
IM = end mass moment of inertia at centroid
Im() = imaginary part of complex number
$k = (i+1)h/\delta_v$
L = one-half length of annular region
l = beam length
l_c = end mass centroid location, Fig. 1
l_E = length of end mass
M = end mass
m = mass/length of beam
m_f = displaced fluid mass/unit length = $\rho\pi R^2$
P = fluid pressure
P_a = ambient pressure outside of the annular region
$p = P/(\rho\omega^2 LR)$
R = radius of end mass
Re() = real part of complex number
(r, ϕ, z) = coordinates, see Fig. 1
T = time
$t = \omega T$
(U, V, W) = velocity components in (r, ϕ, z)-directions, respectively
$(u, v, w) = (U/\omega h, V/\omega R, W/\omega L)$
(x, y, z) = coordinate directions, see Fig. 1
X = central rod displacement in x-direction
$\alpha = (r - R)/h$
$\beta = z/L$
δ_v = viscous penetration depth = $\sqrt{2\nu/\omega}$
ν = fluid kinematic viscosity
ζ = modal viscous damping/critical damping
ρ = fluid mass density
ω = frequency of rod vibration, rad/sec

Downloaded 01 May 2010 to 171.66.16.243. Redistribution subject to ASME license or copyright; see http://www.asme.org/terms/Terms_Use.cfm

Also, the resultant shear forces at the ends of the annular region, $\beta = \pm 1$ and $0 \le \alpha \le 1$ are specified to be zero

$$\int_0^{2\pi} \int_0^1 \frac{\partial w}{\partial \alpha} \cos \phi d\alpha d\phi = 0 \tag{11}$$

$$\int_0^{2\pi} \int_0^1 \frac{\partial w}{\partial \alpha} \sin \phi d\alpha d\phi = 0. \tag{12}$$

Forces could be induced on the rod by fluid shear stresses τ_{rz} and $\tau_{\phi z}$ on the ends of the vibrating rod: $\beta = \pm 1$ and $-R/h \le \alpha \le 0$. Satisfaction of boundary conditions on these surfaces was not attempted, nor were τ_{rz} and $\tau_{\phi z}$ included in the determination of forces on the rod; essentially they were assumed small enough to neglect. However, the resultant shear forces on the ends of the fluid annulus were stipulated to be zero, (11) and (12), since nonzero values could necessitate nonzero shear forces on the ends of the rod for static equilibrium of the fluid outside the annular region.

The pressure p can be eliminated from the last two equations of (1) by differentiation, with the resulting higher-order equations

$$\frac{\partial^2 v}{\partial t \partial \alpha} - \frac{1}{2}\left(\frac{\delta_v}{h}\right)^2 \frac{\partial^3 v}{\partial \alpha^3} = 0,$$

$$\frac{\partial^2 w}{\partial t \partial \alpha} - \frac{1}{2}\left(\frac{\delta_v}{h}\right) \frac{\partial^3 w}{\partial \alpha^3} = 0. \tag{13}$$

Separation of variables solutions to (13) can be derived, which in complex form are

$$v = \frac{a}{h}\left[F_1 + kF_4 \cosh k\alpha + kF_5 \sinh k\alpha\right] \sin \phi \, e^{it}$$

$$w = \frac{a}{h}\left[G_1 + kG_4 \cosh k\alpha + kG_5 \sinh k\alpha\right] \cos \phi \, e^{it} \tag{14}$$

and according to (3)

$$u = -\frac{a}{h}\left[F_1\alpha + F_4 \sinh k\alpha + F_5 \cosh k\alpha + \frac{dG_1}{d\beta}\alpha + \frac{dG_4}{\partial\beta}\sinh k\alpha + \frac{dG_5}{d\beta}\cosh k\alpha + F_6\right] \cos \phi \, e^{it} \tag{15}$$

where the F's and G's are seven complex functions of β. The real parts of (14) and (15) are the desired velocity field solution.

If the nonlinear velocity terms in the governing equations had not been neglected initially, then equations (13) would be

$$\frac{\partial^2 v}{\partial t \partial \alpha} - \frac{1}{2}\left(\frac{\delta_v}{h}\right)^2 \frac{\partial v^3}{\partial \alpha^3} = -\frac{\partial}{\partial \alpha}\left(u\frac{\partial v}{\partial \alpha} + v\frac{\partial v}{\partial \phi} + \frac{\partial v}{\partial \beta}\right)$$

$$\frac{\partial^2 w}{\partial t \partial \alpha} - \frac{1}{2}\left(\frac{\delta_v}{h}\right)^2 \frac{\partial^3 w}{\partial \alpha^3} = -\frac{\partial}{\partial \alpha}\left(u\frac{\partial w}{\partial \alpha} + v\frac{\partial w}{\partial \phi} + w\frac{\partial w}{\partial \beta}\right) \tag{13a}$$

For u and v on the order of $a/h \ll 1$, as assumed, then the nonlinear terms are shown to be negligible, also as assumed. In fact, solutions (14) and (15) represent the first terms in the perturbation expansion solution

$$u = u_1 \frac{a}{h} + u_2 \left(\frac{a}{h}\right)^2 + \ldots$$

$$w = w_1 \frac{a}{h} + w_2 \left(\frac{a}{h}\right)^2 + \ldots$$

Higher-order terms in the solution could be obtained, with appropriate generalization of the boundary conditons; instead the range of utility of the first-order term will be determined by comparison to experimental results. Comparison to experiment was deemed necessary, in any case, because of the assumptions leading to the nondimensionalized governing equations and the treatment of rod and annulus end effects.

The six boundary conditions (4)–(9) allow determination of five of the functions in terms of F_1 and G_1

$$G_4 = -G_1/k$$

$$F_4 = -(F_1 + h/R)/k \tag{16}$$

$$F_5 = (h/R)[\cosh k/(k \sinh k)] - (F_1/k)[(1 - \cosh k)/\sinh k]$$

$$G_5 = -(G_1/k)[(1 - \cosh k)/\sinh k]$$

$$F_6 = \frac{[k(\cosh k - k \sinh k - 1) + (h/R)(\sinh k - k \cosh k]}{k(2 + k \sinh k - 2 \cosh k)}. \tag{16 (Cont.)}$$

The last equation of (2) can be integrated utilizing (14)–(16), to yield

$$p = \frac{a}{h}\frac{R}{L} F_1 \cos \phi \, i \, e^{it} + f(\beta, t) \tag{17}$$

where $f(\beta, t)$ is a function of integration. For (17) to satisfy the second equation of (2), F_1 and G_1 must be related according to

$$\int G_1 d\beta = -\left(\frac{R}{L}\right)^2 F_1 + \text{constant}. \tag{18}$$

The integral-differential equation (18) and the one resulting from boundary condition (7) can be solved simultaneously, employing (16), to obtain

$$G_1 = A \, e^{(L\beta/R)} + B \, e^{-(L\beta/R)}$$

$$F_1 = -A(L/R) \, e^{(L\beta/R)} + B(L/R) \, e^{-(L\beta/R)} + C \tag{19}$$

where

$$C = \frac{k \sinh k}{[2 + k \sinh k - 2 \cosh k]} \tag{20}$$

The remaining constants A, B, and $f(\beta, t)$ are determined by the remaining boundary conditions (10)–(12) with the result

$$-A = B = -C(R/L)/[e^{L/R} + e^{-L/R}]$$

$$f(\beta, t) = p_a. \tag{21}$$

The resultant fluid force per unit length on the oscillating rod in the x-direction is

$$F_x \cong -\int_0^{2\pi} P \cos \phi \, d\phi \tag{22}$$

or with the real part of (17)

$$F_x = \left(1 - \frac{\cosh (z/R)}{\cosh (L/R)}\right) f_x \tag{23}$$

where

$$f_x = m_f(R/h)[\text{Re } (C)\ddot{X} + \omega \text{ Im } (-C)\dot{X}]. \tag{24}$$

Shear stress and other terms are negligible in (22) in comparison to P for $(h/R \ll 1)$. The force in the y-direction is identically zero, as expected. The coefficients of the acceleration $\ddot{X}$ and the velocity $\dot{X}$ in (23) can be likened to added mass and viscosities per unit length. The fluid force per unit length for two-dimensional flow $(L/R \to \infty)$ in an annular region is f_x as can be shown by comparison with [5] or a direct solution of the 2-D Navier-Stokes equations for $h/R \ll 1$ and $(\delta/h) = O(1)$. Variations in the Re (C) and Im (C) are given in Fig. 2 which show the added mass to be insensitive and damping to be sensitive to variations in the viscous penetration depth δ_ν.

The average force/length corresponding to F_x in (23) is

$$\overline{F}_x = K f_x \tag{25}$$

where

$$K = 1 - (R/L) \tanh (L/R). \tag{26}$$

The plot of K versus (L/R) in Fig. 3 indicates that much larger damping forces are associated with primarily circumferential (two-dimensional, $L/R \to \infty$) annular flow in comparison to the damping forces associated with primarily axial flow $(L/R \to 0)$. Another measure of three-dimensional flow effects on the fluid forces is shown in Fig. 4 where $F_x(Z)/F_x(0)$ is plotted versus L/R.

The fluid forces on the rod (23)–(26) represent first-order expres-

Downloaded 01 May 2010 to 171.66.16.243. Redistribution subject to ASME license or copyright; see http://www.asme.org/terms/Terms_Use.cfm

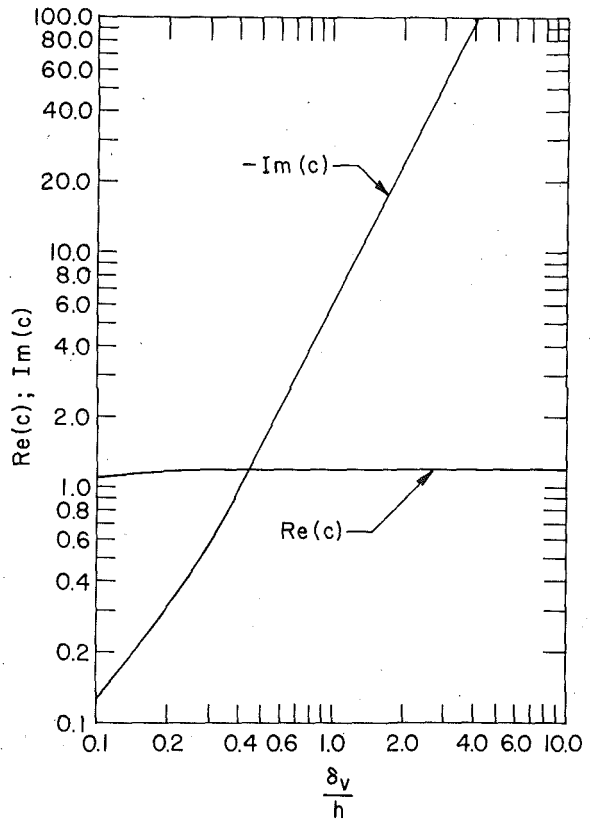

Fig. 2 Added mass and damping multipliers, Re (c) and Im (c), versus viscous penetration depth δ_v

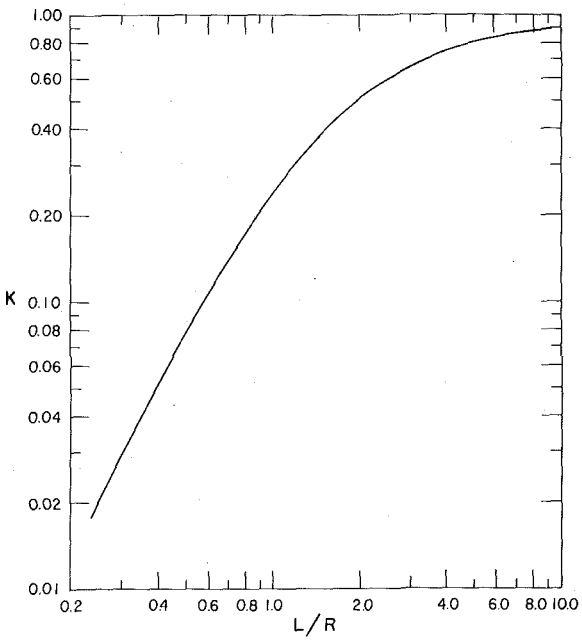

Fig. 3 Variation with L/R of average force/length normalized to $L/R \rightarrow \infty$

sions which are valid for small fluid motions and finite length open ended annular regions where $h/R \ll 1$ and the viscous penetration depth δ_v is of the order of h. Further, although the outside boundary of the annular region has been assumed stationary, the results given are sufficient to characterize the forces for both boundaries moving, as explained in [6].

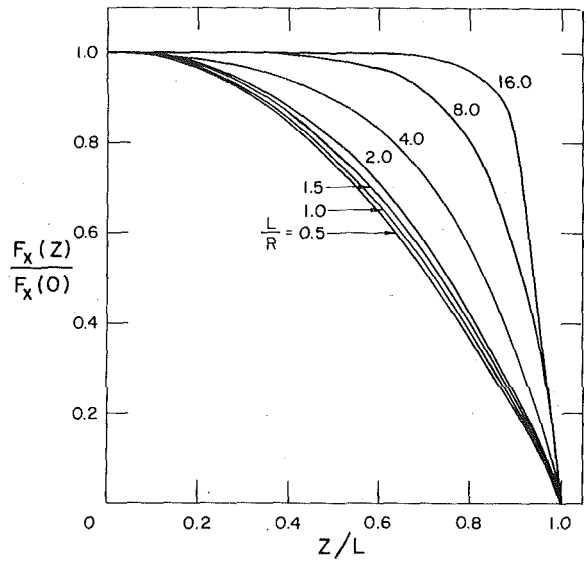

Fig. 4 Normalized fluid force variation with Z/L for several L/R

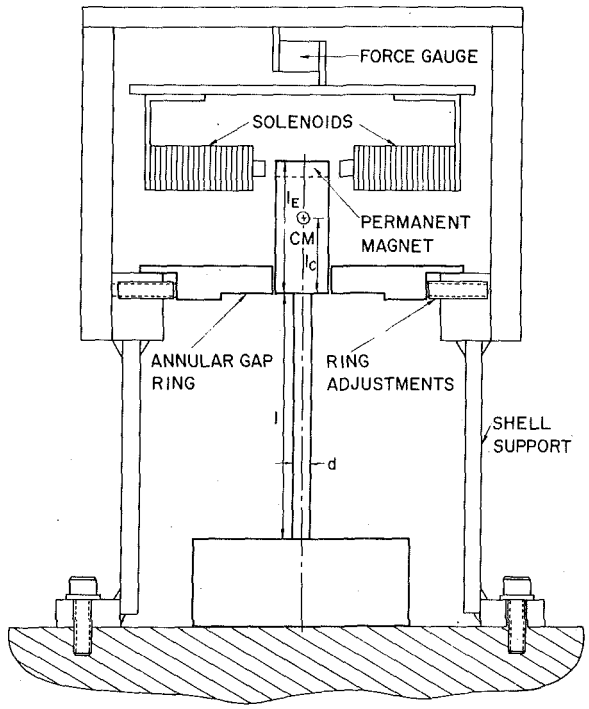

Fig. 5 Cantilevered beam with end mass and annular gap support

Measured Frequencies and Damping

To assess the validity of the force predictions (23) and (24), specific dimensions for the beam geometry of Fig. 5 and Fig. 1 were chosen for testing; see Table 1. The particular configuration of Fig. 5 is considered to include all the important features of a beam with an annular gap support but is simple enough to allow thorough testing and analysis. A constant amplitude force was applied to the structure over a range of frequencies which allowed determination of the beam fundamental frequency and associated modal damping ratio for the test matrix of water filled annular gap widths and lengths given in Table 2. Also, initial tests were performed for the beam in air and water (infinite gap) in order to verify the structural analysis model described in the next section. The geometric and structural parame-

Downloaded 01 May 2010 to 171.66.16.243. Redistribution subject to ASME license or copyright; see http://www.asme.org/terms/Terms_Use.cfm

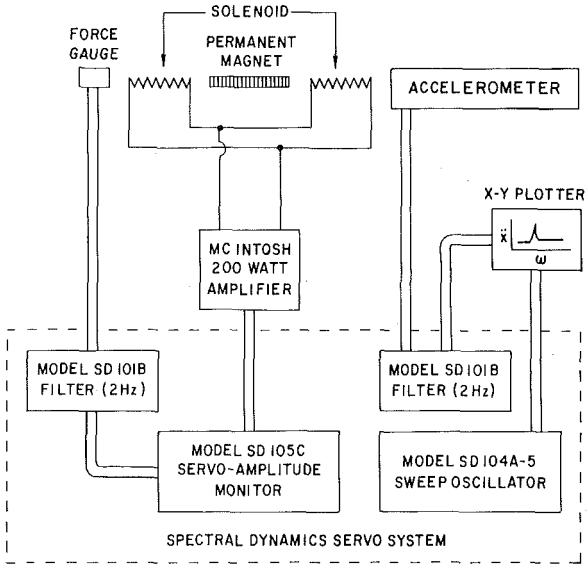

Fig. 6 Force excitation and monitoring instrumentation

Table 1 Beam structural properties

l = 114.3 mm (4.5 in.)	M = 1.094 kg (15.97 slugs)
m = 2.782 kg/m^2 (3.777 × 10^{-2} slugs/ft^2)	l_c = 29.64 mm (1.167 in.)
E = 1.07 × 10^{11} Pa (15.5 × 10^6 lb/in.^{2})	IM = 3.692 kg m^2 (5.79 × 10^{-5} slug ft^2)
I = 0.178 mm^2 (2.76 × 10^{-4} in.^{2})	l_E = 58.75 mm (2.313 in.)
d = 7.95 mm (0.313 in.)	R = 12.2 mm (0.5 in.)

Table 2 Annular gap configurations tested

h/R	L/R	h/R	L/R
0.03	0.5	0.06	0.5
0.03	0.75	0.06	1.25
0.03	1.0	0.06	1.75
0.03	1.25	0.06	2.00

ters chosen are representative of frequencies, mass ratios, and fluid annulus gaps encountered in one-third scale model testing of reactor components. In fact, test results described here also will be employed in conjunction with larger geometrically similar models to empirically verify scale modeling relations.

The different annular gap sizes were obtained by employing different annular gap rings which were held by the rigid (relative to the beam) shell support shown in Fig. 5. Three set screws were provided to allow adjustment of the annular gap ring for concentricity with respect to the beam end mass. Three equally spaced piano wires, undersize by 10 percent at most, were employed to set the annular gap.

A noncontacting method of force excitation was achieved by attaching matched solenoids to the shell structure on opposite sides of a permanent magnet which was implanted in the top of the end mass of the beam; see Fig. 5. The permanent magnet was a 6.35 mm × 25.4 mm (0.25 in. × 1.0 in.) cylinder and the solenoids consisted of ~ 350 turns of 0.9 mm (0.036 in.) diameter Formvar wire wrapped around a steel core the same diameter as the magnet. The gap between the magnet and the solenoid core was varied between 1.56 mm to 12.2 mm (0.0625 in. to 0.5 in.) to obtain well-formed sinusoidal force time histories with peak to peak forces up to 2.22 N (0.5 lb) at a maximum current of 3 amp. The forces were measured by a PCB Piezotronics Model 218A uniaxial piezoelectric force gauge (charge mode) conditioned by an Endevco Model 2730 charge amplifier. Force amplitudes to 0.045 N (0.01 lb) could be resolved.

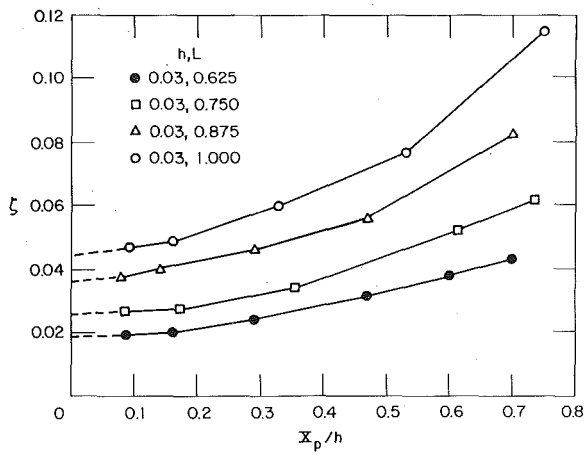

Fig. 7 Damping ratio ζ as a function of peak normalized displacement amplitude X_p/h

The acceleration of the end mass was monitored by two Entran Model EGAL 125-10 piezoresistive accelerometers one of whose sensitive axes was placed in line with the excitation force and the other normal to the direction of excitation at a location immediately below the permanent magnet at the top of the end mass. Endevco Model 4470 signal conditioners and Model 4476.2 bridge conditioners processed the accelerometer signals.

The force excitation system, the force gauge output, and the accelerometer signal were connected with the Spectral Dynamics Servo System shown in Fig. 6. Force amplitudes were held constant, at selected values between 0.089 to 2.22 N (0.02 to 0.5 lb) peak to peak, during frequency sweeps from 20 to 40 Hz. Sweep rates down to 0.001 Hz/sec could be selected to avoid rate effects and instabilities in the servo/mechanical system. Plots of end mass acceleration versus frequency were employed to determine the fundamental structural frequency f_0 associated with the peak response and to find, by the bandwidth method [11], the ratio of modal viscous damping to critical damping

$$\zeta = \frac{\lambda}{2\sqrt{1-\lambda^2}} \frac{\Delta f}{f_0}, \tag{27}$$

where Δf is the frequency bandwidth of the response plot at λ ($0 \leq \lambda \leq 1$) of the peak acceleration level. The value of λ was chosen at the half power point ($\lambda = 1/\sqrt{2}$) and at other values to check for nonlinearities in response. Although the bandwidth method given by (27) is strictly applicable to an amplitude response function, the mechanical system response occurred over such narrow bands that the acceleration signal could be employed just as accurately (± 5 percent).

Testing in air showed the beam to be a very lightly structurally damped system, as desired, with $\zeta \cong 0.0013$ and $f_0 = 36.8$ Hz. In water without any annular gap, $\zeta \cong 0.0016$ and $f_0 = 35.0$ Hz. Test results in water with an annulus were not corrected for structural damping since it was negligible for the configurations of interest. Soon after annular gap testing began, it became apparent that the damping was a nonlinear function of the amplitude of motion as is illustrated by Fig. 7 where ζ is plotted versus the ratio of the normalized peak response X_p/h. The nonlinearity could be due to nonlinear fluid velocity effects for large amplitude motion or due to transition from laminar to turbulent flow [12]. Future studies are planned to investigate the phenomenon. Only ζ at small amplitudes of motion are reported here and plots like those of Fig. 7 were used to obtain them by extrapolation. Note that ζ is not well defined for nonlinear damping.

The measured fundamental beam frequencies f_0 and the damping ratios are shown in Figs. 8 and 9. The trends in the data with a gap length increase or a gap size decrease are as expected: the fundamental frequency decreases due to the increased added mass effect of the fluid and the damping ratio increases because of significant increases in

Downloaded 01 May 2010 to 171.66.16.243. Redistribution subject to ASME license or copyright; see http://www.asme.org/terms/Terms_Use.cfm

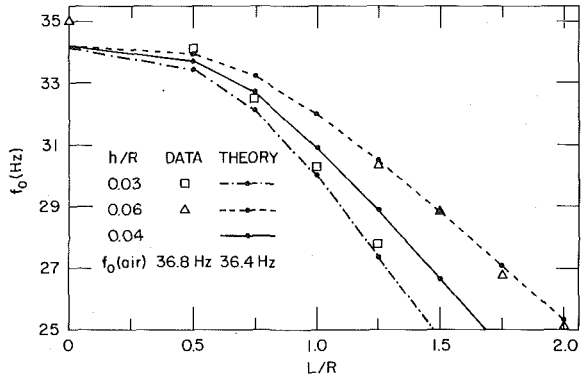

Fig. 8 Measured and predicted fundamental frequencies

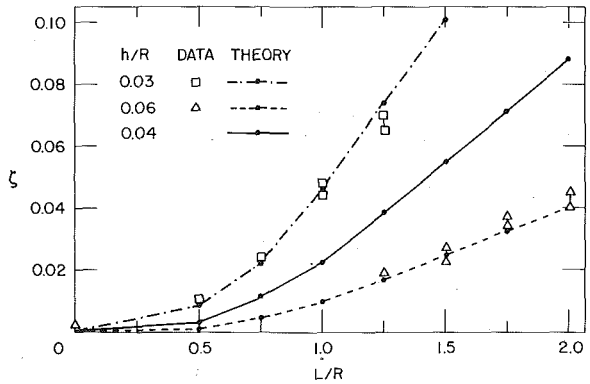

Fig. 9 Measured and predicted damping ratios

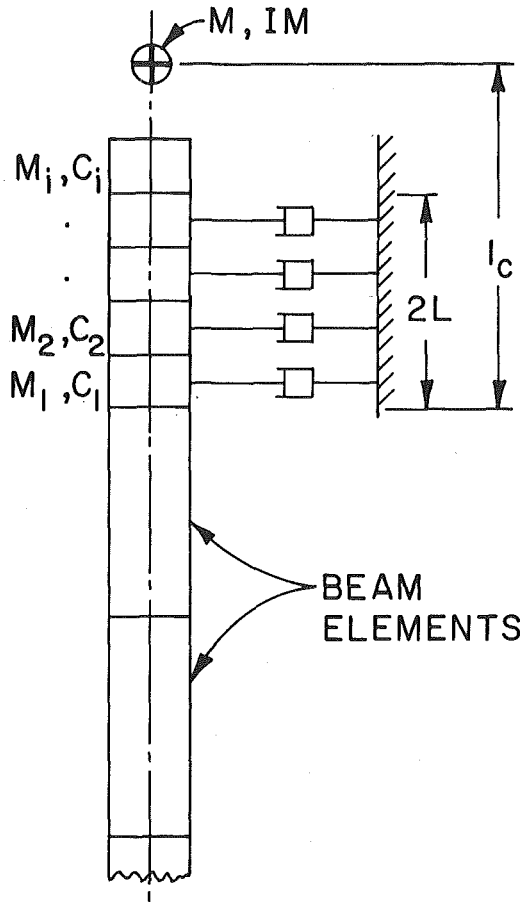

Fig. 10 Structural model of fluid gap with concentrated masses M_i and dashpots C_i

fluid losses. As expected from the force calculations, relatively small differences in natural frequencies were observed (30 percent) for the parameters tested while the damping ratio differences were multifold.

Predictions and Discussion of Results

In order to predict and compare the natural modal frequencies and damping for the beam and annular gap geometries of the experiments, an available computer code (NASTRAN Level 15.5) which had concentrated mass and viscous dampers among its element library was employed to obtain a multidegree of freedom model of the beam and fluid gap. The beam was represented by nine beam elements (including shear and rotary inertia effects) while the end mass was represented by a concentrated mass M and mass moment of inertia IM located at the center of mass, a distance l_c from the end of the beam; see Fig. 10. Table 1 lists the properties. The mass density of the material (brass) was obtained by weighing, and the modulus of elasticity was found by comparing measured and predicted free-free beam frequencies for the beam stock before fabrication of the model. All other properities listed in Table 1 were calculated based on machined dimensions.

In order to represent the added mass and damping effects, every 3.18 mm (0.125 in.) of fluid-filled annular gap length was lumped into a concentrated scalar mass element M_i and linear viscous damper C_i, available elements in the computer code library. The values of (M_i, C_i) were computed with (23), (24), and (20) for an estimated or previously calculated frequency. Because the viscosity coefficients C_i varied significantly with frequency, several iterations could be required before convergence to a free-vibration solution. The added mass M_i were relatively insensitive to frequency variations. The solution to a two-degree-of-freedom model was employed to make initial frequency estimates for the multidegree of freedom model and rarely were more than two iterations required.

The predicted fundamental beam frequencies f_0 and damping ratios ζ are shown in Figs. 8 and 9 for three normalized annular gap widths h/R and a range of L/R. Comparison with the experimental data indicates that frequency predictions are more accurate when the annular gap dominates the response, at larger L/R, but all the predictions are quite satisfactory and within 2.3 percent of the data. The fundamental frequency in air was predicted also and found to be 36.4 Hz in comparison to a measured 36.8 Hz. Undoubtedly the structural (air) model could have been adjusted to give better predictions for smaller L/R. The damping predictions shown in Fig. 9 were not corrected for structural damping, because it was smaller than the error encountered in extrapolating, Fig. 7, for small amplitude damping values. The predictions and data compare within 10 percent, a deviation considered acceptable given the usual scatter encountered in measuring damping values.

The accuracy of another simpler prediction model was investigated which empolyed only a single added mass and viscous damper approximation of the fluid gap at the midlength of the gap. As might be expected the predictions for the first mode, which involves primarily translation of the end mass, were nearly identical to the results of the more elaborate model presented previously. This was true as long as the single added mass approximation included the added mass moment of inertia effects of the fluid gap, otherwise significant errors in predictions would occur. More precisely, to obtain an adequate predictive model for the first mode, the single added mass and damper value could be obtained from (25) but the second moment of the inertia term in (23) and (24) also had to be modeled.

This same model also predicted the second mode natural frequency accurately, but the damping was often significantly in error when the

Downloaded 01 May 2010 to 171.66.16.243. Redistribution subject to ASME license or copyright; see http://www.asme.org/terms/Terms_Use.cfm

node of the mode, consisting primarily of rotation of the end mass, occurred near the damper. For instance, with $L/R = 2.00$ and $h/R = 0.03$, the second mode frequency is predicted to be 343.15 Hz by both the single and multiple mass and damper approximation, but the damping predicted differs by an order of magnitude $\zeta_2 = 0.00135$ as compared to 0.0171, respectively. An angular damper could be used to improve the prediction for this case since the end mass is essentially rigid. The main point is that multiple damper representations, such as shown in Fig. 10, are required for analysis of most vibration modes.

Conclusions

Further characterization of the fluid forces and associated added mass and damping have been achieved for the annular gap support shown in Fig. 1. The three-dimensional Navier-Stokes equations describing the fluid flow in a finite length annular region surrounding a rigid central rod undergoing prescribed translations were solved neglecting nonlinear velocity terms for small rod motions. First-order expressions for the fluid forces on the rod were obtained which are valid for small fluid motions, $h/R \ll 1$, and the viscous penetration depth δ_v on the order of h. A method of representing the forces as added mass and linear viscous dampers in an analysis model was demonstrated for a simple beam geometry, Fig. 2, utilizing an existing structural dynamics computer code (Nastran). The test methods and results of a set of experiments for the same simple geometry were presented, also. Good agreement between the predicted and observed fundamental structural frequencies and modal damping was found. In addition, measurements indicated that the predicted damping probably is a lower bound on the damping for larger amplitude motion.

References

1 Turula, P., and Mulcahy, T. M., "Computer Modeling of Flow-Induced In-Reactor Vibrations," *Journal of Power Division, Proceedings ASCE,* Vol. 103, 1977, pp. 37–49.

2 Pinkus, O., and Sternlicht, B., *Theory of Hydrodynamic Lubrication,* 1st ed., McGraw-Hill, New York, 1961, pp. 1–23.

3 Liu, L. K., "Seismic Analysis of the Boiling Water Reactor," *Seismic Analysis of Pressure Vessel and Piping Components,* Symposium on Analysis of Pressure Vessel and Piping Components, San Francisco, 1971, ASME Publication, New York, 1971, pp. 90–102.

4 Kiss, E., "Analysis of the Fundamental Vibration Frequency of a Radial Vane Steam Separator Structure," *Proceedings of the Conference on Flow-Induced Vibration in Reactor System Components,* Argonne National Laboratory, Argonne, Ill., May 14–15, 1970, ANL-7685, 1970, pp. 335–343.

5 Chen, S. S., Wambsganss, M. W., and Jendrzejczyk, J. A., "Added Mass and Damping of a Vibrating Rod in Confined Viscous Fluid," ASME JOURNAL APPLIED MECHANICS, Vol. 43, 1976, pp. 325–329.

6 Yeh, T. T., and Chen, S. S., "Dynamics of a Cylindrical Shell System Coupled by a Viscous Fluid," *Journal of the Acoustical Society of America,* Vol. 62, No. 2, 1977, pp. 262–270.

7 Yeh, T. T., and Chen, S. S., "The Effect of Fluid Viscosity on Coupled Tube/Fluid Vibrations, *Journal of Sound and Vibration,* Vol. 59, No. 3, 1978, pp. 1–24.

8 Fritz, R. J., "The Effects of Liquids on the Dynamic Motions of Immersed Solids," ASME *Journal of Engineering for Industry,* Vol. 39, 1972, pp. 167–173.

9 Fritz, R. J., and Kiss, E., "The Vibration Response of a Cantilevered Cylinder Surrounded by an Annular Fluid," Knolls Atomic Power Laboratory Report KAPL-M-6539, 1966.

10 Landau, L. D., and Lifshitz, E. M., *Fluid Mechanics,* Addison-Wesley, Mass., 1959.

11 Thompson, W. T., *Vibration Theory and Applications,* Prentice-Hall, Englewood Cliffs, N.J., 1965.

12 Skop, R. A., Rombert, S. E., and Ferer, K. M., "Added Mass and Damping Forces on Circular Cylinders," Joint Petroleum Mechanical Engineering and Pressure Vessel and Piping Conference, September 19–24, 1976, Mexico City, ASME Paper 76-Pet-3.

Downloaded 01 May 2010 to 171.66.16.243. Redistribution subject to ASME license or copyright; see http://www.asme.org/terms/Terms_Use.cfm

M. Kumari
Research Student.

G. Nath
Professor.

Department of Applied Mathematics,
Indian Institute of Science,
Bangalore-560012, India

Unsteady Incompressible Three-Dimensional Asymmetric Stagnation-Point Boundary Layers

The unsteady laminar incompressible boundary-layer flow near the three-dimensional asymmetric stagnation point has been studied under the assumptions that the free-stream velocity, wall temperature, and surface mass transfer vary arbitrarily with time. The partial differential equations governing the flow have been solved numerically using an implicit finite-difference scheme. It is found that in contrast with the symmetric flow, the maximum heat transfer occurs away from the stagnation point due to the decrease in the boundary-layer thickness. The effect of the variation of the wall temperature with time on heat transfer is strong. The skin friction and heat transfer due to asymmetric flow only are comparatively less affected by the mass transfer as compared to those of symmetric flow.

Introduction

The accurate prediction of the unsteady boundary layers when the external stream varies arbitrarily with time is of considerable importance in understanding the flow through turbomachines, over helicopter rotor blades, in jet impingement problems on bodies, and in aircraft response to atmospheric guests. The pertinent literature has been critically reviewed by Stuart [1], Riley [2], and Telionis [3]. Work in this area was initiated by Moore [4], Lighthill [5], and Lin [6]. The unsteady laminar incompressible two-dimensional and axisymmetric stagnation-point boundary-layer flows have been studied by Srivastava [7] and Ishijaki [8] when the free-stream velocity varies arbitrarily with time. The corresponding thermal boundary-layer problem due to step wall temperature change has also been investigated by Chao and Jeng [9] and Jeng, et al. [10]. Subsequently, Ghoshal and Ghoshal [11] have extended the aforementioned analysis to symmetric flows near the three-dimensional stagnation point (for nodal points of attachment only) when the free-stream velocity varies arbitrarily with time. These authors have used approximate methods such as series expansion or momentum integral method for the solutions of partial differential equations governing the flow. As far as authors are aware, the unsteady laminar three-dimensional asymmetric stagnation-point boundary-layer flow which is important in jet impingement problem where a jet is incident on a body at a certain angle, has not been studied so far.

The aim of the present analysis is to study the unsteady laminar incompressible asymmetric stagnation-point boundary-layer flow for three-dimensional bodies when the free-stream velocity, wall temperature, and surface mass transfer vary arbitrarily with time. Both the nodal and saddle points of attachment cases have been included in the analysis. Here the problem has been tackled as an initial value problem starting with a steady-state solution and hence the solution is different from other work [5, 7, 8, 11] where transient motions have been assumed to have died away. The solution in the vicinity of the stagnation point has been obtained by series expansion in longitudinal coordinate. The resulting partial differential equations have been solved numerically using an implicit finite-difference scheme [12]. The results for the steady two-dimensional, axisymmetric, and three-dimensional symmetric stagnation-point flows have been compared with those of Chao and Jeng [9], Jeng, et al. [10], Howarth [13], Davey [14], and Hayday and Bowlus [15] and for the steady three-dimensional asymmetric stagnation-point flow with those of Lesin [16].

Governing Equations

We consider the unsteady laminar incompressible boundary-layer flow with mass transfer near the stagnation point of a three-dimensional porous body. We assume that the free-stream temperature is constant and dissipation terms are negligible near the stagnation point. The free-stream velocity, surface temperature, and mass transfer are assumed to vary arbitrarily with time.

It may be remarked that here, for the sake of simplicity, we have not considered the general distribution of the velocity in the inviscid flow in the neighborhood of the stagnation point. However, in the immediate vicinity of the stagnation point, we expand the velocity components of the inviscid flow in a power series in x neglecting terms higher than the second order. This approximation is valid for asymmetric stagnation-point flows [16]. Further, the quadratic terms with respect to z has also been omitted because the expansion is considered

Contributed by the Applied Mechanics Division for publication in the JOURNAL OF APPLIED MECHANICS.

Discussion on this paper should be addressed to the Editorial Department, ASME, United Engineering Center, 345 East 47th Street, New York, N. Y. 10017, and will be accepted until September 1, 1980. Readers who need more time to prepare a discussion should request an extension from the Editorial Department. Manuscript received by ASME Applied Mechanics Division, March, 1979; final revision, November, 1979.

Copyright © 1980 by ASME
Downloaded 01 May 2010 to 171.66.16.243. Redistribution subject to ASME license or copyright; see http://www.asme.org/terms/Terms_Use.cfm

at the edge of the boundary layer where the square of the boundary-layer thickness is neglected. Under the foregoing assumptions, the velocity components which vary arbitrarily with time can be expressed as [16]

$$u_e = (ax + \alpha x^2)\varphi(t^*), \quad v_e = acy\varphi(t^*),$$
$$w_e = (bz - 2\alpha xz)\varphi(t^*), \tag{1a}$$

where

$$c = b/a, \quad a = (du_e/dx)_0, \quad b = (dv_e/dy)_0, \quad t^* = at. \tag{1b}$$

Here x, y, and z are the longitudinal, transverse, and normal directions, respectively; u, v, and w are the velocity components in the x, y, and z-directions, respectively; t and t^* are the dimensional and dimensionless times, respectively; and the subscripts e and zero denote conditions at the edge of the boundary layer and at the stagnation point, respectively. φ is an arbitrary function of t^* representing the nature of the unsteadiness in the inviscid flow and has a continuous first derivative for $t^* > 0$. The parameter a is the velocity gradient at the stagnation point in the plane of symmetry, the ratio α/a denotes the degree of asymmetry of the flow, and the parameter c represents the three-dimensional properties of the flow ($c = 0$ for a two-dimensional flow and $c = 1$ for an axisymmetric flow). For nodal points of attachment $c \geq 0$ ($0 \leq c \leq 1$) and for saddle points of attachment $c < 0$ ($-1 \leq c < 0$). The parameter b is the velocity gradient at the stagnation point in the y-direction.

We apply the following transformations:

$$\eta = (a/\nu)^{1/2}z, \quad F = f_\eta(\eta, t^*), \quad S = s_\eta(\eta, t^*), \quad M = m_\eta(\eta, t^*)$$
$$u = (axF + \alpha x^2 M)\varphi(t^*), \quad v = acyS\varphi(t^*)$$
$$w = -(a\nu)^{1/2}[f + cs + 2(\alpha x/a)m]\varphi(t^*) \tag{2a}$$

$$(T - T_w)/(T_\infty - T_w) = g(\eta, t^*) + 2(\alpha x/a)G(\eta, t^*) \tag{2b}$$

to the governing boundary-layer equations given in [11] and we find that the equation of continuity is identically satisfied. By equating the coefficients of identical powers in x and y in the momentum and energy equations, we find that

$$F_{\eta\eta} + \varphi[(f + cs)F_\eta + 1 - F^2] + \varphi^{-1}\varphi_t{}^*(1 - F) - F_t{}^* = 0 \tag{3a}$$

$$S_{\eta\eta} + \varphi[(f + cs)S_\eta + c(1 - S^2)] + \varphi^{-1}\varphi_t{}^*(1 - S) - S_t{}^* = 0 \tag{3b}$$

$$\sigma^{-1}g_{\eta\eta} + \varphi(f + cs)g_\eta - g_t{}^* = 0 \tag{3c}$$

$$M_{\eta\eta} + \varphi[(f + cs)M_\eta + 3(1 - MF) + 2mF_\eta] + \varphi^{-1}\varphi_t{}^*(1 - M) - M_t{}^* = 0 \tag{3d}$$

$$\sigma^{-1}G_{\eta\eta} + \varphi[(f + cs)G_\eta + mg_\eta - FG] - G_t{}^* = 0. \tag{3e}$$

The boundary conditions can be expressed as

$$\left.\begin{aligned} &F = S = M = G = 0, \quad g = 1 - R(t^*) \quad \text{at} \quad \eta = 0 \\ &F = S = g = M = 1, \quad G = 0 \quad \text{as} \quad \eta \to \infty \end{aligned}\right\} \text{at} \quad t^* \geq 0 \tag{4a}$$

where

$$f = \int_0^\eta F d\eta + f_w, \quad s = \int_0^\eta S d\eta, \quad m = \int_0^\eta M d\eta$$
$$f_w = -(w)_w(a\nu)^{-1/2}/\varphi(t^*) = A/\varphi(t^*)$$
$$A = -[(w)_w/ax](\mathrm{Re}_x)^{1/2}, \quad \mathrm{Re}_x = ax^2/\nu. \tag{4b}$$

Here η is the similarity variable; f, s, and m are the dimensionless stream functions; F and M are the dimensionless velocities in the x-direction (M and m are the contribution due to the asymmetric nature of the flow); S is the dimensionless velocity in the y-direction; g and G are the dimensionless temperatures (G being the contribution due to the asymmetric nature of the flow); σ and ν are the Prandtl number and kinematic viscosity, respectively; and Re_x is the local Reynolds number. Here $(w)_w$ has been chosen in such a manner that $(w)_w/(ax)$ is a constant. Hence, A is a constant ($A \gtrless 0$ according to whether there is suction or injection) and consequently the surface mass transfer parameter f_w will vary inversely as $\varphi(t^*)$. The subscripts η and t^* denote derivatives with respect to η and t^*, respectively.

Here it has been assumed that the flow is initially steady and changes to unsteady for $t^* > 0$. Therefore, the initial conditions for F, S, g, M, and G at $t^* = 0$ are given by the steady-flow equations obtained by putting

$$\varphi(t^*) = R(t^*) = 1, \quad \varphi_{t^*} = 0, \quad \partial/\partial t^* = 0 \tag{5}$$

in (3). These steady-state equations, which represent the three-dimensional asymmetric stagnation-point flow, are the same as those obtained by Lesin [16]. Furthermore, the first three steady-state equations represent three-dimensional symmetric stagnation-point flow which has been studied by Howarth [13] for nodal points of attachment ($0 \leq c \leq 1$) and by Davey [14] for saddle points of attachment ($-1 \leq c < 0$). The set of equations (3a)–(3c) corresponds to the unsteady symmetric flow near the three-dimensional stagnation point.

The skin-friction coefficients along x and y-directions and the heat-transfer coefficient can be expressed in the form

$$C_f = 2\tau_x/[\rho(u^2{}_{eo})_{t^*=0}] = 2(\mathrm{Re}_x)^{-1/2}\varphi(t^*)(F_\eta + A_1x_1M_\eta)_w \tag{6a}$$

$$\overline{C}_f = 2\tau_y/[\rho(u^2{}_{e0})_{t^*=0}] = 2(\mathrm{Re}_x)^{-1/2}\,(v_e/u_{e0})\varphi(t^*)(S_\eta)_w \tag{6b}$$

$$\mathrm{Nu} = x(T_z)_w/(T_\infty - T_w) = (\mathrm{Re}_x)^{1/2}(g_\eta + 2A_1x_1G_\eta)_w \tag{6c}$$

where

$$\tau_x = \mu(u_z)_w, \quad \tau_y = \mu(v_z)_w, \quad A_1 = \alpha L/a,$$
$$x_1 = x/L, \quad (u_{e0})_{t^*=0} = ax. \tag{6d}$$

Here $(u_{e0})_{t^*=0}$ is the velocity at the edge of the boundary layer for the symmetric flow at $t^* = 0$; τ_x and τ_y are the wall shear stresses in the x and y-directions, respectively; C_f and $\overline{C}_f$ are the skin-friction coefficients in the x and y-directions, respectively; L is the characteristic length; Nu is the Nusselt number which represents heat transfer; and x_1 is the dimensionless longitudinal distance. A_1 is the dimensionless parameter which determines the asymmetry of the flow and it can be determined experimentally. For example, Donaldson and Snedeker [17] have found that for an axisymmetric jet incident at an angle of 60° on an infinite plate, $A_1 = 1$.

Results and Discussion

The set of equations (3) under conditions (4) and (5) has been solved numerically using an implicit finite-difference scheme. Since the detailed description of the method is given by Marvin and Sheaffer [12], its description is not repeated here. Here we have considered two separate unsteady free-stream velocity distributions:

1 $\varphi(t^*) = 1 + t^*$ which corresponds to the case of a body fixed in a stream flowing initially with a constant velocity and then, at a certain instant $t^* = 0$, starting to flow with a constant acceleration.

2 $\varphi(t^*) = 1 + \epsilon \sin(\omega^* t^*)$ which corresponds to the case of a body fixed in a stream fluctuating with a frequency ω^* about a steady mean.

We have also taken the unsteady wall temperature distribution as $R(t^*) = 1 + \epsilon_1 t^*$ which implies that the body has a constant temperature initially and then at a certain instant $t^* = 0$, it (wall temperature) begins to change at a constant rate. Here ϵ and ϵ_1 are small positive constants and ω^* is the frequency parameter.

Computations have been carried out for various values of the parameters $c(-1 \leq c \leq 1)$ and $A(-0.5 \leq A \leq 0.5)$ with $\sigma = 0.72$, $\epsilon = 0.1$, $\epsilon_1 = 0.05$, and $\omega^* = 5.6$. To insure the convergence of the finite-difference scheme to the true solution, several values of step size were utilized. The results presented in subsequent figures are independent of step size within at least 3 significant digits. In order to test the accuracy of the method, we have compared our skin-friction and heat-transfer results for the steady symmetric flow with those of Chao and

Downloaded 01 May 2010 to 171.66.16.243. Redistribution subject to ASME license or copyright; see http://www.asme.org/terms/Terms_Use.cfm

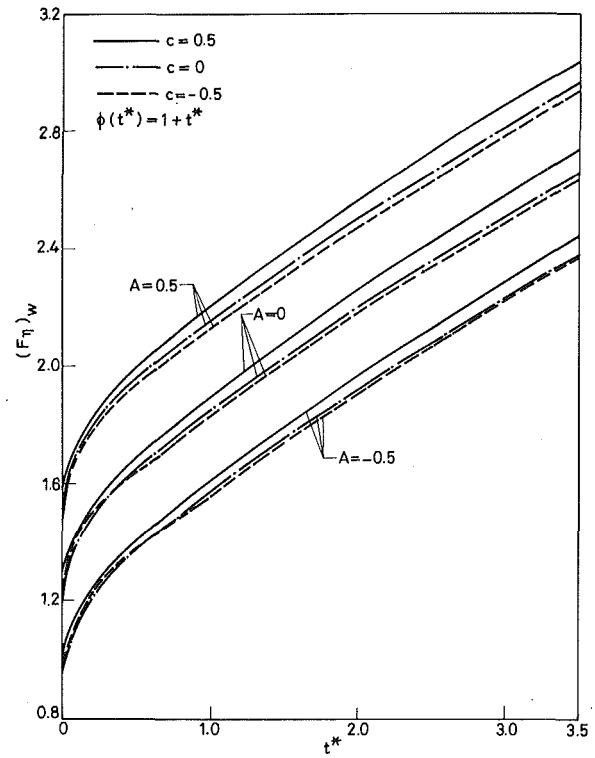

Fig. 1 Skin-friction parameter in the x-direction due to symmetric flow $(F_\eta)_w$ for $\varphi(t^*) = 1 + t^*(t^* \geq 0)$

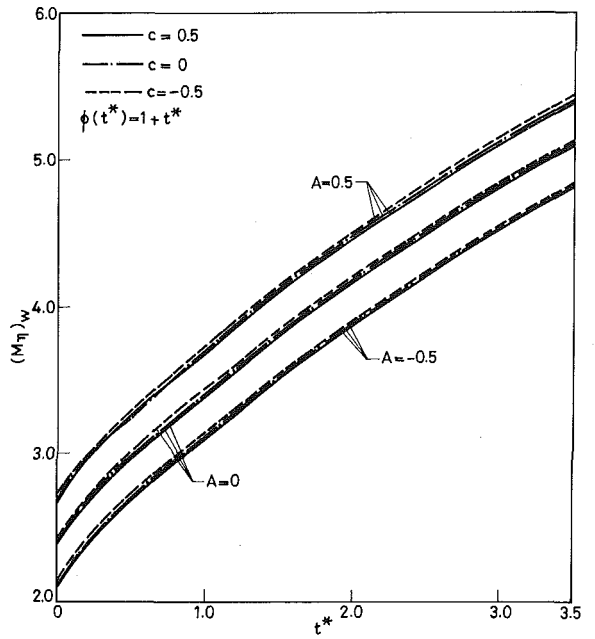

Fig. 2 Skin-friction parameter in the x-direction due to asymmetric flow $(M_\eta)_w$ for $\varphi(t^*) = 1 + t^*(t^* \geq 0)$

Jeng [9], Jeng, et al. [10], Howarth [13], Davey [14], and Hayday and Bowlus [15] and for the steady asymmetric flow with those of Lesin [16] and found them in excellent agreement. The results for the case $\varphi(t^*) = 1 + t^*$ are given in Figs. 1–10 and for the case $\varphi(t^*) = 1 + \epsilon \sin(\omega^* t^*)$ in Figs. 11–15.[1]

[1] The results for $c = 1$ and -1 may be obtained from the authors.

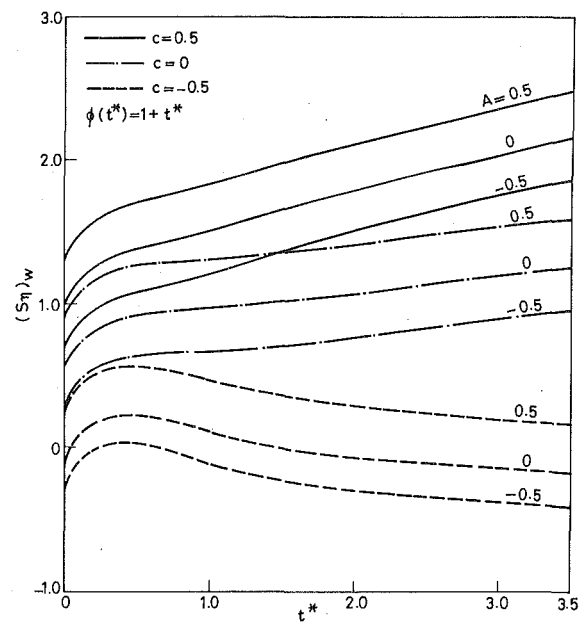

Fig. 3 Skin-friction parameter in the y-direction due to symmetric flow $(S_\eta)_w$ for $\varphi(t^*) = 1 + t^*(t^* \geq 0)$

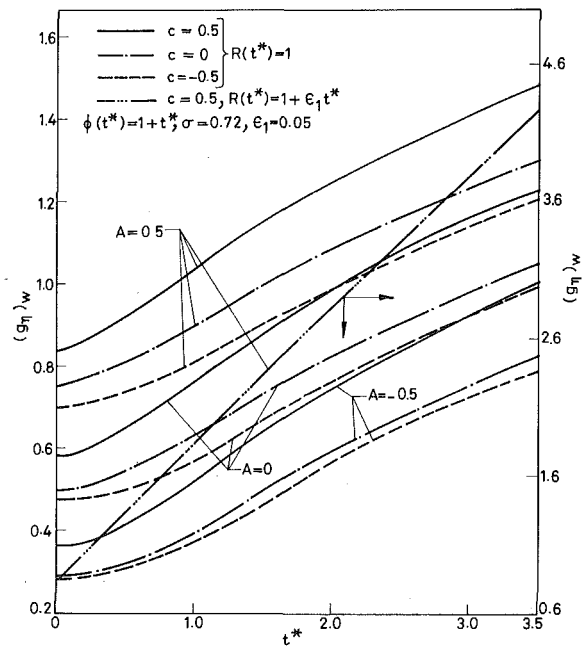

Fig. 4 Heat-transfer parameter due to symmetric flow $(g_\eta)_w$ for $\varphi(t^*) = 1 + t^*(t^* \geq 0)$

The skin-friction parameters $(F_\eta)_w$, $(M_\eta)_w$, and $(S_\eta)_w$ and the heat-transfer parameters $(g_\eta)_w$ and $(G_\eta)_w$ for some values of the parameters are shown in Figs. 1–5. These figures indicate that $(F_\eta)_w$, $(M_\eta)_w$, $(S_\eta)_w$, $(g_\eta)_w$, and $(G_\eta)_w$ all increase as the dimensionless time t^* increases (in some cases after certain time) whatever may be the values of the mass transfer parameter A or the parameter characterizing the nature of the stagnation point c except $(S_\eta)_w$ which for $c < 0$ first increases and then decreases as t^* increases. It is also observed that for $t^* \geq 1$, $(M_\eta)_w$ decreases as c increases irrespective of the values of A. As expected the effect of suction $(A > 0)$ is to increase the skin friction and heat transfer and the effect of injection is just the reverse. The effect of mass transfer is more pronounced on $(F_\eta)_w$, $(S_\eta)_w$, and $(g_\eta)_w$ than on $(M_\eta)_w$ and $(G_\eta)_w$. Furthermore, it is also

Downloaded 01 May 2010 to 171.66.16.243. Redistribution subject to ASME license or copyright; see http://www.asme.org/terms/Terms_Use.cfm

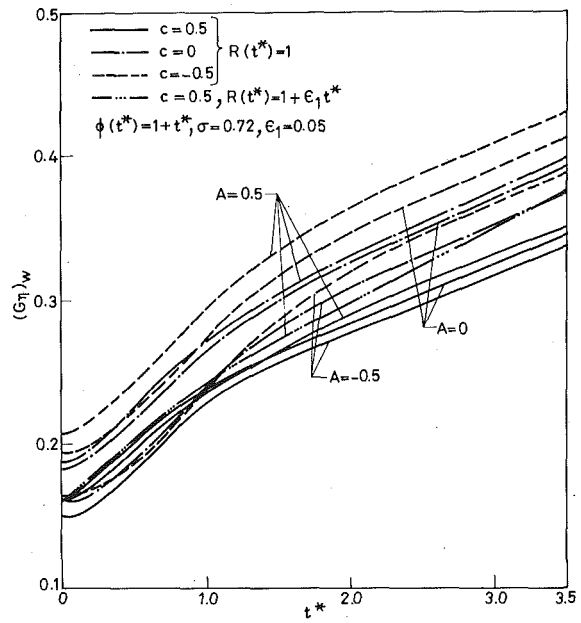

Fig. 5 Heat-transfer parameter due to asymmetric flow $(G_\eta)_w$ for $\varphi(t^*) = 1 + t^*(t^* \geq 0)$

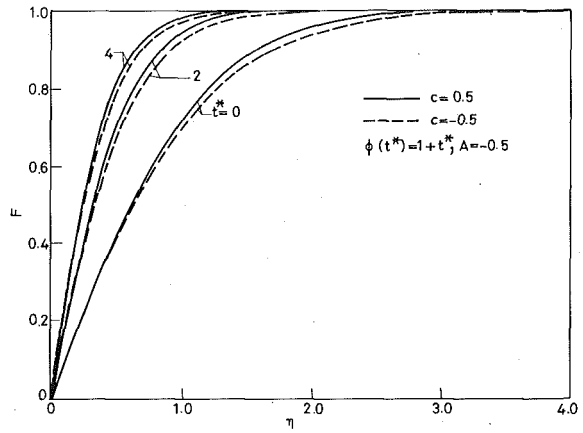

Fig. 6 Velocity in the x-direction due to symmetric flow F for $\varphi(t^*) = 1 + t^*(t^* \geq 0)$

found that for all values of t^* and A, $(F_\eta)_w$, $(M_\eta)_w$, $(S_\eta)_w$, and $(g_\eta)_w$ decrease as c decreases until at some negative c, $(S_\eta)_w$ is reversed and $(F_\eta)_w$, $(M_\eta)_w$, and $(g_\eta)_w$ begin to increase as c decreases but the behavior of $(G_\eta)_w$ is just the reverse (they are not shown here for the sake of brevity[2]). Similar trend has also been observed by Davey [14] for the steady symmetric flow case. The variation of the wall temperature with t^* strongly affects the heat transfer $(g_\eta)_w$. Some representative velocity and temperature profiles (F, M, S, g, G) are shown in Figs. 6–10. It is evident from these fitures that F, S, and g become more steep as t^* or A or c increases. In addition, the profiles M has velocity overshoot and it increases as the rate of injection ($A < 0$) increases or c decreases. Furthermore, G profiles first increase, attain a maximum, then decrease to zero as η increases. This maximum value increases as c decreases.

The skin-friction and heat-transfer results for the oscillatory free-stream velocity distribution $\varphi(t^*) = 1 + \epsilon \sin(\omega^* t^*)$ are presented

[2] They may be obtained from the authors.

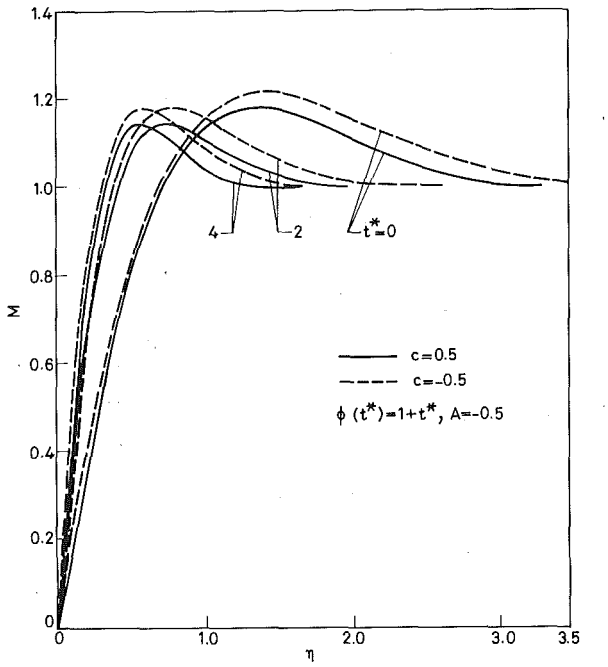

Fig. 7 Velocity in the x-direction due to asymmetric flow M for $\varphi(t^*) = 1 + t^*(t^* \geq 0)$

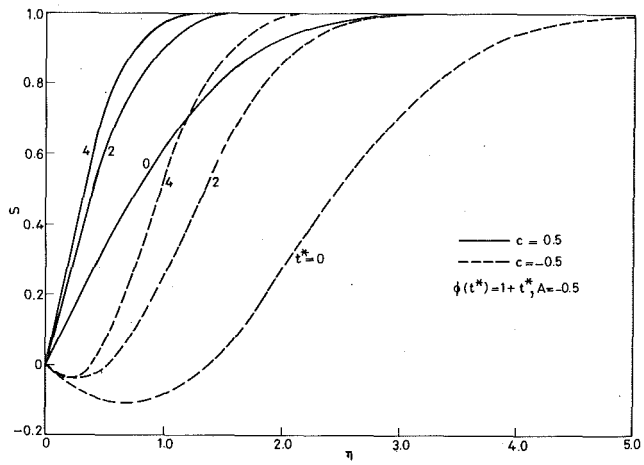

Fig. 8 Velocity in the y-direction due to symmetric flow S for $\varphi(t^*) = 1 + t^*(t^* \geq 0)$

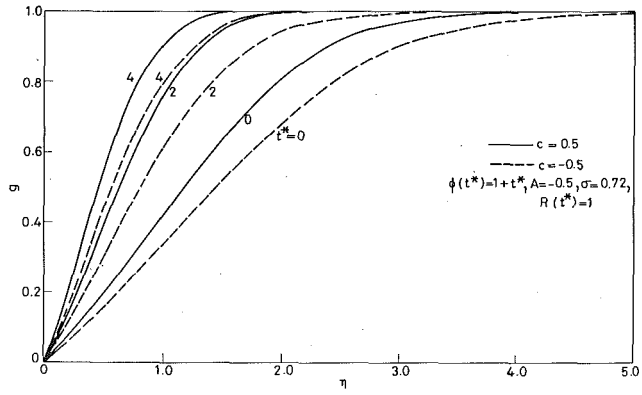

Fig. 9 Temperature due to symmetric flow g for $\varphi(t^*) = 1 + t^*(t^* \geq 0)$

Downloaded 01 May 2010 to 171.66.16.243. Redistribution subject to ASME license or copyright; see http://www.asme.org/terms/Terms_Use.cfm

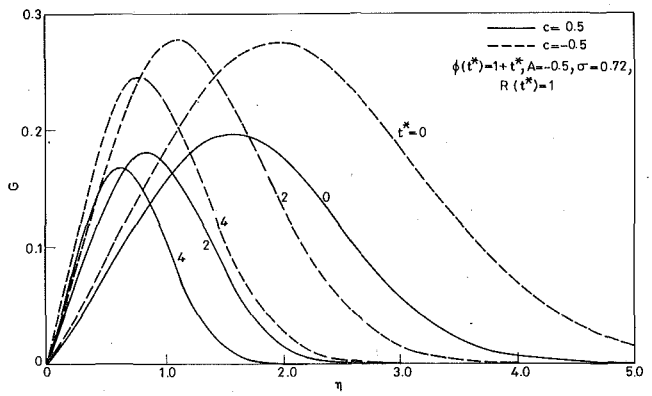

Fig. 10 Temperature due to asymmetric flow G for $\varphi(t^*) = 1 + t^*(t^* \geqslant 0)$

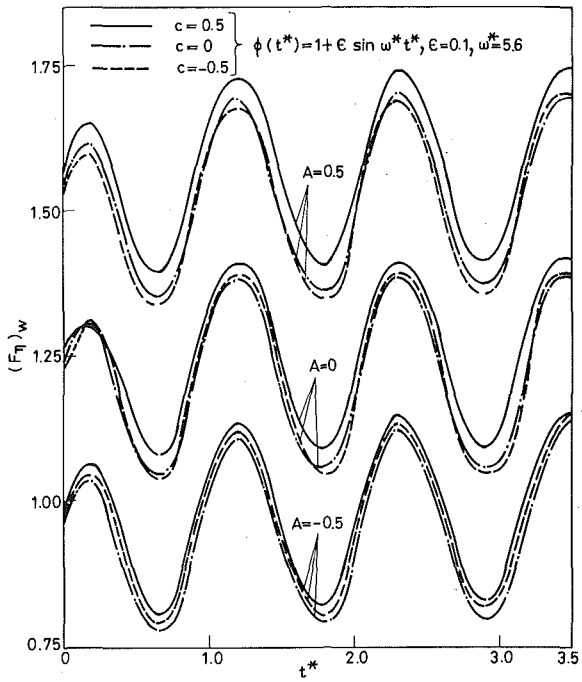

Fig. 11 Skin-friction parameter in the x-direction due to symmetric fow $(F_\eta)_w$ for $\varphi(t^*) = 1 + \epsilon \sin(\omega^* t^*)(t^* \geqslant 0)$

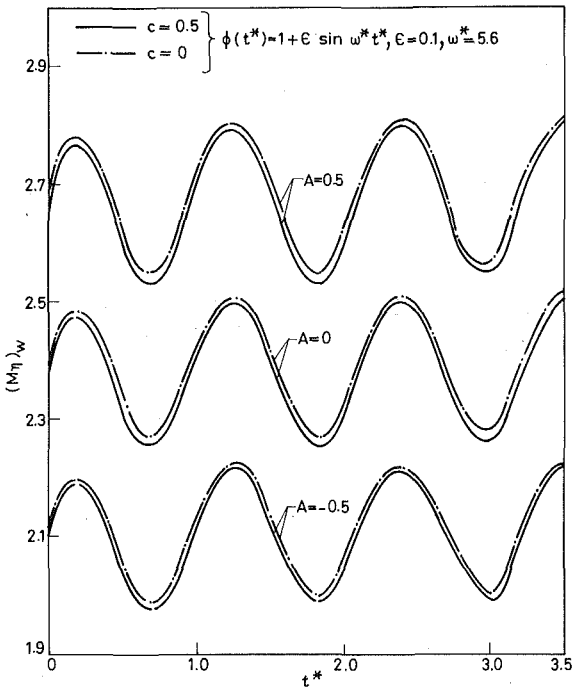

Fig. 12 Skin-friction parameter in the x-direction due to asymmetric flow $(M_\eta)_w$ for $\varphi(t^*) = 1 + \epsilon \sin(\omega^* t^*)(t^* \geqslant 0)$

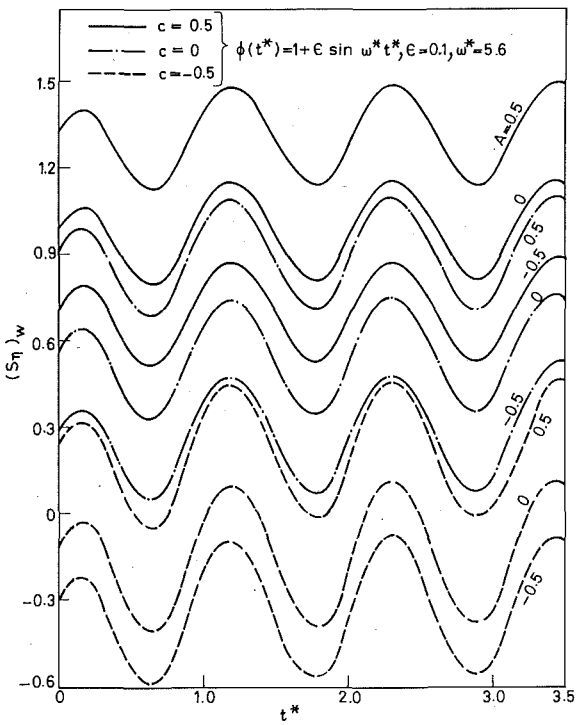

Fig. 13 Skin-friction parameter in the y-direction due to symmetric flow $(S_\eta)_w$ for $\varphi(t^*) = 1 + \epsilon \sin(\omega^* t^*)(t^* \geqslant 0)$

in Figs. 11–15. It is clear from these figures that the parameters $(F_\eta)_w$, $(M_\eta)_w$, $(S_\eta)_w$, and $(G_\eta)_w$ respond more to the free-stream velocity distribution than $(g_\eta)_w$ whatever may be the values of c. However, $(g_\eta)_w$ is more sensitive to the variation of the wall temperature with time. The skin friction and heat transfer are strongly influenced by the parameters A and c except that the effect of c on $(F_\eta)_w$ is comparatively small. It may be noted that for both $\varphi(t^*) = 1 + t^*$ and $\varphi(t^*) = 1 + \epsilon \sin(\omega t^*)$ there is a transient response to the sudden change at $t^* = 0$ which is distinguishable from the long-term effect which appears to have set in by $t^* \geqslant 1.0$.

Finally, we also find that in contrast with the symmetric flow, the maximum heat transfer occurs away from the stagnation point due to the decrease in the boundary-layer thickness (for example, in two-dimensional case it occurs at the leading edge of an airfoil at an angle of attack) whatever may be the values of t^*, A, and c. Similar behavior has also been observed by Lesin [16] for the steady-state case. Since our unsteady solutions for symmetric flow are different from those of Srivastava [7], Ishigaki [8], and Ghoshal and Ghoshal [11] (the reasons were mentioned earlier), it was not possible to compare our results with their results. It may be noted that Chao and Jeng [9] and Jeng, et al. [10], studied the effect of step change in wall temperature on the thermal boundary layer and here we have considered the effect of the continuous variation of the wall temperature and free-stream velocity with time on the boundary layer. Hence we could not compare our unsteady results for heat transfer with the results obtained by them for $c = 0$ and 1.

It may be remarked that the present analysis is also relevant to the

Downloaded 01 May 2010 to 171.66.16.243. Redistribution subject to ASME license or copyright; see http://www.asme.org/terms/Terms_Use.cfm

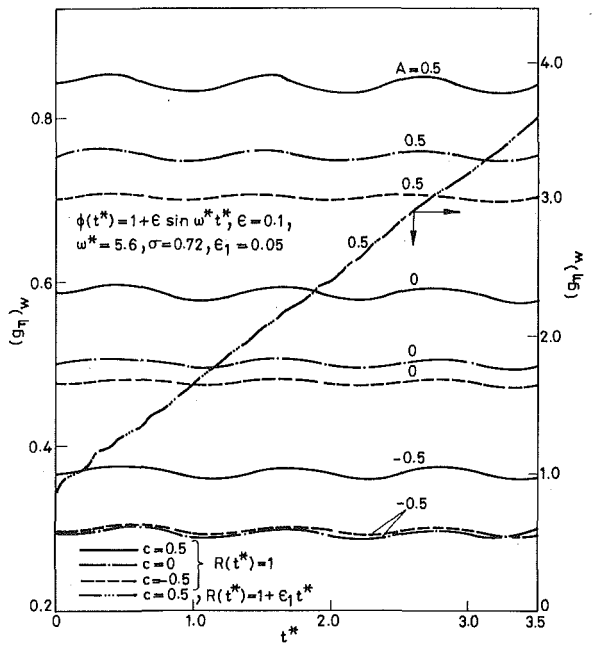

Fig. 14 Heat-transfer parameter due to symmetric flow $(g_\eta)_w$ for $\varphi(t^*) = 1 + \epsilon \sin(\omega^* t^*)(t^* \geq 0)$

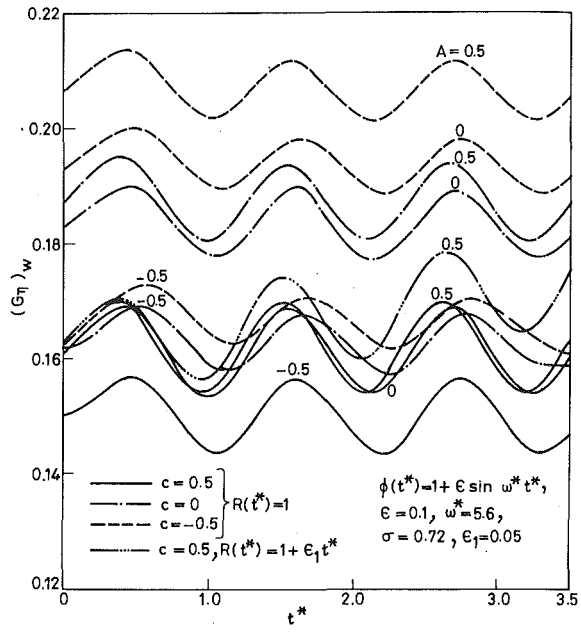

Fig. 15 Heat-transfer parameter due to asymmetric flow $(G_\eta)_w$ for $\varphi(t^*) = 1 + \epsilon \sin(\omega^* t^*)(t^* \geq 0)$

jet problem (i.e., when an incompressible jet is incident at an angle θ on an infinite plate). For example, the heat transfer (Nusselt number) for the jet can be predicted by (6c) with $A_1 = (\pi/2)(\cos\theta/\sin^2\theta)$, where $\theta(\theta \neq 0 \text{ or } \pi)$ is the angle of incidence of the jet on an infinite plate [18].

Conclusions

It is observed from the results that in contrast with the symmetric flow, the maximum heat transfer occurs away from the stagnation point due to the decrease in the boundary-layer thickness whatever may be the values of the mass transfer and the nature of the stagnation point. The effect of mass transfer on the skin friction and heat transfer which is due to asymmetric flow only (i.e., $(M_\eta)_w$ and $(G_\eta)_w$) is less pronounced as compared to those of symmetric flow (i.e., $(F_\eta)_w$, $(S_\eta)_w$, and $(g_\eta)_w$). The longitudinal velocity profiles due to asymmetric flow $(M(\eta)$ have velocity overshoot which increases as the rate of injection increases. The variation of the wall temperature with time has strong effect on the heat transfer. Both skin-friction and heat-transfer results are strongly influenced by the unsteady free-stream velocity distributions.

References

1 Stuart, J. T., "Unsteady Boundary Layers," *Recent Research of Unsteady Boundary Layers*, Eichelbrenner, E. A., ed., Vol. 1, University of Arizona, Tucson, 1971, pp. 1–46.

2 Riley, N., "Unsteady Laminar Boundary Layers," *SIAM Review*, Vol. 17, No. 2, Apr. 1975, pp. 274–297.

3 Telionis, D. P., "Calculations of Time-Dependent Boundary Layers," *Unsteady Aerodynamics*, Kinney, R. B., ed., Vol. 1, Laval University Press, Quebec, 1975, pp. 155–190.

4 Moore, F. K., "Unsteady Laminar Boundary Layer Flow," NACA Tech. Note 2471, 1951.

5 Lighthill, M. J., "The Response of Laminar Skin Friction and Heat Transfer to Fluctuations in the Stream Velocity," *Proceedings of the Royal Society*, London, Series A, Vol. 224, No. 1156, June 1954, pp. 1–23.

6 Lin, C. C., "Motion in the Boundary Layer With a Rapidly Oscillating External Flow," *Proceedings of the 9th International Congress of Applied Mechanics*, Brussels, Vol, 4, 1956, pp. 155–169.

7. Srivastava, A. C., "Note on Fluctuating Flow Near a Stagnation Point," *Journal of Fluid Mechanics*, Vol. 20, Part 3, Nov. 1964, pp. 411–416.

8 Hiroshi, I., "Periodic Boundary Layer Near a Two-Dimensional Stagnation Point," *Journal of Fluid Mechanics*, Vol. 43, Part 3, Sept. 1970, pp. 477–486.

9 Chao, B. T., and Jeng, D. R. "Unsteady Stagnation Point Heat Transfer," ASME *Journal of Heat Transfer*, Vol. 87, No. 2, May 1965, pp. 221–230.

10 Jeng, D. R., Lee, M. H., and Dewitt, K. J., "The Final Approach to Steady State in Nonsteady Stagnation-Point Heat Transfer," *Journal of Engineering Mathematics*, Vol. 10, No. 2, Apr. 1976, pp. 173–185.

11 Ghoshal, S., and Ghoshal, A., "Thermal Boundary-Layer Theory Near the Stagnation Point on Three-Dimensional Fluctuating Flow," *Journal of Fluid Mechanics*, Vol. 43, Part 3, Sept. 1970, pp. 465–476.

12 Marvin, J. G., and Sheaffer, Y. S., "A Method for Solving Nonsimilar Laminar Boundary-Layer Equations Including Foreign Gas Injection," NACA Tech. Note D-5516, 1969.

13 Howarth, L., "The Boundary Layer on Three-Dimensional Flow, Part 2. The Flow Near a Stagnation Point," *Philosophical Magazine*, Series 7, Vol. 42, No. 335, Dec. 1951, pp. 1433–1440.

14 Davey, A., "Boundary-Layer Flow at a Saddle Point of Attachment," *Journal of Fluid Mechanics*, Vol. 10, Part 4, June 1961, pp. 593–610.

15 Hayday, A. A., and Bowlus, D. A., "Integration of Coupled Nonlinear Equations in Boundary-Layer Theory With Specific Reference to Heat Transfer Near the Stagnation-Point in Three-Dimensional Flow," *International Journal of Heat and Mass Transfer*, Vol. 10, No. 4, Apr. 1967, pp. 415–426.

16 Lesin, A. B., "Laminar Heat Transfer Near an Asymmetric Stagnation Point," *Journal of Fluid Dynamics* (translated from Russian), Vol. 11, No. 6, Nov.–Dec. 1976, pp. 940–945.

17 Donaldson, C. D., and Snedeker, R. C., "A Study of Free Jet Impingement, Part 1. Mean Properties of Free and Impinging Jets," *Journal of Fluid Mechanics*, Vol. 45, Part 2, Jan. 1971, pp. 281–320.

18 Birkhoff, G., and Zarantonello, E. H., *Jets, Wakes, and Cavities*, Academic Press, New York, 1957.

Downloaded 01 May 2010 to 171.66.16.243. Redistribution subject to ASME license or copyright; see http://www.asme.org/terms/Terms_Use.cfm

A. S. Popel
Research Associate Professor,
Department of Chemical Engineering,
University of Arizona,
Tucson, Ariz. 85721
Also, Department of Physiology,
University of Arizona College of Medicine,
Tucson, Ariz. 85724
Mem. ASME

A Model of Pressure and Flow Distribution in Branching Networks

The objective of this work is to provide a mechanical description of steady-state flow of Newtonian fluid in a branching network that consists of rigid vessels of different diameters. Solution of this problem is of importance for better understanding of the mechanics of blood flow within the microcirculation. The developed branching network model predicts a wide distribution of the hydrodynamic pressure and flow in the vessels of the same caliber (flow heterogeneity). The obtained results are compared with predictions of a simple series-parallel network model. It is shown that this model provides an accurate approximation to the values of the mean pressure and flow given by the branching network model.

Introduction

Studies of the architecture of the microcirculation reveal rather complex branching structure of the microcirculatory networks (e.g., [1–3]). During the past 15 years new techniques have been developed that made it possible to measure the velocities of red blood cells and the hydrodynamic pressure in single microvessels [4–6]. The results obtained with these techniques indicate that the flow and pressure distributions in the microcirculation are heterogeneous since the characteristics vary substantially from one vessel to another vessel of the same caliber (e.g., [7–10]). These results pose a number of fundamental questions regarding the relationship between the whole organ ("macroscopic") data and the data pertaining to single microvessels. Indeed, one can envision various processes at the microcirculation level that would not be simply translated to the macroscopic level; for example, redistribution of flow in the microvessels without affecting the mean flow. In most cases, the large number of vessels in a given area of the tissue and the complex three-dimensional structure of the system make it impossible to provide a complete experimental description of each individual vessel. A more adequate description of such a system can be given in probabilistic terms, for example, in terms of the frequency (probability) distribution functions. Some examples of experimentally obtained frequency distributions of the velocity of blood and hydrodynamic pressure can be found in [7, 10].

The distribution of pressure and flow in the network is affected by the topology of the network, dimensions of the vessels and many other factors. In order to assess the information contained in these distributions it would be desirable to develop a mathematical model of branching networks that would make it possible to calculate the frequency distributions of pressure and flow in different generations of vessels. This would provide a basis for theoretical investigation of mechanical processes in microvascular networks.

A number of models have been developed to simulate blood flow in the microcirculation. Lee and Nellis [11] considered vascular pattern of the mesentery and calculated the mean blood flow in different generations of vessels. Lipowsky and Zweifach [12] and Lipowsky [13] utilized the data on vessel geometry to develop a more detailed mathematical model of the mesenteric microcirculation, and calculated hemodynamic parameters for each of the considered vessels. Mayrovitz, et al. [14], and Mayrovitz [15] considered a comprehensive model of branching networks and made calculations of resistances and hemodynamic parameters for the vascular network of the bat wing. The calculations resulted in certain mean characteristics of flow and pressure for different generations of vessels [16].

Besides specific branching structure of the network, various other factors may contribute to the complex behavior of flow in the microvasculature among which are

1 Heterogeneous distribution of vessel dimensions (lengths, diameters) within the vessels of the same branching order.
2 Tapering of vessels along the length.
3 Non-Newtonian viscosity of blood.
4 Uneven distribution of red blood cells in the microvessels.
5 Compliance of the vascular walls.

Neither of these factors have been accounted for in the present study. It is clear that taking into account the aforementioned factors would lead to a very sophisticated mathematical model. As a starting point, however, it appears useful to investigate a more simple case of flow of Newtonian fluid in a branching network composed of rigid vessels.

Contributed by the Applied Division for publication in the JOURNAL OF APPLIED MECHANICS.
Discussion on this paper should be addressed to the Editorial Department, ASME, United Engineering Center, 345 East 47th Street, New York, N. Y. 10017, and will be accepted until September 1, 1980. Readers who need more time to prepare a discussion should request an extension from the Editorial Department. Manuscript received by ASME Applied Mechanics Division, July, 1979; final revision, January, 1980.

Copyright © 1980 by ASME
Downloaded 01 May 2010 to 171.66.16.243. Redistribution subject to ASME license or copyright; see http://www.asme.org/terms/Terms_Use.cfm

The results of the present work show that even such a simple system exhibits certain interesting properties, the mechanical interpretation of which is important for understanding of the microcirculatory function.

Geometry of the Network and Governing Equations

Consider a branching network composed of several generations of vessels (vessels of different "branching orders"). The geometry of a vessel of an ith branching order ($i = 1, 2, \ldots, n$) is illustrated in Fig. 1. It is assumed that all vessels of the same branching order are geometrically identical, and each vessel of the ith branching order consists of m_i segments (a segment is a portion of the vessel situated between two adjacent bifurcations). In this work it is assumed that vessels of the branching orders $i = 1, 2, \ldots, n-1$ terminate in two vessels of the next branching order. This geometry appears the most realistic, however, other geometries could easily be considered within the framework of this model. The vessels of the last branching order ($i = n$) consist of a single segment, hence $m_n = 1$. This description completely defines the topology of the network. The network, therefore, contains $N_i = (m_1 + 1)(m_2 + 1) \ldots (m_{i-1} + 1)$ vessels of the ith order, and consists of the total of $N = \sum_{i=1}^{n} N_i$ vessels.

Each node of the ith-order vessel, except for the terminal node, can be associated with a sequence $(i, k_i, k_{i-1}, \ldots, k_1)$, where k_i is the number of nodes preceding the given node in given vessel (including the node from which the vessel originates), and the sequence $(i-1, k_{i-1}, k_{i-2}, \ldots, k_1)$ refers to the node from which the vessel originates considered as a node pertaining to the $(i-1)$st branching order. Terminal nodes are considered as "double" nodes and two sequences are assigned to them: $(i, m_i, k_{i-1}, \ldots, k_1)$ and $(i, m_i + 1, k_{i-1}, \ldots, k_1)$. The two terminal vessels of the $(i+1)$st branching order are considered as originating from different nodes of the double node; for example, the sequences $(i+1, 1, m_i, k_{i-1}, \ldots, k_1)$ and $(i+1, 1, m_i + 1, k_{i-1}, \ldots, k_1)$ identify the second nodes of these vessels. Therefore, the introduced procedure will assign a unique sequence $(i, k_i, k_{i-1}, \ldots, k_1)$ to each node of an ith branching order if terminal nodes are considered as double nodes; in this sequence $i = 1, 2, \ldots, n$; $k_j = 1, 2, \ldots, m_j + 1$ for $1 \leqslant j \leqslant i-1$; $k_i = 0, 1, \ldots, m_i + 1$. Different sequences are assigned to any two nodes of the network. It should be noted, however, that each node is an intersection of vessels of two successive branching orders, and, therefore, can be identified by either $(i, k_i, k_{i-1}, \ldots, k_1)$ or $(i+1, 0, k_i, k_{i-1}, \ldots, k_1)$ with the former referring to the node of the ith branching order, and the latter referring to the node of the $(i+1)$st branching order. Therefore, the introduced notation is unambiguous if the branching order is specified. If a segment of the ith-order vessel has the node $(i, k_i, k_{i-1}, \ldots, k_1)$ at the end then the same sequence is assigned to this segment; the terminal segment is denoted $(i, m_i, k_{i-1}, \ldots, k_1)$.

If the segments are sufficiently long compared to their diameters, and the Reynolds numbers for flow in each segment are small then the hydrodynamic pressure is nearly constant in a cross section of the vessel, and the pressure difference between two adjacent nodes is proportional to the flow through the segment situated between the nodes; the coefficient of proportionality is the hydrodynamic resistance of the segment, [17].

The hydrodynamic pressure at the node $(i, k_i, k_{i-1}, \ldots, k_1)$ is denoted as

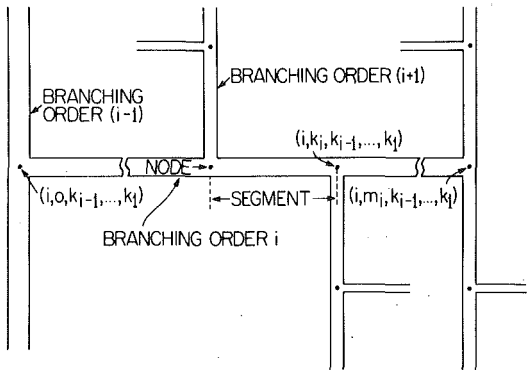

Fig. 1 Topology of the branching network; each vessel of an ith branching order consists of m_i segments

$$p_{i,k_i,k_{i-1},\ldots,k_1} \tag{1}$$

and the volumetric flow rate through the segment $(i, k_i, k_{i-1}, \ldots, k_1)$ is denoted as

$$Q_{i,k_i,k_{i-1},\ldots,k_1} \tag{2}$$

The introduced notation implies the relationships

$$p_{i,k_i,k_{i-1},\ldots,k_1} = p_{i+1,0,k_i,\ldots,k_1},$$

and

$$p_{i,m_i,k_{i-1},\ldots,k_1} = p_{i,m_i+1,k_{i-1},\ldots,k_1}.$$

Using the notations (1), (2) one can express the conservation of mass at each node in the form

$$Q_{i,k_i,k_{i-1},\ldots,k_1} = Q_{i,k_i+1,k_{i-1},\ldots,k_1} + Q_{i+1,1,k_i,\ldots,k_1} \tag{3}$$

where

$$k_j = 1, 2, \ldots, m_j + 1 \quad \text{for} \quad 1 \leqslant j \leqslant i-1;$$

$$k_i = 1, 2, \ldots, m_i - 1$$

and

$$Q_{i,m_i,k_{i-1},\ldots,k_1} = 2Q_{i+1,1,m_i,k_{i-1},\ldots,k_1} = 2Q_{i+1,1,m_i+1,k_{i-1},\ldots,k_1} \tag{4}$$

where

$$k_j = 1, 2, \ldots, m_j + 1 \quad \text{for} \quad 1 \leqslant j \leqslant i-1.$$

Using the definition of the hydrodynamic resistance, ζ_{i,k_i} and the assumption that it is independent of pressure and flow, one can write for each segment

$$p_{i,k_i-1,k_{i-1},\ldots;k_1} - p_{i,k_i,k_{i-1},\ldots,k_1} = \zeta_{i,k_i} Q_{i,k_i,k_{i-1},\ldots,k_1} \tag{5}$$

where

Nomenclature

D_{i,k_i} = segment diameter
L_i = vessel length
L_{i,k_i} = segment length
N_i = number of vessels of an ith branching order
p_a = input pressure
p_v = output pressure
$p_{i,0}$ = mean hydrodynamic pressure at the entrance of the ith branching order, equation (15)
$Q_{i,1}$ = mean flow at the entrance of the ith branching order, equation (16)
Q_i = mean flow, equation (17)
R_{i,k_i} = input hydrodynamic resistance
α = ratio of the lengths, L_i^*/L_i
ξ_{i,k_i} = hydrodynamic resistance
μ = viscosity
Φ = frequency distribution

Subscripts

i = branching order
k_j = node number

Superscript

* = pertaining to the series-parallel network model

Downloaded 01 May 2010 to 171.66.16.243. Redistribution subject to ASME license or copyright; see http://www.asme.org/terms/Terms_Use.cfm

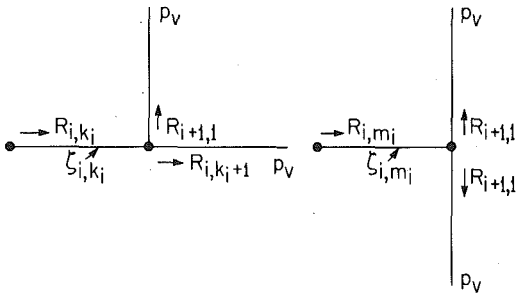

Fig. 2 A scheme illustrating the definition of the input hydrodynamic resistances for two types of bifurcations

$$k_j = 1,2, \ldots, m_j + 1 \quad \text{for} \quad 1 \leqslant j \leqslant i-1;$$
$$k_i = 1, 2, \ldots, m_i.$$

Suppose that the pressure at the entrance of the first branching order, and at the end of the last branching order are specified: $p_{1,0} = p_a$ and

$$p_{n,1,k_{n-1}, \ldots, k_1} = p_v,$$

respectively, for all possible $k_{n-1}, k_{n-2}, \ldots, k_1$, where p_a is the "arterial" pressure and p_v is the "venous" pressure. The problem is to determine the flow in every segment and the pressure at every node providing the resistances of the segments, ζ_{i,k_i}, are given. The problem (3)–(5) is linear due to the assumption that the resistance ζ_{i,k_i} is independent of the flow and pressure in the segment.

In order to obtain the solution of the problem, it is convenient to introduce auxiliary input hydrodynamic resistances analogous to those used by Mayrovitz, et al. [14], and Mayrovitz [15] in modeling vascular networks

$$p_{i,k_i-1,k_{i-1}, \ldots, k_1} - p_v = R_{i,k_i} Q_{i,k_i,k_{i-1}, \ldots, k_1} \tag{6}$$

where

$$k_j = 1, 2, \ldots, m_j + 1 \quad \text{for} \quad 1 \leqslant j \leqslant i-1;$$
$$k_i = 1, 2, \ldots, m_i.$$

For the two cases illustrated in Fig. 2, the following recurrency relationships are formulated that make it possible to compute the matrix R_{i,k_i}:

$$R_{i,k_i} = \zeta_{i,k_i} + \frac{R_{i,k_i+1} R_{i+1,1}}{R_{i,k_i+1} + R_{i+1,1}}$$
$$\text{for} \quad k_i = 1, 2, \ldots, m_i - 1 \tag{7}$$

$$R_{i,m_i} = \zeta_{i,m_i} + 0.5\, R_{i+1,1} \tag{8}$$

$$R_{n,1} = \zeta_{n,1} \tag{9}$$

Therefore, starting with known quantities $R_{n,1}$ and doing calculations in the "reverse" order using (7) and (8) one can determine $\sum_{j=1}^{n-1} m_j$ terms of the sequence

$$R_{n-1,m_{n-1}}; R_{n-1,m_{n-1}-1}; \ldots; R_{n-1,2}; R_{n-1,1};$$
$$R_{n-2,m_{n-2}}; R_{n-2,m_{n-2}-1}; \ldots; R_{n-2,2}; R_{n-2,1};$$
$$\ldots\ldots\ldots\ldots\ldots\ldots\ldots\ldots\ldots$$
$$R_{1,m_1}; R_{1,m_1-1}; \ldots; R_{1,2}; R_{1,1} \tag{10}$$

The knowledge of the input hydrodynamic resistance matrix R_{i,k_i} makes it possible to determine the flow and pressure distribution in the network using the relationships (3)–(5). Thus, for the first segment,

$$Q_{1,1} = \frac{p_a - p_v}{R_{1,1}}, \quad p_{1,1} = p_a - \zeta_{1,1} Q_{1,1} \tag{11}$$

Generally, if the flow $Q_{i,k_i-1,k_{i-1}, \ldots, k_1}$ and the pressure $p_{i,k_i-1,k_{i-1}, \ldots, k_1}$ have already been determined, the flow and pressure further downstream can be found from (4) and the following relationships:

$$Q_{i,k_i,k_{i-1}, \ldots, k_1} = \frac{R_{i+1,1}}{R_{i,k_i} + R_{i+1,1}} Q_{i,k_i-1,k_{i-1}, \ldots, k_1} \tag{12}$$

where

$$k_j = 1, 2, \ldots, m_j + 1 \quad \text{for} \quad 1 \leqslant j \leqslant i-1;$$
$$k_i = 1, 2, \ldots, m_i$$

$$Q_{i+1,1,k_i, \ldots, k_1} = \frac{R_{i,k_i+1}}{R_{i,k_i+1} + R_{i+1,1}} Q_{i,k_i,k_{i-1}, \ldots, k_1} \tag{13}$$

where

$$k_j = 1, 2, \ldots, m_j + 1 \quad \text{for} \quad 1 \leqslant j \leqslant i-1;$$
$$k_i = 1, 2, \ldots, m_i - 1$$

$$p_{i,k_i,k_{i-1}, \ldots, k_1} = p_{i,k_i-1,k_{i-1}, \ldots, k_1} - \zeta_{i,k_i} Q_{i,k_i,k_{i-1}, \ldots, k_1} \tag{14}$$

The values of indices in (14) are the same as in (12).

Certain mean values of the pressure and flow will be calculated. The mean pressure at the entrance of the vessels of the ith branching order is

$$p_{i,0} = \frac{1}{(m_{i-1}+1) \ldots (m_1+1)} \sum_{k_{i-1}=1}^{m_{i-1}+1} \cdots \sum_{k_1=1}^{m_1+1} p_{i,0,k_{i-1}, \ldots, k_1} \tag{15}$$

where the ranges of sums account for the two daughter vessels at the end of given parent vessels. The mean volumetric flow rate in the first segments of the vessels of the ith branching order is

$$Q_{i,1} = \frac{1}{(m_{i-1}+1) \ldots (m_1+1)} \sum_{k_{i-1}=1}^{m_{i-1}+1} \cdots \sum_{k_1=1}^{m_1+1} Q_{i,1,k_{i-1}, \ldots, k_1} \tag{16}$$

and the mean volumetric flow rate in the vessels of the ith branching order averaged over all segments is

$$Q_i = \frac{1}{m_i (m_{i-1}+1) \ldots (m_1+1)} \sum_{k_i=1}^{m_i} \sum_{k_{i-1}=1}^{m_{i-1}+1} \cdots \sum_{k_1=1}^{m_1+1} Q_{i,k_i,k_{i-1}, \ldots, k_1} \tag{17}$$

The conservation of mass yields

$$Q_{i,1,k_{i-1}, \ldots, k_1} = \sum_{k_i=1}^{m_i+1} Q_{i+1,1,k_i, \ldots, k_1} \tag{18}$$

where

$$k_j = 1, 2, \ldots, m_j + 1 \quad \text{for} \quad 1 \leqslant j \leqslant i.$$

Thus, from (16) and (18), it follows that

$$Q_{i+1,1} = \frac{1}{(m_i+1)} Q_{i,1} \tag{19}$$

The relationship (19) shows that the mean flow in the first segment of an $(i+1)$st-order vessel equals the mean flow in the first segment of the ith-order vessel divided by the number of daughter vessels of the $(i+1)$st-order.

Application of the averaging operators defined in (15) and (16) to equation (6) with $k_i = 1$ yields simple relationships between the mean pressure and flow and the input hydrodynamic resistance

$$p_{i,0} - p_v = R_{i,1} Q_{i,1} \tag{20}$$

Relationships (19) and (20) imply

$$p_{i,0} - p_{i+1,0} = (R_{i,1} - R_{i+1,1}/(m_i+1)) Q_{i,1} \tag{21}$$

Therefore, the quantity $R_{i,1} - R_{i+1,1}/(m_i+1)$ may be considered as an effective resistance of an "average" ith-order vessel.

Numerical Examples

For the sake of simplicity, it is assumed that the segments of the

Downloaded 01 May 2010 to 171.66.16.243. Redistribution subject to ASME license or copyright; see http://www.asme.org/terms/Terms_Use.cfm

Table 1 Geometrical parameters of the network

Branching order, i	Length, $L_i(m)$	Diameter, $D_i(m)$	Number of daughter vessels, $m_i + 1$
1	4.0×10^{-2}	97×10^{-6}	13
2	1.7×10^{-2}	52×10^{-6}	12
3	3.5×10^{-3}	19×10^{-6}	10
4	9.5×10^{-4}	7×10^{-6}	5

Table 2 Input hydrodynamic resistances, N/m^5·s

$R_{1,1}$	6.58×10^{13}	9.33×10^{13}	1.20×10^{14}
$R_{2,1}$	5.86×10^{14}	9.37×10^{14}	1.28×10^{15}
$R_{3,1}$	5.68×10^{15}	9.88×10^{15}	1.39×10^{16}
$R_{4,1}$	4.34×10^{16}	8.51×10^{16}	1.26×10^{17}
$R_{5,1}$	1.00×10^{17}	3.00×10^{17}	5.00×10^{17}

vessels are long cylindrical tubes so that the Poiseuille law is applicable; then the hydrodynamic resistance can be expressed in the form

$$\zeta_{i,k_i} = \frac{128\mu L_{i,k_i}}{\pi D^4_{i,k_i}} \tag{22}$$

Here L_{i,k_i} is the length of the segment, D_{i,k_i} is the internal diameter of the segment, and μ is the viscosity of the fluid.

A detailed experimental study of vessel dimensions was performed for the vascular network of the bat wing [1, 15]; these data are utilized here in the numerical examples. Table 1 lists the diameters D_i, the lengths L_i, and the number of daughter branches $m_i + 1$ for four successive branching orders [1, 14, 15]. These quantities are assumed to be connected to the characteristics of the segment by means of relationships: $D_{i,k_i} = D_i$, $L_{i,k_i} = L_i/m_i$, i.e., the diameters of all segments of the ith branching order are identical, and the lengths of all segments of the ith branching order are identical.

The resistances of the vessels located downstream from the forth branching order (terminal arterioles, capillaries and the venous part of the circulation) are "lumped" together, and the effective resistance of this part of the network, $R_{5,1}$, is specified. This terminal resistance is varied within the range $R_{5,1} = 10^{17} - 5 \times 10^{17}$ N/m^5·s. The range $\mu = 0.002 - 0.005$ Pa·s is chosen for viscosity of the fluid (cf. [18]).

Dimensional analysis of the problem suggests [19] that a dimensionless variable

$$\bar{p}_{i,k_i,k_{i-1},\ldots,k_1} = \frac{p_{i,k_i,k_{i-1},\ldots,k_1} - p_v}{p_a - p_v} \tag{23}$$

is independent of a particular choice of the arterial pressure p_a and the venous pressure p_v. The form (23) is used in this study for presentation of the pressure distributions.

Some comments should be made regarding the form of presentation of the results. The number of vessels considered in this particular example is substantial; indeed, there are $N_5 = 13 \times 12 \times 10 \times 5 = 7800$ vessels of the 5th branching order. However, the large volume of data makes it difficult to assess the information pertaining to each individual vessel. Therefore, it is convenient to introduce frequency distribution functions in the following manner. Consider a sequence $\{A_j\}$, $j = 1, 2, \ldots, M$ and let $A_{\min}$ and $A_{\max}$ be the minimum and maximum values of A_j in this sequence. If M_l is the number of terms that satisfy the inequality

$$A_{\min} + \frac{A_{\max} - A_{\min}}{10}(l-1) \leqslant A_j < A_{\min} + \frac{A_{\max} - A_{\min}}{10} l, \quad l = 1, 2, \ldots, 10 \tag{24}$$

with a fixed value of l (the term $A_j = A_{\max}$ is included into the last interval) then the frequency distribution of the quantity A is defined as

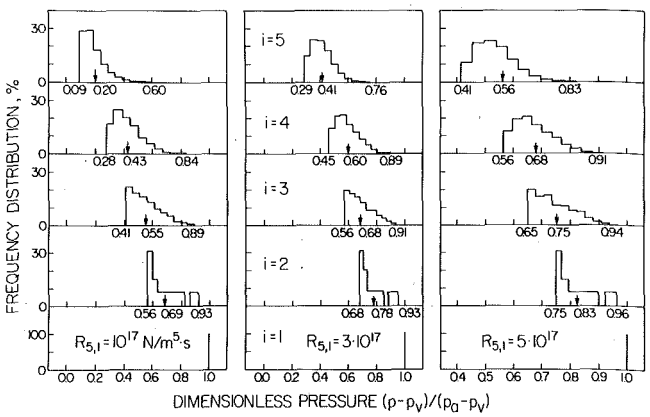

Fig. 3 Frequency distributions of the dimensionless hydrodynamic pressure at the entrance of the vessels,

$$\Phi(\bar{P}_{l,0,k_{i-1},\ldots,k_1}),$$

$l = 1, 2, 3, 4, 5$ for $\mu = 3 \times 10^{-3}$ Pa·s and $R_{5,1} = 10^{17}$, 3×10^{17} and 5×10^{17} N/m^5·s. Vertical arrows indicate the mean values of pressure $\bar{p}_{l,0}$; also shown are the minimum and maximum values of the pressure for each branching order.

$$\Phi(A_j) = 100\, M_l/M \tag{25}$$

The calculations are done in the following order. First, the resistances ζ_{i,k_i} are calculated using the relationships (22), then the matrix of input resistances R_{i,k_i} is computed using the relationships (7)–(9). Finally, the hydrodynamic pressures at all nodes of the network, and the volumetric flow rates through all segments were calculated using the relationships (12)–(14) and (4) and stored in the computer; then these data were utilized in calculations of the frequency distribution functions for pressure and flow.

Table 2 presents the calculated values of $R_{i,1}$ for three different values of the terminal resistance $R_{5,1}$, and the viscosity $\mu = 0.003$ Pa·s. Knowing $R_{1,1}$ one can calculate the total flow through the network, $Q_{1,1}$, in terms of the difference of the input and output pressures using the relationship (11), and then calculate the mean flow for all branching orders, $Q_{i,1}$, using the relationship (19).

Fig. 3 shows the frequency distributions of the dimensionless hydrodynamic pressure at the entrance of the vessels,

$$\Phi(\bar{p}_{i,0,k_{i-1},\ldots,k_1}),$$

for $\mu = 0.003$ Pa·s, and $R_{5,1} = 10^{17}$, 3×10^{17}, and 5×10^{17} N/m^5·s. Arrows indicate the mean values $\bar{p}_{i,0}$ defined by the relationships (15) and (23). The frequency distributions for an ith branching order are based on $N_i = (m_1 + 1)(m_2 + 1)\ldots(m_{i-1} + 1)$ values of pressure. The range of variation of the entrance hydrodynamic pressures in the vessels of the same branching order is substantial and reaches as much as 0.5 on the dimensionless scale. The frequency distribution of pressure may undergo qualitative changes with variation of the terminal resistance $R_{5,1}$. Indeed, the distribution

$$\Phi(\bar{p}_{5,0,k_{i-1},\ldots,k_1})$$

in Fig. 3 (left panel) is skewed to the left which means that a large fraction of vessels have low entrance pressure, whereas the distribution corresponding to a higher terminal resistance (right panel), is more "symmetrical" with respect to the mean pressure $\bar{p}_{5,0}$.

Fig. 4 depicts the quantity $\bar{p}_{5,0}$. It shows that variation of viscosity of fluid significantly affects the pressure distribution. Thus it could be expected that non-Newtonian behavior of fluid would have an impact on the pressure and flow distribution in the network.

The relationship (6) yields

$$Q_{i,1,k_{i-1},\ldots,k_1} = \frac{p_{i,0,k_{i-1},\ldots,k_1} - p_v}{R_{i,1}} \tag{26}$$

which implies that the shape of the frequency distribution of flow

Downloaded 01 May 2010 to 171.66.16.243. Redistribution subject to ASME license or copyright; see http://www.asme.org/terms/Terms_Use.cfm

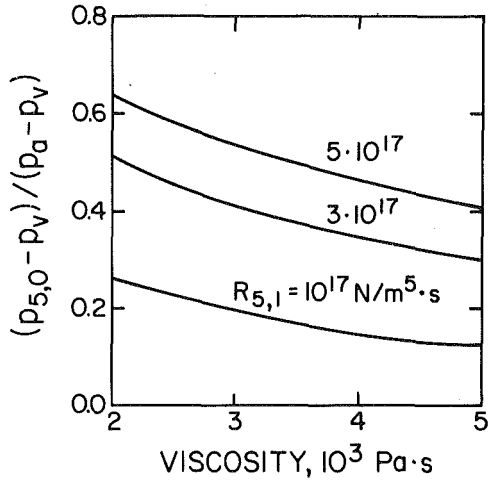

Fig. 4. The dimensionless mean pressure at the entrance of the 5th-order vessels for different values of the viscosity μ, and of the terminal resistance $R_{5,1}$

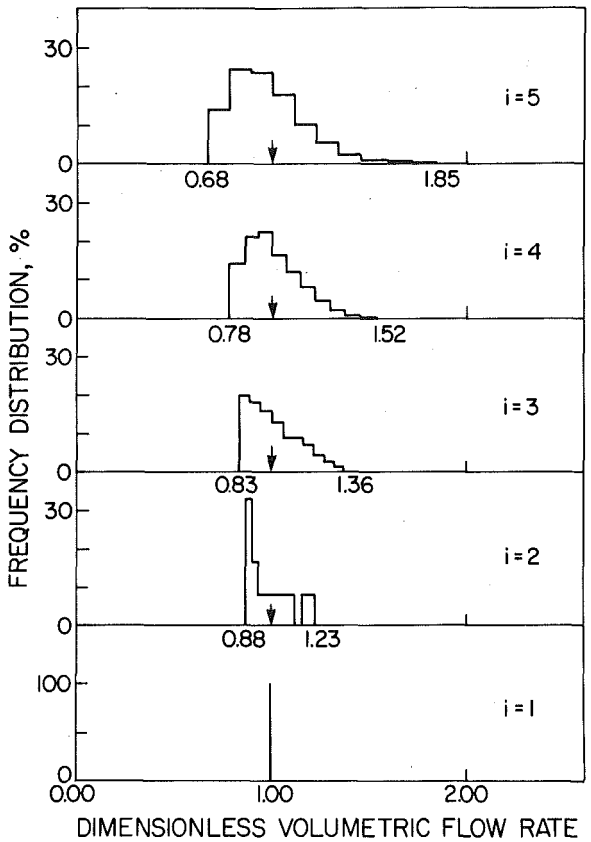

Fig. 5 Frequency distributions of the dimensionless volumetric flow rate at the entrance of the vessels,

$$\Phi(Q_{i,1,k_{i-1},\ldots,k_1}/Q_{i,1})$$

for $\mu = 0.003$ Pa·s and $R_{5,1} = 3 \times 10^{17}$ N/m^5·s. Vertical arrows indicate the dimensionless mean flow, which is equal to unity.

through the first segments of the vessels is similar to the shape of the corresponding frequency distributions of the entrance pressure. Fig. 5 shows the frequency distribution of dimensionless flow at the entrance of the vessels

$$\Phi(Q_{i,1,k_{i-1},\ldots,k_1}/Q_{i,1})$$

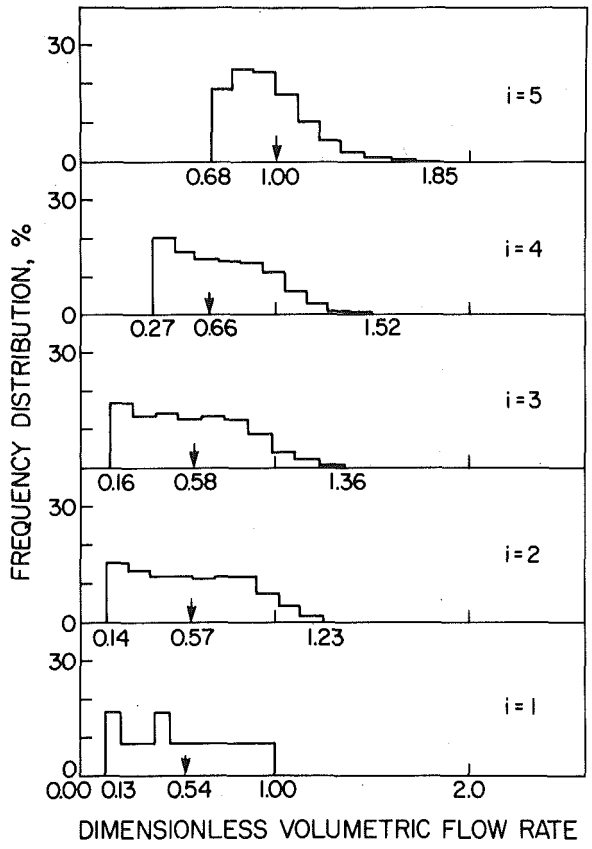

Fig. 6 Frequency distributions of the dimensionless volumetric flow rate,

$$\Phi(Q_{i,k_i,k_{i-1},\ldots,k_1}/Q_{i,1}),$$

for $\mu = 0.003$ Pa·s and $R_{5,1} = 3 \times 10^{17}$ N/m^5·s. Vertical arrows indicate the dimensionless mean flow, which is equal to unity.

normalized for each branching order by the mean flow $Q_{i,1} = (p_a - p_v)/R_{1,1}N_i$, for $R_{5,1} = 3 \times 10^{17}$ N/m^5·s, and $\mu = 0.003$ Pa·s. Note that with such scaling of flow, the distribution of flow becomes wider as the branching order i increases; the dimensionless mean flow is equal to unity. Clearly, the distribution of flow

$$Q_{i,k_i,k_{i-1},\ldots,k_1}$$

in all segments k_i is substantially more heterogeneous than the distribution of flow at the entrance of the vessels,

$$Q_{i,1,k_{i-1},\ldots,k_1}$$

because the loss of fluid into the daughter branches leads to diminution of flow in successive segments of the parent vessel. Fig. 6, which depicts the frequency distribution

$$\Phi(Q_{i,k_i,k_{i-1},\ldots,k_1}/Q_{i,1}),$$

illustrates this difference (compare with Fig. 5). The ratio $Q_i/Q_{i,1}$, where the mean flow Q_i is defined by (17), is also shown for each distribution.

Comparison Between the Branching Network Model and a Series-Parallel Network Model

The results of the previous paragraph manifest that the calculated flow and pressure in the vessels of the same branching order vary within rather wide range from one vessel to another. Of course, this variation cannot be predicted if one considers a model illustrated in Fig. 7 with series-parallel arrangement of the vessels, where the vessels of the same branching order are arranged in parallel, and the vessels of different orders are arranged in series. Such a model yields homo-

Downloaded 01 May 2010 to 171.66.16.243. Redistribution subject to ASME license or copyright; see http://www.asme.org/terms/Terms_Use.cfm

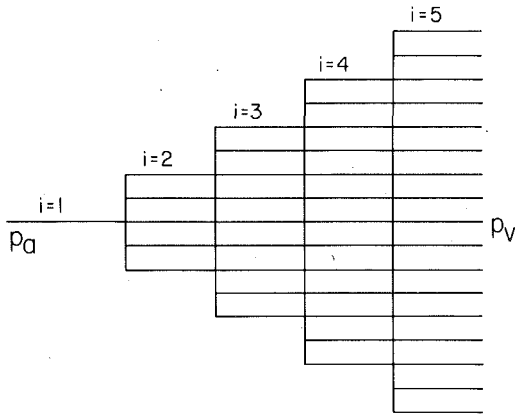

Fig. 7 Topology of the series-parallel network; vessels of the same branching order are arranged in parallel, and vessels of different branching orders are arranged in series

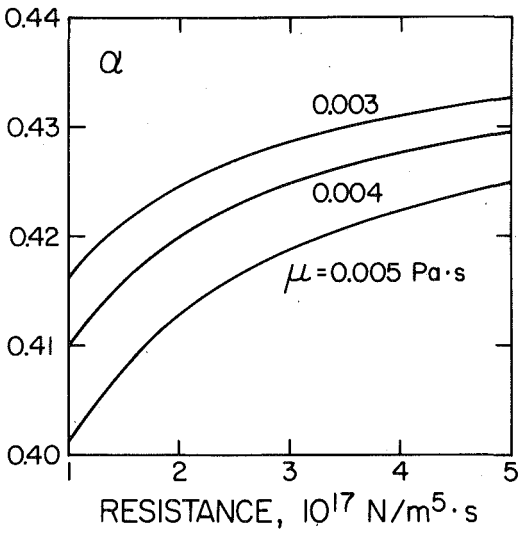

Fig. 8 Dimensionless parameter $\alpha = L_i^*/L_i$ for different values of μ and $R_{5,1}$

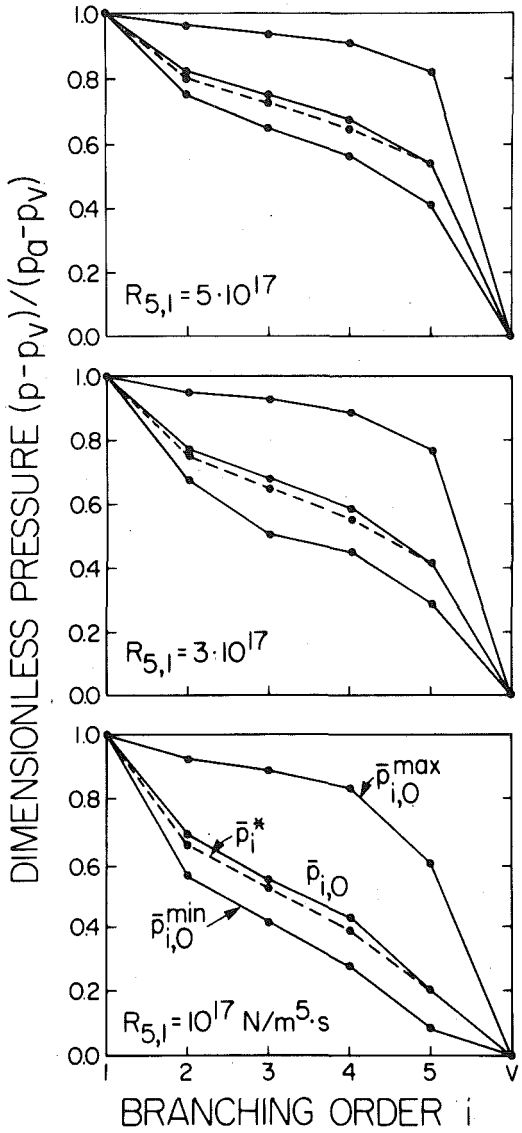

Fig. 9 Distributions of the dimensionless mean pressure $\bar{p}_{i,0}$, the maximum pressure $\bar{p}_{i,0}^{max}$ and the minimum pressure $\bar{p}_{i,0}^{min}$ throughout the network (solid lines) calculated within the framework of the branching network model, and the distributions of $\bar{p}_i^*$ (dotted lines) calculated within the framework of the series-parallel network model, for $\mu = 3 \times 10^{-3}$ Pa·s

geneous flow in vessels of the same branching order. Nevertheless, this model has long been used as an aid in interpretation of experimental data (e.g., [20]). At this point, it is of interest to find out if the values of the mean pressure and flow predicted by the branching network model as described in the preceding paragraphs, could be predicted with a reasonable accuracy by the series-parallel network model.

Consider a network shown in Fig. 7 with the following parameters pertaining to a branching order i: diameter of the vessel D_i, length of the vessel $L_i^* = \alpha L_i$, and number of "parallel" vessels N_i. Therefore, instead of the actual length L_i, an effective length L_i^* is used, where the ratio $\alpha = L_i^*/L_i$ is independent of the branching order i. A condition will be formulated below leading to determination of the parameter α. The hydrodynamic resistance of a single vessel of the ith branching order is calculated as

$$\zeta_i^* = 128\,\mu L_i^*/\pi D_i^4, \quad i = 1, 2, 3, 4 \tag{27}$$

The total flow through the network is then given by

$$Q_1^* = \frac{p_a - p_v}{128\,\mu\alpha\pi^{-1}\sum_{j=1}^{4} L_j D_m^{-4} N_j^{-1} + R_{5,1}N_5^{-1}} \tag{28}$$

The flow through a single vessel of the ith branching order is

$$Q_i^* = Q_1^*/N_i \tag{29}$$

The pressure at the entrance of the ith branching order is

$$p_i^* = p_a - (p_a - p_v)\frac{128\,\mu\alpha\pi^{-1}\sum_{j=1}^{i-1} L_j D_j^{-4} N_j^{-1}}{128\,\mu\alpha\pi^{-1}\sum_{j=1}^{4} L_j D_j^{-4} N_j^{-1} + R_{5,1}N_5^{-1}} \tag{30}$$

It is proposed here to determine the parameter α from the condition that the total flow through the network Q_1^* be equal to the total flow $Q_{1,1}$ given by equation (11), or, in other words, that the total resistance of the series-parallel network be equal to the input resistance $R_{1,1}$ of the branching network as defined by (6). This condition yields

$$\alpha = \frac{R_{1,1} - R_{5,1}N_5^{-1}}{128\,\mu\pi^{-1}\sum_{j=1}^{4} L_j D_j^{-4} N_j^{-1}} \tag{31}$$

As follows from the relationships (19) and (31), the equality $Q_1^* = Q_{1,1}$ implies $Q_i^* = Q_{i,1}$ for $i = 2, 3, 4, 5$, thus the mean flow in the

Downloaded 01 May 2010 to 171.66.16.243. Redistribution subject to ASME license or copyright; see http://www.asme.org/terms/Terms_Use.cfm

vessels of any branching order for the branching network model coincides with the flow in the same branching order for the series-parallel network model. The important result is that the parameter α determined from the relationship (31) remains nearly constant despite variation of $R_{5,1}$ and μ; Fig. 8 shows that fivefold elevation of $R_{5,1}$ causes only 4 percent increase of α when $\mu = 0.002$ Pa·s, and 6 percent increase of α when $\mu = 0.005$ Pa·s.

Now, the question can be raised how well the pressure distributions (30) approximate the mean pressure distributions predicted by the branching network model. Fig. 9 shows the values of $\bar{p}_i^* = (p_i^* - p_v)/(p_a - p_v)$, together with the previously computed characteristics of the branching network model: the dimensionless mean pressure $\bar{p}_{i,0} = (p_{i,0} - p_v)/(p_a - p_v)$, the maximum pressure

$$\bar{p}_{i,0}^{\max} = \max \bar{p}_{i,0,k_{i-1},\ldots,k_1},$$

and the minimum pressure

$$\bar{p}_{i,0}^{\min} = \min \bar{p}_{i,0,k_{i-1},\ldots,k_i}.$$

The agreement between $\bar{p}_i^*$ and $\bar{p}_{i,0}$ is rather remarkable; indeed, the difference between these two quantities does not exceed 0.04 for the considered values of parameters. Equation (20) yields

$$p_{5,0} = p_v + R_{5,1}Q_{5,1} \tag{32}$$

which can be shown to coincide with p_5^* given by (30).

Therefore, the series-parallel network model with effective lengths of the vessels $L_i^* = \alpha L_i$ (with $\alpha \simeq 0.40 - 0.44$) yields the value of total flow that coincides with the total flow predicted by the branching network model, and also yields the distribution of pressure that is very close to the distribution of the mean pressure predicted by the branching network model.

Conclusion

A model of steady-state flow of Newtonian fluid in a branching network of rigid vessels has been developed. Numerical examples have shown that a specific branching structure of the network causes the pressure and flow in the vessels of the same caliber to vary within a wide range. The calculated values of the mean pressure and flow can be accurately predicted within the framework of a simple series-parallel network model. The results of this work may be useful for qualitative assessment of the experimental data on flow and pressure distribution in branching networks. The present model also provides a basis for further development of the theory, in particular accounting for non-Newtonian properties of the fluid.

Acknowledgments

This work was supported by the National Institutes of Health Grants HL-17421 and HL-23362. The author wishes to thank Shen Min Liang for the help in numerical calculations.

References

1 Wiedeman, M. P., "Dimensions of Blood Vessels From Distributing Artery to Collecting Vein," *Circulation Research*, Vol. 12, 1963, pp. 375–378.

2 Hammersen, F., "The Pattern of the Terminal Vascular Bed and Ultrastructure of Capillaries in Skeletal Muscle," *Oxygen Transport in Blood and Tissue*, eds. Lubbers, D. W., Luft, V. C., Thews, G., Witzleb, E., Thieme-Verlag, Stuttgart, 1968, pp. 184–195.

3 Eriksson, E., and Myrhage, R., "Microvascular Dimensions and Blood Flow in Skeletal Muscle," *Acta Physiologica Scandinavica*, Vol. 86, 1972, pp. 211–222.

4 Wiederhielm, C. A., et al., "Pulsatile Pressure in the Microcirculation of the Frog's Mesentery," *American Journal of Physiology*, Vol. 207, 1964, pp. 173–176.

5 Intaglietta, M., Pawula, R. F., and Tompkins, W. R., "Pressure Measurements in the Mammalian Microvasculature," *Microvascular Research*, Vol. 2, 1970, pp. 212–220.

6 Wayland, H., and Johnson, P. C., "Erythrocyte Velocity Measurement in Microvessels by a Two-Slit Photometric Method," *Journal of Applied Physiology*, Vol. 22, 1967, pp. 333–337.

7 Zweifach, B. W., "Quantitative Studies of Microcirculatory Structure and Function, 1. Analysis of Pressure Distribution in the Terminal Bed in Cat Mesentery," *Circulation Research*, Vol. 34, 1974, pp. 843–857.

8 Intaglietta, M., Silverman, N. R., and Tompkins, W. R., "Capillary Flow Velocity Measurements in Vivo and in Situ by Television Methods," *Microvascular Research*, Vol. 10, 1975, pp. 165–179.

9 Burton, K. S., and Johnson, P. C., "Reactive Hyperemia in Individual Capillaries of Skeletal Muscle," *American Journal of Physiology*, Vol. 223, 1975, pp. 517–524.

10 Klabunde, R. E., and Johnson, P. C., "Reactive Hyperemia in Capillaries of Red and White Skeletal Muscle," *American Journal of Physiology*, Vol. 232, 1977, pp. 411–417.

11 Lee, J. S., and Nellis, S., "Modeling Study on the Distribution of Flow and Volume in the Microcirculation of Cat Mesentery," *Annals of Biomedical Engineering*, Vol. 2, 1974, pp. 206–216.

12 Lipowsky, H. H., and Zweifach, B. W., "Network Analysis of Microcirculation of Cat Mesentery," *Microvascular Research*, Vol. 7, 1974, pp. 73–83.

13 Lipowsky, H. H., "In Vivo Studies of the Rheology of Blood in the Microcirculation," PhD Dissertation, University of California, San Diego, 1975.

14 Mayrovitz, H. N., Wiedeman, M. P., and Noordergraaf, A., "Analytical Characterization of Microvascular Resistance Distribution," *Bulletin of Mathematical Biology*, Vol. 38, 1976, pp. 71–82.

15 Mayrovitz, H. N., "The Microcirculation: Theory and Experiment," PhD Dissertation, University of Pennsylvania, Philadelphia, 1974.

16 Mayrovitz, H. N., Tuma, R. F., and Wiedeman, M. P., "Relationship Between Microvascular Blood Velocity and Pressure Distribution," *American Journal of Physiology*, Vol. 232, 1977, pp. 400–405.

17 Shames, I. H., *Mechanics of Fluids*, McGraw-Hill, New York, 1962.

18 Lipowsky, H. H., Kovalcheck, S., and Zweifach, B. W., "The Distribution of Blood Rheological Parameters in the Microvasculature of Cat Mesentery," *Circulation Research*, Vol. 43, 1978, pp. 738–749.

19 Sedov, L. I., *Similarity and Dimensional Methods in Mechanics*, Academic Press, New York, 1959.

20 Burton, A. C., *Physiology and Biophysics of the Circulation*, Year Book, Medical Publishers, Chicago, 1965.

Downloaded 01 May 2010 to 171.66.16.243. Redistribution subject to ASME license or copyright; see http://www.asme.org/terms/Terms_Use.cfm

M. J. Crochet
Mem. ASME

A. Denayer

Université Catholique de Louvain,
Unité de Mécanique Appliquée,
Bâtiment Stévin,
Place du Levant, 2,
B-1348 Louvain-la-Neuve,
Belgium

Transient and Residual Thermo-viscoelastic Stresses in Glass

After discussing the constitutive relations of inorganic glasses and their strong dependence upon temperature history, we construct a numerical algorithm in order to calculate transient and residual stresses during manufacture. The method is applied to calculating stresses generated during the annealing process of bottles.

1 Introduction

The manufacture of inorganic glass covers a wide range of temperature over which it behaves successively like a viscous fluid, a viscoelastic material and an elastic solid. The material functions describing its structural properties depend strongly upon the temperature history. By way of background, let us indicate that a soda-lime commercial glass may be considered as a viscous fluid above 600°C and as an elastic solid below 450°C; between 450°C and 600°C glass behaves like a viscoelastic fluid, in the sense that when subjected to a fixed simple shear state of stress, it will respond with a steady state of flow, after transient effects have died out (see [1, Chapter1]). The present paper will deal mainly with the viscoelastic domain, in which a shear viscosity can be defined.

A comparison of creep and relaxation curves of glass at various *fixed temperatures* reveals that they obey the time-temperature equivalence principle [2]. Isothermal creep and relaxation functions at different temperatures can be superposed by a horizontal shift along a logarithmic time-scale; it is easy to verify that the size of the shift is given by the ratio of isothermal viscosities. The calculation of transient stresses in glass manufacture requests the use of *nonisothermal* constitutive relations, and the thermorheologically simple behavior of glass might lead us to the special model given by Morland and Lee [3] and suggested initially by Hopkins [4] for polymers. However, a careful examination of the physical properties of glass shows that the model proposed in [3] is valid only for very slow and very fast cooling rates in the viscoelastic domain. The strong dependence of material properties upon the temperature history exhibited by inorganic glasses has been taken into account in the special class of simple materials studied by Crochet and Naghdi [5, 6] who introduce a *change of time scale* which depends upon the temperature history. The resulting constitutive relations can be made explicit in order to produce a fairly accurate representation of glass properties, and they will be used in the present paper.

Residual stresses in glass which are known to depend upon the cooling schedule play an essential role; in some cases, high compressive stresses on the surface are obtained by rapid chilling (quenching) in order to obtain glasses of high resistance while for plate glass excessive stresses would impair the cutting process. The amount of residual stresses is controlled by the annealing treatment in which a strict cooling schedule is imposed upon the material. (More details on annealing and on the physical properties of glass may be found in [7]).

Apart from the rough estimate given in [8], a first one-dimensional calculation of residual stresses in plate glass only valid for fast cooling was made by Lee, et al. [9]; the limitation to quenching is due to the fact that temperature history is not taken into account in calculating viscosity and thermal dilatation. The method proposed in [9] was extended to arbitrary temperature histories by Crochet and Tackels in [10, 11] while it was shown in [12] that theoretical results compare well with experimental values.

Here we will deal with three-dimensional bodies like bottles, drinking glasses, etc... Fortunately, most shapes of practical importance are axisymmetric, and a two-dimensional treatment is appropriate. In the present paper we show that transient and residual stresses resulting from an arbitrary temperature history can be calculated by means of a finite-element method. Great difficulties have been encountered in devising an algorithm which is stable in time and finite-element meshes which are well adapted to peculiar geometeries like the shape of a bottle. Moreover, the slowly fading memory of cooling glass imposes a large amount of computer memory storage, and special procedures were used for avoiding prohibitive (if at all possible) calculations.

In Section 2, we shall give a brief synthesis of the field and constitutive equations which are used in the calculations; the dependence of glass properties upon temperature history is made explicit. In Section 3, we explain the time and space discretization used for generating the algorithm. In Section 4, we explain the physical problem of annealing a bottle; detailed results and their comparison with numbers obtained by rough calculations are given in Section 5.

2 Field and Constitutive Relations

For the applications to be discussed in the present paper, we may consider that glass behaves like a linear isotropic viscoelastic material. Let $\mathbf{u}(\mathbf{x}, \tau)$ denote the displacement field from a fixed reference con-

Contributed by the Applied Mechanics Division for publication in the JOURNAL OF APPLIED MECHANICS.

Discussion on this paper should be addressed to the Editorial Department, ASME, United Engineering Center, 345 East 47th Street, New York, N. Y. 10017, and will be accepted until September 1, 1980. Readers who need more time to prepare a discussion should request an extension from the Editorial Department. Manuscript received by ASME Applied Mechanics Division, June, 1979; final revision, October, 1979.

Copyright © 1980 by ASME
Downloaded 01 May 2010 to 171.66.16.243. Redistribution subject to ASME license or copyright; see http://www.asme.org/terms/Terms_Use.cfm

figuration to the position of the body at time τ, $-\infty < \tau \leqslant t$. In the sequel we shall omit explicit reference to the position $\mathbf{x}$, and the time argument τ will not appear when $\tau = t$. In rectangular Cartesian coordinates let ϵ_{ij} denote the components of the infinitesimal strain tensor while the stress components are denoted by σ_{ij}. In the absence of inertia effects they satisfy the equilibrium equations

$$\partial\sigma_{ij}/\partial x_j + f_i = 0, \tag{1}$$

where f_i are the components of the body force per unit volume.

The isothermal constitutive relations at a fixed reference temperature θ_0 of an isotropic linear viscoelastic material are given by

$$s_{ij} = -\int_0^\infty G_1(u)de_{ij}(t-u); \quad s = -\int_0^\infty G_2(u)de(t-u), \tag{2}$$

where $G_1(u)$, $G_2(u)$ denote the relaxation functions in shear and in dilatation, respectively, while $s_{ij}(e_{ij})$ and $s(e)$ denote the deviatoric and the spherical components of the stress (strain) tensor.

Let us consider an isotropic viscoelastic material which remains free of stress while its temperature field is uniform in space and takes the value $\theta(\tau)$, $-\infty < \tau \leqslant t$; the *thermal dilatation* $\alpha(t)$ corresponding to the temperature history $\theta(\tau)$, $-\infty < \tau \leqslant t$, is given by the value of the spherical component of the strain tensor. In general, the thermal dilatation will be a functional of the past temperature history, which is written as

$$\alpha = \mathcal{A}[\theta(t-u); \quad 0 \leqslant u < \infty]. \tag{3}$$

The strain tensor $\epsilon_{ij}(\tau)$ may then be decomposed as the sum of a thermal dilatation strain tensor $\alpha(\tau)1$, and an *isothermal strain tensor* $\bar{\epsilon}_{ij}(\tau)$ as follows:

$$\epsilon_{ij}(\tau) = \bar{\epsilon}_{ij}(\tau) + \alpha(\tau)\delta_{ij}; \tag{4}$$

we shall assume that the absolute value of $\alpha(\tau)$ is much smaller than one.

In order to characterize the nonisothermal behavior of glass, it is necessary to introduce a *modified time scale* for the strain history [6]; the temperature history defines a homeomorphism between the upward time scale u, $0 \leqslant u < \infty$, and a modified time scale v, $0 \leqslant v < \infty$, expressed by a functional relation of the form

$$v = \mathcal{V}[\theta(t-\zeta), \quad 0 < \zeta < \infty; u] = v(t, u), \tag{5}$$

or its inverse

$$u = \mathcal{U}[\theta(t-\zeta), \quad 0 < \zeta < \infty; v] = u(t, v). \tag{6}$$

The thermomechanical behavior of glass is well represented by the special class of simple materials proposed by Crochet and Naghdi [6]; essentially, the constitutive relations are obtained by replacing in the isothermal relations (2) the strain tensor $\epsilon_{ij}(\tau)$ by its isothermal counterpart $\bar{\epsilon}_{ij}(\tau)$, and modifying the time scale of the strain history according to (5). The nonisothermal constitutive relations are given by

$$s_{ij} = -\int_0^\infty G_1(u)de_{ij}(t-v),$$

$$s = -\int_0^\infty G_2(u)d[e(t-v) - \alpha(t-v)], \tag{7}$$

or, equivalently,

$$s_{ij} = \int_{-\infty}^t G_1[u(t, t-\tau)]de_{ij}(\tau),$$

$$s = \int_{-\infty}^t G_2[u(t, t-\tau)]d[e(\tau) - \alpha(\tau)]. \tag{8}$$

It is worth recalling that the classical theory of *thermorheologically simple materials* [3] assumes that the functional $\mathcal{A}$ in (3) reduces to a *function* of the present temperature, and that the ratio du/dv in (6) does not depend upon the history of temperature prior to $(t-v)$, i.e.,

$$\frac{du}{dv} = \Phi[\theta(t-v)]. \tag{9}$$

The dependence of the thermal dilatation upon the temperature history rather than the sole actual temperature has been well established for some polymers by Kovacs [13] and for inorganic glasses by De Bast and Gilard [2] while the modified time scale given by (9) leads to unrealistic responses in relaxation experiments [2].

The asymptotic shape of the creep function for glass at a fixed temperature when time increases is a straight line, the slope of which is known as the viscosity. If the temperature varies, the slope is modified too, and the viscosity η may be expressed as a functional of the temperature history,

$$\eta(t) = H[\theta(t-u); \quad 0 \leqslant u < \infty]. \tag{10}$$

It has been shown elsewhere [11] that for a given time interval dv, the time interval du given by (6) is related to dv by

$$\frac{du}{dv} = \eta_0/\eta(t-v), \tag{11}$$

where η_0 is the viscosity of glass at the reference temperature θ_0 while $\eta(t-v)$ is the actual viscosity in steady creep at time $(t-v)$. The relation between u and v may thus be written as

$$u(t, v) = \int_0^v [\eta_0/\eta(t-\zeta)]d\zeta. \tag{12}$$

Physical properties of glass such as thermal dilatation and viscosity depend strongly upon the temperature history because of the structural modifications of the material which lag behind the temperature variations. A convenient way of evaluating a material property of glass in terms of the thermal history is to express its constitutive relation as a function of the actual temperature θ and an internal variable called the fictive temperature θ_f [14] which is itself a functional of the thermal history,

$$\theta_f(t) = \mathcal{T}[\theta(t-u); \quad 0 < u < \infty]; \tag{13}$$

the functional $\mathcal{T}$ is such that θ_f remains a constant in very fast processes while $\theta_f = \theta$ in very slow processes. We observe that with the definition

$$\xi(\tau) = u(\tau, \tau), \tag{14}$$

we may write from (12)

$$u(t, v) = \xi(t) - \xi(t-v); \tag{15}$$

the constitutive relations (8) may then be written as

$$s_{ij} = \int_{-\infty}^t G_1[\xi(t) - \xi(\tau)]de_{ij}(\tau),$$

$$s = \int_{-\infty}^t G_2[\xi(t) - \xi(\tau)]d[e(\tau) - \alpha(\tau)]. \tag{16}$$

Solving the resulting system of field and constitutive equations by analytical means is impossible in general and one must resort to numerical methods.

3 Time and Space Discretization

Let us assume that the temperature field $\theta(\mathbf{x}, t)$ is known within the body for a time interval $0 \leqslant t \leqslant T$, and that the fictive temperature $\theta_f(\mathbf{x}, t)$, the thermal dilatation $\alpha(\mathbf{x}, t)$ and the viscosity $\eta(\mathbf{x}, t)$ have been calculated.

Consider a set of points on the time axis

$$0 = t_0 < t_1 < \ldots t_i < t_{i+1} \ldots < t_p = T,$$

which divide the time interval into a finite number of segments, and define a set of characteristic functions $l_i(t)$, $0 \leqslant i \leqslant p$ which are shown on Fig. 1. A linear interpolation over the time interval of a function $f(t)$ which takes the value $f^{(i)}$ at time t_i is defined by

$$\tilde{f}(t) = \sum_{i=1}^p f^i l_i(t). \tag{17}$$

If the function $f(t)$ suffers a discontinuity at time t_k, we write $t_k = t_{k+1}$ and define the functions $l_k(t)$, $l_{k+1}(t)$ as shown on Fig. 1; the linear

Downloaded 01 May 2010 to 171.66.16.243. Redistribution subject to ASME license or copyright; see http://www.asme.org/terms/Terms_Use.cfm

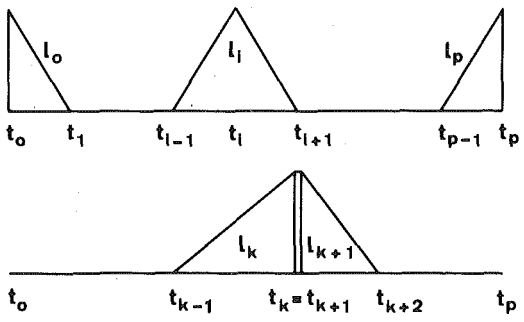

Fig. 1 Interpolating functions

interpolation is still given by (17) where $f^{(k)}$ and $f^{(k+1)}$ now denote the values of $f(t)$ on the left and on the right of $t = t_k$, respectively.

In order to discretize the problem in time, we will replace the unknown displacement field $\mathbf{u}(x, t)$ by its linear interpolation

$$\tilde{\mathbf{u}}(\mathbf{x}, t) = \sum_{i=1}^{p} \mathbf{u}^{(i)}(\mathbf{x})\, l_i(t) \tag{18}$$

from which we obtain the interpolated strain components $\tilde{e}_{kl}(\mathbf{x}, t)$, $\tilde{e}_{kl}(\mathbf{x}, t)$. Similarly, the known thermal dilatation $\alpha(\mathbf{x}, t)$ is replaced by its linear interpolation $\tilde{\alpha}(\mathbf{x}, t)$.

On the basis of (18) and the constitutive relations (16) we may define as follows the stress components $s_{kl}{}^{(i)}$ and $s^{(i)}$ at time t_i,

$$\begin{aligned} s_{kl}{}^{(i)} &= \int_{-\infty}^{t_i} G_1[\xi(t_i) - \xi(\tau)]d\tilde{e}_{kl}(\tau) \\ &= \int_{-\infty}^{t_i} G_1[\xi(t_i) - \xi(\tau)] \sum_{j=0}^{i} e_{kl}{}^{(j)}\, d[l_j(\tau)], \\ s^{(i)} &= \int_{-\infty}^{t_i} G_2[\xi(t_i) - \xi(\tau)]d\,[\tilde{e}(\tau) - \tilde{\alpha}(\tau)] \\ &= \int_{-\infty}^{t_i} G_2[\xi(t_i) - \xi(\tau)] \sum_{j=0}^{i} [e^{(j)} - \alpha^{(j)}]d[l_j(\tau)]. \end{aligned} \tag{19}$$

Let us define the symbols

$$\begin{aligned} \alpha = 1, 2: j \neq 0,\ G_\alpha{}^{ij} &= \int_{-\infty}^{t_i} G_\alpha[\xi(t_i) - \xi(\tau)]d[l_j(\tau)] \\ &= \frac{1}{t_j - t_{j-1}} \int_{t_{j-1}}^{t_j} G_\alpha[\xi(t_i) - \xi(\tau)]d\tau \\ &\quad - \frac{1}{t_{j+1} - t_j} \int_{t_j}^{t_{j+1}} G_\alpha[\xi(t_i) - \xi(\tau)]d\tau, \\ G_\alpha{}^{i0} = G_\alpha[\xi(t_i)] &- \frac{1}{t_i - t_0} \int_{t_0}^{t_i} G_\alpha[\xi(t_i) - \xi(\tau)]d\tau \end{aligned} \tag{20}$$

and rewrite the stress components $s_{kl}{}^{(i)}$ and $s^{(i)}$ as follows:

$$s_{kl}{}^{(i)} = \sum_{j=0}^{i} G_1{}^{ij} e_{kl}{}^{(j)}, \quad s^{(i)} = \sum_{j=0}^{i} G_2{}^{ij}[e^{(j)} - \alpha^{(j)}]. \tag{21}$$

When we proceed to a step by step time integration, the strain components for $j < i$ are known, while the thermal dilatation has been determined at the outset for $j \leqslant i$; we may thus define known partial stress components as follows:

$$p_{kl}{}^{(i)} = \sum_{j=0}^{i-1} G_1{}^{ij} e_{kl}{}^{(j)}, \quad \hat{p}^{(i)} = \sum_{j=0}^{i-1} G_2{}^{ij} e^{(j)} - \sum_{j=0}^{i} G_2{}^{ij} \alpha^{(j)} \tag{22}$$

and separate the stress components $s_{kl}{}^{(i)}$ and $s^{(i)}$ into two parts;

$$s_{kl}{}^{(i)} = \hat{p}_{kl}{}^{(i)} + G_1{}^{ii} e_{kl}{}^{(i)}, \quad s^{(i)} = \hat{p}^{(i)} + G_2{}^{ii} e^{(i)}. \tag{23}$$

Equations (23) show that at time t_i the calculation reduces to solving an elastic problem with an initial stress field given by the partial stress components $\hat{p}_{kl}{}^{(i)}$ and $\hat{p}^{(i)}$. However, expressing the stress components $s_{kl}{}^{(i)}$ and $s^{(i)}$ in terms of the strain components as shown in (21) may lead to large errors of numerical origin whenever the relaxation functions $G_\alpha(t)$ tend asymptotically to zero for large t. In order to see this, let us imagine an isothermal relaxation experiment in which we impose

$$e_{kl}{}^{(j)} = \bar{e}_{kl}, \quad e^{(j)} = 0. \tag{24}$$

In view of (21) we obtain

$$s_{kl}{}^{(i)} = \left(\sum_{j=0}^{i} G_1{}^{ij} \right) \bar{e}_{kl}, \quad s^{(i)} = 0. \tag{25}$$

For a large number of time steps, the sum $(\Sigma_{j=0}^{i} G_1{}^{ij})$, which should vanish when i is large, is in fact replaced by the sum of round-off errors occurring in the numerical calculation of the terms on the right-hand side of (20) and may lead to a considerable relative error in evaluating the relaxation function.

The difficulty is overcome by a step calculation of the *strain increments* which are defined as follows:

$$e_{kl}{}^{(j)} = e_{kl}{}^{(j)} - e_{kl}{}^{(j-1)}, \quad \delta e^{(j)} = e^{(j)} - e^{(j-1)} \tag{26}$$

together with

$$\delta\alpha^{(j)} = \alpha^{(j)} - \alpha^{(j-1)}. \tag{27}$$

It is easy to find that (21) may be written in the form

$$s_{kl}{}^{(i)} = \sum_{j=0}^{i} H_1{}^{ij} \delta e_{kl}{}^{(j)}, \quad s^{(i)} = \sum_{j=0}^{i} H_2{}^{ij} [\delta e^{(j)} - \delta\alpha^{(j)}], \tag{28}$$

where

$$H_\alpha{}^{ij} = \sum_{k=j}^{i} G_\alpha{}^{ik} = \frac{1}{t_j - t_{j-1}} \int_{t_{j-1}}^{t_j} G_\alpha[\xi(t_i) - \xi(\tau)]d\tau, \quad j \neq 0, \tag{29}$$

$$H_\alpha{}^{i0} = \sum_{k=0}^{i} G_\alpha{}^{ik} = G_\alpha[\xi(t_i)].$$

With the use of (28), (25) now becomes

$$s_{kl}{}^{(i)} = H_1{}^{i0} \bar{e}_{kl}, \quad s^{(i)} = 0, \tag{30}$$

and (29) shows that $H_1{}^{i0}$ tends asymptotically to zero with $G_\alpha[\xi(t_i)]$ when t_i and i become large.

By defining partial stress components as

$$p_{kl}{}^{(i)} = \sum_{j=0}^{i-1} H_1{}^{ij} \delta e_{kl}{}^{(j)}, \quad p^{(i)} = \sum_{j=0}^{i-1} H_2{}^{ij} \delta e^{(j)} - \sum_{j=0}^{i} H_2{}^{ij} \delta\alpha^{(j)} \tag{31}$$

we may write (28) as

$$s_{kl}{}^{(i)} = H_1{}^{ii} \delta e_{kl}{}^{(i)} + p_{kl}{}^{(i)}, \quad s^{(i)} = H_2{}^{ii} \delta e^{(i)} + p^{(i)}. \tag{32}$$

At time t_i the calculation again reduces to solving an elastic problem with an initial stress field given by the partial stress components $p_{kl}{}^{(i)}$ and $p^{(i)}$. Equivalently, if $\mathbf{f}^{(i)}$ represents the body force at time t_i and $\bar{\mathbf{t}}^{(i)}$ the surface force on part $\mathcal{S}_\tau$ of the boundary, we request that the potential energy

$$\begin{aligned} W(t_i) = \int_{\mathcal{V}} \Big\{ &\frac{1}{2} \delta e_{kl}{}^{(i)} H_1{}^{ii}\, \delta e_{kl}{}^{(i)} + \delta e_{kl}{}^{(i)}\, p_{kl}{}^{(i)} \\ &+ 3 \left[\frac{1}{2} \delta e^{(i)} H_2{}^{ii} \delta e^{(i)} + \delta e^{(i)} p^{(i)} \right] \\ &- f_k{}^{(i)} \delta u_k{}^{(i)} \Big\} d\nu - \int_{\mathcal{S}_\tau} \bar{t}_k{}^{(i)} \delta u_k{}^{(i)}\, d\mathcal{S} \end{aligned} \tag{33}$$

be a minimum for the displacement field increment $\delta\mathbf{u}^{(i)}(\mathbf{x})$.

Let the domain of integration be covered by a grid of finite elements; the incremental displacement field $\delta\mathbf{u}^{(i)}(\mathbf{x})$ at time t_i is discretized in terms of its nodal values, which are calculated by minimizing the potential energy $W(t_i)$. Sampling points for Gauss-Legendre quadrature are selected in each element. The general algorithm at time $t^{(i)}$ works as follows:[1]

[1] One is led to somewhat simpler calculations when the relaxation function may be expressed as a sum of exponential terms ([15, 16]).

Downloaded 01 May 2010 to 171.66.16.243. Redistribution subject to ASME license or copyright; see http://www.asme.org/terms/Terms_Use.cfm

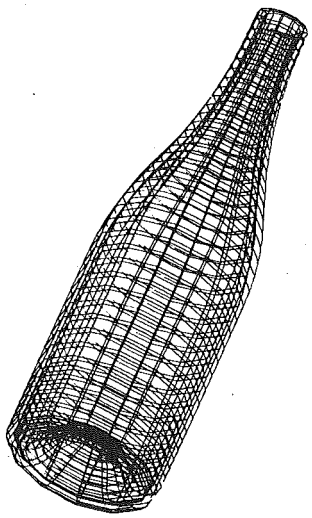

Fig. 2 Shape of the bottle

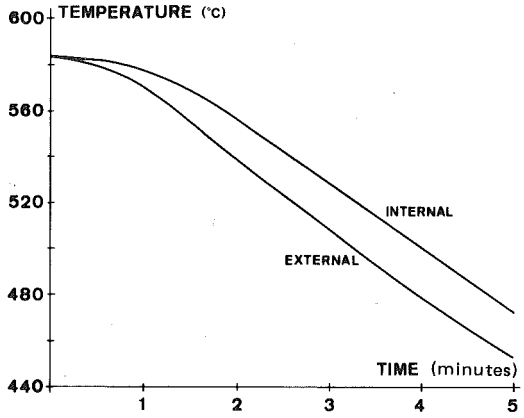

Fig. 3 Measured surface temperatures

1 By solving the transient energy equation, calculate the temperature at every sampling point.

2 By solving (13), calculate the fictive temperature at the sampling points together with the viscosity and the thermal dilatation.

3 Calculate the increment of the modified time scale $\delta\xi_i = [\xi(t_i) - \xi(t_{i-1})]$ at every sampling point on the basis of (12).

4 Calculate the integrals $H_\alpha{}^{ij}$ given by (29) at every sampling point by means of a Taylor series expansion around the point $\{(t_i) - (1/2)[\xi(t_j) + \xi(t_{j-1})]\}$.

5 Calculate the partial stresses $p_{kl}{}^{(i)}$ and $p^{(i)}$ given by (31) at every sampling point.

6 Calculate the stiffness matrix on the basis of (33) by means of Gauss-Legendre quadrature.

7 Calculate the nodal values of the strain increments and the stress components.

8 Save the values of $\delta e_{kl}{}^{(i)}$, $\delta e^{(i)}$, $\delta\xi_i$ for later use and proceed with a new time step.

Below a given temperature which we write as θ_g glass behaves like an elastic solid; this is equivalent to saying that for θ lower than θ_g, the viscosity η becomes infinite. Let us consider the cooling of a volume of glass, and let t_m be such that for $t \geqslant t_m$, $\theta \leqslant \theta_g$ everywhere in the body. By combining (12) and (14) it is easy to find that

$$\xi(t) - \xi(\tau) = \int_\tau^t \frac{\eta_0}{\eta[\theta(t-\zeta);\, \theta_f(t-\zeta)]}\, d\zeta = 0, \quad t > \tau \geqslant t_m, \tag{34}$$

since $1/\eta$ vanishes for $\tau \geqslant t_m$.

Consider a time t_i such that $t_i > t_m$; in view of (34) we have

$$\xi(t_i) = \xi(t_m), \tag{35}$$

and it is easy to deduce from (29) that when $t_j \leqslant t_m \leqslant t_i$,

$$H_\alpha{}^{ij} = H_\alpha{}^{mj}. \tag{36}$$

When $t_m \leqslant t_j \leqslant t_i$ we obtain

$$H^{ij} = \frac{1}{t_j - t_{j-1}} \int_{t_{j-1}}^{t_j} G_\alpha(O)\, d\tau = G_\alpha(O). \tag{37}$$

At time $t_i \geqslant t_m$, the partial stress components given by (31) become, in view of (36) and (37),

$$p_{kl}{}^{(i)} = \sum_{j=0}^{m-1} H_1{}^{mj} \delta e_{kl}{}^{(j)} + \sum_{j=m}^{i-1} G_1(O) \delta e_{kl}{}^{(j)} = p_{kl}{}^{(m)} + G_1(O)[e_{kl}{}^{(i-1)} - e_{kl}{}^{(m-1)}], \tag{38}$$

$$p^{(i)} = p^{(m)} + G_2(O)[e^{(i-1)} - e^{(m-1)}] + G_2(O)[\alpha^{(i)} - \alpha^{(m-1)}], \tag{38}$$

(*Cont.*)

and from (32), (37) and (38) we obtain

$$s_{kl}{}^{(i)} = G_1(O)[e_{kl}{}^{(i)} - e_{kl}{}^{(m-1)}] + p_{kl}{}^{(m)},$$

$$s^{(i)} = G_2(O)[e^{(i)} - e^{(m-1)}] + p^{(m)} + G_2(O)[\alpha^{(i)} - \alpha^{(m-1)}]. \tag{39}$$

Equations (39) show that for times larger than t_m, the number of intermediate time intervals is irrelevant for calculating the actual stresses. In order to calculate the residual stresses at room temperature we may simply consider that time t_{m+1} is the final time t_p and assume a uniform temperature distribution throughout the body. The residual stress tensor components are then given by $s_{kl}{}^{(m+1)}$, $s^{(m+1)}$.

4 Description of the Problem

Let us consider on Fig. 2 a typical bottle of "Champagne" type shaped in order to sustain high internal pressure without fracture. After moulding at high temperature, stresses in the bottle are partially relaxed by slow cooling from a temperature of approximately 600°C down to room temperature in the annealing lehr. Calculating the temperature field within the thickness of the bottle on the basis of the temperature of the surrounding atmosphere is a very difficult problem in view of the convective transfer taking place on the inner walls.

Since we are presently interested mainly in the evaluation of transient and residual stresses, we will base our temperature calculation upon boundary values measured by means of thermocouples on the inner and outer walls in an experimental oven reproducing industrial conditions. Fig. 3 shows these measurements as a function of time; the inner wall is on the average 20°C warmer than the outer wall and the calculated temperature profile within the thickness is almost linear.

An essential difficulty in solving the present problem lies in the thickness of the shell as compared to its meridional dimension, while the stresses and the temperature vary significantly within the thickness. We made use of nine-node quadrilateral isoparametric elements, and our experience in refining the grid toward convergence has shown the need of using eight layers. In view of the large amount of information to be saved in memory for calculating the stresses, and of the ratio of the meridional length to the thickness, it was found necessary to separate the meridional section into three overlapping parts. The length of the overlap which is related to the rate of decay of the edge effects was selected in order to provide a perfect match of stress and displacement contour lines at its middle point. Fig. 4 shows the actual division of the meridional section.

Eventually, each part has been divided into 8 layers of 10 to 12 elements along the meridian line. The time scale has been divided into 25 intervals of 12 sec each. For a time larger that 5 min, the temper-

Downloaded 01 May 2010 to 171.66.16.243. Redistribution subject to ASME license or copyright; see http://www.asme.org/terms/Terms_Use.cfm

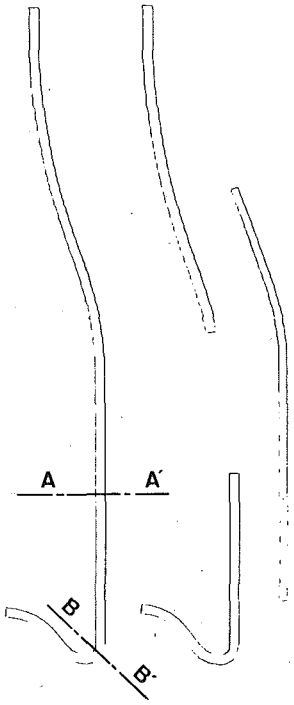

Fig. 4 Division in three segments

ature is such that glass behaves like an elastic material, and the residual stresses can be calculated without further specification of the cooling rate.

The material constants and material functions entering the calculations are proper to a commercial soda-lime silicate glass. On the basis of experiments described in [12], it was found that the following numerical values apply over the considered domain of temperature:

$$G_1(t) = 2\mu\psi(t), \quad G_2(t) = 3k\psi(t),$$

$$\psi(t) = \exp\,[-(Kt/\eta_0)^b], \quad K = 0.302\ 10^{11}\ \text{kg/m sec}^2, \quad b = 0.543,$$

$$\mu = 2.63\ 10^7\ \text{kpa}, \quad k = 4.00\ 10^7\ \text{kpa}; \tag{40}$$

the viscosity η and the thermal dilatation α are given by

$$\alpha - \alpha_0 = [3.47 \times 10^{-5}(\theta_f - \theta_0) + 0.97 \times 10^{-5}(\theta - \theta_f)],$$

$$\ln\,(\eta/\eta_0) = -0.136(\theta_f - \theta_0) - 0.064\,(\theta - \theta_f), \tag{41}$$

where α_0, η_0 are the equilibrium values of α and η at temperature θ_0 and the temperatures are expressed in °C. Here,

$$\theta_0 = 554°\text{C}, \quad \eta_0 = 10^{12.4}\ \text{kg/m sec}.$$

A specific representation of the functional dependence of the fictive temperature θ_f upon the temperature history is given by a rate equation which may be written as

$$\frac{d\theta_f}{dt} = F(\theta, \theta_f). \tag{42}$$

It was suggested by Tool [14] on the basis of physical arguments that the rate of θ_f be proportional to the difference $(\theta - \theta_f)$ and inversely proportional to the viscosity. A better fit with experimental data on a soda-lime silicate glass was obtained by Crochet, et al. [12], with the following equation:

$$\frac{d\theta_f}{dt} = \frac{\eta_0}{\eta}\,(\theta - \theta_f)[a + b(\theta - \theta_f)^2],$$

$$a = 2.2\ 10^{-6}, \quad b = 1.4\ 10^{-8}\ (°\text{C})^{-2}. \tag{43}$$

Before closing this section it is interesting to demonstrate the need

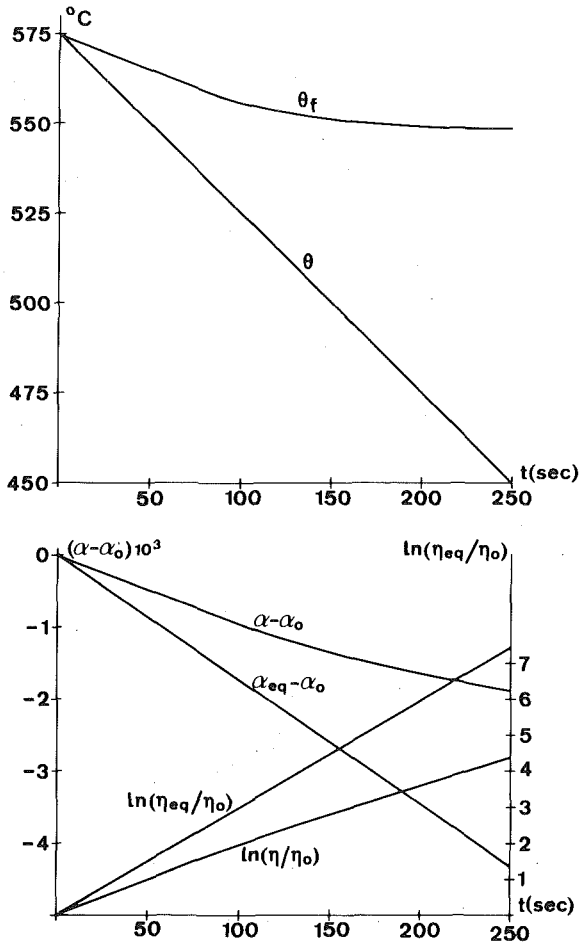

Fig. 5 Influence of the temperature history upon material properties

of introducing the fictive temperature concept in order to calculate the material functions rather than using their equilibrium values. Let us assume that a piece of glass is being cooled from 575°C down to 450 °C in 250 sec; this rate of cooling is close to the rate used in our annealing problem. Fig. 5 shows that θ_f which is initially identical to θ tends to an asymptotic value; the actual values of η and α differ appreciably from their equilibrium values which would have been obtained at a very low cooling rate.

5 Numerical Results

The finite-element method of the displacement type used in the present paper gives rise to a discontinuous stress field across the element boundaries. In order to obtain a continuous representation of the stress field, we have smoothed the discontinuous field by means of a conjugate approximation proposed by Oden [17]; essentially, a continuous stress field is obtained by least-squares approximation from stress components defined piecewise at the integration points.

For clarity, let us define a curvilinear meridional coordinate s along the midsurface of the shell, and let n be a coordinate normal to it. The calculation shows, as we might expect, that the normal stress σ_{nn} and the shear stress σ_{ns} have a value less than a few percent of the stress component σ_{ss} and the hoop stress $\sigma_{\theta\theta}$. We will limit ourselves to exhibiting the values of σ_{ss} and $\sigma_{\theta\theta}$.

In section AA' indicated on Fig. 4 we find a typical stress behavior when time progresses. Fig. 6 shows a perspective view of the stress components σ_{ss} and $\sigma_{\theta\theta}$ throughout section AA' as a function of time. We observe that compressive and traction stresses develop initially on the inner and outer walls, respectively; a reversal occurs after about 3 min. Residual stresses exhibit traction on the inner wall and com-

Downloaded 01 May 2010 to 171.66.16.243. Redistribution subject to ASME license or copyright; see http://www.asme.org/terms/Terms_Use.cfm

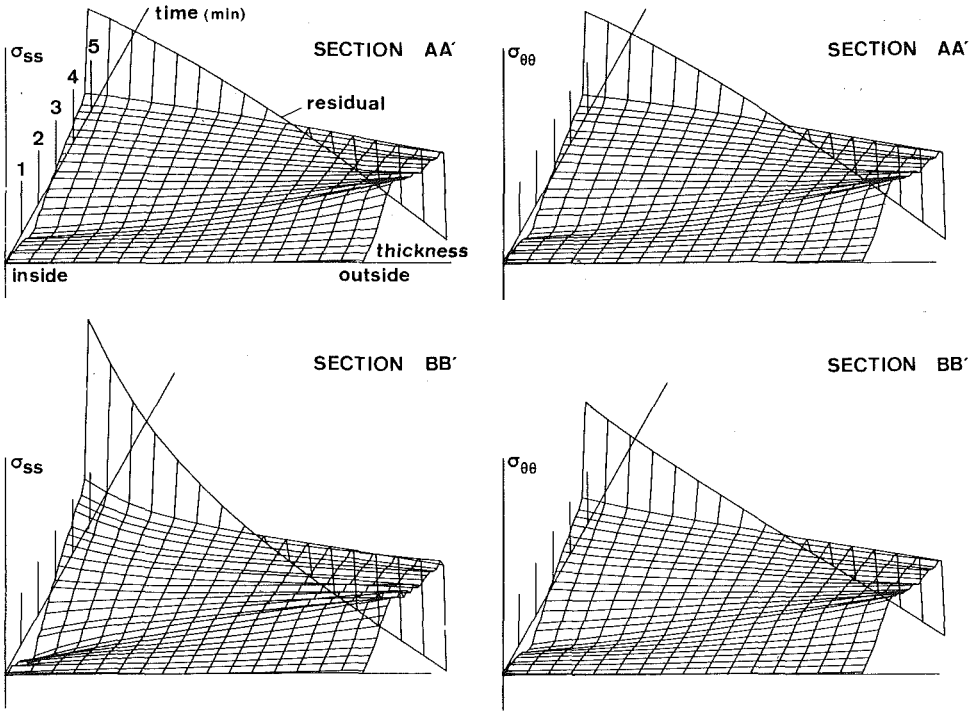

Fig. 6 Perspective view of transient stresses in the thickness

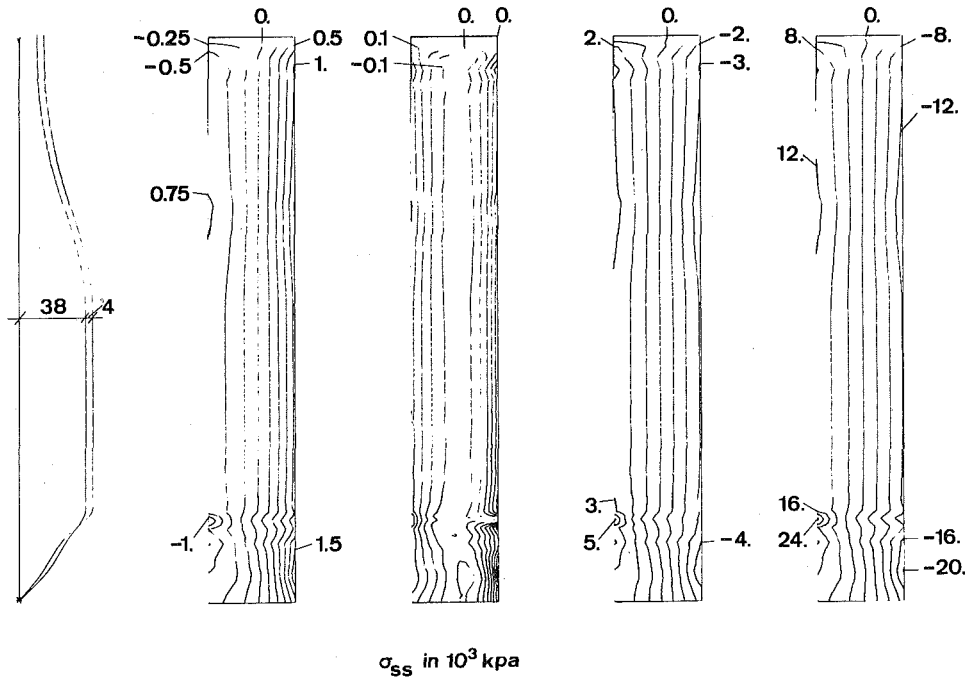

Fig. 7 Stress contour lines of σ_{ss} at time = 1 min, 3 min, 5 min, and residual stresses

pression on the outer wall. Fig. 6 also shows the stress components in section BB' indicated on Fig. 4; the highest stresses occur in that section where the curvature of the midsurface is a maximum, and it is observed that the residual value of σ_{ss} is larger than the residual value of $\sigma_{\theta\theta}$.

A precise evaluation of the stress components is given by the stress contours shown on Fig. 7, where the abscissa corresponds to the thickness expanded by a factor of 10 for clarity. The stress contours are almost vertical, except at the free edge where σ_{ss} vanishes and in the neighborhood of the support where the midsurface has the highest curvature. While σ_{ss} reaches values of $\pm 10^4$ kpa on the walls of the cylindrical part of the bottle, it is found that its value is doubled at the support (where in fact fracture often occurs in destructive tests); the stress values shown on Fig. 7 remain acceptable from a practical point of view since admissible stresses in glass at room temperature lie between 2.5 and 5 10^4 kpa. Our results show clearly that a two-dimensional calculation is necessary for a correct evaluation of the residual stresses.

It is interesting to compare the calculated stresses *in the cylindrical part* of the body with stress distributions obtained by simpler

Downloaded 01 May 2010 to 171.66.16.243. Redistribution subject to ASME license or copyright; see http://www.asme.org/terms/Terms_Use.cfm

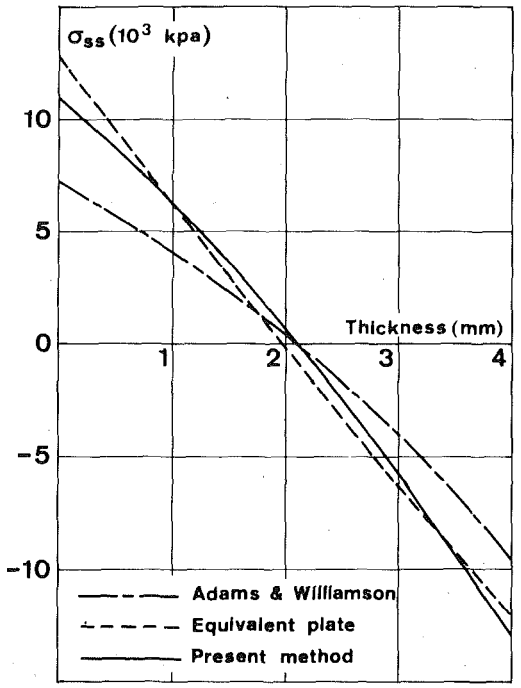

Fig. 8 Residual stresses in the cylindrical portion

methods. A rough estimate is obtained by assuming that glass is totally annealed before thermal uniformization at room temperature, and that thermoelastic stresses are generated by a reversal of the temperature field. Fig. 8 shows that the exact stresses lie 40 percent above the rough estimate. A one-dimensional calculation for plate glass neglecting the curvature of the midsurface has also been applied to the cylindrical part of the bottle; Fig. 8 shows good agreement between this simple method and the two-dimensional results. However, we wish to point out that the maximum stresses are obtained in a region where one-dimensional calculation is not realistic.

Acknowledgments

One of us (A.D.) wishes to acknowledge scholarships received from IRSIA and FNRS during the course of this work.

References

1 Christensen, R. M., *Theory of Viscoelasticity,* Academic Press, 1971.

2 De Bast J., and Gilard, P., "Rhéologie du verre sous contrainte dans l'intervalle de transformation," IRSIA, *Comptes rendus de recherches,* n° 32, 1965.

3 Morland, L. W., and Lee, E. H., "Stress Analysis for Linear Viscoelastic Materials With Temperature Variation," *Trans. of the Society of Rheology,* No. 4, 1960, pp. 233–263.

4 Hopkins, I. L., "Stress Relaxation or Creep of Linear Viscoelastic Substances Under Varying Temperature," *Journal of Polymer Science,* Vol. 28, 1958, pp. 631–633.

5 Crochet, M. J., and Naghdi, P. M., "A Class of Simple Solids With Fading Memory," *International Journal of Engineering Science,* Vol. 7, 1969, pp. 1173–1198.

6 Crochet, M. J., and Naghdi, P. M., "On a Restricted Nonisothermal Theory of Simple Materials," *Journal de Mécanique,* Vol. 13, 1974, pp. 97–114.

7 Jones, G. O., *Glass,* Chapman and Hall, Science Paperbacks, 1971.

8 Adams, L. H., and Williamson, E. D., "The Annealing of Glass, I," *Journal of The Franklin Institution,* Vol. 190, 1920, pp. 597–631.

9 Lee, E. H., Rogers, T. G., and Woo, T. C., "Residual Stresses in a Glass Plate Cooled Symmetrically From Both Surfaces," *Journal of the American Ceram. Society,* Vol. 48, 1965, pp. 480–487.

10 Crochet, M. J., and Tackels, G., "Etude des tensions thermiques dans une feuille de verre," *Silic. Industr.,* Vol. 37, 1972, pp. 101–106.

11 Tackels, G., and Crochet, M. J., "Thermal Stresses During Annealing of a Glass Ribbon," *Rheology Acta,* Vol. 12, 1973, pp. 330–336.

12 Crochet, M. J., et al., "Experimental Study of Stress Relaxation During Annealing," *Journal of Noncrystalline Solids,* Vol. 14, 1974, pp. 242–254.

13 Kovacs, A. J., "Transition vitreuse dans les polymères amorphes. Etude phénoménologique," *Advances in Polymer Science,* Vol. 3-3, 1964, pp. 394–507.

14 Tool, A. Q., "Relation Between Inelastic Deformability and Thermal Expansion of Glass in Its Annealing Range," *Journal Amer. Ceram. Society,* Vol. 29, 1946, pp. 240–253.

15 Taylor, R. L., Pister, K. S., and Goudreau, G. L., "Thermomechanical Analysis of Viscoelastic Solids," *International Journal of Numerical Methods in Engineering,* Vol. 2, 1970, pp. 45–59.

16 Frutiger, R. L., and Woo, T. C., "A Thermoviscoelastic Analysis for Circular Plates of Thermorheologically Simple Material," *Journal of Thermal Stress,* Vol. 2, 1970, pp. 45–60.

17 Oden, J. T., *Finite Elements of Nonlinear Continua,* McGraw-Hill, New York, 1972.

Downloaded 01 May 2010 to 171.66.16.243. Redistribution subject to ASME license or copyright; see http://www.asme.org/terms/Terms_Use.cfm

C. D. Hill
Research Assistant.

A. Bedford
Associate Professor.
Mem. ASME

Department of Aerospace Engineering
and Engineering Mechanics,
The University of Texas at Austin,
Austin, Texas 78712

D. S. Drumheller
Member of the Technical Staff,
Sandia Laboratories,
Albuquerque, New Mex. 87115

An Application of Mixture Theory to Particulate Sedimentation

Equations for two-phase flow are used to analyze the one-dimensional sedimentation of solid particles in a stationary container of liquid. A derivation of the equations of motion is presented which is based upon Hamilton's extended variational principle. The resulting equations contain diffusivity terms, which are linear in the gradient of the particle concentration. It is shown that the solution of the equations for steady sedimentation is stable under small perturbations. Finally, finite-difference solutions of the equations are compared to the data of Whelan, Huang, and Copley for blood sedimentation.

Introduction

The sedimentation of particles in a liquid is of interest in many chemical engineering processes [1], in medicine, where erythrocyte sedimentation has become a standard clinical test [2], and in oceanography [3] as well as other fields.

The analytical study of particulate sedimentation has been approached in three ways. First, some information about sedimentation can be obtained by studying the dynamics of individual particles in liquids [4–7]. Next, by writing the local balance equations for the liquid together with the boundary conditions at the liquid-particle interfaces, and then taking statistical averages over an ensemble of particles, equations which govern the average motions of the liquid and the particles can be obtained [8–13]. Finally, the variables associated with the liquid and the particles can be introduced as continuous fields from the beginning, and balance equations and constitutive relations can be postulated [14–20].[1] These approaches are complementary; each has supported and helped to clarify the predictions of the others.

The objective of this paper is to use the third approach—the continuum theory of two-phase flow—to model the one-dimensional sedimentation of particles through a liquid in a stationary container (Fig. 1). The continuum equations for particulate sedimentation have been derived, for example, by Anderson and Jackson [8], Drew [13], and Soo [17]. In this paper a derivation is presented which uses a variational approach that leads to the sedimentation equations in a particularly direct and simple way [25]. The equations of motion of the particles and of the fluid which are obtained contain diffusivity terms—terms that are linear in the gradient of the particle concentration. Such terms occur in the equations for fluid-particle flow presented by Drew [13] and in the mixture theories of Mills [16] and of Craine [18] and have been formally introduced into the equations for particulate sedimentation by Bedford and Hill [19]. These terms do not appear in the equations for particulate sedimentation pre-

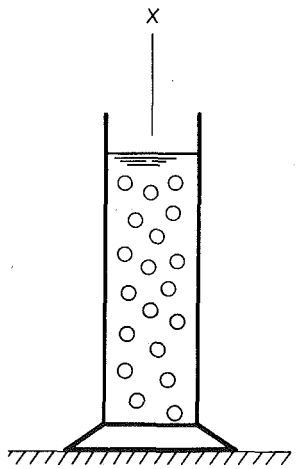

Fig. 1 Sedimentation configuration

[1] In his classical theory of sedimentation, Kynch [21] assumed that the particle velocity is a function only of the local particle concentration. He did not write equations of motion for the particles or the fluid. His approach is still widely used to analyze sedimentation problems [22–24].

Contributed by the Applied Mechanics Division for presentation at the Winter Annual Meeting, Chicago, Ill., November 16–21, 1980, of THE AMERICAN SOCIETY OF MECHANICAL ENGINEERS.

Discussion on this paper should be addressed to the Editorial Department, ASME, United Engineering Center, 345 East 47th Street, New York, N. Y. 10017, and will be accepted until September 1, 1980. Readers who need more time to prepare a discussion should request an extension from the Editorial Department. Manuscript received by ASME Applied Mechanics Division, July, 1979; final revision, December, 1979. Paper No. 80-WA/APM-1.

Copyright © 1980 by ASME
Downloaded 01 May 2010 to 171.66.16.243. Redistribution subject to ASME license or copyright; see http://www.asme.org/terms/Terms_Use.cfm

sented by Soo [17] and by Thacker and Lavelle [20]. From the physical point of view, the diffusivity terms can model the effects of particle-particle impacts due to the Brownian motion of the particles. (See the discussion by Anderson and Jackson [8].) It has also been pointed out to us that such terms can be interpreted as Reynolds stresses [26].

In the absence of the diffusivity terms, the solution for homogeneous, steady sedimentation is known to be unstable under small perturbations [27, 28]. In this paper it is shown that if the coefficients of the diffusivity terms satisfy certain inequalities, then the solution for one-dimensional homogeneous steady sedimentation is stable, and furthermore, the equations are hyperbolic. These results were obtained in a slightly less general form in [26].

Finally, finite-difference solutions of the equations are obtained for the case of blood sedimentation and are compared with the experimental data of Whelan, Huang, and Copley [29].

Equations of Motion

The mass of the ξth constituent ($\xi = p$ for the particles and $\xi = f$ for the liquid) per unit volume of the particle-liquid mixture will be denoted by ρ_ξ. The actual, or local density will be denoted by $\bar{\rho}_\xi$, so that the volume fraction (concentration) ϕ_ξ is

$$\phi_\xi = \rho_\xi / \bar{\rho}_\xi. \tag{1}$$

It is assumed that the particles and the liquid are incompressible, so that $\bar{\rho}_\xi$ = constant. Also, the volume fractions satisfy

$$\sum_\xi \phi_\xi = \phi_p + \phi_f = 1. \tag{2}$$

The conservation of mass equation for each constituent is

$$\dot{\rho}_\xi + \rho_\xi \operatorname{div} \mathbf{v}_\xi = 0, \tag{3}$$

where div denotes the divergence, a dot denotes the material derivative

$$\dot{\rho}_\xi = \frac{\partial}{\partial t} \rho_\xi + \mathbf{v}_\xi \cdot \operatorname{grad} \rho_\xi, \tag{4}$$

$\mathbf{v}_\xi$ is the velocity of the ξth constituent, and grad denotes the gradient. By using equation (1), equation (3) can be written for incompressible constituents as

$$\dot{\phi}_\xi + \phi_\xi \operatorname{div} \mathbf{v}_\xi = 0. \tag{5}$$

An alternative form of equation (5) is

$$J_\xi = \phi_{\xi 0} / \phi_\xi, \tag{6}$$

where J_ξ is the Jacobian and a subscript 0 denotes that a variable is evaluated in a reference configuration.

The equations of motion will be obtained by writing Hamilton's extended principle

$$\delta \int_{t_1}^{t_2} (T - V) dt + \int_{t_1}^{t_2} \delta W \, dt = 0, \tag{7}$$

(where t_1, t_2 are arbitrary times, T and V are the kinetic and potential energies, and δW is the virtual work), for a volume v of the mixture through whose surface s the constituents are not permitted to diffuse [25].[2] The kinetic energy of the mixture in v is written

$$T = \sum_\xi \int_v \frac{1}{2} \rho_\xi \mathbf{v}_\xi \cdot \mathbf{v}_\xi \, dv. \tag{8}$$

The virtual work is written

$$\delta W = \sum_\xi \int_v \left[(\rho_\xi \mathbf{f}_\xi + \mathbf{d}_\xi) \cdot \delta \mathbf{x}_\xi + \frac{b_\xi}{\phi_\xi} \delta \phi_\xi \right] dv, \tag{9}$$

where $\mathbf{x}_\xi$ is the spatial position of a material particle of the ξth constituent. Note that the generalized forces associated with $\delta \mathbf{x}_\xi$ are split into the external body forces $\rho_\xi \mathbf{f}_\xi$ and the interaction (drag) forces $\mathbf{d}_\xi$. The generalized forces associated with $\delta \phi_\xi$, denoted b_ξ / ϕ_ξ, will be seen to give rise to the diffusivity terms, so that they occur naturally in the variational formulation. (In physical terms, if there is a "particle pressure" due to Brownian motion of the particles, a variation of the volume fraction of the particles will give rise to a work term.) Since the constituents are incompressible, a potential energy expression is not required [25].

Equations (2) and (6) will be included in the variational principle as constraints by introducing Lagrange multipliers λ and μ_ξ. Thus equation (7) is written[3]

$$\int_{t_1}^{t_2} \left\{ \delta \sum_\xi \int_v \frac{1}{2} \rho_\xi \mathbf{v}_\xi \cdot \mathbf{v}_\xi \, dv + \sum_\xi \int_v \left[(\rho_\xi \mathbf{f}_\xi + \mathbf{d}_\xi) \cdot \delta \mathbf{x}_\xi + \frac{b_\xi}{\phi_\xi} \delta \phi_\xi \right] dv \right.$$
$$\left. - \int_v \lambda \delta \left(\sum_\xi \phi_\xi - 1 \right) \Big|_{\mathbf{x}} dv + \sum_\xi \int_v \mu_\xi \delta \left(J_\xi - \frac{\phi_{\xi 0}}{\phi_\xi} \right) dv \right\} dt = 0. \tag{10}$$

The resulting equations of motion corresponding to the variations $\delta \mathbf{x}_\xi$, $\delta \phi_\xi$ are

$$\rho_\xi \dot{\mathbf{v}}_\xi = \rho_\xi \mathbf{f}_\xi + \mathbf{d}_\xi + \lambda \operatorname{grad} \phi_\xi - \operatorname{grad} (\mu_\xi J_\xi), \tag{11}$$

$$b_\xi / \phi_\xi - \lambda + \mu_\xi J_\xi / \phi_\xi = 0. \tag{12}$$

By eliminating $\mu_\xi J_\xi$ between equations (11) and (12), the final equations of motion are obtained in the form

$$\rho_\xi \dot{\mathbf{v}}_\xi = \rho_\xi \mathbf{f}_\xi + \mathbf{d}_\xi - \phi_\xi \operatorname{grad} \lambda + \operatorname{grad} b_\xi. \tag{13}$$

To complete the theory, constitutive assumptions are required for $\mathbf{d}_\xi$ and b_ξ. For particulate sedimentation, it will be assumed that

$$\mathbf{d}_\xi = \mathbf{d}_\xi (\phi, \mathbf{v}_p - \mathbf{v}_f), \tag{14}$$

$$b_\xi = b_\xi (\phi, \mathbf{v}_p - \mathbf{v}_f), \tag{15}$$

where $\phi = \phi_p = 1 - \phi_f$. Furthermore, it will be assumed that equations (14) and (15) are isotropic and linear in the relative velocity, so that[4]

$$\mathbf{d}_f = - \mathbf{d}_p = \phi D (\mathbf{v}_p - \mathbf{v}_f), \tag{16}$$

$$b_\xi = B_\xi, \tag{17}$$

where D and B_ξ are scalar functions of ϕ. Equations (2), (5), (13), (16), and (17) are a system of equations in the variables λ, ϕ_ξ, $\mathbf{v}_\xi$, $\mathbf{d}_\xi$, and b_ξ. These equations agree with those obtained by Drew [13] using an averaging approach. The equations also agree with those of Soo [17] and Thacker and Lavelle [20], except that they did not include the diffusivity terms b_ξ. The multiplier λ is the pressure of the liquid.

The One-Dimensional Equations

Consider the one-dimensional sedimentation by gravity of particles in a stationary container of liquid (Fig. 1). The one-dimensional form of equation (5) can be written

$$\frac{\partial \phi_\xi}{\partial t} + \frac{\partial}{\partial x} (\phi_\xi v_\xi) = 0. \tag{18}$$

Writing equation (18) for $\xi = p$ and for $\xi = f$, summing the two equations and using equation (2) yields the equation

$$\frac{\partial}{\partial x} (\phi_p v_p + \phi_f v_f) = 0. \tag{19}$$

The term $\phi_p v_p + \phi_f v_f$ is the volume of the liquid-particle mixture

[2] The mixture can be visualized as occupying a container with impermeable surface s.

[3] Note that since the volume fraction constraint equation (2) applies at a given spatial point, the constraint is introduced in terms of the variation holding $\mathbf{x}$ fixed,

$$\delta \left(\sum_\xi \phi_\xi - 1 \right) \Big|_{\mathbf{x}} = \sum_\xi (\delta \phi_\xi - \operatorname{grad} \phi_\xi \cdot \delta \mathbf{x}_\xi).$$

[4] Note that equation (16) has no zero-order term and equation (17) has no first-order term as a result of the assumption of isotropy.

Downloaded 01 May 2010 to 171.66.16.243. Redistribution subject to ASME license or copyright; see http://www.asme.org/terms/Terms_Use.cfm

which passes a given point x per unit time. For the problem being considered, this volume is zero, so that

$$v_f = -(\phi_p/\phi_f)v_p. \tag{20}$$

Setting $f_\xi = -g$, where g is the acceleration of gravity (the x-axis is positive upward), the one-dimensional forms of equation (13) are

$$\rho_p\left(\frac{\partial v_p}{\partial t} + v_p\frac{\partial v_p}{\partial x}\right) = -\rho_p g - \phi D(v_p - v_f) - \phi_p\frac{\partial \lambda}{\partial x} + \frac{dB_p}{d\phi}\frac{\partial \phi}{\partial x}, \tag{21}$$

$$\rho_f\left(\frac{\partial v_f}{\partial t} + v_f\frac{\partial v_f}{\partial x}\right) = -\rho_f g + \phi D(v_p - v_f) - \phi_f\frac{\partial \lambda}{\partial x} + \frac{dB_f}{d\phi}\frac{\partial \phi}{\partial x}. \tag{22}$$

Eliminating $\partial\lambda/\partial x$ between equations (21) and (22) and using equation (20) to eliminate v_f yields the single equation

$$R\frac{\partial v}{\partial t} + Qv\frac{\partial v}{\partial x} + Sv\frac{\partial \phi}{\partial t} + (K - Uv^2)\frac{\partial \phi}{\partial x} = -(\bar\rho_p - \bar\rho_f)g - \frac{1}{(1-\phi)^2}Dv, \tag{23}$$

where $v = v_p$ and

$$R = \bar\rho_p + \phi\bar\rho_f/(1-\phi), \quad Q = \bar\rho_p - \phi^2\bar\rho_f/(1-\phi)^2,$$
$$S = \bar\rho_f/(1-\phi)^2, \quad U = \phi\bar\rho_f/(1-\phi)^3,$$
$$K = \frac{dB_f}{d\phi}\Big/(1-\phi) - \frac{dB_p}{d\phi}\Big/\phi. \tag{24}$$

Equation (18) for $\xi = p$ is

$$\frac{\partial \phi}{\partial t} + v\frac{\partial \phi}{\partial x} + \phi\frac{\partial v}{\partial x} = 0. \tag{25}$$

Equations (23) and (25) are a system of two quasi-linear equations for the particle concentration ϕ and particle velocity v.

It is easy to show that if

$$K > \bar\rho_f\bar\rho_p\, v^2/\{(1-\phi)^2[\bar\rho_p(1-\phi) + \bar\rho_f\phi]\}, \tag{26}$$

then equations (23) and (25) are hyperbolic [30]. Thus the equations governing the particle motion are hyperbolic if K is positive and sufficiently large.[5] Note from equation (26) that if second-order terms in v are neglected, then the equations are hyperbolic for any positive K.

For a homogeneous distribution of particles with concentration ϕ_0 sedimenting at constant velocity, the solution of equations (23) and (25) is easily seen to be

$$\phi = \phi_0, \tag{27}$$

$$v = v_0 = -(1-\phi_0)^2(\bar\rho_p - \bar\rho_f)g/D_0, \tag{28}$$

where

$$D_0 = D|_{\phi=\phi_0}.$$

Stability Analysis

In an analysis of fluidized beds,[6] Anderson and Jackson [31] obtained numerical results which showed that diffusivity terms have a stabilizing effect on the state of uniform fluidization, which corresponds to homogeneous steady sedimentation. Garg and Pritchett [32] also considered the stability of fluidized beds and obtained an explicit stability criterion which demonstrated that diffusivity terms can stabilize steady sedimentation. However, they used a special constitutive assumption for the coefficient of their diffusivity term. Moreover, since they were concerned with gas-fluidized beds, the equations of motion which they used were simplified by the assumption that (in the present notation) $\bar\rho_p \gg \bar\rho_f$. In this paper, an explicit stability criterion will be derived based on equations (23) and (25).

In the stability analysis we follow Thacker and Lavelle [28]. Let small perturbations be added to the steady sedimentation solution equations (27) and (28) of the forms

$$\phi = \phi_0 + \tilde\phi\exp[i(kx - \omega t)], \tag{29}$$

$$v = v_0 + \tilde v\exp[i(kx - \omega t)], \tag{30}$$

where ω is frequency, k is wave number, and $\tilde\phi$ and $\tilde v$ are constants. When equations (29) and (30) are substituted into equations (25) and (23) and the resulting equations are linearized, they become

$$(\omega - kv_0)\tilde\phi - k\phi_0\tilde v = 0, \tag{31}$$

$$\left[\omega S_0 v_0 + k(U_0 v_0^2 - K_0) + \frac{2iD_0 v_0}{(1-\phi_0)^3} + \frac{iD_0' v_0}{(1-\phi_0)^2}\right]\tilde\phi + \left[\omega R_0 - kQ_0 v_0 + \frac{iD_0}{(1-\phi_0)^2}\right]\tilde v = 0, \tag{32}$$

where a subscript 0 denotes that a function is evaluated at $\phi = \phi_0$, and

$$D_0' = \frac{dD}{d\phi}\Big|_{\phi=\phi_0}$$

The condition for equations (31) and (32) to have a nontrivial solution for $\tilde\phi$ and $\tilde v$ is

$$R_0\omega^2 + \left[kv_0(\phi_0 S_0 - R_0 - Q_0) + \frac{iD_0}{(1-\phi_0)^2}\right]\omega + k^2(Q_0 v_0^2 + \phi_0 U_0 v_0^2 - \phi_0 K_0) + \frac{ikv_0}{(1-\phi_0)^3}[2D_0\phi_0 + (1-\phi_0)(D_0'\phi_0 - D_0)] = 0. \tag{33}$$

It can be shown from equation (33) that the imaginary parts of the roots for ω are ≤ 0 if and only if

$$[\bar\rho_p(1-\phi_0) + \bar\rho_f\phi_0](1-\phi_0)^3 K_0/v_0^2 \ge \bar\rho_p\bar\rho_f(1-\phi_0) + \phi_0\{2\bar\rho_p(1-\phi_0) + \bar\rho_f(2\phi_0 - 1) + (1-\phi_0)[\bar\rho_p(1-\phi_0) + \bar\rho_f\phi_0]D_0'/D_0\}^2. \tag{34}$$

Thus the solution (equations (29) and (30)) is stable if K_0 is positive and sufficiently large. If terms in v_0^2 are neglected, then the solution is stable for any positive K_0. Also note that the solution is unstable when the diffusivity terms are absent, which is the result that was obtained by Jackson [27] and by Thacker and Lavelle [28].

The Linearized Equations

Let the concentration and velocity be expressed as $\phi = \phi_0 + \tilde\phi$, $v = \tilde v$, where ϕ_0 = constant and $\tilde\phi$, $\tilde v$ are small. The linearized forms of equations (23) and (25) are

$$R_0\frac{\partial \tilde v}{\partial t} + K_0\frac{\partial \tilde\phi}{\partial x} = -(\bar\rho_p - \bar\rho_f)g - \frac{1}{(1-\phi_0)^2}D_0\tilde v, \tag{35}$$

$$\frac{\partial \tilde\phi}{\partial t} + \phi_0\frac{\partial \tilde v}{\partial x} = 0. \tag{36}$$

Eliminating $\tilde v$ between equations (35) and (36) yields the single equation for $\tilde\phi$

$$-\frac{R_0}{\phi_0}\frac{\partial^2\tilde\phi}{\partial t^2} + K_0\frac{\partial^2\tilde\phi}{\partial x^2} = \frac{D_0}{\phi_0(1-\phi_0)^2}\frac{\partial\tilde\phi}{\partial t}, \tag{37}$$

which is the damped wave equation if $K_0 > 0$ and $D_0 > 0$. (Note that R_0 is positive.) Then if the acceleration term $R_0(\partial\tilde v/\partial t)$ in equation (35) is neglected (quasi-steady sedimentation), equation (37) becomes the diffusion equation [33]

$$\frac{\partial\tilde\phi}{\partial t} = \beta\frac{\partial^2\tilde\phi}{\partial x^2}, \tag{38}$$

[5] Kynch [21] showed that discontinuities in the particle concentration can exist, and he gave a careful discussion of the circumstances in which they can arise and propagate.

[6] In a typical fluidized bed, fluid flows upward through a "bed" of particles. When the rate of flow is sufficient to lift the particles, the situation is exactly analogous to particulate sedimentation.

Downloaded 01 May 2010 to 171.66.16.243. Redistribution subject to ASME license or copyright; see http://www.asme.org/terms/Terms_Use.cfm

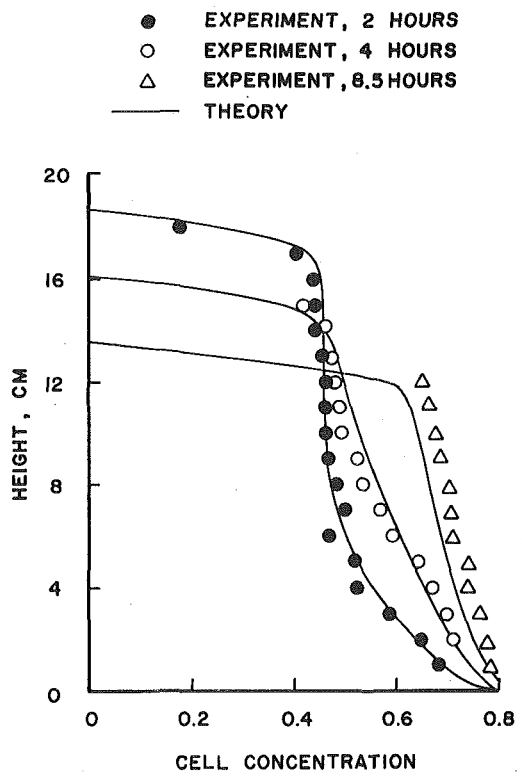

Fig. 2 Cell concentration profiles

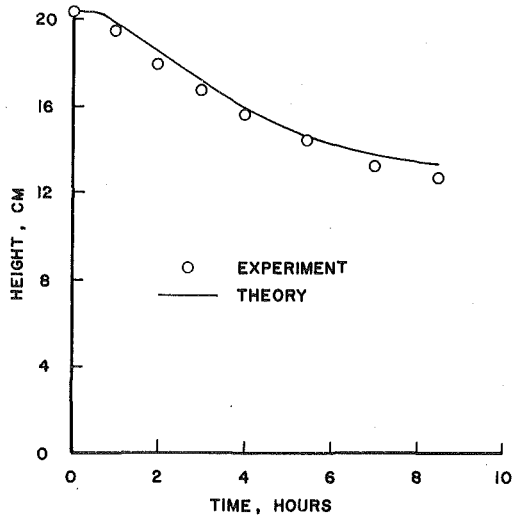

Fig. 3 Upper cell interface position

where the diffusion coefficient β is

$$\beta = \phi_0(1 - \phi_0)^2 K_0/D_0. \tag{39}$$

That a theory of this type leads to the diffusion equation under appropriate assumptions has been pointed out, for example, by Mills [16].

Example

As a brief illustration of the theory, a finite-difference solution of equations (23) and (25) has been obtained for the case of erythrocyte (red cell) sedimentation in human whole blood. In addition to its practical interest, this problem is well suited to the present theory since, as observed by Sartory [34], the diffusivity of the erythrocytes has an important effect on the cell concentration profile. Furthermore, Whelan, Huang, and Copley [29] have made experimental measurements of the concentration profile as a function of time.

The erythrocyte sedimentation test consists of a stationary vertical tube of blood to which anticoagulant has been added. The initial cell concentration (hematocrit) ϕ_0 is uniform. The cells, being slightly denser than the plasma, then settle toward the bottom of the tube. The velocity of the upper cell interface (in mm/hr) is the clinical sedimentation rate.

Huang, et al., [35] have modeled the sedimentation of blood by using the classical convection-diffusion equation [33]. They made the very restrictive assumption that the particle velocity v did not depend upon position or time. Nevertheless they were able to obtain reasonable agreement with their experimental data. However, Sartory [34] pointed out that in order to do so, they had to use a value of the diffusion coefficient that was several orders of magnitude larger than the estimated diffusion coefficient of erythrocytes. Sartory then adopted the approach of Kynch [21] in which the diffusive term in the convection-diffusion equation was neglected and the concentration-dependent convective term was evaluated by comparison with steady homogeneous sedimentation experiments. He noted that the model "is found to give fairly good agreement with the available experiments, at least after 1 hr." A similar model for blood sedimentation has been presented by Puccini, et al. [36].

The initial cell concentration used in the experiments of Whelan, et al., [29] was $\phi_0 = 0.455$ and the height of the blood column was 20.5 cm. It was assumed for the computations that $\bar{\rho}_p = 1.1 \times 10^3$ kg/m^3 and $\bar{\rho}_f = 1.03 \times 10^3$ kg/m^3 [37]. An empirical relation for the drag coefficient D as a function of ϕ which was based on the results of Barnea and Mizrahi [38],

$$D = \alpha(1 - \phi) \exp [1.67\, \phi/(1 - \phi)], \tag{40}$$

where α = constant was used in the computations. In the absence of similar information on the concentration dependence of the diffusivity, it was simply assumed that K = constant.

The solutions were obtained by discretizing the tube into 50 increments and reducing the equations to ordinary equations in time by central differencing. The relative sizes of the coefficients in the equations made it necessary to solve the ordinary equations in time over each time step by using an algorithm for stiff differential equations [39]. The boundary conditions were $v = 0$ at the bottom of the tube and $\phi = 0$ at the upper cell interface.

Fig. 2 shows the measured cell concentration as a function of height in the tube after 2, 4, and 8.5 hr of elapsed time. It was found that using values of $K = 15$ kg/m-s^2 and $\alpha = 3.1 \times 10^7$ kg/m^3-s gave the best match to the experimental data at 2 hr.[7] Using these values of K and α, the calculated results were then compared to the data at 4 and at 8.5 hr. As seen in Fig. 2, the comparison is reasonably good. In Fig. 3, the observed position of the upper cell interface as a function of time is compared to the computed position of the interface. Finally, in Fig. 4 the effect of the empirical drag coefficient equation (40) is illustrated by comparing the concentration profiles at 2 and at 8.5 hr with corresponding profiles obtained by assuming that $D = D|_{\phi=\phi_0}$. The substantial effect of the concentration dependence of D on the profile at later times is clearly seen. In all of the computations, it was assumed that the maximum packing density of the cells was $\phi = 0.8$.

These comparisons, while they are promising, must be regarded as preliminary for two reasons. First, available information on the concentration dependence of the diffusivity for large concentrations is inadequate. Second, an important effect in blood sedimentation, that of aggregation—the tendency of the cells to gather into clumps during the sedimentation process [2]—is not contained in the present model.

[7] From equations (39) and (40), these values of K and α yield a value of the diffusion coefficient of the erythrocytes $\beta = 2.98 \times 10^{-8}$ m^2/s. Based on the data of Whelan, Huang, and Copley [29], Sartory [34] made the order-of-magnitude estimate $\beta \simeq 10^{-8}$ m^2/s. Also, it has been found that the hyperbolicity criterion equation (26) and the stability criterion equation (34) are satisfied for erythrocyte sedimentation.

Downloaded 01 May 2010 to 171.66.16.243. Redistribution subject to ASME license or copyright; see http://www.asme.org/terms/Terms_Use.cfm

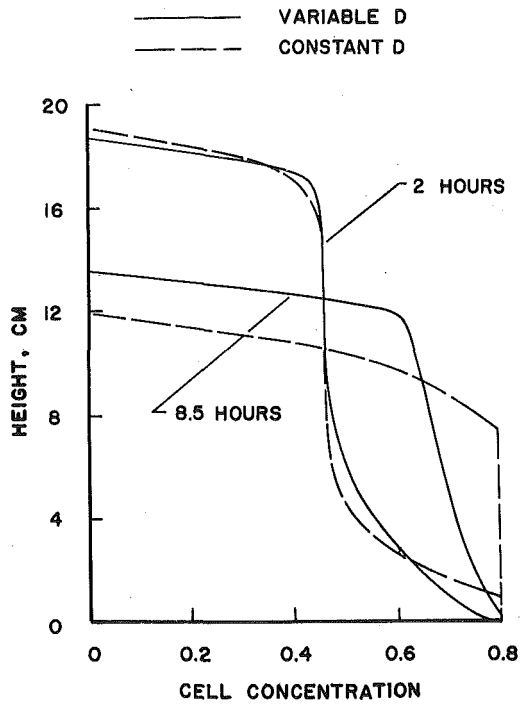

Fig. 4 Comparison of profiles with constant and empirical drag coefficients

Acknowledgments

This research was supported in part by National Science Foundation Grant ENG75-18404 and by the United States Department of Energy. The authors would like to thank Prof. G. B. Thurston for many helpful discussions.

References

1 Zenz, F. A., and Othmer, D. F., *Fluidization and Fluid-Particle Systems,* Reinhold, New York, 1960.

2 Dintenfass, L., *Blood Microrheology-Viscosity Factors in Blood Flow, Ischaemia and Thrombosis,* Appleton-Century-Crofts, New York, 1971.

3 Weyl, P. K., *Oceanography,* Wiley, New York, 1970.

4 Happel, J., and Brenner, H., *Low Reynolds Number Hydrodynamics,* Prentice-Hall, Englewood Cliffs, N. J., 1965.

5 Brenner, H., "Rheology of Two-Phase Systems," *Annual Reviews of Fluid Mechanics,* Vol. 2, 1970, pp. 137–176.

6 Batchelor, G. K., "Sedimentation in a Dilute Dispersion of Spheres," *Journal of Fluid Mechanics,* Vol. 52, 1972, pp. 245–268.

7 Clift, R., Grace, J. R., and Weber, M. E., *Bubbles, Drops and Particles,* Academic Press, New York, 1978.

8 Anderson, T. B., and Jackson, R., "A Fluid Mechanical Description of Fluidized Beds," *Industrial and Engineering Chemistry Fundamentals,* Vol. 6, 1967, pp. 527–539.

9 Panton, R., "Flow Properties for the Continuum Viewpoint of a Non-equilibrium Gas-Particle Mixture," *Journal of Fluid Mechanics,* Vol. 31, 1968, pp. 273–303.

10 Drew, D. A., "Averaged Field Equations for Two-Phase Media," *Studies in Applied Mathematics,* Vol. L, 1971, pp. 133–166.

11 Drew, D. A., and Segel, L. A., "Averaged Equations for Two-Phase Flows," *Studies in Applied Mathematics,* Vol. L, 1971, pp. 205–231.

12 Drew, D. A., and Segel, L. A., "Analysis of Fluidized Beds and Foams Using Averaged Equations," *Studies in Applied Mathematics,* Vol. L, 1971, pp. 233–257.

13 Drew, D. A., "Two-Phase Flows: Constitutive Equations for Lift and Brownian Motion and Some Basic Flows," *Archive for Rational Mechanics and Analysis,* Vol. 62, 1976, pp. 149–163.

14 Van Deemter, J. J., and Van der Laan, E. T., "Momentum and Energy Balances for Two-Phase Flow," *Applied Scientific Research,* Series A, Vol. 10, 1960, pp. 102–108.

15 Murray, J. D., "On the Mathematics of Fluidization Part 1. Fundamental Equations and Wave Propagation," *Journal of Fluid Mechanics,* Vol. 21, 1965, pp. 465–493.

16 Mills, N., "Incompressible Mixtures of Newtonian Fluids," *International Journal of Engineering Science,* Vol. 4, 1966, pp. 97–112.

17 Soo, S., *Fluid Dynamics of Multiphase Systems,* Blaisdell, Waltham, Mass., 1967.

18 Craine, R. E., "Oscillations of a Plate in a Binary Mixture of Incompressible Newtonian Fluids," *International Journal of Engineering Science,* Vol. 9, 1971, pp. 1177–1192.

19 Bedford, A., and Hill, C. D., "A Mixture Theory for Particulate Sedimentation With Diffusivity," *AIChE Journal,* Vol. 23, 1977, pp. 403–404.

20 Thacker, W. C., and Lavelle, J. W., "Two-Phase Flow Analysis of Hindered Settling," *The Physics of Fluids,* Vol. 20, 1977, pp. 1577–1579.

21 Kynch, G. J., "A Theory of Sedimentation," *Transactions of the Faraday Society,* Vol. 48, 1952, pp. 166–176.

22 Aris, R., and Amundson, N. R., *Mathematical Methods in Chemical Engineering,* Vol. 2, Prentice-Hall, Englewood Cliffs, N. J., 1973, pp. 232–249.

23 Kos, P., "Continuous Gravity Thickening of Sludges," *Progress in Water Technology,* Vol. 9, 1977, pp. 291–309.

24 Kos, P., "Fundamentals of Gravity Thickening," *Chemical Engineering Progress,* Vol. 73, 1977, pp. 99–105.

25 Bedford, A., and Drumheller, D. S., "A Variational Theory of Immiscible Mixtures," *Archive for Rational Mechanics and Analysis,* Vol. 68, 1978, pp. 37–51.

26 Hill, C. D., and Bedford, A., "Stability of the Equations for Particulate Sedimentation," *The Physics of Fluids,* Vol. 22, 1979, pp. 1252–1254.

27 Jackson, R., "The Mechanics of Fluidised Beds: Part I: The Stability of the State of Uniform Fluidisation," *Transactions of the Institution of Chemical Engineers,* Vol. 41, 1963, pp. 13–28.

28 Thacker, W. C., and Lavelle, J. W., "Stability of Settling of Suspended Sediments," *The Physics of Fluids,* Vol. 21, 1978, pp. 291–292.

29 Whelan, J. A., Huang, C.-R., and Copley, A. L., "Concentration Profiles in Erythrocyte Sedimentation in Human Whole Blood," *Biorheology,* Vol. 7, 1971, pp. 205–212.

30 Whitham, G. B., *Linear and Nonlinear Waves,* Wiley, New York, 1974, pp. 113–117.

31 Anderson, T. B., and Jackson, R., "Fluid Mechanical Description of Fluidized Beds. Stability of the State of Uniform Fluidization," *Industrial and Engineering Chemistry Fundamentals,* Vol. 7, 1968, pp. 12–21.

32 Garg, S. K., and Pritchett, J. W., "Dynamics of Gas-Fluidized Beds," *Journal of Applied Physics,* Vol. 46, 1975, pp. 4493–4500.

33 Jost, W., *Diffusion in Solids, Liquids, Gases,* Academic Press, New York, 1960.

34 Sartory, W. K., "Prediction of Concentration Profiles During Erythrocyte Sedimentation by a Hindered Settling Model," *Biorheology,* Vol. 11, 1974, pp. 253–264.

35 Huang, C.-R., et al., "A Mathematical Model of Sedimentation Analysis Applied to Human Whole Blood," *Biorheology,* Vol. 8, 1971, pp. 157–163.

36 Puccini, C., Stasiw, D. M., and Cerny, L. C., "The Erythrocyte Sedimentation Curve: A Semiempirical Approach," *Biorheology,* Vol. 14, 1977, pp. 43–49.

37 Burton, A. C., *Physiology and Biophysics of the Circulation,* Year Book Medical Publishers, Chicago, 1972.

38 Barnea, E., and Mizrahi, J., "A Generalized Approach to the Fluid Dynamics of Particulate Systems Part I. General Correlation for Fluidization and Sedimentation of Solid Multiparticle Systems," *Chemical Engineering Journal,* Vol. 5, 1973, pp. 171–189.

39 Hindmarsh, A. C., and Byrne, G. D., "EPISODE: An Experimental Package for the Integration of Systems of Ordinary Differential Equations," Report UCID-30112, Lawrence Livermore Laboratory, May 1975.

Downloaded 01 May 2010 to 171.66.16.243. Redistribution subject to ASME license or copyright; see http://www.asme.org/terms/Terms_Use.cfm

K. Hashiguchi

Research Assistant,
Department of Agricultural Engineering,
Kyushu University, 46-05,
Hakozaki, Higashi-ku,
Fukuoka 812, Japan

Constitutive Equations of Elastoplastic Materials With Elastic-Plastic Transition

Constitutive equations of elastoplastic materials with an elastic-plastic transition observed in the loading state after a first yield are presented by introducing a new parameter denoting the ratio of the size of a loading surface in the transitional state to that of a yield surface in the classical idealization which ignores the transitional state. These equations involve a reasonably simplified rule for the kinematic hardening. They would describe reasonably not only the hardening behavior but especially the softening behavior which requires our careful consideration about the elastic-plastic transition. From these equations, moreover, we derive plastic constitutive equations specifically of metals and granular media which exhibit very different plastic behaviors. Besides, brief discussions are provided concerning the existing constitutive equations describing the elastic-plastic transition.

Introduction

Various types of constitutive equations of elastoplastic materials exhibiting a gradual transition from the elastic to the fully plastic state (abbreviated as an *elastic-plastic transition*) with an isotropic or a kinematic hardening have been proposed by numerous authors: e.g., Mróz [1], Phillips and Sierakowski [2], Eisenberg and Phillips [3], Krieg [4], and Dafalias and Popov [5] along the line of the traditional concept of plasticity whose constitutive equation involves inherently a yield function; Tokuoka [6, 7] within the framework of hypoelasticity; Bernstein [8] by the application of the Lipschitz condition. These constitutive equations, however, have been confined mainly to the description of the hardening behavior of plastically incompressible metals satisfying the von Mises yield condition at least in the initial state of deformation. They seem irrelevant to the description of the deformation of elastoplastic materials such as granular media exhibiting not only hardening but also softening behavior with a plastic volume change. Thus it is desirable to find a reasonable constitutive equation for generalized elastoplastic materials exhibiting these behaviors, without physical contradictions in fundamental laws such as a flow rule and a loading criterion.

In this paper constitutive equations of generalized elastoplastic materials exhibiting the elastic-plastic transition with not only hardening but also softening behavior are derived along the line of the traditional concept of plasticity. First, we provide a basic model of elastoplastic continua within the framework of the classical theory of plasticity idealized to ignore the elastic-plastic transition, exhibiting isotropic and anisotropic hardening or softening behavior. In this model a reasonably simplified rule for the kinematic hardening is incorporated. Then, the concept of a yield surface is extended to a *subyield state* (transitional state) under the distinct *yield state* (fully plastic state) and thus the existence of a *loading surface* in the subyield state is assumed. On this occasion the loading surface is formulated by the same function as the one representing the yield surface in the classical idealization. Further, we introduce a new parameter denoting the ratio of the size of the loading surface to that of the yield surface and thus we extend the basic model so as to describe the elastic-plastic transition. A similar concept of the loading surface was previously introduced by Phillips and Sierakowski [2] and, based on this concept, a constitutive equation describing the elastic-plastic transition has been proposed by Eisenberg and Phillips [3]. This equation, however, is rather complicated and inapplicable to materials exhibiting the softening behavior as will be described in the last section, while the one proposed in the present paper would be a more simple and reasonable generalization of the classical theory of plasticity. Further, from those results we derive two special classes of plastic constitutive equations for metals and granular media which exhibit very different plastic behaviors. And, based on these equations, some calculated results of stress-plastic strain relations in a uniaxial loading or a triaxial compression of these materials are presented.

Constitutive Equations

In this section we first present a basic model of an elastoplastic

Contributed by the Applied Mechanics Division for publication in the JOURNAL OF APPLIED MECHANICS.

Discussion on this paper should be addressed to the Editorial Department, ASME, United Engineering Center, 345 East 47th Street, New York, N.Y. 10017, and will be accepted until September 1, 1980. Readers who need more time to prepare a discussion should request an extension from the Editorial Department. Manuscript received by ASME Applied Mechanics Division, November, 1978; final revision, September, 1979.

Copyright © 1980 by ASME

Downloaded 01 May 2010 to 171.66.16.243. Redistribution subject to ASME license or copyright; see http://www.asme.org/terms/Terms_Use.cfm

continuum within the framework of the classical theory of plasticity and then extend it to describe the elastic-plastic transition.

Throughout this paper, both the standard direct and the Cartesian tensor notations are used. However, we often write the various expressions in component forms and display vector and tensor fields in terms of their rectangular Cartesian components.

A Basic Model of Elastoplastic Continua. For elastoplastic continua we first assume the following linear relation between the stress rate $\dot{\boldsymbol{\sigma}}$ and the strain rate $\dot{\boldsymbol{\epsilon}}$ ($\dot{\epsilon}_{ij} = (\partial v_{i,j} + \partial v_{j,i})/2$, v_i: components of the particle velocity).[1]

$$\dot{\boldsymbol{\epsilon}} = \mathbf{T}[\dot{\boldsymbol{\sigma}}]$$

or

$$\dot{\epsilon}_{ij} = T_{ijkl}\dot{\sigma}_{kl}, \tag{1}$$

where the fourth-order tensor $\mathbf{T}$ with components T_{ijkl} satisfying obvious symmetry conditions in view of the symmetry of $\dot{\epsilon}_{ij}$ and $\dot{\sigma}_{ij}$ is a function of stress and some internal variables describing the effect of the history of plastic deformation on the stress rate-strain rate relation. A superposed dot designates a material time derivative.

In addition, we postulate that the strain rate $\dot{\boldsymbol{\epsilon}}$ can be decomposed into the elastic component $\dot{\boldsymbol{\epsilon}}^e$ and the plastic component $\dot{\boldsymbol{\epsilon}}^p$ as follows:

$$\dot{\boldsymbol{\epsilon}} = \dot{\boldsymbol{\epsilon}}^e + \dot{\boldsymbol{\epsilon}}^p. \tag{2}$$

The definition of these components of the strain rate is given in the following.

Assume that there exists a state in which the integral $\int \dot{\boldsymbol{\epsilon}} dt$ ($= \boldsymbol{\epsilon}$ (t: time)) does not depend on the stress path. The constitutive equation determined by stress-strain characteristics in such a state is termed an *elastic constitutive equation.* And a strain rate prescribed by this equation is defined as an *elastic strain rate* $\dot{\boldsymbol{\epsilon}}^e$. Accordingly, we can write

$$\dot{\boldsymbol{\epsilon}}^e = \mathbf{E}[\dot{\boldsymbol{\sigma}}]$$

or

$$\dot{\epsilon}_{ij}{}^e = E_{ijkl}\dot{\sigma}_{kl}, \tag{3}$$

where the fourth-order tensor $\mathbf{E}$ with components E_{ijkl} is a function of the stress. Since the total differential equation (3) must be completely integrable, the components E_{ijkl} satisfy the exact differential forms

$$\frac{\partial E_{ijmn}}{\partial \sigma_{pq}} = \frac{\partial E_{ijpq}}{\partial \sigma_{mn}} \tag{4}$$

which are deduced from the Frobenius integration theorem (cf., e.g., [10]). When the elastic response changes with plastic deformation, the tensor $\mathbf{E}$ is to be a function not only of the stress but also of some parameters representing the change of the elastic response by the plastic deformation.

From (2) the *plastic strain rate* $\dot{\boldsymbol{\epsilon}}^p$ is defined as $\dot{\boldsymbol{\epsilon}}^p = \dot{\boldsymbol{\epsilon}} - \dot{\boldsymbol{\epsilon}}^e$. Hence, by setting

$$\mathbf{P} \equiv \mathbf{T} - \mathbf{E}, \tag{5}$$

we get from (1)–(3) that

$$\dot{\boldsymbol{\epsilon}}^p = \mathbf{P}[\dot{\boldsymbol{\sigma}}]$$

or

$$\dot{\epsilon}_{ij}{}^p = P_{ijkl}\dot{\sigma}_{kl} \tag{6}$$

which is not completely integrable and is termed a *plastic constitutive equation.*

[1] While the strain rate $\dot{\boldsymbol{\epsilon}}$ is the so-called stretching, the constitutive equations in the following can be given a higher objectivity by replacing the stress rate $\dot{\boldsymbol{\sigma}}$ ($\boldsymbol{\sigma}$: Eulerian stress) included in them by the corotational stress rate $\mathring{\boldsymbol{\sigma}}$ ($\equiv \dot{\boldsymbol{\sigma}} - \mathbf{w}\boldsymbol{\sigma} + \boldsymbol{\sigma}\mathbf{w}$, $\mathbf{w}$: spin) (cf., e. g., [9]).

In what follows we formulate an explicit form of the plastic constitutive equation (6) which describes the relationship of the stress rate to the plastic strain rate.

First we introduce the following yield condition.

$$f(\boldsymbol{\sigma} - \boldsymbol{\alpha}, \boldsymbol{\epsilon}^p) - F(K) = 0 \tag{7}$$

or

$$f(\hat{\boldsymbol{\sigma}}, \boldsymbol{\epsilon}^p) - F(K) = 0, \tag{8}$$

where we set

$$\hat{\boldsymbol{\sigma}} \equiv \boldsymbol{\sigma} - \boldsymbol{\alpha}. \tag{9}$$

By convention let the interior points of the yield surface correspond to $f < F$. In these equations the second-order tensor $\boldsymbol{\alpha}$ is a parameter representing a translation of the yield surface, and the plastic strain $\dot{\boldsymbol{\epsilon}}^p$ ($= \int \dot{\boldsymbol{\epsilon}}^p dt$) and the scalar K describe changes of the shape and the size, respectively, of the yield surface.

Let the rate of change of K, i.e., $\dot{K}$ be a function of $\dot{\boldsymbol{\sigma}}$, $\boldsymbol{\epsilon}^p$, and $\dot{\boldsymbol{\epsilon}}^p$ in degree one satisfying the condition $\dot{K} = 0$ when $\dot{\boldsymbol{\epsilon}}^p = \mathbf{0}$.

Further, let the rate of change of $\boldsymbol{\alpha}$, i.e., $\dot{\boldsymbol{\alpha}}$ be given by

$$\dot{\boldsymbol{\alpha}} = C \operatorname{tr}\left(\dot{\boldsymbol{\epsilon}}^p \frac{\hat{\boldsymbol{\sigma}}}{|\hat{\boldsymbol{\sigma}}|}\right)\frac{\hat{\boldsymbol{\sigma}}}{|\hat{\boldsymbol{\sigma}}|}, \tag{10}$$

where C is a scalar function of K and invariants of $\boldsymbol{\alpha}$, and the notation $|\ |$ is used to represent magnitude. The evolution equation (10) governing the translation of a yield surface is based on the assumption that the yield surface translates in the direction of the vector with components $\hat{\sigma}_{ij}$ in the nine-dimensional stress space and in any of its subspaces. This assumption has been advocated by Ziegler [11]. But in his equation $\dot{\boldsymbol{\alpha}} = \dot{\mu}\hat{\boldsymbol{\sigma}}$ the scalar rate $\dot{\mu}$ is not directly related to $\dot{\boldsymbol{\epsilon}}^p$ but is assumed only to be a proportionality factor, while in our equation (10) $\dot{\boldsymbol{\alpha}}$ is directly and simply related to $\dot{\boldsymbol{\epsilon}}^p$

Adopting the associated flow rule

$$\dot{\boldsymbol{\epsilon}}^p = \dot{\lambda}\frac{\partial f}{\partial \boldsymbol{\sigma}}\left(= \dot{\lambda}\frac{\partial f}{\partial \hat{\boldsymbol{\sigma}}}\right)(\dot{\lambda} > 0), \tag{11}$$

where $\dot{\lambda}$ is a proportionality factor, and considering the consistency condition

$$\operatorname{tr}\left(\frac{\partial f}{\partial \hat{\boldsymbol{\sigma}}}\dot{\boldsymbol{\sigma}}\right) - \operatorname{tr}\left(\frac{\partial f}{\partial \hat{\boldsymbol{\sigma}}}\dot{\boldsymbol{\alpha}}\right) + \operatorname{tr}\left(\frac{\partial f}{\partial \boldsymbol{\epsilon}^p}\dot{\boldsymbol{\epsilon}}^p\right) - \frac{dF}{dK}\dot{K} = 0 \tag{12}$$

which is obtained by taking the time derivative of (8), the plastic strain rate is given as follows:

$$\dot{\boldsymbol{\epsilon}}^p = G \operatorname{tr}\left(\frac{\partial f}{\partial \hat{\boldsymbol{\sigma}}}\dot{\boldsymbol{\sigma}}\right)\frac{\partial f}{\partial \hat{\boldsymbol{\sigma}}}, \tag{13}$$

where

$$G = \frac{1}{C\left[\operatorname{tr}\left(\dfrac{\partial f}{\partial \hat{\boldsymbol{\sigma}}}\dfrac{\hat{\boldsymbol{\sigma}}}{|\hat{\boldsymbol{\sigma}}|}\right)\right]^2 - \operatorname{tr}\left(\dfrac{\partial f}{\partial \boldsymbol{\epsilon}^p}\dfrac{\partial f}{\partial \hat{\boldsymbol{\sigma}}}\right) + \dfrac{dF}{dK}\kappa}, \tag{14}$$

and κ is given by

$$\kappa = \frac{\dot{K}}{\dot{\lambda}}. \tag{15}$$

Therefore κ is a function of $\hat{\boldsymbol{\sigma}}$, $\boldsymbol{\epsilon}^p$, and $\partial f/\partial \hat{\boldsymbol{\sigma}}$ in degree one.

Extended Constitutive Equations With the Elastic-Plastic Transition. A typical stress-strain relation of elastoplastic materials is schematically illustrated in Fig. 1. The yield condition (8) is defined by the relation of $\hat{\boldsymbol{\sigma}}$, $\boldsymbol{\epsilon}^p$, and K in the distinct yield state (fully plastic state) shown as the envelope curve of reloading curves in this figure. In the classical theory of plasticity it is assumed that $\dot{\boldsymbol{\epsilon}}^p = \mathbf{0}$ for $f < F$, so that a discontinuous change of the slope of the stress-strain curve is expressed at the yield point separating the yield state $f = F$ from the elastic state $f < F$. In fact, however, a plastic deformation occurs even in the state $f < F$ and grows up to the *yield* (or *fully plastic*) *state* $f = F$, so that the stress-strain curve appears smooth. Therefore, rather than calling the state $f < F$ the elastic state, we shall use the more

Downloaded 01 May 2010 to 171.66.16.243. Redistribution subject to ASME license or copyright; see http://www.asme.org/terms/Terms_Use.cfm

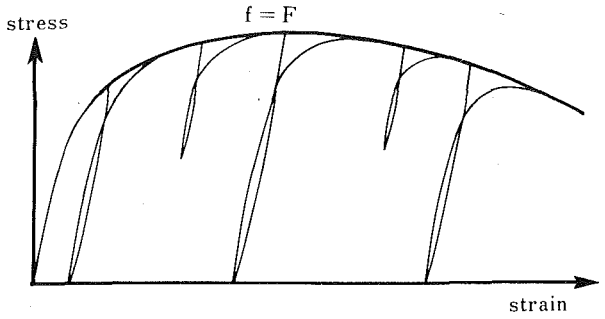

Fig. 1 The yield state ($f = F$) illustrated as the envelope curve of reloading curves

correct term the *subyield state*. In what follows we take into account the plastic deformation produced in the subyield state and thus we extend the foregoing basic model so as to describe the elastic-plastic transition.

Consider the surface expressed by the equation

$$f(\hat{\sigma}, \epsilon^p) = \oint (0 \leqq \oint \leqq F), \tag{16}$$

where $\oint$ is a scalar parameter. When we set formally $\oint = F$ the surface coincides with the yield surface expressed by (8), while when $\oint = 0$ it shrinks to the point $\sigma = \alpha$. For the existing α and ϵ^p the smaller $\oint$ is, the smaller is the surface expressed by (16). Thus, letting the value of $\oint$ change continuously, an interior region of the yield surface is densely covered with these surfaces which do not intersect each other. Among these surfaces, the one for the existing state of stress is termed a *loading surface*, while the one expressed by setting formally $\oint = F$ is called a *yield surface* in accordance with the classical theory (Needless to say, the existing stress does not necessarily satisfy the yield condition $f = F$).

Now, we adopt the quantity $\oint$ as a measure of the size of these surfaces. Then, we denote the ratio of the size of the loading surface ($\oint = f$) to that of the yield surface ($\oint = F$) by the parameter

$$\mathcal{R} \equiv \frac{f}{F} (0 \leqq \mathcal{R} \leqq 1). \tag{17}$$

Assume that the plastic strain rate produced in the general state $0 \leqq \oint \leqq F$, i.e., $0 \leqq \mathcal{R} \leqq 1$ depends on the parameter $\mathcal{R}$ through G in (13). Thus, extending (13), we assume the following plastic constitutive equation for the general state.

$$\dot{\epsilon}^p = \tilde{G} \operatorname{tr}\left(\frac{\partial f}{\partial \hat{\sigma}} \dot{\sigma}\right) \frac{\partial f}{\partial \hat{\sigma}}, \tag{18}$$

where $\tilde{G}$ is a scalar function extended from G by introducing the parameter $\mathcal{R}$ and is explicitly given as follows:

$$\tilde{G} = \frac{U}{C\left[\operatorname{tr}\left(\frac{\partial f}{\partial \hat{\sigma}} \frac{\hat{\sigma}}{|\hat{\sigma}|}\right)\right]^2 - \operatorname{tr}\left(\frac{\partial f}{\partial \epsilon^p} \frac{\partial f}{\partial \hat{\sigma}}\right) + \frac{dF}{dK} \kappa} \tag{19a}$$

or

$$\tilde{G} = \frac{U}{C\left[\operatorname{tr}\left(\frac{\partial f}{\partial \hat{\sigma}} \frac{\hat{\sigma}}{|\hat{\sigma}|}\right)\right]^2 - \operatorname{tr}\left(\frac{\partial f}{\partial \epsilon^p} \frac{\partial f}{\partial \hat{\sigma}}\right) + \frac{dF}{dK} (\kappa + u)} \tag{19b}$$

In these equations the scalars $U (0 \leqq U \leqq 1)$ and $u (\leqq 0)$ are monotonically increasing functions of $\mathcal{R}$ satisfying the following conditions so that (19a, b) coincide with (14) in the yield state.

$$U = 1, \quad u = 0 \quad \text{when} \quad \mathcal{R} = 1. \tag{20}$$

Examples of these functions in simple forms are

$$U = \{(1 - \nu)\mathcal{R}^\gamma + \gamma\}\mathcal{R}, \tag{21}$$

$$u = \zeta \ln \mathcal{R}, \tag{22}$$

where $\nu (0 \leqq \nu \leqq 1)$, $\gamma (\geqq 0)$, and $\zeta (\geqq 0)$ are material constants. U is the ratio of the plastic strain rate produced in a subyield state to that in a yield state. By letting ν take a value close to zero and γ a large value, U can be arbitrarily close to zero until $\mathcal{R}$ reaches a certain value. In that state an elastic deformation proceeds without a considerable plastic deformation. Besides, if it is necessary to give an exact expression for a purely elastic state, we have only to put $U = 0$ for $\mathcal{R} \leqq \mathcal{R}_0$ where $\mathcal{R}_0$ is a material constant. As will be described in a later section, (19a) can be applied to the plastic constitutive equation of metals, while (19b) to that of granular media.

Loading Criteria. For hardening materials the loading criterion can be defined by the sign of the quantity $\operatorname{tr}((\partial f/\partial \sigma)\dot{\sigma})$ as has been done in the traditional theory of plasticity. But this criterion is inapplicable to the generalized elastoplastic continuum with not only hardening but also perfectly plastic and softening behavior, since for such materials the sign of the aforementioned quantity can be zero or negative even in the loading state.

Here, we postulate a loading criterion as follows:

$$\begin{aligned} &\text{Loading: } \dot{\lambda} > 0, \\ &\text{Neutral loading: } \dot{\lambda} = 0, \\ &\text{Unloading: } \dot{\lambda} < 0. \end{aligned} \tag{23}$$

In the constitutive equation (18), $\dot{\lambda}$ is given by

$$\dot{\lambda} \equiv \tilde{G} \operatorname{tr}\left(\frac{\partial f}{\partial \sigma} \dot{\sigma}\right). \tag{24}$$

Note that in the neutral loading state the quantity $\operatorname{tr}((\partial f/\partial \sigma)\dot{\sigma})$ becomes zero, coinciding with $\dot{\lambda}$, as known from (23) and (24), while in the loading and the unloading states the sign of this quantity does not necessarily coincide with that of $\dot{\lambda}$. (23) would be the most general loading criterion that is applicable to the generalized elastoplastic continuum with hardening, perfectly plastic and softening behavior.

Special Plastic Constitutive Equations of Metals and Granular Media

Based on the constitutive equations proposed in the preceding section, two special classes of plastic constitutive equations for metals and granular media which exhibit very different plastic behaviors are derived in this section. Metals are usually analyzed as a hardening and plastically incompressible material, while granular media undergo a considerable softening and a plastic volume change which is the main factor in both hardening and softening phenomena.

Plastic Constitutive Equation of Metals. We first introduce the modified von Mises yield condition

$$\Sigma - F(\xi) = 0, \tag{25}$$

where

$$\Sigma \equiv \sqrt{\frac{3}{2}} |\hat{\sigma}^*|, \quad \hat{\sigma}^* \equiv \hat{\sigma} - \frac{1}{3} \operatorname{tr}(\hat{\sigma}) \mathbf{1}, \tag{26}$$

$$\dot{\xi} \equiv \sqrt{\frac{2}{3}} |\dot{\epsilon}^p|. \tag{27}$$

Adopting (19a) as $\tilde{G}$ and setting $f = \Sigma$ and $K = \xi$, the plastic strain rate is given by

$$\dot{\epsilon}^p = U \frac{\operatorname{tr}(\hat{\sigma}^* \dot{\sigma})}{\left(\frac{2}{3}\Sigma\right)^2 \left[C\left(\frac{\Sigma}{|\hat{\sigma}|}\right)^2 + \frac{dF}{d\xi}\right]} \hat{\sigma}^*, \tag{28}$$

and $\dot{\lambda}$ by

$$\dot{\lambda} = \frac{\operatorname{tr}(\hat{\sigma}^* \dot{\sigma})}{\frac{2}{3}\Sigma \left[C\left(\frac{\Sigma}{|\hat{\sigma}|}\right)^2 + \frac{dF}{d\xi}\right]} \tag{29}$$

Consider the uniaxial loading of a bar. In this state, Σ and $\dot{\xi}$ reduce

Downloaded 01 May 2010 to 171.66.16.243. Redistribution subject to ASME license or copyright; see http://www.asme.org/terms/Terms_Use.cfm

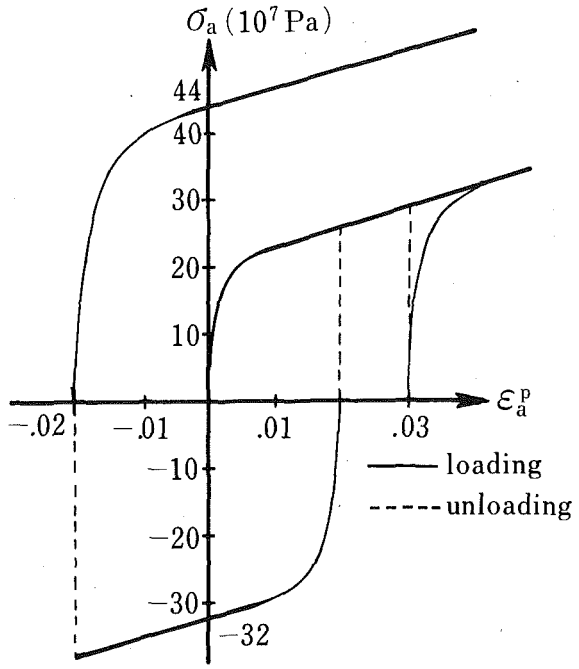

Fig. 2 Stress-plastic strain relation of metals under uniaxial loading; the isotropic hardening

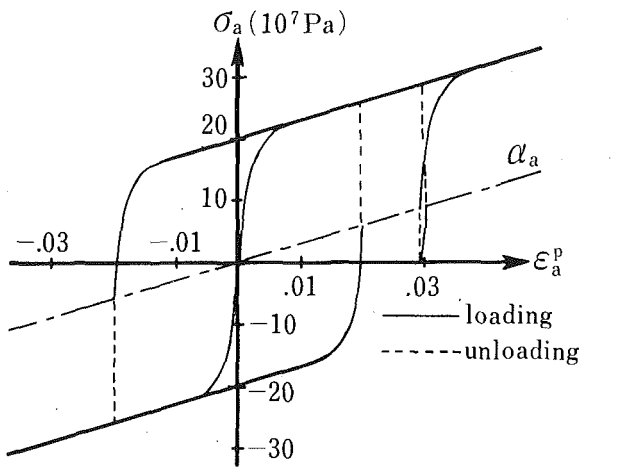

Fig. 3 Stress-plastic strain relation of metals under uniaxial loading; the kinematic hardening

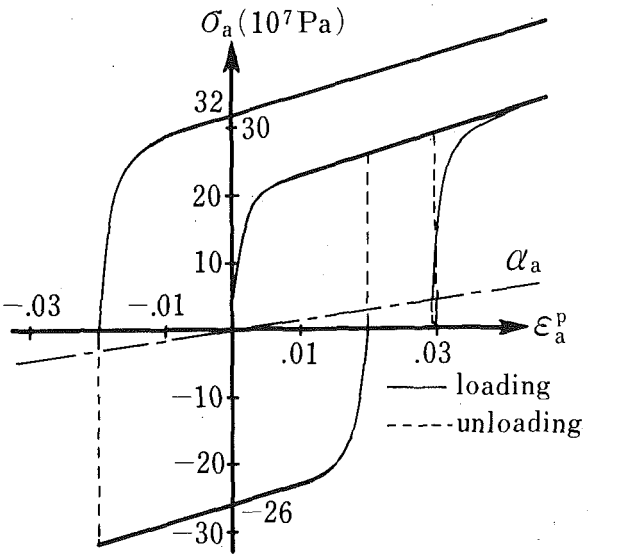

Fig. 4 Stress-plastic strain relation of metals under uniaxial loading; both the isotropic and the kinematic hardening

to $\Sigma = |\hat{\sigma}_a|$ and $\dot{\xi} = |\dot{\xi}_a{}^p|$, and from (28) and (29) $\dot{\epsilon}_a{}^p$ and $\dot{\lambda}$ are given by

$$\dot{\epsilon}_a{}^p = U\frac{\dot{\sigma}_a}{C + \dfrac{dF}{d\xi}}, \tag{30}$$

$$\dot{\lambda} = \frac{\hat{\sigma}_a\dot{\sigma}_a}{|\hat{\sigma}_a|\left(C + \dfrac{dF}{d\xi}\right)}, \tag{31}$$

where

$$\hat{\sigma}_a \equiv \sigma_a - \alpha_a, \tag{32}$$

σ_a, α_a, and $\epsilon_a{}^p$ are the components of the stress, the translation of the loading surface, and the plastic strain along the axis, respectively. From (10) the relation of $\dot{\alpha}_a$ to $\dot{\epsilon}_a{}^p$ is given by the following quite simple equation:

$$\dot{\alpha}_a = C\dot{\epsilon}_a{}^p \tag{33}$$

The relations of σ_a and α_a ($|\hat{\sigma}_a| = f$) to $\epsilon_a{}^p$ are depicted in Figs. 2–4. They are results calculated by selecting the functions included in (30) as follows:

$$\begin{aligned} &F = 20 + 300\xi(10^7\,\mathrm{Pa}), \quad C = 0 \quad : \quad \text{Fig. 2,} \\ &F = 20\,(10^7\mathrm{Pa}), \quad C = 300\,(10^7\mathrm{Pa}) \quad : \quad \text{Fig. 3,} \\ &F = 20 + 150\xi\,(10^7\mathrm{Pa}), \quad C = 150\,(10^7\mathrm{Pa}) \quad : \quad \text{Fig. 4,} \\ &U = (0.9\mathcal{R}^{20} + 0.1)\mathcal{R} \quad : \quad \text{Figs. 2–4.} \end{aligned} \tag{34}$$

In Figs. 2 and 3 the isotropic and the kinematic hardening state are shown, respectively, and in Fig. 4 the state in which both these hardenings proceed concurrently, while the loading ($\dot{\epsilon}_a{}^p \neq 0$) or the unloading ($\dot{\epsilon}_a{}^p = 0$) states are distinguished by the sign of $\hat{\sigma}_a\dot{\sigma}_a$ in (31) according to the loading criterion (24). In these figures we see gradual transitions from the elastic state ($\mathcal{R} < 1$, $\dot{\epsilon}_a{}^p/\dot{\sigma}_a = 0$) through the subyield state ($\mathcal{R} < 1$, $\dot{\epsilon}_a{}^p/\dot{\sigma}_a \neq 0$) to the yield (fully plastic) state ($\mathcal{R} = 1$). Hysteresis loops due to plastic strains increasing gradually in transitional states are depicted by unloading and reloading curves to and from the initial stress $\sigma_a = 0$ in Figs. 3 and 4.

Plastic Constitutive Equation of Granular Media. The existing plastic constitutive equations of granular media, the most representative of which is the Cambridge theory developed by Roscoe and his coworkers [12, 13] motivated by Drucker, Gibson, and Henkel's work [14], could explain to some extent the hardening behavior of granular media. These constitutive equations, however, cannot reasonably describe the softening behavior which occurs in the state subjected to a low confining pressure. In the so-called triaxial compression test, granular media subjected to a low constant lateral pressure undergo a softening gradually after the axial stress reaches a maximal absolute value. However, according to the existing equations adopting the associated flow rule without taking account of the elastic-plastic transition, an excessive softening appears immediately after the axial stress reaches a maximal absolute value at a yield point. Therefore, the stress-strain curve is bent too sharply, and either the maximal absolute value of axial stress or the plastic volume expansion is extremely overestimated. Then, consideration of the elastic-plastic transition is essentially important for the description of the softening behavior of granular media. On the other hand, recently Stutz [15], Romano [16], and Davis and Mullenger [17] have tried to derive a constitutive equation of granular media from the basic equation of hypoelastic body. The derived equations can plausibly express the

Downloaded 01 May 2010 to 171.66.16.243. Redistribution subject to ASME license or copyright; see http://www.asme.org/terms/Terms_Use.cfm

elastic-plastic transition. However, their constitutive equations for the loading state and those for the unloading state do not coincide in the boundary state, ignoring the existence of a neutral loading, i.e., the continuity condition [18]. This physical defect is caused because they, without due consideration, adopted the Green's loading criterion [19] assumed *a priori* for the hypoelastic body. This may be one of the fundamental problems to be solved in the hypoelastic approach to the derivation of constitutive equation of materials exhibiting complex behaviors such as granular media. In what follows we formulate a plastic constitutive equation of granular media, based on the constitutive equation derived in the previous section along the line of the traditional theory of plasticity, to describe reasonably not only hardening but also softening behavior.

In accordance with Drucker, Gibson, and Henkel [14], we assume that the hardening or the softening is caused by a plastic change of volume. Then, we set

$$\dot{K} = \dot{\epsilon}_v{}^p, \tag{35}$$

where $\dot{\epsilon}_v{}^p$ is a plastic volumetric strain rate, namely,

$$\dot{\epsilon}_v{}^p \equiv \mathrm{tr}\,(\dot{\boldsymbol{\epsilon}}^p). \tag{36}$$

Besides, for simplicity, we set $\boldsymbol{\alpha} = \mathbf{0}$ and $\boldsymbol{\epsilon}^p = \mathbf{0}$ in the function f. Therefore, we leave a development of anisotropy out of account. Thus the yield condition is expressed by

$$f(\boldsymbol{\sigma}) - F(\epsilon_v{}^p) = 0. \tag{37}$$

As described previously, we adopt (19b) including the function u in $\tilde{G}$. Consequently, the plastic strain rate is given by

$$\dot{\boldsymbol{\epsilon}}^p = \frac{U}{\dfrac{dF}{d\epsilon_v{}^p}\left[\mathrm{tr}\left(\dfrac{\partial f}{\partial \boldsymbol{\sigma}}\right) + u\right]}\,\mathrm{tr}\left(\frac{\partial f}{\partial \boldsymbol{\sigma}}\,\dot{\boldsymbol{\sigma}}\right)\frac{\partial f}{\partial \boldsymbol{\sigma}}. \tag{38}$$

If the stress in f is expressed by the mean stress P and the stress deviator $\boldsymbol{\sigma}^*$, i.e.,

$$P \equiv \frac{1}{3}\,\mathrm{tr}\,(\boldsymbol{\sigma}), \quad \boldsymbol{\sigma}^* \equiv \boldsymbol{\sigma} - P\mathbf{I}, \tag{39}$$

it can be written that

$$\mathrm{tr}\left(\frac{\partial f}{\partial \boldsymbol{\sigma}}\right) = \frac{\partial f}{\partial P}. \tag{40}$$

Now, as explicit forms of f and F in the yield condition (37) we adopt the following functions [20, 21].

$$f = -P\left[1 + \frac{2(v-2)}{2v-3}\left(\frac{\rho}{M}\right)^{2/3} + \frac{1}{2v-3}\left(\frac{\rho}{M}\right)^{v}\right], \tag{41}$$

$$F = F_0 \exp\,(-\epsilon_v{}^p/\mu), \tag{42}$$

where

$$\rho \equiv -\,|\boldsymbol{\sigma}^*|/P. \tag{43}$$

M, v, and μ are material constants. M is the value of ρ in the so-called *critical state* ($\dot{\epsilon}_v{}^p = \dot{\lambda}\partial f/\partial P = 0$, $\dot{\boldsymbol{\epsilon}}^{p*}$ ($\equiv \dot{\boldsymbol{\epsilon}}^p - 1/3\,\dot{\epsilon}_v{}^p\mathbf{I}$) $\neq \mathbf{0}$). F_0 is the value of F in the reference state ($\epsilon_v{}^p = 0$). The yield condition (37) with (41) and (42) is shown by an axisymmetric closed surface in the principal stress space, which satisfies the following conditions.

$$\begin{aligned} &\rho = 0: \quad P = -f, \quad \partial f/\partial|\boldsymbol{\sigma}^*| = 0, \\ &\rho = M: \quad P = -f/2, \quad \partial f/\partial P = 0, \\ &\rho \to +\infty: \quad P \to -0, \quad \partial f/\partial|\boldsymbol{\sigma}^*| \to +0. \end{aligned} \tag{44}$$

The shape of this surface in the plane (P, $|\boldsymbol{\sigma}^*|$) is depicted in Figs. 5(a) and 6(a).

Now, as to the case of the axisymmetric compression with a constant lateral pressure we display principal features of the foregoing constitutive equation. The relations of $|\boldsymbol{\sigma}^*|$ ($= \sqrt{2/3}|\sigma_a - \sigma_1|$, σ_1: lateral normal stress), f, F, and $\epsilon_v{}^p$ to $\epsilon_a{}^p$ are depicted in Figs. 5 and 6. The

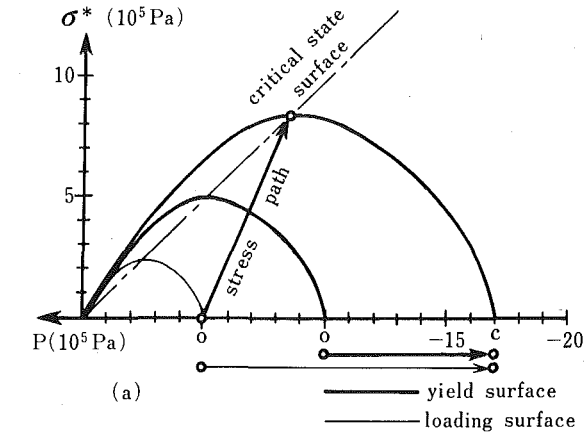

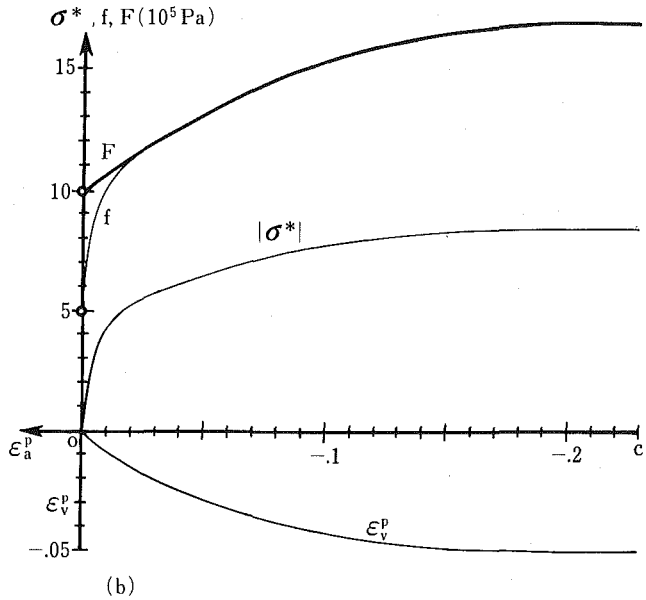

Fig. 5 Stress-plastic strain relation of granular media under axisymmetric compression; the isotropic hardening; (*a*) Stress path and changes of the yield and the loading surfaces; (*b*) Relations of $|\sigma^*|$, *f*, *F*, and $\epsilon_v{}^p$ to $\sigma_a{}^p$

results are calculated by selecting the functions, material constants and F_0 in (38), (41), and (42) as follows:

$$U = \mathcal{R}, \quad u = 20\ln\mathcal{R}, \quad M = 1, \quad v = 10,$$

$$\mu = 0.1, \quad F_0 = 10(10^5\mathrm{Pa}). \tag{45}$$

First, Fig. 5 shows the calculated result in the case of $\sigma_1 = \sigma_{a0}$ (initial value of σ_a) $= -5$ (10^5 Pa). In Fig. 5(a) the stress path is depicted by the line segment starting from the point o and ending in the point c (critical state). The *critical state surface* which represents stresses in the critical state is depicted by the half line arising from the origin of the coordinate system (P, $\boldsymbol{\sigma}^*$). How the yield and the loading surfaces expand is also shown in this figure. In Fig. 5(b) relations of $|\boldsymbol{\sigma}^*|$, f, F, and $\epsilon_v{}^p$ as functions of $\epsilon_a{}^p$ are shown, where f and F correspond to the sizes of the yield surface and the loading surface, respectively.

Next, Fig. 6 shows the calculated result in the case of $\sigma_1 = \sigma_{ao} = -1$ (10^5Pa). The stress path is depicted by the line segment including the turning point m. Namely, it starts from the point o and passes through the point c' in the critical state and rises up once to the point m and then returns finally to the point c in the critical state, while c' is the same point as c in the stress space. Since $\dot{\lambda}$ must be positive and $dF/d\epsilon_v{}^p$ is negative in (38), the following transition occurs as shown in Fig. 6.

Downloaded 01 May 2010 to 171.66.16.243. Redistribution subject to ASME license or copyright; see http://www.asme.org/terms/Terms_Use.cfm

1 Up to the state $\partial f/\partial P = 0$ ($o \sim c'$), $|\sigma^*|$, f and F increase and a slight plastic contraction of volume occurs.

2 In the state $\partial f/\partial P = 0 \sim -u(c' \sim m)$, $|\sigma^*|$ and f increase with the decrease of F and a considerable plastic volume expansion occurs.

3 In the state $\partial f/\partial P = -u(m)$, $|\sigma^*|$ and f take their maximal values. Considering the associated flow rule, we observe that if the loading surface is convex, $|\dot{\epsilon}_v{}^p/\dot{\epsilon}_a{}^p|$ takes a maximal value in this state.

4 If the plastic deformation proceeds further, $|\sigma^*|$, f and F decrease and a plastic volume expansion occurs, while f and F approach to each other asymptotically toward the critical state. In this state a remarkable softening occurs.

Here, remark the important role of the function u. If (38) does not include u, it brings about a divergent plastic deviatoric strain in the state $\partial f/\partial P = 0$ for any low stress level and the stress cannot go out of the critical state surface. Therefore, the function u must be included in the plastic constitutive equation (38).

Discussion

As described previously, Eisenberg and Phillips [3], using the concept of a loading surface similar to ours, have proposed a constitutive equation of metals describing the elastic-plastic transition. But this equation is complicated and inapplicable to the description of the softening behavior, since it is based on the condition $\mathrm{tr}\,(\partial f/\partial \sigma)\dot{\sigma} > 0$ for the loading state. On the other hand, Mroz [1] proposed the model of a field of hardening moduli for metals, which represents an elastic-plastic transition in a piecewise smooth manner, and further Krieg [4] and Dafalias and Popov [5] independently proposed modifications of the Mróz model by incorporating it into the so-called two surface model which represents a smooth elastic-plastic transition. Recently, the attempt to apply these models to the description of the softening behavior of granular media as well as the hardening one has been made [22, 23]. The Mróz model and its modifications assume plural surfaces, namely, an inner one enclosing an elastic region and an outer one corresponding to the yield surface in the present paper, as well as surfaces intermediate between these two. These surfaces approach to or recede from each other by translations. Now, consider the state in which the innermost surface enclosing the elastic region is in contact with the outmost surface. In such a state, reloading (through the point of contact) after a partial unloading within the innermost surface causes an abrupt change from the elastic to the fully plastic state; so the gradual transition is not expressed. Therefore, a softening behavior, to which consideration of the elastic-plastic transition is indispensable could not be suitably described by such models. Besides, the prime aim of the Mróz model may be to describe simply the plastic behavior of metals on the basis of the kinematic hardening. However, it appears doubtful whether the kinematic hardening is a substantial property playing such an important role in the plastic deformation of elastoplastic continua. Further, the constitutive equations of the Mróz model or its modifications are rather complex, since motions of plural surfaces must be formulated individually by different equations.

On the other hand, constitutive equations of metals derived by Tokuoka [7] with the hypoelastic approach and by Bernstein [8] with the application of the Lipschitz condition have fundamental features similar to those of (28) supplemented by the isotropic-linear elastic constitutive equation. For the present, these methods, however, may be only attempts to derive explicit constitutive equations of individual materials. In particular, the loading criterion is not defined rationally. As described previously, none of the existing constitutive equations of granular media derived by the hypoelastic approach satisfies the continuity condition. It is also not satisfied by the constitutive equation of the Tresca material derived by Tokuoka [7] using this approach. In all these constitutive equations the loading criterion is defined by the sign of the stress power according to Green's proposal [19] which has been assumed *a priori* for a hypoelastic body. But, in a strict sense, it is applicable only to such particular constitutive equations that when the stress power vanishes, the higher-order terms of stress related to plastic deformation also vanish to satisfy the continuity condition [18].

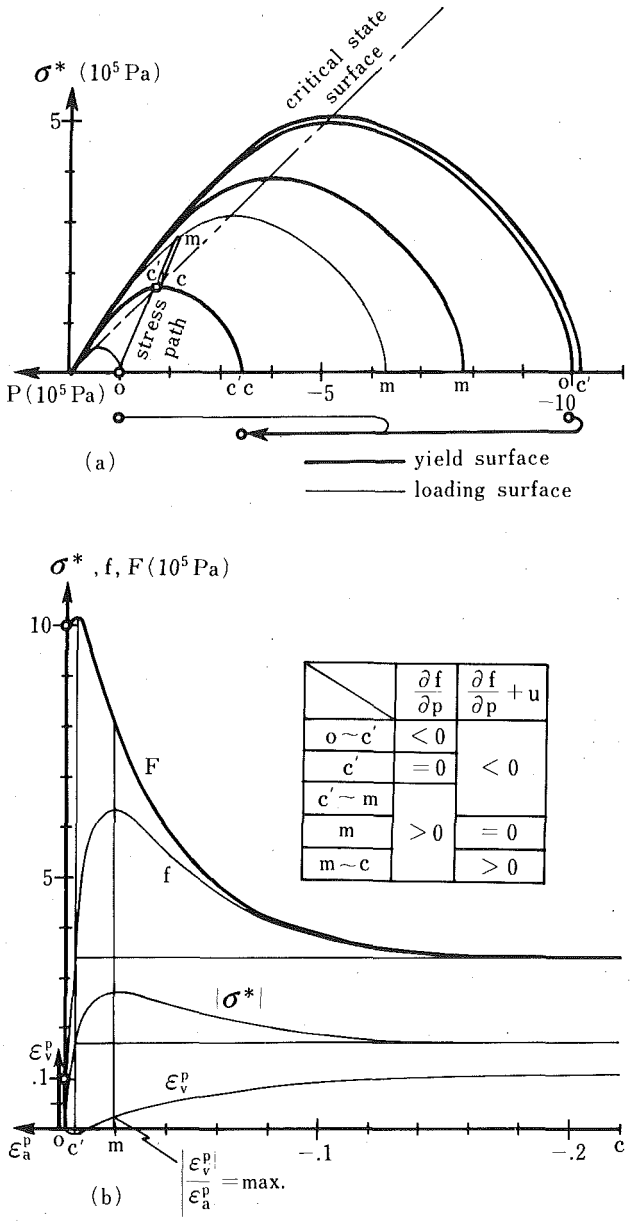

	$\frac{\partial f}{\partial p}$	$\frac{\partial f}{\partial p} + u$
$o \sim c'$	< 0	
c'	$= 0$	< 0
$c' \sim m$		
m	> 0	$= 0$
$m \sim c$		> 0

Fig. 6. Stress-plastic strain relation of granular media under axisymmetric compression; the isotropic hardening and softening; (*a*) Stress path and changes of the yield and the loading surfaces; (*b*) Relations of $|\sigma^*|$, f, F, and $\epsilon_v{}^p$ to $\epsilon_a{}^p$

The traditional concept of plasticity is, for the present, the most reasonable approach to the derivation of plastic constitutive equations. The equation (18) derived along the line of this concept might be regarded as a simple and reasonable plastic constitutive equation to describe the softening behavior as well as the hardening one with the elastic-plastic transition.

Acknowledgment

The author wishes to express his sincere gratitude to Prof. H. Yamaguchi of the Tokyo Institute of Technology for his kind advice and many helpful discussions. The results reported here were obtained in the course of research supported by the Aid for Sientific Researches from the Ministry of Education of Japan under Grant 265140 in 1977 and 355220 in 1978–1979 to the author.

Downloaded 01 May 2010 to 171.66.16.243. Redistribution subject to ASME license or copyright; see http://www.asme.org/terms/Terms_Use.cfm

References

1 Mróz, Z., "On the Description of Anisotropic Workhardening," *Journal of the Mechanics and Physics of Solids,* Vol. 15, 1967, pp. 163–175.

2 Phillips, A., and Sierakowski, R. L., "On the Concept of the Yield Surface," *Acta Mechanica,* Vol. 1, 1965, pp. 29–35.

3 Eisenberg, M. A., and Phillips, A., "A Theory of Plasticity With Noncoincident Yield and Loading Surfaces," *Acta Mechanica,* Vol. 11, 1971, pp. 247–260.

4 Krieg, R. D., "A Practical Two Surface Plasticity Theory," ASME JOURNAL OF APPLIED MECHANICS, Vol. 42, 1975, pp. 641–646.

5 Dafalias, Y. F., and Popov, E. P., "A Model of Nonlinearly Hardening Materials for Complex Loading," *Acta Mechanica,* Vol. 21, 1975, pp. 173–192.

6 Tokuoka, T., "Yield Condition and Flow Rules Derived From Hypo-Elasticity," *Archive for Rational Mechanics and Analysis,* Vol. 42, 1971, pp. 239–252.

7 Tokuoka, T., "Rate Type Plastic Material With General Work-Hardening," *ZAMM,* Vol. 58, 1978, pp. 1–7.

8 Bernstein, B., "An Unified Theory of Elasticity and Plasticity," *International Journal of Engineering Science,* Vol. 15, 1977, pp. 645–660.

9 Truesdell, C., and Noll, W., *The Nonlinear Field Theories of Mechanics,* in *Encyclopedia of Physics,* Flügge, S., ed., Vol. 3, Pt. 3, Springer-Verlag OHG, Berlin, 1965.

10 Flanders, H., *Differential Forms With Applications to the Physical Sciences,* Academic Press Inc., New York, 1963.

11 Ziegler, H., "A Modification of Prager's Hardening Rule," *Quarterly of Applied Physics,* Vol. 17, 1959, pp. 55–60.

12 Roscoe, K. H., Schofield, A. N., and Thurairajah, A., "Yielding of Clays in State Wetter than Critical," *Geotechnique,* Vol. 13, Institution of Civil Engineers, England, 1968, pp. 211–240.

13 Roscoe, K. H., and Burland, J. B., "On the Generalized Stress-Strain Behavior of 'Wet' Clays," *Engineering Plasticity,* Heymann, J., and Leckie, F. A., eds., Cambridge University Press, 1968, pp. 535–609.

14 Drucker, D. C., Gibson, R. E., and Henkel, D. J., "Soil Mechanics and Workhardening Theories of Plasticity, *Transactions ASCE,* Vol. 122, 1957, pp. 338–346.

15 Stutz, P., "Comportement Elasto-plastique des Milieux Granularies," *Foundations of Plasticity,* Sawczuk, A., ed., International Symposium on Foundations of Plasticity, Noordhoff International, Leydon, 1973, pp. 37–49.

16 Romano, M., "A Continuum Theory for Granular Media With a Critical State," *Archives of Mechanics,* Vol. 26, 1974, pp. 1011–1028.

17 Davis, R. O., and Mullenger, G., "A Rate-Type Constitutive Model for Soil With a Critical State," *International Journal for Numerical and Analytical Methods in Geomechanics,* Vol. 2, 1978, pp. 255–282.

18 Prager, W., "Recent Development in the Mathematical Theory of Plasticity," *Journal of Applied Physics,* Vol. 20, 1949, pp. 235–241.

19 Green, A. E., "Hypo-Elasticity and Plasticity," *Proceedings of the Royal Society,* London, Series A, Vol. 234, 1956, pp. 46–60.

20 Hashiguchi, K. "Elastoplastic Constitutive Equation of Granular Media," *Transactions of the Japan Society of Mechanical Engineers,* Vol. 43, 1977, pp. 1242–1250.

21 Hashiguchi, K., and Ueno, M., "Elastoplastic Constitutive Laws of Granular Media," *Constitutive Equations of Soils,* Murayama, S., and Schofield, A. N., eds., Ninth International Conference on Soil Mechanics and Foundation Engineering, Tokyo, 1977, pp. 73–82.

22 Mróz, Z., Norris, V. A., and Zienkiewicz, O. C., "An Anisotropic Hardening Model for Soils and Its Application to Cyclic Loading," *International Journal for Numerical and Analytical Methods in Géomechanics,* Vol. 2, 1978, pp. 203–221.

23 Prevòst, J.-H., "Plasticity Theory for Soil Stress-Strain Behavior," *Journal of the Engineering Mechanics Division, Proceedings ASCE,* Vol. 104, No. EM5, 1978, pp. 1177–1194.

Downloaded 01 May 2010 to 171.66.16.243. Redistribution subject to ASME license or copyright; see http://www.asme.org/terms/Terms_Use.cfm

P. G. Hodge, Jr.
Professor of Mechanics.
Honorary Mem. ASME

D. L. White[2]
Research Assistant.

Department of Aero Engineering and Mechanics,
University of Minnesota,
Minneapolis, Minn. 55455

Nonuniqueness in Contained Plastic Deformation[1]

It is well known that in a well-defined load-controlled boundary-value problem for an elastic/perfectly-plastic structure the displacements are unique if the structure is everywhere elastic, and they are not unique at the yield-point load when the structure becomes a mechanism. The present paper is concerned with the range of contained plastic deformation between these two extremes. Several examples are given in which more than one displacement field exists for loads less than the yield-point load. The significance of this phenomenon is commented on from a physical, mathematical, and computational point of view.

1 Introduction

The solution of boundary-value problems in the mechanics of solids is facilitated by making assumptions about the material and its response to prescribed boundary conditions. These assumptions lead to a mathematical model which approximates the response of the physical system. The accuracy of the approximation varies with the system in question, but frequently much can be learned about a complex system by studying a simple model. However, a simple model may exhibit qualitative phenomena which are not present in the physical system.

The elastic-perfectly plastic model is one such simple model which is useful in the range of contained plastic deformation between the elastic limit and the yield point load. At any fixed point such a material responds elastically until the stresses satisfy the yield function. As long as the stresses continue to satisfy the yield function the material responds plastically with no strain hardening. This paper considers elastic-perfectly plastic structures subjected to a system of loads defined by a single monotonically increasing parameter λ. The structure behaves elastically up to some value of λ, λ_e. For larger values of λ a portion of the structure will be plastic and a portion will be elastic. The elastic portion will limit the displacements and the structure is said to be in the range of contained plastic deformation. At the yield point load, $\lambda = \lambda_y$, deformations can increase indefinitely (assuming geometry changes are ignored). The structure is in the stage of unrestricted plastic flow for the constant load λ_y.

The magnitude of the deformation at $\lambda = \lambda_y$ is not determined, hence the solution is nonunique. It will often be unique to within a single magnitude parameter, but many examples are known of systems with two or more degrees of kinematic freedom at the yield point load.

Considerable theoretical work has been done on the question of uniqueness in elastic-plastic problems. Hill [1] has shown that there is always a unique solution when the total strain is small, the work hardening is monotonic and not zero, and the yield function and plastic potential are identical. Hill [2] has also demonstrated the following necessary condition for the existence of two distinct solutions:

$$I \equiv \int_v (\dot{\sigma}' - \dot{\sigma}'')(\dot{\epsilon}' - \dot{\epsilon}'')\, dV = 0 \tag{1}$$

For an elastic-perfectly plastic structure at the yield point load, $I = 0$. This accommodates the known lack of uniqueness. For contained plastic deformation, I may be positive or zero. If the assumption of two distinct solutions necessarily leads to I being positive, then the solution is unique. Otherwise the question is open.

The purpose of the present paper is to present several simple structures where $I = 0$ and more than one solution does in fact exist in the range of contained plastic deformation. The first example is a simple three bar truss which has frequently been used in the literature [3, 4] to illustrate phenomena which also occur in more complex cases. Section 2 offers a solution to this truss which explcitly demonstrates the lack of uniqueness.

Section 3 carefully examines the characteristics associated with this lack of uniqueness from physical, mathematical, and computational viewpoints. Even though the three bar truss is a simple example, it leads one to observe several general properties defining this type of nonuniqueness.

Section 4 tests these observations on further examples involving trusses, frames, and arches. In each of these examples the general properties proposed in Section 3 are seen to hold. Finally, Section 5 discusses these results and draws some general conclusions.

[1] This research was sponsored by the Office of Naval Research and partially supported by the University of Minnesota Computer Center; the results are taken from a dissertation submitted to the University of Minnesota by one of the authors (D.L.W.) in partial fulfillment of the requirements for a Master of Science degree.

[2] Now at Warner Electric Brake and Clutch Co., Beloit, Wisc. 53511.

Contributed by the Applied Mechanics Division for publication in the JOURNAL OF APPLIED MECHANICS.

Discussion on this paper should be addressed to the Editorial Department, ASME, United Engineering Center, 345 East 47th Street, New York, N. Y. 10017, and will be accepted until September 1, 1980. Readers who need more time to prepare a discussion should request an extension from the Editorial Department. Manuscript received by ASME Applied Mechanics Division, July, 1979; final revision, November, 1979.

Copyright © 1980 by ASME
Downloaded 01 May 2010 to 171.66.16.243. Redistribution subject to ASME license or copyright; see http://www.asme.org/terms/Terms_Use.cfm

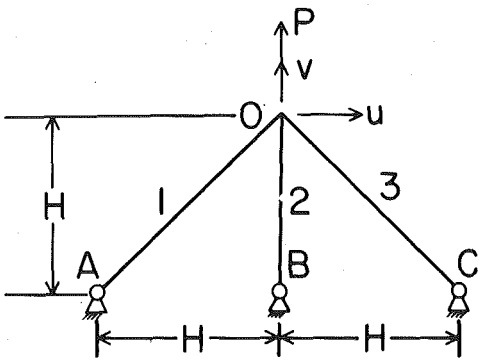

Fig. 1 Three-bar truss

2 Simple Truss

The three bar truss in Fig. 1 offers insight into the nonuniqueness phenomenon and is particularly easy to deal with mathematically. The two-force members OA, OB, and OC join the point O to the fixed points A, B, and C. The structure is symmetric about OB. The load P increases monotonically from zero such that the system is quasi-static. The subscripts 1, 2, and 3 refer to the bars OA, OB, and OC, respectively. Young's modulus E, and the area A are the same for each bar. The yield strength of bar OB is $3\sigma_y$. The yield strength of bars OA and OC is σ_y.

This problem is statically indeterminate to the first degree. There are three types of equations which define the problem: equilibrium, compatibility, and constitutive.

Horizontal and vertical equilibrium of the joint O give

$$F_1 = F_3 \tag{2a}$$

$$F_2 + (F_1 + F_3)/\sqrt{2} = P \tag{2b}$$

Compatibility is assured if the extensions of the bars are defined in terms of u and v, the horizontal and vertical (small) displacements of O:

$$\Delta_1 = (u + v)/\sqrt{2} \tag{3a}$$

$$\Delta_2 = v \tag{3b}$$

$$\Delta_3 = (-u + v)/\sqrt{2} \tag{3c}$$

The constitutive equations may be expressed in several ways. For the present example where all bar forces are positive and nondecreasing they can be written in the simple form

$$F_i \le Y_i \tag{4a}$$

$$\text{If} \quad F_i < Y_i \quad \text{then} \quad \Delta_i = (L_i/AE)F_i \tag{4b}$$

$$\text{Else} \quad F_i = Y_i \quad \text{and} \quad \Delta_i \ge (L_i/AE)Y_i \tag{4c}$$

where $Y_1 = Y_3 = A\sigma_y$ and $Y_2 = 3A\sigma_y$ are the yield forces in the bars, and $L_1 = L_3 = \sqrt{2}H$ and $L_2 = H$ are the lengths.

For P sufficiently small, all bars are elastic and the branch (4b) applies to all three bars. Equations (3) are regarded as definitions of Δ_i, hence equations (2) and (4b) form a system of five nonhomogeneous linear equations in five unknowns: F_1, F_2, F_3, u, and v. The solution of this system is

$$F_1 = F_3 = P/(2 + \sqrt{2}) \quad F_2 = 2P/(2 + \sqrt{2})$$

$$u = 0 \qquad v = F_2H/AE \tag{5}$$

This solution provides the values for stress, strain, and displacement at every point in the structure. The solution is unique in that it is the only set of forces and displacements which satisfies the governing equations. The solution is valid so long as the inequality in (4b) holds for each bar, i.e., until one or more of the bars yields. For the value

$$P_e = (2 + \sqrt{2})\,\sigma_y A \tag{6}$$

bars OA and OC yield and equation (4b) is no longer valid for bars 1 and 3.

As P is further increased, branch (4c) must be used for the two yielded bars. The governing equations are (2) and

$$F_1 = A\sigma_y \tag{7a}$$

$$v = \Delta_2 = (H/AE)F_2 \tag{7b}$$

$$F_3 = A\sigma_y \tag{7c}$$

The four equations (2), (7a), and (7c) contain only the unknowns F_1, F_2, and F_3. However, the system is consistent and the unique solution is

$$F_1 = F_3 = A\sigma_y \quad F_2 = P - \sqrt{2}A\sigma_y \tag{8a}$$

Combination of this result with (7b) gives

$$v = (H/AE)\,(P - \sqrt{2}A\sigma_y) \tag{8b}$$

The inequality in (4b) must hold for bar 2, and the inequality in (4c) must hold for bars 1 and 3. Therefore

$$P < (3 + \sqrt{2})\,A\sigma_y \tag{8c}$$

$$-(H/AE)\,(P - P_e) \le u \le (H/AE)\,(P - P_e) \tag{8d}$$

where P_e is given by (6).

Thus, in the range of contained plastic deformation, i.e.,

$$(2 + \sqrt{2})\,A\sigma_y \le P < (3 + \sqrt{2})\,A\sigma_y \tag{9}$$

(8) provides a complete set of solutions of the system of governing equations and inequalities. Although F_1, F_2, F_3, and v are single-valued, u is not uniquely specified. The range of u is largest at the yield point load. In the limit as P approaches P_y, with $\sigma_y = 200$ MPa and $E = 200$ GPa, v and u are given by

$$v/H = 0.003 \quad -0.001 \le u/H \le 0.001$$

Thus the range of values for u is the same order of magnitude as the vertical deflection.

At the yield point load

$$P = P_y = (3 + \sqrt{2})\,A\sigma_y \tag{10}$$

the branch (4c) holds for all three bars and the forces and displacements satisfy

$$F_1 = F_3 = A\sigma_y \quad F_2 = 3A\sigma_y \tag{11a}$$

$$v \ge 3H\sigma_y/E \quad -(v - 2H\sigma_y E) \le u \le (v - 2H\sigma_y/E) \tag{11b}$$

3 Analysis

In order to see the salient features of the previous example with a view to later generalization, it is desirable to write equations (2) and (3) in rate form, and to rewrite the constitutive equations as

$$F_i^2 \le Y_i^2 \tag{12a}$$

$$\text{If} \quad F_i^2 < Y_i^2 \quad \text{or} \quad F_i\dot{F}_i < 0 \quad \text{then } \dot{\Delta}_i = (L_i/AE)\dot{F}_i \tag{12b}$$

$$\text{Else} \quad \dot{F}_i = 0 \quad \text{and} \quad F_i\dot{\Delta}_i \ge 0 \tag{12c}$$

The equations are trivially integrated in the elastic range to furnish the same results as before. The integration is also simple in the range of contained plastic deformation with initial conditions provided by the results of the elastic range. However, the inequality (12c) combined with (3a) and (3c) gives

$$-\dot{v} \le \dot{u} \le \dot{v} \tag{13}$$

in the range of contained plastic deformation. The remaining governing equations place no further restrictions on u. Thus we see again that the solution is not unique.

Downloaded 01 May 2010 to 171.66.16.243. Redistribution subject to ASME license or copyright; see http://www.asme.org/terms/Terms_Use.cfm

Physically, the lack of uniqueness stems directly from the lack of a unique strain at the yield stress in the elastic-perfectly plastic material model. This is expressed by the inequality (12*c*). If the constitutive equation were an equality, as in a material with strain hardening, this lack of uniqueness would not arise. The inequality is on the rate of extension of the bar, which is a combination of $\dot{u}$ and $\dot{v}$. Now $\dot{v}$ satisfies the strict inequality when $\dot{u} = 0$ and in effect biases the expression in favor of being satisfied. Values of $\dot{u}$ up to the extent of the bias are acceptable. This is the range of possible values for $\dot{u}$.

The lack of uniqueness occurs in variables which are usually not of primary interest in the problem. The stresses, the external work, and the yield point load are all uniquely determined. This last result appeals to one's intuition and is in fact a consequence of the limit analysis theorems [5].

Certain small changes in the model may alter it so that unique results are obtained. For example, an infinitesimal amount of equal strain hardening will lead to the unique result $u = 0$. However, if the hardening coefficients in OA and OC are E' and $2E'$, respectively, then $u = (H/3AE)\,(P - P_e)$ no matter how small E' is compared to E. Alternatively, if the angle AOB is reduced slightly to $45° - \eta$ while angle BOC remains at 45°, then $u = (H/AE)\,(P - P_e)$ whereas a slight increase in the angle of AOB will lead to $u = -(H/AE)\,(P - P_e)$.

A third alternative is to add a small horizontal load ϵP which results in one of the unique values $u = \pm(H/AE)\,(P - P_e)$ depending on whether the horizontal load acts to the right or left. However, if we make *two* changes in the model such as decreasing the angle AOB and adding a horizontal load to the right in such a proportion that $\eta = 2(1 + \sqrt{2})\epsilon$, then the same nonunique solutions are obtained as for the symmetric case.

A more exact analysis in which we include the nonlinearity resulting from applying the loads to the deformed structure gives a unique solution when the load is tensile and a nonunique solution when the load is compressive [4]. Other small changes, such as changing the length of bar OB or changing the angle of both diagonal bars by the same amount will still lead to nonuniqueness. Therefore, since the different modifications lead to different solutions, the lack of uniqueness of the symmetric perfectly plastic case is a real phenomenon.

Mathematically, an essential feature of the nonuniqueness phenomenon is associated with the fact that the equilibrium equation (2*a*) is homogeneous. In rate form it becomes

$$\dot{F}_1 - \dot{F}_3 = 0 \tag{14}$$

Thus, when bars 1 and 3 yield simultaneously, it follows from (12*c*) alone that $\dot{F}_1 = \dot{F}_3 = 0$ and (14) becomes redundant. More generally, for any redundant truss with a single parameter load system, the equilibrium equations can always be written so that all but one of them are homogeneous. If all of the bars appearing in a homogeneous equation except bar k yield, the equation predicts $\dot{F}_k = 0$ regardless of the value of $\dot{\Delta}_k$. If bar k is elastic, this implies $\dot{\Delta}_k = 0$. However, if bar k yields at the same load as the last other bar in the equation, then $\dot{F}_k$ is already known to be zero and the equilibrium equation is redundant. The simultaneous yielding of the last two bars is the simultaneous occurrence of two collapse mechanisms for a portion of the structure. Either mechanism is sufficient to determine the force which this substructure can support.

If a truss is being analyzed with a computer program, the onset of nonuniqueness will cause problems since the stiffness matrix will be singular. The program may interpret this to be a collapse mechanism. If the program uses pivoting to reduce round-off error in the solution of the linear equations, the solver may be stopped by a zero pivot value.

There are at least two techniques which can be used to avoid this difficulty. If the program has been written to include the effects of strain hardening, the use of a small value for the strain-hardening coefficient, for instance $E \times 10^{-5}$, will make the solution unique without noticeably affecting the unique part of the results. NonSAP [6] is a finite-element program capable of handling nonlinear truss problems. With an elastic-perfectly plastic material model, the program stops after the yielding of bars OA and OC. The error message produced is "stop because zero pivot." If a strain-hardening coefficient of $E \times 10^{-5}$ is input, the program runs until the yield of bar OB. At that point the equilibrium iterations do not converge and the error message is "iteration limit reached."

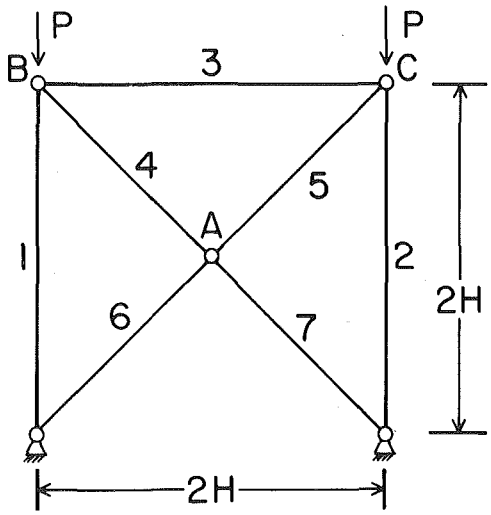

Fig. 2 Conventional truss

For programs written to analyze trusses which are based on the elastic-perfectly plastic material model, the technique is slightly more involved. The usual scheme of such a program is a step by step approach. A load is applied and the elastic problem solved. On the basis of this solution, the bar or bars which yield first are determined. These bars are replaced by the forces acting in them at yield and another elastic analysis is done. The process continues until the stiffness matrix becomes singular. If the truss has a nonunique solution, the stiffness matrix will become singular before the yield point load is reached.

A possible remedy is to replace only one bar at each step, and to infinitesimally increase the yield stress for other bars which were predicted to yield. For the three bar truss, OA and OC are found to yield at the same load. The program arbitrarily picks one of these bars, say OA, and replaces it with the force in the bar at yield. The yield stress in bar OC is increased slightly. In the new elastic solution, the stress in OC does not increase and the next bar to yield is OB. This gives a singular stiffness matrix and is correctly recognized as collapse. This modification will also correctly handle two bars yielding concurrently which do not represent a case of nonuniqueness.

Several characteristics of this lack of uniqueness in the three bar truss can be generalized. First, the stresses, the external work, and the yield point load are uniquely determined. Second, each of the displacements which is not uniquely determined is bounded. Third, one portion of the structure must yield in such a fashion as to allow more degrees of freedom than are specified by the surrounding material. Mathematically, this last requirement amounts to two or more members yielding simultaneously to reduce an equilibrium equation to an identity.

4 Further Examples

The present section considers several other simple structures where nonuniqueness occurs in the range of contained plastic deformation. Only the salient features of the solutions are given here; the details may be found in [7].

The truss in Fig. 2 is composed of bars having the same area, Young's modulus, and yield stress. The loads P are increased monotonically.

This truss is reasonable in appearance and might actually occur in practice. There is no reason for a practising engineer to suspect that the analysis of this truss will present special problems.

Downloaded 01 May 2010 to 171.66.16.243. Redistribution subject to ASME license or copyright; see http://www.asme.org/terms/Terms_Use.cfm

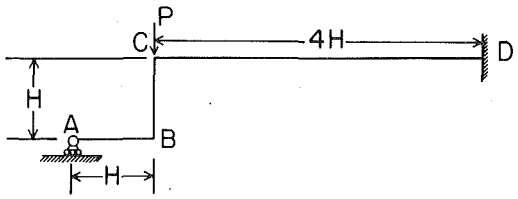

Fig. 3 Simple frame

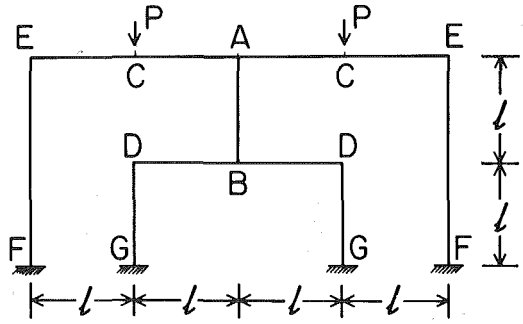

Fig. 4 Conventional frame

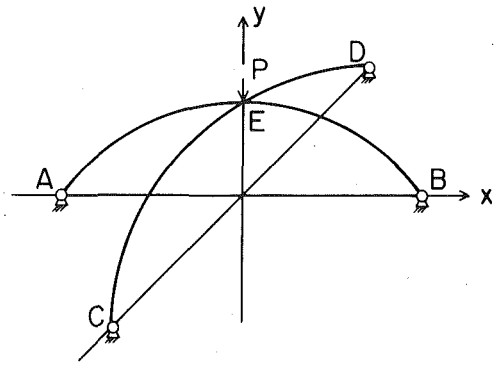

Fig. 5 Intersecting arches

At the elastic limit $P = P_e$, bars 1 and 2 both yield in compression. There is no collapse mechanism associated with this load. Indeed, the only conceivable mechanism is a rotation of the upper triangle about the point A which requires either bar 1 or bar 2 to unload.

As the load is further increased, the vertical displacement of point A is determined by the stresses in bars 6 and 7. The upper triangle is free to rotate about point A within the constraint that the magnitude of the strain in bars 1 and 2 increase monotonically. The yield point load P_y is reached when the diagonal bars yield. At this point there is a collapse mechanism.

Mistaking the load P_e when bars 1 and 2 yield for the yield point of the structure leads to underestimating the strength of this truss by 24 percent. For example, if the area of the bars is 600 mm^2, $E = 20$ GPa, and $\sigma_y = 20$ MPa, then 1 and 2 will yield when P reaches 41 kN, whereas the diagonal bars will yield only when P reaches 53 kN.

This example demonstrates the interesting result that the individual displacements under external loads at B and C are bounded but are not uniquely determined. However, the average displacement $v = (v_B + v_C)/2$ and the total external work $W_{ext} = Pv_B + Pv_C$ are unique, even though the individual deflections are not.

A second example concerns a rectangular frame where each member transmits axial and bending forces. Deformations due to bending moments dominate and deformations due to axial forces are neglected. The effect of axial forces on the yield strength of the members is also neglected.

The frame shown in Fig. 3 has a nonunique solution in the range of contained plastic deformation. All of the members have the same cross-sectional and material properties: E, I, and yield moment M_0. At the support D, the member is fixed against horizontal, vertical, and angular displacements. At A, the member is fixed against vertical displacements. The load P is monotonically increased from zero.

In rate form, the constitutive equations are

$$M_i^2 \le M_0^2 \tag{15a}$$

$$\text{If} \quad M_i^2 < M_0^2 \quad \text{or} \quad M_i\dot{M}_i < 0 \quad \text{then} \quad \dot{\theta}_i = 0 \tag{15b}$$

$$\text{Else} \quad \dot{M}_i = 0 \quad \text{and} \quad M_i\dot{\theta}_i \ge 0 \tag{15c}$$

Static considerations independent of material properties require that the bending moment in BC be constant along the length of the bar. At $P = P_e$, this moment reaches the yield moment, M_0.

For convenience, we assume that the joints are slightly weaker than the adjacent beams so that yield hinges form only at B and C as P is further increased. The moments at these points are then known to be M_0. Equilibrium equations determine the moment distribution throughout the beams AB and BC so long as (15c) holds. This stress distribution is no longer a function of the load P. The incremental deformations in this portion of the frame are due solely to the plastic hinges. At these hinges, the moment-rotation relationship is nonunique.

In the range of contained plastic deformation, the incremental vertical displacement and rotation of CD at the point C are given by the elastic solution to the cantilever beam CD loaded by $(P - P_e)$. Displacements in the mechanism A-B-C are governed by the constitutive equations (15c) and the principle of virtual work:

$$W_{ext} = M_0(\theta_C - \theta_B) \tag{16}$$

W_{ext} is known. Equations (15c) and (16) do not have a unique solution for θ_B and θ_C.

Although this analysis is based on the assumption that hinges form only at joints, the occurrence of the phenomenon does not depend on this assumption. One point of view is that in the structure being modeled, the joints actually are weaker than the beams. In this case the assumption that hinges occur at the joints is necessary to represent the physical situation. A second point of view is to assume that the beam yields every place the moment equals the yield moment. This implies that the entire beam BC is plastic. For a perfectly plastic material, angular displacement is independent of bending moment. There is not enough information to determine whether angular displacements are concentrated at one or more hinges, or whether the rotations are continuously distributed along the beam. Thus this premise also leads to a nonunique solution with, in fact, infinite degrees of freedom.

A more conventional frame exhibiting a lack of uniqueness is shown in Fig. 4. Plastic hinges form at B, then at C for P_e and P_1, respectively. The solution is unique until hinges form simultaneously at A and D for $P = P_2$. For $P_2 < P < P_y$, the incremental displacements at C will be determined by the elastic beams CE and EF whereas the displacement of A will be bounded but not uniquely determined. Physically, the ambiguity is explained by observing that the vertical deflection of C can be accommodated by either rotations at A and C or by a vertical deflection of A and rotations at B and D.

As a final example we consider the two orthogonal intersecting circular arches shown in Fig. 5. Arch CD rests on arch AB with a point of smooth contact at E so that only a vertical force is transmitted there. Both arches are pin-supported and have the same elastic properties, but AB is made of a material with a lower yield stress than that of CD.

As the load P is increased, at some value P_1 three hinges will form in AB while CD is still elastic. For $P > P_1$ the vertical displacement v_E of the center will be determined solely by the properties of arch CD and the increment of the load P.

Downloaded 01 May 2010 to 171.66.16.243. Redistribution subject to ASME license or copyright; see http://www.asme.org/terms/Terms_Use.cfm

Since CD offers no resistance to small deflections of point E in the x-direction, arch AB is the only source of information about u_E. A solution of the collapse load problem for AB will give the location of the plastic hinges and the moments and axial forces at those hinges. As the load P is increased beyond P_1, AB responds as a mechanism and the solution for u_E must come from studying this mechanism with a known vertical force and displacement. However, this mechanism leads to a singular equation which does not determine u_E. As in the other examples, the inequality in the constitutive equation does lead to bounds on u_E.

5 Conclusions

In each of these examples, a portion of the structure reaches its load-carrying capacity at a load below the yield point load for the entire structure. If there is only one collapse mechanism for the substructure, all quantities are determined. If two collapse mechanisms are possible, the solution may be nonunique. Simultaneous yielding at two or more points is a characteristic of this type of nonuniqueness. This concurrent yielding is most easily demonstrated in symmetric structures, but is equally possible in nonsymmetric ones.

Despite the lack of uniqueness, certain parameters are determined. All of the stresses are determined. The total external work, and hence the yield point load, is determined. All of the displacements are not determined, but they are bounded. These bounds increase monotonically, are largest at the yield point load for the entire structure, and are the same order of magnitude as the elastic displacements.

The elastic-perfectly plastic material assumption lies at the root of this lack of uniqueness. Even when the history is given, the stress does not uniquely determine the strain. This allows displacements to be independent of stresses. Kinematic arguments frequently exclude the phenomenon from certain classes of problems, but in a sense, these are the special cases. This paper has demonstrated nonuniqueness in trusses, frames, and arches. Interest in the topic arose because a proposed slip model for finite-element plasticity [8] encountered a lack of uniqueness in a plane strain problem. This type of nonuniqueness must be considered in all problems involving infinitesimal strains and an elastic-perfectly plastic material model. Of particular importance is the effect of nonuniqueness on computer programs for elastic/perfectly plastic structures.

Consider any finite-element problem in which an exact solution predicts simultaneous yielding of two elements at a load P' and an ensuing lack of uniqueness for $P' < P < P_y$. Then the next load step beyond P' should produce a singular stiffness matrix and consequent stopping of the solution at $P = P'$. However, several practical features of any program may alter this situation. If perfect plasticity is handled by a small artificial strain-hardening, then the problem should not arise. If perfect plasticity is handled directly, then round-off error may cause one element to yield before the other and the problem will disappear. Indeed, a NonSAP analysis of several truss problems reported on elsewhere [9] leads to the conclusion that the larger the truss the smaller the probability that the phenomenon will cause computational difficulties.

On the other hand, some programs endeavor to save time by slightly modifying yield stresses so that several elements yield at once in which case the program might predict a nonuniqueness which is not present in the exact solution.

From a practical point of view, when an elastic/plastic computer solution terminates with a message to the effect that a singular matrix has been encountered, the user should be aware of the possibility that the load is still less than P_y and that the displacement solution is still bounded even though it is not unique.

References

1 Hill, R., *The Mathematical Theory of Plasticity,* Clarendon Press, Oxford, 1950.

2 Hill, R., "A General Theory of Uniqueness and Stability in Elastic-Plastic Solids," *Journal of the Mechanics and Physics of Solids,* Vol. 6, 1958, pp. 236–249.

3 Hodge, P. G., Jr., "The Practical Significance of Limit Analysis," *Journal of the Aero/Space Sciences,* Vol. 25, No. 11, 1958, pp. 724–725.

4 Prager, W., "Problem Types in the Theory of Perfectly Plastic Materials, *Journal of the Aeronautical Sciences,* Vol. 15, No. 6, 1948, pp. 337–341.

5 Hodge, P. G., Jr., *Plastic Analysis of Structures,* McGraw-Hill, New York, 1959.

6 Bathe, K.-J., Wilson, E. L., and Iding, R. H., "NonSAP, A Structural Analysis Program for Static and Dynamic Response of Nonlinear Systems," University of California, Berkeley, 1974.

7 Hodge, P. G., Jr., and White, D. L., "Examples of Nonuniqueness in Contained Plastic Deformation," AEM Report H-24, University of Minnesota, July 1979.

8 van Rij, H. M., and Hodge, P. G., Jr., "A Slip Model for Finite-Element Plasticity," ASME JOURNAL OF APPLIED MECHANICS, Vol. 45, Sept. 1978, pp. 527–532.

9 White, D. L., and Hodge, P. G., Jr., "Computation of Nonunique Solutions of Elastic-Plastic Trusses," AEM Report H-25, University of Minnesota, Nov. 1979.

Downloaded 01 May 2010 to 171.66.16.243. Redistribution subject to ASME license or copyright; see http://www.asme.org/terms/Terms_Use.cfm

Eric K. C. Leung

Research Assistant,
Division of Engineering,
Brown University,
Providence, R. I. 02912

An Elastic-Plastic Stress Analysis of the Specimen Used in the Torsional Kolsky Bar

This paper examines the stress concentration, the yielding process, and the growth of the elastic-plastic boundary as a function of applied torque in tubular specimens with a short thin-walled section. Although the analysis is entirely quasi-static, it can, under the proper circumstances, be applied to the deformation of short specimens as generally used for dynamic testing in the torsional Kolsky bar. In the analysis, the governing equations for both elastic and elastic-plastic analyses are presented, the latter taking into account work hardening. Numerical solutions of these equations employ the finite-element method. The elastic stress distribution in the specimen and the elastic-plastic enclaves are presented for various loading stages.

Introduction

The torsional split Hopkinson or Kolsky bar has been employed by a number of investigators to determine the mechanical behavior of materials at high strain rates [1–4]. The materials tested are mostly polycrystalline metals and the specimen generally consists of a thin-walled tube loaded in torsion. The schematic diagram of the Kolsky bar and a photograph of typical specimens are shown in Figs. 1 and 2. The specimen proper is the thin-walled section between the flanges which provide the surface area necessary for mounting the specimen onto the bars. In the analysis of results this thin-walled section deforms plastically while the flanges are presumed to remain elastic. Furthermore, the thin-walled section is presumed to deform homogeneously throughout the entire section during straining. In practice, for a variety of reasons, these idealizations are not met. For instance, the plastic zone extends into the flanges; although experimental results indicate that, even at large strains, it extends only about 5 percent beyond the nominal gauge length. But, does the plastic zone start at the reentrant corners of the specimen and extend across the wall thickness while the remainder of the specimen remains elastic? Were this to occur then deformation would be far from homogeneous. Experimental results indicate that this is probably not occurring (Fig. 3). However, an elastic-plastic analysis of deformation should provide the locus of the elastic-plastic boundary as the applied torque increases and a measure of the homogeneity in stress within the plastic region. It should also bring out those values of the parameters for which nonhomogenous conditions might obtain. The present analysis makes use of a finite-element scheme to provide the static elastic-plastic deformation analysis. This analysis should be applicable to the dynamic problem since in most applications the ratio of the stress pulse length to the specimen length is about 100 to 1. The results are reassuring and consistent with experimental evidence, at least for a material with the mechanical properties of 1100-0 aluminum.

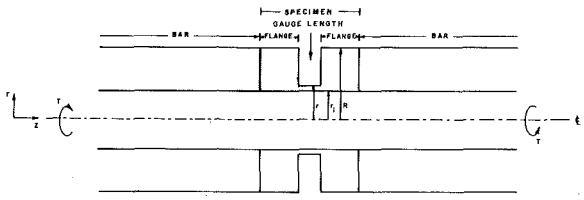

Fig. 1 Longitudinal section through the tube; the shaded portion is the domain used in the finite-element analysis

Formulation

It is desired to determine the state of stress during monotonic torsional loading of the tubular body shown in Fig. 1. The torque is taken as applied quasi-statically and parallel to the axis, and it is presumed that the tube extends to infinity in either direction so that the plane perpendicular to the tube at the center of the gauge length is a plane of symmetry as far as geometry and loading are concerned.

Presentation of the solution is given in two parts: the first deals with the elastic behavior of the body, and the second with the elastic-plastic behavior, including first yield, and providing the locus of the elastic-plastic boundary as a function of the applied torque.

Contributed by the Applied Mechanics Division for publication in the JOURNAL OF APPLIED MECHANICS.

Discussion on this paper should be addressed to the Editorial Department, ASME, United Engineering Center, 345 East 47th Street, New York, N. Y. 10017, and will be accepted until September 1, 1980. Readers who need more time to prepare a discussion should request an extension from the Editorial Department. Manuscript received by ASME Applied Mechanics Division, September, 1979; final revision, November, 1979.

Copyright © 1980 by ASME

Downloaded 01 May 2010 to 171.66.16.243. Redistribution subject to ASME license or copyright; see http://www.asme.org/terms/Terms_Use.cfm

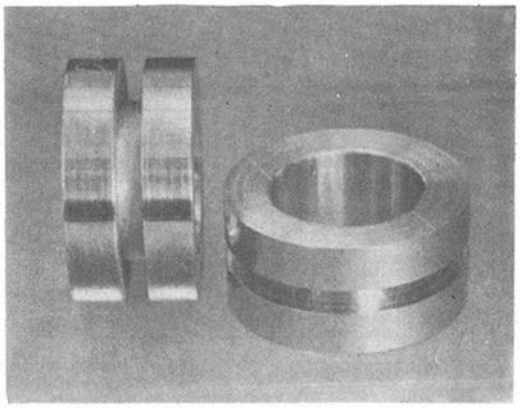

Fig. 2 Photograph of specimens; the narrow section between the integral flanges is the specimen proper

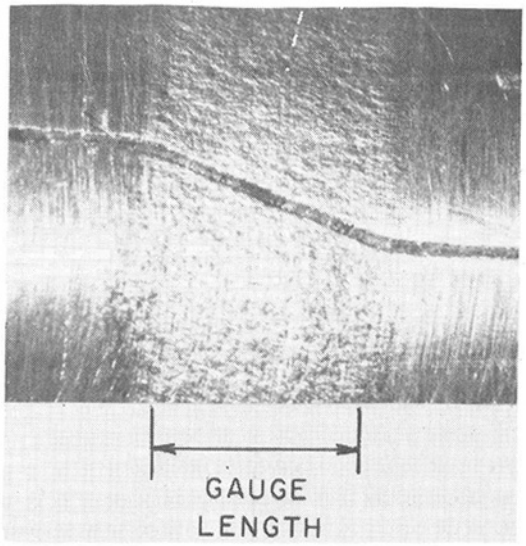

Fig. 3 Photograph of sectioned 1100-0 AL specimen showing scribe line deformed as a result of dynamic loading in shear; scribe line was initially straight and parallel to the axis of rotation

(a) Elastic Analysis. The elastic analysis is guided by the solution of the classical problem of the torsion of a shaft of varying circular cross section. In that case, the only nonvanishing component of displacement at a point is that directed perpendicular to an axial plane through the point. Furthermore, in cylindrical coordinates r, θ, z, this displacement component is a function of r and z, so that

$$u_r = u_z = 0 \quad \text{and} \quad u_\theta = u_\theta(r, z). \tag{1}$$

We seek an approximate solution to the present problem by taking the displacement of each point as consistent with (1). As a result, the nonvanishing strain components are $\epsilon_{r\theta}$ and $\epsilon_{\theta z}$ and hence the nonvanishing stress components are $\sigma_{r\theta}$ and $\sigma_{\theta z}$ by virture of Hooke's law. Following on the classical solution [5, 6] the problem may be solved by defining a stress function $\phi = \phi(r, z)$ which satisfies

$$\frac{\partial}{\partial r}\left(\frac{1}{r^3 G}\frac{\partial \phi}{\partial r}\right) + \frac{\partial}{\partial z}\left(\frac{1}{r^3 G}\frac{\partial \phi}{\partial z}\right) = 0 \tag{2}$$

and which must be constant on the axial bounding surface in order that this surface be traction-free. It should be noted that the shear modulus G need not be constant. The stress components are then derivable from ϕ through the relations

$$\sigma_{r\theta} = -\frac{1}{r^2}\frac{\partial \phi}{\partial z} \quad \text{and} \quad \sigma_{\theta z} = \frac{1}{r^2}\frac{\partial \phi}{\partial r} \tag{3}$$

At a distance sufficiently far from the profile discontinuity the stress component $\sigma_{r\theta}$ vanishes throughout the thickness of the tube while $\sigma_{\theta z}$, the tangential traction component distributed over the cross section, results in the torque T. Hence, at any section far from the specimen we have

$$\frac{\partial \phi}{\partial z} = 0 \tag{4}$$

and

$$T = \int_0^R 2\pi r^2 \sigma_{\theta z} dr = 2\pi \int_0^R \frac{\partial \phi}{\partial r} dr = 2\pi(\phi_0 - \phi_i) \tag{5}$$

where ϕ_0 and ϕ_i correspond, respectively, to the constant values of ϕ on the external and internal boundaries of the tube. One can take $\phi_i = 0$ with no loss in generality thus giving

$$T = 2\pi\phi_0 \tag{6}$$

From symmetry, (4), must also hold for the plane of symmetry of the tubular specimen.

(b) Elastic-Plastic Analysis. Since the external boundary always experiences the maximum strain, plastic flow will start at some point along this boundary. It is expected that the plastic zone will start at the reentrant corners and spread out toward the interior and across the gauge length of the specimen as the applied torque increases monotonically. The problem is to determine how the plastic zone grows and where the elastic-plastic boundary is for a given applied torque. Similar torsion problems have been solved both numerically and experimentally by different investigators [7–9]. However, in their analyses, these investigators modeled the material as elastic-perfectly plastic. This approximation is not suitable for the present application. The mathematical relationship required in the elastic-plastic regime will be derived, taking into account strain hardening.

When the tube is twisted beyond the elastic limit, plastic strains are induced at the highest stressed points and plastic flow begins. If only small geometry changes occur during the entire deformation process and if the assumptions made for the displacement components in the elastic analysis again hold for plastic deformation then $u_\theta \equiv u(r, z)$ is the only nonvanishing displacement component. Hence, the only nonzero strain components are $\epsilon_{r\theta}$ and $\epsilon_{\theta z}$. All stress components vanish except $\sigma_{r\theta}$ and $\sigma_{\theta z}$, which are still related to the stress function $\phi(r, z)$ by (3) and thus satisfy equilibrium.

Hooke's law now reads

$$\sigma_{r\theta} = 2G\epsilon^e_{r\theta} = 2G(\epsilon_{r\theta} - \epsilon^p_{r\theta}) = G\left[r\frac{\partial}{\partial r}\left(\frac{u}{r}\right) - 2\epsilon^p_{r\theta}\right] \tag{7}$$

$$\sigma_{\theta z} = 2G\epsilon^e_{\theta z} = 2G(\epsilon_{\theta z} - \epsilon^p_{\theta z}) = G\left[r\frac{\partial}{\partial z}\left(\frac{u}{r}\right) - 2\epsilon^p_{\theta z}\right]$$

where the superscripts e and p denote, respectively, the elastic and plastic parts of the corresponding strain component. Using (3) and eliminating u from (7) we obtain

$$\frac{\partial}{\partial r}\left(\frac{1}{r^3 G}\frac{\partial \phi}{\partial r}\right) + \frac{\partial}{\partial z}\left(\frac{1}{r^3 G}\frac{\partial \phi}{\partial z}\right) = 2\frac{\partial}{\partial z}\left(\frac{\epsilon^p_{r\theta}}{r}\right) - 2\frac{\partial}{\partial r}\left(\frac{\epsilon^p_{\theta z}}{r}\right) \tag{8}$$

which satisfies compatibility conditions during loading into the elastic-plastic regime. Note that this equation reduces to (2) when the plastic strain components vanish.

For simplicity, assume the material behavior in a uniaxial tension test to be described by a bilinear stress-strain relation

$$\sigma = \begin{cases} E\epsilon & \epsilon \le \epsilon_y \\ \sigma_y + E_t(\epsilon - \epsilon_y) & \epsilon \ge \epsilon_y \end{cases}.$$

Here, σ_y denotes the yield stress in tesion, ϵ_y, the initial yield strain, E, the Young's modulus, and E_t, the tangent modulus. The hardening slope is then given by

$$H' = \frac{EE_t}{E - E_t},$$

and is a constant since E and E_t are constants.

Downloaded 01 May 2010 to 171.66.16.243. Redistribution subject to ASME license or copyright; see http://www.asme.org/terms/Terms_Use.cfm

Employing the incremental theory of plasticity for an isotropic work-hardening material obeying the von Mises yield criterion, the Prandlt-Reuss equations become

$$\frac{\Delta\epsilon^p_{r\theta}}{\sigma_{r\theta}} = \frac{\Delta\epsilon^p_{\theta z}}{\sigma_{\theta z}} = \frac{3}{2}\frac{d\bar{\sigma}}{H'\bar{\sigma}} = \frac{3}{2}\frac{\sigma_{r\theta}\Delta\sigma_{r\theta} + \sigma_{\theta z}\Delta\sigma_{\theta z}}{H'(\sigma^2_{r\theta} + \sigma^2_{\theta z})} \tag{9}$$

where $\bar{\sigma} = \sqrt{3(\sigma^2_{r\theta} + \sigma^2_{\theta z})}$ is the effective stress. On eliminating $\Delta\epsilon^p_{r\theta}$ and $\Delta\epsilon^p_{\theta z}$ from (9) and the incremental form of (8), the governing equation for deformation in the plastic regime can be obtained [10]. In its final form this equation can be expressed as

$$\frac{\partial}{\partial r}\left\{\left[\frac{1}{r^3G} + \frac{3\sigma^2_{\theta z}}{H'r^3(\sigma^2_{r\theta} + \sigma^2_{\theta z})}\right]\frac{\partial\Delta\phi}{\partial r}\right\} + \frac{\partial}{\partial z}\left\{\left[\frac{1}{r^3G} + \frac{3\sigma^2_{r\theta}}{H'r^3(\sigma^2_{r\theta} + \sigma^2_{\theta z})}\right]\frac{\partial\Delta\phi}{\partial z}\right\} - \frac{\partial}{\partial r}\left[\frac{3\sigma_{r\theta}\sigma_{\theta z}}{H'r^3(\sigma^2_{r\theta} + \sigma^2_{\theta z})}\frac{\partial\Delta\phi}{\partial z}\right] - \frac{\partial}{\partial z}\left[\frac{3\sigma_{r\theta}\sigma_{\theta z}}{H'r^3(\sigma^2_{r\theta} + \sigma^2_{\theta z})}\frac{\partial\Delta\phi}{\partial r}\right] = 0 \tag{10}$$

where the Δ quantities indicate small increments. The boundary conditions in the elastic-plastic analysis remain the same as those in the elastic analysis.

Method of Solution

Both equations (2) and (10), the governing equations for torsion in the elastic and plastic regimes, respectively, are second-order partial differential equations of the elliptic type with variable coefficients. The solution to these equations can be obtained by minimizing the functionals corresponding to these differential equations. In cylindrical coordinates, the general second-order elliptic partial equation takes the form

$$\frac{\partial}{\partial x_i}\left(C_{ij}\frac{\partial\phi}{\partial x_j}\right) - b(r,z)\phi = f(r,z) \tag{11}$$

where x_i and x_j correspond, respectively, to the coordinates r and z; the coefficients $C_{ij} = C_{ij}(r,z)$ are nonnegative and symmetric with respect to i and j. If we denote by S_ϕ that part of the boundary where ϕ is prescribed, and by S_n that part where the normal derivative of ϕ is prescribed, then the boundary conditions take the form

$$\phi = \bar{\phi} \text{ on } S_\phi \tag{12}$$
$$\frac{\partial\phi}{\partial n} = \bar{\phi}_n \text{ on } S_n$$

The functional to be minimized corresponding to the differential equation (11) with boundary conditions (12) has the form

$$I = \frac{1}{2}\int_A \left[C_{11}\left(\frac{\partial\phi}{\partial r}\right)^2 + 2C_{12}\frac{\partial\phi}{\partial r}\frac{\partial\phi}{\partial z} + C_{22}\left(\frac{\partial\phi}{\partial z}\right)^2 + b(r,z)\phi^2\right]dA + \frac{1}{2}\int_{S_\phi} f(r,z)\phi dA - \int_{S_n}\bar{\phi}_n\phi dS \tag{13}$$

Since $b(r,z)$ and $f(r,z)$ as well as $\bar{\phi}_n$ vanish for the present problem, (13) reduces to

$$I^e = \frac{1}{2}\int_A \left[\frac{1}{r^3G}\left(\frac{\partial\Delta\phi}{\partial r}\right)^2 + \frac{1}{r^3G}\left(\frac{\partial\Delta\phi}{\partial z}\right)^2\right]dA \tag{14}$$

for the elastic regime, and to

$$I^p = \frac{1}{2}\int_A \left\{\left[\frac{1}{r^3G} + \frac{3\sigma^2_{r\theta}}{H'r^3(\sigma^2_{r\theta} + \sigma^2_{\theta z})}\right]\left(\frac{\partial\Delta\phi}{\partial r}\right)^2 - \frac{6\sigma_{r\theta}\sigma_{\theta z}}{H'r^3(\sigma^2_{r\theta} + \sigma^2_{\sigma z})}\left(\frac{\partial\Delta\phi}{\partial r}\right)\left(\frac{\partial\Delta\phi}{\partial z}\right) + \left[\frac{1}{r^3G} + \frac{3\sigma^2_{\theta z}}{H'r^3(\sigma^2_{r\theta} + \sigma^2_{\theta z})}\right]\left(\frac{\partial\Delta\phi}{\partial z}\right)^2\right\}dA \tag{15}$$

for the plastic regime.

The numerical method used to implement a solution to equations (14) and (15) is based on the finite-element method. Because of the geometric and loading symmetry, only one quarter section of the entire tube need be considered in seeking a solution (see Fig. 1). This domain extends beyond the specimen into the flanges and into the Kolsky bars and then terminates at a sufficiently long distance away from the reentrant corner so that the stress distribution within the specimen can be determined properly.

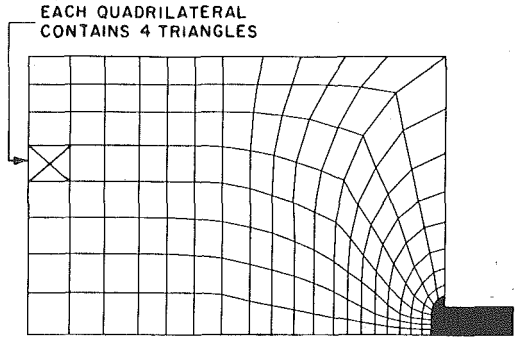

Fig. 4 The finite-element grid; only the shaded portion is used in Figs. 6 and 7

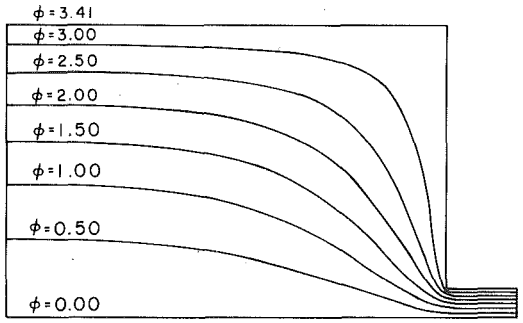

Fig. 5 Contours of stress function at initial yielding at reentrant corner

The finite-element grid shown in Fig. 4 is used in the sequel. It contains 296 quadrilateral elements or 1184 triangular elements having a total of 638 nodes and degrees of freedom. Use of static condensation reduces the number of active degrees of freedom to 342, thus reducing appreciably the size of the highly banded global stiffness matrix. Each triangular element assumes a shape function for ϕ linear in the spatial coordinates r and z so that ϕ is constant within the triangle.

Results and Discussions

As previously mentioned, the present analysis though quasi-static should be applicable to the dynamic problem provided the applied stress pulse is considerably greater than the specimen's length. The actual dimensions of the Kolsky specimen and bars have been used in the computation. Typically, the gauge length of the specimen is 2.5 mm and its wall thickness 0.5 mm. The outer and inner radii of the bar are 12.7 mm and 7.6 mm, respectively. The material properties chosen for the calculations are those of commercially pure aluminum. Its shear modulus and the yield stress in tension are taken to be $G = 2.48 \times 10^4$ MPa and $\sigma_y = 4.3 \times 10^1$ MPa, respectively. The yield stress in shear, k, is related to σ_y, through $k = \sigma_y/\sqrt{3}$. In order to observe the effect of the degree of work hardening, the calculations were carried through twice: once with $H' = 7.8 \times 10^2$ MPa and the second time with H' double the previous value.

Fig. 5 displays the elastic stress distribution within the specimen and a short end portion of a bar in terms of the stress function $\phi(r,z)$. Uniformity in the distribution of the stress function is observed along axial lines in the bar and within the gauge length of the specimen remote from the reentrant corner.

As expected, plastic yielding commences at the reentrant corner. With further increases in the applied torque, the plastic zone grows radially toward the internal boundary as well as across the gauge

Downloaded 01 May 2010 to 171.66.16.243. Redistribution subject to ASME license or copyright; see http://www.asme.org/terms/Terms_Use.cfm

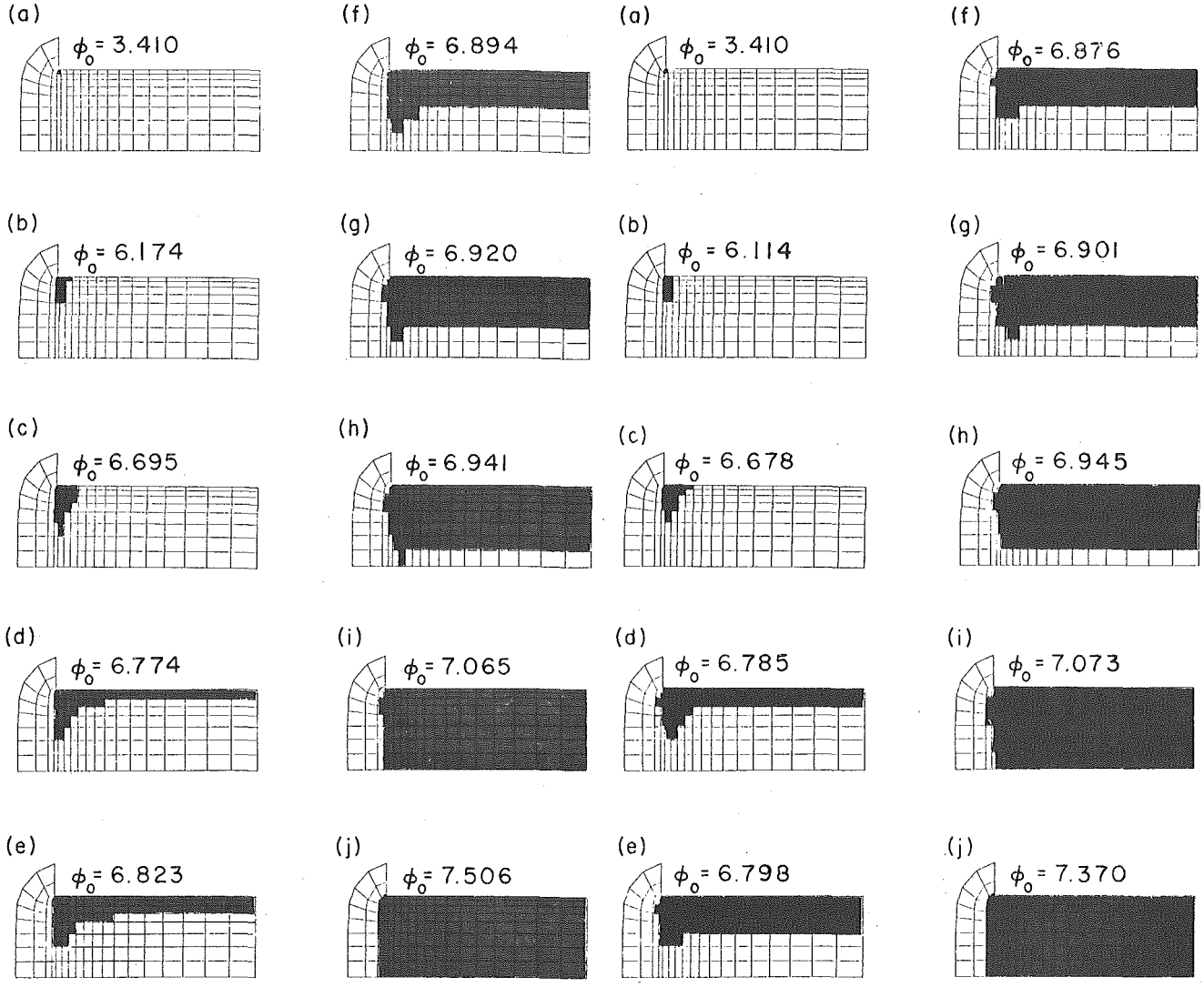

Fig. 6 Spread of the plastic zone at various loading stages; $\sigma_y = 43$ MPa, $H' = 7.8 \times 10^2$ MPa, applied torque is $T = 2\pi \times \phi_0$

Fig. 7 Spread of the plastic zone at various loading stages; $\sigma_y = 43$ MPa, $H' = 1.56 \times 10^3$ MPa; applied torque is $T = 2\pi \times \phi_0$

length along the external boundary of the specimen. The development of the plastic zone and the locations of the elastic-plastic boundaries at various stages of loading are plotted in Figs. 6 and 7. Fig. 6 refers to the material with a lower rate of work hardening. It shows that the plastic zone first expands radially toward the internal boundary of the shaft. However this inward growth does not continue and plastic flow remains contained up to quite a large torque. Indeed the trough in the elastic-plastic boundary at the reentrant corner widens out as more and more elements yield along the gauge length of the specimen. The results indicate that severe stressing takes place only locally and is confined to a very small region around the reentrant corner. Well-contained plastic flow takes place so that the assumption made in the paper by Duffy, et al. [4], that during the deformation process the flanges of the specimen remain elastic is consistent with the results obtained in the present analysis.

On comparing Figs. 6 and 7, the effect of different work-hardening rates is indicated by the shapes of the plastic zones at approximately equal load levels. These plastic enclaves exhibit similar shapes but the trough appears to grow deeper when the slope H' is smaller. Conversely, with high work hardening the growth of the plastic zone is more homogeneous along the entire gauge length of the specimen. A probable explanation is as follows: It is evident that in the material with the greater work hardening, an increasingly greater stress level is required to bring about further plastic yielding in those elements that yielded previously. These higher stress levels cause the neighboring elastic elements to become plastic more rapidly. Hence a high work-hardening rate produces more homogeneous growth of the plastic zone. It might be inferred that if the material is perfectly plastic ($H' = 0$) the trough may extend all the way toward the internal boundary in the early stage of yielding and therefore subsequent failure of the specimen may result upon further application of load to the tube. However, this does not seem to be borne out by the experiments of Costin, et al. [11]. They tested a cold-rolled steel whose work-hardening rate is close to zero. In static tests they obtain a homogeneous state of strain. In dynamic tests they did find shear bands, but these were located away from the reentrant corners.

Finally, it is interesting to compare present results to those found experimentally in dynamic loading, Fig. 3. In the experiment, a straight scribe line was drawn in the axial direction on the interior surface before the torsion experiment was performed. As may be seen in the photograph, the inclination of this line is approximately constant after testing. This indicates that the distribution of shear strain is nearly uniform over the entire gauge length. Furthermore, the plastic deformation in the flanges is confined to a small region compared to the gauge length of the specimen. Experimentally, the plastic deformation in the flanges appears to be nearly equal to, although

Downloaded 01 May 2010 to 171.66.16.243. Redistribution subject to ASME license or copyright; see http://www.asme.org/terms/Terms_Use.cfm

somewhat less than predicted by the present analysis. Hence the results of this analysis taken together with experimental observations, e.g., Fig. 3, would indicate homogeneous deformation in the torsional Kolsky bar.

Acknowledgments

Support for this research was provided by the National Science Foundation under Grant ENG75-18532. The author is grateful to Prof. J. Duffy for his guidance.

References

1 Baker, W. W., and Yew, C. H., "Strain-Rate Effects in the Propagation of Torsional Plastic Waves," ASME JOURNAL OF APPLIED MECHANICS, Vol. 33, 1966, pp. 917–923.

2 Nicholas, T., "Strain-Rate and Strain-Rate History Effects in Several Metlas, in Torsion," *Experimental Mechanics,* Vol. 11, No. 8, 1971, pp. 370–374.

3 Campbell, J. D., Eleiche, A. M., and Tsao, M. C. C., "Strength of Metals and Alloys at High Strains and Strain Rates," *Fundamental Aspects of Structural Alloy Design,* eds., Jaffee, R. I., and Wilcox, B. A., Plenum Publ. Co., 1977, pp. 545–563.

4 Duffy, J., Campbell, J. D., and Hawley, R. H., "On the Use of a Torsional Split Hopkinson Bar to Study Rate Effects in 1100-0 Aluminum," ASME JOURNAL OF APPLIED MECHANICS, Vol. 38, 1971, pp. 83–91.

5 Mitchell, J. H., "Torsion of a Rod of Varying Circular Section," *Proceedings of the London Mathematical Society,* Vol. 31, 1899, pp. 141–142.

6 Love, A. E. H., "Bar of Varying Circular Section," *A Treatise on the Mathematical Theory of Elasticity,* Dover, New York, 1944, pp. 325–326.

7 Rushton, K. R., "Elastic Stress Concentrations for the Torsion of Hollow Shouldered Shafts Determined by an Electrical Analogue," *Aeronautical Quarterly,* Vol. 15, 1964, pp. 83–96.

8 Eddy, R. P., and Shaw, F. S., "Numerical Solution of Elastoplastic Torsion of a Shaft of Rotational Symmetry," ASME JOURNAL OF APPLIED MECHANICS, Vol. 16, pp. 139–148.

9 Zienkiewicz, O. C., and Cheung, Y. K., "Stresses in Shafts," *The Engineer,* Vol. 224, 1967, pp. 696–697.

10 Leung, E. K. C., "An Elastic-Plastic Stress Analysis of the Specimens Used in the Torsional Kolsky Bar," Brown University Technical Report NSF ENG75-18532/10, May 1979.

11 Costin, L. S., et al., "On the Localization of Plastic Flow in Mild Steel Tubes Under Dynamic Torsional Loading," Brown University Technical Report NSF 18532/7, Jan. 1979, presented at the Conference on the Deformation of Materials at High Rates of Strain, Oxford, England, Mar. 1979.

Downloaded 01 May 2010 to 171.66.16.243. Redistribution subject to ASME license or copyright; see http://www.asme.org/terms/Terms_Use.cfm

Y. K. Lee
Student Mem. ASME

J. L. Swedlow
Professor.
Mem. ASME

Center for the Joining of Materials
and Department of Mechanical Engineering,
Carnegie Institute of Technology,
Carnegie-Mellon University,
Pittsburgh, Pa. 15213

Numerical Analysis of Elliptic-Hyperbolic Plastic Flow in Torsion

A method for solving elastic-perfectly plastic problems is presented, such that the mixed elliptic-hyperbolic field may be modeled properly. The method is applied to torsion of a rectangular bar which, although coarsely meshed, exhibits features observed experimentally. In particular, initiation and growth of behavior akin to shear banding is captured. A torque-twist curve is obtained well beyond the peak torque.

Introduction

An often unnoticed aspect of the theory of elastoplastic flow is the distinctive character of the field equations for nonhardening material. That is, in the presence of work-hardening, the theory is amenable to familiar computational methods, especially finite elements, and problem-solving for a given load sequence is straightforward. Absent hardening, however, the equations take a different form: Their ellipticity is lost and hyperbolicity may manifest itself in the form of bands or lines along which shear strain is highly concentrated.[1] In less formal terms, what this suggests is the following sequence of events in a material loaded from a null state. Response is initially elastic everywhere, and behavior may be described in terms of the familiar Saint-Venant principle. For continuous boundary data, the solution is continuous, differentiable, etc. For sufficiently discontinous boundary data, e.g., as caused by a rigid punch, a singularity will occur at the boundary but its effects will diffuse as the point of interest is moved toward the interior, away from the singularity.

The same behavior obtains in the presence of work-hardening elastoplastic flow i.e., a combination of elastic and plastic straining such that the latter is uniquely tied to the stress level through a suitable stress-plastic strain curve having a positive slope. Should the slope of the stress-plastic strain curve become zero, however, it is possible for straining to be concentrated along lines or curves in the field. (In various contexts, these are termed sliplines, shear bands, or characteristic curves, the latter term arising from the mathematical evaluation of the *character* of the equations.)

Certain remarks are in order. This concentration of straining is merely possible in the absence of work-hardening; whether it actually occurs depends on specific problem geometry *and instantaneous load level.* Hence shear banding, as we shall term it, may evolve from an otherwise smooth field and need not occur, fully developed, all at once. This contrasts to the more familiar type of solution in plasticity, commonly designated as slipline solutions. In both cases, we limit our attention to macroscale response, i.e., discussion here does not necessarily extend to slip as observed metallurgically, i.e., on the microscale. Physically, however, macroscale slip in a polycrystal results from tightly confined distributions of microslip.

Our interest in this type of behavior centers on the fact that the solution to a problem of elastoplastic flow may transform from a purely elliptic field to a mixed, elliptic *cum* hyperbolic field as load progresses. Since the use of numerical methods in attempting to solve such problems is inevitable, the question becomes one of establishing methods which will treat both types of response simultaneously. While the question is relatively new to elastoplastic problems, it is not intrinsically so: Gas-dynamics involving trans- and supersonic behavior have long since precipitated the issue. We are then forced to enquire whether methods for the one set of phenomena may be carried over to the other.

The answer, apparently, is in the affirmative. We show here the solution to a relatively simple problem in elastoplastic flow in which the transformation from an entirely elliptic to a mixed field is known to occur. The mechanics of this transformation are not yet fully understood, so far as we are aware, and some interesting theoretical questions remain to be resolved. It is nonetheless evident, however, that the capability for problem-solving may be described, and it is this topic which is pursued here.

Physical Events

In his landmark treatise [4], Nadai reports on experiments conducted many years earlier on torsion of mild steel bars. For each cross section, a set of bars was twisted to a certain level, unloaded, sectioned, and etched; the result shown is the shear band development at a sequence of twist levels. Flow layers, as Nadai terms them, were observed to emanate from the outer boundary—where stress is highest—and to progress inward. (We again prefer the term shear band,

[1] This distinction had been drawn in an earlier analysis of the theory of elastoplastic flow under the assumptions of infinitesimal strain theory and of modeling the material in terms of the second and third invariants of the stress deviator [1]. The latter assumption forces plastic incompressibility without affecting elastic dilation. The first assumption is, in a strict sense, in violation of equilibrium [2,3]; the full theory is nonetheless well posed and appears in practical circumstances not to exhibit serious solution error.

Contributed by the Applied Mechanics Division for publication in the JOURNAL OF APPLIED MECHANICS.

Discussion on this paper should be addressed to the Editorial Department, ASME, United Engineering Center, 345 East 47th Street, New York, N. Y. 10017, and will be accepted until September 1, 1980. Readers who need more time to prepare a discussion should request an extension from the Editorial Department. Manuscript received by ASME Applied Mechanics Division, April, 1979; final revision, December, 1979.

Copyright © 1980 by ASME
Downloaded 01 May 2010 to 171.66.16.243. Redistribution subject to ASME license or copyright; see http://www.asme.org/terms/Terms_Use.cfm

a narrow region of intense shearing.) In all cases, the shear bands developed in a direction normal to the boundary and, except for the vicinity of nonre-entrant corners, were quite uniformly spaced along the bar's periphery. More recently, Richmond [5] repeated the experiment for a circular bar, obtaining the same behavior.

In the context of elastoplastic flow theory, certain aspects are quite important. Even though the observations were made after load (torque) was removed, it is obvious that the interior or centroidal region of the bars was limited to response in the elastic range only; yield progressed from the boundary inward. To the extent that shear banding resulted from the virtually nil degree of hardening that characterizes mild steel, the field is clearly mixed in the sense just outlined. The mixture comprises the interior elastic region to be sure, peripheral areas that may have begun to yield but have not demonstrated shear banding, and the shear bands themselves. Second, we note that the same type of behavior is observed for several cross sections: circular, triangular, square, and rectangular. Finally, virtually uniform spacing of the shear bands—even on the circular bar—suggests a mechanism whereby the banding itself creates a strain gradient such that the bands must be distributed. Nadai discusses this spacing but does not explain it fully; to our knowledge, the matter has yet to be completely resolved.

Problem Statement

The equations of elastoplastic flow have been derived in detail elsewhere in the literature and need not be reiterated here. For torsion, displacement rates $(\dot{u}, \dot{v}, \dot{w})$ take the form [1]

$$\dot{u} = -yz\dot{\theta}, \quad \dot{v} = xz\dot{\theta}, \quad \dot{w} = \dot{W}(x,y)$$

where $\dot{\theta}$ is the rate of twist (per unit bar length). A flow rule may be determined in terms of the two nonvanishing shear stresses (τ_x, τ_y) and their rates $(\dot{\tau}_x, \dot{\tau}_y)$, as depicted in Fig. 1. The inverse flow rule is found to be

$$\dot{\tau}_x = \mu[(1 + \beta T_{yy})(\dot{W}_{,x} - \dot{\theta}y) - \beta T_{xy}(\dot{W}_{,y} + \dot{\theta}x)]/(1 + \beta)$$
$$\dot{\tau}_y = \mu[-\beta T_{xy}(\dot{W}_{,x} - \dot{\theta}y) + (1 + \beta T_{xx})(\dot{W}_{,y} + \dot{\theta}x)]/(1 + \beta) \quad (1)$$

in which μ is the elastic shear modulus, $\beta = \mu/\mu_0^{(p)}$ with $\mu_0^{(p)}$ the octahedral plastic shear modulus, and

$$T_{xx} = \tau_x^2/(\tau_x^2 + \tau_y^2)$$
$$T_{xy} = \tau_x\tau_y/(\tau_x^2 + \tau_y^2) \quad (2)$$
$$T_{yy} = \tau_y^2/(\tau_x^2 + \tau_y^2)$$

It may be shown [1] that, if the stress rates in (1) are subject to an equilibrium rate requirement of the form $\partial\dot{\tau}_x/\partial x + \partial\dot{\tau}_y/\partial y = 0$, the resulting equation for the warping rate $\dot{W}$ is quasi-linear. Its characteristic directions may be computed as

$$\frac{dy}{dx} = \frac{-T_{xy} \pm \sqrt{[-(1 + 1/\beta)/\beta]}}{1/\beta + T_{yy}} \quad (3)$$

Ellipticity is guaranteed so long as dy/dx is complex. Where $1/\beta$ vanishes, i.e., the ratio $\mu_0^{(p)}/\mu \to 0$, however, hyperbolicity may result. Note that this corresponds to "ideal" or "perfect" plasticity (or to "rigid" elasticity).

For the case in which $1/\beta \to 0$, (1) reduces to the simpler form

$$\dot{\tau}_x = \mu[T_{yy}(\dot{W}_{,x} - \dot{\theta}y) - T_{xy}(\dot{W}_{,y} + \dot{\theta}x)]$$
$$\dot{\tau}_y = \mu[-T_{xy}(\dot{W}_{,x} - \dot{\theta}y) + T_{xx}(\dot{W}_{,y} + \dot{\theta}x)] \quad (4)$$

and (3) becomes

$$dy/dx = -T_{xy}/T_{yy} = -\tau_x/\tau_y \quad (5)$$

in the presence of yield, i.e., $\tau_0 = \sqrt{[2(\tau_x^2 + \tau_y^2)/3]} = \tau_l$. (For lower values of τ_0, only elastic behavior occurs.) Orientation of the shear bands is given by (5) in those regions where yield is incipient or in progress.

The problem we wish to solve, using these equations, is twist of a rectangularly shaped bar. Broadly stated, increments of twist will be applied in sequence so that the process of elastoplastic flow is generated and the accumulation may be observed. A detailed discussion of procedure appears elsewhere [6], giving specifics of how the overall process is tracked numerically. Not discussed in that source, and the point of the present discussion, is the implied spatial integration for warping rate (or increment) with growth in the loading (twist) level. Obviously from (5) the characteristic directions are real in certain parts of the field so that the procedure chosen must be able to treat mixed problems.

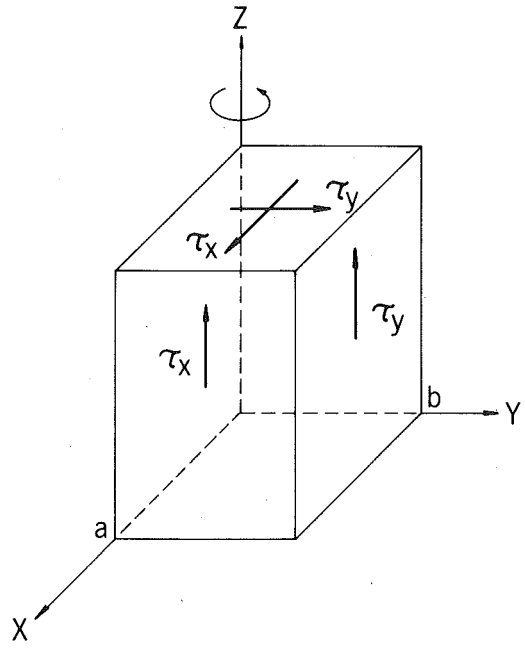

Fig. 1 Stress components in a twisted rectangular bar

Certain difficulties are evident. Any solution method that relies on (spatial) differentiability of warping rate or material state must be excluded, ruling out purely analytical techniques and finite differences. Since the problem is mixed, the usual slipline methods are precluded as well. Ordinary finite-element methods are also problematic because the discontinuities in material response lead to singularities in the coefficient (or stiffness) matrix. The common choices are thereby inappropriate.

An alternative finite-element formulation has been discussed in the literature, apparently as an adjunct to more familiar methods; see, e.g., [7]. The real utility of this formulation has been shown by Fix and Gunzburger [8] in that they have explicitly treated problems of the mixed type. Although initially presented in the framework of transonic flutter analysis, the approach is pertinent here in that ". . . the computational algorithm is the same in elliptic and hyperbolic regions." A capacity of this sort is most attractive for the present purpose, and the Fix-Gunzberger formulation has been adapted to the problem described in the foregoing. We review this formulation briefly and then turn to results of the analysis for the remainder of the paper.

From (1), the limit case of $1/\beta \to 0$ was obtained to find (4) for the yielded region. Similarly, the case of $\beta \to 0$ gives the elastic result. These two sets of relations, each subjected to an equilibrium (rate) requirement, as previously noted, lead to a second-order linear or quasi-linear differential equation for the warping rate $\dot{W}$. The same sets of equations may be used to construct boundary conditions in terms of traction rates, pertinent to a prismatic bar. Recognizing that excitation occurs in terms of the twist rate $\dot{\theta}$, it may be observed that one need add only initial conditions to arrive at a well-posed problem. We take the last to be null values of the dependent variables.

Downloaded 01 May 2010 to 171.66.16.243. Redistribution subject to ASME license or copyright; see http://www.asme.org/terms/Terms_Use.cfm

We next decompose the problem into a first-order system, and the following representation is arbitrarily[2] chosen:

$$U_1 = \partial \dot{W}/\partial x, \quad U_2 = \partial \dot{W}/\partial y, \quad U_3 = \dot{W}$$

It is easily shown that boundary conditions are simple to state, and that equilibrium takes the form

$$U_{1,x} + U_{2,y} = 0 \tag{6a}$$

in the elastic region, and

$$T_{yy}U_{1,x} - T_{xy}U_{1,y} - T_{xy}U_{2,x} + T_{xx}U_{2,y} + \alpha_1 U_1 + \alpha_2 U_2 = (\alpha_1 y - \alpha_2 x)\dot{\theta} \tag{6b}$$

in the plastic region. In (6b), α_1 and α_2 are coefficients resulting from the substitution of (4) into the equilibrium equation. They are

$$\alpha_1 = T_{yy,x} - T_{xy,y}, \quad \alpha_2 = -T_{xy,x} + T_{xx,y}$$

In addition to one or the other of the foregoing equations, we have for consistency

$$U_{3,x} - U_1 = 0, \quad U_{3,y} - U_2 = 0 \tag{7}$$

In the elastic region, we construct the functional

$$\iint_\Omega \{(U_{1,x} + U_{2,y})^2 + (U_{3,x} - U_1)^2 + (U_{3,y} - U_2)^2\}dxdy + \frac{1}{h_y}\int (U_1 - \dot{\theta}y)^2\Big|_{x=a} dy + \frac{1}{h_x}\int (U_2 + \dot{\theta}x)^2\Big|_{y=b} dx \tag{8a}$$

while, for the region undergoing yield, the functional is

$$\iint_\Omega \{[T_{yy}U_{1,x} - T_{xy}U_{1,y} - T_{xy}U_{2,x} + T_{xx}U_{2,y} + \alpha_1 U_1 + \alpha_2 U_2 - (\alpha_1 y - \alpha_2 x)\dot{\theta}]^2 + [U_{3,x} - U_1]^2 + [U_{3,y} - U_2]^2\}dxdy + \frac{1}{h_y}\int (U_1 - \dot{\theta}y)^2\Big|_{x=a} dy + \frac{1}{h_x}\int (U_2 + \dot{\theta}x)^2\Big|_{y=b} dx \tag{8b}$$

In (8a,b), the lines $x = a$ and $y = b$ represent outer boundaries of the quadrant to be analyzed; see Fig. 1. The weights $1/h_x$ and $1/h_y$ do no more than balance the interior and boundary integrals, in that h_x and h_y are the grid spacings along $y = b$ and $x = a$, respectively. Note that the boundary integrals will lead to natural boundary conditions [8].

Simultaneous minimization of (8a,b) will be used to formulate finite-element equations; in effect, (8a,b) replace the energylike functional ordinarily used in such a development [6]. Although any finite-element space could be used, foresight of the nature of results suggests use of linear elements (triangles). Assume that there are M nodes and approximate the unknowns U_1, U_2, U_3 by the expansion

$$\mathbf{U} = \begin{pmatrix} U_1 \\ U_2 \\ U_3 \end{pmatrix} = \sum_{j=1}^{M} \begin{pmatrix} U_{j1} \\ U_{j2} \\ U_{j3} \end{pmatrix} \phi_j(x,y) = \sum_{j=1}^{M} \mathbf{U}_j \phi_j \tag{9}$$

where ϕ_j is a shape function which is unity at node j and zero at all others. By substituting (9) into (8a,b), then minimizing the results with respect to the generalized coordinates of node l, i.e., U_{l1}, U_{l2}, and U_{l3}, we obtain alternate sets (elastic or plastic) of three algebraic equations which can be applied to each element, as appropriate. These equations will form an algebraic system for nodal values which is always linear in the increment. In a fully elastic stage, only the elastic equations need to be satisfied. As load increases beyond initial yield, both elastic and plastic equations have to be satisfied simultaneously. Once we have solved for **U**, the stress and strain increments can then be calculated as indicated, and simple summing gives accumulated values.

[2] It is equally straightforward to use physical variables, i.e., $\dot{\tau}_x, \dot{\tau}_y$, and $\dot{W}$. Normalization of these quantities is required, however, in order to avoid problems of precision in numerical work. Ongoing work uses the latter approach and is to be reported separately.

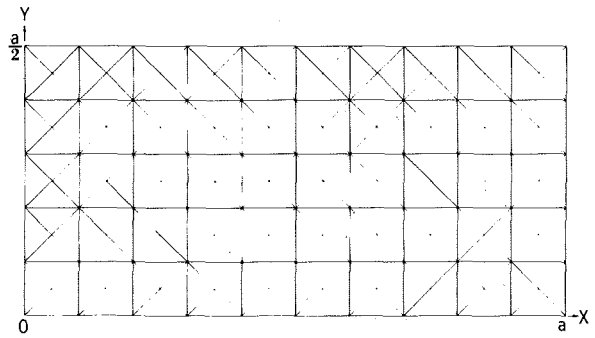

Fig. 2 Finite-element map of one quadrant of the bar under twist; the quadrant is *a* wide and *a*/2 high, with major discretization at intervals of *a*/10

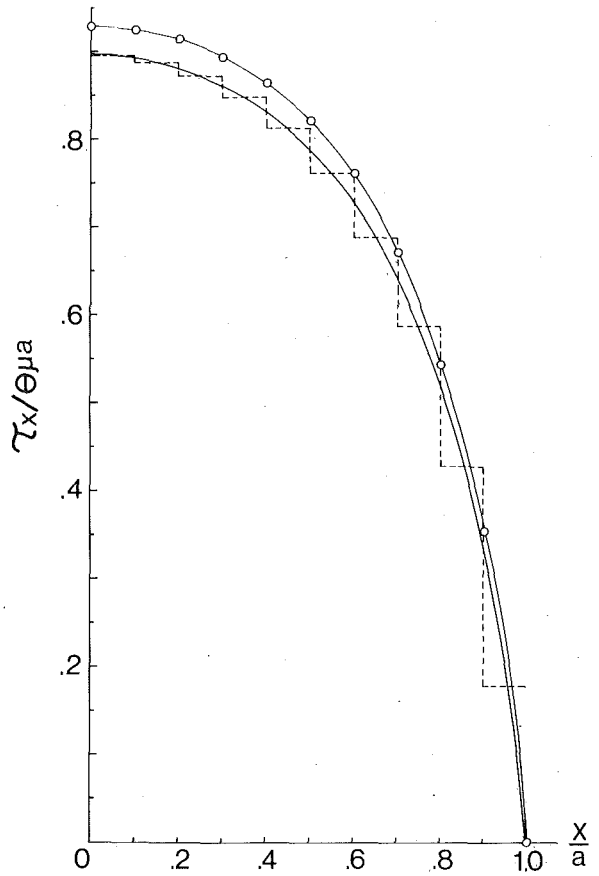

Fig. 3 Comparison of numerical and analytical [10] values of $\tau_x/\theta\mu a$ as a function of x/a, for $y/a = 0.5$ (open circles designate nodal values) and $y/a = 0.4833$ (dashed line designates element values); elastic response

The procedure for solving the problem incrementally follows that based on an energylike and thereby more familiar formulation [6], and need not be described further here. It may be noted, however, that the first "load" (i.e., twist) increment, response is wholly elastic. Beyond that, increments are scaled so that only one element yields at a time; in the example to be shown, 144 increments in θ were used. The finite-element map used in this report is shown in Fig. 2. Its dimensions are $a \times b = 25.4 \times 12.7$ mm. The total number of nodes is 116 and the total number of elements is 200. The material data used in solving this problem are $\mu = 75.8$ GN/m^2 and $\tau_l = 92.9$ MN/m^2. Octahedral strain at yield is therefore 1.23×10^{-3}.

Downloaded 01 May 2010 to 171.66.16.243. Redistribution subject to ASME license or copyright; see http://www.asme.org/terms/Terms_Use.cfm

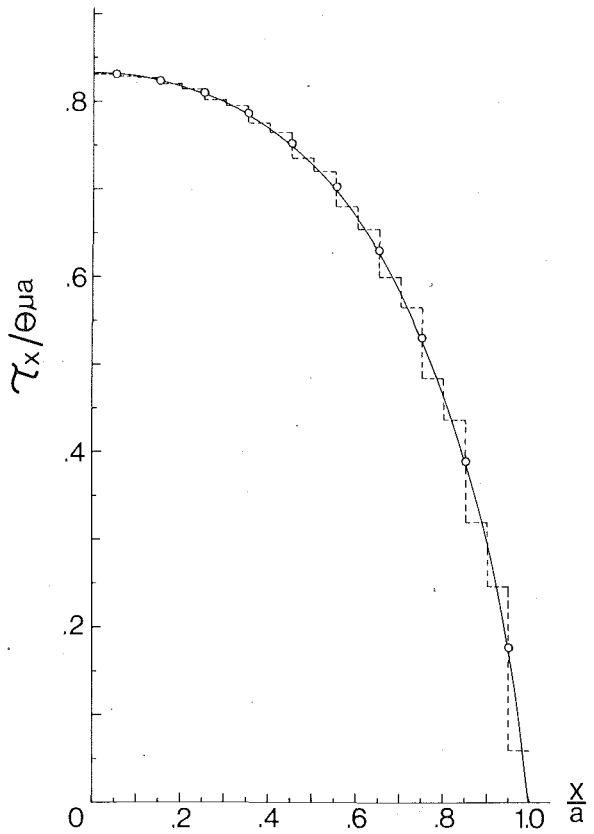

Fig. 4 Comparison of numerical and analytical [10] values of $\tau_x/\theta\mu a$ as a function of x/a, for $y/a = 0.45$ (open circles are nodal values, dashed line gives element values, and solid curve is analytical result); elastic response

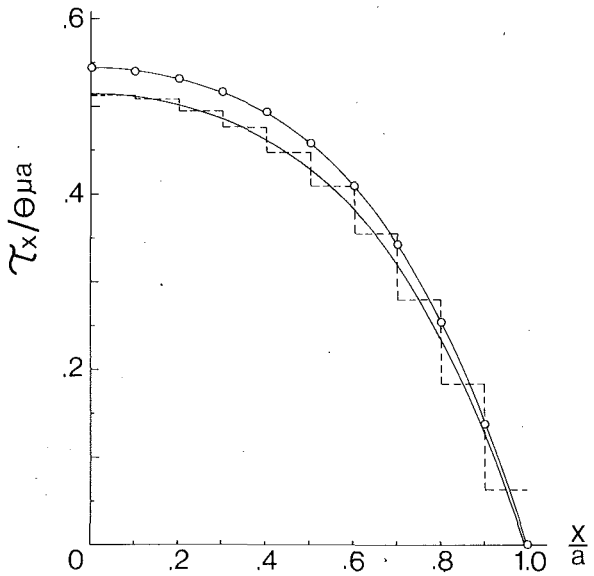

Fig. 5 Comparison of numerical and analytical [10] values of $\tau_x/\theta\mu a$ as a function of x/a, for $y/a = 0.3$ (open circles designate nodal values) and $y/a = 0.2833$ (dashed line designates element values); elastic response

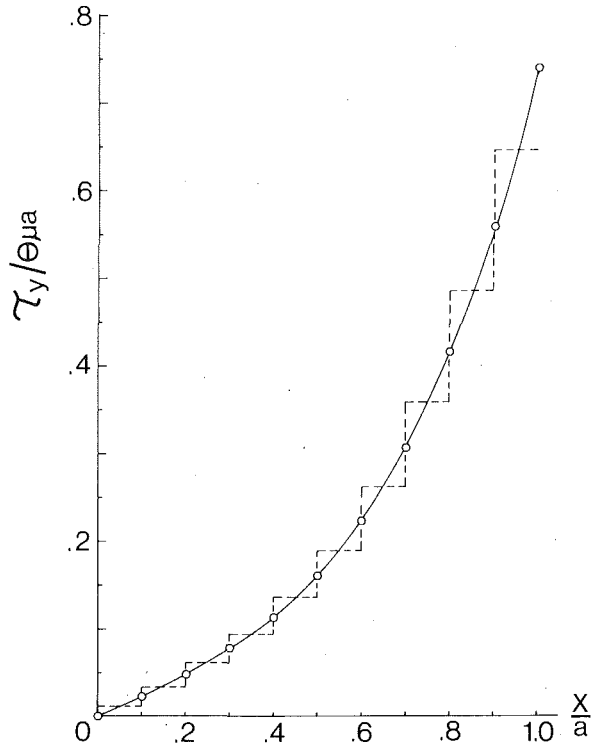

Fig. 6 Comparison of numerical and analytical [10] values of $\tau_y/\theta\mu a$ as a function of x/a, for $y/a = 0$ (open circles are nodal values) and $y/a = 0.01667$ (dashed line gives element values); elastic response. Analytical results (solid curve) for two values of y/a are indistinguishable at scale shown.

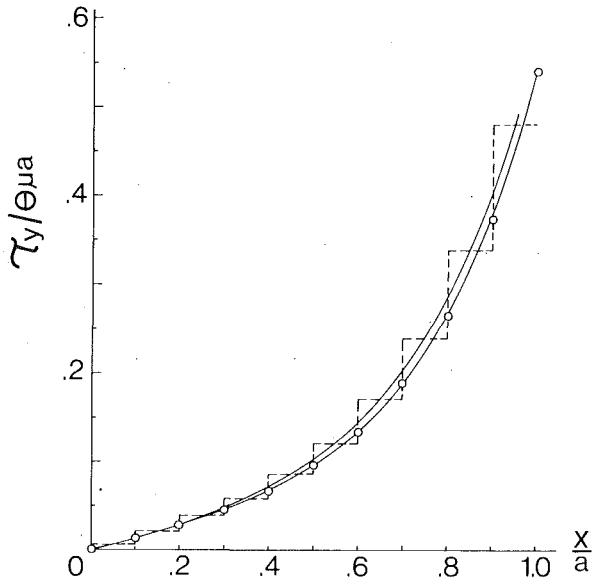

Fig. 7 Comparison of numerical and analytical [10] values of $\tau_y/\theta\mu a$ as a function of x/a, for $y/a = 0.3$ (open circles designate nodal values) and $y/a = 0.2833$ (dashed line designates element values); elastic response

The element map chosen for analysis has the "criss-cross" grid shown in Fig. 2. This array was chosen by Fix, et al., [9] to yield a second-order convergence rate for a series of demonstration problems. This rate of convergence was shown to be consistent for both the primary variable (here U_3) and its gradient (here U_1 and U_2). Thus, apart from mesh spacing, the present grid pattern is optimal—if the work of Fix, et al., carries over—for magnitude and convergence of error. Moreover, Fix, et al., derive optimal order error estimates for problems of this type.

Finally, we remark that this computation required about 25 sec per load step on the CMU DEC 2060.

Elastic Results

Figs. 3–7 show results at load step one at which the octahedral shear

Downloaded 01 May 2010 to 171.66.16.243. Redistribution subject to ASME license or copyright; see http://www.asme.org/terms/Terms_Use.cfm

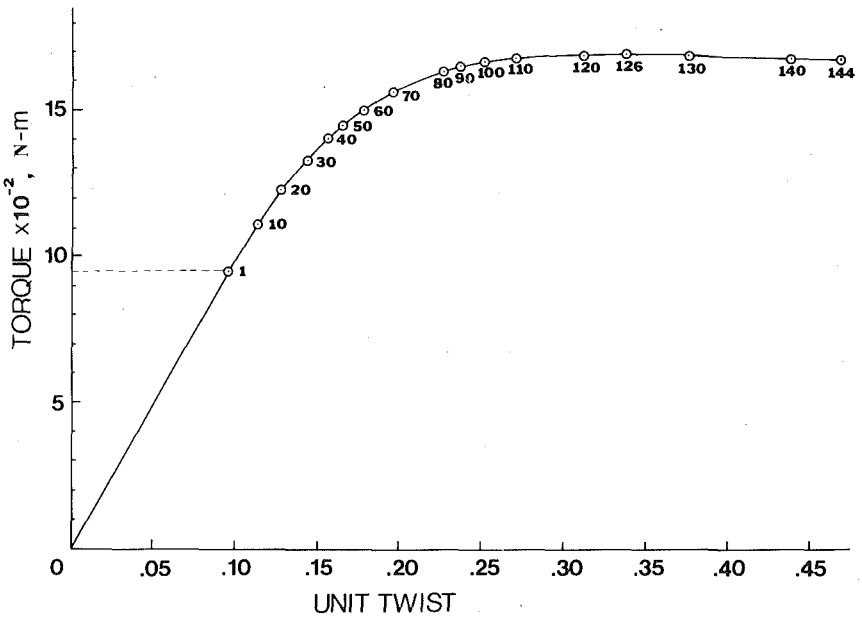

Fig. 8 Torque-twist curve for rectangular bar. Numerals indicate twist step number at position of respective open circles; peak torque at step 126. Unit twist in degrees of rotation per unit (in.) of bar length.

stress at the most highly stressed element just reaches τ_l. At this stage, four nodes along the upper edge ($y = b$) have reached the point of yield almost simultaneously. The point $(x,y) = (0,b)$ of course is first. In Figs. 3–5, normalized stress $\tau_x/\theta\mu a$, as a function of x/a; is given for various values of y/a. The relative difference between numerical and theoretical values of $\tau_x/\theta\mu a$ at the most highly stressed node is only 0.00047. Elemental values are shown by the broken lines for the centroid of each element. Both nodal and elemental values are consistent with the analytical solutions as shown by solid lines. Figs. 6–7 show $\tau_y/\theta\mu a$ versus x/a for different values of y/a. In Fig. 6, the theoretical result for $y/a = 0$ is very close to that for $y/a = 0.01667$. Hence we draw only one solid line. Both Fig. 6 and Fig. 7 show good agreement with the elastic solution. Taking the summation of contributions from each element, the torque is calculated, and it is equal to 949 N-m at load step one. The error is only 0.3 percent when compared to the theoretical value of 952 N-m. It is concluded that numerical results shown surprisingly good agreement for the elastic solution [10].

Elastoplastic Results

Following load step one, yield propagates. The resultant torque-twist curve is shown in Fig. 8. Yield starts at a torque of 949 N-m; as yield progress, the torque and twist both increase. The torque reaches its maximum value of 1689 N-m at load step 126. At this point, it produces a unit twist of 0.3371 deg. Beyond this point, no additional torque is required to cause further twist.[3] The softening is caused by the continued development of the shear bands. The limiting torque for this particular shape is 1.78 × torque at initial yield, a matter of some practical value.

It is interesting next to examine changes to the distribution of stress and strain. In Fig. 9 we show $\tau_x/\mu\theta a$ versus x/a for $y/a = 0.3$ and 0.5 at load steps 126 (peak torque) and 144 (maximum twist achieved in this analysis), and in Fig. 10 $\tau_y/\mu\theta a$ is plotted for $y/a = 0.3$ and 0. Note that all values are nodal data.

These two figures deserve some attention. Consider the open circles in Fig. 9 as compared to their counterpart in Fig. 3. The smooth (elastic) gradient is transformed into a virtually constant value (mean ± 1.8 percent) along most of the bar's upper surface, which then drops sharply to zero. Since θ has changed markedly, the magnitude of the

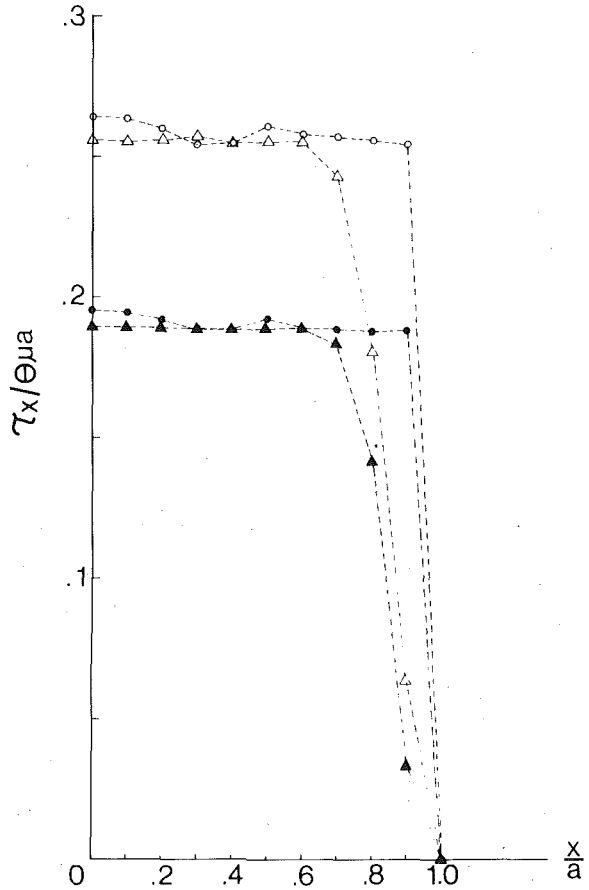

Fig. 9 Distribution of $\tau_x/\theta\mu a$ versus x/a at twist steps 126 (open symbols) and 144 (solid symbols), for $y/a = 0.5$ (circles) and $y/a = 0.3$ (triangles); all data are nodal values

[3] The present analysis is twist-controlled so that torque beyond the maximum can be determined.

Downloaded 01 May 2010 to 171.66.16.243. Redistribution subject to ASME license or copyright; see http://www.asme.org/terms/Terms_Use.cfm

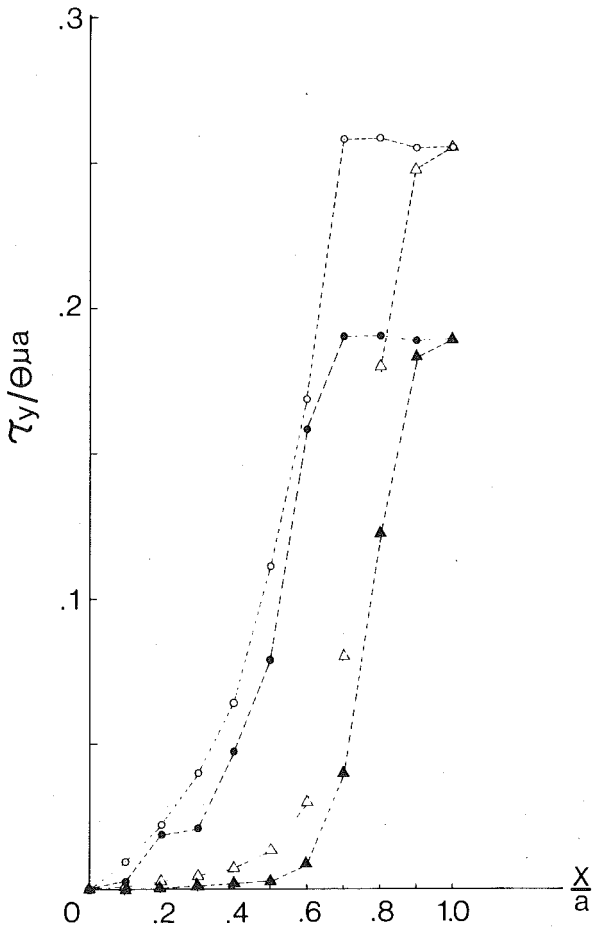

Fig. 10 Distribution of $\tau_y/\theta\mu a$ versus x/a at twist steps 126 (open symbols) and 144 (solid symbols), for $y/a = 0$ (circles) and $y/a = 0.3$ (triangles); all data are nodal values

normalized stress is reduced. Increase in θ from step 126 to step 144 accounts for the reduction in normalized stress along $y/a = 0.5$ (open and solid circles in Fig. 9). In the interior ($y/a = 0.3$), about the same distribution is to be observed (open triangles in Fig. 9). The more moderate gradient for $x/a \rightarrow 1.0$ is reflective of the growth of τ_y along the line $y/a = 0.3$, as shown in Fig. 10. (Recall that it is the quantity $\sqrt{[2(\tau_x{}^2 + \tau_y{}^2)/3]}$ that must be "constant;" we achieve constancy here to a mean value ±1.6 percent.) A similar comparison can be made for the solid triangles in Figs. 9 and 10. Finally, note that the open and solid circles in Fig. 10 pertain to the line $y/a = 0$; along this axis only τ_y is operative.

Elastic strain distributions were not plotted as they follow the behavior shown for stresses, one-to-one. In the presence of yield, however, the situation changes in that there is full coupling between both strains and both stresses. It is instructive then to show data in a fashion such that the components are combined and, moreover, that the distribution picks up both nodal and elemental values. Thus we plot octahedral strain at $y/a = 0.35$ and 0.45 for two load steps, 126 and 144, in Figs. 11 and 12. In these two figures the numerical data are clearly indicated; dotted lines which we believe connect these results in some manner are also shown. While the detailed shape of these dotted lines may be open to interpretation, it is clear that a phenomenon akin to shear banding is in progress.

Finally, we show the characteristic directions in the yielded region, according to (5). At a given twist, the direction at each node where yield is in progress is shown by a solid bar; the absence of a bar signifies that the nodal point is still elastic. Data for load steps 92, 126, and 144 appear in Figs. 13–15. Note that the elastic core persists throughout, that the outer corner remains elastic, but that yield has clearly dominated the field. These figures are suggestive of the shear band field but, in the context of slipline theory, appear not to transfer to a formal calculation of slip. The primary and most compelling reason, of course, is that there is no terminus for the slipline in the familiar sense of that term.

Discussion

Let us turn briefly to a somewhat more physical interpretation of these results. It is evident from the results of Nadai [1] that a mech-

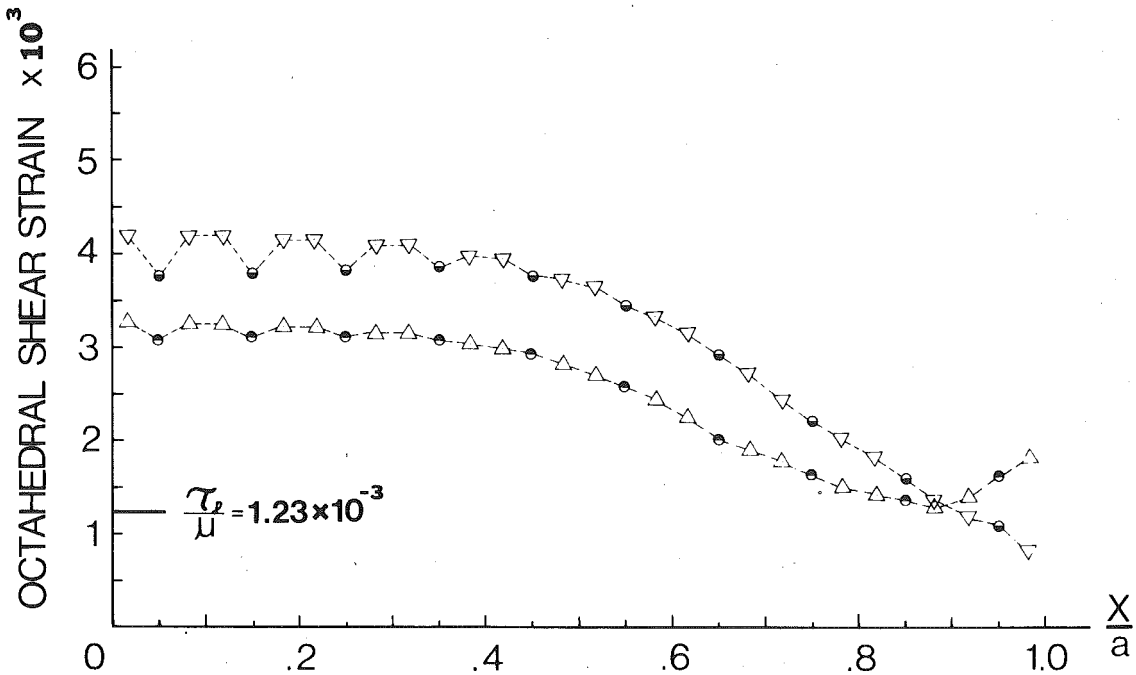

Fig. 11 Octahedral shear strain as a function of x/a for $y = 0.45$ (upper curve) and $y = 0.35$ (lower curve), load step 126. Triangles are element values and circles are nodal values. Dashed lines for convenience of visualization.

Downloaded 01 May 2010 to 171.66.16.243. Redistribution subject to ASME license or copyright; see http://www.asme.org/terms/Terms_Use.cfm

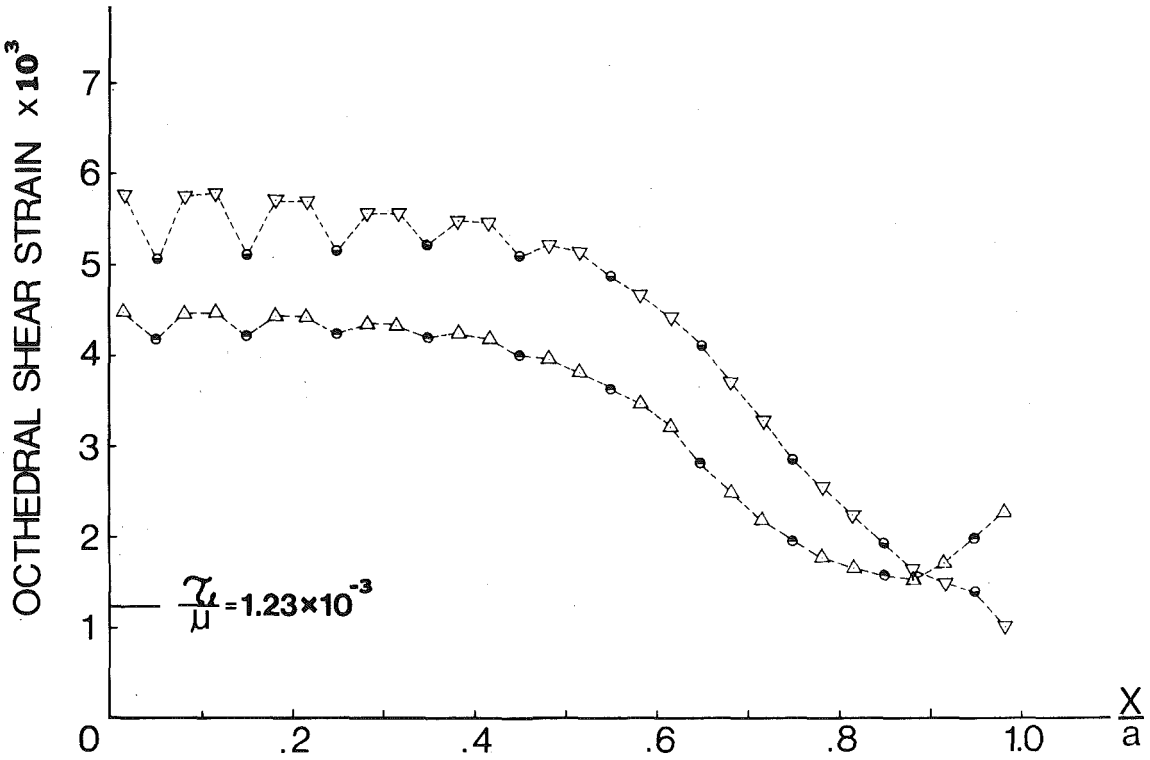

Fig. 12 Octahedral shear strain as a function of x/a for $y = 0.45$ (upper curve) and $y = 0.35$ (lower curve), load step 144. Triangles are element values and circles are nodal values. Dashed lines for convenience of visualization.

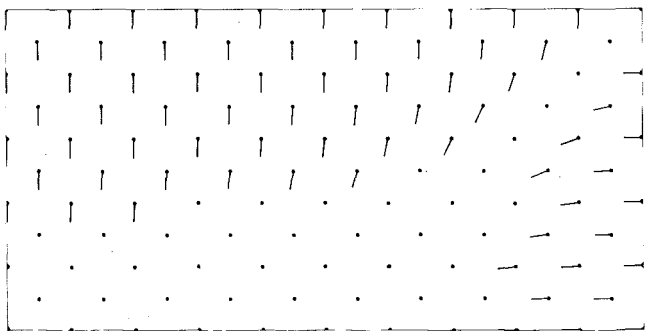

Fig. 13 Characteristic directions at those nodes where yield is in progress; intermediate twist level, twist step 92

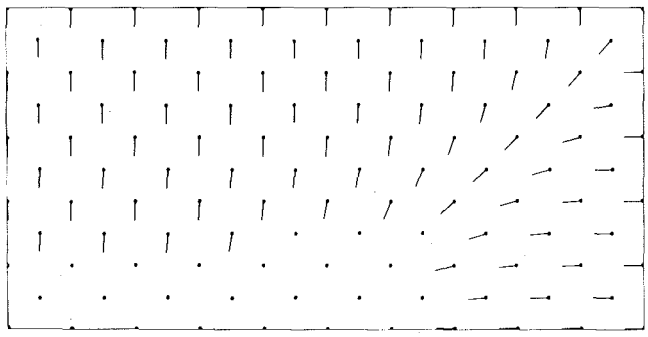

Fig. 14 Characteristic directions at those nodes where yield is in progress; twist corresponding to maximum torque, twist step 126

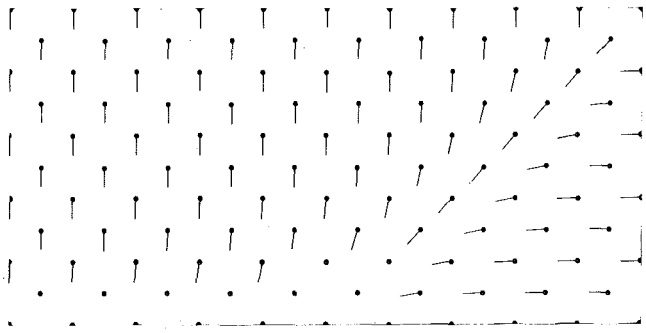

Fig. 15 Characteristic directions at those nodes where yield is in progress; highest twist achieved in this analysis, twist step 144

anism of sequential shear band initiation and development occurs in problems of this type. One might guess that, for the case reported here, the events proceed as follows. The first shear band absorbs some of the local strain, producing a momentary drop in elastic strain and therefore stress as load (twist) is gradually increased. Outside the shear band, the strain and stress reduction can be at most local because the overall (elastic) field will be dominated by the shape of the cross section. Thus, at some modest distance from the initial shear band, stress will again reach τ_i; a second shear band will be generated. The process continues until banding—which in this case all initiates at the boundary and grows gradually inward—has occurred all along the boundary. To the extent that this description is proper, the shear bands will be spaced and will be discrete.

The question then becomes how one might model such a process. In the present analysis, spacing of the phenomena we believe represent shear banding is obviously controlled by the mapping, i.e., by the discretization of the field as shown in Fig. 2. Hence our results, while numerically in parallel to the physical evidence, cannot be taken as definitive in terms of the banding process. However, our intent was not to meet that objective. Rather we have sought to demonstrate that a new method has the capability for attacking the much more difficult problem.

In that context, we have demonstrated that the method is viable. Consider the following aspects. In the formulation, the coefficient matrix is always symmetric and positive-definite and, in the words

Downloaded 01 May 2010 to 171.66.16.243. Redistribution subject to ASME license or copyright; see http://www.asme.org/terms/Terms_Use.cfm

of Fix and his coworkers, ". . . these desirable matrix properties remain valid even if the problems . . . are indefinite . . ." or, in our context, mixed elliptic-hyperbolic [9]. The grid decomposition satisfies the criteria of [9], and we may therefore be confident in having achieved minimal error for the mesh size (i.e., refinement) used here.

To model the process of shear banding, however, would require a significantly refined mesh, relative to that shown in Fig. 2. An increase in discretization such that mesh spacing is reduced by an order of magnitude—in the linear dimension—appears to be a minimal starting point. This suggests a problem of over 5×10^4 degrees of freedom and 2×10^4 elements, well beyond what is needed to establish the methodology itself.

Even with the relatively coarse model in Fig. 2, then, we produce data which meet the requirements of the problem as posed, field equations, initial and boundary conditions. If any deficiency exists in the method as described, it is that precise constancy of τ_0 in yielded regions is not achieved. The slight ($< \pm 2$ percent) variability in τ_0 implied by Figs. 9 and 10 is correctable via tighter control in the computational procedure, but the nature of the remaining data suggest a degree of stability such that no substantive change would occur. This minor variability should be understood to be in terms of local values of τ_l and not to suggest local hardening. That is to say, the material model is forced to deform in an elastic-perfectly plastic manner and, if τ_l is not tightly controlled on an element-to-element basis, the resultant variability produces no more difficulty—and probably much less—than the element mesh relative to that needed for a detailed study of the shear banding process.

Acknowledgments

A special appreciation should be given to Dr. G. J. Fix, III, for his encouragement and permission to use a similar code for solving indefinite problems of the mixed type. Support from the Center for the Joining of Materials at Carnegie-Mellon, through the Materials Research Laboratory Section, National Science Foundation, under Grant No. DMR76-81561, is also gratefully acknowledged.

References

1 Swedlow, J. L., "Character of the Equations of Elastoplastic Flow in Three Independent Variables," *International Journal of Nonlinear Mechanics,* Vol. 3, 1968, pp. 325–336; Vol. 4, 1969, p. 77.

2 Hill, R., "Some Basic Principles in the Mechanics of Solids Without a Natural Time," *Journal of the Mechanics and Physics of Solids,* Vol. 7, 1959, pp. 209–225.

3 Rice, J. R., et al., "Recent Finite Element Studies in Plasticity and Fracture Mechanics," *Computer Methods in Applied Mechanics and Engineering,* Vols. 17/18, 1979, pp. 411–442.

4 Nadai, A., *Theory of Flow and Fracture of Solids,* Vol. 1, McGraw-Hill, New York, 1950, Chapter 36.

5 Richmond, O., private communication, 1978.

6 Swedlow, J. L., "A Procedure for Solving Problems of Elastoplastic Flow," *Computers and Structures,* Vol. 3, 1973, pp. 879–898.

7 Zienkiewicz, O. Z., Owen, D. R. J., and Lee, K. N., "Least Square-Finite Element for Elasto-Static Problems: Use of 'Reduced' Integration," *International Journal for Numerical Methods in Engineering,* Vol. 8, 1974, pp. 341–358.

8 Fix, G. J., and Gunzburger, M. D., "On Least Squares Approximations to Indefinite Problems of the Mixed Type," *International Journal for Numerical Methods in Engineering,* Vol. 12, 1978, pp. 453–469.

9 Fix, G. J., Gunzburger, M. D., and Nicolaides, R. A., "On Finite Element Methods of the Least Squares Type," *Computation and Mathematics With Applications,* Vol. 5, 1979, pp. 87–98.

10 Timoshenko, S. P., and Goodier, J. N., *Theory of Elasticity,* 3rd ed., McGraw-Hill, New York, 1970, Chapter 10.

Downloaded 01 May 2010 to 171.66.16.243. Redistribution subject to ASME license or copyright; see http://www.asme.org/terms/Terms_Use.cfm

M. Morjaria
Postdoctoral Associate.
Student Mem. ASME

S. Mukherjee
Associate Professor.
Mem. ASME

Department of Theoretical and Applied Mechanics,
Cornell University,
Ithaca, N. Y. 14853

Inelastic Analysis of Transverse Deflection of Plates by the Boundary Element Method

A numerical scheme for time-dependent inelastic analysis of transverse deflection of plates of arbitrary shape by the boundary element method is presented in this paper. The governing differential equation is the inhomogeneous biharmonic equation for the rate of small transverse deflection. This complicated boundary-value problem for an arbitrarily shaped plate is solved by using a novel combination of the boundary element method and finite-element methodology. The number of unknowns, however, depends upon the boundary discretization and is therefore less than in a finite-element model. A combined creep-plasticity constitutive theory with state variables is used to model material behavior. The computer code developed can solve problems for an arbitrarily shaped plate with clamped or simply supported boundary conditions and an arbitrary loading history. Some illustrative numerical results for clamped and simply supported rectangular and triangular plates, under various loading histories, are presented and discussed.

Introduction

The boundary element method (BEM-also called the boundary-integral equation method) has been applied to solid mechanics problems for some time. Two recent publications edited by Brebbia [1] and Cruse and Rizzo [2] contain many papers on the subject and references to others. Most of the applications to date address problems in linear elasticity and fracture mechanics while a relatively small number consider nonlinear inelastic problems. Mukherjee and his coworkers recently presented a boundary element method formulation for nonlinear time-dependent inelastic deformation problems [3]. This was followed by numerical implementation of the method for planar problems [4, 5] and a comparison of the BEM with the widely used finite-element method (FEM) [6]. It was demonstrated in references [5, 6] that the BEM is a very powerful method with several potential advantages over the FEM. One of these is that the number of unknowns in the resultant algebraic system obtained by discretization is proportional to the number of boundary nodes in BEM as opposed to the total number of nodes in FEM. Another is the ease of discretization and input data preparation. Even though discretization of the domain must be carried out in these nonlinear problems, this is necessary only for the evaluation of certain integrals with known integrands and the topology of the internal elements is much simpler than for the FEM. Finally, due to the nature of the BEM formulation, the stresses are continuous throughout the domain, are easier to interpret, and are generally more accurate than those obtained by the FEM.

The boundary element method has been applied to problems of *elastic* transverse deflection of plates [7–10]. Jawson, Maiti, et al. [7–8], have solved the associated biharmonic equation by using an integral representation of the solution in terms of certain known kernels and unknown source densities. Recently, a new integral equation formulation for the elastic problems has been presented independently by Benzine and Gamby [9] and Stern [10].

The problem of time-dependent inelastic transverse deflection of plates is the subject of this paper. The governing biharmonic equation for the rate of transverse deflection of a thin plate in the presence of nonelastic strains is first derived. This differential equation is transformed into a pair of coupled Fredholm-type integral equations. The formulation admits any of a number of constitutive models with state variables for material behavior provided that the model has the mathematical structure described in the next section. The governing integral equations are discretized. A computer program capable of solving inelastic deflection problems for plates of *arbitrary* shape, either clamped or simply supported, subjected to arbitrary loading histories, is developed. Finally, numerical solutions are presented for square and triangular plates. The constitutive model due to Hart [11, 12], which has a sound experimental basis [13], is adopted in the numerical calculations. Time integration is carried out by using a recently developed Euler-type scheme with automatic time-step control [14].

Mathematical Structure of State Variable Models

The mathematical structure of many of the state variable models

Contributed by the Applied Mechanics Division for publication in the JOURNAL OF APPLIED MECHANICS.

Discussion on this paper should be addressed to the Editorial Department, ASME, United Engineering Center, 345 East 47th Street, New York, N. Y. 10017, and will be accepted until September 1, 1980. Readers who need more time to prepare a discussion should request an extension from the Editorial Department. Manuscript received by ASME Applied Mechanics Division, June, 1979.

Copyright © 1980 by ASME
Downloaded 01 May 2010 to 171.66.16.243. Redistribution subject to ASME license or copyright; see http://www.asme.org/terms/Terms_Use.cfm

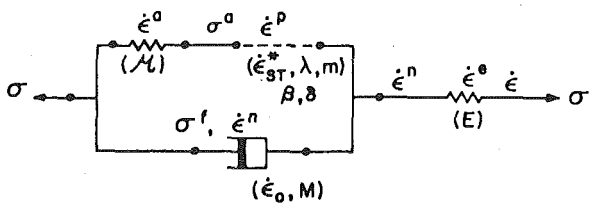

Fig. 1 Hart's model in tension

of inelastic deformation can be summarised by the following equations (see [3–6] for references to other state variable models)

$$\dot{\epsilon}_{ij} = \dot{\epsilon}^e_{ij} + \dot{\epsilon}^n_{ij} + \dot{\epsilon}^T_{ij}, \quad \dot{\epsilon}^n_{ij} = f_{ij}(\sigma_{ij}, q^{(k)}_{ij}, T) \tag{1, 2}$$

$$\dot{q}^{(k)}_{ij} = h_{ij}(\sigma_{ij}, q^{(k)}_{ij}, T), \quad \dot{\epsilon}^n_{kk} = 0 \tag{3, 4}$$

Here $\dot{\epsilon}^e_{ij}$, $\dot{\epsilon}^n_{ij}$, and $\dot{\epsilon}^T_{ij}$ are the elastic, nonelastic, and thermal strain rates, respectively, σ_{ij} is the stress tensor, T the temperature, and $q^{(k)}_{ij}$ are state variables. The number of state variables vary in the different models and they can be scalars or tensors. These state variables are assumed to completely characterize the present deformation state of the material and the history dependence of the rate of nonelastic strain up to the current time is assumed to be completely taken into account by their current values. It is important to note that the rates of the nonelastic strain and state variables at any time depend only on the current values of the stress, state variables, and temperature.

Hart's Model. The specific equations for Hart's constitutive model are presented next. The model in tension is shown in Fig. 1. Material response in dilatation is assumed to be elastic. According to this model, the nonelastic strain is decomposed into two (time-dependent) components

$$\dot{\epsilon}^n_{ij} = \dot{\epsilon}^a_{ij} + \dot{\epsilon}^p_{ij} \tag{5}$$

where ϵ^a_{ij} is the anelastic strain, a stored strain which reflects the magnitude and direction of prior deformation history and ϵ^p_{ij} is the completely irrecoverable and path-dependent permanent strain. The two state variables in the model are the anelastic strain and a scalar σ^*, called hardness, which is similar to an isotropic strain-hardening parameter. The constitutive equations prescribe flow rules for the anelastic strain tensor and the permanent and nonelastic strain rates. Two auxillary tensors s^a_{ij} and s^f_{ij} are used, and their sum equals s_{ij}, the deviatoric part of the stress σ_{ij}. Certain scalar invariants of the relevant tensors are defined in the usual way (e.g., $\sigma^a = \sqrt{(3/2)s^a_{ij}s^a_{ij}}$) and these are related to each other through the uniaxial equations (see Fig. 1)

$$\sigma^a = \mathcal{M}\epsilon^a, \quad \dot{\epsilon}^n = \dot{\epsilon}_0(\sigma^f/\sigma_0)^M \tag{6, 7}$$

$$\dot{\epsilon}^p = \dot{\epsilon}^*(\ln(\sigma^*/\sigma^a))^{-1/\lambda} \tag{8}$$

$$\dot{\epsilon}^* = \dot{\epsilon}^*_{sT}(\sigma^*/\sigma^*_s)^m \exp(Q/RT_B)\exp(-Q/RT) \tag{9}$$

$$\dot{\sigma}^* = \dot{\epsilon}^p\sigma^*\Gamma(\sigma^*, \sigma^a), \quad \Gamma(\sigma^*,\sigma^a) = (\beta/\sigma^*)^\delta(\sigma^a/\sigma^*)^{\beta/\sigma^*} \tag{10, 11}$$

Equation (6) represents a linear anelastic element, (7) a nonlinear dashpot, (8) and (9) a "plastic" element and, finally, (10) and (11) describe strain hardening. The flow parameters are $\mathcal{M}$, M, m, λ, $\dot{\epsilon}_0$ (at a reference stress level σ_0) and $\dot{\epsilon}^*_{sT}$ (at a reference hardness level σ^*_s and reference temperature T_B); β and δ are strain-hardening parameters, R is the gas constant and Q the activation energy for atomic self-diffusion. The material parameters, many of which are temperature-dependent, are obtained from load relaxation and constant strain-rate tension experiments. They are given in Appendix A of the EPRI report by Kumar and others [13].

Analytical Formulation

The analytical formulation of the problem closely follows that for small deflections of thin, laterally loaded elastic plates as discussed in Timoshenko and Woinowsky-Krieger [15]. Let a thin plate of arbitrary shape and thickness h be loaded laterally by a load of intensity q per unit area. The plate deflections are assumed to be small compared to the thickness of the plate and the membrane effects are neglected. The effects of shearing forces and the compressive stress produced by the load q on the plate deformation are neglected. The middle plane of the plate is a plane of symmetry and is assumed to undergo no extension or contraction during bending. It is therefore a neutral surface. The in-plane strains in the plate are assumed to remain proportional to the distance from the neutral surface even in the presence of inelastic deformation. The formulation is carried out in terms of the time rates of change of the relevant variables.

Let the middle plane of the undeformed plate be the x_1x_2 plane and w be the deflection of the middle plane in the x_3-direction. Since the plate deflections and slopes are small, the curvature rates $\dot{\kappa}_1$ and $\dot{\kappa}_2$ and the rate of twist of the middle surface with respect to the x_1 and x_2-axes, $\dot{\kappa}_{12}$, are related to the deflection rate by the following equations:

$$\dot{\kappa}_1 = -\frac{\partial^2\dot{w}}{\partial x_1^2}, \quad \dot{\kappa}_2 = -\frac{\partial^2\dot{w}}{\partial x_2^2}, \quad \dot{\kappa}_{12} = \frac{\partial^2\dot{w}}{\partial x_1\partial x_2} \tag{12}$$

The strain rates in the absence of thermal strains, are, by assumption

$$\begin{aligned}\dot{\epsilon}_{11} &= \dot{\epsilon}^e_{11} + \dot{\epsilon}^n_{11} = x_3\dot{\kappa}_1\\ \dot{\epsilon}_{22} &= \dot{\epsilon}^e_{22} + \dot{\epsilon}^n_{22} = x_3\dot{\kappa}_2\\ \dot{\epsilon}_{12} &= \dot{\epsilon}^e_{12} + \dot{\epsilon}^n_{12} = -x_3\dot{\kappa}_{12}\end{aligned} \tag{13}$$

and the stress rates, from Hooke's law, become

$$\begin{aligned}\dot{\sigma}_{11} &= \frac{E}{1-\nu^2}(\dot{\epsilon}^e_{11} + \nu\dot{\epsilon}^e_{22})\\ &= \frac{Ex_3}{1-\nu^2}(\dot{\kappa}_1 + \nu\dot{\kappa}_2) - \frac{E}{1-\nu^2}(\dot{\epsilon}^n_{11} + \nu\dot{\epsilon}^n_{22})\\ \dot{\sigma}_{22} &= \frac{Ex_3}{1-\nu^2}(\dot{\kappa}_2 + \nu\dot{\kappa}_1) - \frac{E}{1-\nu^2}(\dot{\epsilon}^n_{22} + \nu\dot{\epsilon}^n_{11})\\ \dot{\sigma}_{12} &= 2G\dot{\epsilon}^e_{12} = -2Gx_3\dot{\kappa}_{12} - 2G\dot{\epsilon}^n_{12}\end{aligned} \tag{14}$$

In the following E and ν are the Young's modulus and Poisson's ratio, respectively, of the plate material.

The rates of the bending moments $\dot{M}_1$ and $\dot{M}_2$ and the twisting moment $\dot{M}_{12}$ are

$$\dot{M}_1 = \int_{-h/2}^{h/2}\dot{\sigma}_{11}x_3dx_3, \quad \dot{M}_2 = \int_{-h/2}^{h/2}\dot{\sigma}_{22}x_3dx_3,$$

$$\dot{M}_{12} = -\int_{-h/2}^{h/2}\dot{\sigma}_{12}x_3dx_3 \tag{15}$$

The equilibrium equation of a plate element is

$$\frac{\partial^2\dot{M}_{11}}{\partial x_1^2} + \frac{\partial^2\dot{M}_{22}}{\partial x_2^2} - \frac{2\partial^2\dot{M}_{12}}{\partial x_1\partial x_2} = -\dot{q} \tag{16}$$

Substituting equations (12), (14), and (15) into (16), the governing differential equation for the deflection rate is obtained as

$$\nabla^4\dot{w} = \frac{\dot{q}}{D} - \frac{12}{h^3}f^{(n)}(x_1,x_2,t) \equiv g(x_1,x_2,t) \tag{17}$$

where ∇^2 is the Laplacian operator,

$$f^{(n)} = \frac{\partial^2}{\partial x_1^2}\int_{-h/2}^{h/2}(\dot{\epsilon}^n_{11} + \nu\dot{\epsilon}^n_{22})x_3dx_3 + \frac{\partial^2}{\partial x_2^2}\int_{-h/2}^{h/2}(\dot{\epsilon}^n_{22} + \nu\dot{\epsilon}^n_{11})x_3dx_3 + 2(1-\nu)\frac{\partial^2}{\partial x_1\partial x_2}\int_{-h/2}^{h/2}\dot{\epsilon}^n_{12}x_3dx_3 \tag{18}$$

and $D = Eh^3/(12(1-\nu^2))$.

Equation (18) can be transformed into a pair of Fredholm-type integral equations (see, for example, [16] where the biharmonic equation for the stress functions for a plane elastoplastic problem is considered)

Downloaded 01 May 2010 to 171.66.16.243. Redistribution subject to ASME license or copyright; see http://www.asme.org/terms/Terms_Use.cfm

$$\alpha\pi\nabla^2\dot{w} - \int_A (\ln r) g dA = \int_C \left[\frac{\partial}{\partial n}(\ln r)\nabla^2\dot{w} - \ln r \frac{\partial}{\partial n}(\nabla^2\dot{w})\right] dC \quad (19)$$

$$4\alpha\pi\dot{w} - \int_A (r^2 \ln r) g dA = \int_C \left[\frac{\partial}{\partial n}[\nabla^2(r^2 \ln r)]\dot{w} - \nabla^2(r^2 \ln r)\frac{\partial \dot{w}}{\partial n} + \frac{\partial}{\partial n}(r^2 \ln r)\nabla^2\dot{w} - r^2 \ln r \frac{\partial}{\partial n}(\nabla^2\dot{w})\right] dC. \quad (20)$$

Here A is the area of the plate, C is boundary, r the distance between a source point and a field point, and n is the normal to C at the field point. The value of $\alpha = 1$ if the source point is on the boundary C where it is locally smooth, and $\alpha = 2$ if the source point is inside the plate.

The boundary conditions for the problem are

$$\text{Clamped Plate: } \dot{w} = \frac{\partial \dot{w}}{\partial n} = 0 \quad \text{on} \quad C$$

$$\text{Simply Supported Plate: } \dot{w} = \nabla^2\dot{w} = 0 \quad \text{on} \quad C \quad (21)$$

$$\text{Symmetry Line: } \frac{\partial \dot{w}}{\partial n} = \frac{\partial}{\partial n}(\nabla^2\dot{w}) = 0$$

Thus two of the four quantities $\dot{w}$, $\partial\dot{w}/\partial n$, $\nabla^2\dot{w}$, $\partial/\partial n\,(\nabla^2\dot{w})$ are prescribed on the boundary of the plate, and equations (19) and (20), (for a boundary point with $\alpha = 1$) are integral equations for the remaining two quantities on the boundary. Once these boundary-integral equations are solved, all four of these quantities are known on the boundary, and the values of $\dot{w}$ and $\nabla^2\dot{w}$ can be obtained at any inside point by evaluation of known integrals. The curvature rates throughout the plate are then obtained from equation (12), the stress rates from (14) and the moment rates from (15). The curvature rates are obtained by analytical differentiation of equation (20) under the integral sign.

Numerical Implementation and Solution Strategy

Discretized Equations. A discretized version of equation (19) for a point on the boundary is obtained by dividing the boundary C of the plate into N_s straight boundary elements using N_b ($N_b = N_s$) boundary nodes and the interior A of the plate into n_i triangular internal elements

$$\pi\nabla^2\dot{w} - \sum_{ni} \int_{\Delta A_i} (\ln r) g dA = \sum_{N_s} \int_{\Delta C_i} \left\{\frac{\partial}{\partial n}(\ln r)\nabla^2\dot{w} - (\ln r)\frac{\partial}{\partial n}(\nabla^2\dot{w})\right\} dC \quad (22)$$

A similar equation results from equation (20).

The quantities $\dot{w}$, $\partial\dot{w}/\partial n$, $\nabla^2\dot{w}$, and $\partial/\partial n(\nabla^2\dot{w})$ are assumed to vary linearly over each boundary element with their values assigned at the nodes which lie at the intersection of the elements. Discontinuities in the normal derivatives across corners, if any, are taken care of by placing a "zero length" element between two boundary nodes and assigning different values of $\partial\dot{w}/\partial n$ and $\partial/\partial n\,(\nabla^2\dot{w})$ at each of the nodes. This approach is similar to that used in earlier work to accommodate traction discontinuities in planar problems [5, 6].

Integrals through the thickness of the type

$$I(x_1, x_2, t) = \int_{-h/2}^{h/2} (\dot{\epsilon}^n_{11} + \nu\dot{\epsilon}^n_{22}) x_3 dx_3$$

are evaluated by Gaussian quadrature. Six gauss points are used in the numerical calculations presented later. As mentioned earlier, the integrands are known at any time through the constitutive equations (2) and (4). A quadratic interpolation of such integrals is used on each triangular internal element in the x_1x_2 plane. This FEM-type methodology is more accurate than finite-difference techniques for the determination of second partial derivatives of such integrals that occur in equation (18). However, the topology of the internal elements is simpler than for FEM in that every node need not be shared by neighboring elements (see Fig. 1 of [4]).

Substitution of the functional forms of the variables into equation (22) and the discretized version of (20) with $\alpha = 1$ leads to an algebraic system of the type

$$[A]\{\dot{x}\} = [B]\{\dot{y}\} + \{\dot{d}\} \quad (23)$$

The matrices $[A]$ and $[B]$ depend only on the geometry, i.e., the number of boundary nodes and their distribution. They involve integrals of the type

$$\int_{\Delta C_i} (\ln r) dc, \quad \int_{\Delta C_i} (\ln r) c dc$$

where c is the distance measured along a boundary element. These integrals, some of which become singular when the source point coincides with the field point, are evaluated in *closed form*. They are available in a DOE report with the same title [17]. The vector $\{\dot{x}\}$ contains unknown and the vector $\{\dot{y}\}$ known quantities on the boundary. Finally, the vector $\{\dot{d}\}$ contains integrals of the kernels $r^2 \ln r$ and $\ln r$ over the triangular internal elements, and the nonelastic strain rates $\dot{\epsilon}^n_{11}$, $\dot{\epsilon}^n_{22}$, and $\dot{\epsilon}^n_{12}$ through the function g. This vector is known at any time through the constitutive relations (2) and (4).

Solution Strategy. The initial distribution of state variables is prescribed and the initial nonelastic strain is set to zero. The initial distributions of displacements, stresses, and moments are obtained from the solution of the corresponding elastic problem. This is obtained from the same BEM equations in terms of the variables (rather than their rates). The rates of nonelastic strains at $t = 0$ are obtained from equations (2) and (4) and those of the state variables from (3). These nonelastic strains are used in equation (23) which is solved for the unknown components of $\dot{w}$, $\partial\dot{w}/\partial n$, $\nabla^2\dot{w}$, and $\partial/\partial n\,(\nabla^2\dot{w})$ on the boundary. The displacement rate $\dot{w}$ and its Laplacian $\nabla^2\dot{w}$ are now obtained throughout the plate from discretized versions of equations (19) and (20) for an internal point ($\alpha = 2$). This step only involves evaluation of integrals with known integrands and no new unknowns need to be determined.

The curvature rates are next obtained analytically from the displacement rates. The quantities

$$\left(\frac{\partial^2\dot{w}}{\partial x_1^2} - \frac{\partial^2\dot{w}}{\partial x_2^2}\right) \quad \text{and} \quad \frac{\partial^2\dot{w}}{\partial x_1 \partial x_2}$$

are evaluated at an inside point by analytical differentiation of equation (20) under the integral sign. The curvature rates are obtained by combining these with $\nabla^2\dot{w}$ obtained from equation (19). The stress rates and moment rates are then obtained from equations (14) and (15).

The values of these quantities at a new time Δt are now obtained by integrating forward in time using a suitable numerical procedure and this process is continued in order to determine the time histories of the variables of interest. Since the state variable equations are generally stiff, choice of a suitable time-integration scheme is crucial. A simple but efficient Euler-type strategy with automatic time-step control, described in references [14, 5, 6], is used to advantage.

Boundary Curvature Rates. The rates of curvatures on the boundary of the plate could not be obtained sufficiently accurately by using the solution strategy just described. The boundary curvature rates are obtained instead from the formulas given below, which are derived in [17].

Clamped Plate: On boundary $\dot{w} = \frac{\partial \dot{w}}{\partial n} = 0$

$$\frac{\partial^2\dot{w}}{\partial x_1^2} = (\nabla^2\dot{w})\sin^2\gamma, \quad \frac{\partial^2\dot{w}}{\partial x_2^2} = (\nabla^2\dot{w})\cos^2\gamma$$

$$\frac{\partial^2\dot{w}}{\partial x_1 \partial x_2} = -(\nabla^2\dot{w})\sin\gamma\cos\gamma \quad (24)$$

Simply Supported Plate: On boundary $\dot{w} = \nabla^2\dot{w} = 0$

$$\frac{\partial^2\dot{w}}{\partial x_1^2} = 2\frac{\partial}{\partial c}\left(\frac{\partial \dot{w}}{\partial n}\right)\sin\gamma\cos\gamma$$

$$\frac{\partial^2\dot{w}}{\partial x_2^2} = -2\frac{\partial}{\partial c}\left(\frac{\partial \dot{w}}{\partial n}\right)\sin\gamma\cos\gamma \quad (25)$$

Downloaded 01 May 2010 to 171.66.16.243. Redistribution subject to ASME license or copyright; see http://www.asme.org/terms/Terms_Use.cfm

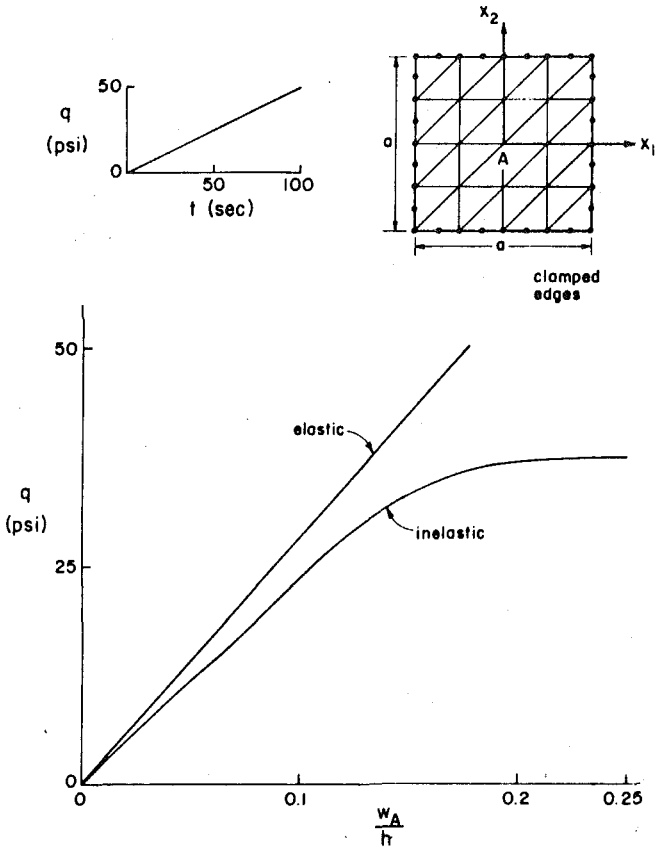

Fig. 2 Load as a function of central displacement for a clamped square plate subjected to a uniform load increasing at a constant rate

$$\frac{\partial^2 \dot{w}}{\partial x_1 \partial x_2} = -\frac{\partial}{\partial c}\left(\frac{\partial \dot{w}}{\partial n}\right)\cos 2\gamma \qquad (25)$$

(Cont.)

In the foregoing, n is the outward normal and c the counterclockwise tangential direction along a boundary element and γ is the angle between the x_1-axis and the direction tangential to the boundary element. The Laplacian of $\dot{w}$ on the boundary is obtained directly in the clamped case from equation (23) and the curvature rates are obtained easily from equation (24). In the simply supported case, $\partial \dot{w}/\partial n$ is obtained directly on the boundary and use of equation (25) involves a first-order numerical differentiation along the boundary element. This procedure leads to determination of boundary curvatures with sufficient accuracy. Unfortunately, curvatures on symmetry lines could not be obtained in this simple manner and symmetry conditions could not be taken advantage of in obtaining the numerical results presented in the next section.

Numerical Results and Discussion

Numerical results for several sample plate bending problems for 304 stainless steel plates at 400°C, using Hart's constitutive model, are presented in this section.

Parameter Values. The values of the various parameters used in the numerical calculations, at 400°C, are given below [13].

$$\lambda = 0.15 \quad M = 7.8 \quad m = 5$$

$$\mathcal{M} = 779 \text{ GPa} \quad (0.113 \times 10^9 \text{ psi})$$

$$E = 168.24 \text{ GPa} \quad (0.244 \times 10^8 \text{ psi}) \quad \nu = 0.298$$

$$\dot{\epsilon}_0 = 1.553 \times 10^4 \text{ sec}^{-1} \quad \text{at} \quad \sigma_0 = 68.95 \text{ MPa (10 ksi)}$$

$$\dot{\epsilon}^*_{sT} = 1.269 \times 10^{-24} \text{ sec}^{-1} \quad \text{at} \quad \sigma^*_s = 68.95 \text{ MPa} \quad T_B = 673°\text{K}$$

$$\beta = 1.234 \text{ GPa} \quad (0.179 \times 10^6 \text{ psi}) \quad \delta = 1.33$$

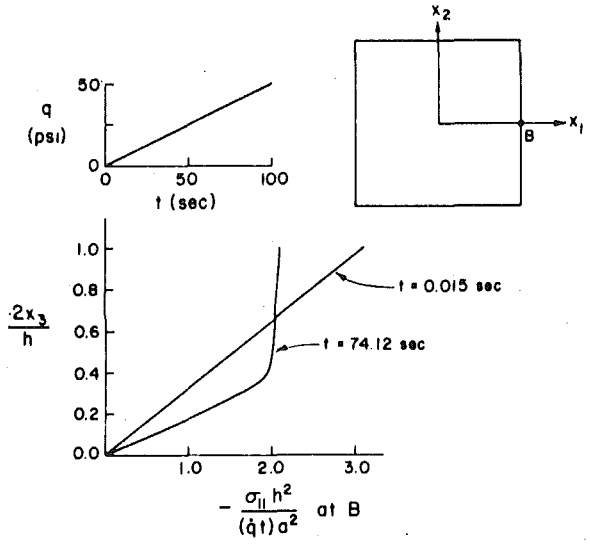

Fig. 3 Redistribution of stress at the midpoint of an edge of the clamped square plate of Fig. 2

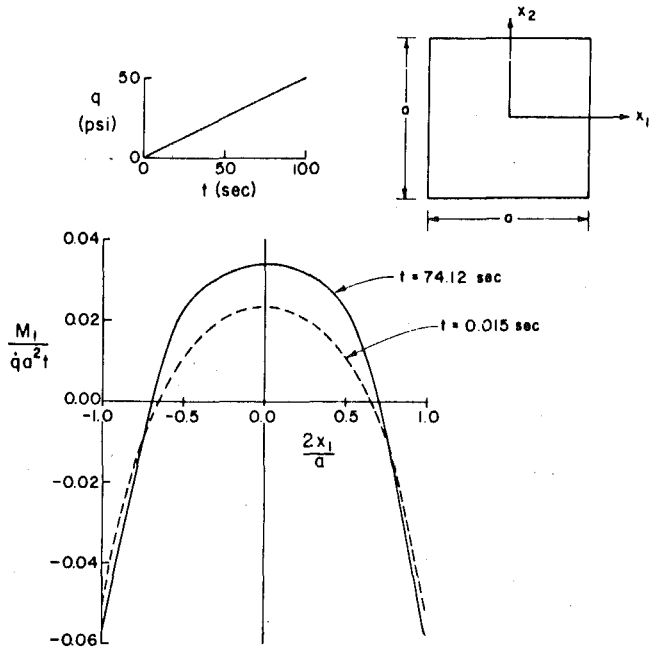

Fig. 4 Redistribution of moment along the line $x_2 = 0$ of the clamped square plate of Fig. 2

The initial values of the state variables for an annealed sample are

$$\sigma^* (\mathbf{x},0) = 117.215 \text{ MPa (17 ksi)}$$

$$\epsilon^a_{ij} (\mathbf{x},0) = 0$$

Square Plates. Numerical results for square plates are shown in Figs. 2–5. The plates are of side $a = 5.08$ cm (2 in.) and the plate thickness is 2 percent of "a" for the clamped plate (Figs. 2–4) and 1 percent of "a" for the simply supported plate in Fig. 5. The loading is an uniform pressure q increasing at a constant rate of 0.5 psi/sec. The boundary and internal mesh are shown as insets in the figures.

The pressure as a function of central displacement is shown in Fig. 2. The short time BEM solution is within 1 percent of the elastic solution from [15].

In order to better understand the behavior of the inelastic curve in Fig. 2, it is instructive to consider an analogous plate made of a

Downloaded 01 May 2010 to 171.66.16.243. Redistribution subject to ASME license or copyright; see http://www.asme.org/terms/Terms_Use.cfm

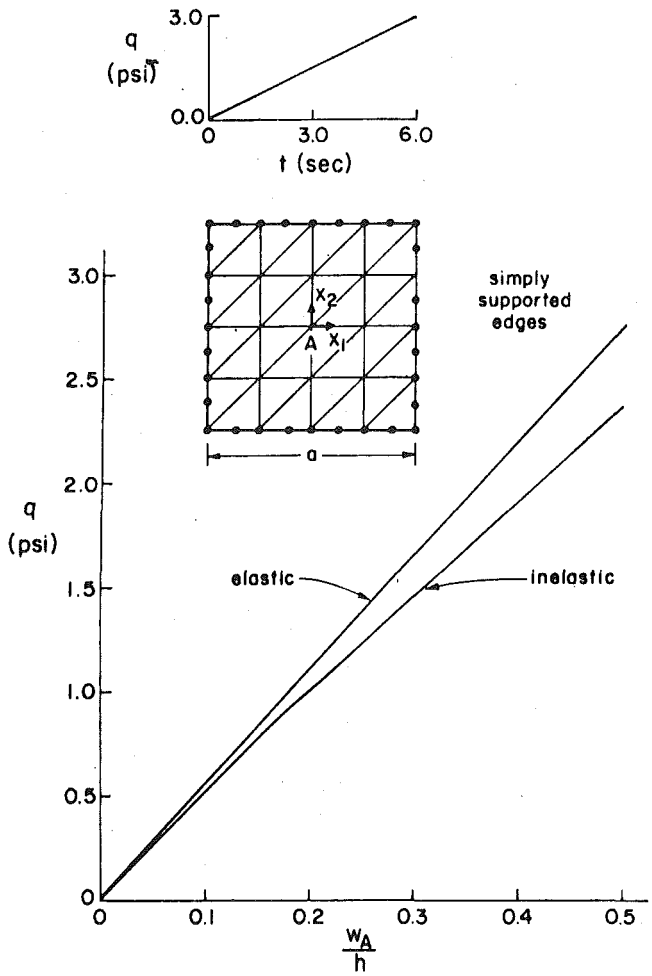

Fig. 5 Load as a function of central displacement for a simply supported square plate subjected to a uniform load increasing at a constant rate

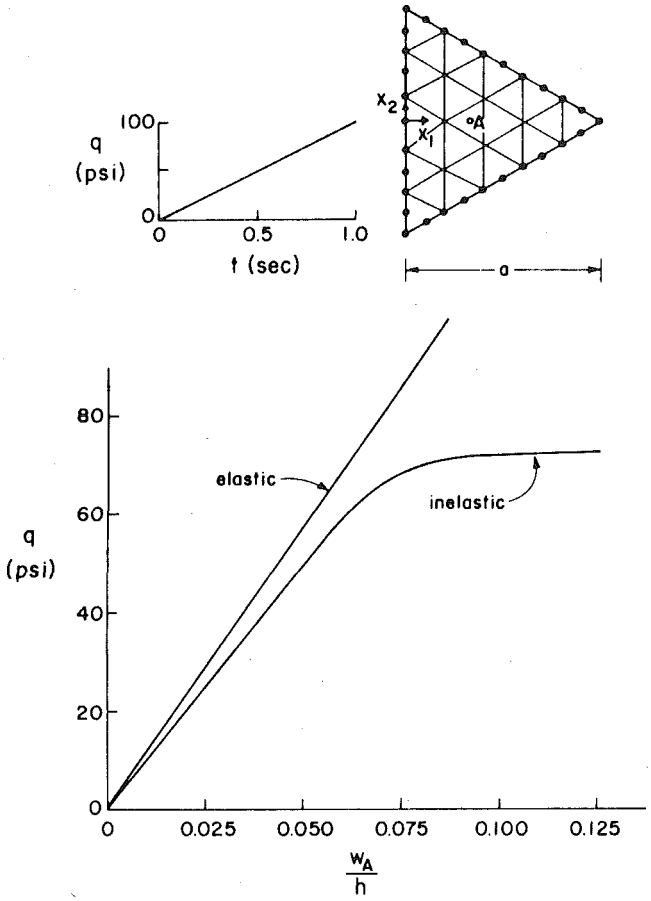

Fig. 6 Load as a function of centroidal displacement for a clamped triangular plate subjected to a uniform load increasing at a constant rate

linear viscoelastic material which is modeled as elastic in dilatation and as a three parameter viscoelastic solid in tension. If the free spring has modulus E and the one parallel to the dashpot has a modulus $\mathcal{M}$, the long time Young's modulus and Poisson's ratio for this model are [18]

$$E_\infty = \frac{\mathcal{M}E}{\mathcal{M}+E}, \quad \nu_\infty = \frac{1}{2} - \frac{E_\infty}{6K}$$

where K is the bulk modulus of the material. In this case, for the plate bending problem, the initial and final slopes, q/w_A, are proportional to the quantities $E/(1-\nu^2)$ and $E_\infty/(1-\nu_\infty^2)$, respectively.

Returning to Hart's model (Fig. 1), it is observed that increases of stress from zero causes deformation of the anelastic spring but substantial permanent deformation of the "plastic" element only begins when the stress in the upper branch, σ^a, approaches the hardness σ^*. Thus, with the plastic element essentially inactive, the behavior in tension is close to that of a nonlinear three parameter viscoelastic solid. The zero time slope of the inelastic curve in Fig. 2, therefore, should be proportional to $E/(1-\nu^2)$ and this should change over to $E_\infty/(1-\nu_\infty^2)$ at, say, $w_A/h = 0.08$. Comparison of the numbers shows that the zero time slope is within 1 percent and the slope at $w_A/h = 0.08$ is within 3 percent of the aforementioned quantities, thus confirming the accuracy of the BEM model. Further increase of pressure causes substantial permanent deformation of the plastic element and the curve has the features of an usual elastic plastic curve. Yielding starts at the midpoints of the outside edges of the plate. The yield front starts moving out along the plate edges and then a second yielding occurs at the center of the plate. The redistribution of stress through the thickness at the midpoint of an edge of the plate (Fig. 3) shows the expected transition from the linear elastic distribution to the nonlinear distribution characteristic of elastic-plastic deformation. Redistribution of the nondimensionalized bending moment M_{11} along a center line of the plate ($x_2 = 0$) is shown in Fig. 4.

Table 1 BEM program statistics

Problem	Number of boundary nodes	Number of Internal elements	Number of Time steps	CPU time on IBM 370/168 (sec)
1. Clamped Square plate	36	32	372	208
2. Simply-supported square plate	36	32	350	210
3. Clamped triangular plate	33	25	200	98

The load-deflection curve for a simply supported square plate is shown in Fig. 5. This time the elastic solution is within 1 percent of the correct one and the slope at $w_A/h = 0.4$ is within 2 percent of the slope expected from the analogous viscoelastic case.

Triangular Plates. Deflection of equilateral triangular plates is also analyzed by the program. Fig. 6 shows the load-deflection curve for a clamped equilateral triangular plate of side 2.54 cm (1 in.) with $h/a = 2$ percent. The elastic solution is within 2 percent of that obtained by Conway [19] and the inelastic solution has the expected elastic-plastic characteristics. Stress redistribution through the

Downloaded 01 May 2010 to 171.66.16.243. Redistribution subject to ASME license or copyright; see http://www.asme.org/terms/Terms_Use.cfm

thickness exhibits the transition from linear elastic to nonlinear elastic-plastic analogous to Fig. 3. The elastic solution for a simply supported equilateral triangular plate under uniform pressure, obtained by the BEM program, is within 0.04 percent of the elastic solution [15]. The nonelastic solution has not been determined in this case.

The number of time-steps and computer times on an IBM 370/168, required for these problems, are given in Table 1.

Conclusions

A numerical procedure for the solution of transverse time-dependent inelastic deflection of plates of arbitrary shape using the boundary element method has been described. This class of problems is complicated because the problems are nonlinear and history dependent and involve redistribution of stress through the thickness and across the plate during deformation. Numerical results for several sample problems for square and triangular plates, using a combined creep-plasticity constitutive model with state variables, are presented. These solutions are obtained accurately and within reasonable amounts of computer times. Successful applications of the boundary-element method to inelastic planar (in earlier work) and transverse deflection problems of plates demonstrates the usefulness of this powerful general purpose technique for this important class of problems.

Acknowledgments

This research was supported by Contract No. EG-77-S-02-2733 of the U.S. Department of Energy with Cornell University.

References

1 Brebbia, C. A., ed., *Recent Advances in Boundary Element Methods,* Pentech Press, London, Plymouth, 1978.

2 Cruse, T. A., and Rizzo, F. J., eds., *Boundary-Integral Equation Method: Computational Applications in Applied Mechanics,* ASME, 1975.

3 Kumar, V., and Mukherjee, S., A Boundary-Integral Equation Formulation for Time-Dependent Inelastic Deformation in Metals, *International Journal of Mechanical Sciences,* Vol. 19, No. 12, Dec. 1977, pp. 713–724.

4 Mukherjee, S., and Kumar, V., "Numerical Analysis of Time-Dependent Inelastic Deformation in Metallic Media Using the Boundary-Integral Equation Method," ASME JOURNAL OF APPLIED MECHANICS, Vol. 45, No. 4, Dec. 1978, pp. 785–790.

5 Morjaria, M., and Mukherjee, S., "Improved Boundary-Integral Equation Method for Time-Dependent Inelastic Deformation in Metals," *International Journal for Numerical Methods in Engineering,* Vol. 15, No. 1, Jan. 1980, pp. 97–111.

6 Morjaria, M., Sarihan, V., and Mukherjee, S., "Comparison of Boundary Element and Finite-Element Methods in Two-Dimensional Inelastic Analysis," *Res Mechanica,* Vol. 1, No. 1, Jan.–Mar. 1980, pp. 3–20.

7 Jawson, M. A., and Maiti, M., "An Integral Equation Formulation of Plate Bending Problems," *Journal of Engineering Mathematics,* Vol. 2, No. 1, Jan. 1968, pp. 83–93.

8 Maiti, M., and Chakrabarty, S. K., "Integral Equation Solutions for Simply Supported Polygonal Plates," *International Journal of Engineering Science,* Vol. 12, No. 10, Oct. 1974, pp. 793–806.

9 Benzine, G. P., and Gamby, D. A., "A New Integral Equation Formulation for Plate Bending Problems," *Recent Advances in Boundary Element Methods,* Brebbia, C. A., ed., Pentech Press, London, Plymouth, 1978, pp. 327–342.

10 Stern, M., "A General Boundary Integral Formulation for the Numerical Solution of Plate Bending Problems," *International Journal of Solids and Structures,* Vol. 15, No. 10, Oct. 1979, pp. 769–782.

11 Hart, E. W., Li, C. Y., and Yamada, H., "Phenomenological Theory: A Guide to Constitutive Relations and Fundamental Deformation Properties, *Constitutive Equations in Plasticity,* Argon, A. S., ed., M.I.T. Press, Cambridge, Mass., 1976, pp. 149–197.

12 Hart, E. W., "Constitutive Relations for the Nonelastic Deformation of Metals," ASME *Journal of Engineering Materials and Technology,* Vol. 98, No. 3, July 1976, pp. 193–202.

13 Kumar, V., et al., "Theoretical and Experimental Analysis of Stresses in Reactor Components-Deformation in Type 304 Austenitic Stainless Steel," EPRI Final Report for Contract No. RP 697-1, Department of Materials Science and Engineering, Cornell University, Ithaca, N.Y., 1980.

14 Kumar, V., Morjaria, M., and Mukherjee, S., "Numerical Integration of Some Stiff Constitutive Models of Inelastic Deformation," ASME *Journal of Engineering Materials and Technology,* Vol. 102, No. 1, Jan. 1980, pp. 92–96.

15 Timoshenko, S., and Woinowsky-Krieger, S., "Small Deflections of Laterally Loaded Plates," *Theory of Plates and Shells,* 2nd ed., McGraw-Hill, New York, 1959, pp. 79–104.

16 Rzasnicki, W., and Mendelson, A., "Application of Boundary Integral Method to Elastoplastic Analysis of *V*-notched Beams," *International Journal of Fracture,* Vol. 11, No. 2, Apr. 1975, pp. 329–342.

17 Morjaria, M., and Mukherjee, S., "Inelastic Analysis of Transverse Deflection of Plates by the Boundary Element Method," DOE Report No. C00-2733-24, Department of Theoretical and Applied Mechanics, Cornell University, Ithaca, N.Y., June 1979.

18 Flügge, W., *Viscoelasticity,* 1st ed., Blaisdell, Waltham, Mass., 1967.

19 Conway, H. D., ""The Approximate Analysis of Certain Boundary-Value Problems," ASME JOURNAL OF APPLIED MECHANICS, Vol. 27, No. 2, June 1960, pp. 275–277.

Downloaded 01 May 2010 to 171.66.16.243. Redistribution subject to ASME license or copyright; see http://www.asme.org/terms/Terms_Use.cfm

W. H. Yang
Department of Mechanical Engineering and Applied Mechanics, University of Michigan, Ann Arbor, Mich. 48109
Mem. ASME

A Generalized von Mises Criterion for Yield and Fracture

Yield and fracture criteria for real materials are to a varying degree affected by a state of hydrostatic stress. Some materials, after certain deformation history, exhibit different yield point when the direction of the stress is reversed, a behavior known as the Bauschinger effect. These physical phenomena are not represented by the von Mises criterion. Based on a convexity theorem of matrices, a generalization of the von Mises criterion is presented. The new criterion satisfies the convexity requirement of plasticity theory and, with two scalar functions of deformation history α and β, produces a class of hardening behavior. The current values of α and β account for the effect of hydrostatic stress and an aspect of the Bauschinger effect on yield and fracture. The generalized criterion reduces to the form of the von Mises criterion as a special case.

Introduction

The von Mises theory [1] has doubtlessly been the most used mathematical description for yield phenomena of materials. The simplicity and smoothness of the function is probably the prime reason behind its popularity. Of course, the existence of a class of materials whose yield surfaces are not significantly altered by the hydrostatic stress has enhanced the applicability of the theory.

Hydrostatic stress certainly plays a role in yield and fracture of many other materials. Early investigations did not distinguish a criterion of yield from that of fracture. They only tried to establish the limit of linear elasticity [2]. The experiments of von Karman [3] and Böker [4] on marble and sandstone supported the Mohr's theory [5] that yield is affected by the hydrostatic stress. This theory is further developed by many researchers into various models whose complex mathematical forms have not induced wide applications.

A generalized von Mises criterion based on a known convexity theorem [11] of matrices is presented in this paper. The new criterion satisfies the convexity requirement of plasticity theory [6] and contains two scalar functions, α and β, of deformation history. Determined experimentally, these functions may produce proper hardening behavior. Given a set of values of α and β, the yield criterion expressed by the function should be regarded as the current yield criterion with respect to a deformation history. The generalized criterion includes the von Mises criterion as a special case.

The functional behavior of α and β will not be discussed here. They are regarded as parameters in this paper.

Although a simple form is chosen for the generalized von Mises criterion, other forms of yield and fracture criteria may be constructed from the convexity theorem given in the next section.

Contributed by the Applied Mechanics Division for publication in the JOURNAL OF APPLIED MECHANICS.

Discussion on this paper should be addressed to the Editorial Department, ASME, United Engineering Center, 345 East 47th Street, New York, N. Y. 10017, and will be accepted until September 1, 1980. Readers who need more time to prepare a discussion should request an extension from the Editorial Department. Manuscript received by ASME Applied Mechanics Division, February, 1979; final revision, August, 1979.

A Convexity Theorem of Matrices

The theorem stated next is valid for Hermitian matrices, but only the real, symmetric stress matrices are encountered in the intended applications.

Theorem. Given any convex, real function of a real variable ($R \to R$), $g(x)$, the corresponding real function F on any n by n symmetric (or Hermitian) matrix A defined by

$$F(A) = \text{Tr}\,(g(A)) \tag{1}$$

is convex. Here the symbol Tr ( ) denotes the trace of a matrix.

Before we prove the theorem, a few words are in order to define $g(A)$ when g is assumed a real function of a real variable. The notation $g(A)$ representing an n by n matrix is standard in mathematics literature. For instance, in the Cayley-Hamilton theorem [7], the characteristic polynomial $y(\lambda)$ is replaced by the matrix polynomial $y(A)$. For a general $R \to R$ function g, we define

$$g(A) = QDQ^t \tag{2}$$

where Q is the orthogonal matrix whose columns are the eigenvectors of A and D is a diagonal matrix with elements $g(\lambda_i)$ being functions of the eigenvalues of A.

It follows from (2) that

$$g(P^tAP) = P^tg(A)P \tag{3}$$

where P is an arbitrary orthogonal matrix.

Since the trace of a matrix is invariant to orthogonal transformation,

$$\text{Tr}\,(g(A)) = \text{Tr}\,(P^tg(A)P) = \text{Tr}\,(g(P^tAP)) \tag{4}$$

are identities.

Now we are ready to prove the theorem. Let $\overline{A}$ be a convex combination of two matrices A and A' such that

$$\overline{A} = \alpha A + (1 - \alpha)A', \quad 0 \le \alpha \le 1 \tag{5}$$

We shall prove that

Copyright © 1980 by ASME
Downloaded 01 May 2010 to 171.66.16.243. Redistribution subject to ASME license or copyright; see http://www.asme.org/terms/Terms_Use.cfm

$$F(\bar{A}) \le \alpha F(A) + (1-\alpha)F(A') \tag{6}$$

if F is to be convex. This is analogous to the convexity property of a $R \to R$ function g such that

$$g(\alpha x + (1-\alpha)x') \le \alpha g(x) + (1-\alpha)g(x') \tag{7}$$

which for a n-point convex combination

$$g\left(\sum_1^n \alpha_i x_i\right) \le \sum_1^n \alpha_i g(x_i), \quad \sum_1^n \alpha_i = 1, \quad \alpha_i \ge 0 \tag{8}$$

is also true.

Let $\bar{Q}$ be the orthogonal matrix whose columns $\bar{q}_i$ are the eigenvectors of $\bar{A}$. Similarly, Q and Q' diagonalize A and A', respectively, such that

$$\bar{Q}^t \bar{A} \bar{Q} = \bar{\Lambda}, \quad Q^t A Q = \Lambda, \quad Q'^t A' Q' = \Lambda' \tag{9}$$

where $\bar{\Lambda}$, Λ, and Λ' are diagonal matrices containing the eigenvalues of $\bar{A}$, A, and A', respectively.

Using (1), (2), (4), and (7),

$$\begin{aligned} F(\bar{A}) = \mathrm{Tr}\,(g(\bar{A})) &= \mathrm{Tr}\,(g(\bar{Q}^t(\alpha A + (1-\alpha)A')\bar{Q})) \\ &= \sum_1^n [g(\alpha\langle \bar{q}_i, A\bar{q}_i\rangle + (1-\alpha)\langle \bar{q}_i, A'\bar{q}_i\rangle)] \\ &\le \alpha \sum_1^n g(\langle \bar{q}_i, A\bar{q}_i\rangle) + (1-\alpha)\sum_1^n g(\langle \bar{q}_i, A'\bar{q}_i\rangle) \\ &= \alpha \sum_1^n g(\langle p_i, \Lambda p_i\rangle) + (1-\alpha)\sum_1^n g(\langle p_i', \Lambda' p_i'\rangle) \end{aligned} \tag{10}$$

where p_i and p_1' are the columns of the orthogonal matrices

$$P = Q^t \bar{Q}, \quad P' = Q'^t \bar{Q} \tag{11}$$

and $\langle\ ,\ \rangle$ denotes the inner product of two vectors.

Consider the first sum in (10). Let p_{ij} be the (i,j)th element of P. Then

$$\begin{aligned} \sum_{i=1}^n g(\langle p_i, \Lambda p_i\rangle) &= \sum_{i=1}^n g\left(\sum_{j=1}^n p_{ij}^2 \lambda_j\right) \\ &\le \sum_{i=1}^n \sum_{j=1}^n p_{ij}^2 g(\lambda_j) = \sum_{j=1}^n \sum_{i=1}^n p_{ij}^2 g(\lambda_j) \\ &= \sum_{j=1}^n g(\lambda_j) = \mathrm{Tr}\,(g(A)) \end{aligned} \tag{12}$$

since

$$\sum_{i=1}^n p_{ij}^2 = \sum_{j=1}^n p_{ij}^2 = 1. \tag{13}$$

A similar expression can be obtained for the second sum of (10). We thus have the result

$$\mathrm{Tr}\,(g(\bar{A})) \le \alpha\,\mathrm{Tr}\,(g(A)) + (1-\alpha)\mathrm{Tr}\,(g(A')) \tag{14}$$

which proves the theorem.

Restating the von Mises Criterion

Let σ denote a 3 by 3 symmetric stress matrix and $p = \mathrm{Tr}\,(\sigma)/3$ denote the hydrostatic stress. The deviatoric stress matrix defined by

$$S = \sigma - pI \tag{15}$$

is symmetric where I is the identity matrix.

A special case of the convex function (1)

$$F(S) = \mathrm{Tr}\,(S^2) \tag{16}$$

where $g(\ ) = (\ )^2$ is chosen, is the well known von Mises yield function although its more familiar form is written in terms of the components of σ [8]

$$\begin{aligned} F(S) = [(\sigma_{xx} - \sigma_{yy})^2 + (\sigma_{yy} - \sigma_{zz})^2 + (\sigma_{zz} - \sigma_{xx})^2]/3 \\ + 2(\sigma_{xy}^2 + \sigma_{yz}^2 + \sigma_{zz}^2) \end{aligned} \tag{17}$$

as shown in most of the plasticity books.

It is known that a state of hydrostatic stress superposed on σ will not change the value of F. It is also known that

$$F(S) = F(Q^t S Q) \tag{18}$$

where Q is any orthogonal matrix. If Q diagonalizes S, then F can be written in terms of the eigenvalues of σ (principal stresses)

$$F(S) = [(\sigma_1 - \sigma_2)^2 + (\sigma_2 - \sigma_3)^2 + (\sigma_3 - \sigma_1)^2]/3 \tag{19}$$

In the Euclidean space of $(\sigma_1, \sigma_2, \sigma_3)$, a constant value of F in (19) represents a circular cylindrical surface whose axis passes through (0, 0, 0) and is oriented in the direction of the unit vector $(1, 1, 1)/\sqrt{3}$.

The fact that $F(S)$ is convex in σ follows from the theorem and from (15). From the theorem, $F(S)$ is convex in S. Since the components of S and that of σ are related by the linear transformation (15), convexity of F is preserved under such a change of variables.

Although the two forms of the von Mises function in (17) and (19) are more familiar, the form in (16) leads to a direct generalization.

A Generalized von Mises Function

We may generate a class of theoretically acceptable yield functions G from arbitrary real to real convex functions g such that

$$G(\sigma) = \mathrm{Tr}\,(g(\sigma)) \tag{20}$$

The usefulness of such an exercise depends on if one can correlate experimental results to some function in the class G. It is conceivable that convex functions of stress matrix generated in this manner could produce correct yield or fracture criteria for some materials.

We shall explore a simple form of (20) in which g is chosen to have the form

$$g(\sigma) = (\sigma - \alpha p I + (1-\alpha)\beta I)^2 \tag{21}$$

where α, β are parameters.

This leads to a generalized von Mises function

$$G(\sigma) = \mathrm{Tr}\,((\sigma - \alpha p I + (1-\alpha)\beta I)^2) \tag{22}$$

For the reason given earlier, G is convex in σ and reduces to the von Mises function when $\alpha = 1$. Using the fact that $\mathrm{Tr}\,(A+B) = \mathrm{Tr}\,(A) + \mathrm{Tr}\,(B)$ and $\mathrm{Tr}\,(\sigma - pI) = 0$, (22) can be written in another form

$$G(\sigma) = \mathrm{Tr}\,((\sigma - pI)^2) + 3(1-\alpha)^2(p+\beta)^2 \tag{23}$$

The foregoing equation can be expressed in terms of the stress invariants, $J_2' = \mathrm{Tr}\,((\sigma - pI)^2)$ and $J_1 = 3p$, such that

$$G(\sigma) = J_2' + \bar{\alpha}^2(J_1 + \bar{\beta})^2 \tag{24}$$

where $\bar{\alpha} = (1-\alpha)/\sqrt{3}$ and $\bar{\beta} = 3\beta$.

The physical and geometrical interpretations of (22)–(24) will be examined in the next section.

Interpretations

$G(\sigma) \le$ constant is a convex set in the space of the components of σ. It would be difficult to visualize the geometry of such a set in the six (independent components of the symmetric stress matrix) dimensional space. Instead, we shall interpret the surfaces of G = constant in the three-dimensional space of principal stresses.

Let Q be the orthogonal matrix which diagonalizes σ such that $Q^t \sigma Q = \mathrm{diag}\,(\sigma_1, \sigma_2, \sigma_3)$. It is obvious that the same Q also diagonalizes the matrices $g(\sigma)$. The function G in terms of the principal stresses is given by

$$\begin{aligned} G(\sigma) = &\left[\left(1 - \frac{\alpha}{3}\right)\sigma_1 - \frac{\alpha}{3}\sigma_2 - \frac{\alpha}{3}\sigma_3 + (1-\alpha)\beta\right]^2 \\ &+ \left[\left(1 - \frac{\alpha}{3}\right)\sigma_2 - \frac{\alpha}{3}\sigma_3 - \frac{\alpha}{3}\sigma_1 + (1-\alpha)\beta\right]^2 \end{aligned} \tag{25}$$

Downloaded 01 May 2010 to 171.66.16.243. Redistribution subject to ASME license or copyright; see http://www.asme.org/terms/Terms_Use.cfm

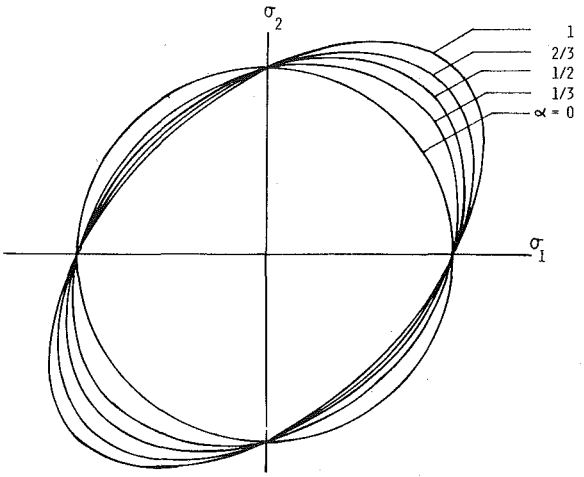

Fig. 1 Yield loci of generalized von Mises criterion

$$+\left[\left(1-\frac{\alpha}{3}\right)\sigma_3-\frac{\alpha}{3}\sigma_1-\frac{\alpha}{3}\sigma_2+(1-\alpha)\beta\right]^2 \qquad (25)$$

(Cont.)

For $\alpha = 0$, $G = Y^2$ is a spherical surface of radius Y centered at $(-\beta, -\beta, -\beta)$, where Y is the uniaxial yield stress. For $\beta = 0$, the maximal elastic hydrostatic stress before yielding or fracture in this case is $Y/\sqrt{3}$. The parameter β produces different yield points when the sign of the stress is reversed, an aspect of the Bauschinger effect.

For $\alpha = 1$, $G = (2/3)Y^2$ is a circular cylindrical surface which intersects σ_1, σ_2, σ_3 axes at Y. The maximum elastic hydrostatic stress is unbounded in this case.

For $\alpha < 1$, the surfaces, G = constant, are closed, therefore, the values of the maximum elastic hydrostatic stress are finite. Since β merely translates the surfaces along the hydrostatic axis, we need only to discuss the case $\beta = 0$. Let the constant values of G be selected for each surface such that the points (Y, O, O) (O, Y, O) and (O, O, Y) are on each surface. The intersections of all surfaces with the $\sigma_1 - \sigma_2$ plane are given by

$$\sigma_1^2 + \sigma_2^2 - \frac{2\alpha(2-\alpha)}{3-\alpha(2-\alpha)}\sigma_1\sigma_2 = Y^2 \qquad (26)$$

and are shown in Fig. 1.

The intersections of these surfaces with the Π-plane, $\sigma_1 + \sigma_2 + \sigma_3 = 0$, are circles. If the radii of all circles are made to equal to $\sqrt{2/3}Y$, the yielding hydrostatic stress is then a function of α as shown in Fig. 2. The yielding hydrostatic stress approaches ∞ as $\alpha \to 1$.

The intersection of $G = (2/3)Y^2$ with a plane passing through origin and perpendicular to Π-plane is an ellipse. This is best interpreted by equation (24). The plane is known as the $\sqrt{J_2'} - J_1$ plane. The ellipse has the minor and major simiaxes $\sqrt{2/3}Y$ and $\sqrt{2/3}Y/\overline{\alpha}$ with its center translated $-\overline{\beta}$ from the origin along the J_1-axis as shown in Fig. 3.

Final Remarks

The generalized von Mises criterion introduced in this paper is perhaps the least general of all other possible generalizations. It nevertheless captures some effects of hydrostatic stress and Bauschinger on yielding (or fracture) and preserves the simplicity of the von Mises criterion. The hardening behavior must be represented by proper choice of functions α and β together with the yield stress Y. The three functions should provide enough freedom to identify a wide class of materials.

In some approaches to rock and soil mechanics, caps are introduced to limit the von Mises cylinder beyond certain hydrostatic stresses [9]. Such approaches destroy the smoothness of the von Mises function and make applications of the criterion cumbersome. The generalized von Mises criterion presented in this paper accomplishes the capping without such shortcomings. It should find immediate applications in soil and rock mechanics.

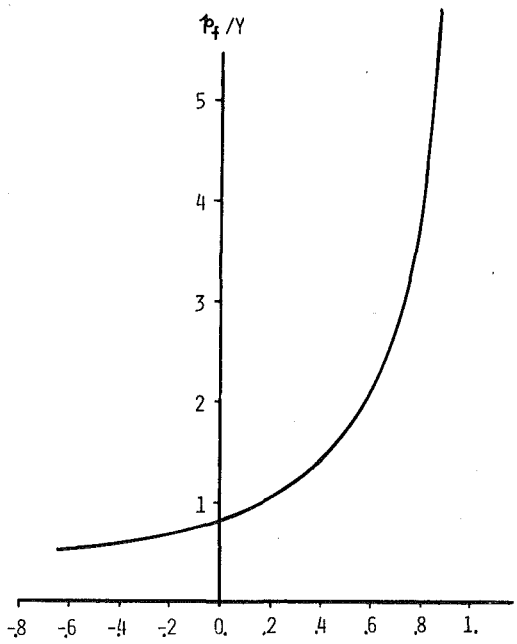

Fig. 2 Yielding hydrostatic stresses as function of α

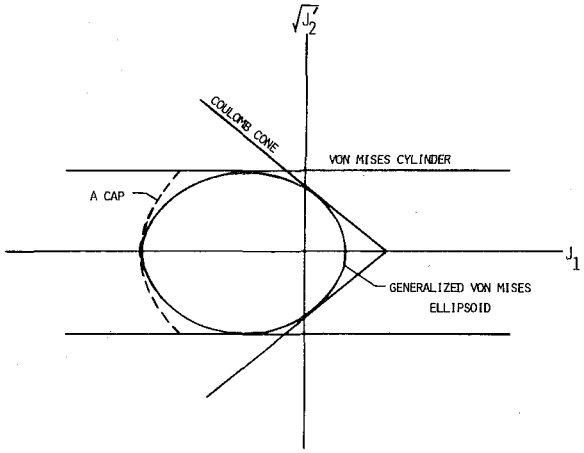

Fig 3 Generalized von Mises ellipsoid in $\sqrt{J_2'} - J_1$ plane

To generate yield functions, which are convex functions of stress matrices, from convex functions of a real variable is the main concept introduced here. This opens up the possibilities of creating other useful limiting criteria from mathematical theorems of convexity. Theorems of this type, more general than the one stated in this paper, are being developed [10]. Further research in this area should produce new yield and fracture criteria for materials which are not describable by the existing theories.

References

1 von Mises, R., "Gottinger Nachrichten," *Math.-Phys. Klasse*, 582, 1913.

2 Westergaard, H. M., *Theory of Elasticity and Plasticity*, Dover, 1952.

3 von Karman, T., "Festigkeitsversuche unter allseitigem Druck," *Mitt. Forschungsarbeit, Gebiete Ingenieurwes*, 118, 1912, pp. 37–68.

4 Böker, R., "Die Mechanik der bleibenden Formänderung in kristallinisch aufgebauten Körpern," *Mitt. Forschungsarbeit, Gebiete Ingenieurwes*, 1915, pp. 175–176, 53 pp.

5 Mohr, O., *Abhandlungen aus dem Gebiete der technischen Mechanik Ernst*, Berlin, ed. 2, 1914, pp. 192–235.

Downloaded 01 May 2010 to 171.66.16.243. Redistribution subject to ASME license or copyright; see http://www.asme.org/terms/Terms_Use.cfm

6 Yang, W. H., "Class Notes on Mathematical Theory of Plasticity," AMES 519, The University of Michigan, 1974.
7 Nobel, B., *Applied Linear Algebra,* Prentice-Hall, Englewood Cliffs, N.J., 1969.
8 Mendelson, A., *Plasticity: Theory and Application,* Macmillan, 1968.
9 DiMaggio, F. L., and Sandler, I. S., "Material Model for Granular Soils," *Journal of Engineering Mechanics Division,* ASCE, June 1971, pp. 935–950.
10 Federbush, P., Taylor, B. A., and Yang, W. H., "A Convexity Theorem for Hermitian Matrices," Preprint, Department of Mathematics, University of Michigan, 1978.
11 Ruelle, D., *Statistical Mechanics,* W. A. Benjamin Inc., New York, 1964, pp. 25–28.

Downloaded 01 May 2010 to 171.66.16.243. Redistribution subject to ASME license or copyright; see http://www.asme.org/terms/Terms_Use.cfm

W. H. Yang

The University of Michigan
Ann Arbor, Mich. 48109
Mem. ASME

A Useful Theorem for Constructing Convex Yield Functions

Known yield functions have been constructed in the three-dimensional space of principal stresses. Their convexity in the six-dimensional space of the stress components is only conjectured. Mathematical theorems of convexity are known for functions of Hermitian matrices but have not been applied to yield functions. In this paper, Drucker's hypothesis is properly restated, leading to convexity requirement for yield functions of elastoplastic materials. Then a special version of a known convexity theorem is presented. The theorem can be applied to construct yield functions for isotropic materials. Examples of such applications are extended to some known yield functions and other theoretically acceptable new ones.

Introduction

Concept and development of yield functions for elastoplastic materials began with the great physical insight of Tresca [1] and the mathematical deduction of von Mises [2]. Their formulations of the yield criteria involved convex functions incidentally. The theory of yielding developed rather slowly after Tresca and von Mises. It is until the hypothesis of Drucker [3], that introduced the convexity requirement to the yield functions.

Convexity based on Drucker's hypothesis has often been argued from a geometrical point of view in the three-dimensional space of principal stresses while convexity must be imposed on a function of six variables of stress components. Convexity of the known yield functions in the six-dimensional stress space is often conjuctured without a proof.

In this paper, Drucker's hypothesis is restated properly as the background for the presentation of a convexity theorem whose usefulness is demonstrated by its power of generating correct new yield functions.

The theorem is a special case of a convexity theorem for Hermitian matrices [4]. The mathematical language used in [4] may not have made it clear to possible applications in the theory of yielding. The presentation of the special case is intended for readers in the field of plasticity.

Finally, the theorem is related to some existing yield functions and is applied to construct theoretically acceptable new yield functions.

Drucker's Hypothesis

The hypothesis of Drucker [3] for a class of elastoplastic materials consists of

1 Existence of a yield function.
2 Non-negative dissipation of mechanical energy.
3 Additivity of elastic and plastic strain increments.

We shall now present these ideas in more details.

At a point P in the material with a current state of stress σ^0, we assume that there exists a yield function $f(\sigma)$ and a set of current states of yield stresses σ^* such that

$$f(\sigma^0) \leq f(\sigma^*) = \text{constant}. \tag{1}$$

Further loading and unloading on the body introduce added stress $\sigma - \sigma^0$ at the point P. Consider only the small deformation theory of deformable solids. The work done by the added stress to a unit volume of material at point P is given by the integral

$$W = \int (\sigma - \sigma^0) : d\epsilon \tag{2}$$

where $d\epsilon$ is the strain increment matrix and $\sigma : d\epsilon$ denotes $\Sigma_{i=1}^{3} \Sigma_{j=1}^{3} \sigma_{ij} d\epsilon_{ij}$.

If the integration is taken along a closed path in the stress space, the Drucker's hypothesis assumes that the work done is non-negative

$$\oint (\sigma - \sigma^0) : d\epsilon \geq 0 \tag{3}$$

If the path reaches a yield stress σ^* and then a point $\sigma^* + d\sigma$ outside the current yield surface $f(\sigma^*) = \text{constant}$, the integral inequality (3) reduces to an algebraic one [5]

$$(\sigma^* - \sigma^0) : d\epsilon^p \geq 0 \tag{4}$$

since no net work is done by the elastic deformation in the closed path. During the loading beyond the current yield surface, the elastic and plastic strain increments are assumed to be additive such that

$$d\epsilon = d\epsilon^e + d\epsilon^p \tag{5}$$

Inequality (4) implies convexity of the set

$$S = \{\sigma : f(\sigma) \leq f(\sigma^*)\} \tag{6}$$

Contributed by the Applied Mechanics Division for publication in the JOURNAL OF APPLIED MECHANICS.

Discussion on this paper should be addressed to the Editorial Department, ASME, United Engineering Center, 345 East 47th Street, New York, N. Y. 10017, and will be accepted until September 1, 1980. Readers who need more time to prepare a discussion should request an extension from the Editorial Department. Manuscript received by ASME Applied Mechanics Division, May, 1979; final revision, October, 1979.

Copyright © 1980 by ASME
Downloaded 01 May 2010 to 171.66.16.243. Redistribution subject to ASME license or copyright; see http://www.asme.org/terms/Terms_Use.cfm

which defines the current elastic range of the material at point P. This can be easily shown by considering two states of initial stresses σ^0 and σ^1 in S. They satisfy the inequality (4) such that $(\sigma^* - \sigma^0):d\epsilon^p \geq 0$ and $(\sigma^* - \sigma^1):d\epsilon^p \geq 0$. Their convex combination $\bar{\sigma} = \alpha\sigma^0 + (1-\alpha)\sigma^1$, $(0 \leq \alpha \leq 1)$, certainly satisfies

$$(\sigma^* - \bar{\sigma}):d\epsilon^p \geq 0 \tag{7}$$

Hence $\bar{\sigma}\epsilon S$ and S is convex.

The condition (4) requires f to be a convex function of six stress components. Tresca and von Mises criteria are presented as cylinders in the principal stress space. Other yield criteria may assume different forms of convex bodies in such a space. It is not clear that the convexity is preserved in the six-dimensional stress space. A simple example should justify raising the question. Consider two real, convex functions of a real variable $f(g)$ and $g(x)$ such that $f'' \geq 0$ and $g'' \geq 0$. The composite function $f(g(x))$ is convex in x, if and only if

$$d^2f/dx^2 = f''g'^2 + f'g'' \geq 0 \tag{8}$$

which is not always true since f' can be negative and large.

Based on Drucker's hypothesis, convexity of a general yield function and normality of a plastic strain increment to a yield surface are required in the six-dimensional stress space. The theorem given in the next section will settle the question of convexity of a class of yield functions in such a space.

A Convexity Theorem

A stress matrix σ being symmetrical may be regarded as equivalent to a vector of six components. The symbol σ shall denote a 3×3-matrix or a 6-vector. Its meaning should be unambiguous in the equations it appears. The eigenvalues of σ known as the principal stresses may take the form of a diagonal matrix or a vector with three components

$$\lambda_i = \lambda_i(\sigma) \qquad i = 1, 2, 3 \tag{9}$$

A yield function $f(\lambda(\sigma))$ is a mapping: $R^6 \to R^3 \to R$.

Theorem. *A convex function $f(\lambda_1, \lambda_2, \lambda_3)$ symmetrical in its* arguments is convex in σ such that its Hessian $H_\sigma(f) = [\partial^2 f/\partial\sigma_i\partial\sigma_j]$ is a 6×6 positive semidefinite matrix.

To prove the theorem, we need first two lemmas.

Lemma 1. Let $\lambda_1 \geq \lambda_2 \geq \lambda_3$ be the eigenvalues of σ and $\mu_1 = \lambda_1$, $\mu_2 = \lambda_1 + \lambda_2$, $\mu_3 = \lambda_1 + \lambda_2 + \lambda_3$. Then $\mu_i(\sigma)$, $i = 1, 2, 3$, are convex in σ.

Proof:

1 Since μ_1 is the largest eigenvalue of σ,

$$\mu_1(\sigma) = \sup_{x \neq 0} \frac{x^t\sigma x}{x^t x} \tag{10}$$

Let $\bar{\sigma} = \alpha\sigma^0 + (1-\alpha)\sigma^1$, $0 \leq \alpha \leq 1$. Then

$$\begin{aligned}\mu_1(\bar{\sigma}) &= \sup_{x \neq 0} \frac{x^t[\alpha\sigma^0 + (1-\alpha)\sigma^1]x}{x^t x} \\ &\leq \alpha \sup_{x \neq 0} \frac{x^t\sigma^0 x}{x^t x} + (1-\alpha) \sup_{x \neq 0} \frac{x^t\sigma^1 x}{x^t x} \\ &= \alpha\mu_1(\sigma^0) + (1-\alpha)\mu_1(\sigma^1)\end{aligned} \tag{11}$$

Hence μ_1 is convex in σ.

2 Since $\mu_3(\sigma) = \mathrm{Tr}\,(\sigma)$, $\mathrm{Tr}\,(\alpha A) = \alpha\,\mathrm{Tr}\,(A)$ and $\mathrm{Tr}\,(A + B) = \mathrm{Tr}\,(A) + \mathrm{Tr}\,(B)$, it follows that

$$\mu_3(\bar{\sigma}) = \alpha\mu_3(\sigma^0) + (1-\alpha)\mu_3(\sigma^1) \tag{12}$$

Therefore $\mu_3(\sigma)$ is both convex and concave. It is a linear function of σ.

3 Since λ_3 is the smallest eigenvalue of σ, it satisfies

$$\lambda_3(\bar{\sigma}) = \inf_{x \neq 0} \frac{x^t\bar{\sigma}x}{x^t x} \geq \alpha \inf_{x \neq 0} \frac{x^t\sigma^0 x}{x^t x} + (1-\alpha) \inf_{x \neq 0} \frac{x^t\sigma^1 x}{x^t x} \tag{13}$$

and is therefore concave in σ or $-\lambda_3$ is convex in σ. Since the sum of convex functions is convex,

$$\mu_2 = \mu_3 - \lambda_3 = \mu_3 + (-\lambda_3) \tag{14}$$

is convex in σ. Hence all μ_1, μ_2, μ_3 are convex in σ.

Lemma 2. Let f be a convex, symmetrical function of $\lambda_1, \lambda_2, \lambda_3$ $(\lambda_1 \geq \lambda_2 \geq \lambda_3)$. Then

$$\frac{\partial f}{\partial\lambda_1} \geq \frac{\partial f}{\partial\lambda_2} \geq \frac{\partial f}{\partial\lambda_3} \tag{15}$$

Proof:

1 Let $\lambda = b = (b_1, b_2, b_3)$, $b' = (b_2, b_1, b_3)$ and

$$\begin{aligned}\phi(\alpha) &= f(\alpha b + (1-\alpha)b') \\ &= f(\alpha b_1 + (1-\alpha)b_2, \alpha b_2 + (1-\alpha)b_1, b_3) \quad 0 \leq \alpha \leq 1\end{aligned} \tag{16}$$

2 Differentiating (16) with respect to α and setting $\alpha = 1$, we obtain

$$\phi'(1) = \left(\frac{\partial f(\lambda)}{\partial\lambda_1} - \frac{\partial f(\lambda)}{\partial\lambda_2}\right)(b_1 - b_2) \tag{17}$$

Since f is symmetrical, $f(b) = f(b')$, and convex,

$$\begin{aligned}\phi(\alpha) &= f(\alpha b + (1-\alpha)b') \\ &\leq \alpha f(b) + (1-\alpha)f(b') = f(b)\end{aligned} \tag{18}$$

The fact $\phi(1) = f(b)$ implies $\phi'(1) \geq 0$. Hence,

$$\frac{\partial f}{\partial\lambda_1} - \frac{\partial f}{\partial\lambda_2} \geq 0 \tag{19}$$

For the case $b_1 = b_2$, we may take $b_1 = b_2 + \delta$ $(\delta > 0)$. The inequality (19) still holds as δ approaches 0.

3 Similarly, $\partial f/\partial\lambda_2 - \partial f/\partial\lambda_3 \geq 0$ can be shown. The lemma is proven.

Proof of the Theorem.

From Lemma 1, we can write

$$\lambda_1 = \mu_1, \quad \lambda_2 = \mu_2 - \mu_1, \quad \lambda_3 = \mu_3 - \mu_2 \tag{20}$$

From Lemma 2, it follows that

$$\frac{\partial f}{\partial\mu_1} = \frac{\partial f}{\partial\lambda_1} - \frac{\partial f}{\partial\lambda_2} \geq 0, \frac{\partial f}{\partial\mu_2} = \frac{\partial f}{\partial\lambda_2} - \frac{\partial f}{\partial\lambda_3} \geq 0 \tag{21}$$

Consider the composite function $f(\lambda(\mu(\sigma)))$. Convexity of f in λ implies convexity of f in μ since the mapping from μ to λ is linear. We shall now proceed to show that a convex function $f(\mu(\sigma))$ is convex in σ.

Let $H_\sigma(f)$, $H_\sigma(\mu_i)$, $i = 1, 2, 3$ denote the 6×6 Hessian matrices of f and μ_i with respect to σ. Since μ_3 is linear in σ, $H_\sigma(\mu_3)$ is a null matrix. Let $H_\mu(f)$ be the 3×3 Hessian matrix of f with respect to μ. By the chain rule of differentiation, we obtain,

$$H_\sigma(f) = [\partial\mu/\partial\sigma]^t H_\mu(f)[\partial\mu/\partial\sigma] + \sum_{i=1}^{2} \frac{\partial f}{\partial\mu_i} H_\sigma(\mu_i) \tag{22}$$

where $[\partial\mu/\partial\sigma]$ is a 3×6 Jacobian matrix. In equation (22), $H_\mu(f)$ is positive-semidefinite since f is convex in μ. $H_\sigma(\mu_i)$, $i = 1, 2$ are positive-semidefinite since μ_1 and μ_2 are convex in σ. Note that $H_\sigma(\mu_3) = 0$ since μ_3 is linear in σ.

To form scalar products, we pre and postmultiply (22) by an arbitrary vector $v \neq 0$. The scalar product formed from the first term in the right-hand side of (22) is obviously non-negative. The scalar products formed from the terms in the summation are also non-negative since $\partial f/\partial\mu_1$ and $\partial f/\partial\mu_2$ are non-negative by Lemma 2. We obtain,

$$v^t H_\sigma(f) v \geq 0 \tag{23}$$

hence $H_\sigma(f)$ is positive-semidefinite and f is convex in σ.

For piecewise differentiable yield functions, we shall treat the corners of the yield function by the limiting process and the theorem can be proven in essentially the same manner.

Downloaded 01 May 2010 to 171.66.16.243. Redistribution subject to ASME license or copyright; see http://www.asme.org/terms/Terms_Use.cfm

Examples

Now we can write arbitrary convex functions of three principal stresses with symmetry in its arguments and be assured of their convexity in the stress space. The theorem provides a convenient way to construct new yield functions for isotropic materials.

The well-known Tresca function

$$T(\sigma) = \max\{|\lambda_1 - \lambda_2|, |\lambda_2 - \lambda_3|, |\lambda_3 - \lambda_1|\} \tag{24}$$

and the von Mises function

$$V(\sigma) = (\lambda_1 - \lambda_2)^2 + (\lambda_2 - \lambda_3)^2 + (\lambda_3 - \lambda_1)^2 \tag{25}$$

certainly fall within the scope of the theorem.

The Coulomb-Mises function may take the form

$$CM(\sigma) = C_1[(\lambda_1 - \lambda_2)^2 + (\lambda_2 - \lambda_3)^2 + (\lambda_3 - \lambda_1)^2] + C_2(\lambda_1 + \lambda_2 + \lambda_3) \tag{26}$$

where C_1, C_2 are constants, The function is convex in σ.

The convex function

$$F(\sigma) = \max\{|2\lambda_1 - \lambda_2 - \lambda_3|, |2\lambda_2 - \lambda_3 - \lambda_1|, |2\lambda_3 - \lambda_1 - \lambda_2|\} \tag{27}$$

has level surfaces in the principal stress space as hexagonal cylinders rotated 30° from the Tresca cylinders.

If $g(x)$ is a convex $R \to R$ function, then

$$f(\sigma) = \sum_{i=1}^{3} g(\lambda_i) \tag{28}$$

is convex in σ.

Many other yield functions may be constructed in this manner. The creation of a useful yield function must be guided by experimental data. The theorem provides an important aid to reduce the data into functional form.

Final Remarks

The theorem given can be stated in another form: For isotropic yield functions, convexity in the principal stress space implies convexity in the stress space.

The theorem presented in this paper can be used to produce new yield functions. Few yield functions are available for materials whose yield surfaces depend on hydrostatic stress and exhibit Bauschinger effect [6]. A generalized von Mises function encompassing such effects is derived recently by Yang [7] using a different convexity theorem.

For anisotropic yield criteria, a new convexity theorem must be developed. There exists no such theorem.

Acknowledgment

The author is grateful for the critical comments of Prof. T. C. T. Ting of University of Illinois at Chicago Circle leading to two improvements in the revised manuscript.

References

1 Tresca, H., *Comptes Rendus Acad. Sci.*, Paris, Vol. 59, 1864, p. 745.

2 von Mises, R., Gottinger Nachrichten, Math.-Phys., Klasse, 1913, p. 582.

3 Drucker, D. C., *Introduction to Mechanics of Deformable Solids*, McGraw-Hill, New York, 1967.

4 Federbush, P., Taylor, B. A., and Yang, W. H., "A Convexity Theorem for Hermitian Matrices," Preprint, Department of Mathematics, University of Michigan, 1978.

5 Martin, J. B., *Plasticity: Fundamentals and General Result*, MIT Press, 1975.

6 Hill, R., *The Mathematical Theory of Plasticity*, Clarendon Press, Oxford, 1956.

7 Yang, W. H., "A Generalized von Mises Criterion for Yield and Fracture," ASME JOURNAL OF APPLIED MECHANICS, Vol. 47, June 1980, pp. 297–300.

Downloaded 01 May 2010 to 171.66.16.243. Redistribution subject to ASME license or copyright; see http://www.asme.org/terms/Terms_Use.cfm

J. F. Dorris
Graduate Student.

S. Nemat-Nasser
Professor of Civil Engineering and Applied Mathematics. Mem. ASME

Northwestern University, Department of Civil Engineering, The Technological Institute, Evanston, Ill. 60201

Instability of a Layer on a Half Space

Unstable deformations of an elastic or elastoplastic layer on an elastic or elastoplastic half space, are studied under compressive forces. Various combinations of material properties are considered, e.g., an elastic layer on an elastoplastic half space, elastoplastic layer on an elastic half space, etc. Both the flow and the total deformation plasticity models are used and the corresponding results compared. The results seem to have relevance to the problem of folding of geological formations and crustal buckling under tectonic stresses.

Introduction

Unstable deformations of a layer which consists of either elastic or elastoplastic materials and which is situated on an elastic or elastoplastic half space, are studied. It is assumed that the layer and the half space are subjected to a constant compressive force parallel to the free surface. The deformations which precede instability are regarded to be finite. For the prediction of the incipience of unstable (quasi-static) motions, an exact rate formulation is employed; see, e.g., Hill [1], Hutchinson [2], Nemat-Nasser [3], and for a comprehensive survey of plastic buckling (up to 1970) see Sewell [4]. In line with Hill's generalization of Shanley's theory [5], no unloading is considered, as the incipience of unstable motions of elastoplastic bodies is predicted to occur at a smaller critical load, if no elastic unloading is included.

The specific material properties assumed for each material are various combinations of elasticity, the flow theory plasticity, and the total deformation plasticity. Qualitatively, the unstable deformations do not vary significantly with a change in material properties. However, quantitatively, the results are significantly affected by the considered constitutive models. Qualitatively, the instability essentially consists of surface buckling which decays exponentially with depth.

The results presented here have application to the unstable deformations of composite materials which have undergone finite homogeneous deformations. Perhaps the most obvious and useful application would correspond to the folding of geological formations and crustal buckling under tectonic stresses. Problems of this kind, but assuming elastic or viscoelastic material properties, have been considered by Biot in a number of pioneering investigations; see his book [6] in which references to earlier works are given. The folding and crustal buckling problem has also been studied by Ramberg [7] who models the earth's crust as a floating elastic or viscoelastic plate being affected by gravity and a lateral tectonic compression. More recently, Brunelle [8] has discussed the surface instability of an elastic half space, using the field equations developed by Novozhilov [9] for small deformations superimposed on large ones. Brunelle, however, does not use objective constitutive relations for the elastic rate problem, nor does he consider the effect of plasticity. In the present work, on the other hand, we use an exact rate formulation and consider various combinations of elastic and elastoplastic models for the layer, the half space, and both combined, and examine the surface instability of an elastic or an elastoplastic half space as a limiting case.

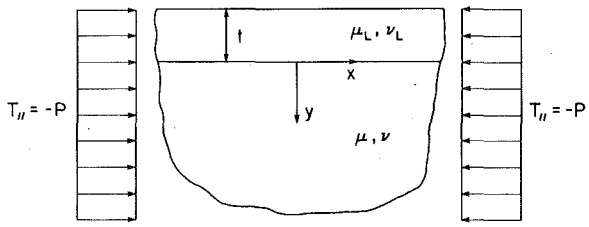

Fig. 1 A layer on a half space

Analysis

The problem considered is the finite deformation due to the horizontal compression of the half space covered by a layer (see Fig. 1). Various material properties are assumed for both the layer and half space. The deformation is assumed to be plane strain and is described by the Lagrangian variable $\mathbf{x} = \mathbf{x}(\mathbf{X}, t) = x_a(\mathbf{X}, t)\mathbf{e}_a$. Here $\mathbf{x}$ and $\mathbf{X}$ denote the position of a typical material point in the current and reference configurations, respectively, and $\mathbf{e}_a$, $a = 1, 2, 3$, defines an orthogonal unit triad for the fixed rectangular coordinate system which will be used throughout this work. With $v_a = v_a(\mathbf{x}, t)$ the instantaneous velocity field, the deformation rate tensor $\mathcal{D}$ is

$$\mathcal{D} = D_{ab}\mathbf{e}_a\mathbf{e}_b = \frac{1}{2}(v_{a,b} + v_{b,a})\mathbf{e}_a\mathbf{e}_b, \tag{1}$$

where a subscript preceeded by a comma denotes partial differentiation, with respect to the corresponding coordinate.

Contributed by the Applied Mechanics Division for publication in the JOURNAL OF APPLIED MECHANICS.

Discussion on this paper should be addressed to the Editorial Department, ASME, United Engineering Center, 345 East 47th Street, New York, N. Y. 10017, and will be accepted until September 1, 1980. Readers who need more time to prepare a discussion should request an extension from the Editorial Department. Manuscript received by ASME Applied Mechanics Division, June, 1979; final revision, October, 1979.

Copyright © 1980 by ASME
Downloaded 01 May 2010 to 171.66.16.243. Redistribution subject to ASME license or copyright; see http://www.asme.org/terms/Terms_Use.cfm

The stress tensor employed in this analysis is the first Piola-Kirchhoff stress tensor $\mathcal{T}^R = T^R_{ab}\mathbf{e}_a\mathbf{e}_b$ since its use yields a simple form for the equations of equilibrium. This stress tensor refers the components of stress to a unit of initial area and is related to the true (Cauchy) stress tensor, $\mathcal{T} = T_{ab}\mathbf{e}_a\mathbf{e}_b$, by

$$T^R_{Aa} = \frac{\rho_0}{\rho} X_{A,b} T_{ba}, \tag{2}$$

where ρ_0 is the density of the material in the initial configuration and ρ is the density in the current configuration. Note that T^R_{Aa} is nonsymmetric.

In the absence of body forces the rate form of the equations of equilibrium for the first Piola-Kirchhoff stress tensor is

$$\dot{T}^R_{Aa,A} = 0. \tag{3}$$

$\dot{T}^R_{Aa}$ denotes the time rate of change of the first Piola-Kirchhoff stress referred to and measured per unit area of the reference configuration. When the current configuration is used as the reference one, we denote this stress rate by $\dot{\tau}^R_{ab}$ and note that it is given by

$$\dot{\tau}^R_{ab} = \frac{\mathcal{D}\tau_{ab}}{\mathcal{D}t} - D_{ac}T_{cb} - D_{bc}T_{ca} + v_{b,c}T_{ca}, \tag{4}$$

where $\mathcal{D}\tau_{ab}/\mathcal{D}t$ denotes the Jaumann rate of the Kirchhoff stress; the Jaumann rates of the Kirchhoff stress referred to the current configuration (τ_{ab}) and Cauchy stress (T_{ab}) are related by

$$\frac{\mathcal{D}\tau_{ab}}{\mathcal{D}t} = \frac{\mathcal{D}T_{ab}}{\mathcal{D}t} + v_{c,c}T_{ab}, \tag{5}$$

where

$$\tau_{ab} = \frac{\rho_0}{\rho} T_{ab} = T_{ab}.$$

The Jaumann rate is referred to a coordinate system which rotates with the material (but does not deform) and hence leads to an objective stress rate.

Since the present problem is concerned only with the onset of buckling which does not involve unloading, the rate problem may be formulated in a manner similar to linear elasticity with prestressing, i.e., the components of the Jaumann rate of the Kirchhoff stress are linearly related to the components of the deformation rate tensor,

$$\frac{\mathcal{D}\tau_{ab}}{\mathcal{D}t} = C_{abce}D_{ce}. \tag{6}$$

The coefficients C_{abce} are determined by the properties of the material being considered, and are as follows.

1 Hypoelastic Solid:

$$\frac{\mathcal{D}\tau_{ab}}{\mathcal{D}t} = (2\mu\delta_{ac}\delta_{be} + \lambda\delta_{ab}\delta_{ce})D_{ce}, \tag{7}$$

where λ and μ are the Lamé constants. For the special case of an incompressible solid (Poisson's ratio, $\nu = 0.5$), the constitutive relation must be modified to include the rate of change of the hydrostatic pressure, $\dot{\mathcal{P}}$. In this case,

$$\frac{\mathcal{D}\tau_{ab}}{\mathcal{D}t} = 2\mu D_{ab} + \dot{\mathcal{P}}\delta_{ab}. \tag{8}$$

Since the pressure rate $\dot{\mathcal{P}}$ is usually unknown, the equations of equilibrium are supplemented with the additional requirement that the condition of incompressibility be satisfied, i.e., $D_{aa} = 0$.

2 Elastoplastic Solid:

$$\frac{\mathcal{D}\tau_{ab}}{\mathcal{D}t} = \left[2\mu\delta_{ac}\delta_{be} + \lambda\delta_{ab}\delta_{ce} - A6\mu^2\frac{T'_{ab}T'_{ce}}{\overline{T}^2}\left(\frac{2}{3}h + 2\mu\right)^{-1}\right]D_{ce}, \tag{9}$$

where

$$A = \begin{cases} 0, & \text{for} \quad T'_{ab}D_{ab} < 0 \\ 1, & \text{for} \quad T'_{ab}D_{ab} \geq 0, \end{cases}$$

$T'_{ab} = T_{ab} - (1/3)\,T_{cc}\delta_{ab}$ is the deviatoric part of the Cauchy stress, $\overline{T}^2 = (3/2)\,T'_{ab}T'_{ab}$ is the effective stress, $h = (1/E_t - 1/E)^{-1}$, E is the initial Young's modulus, and E_t is the instantaneous tangent modulus. For the purpose of calculation it is assumed that the one-dimensional relation between true stress σ and the logarithmic strain ϵ behaves according to the power law

$$\epsilon = \begin{cases} \dfrac{\sigma}{E}, & \text{for} \quad \sigma \leq \sigma_y \\ \dfrac{\sigma}{E}\left(\dfrac{\sigma}{\sigma_y}\right)^{1/n-1}, & \text{for} \quad \sigma \geq \sigma_y, \end{cases}$$

where σ_y is the yield stress and $0 \leq n \leq 1$. Hence the tangent modulus is $E_t = En(\sigma/\sigma_y)^{1-1/n}$. This constitutive relation is based on the Prandtl-Reuss approximation for plasticity. Various aspects of this and related approximations are discussed by McMeeking and Rice [10].

Incompressibility is again accounted for by modifying the constitutive relation to include the pressure rate. Thus, for an incompressible elastoplastic material,

$$\frac{\mathcal{D}\tau_{ab}}{\mathcal{D}t} = \left[2\mu\delta_{ac}\delta_{be} - A6\mu^2\frac{T'_{ab}T'_{ce}}{\overline{T}^2}\left(\frac{2}{3}h + 2\mu\right)^{-1}\right]D_{ce} + \dot{\mathcal{P}}\delta_{ab}. \tag{10}$$

3 Total Deformation Plastic Solid:

$$\frac{\mathcal{D}\tau_{ab}}{\mathcal{D}t} = \left[\frac{2h}{n}\delta_{ac}\delta_{be} - \frac{3h}{n}(1-n)\frac{T'_{ab}T'_{ce}}{\overline{T}^2}\right]D_{ce} + \dot{\mathcal{P}}\delta_{ab}. \tag{11}$$

This constitutive relation, which is derived by Stören and Rice [11], also assumes that the material work hardens according to the power law

$$\bar{\tau} = \tau_0\left(\frac{\bar{\gamma}}{\gamma_0}\right)^n.$$

The instantaneous tangent modulus h is given by

$$h = n\mu\left(\frac{\bar{\tau}}{\tau_0}\right)^{1-1/n},$$

where μ is the shear modulus and τ_0 is a reference stress.

It has been suggested by some authors (e.g., Budiansky [12], Sewell [13], and Stören and Rice [11]) that the total deformation plasticity accounts for a pointed vertex on the yield surface. The possibility of a pointed vertex relaxes the normality condition so that a wider range of loading paths are permitted which will not violate Drucker's postulate. The total deformation plasticity is included here since investigators such as Budiansky [12] and Sewell [13] report that it provides better results than classical plasticity for problems of plastic instability.

For plane strain let $x_1 = x$, $x_2 = y$, and $v_1 = u(x, y)$, $v_2 = v(x, y)$, and $v_3 = 0$. Regardless of the type of material considered the velocity is assumed to be of the form

$$u(x, y) = Ae^{i\beta x + \gamma y}, \quad v(x, y) = Be^{i\beta x + \gamma y}. \tag{12}$$

When incompressibility is considered the pressure rate is assumed to be

$$\dot{\mathcal{P}}(x, y) = Ce^{i\beta x + \gamma y}. \tag{13}$$

The wave number β is positive and real.

The substitution of these field quantities into the equations of equilibrium and the condition of incompressibility when necessary, yields a linear system of homogeneous equations in A, B, and C. A nontrivial solution requires that the determinant of the coefficient matrix vanishes. This requirement yields a fourth-degree polynomial in γ. The four roots are of the form, $\gamma_{1,3} = \pm\beta Z_1$ and $\gamma_{2,4} = \pm\beta Z_2$. For an elastic material Z_1 and Z_2 are real numbers and when plasticity is considered, Z_1 and Z_2 will in general be complex.

Once the γ's are determined, the velocity field and pressure rate can be written as the sum of four terms

Downloaded 01 May 2010 to 171.66.16.243. Redistribution subject to ASME license or copyright; see http://www.asme.org/terms/Terms_Use.cfm

$$u(x,y) = (A_1e^{\gamma_1 y} + A_2e^{\gamma_2 y} + A_3e^{\gamma_3 y} + A_4e^{\gamma_4 y})e^{i\beta x},$$
$$v(x,y) = (B_1e^{\gamma_1 y} + B_2e^{\gamma_2 y} + B_3e^{\gamma_3 y} + B_4e^{\gamma_4 y})e^{i\beta x},$$
$$\dot{\mathcal{P}}(x,y) = (C_1e^{\gamma_1 y} + C_2e^{\gamma_2 y} + C_3e^{\gamma_3 y} + C_4e^{\gamma_4 y})e^{i\beta x}. \quad (14)$$

Returning to the equations of equilibrium and the condition of incompressibility all but one coefficient may be eliminated for each γ. All field quantities can now be written in terms of four unknown coefficients.

Normalize all material properties and the initial stress with respect to a reference shear modulus μ_L. Define $\alpha = P/\mu_L$, $\rho = \mu/\mu_L$ and

$$\kappa = \lambda/\mu_L = \frac{2\mu\nu}{\mu_L(1-2\nu)} = \frac{2\rho\nu}{1-2\nu}.$$

Thus the velocity field and pressure rate for each material considered become functions of the dimensionless parameters α, ρ, ν, and are as follows.

1 Compressible Hypoelastic Solid $(0 < \nu < 0.5)$:

$$u(x,y) = (A_1e^{\beta y} + A_2e^{f(\alpha)\beta y} + A_3e^{-\beta y} + A_4e^{-f(\alpha)\beta y})e^{i\beta x},$$
$$v(x,y) = i\left[-A_1e^{\beta y} - \left(\frac{2\rho+\alpha}{2\rho-\alpha}\right)f(\alpha)A_2e^{f(\alpha)\beta y} + A_3e^{-\beta y} + \left(\frac{2\rho+\alpha}{2\rho-\alpha}\right)f(\alpha)A_4e^{-f(\alpha)\beta y}\right]e^{i\beta x}, \quad (15)$$

where

$$f(\alpha) = \sqrt{\frac{(2\rho-\alpha)(\kappa+2\rho+\alpha)}{(2\rho+\alpha)(\kappa+2\rho)}}.$$

2 Incompressible Hypoelastic Solid $(\nu = 0.5)$:

$$u(x,y) = (A_1e^{\beta y} + A_2e^{g(\alpha)\beta y} + A_3e^{-\beta y} + A_4e^{-g(\alpha)\beta y})e^{i\beta x},$$
$$v(x,y) = i(-A_1e^{\beta y} - \frac{1}{g(\alpha)}A_2e^{g(\alpha)\beta y} + A_3e^{-\beta y} + \frac{1}{g(\alpha)}A_4e^{-g(\alpha)\beta y})e^{i\beta x},$$
$$\dot{\mathcal{P}}(x,y) = -\mu_L i\beta\alpha(A_2e^{g(\alpha)\beta y} + A_4e^{-g(\alpha)\beta y})e^{i\beta x}, \quad (16)$$

where

$$g(\alpha) = \sqrt{\frac{2\rho-\alpha}{2\rho+\alpha}}.$$

3 Compressible Elastoplastic Solid $(0 < \nu < 0.5)$:

$$u(x,y) = (A_1e^{F_1\beta y} + A_2e^{F_2\beta y} + A_3e^{-F_1\beta y} + A_4e^{-F_2\beta y})e^{i\beta x},$$
$$v(x,y) = i(-K_1A_1e^{F_1\beta y} - K_2A_2e^{F_2\beta y} + K_1A_3e^{-F_1\beta y} + K_2A_4e^{-F_2\beta y})e^{i\beta x}, \quad (17)$$

where

$$F_1 = \sqrt{\frac{-C_2+\sqrt{C_2^2-4C_1C_3}}{2C_1}}, \quad F_2 = \sqrt{\frac{-C_2-\sqrt{C_2^2-4C_1C_3}}{2C_1}},$$
$$C_1 = (2\rho+\alpha)(\kappa+2\rho-t\rho\mu m), \quad C_2 = (\alpha^2 - 2\rho\alpha - 4\rho\kappa - 8\rho^2) + 2[(\kappa+2\rho)(r+t) + (t-s)\alpha - 2(\kappa+\rho)s] \times \rho\mu m - 2(s^2-rt)\rho^2\mu^2m^2,$$
$$C_3 = (2\rho-\alpha)(\kappa+2\rho-r\rho\mu m+\alpha), \quad m = A\left(\frac{2}{3}h+2\mu\right)^{-1},$$
$$r = \frac{2}{3}\left(\frac{\nu^2-4\nu+4}{\nu^2-\nu+1}\right), \quad s = \frac{2}{3}\left(\frac{\nu^2-\nu-2}{\nu^2-\nu+1}\right), \quad t = \frac{2}{3}\left(\frac{\nu^2+2\nu+1}{\nu^2-\nu+1}\right),$$
$$K_1 = \frac{(2\kappa+2\rho-2s\rho\mu m+\alpha)F_1}{2(\kappa+2\rho-t\rho\mu m)F_1^2-(2\rho-\alpha)},$$
$$K_2 = \frac{(2\kappa+2\rho-2s\rho\mu m+\alpha)F_2}{2(\kappa+2\rho-t\rho\mu m)F_2^2-(2\rho-\alpha)}.$$

4 Incompressible Elastoplastic Solid $(\nu = 0.5)$:

$$u(x,y) = (A_1e^{G_1\beta y} + A_2e^{G_2\beta y} + A_3e^{-G_1\beta y} + A_4e^{-G_2\beta y})e^{i\beta x}, \quad (18)$$
$$v(x,y) = i\left(-\frac{1}{G_1}A_1e^{G_1\beta y} - \frac{1}{G_2}A_2e^{G_2\beta y} + \frac{1}{G_1}A_3e^{-G_1\beta y} + \frac{1}{G_2}A_4e^{-G_2\beta y}\right)e^{i\beta x},$$
$$\dot{\mathcal{P}}(x,y) = \frac{i\beta\mu_L}{2}(L_1A_1e^{G_1\beta y} + L_2A_2e^{G_2\beta y} + L_1A_3e^{-G_1\beta y} + L_2A_4e^{-G_2\beta y})e^{i\beta x}, \quad (18)\ (Cont.)$$

where

$$G_1 = \sqrt{\frac{4(\rho-4\rho\mu m)+\sqrt{16(\rho-4\rho\mu m)^2-4(2\rho+\alpha)(2\rho-\alpha)}}{2(2\rho+\alpha)}},$$
$$G_2 = \sqrt{\frac{4(\rho-4\rho\mu m)-\sqrt{16(\rho-4\rho\mu m)^2-4(2\rho+\alpha)(2\rho-\alpha)}}{2(2\rho+\alpha)}},$$
$$L_1 = \left[2\rho-\alpha-8\rho\mu m-\frac{(2\rho-\alpha)}{G_1^2}\right],$$
$$L_2 = \left[2\rho-\alpha-8\rho\mu m-\frac{(2\rho-\alpha)}{G_2^2}\right].$$

5 Total Deformation Plastic Solid:

$$u(x,y) = (A_1e^{G_3\beta y} + A_2e^{G_4\beta y} + A_3e^{-G_3\beta y} + A_4e^{-G_4\beta y})e^{i\beta x},$$
$$v(x,y) = i\left(-\frac{1}{G_3}A_1e^{G_3\beta y} - \frac{1}{G_4}A_2e^{G_4\beta y} + \frac{1}{G_3}A_3e^{-G_3\beta y} + \frac{1}{G_4}A_4e^{-G_4\beta y}\right)e^{i\beta x},$$
$$\mathcal{P}(x,y) = \frac{\mu_L i\beta}{2}(L_3A_1e^{G_3\beta y} + L_4A_2e^{G_4\beta y} + L_3A_3e^{-G_3\beta y} + L_4A_4e^{-G_4\beta y})e^{i\beta x}, \quad (19)$$

where

$$G_3 = \sqrt{\frac{4\bar{h}(2n-1)+\sqrt{16\bar{h}^2(2n-1)^2-4(4\bar{h}^2-n^2\alpha^2)}}{2(2\bar{h}+\alpha)}},$$
$$G_4 = \sqrt{\frac{4\bar{h}(2n-1)-\sqrt{16\bar{h}^2(2n-1)^2-4(4\bar{h}^2-n^2\alpha^2)}}{2(2\bar{h}+\alpha)}},$$
$$L_3 = \left[4\bar{h}-\alpha-\frac{2\bar{h}}{n}-\frac{1}{G_3^2}\left(\frac{2\bar{h}}{n}-\alpha\right)\right],$$
$$L_4 = \left[4\bar{h}-\alpha-\frac{2\bar{h}}{n}-\frac{1}{G_4^2}\left(\frac{2\bar{h}}{n}-\alpha\right)\right],$$
$$\bar{h} = \frac{h}{\mu_L} = n\rho\left(\frac{\bar{\tau}}{\tau_0}\right)^{1-1/n}$$

The stress rates for each material are obtained by the appropriate differentiation of the velocity field.

Consider the velocity fields and pressure rates of the plastic constitutive relations when the plasticity effects are eliminated. For the compressible elastoplastic solid it is easily shown that when $m = 0$

$$F_1 = 1, \quad F_2 = \sqrt{\frac{(2\rho-\alpha)(\kappa+2\rho+\alpha)}{(2\rho+\alpha)(\kappa+2\rho)}} = f(\alpha),$$
$$K_1 = 1, \quad K_2 = \frac{(2\rho+\alpha)}{(2\rho-\alpha)}\sqrt{\frac{(2\rho-\alpha)(\kappa+2\rho+\alpha)}{(2\rho+\alpha)(\kappa+2\rho)}} = \frac{(2\rho+\alpha)}{(2\rho-\alpha)}f(\alpha).$$

For the incompressible elastoplastic solid when $m = 0$, we have

$$G_1 = 1, \quad G_2 = \sqrt{\frac{2\rho-\alpha}{2\rho+\alpha}} = g(\alpha),$$
$$L_1 = 0, \quad L_2 = -2\alpha.$$

For the total deformation plastic solid when $n = 1$, we have

$$\bar{h} = \rho, \quad G_3 = 1, \quad G_4 = \sqrt{\frac{2\rho-\alpha}{2\rho+\alpha}} = g(\alpha),$$
$$L_3 = 0, \quad L_4 = -2\alpha.$$

Downloaded 01 May 2010 to 171.66.16.243. Redistribution subject to ASME license or copyright; see http://www.asme.org/terms/Terms_Use.cfm

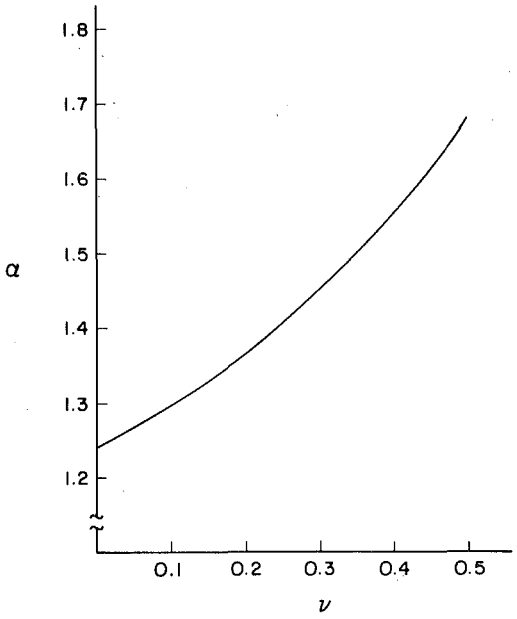

Fig. 2 Buckling load of the hypoelastic half space as a function of Poisson's ratio, ν

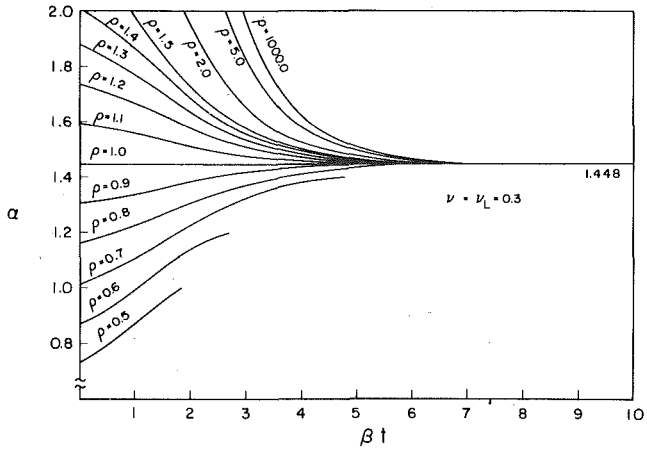

Fig. 3 Buckling loads of the hypoelastic layer and half space for indicated values of $\rho = \mu/\mu_L$ and $\nu = \nu_L = 0.3$

When these substitutions are made it is clear that the field quantities of the plastic solids become equivalent to the field quantities of the hypoelastic solids.

Now that the field quantities have been obtained for each material considered, problems of the horizontal compression of the layer and half space can be solved for any combinations of materials. Since all material properties have been normalized with respect to μ_L, the shear modulus of the layer, $\rho = 1$ for the layer material. The deformation of the half space is required to vanish for large values of $y > 0$. This is obtained by setting the coefficients A_1 and A_2 equal to zero. Hence all field quantities of the half-space decay exponentially from the surface for $y > 0$. There are now six unknown coefficients, four of which describe the field quantities of the layer and two are for the half space.

The unknown coefficients are determined by requiring continuity of velocities and stress rates at the common surface of the layer and half space, and satisfying stress-free boundary conditions on the free surface of the layer. If the subscript L denotes the field quantities associated with the layer, then the six conditions are

$$1 \quad u(x, 0) = u_L(x, 0) \qquad 2 \quad v(x, 0) = v_L(x, 0)$$

$$3 \quad \dot{\tau}^R_{22}(x, 0) = \dot{\tau}^R_{22_L}(x, 0) \qquad 4 \quad \dot{\tau}^R_{21}(x, 0) = \dot{\tau}^R_{21_L}(x, 0)$$

$$5 \quad \dot{\tau}^R_{22_L}(x, -t) = 0 \qquad 6 \quad \dot{\tau}^R_{21_L}(x, -t) = 0.$$

Note that due to the nonsymmetry of $\dot{\tau}^R_{ab}$, $\dot{\tau}^R_{21}$, and not $\dot{\tau}^R_{12}$ must be used for Conditions 4 and 6.

Application of the continuity and boundary conditions yields a linear system of homogeneous equations for the six unknown coefficients. The critical value of α which produces instability is the value of α which causes the determinant of the unknown coefficients to vanish.

Results

Before presenting the results for the surface buckling of the layer on the half space it is useful to consider first the buckling of the elastic half space. The buckling load for the half space is easily calculated by requiring that the stress rates vanish at the free surface. The buckling loads are found to be independent of the wave number β, and are presented in Table 1 for various values of Poisson's ratio. Table 1 will be referred to later when discussing limiting cases of βt, the dimensionless wave number. The buckling load for the half space is

Table 1

ν	$\alpha = P/\mu$
0.1	1.2954
0.2	1.3651
0.3	1.4483
0.4	1.5497
0.5	1.6772

seen to be a function of the Poisson ratio and is illustrated in Fig. 2. This figure differs from the result obtained by Brunelle [8] which shows the buckling load to be a concave downward function of the Poisson ratio.

The first problem considered is the compression of the elastic layer on the elastic half space. The buckling loads are calculated as a function of βt for various material properties. Fig. 3 shows the resulting buckling loads when ρ is varied and the Poisson ratios of the layer and half space are fixed at $\nu = \nu_L = 0.3$. The results shown in Fig. 3 are best interpreted by considering different ranges for the value of ρ.

First consider the results when $\rho < 1$. This case corresponds to a stiff layer on a soft half space. One immediately observes that for $\rho < 1$ the buckling curves are increasing functions of βt. This agrees qualitatively with the theory of plate buckling since for constant t, higher loads are required for the layer to deform into smaller wavelengths. One also observes that for certain values of $\rho < 1$ some curves approach the limiting value $\alpha = 1.4483$ for large βt and other curves only extend over a finite range of βt. Since one of the two terms describing all field quantities of the half space is proportional to

$$\exp\left(-\beta\sqrt{\frac{(2\rho - \alpha)(\kappa + 2\rho + \alpha)}{(2\rho + \alpha)(\kappa + 2\rho)}}\, y\right),$$

it is obvious that we must require $\alpha < 2\rho$ for exponential decay of the field quantities. In particular for Fig. 3 when $2\rho < 1.4483$ all curves will be cut off at $\alpha = 2\rho$. A physical interpretation can be made for the result by fixing β and allowing t to increase from zero. As the thickness increases the layer becomes more rigid and higher loads are required to deform the surface. Once a critical thickness is reached buckling will not occur. Here βt plays a similar role to the slenderness ratio in the Euler buckling theory and incorporates the effect of geometry on the buckling load. As ρ decreases, the layer becomes more rigid with respect to the half space, and the range of βt over which the buckling curves exist will vanish to the point $\beta t = 0$. This point corresponds to a layer of zero thickness and represents the buckling load of the half space alone.

Next consider $\rho > 1$. This case represents a soft layer on a stiff half space. Here the buckling curves are decreasing functions of βt, so that

Downloaded 01 May 2010 to 171.66.16.243. Redistribution subject to ASME license or copyright; see http://www.asme.org/terms/Terms_Use.cfm

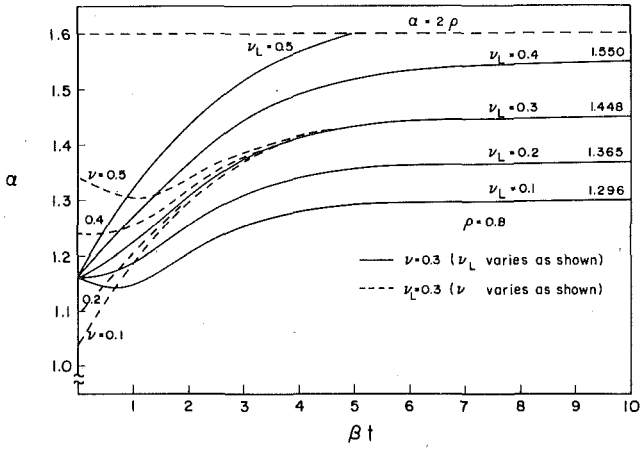

Fig. 4 Buckling loads of the hypoelastic layer and half space for indicated values of Poisson's ratio and $\rho = 0.8$

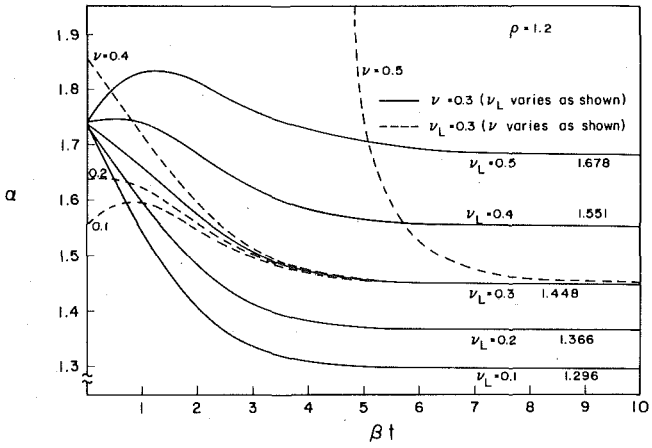

Fig. 5 Buckling loads of the hypoelastic layer and half space for indicated values of Poisson's ratio and $\rho = 1.2$

if t is constant, large loads are required to deform the surface into large wavelengths. This observation becomes physically reasonable when one considers the deformation of the half space. For the elastic half space, whose field quantities decay exponentially, the strain energy resulting from the surface wave exists only to a depth of approximately two times the wavelength of the disturbance. Thus, for the layer to deform into large wavelengths, more energy must be supplied to the half space and hence a higher buckling load is required.

Again it is observed that some of the curves do not exist over the entire range $0 \leq \beta t < \infty$. For large ρ, the half space is rigid with respect to the layer and buckling curves do not exist for small βt. If the boundary conditions of the layer are changed so that the stress rates vanish at the free surface and velocities vanish at the common surface of the layer and half space, then this modified problem becomes an elastic layer on a rigid half space. Physically, β represents the rate of decay of the velocities from the free surface to the fixed surface of the layer. For a given t, small β will not be sufficient to maintain nonzero velocities on one surface of the layer and zero velocities on the other. The buckling curves obtained for this modified problem are the same curves as obtained for the regular problem for large ρ. Furthermore it is found that for large ρ all buckling curves are identical. This independence is apparent by observing that the coefficient matrix of the modified problem does not depend on ρ. For the purpose of calculation the value $\rho = 1000.0$ is used to represent the buckling curve for large ρ.

Finally, consider the case when $\rho \approx 1.0$. Here the stiffness of the half space and layer are well matched and buckling curves exist for all values of βt. Only the relative stiffness between the layer and half space determines whether the curves approach the limiting value $\alpha = 1.4483$ from above or from below. For the special case $\rho = 1.0$ the layer becomes an extension of the half space and the buckling load $\alpha = 1.4483$ is independent of βt.

Next buckling curves are obtained by fixing ρ and varying the Poisson ratios of the two materials. Figs. 4 and 5 are the buckling curves when ρ is fixed at $\rho = 0.8$ and $\rho = 1.2$, respectively. In each figure the solid curves are obtained by fixing the Poisson ratio of the half space at $\nu = 0.3$ and varying ν_L. All solid curves originate from the same point at $\beta t = 0$. The point $\beta t = 0$ corresponds to the buckling load of a half space with material properties μ and $\nu = 0.3$, since for $t = 0$, $\beta t = 0$ for *any* finite value of β. Since the buckling load $\alpha = P/\mu_L$ is normalized with respect to the shear modulus of the layer, α must be adjusted by the factor ρ to obtain the proper buckling load for the half space, i.e., $P/\mu = \alpha/\rho$. In particular for Fig. 4, $P/\mu = 1.1586/0.8 = 1.4483$ and for Fig. 5, $P/\mu = 1.7379/1.2 = 1.4483$. This value agrees with Table 1 for $\nu = 0.3$.

All solid curves approach discrete values of α for large βt. As $t \to \infty$, $\beta t \to \infty$ for *any* nonzero value of β and the layer becomes a half space whose buckling load is independent of β. Thus the limiting values of α for the solid curves in Figs. 4 and 5 represent the buckling loads of the elastic half space with material properties μ_L and ν_L. Again these values are in agreement with the buckling loads found in Table 1.

The dashed curves in Figs. 4 and 5 are obtained by fixing $\nu_L = 0.3$ and varying ν. Here the curves originate from discrete values of α at $\beta t = 0$ and converge to $\alpha = 1.4483$ as $\beta t \to \infty$. The same conclusions concerning the limiting values of βt can be made for the dashed curves as were made for the solid curves.

It is observed that local extrema occur (in Figs. 4 and 5) for small βt when the Poisson ratios of the layer and half space do not match. When a loaded body is constrained in one direction (e.g., plane strain), the pressure required to maintain the constraint is directly related to the Poisson ratio. The layer and half space act to constrain the vertical expansion of each other due to the applied horizontal stresses. When the Poisson ratios of the two bodies are almost equal then the pressure at the common surface due to lateral expansion cancels. Significant differences in the Poisson ratios of the bodies will not cancel the transmitted pressures. Thus a net pressure will be transmitted across the common surface which affects the buckling curves. When $\rho < 1$ and $\nu > \nu_L$ (see Fig. 4), local minimums occur for small βt. For this case the pressure due to vertical expansion will be transmitted from the half space to the layer which will reduce the buckling load of the layer. When $\rho > 1$ and $\nu_L > \nu$ (see Fig. 5), local maximums occur for small βt. Here the pressure is transmitted from the layer to the half space, and consequently higher buckling loads are required.

Buckling curves were also calculated for $\rho = 1000.0$ and various values of ν and ν_L. The results are presented in Fig. 6. When ν is held constant at $\nu = 0.3$ and ν_L is allowed to vary, different curves are obtained for each ν_L. Each curve approaches from above the buckling load of the elastic half space with Poisson's ratio ν_L. When ν_L is held constant at $\nu_L = 0.3$ and ν is varied all of the curves are identical. Thus it is seen that for large ρ buckling will only depend on the Poisson ratio of the layer.

Next the compression of the layer and the half space is considered when plasticity effects are included in the constitutive relation. Results are obtained for an elastoplastic material based on the classical flow theory of plasticity and for a plastic material based on total deformation plasticity. *Plasticity is only considered in the softer of the two materials.* Thus, for $\rho > 1$, we consider only problems of a plastic layer on the elastic half space and for $\rho < 1$ problems of an elastic layer on the plastic half space are considered. For materials which are purely elastic the Poisson ratio is fixed at 0.3. The Poisson ratio of the elastoplastic material is also fixed at 0.3. The total deformation plastic material is incompressible so that the Poisson ratio of that material is 0.5. The yield point of the elastoplastic material is arbitrarily set at 75 percent of the elastic buckling load of the half space with Pois-

Downloaded 01 May 2010 to 171.66.16.243. Redistribution subject to ASME license or copyright; see http://www.asme.org/terms/Terms_Use.cfm

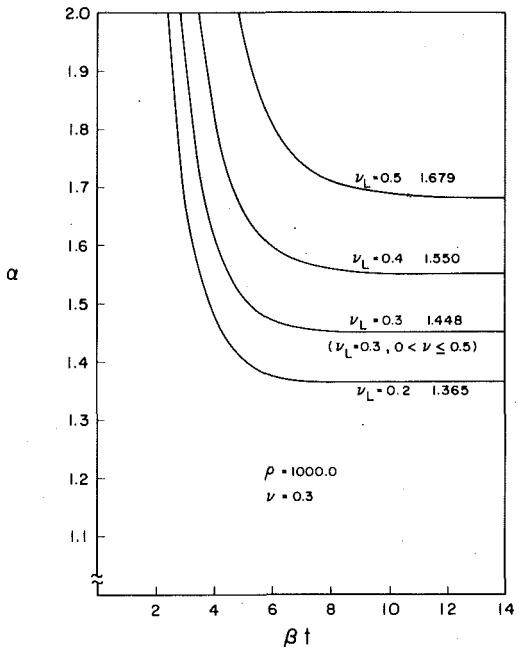

Fig. 6 Buckling loads of the hypoelastic layer and half space for indicated values of Poisson's ratio and $\rho = 1000.0$

son's ratio $\nu = 0.3$. Similarly the reference stress for the total deformation material is 75 percent of the elastic buckling load of the half space with Poisson's ratio $\nu = 0.5$.

As in the previous case of a purely elastic material, buckling curves are calculated as functions of the dimensionless wave number βt. The only difference is the introduction of the parameter n, which is the exponent of the power law describing the work hardening of the plastic material. The particular power law chosen requires $0 \leq n \leq 1$ where $n = 1$ corresponds to an elastic material and $n = 0$ corresponds to a perfectly plastic material.

As in the elastic case, it is useful to consider the buckling of the plastic half space alone. Table 2 presents the buckling loads for the elastoplastic half space for various values of n and Table 3 presents the buckling loads for the total deformation half space.

Fig. 7 presents the buckling curves when the elastoplastic material is considered and Fig. 8 presents the buckling curves when total deformation plasticity is considered. Regardless of the type of plasticity and the value of ρ, all buckling curves will shift downward as the plastic material softens.

As in the elastic case, the limiting values of βt represent the buckling loads of the corresponding half space alone. For $\rho < 1$, the point $\beta t = 0$ represents the buckling curve of a plastic half space with material properties ν and μ and work-hardening exponent n. If the buckling loads for $\beta t = 0$ are adjusted by ρ then these loads will agree with the values in Tables 2 and 3. All curves which exist for $0 \leq \beta t < \infty$ approach from below the buckling load of the elastic half space with material properties ν_L and μ_L. The curves which exist for a finite range of βt are limited by the requirement that the field quantities of the half space must decay exponentially from the surface. For $\rho > 1$ all curves originate at the adjusted buckling load of the elastic half space with material properties ν and μ and approach from above the buckling loads of the plastic half space with material properties ν_L and μ_L and the work-hardening exponent n_L. The buckling loads for $\beta t \to \infty$ also agree with the values in Tables 2 and 3.

The two plasticity theories can be compared by considering the buckling of a plastic half space. In order for the comparison to be valid both theories must be applied to the same material. This is accomplished by insuring that the elastic constants and the work hardening are the same for both constitutive relations. Since the total deformation material is incompressible, the elastoplastic material must be incompressible. Thus the Poisson ratio for each constitutive rela-

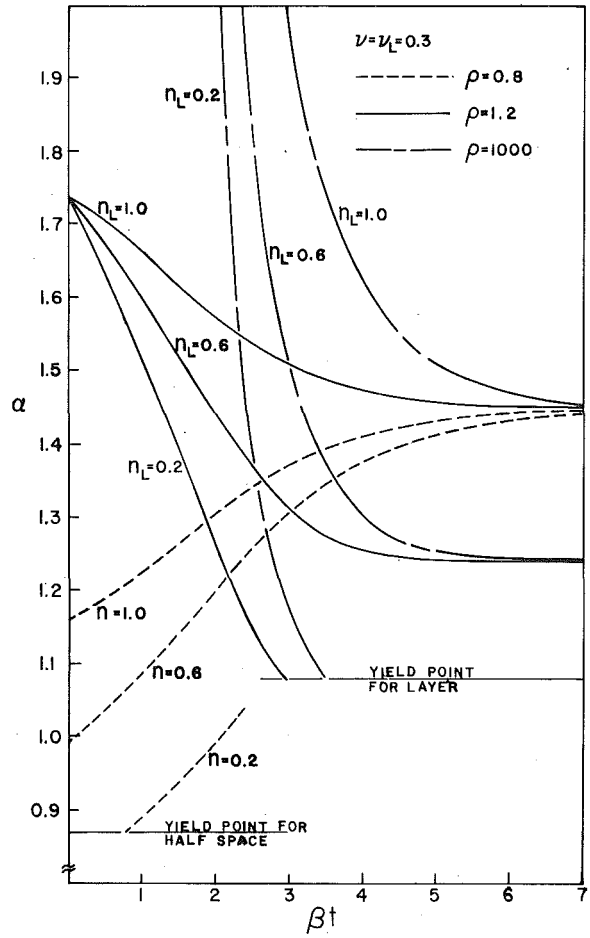

Fig. 7 Buckling loads of the layer on the half space for indicated values of the exponent of the work-hardening law, and $\nu = \nu_L = 0.3$; the softer of the two materials is elastoplastic and the stiffer material is hypoelastic

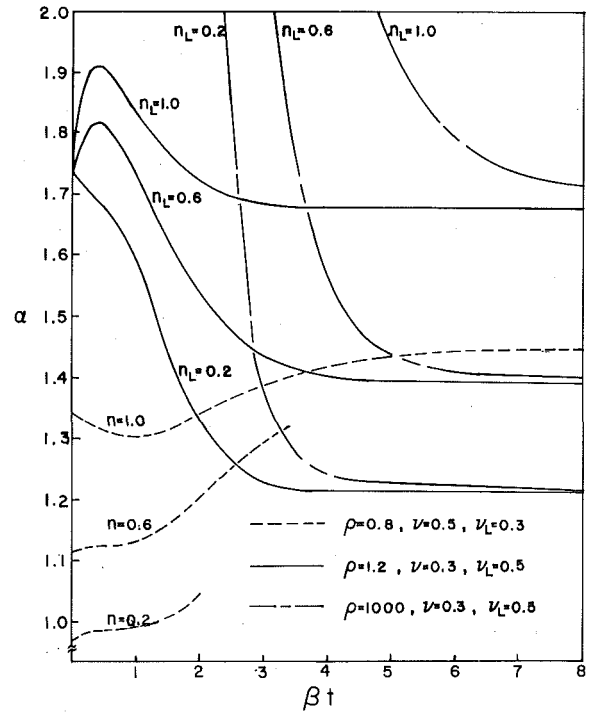

Fig. 8 Buckling loads of the layer on the half space for indicated values of the exponent of the work-hardening law; the softer of the two materials is total deformation plastic with $\nu = 0.5$ and the stiffer material is hypoelastic with $\nu = 0.3$

Downloaded 01 May 2010 to 171.66.16.243. Redistribution subject to ASME license or copyright; see http://www.asme.org/terms/Terms_Use.cfm

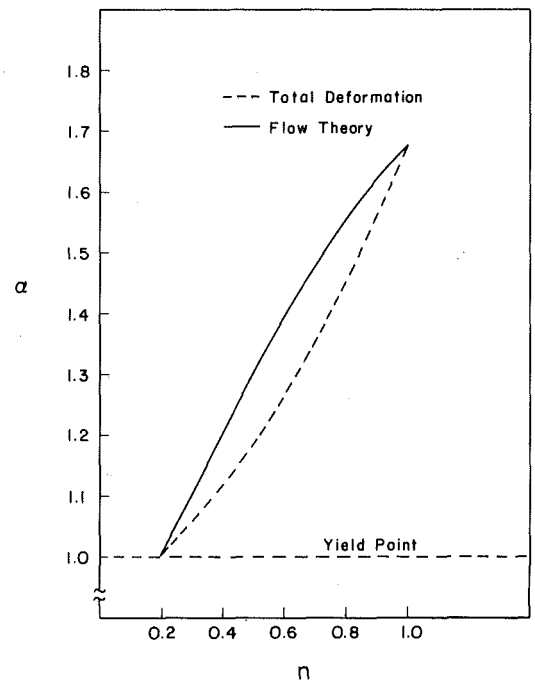

Fig. 9 Comparison of the buckling loads of half spaces with material properties corresponding to the total deformation plasticity and classical elastoplasticity

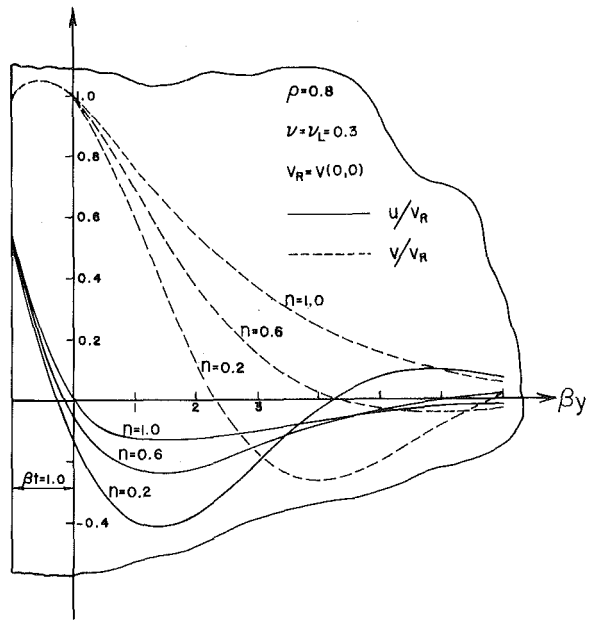

Fig. 10 Horizontal and vertical velocity distribution of the hypoelastic layer on the elastoplastic half space for indicated values of the exponent of the work-hardening law, $\rho = 0.8$, and $\nu = \nu_L = 0.3$

Table 2 Elastoplastic material, $\nu = 0.3$; yield point = 1.086

n	$\alpha = P/\mu$
1.0	1.4483
0.8	1.3519
0.6	1.2408
0.4	1.1190
0.2	— —

Table 3 Total deformation material, $\nu = 0.5$; reference stress = 1.2579

n	$\alpha = P/\mu$
1.0	1.6785
0.8	1.5238
0.6	1.3923
0.4	1.2837
0.2	1.2109

tion must be set at $\nu = 0.5$. The second elastic constant is fixed by performing a hypothetical uniaxial tension test and requiring that the elastic response for both theories be the same. If T_{11} denotes the applied stress and ϵ_{11} denotes the logarithmic strain along the direction of extension then the stress-strain relation for each constitutive relation is

$$T_{11} = 3\mu(1 - 2\mu m)\epsilon_{11} = E(1 - 2\mu m)\epsilon_{11}, \text{ for elastoplastic material;}$$

$$T_{11} = 3h\epsilon_{11} = 3n\mu\left(\frac{\bar{\sigma}}{\sigma_0}\right)^{1-1/n}\epsilon_{11}, \quad \text{for total deformation material.}$$

Clearly for a purely elastic deformation $m = 0$, and $n = 1$. For the elastic response of both constitutive relations to be the same we must require, $3\mu = E$. The same work hardening for both materials is insured by setting the yield point of the elastoplastic material equal to the reference stress of the total deformation solid. For convenience the reference stress is taken to be 1.

The buckling loads were calculated as a function of n for both types of plasticity and are shown in Fig. 9. As expected both theories predict the same buckling load for the elastic case ($n = 1.0$). Both curves also intersect the yield point at the same value of n. However the most significant observation is that the elastoplastic theory predicts higher buckling loads for a given n than the total deformation theory. This supports the results reported by the previously mentioned investigators concerning plastic stability.

Once the buckling load has been found for a particular βt, the field quantities can be calculated. Figs. 10–12 illustrate the field quantities for $\rho = 0.8$ when $\beta t = 1.0$, and Figs. 13–15 show the field quantities for $\rho = 1.2$ when $\beta t = 2.0$. All velocities have been normalized with respect to the reference velocity $v_R = v(0, 0)$, and all stress rates are normalized with respect to the reference stress rate $\dot{\tau}_R = \dot{\tau}^R_{11}(0, 0)$. The distribution of all field quantities are similar in shape to the corresponding field quantities resulting from a Rayleigh surface wave in the elastic half space. The only difference in shape occurs at the interface of the layer and half space. In particular the stress rate $\dot{\tau}^R_{11}$ (Figs. 11 and 14) is discontinuous at the interface, and while all other field quantities are continuous at the interface in accordance with the prescribed continuity conditions, discontinuities in the slopes may develop. Figs. 10, 13, and 15 illustrate field quantities with slope discontinuities at the interface.

The amount of work hardening present in the layer only affects the relative magnitude of the field quantities and not the shape of the distributions. However when plasticity is present in the half space, the distribution of the field quantities change from a pure exponential decay to an oscillating decay as the work hardening decreases.

Conclusion

The surface buckling of the layer on the half space is dependent on the geometry of the deformation and the properties of the two materials. The geometric-dependence is described by the dimensionless wavenumber βt which is a measure of the rate of decay of the field quantities from the common surface of the layer and half space. Material-dependence is described by the Poisson ratios of the two materials and by $\rho = \mu/\mu_L$ which is a measure of the relative stiffness of the two materials.

When $\rho \simeq 1$ the materials are compatible and buckling loads will

Downloaded 01 May 2010 to 171.66.16.243. Redistribution subject to ASME license or copyright; see http://www.asme.org/terms/Terms_Use.cfm

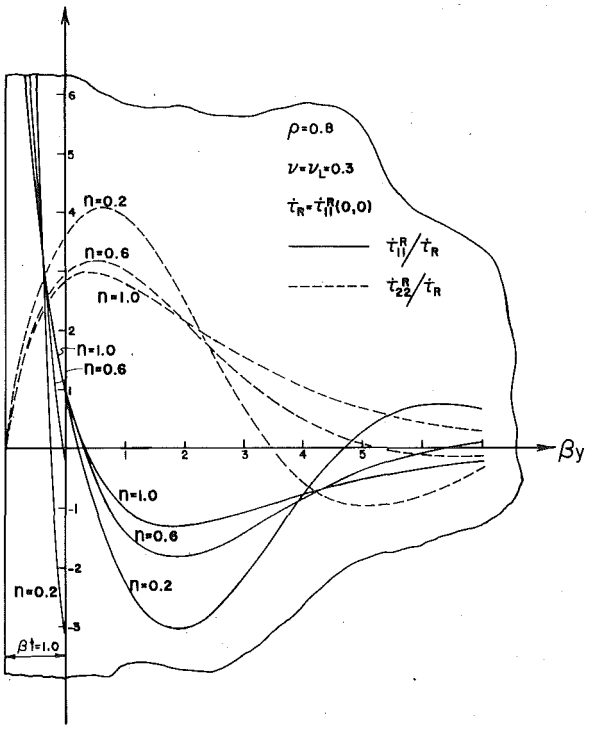

Fig. 11 $\dot{\tau}_{11}^R$ and $\dot{\tau}_{22}^R$ of the hypoelastic layer on the elastoplastic half space for indicated values of the exponent of the work-hardening law, $\rho = 0.8$, and $\nu = \nu_L = 0.3$

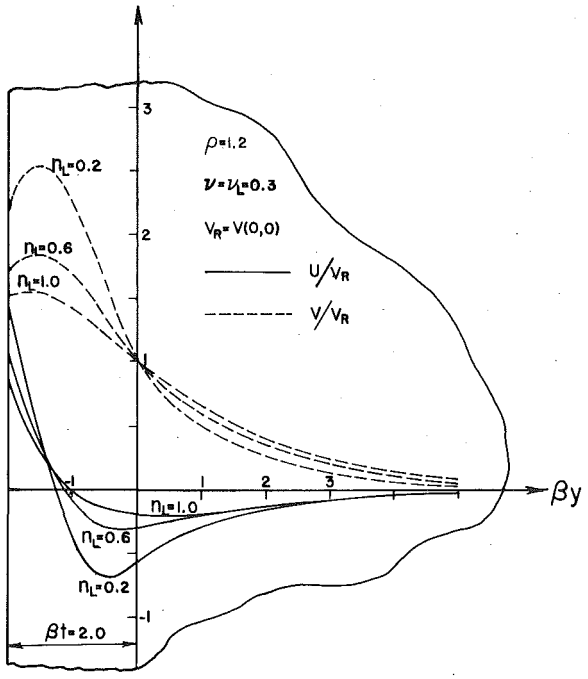

Fig. 13 Horizontal and vertical velocity distributions of the elastoplastic layer on the hypoelastic half space for indicated values of the exponent of the work-hardening law, $\rho = 1.2$, and $\nu = \nu_L = 0.3$

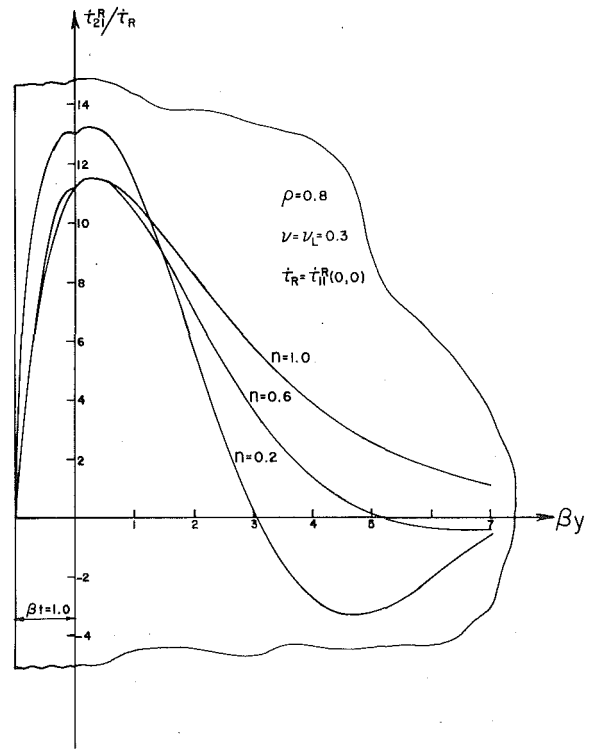

Fig. 12 $\dot{\tau}_{21}^R$ of the hypoelastic layer on the elastoplastic half space for indicated values of the exponent of the work-hardening law, $\rho = 0.8$, and $\nu = \nu_L = 0.3$

exist for all values of βt. The limiting values of βt represent the buckling loads of two half-spaces with the material properties of the two materials. The point $\beta t = 0$ represents the buckling load of the half space alone. As $\beta t \to \infty$ the buckling curves approach the buckling load of a half space with the material properties of the layer.

In general all curves will be monotonic from the buckling load at $\beta t = 0$ to the load at $\beta t \to \infty$ if the Poisson ratio of the two materials match. The relative stiffness ρ determines whether the curves will be monotically increasing or decreasing. If the buckling load is normalized with respect to μ_L, then the buckling curves are monotonically increasing functions of βt when $\rho < 1$, and the curves are monotonically decreasing functions when $\rho > 1$.

If the value of ρ is significantly different from 1.0, the stiffer material will limit the range of βt over which buckling exists. For $\rho < 1$ the stiffness of the layer prevents the existence of buckling for large βt, and for $\rho > 1$ the stiffness of the half space precludes buckling for small βt.

The Poisson ratios of the materials affect the stability of the body by shifting the buckling curves. As the Poisson ratio of either material increases, the buckling curves will shift upward. Local extrema can also develop for small βt if there is a significant difference in the Poisson ratios of the two materials. When $\rho < 1.0$ and $\nu > \nu_L$ local minimums occur for small βt, and when $\rho > 1.0$ and $\nu_L > \nu$ local maximums occur for small βt.

When plasticity is introduced into one of the materials, the buckling curves will shift downward. The downward shift is dependent on the amount of work hardening in the plastic material. As expected smaller work hardening produces lower buckling curves. The amount of work hardening only produces significant changes in the magnitudes of the field quantities, but the general shape of the distributions is unaffected.

Two different constitutive relations are utilized when plasticity is included in one of the materials. The constitutive relations considered are based on the Prandtl-Reuss plasticity and the total deformation plasticity. A comparison of the two theories is made by considering the surface buckling of the plastic half space. The buckling loads predicted by the total deformation theory are lower than the buckling loads of the classical plasticity for a given amount of work hardening.

Downloaded 01 May 2010 to 171.66.16.243. Redistribution subject to ASME license or copyright; see http://www.asme.org/terms/Terms_Use.cfm

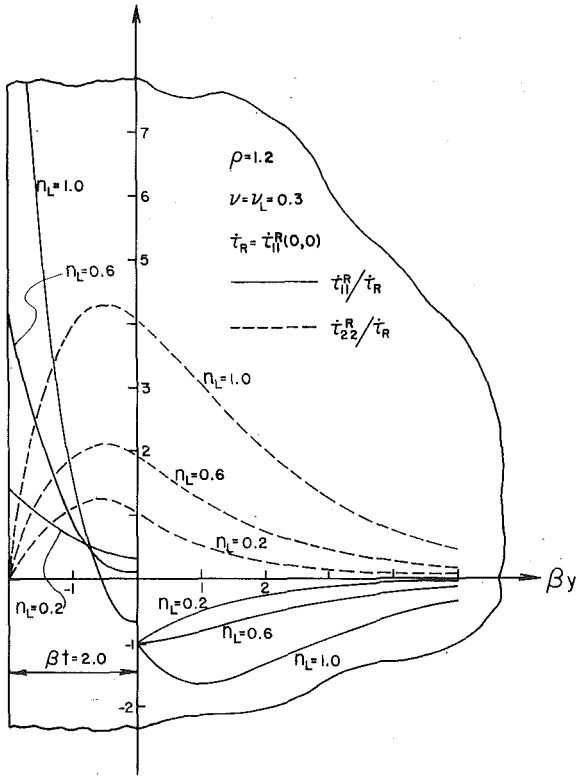

Fig. 14 $\dot{\tau}_{11}^R$ and $\dot{\tau}_{22}^R$ of the elastoplastic layer on the hypoelastic half space for indicated values of the exponents of the work-hardening law, $\rho = 1.2$, and $\nu = \nu_L = 0.3$

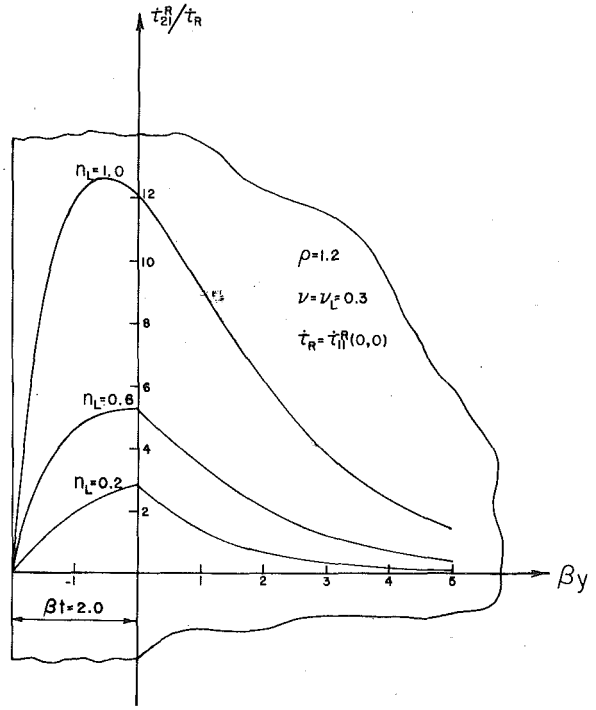

Fig. 15 $\dot{\tau}_{21}^R$ of the elastoplastic layer on the hypoelastic half space for indicated values of the exponent of the work-hardening law, $\rho = 1.2$, and $\nu = \nu_L = 0.3$

Finally we note that constitutive relations for geological materials must include the effects of inelastic volume changes and internal friction. These have been considered in a recent work by Nemat-Nasser and Shokooh [14] but no stability calculations have been presented. We are now completing the corresponding stability analysis which will be reported elsewhere.

Acknowledgment

This work has been supported by the National Science Foundation under Grant No. ENG76-03921 to Northwestern University.

References

1 Hill, R., "A General Theory of Uniqueness and Stability in Elastic-Plastic Solids," *Journal of Mechanics and Physics of Solids,* Vol. 6, 1958, pp. 236–249.

2 Hutchinson, J. W., "Finite Strain Analysis of Elastic-Plastic Solids and Structures," *Numerical Solution of Nonlinear Structural Problems,* ed., Hartung, R. F., ASME, AMD, Vol. 17, 1973, pp. 17–30.

3 Nemat-Nasser, S., "Continuum Bases for Consistent Numerical Formulation of Finite Strains in Elastic and Inelastic Structures," *Finite Element Analysis of Transient Nonlinear Structural Behavior,* eds., Belytschko, T., Osias, J. R., and Marcel, P. V., ASME, AMD, Vol. 14, 1975, pp. 85–98.

4 Sewell, M. J., "A Survey of Plastic Buckling," *Stability,* ed., Leipholz, H. H. E., University of Waterloo, 1972, pp. 85–197.

5 Shanley, F. R., "Inelastic Column Theory," *Journal of Aeronautical Science,* Vol. 14, 1947, pp. 261–267.

6 Biot, M. A., *Mechanics of Incremental Deformations,* Wiley, New York, 1965.

7 Ramberg, H., and Stephansson, O., "Compression of Floating Elastic and Viscuous Plates Affected by Gravity, a Basis for Discussing Crustal Buckling," *Tectonophysics,* Vol. 1, 1964, pp. 101–120.

8 Brunelle, E. J., "Surface Instability due to Initial Compressive Stress," *Bulletin of the Seismological Society of America,* Vol. 63, 1973, pp. 1885–1893.

9 Novozhilov, V. V., *Nonlinear Theory of Elasticity,* Graylock, New York, 1953.

10 McMeeking, R. M., and Rice, J. R., "Finite-Element Formulations for Problems of Large Elastic-Plastic Deformation," *International Journal of Solids and Structures,* Vol. 11, 1975, pp. 601–616.

11 Stören, S., and Rice, J. R., "Localized Necking in Thin Sheets," *Journal of Mechanics and Physics of Solids,* Vol. 23, 1975, pp. 421–441.

12 Budiansky, B., "A Reassessment of Deformation Theories of Plasticity," ASME JOURNAL OF APPLIED MECHANICS, Vol. 26, 1959, pp. 259–264.

13 Sewell, M. J., "A Plastic Flow Rule at a Yield Vertex," *Journal of Mechanics and Physics of Solids,* Vol. 22, 1974, pp. 469–490.

14 Nemat-Nasser, S., and Shokooh, A., "On Finite Plastic Flow of Compressible Materials With Internal Friction," Earthquake Research and Engineering Laboratory, Technical Report No. 79-5-16, May 1979, to appear in *International Journal of Solids and Structures.*

Downloaded 01 May 2010 to 171.66.16.243. Redistribution subject to ASME license or copyright; see http://www.asme.org/terms/Terms_Use.cfm

Y. P. Chiu[1]

Research Scientist,
SKF Industries, Inc.,
King of Prussia, Pa. 19406
Mem. ASME

On the Internal Stresses in a Half Plane and a Layer Containing Localized Inelastic Strains or Inclusions

An Airy stress function has been used to formulate the internal stresses in an isotropic body in terms of the distribution of inelastic strains under the conditions of plane stress and plane strain. Formulation has been first obtained for the stresses in closed forms for an infinite plane containing a rectangular zone with uniform inelastic strains. Using method of Fourier transforms, analytic solutions have been obtained for the stresses due to the inclusion in a half plane with free, fixed and rigid, frictionless boundaries as well as in a layer lying on a rigid, frictionless foundation. Elastic strain energy has been formulated in closed form for the rectangular domain with uniform inelastic strain in an infinite plane and a half plane.

Introduction

We consider an internal stress field arising from the localized zones with misfitting strains, such zones can be caused by plastic deformation, metallurgical transformation as well as the differences in thermal contraction between the zones and the matrix. The elastic fields due to inclusions in infinitely extended media have been investigated by many authors following Eshelby's work [1]. In the studies of plastic mechanisms (due to loading) as well as inclusions, a situation of special interest occurs when these zones are located near a free surface. At present, there are only a limited number of analytic solutions for problems of this type using a half-space assumption [2–6].

The present paper is concerned with the stress solution of a rectangular domain with uniformly distributed inelastic strains in an infinite plane, a half plane, and a layer with specified boundary conditions. The assumptions used in the paper are

1 Plane strain or plane stress.
2 Isotropic elastic material.
3 Identical elastic properties throughout the body.
4 The plastic zone (or the inclusion) is perfectly bonded to the surrounding matrix.

For a plastic zone or an inclusion of arbitrary shape such as that encountered due to surface loading, closed-form solution is not possible. As an alternative to the use of finite-element method [7], an approximate solution technique have been used by the author [8, 9] by subdividing the zone into many rectangular elements (or microelements) each of which is assumed to have a designated set of uniform inelastic strains. Economy in computational time can be achieved by computing and storing "influence coefficients" which are the internal stresses at various locations around or inside a rectangular inclusion with unit plastic strain at various depths from the boundary. Solution superposition is then used to obtain the stress field due to all elements containing inelastic strains. The formulation of the coefficients of stresses and deformations is given in this paper.

This paper begins with the formulation in two dimensions of the Airy stress function in terms of the inelastic strain distribution in an isotropic infinite plane. This problem is first extended, using method of Fourier transform to the half plane with three types of boundary conditions, i.e., a rigid, frictionless boundary, a traction-free surface, and a rigidly constrained boundary. Finally, the solution is extended to a layer lying on a rigid, frictionless boundary and containing a rectangular zone of uniform inelastic strains.

Formulation

We begin with the case of plane stress, i.e., $\sigma_z = 0$. In the presence of inelastic strains ϵ_x^p, ϵ_y^p, and γ_{xy}^p, the displacements u, v are related to the stresses σ_x, σ_y, and τ_{xy} by

$$\epsilon_x = \frac{\partial u}{\partial x} = (\sigma_x - \nu\sigma_y)/E + \epsilon_x^p$$

$$\epsilon_y = \frac{\partial v}{\partial y} = (\sigma_y - \nu\sigma_x)/E + \epsilon_y^p$$

$$\gamma_{xy} = \frac{\partial u}{\partial y} + \frac{\partial v}{\partial x} = \tau_{xy}/\mu + \gamma_{xy}^p \qquad (1)$$

[1] Presently with the Torrington Company, Torrington, Conn. 06790.

Contributed by the Applied Mechanics Division for publication in the JOURNAL OF APPLIED MECHANICS.

Discussion on this paper should be addressed to the Editorial Department, ASME, United Engineering Center, 345 East 47th Street, New York, N. Y. 10017, and will be accepted until September 1, 1980. Readers who need more time to prepare a discussion should request an extension from the Editorial Department. Manuscript received by ASME Applied Mechanics Division, July, 1979; final revision, December, 1979.

Copyright © 1980 by ASME
Downloaded 01 May 2010 to 171.66.16.243. Redistribution subject to ASME license or copyright; see http://www.asme.org/terms/Terms_Use.cfm

where E is the Young's modulus, ν is the Poisson's ratio, and μ is the shear modulus.

The strains satisfy

$$\frac{\partial^2 \epsilon_x}{\partial y^2} + \frac{\partial^2 \epsilon_y}{\partial x^2} = \frac{\partial^2 \gamma_{xy}}{\partial x \partial y} \tag{2}$$

Substituting (1) into (2) and applying the stress equilibrium equations, we obtain

$$E^{-1}\nabla^2(\sigma_x + \sigma_y) = -\frac{\partial^2 \epsilon_x{}^p}{\partial y^2} - \frac{\partial^2 \epsilon_y{}^p}{\partial x^2} + \frac{\partial^2 \gamma_{xy}{}^p}{\partial x \partial y} \tag{3}$$

Introducing Airy stress function φ which satisfies

$$\sigma_x = \frac{\partial^2 \varphi}{\partial y^2}, \quad \sigma_y = \frac{\partial^2 \varphi}{\partial x^2}, \quad \tau_{xy} = -\frac{\partial^2 \varphi}{\partial x \partial y} \tag{4}$$

Equation (3) can be reduced to

$$E^{-1}\nabla^4 \varphi = -\left(\frac{\partial^2 \epsilon_x{}^p}{\partial y^2} + \frac{\partial^2 \epsilon_y{}^p}{\partial x^2}\right) + \frac{\partial^2 \gamma_{xy}{}^p}{\partial x \partial y} \tag{5}$$

For an infinite space in which the inelastic strain components are constant in the z-direction, i.e., the derivatives of $\epsilon_x{}^p$, $\epsilon_y{}^p$, $\epsilon_z{}^p$, $\gamma_{xy}{}^p$, $\gamma_{yz}{}^p$, and $\gamma_{zx}{}^p$ with respect to z vanish. A state of plane strain prevails: We obtain

$$(1-\nu^2)E^{-1}\nabla^4 \varphi = -\left(\frac{\partial^2 \epsilon_x{}^p}{\partial y^2} + \frac{\partial^2 \epsilon_y{}^p}{\partial x^2}\right) + \frac{\partial^2 \sigma_{xy}{}^p}{\partial x \partial y} - \nu \nabla^2 \epsilon_z{}^p \tag{6}$$

$$\nabla^2 w = \frac{\partial \gamma_{zx}{}^p}{\partial x} + \frac{\partial \gamma_{yz}{}^p}{\partial y} \tag{7}$$

where w is the displacement in the z-direction. Knowing φ, the stresses σ_x, σ_y, and γ_{xy} are obtained from equation (4). Using $\epsilon_z = 0$, we have

$$\sigma_z = \nu(\sigma_x + \sigma_y) - E\epsilon_z{}^p$$

Infinite Plane Containing a Rectangular Zone With Uniformly Distributed Plastic Strains

Consider a Cartesian coordinate system (x', y') with its origin at the center of the rectangle having length $2b_1$, $2b_2$ in the x', y'-directions, respectively. We assume uniform plastic strains of values $\boldsymbol{\epsilon}_x$, $\boldsymbol{\epsilon}_y$, $\boldsymbol{\gamma}_{xy}$ inside and zero outside the rectangle, the plastic strain field are expressed as

$$\epsilon_x{}^p = \boldsymbol{\epsilon}_x F(x', y'), \text{ etc.,} \tag{8}$$

where F has a value of unity inside the rectangle and zero outside it. F is given by

$$F = -\sum_{m=1,2}\sum_{n=1,2} \frac{(-1)^{m+n}}{4\pi^2} \int_{-\infty}^{\infty}\int_{-\infty}^{\infty} \frac{e^{i(\xi x_m + \xi y_n)}}{\zeta\xi} d\zeta d\xi \tag{9}$$

with

$$x_1 = x' - b_1, \quad x_2 = x' + b_1, \quad y_1 = y' - b_2, \quad \text{and} \quad y_2 = y' + b_2 \tag{10}$$

Introducing

$$\tilde{F} = -\sum_{m=1,2}\sum_{n=1,2} \frac{(-1)^{m+n}}{4\pi^2} \int_{-\infty}^{\infty}\int_{-\infty}^{\infty} \frac{e^{i(\xi x_m + \xi y_n)}}{\zeta\xi(\zeta^2+\xi^2)^2} d\zeta d\xi \tag{11}$$

which satisfies

$$\nabla^2\nabla^2 \tilde{F} = F \tag{12}$$

Here we deal with plane stress case first. We substitute equations (6) and (10) into (5) and remove the operator $\nabla^2\nabla^2$ on the two sides. The Airy stress function becomes

$$\varphi/E = -\boldsymbol{\epsilon}_x \tilde{F}_{yy} - \boldsymbol{\epsilon}_y \tilde{F}_{,xx} + \boldsymbol{\gamma}_{xy} \cdot \tilde{F}_{,xy} \tag{13}$$

Equations (4) are used to obtain the stresses which require the evaluation of double infinite integrals. For convenience, we obtain first the Fourier transforms of the stresses defined

$$\bar{\sigma}_x = (2\pi)^{-1/2} \int_{-\infty}^{\infty} \sigma_x e^{i\lambda x} \cdot dx \tag{14}$$

The Fourier transforms of the stresses are

$$\bar{\sigma}_{x,\infty}(y') = E \sum_{n=1,2} \chi_n[(|\lambda y_n| - 2) \cdot \operatorname{sgn}(y_n)\boldsymbol{\epsilon}_x - |\lambda| y_n \boldsymbol{\epsilon}_y + i \cdot \operatorname{sgn}(\lambda)(1 - |\lambda y_n|)\boldsymbol{\gamma}_{xy}] \tag{15}$$

$$\bar{\sigma}_{y,\infty}(y') = E \sum_{n=1,2} \chi_n[-|\lambda| y_n \boldsymbol{\epsilon}_x + (|\lambda y_n| + 2) \cdot \operatorname{sgn}(y_n)\boldsymbol{\epsilon}_y + i \operatorname{sgn}(\lambda)(1 + |\lambda y_n|)\boldsymbol{\gamma}_{xy}] \tag{16}$$

$$\bar{\tau}_{xy,\infty}(y') = iE \operatorname{sgn}(\lambda) \sum_{n=1,2} \chi_n[(1 - |\lambda y_n|)\boldsymbol{\epsilon}_x + (1 + |\lambda y_n|)\boldsymbol{\epsilon}_y + i\lambda y_n \boldsymbol{\gamma}_{xy}] \tag{17}$$

with

$$\chi_n \equiv (-1)^n (8\pi)^{-1/2} \lambda^{-1} e^{-|\lambda y_n|} \sin(\lambda b_1) \tag{18}$$

Based on the foregoing expressions of Fourier transforms, we obtain the formulas for the stresses as follows:

$$\begin{pmatrix} \sigma_{x,\infty} \\ \sigma_{y,\infty} \\ \tau_{xy,\infty} \end{pmatrix} = \begin{pmatrix} \sigma_{x,\infty}{}^{(1)} & \sigma_{x,\infty}{}^{(2)} & \sigma_{x,\infty}{}^{(3)} \\ \sigma_{y,\infty}{}^{(1)} & \sigma_{y,\infty}{}^{(2)} & \sigma_{y,\infty}{}^{(3)} \\ \tau_{xy,\infty}{}^{(1)} & \tau_{xy,\infty}{}^{(2)} & \tau_{xy,\infty}{}^{(3)} \end{pmatrix} \cdot \begin{pmatrix} \boldsymbol{\epsilon}_x \\ \boldsymbol{\epsilon}_y \\ \boldsymbol{\gamma}_{xy} \end{pmatrix} \tag{19}$$

where the stress coefficients in the aforementioned matrix are given as follows:

$$\sigma_{x,\infty}{}^{(1)} = \frac{E}{2\pi} \sum_{m=1,2}\sum_{n=1,2} (-1)^{m+n} \left[-\tan\frac{x_m}{y_n} + \frac{x_m y_n}{2(x_m{}^2 + y_n{}^2)}\right] \tag{20}$$

$$\sigma_{y,\infty}{}^{(2)} = \frac{E}{2\pi} \sum_{n=1,2}\sum_{m=1,2} (-1)^{m+n} \left[-\tan\frac{y_n}{x_m} + \frac{x_m y_n}{2(x_m{}^2 + y_n{}^2)}\right] \tag{21}$$

$$\tau_{xy,\infty}{}^{(3)} = \sigma_{x,\infty}{}^{(1)} = \sigma_{x,\infty}{}^{(2)} = -\frac{E}{2\pi} \sum_{n=1,2}\sum_{n=1,2} (-1)^{m+n} \frac{x_m y_n}{2(x_m{}^2 + y_n{}^2)}$$

$$\tau_{xy,\infty}{}^{(1)} = \sigma_{x,\infty}{}^{(3)} = T_2, \quad \tau_{xy,\infty}{}^{(2)} = \sigma_{y,\infty}{}^{(3)} = T_1$$

$$\begin{matrix} T_1 \\ T_2 \end{matrix} = \frac{E}{8\pi} \sum_{m=1,2}\sum_{n=1,2} (-1)^{m+n} [\ln(x_m{}^2 + y_n{}^2) \pm 2y_n{}^2/(x_m{}^2 + y_n{}^2)] \tag{22}$$

Note that the pure dilatational case of the previous formulation (i.e., $\boldsymbol{\epsilon}_x = \boldsymbol{\epsilon}_y = \epsilon_0$ and $\boldsymbol{\gamma}_{xy} = 0$ or uniform thermal expansion inside the rectangle) has been solved by Goodier [10] who gave expressions for the stresses outside the rectangle. The shear stresses contain logarithmic singularity at the corners of the rectangle, which is similar to that found in the solution of a cuboidal inclusion [11, 12].

For the case of plane strain, the foregoing formulation is applicable with some simple modification; the plastic strains $\boldsymbol{\epsilon}_x$, $\boldsymbol{\epsilon}_y$ are replaced by $\boldsymbol{\epsilon}_x + \nu\boldsymbol{\epsilon}_z$ and $\boldsymbol{\epsilon}_y + \nu\boldsymbol{\epsilon}_z$, respectively, E is replaced by $E/(1-\nu^2)$.

Elastic Strain Energy

The elastic strain energy in the rectangular domain is given by

$$W^* = -\frac{1}{2}\int_{-b_2}^{b_2}\int_{-b_1}^{b_1} (\boldsymbol{\epsilon}_x\sigma_x + \boldsymbol{\epsilon}_y\sigma_y + \boldsymbol{\epsilon}_z\sigma_z + \boldsymbol{\gamma}_{xy}\tau_{xy}) dx'dy' \tag{23}$$

in which the stresses are functions of the inelastic strain components and the strains $\gamma_{yz}{}^p$ and $\gamma_{zx}{}^p$ are assumed to be absent. In the following, the strain energy corresponding a single nonzero value of $\boldsymbol{\epsilon}_x$, $\boldsymbol{\epsilon}_y$ and a pure dilatation $\boldsymbol{\epsilon}_x = \boldsymbol{\epsilon}_y = \boldsymbol{\epsilon}_0$ are designated as $W_x{}^*$, $W_y{}^*$, and $W_T{}^*$, respectively, as given below for plane stress:

$$W_x{}^* = -\frac{1}{2}\boldsymbol{\epsilon}_x \int_{-b2}^{b_2}\int_{-b1}^{b_1} \sigma_{x,\infty} dx'dy' = \frac{1}{2}\boldsymbol{\epsilon}_x{}^2 EV\mathbf{g}(b_1, b_2) \tag{24}$$

$$W_y{}^* = -\frac{1}{2}\boldsymbol{\epsilon}_y \int_{-b_2}^{b_2}\int_{-b_1}^{b_1} \sigma_{y,\infty} dx'dy' = \frac{1}{2}\boldsymbol{\epsilon}_y{}^2 EV\mathbf{g}(b_2, b_1) \tag{25}$$

Downloaded 01 May 2010 to 171.66.16.243. Redistribution subject to ASME license or copyright; see http://www.asme.org/terms/Terms_Use.cfm

$$W_T^* = -\frac{1}{2}\epsilon_0 \int_{-b_2}^{b_2}\int_{-b_1}^{b_1} (\sigma_{x,\infty}^{(1)} + \sigma_{x,\infty}^{(2)} + \sigma_{y,\infty}^{(1)} + \sigma_{y,\infty}^{(2)})dx'dy' = \tfrac{1}{2}\epsilon_0^2 EV \quad (26)$$

with

$$V = 4b_1b_2$$

$$\mathbf{g}(b_1, b_2) = \frac{2}{\pi}\tan^{-1}\frac{b_1}{b_2} + \frac{b_1}{4\pi b_2}\ln\frac{b_1^2 + b_2^2}{b_1^2} - \frac{3b_2}{4\pi b_1}\ln\frac{b_1^2 + b_2^2}{b_2^2}$$

For plane strain case, the aforementioned modification is required. In addition, a term $(\frac{1}{2})EV\epsilon_z^2$ is added to the strain energy. Thus, for the plane strain case with $\epsilon_x = \epsilon_y = \epsilon_z = \epsilon_0$, it can be shown $W_{T,\infty}^* = \epsilon_0^2 EV/(1-\nu^2)$ which agrees with the known full space solution [1, 6] of an inclusion of any shape with pure dilatational strains.

A Half Plane ($y > 0$) Containing a Rectangular Zone With Uniform Plastic strains

(A) The Half Plane With a Rigid, Frictionless Boundary. Consider two identical rectangular domains of sides $2b_1$ and $2b_2$ in an infinite plane with centers at $(0, y_c)$ and $(0, -y_c)$. They are arranged in such a way that one is the mirror image of the other. The normal plastic strains are assumed to be equal in the two rectangles but the shear component of plastic strain are equal and opposite in the two domains. The boundary conditions are thus $\tau_{xy,} = 0$ and $v_{,x} = 0$ along $y = 0$. The stress field due to the two domains satisfying the foregoing boundary condition is obtained by superposition and denoted by subscript A as follows:

$$\sigma_{x,A} = [\sigma_{x,\infty}^{(1)}(y - y_c) + \sigma_{x,\infty}^{(1)}(y + y_c)]\epsilon_n + [\sigma_{x,\infty}^{(2)}(y - y_c) + \sigma_{x,\infty}^{(2)}(y + y_c)]\epsilon_y + [\sigma_{x,\infty}^{(3)}(y - y_c) + \sigma_{x,\infty}^{(3)}(y + y_c)]\cdot\gamma_{xy}, \text{ etc.} \quad (27)$$

The elastic strain energy due to various inelastic strain components are given next

$$W^*_{x,A} = W^*_{x,\infty} + \epsilon_x^2 EV(8\pi k)^{-1}(K_2 - 3K_1 - 8K_3) \quad (28)$$

$$W^*_{y,A} = W^*_{y,\infty} + \epsilon_y^2 EV(8\pi k)^{-1}(8K_3 + K_1 - 3K_2) \quad (29)$$

$$W^*_{T,A} = W^*_{T,\infty} \quad (30)$$

with

$$K_1 = (k + k_c)^2\cdot\ln[1 + (k + k_c)^{-2}] + (k_c - k)^2\cdot\ln[1 + (k_c - k)^{-2}] - 2k_c^2\cdot\ln(1 + 1/k_c^2)$$

$$K_2 = \ln\{1 + (k + k_c)^2][1 + (k_c - k)^2]/(1 + k_c^2)^2\}$$

$$K_3 = (k_c + k)\tan^{-1}(k_c + k) + (k_c - k)\cdot\tan^{-1}(k_c - k) - 2k_c\cdot\tan^{-1}k_c$$

and

$$k = b_2/b_1 \quad \text{and} \quad k_c = y_c/b_1$$

(B) Free Boundary, i.e., $\sigma_y = \tau_{xy} = 0$ Along $y = 0$. To derive a solution of a half plane with a free boundary from the preceding solution for the two rectangles, it is necessary to relieve the normal stress $\sigma_{y,A}$ along the boundary $y = 0$, i.e., $(\sigma_{y,A})_{y=0} = 2\sigma_{y,\infty}(y_c)$. The stress field (denoted by a subscript B) is obtained by the superposition of the preceding solution (A) and that of a half plane under normal traction $2\sigma_{y,\infty}$. Using formulation given in the Appendix, we have

$$\sigma_{x,B} = \sigma_{x,A} - [\mathcal{F}(\mathbf{f}_1) - y\cdot\mathcal{F}(|\lambda|\mathbf{f}_1)] \quad (31)$$

$$\sigma_{y,B} = \sigma_{y,A} - [\mathcal{F}(\mathbf{f}_1) + y\mathcal{F}(|\lambda|\mathbf{f}_1)] \quad (32)$$

$$\tau_{xy,B} = \tau_{xy,A} - y\cdot\mathcal{F}(i\lambda\mathbf{f}_1) \quad (33)$$

where $\mathcal{F}(f)$ is a function of x, y, and f as follows:

$$\mathcal{F}(\mathbf{f}) = \frac{1}{\sqrt{2\pi}}\int_{-\infty}^{\infty}\mathbf{f}\cdot\exp(-|\lambda|y - i\lambda x)d\lambda \quad (34)$$

and $\mathbf{f}_1$ is the Fourier transform of the normal surface load of the half plane

$$\mathbf{f}_1 = 2\bar{\sigma}_{y,\infty}(y_c) \quad (35)$$

Using the expression given in equation (16), we obtain in closed form the quantity $\mathcal{F}$ in (41) and (43) in terms of the Fourier transforms of $\lambda^m e^{-\lambda y}$, which are obtainable in closed form using formulas in [13].

The elastic strain energy due to the various inelastic strain components in the rectangular domain in a half plane with free surface can be expressed as follows:

$$W^*_{x,B} = W^*_{x,A} - \epsilon_x^2\cdot EV(16\pi k)^{-1}[K_1 + 2k^2\ln(1 + k_c^{-2})] \quad (36)$$

$$W^*_{y,B} = W^*_{y,A} + \epsilon_y^2\cdot EV(16\pi k)^{-1}(-K_1 + 8K_2 - 16K_3) \quad (37)$$

$$W^*_{T,B} = W^*_{T,A} + \epsilon_0^2 EV(8\pi k)^{-1}(K_2 - K_1 - 4K_3) \quad (38)$$

(C) The Half Plane With a Rigidly Constrained (or Fixed) Boundary. Recall that in previously solved case (A), the displacement v vanishes and $u = 2\cdot u_\infty(y_c)$ along $y = 0$. To satisfy the boundary condition $v = u = 0$, the half plane in case A solved previously is to be superimposed by another half plane which is subjected to a set of boundary conditions $v = 0$ and $u = 2u_\infty(y_c)$. The stresses in the latter case are derived in the Appendix. The resulting stresses for the half plane with a fixed edge and containing a rectangular element with uniform inelastic strains are denoted by a subindex c and given as follows:

$$\sigma_{y,c} = \sigma_{y,A} - 2E_\nu[(1 + \nu)y\cdot\mathcal{F}(|\lambda|\mathbf{f}_2) - (1 - \nu)\mathcal{F}(\mathbf{f}_2)] \quad (39)$$

$$\sigma_{x,c} = \sigma_{x,A} - 2E_\nu[-(1 + \nu)y\cdot\mathcal{F}(|\lambda|\mathbf{f}_2) + (3 + \nu)\mathcal{F}(\mathbf{f}_2)] \quad (40)$$

$$\tau_{xy,c} = \tau_{xy,A} - 2E_\nu[(1 + \nu)y\mathcal{F}(i\lambda\mathbf{f}_2) - 2\cdot\mathcal{F}(i|\lambda|\mathbf{f}_2/\lambda)] \quad (41)$$

with

$$E_\nu = \frac{E}{(1 + \nu)(3 - \nu)}$$

wherein $\mathbf{f}_2$ is the Fourier transform of the gradient of the tangential surface displacement $(u_{,x})$ of the half plane subject to $v = \tau_{xy} = 0$ as in Case A.

$$\mathbf{f}_2 = (\bar{\sigma}_{x,\infty} - \nu\bar{\sigma}_{y,\infty})/E = \sum_{n=1,2}\chi_n\{[(1 + \nu)|\lambda y_n| - 2]\cdot\text{sgn}(y_n)\epsilon_x - [2\nu + (1 + \nu)|\lambda y_n|]\text{sgn}(y_n)\epsilon_y + i[(1 - \nu) - (1 + \nu)|\lambda y_n|\cdot\text{sgn}(\lambda)\gamma_{xy}\} \quad (42)$$

For plane strain, ν and E are replaced by $\nu/(1 - \nu)$ and $E/(1 - \nu^2)$, respectively.

The formulas for the elastic strain energy in the inclusion due to various inelastic strains are obtained from integrating the stresses over the rectangular area. They are, for plane stress

$$W^*_{x,c} = W^*_{x,A} + \epsilon_x^2 E_\nu V(16\pi k)^{-1}[2(3\nu + 7)K_1 - 8K_2 + 16(3 + \nu)K_3 + 2(1 + \nu)^2k^2\ln(1 + k_c^{-2})] \quad (43)$$

$$W^*_{y,c} = W^*_{y,A} + \epsilon_y^2 E_\nu V(16\pi k)^{-1}[(\nu^2 - 6\nu + 1)K_1 - 8\nu^2K_2 - 16\nu(1 - \nu)K_3 + 2(1 + \nu)^2k^2\ln(1 + k_c^{-2})] \quad (44)$$

$$W^*_{T,c} = W^*_{T,A} + 2(1 + \nu)^2E_\nu\epsilon_0^2V(4K_3 + K_1 - K_2)(8\pi k)^{-1} \quad (45)$$

(D) Numerical Results. Figs. 1–3 plot the dimensionless elastic strain energy in plane stress for the rectangular inclusion with given inelastic strain component ϵ_x, ϵ_y and a dilatation strain ϵ_0, respectively, as a function of the ratio b_1/b_2. The curves in the figures consist of the strain-energy solutions for half planes with a rigid, frictionless edge (Curve A), a free surface (Curve B) and a rigidly constrained edge (Curve C) as well as the full plane solution (Curve ∞). The value of Poisson's ratio used in computing Curve C is 0.3.

It is shown in Figs. 2 and 3 that as the distance (y_c) of the inclusion center to the edge increases, the strain energy in each case approaches the full plane solution. It is found that an inclusion located near a rigidly constrained boundary contains greater strain energy than that located near a rigid, frictionless edge and a free surface. The latter case has the smallest strain energy in all cases of half plane and full plane solutions. When an inclusion approaches a rigidly constrained boundary, its strain energy increases.

Downloaded 01 May 2010 to 171.66.16.243. Redistribution subject to ASME license or copyright; see http://www.asme.org/terms/Terms_Use.cfm

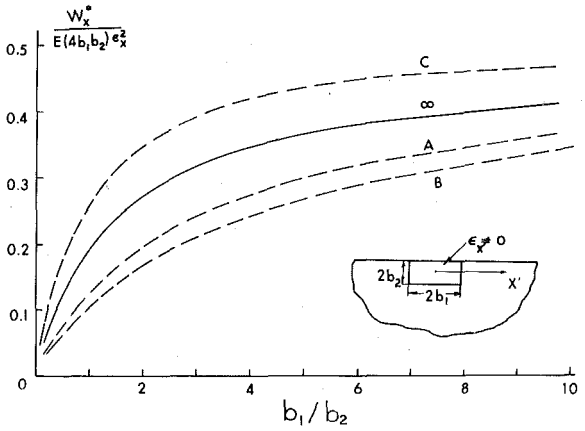

Fig. 1 Dimensionless strain energy in a rectangular inclusion located near the edge of a half plane (*A* for rigid, frictionless edge, *B* for free edge, *C* for fixed edge, and ∞ for the full plane) and having an inelastic strain ϵ_x

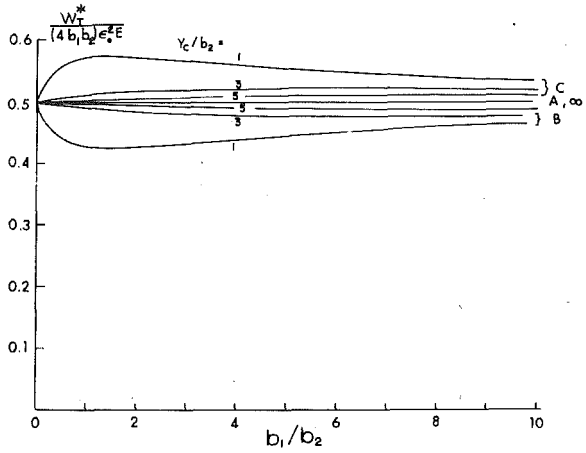

Fig. 3 Same as Fig. 1 except with a dilatational strain ϵ_0

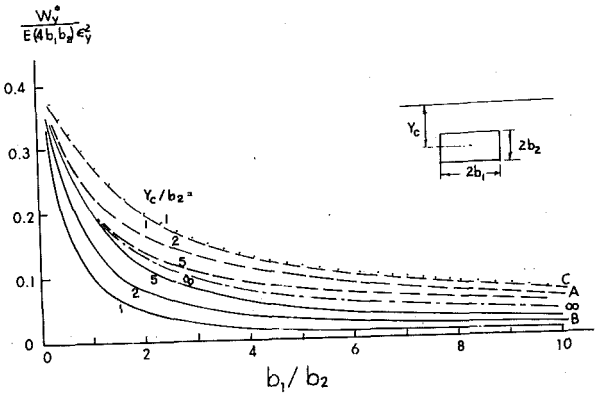

Fig. 2 Same as Fig. 1 except with an inelastic strain ϵ_y inside the element; the numbers around the curves denote values of y_c/b_2

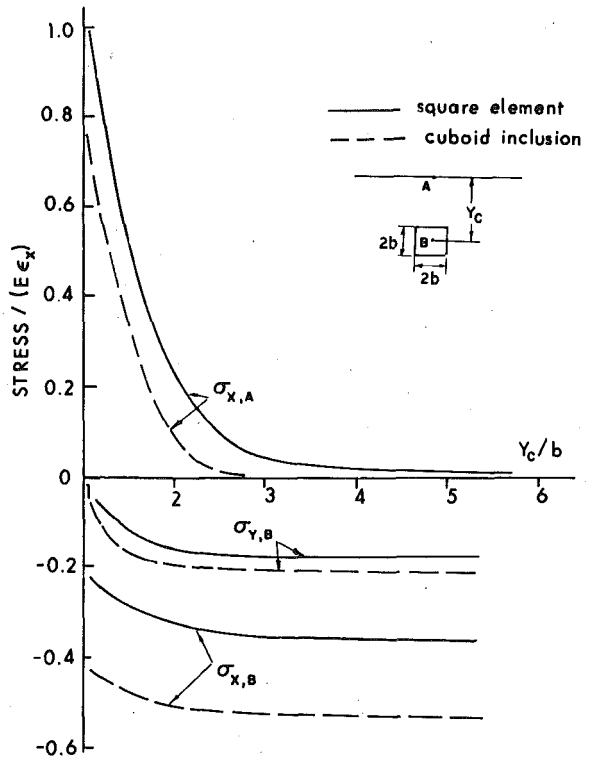

Fig. 4 Variation of internal stresses at the center of a square element (point *B*) and at surface (Point *A*) due to an inelastic strain ϵ_x in a square element of sides $2b$ as a function of the depth of element center (y_c)

For a half plane with a free surface containing a square element ($b_1 = b_2 = b$) in which there is an uniform inelastic strain ϵ_x, Fig. 4 presents the stresses at the center of the element (Point B) and at the free surface immediately above the element (Point A) in solid curves. For purpose of comparison, the dotted curves in Fig. 4 are the stresses calculated in a three-dimensional analysis [5] for a half space containing a cubic element with uniform inelastic strain ϵ_x as a function of the distance of the center of the cube from the free surface. The results reveal that when an inclusion having positive inelastic strain components (ϵ_x, ϵ_y) approaches a free surface, the magnitude of tensile stress at the surface increases. This finding is consistent with the previously obtained solution for a coboid [5] and an ellipsoid [6] within a half space. For a half plane with a rigidly constrained edge and containing a square element with uniform strain component ϵ_x and ϵ_y, respectively, Figs. 5 and 6 plot the stresses at two locations (A at the surface and B at the element center) as a function of the distance from the edge to the center. The solid curves and the dashed curves are for plane strain and plane stress, respectively.

A Layer on a Rigid Frictionless Foundation With Localized Plastic Strains

The layer is assumed to occupy a domain $0 < y < h$, $-\infty < x < \infty$. One of the boundary ($y = h$) is a free surface while along the other boundary ($y = 0$), the shear traction and the displacement v (in the y-direction) vanish. The center of the rectangular plastified zone is assumed to be located at a depth y_c from the free surface.

The foregoing problem is equivalent to that of a layer of thickness $2h$ with two free surfaces along $y = \pm h$ and having two rectangular zones of uniform plastic strains with centers located at $(0, h - y_c)$ and $(0, y_c - h)$. The zones are so situated that one is the mirror images of the other as shown in Fig. 7. In the two zones, the normal components of the plastic strains are equal and the shear components are equal in magnitude and opposite in direction.

Here, we begin with the previously obtained full-plane solution of two rectangular zones of plastic strains as obtained in Case A. The stress field is denoted a subscript A. In the full-plane solution, the tractions along the two fictitious boundaries ($y = \pm h$) are to be removed by superimposing the solution of a layer without localized plastic strain having surface tractions equal and opposite to those occurring along the same boundaries in the full space solution.

Downloaded 01 May 2010 to 171.66.16.243. Redistribution subject to ASME license or copyright; see http://www.asme.org/terms/Terms_Use.cfm

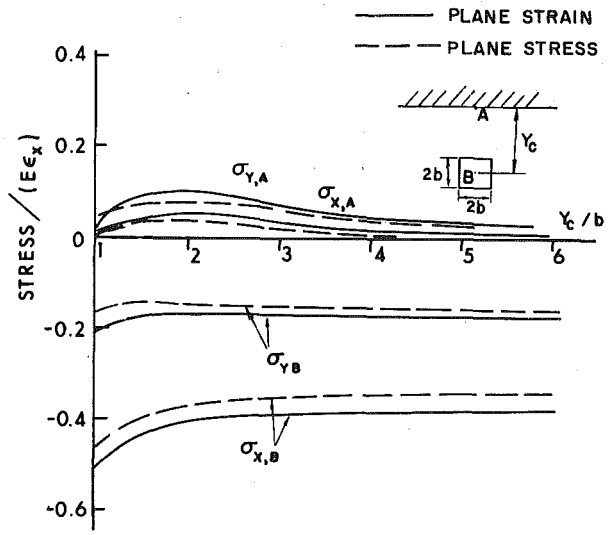

Fig. 5 Variation of stresses at Points A and B with y_c/b in a half plane with a rigidly constrained edge and containing an inelastic strain ϵ_x inside a square element

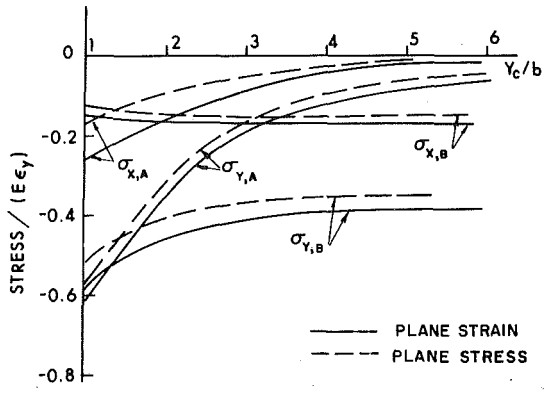

Fig. 6 Same as Fig. 5 except with ϵ_y instead of ϵ_x inside the element

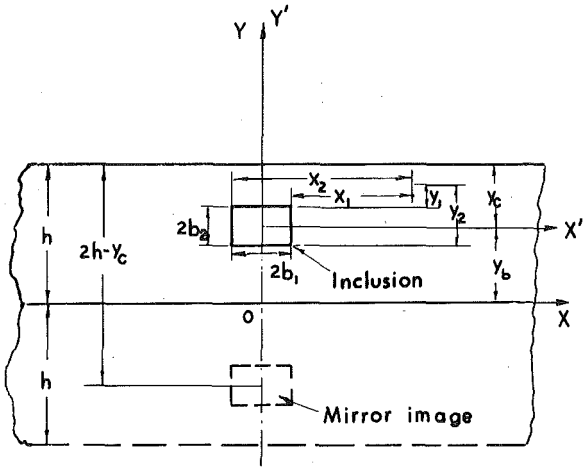

Fig. 7 A rectangular element in a layer with its mirror image

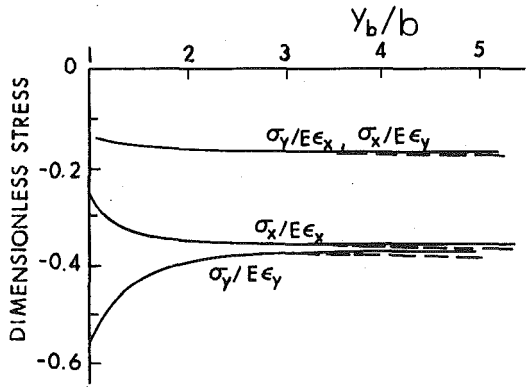

Fig. 8 Variation of stresses at center of the element with inelastic strains ϵ_x and ϵ_y in a layer (solid curves) and a half plane bounded by a rigid, frictionless edge (dashed curves) with the distance from the element center to the base (y_b)

The solution of the present problem is the sum of two parts, i.e., the solution (A) for the full plane with two plastified zones and the solution of a layer with surface traction (prescribed from the solution A). The latter is a boundary-value problem which can be expressed in the form of Fourier integrals [14].

The stresses are

$$\sigma_{y,L} = \sigma_{yA} + \frac{1}{\sqrt{2\pi}} \int_{-\infty}^{\infty} (A \text{ ch } \lambda y + B\lambda y \text{ sh } \lambda y) e^{-i\lambda x} d\lambda \quad (46)$$

$$\sigma_{x,L} = \sigma_{x,A} + \frac{1}{\sqrt{2\pi}} \int_{-\infty}^{\infty} [-(2\beta + A) \text{ ch } \lambda y - B\lambda y \text{ sh } \lambda y] e^{-i\lambda x} d\rho \quad (47)$$

$$\tau_{xy,L} = \tau_{xy,A} + \frac{1}{i\sqrt{2\pi}} \times \int_{-\infty}^{\infty} [A \text{ sh } \lambda y + B(\lambda y \text{ ch } \lambda y + \text{sh } \lambda y)] e^{-i\lambda x} d\lambda \quad (48)$$

with

$$A = 2[(\mu \text{ ch } \mu + \text{sh } \mu)\mathbf{f} - i\mu \, sh \, \mu \cdot \mathbf{g}]/(\text{sh } 2\mu + 2\mu)$$

$$B = 2[-\text{sh } \mu \cdot \mathbf{f} + i \text{ ch } \mu \cdot \mathbf{g}]/(\text{sh } 2\mu + 2\mu), \quad \mu \equiv \lambda h \quad (49)$$

and $\mathbf{f}$ and $\mathbf{g}$ are the Fourier transforms of the normal and tangential traction, respectively, along the boundaries ($y = \pm h$). It is required to relieve the tractions along the same boundaries in the full space solution A.

$$-\mathbf{f} = \epsilon_x[\bar{\sigma}_{y,\infty}{}^{(1)}(y_c) + \bar{\sigma}_{y,\infty}{}^{(1)}(2h - y_c)] + \epsilon_y[\bar{\sigma}_{y,\infty}{}^{(2)}(y_c) + \bar{\sigma}_{y,\infty}{}^{(2)}(2h - y_c)] + \gamma_{xy}[\bar{\sigma}_{y,\infty}{}^{(3)}(y_c) - \bar{\sigma}_{y,\infty}{}^{(3)}(2h - y_c)] \quad (50)$$

$$-\mathbf{g} = \epsilon_x[\bar{\tau}_{xy,\infty}{}^{(1)}(y_c) + \bar{\tau}_{xy,\infty}{}^{(1)}(2h - y_c)] + \epsilon_y[\bar{\tau}_{xy,\infty}{}^{(2)}(y_c) + \bar{\tau}_{xy,\infty}{}^{(2)}(2h - y_c)] + \gamma_{xy}[\bar{\tau}_{xy,\infty}{}^{(3)}(y_c) - \bar{\tau}_{xy,\infty}{}^{(3)}(2h - y_c)] \quad (51)$$

The computation of the stresses and displacements requires the evaluation of infinite integrals of the following form:

$$\mathbf{I}(x, y, m) = \int_{-\infty}^{\infty} \frac{e^{\mu y}\mu^m}{2\mu + \text{sh } 2\mu} e^{-i\mu x} d\mu \quad (52)$$

where m is an integer and $y < 2$. The aforementioned integral has no closed-form solution. It can be evaluated numerically by separating the integral into two parts, i.e.,

$$\mathbf{I}(x, y, m) = 2\mathbf{I}_m + \int_{-\infty}^{\infty} e^{\mu y}\mu^m \left(\frac{1}{2\mu + \text{sh } 2\mu} - 2e^{-2\mu}\right) e^{-i\mu x} d\mu \quad (53)$$

where

$$\mathbf{I}_m = \int_{-\infty}^{\infty} \mu^m e^{-(2-y)\mu} e^{-i\mu x} d\mu \quad (54)$$

Downloaded 01 May 2010 to 171.66.16.243. Redistribution subject to ASME license or copyright; see http://www.asme.org/terms/Terms_Use.cfm

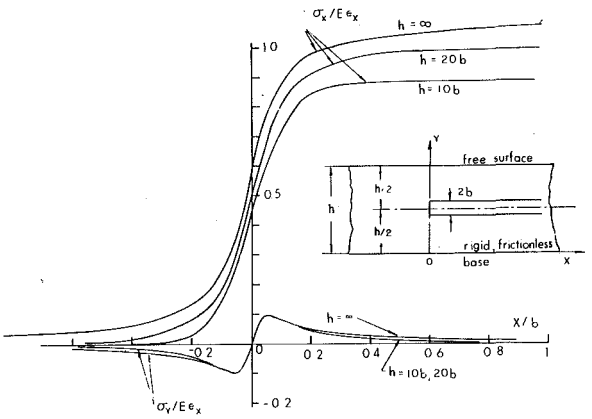

Fig. 9 Variation of stresses along the center line of a semi-infinite domain with uniform ϵ_x in a layer lying on a rigid, frictionless base

The integral I_m can be integrated into closed-form functions of x, y, and m using [13]. The details are omitted here for brevity.

Numerical example has been obtained for a layer of thickness h lying on a rigid frictionless foundation and containing a square element with uniform inelastic strains. Fig. 8 plots for given ϵ_x and ϵ_y, respectively, the stresses at the center of the inclusion (in solid curves) as a function of the distance (y_b) from the center to the rigid, frictionless base. The side of the square ($2b$) are assumed to be $1/12$ of the thickness h. It is found that for $y_b < 3b$, these curves almost coincide with the dashed curves which are obtained for a square inclusion in a half plane with a rigid, frictionless boundary (Solution A). This is so, because, as the inclusion locates close to the base of the layer, it is relatively remote from the free boundary, and the effect of the free surface thus becomes weak. Fig. 9 shows the stresses σ_x and σ_y scaled by $E\epsilon_x$ along the center line of a semi-infinite zone of width $2b$ with uniform inelastic strain ϵ_x in a layer of thickness h. The parameters of the curves are $h/b = 10$, 20 and ∞ with the latter representing a full plane solution. Note that the solution of a rectangular inclusion can be obtained from the superposition of two semi-infinite inclusions; the x coordinates of the end of the semi-infinite domains are let to differ by a distance equal to the width ($2b_1$) of the rectangular inclusion.

The results reveal that as the ratio of the plastic zone thickness to the layer thickness increases, there is a decreases of lateral constraint as compared with that in a half plane or a full plane.

Acknowledgment

This work was partially supported by ARO Durham, North Carolina under Contract No. DAAG-29-76-C-0016. This support and the kind permission of SKF Industries, Inc. to publish this work are gratefully acknowledged.

References

1 Eshelby, J. D., "Elastic Inclusion and Inhomogeneities," *Progress of Solid Mechanics*, Vol. 2, eds., Sneddon, I. N., and Hill, R., North-Holland Publishing Company, 1961, pp. 89–139.

2 Mindlin, R. D., and Cheng, D. H., "Thermoelastic Stress in the Semi-Infinite Solid," *Journal of Applied Physics*, Vol. 21, Sept. 1950, pp. 931–933.

3 Owen, D. R. J., and Mura, T., "Periodic Dislocation Distribution in a Half Space," *Journal of Applied Physics* Vol. 38, No. 5, 1967, pp. 1999–2009.

4 Guell, D. L., and Dundurs, J., "Further Results on Center of Dilatation and Residual Stresses in Joined Elastic Half Space," *Developments in Theoretical and Applied Mechanics*, Vol. 3, Pergamon Press, Oxford, 1967, pp. 105–115.

5 Chiu, Y. P., "On the Stress Field and Surface Deformation in a Half Space With A Cuboidal Zone in Which Initial Strains Are Uniform," ASME JOURNAL OF APPLIED MECHANICS, Vol. 45, 1978, pp. 302–306.

6 Seo, K., and Mura, T., "The Elastic Field in a Half Space Due to Ellipsoidal Inclusions With Uniform Dilatational Eigenstrains," ASME JOURNAL OF APPLIED MECHANICS, Vol. 46, No. 3, 1979, pp. 568–572.

7 Ziewkiewicz, O. C., Villiappan, S., and King, I. P., "Elasto-Plastic Solutions of Engineering Problem, 'Initial Stress', Finite Element Approach," *International Journal of Numerical Method in Engineering*, Vol. 1, 1969, pp. 75–100.

8 Chiu, Y. P., "Analysis of Residual Stresses in Elasto-Plastic Contact of Half-Planes," *Developments in Theoretical and Applied Mechanics*, Vol. 9, May 1978, pp. 77–91.

9 Chiu, Y. P., "On the Plastic Zone and Residual Stresses Within a Strip and a Half Plane Under a Moving Load," presented in International Conference of Numerical Method in Nonlinear Mechanics, TICOM meeting, Mar. 1979, *International Journal of Engineering Science*, Vol. 18, 1980, pp. 277–285.

10 Goodier, J. N., "On the Integration of Thermoelastic Equation," *Philosophical Magazine*, Vol. 23, 1937, p. 1017.

11 Chiu, Y. P., "On the Stress Field Due to Initial Strains in a Cuboid Surrounded by an Infinite Elastic Space," ASME JOURNAL OF APPLIED MECHANICS, Vol. 44, Dec. 1977, pp. 587–590.

12 Lee, J. K., and Johnson, W. C., "Elastic Strain Energy and Interactions of Thin Square Plates Which Have Undergone a Simple Shear," *Scripta Metallurgica*, Vol. 11, 1977, pp. 477–484.

13 Erdelyi, et al., *Table of Integral Transform*, Vol. 1, McGraw-Hill, New York, 1953.

14 Uflyand, Ya.S., "Survey of Articles on the Applications of Integral Transforms in Theory of Elasticity," ed., Sneddon, I. N., North Carolina State University, Oct. 1965, pp. 21–27.

APPENDIX

Fourier Transform of Stress and Displacement in a Half Plane ($y > 0$)

$$\bar{\sigma}_y = -\zeta^2 G \tag{55}$$

$$\bar{\sigma}_x = G'' \tag{56}$$

$$\bar{\tau}_{xy} = i\zeta G' \tag{57}$$

$$\bar{u}_{,x} = (G'' + \nu\zeta^2 G)/E \tag{58}$$

$$\bar{v}_{,x} = -i[G''' - (2+\nu)\zeta^2 G']/\zeta E \tag{59}$$

$$G = (A_1 + A_2 y)\cdot e^{-|\zeta|y} \tag{60}$$

where the prime above G denotes partial derivative with respect to y and the comma denotes partial differentiation, i.e., $(\ )_{,x} = \partial(\ )/\partial x$. Plane stress is assumed.

Under special boundary conditions described next, the previous formulas can be reduced to

(1) For $\tau_{xy} = 0$ at $y = 0$, we have $A_2 = |\zeta| A_1$ and

$$\bar{\sigma}_y = -\zeta^2(1 + |\zeta|y)A_1 e^{-|\zeta|y} \tag{61}$$

$$\bar{\sigma}_x = -\zeta^2(1 - |\zeta|y)A_1 e^{-|\zeta|y} \tag{62}$$

$$\bar{\tau}_{xy} = -i\zeta^3 y A_1 e^{-|\zeta|y} \tag{63}$$

$$\bar{u}_{,x} = (\nu - 1)\zeta^2 A_1/E \quad \bar{v}_{,x} = -\frac{2i}{3E} A_1 |\zeta^3| \tag{64}$$

A is related to the Fourier transform of the normal surface traction by $(\bar{\sigma}_y)_{y=0} = -A_1\zeta^2$

(2) For the case that the displacement v vanishes along the boundary $y = 0$, we have $A_2 = -|\zeta|\cdot A_1(1+\nu)/(1-\nu)$ and $(\bar{u}_{,x})_{y=0} = (1+\nu)(3-\nu)\zeta^2 A_1/(1-\nu)E$

$$(1+\nu)(3-\nu)\bar{\sigma}_y/E = [(1+\nu)|\zeta|y - (1-\nu)](\bar{u}_x)_{y=0} e^{-|\lambda|y} \tag{65}$$

$$(1+\nu)(3-\nu)(\bar{\sigma}_x + \bar{\sigma}_y)/E = 2(1+\nu)(\bar{u}_x)_{y=0} e^{-|\lambda|y} \tag{66}$$

$$(1+\nu)(3-\nu)\bar{\tau}_{xy}/E = i\ \text{sign}\ (\zeta)(\bar{u}_{,x})_{y=0}[(1+\nu)|\zeta|y - 2]\cdot e^{-|\lambda|y} \tag{67}$$

Downloaded 01 May 2010 to 171.66.16.243. Redistribution subject to ASME license or copyright; see http://www.asme.org/terms/Terms_Use.cfm

N. Kamiya

Professor,
Department of Mechanical Engineering,
Mie University,
Kamihamacho, Tsu 514, Japan

Finite Thermoelastic Deformation of Sphere With Temperature-Dependent Properties

The present paper concerns a finite thermoelastostatic analysis considering temperature-dependent mechanical and thermal properties of material. The Lamé elastic parameters, thermal expansion coefficient, and thermal conductivity are expressed by linear functions of temperature. Higher-order terms in terms of temperature and strain invariants are introduced into the free energy expression. Lagrange formulation is employed for derivation of the governing field equations. A hollow sphere under a spherically symmetric stationary thermal field is analyzed numerically. The influence of the temperature-dependent variations of the material properties on stress state is investigated and found to be insignificant over a narrow temperature range where the material remains elastic.

Introduction

Mechanical and thermal properties of material are known to vary with temperature. There have been many analyses of such elastic bodies for stationary thermal fields by Nowinski [1, 2], Chang and Chu [3], Trostel [4, 5], Stanisic and McKinley [6], and Nyuko, Takeuti, and Noda [7] and for nonstationary thermal fields by Nowinski [8], Koizumi and Taniwaki [9], and Hata and Atsumi [10, 11]. In addition, similar analyses have been performed for elastic-plastic and viscoelastic materials.

However, in the field of temperature-dependent finite thermoelasticity, within the author's knowledge, only one thermal stress problem was solved by Craine [12]. Assuming a quadratic representation for the free energy in terms of strain and temperature, in other words, employing the constitutive relation for the linear isotropic elastic material, Craine analyzed finite stationary thermal stress and deformation states of a hollow sphere. In his analysis, the material parameters, i.e., the Lamé elastic parameters and thermal expansion coefficient, appearing in the free energy expression were thought to be invariable, whereas a temperature-dependency of *thermal conductivity*, which affected stresses through thermal field, was introduced. As a result, he showed that there was only invisible discrepancy between the results due to the finite elasticity and the classical linear elasticity provided that the material remained elastic.

In the present paper, as an extension of the aforementioned study [12], we present a method of solution to a finite thermoelastic problem considering temperature-dependent *Lamé parameters, thermal expansion coefficient, and thermal conductivity*. The material is treated here as isotropic and linear elastic and the Lamé two elastic parameters, thermal expansion coefficient, and thermal conductivity are assumed to vary linearly with temperature for a relatively narrow temperature range. Second and third-order terms in terms of temperature and strain tensors are introduced into the free energy formula. Formulation of the governing field equations is referred to the Lagrange coordinate system, which can easily be modified and applied to similar problems with nonlinear elastic and inelastic material behaviors. In order to compare the result with that of Craine, a hollow sphere subjected to a spherically symmetric thermal field is considered. The influence of the temperature-dependent variations of the material parameters on the stress state is investigated by way of numerical calculations. The results show that if we confine our consideration within linear elastic material behavior the inclusion of the temperature-dependent finite deformation in the sphere does not significantly alter the linear elastic solution.

Lagrange Formulation

For the sake of convenience in the subsequent chapters, the fundamental formulas referred to the Lagrange coordinates are explained here (Bland [13]). For repeated indices, we follow the ordinary summation convention rule.

By denoting the original and current coordinates in a fixed rectangular Cartesian frame of reference by a_i and x_i $(i = 1, 2, 3)$, respectively, the Green strain tensor is expressed as

$$\gamma_{ij} = (\partial x_k/\partial a_i \cdot \partial x_k/\partial a_j - \delta_{ij})/2 \quad (i, j, k = 1, 2, 3) \qquad (1)$$

where δ_{ij} stands for Kronecker delta.

The equilibrium equation, if there is no body force, is formulated in terms of Lagrange stress tensor (Piola-Kirchhoff stress tensor) L_{ij} as

Contributed by the Applied Mechanics Division for publication in the JOURNAL OF APPLIED MECHANICS.

Discussion on this paper should be addressed to the Editorial Department, ASME, United Engineering Center, 345 East 47th Street, New York, N. Y. 10017, and will be accepted until September 1, 1980. Readers who need more time to prepare a discussion should request an extension from the Editorial Department. Manuscript received by ASME Applied Mechanics Division, September, 1978; final revision, December, 1979.

Copyright © 1980 by ASME
Downloaded 01 May 2010 to 171.66.16.243. Redistribution subject to ASME license or copyright; see http://www.asme.org/terms/Terms_Use.cfm

$$\partial L_{ij}/\partial a_j = 0 \tag{2}$$

For an isothermal process, we introduce the specific free energy F which is thought here to be a function of the strain tensor γ_{ij} and temperature T,

$$F = F(\gamma_{ij}, T) \tag{3}$$

Expressions of Kirchhoff stress tensor K_{ij} and specific entropy S for a compressible material body are

$$K_{ij} = \rho_0 \partial F/\partial \gamma_{ij}, \quad S = -\partial F/\partial T \tag{4}$$

where ρ_0 is the material density in the undeformed state. In the Cartesian coordinate system, the following relation holds:

$$L_{ij} = \partial x_i/\partial a_k \cdot K_{kj} \tag{5}$$

Free Energy

The following three invariants of the Green strain tensor are defined:

$$J_1 = \gamma_{ii}, \quad J_2 = (\gamma_{ii}\gamma_{jj} - \gamma_{ij}\gamma_{ij})/2,$$
$$J_3 = \det(\gamma_{ij}) \tag{6}$$

As an initial setting, we adopt a homogeneous quadratic expression for the free energy F in terms of the strain and the temperature (in what follows, description due to Dillon [14] and/or Oden [15] is used)

$$\rho_0 F = a_2 J_2 + a_5 J_1^2 + a_7 (T - T_0)^2 + a_8 J_1 (T - T_0) \tag{7}$$

where T_0 denote the reference temperature. If the four coefficients appearing in the foregoing formula are not variable, F takes a quadratic form of γ_{ij} and T with constant coefficients, and thus the constitutive equation reduced from it coincides with that of linear elastic material. If this is the case, the following relations hold between the coefficients and the Lamé constants λ, μ and the thermal expansion coefficient α:

$$a_2 = -2\mu, \quad a_5 = (\lambda + 2\mu)/2, \quad a_8 = -\alpha(3\lambda + 2\mu) \tag{8}$$

Furthermore, a_7 is expressible by the specific heat.

It has been well known that, in general, the mechanical and thermal properties of material vary with change of temperature. Thus we regard the coefficients a_2, a_5, a_7, and a_8 of equation (7) as functions of temperature and express them by the linear functions of $T - T_0$,

$$\rho_0 F = a_2 J_2 [1 + a_2'(T - T_0)] + a_5 J_1^2 [1 + a_5'(T - T_0)] + a_7 (T - T_0)^2 [1 + a_7'(T - T_0)] + a_8 J_1 (T - T_0)[1 + a_8'(T - T_0)] \tag{9}$$

The such formulation is validated if we restrict ourselves within narrow temperature range. By introducing the following notations:

$$a_2' = a_{11}/a_2, \quad a_5' = a_{13}/a_5, \quad a_7' = a_{12}/a_7, \quad a_8' = a_{10}/a_8 \tag{10}$$

Equation (9) becomes

$$\rho_0 F = a_2 J_2 + a_5 J_1^2 + a_7 (T - T_0)^2 + a_8 J_1 (T - T_0) + a_{10} J_1 (T - T_0)^2 + a_{11} J_2 (T - T_0) + a_{12} (T - T_0)^3 + a_{13} J_1^2 (T - T_0) \tag{11}$$

where the fifth to eighth terms in the right-hand side are the higher-order terms of T.

Young's modulus E and Poisson's ratio ν are frequently utilized as the fundamental engineering material parameters. Poisson's ratio is usually treated as a constant because its variation due to temperature change is not remarkable when compared with the other parameters. Consequently, the variations of the Lamé parameters λ, μ and the Young's modulus E become identical. Let us represent the following linear forms for the variations of the parameters:

$$\mu = \mu_0[1 + \mu_1(T - T_0)], \quad \lambda = \lambda_0[1 + \lambda_1(T - T_0)],$$
$$\alpha = \alpha_0[1 + \alpha_1(T - T_0)] \quad (\lambda_1 = \mu_1) \tag{12}$$

where μ_0, λ_0, and α_0 are the values at the reference temperature $T = T_0$ and where μ_1, λ_1, and α_1 are the variational terms. Hence it becomes

$$a_{11}/a_2 = a_{13}/a_5 = \mu_1, \quad a_{10}/a_8 = \mu_1 + \alpha_1 \tag{13}$$

The following comment, however, must be born in mind. Equation (11) was formulated in order to introduce simply the temperature-dependent variations of the mechanical and thermal properties of material by virtue of the linear expression of temperature. Therefore the equation must also be applicable to infinitesimal strain problems where linear relations are available between components of strain and displacement. According to the discussion on the free energy function in the nonlinear thermoelasticity after Dillon [14], the coefficient of $J_1^2(T - T_0)$, a_{13}, vanishes provided that the following conditions holds: that is, "heating of material in compression corresponds to cooling of material in tension (Dillon's condition)." If this is the case, the last term of F, equation (11), vanishes

$$a_{11}/a_2 = \mu_1, \quad a_{10}/a_8 = \mu_1 + \alpha_1, \quad a_{13}/a_5 = 0 \tag{14}$$

Spherically Symmetric Problem [13, 16, 17]

Let us introduce the spherical coordinate systems (r, θ, ϕ) and (R, Θ, Φ) representing, respectively, the undeformed and deformed states. For the spherically symmetric problem

$$R = R(r), \quad \Theta = \theta, \quad \Phi = \phi \tag{15}$$

Nonvanishing components of the strain tensor in the spherically symmetric deformation are γ_{rr}, $\gamma_{\theta\theta}$, and $\gamma_{\phi\phi}$, whose physical components are denoted by the overscored values

$$\bar{\gamma}_{rr} = [(dR/dr)^2 - 1]/2, \quad \bar{\gamma}_{\theta\theta} = \bar{\gamma}_{\phi\phi} = [(R/r)^2 - 1]/2 \tag{16}$$

The equilibrium equation (2) becomes as follows:

$$\left(\frac{2}{r} + \frac{d}{dr}\right)\frac{\partial F}{\partial \bar{\gamma}_{rr}}\frac{dR}{dr} - \frac{R}{r^2}\frac{\partial F}{\partial \bar{\gamma}_{\theta\theta}} = 0 \tag{17}$$

or more concretely

$$\left(\frac{2}{r} + \frac{d}{dr}\right)\frac{\partial F}{\partial (dR/dr)} - \frac{\partial F}{\partial R} = 0 \tag{18}$$

Now, we employ the following variables (Bland [13], Craine [12]):

$$p = R/r, \quad q = dR/dr \tag{19}$$

With the aid of equation (19), equations (16) and (18) are rewritten as follows:

$$\bar{\gamma}_{rr} = (q^2 - 1)/2, \quad \bar{\gamma}_{\theta\theta} = \bar{\gamma}_{\phi\phi} = (p^2 - 1)/2 \tag{20}$$

$$\left(\frac{2}{r} + \frac{d}{dr}\right)\frac{\partial F}{\partial q} - \frac{1}{r}\frac{\partial F}{\partial p} = 0 \tag{21}$$

The first and second invariants of the strain tensors are explicitly expressed, for the present problem, as follows:

$$J_1 = (q^2 + 2p^2 - 3)/2, \quad J_2 = (p^2 - 1)(2q^2 + p^2 - 3)/4 \tag{22}$$

In consequence, by virtue of equations (19), (20), (22) and the expression of F, equation (11), we arrive at the following final equation for equilibrium:

$$\frac{2q}{r}\left[a_2\left\{1 + \frac{a_{11}}{a_2}(T - T_0)\right\}(p^2 - 1) + a_5\left\{1 + \frac{a_{13}}{a_5}(T - T_0)\right\}(q^2 + 2p^2 - 3) + a_8(T - T_0)\left\{1 + \frac{a_{10}}{a_8}(T - T_0)\right\}\right]$$
$$+ \frac{dq}{dr}\left[a_2\left\{1 + \frac{a_{11}}{a_2}(T - T_0)\right\}(p^2 - 1) + a_5\left\{1 + \frac{a_{13}}{a_5}(T - T_0)\right\}(3q^2 + 2p^2 - 3) + a_8(T - T_0)\left\{1 + \frac{a_{10}}{a_8}(T - T_0)\right\}\right]$$
$$+ q\frac{d(T - T_0)}{dr}\left[a_8\left\{1 + \frac{a_{10}}{a_8}(T - T_0)\right\} + a_{10}(T - T_0)\right. \tag{23}$$

Downloaded 01 May 2010 to 171.66.16.243. Redistribution subject to ASME license or copyright; see http://www.asme.org/terms/Terms_Use.cfm

$$+ a_{11}(p^2-1) + a_{13}(q^2+2p^2-3)\Big] + 2pq\frac{dp}{dr}$$
$$\times\left[a_2\left\{1+\frac{a_{11}}{a_2}(T-T_0)\right\} + 2a_5\left\{1+\frac{a_{13}}{a_5}(T-T_0)\right\}\right]$$
$$-\frac{p}{r}\left[a_2\left\{1+\frac{a_{11}}{a_2}(T-T_0)\right\}(q^2+p^2-2)\right.$$
$$+ 2a_5\left\{1+\frac{a_{13}}{a_5}(T-T_0)\right\}(q^2+2p^2-3)$$
$$\left.+ 2a_8(T-T_0)\left\{1+\frac{a_{10}}{a_2}(T-T_0)\right\}\right] = 0 \quad (23)$$

(*Cont.*)

Hollow Sphere

As an application, consider a stationary problem for a hollow sphere which is free from mechanical surface traction and body force except for thermal effect. Its inner and outer surfaces remain at each constant temperature.

Boundary conditions at the surfaces of sphere are that the physical radial component $\bar{L}_{rr}$ of the Lagrange stress tensor vanishes thereupon,

$$\bar{L}_{rr} = 0 \quad \text{at} \quad r = r_1 \quad \text{and} \quad r_2 \tag{24}$$

where r_1 and r_2 denote the inner and outer radii of the undeformed sphere. With the notation of equation (19), it becomes

$$\bar{L}_{rr} = \rho_0 \partial F/\partial q = 0 \tag{25}$$

which, by substitution of F, further reduces to

$$a_2\left[1+\frac{a_{11}}{a_2}(T-T_0)\right](p^2-1) + a_5\left[1+\frac{a_{13}}{a_5}(T-T_0)\right](q^2$$
$$+ 2p^2-3) + a_8(T-T_0)\left[1+\frac{a_{10}}{a_8}(T-T_0)\right] = 0 \quad (26)$$

In the uncoupled thermoelasticity problem, the thermal field can be determined independently of stress and deformation fields. The heat-conduction equation for a stationary thermal field in the Lagrange coordinate system is (Craine [12])

$$\frac{\partial}{\partial a_i}\left(K\frac{\partial T}{\partial a_i}\right) = 0 \tag{27}$$

where K is the thermal conductivity of material. For a spherically symmetric field referred to the spherical coordinate system, equation (27) is simplified to

$$\frac{1}{r^2}\frac{d}{dr}\left(r^2 K\frac{dT}{dr}\right) = 0 \tag{28}$$

The temperatures at the inner and outer surfaces of the sphere are specified at T_1 and T_2, respectively,

$$T = T_1 \quad \text{at} \quad r = r_1, \quad T = T_2\,(\simeq T_0) \quad \text{at} \quad r = r_2 \tag{29}$$

where T_2 is taken as the reference temperature T_0.

Since K varies also with temperature like μ and α, it is here expressed as follows:

$$K = K_0\,[1 + K_1(T-T_0)] \tag{30}$$

where K_0 is the magnitude of K at $T = T_0$. Substituting equation (30) into equation (28) and using equation (29), we obtain the following solution:

$$T - T_0 = \frac{1}{K_1}\left[-1 + \left\{1 - 2K_1(T_1-T_0)\right.\right.$$
$$\left.\left.\times\left[1+\frac{K_1}{2}(T_1-T_0)\right]\frac{r_1(r_2-r)}{r(r_1-r_2)}\right\}^{1/2}\right] \tag{31}$$

If $K_1 = 0$, the solution becomes

$$T - T_0 = (T_1 - T_0)\frac{r_1(r-r_2)}{r(r_1-r_2)} \tag{32}$$

The equilibrium equation (23) along with the defining equation of p and q, equation (19), may be regarded as a system of simultaneous nonlinear differential equation. Either p or q at the inner surface $r = r_1$ can be determined with the aid of the boundary condition (26) if we specify the value of one of them. The equilibrium equation (23) is integrated numerically from $r = r_1$ to $r = r_2$ by a forward integration scheme such as Runge-Kutta method. Trail-and-error procedure for the two-point boundary-value problem is continued repeatedly until the boundary condition at $r = r_2$ is satisfied sufficiently.

Numerical Example and Discussion

The material and geometrical parameters appearing in the foregoing fundamental formulation are as follows:

$$a_2 = -2\mu_0,\ a_5 = (\lambda_0 + 2\mu_0)/2,\ a_8 = -\alpha_0(3\lambda_0 + 2\mu_0),$$
$$a_{10}/a_8 = \mu_1 + \alpha_1,\ a_{11}/a_2 = \mu_1,\ a_{13}/a_5 = \mu_1 \quad \text{or} \quad 0,$$
$$K_1,\ \alpha_0 \quad \text{and} \quad r_2/r_1 \tag{33}$$

where a_7 and a_{12} are excluded in the thermal stress problem. Since the dimension of α_0 and the variational terms μ_1, α_1, and K_1 is [temperature]$^{-1}$ the values multiplied by the difference of the temperature at the inner and outer surfaces $T_1 - T_0\,(= t_0)$ are employed as their dimensionless values.

While in the previous chapters the Lagrange and Kirchhoff stress tensors were thoroughly utilized for convenience of the Lagrange formulation, calculations in the following are carried out for the Euler stress tensor σ_{ij}. The Euler stress tensor can be represented in the Cartesian coordinate system as follows:

$$\sigma_{ij} = \frac{\rho}{\rho_0}\frac{\partial x_j}{\partial a_k}L_{ik} \tag{34}$$

where ρ is the density of the deformed body. The physical components of the nonvanishing stresses in the spherical coordinate system are

$$\bar{\sigma}_{rr} = \rho_0\frac{\partial E}{\partial q}/p^2, \quad \bar{\sigma}_{\theta\theta} = \bar{\sigma}_{\phi\phi} = \rho_0\frac{\partial F}{\partial p}/2pq \tag{35}$$

Now we post as follows:

$$\nu = 1/3, \quad \text{i.e.,} \quad \lambda_0 = 2\mu_0,$$

$\alpha_0 t_0 = 0.002$ (corresponds to $\alpha_0 = 2\times10^{-5}$/deg C when $t_0 = 100$ deg C) together with illustrative magnitudes of the temperature-variational terms listed in Tables 1 and 2. Tables 1 and 2 correspond, respectively, to the calculation results of relatively thick ($r_2/r_1 = 1.5$) and thin ($r_2/r_1 = 1.125$) hollow spheres.

$L1$ to $L4$ are linear solutions and $F1$ to $F4$ and $F3'$ and $F4'$ are the finite solutions. $L1$ and $F1$ correspond to spheres exhibiting temperature-independent properties. $L2$ and $F2$ are solutions with temperature-dependent thermal conductivity, which directly affects thermal field T. When μ and α are functions of temperature, $L3$, $F3$, and $F3'$ are obtained. $L4$, $F4$, and $F4'$ are the most general solutions considering temperature-dependencies of the mechanical and thermal properties of material, μ, α, and K. Discrepancies due to the distinct formulations of F, i.e., with vanishing and nonvanishing coefficients, a_{13}, appear in disagreements between the solutions $F3$, $F4$ and $F3'$, $F4'$.

$F1$ and $F2$ are the solutions obtained earlier by Craine [12] and perfectly coincide with the present numerical solutions. The differences of distributions of stresses are calculated from the results shown in Tables 1 and 2. Since the magnitude of the radial stress is smaller than that of the circumferential stress the present problem for heated sphere, we mainly compare the solutions of the latter component which gains compressive and tensile maxima at the inner and outer surfaces, respectively. Their relative differences with reference to the linear solution $L1$ are shown in Table 3.

The solutions for two kinds of wall thickness, i.e., the ratio of radii $r_2/r_1 = 1.5$ and 1.125, do not offer distinct differences. As Craine pointed out, there are only slight differences between $F1$, $F2$, and $L1$, but the relative differences of $F3$, $F4$ considering the temperature-dependent material properties amount to 2 or 3 percent. If we take the solution $F4$ as the basis for the present problem, there is a conflict

Downloaded 01 May 2010 to 171.66.16.243. Redistribution subject to ASME license or copyright; see http://www.asme.org/terms/Terms_Use.cfm

Table 1 Comparison of solutions ($r_2/r_1 = 1.5$)

	Linear solutions				Finite solutions ($a_{13} \neq 0$)				Finite solutions ($a_{13} = 0$)	
Solution No.	L1	L2	L3	L4	F1	F2	F3	F4	F3'	F4'
$\mu_1 t_o$	0	0	-0.05	-0.05	0	0	-0.05	-0.05	-0.05	-0.05
$\alpha_1 t_o$	0	0	0.05	0.05	0	0	0.05	0.05	0.05	0.05
$K_1 t_o$	0	-0.025	0	-0.025	0	-0.025	0	-0.025	0	-0.025
$\bar{\sigma}_{rr}/2\mu_o \times 10^8$										
$r/r_1 = 1.0$	0	0	0	0	0	0	0	0	0	0
1.1	-32267	-32300	-32923	-32953	-32230	-32263	-32520	-32556	-30922	-30956
1.2	-39474	-39439	-40305	-40625	-39427	-39392	-40091	-40060	-38121	-38091
1.3	-32772	-32688	-33470	-33381	-32734	-32651	-33507	-33425	-31860	-31782
1.4	-18413	-18339	-18804	-18726	-18395	-18320	-18937	-18861	-18006	-17934
1.5	0	0	0	0	0	0	0	0	0	0
$\bar{\sigma}_{\theta\theta}/2\mu_o \times 10^7$										
$r/r_1 = 1.0$	-25263	-25343	-25742	-25820	-25718	-25252	-25167	-25242	-23933	-24009
1.1	-12741	-12718	-13018	-12993	-12715	-12692	-12979	-12958	-12342	-12322
1.2	- 3289	- 3244	- 3369	- 3323	- 3286	- 3241	- 3513	- 3467	- 3340	- 3297
1.3	4068	4091	4153	4177	4066	4090	4029	4054	3831	3833
1.4	9943	9921	10157	10133	9945	9923	10168	10147	9668	9647
1.5	14737	14657	15045	14962	14746	14666	15257	15175	14502	14428

Table 2 Comparison of solutions ($r_2/r_1 = 1.125$)

	Linear solutions				Finite solutions ($a_{13} \neq 0$)				Finite solutions ($a_{13} = 0$)	
Solution No.	L1	L2	L3	L4	F1	F2	F3	F4	F3'	F4'
$\mu_1 t_o$	0	0	-0.05	-0.05	0	0	-0.05	-0.05	-0.05	-0.05
$\alpha_1 t_o$	0	0	0.05	0.05	0	0	0.05	0.05	0.05	0.05
$K_1 t_o$	0	-0.025	0	-0.025	0	-0.025	0	-0.025	0	-0.025
$\bar{\sigma}_{rr}/2\mu_o \times 10^8$										
$r/r_1 = 1.000$	0	0	0	0	0	0	0	0	0	0
1.025	- 8142	- 8159	- 8320	- 8336	- 8133	- 8150	- 8166	- 8184	- 7766	- 7783
1.050	-11544	-11547	-11804	-11806	-11531	-11535	-11662	-11667	-11090	-11095
1.075	-10929	-10912	-11178	-11162	-10916	-10901	-11114	-11100	-10569	-10556
1.100	- 6905	- 6885	- 7066	- 7044	- 6898	- 6878	- 7069	- 7049	- 6723	- 6703
1.125	0	0	0	0	0	0	0	0	0	0
$\bar{\sigma}_{\theta\theta}/2\mu_o \times 10^7$										
$r/r_1 = 1.100$	-21567	-21651	-22019	-22102	-21500	-21583	-21423	-21506	-20375	-20452
1.025	-12379	-12375	-12663	-12657	-12352	-12348	-12525	-12523	-11912	-11909
1.050	- 3847	- 3806	- 3947	- 3905	- 3842	- 3801	- 4056	- 4016	- 3857	- 3819
1.075	4096	4129	4181	4215	4094	4127	4009	4044	3813	3846
1.100	11506	11495	11771	11759	11508	11498	11696	11687	11122	11113
1.125	18433	18349	18864	18777	18449	18365	19026	18940	18091	18009

Table 3 Relative difference of solutions with respect to *L*1 (percent)

		Linear solutions			Finite solutions ($a_{13} \neq 0$)				Finite solutions ($a_{13} = 0$)	
Solution No.		L2	13	L4	F1	F2	F3	F4	F3'	F4'
$r_2/r_1 = 1.5$	$(\bar{\sigma}_{\theta\theta}/2\mu_o)_{r/r_1 = 1.0}$	0.3	1.9	2.2	-0.3	-0.0	-0.4	-0.1	-5.3	-5.0
	$(\bar{\sigma}_{\theta\theta}/2\mu_o)_{r/r_1 = 1.5}$	-0.5	2.1	1.5	0.1	-0.5	3.5	2.9	-1.6	-2.1
$r_2/r_1 = 1.125$	$(\bar{\sigma}_{\theta\theta}/2\mu_o)_{r/r_1 = 1.0}$	0.4	2.1	2.5	-0.3	0.1	-0.7	-0.3	-5.5	-5.2
	$(\bar{\sigma}_{\theta\theta}/2\mu_o)_{r/r_1 = 1..25}$	-0.5	2.3	1.9	0.1	-0.4	3.2	2.8	-1.9	-2.3

Downloaded 01 May 2010 to 171.66.16.243. Redistribution subject to ASME license or copyright; see http://www.asme.org/terms/Terms_Use.cfm

in that $L4$, taking consideration of the temperature-dependent effect of the material properties in the framework of the classical linear elasticity, is hardly more rigorous than the simplest linear solution $L1$. The finite solutions with $a_{13} = 0$ present somewhat detectable contrast to the linear solutions and to the finite solutions with $a_{13} \neq 0$, but as a whole, the difference due to the distinct formulations for the free energy F is not pronounced.

Summary

As an initial attempt, the finite thermoelastic problem of a heated sphere exhibiting temperature-dependent mechanical and thermal properties was analyzed with aid of the Lagrange coordinate formulation. The Lamé two elastic parameters, thermal expansion coefficient, and thermal conductivity were thought to vary linearly with temperature for a relatively narrow temperature range. Two types of the free energy expression with and without the condition due to Dillon were considered.

According to the results of numerical solutions for a simple example, the following were concluded:

1 The temperature-dependence of mechanical and thermal properties has only a slight effect on the stress state and the inclusion of finite deformations does not significantly alter the classical linear elastic solution.

2 If the Dillon's condition is introduced into the free energy expression in the present finite thermoelasticity problem, a somewhat different solution is obtained, but the difference due to the distinct formulation is also insignificant from the practical point of view.

The present problem is confined within the linear elastic behavior of material, but the method of analysis can be extended to problems of finite thermal deformations with inelastic strains, such as plastic or nonlinear elastic deformations. The effect of the temperature-dependence may alter with variations of specified boundary conditions and temperature distributions, which should be clarified in the future studies.

Acknowledgment

The author expresses his thanks to the associate editor Dr. D. S. Griffin and the reviewers for their valuable comments and suggestions.

References

1 Nowinski, J., "Thermal Stresses in a Thick-Walled Cylinder With Variable Elastic Properties (in Polish)," *Archiwum Mechaniki Stoswanej*, Vol. 5, 1953, p. 629.

2 Nowinski, J., "Thermoelastic Problem for an Isotropic Sphere With Temperature Dependent Properties," *Zeitschrift für angewandte Mathematik und Physik*, Vol. 10, 1959, pp. 565–575.

3 Chang, C. C., and Chu, W. H., "Stresses in a Metal Tube Under Both High Radial Temperature Variation," ASME JOURNAL OF APPLIED MECHANICS, Vol. 21, 1954, pp. 101–108.

4 Trostel, R., "Wärmespannungen in Hohlzylindern mit temperaturabhängigen Stoffwerten," *Ingenieur-Archiv*, Vol. 26, 1958, pp. 134–142.

5 Trostel, R., "Wärmespannungen mit temperaturabhängigen Stoffwerten," *Ingenieur-Archiv*, Vol. 26, 1958, pp. 416–432.

6 Stanisic, M. M., and McKinley, R. M., "The Steady-State Thermal Stress Field in an Isotropic Sphere With Temperature-Dependent Properties," *Ingenieur-Archiv*, Vol. 31, 1962, pp. 241–249.

7 Nyuko, N., Takeuti, Y., and Noda, N., "Stationary Thermal Stresses for a Composite Hollow Sphere Exhibiting Temperature-Dependent Properties (in Japanese)," *Transactions of the Japan Society of Mechanical Engineers*, Vol. 44, 1978, pp. 1454–1460.

8 Nowinski, J., "Transient Thermoelastic Problem for an Infinite Medium With a Spherical Cavity Exhibiting Temperature-Dependent Properties," ASME JOURNAL OF APPLIED MECHANICS, Vol. 29, 1962, pp. 399–407.

9 Koizumi, T., and Taniwaki, T., "Thermal Stresses in a Long Solid Cylinder With Temperature-Dependent Properties (in Japanese)," *Transactions of the Japan Society of Mechanical Engineers*, Vol. 31, 1965, pp. 9–15.

10 Hata, T., and Atsumi, A., "Transient Thermoelastic Problem for an Orthotropic Hollow Cylinder With Temperature-Dependent Properties," *Bulletin of the Japan Society of Mechanical Engineers*, Vol. 11, 1968, pp. 404–410.

11 Hata, T., and Atsumi, A., "Transient Thermoelastic Problem for a Transversely Anisotropic Hollow Sphere With Temperature-Dependent Properties," *Bulletin of the Japan Society of Mechanical Engineers*, Vol. 12, 1969, pp. 445–451.

12 Craine, R. E., "Spherically Symmetric Problem in Finite Thermoelastostatics," *Quarterly Journal of Mechanics and Applied Mathematics*, Vol. 21, Part 3, 1968, pp. 279–291.

13 Bland, D. R., *Nonlinear Dynamic Elasticity*, Blaisdel Publishing Company, Waltham, Mass., 1968.

14 Dillon, O. W., "A Nonlinear Thermoelasticity," *Journal of Mechanics and Physics of Solids*, Vol. 10, 1962, pp. 123–131.

15 Oden, J. T., *Finite Elements of Nonlinear Continua*, McGraw-Hill, New York, 1972.

16 Bland, D. R., "Dilatational Waves and Shocks in Large Displacement Isentropic Dynamic Elasticity," *Journal of Mechanics and Physics of Solids*, Vol. 12, 1964, pp. 245–267.

17 Bland, D. R., "*Lagrange's Equations for Finite Elasticity*," *Recent Progress in Applied Mechanics, The Folke Odqvist Volume*, Broberg, B., Hult, J., and Niordson, F., eds., Almqvist and Wiksel, Stockholm/John Wiley & Sons, New York, London, Sydney, 1967, pp. 91–124.

Downloaded 01 May 2010 to 171.66.16.243. Redistribution subject to ASME license or copyright; see http://www.asme.org/terms/Terms_Use.cfm

Z. Hashin[2]

Professor and Chairman,
Department of Solid Mechanics,
Materials, and Structures,
Tel Aviv University,
Tel Aviv, Israel
Fellow ASME

A Reinterpretation of the Palmgren-Miner Rule for Fatigue Life Prediction[1]

It is shown that the simple Palmgren-Miner linear cumulative damage rule is a special case of a general cumulative damage theory previously established. Predictions of lifetimes for families of multistage loadings according to the Palmgren-Miner rule and the general cumulative damage theory are compared with the aim of arriving at qualitative guidelines for applicability of the Palmgren-Miner rule in cyclic loading programs.

1 Introduction

The simplest and most well-known assumption for determination of fatigue lifetime under variable amplitude cyclic loading is due to Palmgren [1] and Miner [2]. Mathematically it is expressed by the statement

$$\sum^{k} \frac{n_k}{N(\sigma_k)} = 1 \tag{1}$$

where the amplitudes of cycling are piecewise constant with kth amplitude σ_k, and number of cycles n_k, and $N(\sigma_k)$ is the lifetime for constant amplitude σ_k cycling.

Equation (1) is easily interpreted for the case where the cyclic amplitude is a continuous function $\sigma(\bar{n})$ of the number of elapsed cycles $\bar{n}$. In that case (1) becomes

$$\int_{\sigma_0}^{\sigma_u} \frac{d\bar{n}(\sigma)}{N(\sigma)} = 1 \tag{2}$$

where $\bar{n}(\sigma)$ is the inverse of $\sigma(\bar{n})$, σ_0 is the initial amplitude and σ_u is the amplitude at failure. The lifetime $\bar{n}_u$ is then given by

$$\bar{n}_u = \bar{n}(\sigma_u) \tag{3}$$

provided that (3) is a single-valued function.

In the following the assumption (1) shall be referred to as the PM rule. It has first been stated in [1] and has been reintroduced in [2] on the basis of some physical assumptions. Other interpretations in terms of assumed crack growth regimes have been given in the literature; see, e.g., [3]. The chief criticisms of (1) are that it ignores sequence of loading effects and that the only material information used is the S-N curve, thus fatigue failure information under constant amplitude only. However, the PM rule does agree with experimental data in certain cases but is also very inaccurate in others.

It is the purpose of the present work to show that (1) is a very special case of a general theory of fatigue lifetime prediction, i.e., cumulative damage theory, and to examine some resulting consequences.

It should, however, be emphasized that the theories of cumulative damage here considered are of deterministic nature. In comparison of the results of such theories to the usual significantly scattered test results there arises the fundamental question: What is the experimental interpretation of a deterministically predicted lifetime? Is it the average of the scattered lifetimes under identical cyclic loading programs or is it some other associated statistical parameter? To the writer's knowledge a satisfactory answer to these questions is not available.

2 Resumé of Cumulative Damage Theory

For present purposes it is necessary to give a brief summary of the cumulative damage theory developed in [4] for prediction of fatigue lifetime under general cyclic loading programs.

It is assumed that there is available a family of "identical" specimens. Each of these specimens is cycled to failure in a two stage loading. The first stages of all of the two stage loadings are identically n_1 cycles at stress amplitude σ_1. The second stages are at different amplitudes σ_j with residual lifetimes $n_j{}^r$. The $n_j{}^r$ are plotted starting from the S-N curve of the material horizontally to the left at ordinates σ_j. The resulting locus is defined as the *damage curve* through n_1, σ_1, Fig. 1.

The following properties of damage curves have been established in [4]:

1 A damage curve is uniquely defined by one of its points. This is based on an equivalent loading postulate which will be explained further.

2 All damage curves pass through the static ultimate point 0, σ_s.

3 Damage curves do not intersect the n or σ-axes, except at 0, σ_s.

[1] Supported by the Naval Air Systems Command, Washington, D. C., and the Office of Naval Research, Structural Mechanics Branch, Arlington, Va., under Contract N00014-70-C-0544 with the University of Pennsylvania.

[2] Also, Adjunct Professor of Engineering and Applied Science, University of Pennsylvania, Philadelphia, Pa. 19104.

Contributed by the Applied Mechanics Division for publication in the JOURNAL OF APPLIED MECHANICS.

Discussion on this paper should be addressed to the Editorial Department, ASME, United Engineering Center, 345 East 47th Street, New York, N. Y. 10017, and will be accepted until September 1, 1980. Readers who need more time to prepare a discussion should request an extension from the Editorial Department. Manuscript received by ASME Applied Mechanics Division, April, 1979; final revision, August, 1979.

Copyright © 1980 by ASME

Downloaded 01 May 2010 to 171.66.16.243. Redistribution subject to ASME license or copyright; see http://www.asme.org/terms/Terms_Use.cfm

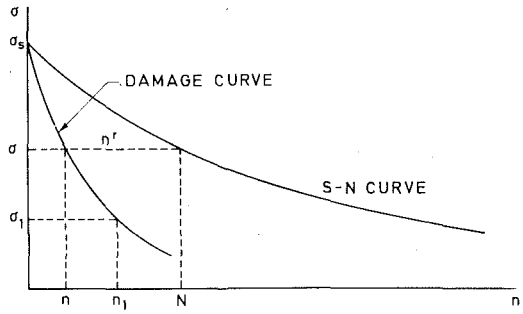

Fig. 1 Damage curve

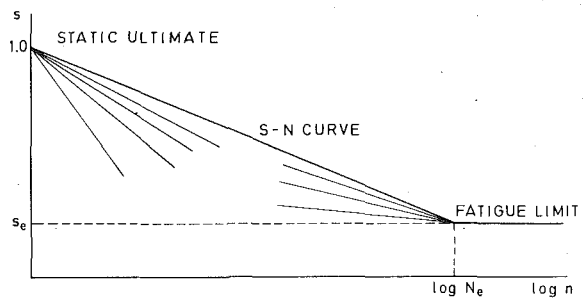

Fig. 2 Linear damage curves; semilog

4 Damage curves do not intersect (if the material is such that additional cycling reduces the residual lifetime) except at static ultimate point and fatigue limit.

It is thus seen that the damage curves form a family of curves which cover the region bounded by the n,σ-axes and the S-N curve. The actual shape of the damage curves is not known. But since the S-N curve is a special case of the damage curves (one stage loading; residual lifetime in second stage vanishes) it is perhaps not unreasonable to assume that the damage curves are expressed by a similar mathematical form as the S-N curve, [4]. Thus, if the S-N curve is represented as

$$s = f(\Gamma, n) \tag{4}$$

where s is nondimensional stress σ/σ_s and Γ is a curve fitting parameter, then the damage curves are represented by the one-parameter family

$$s = f(\gamma, n) \tag{5}$$

where γ is a parameter which changes from curve to curve. It is of course possible to represent damage curves by a family with more than one parameter.

Many S-N curves can be adequately represented by straight lines in semilog or log-log coordinates. Thus

$$s = 1 + \Gamma \log n \qquad \text{semilog} \tag{6a}$$

$$\log s = \Gamma \log n \qquad \text{log-log} \tag{6b}$$

In that case it follows from (5) that the damage curve families have the forms

$$s = 1 + \gamma \log n \tag{7a}$$

$$\log s = \gamma \log n \tag{7b}$$

where γ is determined by the coordinates of any point on the damage curve.

The behavior of the damage curves in the neighborhood of a fatigue limit is not clear at the present time. Let the fatigue limit stress be denoted σ_e and consider two stage loadings with first stage $\sigma_1 > \sigma_e$ for n_1 cycles and second stage σ_e. If a specimen is cycled at constant level σ_e the lifetime will, by definition of the fatigue limit, be infinite (that is, longer than maximum acceptable cycling time). For the two stage loading described it is quite possible to have finite lifetime at σ_e which is more over a decreasing function of σ_1 and n_1. It is also reasonable to assume that for any high-low two stage loading, with first stage σ_1 for n_1 cycles, there will exist a fatigue limit $\bar{\sigma}_e(\sigma_1, n_1)$ which is a decreasing function of σ_1 and n_1. If there is made the simplifying assumption that $\bar{\sigma}_e \sim \sigma_e$ then all damage curves which represent the two stage loading just described must terminate at stress level σ_e. If the S-N curve is a straight line in semilog or log-log coordinates, the fatigue limit is represented by a break in the S-N straight line, Fig. 2. If the damage curves are assumed linear in semilog or log-log representation then they must converge into the fatigue limit point $n = N_e$; $s_e = \sigma_e/\sigma_s$, Fig. 2. The equations of these straight lines are given by

$$s - s_e = \gamma \log\left(\frac{n}{N_e}\right) \qquad \text{semilog} \tag{8a}$$

$$\log(s/s_e) = \gamma \log\left(\frac{n}{N_e}\right) \qquad \text{log-log} \tag{8b}$$

It is to be expected that (7) will approximate the damage curves in the neighborhood of the static ultimate point $n = 0$; $s = 1$ while (8) will approximate them in the neighborhood of the fatigue limit. It is of course possible to construct nonlinear damage curves which will be tangent to the two sets of straight lines at static ultimate and fatigue limit but this subject will not be considered here.

The damage curves determine, by definition, lifetimes under all two stage loadings. It has been shown in [4] that lifetime under any cyclic loading program can be determined on the basis of the damage curves if it is assumed that specimens obey an *equivalent loading postulate*. To explain this postulate it is first necessary to define equivalent cyclic loadings: Consider any variable amplitude loading program which terminates before failure occurs. Subsequently, the specimen is subjected to constant amplitude cycling-to-failure at some stress level, s_1. The residual lifetime under s_1 cycling is $n^r(s_1)$. Among the infinity of possible loading programs there must necessarily be some which have the same $n^r(s_1)$. Such loading programs are defined as equivalent cyclic loadings with respect to s_1. In conventional terms, equivalent loading means that specimens have "suffered the same amount of damage." This vague statement has, here, been precisely expressed in terms of equal residual lifetime under subsequent constant amplitude loading.

Since the stress level, s_1, is arbitrary it is reasonable to believe that if the subsequent constant amplitude is s instead of s_1, residual lifetimes will be the same $n^r(s) \neq n^r(s_1)$ for the cyclic loading programs equivalent with respect to s_1. Hence the *equivalent loading postulate* is stated as: *cyclic loadings which are equivalent for one stress level are equivalent for all stress levels.*

This postulate is schematically illustrated in Fig. 3. The plots show variations of nondimensional amplitude of cyclic loadings. The loadings are equivalent for amplitude s_1 since $n_1{}^r(s_1)$ are the same. The equivalent loading postulate then asserts that they are equivalent for s_2 implying that $n_2{}^r$ are the same and similarly for any other constant s cycling.

Residual lifetimes in two stage loadings are determined by the damage curves, in view of their definition. For a piecewise constant amplitude (multistage) loading the analysis procedure for residual lifetime is shown in Fig. 4. First loading stage, n_1 cycles at s_1 amplitude, is traced in the S-N plane by the horizontal segment n_1 at s_1. For next stage, n_2 cycles at s_2 amplitude, proceed on damage curve through n_1,s_1 until level s_2 and then advance n_2 horizontally. This is repeated for the various loading stages until the S-N curve is reached. The sum of the $n_1, n_2, \ldots$ then defines the lifetime under the multistage loading program.

Now let the cyclic loading have a continuously variable amplitude defined by

$$s = s(\bar{n}) \tag{9}$$
$$\bar{n} = \bar{n}(s)$$

Downloaded 01 May 2010 to 171.66.16.243. Redistribution subject to ASME license or copyright; see http://www.asme.org/terms/Terms_Use.cfm

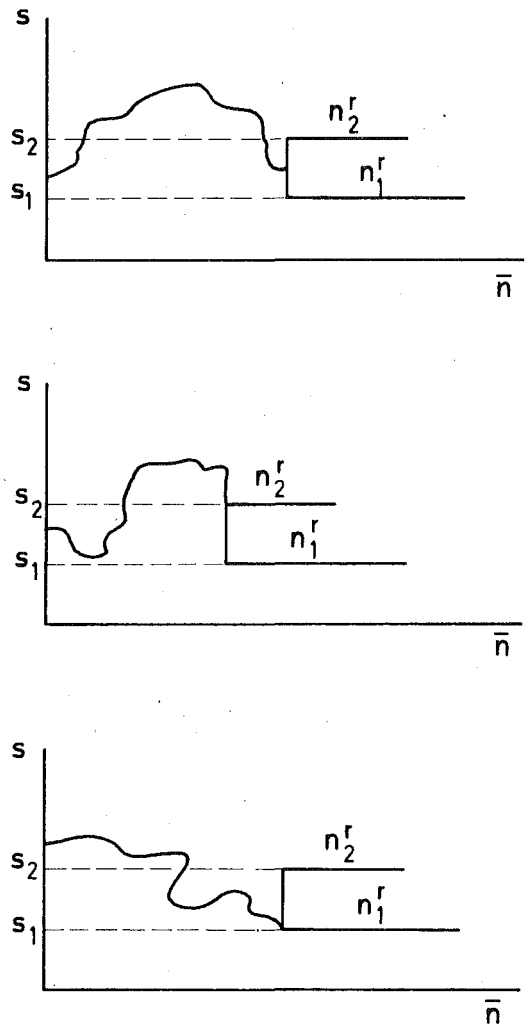

Fig. 3 Equivalent loading postulate

The damage curve equation (5) is written in the alternative forms

$$n = g(\gamma, s) \qquad (10)$$
$$\gamma = \gamma(n, s)$$

In order to find the amplitude s_u at which failure occurs under the cyclic loading (9) it is necessary to solve the differential equation

$$\frac{dn}{ds} = \frac{\partial(\gamma, s)}{\partial s}\bigg|_{\gamma=\gamma(n,s)} + \frac{d\bar{n}}{ds} \qquad (11)$$

with initial condition

$$s(0) = s_0 \qquad (12)$$

where s_0 is the initial amplitude of (9). The solution of (11) defines a curve $s(n)$ in the s-n plane which intersects the S-N curve at failure amplitude s_u. The lifetime $\bar{n}_u$ is then given from (9b) by

$$\bar{n}_u = \bar{n}(s_u) \qquad (13)$$

All of this presupposes that (9) are single-valued functions. If this is not the case the multivalued function must be separated into single-valued branches and the integrations must be carried out separately and successively for the various branches.

Various cases of multistage and continuous cyclic loadings have been treated in [4] on the basis of the damage curves (7) and (8).

3 Palmgren-Miner Cumulative Damage

The PM assumption will now be examined on the basis of the general cumulative damage theory summarized above. To construct the damage curves let a specimen be subjected to a two stage loading n_1 cycles at amplitude s_1 and then n^r cycles to failure at amplitude s. According to the PM assumption

$$\frac{n_1}{N_1} + \frac{n^r}{N} = 1 \qquad (14)$$

and from Fig. 1

$$n^r = N - n \qquad (15)$$

Combination of (14) and (15) yields

$$\frac{n}{N} = \frac{n_1}{N_1} = \text{const} = \gamma \qquad (16)$$

Thus the equation of the damage curves is

$$n(s) = \gamma\, N(s) \qquad 0 \le \gamma \le 1 \qquad (17)$$

where $N(s)$ is the equation of the S-N curve, $\gamma = 1$ corresponds to the S-N curve and $\gamma = 0$ corresponds to the s-axis. The value of γ for any damage curve is determined in terms of the coordinates of a point through which it passes by (16).

Two stage loadings do not in general obey the PM assumption. The following trends have been observed in metal fatigue

$$\frac{n_1}{N_1} + \frac{n_2}{N_2}\begin{cases} > 1 & \text{when } s_1 < s_2 \quad \text{Low-High} \\ < 1 & \text{when } s_1 > s_2 \quad \text{High-Low} \end{cases} \qquad (18)$$

The condition (18) has interesting implications for the damage curves. Writing the left side of (18) in terms of the substitution (15) for n_2 it follows at once that

$$\frac{n(s_L)}{N(s_L)} > \frac{n(s_H)}{N(s_H)} \qquad (19)$$

where L and H indicate lower and higher stress, respectively. In words: the necessary and sufficient condition to fulfill (18) is for $n(s)/N(s)$ to be a monotonically decreasing function of s. In differential form

$$\frac{d}{ds}\frac{n(s)}{N(s)} < 0$$

which can be reduced to

$$\frac{d}{ds}[\log n(s)] < \frac{d}{ds}[\log N(s)] \qquad (20)$$

If the inequalities (18) are reversed, which has been found to be the case in some fiber composite testing, then the inequalities (19) and (20) also reverse. Equations (19) and (20) become equalities if, and only if, the PM assumption is valid. It is easily seen that the logarithmic linear damage curves (7) obey inequalities in the opposite sense to (18) and while the other kind, which converge into the fatigue limit, obey (18). Indeed it has been found, [4], that two stage fatigue life tests for steel are in good agreement with predictions based on (8).

Next the case of multistage loadings is considered. Referring to Fig. 4 the damage curves needed are numbered consecutively. The abscissa of a point with ordinate s_j on the ith damage curve will be denoted n_{ij}. Suppose the loading consists of the three stages n_1 cycles at amplitude s_1, n_2 at s_2 and n_3 to failure at s_3. It is required to find n_3. The procedure is indicated in Fig. 4. The equation of damage curve 1 is

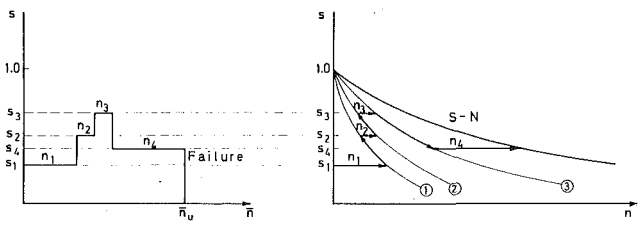

Fig. 4 Analysis of multistage loading

Downloaded 01 May 2010 to 171.66.16.243. Redistribution subject to ASME license or copyright; see http://www.asme.org/terms/Terms_Use.cfm

$$\frac{n}{N} = \frac{n_1}{N_1}$$

It follows that

$$n_{12} = \frac{n_1}{N_1} N(s_2) = \frac{n_1}{N_1} N_2 \quad n_{22} = \frac{n_1}{N_1} N_2 + n_2$$

The equation of damage curve 2 is

$$\frac{n}{N} = \frac{n_{22}}{N_2}$$

It follows that

$$n_{23} = \frac{n_{22}}{N_2} N(s_3) = \frac{n_{22}}{N_2} N_3 \quad n_{33} = n_{23} + n_3$$

Failure at amplitude s_3 cycling occurs when the S-N curve is reached at that level, i.e., when

$$n_{33} = N_3 \tag{21}$$

Combining (21) with the preceding relations it follows easily that

$$\frac{n_1}{N_1} + \frac{n_2}{N_2} + \frac{n_3}{N_3} = 1$$

which is the PM assumption for a three stage loading. It is not difficult to show (by induction) that by this procedure failure in a general multistage loading will be predicted by (1).

It should be carefully noted that the PM assumption has been here adopted only for two stage loadings, whereby the form of the damage curves was determined. The procedure for multistage loading analysis in terms of the damage curves is based on the equivalent loading postulate which refers to any damage curves.

The case of continuous amplitude variation is governed by the differential equation (12). Analytical integration of this equation does not seem feasible in general. Even with the simple damage curves (7) integration could only be carried out numerically, [4]. The situation is however different in the case of the PM damage curves (17). In the present case (10) are given by (17) and (16). It follows that (11) assumes the form

$$\frac{dn}{ds} = \frac{nN'(s)}{N(s)} + \bar{n}'(s) \tag{22}$$

where a prime denotes differentiation. It is easily verified that the solution of (22) is

$$n(s) = N(s) \int_{s_0}^{s} \frac{\bar{n}'(\alpha) d\alpha}{N(\alpha)} \tag{23}$$

Failure is defined by the intersection of $n(s)$ with the S-N curve $N(s)$, i.e., when $n(s) = N(s)$. Thus, for failure,

$$\int_{s_0}^{s_u} \frac{\bar{n}'(\alpha) d\alpha}{N(\alpha)} = 1 \tag{24}$$

It is easily seen that (24) is the same as (2), the continuous amplitude variation version of the PM assumption.

The left sides of (1) and (2) may be termed the PM coefficient. Recall the inequalities (18) for this coefficient for two stage loading and their relations (19) and (20) to the damage curves. It is not difficult to show that (19) and (20) also imply that the general PM coefficient obeys inequalities (18) and also reversed inequalities (19) and (20) for reversed inequalities (18).

Experience accumulated over many years has shown that the PM rule sometimes predicts fatigue life with sufficient engineering accuracy while at other times it is very much in error. To the writer's knowledge no criteria for acceptability or inacceptibility of this rule are available.

In the course of present research, concerning the new cumulative damage theory, fatigue life predictions have been performed for various cyclic loadings on the basis of assumed linear damage curves (7) and (8). It has been found that (8) are more appropriate for metals. For two stage loadings there results the simple formula

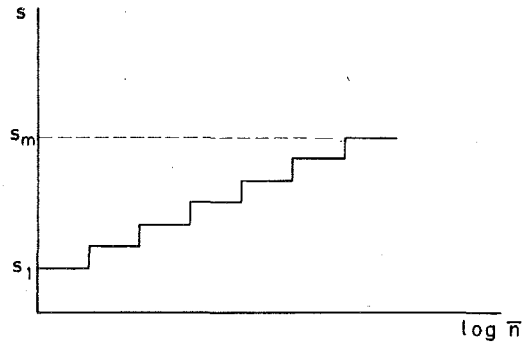

Fig. 5 Ascending staircase loading

$$\left(\frac{n_1}{N_1}\right)^{log\ (N_2/N_e)/log\ (N_1/N_e)} + \frac{n_2}{N_2} = 1 \tag{25}$$

where N_e is lifetime at s_e, the fatigue limit, as determined by the S-N curve. It has been found [4] that (25) is in much better agreement with steel test data than the PM rule.

It is of considerable interest to have some general assessment of the expected differences between lifetime prediction as given by the PM rule and the much more general cumulative damage theory of [4]. While such general assessment is not available at the present time the following example will perhaps serve to establish trends.

Consider a multistage loading program composed of m stages, n_k-cycles at amplitude s_k. The amplitudes increase or decrease monotonically in the interval from initial value s_1 to final value s_m, Fig. 5.

A procedure for lifetime prediction under multistage loading has been given in [4]. This will here be summarized in a modified form. Define the recurrence relations

$$\mu_1 = \frac{n_1}{N_1}$$

$$\mu_2 = \mu_1^{\phi_2/\phi_1} + \frac{n_2}{N_2}$$

$$\mu_k = \mu_{k-1}^{\phi_k/\phi_{k-1}} + \frac{n_k}{N_k} \tag{26}$$

where

n_k = the number of cycles with amplitude s_k in kth stage
$N_k = N(s_k)$ = lifetime at s_k from S-N curve
ϕ_k = functions of stress amplitude defined by the form of damage curves

Then failure is predicted by

$$\mu_k = 1 \tag{27}$$

Choosing the damage curves in the form (8a), that is semilog linear through fatigue limit, the functions ϕ_k assume the form

$$\phi_k = s_k - s_e \tag{28}$$

It is noted in passing that for damage curves (8b)

$$\phi_k = log\ (s_k/s_e) \tag{29}$$

If s_k in (28) and (29) are expressed in terms of N_k from the S-N curves (6) then in both cases

$$\frac{\phi_k}{\phi_{k-1}} = \frac{log\ (N_k/N_e)}{\log\ (N_{k-1}/N_e)} \tag{30}$$

Equation (25) for two stage loading is a special case of (26) with (30).

It is easily seen that the PM rule is obtained as a special case of (26) and (27) when ϕ_k = constant.

Downloaded 01 May 2010 to 171.66.16.243. Redistribution subject to ASME license or copyright; see http://www.asme.org/terms/Terms_Use.cfm

Numerical computations have been carried out for ascending stair case loadings and their descending reverses, with initial and final amplitudes

$$s_1 = 0.3 \qquad s_m = 0.7$$
$$s_1 = 0.7 \qquad s_m = 0.3$$

In all cases

$$s_e = 0.2 \qquad \Gamma = -0.1$$

where Γ refers to S-N curve (6a), and

$$s_k - s_{k-1} = \Delta s = \text{const} = \frac{s_m - s_1}{m} \tag{31}$$

In the first set of computations it was assumed that $n_k = n$ = constant. If a number of stages m is chosen the number of cycles n per stage then becomes the unknown to be determined from (26)–(28). It was found that for these cases the predictions agreed closely with the PM rule. Therefore, introducing (31) into (1), a good approximation is

$$n_u = 1 \Big/ \sum_{k=1}^{k=m} \frac{1}{N_k} \tag{32}$$

In the second set of computations it was assumed that

$$n_k = \beta N_k \tag{33}$$

where β = constant. In this case the unknown for given number of stages is β, which is found numerically by satisfaction of (27). Once β is known the lifetime under given program is the sum of βN_k over all stress values.

The results of the computations are shown in Fig. 6 as ratio of lifetime defined by (33) to lifetime predicted by the PM rule. Note that according to the latter

$$\beta_{\text{PM}} = \frac{1}{m}$$

It easily follows that the ratio plotted in Fig. 6 is simply

$$\frac{\beta}{\beta_{\text{PM}}} = m\beta$$

It is seen that there is substantial disagreement with prediction by the PM rule. Also loading sequence reversal produces substantial changes in lifetime as is seen by the difference between ascending and descending loading program lifetimes.

The differences in agreement with the PM rule in the different loadings are not difficult to explain. In the first case the number of cycles is the same for each stress level. Therefore the damage produced at different stress levels is significant only for the high stress levels. Roughly speaking the loading is equivalent to constant cycling for a certain number of cycles at max stress level of the loading. However for such (constant amplitude) loading the PM rule is (trivially) valid.

In the second kind of loading the damages done at each stress level are of similar magnitudes since the number of cycles in each stage is proportional to the lifetime at the stage stress level. Thus there is no reason to expect validity of the PM rule.

On the basis of the foregoing it may be speculated that the PM rule will be adequate when the most of the "damage" is done at roughly the same stress level. For a rough assessment the PM coefficient (1) or (2) may be computed. If in (1) one of the terms is dominant (larger than 0.9, say) or if in (2) the major contribution to the integral comes from a narrow stress band then it may be surmised that the PM rule would be an adequate approximation.

4 Conclusion

It has been shown that the well-known Palmgren-Miner linear cumulative damage rule is a special case of a general cumulative damage theory. In this respect it should be noted that according to present development it is necessary to assume validity of the PM rule only for two stage loadings. Its validity for multistage loadings then follows from a general equivalent loading postulate which is assumed valid for any cumulative damage theory.

It has been shown by means of numerical examples that there are classes of multistage loadings for which the general cumulative damage theory and the PM rule are in close agreement while substantial disagreement is found for others.

It must be emphasized again that all theories included here are phenomenological and deterministic. The fit of any such theory to test data is obscured by the significant scatter observed. It is therefore most important to generalize the theory developed so as to take into account the scatter of lifetime test data.

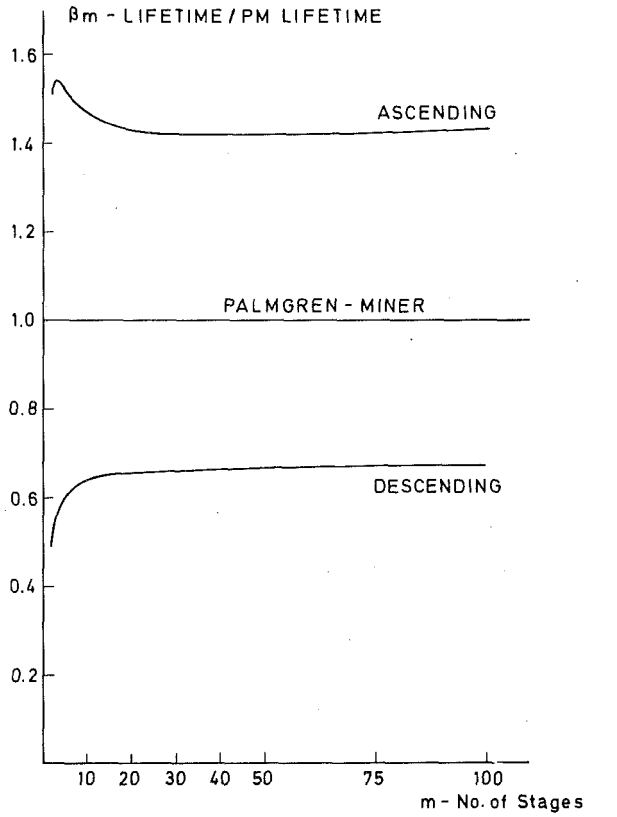

Fig. 6 Lifetimes for staircase loading programs: comparison with Palmgren-Miner prediction

Acknowledgment

It is a pleasure to acknowledge helpful and stimulating discussions with Dr. Campbell Laird.

References

1 Palmgren, A. Z., "Die Lebensdauer von Kugellagern," *Zeitschrift des Verein Deutscher Ingenieure,* Vol. 68, 1924, pp. 339–341.

2 Miner, M. A., "Cumulative Damage in Fatigue," ASME JOURNAL OF APPLIED MECHANICS, Vol. 12, 1945, pp. A159–A164.

3 Frost, N. E., Marsh, K. J., and Pook, L. P., *Metal Fatigue,* Chapter 6, Oxford University Press, 1974.

4 Hashin, Z., and Rotem, A., "A Cumulative Damage Theory of Fatigue Failure," *Materials Science and Engineering,* Vol. 34, 1978, pp. 147–160.

Downloaded 01 May 2010 to 171.66.16.243. Redistribution subject to ASME license or copyright; see http://www.asme.org/terms/Terms_Use.cfm

Z. Hashin[2]

Professor and Chairman,
Department of Solid Mechanics,
Materials, and Structures,
Tel Aviv University,
Tel Aviv, Israel
Fellow ASME

Failure Criteria for Unidirectional Fiber Composites[1]

Three-dimensional failure criteria of unidirectional fiber composites are established in terms of quadratic stress polynomials which are expressed in terms of the transversely isotropic invariants of the applied average stress state. Four distinct failure modes—tensile and compressive fiber and matrix modes—are modeled separately, resulting in a piecewise smooth failure surface.

1 Introduction

One of the outstanding problems in the analysis of mechanical properties of fiber composites is the prediction of failure due to a specified state of stress. The microstructural aspects of failure are of such complexity that there is little hope of resolution of this problem on the basis of micromechanics methods. Such methods would require analytical detection of successive microfailures in terms of microstress analysis and microfailure criteria and prediction of the coalescence of some of them to form macrofailures which is an intractable task.

A more hopeful approach is to assume the existence of a three-dimensional failure criterion in terms of macrovariables, such as average stresses or strains. A convenient mathematical representation of such criteria is in terms of polynomials. It is then necessary to determine the coefficients of the polynomial in terms of test results which can be conveniently obtained in the laboratory, such as uniaxial tension or compression, pure shear, etc.

The problem in this sense is superficially reminiscent of that of the construction of an initial yield criterion for an elasto-plastic material. Indeed, in one of the first contributions to the subject Tsai [1] assumed that the failure criterion of a unidirectional fiber composite has the same mathematical form as the yield criterion of an orthotropic ideally plastic material as given by Hill [2] in the form

$$A(\sigma_{11}-\sigma_{22})^2+B(\sigma_{22}-\sigma_{33})^2+C(\sigma_{33}-\sigma_{11})^2+2D\sigma_{12}^2+2E\sigma_{23}^2+2F\sigma_{31}^2=1 \quad (1)$$

The advantage of the form (1) is that it permits easy determination of the coefficients in terms of one-dimensional uniaxial and shear failure stresses. But its disadvantage is that it is based on the assumption that isotropic stress has no effect. It is for that reason that only squares of normal stress differences enter into the criterion. While such an assumption may be a good approximation for initial yielding of a metal, it is certainly not valid for isotropic tension of a fiber composite. Hoffman [3] has modified (1) by adding linear stress terms to it so as to account for unequal failure stresses in tension and compression with a single quadratic expression.

Tsai and Wu [4] represented the failure criterion as a general quadratic in the stresses, thereby eliminating the special dependence on the normal stresses of (1). In their notation

$$F_{ij}\sigma_i\sigma_j+F_i\sigma_i=1 \quad (2)$$

where

$$i=1,2,3,4,5,6$$

$$1\equiv 11,\ 2\equiv 22,\ 3\equiv 33,\ 4\equiv 31,\ 5\equiv 23,\ 6\equiv 12.$$

For an orthotropic material with unequal strengths in tension and compression

$$F_{11}=\frac{1}{N_1^+N_1^-} \quad (3a)$$

$$F_1=\frac{1}{N_1^+}-\frac{1}{N_1^-} \quad (3b)$$

$$F_{66}=\frac{1}{S_6^2} \quad (3c)$$

where N_1^+, N_1^- are tensile and compressive strengths, respectively, in 1-direction and S_6 is shear strength in the 12 plane. The coefficients F_{22}, F_{33}, F_{44}, F_{55}, F_2, F_3, are given by analogous expressions.

Since the failure of the material is insensitive to a change of sign of shear stress (in contrast to a change of sign of normal stress) all terms containing a shear stress to first power must vanish. Therefore, the only surviving unknown coefficients are F_{12}, F_{23}, and F_{13}. Tsai and Wu propose to determine these coefficients by biaxial failure tests. Unfortunately, such tests are complicated and expensive.

The criterion (2) is a definite improvement over previous criteria because of its generality and versatility and has also provided good fit with test data. Nevertheless, its utilization and interpretation raise some intrinsic problems. Underlying these is the fact that a fiber composite consists of mechanically very dissimilar phases: stiff elastic brittle fibers and a compliant yielding matrix. Consequently, the

[1] Supported in part by the U.S. Naval Research Laboratory under Contract N00173-78-C-0170 with Materials Sciences Corporation, Blue Bell, Pa.

[2] Also, Scientific Advisor, Materials Sciences Corporation.

Contributed by the Applied Mechanics Division for publication in the JOURNAL OF APPLIED MECHANICS.

Discussion on this paper should be addressed to the Editorial Department, ASME, United Engineering Center, 345 East 47th Street, New York, N.Y. 10017, and will be accepted until September 1, 1980. Readers who need more time to prepare a discussion should request an extension from the Editorial Department. Manuscript received by ASME Applied Mechanics Division, April, 1979; final revision, July, 1979.

Copyright © 1980 by ASME
Downloaded 01 May 2010 to 171.66.16.243. Redistribution subject to ASME license or copyright; see http://www.asme.org/terms/Terms_Use.cfm

failure occurs in very different modes. Thus the fibers may rupture in tension or buckle in compression, or the matrix may fail due to loads transverse to the fibers. It is not evident that all of the distinct failure modes can be represented by a single smooth function such as (2).

An hexagonal crystal has macroscopically the same symmetry as a transversely isotropic fiber composite, yet the failure modes of these materials are entirely different. It would hardly be possible to bring forth these differences by mathematically similar smooth failure criteria which only differ in the numerical values of the coefficients.

To point out some difficulties specific to fiber composites let (2) be specialized to a unidirectionally reinforced lamina in plane stress. Then the failure criterion is

$$F_{11}\sigma_{11}^2 + F_{22}\sigma_{22}^2 + 2F_{12}\sigma_{11}\sigma_{22} + F_{66}\sigma_{12}^2 + F_1\sigma_{11} + F_2\sigma_{22} = 1 \quad (4)$$

where x_1 is fiber direction and x_2 transverse to it.

All coefficients except F_{12} are determined by expressions of type (3). To determine F_{12} one can use a variety of biaxial failure tests: tension-tension, compression-compression, tension-compression. It is not evident that the values of F_{12} determined by these different tests will be the same or even close.

Suppose F_{12} has been determined and it is desired to utilize (4) to predict failure for the biaxial tensile state of stress:

$$\sigma_{11} = \sigma \quad \sigma_{22} = \alpha\sigma \quad \sigma_{12} = 0$$

where α is a given number and σ is to be determined. Insertion of this state of stress into (4) will result in a quadratic equation for σ. Because of the forms (3*a*,*b*) the coefficients of the quadratic depend on the tensile and compressive failure stresses $N_1^+, N_1^-, N_2^+, N_2^-$. It follows that failure under biaxial *tensile* stress depends on the values of the *compressive* failure stresses and this is physically unacceptable.

The foregoing difficulties provide the motivation to represent the failure criterion of a unidirectional fiber composite in *piecewise* smooth form, where each smooth branch represents one distinct failure mode. Such an approach has been introduced in [5] in the context of static and fatigue failure of fiber composites in plane stress.

2 Development of Failure Criteria

The failure criteria just discussed, as well as the ones to be established, are quadratic in the stresses. It should be emphasized that the choice of quadratics is based on curve fitting considerations and not on physical reasoning. The actual failure criterion is some closed surface in stress space, when all failure stresses are finite. An infinite failure stress may be used as a convenient idealization to indicate an order of magnitude difference, e.g., failure under isotropic pressure.

The simplest approximation of a failure surface is by planes parallel to coordinate planes, e.g., rectangular parallelepiped in three-dimensional stress space. Such representations have their uses for constant stress criteria in fixed directions with respect to material axes, but are in general of insufficient accuracy due to neglect of stress interaction effects.

The next approximation would consist of oblique planes which intersect the stress axes at the appropriate one-dimensional ultimate stresses. This may be termed the linear approximation and our experience shows that it underestimates the strength of the material and is therefore inscribed within the actual failure surface. However, linear approximations are very useful to model failure criteria of rocks [6].

The next order of approximation is quadratic, Fig. 1. It is the simplest presentation which can fit the data reasonably well, and in view of the significant scatter of failure test data it hardly seems worthwhile to employ cubic or higher approximations. It is unfortunate that the quadratic nature of stress-energy density forms has at times led to "physical" interpretation of quadratic failure criteria (or of quadratic initial yielding criteria in plasticity).

Literally all unidirectional fiber composites are transversely isotropic with respect to fiber direction, since the fibers are randomly

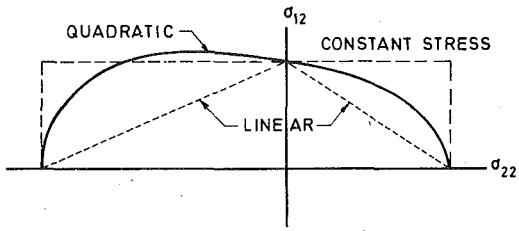

Fig. 1 Failure surfaces—schematic

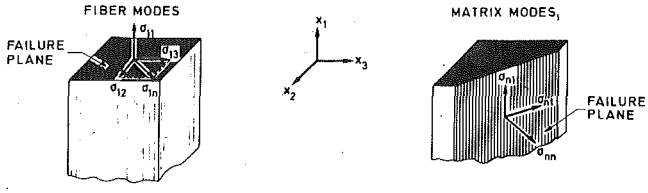

Fig. 2 Failure modes and failure planes

placed. Consider such a fiber-reinforced cylindrical specimen which is referred to a system of axes x_1 in fiber direction and x_2, x_3 in the transverse directions. It follows from the transverse isotropy that the failure criterion must be invariant under any rotation of the x_2, x_3-axes around x_1. Therefore the failure criterion can be at most a function of the stress invariants under such rotations. Such invariants are (see, e.g., [7]):

$$I_1 = \sigma_{11} \quad (5a)$$

$$I_2 = \sigma_{22} + \sigma_{33} \quad (5b)$$

$$I_3 = \sigma_{23}^2 - \sigma_{22}\sigma_{33} \quad \text{or} \quad \frac{1}{4}(\sigma_{22} - \sigma_{33})^2 + \sigma_{23}^2 \quad (5c)$$

$$I_4 = \sigma_{12}^2 + \sigma_{13}^2 \quad (5d)$$

$$I_5 = 2\sigma_{12}\sigma_{23}\sigma_{13} - \sigma_{22}\sigma_{13}^2 - \sigma_{33}\sigma_{12}^2 \quad (5e)$$

A simple construction of these invariants is given in the Appendix to this paper. It is of interest to note that the second of (5*c*) is the square of the maximum transverse shear stress while (5*d*) is the square of maximum axial shear stress. The two alternative forms (5*c*) are related in terms of (5*b*). For present purposes it is more convenient to use the first of (5*c*).

In view of the choice of quadratic approximation (5*e*) cannot appear in the failure criterion. Thus the most general transversely isotropic quadratic approximation will have the form

$$A_1I_1 + B_1I_1^2 + A_2I_2 + B_2I_2^2 + C_{12}I_1I_2 + A_3I_3 + A_4I_4 = 1 \quad (6)$$

The one-dimensional failure stresses of the material are denoted as follows:

σ_A^+ = tensile failure stress in fiber direction
σ_A^- = compressive failure stress in fiber direction (absolute value)
σ_T^+ = tensile failure stress transverse to fiber direction
σ_T^- = compressive failure stress transverse to fiber direction (absolute value)
τ_T = transverse failure shear; σ_{nt} in Fig. 2(*b*)
τ_A = axial failure shear; σ_{ln} in Fig. 2(*b*)

It follows at once by application of (5) and (6) to pure transverse or axial shear:

$$A_3 = \frac{1}{\tau_T^2}$$

$$A_4 = \frac{1}{\tau_A^2} \quad (7)$$

Observation of failure in unidirectional fiber composites indicates

Downloaded 01 May 2010 to 171.66.16.243. Redistribution subject to ASME license or copyright; see http://www.asme.org/terms/Terms_Use.cfm

that there are two primary failure modes: a *fiber mode* in which the composite fails due to fiber rupture in tension or because of fiber buckling in compression and a *matrix mode* in which a plane crack parallel to the fibers occurs.

It may be argued that in the event that a failure plane can be identified, the failure is produced by the normal and shear stresses on that plane. For the fiber mode the failure plane is approximately the x_2x_3 plane. Therefore, the stresses producing this failure are σ_{11}, σ_{12}, and σ_{13}; Fig. 2(*a*). A possible counter argument is that transversely isotropic compression $\sigma_{22} = \sigma_{33} = -\sigma$ would impede fiber buckling produced by compressive σ_{11}, thus requiring an interaction mechanism of these normal stresses. However, an analysis due to Rosen [8] indicates that fibers under axial compression buckle in a shear mode, thus independently of transverse normal stress. Accordingly such interaction will be assumed negligible, pending experimental investigation of this failure mode.

The matrix mode is a planar fracture in fiber direction, Fig. 2(*b*). The stresses on this plane are σ_{nn}, σ_{nt}, and σ_{ln}. The first two are expressed in terms of the stresses, σ_{22}, σ_{33}, and σ_{23}, while the last is expressed in terms of σ_{12} and σ_{13}. Therefore, σ_{11} does not enter into this failure mode.

If these conclusions are combined with the quadratic approximation (6) and the results (7) it follows that the failure criteria for these two modes are:

Fiber Mode

$$A_f\sigma_{11} + B_f\sigma_{11}^2 + \frac{1}{\tau_A^2}(\sigma_{12}^2 + \sigma_{13}^2) = 1 \tag{8}$$

Matrix Mode

$$A_m(\sigma_{22} + \sigma_{33}) + B_m(\sigma_{22} + \sigma_{33})^2 + \frac{1}{\tau_T^2}(\sigma_{23}^2 - \sigma_{22}\sigma_{33}) + \frac{1}{\tau_A^2}(\sigma_{12}^2 + \sigma_{13}^2) = 1 \tag{9}$$

Failure mechanisms and failure stresses are quite different for tension and compression in fiber direction as well as for tension and compression transverse to fibers. Consequently each primary mode is further subdivided into tensile and compressive modes. These will now be discussed and modeled, separately.

Tensile Fiber Mode $\sigma_{11} > 0$. The simple uniaxial tensile test information, $\sigma_{11}^u = \sigma_A^+$, provides only one equation for determination of the two coefficients A_f and B_f. Failure data for combined σ_{11}, σ_{12} stressing (e.g., tension-torsion) are necessary to provide a necessary additional equation.

It is to be expected that tensile σ_{11} and shear σ_{12} are mutually weakening. If so, the failure locus for these two stresses must be convex. A possibly satisfactory simple approximation would be an ellipse quadrant with intercept σ_A^+ and τ_A with the axes. With this approximation (8) becomes

$$\left(\frac{\sigma_{11}}{\sigma_A^+}\right)^2 + \frac{1}{\tau_A^2}(\sigma_{12}^2 + \sigma_{13}^2) = 1 \tag{10}$$

A still more drastic approximation is to simply use the maximum stress criterion

$$\sigma_{11} = \sigma_A^+ \tag{11}$$

for tensile failure in fiber direction, thus disregarding the shear contribution.

Compressive Fiber Mode $\sigma_{11} < 0$. The only available information is that $\sigma_{11}^u = -\sigma_A^-$, so again there is insufficient information to find A_f and B_f in (8). It is not known to the writer whether axial shear stress produces a weakening or strengthening effect on compressive strength in fiber direction. Consequently the failure criterion is represented temporarily in the simple maximum stress form

$$\sigma_{11} = -\sigma_A^- \tag{12}$$

The dependence of both fiber modes on the axial shear stresses does not appear well understood at the present time and deserves careful experimental investigation.

Matrix Modes. Matrix mode modeling is more complicated since the failure plane, Fig. 2(*b*), is not *a priori* identified. One possible procedure would be to formulate a surface failure criterion which would depend on σ_{nn}, σ_{nt}, and σ_{ln}. For example, a simple choice is

$$f(\sigma_{nn}, \sigma_{nt}, \sigma_{ln}) = \left(\frac{\sigma_{nn}}{\sigma_T^+}\right)^2 + \left(\frac{\sigma_{nt}}{\tau_T}\right)^2 + \left(\frac{\sigma_{ln}}{\tau_A}\right)^2 = 1 \tag{13}$$

for the case of tensile transverse normal stress. A different failure criterion should be used for compressive σ_{nn}. If σ_{nn}, σ_{nt}, σ_{ln} are expressed by tensor transformation in terms of the stresses σ_{22}, σ_{33}, σ_{23}, σ_{12}, σ_{13} and the angle $(x_2, n) = \theta$, then (13) will be of the general form

$$g(\sigma_{22}, \sigma_{33}, \sigma_{23}, \sigma_{12}, \sigma_{13}, \theta) = 1 \tag{14}$$

and failure will occur on the plane defined by a θ_0 which makes the left side of (14) a maximum. The failure criterion would then be given by (14) with $\theta = \theta_0$.

This procedure is somewhat reminiscent of Mohr failure theory as used in soil mechanics. While it may appear attractive because of its sound physical basis, it is unfortunately difficult to use. Even with the simple surface failure criterion (13) the extremum problem is quite complicated and the angle θ_0 must be found by solution of a quartic equation in $\sin 2\theta_0$. The resulting failure criterion (14) is complicated and definitely not quadratic. Furthermore, the failure criterion (13) is subject to the same difficulty encountered in the fiber modes in that presence of a linear term in σ_{11} may be necessary. Similar difficulties are encountered for surface failure criterion for compressive σ_{nn}. Finally, the extremum problem which must be solved is even more complicated than the one previously mentioned, since it must take into account the difference of failure criteria for tensile and compressive σ_{nn}. Consequently, the approach outlined will not be pursued at the present time.

Returning to the simple matrix mode criterion (9) it will be assumed that it represents a tensile mode defined by $\sigma_{nn} > 0$ and a compressive mode defined by $\sigma_{nn} < 0$. The coefficients A_m, B_m for each mode are different and will be distinguished by + and − superscripts.

Tensile Mode $\sigma_{nn} > 0$. The available simple information is $\sigma_{22}^u = \sigma_T^+$ which, when used in (9) implies that

$$A_m^+\sigma_T^+ + B_m^+\sigma_T^{+2} = 1 \tag{15}$$

Using arguments similar to those leading to (10), A_m^+ is set equal to zero as an approximation. This results in the failure criterion

$$\frac{1}{\sigma_T^{+2}}(\sigma_{22} + \sigma_{33})^2 + \frac{1}{\tau_T^2}(\sigma_{23}^2 - \sigma_{22}\sigma_{33}) + \frac{1}{\tau_A^2}(\sigma_{12}^2 + \tau_{13}^2) = 1 \tag{16}$$

Compressive Mode $\sigma_{nn} < 0$. In this case the available simple information is $\sigma_{22}^u = -\sigma_T^-$, which when used in (9) implies that

$$-A_m^-\sigma_T^- + B_m^-\sigma_T^{-2} = 1 \tag{17}$$

To obtain additional information it may be argued that if the material is failed in transversely isotropic pressure $\sigma_{22} = \sigma_{33} = -\sigma$, all others vanish, this pressure will be very much larger than the compressive uniaxial failure stress. Thus

$$\sigma \gg \sigma_T^- \tag{18}$$

To utilize this condition A_m^- and B_m^- are first determined in terms of σ_T^- and σ and the condition (18) is then taken into account by retention of only first-order tems in σ_T^-/σ in the expressions. The resulting failure criterion is

$$\frac{1}{\sigma_T^-}\left[\left(\frac{\sigma_T^-}{2\tau_T}\right)^2 - 1\right](\sigma_{22} + \sigma_{33}) + \frac{1}{4\tau_T^2}(\sigma_{22} + \sigma_{33})^2 + \frac{1}{\tau_T^2}(\sigma_{23}^2 - \sigma_{22}\sigma_{33}) + \frac{1}{\tau_A^2}(\sigma_{12}^2 + \sigma_{13}^2) = 1 \tag{19}$$

In order to determine which of the failure criteria (16), (19) should be used it is necessary to know the sign of σ_{nn} on the failure plane.

Downloaded 01 May 2010 to 171.66.16.243. Redistribution subject to ASME license or copyright; see http://www.asme.org/terms/Terms_Use.cfm

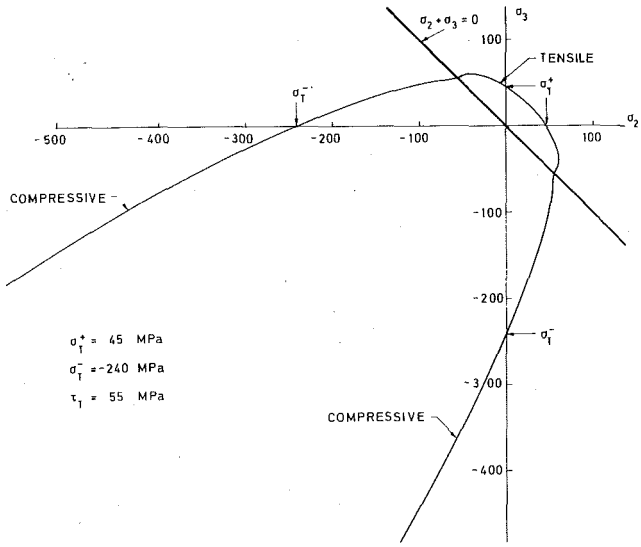

Fig. 3 Failure locus for matrix modes; principal transverse plane stress

Unfortunately, however, this requires prior identification of the failure plane in terms of the extremum problem previously discussed. Not only is such a procedure very complicated but, as has been pointed out in the foregoing, is incompatible with the quadratic approximation of failure criteria. Present development will be continued in terms of quadratic representations, but this will inevitably lead to certain requirements with regard to the failure plane location.

To simplify matters and without any loss of generality, the matrix mode failure criteria will be expressed in terms of the principal stresses σ_2, σ_3 associated with the plane stress system σ_{22}, σ_{33}, σ_{23} and the maximum axial shear stress $\tau_n = \sqrt{\sigma_{12}^2 + \sigma_{13}^2}$. This permits representation of matrix mode failure criteria in three-dimensional stress space σ_2, σ_3, τ_n.

The normal stress σ_{nn} on a plane with orientation θ relative to x_2-axis is given by

$$\sigma_{nn} = \sigma_2 \cos^2\theta + \sigma_3 \sin^2\theta$$

Evidently

$$\sigma_{nn} \geq 0 \quad \text{when} \quad \sigma_2, \sigma_3 \geq 0 \tag{20a}$$

$$\sigma_{nn} \leq 0 \quad \text{when} \quad \sigma_2, \sigma_3 \leq 0 \tag{20b}$$

Thus (16) applies for the first quadrant and (19) for the third quadrant of the σ_2, σ_3-plane, but in the second and fourth quadrants σ_{nn} can have either sign.

Let (16), (19) be represented in the general form (9) in present stress variables. Thus

$$A_m^+(\sigma_2+\sigma_3) + B_m^+(\sigma_2+\sigma_3)^2 - \frac{\sigma_2\sigma_3}{\tau_T^2} + \frac{\tau_n^2}{\tau_A^2} = 1 \tag{21a}$$

$$A_m^-(\sigma_2+\sigma_3) + B_m^-(\sigma_2+\sigma_3)^2 - \frac{\sigma_2\sigma_3}{\tau_T^2} + \frac{\tau_n^2}{\tau_A^2} = 1 \tag{21b}$$

The trace of the intersection of (21a,b) in the σ_2, σ_3-plane is given by either of the two straight lines

$$\sigma_2 + \sigma_3 = 0 \tag{22a}$$

$$\sigma_2 + \sigma_3 = -\frac{A_m^+ - A_m^-}{B_m^+ - B_m^-} \tag{22b}$$

The criterion (16) must apply above the straight line and the criterion (19) below it. If (22b) is the intersection trace then it must intersect either the first or the third quadrants. In the first case it would follow that (21b) applies to part of the first quadrant which contradicts (20a). In the second case it would follow that (20a) applies to part of the third quadrant which contradicts (20b). The conclusion is that only (22a) is compatible with (20) and is therefore the only acceptable intersection trace. Therefore

$$\sigma_{nn} \geq 0 \quad \text{when} \quad \sigma_2 + \sigma_3 \geq 0 \tag{23a}$$

$$\sigma_{nn} \leq 0 \quad \text{when} \quad \sigma_2 + \sigma_3 \leq 0 \tag{23b}$$

In view of (19) it is not difficult to see that the inequalities (21) and (23) are compatible only when $\theta = \pm 45°$. (This is easily perceived by consideration of the regions of validity of the inequalities in the σ_2, σ_3-plane.) *It follows that the quadratic representation implies that* failure always occurs on the maximum transverse shear plane. This is difficult to accept as a general conclusion. A counterexample is a state of stress dominated by axial shear in which case the failure plane or orientation would more likely be governed by the direction of the maximum axial shear.

However, this difficulty is a direct consequence of the quadratic approximation. Higher-order approximations contain more disposable coefficients, are therefore more flexible and can better accommodate necessary physical ingredients but they would also require complicated and expensive combined stress testing in order to determine the increased number of coefficients.

The quadratic failure criteria derived are now summarized:

Tensile Fiber Mode $\sigma_{11} > 0$

$$\left(\frac{\sigma_{11}}{\sigma_A^+}\right)^2 + \frac{1}{\tau_A^2}(\sigma_{12}^2 + \sigma_{13}^2) = 1 \tag{10}$$

or

$$\sigma_{11} = \sigma_A^+ \tag{11}$$

Compressive Fiber Mode $\sigma_{11} < 0$

$$\sigma_{11} = -\sigma_A^- \tag{12}$$

Tensile Matrix Mode $\sigma_{22} + \sigma_{33} > 0$

$$\frac{1}{\sigma_T^{+2}}(\sigma_{22}+\sigma_{33})^2 + \frac{1}{\tau_T^2}(\sigma_{23}^2 - \sigma_{22}\sigma_{33}) + \frac{1}{\tau_A^2}(\sigma_{12}^2 + \sigma_{13}^2) = 1 \tag{16}$$

Compressive Matrix Mode $\sigma_{22} + \sigma_{33} < 0$

$$\frac{1}{\sigma_T^-}\left[\left(\frac{\sigma_T^-}{2\tau_T}\right)^2 - 1\right](\sigma_{22}+\sigma_{33}) + \frac{1}{4\tau_T^2}(\sigma_{22}+\sigma_{33})^2 + \frac{1}{\tau_T^2}(\sigma_{23}^2 - \sigma_{22}\sigma_{33}) + \frac{1}{\tau_A^2}(\sigma_{12}^2 + \sigma_{13}^2) = 1 \tag{19}$$

A schematic drawing of matrix failure criteria in the four quadrants of transverse plane principal stress is shown in Fig. 3. It should be noted that the ultimate transverse shear stress, τ_T, which appears in the failure criteria is notoriously difficult to measure. However, no general failure criterion could avoid inclusion of this quantity.

3 Plane Stress Failure Criteria

The case of plane stress is of considerable practical significance since such is the state of stress in the laminae of a laminate at sufficient distance from the edges. Let the nonvanishing stress components be σ_{11}—in fiber direction, σ_{22}—transverse to fibers and σ_{12}—in plane or axial shear. It then follows from the three-dimensional failure criteria that failure modes and their analytical descriptions are

Tensile Fiber Mode

$$\left(\frac{\sigma_{11}}{\sigma_A^+}\right)^2 + \left(\frac{\sigma_{12}}{\tau_A}\right)^2 = 1 \quad \sigma_{11} > 0 \tag{24}$$

Fiber Compressive Mode

$$\sigma_{11} = -\sigma_A^- \quad \sigma_{11} < 0 \tag{25}$$

Tensile Matrix Mode $\sigma_{22} > 0$

$$\left(\frac{\sigma_{22}}{\sigma_T^+}\right)^2 + \left(\frac{\sigma_{12}}{\tau_A}\right)^2 = 1 \tag{26}$$

Downloaded 01 May 2010 to 171.66.16.243. Redistribution subject to ASME license or copyright; see http://www.asme.org/terms/Terms_Use.cfm

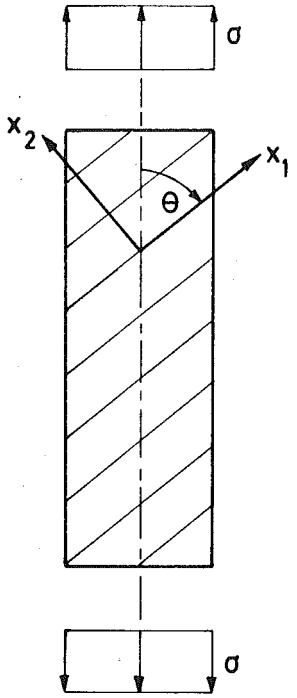

Fig. 4 Off-axis specimen

Compressive Matrix Mode $\sigma_{22} < 0$

$$\left(\frac{\sigma_{22}}{2\tau_T}\right)^2 + \left[\left(\frac{\sigma^-_T}{2\tau_T}\right)^2 - 1\right]\frac{\sigma_{22}}{\sigma^-_T} + \left(\frac{\sigma_{12}}{\tau_A}\right)^2 = 1 \tag{27}$$

The case of tensile modes (24), (26) can be conveniently tested by means of an off-axis specimen, Fig. 4, under uniaxial tension σ. The state of stress with respect to the material axes is then

$$\sigma_{11} = \sigma \cos^2\theta$$

$$\sigma_{22} = \sigma \sin^2\theta$$

$$\sigma_{12} = \sigma \sin\theta \cos\theta \tag{28}$$

Insertion of (28) into (24) and (26) predicts the off-axis failure stresses

$$\sigma^2_{fu} = \frac{1}{\cos^2\theta[\cos^2\theta/\sigma^2_T + \sin^2\theta/\tau^2_A]}$$

$$\sigma^2_{mu} = \frac{1}{\sin^2\theta[\sin^2\theta/\sigma^2_T + \cos^2\theta/\tau^2_A]} \tag{29}$$

where subscripts f and m indicate fiber and matrix modes, respectively.

Many off-axis test results have been reported in the literature, but in numerous cases coefficients of a polynomial which is supposed to represent a failure criterion have been obtained by best fit with the data. Such a procedure does not provide critical examination of a failure criterion.

In order to test a failure criterion it is necessary to examine prediction of failure under combined states of stress in terms of failure under single stress components. It also must be remembered that the significant scatter of test results tends to obscure verification. In this respect it should be noted that it is generally tacitly expected that a failure criterion will predict the mean of combined stress failure results in terms of the mean of one-dimensional failure stress results. There is in principle no statistical reason for such an assumption, but this subject is beyond the scope of the present discussion.

Pipes and Cole [9] reported off-axis tensile failure results for unidirectional boron-epoxy. In attempting to fit their results to the plane stress Tsai-Wu criterion (4) they found that F_{12} assumed considerably

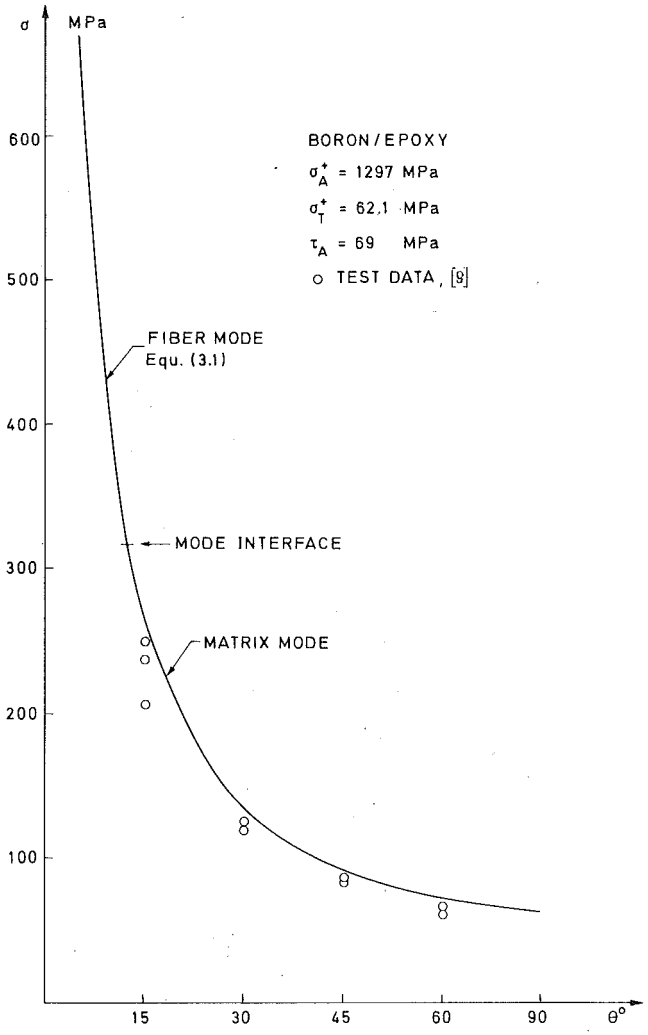

Fig. 5 Comparison of failure criteria with test data; boron-epoxy off-axis specimens

different values for the fiber orientations used (15°, 30°, 45°, 60°), the ratio of max F_{12} to min F_{12} being −51! They obtained good fit of (4) with experimental data by empirically setting $F_{12} = 0$.

The question of F_{12} significance has recently been considered in [10]. It was concluded on the basis of numerical computations that setting $F_{12} = 0$ in (4) or using the Hoffman criterion [3] would be practically acceptable as the expected errors would not exceed 10 percent. However, until physical arguments are supplied why F_{12} should vanish in a criterion such as (4) which contains *a priori* all terms on an equal rights basis, this must remain an empirical finding.

It should be pointed out that F_{12} is also absent from the present failure criterion, but this is due to consideration of the two different failure modes: fiber mode which is independent of σ_{22} and matrix mode which is independent of σ_{11}.

Fig. 5 shows the experimental results of [9] and the failure criteria (24), (26) in terms of one-dimensional failure stresses reported in [9], showing reasonable agreement. It should be remembered that these failure criteria are based on (8), (9) with vanishing A_f and A_m. No doubt better fit with data could be obtained by retaining such coefficients in (24), (26) and obtaining them from fit to the data; but it is believed that the price paid in complication is hardly worth the return in accuracy.

Fig. 6 shows comparison with the failure criteria of experimental data for Glass/Epoxy off-axis specimens as reported in [5], demonstrating very good agreement. It should be noted in this respect that

Downloaded 01 May 2010 to 171.66.16.243. Redistribution subject to ASME license or copyright; see http://www.asme.org/terms/Terms_Use.cfm

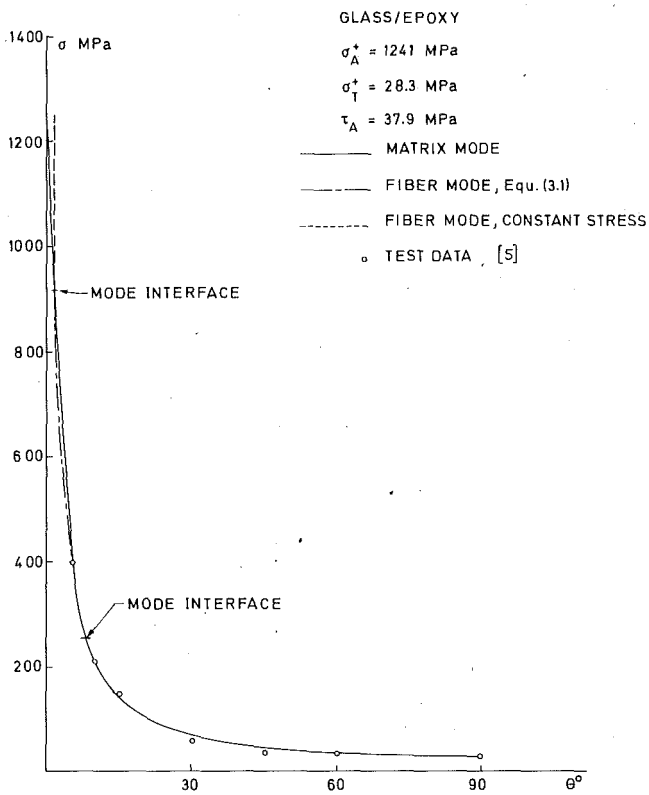

Fig. 6 Comparison of failure criteria with test data; glass-epoxy off-axis specimens

in [5] the fiber mode was modeled by the simple maximum stress criterion $\sigma_{11} = \sigma_A^+$. This of course does not affect the form of the matrix mode, but is of importance for the value of the reinforcement angle, θ_{fm}, which separates the two modes. With the present criteria this separation angle is about 8°, while with maximum stress in fiber direction the angle is 1°45′. Test data for small angles θ are needed in order to establish the relative accuracy of the two different fiber mode descriptions.

5 Conclusion

The principal theme of the present work is that a general failure criterion for unidirectional fiber composites should distinguish among the various different failure modes of the composite and model each of the modes separately. Consequently, the general failure criterion cannot be smooth but is piecewise smooth, consisting of smooth branches each of which models a distinct failure mode.

Such a failure criterion is physically more realistic than a completely smooth criterion since it avoids prediction of multiaxial tensile (compressive) modes in terms of compressive (tensile) failure stresses. Furthermore, the recognition of the separate modes identifies certain troublesome interaction coefficients in polynomial criteria as being of secondary importance. The neglect of these much facilitates experimental determination of needed failure criterion parameters.

It should also be noted that failure mode identification is a required feature if the criterion is to be useful for progressive damage analysis of a fiber composite structural element (e.g., notched laminate) by a finite-element scheme. Such a computational procedure starts with a finite-element stress analysis. Certain elements will fail when their stresses satisfy the failure criteria, but in order to continue the analysis it is essential to know *how* the elements have failed; by fiber rupture, matrix crack or delamination from adjacent lamina. With this information it is possible to set up a new finite-element configuration with appropriate stiffness changes or new free surfaces and the analysis can proceed to identification of new failures. But clearly this procedure is not possible with a criterion which predicts "failure" but does not identify a failure mode.

The actual mathematical modeling of the failure modes, given here, should not be considered definitive in any sense. It is merely a simple mathematical description in terms of available experimental information. In certain cases—fiber modes and tensile-tensile matrix modes—the simple available information was not sufficient to determine the coefficients in unambiguous fashion. A most important task is to provide carefully controlled test data for accurate modeling of failure modes. Such tests should also clarify the question of the validity of the quadratic approximation. As has been pointed out, quadratic failure criteria imply that the matrix mode failure plane is the maximum transverse shear plane and this does not seem acceptable in a general sense. It can only be hoped that the quadratic approximation will prove sufficiently accurate in spite of this physical shortcoming, for the alternative of higher-order failure criteria is very complicated.

Finally, the statistical scatter aspects of the failure must be recognized and incorporated by a theory which would predict statistical parameters of failure under combined stress in terms of known statistics of failure under simple stress.

Acknowledgment

It is a pleasure to acknowledge helpful discussions with B. Walter Rosen.

References

1 Tsai, S. W., "Strength Characteristics of Composite Materials," NASA CR-224, 1965.

2 Hill, R., "A Theory of the Yielding and Plastic Flow of Anisotropic Materials," *Proceedings of the Royal Society*, Series A, Vol. 193, 1948, p. 281.

3 Hoffman, O., "The Brittle Strength of Orthotropic Materials," *Journal of Composite Materials*, Vol. 1, 1967, p. 200.

4 Tsai, S. W., and Wu, E. M., "A General Theory of Strength for Anisotropic Materials," *Journal of Composite Materials*, Vol. 5, 1971, p. 58.

5 Hashin, Z., and Rotem, A., "A Fatigue Failure Criterion for Fiber-Reinforced Materials," *Journal of Composite Materials*, Vol. 7, 1973, p. 448.

6 Paul, B., "Macroscopic Criteria for Plastic Flow and Brittle Fracture," *Fracture*, Liebowitz, H., ed., Academic Press, 1968, Vol. III, Chapter 4.

7 Mulhern, J. F., Rogers, T. G., and Spencer, A. J. M., "A Continuum Model for Fiber-Reinforced Plastic Materials," *Proceedings of the Royal Society*, Series A, Vol. 301, 1967, p. 473.

8 Rosen, B. W., "Mechanics of Composite Strengthening," in *Fiber Composite Materials*, American Society for Metals, 1965, pp. 37–76.

9 Pipes, R. B., and Cole, B. W., "On the Off-Axis Strength Test for Anisotropic Materials," *Journal of Composite Materials*, Vol. 7, 1973, p. 246.

10 Narayanaswami, R., and Adelman, H., "Evaluation of the Tensor Polynomial and Hoffman Strength Theories for Composite Materials," *Journal of Composite Materials*, Vol. 11, 1977, p. 366.

APPENDIX

Transversely Isotropic Invariants of Second Rank Symmetric Tensor

The usual isotropic invariants of the stress tensor or any other second rank symmetric tensor are

$$I_1^i = \sigma_{11} + \sigma_{22} + \sigma_{33} \tag{30a}$$

$$I_2^i = \sigma_{11}\sigma_{22} + \sigma_{22}\sigma_{33} + \sigma_{33}\sigma_{11} - \sigma_{12}^2 - \sigma_{23}^2 - \sigma_{31}^2 \tag{30b}$$

$$I_3^i = \sigma_{11}\sigma_{22}\sigma_{33} + 2\sigma_{12}\sigma_{23}\sigma_{31} - \sigma_{11}\sigma_{23}^2 - \sigma_{22}\sigma_{31}^2 - \sigma_{33}\sigma_{12}^2 \tag{30c}$$

Expressions (1) are invariants for the set of *all* rotations of a coordinate system. Consider the subset of rotations in which the x_1-axis remains fixed. Evidently (1) are invariants also for such rotations.

A most elementary calculation shows that (5*a*) and (5*d*) are invariants for rotation around x_1-axis. It follows from (30*a*) and (5*a*) that (5*b*) is an invariant. It then follows from (5*a*,*b*,*d*) and (30*b*) that (5*c*) is an invariant.

Finally, from (5*a*,*c*) and (30*c*) there follows the invariance of (5*e*).

Downloaded 01 May 2010 to 171.66.16.243. Redistribution subject to ASME license or copyright; see http://www.asme.org/terms/Terms_Use.cfm

J. F. Yau[1]
Graduate Student.

S. S. Wang
Assistant Professor.
Assoc. Mem. ASME

H. T. Corten
Professor.
Mem. ASME

Department of Theoretical and Applied Mechanics,
University of Illinois,
Urbana, Ill. 61801

A Mixed-Mode Crack Analysis of Isotropic Solids Using Conservation Laws of Elasticity

A simple and convenient method of analysis for studying two-dimensional mixed-mode crack problems is presented. The analysis is formulated on the basis of conservation laws of elasticity and of fundamental relationships in fracture mechanics. The problem is reduced to the determination of mixed-mode stress-intensity factor solutions in terms of conservation integrals involving known auxiliary solutions. One of the salient features of the present analysis is that the stress-intensity solutions can be determined directly by using information extracted in the far field. Several examples with solutions available in the literature are solved to examine the accuracy and other characteristics of the current approach. This method is demonstrated to be superior in its numerical simplicity and computational efficiency to other approaches. Solutions of more complicated and practical engineering fracture problems dealing with the crack emanating from a circular hole are presented also to illustrate the capacity of this method.

1 Introduction

Conservation laws in elasticity have recently received much attention due to their wide range of application to mechanics problems. The mathematical form of each law states that the integral of a certain function, F, of field elastic variables over the closed surface, S, of a subregion in an elastically deformed body vanishes, i.e.,

$$J_i = \int_S F(u_i, u_{i,j}, \sigma_{ij})dS = 0, \tag{1}$$

where u_i is the displacement vector, σ_{ij} is the stress tensor, and the comma (,) in the subscript represents a partial derivative of the variable. Earlier work by Günther [1], Eshelby [2], and later by Rice and Budiansky [3] laid the foundation of conservation laws in elasticity. Knowles and Sternberg [4], Green [5], Chen and Shield [6], and Shield [7] have established additional conservation laws for linearized and finite elastostatics of homogeneous solids.

Applications of conservation laws to the important field of fracture mechanics have led to the establishment of useful conservation integrals, e.g., the so-called path-independent integrals. The well-known Eshelby-Rice J-integral [8, 9] is one of these kind and has been used widely in many fracture testing and engineering fracture problems [10–12]. The integral has been shown to be identical to Irwin's energy release rate associated with the colinear extension of a crack in an elastic solid [8]. It has been related to crack-tip stress-intensity factors in both linear and nonlinear elastic solids subjected to infinitesmal deformations [8, 13]. Stern, et al. [14], have employed another path-independent integral based on Betti's reciprocal work theorem to examine elastic crack problems. Gurtin [15] has extended conservation law formulation further to problems of elastodynamics. The conservation integral in a dynamic case has been shown to be related to dynamic stress-intensity factors in a fashion similar to that in the elastostatic case. More recently, Freund [16] has applied a conservation integral, called the M-integral, to a class of plane elastic crack problems, provided the problems possess certain required characteristics. Both the J and M-integral approaches have an inherent limitation which cannot, in a mixed-mode fracture problem, allow the individual stress-intensity factor for each mode to be determined explicitly and separately. This paper presents a new method of analysis for studying mixed-mode crack problems in isotropic elastic solids, which can evaluate directly the individual stress-intensity factor solution for each fracture mode.

The fundamental basis of the present approach lies in the introduction of the conservation integral for two equilibrium states of a cracked elastic body. The analysis requires evaluation of the new conservation integral along a selected contour in the far field. Several important properties of the conservation integral, J_i, are used in the formulation of the problem. Stress-intensity factor solutions are then obtained in terms of known auxiliary solutions and field variables along a selected contour. The general concept of applying this method to elastic fracture mechanics problems has been discussed in [6]. One of the salient features of the current approach is that the mixed-mode

[1] Presently, Engineer, Aircraft Engine Group, General Electric Company, Evendale, Ohio 45215.

Contributed by the Applied Mechanics Division for publication in the JOURNAL OF APPLIED MECHANICS.

Discussions on this paper should be addressed to the Editorial Department, ASME, United Engineering Center, 345 East 47th Street, New York, N.Y. 10017, and will be accepted until September 1, 1980. Readers who need more time to prepare a discussion should request an extension from the Editorial Department. Manuscript received by ASME Applied Mechanics Division, December, 1978, final revision, July, 1979.

Copyright © 1980 by ASME
Downloaded 01 May 2010 to 171.66.16.243. Redistribution subject to ASME license or copyright; see http://www.asme.org/terms/Terms_Use.cfm

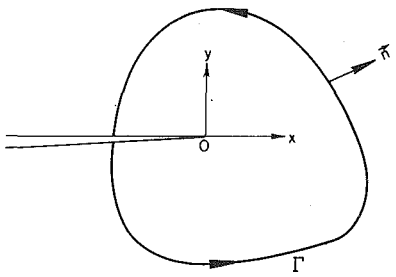

Fig. 1 Coordinates and path of *J*-integral

stress-intensity factor solutions at the crack tip can be determined accurately and conveniently from information extracted in the far field. In the next section, the development of the fundamental theory for the analysis is presented. The solution procedure for the mixed-mode crack problems is given in Section 3. Numerical examples are shown in Section 4 to illustrate the capacity of the current approach and its superiority to conventional ones.

2 Formulation

For infinitesimal deformations of homogeneous elastic bodies, a general form of conservation laws in plane isotropic elasticity problems may be written [6] as

$$J_i = \int_S \left[W n_i - \frac{\partial W}{\partial u_{j,k}} u_{j,i}\, n_k \right] ds = 0 \tag{2}$$

for an arbitrary closed boundary S which encloses a portion of the continuum, where W is the strain energy density, n_i is the outward unit normal of S, and u_i is the displacement vector referred to a Cartesian coordinate system. The conservation law can be reduced to the path-independent J-integral along an arbitrary path Γ enclosing the crack tip located at the origin of the coordinates as shown in Fig. 1 by

$$J \equiv J_1\{\Gamma\} = \int_\Gamma \left\{ W dy - T_i \frac{\partial u_i}{\partial x}\, ds \right\}, \tag{3}$$

where

$$T_i = \sigma_{ij}\, n_j. \tag{4}$$

The J-integral has been shown [8] to be identical to Irwin's energy release rate in an elastic solid during mixed-mode crack extension, i.e.,

$$J = G_{\mathrm{I}} + G_{\mathrm{II}} = G_{\mathrm{total}}. \tag{5}$$

The energy release rates G_{I} and G_{II} are related to the crack-tip stress-intensity factors K_{I} and K_{II} by the well-known relationships:

$$G_{\mathrm{I}} = \alpha K_{\mathrm{I}}^2 \tag{6}$$

and

$$G_{\mathrm{II}} = \alpha K_{\mathrm{II}}^2, \tag{7}$$

where

$$\alpha = \begin{cases} \dfrac{(1-\nu^2)}{E} & \text{(plane strain)} \qquad (8a) \\ \dfrac{1}{E} & \text{(plane stress),} \qquad (8b) \end{cases}$$

and E and ν are the Young's modulus and Poisson's ratio, respectively. Therefore, J can be expressed in terms of the stress-intensity factors by

$$J = \alpha(K_{\mathrm{I}}^2 + K_{\mathrm{II}}^2). \tag{9}$$

It should be noted here that the J-integral in equation (9) alone does not provide adequate information for determining the individual values of K_{I} and K_{II} in a mixed-mode crack problem. If, however, equation (9) is used in conjunction with the recently developed conservation law for two independent equilibrium states of an elastic solid, the deficiency for solving the mixed-mode fracture problem can be removed.

Now consider two independent equilibrium states of an elastically deformed body. Field variables associated with the two states are denoted by the superscripts 1 and 2. Superposition of the two equilibrium states leads to another equilibrium state 0. The J-integral of the superimposed state can be shown to have the following form:

$$J^{(0)} = J^{(1)} + J^{(2)} + M^{(1,2)}, \tag{10}$$

in which

$$M^{(1,2)} = \int_\Gamma \left(W^{(1,2)}\, dy - \left[T_i^{(1)} \frac{\partial u_i^{(2)}}{\partial x} + T_i^{(2)} \frac{\partial u_i^{(1)}}{\partial x} \right] ds \right), \tag{11}$$

where $W^{(1,2)}$ is the mutual potential energy density of the elastic body, defined by

$$W^{(1,2)} = C_{ijkl} u_{i,j}^{(1)} u_{k,l}^{(2)} = C_{ijkl} u_{i,j}^{(2)} u_{k,l}^{(1)}. \tag{12}$$

Recalling the J–K relationships in equation (9) and the orthogonality of stress-intensity factors, one finds that the J-integral for the 0 state may be expressed as

$$J^{(0)} = \alpha([K_{\mathrm{I}}^{(1)} + K_{\mathrm{I}}^{(2)}]^2 + [K_{\mathrm{II}}^{(1)} + K_{\mathrm{II}}^{(2)}]^2). \tag{13}$$

More explicitly, equation 13 can be written as

$$J^{(0)} = J^{(1)} + J^{(2)} + 2\alpha(K_{\mathrm{I}}^{(1)} K_{\mathrm{I}}^{(2)} + K_{\mathrm{II}}^{(1)} K_{\mathrm{II}}^{(2)}). \tag{14}$$

A direct comparison between equations (10) and (14) reveals that

$$M^{(1,2)} = 2\alpha[K_{\mathrm{I}}^{(1)} K_{\mathrm{I}}^{(2)} + K_{\mathrm{II}}^{(1)} K_{\mathrm{II}}^{(2)}]. \tag{15}$$

The M-integral shown in equations (11) and (15) deals with interaction terms only and will be used directly for solving mixed-mode crack problems in a linear elastic solid. It should be noted here that the M-integral is related to the details of the stresses and deformation at the crack tip (i.e., K_{I} and K_{II} in equation (15)) but yet may be evaluated in the region away from the crack tip (i.e., the integral in equation (11)), where such a calculation can be carried out with greater accuracy and convenience than near the crack tip.

3 Solution Procedure

Equation (11) together with equation (15) provides, in fact, sufficient information for determining the stress-intensity factor solution for a mixed-mode fracture problem, when proper known auxiliary solutions are introduced. Let the first auxiliary solution be denoted by a superscript $2a$. For a cracked body subjected to mode-I deformation only, i.e.,

$$K_{\mathrm{I}}^{(2a)} = 1 \quad \text{and} \quad K_{\mathrm{II}}^{(2a)} = 0, \tag{16}$$

equation (15) can be simplified as

$$M^{(1,2a)} = 2\alpha K_{\mathrm{I}}^{(1)}, \tag{17}$$

where $M^{(1,2a)}$ has the form

$$M^{(1,2a)} = \int_\Gamma \left(C_{ijkl} u_{i,j}^{(1)} u_{k,l}^{(2a)}\, dy - \left[T_i^{(1)} \frac{\partial u_i^{(2a)}}{\partial x} + T_i^{(2a)} \frac{\partial u_i^{(1)}}{\partial x} \right] ds \right). \tag{18}$$

In equation (18), $T_i^{(1)}$ and $u_i^{(1)}$ can be determined by any convenient method along a properly selected integration path Γ, which will be discussed later. In a plane-strain crack problem subjected to the loading condition of equation (16), $T_i^{(2a)}$ and $u_i^{(2a)}$ can be calculated from the following expressions [17]:

$$T_i^{(2a)} = \sigma_{ij}^{(2a)} n_j, \tag{19}$$

and

Downloaded 01 May 2010 to 171.66.16.243. Redistribution subject to ASME license or copyright; see http://www.asme.org/terms/Terms_Use.cfm

$$u^{(2a)} = \frac{1}{G}\sqrt{\frac{r}{2\pi}}\cos\frac{\theta}{2}\left(1 - 2\nu + \sin^2\frac{\theta}{2}\right), \tag{20a}$$

$$v^{(2a)} = \frac{1}{G}\sqrt{\frac{r}{2\pi}}\sin\frac{\theta}{2}\left(2 - 2\nu - \cos^2\frac{\theta}{2}\right), \tag{20b}$$

where

$$\sigma_{xx}{}^{(2a)} = \frac{1}{\sqrt{2\pi r}}\cos\frac{\theta}{2}\left(1 - \sin\frac{\theta}{2}\sin\frac{3\theta}{2}\right) + O(\sqrt{r}), \tag{21a}$$

$$\sigma_{yy}{}^{(2a)} = \frac{1}{\sqrt{2\pi r}}\cos\frac{\theta}{2}\left(1 + \sin\frac{\theta}{2}\sin\frac{3\theta}{2}\right) + O(\sqrt{r}), \tag{21b}$$

and

$$\sigma_{xy}{}^{(2a)} = \frac{1}{\sqrt{2\pi r}}\cos\frac{\theta}{2}\sin\frac{\theta}{2}\cos\frac{3\theta}{2} + O(\sqrt{r}). \tag{21c}$$

The second auxiliary solution denoted by the superscript, 2*b*, for pure mode-II deformation of the cracked body is also introduced so that

$$K_{\mathrm{I}}{}^{(2b)} = 0 \quad \text{and} \quad K_{\mathrm{II}}{}^{(2b)} = 1. \tag{22}$$

This gives

$$M^{(1,2b)} = 2\alpha K_{\mathrm{II}}{}^{(1)}, \tag{23}$$

and

$$M^{(1,2b)} = \int_\Gamma \left(C_{ijkl}\, u_{i,j}{}^{(1)}\, u_{k,l}{}^{(2b)}\, dy - \left[T_i{}^{(1)}\frac{\partial u_i{}^{(2b)}}{\partial x} + T_i{}^{(2b)}\frac{\partial u_i{}^{(1)}}{\partial x}\right] ds\right). \tag{24}$$

The quantities $T_i{}^{(2b)}$ and $u_i{}^{(2b)}$ can be determined by

$$T_i{}^{(2b)} = \sigma_{ij}{}^{(2b)}\, n_j, \tag{25}$$

and

$$u^{(2b)} = \frac{1}{G}\sqrt{\frac{r}{2\pi}}\sin\frac{\theta}{2}\left(2 - 2\nu + \cos^2\frac{\theta}{2}\right), \tag{26a}$$

$$v^{(2b)} = \frac{1}{G}\sqrt{\frac{r}{2\pi}}\cos\frac{\theta}{2}\left(1 - 2\nu + \sin^2\frac{\theta}{2}\right), \tag{26b}$$

where

$$\sigma_{xx}{}^{(2b)} = \frac{-1}{\sqrt{2\pi r}}\sin\frac{\theta}{2}\left(2 + \cos\frac{\theta}{2}\cos\frac{3\theta}{2}\right) + O(\sqrt{r}), \tag{27a}$$

$$\sigma_{yy}{}^{(2b)} = \frac{1}{\sqrt{2\pi r}}\sin\frac{\theta}{2}\cos\frac{\theta}{2}\cos\frac{3\theta}{2} + O(\sqrt{r}), \tag{27b}$$

and

$$\sigma_{xy}{}^{(2b)} = \frac{1}{\sqrt{2\pi r}}\cos\frac{\theta}{2}\left(1 - \sin\frac{\theta}{2}\sin\frac{3\theta}{2}\right) + O(\sqrt{r}). \tag{27c}$$

Equations (17), (18), and (23), (24) provide sufficient information to determine $K_{\mathrm{I}}{}^{(1)}$ and $K_{\mathrm{II}}{}^{(1)}$ directly. It should be noted that, in solving for $K_{\mathrm{I}}{}^{(1)}$ and $K_{\mathrm{II}}{}^{(1)}$, the integrals, $M^{(1,2a)}$ and $M^{(1,2b)}$, have to be evaluated accurately and explicitly. For a mixed-mode fracture problem with a given crack geometry and loading condition, this can be achieved by integrating equations (18) and (24) numerically along a properly selected path Γ in the far field so as to avoid crack-tip complications. A finite-element method, using eight-node isoparametric elements, is currently employed to calculate $T_i{}^{(1)}$ and $u_i{}^{(1)}$ along Γ. The M-integral is then evaluated by the following second-order Gaussian quadrature:

$$M = \sum_{n=1}^{N}\sum_{m=1}^{3}[H_m F_n(x_m, y_m)]\Delta s_n, \tag{28}$$

along the contour Γ passing through Gaussian stations of each element (Fig. 2), where

$$F_n(x_m, y_m) = \left(W^{(1,2)}\, n_1 - \left[T_i{}^{(1)}\frac{\partial u_i{}^{(2)}}{\partial x} + T_i{}^{(2)}\frac{\partial u_i{}^{(1)}}{\partial x}\right]\right)_{(x_m, y_m)}, \tag{29}$$

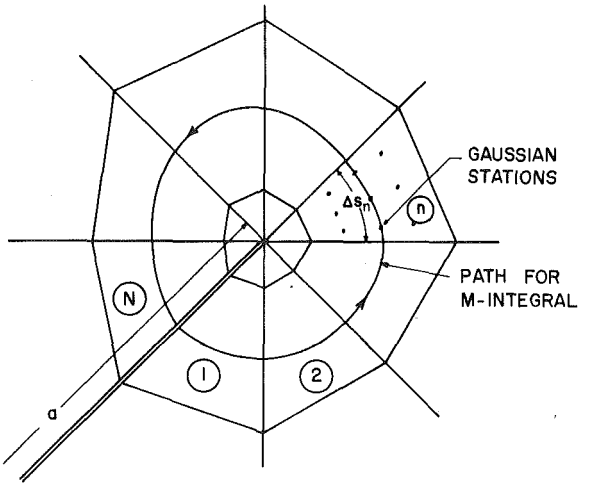

Fig. 2 Gaussian stations, finite-element mesh, and integration path of *M*-integral around crack tip

and H_m is a weight coefficient of the Gaussian quadrature formula; (x_m, y_m) are the Cartesian coordinates of Gaussian stations; N, the total number of elements included in the integration path Γ, and Δs_n is a segment of Γ within the nth element.

4 Numerical Results

The procedure just outlined has been programmed for studying general two-dimensional mixed-mode crack problems in isotropic elastic solids. Evaluation of the conservation contour integrals have been conducted in conjunction with a conventional finite-element method, using eight-node isoparametric elements. The primary objective of this section is to illustrate the effectiveness of the current approach. Of particular interest are the numerical simplicity and computational efficiency of the analysis. Stress-intensity factor solutions have been obtained by solving equations (17) and (23) directly for several examples whose solutions are available in the literature. Direct comparisons of current results with the published solutions are made to demonstrate the accuracy, convergence and other characteristics of the current approach. More complex and practical fracture problems of crack emanation from a circular hole in a tension plate are studied also to illustrate the capacity of the method in dealing with mixed-mode fracture problems.

4.1 Crack Oriented at an Angle θ in an Infinite Plate. The first numerical example studied in this section deals with a crack in an infinite plate subjected to a uniaxial nominal stress, σ_∞, as shown in Fig. 3. The crack is assumed to have a length of $2a$ and is oriented at an angle θ with respect to the tensile loading direction. This problem is chosen deliberately and studied first because an analytically derived and unquestionably correct, exact solution is available in the literature. The exact solution for the problem has been shown [17] to have the form

$$K_1{}^\infty = \sigma_\infty \sin^2\theta\,\sqrt{\pi a}\,,$$

and

$$K_{\mathrm{II}}{}^\infty = \sigma_\infty \sin\theta\cos\theta\,\sqrt{\pi a}.$$

For simplicity without loss of generality, the following geometric and loading variables are assumed: $\theta = 45°$, $a = \sqrt{2}$ in. and $\sigma_\infty = 1$ psi. Thus the exact solution for the problem is found to be $K_{\mathrm{I}}{}^\infty = K_{\mathrm{II}}{}^\infty = 1.0538$ psi $\sqrt{\text{in.}}$ Since the finite-element method is chosen here to evaluate the tractions and displacements, $T_i{}^{(1)}$ and $u_i{}^{(1)}$, along a selected contour Γ in the far field, an inherent disadvantage is associated with the numerical approach. This results from the fact that the infinite plate cannot be modeled exactly by the present finite-element discretization. This, however, does not prevent the fundamental na-

Downloaded 01 May 2010 to 171.66.16.243. Redistribution subject to ASME license or copyright; see http://www.asme.org/terms/Terms_Use.cfm

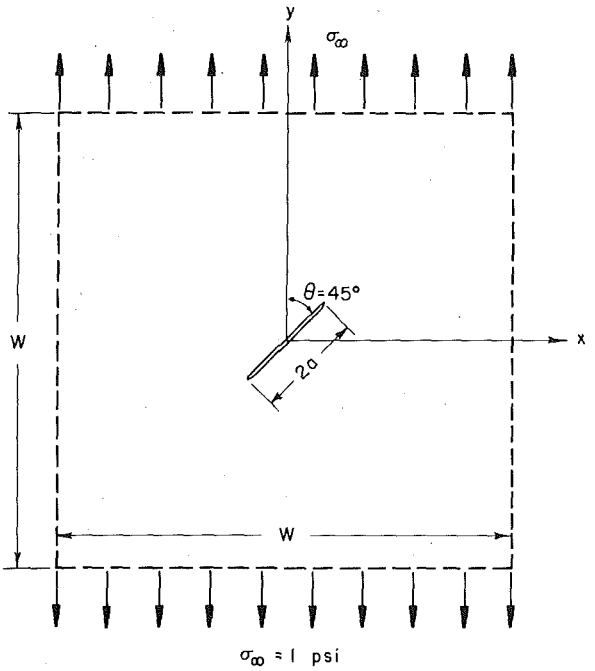

Fig. 3 Crack oriented at an angle θ in an infinite plate subjected to uniform axial tension

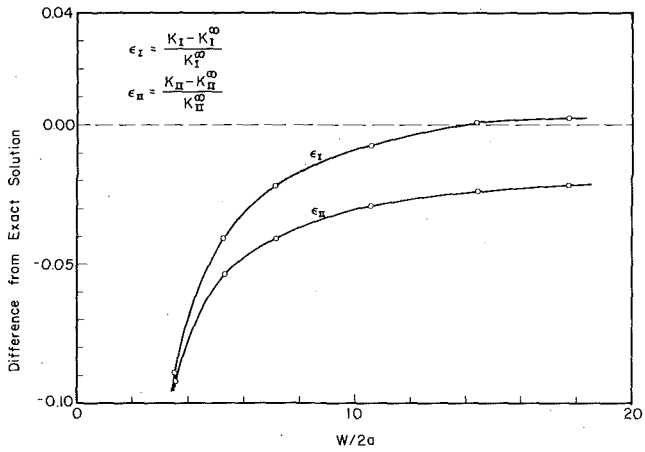

Fig. 4 Difference from exact solution for crack oriented at 45° with loading direction in tension plate

ture of current solutions for the cracked infinite plate problem from being examined. Examining finite dimensional plates of increasingly larger panel sizes, one can study the accuracy and related characteristics of the numerical solutions for the present problem. Panels (containing a crack of fixed length) of increasingly larger dimensions are used to approximate the infinite plate; the crack-tip stress-intensity solution for the infinite plate is asymptotically approached by the present results as $W/2a$ approaches infinite. Solutions of K_I and K_{II} obtained by the present analysis are compared with the exact solution K_I^∞ and K_{II}^∞. Fig. 4 gives the numerical results, indicating differences, ϵ_I and ϵ_{II}, between the K_I and K_{II} in cracked finite-dimensional plates with various $W/2a$ values and that in an infinite case. It is observed that ϵ_I and ϵ_{II} decrease very rapidly as the dimension of the plate increases. In the calculation, the plate is discretized into 90 elements for all of the cases studied. The results also reveal that, as $W/2a$ exceeds 10, current solutions and the exact ones are within 1 percent difference in K_I and 3 percent in K_{II}, respectively. The fact

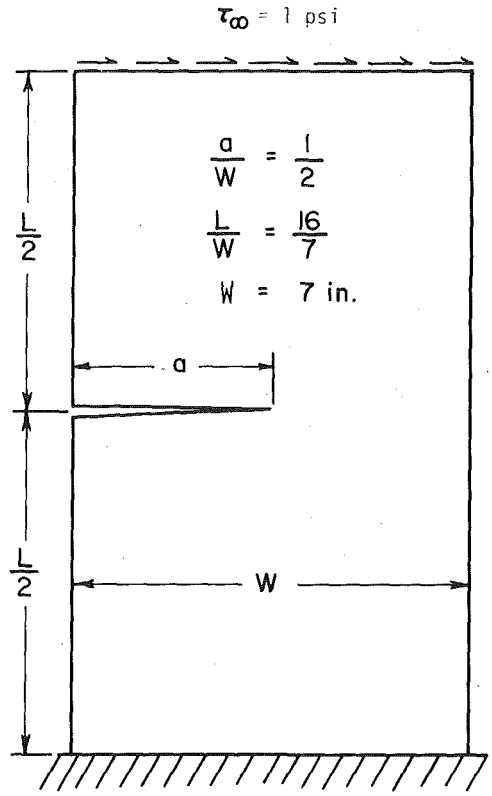

Fig. 5 Edge-notched plate subjected to nominal shear stress τ_∞

that ϵ_I and ϵ_{II} do not vanish, as shown in the figure, may be attributed to the following two sources: (*i*) the inherent approximation introduced by the finite-element method, and (*ii*) the finite width and length effects (i.e., the so-called K-calibrations). The effect of contour path selection on the accuracy of the stress-intensity factor solutions has been examined and will be discussed in the next section.

4.2 Edge Crack in Finite-Dimensional Plates. The second problem investigated in this paper deals with an edge crack in a finite-dimensional plate subjected to a uniformly distributed nominal shear stress τ_∞ as shown in Fig. 5. The geometry and linear dimensions of the cracked plate are given in the figure. Mixed-mode stress-intensity factors, $K_I°$ and $K_{II}°$, calculated by a boundary collocation method [18], are used as the reference solution:

$$K_I° = 34.0 \text{ psi}\sqrt{\text{in.}} \quad \text{and} \quad K_{II}° = 4.55 \text{ psi}\sqrt{\text{in.}}$$

Results obtained by the current numerical procedure are expected to be affected by the discretization of the continuum (i.e., the number of elements in the analysis) and the path of integration. Assessments of solution accuracy and convergence by evaluating their relative differences from the reference solution were made to examine the optimum mesh configuration and integration path for computation. Fig. 6 indicates that differences from the reference solution increase drastically with coarser grids. When finer meshes are used, say, with more than 30 elements, the solutions become quite accurate and are relatively insensitive to mesh arrangements. Contours with circular paths of different radii, r's, are chosen to evaluate the M-integral and therby the stress-intensity factor solutions. Effects of different integration paths on solution accuracy and convergence for a discretized panel of 52 elements and 173 nodes are shown in Fig. 7. Significant deviations from the reference solution are observed as the contours become very close to the crack tip due to the fact that the conventional elements used in the crack-tip region can not describe the singular near field behavior accurately. More stable and accurate results are obtained in the cases with integration paths farther away from the crack-tip region, and the solutions become insensitive to the integration paths chosen when the contours are well removed from the

Downloaded 01 May 2010 to 171.66.16.243. Redistribution subject to ASME license or copyright; see http://www.asme.org/terms/Terms_Use.cfm

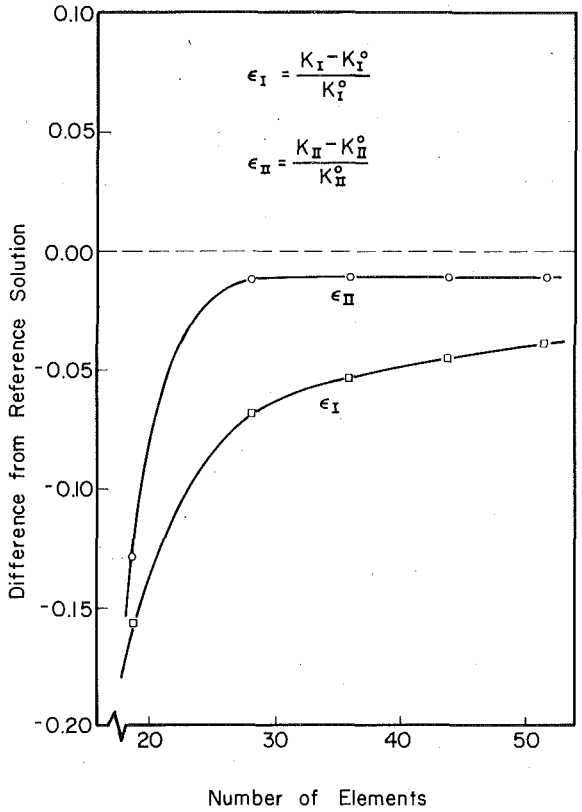

Fig. 6 Effects of number of elements on solution accuracy and convergence

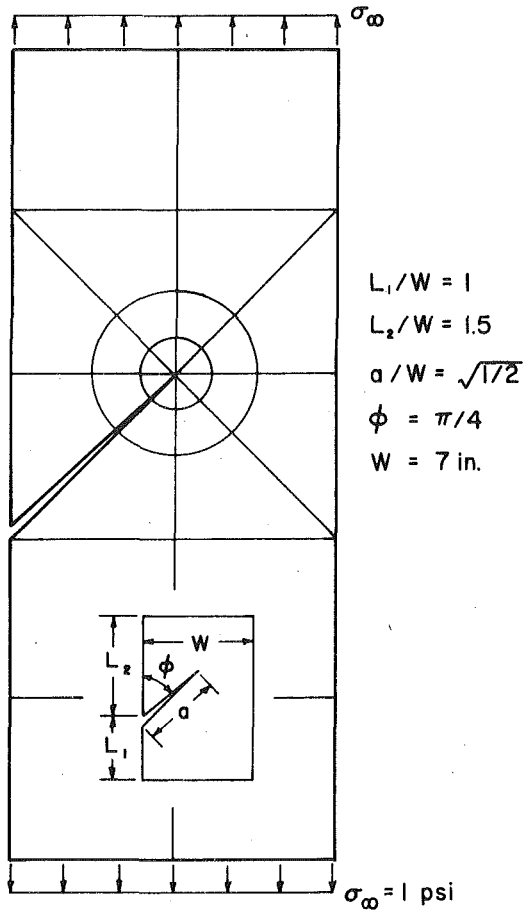

Fig. 8 Slanted edge crack in a tension plate

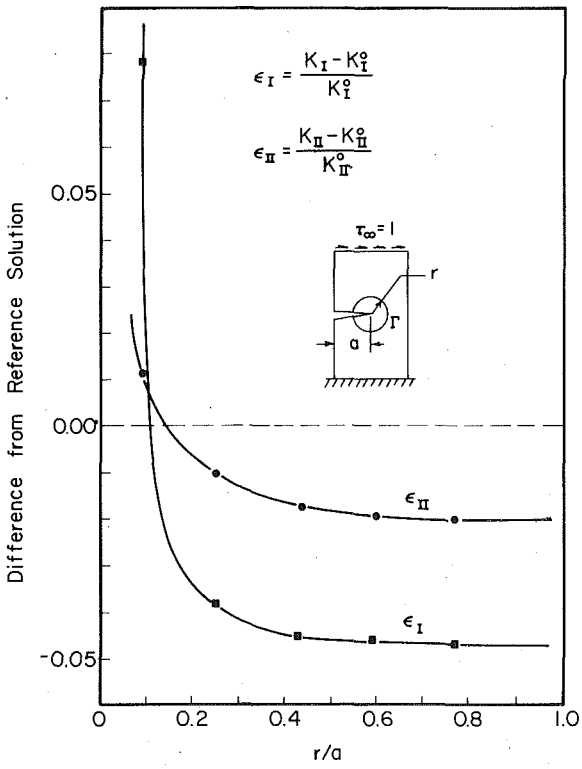

Fig. 7 Effects of different integration paths on accuracy of solutions (52 elements)

crack tip. This is expected in view of the nature of the problem, since calculation of the conservation integral is conducted along a path in the far field where field variables are generally smooth. Both K_I and K_{II} reach a range of a few percent difference from the reference solution for a typical mesh of about 30 elements when an integration contour of $r/a > 0.5$ is selected. More precisely, an analysis using 52 elements gives 3.7 percent and 1.01 percent differences in the values of K_I and K_{II}, respectively, from the boundary collocation results [18].

The next problem studied in this investigation contains an edge crack inclined at an angle 45° to the loading direction in a finite-dimensional plate subjected to a uniformly distributed nominal stress σ_∞ at its ends. The geometry of the problem and a typical finite-element discretization of the cracked plate are shown in Fig. 8. A numerical solution, which involves only 30 elements and 103 nodes, gives the following values of stress-intensity factors:

$$\frac{K_I}{(\sigma_\infty\sqrt{\pi a})} = 1.825 \quad \text{and} \quad \frac{K_{II}}{(\sigma_\infty\sqrt{\pi a})} = 0.831.$$

The results are compared with the available solution for this problem obtained by a boundary collocation method [18]. A difference of 1.67 percent in the value of K_I and 0.43 percent in K_{II} are observed.

4.3 Crack Emanating From a Circular Hole. More complicated fracture problems of crack emanation from a circular hole in an isotropic finite plate are studied also to demonstrate the capacity and versatility of the present method of analysis. Fig. 9 shows the geometry of the problem and individual dimensions of the plate. A crack of length a is assumed to emanate at (R,ϕ) of the hole boundary, where R is the hole radius and ϕ is the direction along which the crack

Downloaded 01 May 2010 to 171.66.16.243. Redistribution subject to ASME license or copyright; see http://www.asme.org/terms/Terms_Use.cfm

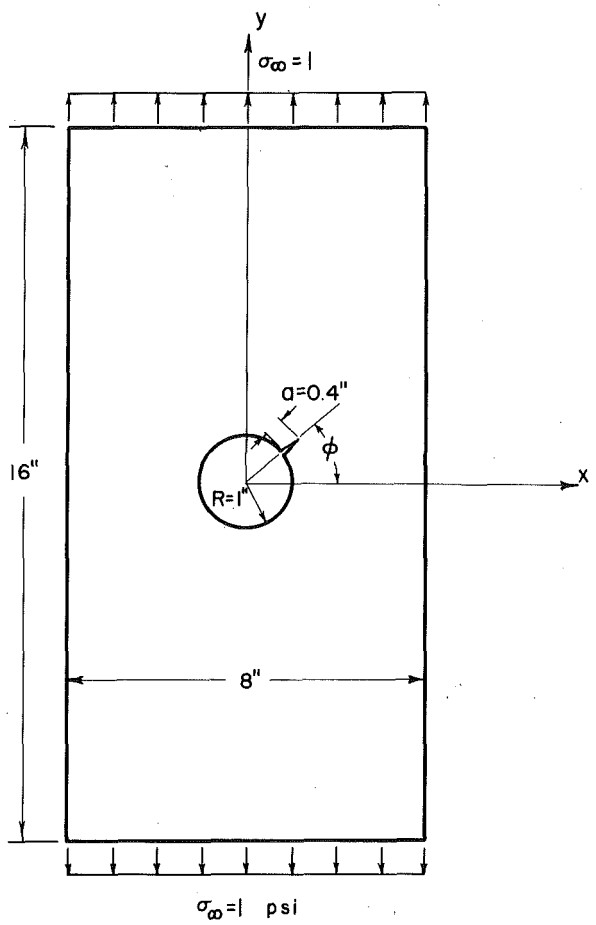

Fig. 9 Crack emanating from a circular hole in a tension plate

Table 1 Stress-intensity factors for a crack emanating from a circular hole in an isotropic panel*

	K_I (psi-$\sqrt{\text{in.}}$)	K_{II} (psi-$\sqrt{\text{in.}}$)
Stalk and Orringer [19]	2.302	0.000
Present Solution	2.333	0.000

*a/(2R) = 0.2, ϕ = 0°, 56 eight-node isoparametric elements

extends. For comparative purposes, the problem with $\phi = 0°$ was studied first to examine the accuracy of the solution. The current analysis, employing only 56 elements in the numerical computation, gives the result (Table 1), which is in very good agreement with the solution reported by Stalk and Orringer [19] using a singular hybrid-stress finite-element approach. For a more general case, for example, when the crack is oriented at 45° with respect to the loading direction in a plate with the same geometry, the analysis, using the same discretization, provides the following results:

$$K_I = 1.415 \text{ psi } \sqrt{\text{in.}}$$

and

$$K_{II} = 0.726 \text{ psi } \sqrt{\text{in.}}$$

5 Conclusions

A method of analysis, based on conservation laws of elasticity and fundamental relationships in fracture mechanics, has been presented for studying mixed-mode crack problems in two-dimensional solids. The analysis is formulated by using conservation integrals of two independent equilibrium states of an elastic isotropic solid. The method is distinct from the J and M-integral approaches for plane crack problems in that it can determine directly the individual stress-intensity factor solution for each mode in mixed-mode fracture. The solution procedure has been established and shown to be computationally efficient and operationally simple, involving only known auxiliary solutions and evaluation of conservation integrals along a suitably selected path. One of the salient features of the present approach is that the stress-intensity factor solutions can be determined accurately and directly by information obtained in the far field. The evaluation of the path-independent conservation integral can be performed along a contour well removed from the singular crack-tip region so as to avoid crack-tip complications. The present analysis can be conveniently conducted with the aid of any numerical method which can provide far-field information of field variables. Thereby complex mixed-mode fracture problems can be solved easily. When used in conjunction with a finite-element method such as the one discussed in this paper, the approach leads to stress-intensity solutions with high accuracy and fast convergence. The accuracy of the results is found to be insensitive to the discretization of the continuum and the path of integration, as long as the contour is sufficiently removed from the crack tip. Extension of the present formulation to other fracture mechanics problems, involving material anisotropy and time-dependent properties, can be achieved easily. These further developments have been successful and are reported elsewhere [20].

6 Acknowledgments

The authors wish to express their appreciation to Dr. N. Ashbaugh of System Research Laboratory, Inc., for the discussion in the early stages of this study. The computational work was carried out in the Digital Computer Laboratory of the University of Illinois and supported in part by the Research Board of the University and by NASA-Lewis Research Center through Grant NSG 3044.

7 References

1 Günther, W., "Über einige Randintegrale der Elastomechanik," *Abhandlungen der Braunschweigischen Wissenschaftlichen Gesellschaft,* Vol. 14, 1962, pp. 54–72.

2 Eshelby, J. D., "The Continuum Theory of Lattice Defects," *Solid State Physics,* eds., Seitz, F., and Turnbull, D., Vol. 3, Academic Press, New York 1956, pp. 79–144.

3 Budiansky, B., and Rice, J. R., "Conservation Laws and Energy-Release Rates," ASME JOURNAL OF APPLIED MECHANICS, Vol. 40, 1973, pp. 201–203.

4 Knowles, J. K., and Sternberg, E., "On a Class of Conservation Laws in Linearized and Finite Elastostatics," *Archive of Rational Mechanics and Analysis,* Vol. 44, 1972, pp. 187–211.

5 Green, A. E., "On Some General Formulas in Finite Elastostatics," *Archive of Rational Mechanics and Analysis,* Vol. 50, 1973, pp. 73–80.

6 Chen, F. H. K., and Shield, R. T., "Conservation Laws in Elasticity of the J-Integral Type," *Journal of Applied Mathematics and Physics (ZAMP),* Vol. 28, 1977, pp. 1–22.

7 Shield, R. T., "Conservation Laws in Finite Elasticity," *Finite Elasticity,* ed., Rivlin, R. S., AMD, Vol. 27, ASME, 1977, pp. 1–10.

8 Rice, J. R., "A Path-Independent Integral and Approximate Analysis of Strain Concentrations by Notches and Cracks," ASME JOURNAL OF APPLIED MECHANICS, Vol. 35, 1968, pp. 379–386.

9 Rice, J. R., "Mathematical Analysis in the Mechanics of Fracture," *Fracture,* Vol. II, ed., Liebowitz, H., Academic Press, New York, 1968, pp. 191–311.

10 Begley, J. A., and Landes, J. D., "The J-Integral as a Fracture Criterion," *Fracture Toughness, Part II,* ASTM STP 514, American Society for Testing and Materials, 1972, pp. 1–20.

11 Bucci, R. J., et al., "J-Integral Estimation Procedures," *Fracture Toughness, Part II,* ASTM STP 514, American Society for Testing and Materials, 1972, pp. 40–69.

12 Landes, J. D., and Begley, J. A., "Recent Developments in J_{Ic} Testing," *Developments in Fracture Mechanics Test Methods Standardizations,* ASTM STP 632, American Society for Testing and Materials, 1977, pp. 57–81.

13 Hutchinson, J. W., "Singular Behavior at the End of a Tensile Crack in a Hardening Material," *Journal of Mechanics and Physics of Solids,* Vol. 16, 1968, pp. 13–31.

14 Stern, M., Becker, E. B., and Dunham, R. S., "A Contour Integral Computation of Mixed-Mode Stress-Intensity Factors," *International Journal of Fracture,* Vol. 12, No. 3, 1976, pp. 359–368.

Downloaded 01 May 2010 to 171.66.16.243. Redistribution subject to ASME license or copyright; see http://www.asme.org/terms/Terms_Use.cfm

15 Gürtin, M. E., "On a Path-Independent Integral for Elastodynamics," *International Journal of Fracture,* Vol. 12, 1976, pp. 643–644.

16 Freund, L. B., "Stress-Intensity Factor Calculations Based on a Conservation Integral," *International Journal of Solids and Structures,* Vol. 14, 1978, pp. 241–250.

17 Paris, P. C., and Sih, G. C., "Stress Analysis of Cracks," *Fracture Toughness Testing and Its Application,* ASTM STP 381, American Society for Testing and Materials, 1965, pp. 30–83.

18 Wilson, W. K., "Combined-Mode Fracture Mechanics," PhD Dissertation, University of Pittsburgh, 1969.

19 Stalk, G., and Orringer, O., "Fracture Mechanics Analysis of Centered and Offset Fastener Holes in Stiffened and Unstiffened Panels Under Uniform Tension," Technical Report AFFDL-TR-75-70, Air Force Flight Dynamics Laboratory, Wright-Patterson Air Force Base, Ohio, 1976.

20 Yau, J. F., PhD Thesis, Department of Theoretical and Applied Mechanics, University of Illinois, Urbana, Ill., 1979.

Downloaded 01 May 2010 to 171.66.16.243. Redistribution subject to ASME license or copyright; see http://www.asme.org/terms/Terms_Use.cfm

P. S. Theocaris
Chair of Mechanics A'.
Mem. ASME

N. I. Ioakimidis
Chair of Mechanics B'.
Assoc. Mem. ASME

Athens National Technical University,
5 K. Zographou Street,
Zographou,
Athens 624, Greece

Stress-Intensity Factors and Complex Path-Independent Integrals

Path-independent integrals about crack tips may be used to estimate stress-intensity factors at crack tips in plane and antiplane elasticity problems. In this paper a new class of such integrals is established by using complex stress functions and the trivial application of the Cauchy theorem of complex analysis. Both the simple Westergaard complex potentials of plane and antiplane elasticity and the more general Muskhelishvili complex potentials will be used for the construction of appropriate path-independent integrals. Two applications of these integrals to the theoretical determination of stress-intensity factors at crack tips are presented. An optical method for the experimental determination of stress-intensity factors at crack tips, based on the use of appropriate complex path-independent integrals, is also proposed.

Introduction

The path-independent integrals, initially proposed by Rice [1], afford a direct method of evaluating the stress-intensity factors associated with notches and cracks, by bypassing the detailed solution of the corresponding boundary-value problems. This theory consists of two stages: (*i*) Establishment of path-independence of an integral which has been properly selected, in accordance with the (plane) elastic problem considered. (*ii*) Determination of the stress-intensity factor associated with the aforementioned elastic problem, by shifting the path of integration to two "convenient" positions (e.g., to infinity and on the crack) and by equating the values of the two integrals, since they have been proved in (*i*) to be path-independent.

Now, for the establishment of path-independence: (*a*) The integrand is chosen to be the mathematical expression of some basic law of (plane) elasticity (e.g., Hooke's law, Betti's reciprocal work theorem, or, as proposed in this paper, the complex potentials due either to MacGregor-Westergaard [7, 8] or to Kolosov-Muskhelishvili [9]). This expression may be properly modified (e.g., by multiplication by an appropriate factor) so that it conforms with the elastic problem considered. (*b*) The path-independence of the resulting integral is proved by application of appropriate theorems of mathematical analysis (e.g., Green's integral theorem [1] or, as proposed in this paper, Cauchy's theorems of complex analysis [10]).

It should be mentioned that, although considerable contributions have followed [1] in this field (e.g., references [2–6]), still none of the various path-independent integrals are based directly on the complex potentials. The only attempt to incorporate complex formulation in such an integral, to the best of the author's knowledge, has been made by Budiansky and Rice [19] who, based on the laws of energy conservation, gave their complex-variable forms in the cases of linear, isotropic, plane elasticity.

In the next section, using the MacGregor-Westergaard complex potentials, path-independence is proved for a certain integral, as well as its relation to the corresponding stress-intensity factor and various other path independent integrals are proposed.

In the following sections the application of complex path-independent integrals to the evaluation of stress-intensity factors is exhibited in two specific crack problems: a theoretical one and another, in which the evaluation is based on experimental data.

In the final section, the same ideas are developed on the basis of the Kolosov-Muskhelishvili complex potentials.

Use of the MacGregor-Westergaard Complex Potentials

First Mode Conditions. This is the case of straight cracks lying along the Ox-axis under symmetrical loading conditions. Only the K_I stress-intensity factor is present and the stress and displacement fields can be described by the complex potential $Z_I(z)$, $z = x + iy$, of MacGregor-Westergaard [7–8] or the modified one [12] $Z_I^* = Z_I + A_I$, where A_I is a real constant related to the loading conditions at infinity. The stress components are

$$\sigma_{xx} = \text{Re } Z_I^* - y \text{ Im } Z_I^{*\prime} - 2A_I \tag{1a}$$

$$\sigma_{yy} = \text{Re } Z_I^* + y \text{ Im } Z_i^{*\prime} \tag{1b}$$

$$\sigma_y = -y \text{ Re } Z_I^{*\prime} \tag{1c}$$

It should be mentioned, in passing, that the addition of the constant A_I to Westergaard's equations was shown [11] to be indispensable for the determination of the stress field in certain cases, but it is indifferent if we are interested in the stress-intensity factor only, as it does not affect the stress singularity. Actually, for the crack BA, shown in Fig. 1, the asymptotic behavior of the complex potential at the crack tip $A(x = a, y = 0)$ is [13]:

$$Z_I \sim Z_I^* \sim K_I[2\pi(z - a)]^{-1/2}. \tag{2}$$

Contributed by the Applied Mechanics Division for publication in the JOURNAL OF APPLIED MECHANICS.

Discussion on this paper should be addressed to the Editorial Department, ASME, United Engineering Center, 345 East 47th Street, New York, N. Y. 10017, and will be accepted until September 1, 1980. Readers who need more time to prepare a discussion should request an extension from the editorial Department. Manuscript received by ASME Applied Mechanics Division, July, 1979; final revision, October, 1979.

Copyright © 1980 by ASME
Downloaded 01 May 2010 to 171.66.16.243. Redistribution subject to ASME license or copyright; see http://www.asme.org/terms/Terms_Use.cfm

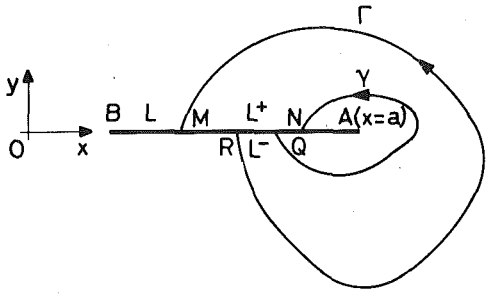

Fig. 1

To prove now the path-independence for the integrand $Z_I{}^{*2}$ we employ Cauchy's theorem [10] according to which for a closed contour C:

$$\int_C f(z)dz = 0 \tag{3}$$

if $f(z)$ is holomorphic inside and on C, while, if $f(z)$ has certain (simple) poles inside C, then the same integral is equal to the sum of the residues at these poles, e.g., in the case of one simple pole

$$\int_C \frac{f(z)}{z-\zeta}dz = 2\pi i f(\zeta). \tag{4}$$

Indeed, if $C = \Gamma \cup L_{MN}{}^{+} \cup (-\gamma) \cup L_{QR}{}^{-}$ where $L_{MN}{}^{+}$, $L_{QR}{}^{-}$ are segments of the upper and lower edges of the crack, respectively, the positive sense being indicated by the arrows in Fig. 1, then $f(z) \equiv Z_I{}^{*2}$ is holomorphic inside and on C and, by equation (3), it is valid that

$$\int_C Z_I{}^{*2}dz = 0 \tag{5}$$

where

$$Z_I{}^{*2} = (\text{Re } Z_I{}^{*2} - \text{Im } Z_I{}^{*2}) + 2i(\text{Re } Z_I{}^{*})(\text{Im } Z_I{}^{*}). \tag{6}$$

Assuming now that no real loading in the direction of the Oy-axis exists along $L_{MN}{}^{+}$, $L_{QR}{}^{-}$, that is

$$\sigma_{yy} = 0 \quad \text{for} \quad y = 0 \tag{7}$$

which is not unrealistic if M, N, Q, R lie in the vicinity of the tip A (this being the only restriction imposed on the curves Γ, γ), we have from equations (1b) and (7) that Re $Z_I{}^{*} = 0$ and therefore, from equation (6)

$$\int_S Z_I{}^{*2}dz = -\int_S \text{Im } Z_I{}^{*2}dx \quad \text{for} \quad S = L_{NM}{}^{+}, L_{QR}{}^{-}. \tag{8}$$

Now, from equation (5)

$$\text{Im} \int_C Z_I{}^{*2}dz = \text{Im}\left[\int_\Gamma Z_I{}^{*2}dz - \int_\gamma Z_I{}^{*2}dz + \int_{L_{MN}{}^{+}} Z_I{}^{*2}dz + \int_{L_{QR}{}^{-}} Z_I{}^{*2}dz\right] = 0.$$

But the last two integrals in the square brackets above are, by equation (8), real and hence

$$\text{Im} \int_\Gamma Z_I{}^{*2}dz = \text{Im} \int_\gamma Z_I{}^{*2}dz \tag{9}$$

which establishes the path-independence of the integral

$$I \equiv \text{Im} \int_\gamma Z_I{}^{*2}dz\,. \tag{10}$$

Finally, to determine the relation of this constant integral I to the stress-intensity factor, consider γ to be a "small" curve surrounding the crack tip A—e.g., a circle with center at A and radius $\epsilon \to 0$—so that $Z_I{}^{*}$ may be substituted by its asymptotic expression in equation (2). By applying equation (4) with $f(z) = K_I{}^2/(2\pi)$ and closing γ over the crack—which is permissible since $K_I{}^2/(2\pi)$ is holomorphic—we find

$$K_I{}^2 = I \equiv Im \int_\Gamma Z_I{}^{*2}dz. \tag{11}$$

Thus K_I is determined by evaluating the integral in equation (11) along any (convenient) path Γ, which may lie even far from the crack tip A. Equation (11) can be compared with the corresponding equation

$$J_R = K_I{}^2/E' \tag{12}$$

for the J-integral of Rice [1], where $E' = E$ for generalized plane stress conditions and $E' = E/(1-\nu^2)$ for plane strain conditions, E and ν denoting Young's modulus and the Poisson ratio of the elastic material of the cracked medium. The integral J_R is more general than I since it is also applicable to nonlinear elastic materials.

Finally, it can be mentioned that analogous results hold also for the left tip B of the crack L, existing if L is a crack of finite length.

Second and Third Mode Conditions. In the case of second mode conditions the stresses are expressed in terms of the MacGregor-Westergaard function Z_{II} as follows [11]:

$$\sigma_{xx} = 2\text{Im } Z_{II} + y \text{ Re } Z_{II}' \tag{13a}$$

$$\sigma_{yy} = -y \text{ Re } Z_{II}' \tag{13b}$$

$$\sigma_{xy} = \text{Re } Z_{II} - y \text{ Im } Z_{II}' + A_{II} \tag{13c}$$

and the asymptotic expression near the crack tip $A(x = a, y = 0)$ is

$$Z_{II} \sim K_{II}[2\pi(z-a)]^{-1/2}. \tag{14}$$

Assuming again that the crack edges are not loaded near the crack tip A (hence Re $Z_{II} = 0$ along the crack edges near A) we can, repeating the reasoning for the case of first mode conditions, establish the path-independence of the integral

$$I \equiv \text{Im} \int_\gamma Z_{II}{}^2dz \tag{15}$$

and its relation to the second mode stress-intensity factor

$$K_{II}{}^2 = I \tag{16}$$

We observe that equation (12) of [1] holds in this case with K_I replaced by K_{II} and can be compared with equation (16).

In the case when both first and second-mode conditions are present, i.e., both Z_I and Z_{II} are meaningful, we give following [12], their relation to Kolosov-Muskhelishvili's complex potential $\Phi(z)$ and $\Psi(z)$:

$$\Phi(z) = \frac{1}{2}[Z_I(z) - iZ_{II}(z)] \tag{17}$$

$$\Psi(z) = \tfrac{1}{2}\, z[Z_I'(z) - iZ_{II}'(z)]z + iZ_{II}(z). \tag{18}$$

These equations will be used in the examples which follow, to interrelate results found within the framework of the MacGregor-Westergaard complex formulation to those of Muskhelishvili.

We now consider the third mode of loading, that is antiplane loading conditions in the cracked medium. In this case the stress and displacement fields can be expressed in terms of the complex potential $Z_{III}(z)$ and only the third-mode stress-intensity factor K_{III} is present at the crack tip A of Fig. 1. In this case the only existing stress components σ_{xw} and σ_{yw}, where w denotes the normal direction to the plane Oxy of Fig. 1, are determined by [11]:

$$\sigma_{xw} = \text{Im } Z_{III}(z), \qquad \sigma_{yw} = \text{Re } Z_{III}(z). \tag{19}$$

By assuming again that the crack edges are not loaded in the neighborhood of the crack tip A, we find that Re $Z_{III}(z) = 0$ along these edges and further we deduce once more equations (14)–(16), but with the subscript (II) replaced now by the subscript (III). Finally, we can mention that in the third-mode case the Rice integral J_R is related to the third-mode stress-intensity factor K_{III} by

Downloaded 01 May 2010 to 171.66.16.243. Redistribution subject to ASME license or copyright; see http://www.asme.org/terms/Terms_Use.cfm

$$J_R = [(1 + \nu)/E]K_{III}^2 \tag{20}$$

that is the Rice integral J_R is $(1 + \nu)/E$ times our integral I.

Several more path-independent integrals can be constructed on the basis of the complex functions Z_I, Z_{II}, Z_{III} in accordance with the specific elastic problem treated. Thus, under a combination of all three modes and if the stress field can be described by Z_I, Z_{II}, Z_{III}, then one can consider the path-independent integral:

$$I_3 \equiv \text{Im} \int_\gamma [Z_I^2 + Z_{II}^2 + Z_{III}^2]dz. \tag{21}$$

Also, from the expression of Z_I^*:

$$Z_I^* = \sum_{k=0}^{\infty} A_k(z - a)^{k-1/2} \tag{22}$$

with A_k being real constants, valid near the crack tip A under the assumption of unloaded crack edges there [13], one is led to the path-independent integral:

$$Q_I \equiv \text{Im} \int_\gamma (z - a)^{-1/2} Z_I^* dz \tag{23}$$

and to corresponding Q_{II} and Q_{III} integrals for the second and third-mode conditions.

Finally, for integrals of the form

$$R_\delta^{(t)} = \frac{1}{b - a} \text{Im} \int_\delta (z - t)Z^2 dz, \quad t = a, b \tag{24}$$

where a, b are the abscissae of the tips A, B, respectively, and the contour δ surrounds the whole crack BA, path-independence can be established without the restriction of unloaded crack edges near the tips B, A and the ensuing relations to the stress-intensity factors are

$$K_b^2 = R_\delta^{(b)}, \quad K_a^2 = -R_\delta^{(a)}. \tag{25}$$

This is exhibited in detail in the following application.

An Application to a Theoretical Problem

Consider the crack L of length $2a$ along the Ox-axis, loaded symmetrically by the concentrated force P acting at point C on the crack edges with abscissae $x = c$ (Fig. 2). The cracked medium is assumed isotropic and elastic under generalized plane stress or plane strain conditions. The problem is to determine the stress intensity factor K_I at the tip A.

The stress field can be described by the complex function $Z_I(z)$, having the following asymptotic behavior:

(i) At infinity, since the resultant of external loading on the crack L vanishes:

$$Z_I \sim O(z^{-2}) \tag{26}$$

(ii) At the crack tip A (or B) the asymptotic behavior is described by equation (9).

(iii) Near the point $C(x = c)$ of application of the load P, according to Muskhelishvili's [9] theory for the loaded half plane:

$$Z_I \sim \mp iP/[\pi(z - c)]. \tag{27}$$

Hence we consider the following integral:

$$Q_\delta^{(a)} = \int_\delta (z + a)(z - c)Z_I^2(z)dz. \tag{28}$$

The integrand is holomorphic inside and on δ, with the exception of points $z = c$ and $z = a$, where it presents, by equations (9) and (27), simple poles, therefore it has the same value for any path δ surrounding the crack L. We consider two characteristic paths: δ_∞, that is δ tending to infinity and δ_c, that is, δ tending on the crack edges. Then, by equation (26) it is

$$Q_\delta^{(a)} = Q_{\delta_\infty}^{(a)} = 0 \tag{29a}$$

and for δ tending to δ_c, $Q_{\delta_c}^{(a)}$ is equal to the sum of the residues at $z = c$ and $z = a$:

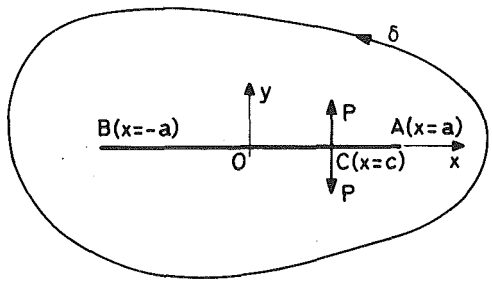

Fig. 2

$$Q_\delta^{(a)} = Q_{\delta_c}^{(a)} = 2a(a - c)K_I^2 - 2(c + a)P^2/\pi. \tag{29b}$$

From equations (29a, b):

$$K_I = P\left(\frac{1}{\pi a}\frac{a + c}{a - c}\right)^{1/2}. \tag{30}$$

Furthermore, if it is assumed that the symmetric concentrated loads P are replaced by opposite pressure distributions $p(x)$ along the crack edges, then, by using the principle of superposition, we obtain from equation (30):

$$K_I = \frac{1}{(\pi a)^{1/2}} \int_{-a}^{a} p(x)\left(\frac{a + x}{a - x}\right)^{1/2} dx. \tag{31}$$

These are well-known results of plane isotropic elasticity and can be derived by various techniques. For example, from the results of Muskhelishvili [9], one obtains for the present application

$$\Phi(z) = \frac{1}{2\pi i(z^2 - a^2)^{1/2}} \int_{-a}^{a} \frac{(x^2 - a^2)^{1/2} p(x)}{x - z} dx. \tag{32}$$

This result was established by reduction of the whole problem to a Riemmann-Hilbert boundary-value problem. By taking into account equations (9) and (18a) and letting z tend to $x = a$ in equation (32), we obtain again equation (31). So, if we are interested not in the complete information about the stress field, but only in the stress-intensity factor at the crack tip(s), we can avoid the complicacies of Muskhelishvili's method by bypassing the solution of the boundary-value problem and directly determining K_I, as suggested in this section.

It is worth mentioning at this point that equation (31) was also deduced by Eshelby [2] in the simpler third-mode (antiplane) case through the use of an appropriate real path-independent integral.

An Application to an Experimental Problem

As a further application we consider the problem of the experimental determination of the stress-intensity factor at a crack tip. In this case the method, based on the derivation of light rays when a light beam impinges on a specimen, has been successfully used by Theocaris when a caustic is formed on a screen either parallel to the specimen or not. The complex coordinate W of a point on the screen corresponding to a point with a complex coordinate z on the specimen is determined by [14]:

$$W = \lambda_m z + C\Phi'(z) \tag{33}$$

where λ_m is the magnification ratio of the optical setup and C an overall constant. In the cases of first and second loading modes, because of equation (17), equation (33) is written:

$$W = \lambda_m z + (C/2)Z_I'(z), \quad W = \lambda_m z - i(C/2)Z_{II}'(z). \tag{34}$$

Now, if the correspondence between z and W can be experimentally established (which can be attained by several methods, e.g., by creating small reflective areas at the specific positions z of the specimen's surface we are interested in, as proposed by Sharpe and Martin [15]) then either $\Phi'(z)$ or $Z_I'(z)$ and $Z_{II}'(z)$ can be determined from equations (33) or (34). Further on, by constructing appropriate path-independent integrals involving Φ' and Z', we can relate these,

Downloaded 01 May 2010 to 171.66.16.243. Redistribution subject to ASME license or copyright; see http://www.asme.org/terms/Terms_Use.cfm

experimentally determined, derivatives to the sought stress-intensity factors.

As an example consider the first mode case, assuming unloaded the crack edges L^+, L^- near the crack tip $z = a$ (Fig. 1). Since, from equation (22):

$$(z-a)^{1/2}Z_I^{*\prime} \sim -\frac{A_0}{2}\frac{1}{z-a} \quad \text{and} \quad A_0 = \frac{K_I}{\sqrt{2\pi}},$$

we construct the integral Q_γ which is easily proved to be path-independent and related to K_I as follows:

$$Q_\gamma \equiv \text{Im} \int_\gamma (z-a)^{1/2}Z_I^{*\prime}(z)dz = -K_I\sqrt{\frac{\pi}{2}}. \tag{35}$$

We should observe that, due to the path-independence, equation (35) permits the evaluation of K_I even with values of $Z_I^{*\prime}$ experimentally determined at points z far away from the crack tip $z = a$. Finally, it should be emphasized that with this experimental method of evaluating stress-intensity factors, the analytical approximation of truncating the series in equation (22) to the first two or three terms (as has always been done near the crack tip up to now [16]) is avoided.

Use of the Kolosov-Muskhelishvili Complex Potentials

The complex potentials $\Phi(z)$ and $\Psi(z)$ of Kolosov-Muskhelishvili afford an alternative elastotheoretical basis for the construction of path-independent integrals, the mathematical counterpart remaining the same: Cauchy's integral formulas (3) and (4).

The advantage of Φ, Ψ, compared to Z_I, Z_{II}, Z_{III}, is that the former are more general, that is applicable to any type of loading conditions. The integrands, as has been already shown in the previous sections, consist of products of an appropriate expression of Φ and/or Ψ with a holomorphic complex factor, thus leading to a variety of path-independent integrals, their choice depending usually on the specific problem treated.

As a simple example to illustrate the foregoing ideas, consider the familiar crack of Fig. 3 with one concentrated force P acting at the origin O in the direction of the positive Oy-axis. Following Muskhelishvili [9] we replace $\Psi(z)$ by

$$\Omega(z) \equiv \overline{\Phi}(z) + z\overline{\Phi}'(z) + \overline{\Psi}(z) \tag{36}$$

hence

$$\sigma_{yy} - i\sigma_{xy} = \Phi(z) + \Omega(\bar{z}) + (z-\bar{z})\overline{\Phi'(z)}. \tag{37}$$

Then, according to the same reference [9], the problem exhibits the following asymptotic behavior:

(i) At infinity:

$$\Phi(z) + \Omega(z) \sim \frac{(\kappa-1)Pi}{2\pi(\kappa+1)z} \tag{38}$$

where κ: denotes the well-known constant of Muskhelishvili.

(ii) At the crack tip A:

$$\Phi(z) \sim \Omega(z) \sim \frac{1}{2}(K_I - iK_{II})[2\pi(z-a)]^{-1/2} \tag{39a}$$

and at the crack tip B:

$$\Phi(z) \sim \Omega(z) \sim \frac{1}{2i}(K_I + iK_{II})[2\pi(z+a)]^{-1/2}. \tag{39b}$$

(iii) At the origin 0 (point of application of P):

$$\Phi(z) + \Omega(z) \sim -\frac{P}{2\pi zi}. \tag{40}$$

We consider the integral:

$$T_\delta \equiv \int_\delta z[\Phi(z) + \Omega(z)]^2 dz \tag{41}$$

whose independence of the contour δ (Fig. 3) may be easily shown. To find its relation to the stress-intensity factor, we equate the values of this integral obtained for two limiting positions of the path δ: T_∞, for δ tending to infinity with T_C for δ tending into the crack.

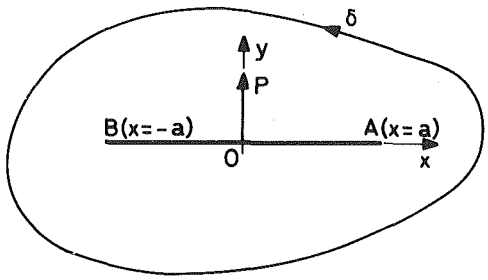

Fig. 3

Since the integrand in equation (41) is holomorphic inside and along δ with simple poles at $z = \pm a$, $z = 0$, as indicated by equations (39a, b), (40), these integrals are, because of equation (38):

$$T_\infty = -\frac{P^2}{4\pi^2}\left(\frac{\kappa-1}{\kappa+1}\right)^2 \int_\delta \frac{dz}{z} = -i\frac{P^2}{2\pi}\left(\frac{\kappa-1}{\kappa+1}\right)^2 \tag{42}$$

and because of equations (39a, b) and (40):

$$T_C = -i\frac{P^2}{2\pi} + ia(K_I - iK_{II})^2 + ia(K_I + iK_{II})^2. \tag{43}$$

By equating the right-hand sides of equations (42) and (43):

$$K_I{}^2 - K_{II}{}^2 = \frac{P^2}{4\pi a}\left[1 - \left(\frac{\kappa-1}{\kappa+1}\right)^2\right] \tag{44}$$

which is in agreement with the corresponding results obtained by Ouchterlony [6] by using real path-independent integrals.

References

1 Rice, J. R., "A Path-Independent Integral and the Approximate Analysis of Strain Concentration by Notches and Cracks," ASME JOURNAL OF APPLIED MECHANICS, Vol. 35, 1968, pp. 379–386.

2 Eshelby, J. P., "The Calculation of Stress Energy Release Rates," in *Prospects of Fracture Mechanics*, eds., Sih, G. C., et al., Noordhoff, Leyden, The Netherlands, 1974, pp. 69–84.

3 Carlsson, A. J., "Path-Independent Integrals in Fracture Mechanics and Their Relation to Variational Principles," in *Prospects of Fracture Mechanics*, eds., Sih, G. C., et al., Noordhoff, Leyden, The Netherlands, 1974, pp. 139–158.

4 Chen, F. H.-P., "Conservation Laws in Elasticity of the J-Integral Type," PhD Thesis at the University of Illinois, Urbana-Champaign, Ill., 1976 [Available from University Micr. Int. order No. 77-8955].

5 Stern, M., Becker, E. B., and Dunham, R. S., "A Contour Integral Computation of Mixed-Mode Stress-Intensity Factors," *International Journal of Fracture*, Vol. 12, 1976, pp. 359–368.

6 Ouchterlony, F., "Some Stress-Intensity Factors for Self-Similar Cracks, Derived From Path-Independent Integrals," *Journal of Elasticity*, Vol. 8, 1978, pp. 259–271.

7 MacGregor, C. W., "The Potential Function Method for the Solution of Two-Dimensional Stress Problems," *Transactions of the American Mathematical Society*, Vol. 38, 1935, pp. 177–186.

8 Westergaard, H. M., "Bearing Pressures and Cracks," ASME JOURNAL OF APPLIED MECHANICS, Vol. 6, 1939, pp. A49–A53.

9 Muskhelishvili, N. I., *Some Basic Problems of the Mathematical Theory of Elasticity*, 4th ed., P. Noordhoff, Groningen, 1963.

10 Phillips, E. G., *Functions of a Complex Variable*, 8th ed., Oliver and Boyd, Edinburgh, 1957, pp. 89–95.

11 Paris, P. C., and Sih, G. C., "Stress Analysis of Cracks," in *Fracture Toughness Testing and Its Applications*, ASTM Special Technical Publication No 381, The American Society for Testing and Materials and the National Aeronautics and Space Administration, Philadelphia, Pa., 1964, pp. 30–83.

12 Eftis, J., and Liebowitz, H., "On the Modified Westergaard Equations for Certain Plane Crack Problems," *International Journal of Fracture Mechanics*, Vol. 8, 1972, pp. 383–392.

13 Bueckner, H. F., "Field Singularities and Related Integral Representations," in *Methods of Analysis and Solution of Crack Problems* (*Mechanics of Fracture*, Vol. 1, ed., Sih G. C., Noordhoff, Leyden, The Netherlands, 1973, Chapter 5, pp. 239–314.

14 Theocaris, P. S., "A Theoretical Consideration of the Constrained Zones in an Array of Interacting Collinear and Asymmetric Cracks," *Acta Mechanica*, Vol. 17, 1973, pp. 169–189.

15 Sharpe, W. N., and Martin, D. R., "Optical Measurement of the In-Plane Strain/Displacement Near Crack Tips at HighTemperature," *VDI-Berichte*, Nr. 313, 1978, pp. 195–201.

16 Theocaris, P. S., and Ioakimidis, N. I., "An Improved Method for the

Downloaded 01 May 2010 to 171.66.16.243. Redistribution subject to ASME license or copyright; see http://www.asme.org/terms/Terms_Use.cfm

Determination of Mode I Stress Intensity Factors by the Experimental Method of Caustics," *Journal of Strain Analysis,* Vol. 14, No. 2, July 1979.

17 Freund, L. B., "Stress Intensity Factor Calculations Based on a Conservation Integral," *International Journal of Solids and Structures,* Vol. 14, 1978, p. 241.

18 Ouchterlony, F., "Symmetric Branching of a Wedge by Transverse Displacements," *Journal of Elasticity,* submitted for publication.

19 Budiansky, B., and Rice, J. R., "Conservation Laws and Energy-Release Rates," ASME JOURNAL OF APPLIED MECHANICS, Vol. 40, 1973, pp. 201–203.

Downloaded 01 May 2010 to 171.66.16.243. Redistribution subject to ASME license or copyright; see http://www.asme.org/terms/Terms_Use.cfm

A. F. Mak
Department of Civil Engineering.
Student Mem. ASME.

L. M. Keer
Professor,
Department of Civil Engineering.
Mem. ASME

S. H. Chen[2]
Department of Mechanical Engineering.
Assoc. Mem. ASME

J. L. Lewis
Departments of Civil Engineering
and Orthopaedic Surgery.
Mem. ASME

Northwestern University,
Evanston, Ill. 60201

A No-Slip Interface Crack[1]

Adhesive fracture of an interdigitated or very rough interface is investigated by considering an interface crack with no-slip zones. Both the normal and the shear stresses are singular at the crack tip with the Mode II stress-intensity factor being generally smaller than that of the Mode I.

Introduction

The mechanics of cracks at a bimaterial interface, so called adhesive fracture mechanics, has received considerable attention recently. Previous solutions of interface cracks [1, 2] have contained oscillating singularities at the crack tip and result in the physically unrealistic feature of material interpenetrations. Comninou [3] eliminated this problem by assuming contact regions near the crack tips, leading to a physically acceptable solution. The crack considered by Comninou could undergo relative shear slip within the crack. In several applications relative slip between the crack faces is not possible. An analysis for such a no-slip interface crack is presented in this paper. Although the solution does not contain oscillating singularities at the crack tips, considerations of contact zones need not be made since a no-slip transition region introduces only square root singularities.

The solution is motivated by problems in internal artificial human joints, in which the artificial material forming the articulating surface is connected to the bone by room temperature hardening polymer, polymethylmethacrylate (PMMA). This material does not adhere to the bone, but rather forms a mechanical interlock. A significant problem with the artificial joints is that they can come loose from the bone. Although the exact mechanism of loosening is unknown, the process probably involves mechanical crack propagation along the bone—PMMA interface. A hypothesized loosening process is, first, propagation of initial interface flaws to complete interface failure, next growth of fibrous material at the interface due to relative motion, and finally degradation of the lining material to cause joint pain and symptoms of clinical loosening. The first step in establishing the validity of this hypothesis is a study of the crack propagation phenomena and the mechanics of interface cracks. Of primary concern is the loosening of knee prostheses which are afixed to cancellous bone. This bone is spongelike in appearance with pore sizes of the order of 1 mm. Because of this structure the bone-PMMA interface is very irregular, with typical perturbations of greater than 1 mm. In such a surface, failure would be expected to be primarily tensile, since the interdigitation would prevent shear slip. A certain relative normal displacement could occur. For minimal normal displacement the crack would be a "no-slip interface crack," in which there is no relative shear displacement along the entire interface. As the crack opened to a value greater than the interdigitation height, a shear stress free zone would form, forming a "mixed no-slip interface crack" in which the center region could transmit neither tension nor shear stress and the end zones could transmit shear in a no-slip condition, but not tensile stress. Such a crack may be physically realistic in other applications where crack interface surfaces are very rough. The no-slip crack would be a limiting case for a conventional interface crack with friction. The solution for such an interfacial crack follows.

Interface Crack With Transition Zones of Nonslip

From superposition considerations, it can be shown that the strength of the stress singularity at the tips of an interface crack in a uniform tensile field P_0 is equivalent to that associated with the

[1] This work was supported by Grants RSA 23P-55898, NIH AM00081.
[2] Presently, Research Engineer, Deere & Co., Moline, Ill. 61265.
Contributed by the Applied Mechanics Division for publication in the JOURNAL OF APPLIED MECHANICS.
Discussion on this paper should be addressed to the Editorial Department, ASME, United Engineering Center, 345 East 47th Street, New York, N. Y. 10017, and will be accepted until September 1, 1980. Readers who need more time to prepare a discussion should request an extension from the Editorial Department. Manuscript received by ASME Applied Mechanics Division, May, 1979; final revision, October, 1979.

Copyright © 1980 by ASME
Downloaded 01 May 2010 to 171.66.16.243. Redistribution subject to ASME license or copyright; see http://www.asme.org/terms/Terms_Use.cfm

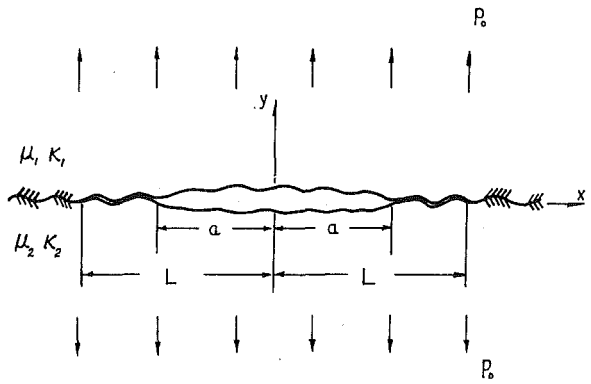

Fig. 1 Geometry and coordinate system for interfacial crack

same crack being subjected to an internal pressure P_0. The mathematical formulation of such a problem is given next.

Consider two elastic isotropic materials represented by two half planes $y > 0$ and $y < 0$ that are bonded along the interface $y = 0$ except for a region $-L < x < L$ where adhesion is lost (Fig. 1). The symbols μ and ν are, respectively, the shear modulus and Poisson's ratios. Note that due to interdigitations, relative shear motions are prohibited at the crack tip regions $a < |x| < L$; while on $|x| < a$, it is assumed that the crack has opened to sufficient extent that the surface are cleared of the mechanical interlocking and relative tangential slip can occur. The boundary conditions at $y = 0$ are as follows:

$$|x| \geq 0, \quad \sigma_{xy}{}^1 = \sigma_{xy}{}^2, \quad \sigma_{yy}{}^1 = \sigma_{yy}{}^2 \tag{1a,b}$$

$$|x| < L, \quad \sigma_{yy}{}^1 = \sigma_{yy}{}^2 = -P_0 \tag{1c}$$

$$|x| < a, \quad \sigma_{xy}{}^1 = \sigma_{xy}{}^2 = 0 \tag{1d}$$

$$|x| > L, \quad u_y{}^1 = u_y{}^2 \tag{1e}$$

$$|x| > a, \quad u_x{}^1 = u_x{}^2, \tag{1f}$$

where the σ's and u's are stresses and displacements, respectively. Superscripts are used to distinguish the two materials.

The Papkovitch-Neuber potentials φ and ψ are used to represent displacements as

$$2\mu_i u_x{}^i = -\frac{\partial \varphi_i}{\partial x} - y\frac{\partial \psi_i}{\partial x}$$

$$2\mu_i u_y{}^i = (3 - 4\nu_i)\psi_i - \frac{\partial \varphi_i}{\partial y} - y\frac{\partial \psi_i}{\partial y}, \qquad i = 1,2$$

where φ_i and ψ_i are harmonic functions of x,y.

If one now writes φ_i and ψ_i in their representations as Fourier integrals,

$$\varphi_{1,2} = (2/\pi)^{1/2} \int_0^\infty \xi^{-1} A_{1,2}(\xi) e^{\mp \xi y} \cos(\xi x) d\xi$$

$$\psi_{1,2} = (2/\pi)^{1/2} \int_0^\infty B_{1,2}(\xi) e^{\mp \xi y} \cos(\xi x) d\xi,$$

then stresses and displacements can be obtained in terms of A_i, B_i. If conditions of stress continuity (1a, 1b) are applied, then two of the four transformations, A_i, B_i, can be found in terms of the other two and the remaining mixed boundary conditions (1c)–(1f) can be written as

$$(2/\pi)^{1/2} \int_0^\infty \xi[\beta G(\xi) + \alpha H(\xi)] \cos \xi x \, d\xi = -P_0, \qquad |x| < L, \tag{2a}$$

$$(2/\pi)^{1/2} \int_0^\infty \xi[\alpha G(\xi) + \beta H(\xi)] \sin \xi x \, d\xi = 0, \qquad |x| < a, \tag{2b}$$

$$(2/\pi)^{1/2} \int_0^\infty \xi H(\xi) \sin \xi x \, d\xi = 0, \qquad |x| > L, \tag{2c}$$

$$(2/\pi)^{1/2} \int_0^\infty \xi G(\xi) \cos \xi x \, d\xi = 0, \qquad |x| > a, \tag{2d}$$

where

$$\alpha = [(1 - \nu_1)\mu_1 + (1 - \nu_2)/\mu_2]/R$$

$$\beta = [(1 - 2\nu_1)/2\mu_1 - (1 - 2\nu_2)/2\mu_2]/R$$

$$R = [(1 - \nu_1)/\mu_1 + (1 - \nu_2)/\mu_2]^2 - [(1 - 2\nu_1)/2\mu_1 - (1 - 2\nu_2)/2\mu_2]^2.$$

Note that $\beta/\alpha = \tilde{\beta}$ is Dundurs constant [4]. $G(\xi)$ and $H(\xi)$ are simply redefinition of the transforms and are used for convenience. Now if $\xi H(\xi)$ and $\xi G(\xi)$ are written as

$$\xi H(\xi) = -(2/\pi)^{1/2} \int_0^L b_y(x) \sin \xi x \, dx$$

$$\xi G(\xi) = -(2/\pi)^{1/2} \int_0^a b_x(x) \cos \xi x \, dx,$$

then equations (2a) and (2b) reduce to the following dual singular integral equations:

$$\tilde{\beta} b_x(x) - \frac{1}{\pi} \int_{-L}^{L} \frac{b_y(\xi)}{\xi - x} d\xi = P_0/\alpha \quad |x| < L \tag{3a}$$

$$\tilde{\beta} b_y(x) + \frac{1}{\pi} \int_{-a}^{a} \frac{b_x(\xi)}{\xi - x} d\xi = 0 \quad |x| < a, \tag{3b}$$

where

$$b_y(x) = 0 \quad |x| > L; \quad b_x(x) = 0 \quad |x| > a \tag{3c,3d}$$

$$b_y(x) \equiv \frac{\partial}{\partial x}[u_y{}^1(x,0) - u_y{}^2(x,0)]$$

$$b_x(x) \equiv \frac{\partial}{\partial x}[u_x{}^1(x,0) - u_x{}^2(x,0)].$$

Note that equations (3a) and (3b) can also be derived very quickly from the results of Achenbach, et al. [5], by using their equations (2.29)–(2.31) and requiring that A and T be zero. However, the solution of equations (3) will be somewhat different.

From equations (3a) and (3d), and the requirement that $b_y(x)$ be unbounded at $x = \pm L$, we can express $b_y(x)$ in terms of $b_x(\xi)$ as follows:

$$b_y(x) = \frac{\tilde{\beta}(L^2 - x^2)^{-1/2}}{\pi} \int_{-a}^{a} \frac{b_x(\xi) d\xi}{(L^2 - \xi^2)^{-1/2}(\xi - x)} - \frac{P_0 x}{\alpha(L^2 - x^2)^{1/2}} \quad |x| < L. \tag{4}$$

Substituting the foregoing equations into (3b), we have

$$\frac{(1 - \tilde{\beta}^2)}{\pi} \int_{-a}^{a} \frac{b_x(\xi) d\xi}{\xi - x} - \frac{\tilde{\beta}^2}{\pi} \int_{-a}^{a} b_x(\xi) K(\xi,x) d\xi = \frac{\tilde{\beta} P_0 x}{\alpha(L^2 - x^2)^{1/2}}, \tag{5}$$

where

$$K(\xi,x) = \frac{1}{\xi - x}\left[\left(\frac{L^2 - \xi^2}{L^2 - x^2}\right)^{1/2} - 1\right].$$

Subsidiary conditions for b_x and b_y are

$$\int_{-L}^{L} b_y(x) dx = 0 \quad \text{and} \quad \int_{-a}^{a} b_x(x) dx = 0. \tag{6a,b}$$

By symmetry, equation (6a) is automatically satisfied and the equations remaining are equations (5) and (6b).

Numerical Analysis and Results

Normalizing all lengths with respect to a and writing $\xi = aw$, $x = a\zeta$, $a' = a/L$ and

$$b_x(\omega) = \frac{F(\omega)}{(1 - \omega^2)^{1/2}},$$

Downloaded 01 May 2010 to 171.66.16.243. Redistribution subject to ASME license or copyright; see http://www.asme.org/terms/Terms_Use.cfm

equations (5) and (6b) become

$$\frac{1}{\pi}\int_{-1}^{1}\frac{F(\omega)d\omega}{(\omega-\zeta)(1-\omega^2)^{1/2}}+\int_{-1}^{1}\frac{F(\omega)}{(1-\omega^2)^{1/2}}k(\omega,\zeta)d\omega=g(\zeta), \tag{7a}$$

where

$$k(\omega,\zeta)=-\frac{1}{\pi}\frac{\tilde{\beta}^2}{1-\beta^2}\frac{1}{\omega-\zeta}\left[\left(\frac{1-a'^2\omega^2}{1-a'^2\zeta^2}\right)^{1/2}-1\right],$$

$$g(\zeta)=\frac{P_0a'\zeta}{\alpha(1-a'^2\zeta^2)^{1/2}}\cdot\frac{\tilde{\beta}}{1-\tilde{\beta}^2},$$

and

$$\int_{-1}^{1}\frac{F(\omega)d\omega}{(1-\omega^2)^{1/2}}=0. \tag{7b}$$

Using the Gauss-Chebyshev integration formula [6], equations (7) can be represented discretely as

$$\sum_{k=1}^{n}\frac{1}{n}F(\omega_k)\left[\frac{1}{\omega_k-\zeta_i}+\pi k(\omega_k,\zeta_i)\right]=g(\zeta_i)\quad i=1,\ldots,n-1$$

$$\sum_{k=1}^{n}\frac{\pi}{n}F(\omega_k)=0; \tag{8}$$

where

$$\omega_k=\cos\frac{\pi}{2n}(2k-1),$$

and

$$\zeta_i=\cos\frac{\pi i}{n}.$$

Equations (8) represent a system of n linear algebraic equations which can be solved for the n unknowns $F(\omega_1),\ldots,F(\omega_n)$.

In practical situations, the values of a/L are determined by the heights of the interdigitations. We assume that free slip only occurs in regions where the crack opening displacements become greater than the interdigitation heights. Thus, if δ denotes the average physical interdigitation height, the values of a/L will be determined by the following relation:

$$2\delta/L=-\int_{a'}^{1}b_y(\zeta)d\zeta. \tag{9}$$

However in the foregoing solution, for the sake of convenience, we have assumed known values of a/L and used equation (9) to compute the corresponding δ's afterwards.

The stress-intensity factors K_I at $x=\pm L$, K_{II} at $x=\pm a$ and $x=\pm L$ can be found from $F(\omega_k)$, [7]

$$K_{I_{x=\pm L^+}}=\lim_{x\to L^+}[2\pi(x-L)]^{1/2}\sigma_{yy}(x,0)=$$

$$-a\tilde{\beta}\sum_{k=1}^{n}\left[\frac{1}{n}F(\omega_k)(1+a'\omega_k)^{1/2}\right]+1, \tag{10a}$$

$$K_{II_{x=\pm a}}=\lim_{x\to a^+}[2\pi(x-a)]^{1/2}\sigma_{xy}(x,0)=$$

$$-\frac{1}{n}\sum_{k=1}^{n}\frac{\sin\left[\frac{2n-1}{4n}(2k-1)\pi\right]}{\sin\left[\frac{2k-1}{4n}\pi\right]}F(\omega_k), \tag{10b}$$

and

$$K_{II_{x=\pm L}}=\lim_{x\to L^-}[2\pi(L-x)]^{1/2}\sigma_{xy}(x,0)$$

$$=\tilde{\beta}^2\sum_{k=1}^{n}\left[\frac{1}{n}F(\omega_k)(1+a'\omega_k)^{1/2}\right]-\tilde{\beta}. \tag{10c}$$

Their values for various a/L and the corresponding interdigitation height δ are presented in Table 1. It will be later noted (see equation (13)) that if the interface interdigitations are greater than $P_0L/2\alpha$, or in other words, if the loading P_0 is less than $2\delta\alpha/L$, the entire crack surfaces will remain interlocked and the no-slip condition will apply to the whole interface, including the crack region.

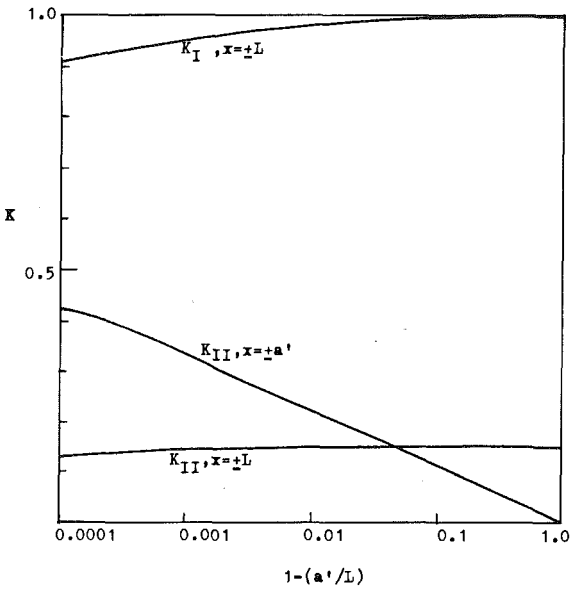

Fig. 2 The dependence of the stress-intensity factors on the size of the no-slip zone

Table 1 Stress-intensity factors versus interdigitation heights for crack of length 2 units and unit tensile loading; ($\tilde{\beta}=-0.147$)

$\frac{2\delta\cdot\alpha}{P_0L}$	$1-\frac{a'}{L}$	K_I $x=\pm L$	K_{II} $x=\pm a'$	K_{II} $x=\pm L$
0.013	0.0001	0.91	0.42	0.13
0.042	0.001	0.95	0.33	0.14
0.136	0.01	0.98	0.22	0.14
0.342	0.0625	0.99	0.14	0.15
0.479	0.125	1.00	0.11	0.15
0.595	0.2	1.00	0.09	0.15
0.657	0.25	1.00	0.08	0.15
0.741	0.333	1.00	0.06	0.15
0.863	0.5	1.00	0.04	0.15
0.967	0.75	1.00	0.02	0.15
0.991	0.875	1.00	0.01	0.15

Comparing the first and the last row of results in Table 1, it is noted that for a reduction to 1 percent of the interdigitation heights from their critical value $P_0L/2\alpha$ (which corresponds roughly to a 10^4 times reduction of the size of the no-slip zone) the K_I at $x_1=\pm1$ drops about 10 percent, that is, K_I is not very sensitive to the presence or size of the slip or no shear stress zone. These results are presented again in Fig. 2 by plotting K_I, K_{II} versus various $1-a'/L$.

Interface Crack With No Tangential Slip

The condition of no tangential slip over the entire interface, is of considerable practical interest. Rather than attempt to deduce it as a limiting case of the mixed no-slip crack solution, it is more illustrative to solve this crack problem directly.

In situations where the entire crack remains interlocked in the tangential direction, $b_x(\omega)=0$ and equations (3) reduce to

$$\int_{-1}^{1}\frac{b_y(\omega)}{\omega-\zeta}d\omega=\frac{-P_0}{\pi\alpha},\quad |x|<1 \tag{11a}$$

where b_y must satisfy

$$\int_{-1}^{1}b_y(\omega)d\omega=0. \tag{11b}$$

Downloaded 01 May 2010 to 171.66.16.243. Redistribution subject to ASME license or copyright; see http://www.asme.org/terms/Terms_Use.cfm

The solution of equations (11) yields

$$b_y(\zeta) = \frac{-P_0\zeta}{\alpha(1-\zeta^2)^{1/2}}. \tag{12}$$

The crack opening displacement in the region $|\zeta| \leq 1$ can be obtained by integrating $b_y(\zeta)$ and is

$$\Delta u_y(\zeta,0) = P_0(1-\zeta^2)^{1/2}/\alpha \quad |\zeta| \leq 1. \tag{13}$$

Equation (12) is put into the equation for σ_{yy}, and when it is evaluated for $|\zeta| > 1$, we obtain

$$\sigma_{yy} = -P_0[(\zeta^2-1)^{1/2} - |\zeta|](\zeta^2-1)^{-1/2} \quad |\zeta| > 1, \tag{14}$$

which we observe to be independent of the elastic constants.

Similarly,

$$\sigma_{xy} = \begin{cases} -P_0\tilde{\beta}\zeta/(1-\zeta^2)^{1/2} & |\zeta| > 1 \\ 0 & |\zeta| > 1 \end{cases} \quad y = 0. \tag{15}$$

The Mode I stress-intensity factor K_I can be determined from

$$K_I = P_0(\pi L)^{1/2}, \tag{16a}$$

and similarly for Mode II

$$K_{II} = -\tilde{\beta}P_0(\pi L)^{1/2}. \tag{16b}$$

In a shear field, following the foregoing formulation scheme, equation (11a) becomes

$$\int_{-1}^{1} \frac{b_y(\omega)d\omega}{\omega - \zeta} = 0 \tag{17}$$

implying $b_y(\omega) = 0$. Thus the crack will not open under shear loading. This results in the desirable feature that in a biaxial stress field, if the crack remains tangentially interlocked, only the normal tensile stress component influences crack behavior.

Discussion and Conclusions

The consideration of a no-slip condition due to interface roughness has eliminated the physically undesirable feature of material overlapping obtained by the conventional modeling of interface cracks. Both the singularities which occur at $x = a,L$ are of the square-root type commonly associated with cracks in homogeneous media. Furthermore, if one lets a/L approach zero, then the results approach the limit solution for an interface crack with no tangential slip. The solution for the no-slip interface crack is considerably simpler than the solution for the mixed crack, but the K_I-values are very similar, even for small a/L. Thus, in most cases of practical interest, the no-slip crack would be an adequate approximation to the mixed crack and the simpler no-slip crack solution could be used.

The energy release rate, G, which can be obtained by letting the crack extend for an infinitesimal amount and then calculating the work done by the traction at the original crack tip region is found to be

$$G = \frac{K_I^2}{4\alpha}.$$

Table 2 The elastic properties of PMMA and cancellous bone

Material	Properties	
	μ(N/m^2)	ν
(I) PMMA	2.0×10^9	0.4
(II) Canc. bone	1.3×10^8	0.32

Applying the aforementioned results in our PMMA-cancellous bone system with material properties listed in Table 2, α and β are found to be 1.92×10^8 and -0.462×10^8 N/m^2, respectively.

From three-dimensional finite-element models of prostheses in the proximal tibia, a typical high tensile stress level at the interface is of the order of 10^5 N/m^2. From equation (13), the resulting displacement jump would be of the order of $10^{-4} \times Lm$, where L is the crack length. Typical values of L would be 0.01 m, giving an opening displacement of 10^{-6} m. This suggests that for our PMMA-cancellous bone interface, the no-slip condition will generally be satisfied even within the crack region.

Also, for this PMMA-cancellous bone combination, $K_{II} \simeq 0.24\,K_I$. Since any Mode II interface fracture will involve cohesive fracture at the interlocks, it is expected that the Mode II critical stress-intensity factor is much larger than that of Mode I for this type of interface. Hence, the interface is more likely to fail in Mode I.

References

1 Williams, M. L., "The Stresses Around a Fault or Crack in Dissimilar Media," *Bulletin of the Seismological Society of America*, Vol. 49, 1959, pp. 199–204.

2 England, A. H., "A Crack Between Dissimilar Media," ASME JOURNAL OF APPLIED MECHANICS, Vol. 32, 1965, pp. 400–402.

3 Comninou, M., "The Interface Crack," ASME JOURNAL OF APPLIED MECHANICS, Vol. 44, 1977, pp. 631–636.

4 Dundurs, J., Discussion, ASME JOURNAL OF APPLIED MECHANICS, Vol. 36, 1967, pp. 650–652.

5 Achenbach, J. D., *et al.*, "Loss of Adhesion at the Tip of an Interface Crack," *Journal of Elasticity*, Vol. 9, 1979, pp. 397–424.

6 Erdogan, F., Gupta, G. D., and Cook, T. S., "Numerical Solution of Singular Integral Equations," *Mechanics of Fracture*, Vol. 1, ed., Sih, G., Noordhoff International Publishing, Leyden, 1973.

7 Krenk, S., "On the Use of the Interpolation Polynomial for Solutions of Singular Integral Equations," *Quarterly of Applied Mathematics*, Vol. 32, 1975, pp. 479–484.

Downloaded 01 May 2010 to 171.66.16.243. Redistribution subject to ASME license or copyright; see http://www.asme.org/terms/Terms_Use.cfm

G. C. Sih
Professor of Mechanics.
Fellow ASME

E. P. Chen[2]
Mem. ASME

Institute of Fracture and Solid Mechanics,
Lehigh University,
Bethlehem, Pa. 18015

Normal and Shear Impact of Layered Composite With a Crack: Dynamic Stress Intensification[1]

The dynamic response of a layered composite under normal and shear impact is analyzed by assuming that the composite contains an initial flaw in the matrix material. Because of the complexities that arise from the interaction of waves scattered by the crack with those reflected by the interfaces within the composite, dynamic analyses of composites with cracks have been treated only for a few simple cases. One of the objectives of the present work is to develop an effective analytical method for determining dynamic stress solutions. This will not only lead to an in-depth understanding of the failure of composites due to impact but also provide reliable solutions that can guide the development of numerical methods. The analysis method utilizes Fourier transform for the space variable and Laplace transform for the time variable. The time-dependent angle loading is separated into two parts: one being symmetric and the other skew-symmetric with reference to the crack plane. By means of superposition, the transient boundary conditions consist of applying normal and shear tractions to a crack embedded in a layered composite. One phase of the composite could represent the fiber while the other could be the matrix. Mathematically, these conditions reduce the problem to a system of dual integral equations which are solved in the Laplace transform plane for the transform of the dynamic stress-intensity factor. The time inversion is carried out numerically for various combinations of the material properties of the composite and the results are displayed graphically.

Introduction

Past work on the development of high performance composite materials was mainly concerned with achieving high strength and modulus. This requirement alone, however, may result in a composite that is excessively brittle and lacks the ability to resist impact loading. The energy absorption or toughness of the composite is also an important property that must be accounted for in addition to strength and stiffness.

The concept of fracture toughness has mostly been applied to homogeneous isotropic materials [1] based on the linear fracture mechanics theories such as those advanced by Griffith, Irwin, and others. These theories, developed for single-phase materials, have had limited success in characterizing the fracture behavior of composites which are inherently nonhomogeneous and anisotropic. This is mainly because the fracture modes in composites are multifacet and can include interface failure, fiber breaking, matrix fracture, etc. The individual contribution of each of these failure modes is not clearly accounted for and/or not related to the critical failure load. As a result, large discrepancies between the theory and experiment can result.

A study on the selection of appropriate mathematical models for different unidirectional composite systems was made [2] in the case of static loading. Many of the assumptions in [2] will also be used in the dynamic problem treated here. One of them is the existence of inherent flaws or cracks which are the sites of failure initiation.

Analytical investigation of the fracture of fibrous composite materials subjected to impact loading has been meager because the elastodynamic stress analysis involves numerous parameters and is enormously complex. This is necessitated by the complex nature of the dynamic load transfer characteristics in composites containing initial imperfections such as flaws or cracks. The stress wave solution is not only time-dependent but it interacts with the material properties of the constituents of the composite and the various geometric parameters. The influence of these parameters will be analyzed in this

[1] This work was completed during Dr. Chen's tenure at Lehigh University.
[2] Presently, Division 4442, Sandia Laboratories, Albuquerque, New Mexico 87115.

Contributed by the Applied Mechanics Division for publication in the JOURNAL OF APPLIED MECHANICS.
Discussion on this paper should be addressed to the Editorial Department, ASME, United Engineering Center, 345 East 47th Street, New York, N. Y. 10017, and will be accepted until September 1, 1980. Readers who need more time to prepare a discussion should request an extension from the Editorial Department. Manuscript received by ASME Applied Mechanics Division, August, 1979; final revision, November, 1979.

Copyright © 1980 by ASME
Downloaded 01 May 2010 to 171.66.16.243. Redistribution subject to ASME license or copyright; see http://www.asme.org/terms/Terms_Use.cfm

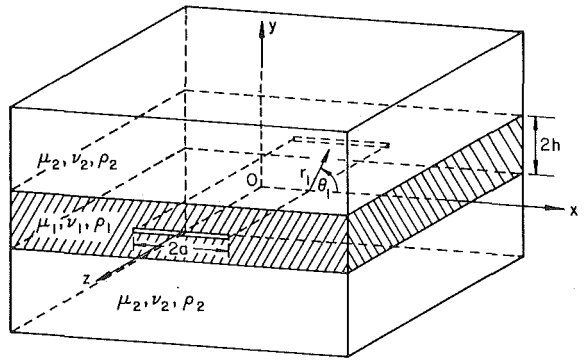

Fig. 1 Stress element near crack in matrix of fiber-reinforced composite

impact study with particular emphasis placed on determining the dynamic stress-intensity factors k_1 and k_2 arising from normal and shear loading. Their combination determines the response to loading of a more general nature and reflects the energy absorption property of the composite. Several examples of how k_1 and k_2 can be combined to predict crack behavior in dynamic stress fields are found in [3]. The question of whether there is the need of how to define a dynamic fracture toughness parameter differing from its corresponding static value has been the subject of many past and present debates within the fracture mechanics community. Thus far, no general agreement has been achieved.

This paper is concerned with dynamic fracture analysis and, particularly, with the development of an analytical method for obtaining effective dynamic stress solutions to layered composites with cracks embedded in one of the layers. Other possible failure modes will be dealt with in future communications. Effective stress solutions for k_1 and k_2 are essential as they are the prerequisites for formulating failure criteria and guiding the development of numerical procedures.

Layered Composite

Fig. 1 considers a crack in a layer of material of thickness $2h$. The composite is subjected to a time-dependent applied stress. Without serious loss in generality, the composite is assumed to be modeled by a layer of cracked material with elastic properties μ_1, ν_1, and ρ_1 sandwiched in between two dissimilar media with properties μ_2, ν_2, and ρ_2. The number of layers surrounding the cracked layer is reasonably large so that the average shear modulus μ_2, Poisson's ratio ν_2, and mass density ρ_2 can be used.

The basic two-dimensional elastodynamic equations in the theory of elasticity can be expressed in terms of two scalar potentials $\phi_j(x, y, t)$ and $\psi_j(x, y, t)$ where $i, j = 1, 2$ with 1 and 2 referring to the cracked layer and the surrounding material, respectively. In terms of the Lamé coefficients λ_j and μ_j, the dynamic stress components are

$$(\sigma_x)_j = \lambda_j \nabla^2 \phi_j + 2\mu_j \left(\frac{\partial^2 \phi_j}{\partial x^2} + \frac{\partial^2 \psi_j}{\partial x \partial y} \right)$$

$$(\sigma_y)_j = \lambda_j \nabla^2 \phi_j + 2\mu_j \left(\frac{\partial^2 \phi_j}{\partial y^2} - \frac{\partial^2 \psi_j}{\partial x \partial y} \right)$$

$$(\sigma_z)_j = \frac{\lambda_j}{2} \left(\frac{\lambda_j + 2\mu_j}{\lambda_j + \mu_j} \right) \nabla^2 \phi_j$$

$$(\tau_{xy})_j = \mu_j \left(2 \frac{\partial^2 \phi_j}{\partial x \partial y} + \frac{\partial^2 \psi_j}{\partial y^2} - \frac{\partial^2 \psi_j}{\partial x^2} \right) \quad (1)$$

where $\nabla^2 = \partial^2/\partial x^2 + \partial^2/\partial y^2$ and the thickness shear stresses are assumed to vanish. The corresponding in-plane displacements are given by

$$(u_x)_j = \frac{\partial \phi_j}{\partial x} + \frac{\partial \psi_j}{\partial y} \quad (2)$$

$$(u_y)_j = \frac{\partial \phi_j}{\partial y} - \frac{\partial \psi_j}{\partial x} \quad (2)$$

(Cont.)

Under plane strain, the material elements are constrained in the z-direction. The governing differential equations can then be obtained from the equations of motion

$$\nabla^2 \phi_j = \frac{1}{c_{1j}^2} \frac{\partial^2 \phi_j}{\partial t^2}$$

$$\nabla^2 \psi_j = \frac{1}{c_{2j}^2} \frac{\partial^2 \psi_j}{\partial t^2} \quad (3)$$

in which c_{1j} and c_{2j} are the dilatational and shear wave velocities defined as

$$c_{1j} = \left(\frac{\lambda_j + 2\mu_j}{\rho_j} \right)^{1/2}, \quad c_{2j} = \left(\frac{\mu_j}{\rho_j} \right)^{1/2} \quad (4)$$

The problem involves the determination of the potentials $\phi_j(x, y, t)$ and $\psi_j(x, y, t)$ in equations (3) from the transient boundary conditions of the crack problem.

The analysis may be simplified considerably if the problem is separated into two parts. The first concerns with normal stresses applied to the crack such that symmetry prevails about the x-axis in Fig. 1 while the second deals with shear surface tractions so that the problem is skew-symmetric with reference to the x-axis. Both of these problems will be presented separately.

Normal Impact

Let the composite body be initially at rest such that the stresses are zero everywhere. Suddenly, at $t = 0$, a normal stress of magnitude $-\sigma_0$ is applied to the top and bottom crack surfaces in Fig. 1 and kept on the crack of length $2a$ thereafter. Referring to the set of axes x and y that are placed parallel and normal to the line crack, the following conditions are prescribed:

$$(\sigma_y)_1(x, 0, t) = -\sigma_0 H(t); \quad (\tau_{xy})_1(x, 0, t) = 0, \quad 0 \le x < a; t > 0 \quad (5)$$

where $H(t)$ is the Heaviside unit step function. The symmetry conditions about the axis $y = 0$ are enforced by noting

$$(u_y)_1(x, 0, t) = 0; \quad (\tau_{xy})_1(x, 0, t) = 0, \quad x \ge a; t > 0 \quad (6)$$

Perfect bonding will be assumed along the interfaces between material 1 and material 2. This requires the stresses and displacements to be continuous across $y = \pm h$. On account of symmetry, only the upper half plane $y \ge 0$ need to be considered, i.e.,

$$(\sigma_y)_1(x, h, t) = (\sigma_y)_2(x, h, t)$$
$$(\tau_{xy})_1(x, h, t) = (\tau_{xy})_2(x, h, t) \quad (7)$$

and for the stresses and

$$(u_x)_1(x, h, t) = (u_x)_2(x, h, t)$$
$$(u_y)_1(x, h, t) = (u_y)_2(x, h, t) \quad (8)$$

for the displacements.

Dual Integral Equations. It is convenient at this point to apply the Laplace transform to the time variable t which corresponds to p in the transformed plane. Consider the standard Laplace transform on $f(t)$

$$f^*(p) = \int_0^\infty f(t) e^{-pt} dt \quad (9)$$

whose inversion is

$$f(t) = \frac{1}{2\pi i} \int_{Br} f^*(p) e^{pt} dp \quad (10)$$

in which Br stands for the Bromwich path of integration. The application of equation (9) to equations (3) yields

Downloaded 01 May 2010 to 171.66.16.243. Redistribution subject to ASME license or copyright; see http://www.asme.org/terms/Terms_Use.cfm

$$\nabla^2\phi_j^* = \frac{p^2}{c_{ij}^2}\phi_j^*$$

$$\nabla^2\psi_j^* = \frac{p^2}{c_{2j}^2}\psi_j^* \tag{11}$$

Again, the condition of symmetry requires only the consideration of x and y in the first quadrant. The Fourier cosine and sine transforms defined by

$$f^c(s) = \int_0^\infty f(x)\cos(sx)dx$$

$$f(x) = \frac{2}{\pi}\int_0^\infty f^c(s)\cos(sx)ds \tag{12}$$

and

$$f^s(s) = \int_0^\infty f(x)\sin(sx)dx$$

$$f(x) = \frac{2}{\pi}\int_0^\infty f^s(s)\sin(sx)ds \tag{13}$$

are now applied to the space variable x. This simplifies equations (3) to a set of ordinary differential equations which can be solved giving

$$\phi_1^*(x, y, p) = \frac{2}{\pi}\int_0^\infty [A^{(1)}(s, p)e^{-\gamma_{11}y} + A^{(2)}(s, p)e^{\gamma_{11}y}]\cos(sx)ds$$

$$\psi_1^*(x, y, p) = \frac{2}{\pi}\int_0^\infty [B^{(1)}(s, p)e^{-\gamma_{21}y} + B^{(2)}(s, p)e^{\gamma_{21}y}]\sin(sx)ds \tag{14}$$

for the cracked matrix and

$$\phi_2^*(x, y, p) = \frac{2}{\pi}\int_0^\infty C^{(1)}(s, p)e^{-\gamma_{12}y}\cos(sx)ds$$

$$\psi_2^*(s, y, p) = \frac{2}{\pi}\int_0^\infty C^{(2)}(s, p)e^{-\gamma_{22}y}\sin(sx)ds \tag{15}$$

for the averaged fiber-matrix material. In equations (14) and (15), the quantities γ_{1j} and γ_{2j} are given by

$$\gamma_{1j} = \left(s^2 + \frac{p^2}{c_{1j}^2}\right)^{1/2}, \quad \gamma_{2j} = \left(s^2 + \frac{p^2}{c_{2j}^2}\right)^{1/2} \tag{16}$$

The functions $A^{(1)}, A^{(2)}, B^{(1)}, \ldots, C^{(2)}$ in equations (14) and (15) are determined from the transient boundary conditions. To this end, equations (5) and (6) will be written in the Laplace transform plane

$$(\sigma_y^*)_1(x, 0, p) = -\frac{\sigma_0}{p}; \quad (\tau_{xy}^*)_1(x, 0, p) = 0, \quad 0 \le x < a \tag{17}$$

and

$$(u_y^*)_1(x, 0, p) = 0; \quad (\tau_{xy}^*)_1(x, 0, p) = 0, \quad x \ge a \tag{18}$$

In the same way, equations (7) become

$$(\sigma_y^*)_1(x, h, p) = (\sigma_y^*)_2(x, h, p)$$

$$(\tau_{xy}^*)_1(x, h, p) = (\tau_{xy}^*)_2(x, h, p) \tag{19}$$

and equations (8) take the forms

$$(u_x^*)_1(x, h, p) = (u_x^*)_2(x, h, p)$$

$$(u_y^*)_1(x, h, p) = (u_y^*)_2(x, h, p) \tag{20}$$

The stresses and displacements in equations (1) and (2) may also be transformed into the Laplace transform plane. Without going into details, the appropriate Laplace transform of the stress and displacement expressons in equations (17) to (20) may be used to satisfy all of the necessary boundary, symmetry and continuity conditions. This leads to the following set of dual integral equations:

$$\int_0^\infty A(s, p)\cos(sx)ds = 0, \quad x \ge a \tag{21}$$

$$\int_0^\infty sF_I(s, p)A(s, p)\cos(sx)ds = -\frac{\pi\sigma_0}{4\mu_1 p(1-\kappa_1^2)}, \quad x < a \tag{21}$$

(*Cont.*)

in which $F_I(s, p)$ stands for the known function

$$F_I(s, p) = \frac{1}{s(1-\kappa_1^2)\Delta_I}\left\{\left[\frac{1}{4}(s^2+\gamma_{21}^2)^2 - s^2\gamma_{11}\gamma_{21}\right]\right.$$
$$\times [\beta^{(2)} - \beta^{(3)}e^{-2(\gamma_{11}+\gamma_{21})h}]$$
$$+ s(s^2+\gamma_{21}^2)[\gamma_{21}(\beta^{(1)}\beta^{(4)} - \beta^{(2)}\beta^{(3)}) - \gamma_{11}]e^{-(\gamma_{11}+\gamma_{21})h}$$
$$\left. + \left[\frac{1}{4}(s^2+\gamma_{21}^2)^2 + s^2\gamma_{11}\gamma_{21}\right][\beta^{(4)}e^{-2\gamma_{21}h} - \beta^{(1)}e^{-2\gamma_{11}h}]\right\} \tag{22}$$

while the quantities κ_1 and Δ_I are defined as

$$\kappa_1 = (c_{21}/c_{11})^{1/2}$$

$$\Delta_I = \frac{p^2}{2c_{21}^2}\gamma_{11}[\beta^{(2)} + \beta^{(3)}e^{-2(\gamma_{11}+\gamma_{21})h} + \beta^{(4)}e^{-2\gamma_{21}h}$$
$$+ \beta^{(1)}e^{-2\gamma_{11}h}] \tag{23}$$

such that $\beta^{(1)}, \beta^{(2)}, \ldots, \beta^{(4)}$ are given by

$$\beta^{(1)} = (\alpha^{(3)}\alpha^{(6)} - \alpha^{(2)}\alpha^{(7)})/\Delta_0; \quad \beta^{(2)} = (\alpha^{(4)}\alpha^{(6)} - \alpha^{(2)}\alpha^{(8)})/\Delta_0$$

$$\beta^{(3)} = (\alpha^{(1)}\alpha^{(7)} - \alpha^{(3)}\alpha^{(5)})/\Delta_0; \quad \beta^{(4)} = (\alpha^{(1)}\alpha^{(8)} - \alpha^{(4)}\alpha^{(5)})/\Delta_0 \tag{24}$$

where Δ_0 is

$$\Delta_0 = \alpha^{(1)}\alpha^{(6)} - \alpha^{(2)}\alpha^{(5)} \tag{25}$$

The quantities $\alpha^{(1)}, \alpha^{(2)}, \ldots, \alpha^{(8)}$ in equations (25) are complicated functions of s, p and the material constants. They are given by equations (46) in Appendix A.

The problem is now reduced to finding the single unknown $A(s, p)$ governed by equations (21). Once $A(s, p)$ is known, the functions $A^{(1)}$, $A^{(2)}, \ldots, C^{(2)}$ that are required in equations (14) and (15) for the Laplace transform of the potentials $\phi_j^*(x, y, p)$ and $\psi_j^*(x, y, p)$ can be obtained from equations (47) outlined in Appendix A. What remains is the determination of a solution for the dual integral equations (21). This will be accomplished with the help of a method by Copson [5] which has been used by Chen and Sih [6] for solving dynamic crack problems involving single-phase homogeneous materials. Following the details in [5, 6], it can be shown that

$$A(s, p) = -\frac{\pi\sigma_0 a^2}{4\mu_1 p(1-\kappa_1^2)}\int_0^1 \sqrt{\xi}\,\Phi_I^*(\xi, p)J_0(sa\xi)d\xi \tag{26}$$

is a solution of equations (21) with J_0 being the zero-order Bessel function of the first kind. The function $\Phi_I^*(\xi, p)$ is calculated numerically from a Fredholm integral equation of the second kind

$$\Phi_I^*(\xi, p) + \int_0^1 \Phi_I^*(\eta, p)K_I(\xi, \eta, p)d\eta = \sqrt{\xi} \tag{27}$$

whose kernel

$$K_I(\xi, \eta, p) = \sqrt{\xi\eta}\int_0^\infty s\left[F_I\left(\frac{s}{a}, p\right) - 1\right]J_0(s\xi)J_0(s\eta)ds \tag{28}$$

is symmetric in ξ and η.

Mode I Dynamic Stress-Intensity Factor. The transmission of the time-dependent load to the vicinity of the crack tip can be best described by the intensification of the local stresses. A quantity that has been used widely in the static theory of fracture mechanics is the "stress-intensity factor" which can be extracted from the asymptotic expansions of the stresses near the crack tip. Referring to Fig. 1, let r_1 and θ_1 be a set of local polar coordinates measured from the right-hand crack tip located at $x = a$ and $y = 0$ in the matrix material, the singular character of the dynamic stresses is described only by the space variables and hence can be more easily determined in the Laplace transform domain. This observation was first made by Sih, Ravera, and Embley [7]. Following their procedure, the local stresses in terms of r_1 and θ_1 are found:

Downloaded 01 May 2010 to 171.66.16.243. Redistribution subject to ASME license or copyright; see http://www.asme.org/terms/Terms_Use.cfm

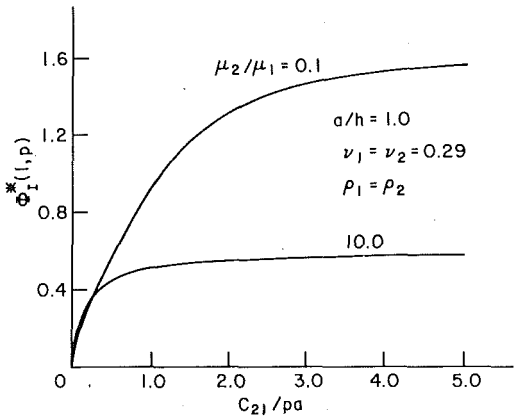

Fig. 2 Variations of $\Phi_I^*(1, p)$ with $c_{21}\,pa$ for $a/h = 1.0$

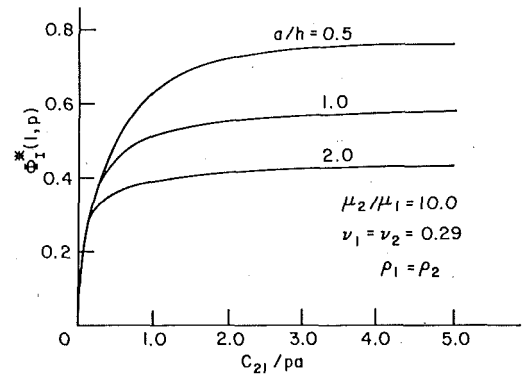

Fig. 3 Variations of $\Phi_I^*(1, p)$ with $c_{21}\,pa$ for $\mu_2/\mu_1 = 10$

$$(\sigma_x^*)_1(r_1, \theta_1, p) = \frac{k_1^*(p)}{\sqrt{2r_1}}\cos\frac{\theta_1}{2}\left(1 - \sin\frac{\theta_1}{2}\sin\frac{3\theta_1}{2}\right) + O(r_1^\circ)$$

$$(\sigma_y^*)_1(r_1, \theta_1, p) = \frac{k_1^*(p)}{\sqrt{2r_1}}\cos\frac{\theta_1}{2}\left(1 + \sin\frac{\theta_1}{2}\sin\frac{3\theta_1}{2}\right) + O(r_1^\circ)$$

$$(\sigma_z^*)_1(r_1, \theta_1, p) = \frac{k_1^*(p)}{\sqrt{2r_1}}2\nu_1\cos\frac{\theta_1}{2} + O(r_1^\circ)$$

$$(\tau_{xy}^*)_1(r_1, \theta_1, p) = \frac{k_1^*(p)}{\sqrt{2r_1}}\sin\frac{\theta_1}{2}\cos\frac{\theta_1}{2}\cos\frac{3\theta_1}{2} + O(r_1^\circ) \quad (29)$$

Only the dynamic stress-intensity factor, $k_1^*(p)$, in equations (29) need to be inverted to real time t

$$k_1^*(p) = \frac{\Phi_I^*(1, p)}{p}\sigma_0\sqrt{a} \quad (30)$$

where the function $\Phi_I^*(1, p)$ is found from $\Phi_I^*(\xi, p)$ by letting the nondimensional parameter $\xi = 1$ representing the crack tip location. The functional dependence of the stresses in r_1 and θ_1 as shown by equations (29) reveals that the dynamic stresses also possess the inverse square root singularity in terms of r_1 and that the angular distribution in θ, is the same as the case for static loading.

Applying the Laplace inversion formula in equation (10)–(30) renders the factor $k_1(t)$ as a function of time, i.e.,

$$k_1(t) = \frac{\sigma_0\sqrt{a}}{2\pi i}\int_{Br}\frac{\Phi_I^*(1, p)}{p}e^{pt}dp \quad (31)$$

It is apparent that $\Phi_I^*(1, p)$ must be first known before the integration of equation (31) can be performed. Refer to [6] for a detailed account of the procedure used for evaluating equation (31). Three different sets of $\Phi_I^*(1, p)$ values are plotted against the dimensionless Laplace

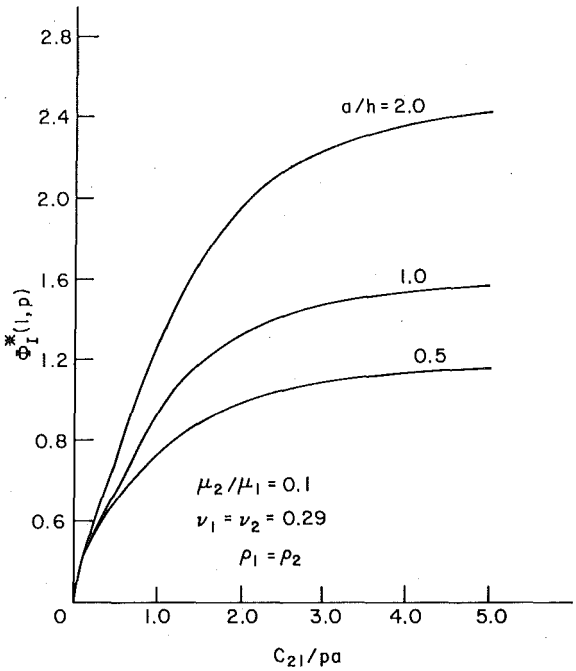

Fig. 4 Variations of $\Phi_I^*(1, p)$ with $c_{21}\,pa$ for $\mu_2\,\mu_1 = 0.1$

transform wave number c_{21}/pa. They are given in Figs. 2–4 for $\rho_1 = \rho_2$ and $\nu_1 = \nu_2 = 0.29$ while the ratios a/h and μ_2/μ_1 are varied. In general, all the curves tend to rise quickly and then flatten out. It would be more meaningful to discuss the influence of a/h and μ_2/μ_1 on the stress-intensity factor $k_1(t)$.

Figs. 5–7 display the normalized stress-intensity factor $k_1(t)/\sigma_0\sqrt{a}$ as a function of $c_{21}t/a$. In Fig. 5, the crack length to layer thickness ratio, a/h, is fixed at unity while the shear moduli ratio, μ_2/μ_1 is increased from 0.1 to 10.0 as indicated. The $k_1(t)$ factor is oscillatory in nature reaching a peak and then decreases in magnitude as time increases. The oscillation is more pronounced when the shear modulus of the cracked material is greater than that of the surrounding material, i.e., $\mu_1 > \mu_2$. The values of $k_1(t)$ decrease below those of the corresponding homogeneous case, $\mu_1 = \mu_2$, solved previously by Chen and Sih [6] when $\mu_1 < \mu_2$. The influence of a/h on $k_1(t)$ is exhibited in Figs. 6 and 7 for the two cases of $\mu_2/\mu_1 = 0.1$ and 10.0, respectively. For $\mu_2/\mu_1 = 0.1$ in Fig. 6, a decrease in a/h tends to lower the stress-intensity factor. Observed also is a small step in the curve for $a/h = 2.0$ and small time t. A possible explanation for this discontinuity is the reflection of elastic waves from the material interface.[3] The size and time scale are such that this effect showed up quantitatively in the graph while the same effect was not noticeable in the other curves. For the smaller ratios of a/h such as 0.5 and 1.0, the crack tips are further away from the interface and the influence of the reflected waves are not as pronounced. The opposite trend is observed in Fig. 7 for $\mu_2/\mu_1 = 10.0$. When the outer material is more rigid than that of the center layer, $k_1(t)$ tends to increase in magnitude as a/h is decreased. Again, a distinct step in the curve for $a/h = 2.0$ is seen for small time t. As time increases, all of the results here reduce to the corresponding static solutions of Hilton and Sih [8].

Shear Impact

Suppose that the crack in Fig. 1 is now sheared suddenly by a pair of shear stresses of magnitude $-\tau_0$ such that the upper and lower crack surfaces move in the opposite direction. This creates a defor-

[3] The numerical results are not accurate enough to determine the exact time at which this phenomenon occurs.

Downloaded 01 May 2010 to 171.66.16.243. Redistribution subject to ASME license or copyright; see http://www.asme.org/terms/Terms_Use.cfm

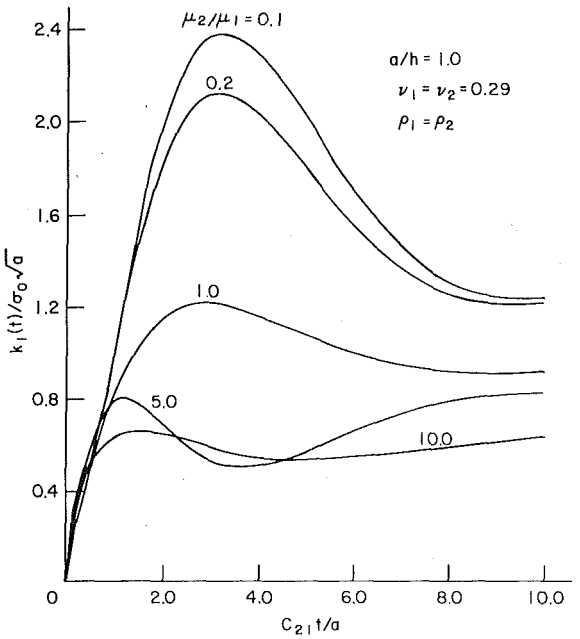

Fig. 5 Dynamic stress-intensity factor $k_1(t)$ versus time for $a/h = 1.0$

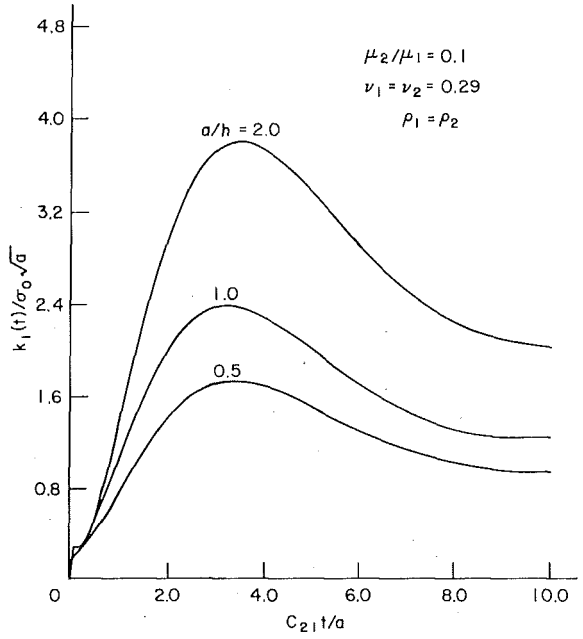

Fig. 6 Dynamic stress-intensity factor $k_1(t)$ versus time $\mu_2/\mu_1 = 0.1$

mation field that is skew-symmetric with respect to the $y = 0$ plane. Following the footstep laid out in the previous example on normal impact, the Laplace transform of the transient boundary conditions on the x-axis inside the crack are

$$(\tau_{xy}^*)_1(x, 0, p) = -\frac{\tau_0}{p}; \quad (\sigma_y^*)_1(x, 0, p) = 0, \quad 0 \le x < a \tag{32}$$

and the skew-symmetric conditions outside the crack are given by

$$(u_x^*)_1(x, 0, p) = 0; \quad (s_y^*)_1(x, 0, p) = 0, \quad x \ge a \tag{33}$$

Continuity of the stresses across $y = h$ is expressed by

$$\begin{aligned}(\sigma_y^*)_1(x, h, p) &= (\sigma_y^*)_2(x, h, p)\\ (\tau_{xy}^*)_1(x, h, p) &= (\tau_{xy}^*)_2(x, h, p)\end{aligned} \tag{34}$$

while the displacements are also required to be continuous, i.e.,

$$\begin{aligned}(u_x^*)_1(x, h, p) &= (u_x^*)_2(x, h, p)\\ (u_y^*)_1(x, h, p) &= (u_y^*)_2(x, h, p)\end{aligned} \tag{35}$$

Integral Representations. Under the foregoing considerations, the following wave potentials $\phi_j^*(x, y, p)$ and $\psi_j^*(x, y, p)$ are selected:

$$\begin{aligned}\phi_1^*(x, y, p) &= \frac{2}{\pi}\int_0^\infty [A^{(1)}(s, p)e^{-\gamma_{11}y} + A^{(2)}(s, p)e^{\gamma_{11}y}] \sin(sx)ds\\ \psi_1^*(x, y, p) &= \frac{2}{\pi}\int_0^\infty [B^{(1)}(s, p)e^{-\gamma_{21}y} + B^{(2)}(s, p)e^{\gamma_{21}y}] \cos(sx)ds\end{aligned} \tag{36}$$

for the cracked layer and

$$\begin{aligned}\phi_2^*(x, y, p) &= \frac{2}{\pi}\int_0^\infty C^{(1)}(s, p)e^{-\gamma_{12}y} \sin(sx)ds\\ \psi_2^*(x, y, p) &= \frac{2}{\pi}\int_0^\infty C^{(2)}(s, p)e^{-\gamma_{22}y} \cos(sx)ds\end{aligned} \tag{37}$$

for the outside material.

Equations (6) and (7) may now be substituted into the Laplace transform of the stresses and displacements in equations (1) and (2). Making use of the conditions in equations (2)–(5), the solution can

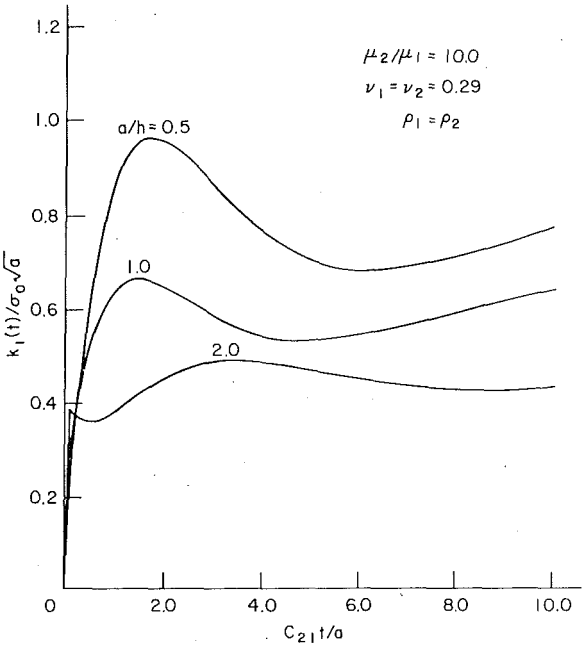

Fig. 7 Dynamic stress-intensity factor $k_1(t)$ versus time $\mu_2/\mu_1 = 10.0$

be expressed in terms of the functions $A^{(1)}, A^{(2)}, \ldots, C^{(2)}$ which are related to a single unknown $B(s, p)$ as shown by equations (48) in Appendix B. The function $B(s, p)$ is governed by the system of dual integral equations

$$\begin{aligned}\int_0^\infty B(s, p) \cos(sx)ds &= 0, \quad x \ge a\\ \int_0^\infty sF_{II}(s, p)B(s, p) \cos(sx)ds &= \frac{\pi\tau_0}{4\mu_1 p(1 - \kappa_1^2)}, \quad x < a\end{aligned} \tag{38}$$

The function $F_{II}(s, p)$ is related to $F_I(s, p)$ in equation (22) as

$$F_{II}(s, p) = \frac{\Delta_I}{\Delta_{II}} F_I(s, p) \tag{39}$$

Downloaded 01 May 2010 to 171.66.16.243. Redistribution subject to ASME license or copyright; see http://www.asme.org/terms/Terms_Use.cfm

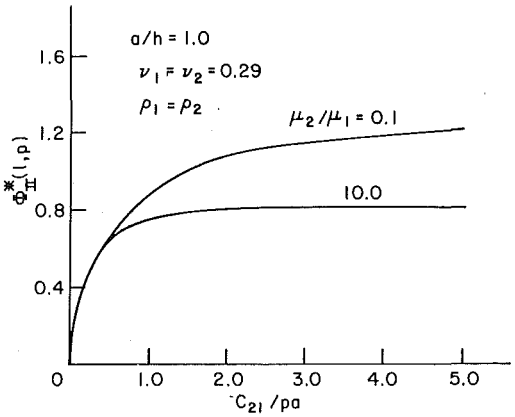

Fig. 8 Variations of $\Phi^*_{II}(1, p)$ with c_{21}/pa

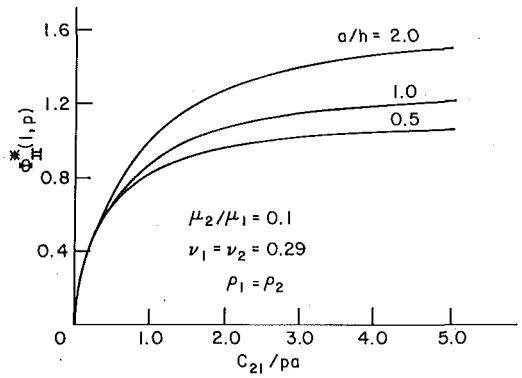

Fig. 9 Variations of $\Phi^*_{II}(1, p)$ with c_{21}/pa

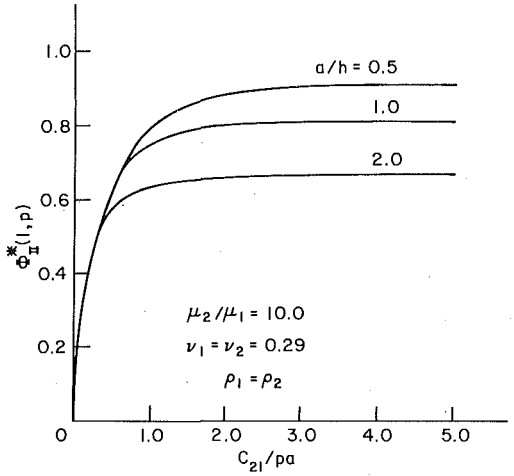

Fig. 10 Variations of $\Phi^*_{II}(1,p)$ with c_{21}/pa

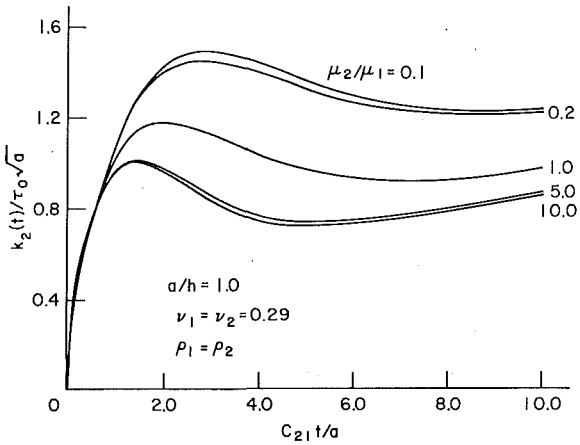

Fig. 11 Dynamic stress-intensity factor $k_2(t)$ versus time for $a/h = 1.0$

where

$$\Delta_{II} = \frac{p^2}{2c_{21}^2}\gamma_{21}[\beta^{(2)} + \beta^{(3)}e^{-2(\gamma_{11}+\gamma_{21})h} - \beta^{(4)}e^{-2\gamma_{21}h} - \beta^{(1)}e^{-2\gamma_{11}h}] \quad (40)$$

The other parameters such as κ_1, Δ_1, $\beta^{(1)}$, $\beta^{(2)}$, etc., are the same as those defined earlier for the case of normal impact.

A solution to equations (38) is again found by application of the Copson's method [5]

$$B(s, p) = \frac{\pi\tau_0 a^2}{4\mu_1 p(1-\kappa_1^2)}\int_0^1 \sqrt{\xi}\,\Phi^*_{II}(\xi, p)J_0(sa\xi)d\xi \quad (41)$$

provided that $\Phi^*_{II}(\xi, p)$ satisfies a Fredholm integral equation of the second kind

$$\Phi^*_{II}(\xi, p) + \int_0^1 \Phi^*_{II}(\eta, p)K_{II}(\xi, \eta, p)d\eta = \sqrt{\xi} \quad (42)$$

whose kernel $K_{II}(\xi, \eta, p)$ takes the form

$$K_{II}(\xi, \eta, p) = \sqrt{\xi\eta}\int_0^\infty s\left[F_{II}\left(\frac{s}{a}, p\right) - 1\right]J_0(s\xi)J_0(s\eta)ds \quad (43)$$

Mode II Dynamic Stress-Intensity Factor. As in the case of Mode I, the asymptotic expressions of the dynamic stresses in the Laplace transform plane are first obtained in terms of r_1 and θ_1 defined in Fig. 1. The results for the angular distribution of the stresses are the same as the static case and will not be repeated here. The dynamic stress-intensity factor in the Laplace transform domain takes the form

$$k_2^*(p) = \frac{\Phi^*_{II}(1, p)}{p}\tau_0\sqrt{a} \quad (44)$$

Equation (10) is then applied to invert the Laplace transform of the stress-intensity factor in equation (44). This gives

$$k_2(t) = \frac{\tau_0\sqrt{a}}{2\pi i}\int_{Br}\frac{\Phi^*_{II}(1, p)}{p}e^{pt}dp \quad (45)$$

in which $\Phi^*_{II}(1, p)$ is computed numerically from equation (42).

Figs. 8–10 display the values of $\Phi^*_{II}(1, p)$ as a function of the normalized quantity c_{21}/pa for various values of a/h and μ_2/μ_1 while $\nu_1 = \nu_2 = 0.29$ and $\rho_1 = \rho_2$ are used for all cases. With a knowledge of $\Phi^*_{II}(1, p)$, the integral in equation (45) may be evaluated by a procedure outlined in [6]. In general, $k_2(t)$ increases with time reaching a maximum and then decreases to the static value for sufficiently large time. The trend is very similar to $k_1(t)$ for the case of normal impact in that a higher value of $k_2(t)$ is obtained when the modulus of the surrounding material is less than that of the cracked layer, i.e., $\mu_2/\mu_1 < 1$. Comparing the results in Figs. 5 and 10, it is seen that for $\mu_2/\mu_1 < 1$, normal impact yields a higher crack tip stress-intensity factor than shear impact, i.e., $k_1(t) > k_2(t)$. The opposite is observed when $\mu_2/\mu_1 > 1$, i.e., $k_2(t) > k_1(t)$. The curves in Figs. 12 and 13 for $k_2(t)$ also show the absence of a small fluctuation for small time which was present in Figs. 6 and 7 for $k_1(t)$. This is because the influence of the reflected incident shear wave from the interface is considerably weaker even for the ratio of $a/h = 2.0$.

Conclusion

As composite materials are currently being applied to major pri-

Downloaded 01 May 2010 to 171.66.16.243. Redistribution subject to ASME license or copyright; see http://www.asme.org/terms/Terms_Use.cfm

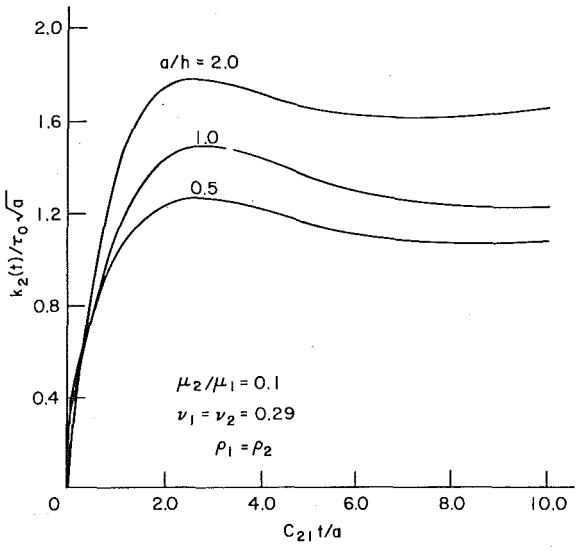

Fig. 12 Dynamic stress-intensity factor $k_2(t)$ versus time for $\mu_2/\mu_1 = 0.1$

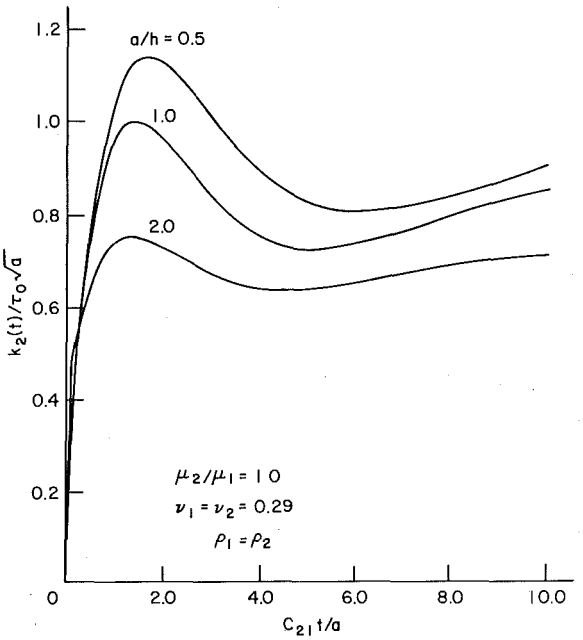

Fig. 13 Dynamic stress-intensity factor $k_2(t)$ versus time for $\mu_2/\mu_1 = 10.0$

mary structure designs, it is necessary to have an in-depth understanding of the mechanical behavior of these materials, particularly with reference to the allowable applied load both statically and dynamically. This investigation is concerned with the dynamic stress distribution around a crack embedded in a layered composite. The time-dependent loading can be of a general nature applied to the crack. For those composites which fail predominantly by matrix cracking under impact, the present results can be used effectively for determining the ability of the composite to absorb energy and to withstand load prior to total destruction.

The other modes of failure such as fiber breaking and/or debonding of fibers from matrix are not treated but may be significant in other composite systems. The redistribution of dynamic stresses in these cases may also be analyzed such that their individual contribution can be assessed quantitatively. These cases will be left for future investigations.

Acknowledgments

This research was performed under Grant No. NSG-3179 supported by the National Aeronautics and Space Administration, Lewis Research Center, Cleveland, Ohio. The financial support of NASA and the encouragement of Dr. C. C. Chamis are gratefully acknowledged. Dr. E. P. Chen's contribution to this work is also acknowledged. He has recently left Lehigh University and joined the staff at the Sandia Laboratories in Albuquerque, New Mexico.

References

1 *Linear Fracture Mechanics,* eds., Sih, G. C., Wei, R. P., and Erdogan, F., Envo Publishing Co., Inc., Bethlehem, Pa., 1975.

2 Sih, G. C., et al., "Material Characterization on the Fracture of Filament-Reinforced Composites," *Journal of Composite Materials,* Vol. 9, 1975, pp. 167–186.

3 Sih, G. C., "Dynamic Crack Problems: Strain Energy Density Fracture Theory," *Mechanics of Fracture,* Vol. IV, ed., Sih, G. C., Sijthoff and Noordhoff International Publishing, Alphen, 1977, pp. XVII–XLVII.

4 "Response of Metals and Metallic Structures to Dynamic Loading," Publication NMAB-341, National Academy of Sciences, Washington, D.C., 1978.

5 Copson, E. T., "On Certain Dual Integral Equations," *Proceedings of Glasgow Mathematical Association,* Vol. 5, 1961, pp. 19–24.

6 Chen, E. P., and Sih, G. C., "Transient Response of Cracks to Impact Loads," *Mechanics of Fracture,* Vol. IV, ed., Sih, G. C., Sijthoff and Noordhoff International Publishing, Alphen, 1977, pp. 1–58.

7 Sih, G. C., Ravera, R. S., and Embley, G. T., "Impact Response of a Finite Crack in Plane Extension," *International Journal of Solids and Structures,* Vol. 8, 1972, pp. 977–993.

8 Hilton, P. D., and Sih, G. C., "A Sandwiched Layer of Dissimilar Material Weakened by Crack-Like Imperfections," *Proceedings of the 5th Southeastern Conference on Theoretical and Applied Mechanics.*

9 Papoulis, A., "A New Method of Inversion of the Laplace Transform," *Quarterly of Applied Mathematics,* Vol. 14, 1957, pp. 405–414.

10 Miller, M. K., and Guy, W. T., "Numerical Inversion of the Laplace Transform by Use of Jacobi Polynomials," *SIAM Journal of Numerical Analysis,* Vol. 3, 1966, pp. 624–635.

APPENDIX *A*

Expressions for $\alpha^{(i)}$ and $A^{(i)}(s, p), \ldots, C^{(i)}(s, p)$ in Normal Loading

This section gives the expressions for $\alpha^{(1)}, \alpha^{(2)}, \ldots, \alpha^{(8)}$ in equations (25) in terms of the variables s, p and the material constants

$$\alpha^{(1)} = -s\left[\left(1-\frac{\mu_2}{\mu_1}\right)\gamma_{21} - \frac{\mu_2}{\mu_1}\left(\frac{p^2}{2c_{22}^2}\right)\left(\frac{\gamma_{21}-\gamma_{22}}{s^2-\gamma_{12}\gamma_{22}}\right)\right]$$

$$\alpha^{(2)} = s\left[\left(1-\frac{\mu_2}{\mu_1}\right)\gamma_{21} - \frac{\mu_2}{\mu_1}\left(\frac{p^2}{2c_{22}^2}\right)\left(\frac{\gamma_{21}+\gamma_{22}}{s^2-\gamma_{12}\gamma_{22}}\right)\right]$$

$$\alpha^{(3)} = \frac{1}{2}(s^2+\gamma_{21}^2) - \frac{\mu_2}{\mu_1}\left[s^2 + \frac{p^2}{2c_{22}^2}\left(\frac{s^2-\gamma_{11}\gamma_{22}}{s^2-\gamma_{12}\gamma_{22}}\right)\right]$$

$$\alpha^{(4)} = \frac{1}{2}(s^2+\gamma_{21}^2) - \frac{\mu_2}{\mu_1}\left[s^2 + \frac{p^2}{2c_{22}^2}\left(\frac{s^2+\gamma_{11}\gamma_{22}}{s^2-\gamma_{12}\gamma_{22}}\right)\right]$$

$$\alpha^{(5)} = -\frac{1}{2}(s^2+\gamma_{21}^2) + \frac{\mu_2}{\mu_1}\left[s^2 + \frac{p^2}{2c_{22}^2}\left(\frac{s^2-\gamma_{12}\gamma_{21}}{s^2-\gamma_{12}\gamma_{22}}\right)\right]$$

$$\alpha^{(6)} = -\frac{1}{2}(s^2+\gamma_{21}^2) + \frac{\mu_2}{\mu_1}\left[s^2 + \frac{p^2}{2c_{22}^2}\left(\frac{s^2+\gamma_{12}\gamma_{21}}{s^2-\gamma_{12}\gamma_{22}}\right)\right]$$

$$\alpha^{(7)} = s\left[\left(1-\frac{\mu_2}{\mu_1}\right)\gamma_{11} - \frac{\mu_2}{\mu_1}\left(\frac{p^2}{2c_{22}^2}\right)\left(\frac{\gamma_{11}-\gamma_{12}}{s^2-\gamma_{12}\gamma_{22}}\right)\right]$$

$$\alpha^{(8)} = -s\left[\left(1-\frac{\mu_2}{\mu_1}\right)\gamma_{11} - \frac{\mu_2}{\mu_1}\left(\frac{p^2}{2c_{22}^2}\right)\left(\frac{\gamma_{11}+\gamma_{12}}{s^2-\gamma_{12}\gamma_{22}}\right)\right] \qquad (46)$$

in which γ_{ij} is given by equations (16).

The functions $A^{(1)}, A^{(2)}, \ldots, C^{(2)}$ are related to the single function $A(s, p)$ as follows:

Downloaded 01 May 2010 to 171.66.16.243. Redistribution subject to ASME license or copyright; see http://www.asme.org/terms/Terms_Use.cfm

$$A^{(1)}(s,p) = \frac{A(s,p)}{\Delta_I}\left[\frac{1}{2}(s^2+\gamma_{21}^2)(\beta^{(2)}+\beta^{(4)}e^{-2\gamma_{21}h}) - s\gamma_{11}e^{-(\gamma_{11}+\gamma_{21})h}\right]$$

$$A^{(2)}(s,p) = -\frac{A(s,p)}{\Delta_I}\left[s\gamma_{11}e^{-(\gamma_{11}+\gamma_{21})h} + \frac{1}{2}(s^2+\gamma_{21}^2)e^{-2\gamma_{11}h}(\beta^{(1)}+\beta^{(3)}e^{-2\gamma_{21}h})\right]$$

$$B^{(1)}(s,p) = \beta^{(1)}e^{-(\gamma_{11}-\gamma_{21})h}A^{(1)}(s,p) + \beta^{(2)}e^{(\gamma_{11}+\gamma_{21})h}A^{(2)}(s,p)$$
$$B^{(2)}(s,p) = \beta^{(3)}e^{-(\gamma_{11}+\gamma_{21})h}A^{(1)}(s,p) + \beta^{(4)}e^{(\gamma_{11}-\gamma_{21})h}A^{(2)}(s,p)$$

$$C^{(1)}(s,p) = \frac{e^{\gamma_{12}h}}{s^2-\gamma_{12}\gamma_{22}}[(s^2-\gamma_{11}\gamma_{22})e^{-\gamma_{11}h}A^{(1)}(s,p) + (s^2+\gamma_{11}\gamma_{22})e^{\gamma_{11}h}A^{(2)}(s,p) + s(\gamma_{21}-\gamma_{22})e^{-\gamma_{21}h}B^{(1)}(s,p) - s(\gamma_{21}+\gamma_{22})e^{\gamma_{21}h}B^{(2)}(s,p)]$$

$$C^{(2)}(s,p) = \frac{e^{\gamma_{22}h}}{s^2-\gamma_{12}\gamma_{22}}[s(\gamma_{11}-\gamma_{12})e^{-\gamma_{11}h}A^{(1)}(s,p) - s(\gamma_{11}+\gamma_{22})e^{\gamma_{11}h}A^{(2)}(s,p) + (s^2-\gamma_{12}\gamma_{21})e^{-\gamma_{21}h}B^{(1)}(s,p) + (s^2+\gamma_{12}\gamma_{21})e^{\gamma_{21}h}B^{(2)}(s,p)] \quad (47)$$

APPENDIX *B*

Expressions for $A^{(i)}(s,p), \ldots, C^{(i)}(s,p)$ in Shear Loading

In the skew-symmetric problem, the unknown functions in equations (36) and (37) can also be expressed in terms of a single unknown $B(s,p)$ in accordance with the following relationships:

$$A^{(1)}(s,p) = -\frac{B(s,p)}{\Delta_{II}}\left[s\gamma_{21}(\beta^{(2)}-\beta^{(4)}e^{-2\gamma_{21}h}) + \frac{1}{2}(s^2+\gamma_{21}^2)e^{-(\gamma_{11}+\gamma_{21})h}\right]$$

$$A^{(2)}(s,p) = \frac{B(s,p)}{\Delta_{II}}\left[s\gamma_{21}e^{-2\gamma_{11}h}(\beta^{(1)}-\beta^{(3)}e^{-2\gamma_{21}h}) + \frac{1}{2}(s^2+\gamma_{21}^2)e^{-(\gamma_{11}+\gamma_{21})h}\right]$$

$$B^{(1)}(s,p) = -\beta^{(1)}e^{-(\gamma_{11}-\gamma_{21})h}A^{(1)}(s,p) - \beta^{(2)}e^{(\gamma_{11}+\gamma_{21})h}A^{(2)}(s,p)$$
$$B^{(2)}(s,p) = -\beta^{(3)}e^{-(\gamma_{11}+\gamma_{21})h}A^{(1)}(s,p) - \beta^{(4)}e^{(\gamma_{11}-\gamma_{21})h}A^{(2)}(s,p)$$

$$C^{(1)}(s,p) = \frac{e^{\gamma_{12}h}}{s^2-\gamma_{12}\gamma_{22}}[(s^2-\gamma_{11}\gamma_{22})e^{-\gamma_{11}h}A^{(1)}(s,p) + (s^2+\gamma_{11}\gamma_{22})e^{\gamma_{11}h}A^{(2)}(s,p) - s(\gamma_{21}-\gamma_{22})e^{-\gamma_{21}h}B^{(1)}(s,p) + s(\gamma_{21}+\gamma_{22})e^{\gamma_{21}h}B^{(2)}(s,p)]$$

$$C^{(2)}(s,p) = \frac{e^{\gamma_{22}h}}{s^2-\gamma_{21}\gamma_{22}}[s(\gamma_{12}-\gamma_{11})e^{-\gamma_{11}h}A^{(1)}(s,p) + s(\gamma_{12}+\gamma_{11})e^{\gamma_{11}h}A^{(2)}(s,p) + (s^2-\gamma_{21}\gamma_{12})e^{-\gamma_{21}h}B^{(1)}(s,p) + (s^2+\gamma_{21}\gamma_{12})e^{\gamma_{21}h}B^{(2)}(s,p)] \quad (48)$$

where Δ_{II} is given by equation (40).

Downloaded 01 May 2010 to 171.66.16.243. Redistribution subject to ASME license or copyright; see http://www.asme.org/terms/Terms_Use.cfm

S. F. Stone
Graduate Student.

M. L. Ghosh
Postdoctoral Fellow.

A. K. Mal
Professor.

Department of Mechanics and Structures,
University of California,
Los Angeles, Calif. 90024

Diffraction of Antiplane Shear Waves by an Edge Crack

The diffraction of time harmonic antiplane shear waves by an edge crack normal to the free surface of a homogeneous half space is considered. The problem is formulated in terms of a singular integral equation with the unknown crack opening displacement as the density function. A numerical scheme is utilized to solve the integral equation at any given finite frequency. Asymptotic solutions valid at low and high frequencies are obtained. The accuracy of the numerical solution at high frequencies and of the high frequency asymptotic solution at intermediate frequencies are examined. Graphical results are presented for the crack opening displacement and the stress intensity factor as functions of frequency and the incident angle. Expressions for the far-field displacements at high and low frequencies are also presented.

Introduction

The problem of the diffraction of elastic waves by an edge crack is of considerable importance in a variety of engineering applications. In fracture mechanics the interest is in the determination of the stress field near the crack tip as a prerequisite to the study of crack propagation under dynamic loading. In ultrasonic nondestructive evaluation (NDE) techniques, the interest is in the scattered wave field whose characteristics depend upon the depth of penetration of the crack.

The solution of the diffraction problem is complicated by the presence of the free surface of the medium in addition to the crack surfaces and the associated sharp corners. To the authors' knowledge, the only available solution is that given by Datta [1] where an appropriate low frequency solution for the diffraction of antiplane shear waves by an edge crack was obtained.

In the present paper the diffraction of antiplane shear waves by an edge crack normal to the free surface of an otherwise homogeneous half space is considered. A numerical scheme is developed for the calculation of the scattered field at any finite frequency. Asymptotic solutions at low and high frequencies are also obtained. The accuracy of the high frequency solution is examined. Graphical results are presented for the stress-intensity factor and the crack opening displacement. Expressions are given for the far-field scattered waves at low and high frequencies.

Formulation

The Cartesian coordinate system (x, y, z) is located on the free surface, so that the crack occupies the region $x = 0, 0 < y < l, -\infty < z < \infty$ (Fig. 1). A plane harmonic shear wave, polarized along the z-axis, is incident at angle θ with the x-axis. Let $W_I(x, y)e^{-i\omega t}$ denote the displacement due to the incident wave alone. Then

$$W_I(x, y) = A_0F_0(x, y)$$

where

$$F_0(x, y) = e^{ik(x\cos\theta - y\sin\theta)}, \quad (1)$$

A_0 is the amplitude and k, the wave number.

The total wave field $W(x, y)e^{i\omega t}$ may be expressed in the form,

$$W(x, y) = A_0F_0(x, y) + A_0F_0(x, -y) + W_s(x, y), \quad y > 0. \quad (2)$$

where the second term represents the reflected wave and the third term the scattered waves. Due to the scalar nature of the problem the domain of W_s can be extended to $y < 0$ by defining,

$$W_s(x, -y) = W_s(x, y), \quad y < 0.$$

Then W_s, assumed continuous across $y = 0$, satisfies the zero traction

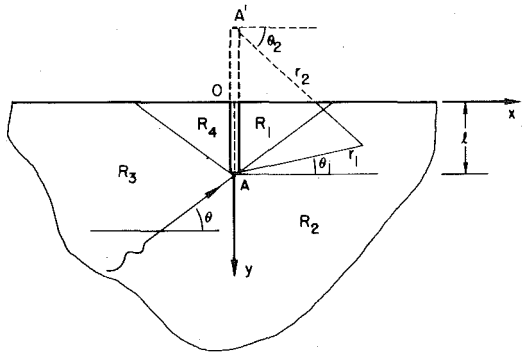

Fig. 1 Geometry of the problem and the shadow boundaries

Contributed by the Applied Mechanics Division for publication in the JOURNAL OF APPLIED MECHANICS.

Discussion on this paper should be addressed to the Editorial Department, ASME, United Engineering Center, 345 East 47th Street, New York, N.Y. 10017, and will be accepted until September 1, 1980. Readers who need more time to prepare a discussion should request an extension from the Editorial Department. Manuscript received by ASME Applied Mechanics Division, June, 1979; final revision, November, 1979.

Copyright © 1980 by ASME
Downloaded 01 May 2010 to 171.66.16.243. Redistribution subject to ASME license or copyright; see http://www.asme.org/terms/Terms_Use.cfm

condition on $y = 0$, and is the solution of the boundary-value problem,

$$(\nabla^2 + k^2)W_s = 0, \quad -\infty < x, y < \infty. \tag{3a}$$

$$\lim_{x\to 0} \frac{\partial W_s}{\partial x} = -2ik\, A_0 \cos\theta \cos(ky \sin\theta), \quad |y| < l \tag{3b}$$

In order to insure uniqueness, W_s must be subjected to the usual edge conditions at the crack tips, $x = 0$, $|y| = l$ as well as a radiation condition at infinity.

Solution at Moderate Frequencies

Let $P(y)$ denote the crack opening displacement, i.e.,

$$P(y) = W_s(0+, y) - W_s(0-, y), \quad 0 \le y \le l \tag{4}$$

It can be shown that $P(y)$ satisfies the weakly singular integral equation (c.f., Noble, [6]).

$$\int_{-l}^{l} P(y')\{H_0^1(k|y - y'|) - \cos(ky) - H_0^1(k|y'|)\}dy' = \frac{8A_0}{k\cos\theta}\{\cos ky \cos(ky \sin\theta)\} \tag{5}$$

Let (5) be normalized by writing

$$y/l = \xi, \quad y'/l = \eta, \quad kl = \Omega, \quad P(y')/4i\Omega A_0 = f(\eta, \Omega, \theta)$$

to give

$$\int_{-1}^{1} f(\eta, \Omega, \theta)\{H_0^1(\Omega|\xi - \eta|) - \cos\Omega\xi H_0^1(\Omega|\eta|)\}d\eta = \frac{-2i}{\Omega^2\cos\theta}\{\cos(\Omega\xi) - \cos(\Omega\xi \sin\theta)\}, \quad |\xi| < 1 \tag{6}$$

Equation (6) is convenient for approximate solution at low frequencies by means of standard perturbation techniques (see, e.g., Millar, [5]). It can be shown that

$$f(\eta, \Omega, \theta) = \cos\theta\sqrt{1-\eta^2}\left[1 - \frac{\Omega^2}{4}\ln\Omega - \frac{\Omega^2}{2}\left\{\frac{C}{2} + \frac{\sin^2\theta}{6} + \frac{1}{3}\left(\frac{1}{2} + \sin^2\theta\right)(1-\eta^2)\right\} + O(\Omega^2\ln\Omega)^2\right] \tag{7}$$

where $C = \ln(\gamma/4) - i\pi/2 - 5/6$, γ being the Euler's constant.

The singular part of the stress in the vicinity of the crack tip is,

$$\tau_{xz}{}^s(0, y) = -\frac{2\mu A_0 i\Omega\cos\theta}{\sqrt{2l}\sqrt{1-\xi}} \times \left\{1 - \frac{\Omega^2}{4}\ln\Omega - \frac{\Omega^2}{4}\left(C + \frac{\sin^2\theta}{3}\right) + O(\Omega^2\ln\Omega)^2\right\} \tag{8}$$

The normalized stress-intensity factor, $K(\Omega, \theta)$ may be defined by,

$$K(\Omega, \theta) = \lim_{\xi\to 1}\frac{\sqrt{1-\xi}\,\tau_{xz}{}^s(0, y)}{\sqrt{2}\,ikA_0\mu} = \cos\theta\left\{1 - \frac{\Omega^2}{4}\ln\Omega - \frac{\Omega^2}{4}\left(C + \frac{\sin^2\theta}{3}\right) + O(\Omega^2\ln\Omega)^2\right\} \tag{9}$$

It can be further shown that the scattered wave in the far-field region is given by,

$$W_s(r, \phi) \simeq A_0\sqrt{\frac{\pi}{2kr}}\, e^{i(kr+\pi/4)}\,\Omega^2 R(\phi, \Omega) \tag{10}$$

where $x = r\sin\phi$, $y = r\cos\phi$, and

$$R(\phi, \Omega) = \sin\phi\cos\theta\left[1 - \frac{\Omega^2}{4}\ln\Omega - \frac{\Omega^2}{4}\left\{C + \frac{1}{12} + \frac{1}{2}(\sin^2\theta + \cos^2\phi)\right\} + O(\Omega^2\ln\Omega)^2\right] \tag{11}$$

Equations (7), (9), and (10) give the low frequency estimates to $0(\Omega^2)$ of quantities of physical interest. Although no error estimates have been presented here, it can be inferred from similar studies that these expressions give accurate values only in a small neighborhood of $\Omega = 0$ (c.f. Mal [3]). In many practical applications the wavelengths are on the order of the crack length or smaller, i.e., $\Omega \ge 2\pi$. For these values of Ω it is necessary to obtain a numerical solution of (6). It is more convenient to work with the differentiated form

$$\mathcal{P}\int_{-1}^{1}\frac{f(\eta)}{\xi - \eta}d\eta + \int_{-1}^{1} f(\eta)\,\mathcal{H}(\xi, \eta)d\eta = f_0(\xi), \quad |\xi| < 1 \tag{12}$$

where $\mathcal{P}$ indicates principal value,

$$\mathcal{H}(\xi, \eta) = \frac{\pi\Omega}{2i}\left\{H_0{}^{1\prime}(\Omega|\xi - \eta|)\,\mathrm{sgn}(\xi - \eta) - \frac{2i}{\pi\Omega(\xi - \eta)} + \sin(\Omega\xi)H_0^1(\Omega|\eta|)\right\} \tag{13}$$

and

$$f_0(\xi) = \frac{2\pi}{\Omega\cos\theta}\{\sin(\Omega\xi) - \sin\theta\sin(\Omega\xi\sin\theta)\} \tag{14}$$

In (12) and in subsequent discussions the arguments Ω, θ in f are dropped for convenience.

It is to be noted that the kernel $\mathcal{H}(\xi, \eta)$ has only a weak logarithmic singularity at $\eta = 0$. Thus (12) is a singular integral equation of the standard Cauchy type and can be transformed into a Fredholm equation of the second kind. The difficulty with this approach is that the kernel appears as an integral, the numerical evaluation of which becomes impractical at moderately high frequencies.

In the present study an alternative procedure developed by Erdogan and Gupta [2] is used. In this approach $f(\eta)$ is written in the form,

$$f(\eta) = \sqrt{1-\eta^2}\,g(\eta) \tag{15}$$

where $g(\eta)$ is bounded in the closed interval $[-1, 1]$. It can be shown that the normalized stress intensity factor is given by

$$K(\Omega, \theta) = g(1) \tag{16}$$

Application of the Gauss-Chebyshev integration formulas to the integrals in (12) yields the system of linear algebraic equations,

$$\sum_{i=1}^{n}\frac{1-\eta_i{}^2}{n+1}g(\eta_i)\left\{\frac{1}{\xi_j - \eta_i} + \pi\mathcal{H}(\xi_j, \eta_i)\right\} = f_0(\xi_j), \tag{17}$$

where

$$j = 1, 2, \ldots n+1,$$

and

$$\xi_j = \cos\{\pi(2j-1)/2(n+1)\}$$
$$\eta_i = \cos\{\pi i/(n+1)\} \tag{18}$$

It should be noted that there are $(n+1)$ equations in (17) for the determination of the n unknowns $g(\eta_i)$. In the present calculations n was chosen as an even integer and the equation corresponding to $j = (n/2) + 1$ was ignored. Furthermore, equations (17) do not contain $g(\pm 1)$. A three point extrapolation scheme was used to calculate $g(1)$ in terms of $g(\eta)$ at η_1, η_2, η_3.

The system of equations (17) was solved by assuming $n = 10$ and increasing its value successively by 10 until an accuracy of 0.01 percent in the calculated value of $g(1)$ was achieved. The required minimum value of n varied from $n = 20$ at $\Omega = 0$ to $n = 50$ for $\Omega = 20$. At higher frequencies the numerical scheme becomes impractical due to the highly oscillatory nature of the solution. Thus, at these frequencies, an asymptotic solution should be provided for completeness.

Solution at High Frequencies

It does not seem possible to obtain high frequency asymptotic solution of (12). However, the first few lowest-order terms in the asymptotic solution can be obtained by means of a number of available

Downloaded 01 May 2010 to 171.66.16.243. Redistribution subject to ASME license or copyright; see http://www.asme.org/terms/Terms_Use.cfm

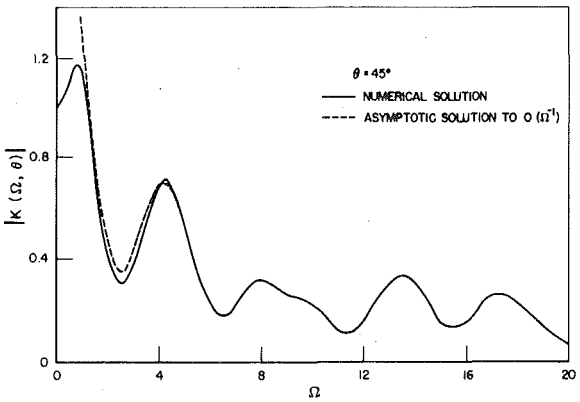

Fig. 2 Normalized stress-intensity factor; comparison between numerical and asymptotic solutions

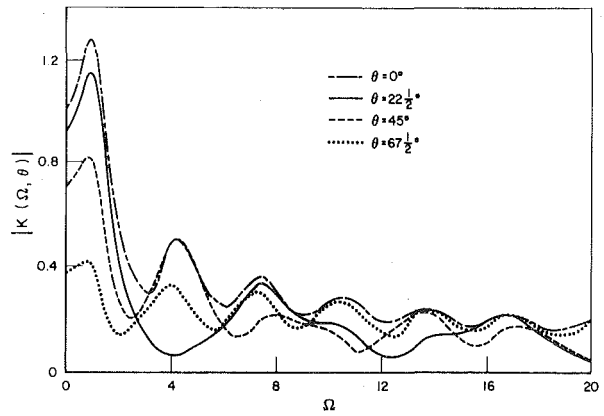

Fig. 3 Normalized stress-intensity factor versus normalized frequency and incident angle; numerical solution

techniques. An extended Wiener-Hopf technique described in Noble [6] was used to obtain the first two lowest-order terms.

It can be shown that at high frequencies the scattered wave field may be written in the form,

$$W_s = W_g + W_d \tag{19}$$

where W_g is the geometric solution given by

$$\begin{aligned} W_g(x, y) &= 0, && x, y \in R_2 \\ &= -W_I(x, y) - W_I(x, -y), && x, y \in R_1 \text{ (shadow zone)} \\ &= W_I(-x, y) + W_I(-x, -y), && x, y \in R_4 \\ &= W_I(-x, -y), && x, y \in R_3 \end{aligned} \tag{20}$$

The regions R_1, R_2, R_3, R_4 are shown in Fig. 1. W_d represents the *diffracted* field given by

$$A_0 W_d = P(x, y, \theta) + P(x, y, -\theta) \tag{21}$$

where

$$\begin{aligned} P(x, y, \theta) &= \alpha(\theta, \theta_1)\frac{e^{ikr_1}}{\sqrt{kr_1}} + \alpha(\theta, \theta_2)\frac{e^{ikr_2}}{\sqrt{kr_2}} \\ &\quad + \beta(\theta, \theta_1)\frac{e^{ik(r_1+2l)}}{k\sqrt{r_1 l}} + \beta(\theta, \theta_2)\frac{e^{ik(r_2+2l)}}{k\sqrt{r_2 l}} + O(kl)^{-3/2} \\ \alpha(\theta, \theta_1) &= -\frac{ie^{-i\pi/4}}{\sqrt{2\pi}}\frac{\cos\theta\cos\theta_1\, e^{-ikl\sin\theta}}{\sqrt{(1+\sin\theta)(1-\sin\theta_1)}\,(\sin\theta - \sin\theta_1)} \\ \beta(\theta, \theta_1) &= \frac{-\sqrt{2}ie^{-ikl\sin\theta}}{\sqrt{(1-\sin\theta)(1+\sin\theta_1)}} \end{aligned} \tag{22}$$

The polar coordinates (r_1, θ_1), (r_2, θ_2) are defined in Fig. 1. It should be noted that the asymptotic expressions are not valid near the boundaries between the regions R_1, R_2, R_3, R_4.

Each term in the foregoing expression for W_d can be identified as a reflected and/or diffracted ray arrival at the field point. $P(x, y, \theta)$ gives all of the rays resulting from the incident wave $W_I(x, y)$, while $P(x, y, -\theta)$ are those due to the reflected wave $W_I(x, -y)$ from the free surface of the half space. The first term in (22) represents the first-order diffracted cylindrical wave from the crack tip $y = l$. The second term represents the result of the reflection of this wave from the free surface $y = 0$. The third term is generated by the reflection of the once diffracted wave by the 90° corner at the origin and its subsequent diffraction at the crack tip. The fourth term is the result of reflection of this doubly diffracted wave at the free surface. It should be mentioned that no diffracted waves are generated by the corners at the origin. The results can be extended to higher order in Ω by including higher-order diffractions and reflections, although this will not be done here.

The normalized stress-intensity factor can also be calculated. It can be shown that

$$K(\Omega, \theta) = Q(\theta) + Q(-\theta) \tag{23}$$

where

$$Q(\theta) = \frac{e^{-i\pi/4}\cos\theta e^{-i\Omega\sin\theta}}{\sqrt{2\pi\Omega(1+\sin\theta)}}\left\{1 - \frac{e^{2i\Omega+i\pi/4}}{\sqrt{\pi\Omega}(1-\sin\theta)}\right\} + O(\Omega^{-3/2}). \tag{24}$$

The normalized crack opening displacement may be written in the form,

$$f(\eta) = \{S(\eta, \theta) + S(\eta, -\theta)\}/4i\Omega \tag{25}$$

where

$$\begin{aligned} S(\eta, \theta) &= -2e^{-i\Omega\eta\sin\theta} \\ &\quad + \frac{4}{\sqrt{\pi}}e^{-i\Omega\eta\sin\theta - i\pi/4}F(\sqrt{\Omega(1-\eta)(1-\sin\theta)}) \\ &\quad + \frac{4}{\sqrt{\pi}}e^{i\Omega\eta\sin\theta - i\pi/4}F(\sqrt{\Omega(1+\eta)(1-\sin\theta)}) \\ &\quad - \frac{2\sqrt{2}}{\pi}\frac{e^{i\Omega(\eta+1-\sin\theta)}}{\sqrt{\Omega(1-\sin\theta)}}F(\sqrt{2\Omega(1-\eta)}) \\ &\quad - \frac{2\sqrt{2}}{\pi}\frac{e^{-i\Omega(\eta-1+\sin\theta)}}{\sqrt{\Omega(1-\sin\theta)}}F(\sqrt{2\Omega(1+\eta)}) + \ldots \end{aligned} \tag{26}$$

$F(z)$ is the Fresnel integral defined by

$$F(z) = \int_z^\infty e^{iu^2}du \tag{27}$$

Clearly,

$$S(1, \theta) = O(\Omega^{-1}) \tag{28}$$

and

$$\begin{aligned} S(\eta, \theta) &= -2e^{-i\Omega\eta\sin\theta} + \frac{2e^{i\Omega(1-\eta-\sin\theta)+i\pi/4}}{\sqrt{\pi\Omega(1-\eta)(1-\sin\theta)}} \\ &\quad + \frac{2e^{i\Omega(1+\eta-\sin\theta)+i\pi/4}}{\sqrt{\pi\Omega(1+\eta)(1-\sin\theta)}} - \frac{i}{\pi}\frac{e^{i\Omega(3-\eta-\sin\theta)}}{\Omega\sqrt{(1-\eta)(1-\sin\theta)}} \\ &\quad - \frac{i}{\pi}\frac{e^{i\Omega(3+\eta-\sin\theta)}}{\Omega\sqrt{(1+\eta)(1-\sin\theta)}} + O(\Omega^{-3/2}), \quad 0 \le \eta < 1, \theta < \pi/2 \end{aligned} \tag{29}$$

It should be noted that the asymptotic expressions (22), (24), (28), and (29) are consistent with the approximation used in the Wiener-Hopf procedure. The change in the order of the neglected terms in (28) at the crack tip indicates that the asymptotic solution (29) loses accuracy near $\eta \simeq 1$. In expression (26) the Fresnel integrals contain terms of order higher than Ω^{-1}, which appears to be inconsistent with the asymptotic solution obtained by the Wiener-Hopf technique. However, the same expression can be derived from the solution of the

Downloaded 01 May 2010 to 171.66.16.243. Redistribution subject to ASME license or copyright; see http://www.asme.org/terms/Terms_Use.cfm

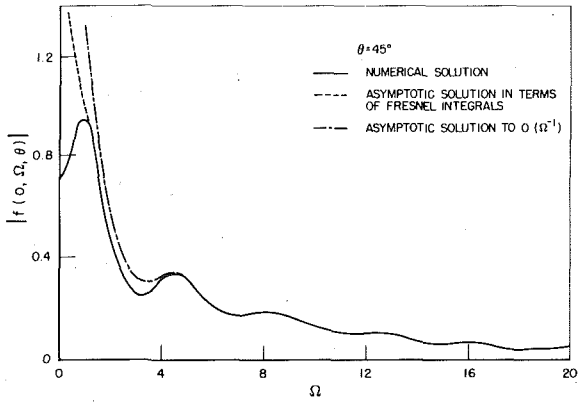

Fig. 4 Normalized crack opening displacement, comparison between numerical and asymptotic solutions

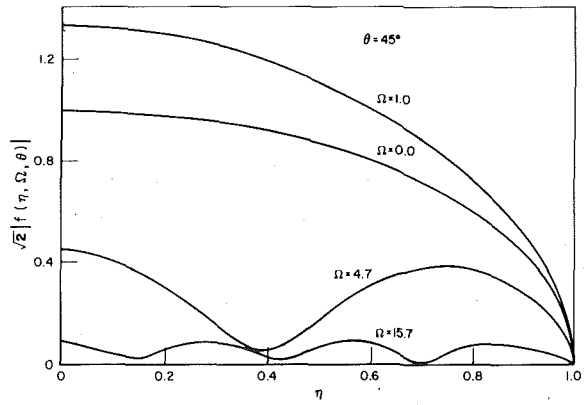

Fig. 6 Normalized crack opening displacement versus depth and frequency

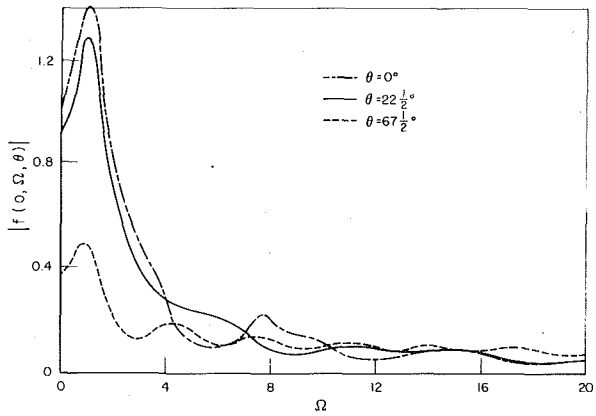

Fig. 5 Normalized crack opening displacement versus normalized frequency and incident angle; numerical solution

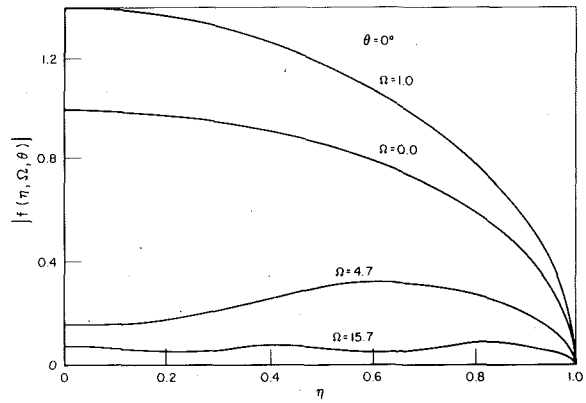

Fig. 7 Same as Fig. 6

Sommerfeld diffraction problem by ray construction. Thus, inspite of the inconsistency, equation (26) may in fact yield a more accurate representation of the crack opening displacement than (29).

Numerical Results

The normalized stress-intensity factor $|K(\Omega, \theta)|$ is plotted against the dimensionless frequency Ω in Figs. 2 and 3, for several values of the incident angle θ. It can be seen from Fig. 2 that the high frequency asymptotic solution (23) gives accurate values of K for $\Omega > 4$, i.e., $\lambda/l < \pi/2$. The range of accuracy of the asymptotic solution is somewhat surprising considering the fact that it contains only two lowest-order terms. In Fig. 3 the curve for $\theta = 0$ represents the stress-intensity factor for a crack of length $2l$ in an infinite medium and therefore agrees with that given in Mal [4]. The effect of interference between the incident and reflected waves can be clearly seen in the curves for incident angles different from zero, especially at higher frequencies.

The normalized crack opening displacement at the intersection of the crack with the free surface is presented in Figs. 4 and 5 as functions of Ω and θ. The numerical solution is compared with the asymptotic solutions (26) and (29) in Fig. 4. The high frequency solution (29) to Ω^{-1} again gives accurate results for $\Omega > 4$. The latter result indicates that the coefficients of the higher-order terms neglected in the asymptotic solution must be negligibly small.

Finally, the shape of the crack at different frequencies and incident angles are shown in Figs. 6 and 7. These results are obtained from the numerical solution only, since the asymptotic solutions break down near $\eta = 1$. It should be noted that the change in the incident angle from 0 to 45 deg causes significant changes in the nature of the crack opening displacement.

Acknowledgments

This research was carried out under Contract No. W-7405-ENG-48 with the U.S. Department of Energy. We wish to thank Dr. John Opsal of Lawrence Livermore Laboratory for helpful discussions.

References

1 Data, S. K., "Diffraction of SH waves by an Edge Crack," ASME JOURNAL OF APPLIED MECHANICS, Vol. 46, 1979, pp. 101–106.

2 Erdogan, F., and Gupta, G. D., "On the Solution of Singular Integral Equations," *Quarterly of Applied Mathematics*, Vol. 29, 1972, p. 525.

3 Mal, A. K., "A Note on the Low Frequency Diffraction of Elastic Waves by a Griffith Crack," *International Journal of Engineering Science*, Vol. 10, 1972a, pp. 609–612.

4 Mal, A. K., "Interaction of Elastic Waves With a Griffith Crack," *International Journal of Engineering Science*, Vol. 8, 1970, p. 763.

5 Millar, R. F., "A Note on Diffraction by a Slit," *Canadian Journal of Physics*, Vol. 38, 1960, pp. 38–47.

6 Noble, B., *Methods Based on the Wiener-Hopf Technique for the Solution of Partial Differential Equations*, Pergamon Press, 1958.

Downloaded 01 May 2010 to 171.66.16.243. Redistribution subject to ASME license or copyright; see http://www.asme.org/terms/Terms_Use.cfm

J. W. Nicholson
Assistant Professor.

J. G. Simmonds
Professor.

Department of Applied Mathematics and Computer Science, University of Virginia, Charlottesville, Va. 22901

Sanders' Energy-Release Rate Integral for Arbitrarily Loaded Shallow Shells and Its Asymptotic Evaluation for a Cracked Cylinder[1]

Sanders' path-independent, energy-release rate integral I is specialized to an arbitrarily loaded shallow shell containing a stress-free void, assuming linear theory. Two forms of I are given. When the void is a crack, one form reduces to integrals over circles of vanishing radius centered at the tips and is expressible in terms of bending and stretching stress-intensity factors. The other form reduces to an integral along the crack. For an elastically isotropic cylindrical shell containing a longitudinal crack and subject to a uniform bending stress at large distances from the crack, the dimensionless form of I depends on Poisson's ratio ν and a dimensionless crack length λ. When λ is small the shell is nearly flat; when λ is large the shell is very thin. An asymptotic formula is obtained for I as $\lambda \to \infty$. This is done by reducing the boundary-value problem to a coupled set of singular integral equations, scaling, taking the limit as $\lambda \to \infty$ to obtain inner and outer integral equations, solving the outer equations analytically, and, finally, evaluating I along the crack where the outer solutions dominate. As the evaluation of I does not require an explicit solution of the inner integral equations, an apparently intractible coupled Wiener-Hopf problem is evaded.

Introduction

The path-independent integrals of elastostatics discovered by Eshelby [1], Sanders [2], Günter [3], Cherepanov [4], Rice [5], and Knowles and Sternberg [6] can be interpreted as release rates of potential energy with respect to various motions of a void [7]. For this reason the values of these integrals can be useful predictors of void movement in brittle materials. Moreover, for stress-free cracks, certain of these integrals, because of their path-independence, can be evaluated in the immediate neighborhood of the crack tip. In particular, within the framework of linear, two-dimensional theory, these integrals may be expressed in terms of stress-intensity factors that measure the amplitude of the inverse square root singularities of the stress field at the crack tip.

The present paper first derives two forms of Sanders' path-independent, energy-release rate integral I for an arbitrarily loaded elastic body containing a stress-free void. Linearity is assumed. Although the analysis is motivated with an eye on shallow shell theory, the results can be applied easily to any two or three-dimensional elastic body.

The remaining part of the paper evaluates I, asymptotically, for a very thin cylindrical shell containing a longitudinal crack. The shell is acted upon at large distances from the crack by a uniform circumferential stress couple M_0 and a uniform axial stress couple νM_0, where ν is Poisson's ratio. (The axial stress couple is imposed to insure that, far from the crack, each transverse cross section of the shell undergoes identical ring bending.) Although we shall analyze a very specific problem, it will become clear as we proceed that our method works whenever an asymptotic expansion is available for the fundamental solution of the shallow shell equations and the asymptotic forms of the integral equations for the stress field away from the crack tips can be solved.

The symmetry of our problem implies that if the crack grows, it does so by expanding uniformly, i.e., both tips extend at the same rate. Were we considering the bending of a cracked *plate*, the associated energy-release rate would be given by the path-independent integral $M = \int x_\alpha P_{\alpha\beta}\nu_\beta ds$, where x_α, $\alpha = 1, 2$, are the Cartesian coordinates of a point on the integration path, $P_{\alpha\beta}$ are the Cartesian components of the energy-momentum tensor and $\nu_\beta ds$ is a directed element of arc length. Following Eshelby's recipe [8], we can also construct $P_{\alpha\beta}$ for a shallow *shell*. However, for a quadratic midsurface, $x_\alpha P_{\alpha\beta}$ is *not*

[1] This work was supported by the National Science Foundation under Grant MCS-76-10454.

Contributed by the Applied Mechanics Division for publication in the JOURNAL OF APPLIED MECHANICS.

Discussion on this paper should be addressed to the Editorial Department, ASME, United Engineering Center, 345 East 47th Street, New York, N. Y. 10017, and will be accepted until September 1, 1980. Readers who need more time to prepare a discussion should request an extension from the Editorial Department. Manuscript received by ASME Mechanics Division, August, 1979; final revision, November, 1979.

Copyright © 1980 by ASME
Downloaded 01 May 2010 to 171.66.16.243. Redistribution subject to ASME license or copyright; see http://www.asme.org/terms/Terms_Use.cfm

divergence free, i.e., M is *path-dependent*. We therefore turn to the more general path-independent integral I of Sanders. Unlike M, I involves derivatives of the field variables with respect to crack length.

The first step in the analysis of a cracked shell is to compute the stresses and displacements that would exist in the absence of the crack. By linearity, the original problem reduces to the analysis of a shell with a crack subject to stresses that are equal and opposite to those in the uncracked shell. This is the so-called *residual problem*. Because the loading in the residual problem is self-equilibrating and because, in practice, the crack length $2c$ is small compared to some typical radius of curvature R of the shell midsurface, shallow shell theory may be used.

In [9] the equations for a cracked shallow shell with a quadratic midsurface were reduced to coupled singular integral equations (IE's) along the crack. The nondimensionalized IE's depend on ν and the dimensionless parameter

$$\lambda = [(3/4)(1 - \nu^2)]^{1/4}\, c/\sqrt{hR}, \tag{1}$$

where h is the shell thickness (taken constant). For c fixed, the shell is nearly flat if $\lambda \ll 1$ and very thin if $\lambda \gg 1$. Thus all non-negative values of λ are of interest. If $\lambda \ll 1$, the IE's may be solved, approximately, by perturbing about the flat plate solution. If $\lambda = 0(1)$, numerical methods are needed.[2] If $\lambda \gg 1$, asymptotic methods must be considered.

By an appropriate scaling of the dependent and independent variables, the IE's may be split, to a first approximation, into outer and inner equations. In the outer equations the domain is finite but certain integrals of the kernels are replaced by the first term in their asymptotic expansions. In the inner equations, the domain becomes semi-infinite and certain kernels are differentiated. If these outer and inner IE's can be solved, the conventional bending and stretching stress-intensity factors, $B(\lambda, \nu)$ and $S(\lambda, \nu)$, can be found by matching. For example in [11], a matching procedure was applied to a pressurized cylindrical shell with a *clamped* crack—an admittedly artificial case leading to a *single* complex-valued IE—to yield

$$S \sim \frac{2^{7/4}\cos(3\pi/16)}{3\Gamma(3/4)}\lambda^{3/4}$$
$$= (0.7607\ldots)\lambda^{3/4} \quad \text{as} \quad \lambda \to \infty. \tag{2}$$

However, for stress-free cracks, the inner IE's are of the coupled Wiener-Hopf type and there is no known general method of solution. On the other hand the outer IE's are sometimes amenable to solution.

Suppose that we are concerned only with evaluating Sanders' energy-release rate integral I. Then we may do so by taking a contour along which the solutions of the outer IE's dominate the integrand. The second form of I that we derive involves such a contour. Thus we bypass the matching procedure that otherwise would require at least an asymptotic solution of the inner IE's.

It is possible, of course, to express all stresses and displacements in the immediate neighborhood of the crack tips in terms of B and S. By virtue of its path-independence, I may be evaluated also along a closed contour taken arbitrarily close to the crack. As its integrand vanishes along the crack, I reduces to two identical integrals over arbitrarily small circles centered at the crack tips. We find that

$$\frac{D}{2\pi c M_0^2} I(\lambda, \nu) = S^2(\lambda, \nu) + \frac{B^2(\lambda, \nu)}{(3 + \nu)(1 - \nu)} \equiv C^2(\lambda, \nu), \tag{3}$$

where

$$D = \frac{Eh^3}{12(1 - \nu^2)} \tag{4}$$

[2] Using the recently proposed method of Theocaris and Ioakimidis [10], C. K. Carrington, who has kindly performed the numerical calculations in the present paper, has found that numerical solutions for a number of crack problems are feasible, economically, for values of λ up to about 40.

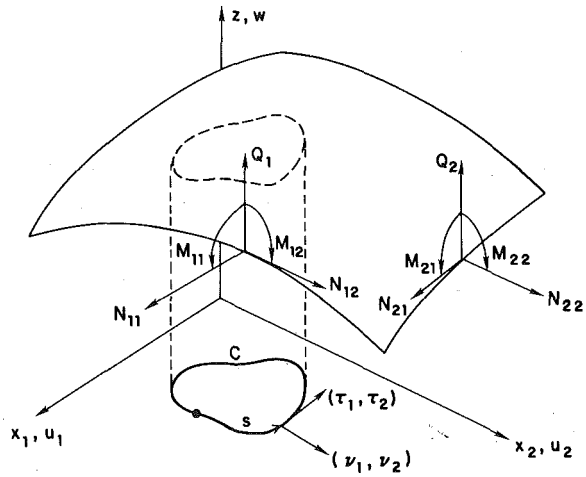

Fig. 1 Stress, displacement, and geometric conventions

is the bending stiffness and E is Young's modulus. Equation (3) indicates that the combined stress-intensity factor $C(\lambda, \nu)$ is the appropriate measure of incipient crack growth and not S or B individually. A similar result was obtained by Amazigo [12] who evaluated Rice's J-integral around the tip of a semi-infinite crack in a pressurized cylindrical shell.

The end product of the present paper is the asymptotic formula

$$C(\lambda,\nu) \sim (2^{3/2}/\pi)|\Gamma(5/4 - ib)\lambda|^{-1/4}$$
$$= (0.7879\ldots)\lambda^{-1/4} \quad \text{as} \quad \lambda \to \infty, \tag{5}$$

where b is given by equation (108) of the text. This result is corroborated by a numerical solution of the exact IE's and the subsequent computation of the right side of (3) for values of λ up to 40.

The Equations of Linear Shallow Shell Theory

These consist of the reduced force equilibrium equations

$$N_{\alpha\beta,\beta} + p_\alpha = 0, \quad M_{\alpha\beta,\alpha\beta} + z_{,\alpha\beta}N_{\alpha\beta} + p = 0 \tag{6, 7}$$

plus stress-displacement relations that, for an elastically isotropic shell, take the form

$$\tfrac{1}{2}(u_{\alpha,\beta} + u_{\beta,\alpha}) - z_{,\alpha\beta}w = A[(1 + \nu)N_{\alpha\beta} - \nu\delta_{\alpha\beta}N_{\gamma\gamma}] \tag{8}$$

$$M_{\alpha\beta} = -D[(1 - \nu)w_{,\alpha\beta} + \nu\delta_{\alpha\beta}\, w_{,\gamma\gamma}]. \tag{9}$$

Here $N_{\alpha\beta}$ and $M_{\alpha\beta}$ are, respectively, the Cartesian components of the stress resultant and stress couple tensors (u_α, w) and (p_α, p) are the tangential and normal components of the midsurface displacement and load vectors $\mathbf{u}$ and $\mathbf{p}$, $z = f(x_1, x_2)$ is the equation of the midsurface, $\delta_{\alpha\beta}$ is the Kronecker delta, $A = 1/Eh$, and a comma denotes partial differentiation. The standard conventions of Cartesian tensor theory are employed. Stresses and displacements are reckoned positive as indicated in Fig. 1.

Let C denote a piecewise smooth curve, parameterized by its arc length s and having unit tangent and normal vectors with components τ_α and $\nu_\alpha = \epsilon_{\alpha\beta}\tau_\beta$, where $\epsilon_{\alpha\beta}$ are the components of the alternating tensor. If $\dot{\mathbf{u}}$ denotes velocity (or virtual displacement), then the rate of work (or virtual work) of the tractions along C is denoted and defined by

$$\int_C T \cdot \dot{U} ds \equiv \int_C (N_{\alpha\beta}\nu_\beta\dot{u}_\alpha + Q_\alpha\nu_\alpha\dot{w} - M_{\alpha\beta}\nu_\beta\dot{w}_{,\alpha})ds$$
$$= \int_C (T_\alpha\dot{u}_\alpha + V\dot{w} + M\dot{\phi})ds + \sum[H]_i\dot{w}(s_i), \tag{10}$$

where ds is a differential element of arc length and

$$V = Q_\alpha\nu_\alpha + H_{,s}, \quad Q_\alpha = M_{\alpha\beta,\beta} \tag{11, 12}$$

Downloaded 01 May 2010 to 171.66.16.243. Redistribution subject to ASME license or copyright; see http://www.asme.org/terms/Terms_Use.cfm

$$H = M_{\alpha\beta}\tau_\alpha\nu_\beta, \quad M = M_{\alpha\beta}\nu_\alpha\nu_\beta, \quad \phi = -w_{,\beta}\nu_\beta \quad (13, 14, 15)$$

$$[H]_i = \lim_{\epsilon \to 0} [H(s_i + \epsilon) - H(s_i - \epsilon)]. \quad (16)$$

The summation in (10) arises from an integration by parts and is to be taken over the corners of C represented by the points s_i. The notation $T\cdot U$ represents the inner product of the 4-dimensional traction vector (T_1, T_2, V, M) with the 4-dimensional displacement vector (u_1, u_2, w, ϕ). From (10) we may infer the appropriate form of the boundary conditions to be imposed on an edge of the shell.

Sanders' Path-Independent Integral I

Consider a family of shallow shells, all identical save that each contains a void whose shape depends on a parameter τ. Specifically, let the boundary of the void be a piecewise smooth curve $\partial V(\tau)$ having the parametric representation

$$\mathbf{x} = \mathbf{r}(\sigma) + \tau v(\sigma)\boldsymbol{\nu}(\sigma), \quad (17)$$

where $\boldsymbol{\nu}$ is an outward unit normal vector, σ is arc length along $\partial V(0)$, and $v(\sigma)$ represents the normal "velocity" of the void. Let the void be stress-free and let the midsurface and the other edges of the shell be subject to static or kinematic conditions that are *independent* of τ. Each shell of the family has a unique midsurface displacement vector of the form $\mathbf{u}(x_\alpha, \tau)$. Finally, let C be an arbitrary, piecewise smooth curve *fixed* in the x_1x_2 plane (i.e., independent of τ), surrounding the void, and let a dot denote differentiation with respect to τ. Then, if we multiply (6) by $\dot{u}_\alpha$ and (7) by $\dot{w}$, and apply the divergence theorem to the region $A(\tau)$ contained between C and ∂V, we obtain the identity

$$\int_C T\cdot\dot{U}ds + \iint_{A(\tau)} \mathbf{p}\cdot\dot{\mathbf{u}}\, dA \equiv \iint_{A(\tau)} \dot{W}\, dA, \quad (18)$$

where W is the strain-energy density. As Budiansky and Rice have noted [7],

$$\left(\iint_{A(\tau)} F dA\right)^{\cdot} = \iint_{A(\tau)} \dot{F} dA - \int_{\partial V(\tau)} F v_* ds \quad (19)$$

for any scalar function F. In (19), $v_* = v(1 + \kappa\tau v)\, d\sigma/ds$, where $\kappa = |\boldsymbol{\nu}'|$, and the minus sign occurs because v_* measures the *outward* velocity of the void. Hence (18) may be expressed in the form

$$I(\tau) \equiv \int_C T\cdot\dot{U}ds + \left[\iint_{A(\tau)} (\mathbf{p}\cdot\mathbf{u} - W)dA\right]^{\cdot} = \int_{\partial V(\tau)} (W - \mathbf{p}\cdot\mathbf{u})v_* ds. \quad (20)$$

I is Sanders' integral [2]. Clearly I is path-independent because the right side of (20) does not depend on C.

Linearity and the absence of stress along the void allows us to set

$$\iint_{A(\tau)} W dA = \frac{1}{2}\int_C T\cdot U\, ds + \frac{1}{2}\iint_{A(\tau)} \mathbf{p}\cdot\mathbf{u}\, dA. \quad (21)$$

Hence (20) reduces to

$$I(\tau) = \frac{1}{2}\int_C (T\cdot\dot{U} - \dot{T}\cdot U)ds + \frac{1}{2}\left(\iint_{A(\tau)} \mathbf{p}\cdot\mathbf{u}\, dA\right)^{\cdot}. \quad (22)$$

The physical interpretation of I follows upon taking C in (20) to coincide with the edge of the shell, C_*. If the prescribed boundary conditions are independent of τ, then

$$I(\tau) = -\dot{\Pi} \equiv \left[\iint_{A_*(\tau)} (\mathbf{p}\cdot\mathbf{u} - W)dA + \int_{C_*} T\cdot U ds\right]^{\cdot} = \int_{\partial V(\tau)} (W - \mathbf{p}\cdot\mathbf{u})v_* ds. \quad (23)$$

But Π is just the potential energy of the shell. Hence (23) states that Sanders' path-independent integral I is equal to the rate of flow of potential energy from the shell into the void (so that I is positive if the void expands).

An Alternate Form For $I(0)$

With the aid of the Betti reciprocity principle, we now show that $I(0)$ may be expressed as an integral along the void.

Let T_0, U_0, $\mathbf{p}$ denote the traction, displacement, and surface load vectors that would exist were there no void and let T_r, U_r denote residual traction and displacement vectors such that $T = T_0 + T_r$, $U = U_0 + U_r$. Clearly

1 T_0, U_0, $\mathbf{p}$ are independent of τ.
2 $T_0 = -T_r$ on ∂V, because the void is stress-free.
3 T_r and U_r vanish identically, as functions of τ, on C_* because on the edge, T, U and T_0, U_0 satisfy the same boundary conditions. By assumption these boundary conditions are independent of τ.

Because of Condition 1, equation (21) yields

$$\left(\iint_{A(\tau)} W dA\right)^{\cdot} = \frac{1}{2}\left[\int_C (T_0\cdot U_r + T_r\cdot U_0 + T_r\cdot U_r)ds + \iint_{A(\tau)} \mathbf{p}\cdot(\mathbf{u}_0 + \mathbf{u}_r)dA\right]. \quad (24)$$

As T_0, U_0, $\mathbf{p}$ and T_r, U_r are equilibrium solutions, the Betti reciprocity principle implies that

$$\int_{C+\partial V(\tau)} T_r\cdot U_0\, ds = \int_{C+\partial V(\tau)} T_0\cdot U_r\, ds + \iint_{A(\tau)} \mathbf{p}\cdot\mathbf{u}_r\, dA \quad (25)$$

or, by Condition 2

$$\int_C T_r\cdot U_0\, ds = \int_C T_0\cdot U_r + \int_{\partial V(\tau)} T_0\cdot U\, ds + \int_{A(\tau)} \mathbf{p}\cdot\mathbf{u}_r\, dA. \quad (26)$$

Substitute (26) into (24) and note from (17) that

$$\left[\int_{\partial V(\tau)} \mathrm{F}(\sigma, \tau)ds\right]^{\cdot}(0) = \int_{\partial V(0)} [\dot{F}(\sigma, 0) + \kappa(\sigma)v(\sigma)F(\sigma, 0)]d\sigma, \quad (27)$$

for any scalar function F. Hence with the aid of (19) we have, at $\tau = 0$,

$$\left(\iint_{A(\tau)} W dA\right)^{\cdot}(0) = \int_C [T_0\cdot\dot{U}_r + \tfrac{1}{2}(T_r\cdot U_r)^{\cdot}]ds + \iint_{A(\tau)} \mathbf{p}\cdot\dot{\mathbf{u}}_r dA + \frac{1}{2}\int_{\partial V(0)} [T_0\cdot(\dot{U} + \kappa v U) - \mathbf{p}\cdot(\mathbf{u}_0 + 2\mathbf{u}_r)v]d\sigma. \quad (28)$$

Now set $\tau = 0$ in (20), insert (28), and take $C = C_*$. With the aid of Conditions 1 and 3, it follows that

$$I(0) = -\frac{1}{2}\int_{\partial V(0)} [T_0\cdot(\dot{U} + \kappa v U) + \mathbf{p}\cdot\mathbf{u}_0 v]d\sigma. \quad (29)$$

It is evident that the results of this and the preceeding section, with trivial changes in notation, apply to any elastic body described by linear equations.

Nondimensionalization

Consider an arbitrary shallow shell containing a straight crack of length $2c$. Take $\tau = c$ and assume that the crack extends symmetrically, so that $v = 0$. Let σ denote a reference stress and introduce dimensionless variables by setting

$$x_\alpha = c\bar{x}_\alpha, \quad z = (c^2/R)\bar{z}, \quad N_{\alpha\beta} = \sigma h\overline{N}_{\alpha\beta} \quad (30, 31, 32)$$

$$M_{\alpha\beta} = \sigma h^2[12(1 - \nu^2)]^{-1/2}\overline{M}_{\alpha\beta}, \quad (p_\alpha, p) = \sigma h(\overline{p}_\alpha/c, \overline{p}/R) \quad (33, 34)$$

Downloaded 01 May 2010 to 171.66.16.243. Redistribution subject to ASME license or copyright; see http://www.asme.org/terms/Terms_Use.cfm

$$u_\alpha = (\sigma c/E)\bar{u}_\alpha, \quad w = (\sigma c^2/Eh)[12(1-\nu^2)]^{1/2}\bar{w}. \quad (35, 36)$$

Then, with the overbars dropped, (6)–(9) take the form

$$N_{\alpha\beta,\beta} + p_\alpha = 0, \quad M_{\alpha\beta,\alpha\beta} + 4\lambda^2(z_{,\alpha\beta}N_{\alpha\beta} + p) = 0 \quad (37, 38)$$

$$\tfrac{1}{2}(u_{\alpha,\beta} + u_{\beta,\alpha}) - 4\lambda^2 z_{,\alpha\beta}w = (1+\nu)N_{\alpha\beta} - \nu\delta_{\alpha\beta}N_{\gamma\gamma} \quad (39)$$

$$M_{\alpha\beta} = -(1-\nu)w_{,\alpha\beta} - \nu\delta_{\alpha\beta}w_{,\gamma\gamma}, \quad (40)$$

where λ is given by (1).

For a shell of infinite extent, the solution for the dimensionless stresses and displacements will have the functional form $f(\bar{x}_\alpha;\lambda)$. Hence

$$\begin{aligned}\dot{N}_{\alpha\beta} &= \partial\{\sigma h\,\bar{N}_{\alpha\beta}[\bar{x}_\gamma(c);\,\lambda(c)]\}/\partial c \\ &= \sigma h[(\bar{N}_{\alpha\beta,\gamma})(\partial\bar{x}_\gamma/\partial c) + (\partial\bar{N}_{\alpha\beta}/\partial\lambda)(\partial\lambda/\partial c)] \\ &= (\sigma h/c)(-\bar{x}_\gamma\bar{N}_{\alpha\beta,\gamma} + \lambda\partial\bar{N}_{\alpha\beta}/\partial\lambda) \quad (41)\\ \dot{u}_\alpha &= \partial\{(\sigma c/E)\bar{u}_\alpha\,[x_\beta(c);\,\lambda(c)]\}/\partial c \\ &= (\sigma/E)(\bar{u}_\alpha - \bar{x}_\beta\bar{u}_{\alpha,\beta} + \lambda\,\partial\bar{u}_\alpha/\partial\lambda), \quad \text{etc.} \quad (42)\end{aligned}$$

Now set

$$I = (\sigma^2 hc/E)\bar{I}, \quad s = c\bar{s} \quad (43, 44)$$

denote differentiation with respect to λ by a dot, define T_α, V, Q_α, H, M, and ϕ as in (10)–(15) but now in terms of dimensionless variables, and drop overbars to obtain from (22)

$$\begin{aligned}2I = \int_C &[N_{\alpha\beta}(u_\alpha - x_\gamma u_{\alpha,\gamma}) + x_\gamma N_{\alpha\beta,\gamma}u_\alpha + Q_\beta(3w - x_\gamma w_{,\gamma}) \\ &+ x_\gamma Q_{\beta,\gamma}w - M_{\alpha\beta}(w_{,\alpha} - w_{,\alpha\gamma}x_\gamma) - x_\gamma M_{\alpha\beta,\gamma}w_{,\alpha} \\ &+ \lambda(N_{\alpha\beta}\dot{u}_\alpha - \dot{N}_{\alpha\beta}u_\alpha + Q_\beta\dot{w} - \dot{Q}_\beta w - M_{\alpha\beta}\dot{w}_{,\alpha} + \dot{M}_{\alpha\beta}w_{,\alpha})]\nu_\beta\,ds \\ &+ \iint_{A(\tau)}[p_\alpha(u_\alpha - x_\beta u_{\alpha,\beta} + \lambda\dot{u}_\alpha) \\ &+ 4\lambda^2 p\,(2w - x_\alpha w_{,\alpha} + \lambda\dot{w})]dA. \quad (45)\end{aligned}$$

To render (29), the second form of $I(0)$, dimensionless, let the crack run from -1 to 1 along the x_1 axis. Then, using (10)–(15), (30)–(36), and (41)–(43), dropping overbars, and denoting uncracked values by "o," we obtain

$$\begin{aligned}I(0) &= \frac{1}{2}\int_{-1}^{1}\{\mathring{N}_{12}[u_1 - x_1u_{1,1} + \lambda\dot{u}_1] + \mathring{N}_{22}[u_2 - x_1u_{2,1} + \lambda\dot{u}_2] \\ &+ (\mathring{Q}_2 + \mathring{H}_{,1})[2w - x_1w_{,1} + \lambda\dot{w}] - \mathring{M}_{22}[w_{,2} - x_1w_{,21} + \lambda\dot{w}_{,2}]\}dx_1 \\ &= \frac{1}{2}\int_{-1}^{1}\{\mathring{N}_{12}[2u_1 + \lambda\dot{u}_1] + \mathring{N}_{22}[2u_2 + \lambda\dot{u}_2] \\ &+ (\mathring{Q}_2 + \mathring{H}_{,1})[3w + \lambda\dot{w}] - \mathring{M}_{22}[2w_{,2} + \lambda\dot{w}_{,2}]\}dx_1. \quad (46)\end{aligned}$$

The brackets denote the jump across the crack of the enclosed quantity, i.e., $[f](x) \equiv \lim[f(x,\epsilon) - f(x,-\epsilon)]$ as $\epsilon \to 0$.

Integral Equations for a Cracked Cylindrical Shell

We now set $x_1 = x$, $x_2 = y$, $u_1 = u$, $u_2 = v$, $\mathbf{p} = 0$, $N_{11} = N_x$, $N_{12} = N_{xy}$, etc., and consider a cylindrical shell with midsurface $z = (\frac{1}{2})y^2$, acted upon at infinity by uniform stress couples. We take for the reference stress

$$\sigma = [12(1-\nu^2)]^{1/2}M_0/h^2, \quad (47)$$

so that $M_y \to 1$ and $M_x \to \nu$ as $r = (x^2+y^2)^{1/2} \to \infty$.

The displacements in the uncracked shell are

$$\mathring{u} = 0, \quad \mathring{v} = -(\tfrac{2}{3})\lambda^2 y^3, \quad \mathring{w} = -(\tfrac{1}{2})y^2, \quad (48)$$

and represent a state of pure ring bending. From (10) and (37)–(40), the *residual* boundary-value problem for the uncracked shell reads

$$N_{x,x} + N_{xy,y} = 0, \quad N_{xy,x} + N_{y,y} = 0 \quad (49, 50)$$

$$-\Delta\Delta w + 4\lambda^2 N_y = 0 \quad (51)$$

$$u_{,x} = N_x - \nu N_y, \quad v_{,y} - 4\lambda^2 w = N_y - \nu N_x \quad (52, 53)$$

$$u_{,y} + v_{,x} = 2(1+\nu)N_{xy} \quad (54)$$

$$N_y(x,\pm 0) = N_{xy}(x,\pm 0) = 0, \quad |x| \le 1 \quad (55, 56)$$

$$w_{,yy}(w,\pm 0) + \nu w_{,xx}(x,\pm 0) = 1, \quad |x| \le 1 \quad (57)$$

$$(2-\nu)w_{,xyy}(x,\pm 0) + w_{,yyy}(x,\pm 0) = 0, \quad |x| \le 1, \quad (58)$$

where Δ is the Laplacian and the stress couples have been expressed in terms of the midsurface normal displacement w. As $r \to \infty$, all stresses must vanish. In (55)–(58), the plus or minus sign, $\pm$, distinguishes the two faces of the crack.

In [9] the field equations and boundary conditions for a cracked shell with a quadratic midsurface were reduced to singular *IE*'s along the crack. Specialized to the case at hand, these equations take the form

$$\begin{aligned}&\text{⨍}\!\!\!\!\!\!-\!\!\int_{-1}^{1} H_{11}(\lambda x - \lambda t)F_1(t;\lambda,\nu)dt \\ &\qquad + \int_{-1}^{1} H_{12}(\lambda x - \lambda t;\nu)F_2(t;\lambda,\nu)dt = 0 \quad (59)^3\end{aligned}$$

$$\begin{aligned}&\lambda\int_{-1}^{1} H_{12}(\lambda x - \lambda t;\nu)F_1(t;\lambda,\nu)dt \\ &\qquad + \lambda\,\text{⨍}\!\!\!\!\!\!-\!\!\int_{-1}^{1} H_{22}(\lambda x - \lambda t;\nu)F_2(t;\lambda,\nu)dt = 1, \quad (60)\end{aligned}$$

where $|x|<1$, ⨍ denotes the Cauchy principal value, and

$$F_1 = \int_0^x [N_{x,y}]dt, \quad F_2 = -[w_{,xy}] \quad (61, 62)$$

$$H_{11}(x) = \mathcal{R}\{g_{,xxx}(x,0)\} = (4\pi x)^{-1} + O(x) \quad (63)$$

$$H_{12}(x) = \mathcal{I}\{g_{,xyy}(x,0) + \nu g_{,xxx}(x,0)\} = O(x\ln|x|) \quad (64)$$

$$\begin{aligned}H_{22}(x) = \mathcal{R}\{&(1-\nu^2)g_{,xxx}(x,0) + 2(1-\nu)g_{,xyy}(x,0)\} \\ &+ 4\mathcal{I}\{g_{,x}(x,0)\} = (3+\nu)(1-\nu)(4\pi x)^{-1} + O(x). \quad (65)\end{aligned}$$

In (63)–(65), $\mathcal{R}$ and $\mathcal{I}$ denote, respectively, the "real part of" and the "imaginary part of." Further, g is the fundamental solution for a shallow cylindrical shell, satisfying

$$\Delta\Delta g - 4ig_{,xx} = \delta(x)\delta(y) \quad (66)$$

and having the *formal* Fourier integral representation [13]

$$g(x,y) = \frac{1}{4\pi^2}\int_{-\infty}^{\infty}\int_{-\infty}^{\infty}\frac{e^{-i(\alpha x+\beta y)}d\alpha d\beta}{(\alpha^2+\beta^2)^2 + 4i\alpha^2}. \quad (67)$$

Although g cannot be expressed in terms of known transcendental functions of one variable, the following explicit representations for various derivatives of g, obtained from [13], are sufficient for our purposes. In what follows $i^{1/2}$ is short for $e^{i\pi/4}$.

$$4\pi g_{,x}(x,y) = i^{3/2}\sinh(i^{1/2}x)K_0(i^{1/2}r) \quad (68)$$

$$4\pi g_{,xx}(x,y) = (x/r)\sinh(i^{1/2}x)K_1(i^{1/2}r) - \cosh(i^{1/2}x)K_0(i^{1/2}r) \quad (69)$$

$$\begin{aligned}4\pi g_{,yy}(x,y) = -[&(x/r)\sinh(i^{1/2}x)K_1(i^{1/2}r) \\ &+ \cosh(i^{1/2}x)K_0(i^{1/2}r)] \quad (70)\end{aligned}$$

$$\begin{aligned}4\pi g_{,xxx}(x,y) = &-i^{1/2}(1 + x^2/r^2)\sinh(i^{1/2}x)K_0(i^{1/2}r) \\ &- [(x^2-y^2)/r^3]\sinh(i^{1/2}x)K_1(i^{1/2}r) \\ &+ 2i^{1/2}(x/r)\cosh(i^{1/2}x)K_1(i^{1/2}r) \quad (71)\end{aligned}$$

$$\begin{aligned}4\pi g_{,xyy}(x,y) = \sinh(i^{1/2}x)\{&i^{1/2}(y/r)^2K_0(i^{1/2}r) \\ &+ [(x^2-y^2)/r^3]K_1(i^{1/2}r)\}, \quad (72)\end{aligned}$$

where K_0 and K_1 are the modified Bessel functions of the first kind.

[3] Whenever convenient, we supress the arguments λ and ν.

Downloaded 01 May 2010 to 171.66.16.243. Redistribution subject to ASME license or copyright; see http://www.asme.org/terms/Terms_Use.cfm

The *IE*'s (59) and (60) are of the same form as those derived by Copley and Sanders [14]. By symmetry, $F_1(t)$ and $F_2(t)$ are *odd* functions of t.

The Form of the Exact Solutions of the Integral Equations

A closed-form solution of (59) and (60) valid for all $\lambda \geq 0$ seems out of the question, especially since much simpler problems of the same type such as the two-dimensional diffraction of a plane wave by a slit continue to defy exact solution. Nevertheless, representations for F_1 and F_2 that explicitly display the singularities in these functions may be extracted from (59) and (60).

Assume that F_1 and F_2 are integrable. Then with the aid of (63)–(65), (59) and (60) may be put into the form

$$\frac{1}{4\pi} \int\!\!\!\!\!\!- _{-1}^{1} \frac{F_\alpha(t)dt}{x - t} = B_\alpha(x), \quad \alpha = 1,2 \tag{73}$$

where the B_α are unknown (because they depend on the F_α) but integrable. But these are "airfoil" equations, the left sides of which may be inverted by formula [15], yielding

$$F_\alpha(t; \lambda) = (1 - t^2)^{-1/2} G_\alpha(t; \lambda), \quad |t| < 1, \quad \lambda \geq 0, \tag{74}$$

where the G_α are continuous on $[-1, 1]$. This representation is useful for both analytic and numeric work.

Stresses and Displacements in a Neighborhood of a Crack Tip

Stresses and displacements may be expressed as double inverse Fourier transforms involving $[(\alpha^2 + \beta^2)^2 - 4i\lambda^2\alpha^2]^{-1}$, the double Fourier transform of $\lambda^{-2}\bar{g}(\lambda x, \lambda y)$, and $f_\beta(\alpha) \equiv \int_{-1}^{1} e^{-i\alpha x} F_\beta(x)dx$, the *double* Fourier transform of the *distribution* $(1/2)F_\beta(x)[H(x + 1) - H(x - 1)]\delta(y)$. Here H is the Heaviside step function and an overbar now denotes complex conjugation. As the singularities of a function are reflected in the asymptotic behavior of its Fourier transform [16,17], we may, ultimately, express the dominant behavior of the stresses and displacement near the crack tips in terms of the dominant term in the large-α expansion of $f_\beta(\alpha)$. From (74) and equation (12.1) on page 24 of [18], we have, recalling that $G_\alpha(x)$ is odd,

$$\begin{aligned} f_\beta(\alpha) &= \int_{-1}^{1} \frac{e^{i\alpha x} G_\beta(x)dx}{(1 - x^2)^{1/2}} \\ &= i\sqrt{\frac{2\pi}{|\alpha|}}\, G_\beta(1) \sin\left(\alpha - \frac{\pi}{4}\operatorname{sgn}\alpha\right) + O(|\alpha|^{-3/2}). \end{aligned} \tag{75}$$

Let (ρ, θ) denote a set of polar coordinates centered at the right crack tip, such that $x = 1 + \rho\cos\theta$, $y = \rho\sin\theta$. By a straightforward but tedious analysis that is too lengthy to reproduce here (see Chapter 5 of [19] as well as a related analysis by Krenk [20] involving a 10th-order shell theory), we find that as $\rho \to 0$,

$$\begin{Bmatrix} N_x \\ N_{xy} \\ N_y \end{Bmatrix} \sim \frac{G_1(1)}{16\sqrt{2\rho}} \begin{Bmatrix} 3\cos(\theta/2) + \cos(5\theta/2) \\ -\sin(\theta/2) + \sin(5\theta/2) \\ 5\cos(\theta/2) - \cos(5\theta/2) \end{Bmatrix} \tag{76}$$

$$\begin{Bmatrix} M_x \\ M_{xy} \\ M_y \end{Bmatrix} \sim \frac{(1 - \nu)G_2(1)}{16\sqrt{2\rho}} \begin{Bmatrix} -(1 + \nu)[3\cos(\theta/2) + \cos(5\theta/2)] \\ -[(7 + \nu)\sin(\theta/2) + (1 - \nu)\sin(5\theta/2)] \\ (11 + 5\nu)\cos(\theta/2) + (1 - \nu)\cos(5\theta/2) \end{Bmatrix} \tag{77}$$

$$\begin{Bmatrix} u \\ v \end{Bmatrix} \sim \begin{Bmatrix} U(\lambda,\nu) \\ V(\lambda,\nu) \end{Bmatrix} + \sqrt{2\rho}\,\frac{G_1(1; \lambda,\nu)}{16} \begin{Bmatrix} (5 - 3\nu)\cos(\theta/2) - (1 + \nu)\cos(3\theta/2) \\ (7 - \nu)\sin(\theta/2) - (1 + \nu)\sin(3\theta/2) \end{Bmatrix} \tag{78}$$

$$w \sim W(\lambda,\nu) - [(2\rho)^{3/2}/48]G_2(1; \lambda, \nu) \times [3(1 - \nu)\cos(\theta/2) - (7 + \nu)\cos(3\theta/2)], \tag{79}$$

where U, V, and W are unknown constants. These formulas are of the same form as those predicted by the classical theory of plate stretching and bending.

I in Terms of Stress-Intensity Factors

Being path-independent, I, defined by (20) and nondimensionalized by (45), may be reduced to an integral along the two straight lines $|x| \leq 1 - \delta$, $y = \pm 0$, plus two identical integrals over circles of radius δ centered at the crack tips. The integrand vanishes along the straight lines because the crack is stress-free. Into the dimensionless form of I given by (45) and taken along the circle about the right crack tip, we substitute (76)–(79). In the limit as $\delta \to 0$ the contributions from the crack tip displacements, U_α and W vanish, and we obtain (3). Here we have followed Copley and Sanders and defined the stretching and bending stress-intensity factors

$$S(\lambda, \nu) = -\lim_{\rho \to 0} \sqrt{2\rho}\, N_y(\rho, 0) = -(1/4)G_1(1; \lambda, \nu) \tag{80}$$

$$B(\lambda, \nu) = -\lim_{\rho \to 0} \sqrt{2\rho}\, M_y(\rho, 0) = -(1/4)(3 + \nu)(1 - \nu)G_2(1; \lambda, \nu). \tag{81}$$

I in Terms of the Unknown $F_2(x;\lambda,\nu)$

The alternate dimensionless form of I given by (46) reduces to

$$I = -\int_{-1}^{1} [w_{,y} + (1/2)\lambda\dot{w}_{,y}]dx \tag{82}$$

But from (62),

$$[w_{,y}](x) = -\int_{-1}^{x} F_2(t)dt. \tag{83}$$

Hence

$$I(\lambda,\nu) = -\int_{-1}^{1} x[F_2(x; \lambda, \nu) + (1/2)\lambda\dot{F}_2(x; \lambda, \nu)]dx. \tag{84}$$

Approximate Solutions of the Integral Equations

To determine the explicit dependence of I on λ and ν we need to solve (59) and (60), if only approximately.

If $\lambda \ll 1$, we may use a perturbation method. Omitting the details that are virtually the same as those spelled out in [21], we find that

$$F_2(x; \lambda, \nu) = \frac{-4x}{(3 + \nu)(1 - \nu)(1 - x^2)^{1/2}} \times \left[1 - \frac{\lambda^2\pi}{16}\frac{(1 + 2\nu + 5\nu^2)}{(3 + \nu)(1 - \nu)} + \ldots\right]. \tag{85}$$

Hence, from (3) and (84),

$$C(\lambda, \nu) = \frac{1}{[(3 + \nu)(1 - \nu)]^{1/2}} \left[1 - \frac{\lambda^2\pi}{16}\frac{(1 + 2\nu + 5\nu^2)}{(3 + \nu)(1 - \nu)} + \ldots\right]. \tag{86}$$

If $\lambda = O(1)$, (59) and (60) may be solved numerically; Copley and Sanders [14] did so for $0 \leq \lambda \leq 4$. Carrington has obtained numerical solutions of (59) and (60) using the method of Theocaris and Ioakimidis [10]—a method particularly suited to computing stress-intensity factors because the $G_\alpha(1;\lambda, \nu)$ are among the discretized unknowns. Her values for C for $\nu = 0.3$ and selected values of λ up to 40 are shown in Fig. 1.

If $\lambda \gg 1$, asymptotic methods beckon. In the limit as $\lambda \to \infty$, there are two ways in which (59) and (60) may be scaled so that nontrivial, parameter-free *IE*'s emerge. The first scaling highlights the very strong coupling between bending and stretching that exists away from the crack tips and leads to what we call the (first-approximation) *outer IE's*. The second scaling highlights the platelike behavior of the shell near the crack tips and leads to what we call the (first-approximation) *inner IE's*.

The Outer Integral Equations

These are obtained by bounding x away from the crack tips and

Downloaded 01 May 2010 to 171.66.16.243. Redistribution subject to ASME license or copyright; see http://www.asme.org/terms/Terms_Use.cfm

considering the forms of the kernels in (59) and (60) as $\lambda \to \infty$. As the dominant terms in some of the large argument expansions of the kernels are nonintegrable, we first integrate (59) twice and (60) once with respect to x. Introducing $[w_{,y}]$ from (62) as a new unknown, integrating by parts, and noting that the left sides of the resulting equations are, respectively, even and odd in x, we have

$$\int_{-1}^{1} H_{11}^{(-2)}(\lambda x - \lambda t) F_1(t)dt - \lambda \int_{-1}^{1} H_{12}^{(-1)}(\lambda x - \lambda t)[w_{,y}](t)dt = K(\lambda, \nu) \quad (87)$$

$$\int_{-1}^{1} H_{12}^{(-1)}(\lambda x - \lambda t) F_1(t)dt - \lambda \int_{-1}^{1} H_{22}(\lambda x - \lambda t)[w_{,y}](t)dt = x, \quad (88)$$

where $K(\lambda,\nu)$ is an unknown constant of integration and

$$H_{11}^{(-2)}(x) = \mathcal{R}\{g_{,x}(x, 0)\} \quad (89)$$

$$H_{12}^{(-1)}(x) = \mathcal{I}\{g_{,yy}(x, 0) + \nu g_{,xx}(x, 0)\}. \quad (90)$$

The superscript $(-n)$ indicates that a kernel, defined by (63) or (64), has been integrated n times. From (65), (68)–(72), (89), (90), and equation 9.7.2 of [22], it follows that as $x \to \infty$,

$$H_{11}^{(-2)}(x) \sim -\frac{\operatorname{sgn} x \cos(3\pi/8)}{8\sqrt{2\pi}\,|x|^{1/2}} \quad (91)$$

$$H_{12}^{(-1)}(x) \sim \frac{\sin(\pi/8)}{4\sqrt{2\pi}\,|x|^{1/2}} \quad (92)$$

$$H_{22}(x) \sim -\frac{\operatorname{sgn} x \sin(3\pi/8)}{2\sqrt{2\pi}\,|x|^{1/2}}. \quad (93)$$

Let $\lambda \to \infty$ in (87) and (88). With

$$p(t) = \lim_{\lambda\to\infty} \lambda^{-1/2} F_1(t; \lambda, \nu) \quad (94)$$

$$q(t) = -\lim_{\lambda\to\infty} \lambda^{1/2}[w_{,y}](t; \lambda, \nu), \quad (95)$$

we obtain

$$\int_{-1}^{1} \frac{q(t)dt}{|x-t|^{1/2}} - \frac{1}{2}\int_{-1}^{1} \frac{p(t)\operatorname{sgn}(x-t)dt}{|x-t|^{1/2}} = \frac{4\sqrt{2\pi}K_*}{\sin(\pi/8)} \quad (96)$$

$$\int_{-1}^{1} \frac{q(t)\operatorname{sgn}(x-t)dt}{|x-t|^{1/2}} + \frac{1}{2}\tan\left(\frac{\pi}{8}\right)\int_{-1}^{1} \frac{p(t)dt}{|x-t|^{1/2}} = \frac{2\sqrt{2\pi}\,x}{\cos(\pi/8)}, \quad (97)$$

where $K_* = K(\infty, \nu)$.

Solution of the Outer Integral Equations

We first convert (96) and (97) to Cauchy form, using a method suggested by Latta and carried out in detail in [11], [19], and [23].

For convenience, map to the interval (0,1) via $x = 2\xi - 1$, $t = 2\tau - 1$. Next introduce the fractional integral operators

$$I^{1/2} f = \pi^{-1/2}\int_0^{\xi} f(t)(\xi - t)^{-1/2}dt \quad (98)$$

$$J^{1/2} f = \pi^{-1/2}\int_{\xi}^{1} f(t)(t - \xi)^{-1/2}dt, \quad (99)$$

so that (96) and (97) take the form

$$(I^{1/2} + J^{1/2})q(\xi) - \frac{1}{2}(I^{1/2} - J^{1/2})p(\xi) = 4K_* \csc(\pi/8) \quad (100)$$

$$(I^{1/2} - J^{1/2})q(\xi) + \frac{1}{2}\tan(\pi/8)(I^{1/2} + J^{1/2})p(\xi) = 2(2\xi - 1)\sec(\pi/8). \quad (101)$$

Operate on (100) and (101) by $I^{1/2}$ and differentiate the resulting equations, noting that $[I^{1/2}J^{1/2}f(\xi)]' = \xi^{-1/2}T[\xi^{1/2}f(\xi)]$, where

$$Tf = \frac{1}{\pi}\int_0^1 \frac{f(t)dt}{t - \xi}. \quad (102)$$

With $P = (1/2)\sqrt{\pi\xi}\,p(\xi)$ and $Q = (1/2)\sqrt{\pi\xi}q(\xi)$, there follows:

$$Q(\xi) + TQ(\xi) - \frac{1}{2}[P(\xi) - TP(\xi)] = 2K_* \csc(\pi/8) \quad (103)$$

$$Q(\xi) - TQ(\xi) + \frac{1}{2}\tan(\pi/8)[P(\xi) + TP(\xi)] = (4\xi - 1)\sec(\pi/8). \quad (104)$$

Multiplying (103) by the complex constant $i\sqrt{\tan(\pi/8)} \equiv iC$, we obtain the single, complex-valued Cauchy singular IE

$$(T + \beta)f(\xi) = -2^{1/4}(C^{-1} - 1)(1 + iC)(4\xi - 1 + 2iC^{-1}K_*), \quad (105)$$

where

$$f = Q - (1/2)iCP \quad (106)$$

$$\beta = -\frac{1 - C^2 + 2iC}{1 + C^2}. \quad (107)$$

Carleman's method [24] solves (105); see [19] for details. The respective oddness and evenness of $p(x)$ and $q(x)$ implies that

$$b \equiv -4K_*C^{-1} = \frac{1}{2\pi}\ln\left(\frac{\sqrt{1+\sqrt{2}}+1}{\sqrt{1+\sqrt{2}}-1}\right) = 0.2433\ldots, \quad (108)$$

yielding the first approximation outer solutions

$$p(x) = 8\sqrt{2(1+\sqrt{2})/\pi}\,(1 - x^2)^{1/4}\sin\psi(x) \quad (109)$$

$$q(x) = 4\sqrt{2/\pi}\,(1 - x^2)^{1/4}\cos\psi(x), \quad (110)$$

where

$$\psi(x) = b[\ln(1 - x) - \ln(1 + x)]. \quad (111)$$

The Inner Integral Equations

Noting that λ enters the kernels of (87) and (88) only in the combination $\lambda x - \lambda t$, and focusing on a neighborhood of the left crack tip, we introduce the scaled variables

$$\xi = \lambda(x + 1), \quad \tau = \lambda(t + 1). \quad (112, 113)$$

The dependent variables in (87) and (88) must be scaled so that "the outer limit of the inner solutions matches the inner limit of the outer solutions" [25]. If we insert (112) into (109) and (110) and refer to (94) and (95), it follows that as $\xi \to 0$,

$$\lambda^{1/2}[w_{,y}] + (1/2)iC\lambda^{-1/2}F_1 \sim -(8/\sqrt{\pi})(\xi/2\lambda)^{1/4+ib}. \quad (114)$$

Hence we introduce scaled inner dependent variables by setting

$$[w_{,y}] = \lambda^{-3/4-ib}M(\xi) \quad (115)$$

$$F_1 = \lambda^{1/4-ib}\Lambda(\xi). \quad (116)$$

However, if we insert (112), (113), (115), and (116) into (87) and (88) and multiply each equation by $\lambda^{3/4-ib}$, then, although the left sides become independent of λ as $\lambda \to \infty$, the right sides approach infinity. To avoid such a situation, (encountered in [11] in a simpler problem) we must work with homogeneous inner IE's. Thus we return to the original IE's, (59) and (60), differentiate (60) with respect to x, insert (112) and (113), take

$$F_2' = -[w_{,y}]_{,xx} = \lambda^{5/4-ib}N(\xi) \quad (117)$$

as a new unknown, and take the limit as $\lambda \to \infty$ to obtain the first approximation inner IE's

$$\int_0^{\infty} H_{11}(\xi - \tau)\Lambda_0(\tau)d\tau + \int_0^{\infty} H_{12}^{(1)}(\xi - \tau)N_0(\tau)d\tau = 0 \quad (118)$$

$$\int_0^{\infty} H_{12}^{(1)}(\xi - \tau)\Lambda_0(\tau)d\tau + \int_0^{\infty} H_{22}(\xi - \tau)N_0(\tau)d\tau = 0, \quad (119)$$

where $\Lambda_0(\tau) = \Lambda(\tau, \infty)$ and $N_0(\tau) = N(\tau, \infty)$.

Downloaded 01 May 2010 to 171.66.16.243. Redistribution subject to ASME license or copyright; see http://www.asme.org/terms/Terms_Use.cfm

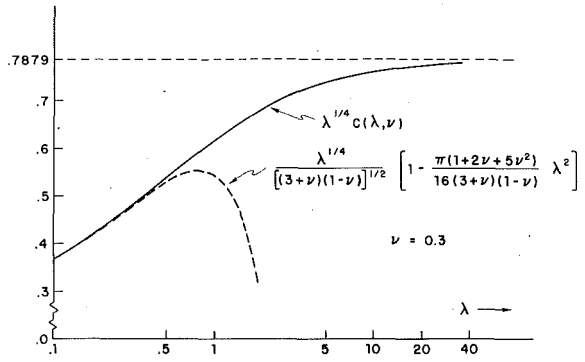

Fig. 2 Combined stress-intensity factor $\lambda^{1/4}C(\lambda,\nu)$ versus λ for $\nu = 0.3$

Asymptotic Evaluation of I

We use (82) to evaluate I as $\lambda \to \infty$. Set

$$\int_{-1}^{1}[w_{,y}]dx = 2\int_{-1}^{-1+\lambda^{-1/2}}[w_{,y}]dx + \int_{-1+\lambda^{-1/2}}^{1-\lambda^{-1/2}}[w_{,y}]dx \equiv 2J_1 + J_2. \quad (120)$$

To estimate J_1 consider the first-approximation inner solution for $[w_{,y}]$. Although the inner IE's (118) and (119) are of the coupled Wiener-Hopf type for which there is no known general method of solution, we need only note for our purpose that $[w_{,y}]$ is integrable at $x = -1$, by (74), and $O(\lambda^{-5/8})$ on $-1 \le x \le \lambda^{-1/2}$, by (114). Hence $J_1 = 0(\lambda^{-9/8})$.

In J_2, replace $[w_{,y}]$ by the first-approximation outer solution $\lambda^{-1/2}q$, thereby introducing a *relative* error of $O(\lambda^{-1})$. As q is integrable on $(-1,1)$, we may extend the range of integration in J_2 from -1 to 1. Thus

$$J_2 = -\lambda^{-1/2}\int_{-1}^{1}q(t)dt + O(\lambda^{-1}) \quad (121)$$

From (110)

$$\int_{-1}^{1}q(t)dt = 4\sqrt{2/\pi}\int_{-1}^{1}(1-t^2)^{1/2}\cos\psi(t)dt$$
$$= 4\sqrt{2/\pi}\int_{-1}^{1}(1-t)^{1/4-ib}(1+t)^{1/4+ib}dt$$
$$= (2^6/3\pi)|\Gamma(5/4-ib)|. \quad (122)$$

Concatenating (3), (43), (82), (120), and (122), we obtain (5). Fig. 2 is a graph of $\lambda^{1/4}C(\lambda,0.3)$ as determined from a numerical solution of the exact IE's (59) and (60), and as determined from the small and large λ analytic solutions, (86) and (5).

Conclusions

We have determined the form of Sanders' path-independent energy-release rate integral in the linear theory of arbitrarily loaded shallow shells and have used it to compute the asymptotic behavior of a combined stress-intensity factor for a bent cylindrical shell with a longitudinal crack.

Our approach should work for *any* cracked, elastic shell so long as the crack is short and straight and does not lie too close to an edge or other geometric discontinuity. This *assumes* that we can solve the outer IE's (even a numerical solution will suffice if we can extract the analytic dependence on λ). Of course to formulate the outer IE's, we need asymptotic expansions of the fundamental solution of shallow shell theory. To date these are known for spherical [26], cylindrical [13], and hyperbolic paraboloidal [27] shells only, but asymptotic expansions for shallow shells with arbitrary quadratic midsurfaces are under study.

References

1 Eshelby, J. D., "The Continuum Theory of Lattice Defects," *Solid State Physics,* eds., Seitz, F., and Turnbull, D., Vol. 3, Academic Press, 1956, pp. 79–144.

2 Sanders, J. L., Jr., "On the Griffith-Irwin Fracture Theory," ASME JOURNAL OF APPLIED MECHANICS, Vol. 27, 1960, pp. 352–353.

3 Günter W., "Über einige Randintegrale der Elastomechanik," *Braunschweigische Wissenschaftliche Gellschaft Abhandlungen,* Vol. 14, 1962, pp. 53–72.

4 Cherepanov, G. P., "Crack Propagation in Continuous Media," *Journal of Applied Mathematics and Mechanics* (Translation of *P.M.M*), Vol. 31, 1967, pp. 503–512.

5 Rice, J. R., "A Path-Independent Integral and the Approximate Analysis of Strain Concentration by Notches and Cracks," ASME JOURNAL OF APPLIED MECHANICS, Vol. 35, 1968, pp. 379–386.

6 Knowles, J. K., and Sternberg, E., "On a Class of Conservation Laws in Linearized and Finite Elastostatics," *Archive for Rational Mechanics and Analysis,* Vol. 44, 1972, pp. 187–211.

7 Budiansky, B., and Rice, J. R., "Conservation Laws and Energy-Release Rates," ASME JOURNAL OF APPLIED MECHANICS, Vol. 40, 1973, pp. 201–203.

8 Eshelby, J. D., "The Elastic Energy-Momentum Tensor," *Journal of Elasticity,* Vol. 5, 1975, pp. 321–335.

9 Simmonds, J. G., Bradley, M. R., and Nicholson, J. W., "Stress-Intensity Factors for Arbitrarily Oriented Cracks in Shallow Shells," ASME JOURNAL OF APPLIED MECHANICS, Vol. 45, 1978, pp. 135–141.

10 Theocaris, P. S., and Ioakimidis, N. I., "Numerical Integration Methods for the Solution of Singular Integral Equations," *Quarterly Journal of Applied Mathematics,* Vol. 35, 1977, pp. 173–183.

11 Latta, G. E., Simmonds, J. G., and Bradley, M. R., "Analytical and Numerical Calculation of Stress-Intensity Factors in a Pressurized Cylindrical Shell With a Clamped Crack," ASME JOURNAL OF APPLIED MECHANICS, Vol. 44, 1977, pp. 264–270.

12 Amazigo, J. C., "On the J Integral for an Internally Pressurized Cylindrical Shell With Longitudinal Crack," *International Journal of Fracture,* Vol. 9, 1973, pp. 492–494.

13 Sanders, J. L., Jr., and Simmonds, J. G., "Concentrated Forces on Shallow Cylindrical Shells," ASME JOURNAL OF APPLIED MECHANICS, Vol. 37, 1970, pp. 367–373.

14 Copley, L. G., and Sanders, J. L., Jr., "A Longitudinal Crack in a Cylindrical Shell Under Internal Pressure," *International Journal of Fracture Mechanics,* Vol. 5, 1969, pp. 117–131.

15 Latta, G. E., "Transform Methods," Chapter 11 of *Handbook of Applied Mathematics,* ed., Pearson, C. E., Van Nostrand Rienhold, 1974.

16 Lighthill, M. J., *Fourier Analysis and Generalized Functions,* Cambridge University Press, 1959, Chapter 4.

17 Jones, D. S., *Generalized Functions,* McGraw-Hill, New York, 1966, Chapter 9.

18 Copson, E. T., *Asymptotic Expansions,* Cambridge University Press, 1965.

19 Nicholson, J. W., "Asymptotic Evaluation of Stress-Intensity Factors in Cracked Shells Via a Path Independent Integral," PhD Dissertation, University of Virginia, Charlottesville, Va., 1979.

20 Krenk, S., "Influence of Transverse Shear on an Axial Crack in a Cylindrical Shell," *International Journal of Fracture,* Vol. 14, 1978, pp. 123–143.

21 Simmonds, J. G., and Bradley, M. R., "Stress-Intensity Factors for Very Short Cracks in Arbitrary Pressurized Shells," ASME JOURNAL OF APPLIED MECHANICS, Vol. 43, 1976, pp. 657–662.

22 Abramowitz, M., and Stegun, I. A., *Handbook of Mathematical Functions,* U.S. Government Printing Office, 1964.

23 Bradley, M. R., "Cracks in Shells," PhD Dissertation, University of Virginia, Charlottesville, Va., 1977.

24 Carrier, G. F., Krook, M., and Pearson, C. E., *Functions of a Complex Variable,* McGraw-Hill, New York, 1966, Chapter 8.

25 Van Dyke, M., *Perturbation Methods in Fluid Mechanics,* Annotated Edition, Parabolic Press, 1975, Chapter 5.

26 Reissner, E., "Stresses and Small Displacements in Shallow Spherical Shells, I, II," *Journal of Mathematics and Physics,* Vol. 25, 1947, pp. 80–85, 279–300.

27 Simmonds, J. G., and Tropf, C., "The Fundamental (Normal Point Load) Solution for a Shallow Hyperbolic Paraboloidal Shell," *SIAM Journal of Applied Mathematics,* Vol. 27, 1974, pp. 102–120.

Downloaded 01 May 2010 to 171.66.16.243. Redistribution subject to ASME license or copyright; see http://www.asme.org/terms/Terms_Use.cfm

K. C. Park

Staff Scientist,
Applied Mechanics Laboratory,
Lockheed Palo Alto Research Laboratory,
3251 Hanover Street,
Palo Alto, Calif. 94304
Mem. ASME

Partitioned Transient Analysis Procedures for Coupled-Field Problems: Stability Analysis

A general partitioned transient analysis procedure is proposed, which is amenable to a unified stability analysis technique. The procedure embodies two existing implicit-explicit procedures and one existing implicit-implicit procedure. A new implicit-explicit procedure is discovered, as a special case of the general procedure, that allows degree-by-degree implicit or explicit selections of the solution vector and can be implemented within the framework of the implicit integration packages. A new element-by-element implicit-implicit procedure is also presented which satisfies program modularity requirements and enables the use of single-field implicit integration packages to solve coupled-field problems.

Introduction

The transient response analysis of many engineering systems involves the formulation of semidiscrete coupled-field equations of motion which are then solved by direct time integration methods. Such coupled-field equations, for example, arise in the modeling of structure-medium interaction problems, thermal-fluid flow problems, and structure-structure interaction problems. The direct time integration of these equations presents computational difficulties that are not normally encountered in single-field problems or in structure-structure interaction problems where mesh sizes are more or less uniform. There are two major sources of difficulties, one related to computational aspects and the other to implementation.

First, the isolated fields may have vastly different response characteristics. This suggests that for computational efficiency different integration algorithms and/or different time step sizes for each solution vector should be adopted. In fluid-structure interaction problems, for instance, the characteristic response time scale of the fluid-field solution vector is typically much slower than that of the structure-field vector.

Second, the bulk of existing engineering analysis software has been developed primarily for the treatment of single-field problems. One is thus motivated to make use of existing single-field analysis software to solve the coupled-field equations of motions; this imposes modularity constraints on software architecture. If modularity requirements are met, the direct time integration of the entire equations can be performed either by sequential or parallel execution of single-field analyzers. Solution procedures geared to this operation mode will be termed *partitioned transient analysis procedures* (or simply *partitioned procedures*). As shown in the paper, there is a multitude of possible partitioned transient analysis procedures for each coupled-field system. Therefore, the task of selecting a "best" procedure can become formidable. This is because the analysis of the stability and accuracy of partitioned procedures is much harder than that of single-field solution procedures. Furthermore, the assessment of the relative merit of competing procedures may be difficult to settle if different analysis techniques are employed for each procedure.

Partitioned procedures for structural dynamic problems were first proposed by Belytschko and Mullen [1–2]. They described an implicit-explicit (I–E) partition through which meshes that exhibit high (low) frequency response characteristics are treated by implicit (explicit) integration formulas. Hughes and Liu [3–4] proposed an alternative I–E partition, which apparently leads to a simpler implementation in finite-element programs.

Few systematic studies of partitioned procedures for specific coupled-field problems have appeared in the literature. An analysis of integration procedures for the coupled sound and heat flow problems by Morimoto [5] appears to be the first study on the subject. Recently, Park, Felippa, and DeRuntz [6] studied implicit-implicit partitioned procedures for a class of fluid-structure interaction equations. Their objective was to treat the symmetric parts of both the fluid and structural equations by implicit integration formulas and coupling terms by extrapolation formulas. The two primary solution vectors were the scattered fluid pressure on the "wet" structural surface and the structural displacements. Hence, the solution of these coupled-field equations was obtained by a sequential execution of fluid and structural analyzers, which led to the term "*staggered solution pro-*

Contributed by the Applied Mechanics Division for publication in the JOURNAL OF APPLIED MECHANICS.

Discussion on this paper should be addressed to the Editorial Department, ASME, United Engineering Center, 345 East 47th Street, New York, N. Y. 10017, and will be accepted until September 1, 1980. Readers who need more time to prepare a discussion should request an extension from the Editorial Department. Manuscript received by ASME Applied Mechanics Division, March, 1979; final revision, August, 1979.

Copyright © 1980 by ASME
Downloaded 01 May 2010 to 171.66.16.243. Redistribution subject to ASME license or copyright; see http://www.asme.org/terms/Terms_Use.cfm

cedures." Unconditional stabilization of such implicit-implicit procedures was made possible by exploiting the availability of the fluid radiation damping term in the equations of motion, which is the result of treating the infinite fluid domain by a doubly asymptotic approximation [7]. The idea of introducing damping for stabilization was subsequently pursued by Belytschko, Yen, and Mullen [8] in their study of an implicit-implicit procedure for a two-degree-of-freedom model problem which describes certain fluid-structure interaction problems.

Common to the aforementioned studies is the use of a specific partitioned procedure and/or restriction to special classes of problems. The present study endeavors to consider a general partitioned procedure which is amenable to a unified stability analysis technique. Motivation for undertaking this study is twofold: it eliminates case-by-case stability analysis of each particular partitioned procedure, and it provides a common ground for evaluating competing procedures.

As a means to achieve the preceding objectives, the present paper utilizes the following three basic formulation steps. First, the entire semidiscrete equations of motion are treated by implicit integration formulas. Second, the resulting difference equations are partitioned. Finally, coupling terms that are transferred to the right-hand side in the difference equations are extrapolated. In other words, the first step completes the temporal discretization. The second defines computer implementation as regards matrix configurations that have to be treated in each single-field analyzer. The last step determines which parts or portion of the entire solution vector should be treated explicitly. It will be shown that the present formulation can embody existing partitioned procedures plus hitherto untried ones that may offer algorithmic and/or implementation advantages.

Linear Coupled-Field Equations of Motion

We consider problems governed by the general matrix equation

$$\mathbf{A}\,\underline{\ddot{u}} + \mathbf{B}\,\underline{\dot{u}} + \mathbf{C}\,\underline{u} = \underline{f} \tag{1a}$$

where $\underline{u}$ is the complete solution vector

$$\underline{u}^T = (\underline{u}^x, \underline{u}^y, \ldots)^T \tag{1b}$$

and $\underline{u}^x$, $\underline{u}^y$. . . represent single-field solution state vectors; a superposed dot denotes time (t) differentiation and the superscript T on a matrix or vector denotes transposition. Matrices **A**, **B**, and **C** represent generalized mass, damping, and stiffness matrices, respectively, and $\underline{f}$ is the generalized force vector.

The term "generalized" is used to indicate that no specific form of matrices **A**, **B**, and **C** is required for carrying out the basic three formulation steps outlined in the Introduction. For example, if **A** is diagonal, **B** is null, and **C** is positive-definite, equation (1) represents a lumped-mass and stiffness system that describes undamped oscillatory problems. If the entries in **A** corresponding to $\underline{u}^y$ and those in **B** corresponding to $\underline{u}^x$ are zero, equation (1) represents a coupled hyperbolic ($\underline{u}^x$) and parabolic ($\underline{u}^y$) system that describes fluid-structure interaction problems via a doubly asymptotic approximation [7]. Other coupled-field problems can be defined by appropriate selection of entries in matrices **A**, **B**, and **C**. Thus the application of the basic three formulation steps to equation (1) can cover fairly general partitioned transient analysis procedures applicable to a wide class of coupled-field problems.

Implicit Integration, General Partitioning and Extrapolation

Implicit linear multistep formulas can be expressed in a compact form (see Felippa and Park [9] for details):

$$\underline{u}_n = \delta\,\underline{\dot{u}}_n + \underline{h}^u_n \tag{2}$$

where $\underline{h}^u_n$ represents the contribution of historical terms and δ is a formula-dependent generalized step size. It is noted that each field solution state vector in equation (1b) can be integrated by different integration formulas. Therefore, equation (2) is to be viewed as a symbolic representation of these different integration formulas, viz., for $\underline{u}^T = (\underline{u}^x, \underline{u}^y, \ldots)^T$, we have $\delta = \text{diag}\,(\delta_x, \delta_y, \ldots)$, and similarly for the historical vector $\underline{h}^u_n$. Substitution of equation (2) into equation (1) yields

$$\mathbf{E}\,\underline{u}_n = \underline{g}_n \tag{3}$$

where

$$\mathbf{E} = \mathbf{A} + \delta\,\mathbf{B} + \delta^2\,\mathbf{C} \tag{4}$$

$$\underline{g}_n = \delta^2\,\underline{f}_n + (\mathbf{A} + \delta\,\mathbf{B})\,\underline{h}^u_n + \delta\,\mathbf{A}\,\underline{h}^{\dot{u}}_n \tag{5}$$

Now we wish to solve the difference equation (3) for the entire coupled-field equations by making use of single-field analysis software. To this end we restrict our considerations to two-field problems and consider the following general matrix partitioning:

$$\mathbf{E} = \mathbf{E}_x + \mathbf{E}_y \tag{6}$$

where

$$\mathbf{E}_x = \mathbf{A} + \delta\,\mathbf{B}_x + \delta^2\,\mathbf{C}_x \tag{7}$$

$$\mathbf{E}_y = \delta\,\mathbf{B}_y + \delta^2\,\mathbf{C}_y \tag{8}$$

Equation (3) is rearranged using equation (6) in the form

$$\mathbf{E}_x\,\underline{u}_n = \underline{g}_n - \mathbf{E}_y\,\underline{u}^{(P)}_n \tag{9}$$

where $\underline{u}^{(P)}_n$ is a suitable extrapolator for $\underline{u}_n$.

We call the formulation as given by equations (2)–(9) an *implicit-explicit* (*I-E*) procedure if $\mathbf{E}_y$ contains nonzero diagonal entries, and an *implicit-implicit* (*I-I*) procedure if $\mathbf{E}_y$ *contains only off-diagonal entries.*

We use here the term partitioning in preference to *splitting* for the following reason. The term "matrix splitting" is often associated with procedures in which one wishes to reduce the bandwidth of the semi-implicit iteration matrix or to treat directional-sensitive matrix coefficients separately in alternating direction methods [10–12]. Thus, in splitting procedures, one solves for the entire solution state vector simultaneously. On the other hand, in partitioned procedures one solves first for part of the entire solution state vector, which is then used to solve a portion of the remaining solution vector. This distinction with be clarified by the following examples which arise in structural dynamics.

Examples of Partitioning

For reasons discussed later, matrix **A** is *not* partitioned and the same partitioning is applied to **B** and **C**. Hence, we will deal only with matrix **C** in the following examples.

Let us represent the matrix **C** as a 3×3 block matrix

$$\mathbf{C} = \begin{bmatrix} \mathbf{C}_{xx} & \mathbf{C}_{xb} & \mathbf{0} \\ \mathbf{C}_{bx} & \mathbf{C}_{bb} & \mathbf{C}_{by} \\ \mathbf{0} & \mathbf{C}_{yb} & \mathbf{C}_{yy} \end{bmatrix} \tag{10}$$

and the corresponding solution state vector $\underline{u}$ by

$$u^T = (\underline{u}^x, \underline{u}^b, \underline{u}^y)^T \tag{11}$$

where super or subscripts x and y designate the two domains, and b designates the boundary as shown in Fig. 1. We now illustrate some useful partitions.

Example 1: Belytschko and Mullen Node-by-Node Partitioning [1–2]. This partitioning is achieved from equation (10) by grouping the boundary contributions to either one of the domains and choosing $\mathbf{C}_y$ as

$$\mathbf{C}_y = \begin{bmatrix} \mathbf{0} & \mathbf{0} & \mathbf{0} \\ \mathbf{0} & \mathbf{0} & \mathbf{0} \\ \mathbf{0} & \mathbf{C}_{yb} & \mathbf{C}_{yy} \end{bmatrix} \tag{12}$$

This partition was used in an implicit-explicit procedure. Partition (12) enables us to obtain the entire soution vector $\underline{u}$ in two separate

Downloaded 01 May 2010 to 171.66.16.243. Redistribution subject to ASME license or copyright; see http://www.asme.org/terms/Terms_Use.cfm

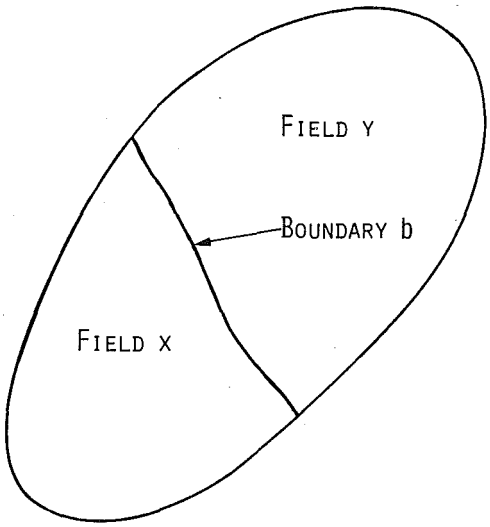

Fig. 1 Coupling of two fields with a common boundary

solution stages. First, the solution vector $\underline{u}^y$ is obtained explicitly as $\mathbf{A}$ *is assumed diagonal. Then the remaining vector* $(\underline{u}^x, \underline{u}^b)^T$ is obtained by solving the implicit algebraic equations once $\underline{u}^y$ is available.

Example 2: Hughes and Liu Element-by-Element Partitioning [3–4]. If we decompose the boundary matrix $\mathbf{C}_{bb}$ in equation (10) into two element-level matrices according to the two groups of boundary-adjacent finite elements, the following partitioning for $\mathbf{C}_y$ results:

$$\mathbf{C}_y = \begin{bmatrix} \mathbf{0} & \mathbf{0} & \mathbf{0} \\ \mathbf{0} & \mathbf{C}^y_{bb} & \mathbf{C}_{by} \\ \mathbf{0} & \mathbf{C}_{yb} & \mathbf{C}_{yy} \end{bmatrix} \tag{13}$$

where $\mathbf{C}_{bb} = \mathbf{C}^x_{bb} + \mathbf{C}^y_{bb}$, in which $\mathbf{C}^x_{bb}$ is the contribution of the element-level matrices that belong to elements in the spatial domain x, and similarly for $\mathbf{C}^y_{bb}$.

Example 3: A New DOF-by-DOF Partitioning. A partitioning suitable for working at the degree-of-freedom (DOF) level results if we take

$$\mathbf{C}_y = \begin{bmatrix} \mathbf{0} & \mathbf{0} & \mathbf{0} \\ \mathbf{0} & \mathbf{0} & \mathbf{0} \\ \mathbf{0} & \mathbf{0} & \mathbf{C}_{yy} \end{bmatrix} \tag{14}$$

It will be shown later on in the paper that this partition gives the same stability condition as the node-by-node partition (12). Nevertheless, this DOF-by-DOF partition (14) offers one computational advantage over the node-by-node partition: it can be implemented within a single-field implicit integration package as the implicit-portion of the stiffness matrix remains symmetric. On the other hand, the node-by-node partition (12) requires that integration be carried out in two separate integration packages: explicit and implicit, because the implicit-portion stiffness matrix is not symmetric.

Stability of General Partitioned Procedure

The stability of the general partitioned equation (9) can be examined by seeking nontrivial solutions for $f_n = \underline{0}$ in the form:

$$\underline{u}_n = \lambda\, \underline{u}_{n-1} \tag{15}$$

where λ is the solution amplification factor. The integration formula (2) can now be expressed in terms of its associated characteristic polynomial (see Appendix A)

$$\rho(\lambda)\underline{u}_{n-m} = \delta\, \sigma(\lambda)\, \underline{\dot{u}}_{n-m} \tag{16}$$

and similarly for the extrapolator (47) (see Appendix A)

$$\underline{u}^{(p)}_n = e(\lambda)\, \underline{u}_{n-m} \tag{17}$$

where the subscript m denotes the number of step intervals used in the formula (2). Substituting equations (16) and (17) into equation (9) one obtains the characteristic system

$$\mathbf{J}(\lambda)\, \underline{u}_{n-m} = \underline{0} \tag{18}$$

where

$$\mathbf{J}(\lambda) = [\rho^2 \mathbf{A} + \delta\, \rho\, \sigma\, \mathbf{B}_x + \delta\, \rho\, (\sigma - \lambda^m + e)\, \mathbf{B}_y + \delta^2\, \sigma^2\, \mathbf{C}_x + \delta^2(\sigma^2 - \lambda^m\, \rho + \rho\, e)\, \mathbf{C}_y] \tag{19}$$

in which ρ stands for $\rho(\lambda)$, etc.

Remark: It is important that velocities be updated by the integration formula

$$\underline{\dot{u}}_n = \delta\, \underline{\ddot{u}}_n + \underline{h}^{\dot{u}}_n \tag{20}$$

and not by the differentiation formula

$$\underline{\ddot{u}}_n = (\underline{u}_n - \underline{h}^u_n)/\delta \tag{21}$$

in order to avoid numerical instability (see Appendix A).

For algebraic convenience we introduce the transformation

$$\lambda = \frac{1+z}{1-z} \tag{22}$$

which maps the solution-bounding unit disk $|\lambda| \le 1$ onto the entire left-hand z-plane. The characteristic equation in the z variable is

$$\det \mathbf{J}\left(\frac{1+z}{1-z}\right) = 0 \tag{23}$$

For stability the roots of the characteristic equation (23) must satisfy

$$\mathrm{Re}\,(z_i) \le 0, \quad i = 1, \ldots\ldots\ldots\ldots, 2mN \tag{24}$$

where N is the size of equation (1) and m is the number of steps entering in the integration formula (2).

The major thrust of the present paper is to treat various partitioned procedures and their stability conditions by a general partitioned procedure (9) and a unified stability analysis. To this end we will limit ourselves to the use of the trapezoidal formula and one term extrapolator in the sequel, viz:

$$\begin{aligned} \rho(\lambda) &= \lambda - 1 \\ \sigma(\lambda) &= \lambda + 1 \\ \delta &= 0.5\, h \\ e(\lambda) &= 1 \end{aligned} \tag{25}$$

so that equations (19) and (23), respectively, reduce to

$$\mathbf{J}_T(\lambda) = (\lambda - 1)^2 \mathbf{A} + \delta(\lambda^2 - 1)\, \mathbf{B}_x + \delta^2(\lambda + 1)^2\, \mathbf{C}_x + 2\,\delta(\lambda - 1)\, \mathbf{B}_y + 4\delta^2\, \lambda\, \mathbf{C}_y \tag{26}$$

$$\det [(\mathbf{A} - \delta\, \mathbf{B}_y - \delta^2\, \mathbf{C}_y)\, z^2 + \delta\, \mathbf{B}\, z + \delta^2\, \mathbf{C}] = 0 \tag{27}$$

The stability of the general partitioned procedure (9), when the trapezoidal integration formula and one term extrapolator are used, can now be examined via the characteristic z-polynomial equation (27) subject to the constraints (24). As basic means for evaluating the stability condition (24) we cite the classical theorems of Routh-Hurwitz and Lyapunov (see Chapter XV of Gantmacher [13]). For the case in which all matrices appearing in equation (27) are symmetric, it is convenient to use a theorem of Bellman [14].

Theorem 1 (Bellman). If $(\mathbf{A} - \delta\, \mathbf{B}_y - \delta^2\, \mathbf{C}_y)$, $\mathbf{B}$ and $\mathbf{C}$ are nonnegative definite, and either $(\mathbf{A} - \delta\, \mathbf{B}_y - \delta^2\, \mathbf{C}_y)$ or $\mathbf{C}$ is positive-definite, then equation (27) has no roots with positive real parts.

If a particular partitioning gives rise to an unsymmetric system in

Downloaded 01 May 2010 to 171.66.16.243. Redistribution subject to ASME license or copyright; see http://www.asme.org/terms/Terms_Use.cfm

equation (27), i.e., the node-by-node partition (12), the theorem of Bellman is not applicable. For this case one may invoke Siljak's algebraic criteria [15] to examine the positive realness of equation (27).

Alternatively, a perturbation theory such as the one expounded by Vidyasagar [16] can be employed to assess the asymptotic stability of equation (27) for $\delta \to (0, \infty)$. Stability for intermediate stepsize ranges can then be determined by a model problem as successfully exploited in [6].

If we restrict ourselves to undamped cases, i.e., $\mathbf{B} = \mathbf{0}$ in equation (27), a simple criterion can be derived for the positive realness of equation (27) which involves unsymmetric matrices. To this end we rewrite equation (27) as

$$\det\left(\begin{bmatrix} \mathbf{A}_x & \mathbf{0} \\ -\delta^2 \mathbf{C}_y^{yx} & \mathbf{A}_y - \delta^2 \mathbf{C}_y^{yy} \end{bmatrix} z^2 + \delta^2 \mathbf{C}\right) = 0 \tag{28}$$

in which

$$\begin{aligned} \mathbf{C}_y^{yy} &= \text{Sym}\,[\mathbf{C}_y] \\ \mathbf{C}_y^{yx} &= \mathbf{C}_y - \mathbf{C}_y^{yy} \end{aligned} \tag{29}$$

In equation (29), we have $\mathbf{C}_y^{yy} = \mathbf{C}_{yy}$ and $\mathbf{C}_y^{yx} = \mathbf{C}_{yx}$ for partition (12), and $\mathbf{C}_y^{yy} = \mathbf{0}$ for partitions that render I-I procedures. We now state a theorem for equation (28) (see Appendix B).

Theorem 2. If $\mathbf{A}_x$ and $(\mathbf{A}_y - \delta^2 \mathbf{C}_y^{yy})$ are non-negative definite and $\mathbf{C}$ is positive-definite, then equation (28) has no roots with positive real parts.

Remark: Theorem 2 is applicable to damped cases ($\mathbf{B} \neq \mathbf{0}$) if $\mathbf{B}$ is a Rayleigh-type [17]. This is because $\mathbf{B}$ can be made parts of $\mathbf{A}$ and $\mathbf{C}$ by a commutable matrix transformation [18]. The ensuing stepsize restriction for unsymmetrically partitioned I-E procedures can be obtained by replacing appropriate transformed matrices in Theorem 2.

Implicit-Explicit Procedures in Structural Dynamics

In the previous section we have presented a technique for determining the stability of the general partitioned procedure (9) through the concept of the solution amplification factor. We now examine the three partitions defined by equations (12)–(14) as applied to structural dynamics problems when the trapezoidal formula and one-term extrapolator (25) are used. It will be shown that the three resulting procedures have algorithmic characteristics identical to those which would result from the combined use of the central-difference formula for the explicit partitions and of the trapezoidal formula for the implicit partitions.

In the sequel we replace the matrices in equation (1) by the more familiar notation

$$(\mathbf{A}, \mathbf{B}, \mathbf{C}) = (\mathbf{M}, \mathbf{D}, \mathbf{K}) \tag{30}$$

Node-by-Node I-E Partition. The general characteristic z-polynomial equation (27) for the partition (12) becomes for $\mathbf{D} = 0$:

$$\det\left[(\mathbf{M} - \delta^2 \mathbf{K}_y)\, z^2 + \delta^2 \mathbf{K}\right] = 0 \tag{31}$$

Application of Theorem 2 to equation (31) in conjunction with equations (12) and (29) indicates that this procedure remains stable provided

$$h \leq 2/(\omega_{BM})_{\max} \tag{32}$$

where $(\omega_{BM})_{\max}$ is the largest eigenvalue of

$$\omega_{BM}^2\, \mathbf{M}\, \underline{u} = \begin{bmatrix} \mathbf{0} & \mathbf{0} \\ \mathbf{0} & \mathbf{K}_{yy} \end{bmatrix} \underline{u} \tag{33}$$

If the trapezoidal and the central difference formulas are used to integrate $(\underline{u}^x, \underline{u}^b)^T$ and $\underline{u}^y$, respectively, it can be shown that the resulting characteristic matrix is

$$\mathbf{J}_B(\lambda) = (\lambda - 1)^2\, \mathbf{M} + \delta^2\, (\lambda + 1)^2\, (\mathbf{K} - \mathbf{K}_y) + 4\delta^2\, \lambda\, \mathbf{K}_y \tag{34}$$

It is noted that equation (26), which is obtained by specializing the general characteristic equation (19) for the trapezoidal formula with one-term extrapolator, is identical to equation (34), with $\mathbf{B} = \mathbf{O}$.

Element-by-Element I-E Partition. For the partition (13), Bellman's theorem is directly applicable and provides the following stability condition:

$$h \leq 2/(\omega_{HL})_{\max} \tag{35}$$

in which $(\omega_{HL})_{\max}$ is the largest eigenvalue of

$$\omega_{HL}^2\, \mathbf{M}\, \underline{u} = \begin{bmatrix} 0 & 0 & 0 \\ 0 & \mathbf{K}_{bb}^{\gamma} & \mathbf{K}_{by} \\ 0 & K_{yb} & \mathbf{K}_{yy} \end{bmatrix} \underline{u} \tag{36}$$

The foregoing stability condition (35) is identical to that obtained by Hughes and Liu [3] by an energy stability criterion. It can also be shown that the combined use of the Newmark-family predictor-corrector pairs for the partition (13) gives the same algorithmic characteristics as equation (34). The presence of damping can be accounted for to give the same stability condition as that derived in [3].

DOF-by-DOF I-E Partition. As the partition (14) renders a symmetric system, we can invoke Bellman's theorem to determine its stability. It can be shown that the resulting stability condition of this partition is identical to that of the node-by-node partition (32). The algorithmic characteristic equation is obtained from equation (34) by taking $\mathbf{K}_y$ in the form

$$\begin{bmatrix} 0 & 0 & 0 \\ 0 & 0 & 0 \\ 0 & 0 & \mathbf{K}_{yy} \end{bmatrix} \tag{37}$$

Remark 1: Examination of the three I-E partitions demonstrates that regardless of the particular partition selected, the computer implementation of the present procedure, equations (3)–(9), can be accomplished within the framework of implicit integration formulas. Hence, any need for explicit or predictor formulas to integrate separately the explicit partitions is eliminated.

Remark 2: An important feature of the general partitioned procedure (9) is that it allows the combined use of the element-by-element and the DOF-by-DOF partitions simultaneously. This is possible because the two partitions preserve symmetry of the matrix in the left-hand side in equation (9) and a single extrapolated vector is applicable to the coupling term in the right-hand side of equation (9). For example, the element-by-element partition can be used for partitioning different elements (shells, beams, low and high-order isoparametric elements for solid continua) or different media (fluid, structure, soil subdomains). At the same time, the DOF-by-DOF partition can be applied within each element or subdomain to integrate the DOF's exhibiting low (high) frequencies explicitly (implicitly).

Implicit-Implicit Procedures

The need for implicit-implicit (I-I) partitioned procedures arises when the coupled-field equations are to be integrated implicitly by sequentially employing single-field integration packages. We will now consider two possible I-I partitioned procedures that may be useful for structure-soil interaction and structure-fluid interaction problems.

Staggered I-I Partition. Let us consider the partitioned matrix

$$\mathbf{K}_y = \begin{bmatrix} \mathbf{0} & \mathbf{0} & \mathbf{0} \\ \mathbf{0} & \mathbf{0} & \mathbf{0} \\ \mathbf{0} & \mathbf{K}_{yb} & \mathbf{0} \end{bmatrix} \tag{38}$$

For this I-I partition the solution-advancing cycle proceeds as follows. First, the vector $\underline{u}^y$ [see equation (11)] is implicitly obtained by extrapolating $\underline{u}^b$. Then use $\underline{u}^y$ to obtain implicitly the vector $(\underline{u}^x, \underline{u}^b)^T$.

Notice that the characteristic z-polynomial equation (28) is ap-

Downloaded 01 May 2010 to 171.66.16.243. Redistribution subject to ASME license or copyright; see http://www.asme.org/terms/Terms_Use.cfm

plicable to this I-I partition. Applying Theorem 2 to this partition in conjunction with equation (38) indicates that the preceding I-I procedure is unconditionally stable.

This is in striking contrast to the result of Belytschko, Yen, and Mullen [8] from their study of a model two-DOF system, in which they proved that the preceding partitioned procedure becomes "unconditionally unstable." We offer the following explanation for this discrepancy.

The difference equations employed in [8] are

$$\begin{aligned} \underline{u}_n^P &= \underline{u}_{n-1} \\ (\mathbf{M} + \delta^2 \mathbf{K}_x)\, \underline{u}_n &= 2\,(\mathbf{M} - \delta^2 \mathbf{K})\, \underline{u}_{n-1} - (\mathbf{M} + \delta^2 \mathbf{K})\, \underline{u}_{n-2} \\ &\quad - \delta^2 \mathbf{K}_y\, \underline{u}_n^{(P)} \end{aligned} \tag{39}$$

The foregoing difference equation (39) can be written equivalently by a pair of difference equations and the integrator for velocity as

$$\begin{aligned} (\mathbf{M} + \delta^2 \mathbf{K}_x)\, \underline{u}_n &= (\mathbf{M} - \delta^2 \mathbf{K})\, \underline{u}_{n-1} + 2\,\delta\, \mathbf{M}\, \underline{\dot{u}}_{n-1} \\ \mathbf{M}\, \underline{\dot{u}}_n &= \mathbf{M}\, \underline{\dot{u}}_{n-1} - \delta\, \mathbf{K}\, (\underline{u}_{n-1} + \underline{u}_n) \end{aligned} \tag{40}$$

On the other hand, our procedure (9), when specialized to the case of the trapezoidal formula and one-term extrapolation (35), becomes

$$\begin{aligned} \underline{u}_n^{(P)} &= \underline{u}_{n-1} \\ (\mathbf{M} + \delta^2 \mathbf{K}_x)\, \underline{u}_n &= (\mathbf{M} - \delta^2 \mathbf{K})\, \underline{u}_{n-1} + 2\,\delta\, \mathbf{M}\, \underline{\dot{u}}_{n-1} - \delta^2 \mathbf{K}_y\, \underline{u}_n^{(P)} \\ \mathbf{M}\, \underline{\dot{u}}_n &= \mathbf{M}\, \underline{\dot{u}}_{n-1} - \delta\, \mathbf{K}\, (\underline{u}_{n-1} + \underline{u}_n) \end{aligned} \tag{41}$$

Comparing equations (40) with (41) one sees that the latter is equivalent to the former if $\underline{u}^{(P)} = 0$ in equation (41). The characteristic z-polynomial equation for equation (40) can be derived as

$$\det \left[\left(\mathbf{M} - \frac{1}{2} \delta^2 \mathbf{K}_y \right) z^2 - \frac{\delta^2}{2} \mathbf{K}_y\, z + \delta^2 \mathbf{K} \right] = 0 \tag{42}$$

from which one can establish that the procedure is "unconditionally unstable" for the model problem considered in [8].

Remark: If the extrapolator in equation (39) is changed to

$$\underline{u}_n^{(p)} = 2\underline{u}_{n-1} - \underline{u}_{n-2} \tag{43}$$

it can be shown that the resulting characteristic equation is identical to that of the present procedure (41). This is a direct consequence of the well-known property that the order of accuracy of difference equations for second-order systems maintains that of the integration formula when discretized by one-derivative formulas and it decreases by one from that of the integration formula when discretized by two-derivative formulas. Therefore, from the viewpoint of our procedure (41) the procedure of [8] corresponds to neglecting the coupling term when computing $\underline{u}^y$.

Although the present staggered I-I procedure (41) which is a special case of the general procedure (9) is unconditionally stable, it does not meet the modularity requirement. The reason for this is that the entries in the matrix $\mathbf{K}_y$ in equation (38) cannot be decomposed into the two subdomains as shown in Fig. 1. The remedy to this shortcoming is an element-by-element I-I partitioned procedure.

Element-by-Element I-I Partition. If the partitioned matrix $\mathbf{E}_y$ in equation (9) contains nonzero diagonal entries, the solution vector pertaining to $\mathbf{E}_y$ is necessarily obtained by an explicit process as shown in the section on Implicit-Explicit Procedures. One can overcome this deficiency by implicitly solving two sets of difference equations for both partitioned subdomains (see Fig. 1). This is accomplished by the following I-I procedure:

$$\begin{aligned} (\mathbf{M} + \delta^2 \mathbf{K}_x)\, \underline{u}_{nt} &= \underline{g}_n - \delta^2 \mathbf{K}_y\, \underline{u}_{n-1} \\ (\mathbf{M} + \delta^2 \mathbf{K}_y)\, \underline{u}_n &= \underline{g}_n - \delta^2 \mathbf{K}_x\, \underline{u}_{nt} \end{aligned} \tag{44}$$

where $\mathbf{K}_y$ takes the partition (13).

For the particular case: $\mathbf{A} = \mathbf{M}$, $\mathbf{E}_x = \mathbf{M} + \delta^2 \mathbf{K}_x$, and $\mathbf{E}_y = \delta^2 \mathbf{K}_y$, the stability of the element-by-element I-I procedure (44) can be analyzed and the resulting z-polynomial stability equation can be shown as

$$\begin{aligned} \det [(4\mathbf{M} + 2\,\delta^4 [\mathbf{K}_x\, \mathbf{M}^{-1}\, \mathbf{K}_y + \mathbf{K}_y\, \mathbf{M}^{-1}\, \mathbf{K}_x])\, z^2 \\ + 2\,\delta^4\, (\mathbf{K}_x\, \mathbf{M}^{-1}\, \mathbf{K}_y - \mathbf{K}_y\, \mathbf{M}^{-1}\, \mathbf{K}_x)\, z + 4\,\delta^2 \mathbf{K}] = 0 \end{aligned} \tag{45}$$

The first and the third coefficient matrices are positive-definite. The second matrix $(\mathbf{K}_x\, \mathbf{M}^{-1}\, \mathbf{K}_y - \mathbf{K}_y\, \mathbf{M}^{-1}\, \mathbf{K}_x)$ is antisymmetric and therefore has purely imaginary eigenvalues only. Hence, the element-by-element I-I procedure (44) is stable by Theorem 1.

It is noted that the preceding I-I partitioned procedure (44) preserves the program modularity of each single-field implicit integration package. As the preceding I-I procedure is new we will describe its computational aspects in some detail.

First, equation (44a) is implicitly solved for the vector $(\underline{u}_{nt}^x, \underline{u}_{nt}^b)^T$ by utilizing the extrapolated vector $(\underline{u}_{n-1}^b, \underline{u}_{n-1}^y)^T$. Then solve equation (44b) for the vector $(\underline{u}_n^b, \underline{u}_n^y)^T$ by utilizing the temporary solution vector $(\underline{u}_{nt}^x, \underline{u}_{nt}^b)^T$. The final solution vector to be used for the next step integration is thus $(\underline{u}_{nt}^x, \underline{u}_n^b, \underline{u}_n^y)^T$. In the next step equation (44b) is solved first. The integration process is continued by solving equations (44a) and (44b) alternatively.

From the foregoing examination of the computational sequence of the element-by-element I-I procedure (44), it is evident that two implicit solutions are required for the boundary vector $\underline{u}^b$ per step. Therefore, the price paid for realizing the computational modularity by the element-by-element I-I procedure is one additional implicit solution of the boundary vector $\underline{u}^b$ as compared to that of the staggered I-I procedure (41).

Discussion and Conclusions

In this paper the complete set of coupled-field equations of motion is discretized by implicit integration formulas. A general partition is then introduced to the resulting implicit difference equations. Finally, the coupling terms that end up in the right-hand side as unknowns are extrapolated to advance the solution cycle. The ensuing stability analysis for the general partitioned procedure (9) is carried out via the concept of solution amplification of the difference equations. We now summarize the main results of the present study.

It is demonstrated that a unified stability analysis is applicable to all existing and some new partitioned procedures even if the matrix equations that describe the stability characteristics of the partitioned procedures are not simultaneously diagonalizable. This applicability is in fact due to the equivalence between the well-known energy technique [19] and the positive-definiteness of quadratic polynomials in the matrix theory that underlies the theorems of Routh-Hurwitz and Lyapunov.

Our partitioned procedure (9) can be specialized to a general implicit-explicit procedure that embodies those of Belythshko and Mullen [1–2] and Hughes and Liu [3–4]. In particular, it led to the discovery of a new DOF-by-DOF implicit-explicit procedure that preserves the symmetry of the partitioned matrices and allows degree-by-degree implicit or explicit selections of the solution vector. Furthermore, our implicit-explicit procedure can accommodate, within the framework of implicit integration implementation, the concurrent use of the element-by-element and the DOF-by-DOF I-E procedures.

Our procedure (9) becomes the staggered I-I procedure (41) when the partitioned matrix does not contain nonzero diagonal entries. The staggered I-I procedure is unconditionally stable if the extrapolator is judiciously selected. On the other hand, the cause of unconditional instability of the I-I procedure of Belytschko, Yen, and Mullen [8] can be traced to an improper choice of the extrapolation vector.

A new element-by-element I-I procedure (44) is presented, which preserves the program modularity of each single-field integration package when used to solve coupled-field problems. The procedure is stable and its only computational overhead as compared to that of the staggered I-I procedure is the requirement of an additional implicit solution of the boundary state vector.

So far we have proposed and analyzed that integrate field solution vectors with the same time step size. The stability analysis of procedures which integrate field solution vectors with different time step sizes is much more involved and the resulting computational gain

Downloaded 01 May 2010 to 171.66.16.243. Redistribution subject to ASME license or copyright; see http://www.asme.org/terms/Terms_Use.cfm

margins are in general harder to assess. Study of such fractional-step partitioned procedures is now being actively pursued and will be reported in a separate communication.

Acknowledgments

The author wishes to thank Dr. C. A. Felippa for his many stimulating discussions during the course of the present study and, in particular, for his literature search which brought the theorem of Vidyasagar to the author's attention and his consultation in formulating Theorem 2 in the paper. This study was supported by the U.S. Defense Nuclear Agency under Contract DNA 001-78-C-0026 and the Office of Naval Research under Contract N00014-74-C-0355.

References

1 Belytschko, T., and Mullen, R., "Mesh Partitions of Explicit-Implicit Time Integration," *Formulations and Computational Algorithms in Finite Element Analysis,* eds., Bathe, J., et al., M.I.T. Press, 1977.

2 Belytschko, T., and Mullen, R., "Stability of Explicit-Implicit Mesh Partitions in Time Integration," *International Journal Num. Meth. in Engineering,* Vol. 12, 1978, pp. 1575–1586.

3 Hughes, T. J. R., and Liu, W. K., "Implicit-Explicit Finite Elements in Transient Analysis: Stability Theory," ASME JOURNAL OF APPLIED MECHANICS, Vol. 45, 1978, pp. 371–374.

4 Hughes, T. J. R., and Liu, W. K., "Implicit-Explicit Finite Elements in Transient Analysis: Implementation and Numerical Examples," ASME JOURNAL OF APPLIED MECHANICS, Vol. 45, 1978, pp. 375–378.

5 Morimoto, H., "Stability in the Wave Equation Coupled With Heat Flow," *Numerische Mathematik,* Vol. 4, 1962, pp. 136–145.

6 Park, K. C., Felippa, C. A., and DeRuntz, J. A., "Stabilization of Staggered Solution Procedures for Fluid-Structure Interaction Analysis," *Computational Methods for Fluid-Structure Interaction Problems,* ed., Belytschko, T., and Geers, T. L., ASME Applied Mechanics Symposia Series, AMD-Vol. 26, 1977, pp. 94–124.

7 Geers, T. L., "Doubly Asymptotic Approximations for Transient Motions of Submerged Structures," *Journal of the Acoustical Society of America,* Vol. 64, 1978, pp. 1500–1508.

8 Belytschko, T., Yen, H. J., and Mullen, R., "Mixed Methods for Time Integration," *Proceedings of the International Conference on Finite Elements in Nonlinear Mechanics (FENOMECH 78),* University of Stuttgart, Stuttgart, Germany, Sept. 1978.

9 Felippa, C. A., and Park, K. C., "Computational Aspects of Time Integration Procedures in Structural Dynamics," ASME JOURNAL OF APPLIED MECHANICS, Vol. 45, 1978, pp. 595–602.

10. Peaceman, D. W., and Rachford, H. H., "The Numerical Solution of Parabolic and Elliptic Differential Equations," *J. Soc. Ind. Appl. Math.,* Vol. 3, 1955, pp. 28–41.

11 Douglas, J., Jr., "On the Numerical Integration of $u_{xx} + u_{yy} = u_t$ by Implicit Methods," *J. Soc. Ind. Appl. Math.,* Vol. 3, 1955, pp. 42–65.

12 Yanenko, N. N., *The Method of Fractional Steps,* Springer-Verlag, New York, 1971.

13 Gantmacher, F. R., *The Theory of Matrices,* Vol. 2, Chelsea Publishing Co., New York, 1960.

14 Bellman, R., *Introduction to Matrix Analysis,* 2nd Edition, McGraw-Hill, New York, 1970, pp. 249–262.

15 Siljak, D. D., "New Algebraic Criteria for Positive Realness," *Journal of The Franklin Institute,* Vol. 29, No. 2, 1971, pp. 109–120.

16 Vidyasagar, M., *Nonlinear Systems Analysis,* Prentice-Hall, Englewood Cliffs, N. J., 1978, pp. 124–130.

17 Caughey, T. K., "Classical Normal Modes in Damped Linear Systems," ASME JOURNAL OF APPLIED MECHANICS, Vol. 27, 1960, pp. 269–271.

18 Servin, S. M., "On the Construction and Analysis of Approximations of Arbitrarily High-Order for Proportionally Damped Second-Order Systems," Department of Mathematics, University of Tennessee, Knoxville, Tenn., 1979.

19 Richtmeyer, R. D., and Morton, K. W., *Difference Methods for Initial Value Problems,* 2nd edition, Interscience Publishers, New York, 1967.

APPENDIX *A*

Derivation of Characteristic Polynomial Equation

The linear multistep formula (2) can be expressed in the form

$$\sum_{j=0}^{m} (\alpha_j \underline{u}_{n-j} - \delta \beta_j \underline{\dot{u}}_{n-j}) = 0 \tag{46}$$

and a stable form of extrapolators is found to be [6]

$$\underline{u}_n^{(P)} = \sum_{j=1}^{m} \hat{\alpha}_j \underline{u}_{n-j} \tag{47}$$

The historical vector $\underline{h}_n^u$ in equation (2) is

$$\underline{h}_n^u = \sum_{j=1}^{m} (\delta \beta_j \underline{\dot{u}}_{n-j} - \alpha_j \underline{u}_{n-j}) \tag{48}$$

provided $\alpha_0 = 1$, which we assume.

Equations (46)–(48) can be expressed in terms of the characteristic value λ of the difference equation (10) and $\underline{u}_{n-m}$, viz.:

$$\rho(\lambda)\, \underline{u}_{n-m} - \delta\, \sigma(\lambda)\, \underline{\dot{u}}_{n-m} = 0$$

$$\underline{u}_n^{(P)} = e(\lambda)\, \underline{u}_{n-m}$$

$$\underline{h}_n^u = \delta[\sigma(\lambda) - \lambda^m]\, \underline{\dot{u}}_{n-m} + [\lambda^m - \rho(\lambda)]\, \underline{u}_{n-m}$$

where

$$\rho(\lambda) = \sum_{j=0}^{m} \alpha_j\, \lambda^{m-j}$$

$$\sigma(\lambda) = \sum_{j=0}^{m} \beta_j\, \lambda^{m-j} \tag{49}$$

$$e(\lambda) = \sum_{j=1}^{m} \hat{\alpha}_j\, \lambda^{m-j}$$

The partitioned equation (9) can now be expressed as

$$\lambda^m\, \mathbf{E}_x\, \underline{u}_{n-m} - (\mathbf{A} + \delta \mathbf{B})\, [(\lambda^m - \rho)\, \underline{u}_{n-m} - \delta(\lambda^m - \sigma)\, \underline{\dot{u}}_{n-m}] - \delta\, \mathbf{A}\, (\lambda^m - \rho)\, \underline{\dot{u}}_{n-m} - \delta^2\, (\lambda^m - \sigma)\, (\mathbf{B}\, \underline{\dot{u}}_{n-m} + \mathbf{C}\, \underline{u}_{n-m}) + e\, \mathbf{E}_y\, \underline{u}_{n-m} = 0 \tag{50}$$

where ρ, σ, and e stand for $\rho(\lambda)$, $\sigma(\lambda)$, and $e(\lambda)$, respectively.

The auxiliary equation needed to eliminate $\underline{\dot{u}}_{n-m}$ from (50) is

$$\mathbf{A}\, \rho\, \underline{\dot{u}}_{n-m} = \delta\, \mathbf{A}\, \sigma\, \underline{\ddot{u}}_{n-m} \tag{51}$$

Substituting the equation of motion (1) into (51), one obtains for $\underline{f} = \underline{0}$

$$\mathbf{A}\, \rho\, \underline{\dot{u}}_{n-m} = -\delta\, \sigma(\mathbf{B}\, \underline{\dot{u}}_{n-m} + \mathbf{C}\, \underline{u}_{n-m}) \tag{52}$$

Combining (50) and (52) yields

$$[\rho^2\, \mathbf{A} + \delta^2\, \sigma^2\, \mathbf{C}_x + \delta^2\, (\sigma^2 - \lambda^m\, \rho + \rho\, e)\, \mathbf{C}_y + \delta\, \rho^2\, \mathbf{B}_x + \delta(\rho^2 - \lambda^m \rho + e\rho)\, \mathbf{B}_y]\, \underline{u}_{n-m} + \delta^2\, (\sigma - \rho)\, \sigma\, \mathbf{B}\, \underline{\dot{u}}_{n-m} = 0 \tag{53}$$

The velocity term (53) can only be eliminated by differentiation formula resulting from (49*a*)

$$\underline{\dot{u}}_{n-m} = (\rho/\delta\sigma)\, \underline{u}_{n-m} \tag{54}$$

which is substituted into (53) to yield

$$[\rho^2\, \mathbf{A} + \delta\sigma\rho\, \mathbf{B}_x + \delta^2\, \sigma^2\, \mathbf{C}_x + \delta(\rho\sigma - \lambda^m \rho + \rho e)\, \mathbf{B}_y + \delta^2(\sigma^2 - \lambda^m \rho + \rho e)\, \mathbf{C}_y]\, \underline{u}_{n-m} = 0 \tag{55}$$

It should be noted that if the differentiation formula (54) is used in place of (51), the following equation results:

$$[\rho^2\, \mathbf{A} + \delta\, \rho\sigma\, \mathbf{B}_x + \delta(\rho\sigma - \lambda^m \sigma + \sigma e)\, \mathbf{B}_y + \delta^2\, \sigma^2\, \mathbf{C}_x + \delta^2(\sigma^2 - \lambda^m \sigma + \sigma e)\, \mathbf{C}_y]\, \underline{u}_{n-m} = 0 \tag{56}$$

This has roots whose magnitudes are greater than unity in general for consistent integration formulas; thus the integration process is unstable. The reader can verify this assertion for the trapezoidal rule and one-term extrapolator.

APPENDIX *B*

Proof of Theorem 2

Let us consider the undamped system from equation (1)

$$\mathbf{A}\, \underline{\ddot{u}} + \mathbf{C}\, \underline{u} = \underline{0} \tag{57}$$

Equation (57) can be transformed to an equivalent form

$$\underline{\ddot{q}} + \hat{\mathbf{C}}\, \underline{q} = \underline{0}$$

where

Downloaded 01 May 2010 to 171.66.16.243. Redistribution subject to ASME license or copyright; see http://www.asme.org/terms/Terms_Use.cfm

$$\underline{q} = \mathbf{L}^{-T}\,\underline{u} \tag{58}$$

$$\mathbf{A} = \mathbf{L}\,\mathbf{L}^T \quad \text{and} \quad \hat{\mathbf{C}} = \mathbf{L}^{-1}\,\mathbf{C}\,\mathbf{L}^{-T}$$

The characteristic system for (58) which corresponds to equation (28) can be derived as

$$z^2\,\mathbf{G}\,\underline{q} + \delta^2\,\hat{\mathbf{C}}\,\underline{q} = \underline{0}$$

where

$$\mathbf{G} = \begin{bmatrix} \mathbf{I} & \mathbf{0} \\ -\delta^2\,\hat{\mathbf{C}}_y^{yx} & \mathbf{I} - \delta^2\,\hat{\mathbf{C}}_y^{yy} \end{bmatrix} \tag{59}$$

Equation (59) can be further reduced by the orthogonal transformation

$$\underline{q} = \begin{bmatrix} \mathbf{I} & 0 \\ 0 & \mathbf{T} \end{bmatrix} \underline{v} \tag{60}$$

so that

$$\mathbf{T}^T\,\hat{\mathbf{C}}_{yy}\,\mathbf{T} = \Lambda = \text{diag}\,(\Omega_1^2, \ldots, \Omega_k^2) \tag{61}$$

where k is the size of $\mathbf{C}_{yy}$.

Using equations (60) and (61), one transforms equation (59) to

$$z^2\,\hat{\mathbf{G}}\,\underline{v} + \delta^2\,\hat{\hat{\mathbf{C}}}\,\underline{v} = 0$$

where

$$\hat{\mathbf{G}} = \begin{bmatrix} \mathbf{I} & \mathbf{0} \\ -\delta^2\,\mathbf{T}^T\,\mathbf{C}_y^{yx} & \mathbf{I} - \delta^2\,\mathbf{T}^7\,\mathbf{C}_y^{yy}\,\mathbf{T} \end{bmatrix} \tag{62}$$

$$\hat{\hat{\mathbf{C}}} = \begin{bmatrix} \hat{\mathbf{C}}_{xx} & \mathbf{B} \\ \mathbf{B}^T & \Lambda \end{bmatrix}$$

in which $\mathbf{B} = \hat{\mathbf{C}}_{xy}\,\mathbf{T}$.

Case: $\hat{\mathbf{C}}_y^{yy} = \hat{\mathbf{C}}_{yy}$ and $\hat{\mathbf{C}}_y^{yx} = \hat{\mathbf{C}}_{yx}$. For this case we have

$$\begin{aligned} \mathbf{T}^T\,\hat{\mathbf{C}}_y^{yx} &= \mathbf{B}^T \\ \mathbf{T}^T\,\hat{\mathbf{C}}_y^{yy}\,\mathbf{T} &= \Lambda \end{aligned} \tag{63}$$

Now, equation (62a) can be expressed in the form

$$z^2 \begin{bmatrix} \mathbf{I} & \mathbf{0} \\ \mathbf{0} & \mathbf{I} - \delta^2\Lambda \end{bmatrix} \hat{v} + \delta^2\,\mathbf{H}^{-1}\,\hat{\hat{\mathbf{C}}}\mathbf{H}\hat{v} = 0 \tag{64}$$

where $\mathbf{H}$ is a similarity transformation matrix

$$\mathbf{H} = \begin{bmatrix} \mathbf{I} & \mathbf{0} \\ -\Lambda^{-1}\,\mathbf{B}^T & \mathbf{I} \end{bmatrix} \tag{65}$$

Note that if $(\mathbf{I} - \delta^2\Lambda)$ and $\hat{\hat{\mathbf{C}}}$ are positive-definite, all z_i^2, $i = 1, \ldots, N$ are negative real as the similarity transformation preserves the eigenvalues of original system (62a)

Case: $\hat{\mathbf{C}}_y^{yy} = \mathbf{0}$, $\hat{\mathbf{C}}_y^{yx} = \mathbf{C}_{yx}$. In this case, we have

$$z^2\,\hat{\mathbf{G}}^I\,v + \delta^2\,\hat{\hat{\mathbf{C}}}\,\underline{v} = 0$$

where

$$\hat{\mathbf{G}}^I = \begin{bmatrix} \mathbf{I} & \mathbf{0} \\ -\delta^2\mathbf{B}^T & \mathbf{I} \end{bmatrix} \tag{66}$$

As $\hat{\mathbf{G}}^I$ is not diagonalizable, we perturb it to the form

$$\hat{\mathbf{G}}^{IP} = \begin{bmatrix} \mathbf{I} & \mathbf{0} \\ -\delta^2\,\mathbf{B}^T & \mathbf{I} + \delta^2\,\epsilon\,\mathbf{I} \end{bmatrix} \tag{67}$$

where $0 < \delta^2\,\epsilon \ll 1$. Substituting the perturbed matrix (67) into (66a) and following similar steps as used in deriving equation (62a), one can obtain

$$z^2 \begin{bmatrix} I & \mathbf{0} \\ \mathbf{0} & \mathbf{I} + \delta^2\,\epsilon\mathbf{I} \end{bmatrix} \underline{v} + \mathbf{H}^{-P}\,\hat{\hat{\mathbf{C}}}\,\mathbf{H}^P\,\underline{\hat{v}} = 0 \tag{68}$$

where

$$\mathbf{H}^P = \begin{bmatrix} \mathbf{I} & \mathbf{0} \\ \dfrac{1}{\epsilon}\,\mathbf{B}^T & \mathbf{I} \end{bmatrix} \tag{69}$$

We note that the eigenvalues of a matrix depend continuously on the elements of the matrix (see, e.g., Vidyasagar [16]). Therefore, as $\epsilon \to 0$, equation (68) contains the eigenvalues of the system (66). Furthermore, $\mathbf{H}^P$ is a similarity transformation matrix; hence, if $\hat{\hat{\mathbf{C}}}$ is positive-definite, all eigenvalues z_i^2, $i = 1, \ldots, N$ in equation (66) are negative real. This completes the proof of Theorem 2.

Downloaded 01 May 2010 to 171.66.16.243. Redistribution subject to ASME license or copyright; see http://www.asme.org/terms/Terms_Use.cfm

K. Miya
Associate Professor.

T. Takagi
Graduate Student.

Nuclear Engineering Research Laboratory,
Faculty of Engineering,
The University of Tokyo,
Tokaimura, Ibaraki-Prefecture,
Japan

Y. Ando
Professor,
Department of Nuclear Engineering,
Faculty of Engineering,
Hongo, Tokyo, Japan

Finite-Element Analysis of Magnetoelastic Buckling of Ferromagnetic Beam Plate

Some corrections have been made hitherto to explain the great discrepancy between experimental and theoretical values of the magnetoelastic buckling field of a ferromagnetic beam plate. To solve this problem, the finite-element method was applied. A magnetic field and buckling equations of the ferromagnetic beam plate finite in size were solved numerically assuming that the magnetic torque is proportional to the rotation of the plate and by using a disturbed magnetic torque deduced by Moon. Numerical and experimental results agree well with each other within 25 percent.

Introduction

The magnetoelastic buckling of a ferromagnetic thin plate was first solved analytically by Moon and Pao [1]. Their paper gave us a better understanding of the phenomenon, but left the interesting issue of how to explain the big discrepancy between theoretical and experimental results. The magnetoelastic buckling phenomenon can be considered essentially the same as that of superconducting toroidal magnets arrayed in a torus of a magnetic fusion reactor. A proof of the buckling of the toroidal coil was shown by Moon, et al. [2], the finite-element analysis of the buckling of the toroidal coil constrained with lateral supports was conducted by Miya and Takagi [3], where the concept of an equivalent plate magnet, as a first approximation, was applied for the calculation of the magnetic energy. Thus it is meaningful for a development of methodology which can solve the buckling of the toroidal coils to give a final explanation to the discrepancy between experiment and theory, which has not yet been resolved. Several investigators conducted experiments and discussed the problem based on a nonuniformity of the magnetic field due to pole dimension and gap distance, misorientation of the ferromagnetic specimen due to an initial defect, magnetization of the specimen and concentration of the magnetic induction near an edge of the finite specimen.

Wallerstein and Peach [4] analyzed a perturbed field around a wide cantilever beam based on the amperian current model and coupled it with the differential equation of the plate bending. As a result of the analysis, they concluded that the big discrepancy occurred in Moon's experiment could be corrected within 12–20 percent if an applied critical field B_{0c} is substituted with the field at a surface of the ferromagnetic specimen. Numerical results given in Fig. 2 in their paper show that the magnetic induction at the surface is 1.8 times greater than the applied field; namely, according to their discussion the applied experimental buckling field should be multiplied by the coefficient. However, the authors do not agree with this formal correction. The reason is that their result shown in the figure does not agree with the result of the numerical analysis by the finite-element method given by Miya, Hara, and Someya [5]. If the specimen set normal to the applied field is so long and wide that the magnetic field concentration near the edge has no significant effect on the buckling field, the field at the surface should exactly equate to the applied field. This will be later discussed in detail.

Dalrymple, Peach, and Viegelahn [6] showed that the discrepancy between theory and experiment can be attributed to the magnetic field concentration near an edge of the finite specimen. This fact was also confirmed in Miya's experiment [5] where the width of the beam plate was changed systematically. If the width becomes large enough in comparison with the thickness of the specimen, the experimental buckling fields are expected to approach the theoretical ones. The foregoing discussion could allow us to conclude that a primary reason for the big discrepancy is the magnetic field concentration, so long as an experiment is conducted with a great care to minimize initial defects and demagnetize fully the specimen before applying the field to it. And this conclusion suggests to us to try to calculate numerically the critical buckling field of the finite ferromagnetic specimen not referring to the following theoretical formula deduced by Moon and Pao [1],

$$\frac{B_c}{\sqrt{\mu_0 E}} = \frac{\pi^{3/2}}{\sqrt{192(1-\nu^2)}} \left(\frac{t}{L}\right)^{3/2} \tag{1}$$

Contributed by the Applied Mechanics Division for publication in the JOURNAL OF APPLIED MECHANICS.

Discussion on this paper should be addressed to the Editorial Department, ASME, United Engineering Center, 345 East 47th Street, New York, N. Y. 10017, and will be accepted until September 1, 1980. Readers who need more time to prepare a discussion should request an extension from the Editorial Department. Manuscript received by ASME Applied Mechanics Division, May, 1979; final revision, November, 1979.

Copyright © 1980 by ASME
Downloaded 01 May 2010 to 171.66.16.243. Redistribution subject to ASME license or copyright; see http://www.asme.org/terms/Terms_Use.cfm

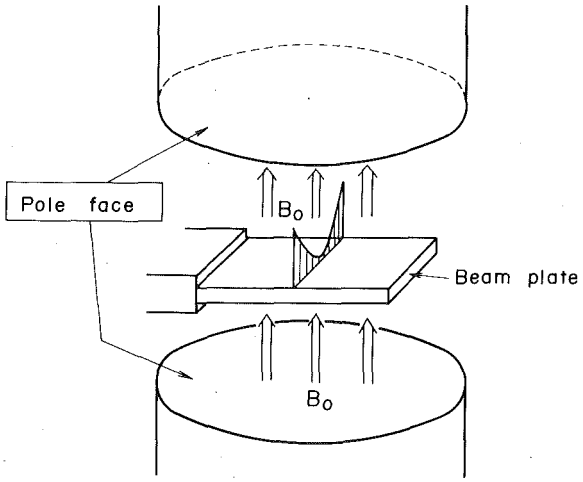

Fig. 1 Cantilevered plate inserted in an applied magnetic field and field concentration near edge

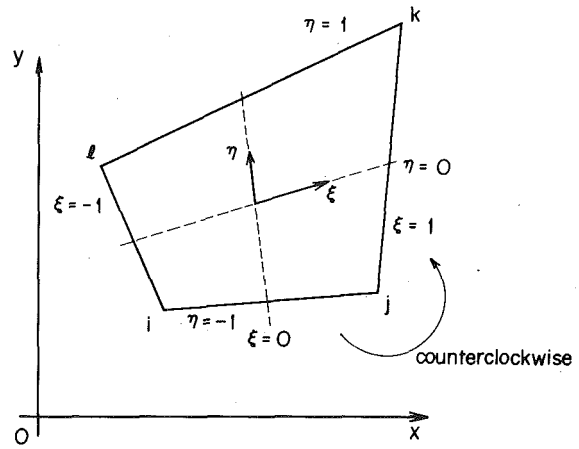

Fig. 2 Two-dimensional quadrilateral simplex element and natural coordinates system

In this paper is shown the finite-element scheme which solves the magnetic field problem around the finite ferromagnetic beam plate and couples it with the buckling equation of the elastic plate to get the buckling field. In the analysis restrictions arising from the finiteness of the specimen should be removed and its results could be expected to explain well the discrepancy between theory and experiment.

Finite-Element Analysis of Magnetic Field

Basic Equations and Formulation for Magnetic Field. In the previous paper [5] is shown the finite-element formulation of the axisymmetric field problem where cylindrical coordinates are used. In the paper was considered the fact that a governing equation of the magnetic field expressed in terms of the cylindrical coordinates could be reduced to that in terms of the Cartesian coordinates if the radius is sufficiently large compared to the dimension of the ferromagnetic beam plate. But the authors here analyze the Laplace equation governing the magnetic field in Cartesian coordinates.

As shown in the previous paper [5], Maxwell's equations determining the static magnetic field can be deduced to [7, 8],

$$\frac{1}{\mu}\,\mathrm{rot}\,(\mathrm{rot}\,\mathbf{A}) = 0 \tag{2}$$

if the vector potential **A** is used. A magnetic induction **B** is given by

$$\mathbf{B} = \mathrm{rot}\,\mathbf{A} \tag{3}$$

once the vector potential is solved numerically.

A functional of equation (2) could be found by applying the variational method. A variation of it, "δI," is obtained by multyplying equation (2) by $\delta\mathbf{A}$ and integrating that over the whole domain "V."

$$\delta I = \iiint_V \frac{1}{\mu}\,\mathrm{rot}\,(\mathrm{rot}\,\mathbf{A})\,\delta\mathbf{A}\,dv \tag{4}$$

Integrating by parts we get,

$$\delta I = \frac{1}{2\mu}\,\delta\left[\iiint_V (\mathrm{rot}\,\mathbf{A})(\mathrm{rot}\,\mathbf{A})dv\right] + \frac{1}{\mu}\iint_R (\mathrm{rot}\,\mathbf{A}\times\delta\mathbf{A})\,\mathbf{n}\,ds \tag{5}$$

where "R" is a surface of the domain "V", and "**n**" is an outward normal unit vector to the surface. Now we can choose the variation of the vector potential $\delta\mathbf{A}$ as zero on the surface and thus from equation (5) we get

$$I = \frac{1}{2\mu}\iiint_V \left[\left(\frac{\partial A_z}{\partial y} - \frac{\partial A_y}{\partial z}\right)^2 + \left(\frac{\partial A_x}{\partial z} - \frac{\partial A_z}{\partial x}\right)^2 + \left(\frac{\partial A_y}{\partial x} - \frac{\partial A_x}{\partial y}\right)^2\right] dv \tag{6}$$

where y-axis is normal to the beam-plate and x-axis is along a length of the plate. Equation (6) is simplified as follows for the present problem illustrated in Fig. 1:

$$I = \frac{1}{2\mu}\iint_s \left\{\left(\frac{\partial A}{\partial x}\right)^2 + \left(\frac{\partial A}{\partial y}\right)^2\right\} dxdy \tag{7}$$

because x and y-components of the vector potential are constant and there is no current source in the domain. "s" is a two-dimension integral area. The z-component of the vector potential in an element is expressed in terms of nodal values $\{A_i\}$ as follows:

$$A = [N]\{A_i\}. \tag{8}$$

The shape function $[N]$ for a two-dimensional quadrilateral simplex element is given by

$$N_i = \frac{1}{4}(1+\xi)(1+\eta)$$

$$N_j = \frac{1}{4}(1-\xi)(1+\eta)$$

$$N_k = \frac{1}{4}(1-\xi)(1-\eta)$$

$$N_l = \frac{1}{4}(1+\xi)(1-\eta) \tag{9}$$

where notations in the aforementioned equations are shown in Fig. 2 together with the element shape. Substitution of equation (8) in equation (7) yields,

$$I = \frac{1}{2\mu}\iint_s \left[\{A_i\}^T\frac{\partial[N]^T}{\partial x}\frac{\partial[N]}{\partial x}\{A_i\} + \{A_i\}^T\frac{\partial[N]^T}{\partial y}\frac{\partial[N]}{\partial y}\{A_i\}\right] dxdy. \tag{10}$$

To minimize I, equation (10) should be differentiated with respect to $\{A_i\}$.

$$\frac{\partial I}{\partial\{A_i\}} = \frac{1}{\mu}\iint_s \left[\frac{\partial[N]^T}{\partial x}\frac{\partial[N]}{\partial x} + \frac{\partial[N]^T}{\partial y}\frac{\partial[N]}{\partial y}\right] dxdy\,\{A_i\} = \{0\} \tag{11}$$

Equation (11) reduces to the next simple matrix equation.

$$[P]\,\{A\} = \{0\} \tag{12}$$

A solution of this equation satisfying boundary conditions gives nodal

Downloaded 01 May 2010 to 171.66.16.243. Redistribution subject to ASME license or copyright; see http://www.asme.org/terms/Terms_Use.cfm

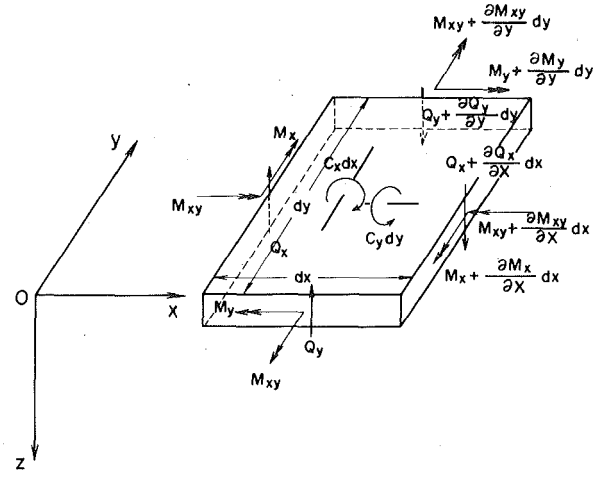

Fig. 3 Stress resultants and magnetic torque

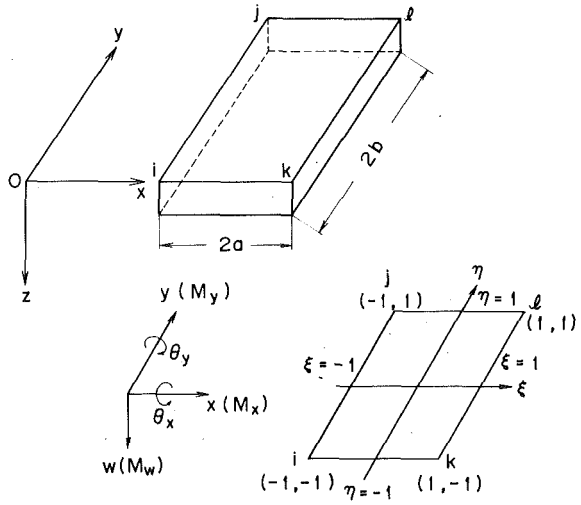

Fig. 4 A rectangular plate element and local coordinates system

vector potentials and from those the magnetic induction **B** can be calculated from equation (3) as follows:

$$B_x = \frac{\partial A}{\partial y} = \frac{\partial [N]}{\partial y}\{A_i\} \tag{13}$$

$$B_y = -\frac{\partial A}{\partial x} = -\frac{\partial [N]}{\partial x}\{A_i\}. \tag{14}$$

Formulation for Magentoelastic Buckling of Ferromagnetic Plate

In this analysis two assumptions are made

1 The classical theory of the thin plate can be applied,

2 The magnetic torque **C** produced in the plate as a result of interaction between the applied field $\mathbf{B}_0$ and the magnetization **m** is given by $\mathbf{m} \times \mathbf{B}_0$ and is proportional to a rotation of the plate as assumed by Moon and Pao.

General stresses and strains in the bending problem of a plate are defined in such a way that a scalar product of them gives internal work. Thus the general strain $\{\epsilon\}$ is defined as second derivatives of lateral displacement w or its curvatures,

$$\{\epsilon\} = \left\{-\frac{\partial^2 w}{\partial x^2}, -\frac{\partial^2 w}{\partial y^2}, 2\frac{\partial^2 w}{\partial x \partial y}\right\}^T \tag{15}$$

and the general stress $\{\sigma\}$ is defined as bending moments,

$$\{\sigma\} = \{M_x, M_y, M_{xy}\}^T \tag{16}$$

where M_x and M_y are the bending moments around y and x- axes and M_{xy} is the twisting moment as shown in Fig. 3.

The general stress is connected to the general strain with the elasticity matrix $[D]$ defined as follows:

$$\{\sigma\} = [D]\{\epsilon\} \tag{17}$$

where

$$[D] = \frac{Et^3}{12(1-\nu^2)}\begin{bmatrix} 1 & \nu & 0 \\ \nu & 1 & 0 \\ 0 & 0 & (1-\nu)/2 \end{bmatrix} \tag{18}$$

where E, t, and ν are Young's modulus, thickness, and Poisson's ratio, respectively. Next we consider equilibrium equations of moment and force referring to an infinitesimal element shown in Fig. 3. The equilibrium equations of moment about the y and x-axes and force are, respectively, [9],

$$Q_x + C_x - M_{x,x} + M_{xy,y} = 0 \tag{19}$$

$$-Q_y + C_y + M_{y,y} - M_{xy,x} = 0 \tag{20}$$

$$Q_{x,x} + Q_{y,y} = 0 \tag{21}$$

where $M_{x,x} = \partial M_x/\partial x$ for example. C_x and C_y are the magnetic torques calculated later using the result of the magnetic field analysis, and Q_x and Q_y are the shearing forces. Elimination of the shearing forces Q_x and Q_y from the foregoing three equations (19)–(21) yields,

$$M_{x,xx} + M_{y,yy} - 2M_{xy,xy} - C_{x,x} + C_{y,y} = 0. \tag{22}$$

A variation of the functional of equation (22) can be given as

$$\delta I = \iint_s (M_{x,xx} + M_{y,yy} - 2M_{xy,xy} - C_{x,x} + C_{y,y})\,\delta w dx dy \tag{23}$$

where w is the deflection of the midplane of the plate. Integration by parts of equation (23) gives

$$\delta I = \delta I_1 + \delta I_2 + \delta I_3 \tag{24}$$

where

$$\delta I_3 = \iint M_x \frac{\partial^2 \delta w}{\partial x^2} dx dy + \iint M_y \frac{\partial^2 \delta w}{\partial y} dx dy - 2\iint M_{xy}\frac{\partial^2 \delta w}{\partial x \partial y} dx dy + \iint C_x \frac{\partial \delta w}{\partial x} dx dy - \iint C_y \frac{\partial \delta w}{\partial y} dx dy \tag{25}$$

The first two terms of equation (24), δI_1 and δI_2, correspond to boundary conditions and can be proved to be zero. The proof is lengthy and so is not presented here (see reference [9]). Substitution of equations (15) and (16) in equation (25) yields,

$$\delta I = \delta I_3 = -\iint \{\sigma\}^T \delta\{\epsilon\}\, dx dy + \iint (C_x \delta\theta_y + C_y \delta\theta_x)\, dx dy$$

From this equation, the functional is

$$I = I_e - I_m \tag{26}$$

$$I_e = \frac{1}{2}\iint \{\sigma\}^T\{\epsilon\}\, dx dy \tag{27}$$

$$I_m = \frac{1}{2}\iint (C_x\theta_y + C_y\theta_x)\, dx dy \tag{28}$$

I_e and I_m correspond to the internal work and the external work done by the magnetic torque, respectively.

The rectangular plate element shown in Fig. 4 was chosen for the

Downloaded 01 May 2010 to 171.66.16.243. Redistribution subject to ASME license or copyright; see http://www.asme.org/terms/Terms_Use.cfm

analysis of buckling. This element has four nodal points, and the following three nodal parameters are defined at each node:

$$\{\delta_i\} = \{w_i, (\theta_x)_i, (\theta_y)_i,\}^T \tag{29}$$

and thus

$$\{\delta\} = \{\delta_i \delta_j \delta_k \delta_1\}^T \tag{30}$$

where w_i, $(\theta_x)_i$ $(= -(\partial w/\partial y)_i)$ and $(\theta_y)_i$ $(= (\partial w/\partial x)_i)$ are the lateral displacement and the rotations about x and y-axes, respectively. "T" means a transpose of the vector. The element displacement vector $\{\delta\}$ has 12 components and thus a polynomial function for "w" is as follows:

$$w = \alpha_1 + \alpha_2 x + \alpha_3 y + \alpha_4 x^2 + \alpha_5 xy + \alpha_6 y^2 + \alpha_7 x^3 + \alpha_8 x^2 y + \alpha_9 xy^2 + \alpha_{10} y^3 + \alpha_{11} x^3 y + \alpha_{12} xy^3 = [p]\{\alpha\} \tag{31}$$

From equations (29) and (31) we get the next equation with use of $\{\delta\} = [G]\{\alpha\}$.

$$w = [p][G]^{-1}\{\delta\} = [N]\{\delta\} \tag{32}$$

where

$$N_i = \frac{1}{8}(\xi_0 + 1)(\eta_0 + 1)\{(2 + \xi_0 + \eta_0 - \xi^2 - \eta^2), - b\eta_i(\eta_0 + 1)(\eta_0 - 1), a\xi_i(\xi_0 + 1)(\xi_0 - 1)\} \tag{33}$$

and

$$\xi = (x - x_c)/a,\ \eta = (y - y_c)/b$$

$$\xi_0 = \xi\xi_i,\ \eta_0 = \eta\eta_i$$

where (x_c, y_c) and (ξ_i, η_i) are the center of the element and the coordinates of the node "i" in the local coordinates system, respectively, as shown in Fig. 4. Substitution of equation (31) in equation (15) gives an expression for the general strain,

$$\{\epsilon\} = [Q]\{\alpha\} = [Q][G]^{-1}\{\delta\} = [H]\{\delta\}. \tag{34}$$

Therefore,

$$I_e = \frac{1}{2}\{\delta\}^T\{[G]^{-1}\}^T\left\{\iint [Q]^T[D][Q]\,dxdy\right\}[G]^{-1}\{\delta\}. \tag{35}$$

As assumed before the magnetic torque is proportional to the rotation of the plane. A normal component (z-component) of the magnetic induction of the ferromagnetic specimen may be calculated as follows with use of the computer code based on equations (2)–(14):

$$B_y = B_0 \cdot \beta(x,y) \tag{36}$$

and a small perturbation of the magnetic torque is given by the equation deduced by Moon and Pao (equation (22) in reference [1]) as follows:

$$C_x = +\frac{\chi^2 B_0^2}{\mu_0 \mu_r} \cdot \frac{\beta(x,y)t}{(\mu_r \pi t/\lambda_x + 1)} \frac{\partial w}{\partial x} \tag{37}$$

$$C_y = -\frac{\chi^2 B_0^2}{\mu_0 \mu_r} \cdot \frac{\beta(x,y)t}{(\mu_r \pi t/\lambda_y + 1)} \frac{\partial w}{\partial y} \tag{38}$$

where wavelengths λ_x and λ_y are equal to the quadruple length of the specimen and the double width, respectively, in the present calculation. Substitution of equations (37) and (38) in equation (28) gives

$$I_m = \frac{1}{2}\frac{\chi^2 B^2{}_0 t}{\mu_0 \mu_r} \iint \left[\frac{\beta(x,y)}{\pi\mu_r t/\lambda_x + 1}\left(\frac{\partial w}{\partial x}\right)^2 + \frac{\beta(x,y)}{\pi\mu_r t/\lambda_y + 1}\left(\frac{\partial w}{\partial y}\right)^2\right] dxdy \tag{39}$$

Then the functional "I" can be finally obtained as a sum of equations (35) and (39). By differentiating the functional with respect to $\{\delta\}$ in order to minimize it, two matrices $[K_e]$ and $[K_m]$ can be obtained.

$$[K_e] = \{[G]^{-1}\}^T\left[\int_{-b}^{b}\int_{-a}^{a} [Q]^T[D][Q]\,dxdy\right][G]^{-1}dxdy \tag{40}$$

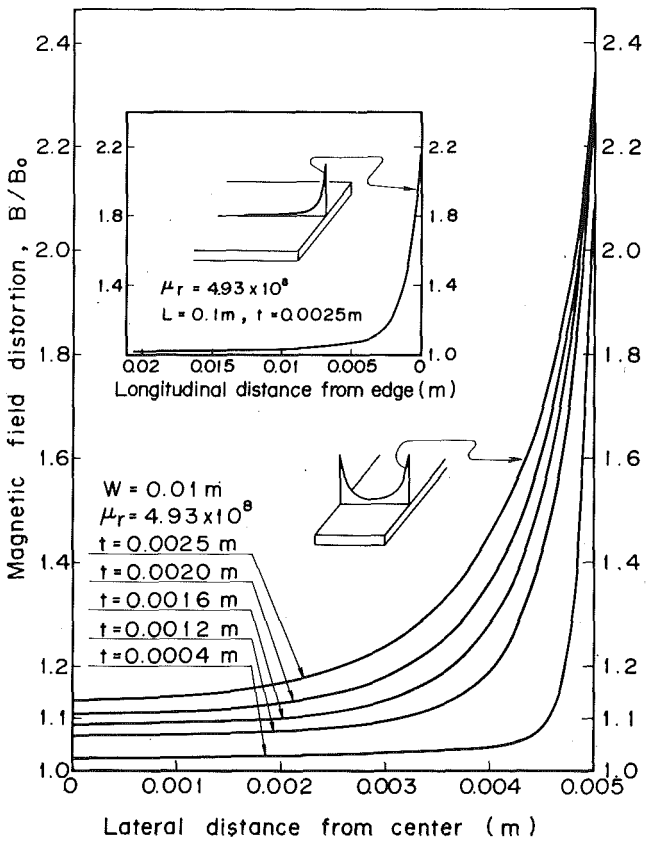

Fig. 5 Lateral and longitudinal distribution of magnetic induction in ferromagnetic beam plate

$$[K_m] = \frac{\chi^2 t}{\mu_0 \mu_r}\int_{-1}^{1}\int_{-1}^{1}\beta(x,y)\left[\frac{1}{\mu_r \pi t/\lambda_x + 1}\frac{\partial[N]^T}{\partial x}\frac{\partial[N]}{\partial x} + \frac{1}{\mu_r \pi t/\lambda_y + 1}\frac{\partial[N]^T}{\partial y}\frac{\partial[N]}{\partial y}\right] abd\xi d\eta \tag{41}$$

Therefore, a final eigenvalue equation can be obtained as follows:

$$|[K_e] - B_0{}^2[K_m]| = 0 \tag{42}$$

where matrices $[K_e]$ and $[K_m]$ in equation (42) are ones summed up over the whole elements while those in equations (40) and (41) refer to just one element. Equation (42) gives eigenvalues, the smallest of which corresponds to the buckling field of the ferromagnetic beam plate.

Results of Numerical Analysis and Discussions

The distribution of the magnetic induction in and around the ferromagnetic specimen can be obtained by solving equation (12) while satisfying a boundary condition that the magnetic induction on the boundary (both the pole faces shown in Fig. 1) should be the applied field B_0. This boundary condition is represented with $A = B_0 x$ on the pole faces. The factor, $\beta(x,y)$, in equation (37) can be determined from y-component of the calculated magnetic induction in the specimen. It should be noted here that the distribution of the magnetic induction is regardless of the permeability, μ_r, of the specimen if it is larger than 50. This corresponds to the fact that the theoretical buckling field deduced by Moon and Pao [1] is independent of the permeability of the material.

In Fig. 5 are shown distributions of the y-component of the magnetic induction, which is averaged through the thickness, using a parameter of the thickness of the specimen. The width and the permeability of the specimen are always 0.01 m and 4.93×10^8, respectively, in those cases. The results in the figure differ from those given in the paper [4] which show the uniform field distribution of the

Downloaded 01 May 2010 to 171.66.16.243. Redistribution subject to ASME license or copyright; see http://www.asme.org/terms/Terms_Use.cfm

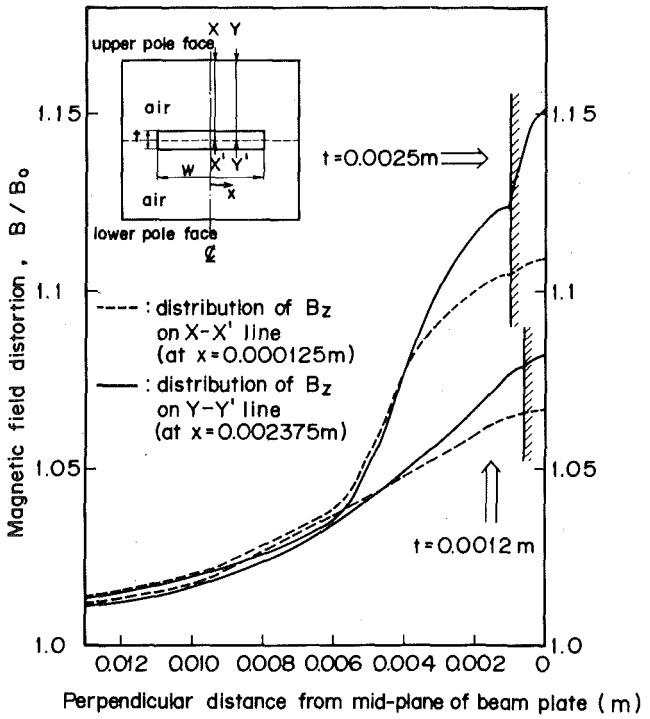

Fig. 6 Distributions of magnetic induction B_z in air and ferromagnetic beam plate

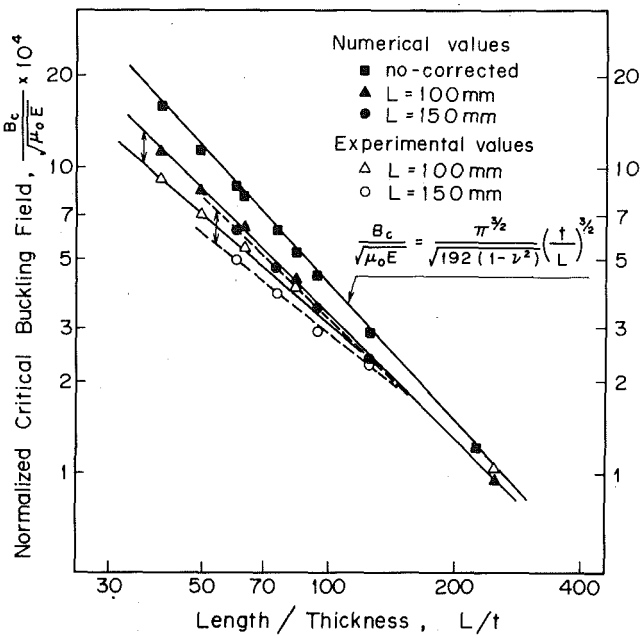

Fig. 7 Relation between critical buckling field and length-to-thickness ratio

surface. The field distribution near a longitudinal edge is also shown upper in Fig. 5. It seems very similar with the lateral field distribution if the thickness is equal. As pointed out by Dalrymple, et al. [6], a magnitude of the field concentration would become much larger as the width becomes smaller. This could correspond to the fact that experimental results are always smaller than the theoretical ones given by equation (1) because the theoretical prediction assumes that the ferromagnetic beam plate extends infinitely, while actually its thickness is kept finite and constant.

In Fig. 6 are shown field distributions on two lines extending upper from a midplane of the beam plate. Two groups of four curves in the figure correspond to two specimens of which thicknesses are 0.0025 and 0.0012 m. The analysis by Wallerstein, et al. [4], showed that the axial component, B_y, of the magnetic induction in a region over 0.0048 m above the surface is equal to the applied field, but the present analysis shows that there is a slight gradient of B_y while a pole gap is finite (=0.2 m) in this case. It is clear in the figure that the axial fields at the surface are much smaller than the value of $1.86 \times B_0$ given by them and the field in the specimen. The value depends on the specimen thickness as stated by them. However, they suggested that experimental values should be multiplied by a factor of 1.86 regardless of the thickness saying "a variation of as much as 60 percent in t/L produces a variation in B_{yc}/B_{oc} of less than 3.5 percent."

The next interesting issue is how exactly the finite-element coupling solution of equation (12) and equation (42) can explain experimental results. Numerical results are shown in Fig. 7. Experimental results shown with blank circle and triangle were given in the previous paper

Table 1 Comparison of theoretical, experimental, and numerical results

SPECIMEN	DIMENSION (m)			$C_{th}(\frac{C_{th}-C_{ex}}{C_{ex}}\times 100)$	C_{ex}	$C_n(\frac{C_n-C_{th}}{C_{th}}\times 100)$	$C_{nw}(\frac{C_{nw}-C_{ex}}{C_{ex}}\times 100)$	$C_{nwl}(\frac{C_{nwl}-C_{ex}}{C_{ex}}\times 100)$
	length	width	thickness					
1	0.10	0.01	0.0004	1.07(3.9)	1.03	1.02(-4.7)	0.956(- 7.2)	0.949(- 7.8)
2	0.09	0.01	0.0004	1.25(-21.9)	1.60	1.20(-4.0)	1.12 (-30.0)	1.11 (-30.6)
3	0.15	0.01	0.0012	3.01(30.3)	2.31	2.88(-4.3)	2.40 (4.1)	2.37 (2.6)
4	0.10	0.01	0.0012	5.54(36.5)	4.06	5.30(-4.3)	4.42 (8.9)	4.31 (6.3)
5	0.15	0.01	0.0016	4.64(59.5)	2.91	4.44(-4.3)	3.57 (22.8)	3.51 (20.7)
6	0.10	0.01	0.0016	8.53(55.7)	5.48	8.16(-4.3)	6.57 (19.9)	6.39 (16.6)
7	0.15	0.01	0.0020	6.49(66.8)	3.89	6.20(-4.5)	4.83 (24.1)	4.73 (21.7)
8	0.10	0.01	0.0020	11.9 (69.5)	7.02	11.4 (-4.2)	8.88 (26.4)	8.53 (21.5)
9	0.15	0.01	0.0025	9.06(80.5)	5.02	8.67(-4.3)	6.49 (29.3)	6.31 (25.7)
10	0.10	0.01	0.0025	16.7 (79.8)	9.29	15.9 (-4.6)	11.9 (28.5)	11.4 (22.2)

C_{th} : Theoretical value of normalized critical buckling field (from Moon [1] et al)

C_{ex} : Experimental value of normalized critical buckling field

C_{n} : Numerical result of normalized critical buckling field (without correction)

C_{nw} : Numerical result of normalized critical buckling field (involves magnetic field concentration over the direction of width)

C_{nwl} : Numerical result of normalized buckling field (involves magnetic field concentration over the direction of length as well as that of width)

Downloaded 01 May 2010 to 171.66.16.243. Redistribution subject to ASME license or copyright; see http://www.asme.org/terms/Terms_Use.cfm

[5]. As usual, the validity of the computer code based on the previously stated process should be proved in advance of the numerical analysis of the experimental results. If the field correction factor, $\beta(x,y)$, appearing in equation (38) is equal to one, a solution of equation (42) can be expected equal to a value predicted by equation (1) deduced for a cantilever. The upper solid line in Fig. 7 was calculated analytically from the equation (1). And solid rectangles are solutions of equation (42). They agree well with each other. Differences between the numerical and analytical results are listed up in the seventh column in Table 1. The errors are within 4.0–4.7 percent, from which we can consider the computer code valid. Maximum error between the experiment and the theory of equation (1) is 80.5 percent as shown in the fifth column. In the column of C_{nw} are shown the buckling fields obtained when the lateral field correction only was taken into account. In the last column is shown the buckling field when both the lateral and longitudinal field corrections were made. Differences between the experimental and the numerical results are all below 25 percent while some of the differences between the experiment and the theory are above 50 percent. The results in the last column in Table 1 are plotted in Fig. 7. As is clear from the results in the figure, slopes of the experimental results are not parallel to that given by equation (1); namely, the slope of the buckling field of the finite ferromagnetic beam plate is smaller than 3/2. The numerical analysis also supports this fact.

As shown in Fig. 7 the experimental results for the higher L/t agree very well with the predicted one while those for the lower L/t differ by more than 50 percent. The numerical results shown in Fig. 5 explain the reason why the magnitude of the field concentration for a thinner specimen (L is constant and so L/t is large) could be negligible, which leads to a better coincidence with the predicted value, while it of the thicker specimen is relatively large, thus resulting in the big discrepancy. But the big discrepancy was well estimated by the present numerical analysis within 25 percent (see the last column in Table 1). The lateral field concentration is dominant in the correction of the experiment as seen in Table 1 while the longitudinal correction rate is about 5 percent. A contribution of the magnetic energy of the buckling around the x-axis corresponding to the second term in equation (41) was negligible, as is easily estimated from the very small value of λ_y compared to λ_x.

There still remains the essential question of why the maximum difference of 25.7 percent cannot be corrected although the finite-element analysis could explain comparatively well the experimental results. Possible reasons for the question may be experimental errors such as the existence of an actual gradient of the applied field, initial defects not recognized when conducting the experiment. Another reason may be placed on the validity of the dipole model employed here. However, we cannot draw any conclusion of this problem in the present study. An advanced experiment and theory must be developed for a final solution.

Conclusion

The difficulty to deduce an analytical expression for the buckling field of a ferromagnetic beam plate finite in size suggests to us to apply a numerical method to the problem. An example of the application of the finite-element method to it is presented in this paper with a considerably better estimate of the experimental results. The code made here can be applied to any magnetoelastic buckling problem, if that problem is two-dimensional.

Acknowledgment

This work has been done with a financial support from the Controlled Thermonuclear Reactor Committee (Chairman, Prof. A. Sekiguchi), Faculty of Engineering, University of Tokyo. The authors also would appreciate discussions on this work with Dr. F. C. Moon, Cornell University and Dr. J. E. Akin, University of Tennessee.

References

1 Moon, F. C., and Pao, Y. W., "Magnetoelastic Buckling of a Thin Plate," ASME JOURNAL OF APPLIED MECHANICS, Vol. 35, 1968, pp. 53–58.

2 Moon, F. C., and Swanson, C., "Experiments on Buckling and Vibration of Superconducting Coils," ASME JOURNAL OF APPLIED MECHANICS, Vol. 44, 1977, pp. 707–713.

3 Miya, K., and Takagi, T., "Finite-Element Analysis of Electromagnetoelastic Buckling of Superconducting Magnet in Magnetic Fusion Reactor," ASME *Journal of Pressure Vessel Technology,* Vol. 100, 1978, pp. 1–24.

4 Wallerstein, D. V., and Peach, M. O., "Magnetoelastic Buckling of Beam and Thin Plates of Magnetically Soft Material," ASME JOURNAL OF APPLIED MECHANICS, Vol. 39, 1972, pp. 451–455.

5 Miya, K., Hara, K., and Someya, K., "Experimental and Theoretical Study on Magnetoelastic Buckling of a Ferromagnetic Cantilevered Beam-Plate," ASME JOURNAL OF APPLIED MECHANICS, Vol. 45, 1978, pp. 355–360.

6 Dalrymple, J. M., Peach, M. O., and Viegelahn, G. L., "Magnetoelastic Buckling; Theory Versus Experiment, "*Journal of Experimental Mechanics,* Vol. 17, No. 1, 1976, pp. 26–31.

7 Miya, K., An, S., etc., "Application of Finite-Element Method to Electro-Magneto-Mechanical Dynamics of Superconducting Magnet Coil and Vacuum Vessel," *Proceedings of the 6th Symposium on Engineering Problems of Fusion Research,* San Diege, Nov. 1975.

8 Miya, K., Takagi, T., and Tabata, Y., "Three-Dimensional Analysis of Magnetic Field and Magnet Stress Induced Into Vessel by Plasma Motion," *Proceedings of the 7th Symposium on Engineering Problems of Fusion Research,* ORNL, Nov. 1977.

9 Washizu, K., *Variational Methods in Elasticity and Plasticity,* 2nd ed., Pergamon Press, 1975, pp. 152–167.

Downloaded 01 May 2010 to 171.66.16.243. Redistribution subject to ASME license or copyright; see http://www.asme.org/terms/Terms_Use.cfm

K. Kemmochi
Senior Researcher,
Industrial Products Research Institute,
Agency of Industrial Science and Technology,
1-4, Higashi 1-Chome, Yatabe-Cho,
Tsukuba-Gun,
Ibaragi, 305 Japan
Mem. ASME

T. Akasaka
Professor,
Faculty of Science and Engineering,
Chuo University,
Kasuga-Cho,
Tokyo, Japan

R. Hayashi
Senior Researcher.

K. Ishiwata
Senior Researcher.

Industrial Products Research Institute,
Agency of Industrial Science and Technology,
1-4, Higashi 1-Chome, Yatabe-Cho, Tsukuba-Gun,
Ibaragi, 305 Japan

Shear-Lag Effect in Sandwich Panels With Stiffeners Under Three-Point Bending[1]

In this paper, a modified theory based upon Reissner's procedure for the shear-lag effect of the sandwich panel is presented, which includes the effects of the anisotropy of the faces and the shearing rigidity of the core. In order to verify this theory, bending experiments were performed with sandwich panels composed of a soft core, stiffeners, and orthotropic faces. It was found that the effective bending rigidity calculated from this theory was lower than that derived from the classical bending theory and that the theoretical strain distribution on the faces agreed well with the experimental results.

Introduction

The use of sandwich constructions began in aircraft structures in which high specific strength and rigidity are required. However, in recent years, sandwich panels have also been used in many other industrial products, such as trains, ships, and housing components.

It is well known that the sandwich core, which is an expanded high polymer (plastic foam), a grid (honeycomb construction), or balsawood with its grain perpendicular to the faces, is so weak in comparison with the face materials that normal stresses in the core can be neglected in the plane of the sandwich. In order to increase the bending rigidity of the sandwich panels, the soft core in between the stiffeners and/or ribs may be further reinforced high rigidity stiffeners. However, a proper analysis should account for the possible shear between the core and stiffeners. In the sequel such a structure is referred to as a composite core.

When the sandwich panel with composite core is subjected to a bending load, the stress distributions across the faces is nonuniform, i.e., the displacements near the stiffeners are larger than in the region where the faces are attached only to the core. The part of the face restrained by a stiffener of high bending rigidity is stretched (or compressed) more than regions of the face covering the weak core. This gives rise to a nonuniform stress distribution in the faces and it reduces the bending rigidity of the sandwich panel. This phenomenon is called shear lag. If one ignores the shear-lag effect, he overestimates the strength and the rigidity of the sandwich panel.

Therefore, box beams used in airplane structural elements are always designed with consideration of the shear-lag effect and they have a high structural efficiency. The effective width of the face plate can be calculated theoretically [1]. It is very important to note that the shear-lag effect in the faces is just as significant as it is in box or I-beams.

Reissner derived formulas for the shear-lag effect in the box beam with isotropic cover sheets under bending load [2]. The present paper assumes that the faces are orthotropic plates and extends Reissner's equation to add the effects of bending and shearing deformations of the core. Solutions of the modified equations have been obtained and compared with results of bending tests of sandwich panels with composite core.

Stresses and deflections calculated from Reissner's modified theory are in good agreement with those measured. Thus the theoretical prediction of a decrease in bending rigidity due to shear-lag has been verified quantitatively.

[1] This paper was completed when one of the authors (K.K.) was visiting the Department of Mechanical Engineering, Aeronautical Engineering and Mechanics, Rensselaer Polytechnic Institute, Troy, N. Y. 12181, as Research Associate from September 1, 1978 to August 30, 1979.

Contributed by the Applied Mechanics Division for publication in the JOURNAL OF APPLIED MECHANICS.

Discussion on this paper should be addressed to the Editorial Department, ASME, United Engineering Center, 345 East 47th Street, New York, N. Y. 10017, and will be accepted until September 1, 1980. Readers who need more time to prepare a discussion should request an extension from the Editorial Department. Manuscript received by ASME Applied Mechanics Division, March, 1979; final revision, July, 1979.

Copyright © 1980 by ASME
Downloaded 01 May 2010 to 171.66.16.243. Redistribution subject to ASME license or copyright; see http://www.asme.org/terms/Terms_Use.cfm

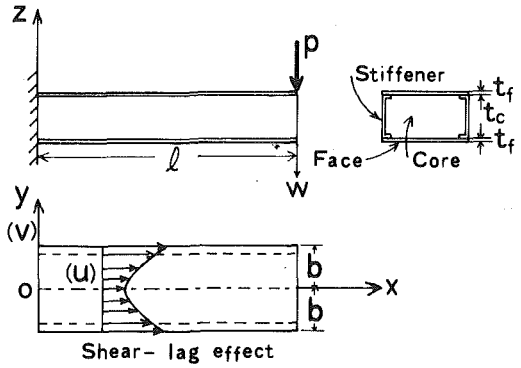

Fig. 1 Coordinates and geometry of a sandwich panel with stiffeners for analysis

Formulation of the Problem

Consider a sandwich panel of stiffener height t_c, face width $2b$, and core depth t_c which is bent as shown in Fig. 1. Evidently one of the faces is in tension while the opposite face is in compression.

The spanwise coordinate being x, let y be the coordinate in the plane of the faces perpendicular to the x-direction, and $w(x)$ the deflection of the neutral plane of the panel.

The assumptions are as follows:

1 Local buckling of the faces of the sandwich panel does not occur.

2 The face-to-core bonds are strong enough so that under bending loads no bond failure occurs.

3 The faces are of equal thickness, orthotropic, and having the same mechanical properties, while the core is isotropic.

4 A plane state of stress (not uniformity) exists on the faces.

5 The Navier-Kirchhoff hypothesis holds for the faces, i.e., straight lines initially normal to the middle surface of the faces remain straight and normal to the middle surface of the faces after bending.

6 Transverse normal strain of the core is neglected.

These assumptions have been used previously and are known to represent very well [3, 4] the actual behavior of sandwich structures.

In deriving analytical solutions, the following three additional assumptions about displacement of faces are made:

1 The deflection $w(x)$ is considered to be a function of the length coordinate x.

2 Normal strains in the width direction are not accounted for. Such displacements of the faces are negligible, $v(x, y) \equiv 0$.

3 Because of the assumption of a parabolic variation of u, a reasonable assumption for the spanwise face displacements is

$$u(x, y) = \pm h\left[\frac{dw}{dx} + \left(1 - \frac{y^2}{b^2}\right)\zeta(x)\right], \tag{1}$$

where $h = (t_f + t_c)/2$ and $h\{dw/dx + \zeta(x)\}$ is the displacement in the middle of the faces ($y = 0$).

The potential energy of the sandwich panel may be considered as composed of the following five parts, i.e.,

1 The strain energy U_s of the two stiffeners.

2 The strain energy U_{fm} of the two faces holding the distance h to each other.

3 The bending strain energy in the faces themselves (upper and lower) U_{fb}.

4 The shear strain energy in the core U_c.

5 The load system V.

The total potential energy π for the system can be given by

$$\pi = U_s + U_{fm} + U_{fb} + U_c - V = \frac{D_s}{2}\int_0^l (w'')^2\,dx + \frac{D_0}{2}\int_0^l \left\{(w'')^2 + \frac{4}{3}w''\zeta' + \frac{8}{15}(\zeta')^2 + \frac{4}{3}\frac{G_{xy}}{b^2 E_x'}\zeta^2\right\}dx + \frac{D_f}{2}\int_0^l (w'')^2 dx + \frac{1}{2}\Gamma_c\int_0^l \zeta^2 dx - \int_0^l M(x)(w'')dx = \int_0^l \left\{\frac{D}{2}(w'')^2 - Mw''\right\}dx + \frac{D_0}{2}\int_0^l \left\{\frac{4}{3}w''\zeta' + \frac{8}{15}(\zeta')^2\right\}dx + \frac{\Gamma}{2}\int_0^l \zeta^2\,dx \tag{2}$$

where D and Γ are the bending stiffness and shearing rigidity of the sandwich panel

$$\left.\begin{aligned} D_s + D_0 + D_f &\equiv D \\ D_0\frac{4}{3b^2}\frac{G_{xy}}{E_x} + \Gamma_c &\equiv \Gamma \end{aligned}\right\} \tag{3}$$

and

$$E_s I_s \equiv D_s, \quad 4t_f h^2 b \equiv I_0, \quad E_x/(1 - \nu_x\nu_y) \equiv E_x', \quad E_x' I_0 \equiv D_0,$$
$$4t_f^3 b E_x'/12 \equiv D_f, \quad 16G_c t_c b/15 \equiv \Gamma_c.$$

The differential equations and boundary condition for w and ζ are obtained from the theorem of minimum potential energy which states that $\delta\pi = 0$.

Carrying out the usual manipulations

$$\delta\pi = \int_0^l \left(Dw'' - M + \frac{2}{3}D_0\zeta'\right)\delta w''dx + \int_0^l \left\{\Gamma\zeta - D_0\left(\frac{2}{3}w''' + \frac{8}{15}\zeta''\right)\right\}\delta\zeta dx + \left[D_0\left(\frac{2}{3}w'' + \frac{8}{15}\zeta'\right)\delta\zeta\right]_0^l = 0. \tag{4}$$

In the solution of cantilever beam with concentrated load on the edge, the moment distribution $M(x)$ is defined by

Nomenclature

$2b$, B = beam width and panel width, respectively
D = flexural rigidity in theoretical analysis
D^* = flexural rigidity of a sandwich panel
E_s = Young's modulus of elasticity of stiffener (subscript "s" denotes stiffener)
E_x, ν = Young's modulus of elasticity and Poisson's ratio of faces
G_{xy}, G_c = shear moduli of faces in xy-plane and core, respectively
$h(x)$ = distance between neutral plane of upper and lower face ($= t_f + t_c$)
$I(x)$ = moment of inertia
n, k = dimensionless parameter
l, L = beam span for cantilever and panel span length for three-point bending, respectively
$M(x)$ = applied bending moment
p, W = theoretical and experimental load, respectively
t, t_f, t_c = total thickness, thickness of face, and thickness of core, subscripts "f" and "c" denote face and core, respectively
u, v, w = face displacements in x, y, and z-directions, respectively
U = strain energy
x, y = rectangular coordinates in the plane of the faces; x spanwise and measured from tip to root, y transverse and measured from middle line between stiffeners to edge
z = coordinate perpendicular to neutral plane of panel, counted positive from middle plane to upper face
$\epsilon(x)$ = strain distribution in xy-plane of faces

Downloaded 01 May 2010 to 171.66.16.243. Redistribution subject to ASME license or copyright; see http://www.asme.org/terms/Terms_Use.cfm

$$M(x) = M_0\left(1 - \frac{x}{l}\right), \quad M_0 = Pl \tag{5}$$

and a system of boundary conditions at each end ($x = 0$ and $x = l$) of the beam, the following relations are obtained:

$$w'' = \frac{M_0}{D}\left\{\left(1 - \frac{x}{l}\right) - \frac{n-1}{kl}\left[\sinh(kx) - \tanh(kl)\cdot\cosh(kx)\right]\right\}, \tag{6}$$

and

$$\zeta'' = \frac{3D}{2D_0}\cdot\frac{M_0}{D}\frac{(n-1)}{kl}\{\sinh(kx) - \tanh(kl)\cdot\cosh(kx)\} \tag{7}$$

where k and n are nondimensional parameters as defined in the following:

$$\left.\begin{aligned}\left(\frac{3D}{2D_0} - \frac{5}{4}\right)\cdot\frac{16}{45}\frac{D_0^2}{\Gamma D} &\equiv \frac{1}{k^2}\\ \frac{3D}{2D_0}\cdot\frac{16}{45}\frac{D_0^2}{\Gamma D} &\equiv \frac{n}{k^2}\end{aligned}\right\} \tag{8}$$

Strain Distribution in the Faces. The strain distribution in the middle plane of the faces is given by equations (1), (6), and (7) as follows:

$$\epsilon_x = \pm\frac{du}{dx} = \pm h\frac{M_0}{D}\left[\left(1 - \frac{x}{l}\right) - \frac{n-1}{kl}\left\{1 - \frac{3D}{2D_0}\left(1 - \frac{y^2}{b^2}\right)\right\}\right.$$
$$\left.\times\{\sinh(kx) - \tanh(kl)\cdot\cosh(kx)\}\right] \tag{9}$$

where the upper (positive) refers to the lower (tensile) face, and the lower (negative) sign to the upper (compressive) face.

Deflections. The deflection of the beam is obtained from equation (6) and the boundary condition. When the beam is fixed at $x = 0$, the equation takes the form

$$w = \frac{M_0}{D}\left[\frac{x^2}{2} - \frac{x^3}{6l} - \frac{n-1}{kl^3}\{\tanh(kl) - kx\right.$$
$$\left.+ \sinh(kx) - \tanh(kl)\cdot\cosh(kx)\}\right]. \tag{10}$$

The maximum deflection w_{max} is at the free end ($x = l$) and is given by

$$w_{max} = \frac{Pl^3}{3D}\left[1 + \frac{3(n-1)}{(kl)^2}\left\{1 - \frac{\tanh(kl)}{kl}\right\}\right] \tag{11}$$

where the relation $M_0 = Pl$ has been employed.

The middeflection of the beam on two simple supports is

$$\delta_{max} = \frac{wL^3}{48\,D^*}\left[1 + \frac{3(n-1)}{(kL)^2}\left\{1 - \frac{\tanh(kL)}{kL}\right\}\right], \tag{12}$$

where δ_{max} is the maximum deflection of the specimens, $L = 2l$, D^* is to be replaced by $2D_1$ and $3D_2$ for specimens, D_1 and D_2 denote one element of bending rigidity in Specimen No. 1 ($2b$ = 150 mm, 5.91 in.) and Specimen No. 2 ($2b$ = 100 mm, 3.94 in.), respectively, and W is to be replaced by $4P$ for Specimen No. 1 and by $6P$ for Specimen No. 2.

In equation (12), the first factor in the right-hand member agrees with the result of classical beam theory, and the second term in brackets represents the additional shearing deflection due to the shear-lag effects.

Experimental Investigation

As a result of the foregoing calculations, the shear-lag effect of sandwich panels with stiffeners has been obtained. In the present section, experiments on actual sandwich panels with stiffeners are described. These were carried out in order to ascertain the validity of the previous calculations.

Test Specimens. The composite core of the sandwich panels was composed of aluminum alloy stiffeners and a synthetic foam (acrylic resin foam). There was a light transverse wood rib to facilitate the introduction of the load. Decorative phenolic resin laminates were used as the anisotropic face material.

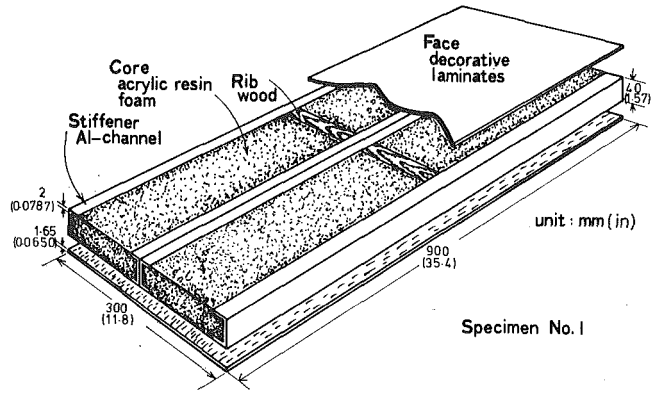

Fig. 2 Test Specimen No. 1

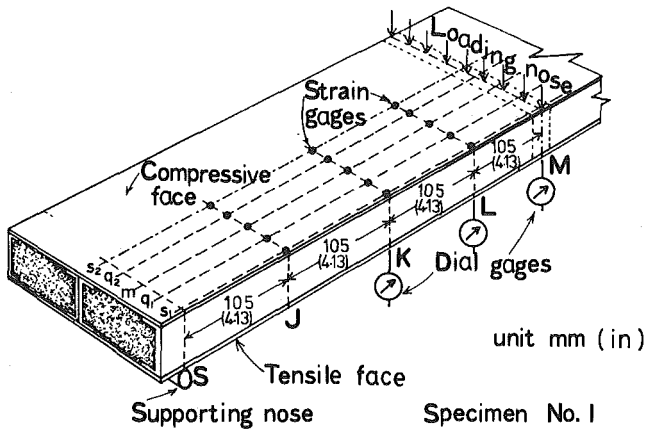

Fig. 3 Positions where the strain and deflection were measured

The specimen is shown in Fig. 2 as an example of No. 1 specimen. Specimen No. 2 is of the same size as No. 1, but it has three stiffeners; one of the stiffeners is composed of two aluminum alloy channels.

Measurement of Strain and Deflection. Each of the specimens was tested using three-point bending by the Instron-type testing machine (with the capacity of 49000 N). The deflection was measured at five equidistant lines along the sandwich panel and strain was measured at four to six points across the width of the panel depending upon the specimen. The location of the dial and strain gages is shown in Fig. 3. Line "s" was on the stiffener face, "m" along the center line of the face between the two stiffeners and "q" halfway between "s" and "m". These 40 to 60 measuring points were provided on both sides of the specimens (on both the tensile face and the compressive face) for the determination of the stress distribution (with the exception of the line of load application on the compressive face).

The deflections of the sandwich panel at points K, L, and M were measured by the extensometers similar to dial gages (see Fig. 3).

The loads were increased gradually up to the maximum load of the specimen, and strains and deflections were measured for each of 490 or 980 N increment by means of a multistrain meter (DATRAN II, made by Vishay Intertechnology, Inc.). As the instrument was able to measure strains of all the points (40 to 60) within 4 to 6 sec, it is believed that stress relaxation or strain increases could not occur during the incremental loading.

Experimental Results

The Mechanical Properties of Fabricating Materials in the

Downloaded 01 May 2010 to 171.66.16.243. Redistribution subject to ASME license or copyright; see http://www.asme.org/terms/Terms_Use.cfm

Table 1 Mechanical properties of the face materials

Degree		0°	45°	90°
E_f	GPa (Msi)	15.46 (2.24)	13.94 (2.02)	12.56 (1.82)
F_t	MPa (ksi)	117 (16.9)	102 (14.8)	87.6 (12.7)
ν_f		0.349	0.391	0.256
G_{xy}	GPa (Msi)	5.14 (0.745)		

Table 2 Calculated values due to classical theory

Specimen		No. 1	No. 2
D^*	kN - m^2	16.20	20.66
W^*	kN	27.0	34.4
b_{eff}		0.825	0.878
D^{**}	kN-m^2	14.92	19.77

Specimens. The mechanical properties of each material used were determined by standard test methods (ASTM and JAPAN Industrial Standard).

To obtain the strength properties and the elastic moduli of the face material, tensile tests were carried out for three orientations of the fibers, namely 0°, 45°, and 90° subtended with the spanwise direction. All the characteristic quantities (E_f, F_t, and ν_f) measured are compiled in Table 1.

The shear modulus of the face G_{xy} was calculated from Hayashi's equation for anisotropic plates

$$\frac{1}{G_{xy}} = \frac{4}{E_{45°}} - \left(\frac{1}{E_{0°}} + \frac{1}{E_{90°}} - \frac{2\nu_{0°}}{E_{0°}}\right). \tag{13}$$

Young's modulus of the aluminum-alloy channel E_s was determined by bending tests of I-beams constructed by epoxy-welding together the webs of two aluminum-alloy channels back to back.

Also, the shear rigidity of the acrylic resin foam core G_c was determined with the aid of torsion tests of columns of square section made of the core.

The resulting numerical values employed in the analysis are as follows:

t_f = 1.65 mm (0.0394 in.), t_c = 40 mm (1.575 in.),
$h = (t_c + t_f)/2$ = 20.83 mm (0.820 in.)

b = 75 (2.95) (for specimen No. 1)
and 50 (1.97) (for specimen No. 2) mm (in.)

l = 420 mm (16.54 in.), E_x = 15.46 GPa (2.24 Msi),
G_{xy} = 5.14 GPa (0.745 Msi),

ν_x = 0.349, ν_y = 0.256, E_s = 60.9 GPa (8.86 Msi),
G_c = 24.4 MPa (3.56 Ksi).

Comparison of the Experimental Results With Classical Beam Theory. When the failure of the specimen occurs at the tensile strength F_t of the face, the maximum load W^* is estimated to be

$$W^* = \frac{8F_tD^*}{t \cdot LE_x}, \tag{14}$$

where $t = 2t_f + t_c$.

The bending rigidity D^* and estimated load W^* of the specimen are shown in Table 2. On the other hand, the experimental results, such as the maximum load W_{max}, the maximum midpoint deflection δ_{max}, and the rigidity D_{exp} are presented in Table 3.

The quantity D_{exp} was calculated from the following equation:

$$D_{exp} = \frac{WL^3}{128(2\delta_L - \delta_M)}, \tag{15}$$

where δ_L and δ_M are the deflections at points L and M along the span, respectively (see Fig. 3).

The failure of each specimen occurred when the tensile strength of the face at the middle of the span was reached (see Tables 1–3). The maximum load W_{max} and the maximum stress σ_{max} were almost equal to 50 ~ 60 percent of W^* and F_t, respectively. The apparent bending rigidity D amount to about 65 ~ 75 percent of D^*.

Table 3 Experimental results by three-point bending

Specimen		No. 1	No. 2
ρ	g/cm^3 (lb/in^3)	0.34 (0.012)	0.39 (0.014)
W_{max}	kN	12.74	18.67
δ_{max}	mm (in)	11.32 (0.446)	15.45 (0.608)
D_{exp}	kN - m^2	14.21	16.0
σ_{max}	MPa (ksi)	55.3 (8.01)	63.5 (9.20)

ρ: mass density

Table 4 Comparison of theoretical strain and deflection with experimental ones

Specimen / Value		No. 1 exp	No. 1 cal	No. 1 exp/cal	No. 2 exp	No. 2 cal	No. 2 exp/cal
Strain (μ)	s	2075	2089	0.99	1600	1578	1.01
	q	1520	1678	0.91	1338	1361	0.98
	m	1477	1542	0.96	1180	1289	0.92
Deflection mm (in)	M	6.17 (0.243)	5.39 (0.212)	1.14	4.55 (0.179)	4.15 (0.163)	1.10

These differences between the experimental results and the classical beam theory are caused by the redistribution of the stresses known as the shear-lag effect.

Comparison of Experiment With the Theoretical Solutions of the Shear-Lag Effect. The strain application on the "M" line on the tensile face, near the point of load was slightly lower than the theoretical value. With increasing load, it attained good agreement with the theoretical value in the elastic range ($W \geq 5880 \sim 7840$ N) and then, with the addition of more loads, it was higher than the theoretical value in the plastic range. The strain distributions in the two specimens are shown to be approximately the same. Therefore, the behavior of specimens No. 1 and 2 at W = 6860 N was plotted in Figs. 4(a, b), respectively. The theoretical values and classical beam theory are also shown in the same figures.

The deflections that were measured at the points "K", "L", and "M" are in good agreement with the theoretical values within the elastic range, and an anticlastic [5] curvature effect was noticed in the deflections along the width.

All of the experimental and theoretical values are shown in Table 4. While it is known that the experimental stress distributions are

Downloaded 01 May 2010 to 171.66.16.243. Redistribution subject to ASME license or copyright; see http://www.asme.org/terms/Terms_Use.cfm

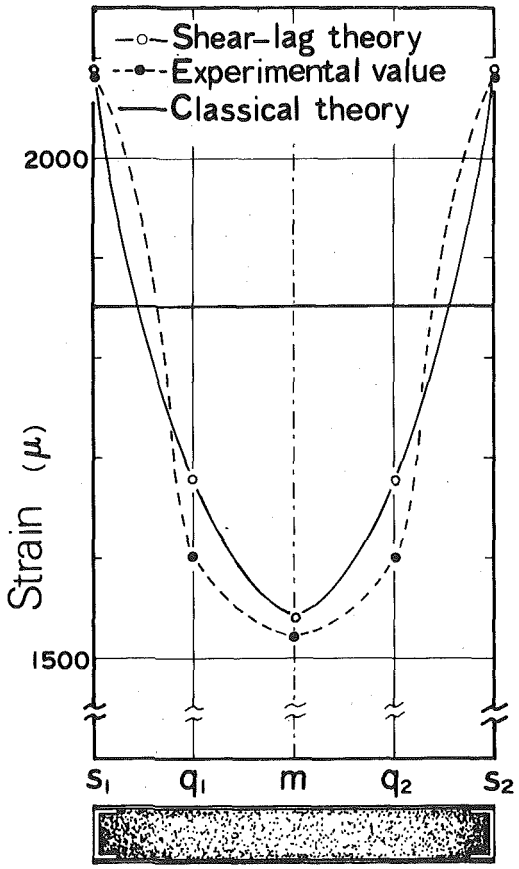

Fig. 4(*a*) Specimen No. 1

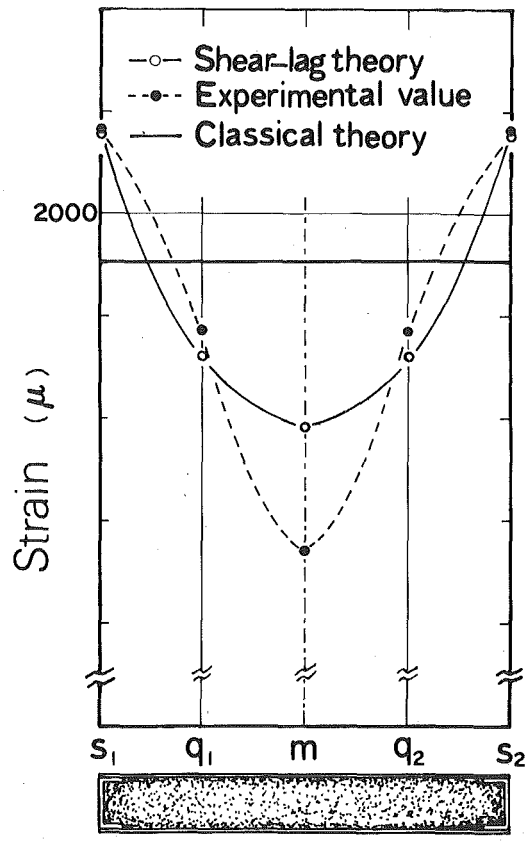

Fig. 4(*b*) Specimen No. 2

Fig. 4 Comparison of the experimental strain distribution with the values of shear-lag theories in the tensile face at $W = 6.8$ kN

close to the shear-lag theory, the maximum differences between the experimental deflection and the theoretical ones is within 15 percent.

The mid-deflections from the experiments, the shear-lag theory and the classical beam theory in Specimens No. 1 and 2 are shown in Fig. 4.

From Fig. 4, the experimental values are about 10 percent larger than the shear-lag theory and the theory including shear lag effects is not very different from the classical theory. The possible reasons for the discrepancy between the experimental and calculated values are as follows:

1 The bending rigidity of the stiffeners was too high compared with the face rigidity of the specimens. If a stiffener with almost the same rigidity as that of the faces had been used, the shear-lag effect would be more pronounced.

2 As the deflections were measured by means of extensometers along the edge line of the tensile face, the deflections measured included the effect of the anticlastic curvature.

The strain distribution along lines *J*, *K*, *L*, and *M* in the tensile face of Specimen No. 1 is shown in Fig. 6. From this figure it is clear that the experimental strain distribution is in good agreement with the shear-lag theory. On the opposite side of the specimen, compressive strain distributions are shown in Fig. 7; the comparison between the experimental and the theoretical values is not so good as in the tensile strain case.

It was impossible to measure the distribution along the *M* line on the compressive side because of the load application.

As all the specimens failed at midspan on the tensile face, it is concluded that the tensile strain caused the fracture.

Discussion of the Results

It is clear that the strain distribution on the tensile face is in good agreement with the shear-lag theory within the elastic limit. From the experimental standpoint, it is proposed to quantify the value of the shear-lag effect in a sandwich plate with stiffeners with the aid of the concept of an effective width.

The following equation defines the effective width

$$b_{\text{eff}} = \frac{\int_0^b \epsilon_x dy}{(\epsilon_x)_{y=b}} = \frac{1 + \dfrac{n-1}{kl}\tanh(kl)\left(1 - \dfrac{D}{D_0}\right)}{1 + \dfrac{n-1}{kl}\tanh(kl)} \tag{16}$$

Therefore, the bending rigidity D^{**} of the sandwich panel with stiffeners can be given as

$$D^{**} = D_s + (D_f + D_0) \times b_{\text{eff}}. \tag{17}$$

Values of D^{**} for each specimen are shown in Table 2. If D^{**} is substituted for D in the classical beam theory, the deflection of each specimen can be calculated; results so obtained are shown in Fig. 5.

From Fig. 5 it can be seen that the classical theory modified to include the effective width concept is closer to the experimental values than the shear-lag theory. Moreover, if $\tanh(kl)$ is set equal to unity, equation (16) is reduced to the following approximate equation:

$$b_{\text{eff}} = 1 - \frac{\dfrac{n-1}{kl}\cdot\dfrac{D}{D_0}}{1 + \dfrac{n-1}{kl}}. \tag{18}$$

The two nondimensional parameters involved $(n-1)/kl$ and D/D_0

Downloaded 01 May 2010 to 171.66.16.243. Redistribution subject to ASME license or copyright; see http://www.asme.org/terms/Terms_Use.cfm

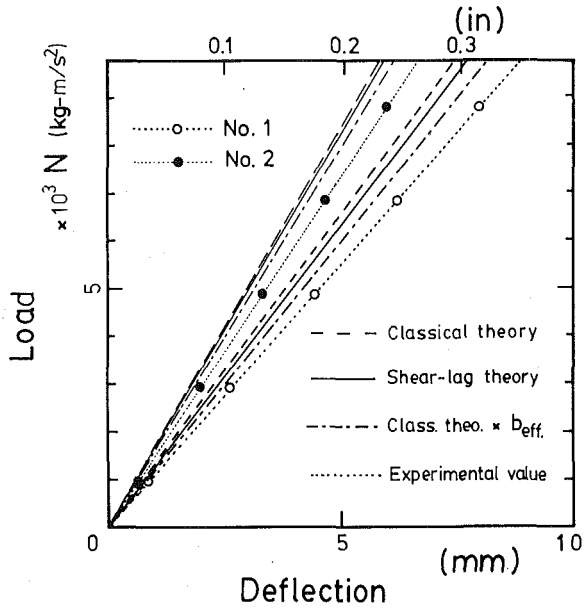

Fig. 5 Relationships between load and deflection

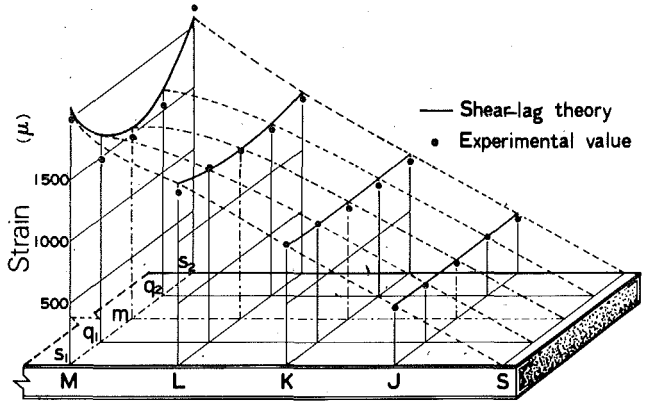

Fig. 6 Strain distribution in tensile face at $W = 6.8$ kN of Specimen No. 1

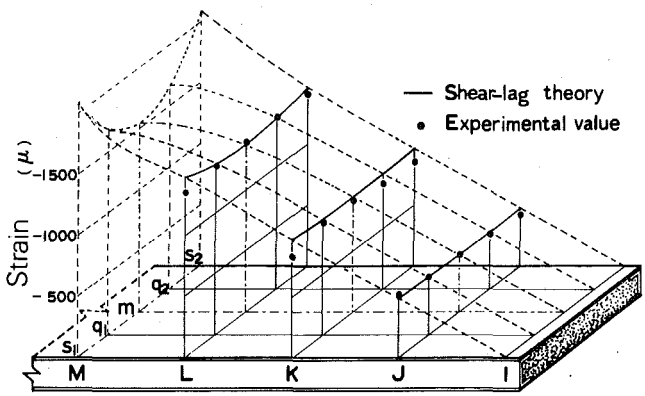

Fig. 7 Strain distribution in compressive face at $W = 6.8$ kN of Specimen No. 1

are given by the simple equations (3) and (8); therefore, the value of b_{eff} can be obtained easily.

Thus sandwich panels with stiffeners can be designed and their mechanical properties can be estimated through use of the modified classical beam theory.

Conclusions

The following are a few conclusions obtained from the aforementioned experimental and theoretical investigations:

1 The shear-lag theory of sandwich panels with stiffeners, obtained from a modified Reissner theory dealing with isotropic box beams, shows good agreement with the strain (or stress) distribution measured in the faces of test specimens.

2 The theoretical deflections including the shear-lag effect are about 10 percent smaller than the experimental values. In the experiments described, a striking difference between the shear-lag theory and the classical beam theory could not be seen, because of the use of stiffeners having a higher bending rigidity than the rigidity of the faces. If the sandwich panels had incorporated stiffeners having almost the same bending rigidity as the faces, the difference between the two analyses would have amounted to about 15 percent.

3 When the shear-lag effect is accounted for by means of the concept, it is possible to estimate more accurate values of the deflections of sandwich panels with stiffeners by using the modified classical beam theory.

Acknowledgment

The authors wish to thank Prof. N. J. Hoff of the Department of Mechanical Engineering, Aeronautical Engineering, and Mechanics at Rensselaer Polytechnic Institute, for his helpful suggestions.

References

1 Reissner, E., "Least Work Solutions of Shear-Lag Problems," *Journal of the Aeronautical Science*, Vol. 8, No. 7, 1941, pp. 284–291.

2 Reissner, E., "Analysis of Shear-Lag in Box Beam by the Principle of Minimum Potential Energy," *Quarterly of Applied Mathematics*, Vol. IV, No. 3, 1946, pp. 268–278.

3 Hoff, N. J., "Bending and Buckling of Rectangular Sandwich Plates," NACA TN 2225, Nov. 1950.

4 Chang, C. C., and Ebcioglu, I. K., "Elastic Instability of Rectangular Sandwich Panel of Orthotropic Core With Different Face Thicknesses and Materials," ASME JOURNAL OF APPLIED MECHANICS, Vol. 82, No. 3, 1960, pp. 474–480.

5 Timoshenko, S. P., and Goodier, J. N., *Theory of Elasticity*, 3rd ed., McGraw-Hill, New York, 1934, Chapter 9.

Downloaded 01 May 2010 to 171.66.16.243. Redistribution subject to ASME license or copyright; see http://www.asme.org/terms/Terms_Use.cfm

A. Rosen

Senior Lecturer,
Department of Aeronautical Engineering,
Technion–Israel Institute of Technology,
Technion City,
Haifa, Israel

The Effect of Initial Twist on the Torsional Rigidity of Beams—Another Point of View

Introduction

It was first pointed out by Chu [1] that if a thin prismatical bar or noncircular thin tube possesses an initial twist, its torsional rigidity will be greater than the same bar or tube without an initial twist. The relative increase of torsional rigidity depends on the amount of initial twist, the shape of cross section, the wall thickness, and the material of the beam. Chu derived a theory to calculate this increase in torsional rigidity and got a very good agreement when he compared theoretical and experimental results in the case of initially twisted rectangular steel strips. Chu's results became more familiar to the engineering community after appearing in the *Handbook of Engineering Mechanics* [2], edited by Flügge. The effect of increasing torsional rigidity by introducing initial twist is of interest in aircraft propellers, turbine blades, etc.

It was recently pointed out by Rosen and Friedman [3] that the system of coordinates which was used by Chu [1] and others who investigated the behavior of initially twisted beams, is in fact a nonorthogonal curvilinear system of coordinates. It was shown in that report that if the appropriate theory for curvilinear system of coordinates is used, certain terms which appeared using the inappropriate theory, disappear.

The weakness of the previous derivation appears if we imagine a solid circular beam that has a pretwist. This can be presented visually by simply painting some spirals on its surface. According to the results of [1] the torsional stiffness of the circular beam will increase. But, as pointed out by Chu [1], we certainly cannot increase the torsional rigidity of the beam in this way. Therefore, Chu restricted this theory to thin-walled sections.

As pointed out in [3] the derivation there does not include warping in order to compare the results with another derivation which also does not include warping. But, on the other hand, it was pointed out clearly that "Another phenomenon, known from the literature [1], is the fact that due to warping, pretwist can cause an increase in the torsional rigidity of thin prismatic bars." In addition, it was also noted that inclusion of warping and determination of its influence on the derivation can be observed by applying the same technique.

Contributed by the Applied Mechanics Division for publication in the JOURNAL OF APPLIED MECHANICS.

Discussion on this paper should be addressed to the Editorial Department, ASME, United Engineering Center, 345 East 47th Street, New York, N. Y. 10017, and will be accepted until September 1, 1980. Readers who need more time to prepare a discussion should request an extension from the Editorial Department. Manuscript received by ASME Applied Mechanics Division, March, 1978; final revision, November, 1979.

Following these notes the author of this paper in another report [4] traces the influence of initial twist on torsional rigidity, to the influence of initial twist on warping contributions. It is shown [4] that results which are obtained in this way overcome the problem of the pretwisted solid circular beam which was described previously. It is also shown why in certain cases a very good agreement between experimental and theoretical results was obtained, using the theory of [1]. In the report itself, the derivation is done using an orthogonal system of coordinates. In the Appendix a consistent derivation of the equations in a curvilinear-nonorthogonal system of coordinates, like the one used in [1] and other reseach, is presented. It is shown that using a nonorthogonal system of coordinates complicates the derivation considerably, but at the end yields the same results which are obtained using the simpler orthogonal system of coordinates.

In the present paper, the main derivations and results of [4] will be presented.

Theoretical Derivation

An initially twisted slender beam is shown in Fig. 1. The length of the beam is l and all the cross sections are identical. The initial twist is presented by a rotation β of the cross section about the x-axis. β is a function of x which can be either a linear function which represents constant initial twist, or any other function. As in [1] the derivation will be restricted to the case of constant initial twist given by k which implies

$$k = \frac{d\beta}{dx} \tag{1}$$

In Fig. 1 two different systems of coordinates are presented. The first system is the x,y,z system which is a fixed-in-space system. The axes y and z are orthogonal to x and to each other, which yields an orthogonal system of coordinates. The second system is the x,η,ζ system where η and ζ are the principal axes of the cross section of the beam, perpendicular to each other, and rotate with the cross section along x. The angle between the axis η and y equals β. It is clear that this system of coordinates is nonorthogonal (see also Appendix A of [4]). It must be emphasized that the initial state, including the initial twist, is stress-free.

At this stage a torque M_t is applied at the end of the beam, while no other external forces are applied. The beam deforms and the displacement vector of each point of the beam, $\overline{W}$, is given by

$$\overline{W} = u\hat{e}_x + v\hat{e}_y + w\hat{e}_z \tag{2}$$

where $\hat{e}_x$, $\hat{e}_y$, and $\hat{e}_z$ are unit vectors in the directions x,y, and z, re-

Copyright © 1980 by ASME
Downloaded 01 May 2010 to 171.66.16.243. Redistribution subject to ASME license or copyright; see http://www.asme.org/terms/Terms_Use.cfm

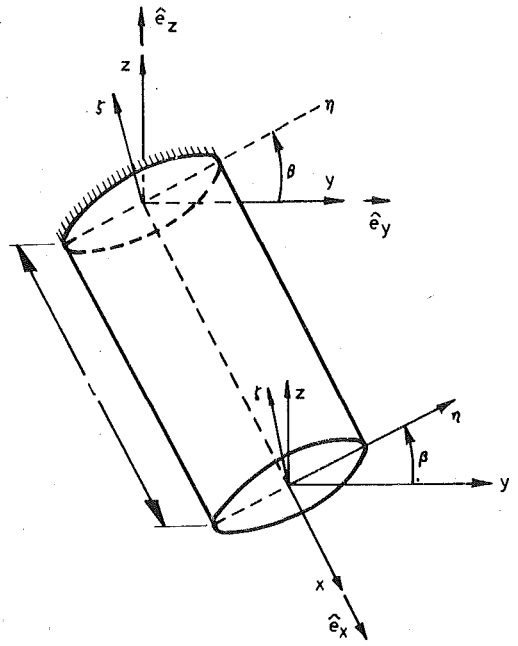

Fig. 1 General description of a beam with initial twist

spectively. It is assumed, as was done by Chu [1], that the deformation is a superposition of a Saint-Venant torque together with some axial motion u_1 of each cross section, unknown at this stage. The displacement components will then be

$$u = u_1 + \theta\Psi \tag{3a}$$
$$v = -\varphi z \tag{3b}$$
$$w = \varphi y \tag{3c}$$

Ψ is the warping function, φ is the angle of rotation of the cross section, and θ is the change in φ per unit length (for more details see, for example, Timoshenko [5]). At this stage it will be assumed that, at the ends, the beam is free to warp and so the torsion will be uniform along the beam. This means that θ is constant and if at the end $z = 0$, also $\varphi = 0$, one obtains

$$\varphi = \theta x \tag{4}$$

This assumption of ends free to warp is not essential and it is introduced only in order to simplify the derivation and present the scope of the paper more clearly. With a little more effort the equations for the case where warping is restrained at the ends, can be derived.

With the help of equations (2)–(4) the strain components are obtained as

$$\epsilon_{xx} = \frac{\partial u}{\partial x} = \frac{\partial u_1}{\partial x} + \theta\frac{\partial \Psi}{\partial x} \tag{5a}$$
$$\epsilon_{xy} = \frac{1}{2}\left(\frac{\partial u}{\partial y} + \frac{\partial v}{\partial x}\right) = \frac{1}{2}\theta\left(-z + \frac{\partial \Psi}{\partial y}\right) \tag{5b}$$
$$\epsilon_{xz} = \frac{1}{2}\left(\frac{\partial u}{\partial z} + \frac{\partial w}{\partial x}\right) = \frac{1}{2}\theta\left(y + \frac{\partial \Psi}{\partial z}\right) \tag{5c}$$
$$\epsilon_{yy} = \epsilon_{zz} = \epsilon_{yz} = 0 \tag{5d}$$

The strain energy of the beam per unit volume, using the assumptions of the beam theory (see, for example, Wempner [6, equation (8.131)] is

$$U = \frac{E}{2}\epsilon_{xx}^2 + 2G(\epsilon_{xy}^2 + \epsilon_{xz}^2) \tag{6}$$

Substituting equations (5) into (6) and adding the potential of the external load yields the potential of all the internal and external forces, V.

$$V = \int_0^l \iint_A \left\{\frac{E}{2}\left(\frac{\partial u_1}{\partial x} + \theta\frac{\partial \Psi}{\partial x}\right)^2 + \frac{G}{2}\theta^2\left[\left(-z + \frac{\partial \Psi}{\partial y}\right)^2 + \left(y + \frac{\partial \Psi}{\partial z}\right)^2\right]\right\} dx\, dy\, dz - M_t\int_0^l \theta dz \tag{7}$$

Integration of equation (7) over the cross section (y,z-directions) implies

$$V = \int_0^l \left\{\frac{E}{2}\left[A\left(\frac{\partial u_1}{\partial x}\right)^2 + 2\frac{\partial u_1}{\partial x}\theta S + \theta^2 K\right] + \frac{G}{2}J_s\theta^2 - M_t\theta\right\} dx \tag{8}$$

where

$$J_s = \iint_A \left[\left(-z + \frac{\partial \Psi}{\partial y}\right)^2 + \left(y + \frac{\partial \Psi}{\partial z}\right)^2\right] dy\, dz \tag{9a}$$
$$S = \iint_A \frac{\partial \Psi}{\partial x} dy\, dz \tag{9b}$$
$$K = \iint_A \left(\frac{\partial \Psi}{\partial x}\right)^2 dy\, dz \tag{9c}$$

J_s is the well known torsional stiffness of the uniform beam, without the initial twist, according to Saint-Venant torsion (see, for example, [5]). S and K are integrals associated with the change of the warping function with x. In the present case this change is associated with the initial twist only.

If the beam is in equilibrium V obtains a stationary value. This means that due to virtual variations δu and $\delta\theta$ in the deformation, the first variation of V becomes zero. Applying this principle to equation (8) yields

Nomenclature

A = cross-sectional area of the beam
B = section constant defined by equations (36.60) of [2].
E = Young's modulus of elasticity
$\hat{e}_x,\hat{e}_y,\hat{e}_z$ = unit vectors in the directions x, y, and z, respectively
G = shear modulus of elasticity
h = thickness of the thin prismatical cross section
I_p = polar moment of inertia of the cross section
J = torsional stiffness of the beam with an initial twist
J_s = torsional stiffness of the beam without an initial twist
K = section constant defined by equation (9c)
k = initial twist of the beam defined by equation (1)
l = length of the beam
M_t = torsional moment which is applied to the beam
S = section constant defined by equation (9b)
U = strain energy of the deformed beam
u,v,w = displacement components
u_1 = axial motion of the cross sections
V = total potential of the deformed beam
$\overline{W}$ = displacement vector of each point of the beam
x,y,z = orthogonal fixed-in-space system of coordinates
β = angle of initial twist of each cross section of the beam
ϵ_{ij} = components of the strain tensor in the x,y,z system of coordinates
η,ζ = principal axes of each cross section of the beam (see Fig. 1)
θ = elastic twist
φ = angle of elastic torsional rotation
Φ = torsion stress function of Prandtl
Ψ = warping function

Downloaded 01 May 2010 to 171.66.16.243. Redistribution subject to ASME license or copyright; see http://www.asme.org/terms/Terms_Use.cfm

$$\int_0^l \left\{ E\left(A\frac{\partial u_1}{\partial x} + S\theta\right)\frac{\partial \delta u_1}{\partial x} + \left[E\left(S\frac{\partial u_1}{\partial x} + K\theta\right) + GJ_s\theta - M_t\right]\delta\theta \right\} dx = 0 \quad (10)$$

Since δu_1 and $\delta\theta$ are arbitrary along the beam, equation (10) implies the following equations:

$$A\frac{\partial u_1}{\partial x} + S\theta = 0 \quad (11a)$$

$$GJ_s\theta + E\left(S\frac{\partial u_1}{\partial x} + K\theta\right) = M_t \quad (11b)$$

Substitution of the value of $\partial u_1/\partial x$ according to equation (11a) into equation (11b) implies

$$G\left[J_s + \frac{E}{G}\left(K - \frac{S^2}{A}\right)\right]\theta = M_t \quad (12)$$

If the total torsional stiffness of the beam with initial twist is denoted by J, then equation (12) implies

$$\frac{J}{J_s} = 1 + \frac{E}{GJ_s}\left(K - \frac{S^2}{A}\right) \quad (13)$$

One should note the similarity in the structure of equations (36.61) of [2] although the terms K and S are essentially different from B and I_p.

Equation (13) overcomes the difficulties which have been pointed out in the previous section. In the case of a circular shaft or circular tube Ψ is identically zero and so according to equations (9) S and K become zero. Therefore equation (13) implies that $J/J_s = 1$, as one expects from simple physical reasoning.

In what follows equation (13) will be used to calculate the increase in torsional stiffness due to initial twist in the case of thin-walled prismatical beams with initial twist.

Thin-Walled Prismatical Beam With Initial Twist

Fig. 2 presents the cross section of a thin prismatical beam. The cross section is symmetric around η and ζ and it may have any thin symmetric shape.

Using the Saint-Venant torsion theory one can write down the expression for Ψ. Since all the cross sections are identical, except for the initial rotation β, Ψ will not be a function of x, if described in η and ζ coordinates. Therefore

$$\frac{\partial \Psi}{\partial x}(\eta,\zeta) = \frac{\partial \Psi}{\partial \eta}\frac{\partial \eta}{\partial x} + \frac{\partial \Psi}{\partial \zeta}\frac{\partial \zeta}{\partial x} \quad (14)$$

From Fig. 2 one obtains

$$\eta = y\cos\beta + z\sin\beta$$
$$\zeta = -y\sin\beta + z\cos\beta \quad (15)$$

Differentiating (15) with respect to x, using equation (1), implies

$$\frac{\partial \eta}{\partial x} = (-y\sin\beta + z\cos\beta)\frac{d\beta}{dx} = \zeta k$$
$$\frac{\partial \zeta}{\partial x} = -(y\cos\beta + z\sin\beta)\frac{d\beta}{dx} = -\eta k \quad (16)$$

Substitution of equation (16) into (14) and then into equations (9b) and (9c) implies

$$S = k\iint_A \left(\frac{\partial \Psi}{\partial \eta}\zeta - \frac{\partial \Psi}{\partial \zeta}\eta\right) d\eta\, d\zeta \quad (17a)$$

$$K = k^2\iint_A \left(\frac{\partial \Psi}{\partial \eta}\zeta - \frac{\partial \Psi}{\partial \zeta}\eta\right)^2 d\eta\, d\zeta \quad (17b)$$

It is known from the Saint-Venant torsion theory that instead of using the warping function Ψ one can use the Prandtl stress function Φ (see, for example, Timoshenko [5] or Wempner [6], and the stress function of [5] must be divided by $G\theta$ to give the stress function of [6]). Here Wempner's notation is used. According to equations (6.201) of [6]:

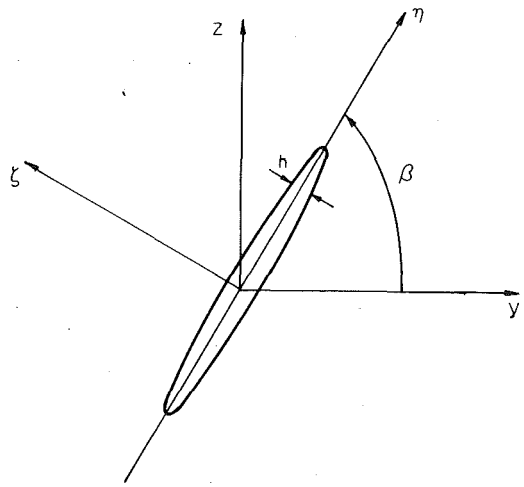

Fig. 2 Cross section of a thin-walled prismatical beam with initial twist

$$\frac{\partial \Psi}{\partial \eta} = \zeta + \frac{\partial \Phi}{\partial \zeta};\quad \frac{\partial \Psi}{\partial \zeta} = -\eta - \frac{\partial \Phi}{\partial \eta} \quad (18)$$

In the case of thin-walled cross section, like the one presented in Fig. 2, the stress function Φ can be approximated (recall the membrane analogy—for more details see [5 or 6]) as

$$\Phi \simeq \left(\frac{h}{2}\right)^2 - \zeta^2 \quad (19)$$

where h is the thickness of the cross section at each point along the η-axis. Substitution of equation (19) into equation (18) and then into equations (17) implies

$$S = k\iint_A \eta^2\left(1 - \underline{\frac{\zeta^2}{\eta^2}}\right) d\eta\, d\zeta \quad (20a)$$

$$K = k^2\iint \eta^4\left(1 - \underline{\frac{\zeta^2}{\eta^2}}\right)^2 d\eta\, d\zeta \quad (20b)$$

Since the cross section is thin, the underlined terms in equations (20) can be neglected. Then substitution of equations (20) into equation (13) gives the same result as one obtains from equation (36.61) of [2] under the same assumptions of thin cross sections.

Therefore it can be concluded that the present derivations give identical results to those of Chu [1] for the case of pretwisted thin-walled prismatical beams. According to experimental results which were obtained by Chu, the agreement between theory and experiment in this case is very good.

Conclusions

It was shown that when Chu's theory about torsional rigidity increase due to initial twist is applied to the case of a solid circular shaft or a thin circular tube, it gives results which contradict simple physical reasoning. It was also pointed out that while Chu uses the relations from the theory of elasticity which are only applicable to orthogonal systems of coordinates, he in fact applies them to nonorthogonal systems.

The present paper indicates that the increase in the torsional stiffness of a beam due to initial twist can be traced to the influence of this initial twist on the contributions of the warping of the cross sections. By doing this, all the difficulties associated with Chu's results are overcome. In the case of thin prismatical beams with initial twist, Chu obtained a very good agreement between theoretical and experimental results. It was shown that for this case the theoretical results of Chu are identical to those which are obtained using the present derivations. It must be emphasized that, unlike Chu's theory, the present approach does not limit the applicability of the theory to thin-walled cross sections, or small initial twist. The only limitation

Downloaded 01 May 2010 to 171.66.16.243. Redistribution subject to ASME license or copyright; see http://www.asme.org/terms/Terms_Use.cfm

is that the usual assumptions of the beam theory will be applicable to the case which is under consideration.

It is further shown in Appendix *A* of the detailed report [4] that using the nonorthogonal curvilinear system of coordinates properly gives the same results as the orthogonal system presented here, but the derivation is much more tedious and complicated.

References

1 Chen, C., "The Effect of Initial Twist on the Torsional Rigidity of Thin Prismatical Bars and Tubular Members," *Proceedings of the First U.S. National Congress of Applied Mechanics*, June 11–16, 1951, pp. 265–269.

2 Goodier, J. N., "Torsion," in *Handbook of Engineering Mechanics*, Flügge, W., ed., McGraw-Hill, New York, 1962, pp. 36–16—36–18, Chapter 36.

3 Rosen, A., and Friedman, P., "Nonlinear Equations of Equilibrium for Elastic Helicopter or Wind Turbine Blades Undergoing Moderate Deformations," UCLA-ENG-7718, Rev. ed., June 1977.

4 Rosen, A., "The Effect of Initial Twist on the Torsional Rigidity of Beams—Another Point of View," Technion—Israel Institute of Technology, Department of Aeronautical Engineering, TAE Report No. 360, Apr. 1978.

5 Timoshenko, S. P., and Goodier, J. N., "Torsion," in *Theory of Elasticity*, 3rd ed., McGraw-Hill, Kogakusha Ltd, 1970, Chapter 10.

6 Wempner, G., *Mechanics of Solids With Applications to Thin Bodies*, McGraw-Hill, New York, 1973.

Downloaded 01 May 2010 to 171.66.16.243. Redistribution subject to ASME license or copyright; see http://www.asme.org/terms/Terms_Use.cfm

D. H. Hodges

Aeromechanics Laboratory,
U. S. Army Research and Technology
Laboratories (AVRADCOM),
Ames Research Center,
Moffett Field, Calif. 94035

Torsion of Pretwisted Beams Due to Axial Loading

The equations for static torsional deformation of a pretwisted beam under axial loading are obtained from the principle of virtual work. Theory appropriate for a curvilinear coordinate system is used, and warp is included in the analysis from the outset. The present formulation yields the expected result that a pretwisted beam of noncircular cross section will untwist under tensile loading. A slender-beam approximation of the present theory is offered, and the resulting torsion-extension coupling terms are similar but not identical to those in common use in analyses of rotating blades. Numerical results indicate that the effect is not negligible when the ratio of shear modulus to extension modulus is small.

Introduction

In the analysis of pretwisted rotating blades it is necessary to consider the influence of axial forces on the torsion deformation. It is well known that the torsional rigidity is effectively increased in the presence of tensile stress [1, 2]. In the equations of Houbolt and Brooks [3] a term appears that is linear in pretwist, very similar to the term reflecting the increase in effective torsional rigidity due to tensile stress. This term gives rise to a torsion moment tending to untwist the pretwisted beam under tensile load. Researchers in rotor blade dynamics have tended to take this term for granted [4–6], leaving it in their equations without considering its origin.

The increase of torsional rigidity due to axial stress was first considered theoretically by Buckley [7] and extended by Wagner [8]. What has come to be known as Wagner's hypothesis is that the beam consists of straight "fibers" in the untwisted state that carry the axial stress. These fibers then run through the cross section in a twisted pattern when the beam is twisted. The axial stresses, assumed to act along the fibers, would then produce a couple in the twisted state about the neutral axis. Biot has shown, however, that the same increase in torsional rigidity can be obtained from application of general elasticity theory to untwisted beams [1] without the use of Wagner's hypothesis. Note that Wagner's hypothesis does *not* hold for a pretwisted beam. Although not specifically stated, the theory involving torsion of a pretwisted beam under axial stress embodied in the derivation found in [3] is based on Wagner's hypothesis. Thus the term involving an increase in the effective torsion rigidity is correct in [3–6], but the corresponding torsion moment that is due to pretwist must be reexamined.

Rosen and Friedmann [9] have examined the term that describes the torsion moment due to axial load and pretwist of [3]. They correctly point out that the term in [3] does not vanish for a beam of circular cross section, as it intuitively should, and that theory appropriate for a curvilinear coordinate system should be used. Through an argument based on values of G/E typical for isotropic materials, they conclude that the term in [3] is negligible even if correct. Since some rotor blades are built out of composite materials so that equivalent G/E-values may be much less than unity, this term may be more significant than indicated in [9]. After a lengthy derivation ignoring warp and based on a curvilinar coordinate system to describe the cross-section geometry, Rosen and Friedmann [9] conclude that there is *no* torsion of a pretwisted beam due to axial stress.

This conclusion is made in [9] contrary to physical reasoning and established theoretical and experimental results. Knowles and Reissner [10] showed that a pretwisted beam of thin rectangular cross section would experience torsional deformation in the presence of axial loads. Similar results hold for beams of general noncircular cross section [11]. Ohtsuka [12], using a generalized beam theory including warp as done in [11], obtained theoretical results with experimental confirmation indicating that rotating blades untwist. Hand calculation indicates that the two components of untwist, one due to axial stress in the presence of pretwist and the other due to propeller moment effects, are of the same order of magnitude.

The basic theory needed to examine the effect of axial stress on a pretwisted beam is found in Washizu's paper on pretwisted and curved beams [11]. In [11] the derivation begins with a nonorthogonal curvilinear coordinate system to describe the undeformed state. A warp variable is included, separate from torsion. Standard relations [13] are then invoked through the principle of virtual work to obtain the equilibrium equations for beams under arbitrary end loading. It

Contributed by the Applied Mechanics Division for publication in the JOURNAL OF APPLIED MECHANICS.

Discussion on this paper should be addressed to the Editorial Department, ASME, United Engineering Center, 345 East 47th Street, New York, N. Y. 10017, and will be accepted until September 1, 1980. Readers who need more time to prepare a discussion should request an extension from the Editorial Department. Manuscript received by ASME Applied Mechanics Division, April, 1979; final revision, September, 1979.

Copyright © 1980 by ASME
Downloaded 01 May 2010 to 171.66.16.243. Redistribution subject to ASME license or copyright; see http://www.asme.org/terms/Terms_Use.cfm

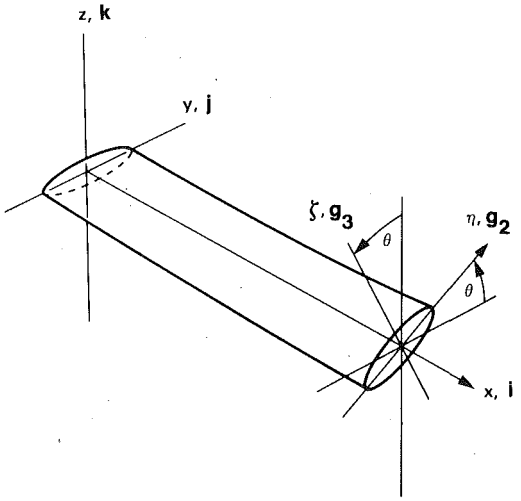

Fig. 1 Schematic of a pretwisted beam showing coordinate systems

is this approach that is also utilized in this paper, in somewhat specialized form, to concentrate on torsion of pretwisted beams under axial stress. A specialized version of the present theory suitable for slender-beam applications is proposed, and results obtained through it are compared with those of [3].

Undeformed State Geometry

We must first specify the geometry of the undeformed state of the beam. We assume that the pretwist angle is $\theta(x)$ where x is the axial coordinate (see Fig. 1). Bending of the beam is not considered and the beam elastic axis is straight. For loading, an axial force is applied that varies along the beam. At the root axial deflection, torsion, and warp are restrained. In a Cartesian coordinate system, the position vector of any point P in the beam interior is

$$\mathbf{r}_0 = x\mathbf{i} + y\mathbf{j} + z\mathbf{k}$$

where

$$y = \eta\cos\theta - \zeta\sin\theta \qquad (2)$$
$$z = \eta\sin\theta + \zeta\cos\theta$$

The coordinates η and ζ are along the local cross section major and minor axes, respectively, through the shear center. We define curvilinear coordinates ψ^1,ψ^2,ψ^3 as x,η,ζ and proceed as outlined in [11] and Chapter 4 of [13]. The covariant base vectors $\mathbf{g}_i = \partial\mathbf{r}_0/\partial\psi^i$ are

$$\left.\begin{aligned}\mathbf{g}_1 &= \mathbf{i} - \mathbf{j}\theta'(\eta\sin\theta + \zeta\cos\theta) + \mathbf{k}\theta'(\eta\cos\theta - \zeta\sin\theta)\\ \mathbf{g}_2 &= \mathbf{j}\cos\theta + \mathbf{k}\sin\theta\\ \mathbf{g}_3 &= -\mathbf{j}\sin\theta + \mathbf{k}\cos\theta\\ \theta' &= \frac{d\theta}{dx}\end{aligned}\right\} \qquad (3)$$

The elements of the covariant metric tensor for the undeformed state $g_{ij} = \mathbf{g}_i\cdot\mathbf{g}_j$ are given as

$$\left.\begin{aligned}g_{11} &= 1 + \theta'^2(\eta^2 + \zeta^2)\\ g_{12} &= -\zeta\theta' = g_{21}\\ g_{13} &= \eta\theta' = g_{31}\\ g_{22} = g_{33} &= 1; \quad g_{23} = g_{32} = 0\end{aligned}\right\} \qquad (4)$$

For later use we define a local Cartesian system y^1,y^2,y^3 [13, pp. 84, 85], at the point P. Now,

$$d\mathbf{r}_0 = \frac{\partial\mathbf{r}_0}{\partial\psi^i}d\psi^i = \mathbf{j}_i dy^i \quad \text{(summation convention)} \qquad (5)$$

where locally the vectors $\mathbf{j}_i$ are along $\mathbf{i},\mathbf{g}_2,\mathbf{g}_3$. Thus

$$\frac{\partial\psi^k}{\partial y^i} = g^{kl}(\mathbf{j}_i\cdot\mathbf{g}_l) \qquad (6)$$

where the tensor g^{kl} is the contravariant metric tensor for the undeformed state and

$$g^{ik}g_{kj} = \delta^i_j \text{ (Kronecker delta)} \qquad (7)$$

thus

$$\left.\begin{aligned}g^{11} &= 1\\ g^{12} = g^{21} &= \zeta\theta'\\ g^{13} = g^{31} &= -\eta\theta'\\ g^{22} &= 1 + \zeta^2\theta'^2\\ g^{23} = g^{32} &= -\eta\zeta\theta'^2\\ g^{33} &= 1 + \eta^2\theta'^2\end{aligned}\right\} \qquad (8)$$

and

$$\left.\begin{aligned}&\frac{\partial\psi^1}{\partial y^1} = \frac{\partial\psi^2}{\partial y^2} = \frac{\partial\psi^3}{\partial y^3} = 1\\ &\frac{\psi^1}{\partial y^2} = \frac{\partial\psi^1}{\partial y^3} = \frac{\partial\psi^2}{\partial y^3} = \frac{\partial\psi^3}{\partial y^2} = 0\\ &\frac{\partial\psi^2}{\partial y^1} = \zeta\theta'; \quad \frac{\partial\psi^3}{\partial y^1} = -\eta\theta'\end{aligned}\right\} \qquad (9)$$

Deformed State Geometry

The covariant metric tensor for the deformed state is needed for deriving the strains. We start with the position vector for the deformed state assumed to be

$$\mathbf{r} = [x + u + \lambda(x,\eta,\zeta)\alpha]\mathbf{i} + [\eta\cos(\theta+\phi) - \zeta\sin(\theta+\phi)]\mathbf{j} + [\eta\sin(\theta+\phi) + \zeta\cos(\theta+\phi)]\mathbf{k} \qquad (10)$$

where ϕ is the torsion deflection, u is the axial deflection, $\lambda(x,\eta,\zeta)$ is the warp function for the cross section at x, and α is the warp amplitude. Now, covariant base vectors for the deformed state, $\mathbf{G}_i = \partial\mathbf{r}/\partial\psi^i$ are obtained from equation (10)

$$\left.\begin{aligned}\mathbf{G}_1 &= (1 + u' + \lambda_x\alpha + \lambda\alpha')\mathbf{i}\\ &- (\theta' + \phi')[\eta\sin(\theta+\phi) + \zeta\cos(\theta+\phi)]\mathbf{j}\\ &+ (\theta' + \phi')[\eta\cos(\theta+\phi) - \zeta\sin(\theta+\phi)]\mathbf{k}\\ \mathbf{G}_2 &= \lambda_\eta\alpha\mathbf{i} + \mathbf{j}\cos(\theta+\phi) + \mathbf{k}\sin(\theta+\phi)\\ \mathbf{G}_3 &= \lambda_\zeta\alpha\mathbf{i} - \mathbf{j}\sin(\theta+\phi) + \mathbf{k}\cos(\theta+\phi)\end{aligned}\right\} \qquad (11)$$

where $\lambda_x = \partial\lambda/\partial x$, $\lambda_\eta = \partial\lambda/\partial\eta$, $\lambda_\zeta = \partial\lambda/\partial\zeta$. The elements of the covariant metric tensor for the deformed state are $G_{ij} = \mathbf{G}_i\cdot\mathbf{G}_j$ and are obtained from equation (11).

$$\left.\begin{aligned}G_{11} &= 1 + 2u' + 2\lambda_x\alpha + 2\lambda\alpha' + u'^2 + 2u'\lambda_x\alpha + 2u'\lambda\alpha'\\ &+ \lambda_x^2\alpha^2 + 2\lambda_x\lambda\alpha\alpha' + \lambda^2\alpha'^2 + (\theta' + \phi')^2(\eta^2 + \zeta^2)\\ G_{12} = G_{21} &= \lambda_\eta\alpha(1 + u' + \lambda_x\alpha + \lambda\alpha') - \zeta(\theta' + \phi')\\ G_{13} = G_{31} &= \lambda_\zeta\alpha(1 + u' + \lambda_x\alpha + \lambda\alpha') + \eta(\theta' + \phi')\\ G_{22} &= 1 + \lambda_\eta^2\alpha^2\\ G_{23} = G_{32} &= \lambda_\eta\lambda_\zeta\alpha^2\\ G_{33} &= 1 + \lambda_\zeta^2\alpha^2\end{aligned}\right\} \qquad (12)$$

The components of the Green strain tensor (symmetric) are obtained from equations (4) and (12) using the relation $2f_{ij} = G_{ij} - g_{ij}$ so that

Downloaded 01 May 2010 to 171.66.16.243. Redistribution subject to ASME license or copyright; see http://www.asme.org/terms/Terms_Use.cfm

$$
\left.
\begin{aligned}
f_{11} &= u' + \lambda_x\alpha + \lambda_x a' + \frac{u'^2}{2} + u'\lambda_x\alpha + u'\lambda\alpha' + \frac{\lambda_x^2\alpha^2}{2} \\
&\quad + \lambda_x\lambda\alpha\alpha' + \frac{\lambda^2\alpha'^2}{2} + \left(\theta'\phi' + \frac{\phi'^2}{2}\right)(\eta^2 + \zeta^2) \\
2f_{12} &= 2f_{21} = \lambda_\eta\alpha(1 + u' + \lambda_x\alpha + \lambda\alpha') - \zeta\phi' \\
2f_{13} &= 2f_{31} = \lambda_\zeta\alpha(1 + u' + \lambda_x\alpha + \lambda\alpha') + \eta\phi' \\
f_{22} &= \frac{\lambda_\eta^2\alpha^2}{2} \\
2f_{23} &= 2f_{32} = \lambda_\eta\lambda_\zeta\alpha^2 \\
f_{33} &= \frac{\lambda_\zeta^2\alpha^2}{2}
\end{aligned}
\right\} \quad (13)
$$

Principle of Virtual Work and Equilibrium Equations

The principle of virtual work with stresses and strains expressed in the local Cartesian reference system y^1, y^2, y^3 for an arbitrary three-dimensional body in the absence of surface forces is found in [13] as

$$
\int\int\int_V \sigma^{ij}\delta e_{ij}\, dV = \int\int\int_V \mathbf{P}\cdot\delta\mathbf{r}\, dV \qquad (14)
$$

where V is the volume of the body in its undeformed state. The stresses σ^{ij} are assumed to be related to the strains e_{ij} in the following way:

$$
\sigma^{ij} = \frac{E}{1-2\nu}\frac{e_{kk}}{3}\delta_{ij} + 2G\left(e_{ij} - \frac{e_{kk}}{3}\delta_{ij}\right) \qquad (15)
$$

where G and E are shear and extension moduli, respectively, and ν is Poisson's ratio. For a pretwisted beam, the stresses associated with coordinates normal to g_1 should be negligible. It is much simpler, however, to neglect stresses associated with cross-section principal axes $\eta(y^2)$ and $\zeta(y^3)$ so that $\sigma^{22} = \sigma^{23} = \sigma^{33} = 0$. Equation (15) then reduces to

$$
\left.
\begin{aligned}
\sigma^{11} &= Ee_{11} \\
\sigma^{12} &= 2Ge_{12} \\
\sigma^{13} &= 2Ge_{13}
\end{aligned}
\right\} \quad (16)
$$

The differences introduced by the present simpler approach are on the order of elongations and shears with respect to unity and are thus negligible for a small strain analysis. Behavior of a composite beam may be analyzed using equation (16) if G and E are allowed to be independent quantities.

The principle of virtual work becomes

$$
\int_0^L \iint_A (\sigma^{11}\delta e_{11} + 2\sigma^{12}\delta e_{12} + 2\sigma^{13}\delta e_{13})dA\, dx = \int_0^L P\,\delta u\, dx \qquad (17)
$$

where P is the applied axial load per unit length. The strains e_{11}, e_{12}, e_{13} must now be found. Washizu [13, p. 85] relates the strains in the local Cartesian system e_{ij} to components of Green strain f_{kl} as follows:

$$
e_{ij} = \frac{\partial\psi^k}{\partial y^i}\frac{\partial\psi^l}{\partial y^j}f_{kl} \qquad (18)
$$

If squares and products of elongation and shears are neglected, the strain components may be written on the basis of equations (9), (13), and (18).

$$
\left.
\begin{aligned}
e_{11} &= u' + \lambda_x\alpha + \lambda\alpha' + (\eta^2 + \zeta^2)\frac{\phi'^2}{2} + (\lambda_\eta\zeta - \lambda_\zeta\eta)\alpha\theta' \\
2e_{12} &= \lambda_\eta\alpha - \zeta\phi' \\
2e_{13} &= \lambda_\zeta\alpha + \eta\phi'
\end{aligned}
\right\} \quad (19)
$$

While the term $(\eta^2 + \zeta^2)\phi'^2/2$ may appear to be composed of the squares of shears, it is shown clearly to represent an elongation in [14]. Straightforward application of the principle of virtual work, equation (17), yields the equilibrium equations. If we assume the analogous untwisted beam to be prismatic, then $\lambda_x = 0$. For simplicity we assume also that the cross section is homogeneous and doubly symmetric. The equations of equilibrium become

$$
\left.
\begin{aligned}
&-\left(EAu' + EI_p\frac{\phi'^2}{2} + ED\theta'\alpha\right)' = P \\
&\left(EI_pu' + EB\frac{\phi'^2}{2} + ED_1\theta'\alpha + GI_p\right)\phi' - GD\alpha = 0 \\
&-(EC\alpha')' + ED\theta'u' + ED_1\theta'\frac{\phi'^2}{2} \\
&\qquad + ED_2\theta'^2\alpha + GD(\alpha - \phi') = 0
\end{aligned}
\right\} \quad (20)
$$

where

$$
\begin{aligned}
A &\equiv \iint_A d\eta\, d\zeta; \quad C \equiv \iint_A \lambda^2 d\eta\, d\zeta \\
I_p &\equiv \iint_A (\eta^2 + \zeta^2)d\eta\, d\zeta; \quad D_2 \equiv \iint_A (\zeta\lambda_\eta - \eta\lambda_\zeta)^2 d\eta\, d\zeta \\
D &\equiv \iint_A (\zeta\lambda_\eta - \eta\lambda_\zeta)d\eta\, d\zeta = \iint_A (\lambda_\eta^2 + \lambda_\zeta^2)d\eta\, d\zeta \qquad (21) \\
D_1 &\equiv \iint_A (\eta^2 + \zeta^2)(\zeta\lambda_\eta - \eta\lambda_\zeta)d\eta\, d\zeta; \quad B \equiv \iint_A (\eta^2 + \zeta^2)^2 d\eta\, d\zeta
\end{aligned}
$$

The section constants associated with the warp function λ may be evaluated analytically, where possible, by simple power series approximations [13, p. 128] or by finite-element discretization [12].

Equations (20) are in agreement with similar equations in [11] except that nonlinear terms are retained. The boundary conditions are

$$
u = 0,\ \phi = 0,\ \alpha = 0 \quad \text{at} \quad x = 0 \qquad (22a)
$$

$$
\left.
\begin{aligned}
EC\alpha' &= 0 \\
EAu' + EI_p\frac{\phi'^2}{2} + ED\theta'\alpha &= 0
\end{aligned}
\right\} \quad \text{at} \quad x = L \qquad (22b)
$$

The local tension force T is

$$
T = EAu' + EI_p\frac{\phi'^2}{2} + ED\theta'\alpha \qquad (23)
$$

Equations (20) and (22b) reveal that

$$
T = \int_x^L P dx \qquad (24)
$$

and u' may be eliminated by making use of

$$
u' = \frac{T}{EA} - \frac{I_p}{A}\frac{\phi'^2}{2} - \frac{D\theta'}{A}\alpha \qquad (25)
$$

Thus the second and third of equations (20) become

$$
\left(GI_p + \frac{TI_p}{A}\right)\phi' - GD\alpha + E\left(B - \frac{I_p^2}{A}\right)\frac{\phi'^3}{2} + E\theta'\left(D_1 - \frac{DI_p}{A}\right)\alpha\,\phi' = 0 \qquad (26a)
$$

$$
-(EC\alpha')' + E\theta'\left(D_1 - \frac{DI_p}{A}\right)\frac{\phi'^2}{2} + E\theta'^2\left(D_2 - \frac{D^2}{A}\right)\alpha + GD(\alpha - \phi') = -\frac{TD\theta'}{A} \qquad (26b)
$$

Equations (26) constitute the coupled warp-torsion equations for a pretwisted beam under axial load. The equations contain terms analogous to those noted as important for high twist in [3, 6, 15]. The terms in equations (26), however, are not identical to those of [3, 4–6, 15] because a curvilinear coordinate system was not used in the earlier work. While the differences introduced by a curvilinear coordinate

Downloaded 01 May 2010 to 171.66.16.243. Redistribution subject to ASME license or copyright; see http://www.asme.org/terms/Terms_Use.cfm

system are not large for some configurations, it is not known just how significant the effects may be for the general case. These points are also discussed in [16] in which the torsion of pretwisted beams in the *absence* of axial loads is analyzed. Slight differences in the results of the present paper when specialized for no axial loads and those of [16] when specialized for no applied torsion moment can be traced to the use in this paper of an independent warp variable.

For a circular cross section $\lambda = D = D_1 = D_2 = C = 0$, the second of equations (26) vanishes completely and thus α is arbitrary and $\phi' \equiv 0$ for all T, as expected.

Slender-Beam Approximation

A linear, slender-beam approximation of equations (26) is desirable to simplify the analysis and is sufficient to illustrate the effect we have set out to examine. Thus we can use the relation

$$GD\alpha \cong \left(GI_p + \frac{TI_p}{A}\right)\phi' \tag{27}$$

from equations (26*a*) and eliminate α in equation (26*b*) obtaining

$$\left(GI_p + \frac{TI_p}{A} - GD\right)\phi' = -\frac{TD\theta'}{A} \tag{28}$$

The other linear terms in equation (26*b*) are negligible for beams that are sufficiently slender. The standard torsion constant J is given by [13, pp. 116, 119]

$$\left.\begin{aligned} J &\equiv \iint_A [(\zeta - \lambda_\eta)^2 + (\eta + \lambda_\zeta)^2]d\eta\, d\zeta \\ &= \iint_A (\eta^2 + \zeta^2 - \zeta\lambda_\eta + \eta\lambda_\zeta)d\eta\, d\zeta = I_p - D \end{aligned}\right\} \tag{29}$$

Thus equation (28) becomes

$$\left(GJ + \frac{TI_p}{A}\right)\phi' = -\underline{\underline{\frac{T}{A}(I_p - J)\theta'}} \quad \text{(present)} \tag{30}$$

The single underlined term reflects the increase in torsion rigidity due to axial tension T [1, 2]. This term can be obtained using Wagner's hypothesis as well [3, 7, 8]. The double underlined term is the moment due to pretwist and is different from the corresponding term derived from Wagner's hypothesis [3]

$$\left(GJ + \frac{TI_p}{A}\right)\phi' = -\frac{TI_p}{A}\theta' \quad \text{(Houbolt and Brooks)} \tag{31}$$

and from the analogous result in [9]

$$\left(GJ + \frac{TI_p}{A}\right)\phi' = 0 \quad \text{(Rosen and Friedmann)} \tag{32}$$

Equation (32) is clearly unreasonable for any general noncircular cross section. Rosen and Friedmann [9] neglected warp *a priori* rather than taking a slender-beam approximation for its effects. Equation (31) is only unreasonable for circular cross sections. Examination of equation (30), however, reveals that the right-hand side vanishes, as it should, for circular cross sections for which $\lambda = 0$ and $J = I_p$. To ascertain the numerical difference in the foregoing relations it is necessary to treat a specific configuration.

It should be noted that the term involving θ'^2 in equation (26*b*) can have a significant effect on the torsional rigidity for beams with very thin cross sections [15, 16]. It is beyond the scope of the present paper, however, to examine the effects of this term in detail. The term is negligible for slender beams that have thin elliptical cross sections with principal axes $2a$ and $2b$ if

$$\frac{\theta'^2 r^2}{16(G/E)t^2 + 4(T/EA)} \ll 1 \tag{33}$$

where t is the thickness ratio b/a, and r is the slenderness ratio a/L. We assume that the condition in equation (33) is satisfied so that the torsion per unit pretwist for a slender beam with elliptical cross section is given by

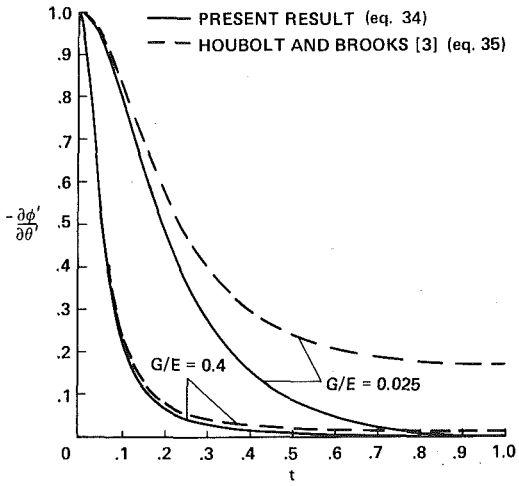

Fig. 2 Torsion per unit pretwist of a slender beam with elliptical cross section

$$\frac{\partial\phi'}{\partial\phi'} = -\frac{(T/EA)(1 - t^2)^2}{4(G/E)t^2 + (T/EA)(1 + t^2)^2} \quad \text{(present)} \tag{34}$$

Based on [3], the analogous expression is

$$\frac{\partial\phi'}{\partial\theta'} = -\frac{(T/EA)(1 + t^2)^2}{4(G/E)t^2 + (T/EA)(1 + t^2)^2} \quad \text{(Houbolt and Brooks)} \tag{35}$$

Results from equations (34) and (35) are plotted in Fig. 2 for $T/EA = 0.005$ and two values of $G/E = 0.4$ and 0.025. The larger value is typical for isotropic materials whereas the smaller value is typical for some composite materials. For the larger value of G/E the Houbolt and Brooks expression agrees well with the present result. Although the disparity increases with t, the amount of torsion itself decreases sharply. For the larger value of G/E, however, the difference between the two results is greater and the torsion due to axial load of a pretwisted beam is a non-negligible effect. The present theory, unlike that of [3], gives the correct result of no torsion for a circular cross section ($t = 1$).

Conclusion

The equilibrium equations for static torsional deformation of a pretwisted beam are obtained from the principle of virtual work. Theory appropriate for a curvilinear coordinate system is used in the present paper, and a warping variable is included in the analysis from the outset. The present results show clearly that a pretwisted beam of noncircular cross section does in fact untwist under tensile load. The commonly used expression for the coupling of torsion and extension through pretwist derived in [3] is seen to be in good agreement with the slender-beam approximation offered at the end of the present derivation when the cross section is thin and when the ratio of shear modulus to extension modulus is typical of isotropic materials. When the ratio of moduli is small, typical of some composite materials, the effect is more pronounced than otherwise, and the agreement between the present result and that of [3] is not as good.

References

1 Biot, M. A., "Increase of Torsional Stiffness of a Prismatic Bar Due to Axial Tension," *Journal of Applied Physics*, Vol. 10, 1939, pp. 860–864.

2 Goodier, J. N., "Elastic Torsion in the Presence of Initial Axial Stress," ASME JOURNAL OF APPLIED MECHANICS, Vol. 17, Dec. 1950, pp. 383–387.

3 Houbolt, J C., and Brooks, G. W., "Differential Equations of Motion of Combined Flapwise Bending, Chordwise Bending, and Torsion of Twisted, Nonuniform Rotor Blades," NACA Report 1346, 1958.

4 Hodges, D. H., and Dowell, E. H., "Nonlinear Equations of Motion for the Elastic Bending and Torsion of Twisted Nonuniform Rotor Blades," NASA TN D-7818, 1974.

5 Friedmann, P., "Influence of Structural Damping, Preconing, Offsets

Downloaded 01 May 2010 to 171.66.16.243. Redistribution subject to ASME license or copyright; see http://www.asme.org/terms/Terms_Use.cfm

and Large Deflections on the Flag-Lag-Torsional Stability of a Cantilevered Rotor Blade," *AIAA Journal*, Vol. 15, No. 2, Feb. 1977, pp. 149–158.

6 White, W. F., "The Influence of High Twist on the Dynamics of Rotating Blades," Fourth European Rotorcraft and Powered Lift Aircraft Forum, Stresa, Italy, Paper No. 25, Sept. 1978.

7 Buckley, J. C., "Bifilar Property of Twisted Strips," *Philosophical Magazine*, Vol. 28, 1914, pp. 778–787.

8 Wagner, H., "Torsion and Buckling of Open Sections," NACA TM 807, 1936.

9 Rosen, A., and Friedmann, P., "Nonlinear Equations of Equilibrium for Elastic Helicopter or Wind Turbine Blades Undergoing Moderate Deformation," University of California, Los Angeles, School of Engineering and Applied Science Report UCLA-ENG-7718 (revised edition), June 1977.

10 Knowles, J. K., and Reissner, E., "Torsion and Extension of Helicoidal Shells," *Quarterly of Applied Mathematics*, Vol. 17, No. 4, 1960, pp. 409–422.

11 Washizu, K., "Some Considerations on a Naturally Curved and Twisted Slender Beam," *Journal of Mathematics and Physics*, Vol. 43, No. 2, June 1964, pp. 111–116.

12 Ohtsuka, M., "Untwist of Rotating Blades," ASME *Journal of Engineering for Power*, Vol. 97, No. 2, Apr. 1975, pp. 180–187.

13 Washizu, K., *Variational Methods in Elasticity and Plasticity*, 2nd ed., Pergamon Press, Oxford, 1968.

14 Dixon, P. G. C., "Derivation of Control Loads for Bearingless Rotor Systems," *Proceedings of the AHS/NASA Ames Conference on Helicopter Structures Technology*, Paper No. 3, Nov. 1977.

15 Chu, C., "The Effect of Initial Twist on the Torsional Rigidity of Thin Prismatical Bars and Tubular Members," *Proceedings of the First U.S. National Congress of Applied Mechanics*, 1952, pp. 265–269.

16 Rosen, A., "The Effect of Initial Twist on the Torsional Rigidity of Beams—Another Point of View," TAE Report No. 360, Technion Israel Institute of Technology, Apr. 1978.

Downloaded 01 May 2010 to 171.66.16.243. Redistribution subject to ASME license or copyright; see http://www.asme.org/terms/Terms_Use.cfm

D. A. Peters

Professor,
Department of Mechanical Engineering,
Washington University,
Box 1185,
St. Louis, Mo. 63130
Mem. ASME

D. H. Hodges

Research Scientist,
Aeromechanics Laboratory,
U. S. Army R & T Laboratories
(AVRADCOM),
Ames Research Center,
Moffett Field, Calif. 94035

In-Plane Vibration and Buckling of a Rotating Beam Clamped Off the Axis of Rotation

Some work on the in-plane vibrations and buckling of rotating beams, clamped off the axis of rotation, is unclear as to behavior in the limit of small stiffness and small off-clamping. In this paper, asymptotic expansion formulas are developed for both small and large values of stiffness and off-clamping parameters. A composite expansion formula is also introduced as an engineering approximation to the buckling curve for all values of parameters. The present results agree quite well with an exact numerical solution and indicate that buckling can occur for arbitrarily small stiffness and off-clamping.

Introduction

The vibration of rotating beams in the limit of small bending stiffness (or, equivalently, large rotational speed) is a problem of practical as well as mathematical interest. The practical interest stems from the interest in helicopter rotor blades and spinning satellites, which have small stiffness, and the mathematical interest stems from the interesting behavior of the solution when the nondimensional ratio, η (proportional to bending stiffness and inversely proportional to the square of rotational speed), tends toward zero. The practical and mathematical interests are closely related to each other because conventional Ritz-Galerkin procedures (used for practical frequency calculations) show poor convergence when η is small compared to unity. Perturbation solutions have been found to be, therefore, helpful in obtaining practical frequency calculations for beams with small stiffness.

The first approximate solutions to this problem based on asymptotic expansions were developed independently and simultaneously by three investigators [1–3]. Colin [1], the first to publish asymptotic frequency and mode-shape formulas for out-of-plane bending, analyzed primarily the first-order characteristics of the first two natural frequencies. He then used the result as a tool in a general stability analysis. Peters [2] analyzed both out-of-plane and in-plane bending and developed general, first-order formulas for all natural frequencies and modes. He also developed second-order formulas for the fundamental frequency and mode. Peters also developed expansions in the limit of large η, and he combined those with the small-η expansions to obtain "composite expansions" that give accurate frequencies and modes throughout the entire range of η.

In contrast to [1, 2], in which the expansion formulas were developed as tools in an overall engineering analysis, Lakin [3] concentrated primarily on the mathematical aspects of the problem and especially on the turning point of the equation, which occurs at the beam tip. Although no frequency formulas are given in [3], the paper gives a very carefully done analysis of the mathematical intricacies of the problem, intricacies which were generally overlooked in [1, 2]. In [4], Lakin and Ng continue the rigorous development of [3] and obtain complete frequency and mode-shape formulas. The results of [4] confirm that the less careful expansions in [1, 2] are indeed correct; and all three solutions are thus consistent, although the results in [4] certainly go much further than those in [1, 2].

During the time that the aforementioned work was being performed on the frequency of rotating beams, related work was being performed on the buckling of rotating beams clamped off the axis of rotation (Fig. 1). The off-clamping allows for destabilizing centrifugal loads, whereas the centrally clamped beam cannot buckle. Mostaghel and Tadjbachsh [5] outlined the general behavior of off-clamped beams in terms of the η required for buckling as a function of off-clamping, $\alpha = R/L$. Their results were for generally large values of η and α, although they did present results for η as low as 0.05 ($\alpha = 0.5$). They also noted that for $\eta < 0.05$ ($\alpha < 0.5$) the computation time becomes prohibitive, as is also the case for frequency calculations, [2]. Nachman [6], commenting on the work in [5], concluded that buckling is impossible for $\alpha < 0.5$. He also obtained a perturbation expansion for the buckling curve at large values of η and α, based on a supposed singularity at $\alpha = 0.5$.

Lakin [7], presumably motivated by the work in [5, 6], extended his perturbation analysis to include the calculation of frequencies of off-clampled beams. Subsequently, Lakin and Nachman collaborated to develop perturbation solutions for the buckling of off-clamped beams, [8]. Reference [8], although following the same high mathematical standards as Lakin's other work, also offers three physical interpretations that need to be clarified:

1 The paper speaks of "unstable vibrations" for off-clamped beams. Since one does not encounter unstable vibrations in a con-

Contributed by the Applied Mechanics Division for publication in the JOURNAL OF APPLIED MECHANICS.

Discussion on this paper should be addressed to the Editorial Department, ASME, United Engineering Center, 345 East 47th Street, New York, N. Y. 10017, and will be accepted until September 1, 1980. Readers who need more time to prepare a discussion should request an extension from the Editorial Department. Manuscript received by ASME Applied Mechanics Division, August, 1979; final revision, December, 1979.

Copyright © 1980 by ASME
Downloaded 01 May 2010 to 171.66.16.243. Redistribution subject to ASME license or copyright; see http://www.asme.org/terms/Terms_Use.cfm

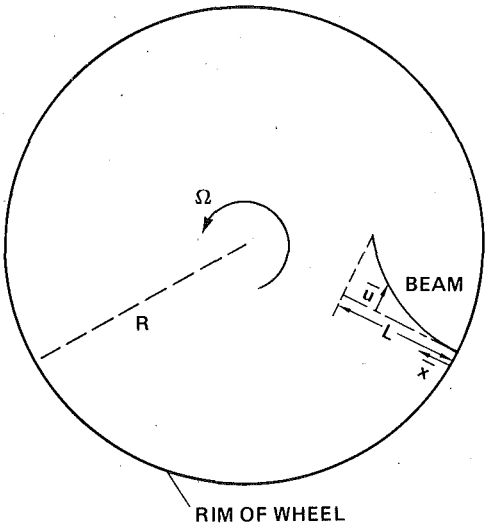

Fig. 1 Flexible beam cantilevered to the rim of a rigid wheel

servative system, this terminology is unfortunate. The physical mechanism (buckling, not true vibration) is clarified, however, by a statement in [8] that the "vibrations will grow in time without oscillations."

2 According to the last paragraph of [8], asymptotic methods imply that $1/\eta$ for buckling "cannot be both large and positive." This appears to be incorrect on physical grounds in that small η (large $1/\eta$) should imply a soft (and thus easily buckled) configuration.

3 The last paragraph of [8] states that a Ritz-Galerkin technique shows that buckling can occur for values of the off-clamping parameter, α, as low as 0.05. The frequency formulas in [2], however, indicate that buckling is possible even when α tends toward zero, because the in-plane frequency vanishes for $\alpha = \eta = 0$, thus contradicting conclusions 2 and 3 as well as most of the conclusions of [6]. Fig. 4 of [8] also seems to show that the point $\alpha = \eta = 0$ is a point on the buckling boundary, although this point is actually excluded if the limiting conditions specified in [8] are strictly enforced.

Recently Lakin and Nachman [9], proceeding on the suggestion of the present authors, obtained an asymptotic approximation of the frequency parameter for small η and α. The resulting small η and α buckling formula was first obtained by the present authors in a different manner, details of which are presented herein. In this paper we endeavor to clarify the earlier conclusions of [6, 8] and also analyze the off-clamped beams for large values of η and α. The two analyses (small and large η, α) are combined to give an approximate, composite expansion for all values of η and α. Results of this expansion are then compared with previous work.

Mathematical Description

The physical model of a rotating, off-clamped beam is sketched in Fig. 1. The nondimensional equations for vibrations in the plane of rotation are given from [5] as

$$\eta u'''' - \frac{1}{2}[(1-x^2)u']' - (\lambda+1)u + \alpha[(1-x)u']' = 0 \quad (1a)$$

$$u(0) = u'(0) = u''(1) = u'''(1) = 0 \quad (1\,b\text{–}e)$$

where

$$u = \frac{\bar{u}}{L};\quad \lambda = \frac{\omega^2}{\Omega^2};\quad \eta = \frac{EI}{\mu\Omega^2 L^4};\quad \alpha = \frac{R}{L};\quad x = \frac{\bar{x}}{L};\quad (\,)' = \frac{d}{dx} \quad (2\,a\text{–}f)$$

The parameter η is the bending stiffness (or rotational speed) parameter. When $\eta = 0$, the u', u'', and u''' boundary conditions are relaxed, and the system degenerates to a second-order equation with turning points at $x = 1$ and $x = 2\alpha - 1$. The parameter α is the off-clamping parameter. For $\alpha < 0$, the beam is clamped, directed outward from the axis of rotation, and entirely in tension. For $\alpha > 0$ the axis of rotation is on the beam. For $0 < \alpha < \frac{1}{2}$, the beam is in tension; for $\frac{1}{2} < \alpha < 1$, the beam is partially in tension and partially in compression. Finally, for $\alpha > 1$, the beam is entirely in compression. For this paper we consider only the smallest critical rotation speed for buckling (the largest η). When $0 < \alpha < \frac{1}{2}$, this is the only buckling mode [8]. When $\alpha > \frac{1}{2}$, other buckling modes also exist but are not treated here.

(a) Small η, α Expansion. It is known from [1, 2, 4, 7] that the frequency parameter λ varies as $\eta^{1/2}$ for small α and also varies as α^1 for small η. Therefore, it is reasonable to assume that α should be order $\eta^{1/2}$ for a small η, α expansion. We thus follow the analysis of [2] with the addition of the parameter α proportional to $\eta^{1/2}$. The parameters α and λ take the form

$$\alpha = a\eta^{1/2},\quad \lambda = \eta^{1/2}\lambda_1 \quad (3\,a,\,b)$$

The outer expansion then becomes

$$[(1-x^2)u_0']' + 2u_0 = 0 \quad (4a)$$

$$[(1-x^2)u_1']' + 2u_1 = -2\lambda_1 u_0 + 2a[(1-x)u_0']' \quad (4b)$$

$$u_0 = x \quad (4c)$$

$$u_1 = \frac{2}{3}\lambda_1[x\ln(1+x) - 1] - a \quad (4d)$$

The matching condition with the inner solution (near the root) [2] gives

$$u(0) = -\sqrt{2},\quad \lambda_1 = \frac{3}{2}(\sqrt{2} - a) \quad (5\,a,\,b)$$

$$\lambda = \frac{3\eta^{1/2}}{\sqrt{2}} - \frac{3}{2}\alpha \quad (5c)$$

Equation (5c) is the frequency formula for the case of simultaneously small η and α with η of the order α^2 and is similar to the result obtained in [9] except for an additional factor of $\pi^{-1/2}$ in [9]. Numerical results, discussed below, lead us to conclude that equation (5c) is correct.

It is interesting to compare equation (5c) with similar results in the

Nomenclature

A, B, C = undetermined coefficients
a = proportionality constant, $\alpha = a\eta^{1/2}$
EI = bending stiffness, N m^2
$J_{-1/3}$ = Bessel function of fractional order $-\frac{1}{3}$
L = length of beam, m
Q = ratio α/η
Q_0, Q_1 = expansion terms for Q
R = distance from beam root to axis of rotation, positive when beam is directed toward the axis of rotation, m
s = independent variable, $1 - x$
u = nondimensional deflection, $\bar{u}/L$
$\bar{u}$ = deflection of beam, m
v = slope of beam
v_0, v_1 = expansion terms for v
x = nondimensional beam coordinate, $\bar{x}/L$
$\bar{x}$ = dimensional beam coordinate, m
α = off-clamping parameter, R/L
ϵ = small parameter, $1/\eta$, for large η expansion
λ = nondimensional frequency parameter, ω^2/Ω^2
η = nondimensional stiffness, $EI/\mu L^4\Omega^2$
μ = mass per unit length, kg/m
ω = natural frequency, rad/sec
Ω = rotational frequency, rad/sec
$(\,)' = d/dx$

Downloaded 01 May 2010 to 171.66.16.243. Redistribution subject to ASME license or copyright; see http://www.asme.org/terms/Terms_Use.cfm

literature. For example, when $\alpha \equiv 0$, equation (5c) reduces to the results of [1, 2, 4]. On the other hand, when $\eta \equiv 0$, equation (5c) becomes

$$\lambda = -3/2\ \alpha \tag{6a}$$

which is different from the results of [7], for example, where for α small (but larger in order than $\eta^{1/2}$), λ is given by

$$\lambda = -\frac{6}{\pi}\alpha \tag{6b}$$

It appears that the limiting behavior of λ with α small and η held constant is different from the case of α and η tending toward zero simultaneously. It is beyond the scope of the present paper, however, to attempt explanation for the different results obtained here and in [7].

Equation (5c) with $\lambda = 0$ gives the correct buckling curve for simultaneously small η and α.

$$\alpha = \sqrt{2\eta}\,, \qquad \eta = \alpha^2/2 \tag{7 a, b}$$

The original assumption, $\alpha \sim \eta^{1/2}$, results in a continuous curve down to the point $\eta = \alpha = 0$, in contradiction to [6, 8]. Thus the use of equation (5c) is a key in obtaining the actual buckling behavior for small η and α. Note that the formula in equation (5c) may be valid, however, only for small η ($\eta < 0.005$) and for α of the order $\eta^{1/2}$ or less.

(b) Large η and α. In [2], it was shown that a small-parameter expansion could be combined with a large-parameter expansion to give an overall frequency approximation in closed form. The overall approximation, called a "composite expansion," has proved to be a valuable engineering tool for describing system behavior. Therefore, we wish to pursue a composite buckling expansion. First, we derive an expansion for large η and α. By "large," we do not necessarily mean large with respect to unity (although that case is certainly included). "Large η and α" implies that these parameters are large enough to dominate the solution of the differential equations.

We begin with equation (1a) with $\lambda = 0$ to give immediately the buckling equation for large α and η

$$u'''' + Q[(1-x)u']' = \epsilon u + (1/2)\epsilon[(1-x^2)u']' \tag{8a}$$

where

$$Q = \alpha/\eta, \quad \epsilon = 1/\eta \tag{8 b, c}$$

We follow a similar development in [10], simplify equation (8) by the following changes of variable:

$$s = 1 - x, \quad v(s) = du(x)/dx \tag{9 a, b}$$

and obtain a first integral.

$$v'' + Qsv = -\epsilon \int_0^s \int_{s_1}^1 v(s_2)ds_2ds_1 + \epsilon s(1 - s/2)v$$

$$v'(0) = 0, \quad v(1) = 0 \tag{10 a–c}$$

We now expand Q and v in powers of ϵ

$$Q = Q_0 + \epsilon Q_1 \tag{11a}$$

$$v = v_0 + \epsilon v_1 \tag{11b}$$

to give

$$v_0'' + Q_0 s v_0 = 0 \tag{12a}$$

$$v_1'' + Q_0 s v_1 = s(1 - s/2)v_0(s) - Q_1 s v_0(s) - \int_0^s \int_{s_1}^1 v_0(s_2)ds_2ds_1 \tag{12b}$$

The solution to equation (12a) is well known.

$$v_0 = \sqrt{s}\, J_{-1/3}\left(\frac{2\sqrt{Q_0}}{3}\, s^{3/2}\right) \tag{13}$$

The boundary condition in equation (10c) yields

$$J_{-1/3}\left(\frac{2\sqrt{Q_0}}{3}\right) = 0, \quad Q_0 = 7.837347439 \tag{14 a, b}$$

The solution to equation (12b) follows from the substitution

$$v_1 = \phi(s)v_0(s) \tag{15}$$

which yields

$$\frac{d\phi}{ds} = -\frac{1}{{v_0}^2}\int_s^1 f(s_1)v_0(s_1)ds_1 \tag{16}$$

where

$$f(s) \equiv -\int_0^s \int_{s_1}^1 v_0(s_2)ds_2ds_1 + s(1 - s/2)v_0(s) - Q_1 s v_0(s) \tag{17}$$

The boundary condition $dv_1/ds(0) = 0$ gives

$$\int_0^1 f(s)v_0(s)ds = 0 \tag{18}$$

from which we obtain

$$Q_1 = \frac{\int_0^1 s(1-s/2){v_0}^2 ds - \int_0^1 \left(\int_s^1 v_0 ds_1\right)^2 ds}{\int_0^1 s{v_0}^2 ds} = 0.1319937523 \tag{19}$$

The same answer can be obtained by Rayleigh's method or by noting that the solution for v_1 only exists if the right-hand side of equation (12b) is orthogonal to v_0. Therefore the large η, α expansion is

$$Q = \frac{\alpha}{\eta} = Q_0 + \frac{1}{\eta}Q_1 \tag{20a}$$

or

$$\alpha = Q_1 + Q_0\eta \tag{20b}$$

where the values of the parameters Q_0 and Q_1 are calculated numerically and are

$$Q_0 = 7.837347439 \tag{20c}$$

$$Q_1 = 0.1319937523 \tag{20d}$$

The foregoing development follows very closely a similar development in [6], but is not identical to it. The earlier work of [6] expands $\eta/(\alpha - 1/2)$ in powers of $1/(\alpha - 1/2)$ whereas the present work expands α/η in powers of $1/\eta$. For α close to 1/2, therefore, one would expect large differences in the two theories. For $\alpha \gg 1/2$, on the other hand, one might expect the two expansions to give identical results. This is not the case, however. The results in [6] yield

$$\frac{\alpha - 1/2}{\eta} = 7.83 + \frac{4.18}{\alpha - 1/2} \tag{21a}$$

which, for $\alpha \gg 1/2$, is equivalent to

$$\alpha = 7.83\,\eta + 1.03 \tag{21b}$$

A comparison of equations (20b) and (21b) shows that, although the slopes of the two curves are the same, the offsets are considerably different. Upon recalculating the integrals in [6], we obtain −2.88 instead of the factor +4.18 in equation (21a), which brings the large η, α behavior into agreement with equation (20b). Further comparisons between the two expansions will be given later.

(c) Composite Expansion. Here we follow the methodology of [2] and assume a function of the form

$$\alpha = A\eta^{1/2}\tan^{-1}[B/\eta^{1/2}] + C\eta \tag{22}$$

Downloaded 01 May 2010 to 171.66.16.243. Redistribution subject to ASME license or copyright; see http://www.asme.org/terms/Terms_Use.cfm

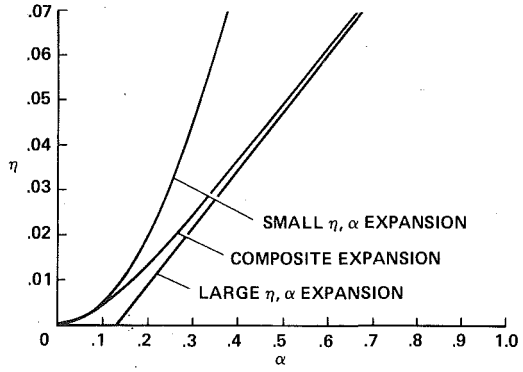

Fig. 2 Small, large, and composite expansions for buckling boundary

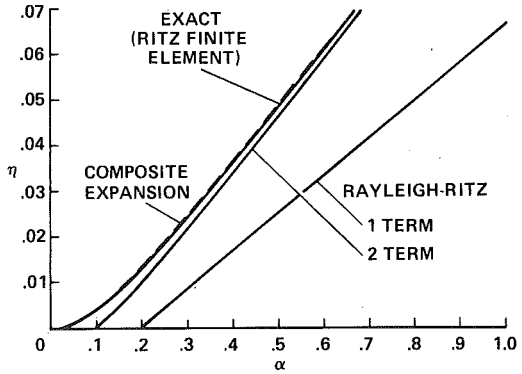

Fig. 3 Exact, composite expansion, and Rayleigh-Ritz solutions for buckling boundary

for use in our composite expansion.[1] Equation (22) has the property that, in the limit of small η, it gives an expansion in powers of $\eta^{1/2}$;

$$\alpha = \frac{\pi}{2} A\eta^{1/2} + O(\eta) \tag{23}$$

but for large η, it gives an expansion in powers of $1/\eta$

$$\alpha = C\eta + AB + O(1/\eta) \tag{24}$$

The parameters A, B, and C are chosen so that the function has the correct limiting behavior as derived in equations (7a) and (20b).

$$A = \frac{2\sqrt{2}}{\pi} \tag{25a}$$

$$B = \frac{\pi Q_1}{2\sqrt{2}} \tag{25b}$$

$$C = Q_0 \tag{25c}$$

The composite expansion is, therefore,

$$\alpha = \frac{2\sqrt{2\eta}}{\pi} \tan^{-1}\left(\frac{\pi Q_1}{2\sqrt{2\eta}}\right) + Q_0\eta \tag{27}$$

where Q_0 and Q_1 are given in equation (20).

The composite expansion is compared in Fig. 2 with both the small η expansion and the large η expansion. We see that the single term, small η, α expansion is accurate only for $\eta \lesssim 0.005$. On the other hand, the "large η, α" expansion (the straight line) is fairly accurate for $\eta \gtrsim 0.05$. This indicates that even for η relatively small with respect to unity (i.e., 0.05), the η terms may still dominate the equations.

We also note the convergence of a conventional Rayleigh-Ritz solution for buckling, Fig. 3. Although the convergence is reasonable for $\eta \gtrsim 0.05$ (for which η dominates), the convergence is characteristically poor at small η. The Rayleigh-Ritz solutions give the erroneous results that no buckling is possible for $\alpha < 0.2$ (1 term) or for $\alpha < 0.1$ (2 terms). It is believed that this type of Rayleigh-Ritz error is what led to the conclusion in [8] that buckling was possible only for $\alpha > 0.05$. Also shown in Fig. 3 is the essentially exact solution from high-order Ritz finite elements, [11]. The composite solution is very accurate and is barely distinguishable on the graph from the exact solution. Nonetheless, the composite curve is only an approximation, and an error in α of about 1.5 percent is obtained near $\eta = 0.006$. The error diminishes, however, for larger or smaller η's.

It is also interesting to compare the exact solution with results published earlier in [5, 6], Fig. 4. We plot $\alpha^2/\sqrt{\eta}$ to more easily compare with [5]. First, we note that the results of [5] are essentially exact

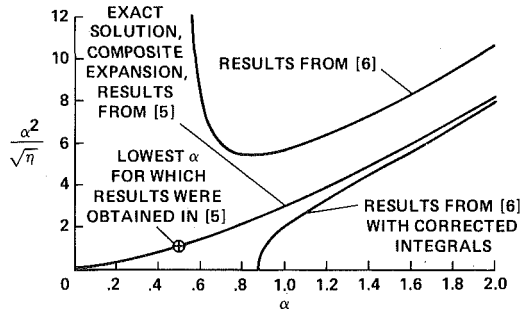

Fig. 4 Comparison with other work

for $\alpha \geq 1/2$ ($\alpha = 1/2$ is the smallest α calculated in [5]). Second, we note that the results of [6], both those plotted directly from equation (21a) and those with corrected integrals, are generally inaccurate. Although the curve directly from [6] approaches the correct slope $\alpha \to \infty$, the offset is considerably in error, as we noted previously. Furthermore, we note that, even when the curve is adjusted for offset by the corrected integrals, the buckling formula of [6] is still in error for $\alpha < 1$. The reason for this is the expansion in terms of $1/(\alpha - 1/2)$. The purpose of the $1/(\alpha - 1/2)$ expansion was to capture the supposed effect that buckling is impossible for $\alpha < 1/2$. Since buckling is possible for $\alpha < 1/2$, however, the $1/(\alpha - 1/2)$ expansion simply causes the expansion to diverge from the true solution for $\alpha < 1$.

Conclusions

The correct in-plane buckling behavior has been obtained for rotating beams clamped off the axis of rotation. The correct behavior in the limit of small stiffness (η) and small off-clamping (α) requires that η and α approach zero simultaneously, as demonstrated by asymptotic expansions for frequency with the frequency parameter set to zero. These expansions show that η for buckling varies as α for large η but varies as α^2 for small η. A composite expansion, derived in the text, provides a good approximation to the buckling curve for all values of η and α with a maximum error of 1.5 percent. Previous statements in the literature that buckling is not possible for small off-clamping and small stiffness are demonstrated to be incorrect.

References

1 Colin, A. D., "Modal Analysis for Liapunov Stability of Rotating Elastic Bodies," PhD Thesis, University of California at Los Angeles, 1973, pp. 11–43.

2 Peters, D. A., "An Approximate Solution for the Free Vibrations of Rotating Uniform Cantilever Beams," NASA TM X-62, 299, Sept. 1973.

3 Lakin, W. D., "On the Differential Equation of a Rapidly Rotating Slender Rod," *Quarterly of Applied Mathematics*, Vol. 32, Apr. 1974, pp. 11–27.

[1] It is obvious that functions other than $\tan^{-1}$ could serve just as well. Our experience indicates that the accuracy of the expansion is not sensitive to the function used as long as the behavior at large and small values of the argument is appropriate.

Downloaded 01 May 2010 to 171.66.16.243. Redistribution subject to ASME license or copyright; see http://www.asme.org/terms/Terms_Use.cfm

4 Lakin, W. D., and Ng, B. S., "A Fourth-Order Eigenvalue Problem With a Turning Point at the Boundary," *Quarterly Journal of Mechanics and Applied Mathematics,* Vol. 28, Mar. 1975, pp. 107–121.

5 Mostaghel, N., and Tadjbachsh, I., "Buckling of Rotating Rods and Plates," *International Journal of the Mechanical Sciences,* Vol. 15, June 1973, pp. 429–434.

6 Nachman, A., "The Buckling of Rotating Rods," ASME JOURNAL OF APPLIED MECHANICS, Vol. 42, Mar. 1975, pp. 222–224.

7 Lakin, W. D., "Vibrations of a Rotating Flexible Rod Clamped Off the Axis of Rotation," *Journal of Engineering Mathematics,* Vol. 10, Oct. 1976, pp. 313–321.

8 Lakin, W. D., and Nachman, A., "Unstable Vibrations and Buckling of Rotating Flexible Rods," *Quarterly Journal of Applied Mathematics,* Vol. 35, Jan. 1978, pp. 479–493.

9 Lakin, W. D., and Nachman, A., "Vibration and Buckling of Rotating Flexible Rods at Transitional Parameter Values," *Journal of Engineering Mathematics,* Vol. 13, No. 4, Oct. 1979, pp. 339–346.

10 Peters, D. A., and Wu, J. J., "Asymptotic Solutions to a Stability Problem," *Journal of Sound and Vibration,* Vol. 59, No. 4, Aug. 1978, pp. 591–610.

11 Hodges, D. H., "Vibration and Response of Nonuniform Rotating Beams With Discontinuities," *Journal of the American Helicopter Society,* Vol. 24, No. 5, Oct. 1979, pp. 43–50.

Downloaded 01 May 2010 to 171.66.16.243. Redistribution subject to ASME license or copyright; see http://www.asme.org/terms/Terms_Use.cfm

Isaac Elishakoff[1]

Associate Professor,
Department of Aerospace Engineering,
Delft University of Technology,
Delft, The Netherlands

Hoff's Problem in a Probabilistic Setting

Hoff's problem—that of investigation of the maximum load supported by an elastic column in a compression test—is considered in a probabilistic setting. The initial imperfections are assumed to be Gaussian random fields with given mean and autocorrelation functions, and the problem is solved by the Monte Carlo Method. The Fourier coefficients of the expansion for the initial imperfection function are simulated numerically; for each realization of the initial imperfection function, the maximum load supported by an elastic column in a compression test is found by the solution of a set of coupled nonlinear differential equations. For slightly imperfect columns, the closed solution is given in terms of Bessel and Lommel functions and turns out to compare well with the result of numerical integration. Results of the Monte Carlo solution are used in constructing the reliability function at a specified load. Reliability functions for different manufacturing processes (represented by different autocorrelation functions with equal variance) are calculated; design requirement suggests then that, other conditions being equal, the preference should be given to the manufacturing process resulting higher reliability.

Introduction

The theoretical buckling load of a column is usually obtained by the Euler method, which reduces the job of stability analysis of a form of equilibrium to the simpler one of finding the minimum eigenvalue of a certain linear boundary-value problem. As for the experimental buckling load, it is usually determined as the maximum load recorded in a standard buckling test. The first to take interest in the intercorrelation between the two loads was Hoff, who noted in the Forty-First Wilbur Wright Memorial Lecture [1]: "It is a fortunate coincidence from the standpoint of practical applications, but perhaps unfortunate for the development of a more accurate theory, that the column test carried out in a routine manner in an ordinary testing machine gives results in excellent agreement with the classical theory when the column is slender." On an earlier occasion [2], Hoff considered the motion of an elastic, initially slightly imperfect column when one of its ends is displaced axially at a constant rate in a perfectly rigid testing machine. An interesting corollary was that the maximum axial force recorded in the test may be a multiple of the Euler load, when the so-called dynamic similarity number and the initial imperfection are small.

This pioneering work was followed by many others. The linear differential equation associated with the original nonlinear one, which was found to approximate satisfactorily the motion below the "Euler displacement," was solved by Hoff himself in terms of Bessel functions; later on, Tyler [3] presented an alternative solution in terms of Airy integral functions, which were also used by Markin [4] in analyzing the motion of the column under general, monotonically increasing loading. Hoff, et al. [5], presented four different methods for integration of the differential equation below the "Euler displacement." Subsequent contributions, both numerical and experimental, are found in references [6–13]; in particular, Sevin [13] showed that the axial inertia effect in Hoff's problem may be neglected.

In most of the analyses, the initial deviation of the column axis from the straight line of action of the compressive load was represented by a half sine-wave, its magnitude being treated as a deterministic quantity. The difficulty with this type of theory lies in proper choice of the imperfection, as it is conditional on prior knowledge of the imperfection function, which varies from case to case—seeing that both shape and magnitude derive from an arbitrary manufacturing process, itself subject to a large number of random factors. This was apparently also first noted by Hoff as early as 1949 [14]: ". . . For the engineer stability means that he need not worry whether the equilibrium of the structural element or part of machinery he designed will be upset by some disturbance. He can rely upon the equilibrium . . . The nature and the magnitude of the disturbance must be established from a statistical investigation of the conditions under which the structural element or the part of machinery will be used. The safety of the system can be safeguarded if it is made stable for all disturbances which have a probability greater than a required minimum . . ."

In the light of these considerations, it is clear that practicability of available theories is conditional on their being combined with a statistical analysis of the imperfections and critical loads. The notion

[1] On sabbatical leave from Technion, Israel Institute of Technology, Department of Aerospace Engineering, Haifa, Israel.

Contributed by the Applied Mechanics Division for publication in the JOURNAL OF APPLIED MECHANICS.

Discussion on this paper should be addressed to the Editorial Department, ASME, United Engineering Center, 345 East 47th Street, New York, N. Y. 10017, and will be accepted until September 1, 1980. Readers who need more time to prepare a discussion should request an extension from the Editorial Department. Manuscript received by ASME Applied Mechanics Division, October, 1978; final revision, August, 1979.

Copyright © 1980 by ASME
Downloaded 01 May 2010 to 171.66.16.243. Redistribution subject to ASME license or copyright; see http://www.asme.org/terms/Terms_Use.cfm

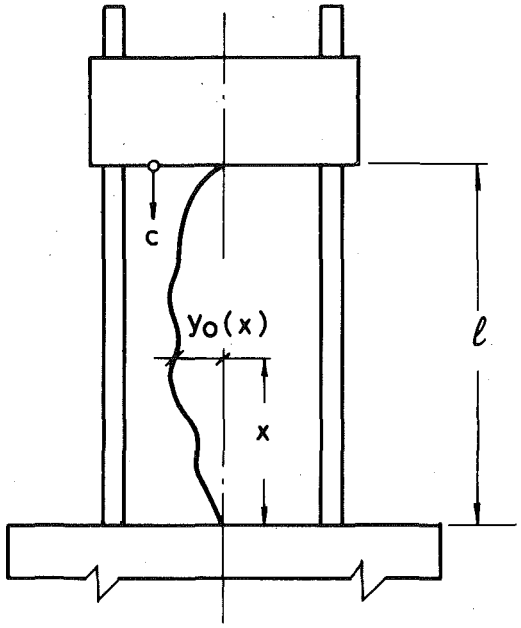

Fig. 1 Imperfect column in testing machine

of stochasticity of the initial imperfections for impact problems was first applied by Lindberg [15], who treated the former as "white noise." Later on Elishakoff [16] generalized this work, dispensing with this restriction and presenting a simulation procedure of the initial imperfections with an arbitrary autocorrelation function.

This simulation procedure is used in the present analysis, in which Hoff's problem is considered in a probabilistic setting, using the Monte Carlo Method. The initial imperfections are expanded in terms of modes of stability loss of the corresponding perfect structure, and the Fourier coefficients are treated as random vectors with appropriate probabilistic characteristics, obtainable from the given mean and autocorrelation functions of the initial imperfections. By this means, a large number of imperfection vectors are constructed; for each "trial" (realization) of these vectors, the corresponding buckling load is calculated and the reliability function of the system is studied.

Basic Equations and Method of Solution

The equation of motion of the column test was derived in reference [2] under the assumption that the loading head descends at a constant velocity c and that the column is perfectly elastic (Fig. 1). The equation of motion reads

$$EI\frac{\partial^4 y}{\partial x^4}+\frac{\partial}{\partial x}\left(P\frac{\partial y}{\partial x}\right)+\rho A\frac{\partial^2 y}{\partial t^2}=0 \tag{1}$$

where

$$P=\frac{EA}{l}\left\{ct-\frac{1}{2}\int_0^l\left[\left(\frac{\partial y}{\partial x}\right)^2-\left(\frac{\partial y_0}{\partial x}\right)^2\right]dx\right\} \tag{2}$$

x is the axial coordinate, t time, $y_0(x)$ the initial imperfection (a small perturbation to the initial shape of the unstressed column), $y(x, t)$ the total deviation of the column axis from the straight line between its end points, $x = 0, x = l$; E Young's modulus, I the moment of inertia, A the cross-sectional area, l the length (actually the initial distance between the ends of the column measured along the x-axis of the column), ρ mass density, and $P(x, t)$ the compressive force in section x of the column at time t.

The foregoing equations are supplemented by the boundary conditions

$$y(x,t)=0,\quad \frac{\partial^2}{\partial x^2}y(x,t)=0 \quad \text{at} \quad x=0,l \tag{3}$$

and the initial conditions

$$y(x,t)=y_0(x),\quad \frac{\partial}{\partial t}y(x,t)=0 \quad \text{at} \quad t=0 \tag{4}$$

The initial imperfection function $y_0(x)$ is presented in a probabilistic sense. In particular, the mean imperfection function

$$Y_0(x)=E[y_0(x)] \tag{5}$$

and the autocorrelation function

$$K_{y_0}(x_1,x_2)=E\{[y_0(x_1)-Y_0(x_1)][y_0(x_2)-Y_0(x_2)]\} \tag{6}$$

can be assumed to be given. In equations (5), (6), $E[\ldots]$ denotes the mathematical expectation.

The problem reads as follows: *Given the probabilistic characteristics of the initial imperfections, find those of the maximum axial forces recorded on the testing machine.*

For the stochastic boundary-value problem we resort to the normal-mode approach, which consists in expanding the probabilistically given and sought functions in series in terms of the modes of stability loss of a perfect bar. Following Lavrent'ev and Ishlinsky [17], the initial imperfections and the total deflections are represented as follows:

$$y_0(x)=\sum_{n=1}^{\infty}a_n\sin\frac{n\pi x}{l},\quad y(x,t)=\sum_{n=1}^{\infty}F_n(t)\sin\frac{n\pi x}{l} \tag{7}$$

Substituting equation (7) in (1) and (2), we apply the Galerkin method, namely, multiply both sides of the resulting equation by $\sin(m\,x/l)$, $m = 1, 2, \ldots$, and integrate over the length of the column. The result reads

$$f_m''+\Omega m^2(m^2-\xi)f_m+(\Omega m^2/4)\sum_{n=1}^{\infty}n^2(f_n{}^2-e_n{}^2)f_m = \Omega m^4 e_m,\quad m=1,2,\ldots \tag{8}$$

the primes denoting differentiation with respect to the nondimensional time parameter ξ.

In equation (8) the following nondimensional quantities were introduced:

$$f_m=F_m/\Delta,\ e=a_m/\Delta,\ \xi=ct/\epsilon_E l,\ \epsilon_E=\pi^2(\Delta/l)^2,\ \Omega=\pi^2\epsilon_E{}^3(E/\rho c^2) \tag{9}$$

where Δ is the radius of gyration of the cross section. Equation (8) is supplemented by the initial conditions

$$f_m(\xi)=e_m,\quad df_m(\xi)/d\xi=0 \quad \text{at}\ \xi=0 \tag{10}$$

For the particular case of a single-term Galerkin approximation ($m = 1$), equation (8) reduces to equation (11) of reference [2], where the quantity Ω is characterized as the *dynamic similarity number.* In the case under consideration, two elastic bars are "dynamically similar" if Ω and the initial imperfection function $y_0(x)$ (and consequently the e_m values) are the same for both. After similar transformation, equation (2) can be written as

$$P/P_E=\xi-\sum_{n=1}^{\infty}n^2(f_n{}^2-e_n{}^2)/4 \tag{11}$$

In what follows we truncate the series (7) to some N (number of the terms taken into account), satisfying the requirement that the probabilistic characteristics of the maximum loads supported by the columns in a compression test be obtainable with sufficient accuracy. The mean values of the line-vector $\mathbf{e}^T = (e_1, e_2, \ldots, e_N)$ and corresponding column vector $\mathbf{e}$ are determined as

$$\mu_m\equiv E(\mathbf{e})=(2/l)\int_0^l E[y_0(x)/\Delta]\sin(m\pi x/l)\,dx \tag{12}$$

whereas the covariance matrix is

$$\mathbf{C}=\{\mathrm{cov}\,(e_m,e_n)\}_{N\times N}\equiv\{C_{mn}\}_{N\times N} \tag{13}$$

with elements

Downloaded 01 May 2010 to 171.66.16.243. Redistribution subject to ASME license or copyright; see http://www.asme.org/terms/Terms_Use.cfm

$$C_{mn} = (4/l^2\Delta^2) \int_0^l \int_0^l E\{y_0(x') - E[y_0(x')]\}\{y_0(x'') - E[y_0(x'')]\} \sin(m\pi x'/l) \sin(n\pi x''/l)\, dx'\, dx'' \quad (14)$$

so that the joint probabilistic density of $\mathbf{e}$ is

$$P_{\mathbf{e}}(e_1, e_2, \ldots, e_N) = (\det \mathbf{C})^{-1/2} (2\pi)^{-N/2} \times \exp\left[-\frac{1}{2}(\mathbf{e}-\boldsymbol{\mu})^T \mathbf{C}^{-1} (\mathbf{e}-\boldsymbol{\mu})\right] \quad (15)$$

$\mathbf{C}^{-1}$ being inverse of $\mathbf{C}$.

The problem now reduces to the well-known one of simulation of random normal vectors [20] (see also references [16, 21]). Linear nondegenerative transformation of the normal random vector results in another random normal vector with different mean vector and covariance matrix. Since $\mathbf{C}$ is positive-definite and symmetric, it can be decomposed as

$$\mathbf{C} = \mathbf{S}\mathbf{S}^T \quad (16)$$

where $\mathbf{S}$ is a triangular matrix. Then

$$\mathbf{C}^{-1} = (\mathbf{S}\mathbf{S}^T)^{-1} = (\mathbf{S}^T)^{-1} \mathbf{S}^{-1} \quad (17)$$

and

$$(\mathbf{e}-\boldsymbol{\mu})^T \mathbf{C}^{-1} (\mathbf{e}-\boldsymbol{\mu}) = (\mathbf{e}-\boldsymbol{\mu})^T (\mathbf{S}^T)^{-1} \mathbf{S}^{-1} (\mathbf{e}-\boldsymbol{\mu}) = [\mathbf{S}^{-1}(\mathbf{e}-\boldsymbol{\mu})]^T [\mathbf{S}^{-1}(\mathbf{e}-\boldsymbol{\mu})] \quad (18)$$

Denoting further

$$\mathbf{b} = \mathbf{S}^{-1}(\mathbf{e}-\boldsymbol{\mu}) \quad (19)$$

The joint probability density of $\mathbf{b}$ is

$$P_{\mathbf{b}}(b_1, b_2, \ldots, b_N) = (2\pi)^{-N/2} \exp[-(1/2)\mathbf{b}^T\mathbf{b}] \quad (20)$$

Accordingly, to obtain realizations of a normal random vector $\mathbf{e}-\boldsymbol{\mu}$, it is necessary to take N independent realizations of one-dimensional normal vector $b_1, b_2, \ldots, b_N$ (resulting in realization of $\mathbf{b}$ with zero mean values and unit variances), and multiply by $\mathbf{S}$ on the left; consequently realizations of $\mathbf{e}$ are obtained as follows:

$$\mathbf{e} = \boldsymbol{\mu} + \mathbf{S}\mathbf{b} \quad (21)$$

It should be noted that the autocorrelation function of the initial imperfections

$$K_{y_0/\Delta}(\eta_1, \eta_2) \equiv E\{y_0(x') - E[y_0(x')]\}\{y_0(x'') - E[y_0(x'')]\}/\Delta^2 \quad (22)$$

in equation (17) should, strictly speaking, be nonhomogeneous, subject to boundary conditions

$$y_0(0) = y_0(l) = 0 \quad (23)$$

and this may introduce a further dependence on length. It can be visualized that the finite column is obtained by the cutting of an infinitely long one to a given length and fixing the ends. Let the initial deviations $v(x)$ from a middle line before cutting to length l and fixing the ends be a homogeneous Gaussian field with mean field zero, and an autocorrelation function

$$K_v(x_1 - x_2) = E[v(x_1)\, v(x_2)] \quad (24)$$

The column is now cut and the line between the end points used as axis. Assumption of small angles yields

$$y_0(x) = v(x) - v(0) - (x/l)[v(l) - v(0)] \quad (25)$$

thus satisfying the requirement (23). From the definitions of $y_0(x)$ in terms of $v(x)$, we obtain

$$E[y_0(x)] = 0 \quad (26)$$

$$K_{y_0}(x_1, x_2) = K_v(x_1 - x_2) + K_v(0) - [K_v(0) - K_v(l)][(l - x_1)x_2 + (l - x_2)x_1]l^{-2} - K_v(l - x_2)x_1 l^{-1} - K_v(l - x_1)x_2 l^{-1} - K_v(x_2)(1 - x_1 l^{-1}) - K_v(x_1)(1 - x_2 l^{-1}) \quad (27)$$

(Cont.)

The autocorrelation function (27) has the following interesting properties

$$K_{y_0}(0, x) \equiv 0, \quad K_{y_0}(l, x) \equiv 0$$
$$K_{y_0}(x_1, x_2) \equiv K_{y_0}(l - x_1, l - x_2) \quad (28)$$

and provides an indication of the influence of length through Var $[y_0(l/2)]$

$$\text{Var}\,[y_0(l/2)] = \frac{1}{2}[3K_v(0) + K_v(l) - 4K_v(l/2)] \quad (29)$$

Finally, after nondimensionalization, equation (27) becomes

$$K_{y_0/\Delta}(\eta_1, \eta_2) = K_{v/\Delta}(\eta_1 - \eta_2) + K_{v/\Delta}(0) - [K_{v/\Delta}(0) - K_{v/\Delta}(1)][(1 - \eta_1)\eta_2 + (1 - \eta_2)\eta_1] - \eta_1 R(1 - \eta_2) - \eta_2 R(1 - \eta_1) - (1 - \eta_1)R(\eta_2) - (1 - \eta_2)R(\eta_1) \quad (30)$$

Calculations using equation (14) result in

$$C_{mn} = \overline{C}_{mn} + \frac{4}{mn\pi^2} K_{v/\Delta}(0)[(-1)^m - 1][(-1)^n - 1] + \frac{4}{mn\pi^2}[K_{v/\Delta}(0) - K_{v/\Delta}(1)][(-1)^m + (-1)^n] - \frac{4}{m\pi}[1 + (-1)^{m+n}] \int_0^1 K_{v/\Delta}(\eta) \sin(n\pi\eta)\, d\eta - \frac{4}{n\pi}[1 + (-1)^{m+n}] \int_0^1 K_{v/\Delta}(\eta) \sin(m\pi\eta)\, d\eta \quad (31)$$

where

$$\overline{C}_{mn} = 4 \int_0^1 \int_0^1 K_{v/\Delta}(\eta_1 - \eta_2) \sin(m\pi\eta_1) \sin(n\pi\eta_2)\, d\eta_1\, d\eta_2 \quad (32)$$

can be put as a single integral (after introduction of a new coordinate system $\eta = 2^{-1/2}(\eta_2 - \eta_1)$, $\kappa = 2^{-1/2}(\eta_2 + \eta_1)$):

$$\overline{C}_{mm} = 4 \int_0^1 [(1 - \eta)\cos(m\pi\eta) + (1/m\pi)\sin(m\pi\eta)] K_{v/\Delta}(\eta)\, d\eta, \quad m = n \quad (33)$$

$$\overline{C}_{mn} = \frac{4[1 - (-1)^{m+n+1}]}{\pi(n^2 - m^2)} \int_0^1 [n \sin(m\pi\eta) - m \sin\sin(n\pi\eta)] K_{v/\Delta}(\eta)\, d\eta, \quad m \neq n \quad (34)$$

Numerical Examples

The numerical examples were worked out on an IBM 360/178 computer at the Technion, using the following autocorrelation function of the initial deviations $v(x)$ from a middle line before cutting [22, 23]:

$$K_{v/\Delta}(\eta_1, \eta_2) = 2Q[\sin T(\eta_1 - \eta_2)]/(\eta_1 - \eta_2), \quad (\eta \equiv x/l) \quad (35)$$

$2QT$ being the variance, with their mean function chosen as zero.

The Fourier coefficients C_{mn} were approximated from equations (31–34) by numerical quadrature and the elements of matrix $\mathbf{S}$ obtained by Cholesky's decomposition procedure. Equations (8) were integrated for numerous "trial" values of the random Fourier coefficients $e_1, e_2, \ldots, e_N$ (N being the number of imperfection modes taken into account), using Hamming's predictor-corrector method with varying step size. For each realization the dimensionless maximum compressive force ($P_{k,max}/P_E$) was determined numerically (k being the realization number, and P_E the buckling load for a perfect column). An empirical reliability function $R^*(\lambda)$ of the maximum load supported by an elastic column in a compression test was defined as

Downloaded 01 May 2010 to 171.66.16.243. Redistribution subject to ASME license or copyright; see http://www.asme.org/terms/Terms_Use.cfm

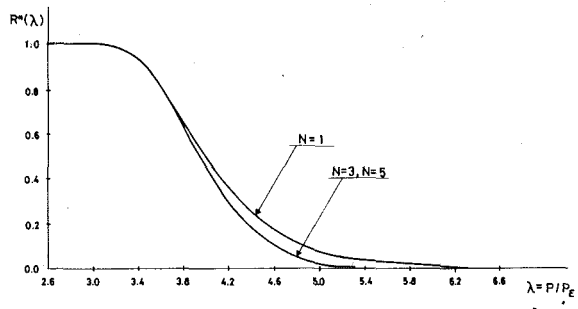

Fig. 2 Emprical reliability function versus nondimensional force $\lambda = P/P_E$ ($\Omega = 1$, $Q = 10^{-4}/3$, $T = 3\pi$)

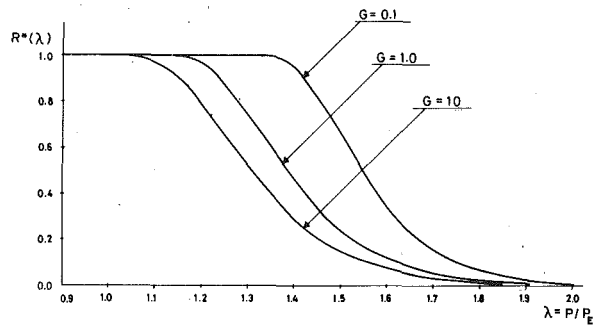

Fig. 4 Influence of parameters of initial imperfection autocorrelation function (39) on empirical reliability at constant variance ($\Omega = 100$, $D = 2\cdot10^{-4}\pi$, $N = 3$, $M = 1089$)

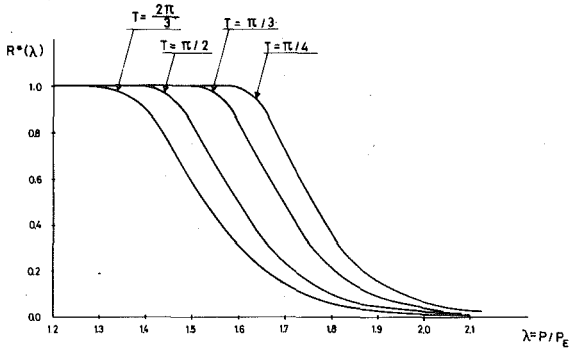

Fig. 3 Influence of parameters of initial imperfection autocorrelation function (35) on empirical reliability at constant variance $2QT = 2\cdot10^{-4}\pi$ ($\Omega = 100$, $N = 3$, $M = 1089$)

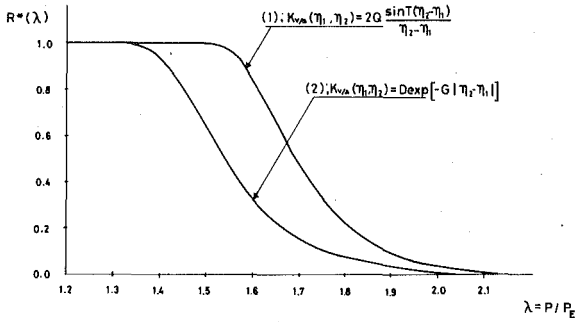

Fig. 5 Comparison of reliabilities associated with different manufacturing processes ($Q = 3\cdot10^{-4}$, $T = \pi/3$, $D = 2\cdot10^{-4}\pi$, $G = 0.1$)

$$R^*(\lambda) = \nu_M(\lambda)/M \tag{36}$$

where $\nu_M(\lambda)$ us the number of $P_{k,\max}/P_E$ exceeding λ, M the ensemble size and $P_{k,\max}$ the maximal force supported by the kth column. For $M = 1089$, according to the Kolmogorov-Smirnov test of goodness of fit [24], the critical value of the maximum absolute difference between the theoretical $R(\lambda)$ and empirical $R^*(\lambda)$ reliability function is $1.36/\sqrt{1089} \simeq 0.041$ at a level of significance of 0.05. It turned out that retention of three terms in series (7) suffices for satisfactory description of the statistical characteristics of buckling loads. Fig. 2 shows that the percentage difference between the reliability function and its approximation obtained with $N = 1$ may be considerable; at the nondimensional force level $\lambda = 4.7$ it is almost 100 percent whereas for larger values of λ it is even greater. It should be noted that higher values of Hoff's dynamic similarity number are generally associated with a smaller number of imperfection "modes" to be taken into account for satisfactory determination of the empirical reliability function $R^*(\lambda)$. Fig. 3 shows the influence of the parameters of the autocorrelation function Q and T on the reliability function, all curves being associated with the same level of variance ($2\pi\cdot10^{-4}$). Curve 1 corresponds to $Q = 4 \times 10^{-4}$, $T = \pi/4$; curve 2 to $Q = 3 \times 10^{-4}$, $T = \pi/3$; curve 3 to $Q = 2 \times 10^{-4}$, $T = \pi/2$, and curve 4 to $Q = 1.5 \times 10^{-4}$, $T = 2\pi/3$. As is seen from this figure, the reliability of the column increases with the decrease of the "spatial cutoff frequency" T at constant variance of the initial imperfection.

Note that the single-term approximation may be good enough for the nonhomogeneous imperfections with the following autocorrelation function:

$$K_{y_0/\Delta}(\eta_1,\eta_2) = C_{pp} \sin(p\pi\eta_1) \sin(p\pi\eta_2) \tag{37}$$

where C_{pp} is some positive constant and p is some positive integer. Initial imperfections of the type

$$y_0/\Delta = e_p \sin(p\pi\eta) \tag{38}$$

have autocorrelation function (37) with C_{pp} being the variance of the random variable e_p; consequently $e_m = e_p\delta_{mp}$ in equations (8). For the case when the radius of gyration is much higher than $E(e_p)$ or $C_{pp}^{1/2}$ (i.e., for the nearly perfect column), the linearized analysis (see Appendix) turns out to be a very satisfactory one.

Fig. 4 shows the behavior of the empirical function versus λ for another autocorrelation function of the initial deviations $v(x)$ from a middle line before cutting to length:

$$K_{v/\Delta}(\eta_1,\eta_2) = D \exp[-G|\eta_2 - \eta_1|] \tag{39}$$

where D and G are positive constants. The constant variance level chosen was $D = 2 \times 10^{-4}\pi$, while G ranged from 0.1 to 10, as shown in the figure.

It can be assumed that the autocorrelation functions (35) and (39) are associated with different manufacturing processes with constant variance $2QT = D$. Other conditions being equal, preference should then be given to the process with better reliability (Fig. 5, curve 1).

Conclusion

The Monte Carlo Method was applied to Hoff's problem. The initial imperfections of the column tested in an ordinary testing machine were assumed to be a normally distributed random function of the space coordinate with given mean and autocorrelation functions. The Fourier coefficients of the expansion of the initial imperfection function were simulated numerically and the statistical behavior of the buckling force (maximum force supported by the column) was determined. The reliability functions associated with different autocorrelation functions of the initial imperfections were calculated and compared for design purposes.

Acknowledgments

I wish to thank Messrs. Dov Verbin and Nyunya Nitskansky for performing the calculations, and Mrs. Elizabeth Youdim for typing the manuscript. I am also indebted to the referee for his useful comments. The study was supported by the Technion Research and Development Foundation.

Downloaded 01 May 2010 to 171.66.16.243. Redistribution subject to ASME license or copyright; see http://www.asme.org/terms/Terms_Use.cfm

References

1 Hoff, N. J., "Buckling and Stability" (Forty-First Wilbur Wright Memorial Lecture), *Journal of the Royal Aeronautical Society,* Vol. 58, 1954, pp. 3–52.

2 Hoff, N. J., "The Dynamics of the Buikling of Elastic Columns," ASME JOURNAL OF APPLIED MECHANICS, Vol. 18, Mar. 1951, pp. 68–74.

3 Tyler, C. M., Jr., Discussion of reference [2], ASME JOURNAL OF APPLIED MECHANICS, Vol. 18, sept. 1951, p. 317.

4 Markin, A. V., "Buckling of Elastic Beams During Varying Intensive Loading," *Journal of Applied Mathematics and Technical Physics,* No. 1, Jan.–Feb. 1977, pp. 155–161 (in Russian).

5 Hoff, N. J., Nardo, S. V., and Erickson, B., "The Maximum Load Supported by an Elastic Column in a Rapid Compression Test," *Proceedings of the First National Congress of Applied Mechanics,* The American Society of Mechanical Engineers, 1951, pp. 419–423.

6 Chawla, J. P., "Numerical Analysis of the Process of Buckling of Elastic and Inelastic Columns," *Proceedings of the First National Congress of Applied Mechanics,* The American Society of Mechanical Engineers, 1951, pp. 435–441.

7 Hoff, N. J., Nardo, S. V., and Erickson, B., "An Experimental Investigation of the Process of Buckling of Columns," *Proceedings of the Society for Experimental Stress Analysis,* Vol. 13, No. 1, 1955, pp. 201–208.

8 Erickson, B., et al., "An Experimental Investigation of the Maximum Loads Supported by Elastic Columns in Rapid Compression Tests," *Proceedings of the Society for Experimental Stress Analysis,* Vol. 14, No. 1, 1956, pp. 13–20.

9 Schmitt, A. F., "A Method of Stepwise Integration in Problems of Impact Loading," ASME JOURNAL OF APPLIED MECHANICS, Vol. 23, June 1956, pp. 291–294.

10 Hegglin, B., "Dynamic Buckling of Columns," SUDAER Report No. 129, Department of Aeronautics and Astronautics, Stanford University, June 1962.

11 Vol'mir, A. S., *Stability of Deformable Bodies,* Nauka Publishing House, Moscow, 1967, pp. 264–269 (in Russian).

12 Hoff, N. J., "Dynamic Stability of Structures" (Keynote Address) in *Dynamic Stability of Structures,* Herrmann, G., ed., Pergamon, 1965, pp. 7–77.

13 Sevin, E., "On the Elastic Bending of Columns Due to Dynamic Axial Forces Including Effects of Axial Inertia," ASME JOURNAL OF APPLIED MECHANICS, Vol. 27, Mar. 1960, pp. 125–131.

14 Hoff, N. J., *Dynamic Criteria of Buckling,* Research, Engineering Structures Supplement, Butterworth Scientific Publications, London, and Academic Press, New York, 1949, p. 121.

15 Lindberg, H. E., "Impact Buckling of Thin Bar," ASME JOURNAL OF APPLIED MECHANICS, Vol. 32, June 1965, pp. 312–322.

16 Elishakoff, I., "Impact Buckling of Thin Bar Via Monte Carlo Method," ASME JOURNAL OF APPLIED MECHANICS, Vol. 45, Sept. 1978, pp. 566–570.

17 Lavrent'ev, M. A., and Ishlinsky, A. V., "Dynamic Forms of Loss of Stability of Elastic Systems," *Doklady Akademii Nauk SSSR,* Vol. 64, 1949, pp. 779–782 (English translation by R. Cooper in STL-TR-61-5110-41, Space Technology Laboratories, Los Angeles, Calif.).

18 Watson, G. N., *A Treatise of the Theory of Bessel Functions,* Cambridge University Press, Cambridge, Mass., 1962.

19 Luke, Yu. L., *Integrals of Bessel Functions,* McGraw-Hill, New York, 1962.

20 Sheuer, E. M. and Stoller, D. S., "On the Generation of Normal Random Vectors," *Technometrics,* Vol. 4, 1962, pp. 278–281.

21 Elishakoff, I., "Buckling of a Stochastically Imperfect Finite Column on a Nonlinear Elastic Foundation—A Reliability Study," ASME JOURNAL OF APPLIED MECHANICS, Vol. 46, June 1979, pp. 411–416.

22 Boyce, W. C., "Buckling of a Column With Random Initial Displacements," *Journal of Aerospace Sciences,* Vol. 28, 1961, pp. 308–320.

23 Singh, M. P., and Ang, A. H. S., "Columns With Randon Imperfections and Associated Bracing Requirements," *Journal of Structural Mechanics,* Vol. 4, No. 2, 1976, pp. 161–180.

24 Massey, F. J., Jr., "The Kolmogorov-Smirnov Test for Goodness of Fit," *Journal of the American Statistical Association,* Vol. 46, No. 253, 1951, pp. 68–78.

25 Elishakoff, I., "Hoff's Problem in a Statistical Setting," TAE Report No. 348, Oct. 1978, Department of Aeronautical Engineering, Technion-Israel Institute of Technology, Haifa, Israel.

Table 1 Values of $f_1(1)/e_1$ for different values of Ω (comparison with results of Hoff, et al. [7])

Method	1 [7]	2 [7]	3 [7]	4 [7]	Present method
$\Omega = 2.25$	1.363			1.356	1.36
$\Omega = 10$	2.3976	2.414		2.399	2.41
$\Omega = 10^2$		5.896	5.87941	5.913	5.89
$\Omega = 10^3$			12.8395		12.82
$\Omega = 10^4$			27.7609		27.75
$\Omega = 10^5$			59.7541		59.74
$\Omega = 10^6$			128.977		128.71
$\Omega = 10^7$			278.119		277.03

$$f_m'' + \Omega m^2(m^2 - \xi)f_m = \Omega^4 e_m \tag{40}$$

Introducing the new nondimensional time parameter

$$z = 1 - \xi/m^2 \tag{41}$$

we have

$$\ddot{f}_m + \Omega m^8 z f_m = \Omega m^8 e_m \tag{42}$$

where the dots denote differentiation with respect to z. The complementary solution of the ordinary differential equation (3) is given in terms of Bessel functions of the first kind

$$f_{m,c}(z) = z^{1/2}\{A'J_{1/3}[(2/3)m^4\Omega^{1/2}z^{3/2}] + B'J_{-1/3}[(2/3)m^4\Omega^{1/2}z^{3/2}]\} \tag{43}$$

while the particular solution can be formulated in any of the following ways:

$$f_{m,p}(z) = (2/3)m^4\Omega^{1/2}z^{1/2}s_{0,1/3}[(2/3)m^4\Omega^{1/2}z^{3/2}]e_m \tag{44}$$

$$f_{m,p}(z) = (2/3)m^4\Omega^{1/2}z^{1/2}S_{0,1/3}[(2/3)m^4\Omega^{1/2}z^{3/2}]e_m \tag{45}$$

where $s_{\mu,\nu}(z)$ and $S_{\mu,\nu}(z)$ are Lommel functions [18, 19] defined as

$$s_{\mu,\nu}(z) = \sum_{k=0}^{\infty} \frac{(-1)^k z^{\mu+2k+1}}{[(\mu+1)^2 - \nu^2][(\mu+3)^2 - \nu^2]\cdots[(\mu+2k+1)^2 - \nu^2]} \tag{46}$$

$$S_{\mu,\nu}(z) = s_{\mu,\nu}(z) + \frac{2^{\mu-1}}{\sin(\nu\pi)}\Gamma\left[\frac{1}{2}(\mu-\nu+1)\right]\Gamma\left[\frac{1}{2}(\mu+\nu+1)\right] \times \left\{\cos\left[\frac{1}{2}(\mu-\nu)\pi\right]J_{-\nu}(z) - \cos\left[\frac{1}{2}(\mu+\nu)\pi\right]J_\nu(z)\right\} \tag{47}$$

and $\Gamma(\cdots)$ is the Gamma function. In the case under consideration, $\mu = 0$, $\gamma = 1/3$, so that neither of the numbers $\mu \pm \nu$ is an odd negative integer, and the denominator for $s_{\mu,\nu}$ is determined accordingly. It should be noted that integration of the differential equation (42), using the method of variation of parameters, yields the integral representation of the Lommel function

$$s_{\mu,\nu}(z) = \frac{\pi}{2\sin(\nu\pi)}\left[J_\nu(z)\int_0^z z^\mu J_{-\nu}(z)dz + J_{-\nu}(z)\int_0^z z^\mu J_\nu(z)dz\right] \tag{48}$$

Applying equation (32) for $m = 1$, and $s_{0,1/3}(z)$ in the form (48), we arrive at Hoff's [2] representation of the particular solution.

Note that for high values of the argument $(2/3)m^4\Omega^{1/2}z^{3/2}$, the following expansion may be used for $s_{0,1/3}(z)$:

$$S_{0,1/3}(z) = z^{-1}\{1 - [1 - (1/3)^2]z^{-2} + [1 - (1/3)^2][3^2 - (1/3)^2]z^4 + \cdots\} \tag{49}$$

Substitution of

$$f_m = f_{m,c} + f_{m,p} \tag{50}$$

APPENDIX

Deterministic Analysis for the Nearly Perfect Column

Motion Below "Euler Displacement." When the Fourier coefficients of both the initial imperfection and the total deflection are small (for a nearly perfect column), the terms containing $f_n{}^2 f_m$ and $e_n{}^2 f_m$ in equation (8) may be neglected, and the equation reduces to

Downloaded 01 May 2010 to 171.66.16.243. Redistribution subject to ASME license or copyright; see http://www.asme.org/terms/Terms_Use.cfm

in the initial condition (10) yields

$$A'J_{1/3}[(2/3)_m{}^4\Omega^{1/2}] + B'J_{-1/3}[(2/3)m^4\Omega^{1/2}] + (2/3)m^4\Omega^{1/2}S_{0,1/3}[(2/3)m^4\Omega^{1/2}] = e_m \quad (51)$$

$$A'm^4\Omega^{1/2}J_{-2/3}[(2/3)m^4\Omega^{1/2}] - B'm^4\Omega^{1/2}J_{2/3}[(2/3)m^4\Omega^{1/2}] + (2/3)\Omega m^8\{(-2/3)S_{-1,-2/3}[(2/3)m^4\Omega^{1/2}] - (1/2)m^{-4}\Omega^{-1/2}S_{0,1/3}[(2/3)m^4\Omega^{1/2}\} = 0 \quad (52)$$

Having determined A' and B' from equations (51) and (52), we can calculate $f_m(1)$ and $f_m'(1)$ at the "Euler displacement" $\xi = 1$. Table 1 lists, as an example, the values of $f_1(1)$ for a range of Ω, from 2.25 to 10^7; it also lists values obtained by four different methods by Hoff, et al. [7]. As is seen, representation of the solution in terms of Bessel and Lommel functions permits very accurate determination of $f_m(1)$ for all the values of Hoff's dynamic similarity numbers Ω reported in reference [7].

Motion Above "Euler Displacement." When the nondimensional time parameter ξ exceeds m^2 and the Fourier coefficients of the initial imperfection and total deflection are small, nonlinear terms in equation (8) may be neglected, and using the notation

$$\zeta = \xi/m^2 - 1 \quad (53)$$

the equation reduces to

$$\ddot{f}_m - \Omega m^8 \zeta f_m = \Omega m^8 e_m \quad (54)$$

where the dots now denote differentiation with respect to ζ. The complementary solution can be written as [2, 11]

$$f_{m,c}(\zeta) = \zeta^{1/2}\{A''I_{1/3}[(2/3)\Omega^{1/2}\zeta^{3/2}] + B''I_{-1/3}[(2/3)\Omega^{1/2}\zeta^{3/2}]\} \quad (55)$$

where $I_{1/3}(\cdots)$ and $I_{-1/3}(\cdots)$ are modified Bessel functions, and the particular solution can be formulated as

$$f_{m,p}(\zeta) = (2/3)m^4\Omega^{1/2}\zeta^{1/2}E_{0,1/3}[(2/3)m^4\Omega^{1/2}\zeta^{3/2}]e_m \quad (56)$$

here the function $E_{\mu,\nu}(z)$ is defined as

$$E_{\mu,\nu}(\zeta) = \sum_{k=0}^{\infty} \frac{\zeta^{\mu+2k+1}}{[(\mu+1)^2-\nu^2][\mu+3)^2-\nu^2]\cdots[(\mu+2k+1)^2-\nu^2]} \quad (57)$$

This representation of the particular solution of equation (54) is apparently new. The function $E_{\mu,\nu}(\zeta)$ is connected formally with the Lommel function $s_{\mu,\nu}$

$$E_{\mu,\nu}(\zeta) = s_{\mu,\nu}(i\zeta)/i^{\mu+1} \quad (58)$$

where $i = \sqrt{-1}$. Note that the derivative of $E_{\mu,\mu}(\zeta)$ reads

$$\frac{d}{d\xi}E_{\mu,\nu}(\zeta) = (\mu+\nu-1)E_{\mu-1,\nu-1}(\zeta) - \frac{\nu}{\zeta}E_{\mu,\nu}(\zeta) \quad (59)$$

The integration constants A'' and B'' are determined from the continuity conditions at $\zeta = 0$. Reference [25], of which this paper represents an abridged version, contains a comparison of linearized and nonlinear solutions for the case where a single-term Galerkin approximation is used in equation (8). It turns out that the linearized solution satisfactorily predicts the motion of the column up to $\xi = 1.1$ for $e_1 = 10^{-2}$ and up to $\xi = 1.3$ for $e_1 = 10^{-3}$. Fig. 6 gives a comparison of the dimensionless maximum compressive force P_{max}/P_E (computed as per equation (11)) as against the dimensionless Fourier coefficient e_1. Consequently, for nearly perfect columns the linearized solution represents a very good approximation for determining the maximum compressive forces and thus for constructing the reliability functions.

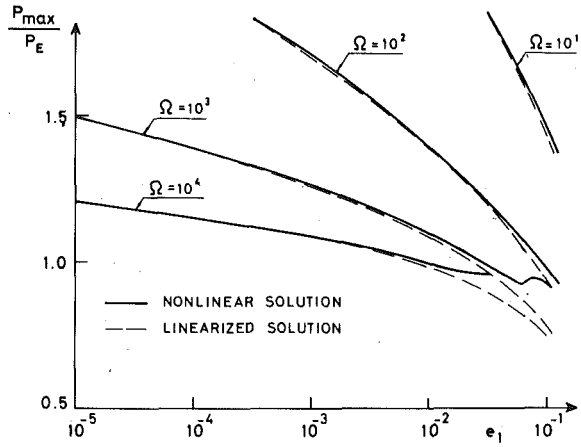

Fig. 6 Comparison of maximum compressive forces for slightly imperfect columns via nonlinear and linearized solutions

Downloaded 01 May 2010 to 171.66.16.243. Redistribution subject to ASME license or copyright; see http://www.asme.org/terms/Terms_Use.cfm

M. R. M. Crespo da Silva

Associate Professor,
Department of Engineering Science,
University of Cincinnati,
Cincinnati, Ohio 45221
Mem. ASME

Nonlinear Resonances in a Column Subjected to a Constant End Force

A canonical perturbation method based on Hamilton-Jacobi theory, used together with Galerkin's method, is employed to analyze the nonlinearly coupled transverse free oscillations of columns subjected to a constant end force. Integrals of motion, readily obtained from this type of analysis, are used to allow the analytical determination of the main characteristics of the resonant motion and of the region of resonance of the system.

1 Introduction

Nonlinear coupling between the modes of oscillation about a Liapunov stable equilibrium of multidegree-of-freedom dynamical systems may give rise to a resonant energy exchange between such modes. In unforced systems this coupling may cause the amplitude of one or more of the generalized coordinates of the system to grow to relatively large values that are independent of the initial conditions for those coordinates. This phenomenon is generally considered undesirable. The determination of the main characteristics of these nonlinear resonant motions, as well as finding ways to reduce or even eliminate such phenomenon, are important aspects of research in nonlinear system dynamics. A comprehensive study of nonlinear systems and their features is presented in recent books by Nayfeh [1] and by Nayfeh and Mook [2].

Dynamical systems exhibit the aforementioned nonlinear resonance phenomenon when the frequencies of their linearized oscillation modes is *a* near a ratio m/n, where m and n are integers; the actual value of m/n is determined by the nonlinearities present in the differential equations of motion of the system. This phenomenon may also be observed in elastic systems, such as beams or columns, able to exhibit flexure in two normal directions in space. The analysis of nonplanar motions is inherently more complex than the planar ones since it also requires special attention in the formulation of the differential equations of motion so that the nonlinearities in the system are consistently taken into account. Ho, Scott, and Eisley [3] considered the free motion of beams with immovable ends and no torsion, and Crespo da Silva and Glynn [4] considered such motion in fixed-free beams including the effects of support asymmetry and torsion. A more extensive bibliography for nonlinear beam oscillations is given in [4, 5].

The objective of this paper is to investigate the free nonlinear resonant oscillations in columns subjected to a constant (i.e., in magnitude and direction) end force, and to determine the effect of this force on the resonance region of the system and on the main characteristics of its motion. The formulation presented in [5] is used to obtain the equations of motion and the boundary conditions of the system. A canonical perturbation method [1, 6–8] based on Hamilton-Jacobi theory [9–11], used together with Galerkin's method [12] is employed to analyze the motion. The canonical perturbation method just mentioned has been used mainly in classical dynamics, especially in space mechanics problems, e.g., [6–8]. Coupled with a method such as Galerkin's, it is particularly useful in facilitating the extraction of integrals of motion for the system.

2 Problem Formulation and Method of Solution

Consider an initially straight thin inextensional column of length L and total mass mL, capable of undergoing flexure in two directions and torsion, and subjected to a constant force $\mathbf{F} = -F\hat{x}_1$ applied at its end $s = 1$, as shown in Fig. 1. In that figure, sL denotes arc-length measured along the neutral axis of the column, and $Lu(s, \tau)$, $Lv(s, \tau)$, and $Lw(s, \tau)$, with τ denoting time, are the elastic displacements of the centroid of the column's cross-sectional area, at location s, along the inertial directions x_1, x_2, and x_3, respectively. The unit vectors along these directions are denoted by $\hat{x}_1$, $\hat{x}_2$, and $\hat{x}_3$ and the virtual work done by $\mathbf{F}$ is seen to be given as $\delta W_B = -FL\delta u(s = 1, \tau = \tau)$. Note that s, $u(s, \tau)$, $v(s, \tau)$, and $w(s, \tau)$ are nondimensional quantities. The column is assumed to be thin enough so that its distributed mass moments of inertia are of higher order than the order of approximations to be carried out in the analysis that will follow. Let D_1, D_2, and D_3 denote, respectively, the torsional and flexural stiffness of the column, which are assumed to be constants; the "2" and "3" axes are the principal axes of the column's cross section that is normal, at all times, to the neutral "1" axis. When the column is undeflected, the 1 and x_1-axes coincide with each other, while the 2 and 3-axes are parallel to x_2 and x_3, respectively. We assume here that $u(0, \tau) = 0$ and that the column is free to twist at the boundary $s = 1$ but not at $s = 0$.

With the foregoing assumptions the differential equations of motion governing the flexural deflections $v(s, \tau)$ and $w(s, \tau)$ can be readily

Contributed by the Applied Mechanics Division for publication in the JOURNAL OF APPLIED MECHANICS.

Discussion on this paper should be addressed to the Editorial Department, ASME, United Engineering Center, 345 East 47th Street, New York, N. Y. 10017, and will be accepted until September 1, 1980. Readers who need more time to prepare a discussion should request an extension from the Editorial Department. Manuscript received by ASME Applied Mechanics Division, October, 1979.

Copyright © 1980 by ASME
Downloaded 01 May 2010 to 171.66.16.243. Redistribution subject to ASME license or copyright; see http://www.asme.org/terms/Terms_Use.cfm

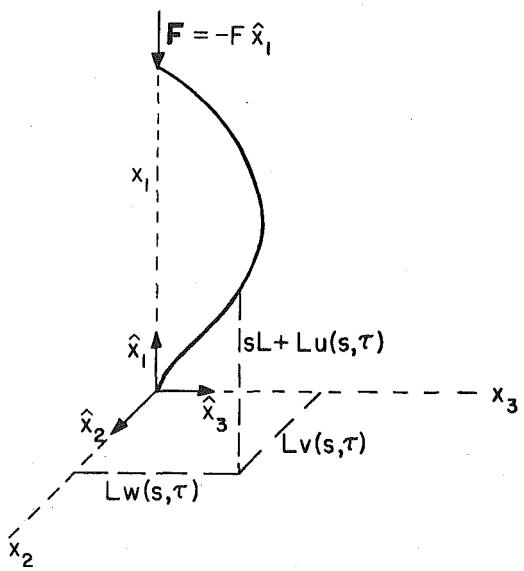

Fig. 1 Elastic displacements of the column at location s, along the inertial directions x_1, x_2, x_3

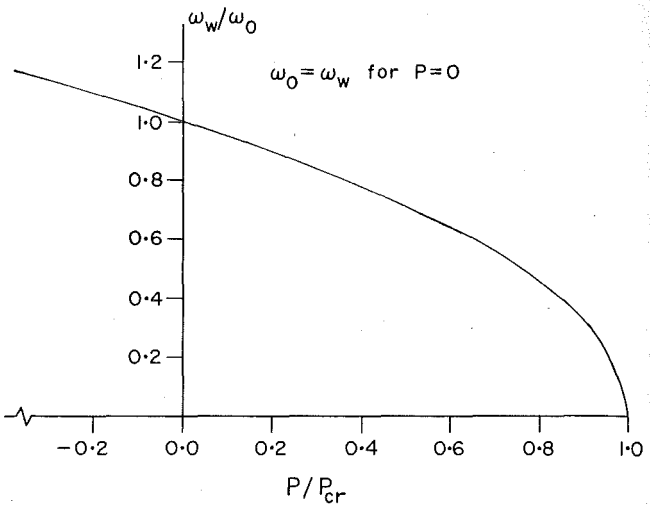

Fig. 2 Normalized frequency ω_w versus the load parameter P for Cases 1 and 2 (for Case 1, $P_{cr} = 4\pi^2$ and $\omega_0 \approx 4.73^2$; for Case 2, $P_{cr} \approx (4.4934)^2$, and $\omega_0 \approx (3.9266)^2$)

obtained by using the formulation presented earlier by Crespo da Silva and Glynn [5, 13]. When written in integro differential form, and in terms of nondimensional variables, these equations when expanded to cubic nonlinearities are obtained as

$$\ddot{v} + Pv'' + \beta_y v'''' = -[\beta_y v'(v'^2 + w'^2)'' + Pv'(v'^2 + w'^2)]'/2 - \left\{\frac{1}{2}v' \int_1^s \left[\int_0^s (v'^2 + w'^2)ds\right]^{\cdot\cdot} ds - (1-\beta_y)\left[w'' \int_1^s v''w''ds - w''' \int_0^s v''w'ds\right]\right\}' - [(1-\beta_y)^2/\beta_\gamma]\left[w'' \int_0^s \int_1^s v''w''dsds\right]'' \quad (1a)$$

$$\ddot{w} + Pw'' + w'''' = -[w'(v'^2 + w'^2)'' + Pw'(v'^2 + w'^2)]'/2 - \left\{\frac{1}{2}w' \int_1^s \left[\int_0^s (v'^2 + w'^2)ds\right]^{\cdot\cdot} ds + (1-\beta_y)\left[v'' \int_1^s v''w''ds - v''' \int_0^s v'w''ds\right]\right\}' - [(1-\beta_y)^2/\beta_\gamma]\left[v'' \int_0^s \int_1^s v''w''dsds\right]'' \quad (1b)$$

where $\beta_y = D_3/D_2$, $\beta_\gamma = D_1/D_2$ and $P = FL^2/D_2$; primes denote partial differential with respect to the normalized arc-length s, and dots denote partial differentiation with respect to a nondimensional time $t = \tau[D_2/(mL^4)]^{1/2}$.

For simplicity, we consider here cases for which the boundary conditions for $v(s, t)$ and $w(s, t)$ are linear functions of v and w and their partial derivatives. We will address the following two cases:

Case 1: Clamped-Clamped/Sliding Column

$$v(0, t) = w(0, t) = v'(0, t) = w'(0, t) = 0 \quad (2a)$$

$$v(1, t) = w(1, t) = v'(1, t) = w'(1, t) = 0 \quad (2b)$$

Case 2: Clamped-Pinned/Sliding Column

$$v(0, t) = w(0, t) = v'(0, t) = w'(0, t) = 0 \quad (3a)$$

$$v(1, t) = w(1, t) = v''(1, t) = w''(1, t) = 0 \quad (3b)$$

If the response of the column to the initial conditions is approximated by one mode of oscillation, the solution to the associated linearized differential equations of motion, satisfying the boundary conditions given by equations (2a, b) or (3a, b), can be readily obtained for arbitrary values of β_y as

$$v(s, t) \approx F_v(s)A_v \cos \omega_v(t + \beta_v) \quad (4a)$$

$$w(s, t) \approx F_w(s)A_w \cos \omega_w(t + \beta_w) \quad (4b)$$

The function $F_w(s)$, for example, is the solution to the differential equation

$$F_w'''' + PF_w'' - \omega_w{}^2F_w = 0 \quad (4c)$$

with the boundary conditions $F_w(0) = F_w'(0) = F_w(1) = 0$ and $F_w'(1) = 0$, for Case 1, or $F_w''(1) = 0$ for Case 2. For both cases, it is given as

$$F_w(s) = C[r_2 \sin r_1 s - r_1 \sinh r_2 s + K(\cosh r_2 s - \cos r_1 s)] \quad (4d)$$

with $C \neq 0$ arbitrary (later on it will be chosen such that

$$\int_0^1 F_w{}^2(s)ds = 1,$$

for convenience) and

$$K = (r_1 \sinh r_2 - r_2 \sin r_1)/(\cosh r_2 - \cos r_1) \quad (4e)$$

$$r_1{}^2 = [(P^2 + 4\omega_w{}^2)^{1/2} + P]/2; \quad r_2{}^2 = [(P^2 + 4\omega_w{}^2)^{1/2} - P]/2 \quad (4f)$$

The constants r_1 and r_2 satisfy the following characteristic equations:

$$2r_1r_2[1 - (\cos r_1)\cosh r_2] - P(\sin r_1)\sinh r_2 = 0 \quad \text{(for Case 1)} \quad (4g)$$

$$r_2 \tan r_1 = r_1 \tanh r_2 \quad \text{(for Case 2)} \quad (4h)$$

which can be solved numerically. Fig. 2 shows the dependence of the normalized frequency ω_w on the load parameter P, for both $P > 0$ and $P < 0$. The critical value of P, $P = P_{cr}$, corresponds to $\omega_w = 0$ (or $\omega_v = 0$). Buckling occurs in the x_3 direction (see Fig. 1) when $\beta_y > 1$ (i.e., $D_3 > D_2$) and in the x_2-direction when $\beta_y < 1$. For buckling in the x_3-direction, $P_{cr} = FL^2/D_2 \approx (4.4934)^2$ for Case 2, and $4\pi^2$ for Case 1; for buckling in the x_2-direction these values correspond to $P_{cr}/\beta_y = FL^2/D_3$. Since these critical loads correspond to zero frequencies, they may also be determined by a static stability analysis.

For infinitesimal oscillations, A_v and A_w in equations (4a, b) are constants determined by the initial conditions of the motion. When β_y is "near" unity, $F_v(s) \approx F_w(s)$ and the natural frequencies ω_v and ω_w are approximately equal to each other. In this case, the nonlinearities in the right-hand side of equations (1a, b) generate a

Downloaded 01 May 2010 to 171.66.16.243. Redistribution subject to ASME license or copyright; see http://www.asme.org/terms/Terms_Use.cfm

number of periodic terms in the response, among which are terms with frequency $\omega_v \approx \omega_w$. This causes the v and w motions to be in a state of nonlinear resonance. This state, which is characterized by an energy exchange between the v and w motions, persists for a certain range of the ratio ω_v/ω_w—called the "nonlinear resonant region" of the system. In this case, both A_v and A_w are slowly varying functions of time. Here, we will analyze these resonant motions and determine the influence of the normalized force P on the resonant region of the column. For this we will use a canonical perturbation method based on Hamilton's differential equations of motion [1, 6–8]. To apply this method we first transform equations (1*a*, *b*) to ordinary differential equations through Galerkin's method [12]. For $\beta_y \approx 1$, the solutions to those equations are approximated as

$$v(s, t) \approx F_w(s)V(t); \quad w(s, t) \approx F_w(s)W(t) \tag{5}$$

With $F_w(s)$ normalized so that

$$\int_0^1 F_w{}^2(s)ds = 1,$$

the following differential equations with cubic nonlinearities are obtained for $V(t)$ and $W(t)$,

$$\ddot{V} + \omega_v{}^2V + V\{\alpha_4(V\dot{V} + W\dot{W})\cdot + (\beta_y\alpha_{30} + \alpha_3 - \alpha_{30})(V^2 + W^2) - [\alpha_1(1 - \beta_y) - \alpha_2(1 - \beta_y)^2/\beta_\gamma]W^2\} = 0 \tag{6a}$$

$$\ddot{W} + \omega_w{}^2W + W\{\alpha_4(V\dot{V} + W\dot{W})\cdot + \alpha_3(V^2 + W^2) + [\alpha_1(1 - \beta_y) + \alpha_2(1 - \beta_y)^2/\beta_\gamma]V^2\} = 0 \tag{6b}$$

where

$$\alpha_1 = \int_0^1 F_w(s)\left\{F_w''(s)\int_1^s F_w''^2(s)ds - F_w'''(s)\int_0^s F_w'(s)F_w''(s)ds\right\}'ds \tag{6c}$$

$$\alpha_2 = \int_0^1 F_w(s)\left\{F_w''(s)\int_0^s\int_1^s F_w''^2(s)dsds\right\}''ds \tag{6d}$$

$$\alpha_{30} = \frac{1}{2}\int_0^1 F_w(s)\{F_w'(s)[F_w'^2(s)]''\}'ds \tag{6e}$$

$$\alpha_3 = \alpha_{30} + \frac{1}{2}P\int_0^1 F_w(s)[F_w'^3(s)]'ds \tag{6f}$$

$$\alpha_4 = \int_0^1 F_w(s)\left\{F_w'(s)\int_1^s\int_0^s F_w'^2(s)dsds\right\}'ds \tag{6g}$$

$$\omega_v{}^2 = \beta_y\omega_w{}^2 + P\alpha_P(1 - \beta_y); \quad \alpha_P = \int_0^1 F_w(s)F_w''(s)ds \tag{6h}$$

The foregoing definite integrals may be evaluated numerically for any chosen value of P.

3 The Hamiltonian for the System

Equations (6*a*, *b*) can be obtained from Lagrange's equations, in terms of the generalized coordinates $V(t)$ and $W(t)$, with a Lagrangian $L(V, W, \dot{V}, \dot{W})$ given as

$$L = (\dot{V}^2 - \omega_v{}^2V^2 + \dot{W}^2 - \omega_w{}^2W^2)/2 + [2\alpha_4(V\dot{V} + W\dot{W})^2 - \beta_3V^4 - \alpha_3W^4 - 2K_1V^2W^2]/4 \tag{7a}$$

where

$$\beta_3 = \alpha_3 - \alpha_{30}(1 - \beta_y) \tag{7b}$$

$$K_1 = \beta_3 - \alpha_1(1 - \beta_y) + \alpha_2(1 - \beta_y)^2/\beta_\gamma \tag{7c}$$

The validity of the foregoing Lagrangian can be verified with the aid of the following proposition:

Proposition: For α_1 and α_{30} defined by equations (6*c*, *e*), $\alpha_{30} + 2\alpha_1 = 0$.

Proof: From the definitions of α_1 and α_{30} it follows that:

$$\alpha_{30} + 2\alpha_1 = \int_0^1 F_w(s)\left\{F_w'(s)[F_w'(s)F_w'''(s) + F_w''^2(s)] + 2F_w''(s)\int_1^s F_w''^2(s)ds - F_w'''(s)[F_w'^2(s) - F_w'^2(0)]\right\}'ds \tag{8a}$$

(*Cont.*)

Noticing that $F_w(0) = F_w'(0) = 0$, $F_w(1) = 0$, and $F_w'(1)$. $F_w''(1) = 0$, integration by parts yields,

$$\alpha_{30} + 2\alpha_1 = -\int_0^1\left[F_w'^2(s)F_w''^2(s)ds - \int_0^1[F_w'^2(s)]'\int_1^s F_w''^2(s)dsds\right] = -\int_0^1 F_w'^2(s)F_w''^2(s)ds - \left[F_w'^2(s)\int_1^s F_w''^2(s)ds\right]_0^1 - \int_0^1 F_w'^2(s)F_w''^2(s)ds = 0 \tag{8b}$$

The Hamiltonian H corresponding to the Lagrangian L is defined as

$$H = [\partial L/\partial\dot{V} \;\; \partial L/\partial\dot{W}]\begin{bmatrix}\dot{V}\\ \dot{W}\end{bmatrix} - L = (\dot{V}^2 + \omega_v{}^2V^2 + \dot{W}^2 + \omega_w{}^2W^2)/2 + [2\alpha_4(V\dot{V} + W\dot{W})^2 + 2K_1V^2W^2 + \beta_3V^4 + \alpha_3W^4]/4 \tag{9}$$

In terms of the generalized momenta p_v and p_w given by

$$p_v = \partial L/\partial\dot{V} = \dot{V} + \alpha_4V(V\dot{V} + W\dot{W}) \tag{10a}$$

$$p_w = \partial L/\partial\dot{W} = \dot{W} + \alpha_4W(V\dot{V} + W\dot{W}) \tag{10b}$$

the Hamiltonian becomes, when expanded to fourth-order nonlinearities in (V, W, p_v, p_w),

$$H(V, W, p_v, p_w) = [(p_v{}^2 + \omega_v{}^2V^2)/2 + (p_w{}^2 + \omega_w{}^2W^2)/2] + [\beta_3V^4 + \alpha_3W^4 + 2K_1V^2W^2 - 2\alpha_4(p_vV + p_wW)^2]/4 + \ldots = H_2 + H_4 + \ldots \tag{11}$$

where H_2 and H_4 stand, respectively, for the second and fourth-order terms. With H given as in the foregoing, the differential equations of motion (6*a*, *b*) may be obtained from Hamilton's canonical equations as

$$\partial H/\partial p_v = \dot{V}; \quad \partial H/\partial p_w = \dot{W} \tag{12a}$$

$$\partial H/\partial V = -\dot{p}_v; \quad \partial H/\partial W = -\dot{p}_w \tag{12b}$$

4 Integration of the Canonical Differential Equations

To a first approximation, the generalized momenta p_v and p_w are equal to the generalized velocities $\dot{V}$ and $\dot{W}$, respectively [equations (10*a*, *b*)]. If the H_4 term in the expresion for the Hamiltonian H is neglected when compared to H_2, equations (12*a*, *b*) yield the linearized differential equations of motion to which an exact solution can be readily found. According to the method of variation of parameters applied to Hamilton's equations [1, 6–8], an approximate solution to equations (12*a*, *b*) may be obtained from the linearized solutions when the higher-order term H_4 is included in H. To obtain these approximate solutions, we first transform the variables (V, W) and (p_v, p_w) into a new set of generalized coordinates (β_v, β_w) and momenta (α_v, α_w), respectively. Two conditions are imposed on the transformation, namely,

1 That the new variables $(\beta_v, \beta_w, \alpha_v, \alpha_w)$ be constants when H_4 is neglected when compared to H_2.

2 That the new variables be canonically associated with a new Hamiltonian H^*.

The latter condition is mathematically expressed as

Downloaded 01 May 2010 to 171.66.16.243. Redistribution subject to ASME license or copyright; see http://www.asme.org/terms/Terms_Use.cfm

$$\partial H^*/\partial\alpha_i = \dot{\beta}_i; \quad \partial H^*/\partial\beta_i = -\dot{\alpha}_i \quad (i = v, w) \tag{13}$$

The aforementioned equations disclose that if $H^* = 0$ [when H_4 is neglected in comparison to H_2 in equation (11)], the new variables α_i and β_i ($i = v, w$) are constants, as desired. According to Hamilton-Jacobi theory [9-11], the transformation $(V, W) \rightarrow (\beta_v, \beta_w)$, $(p_v, p_w) \rightarrow (\alpha_v, \alpha_w)$ may be obtained through a generating function $S(V, W, \alpha_v, \alpha_w, t)$, with $p_v = \partial S/\partial V$ and $p_w = \partial S/\partial W$, satisfying the Hamilton-Jacobi equation

$$H_2(V, W, p_v = \partial S/\partial V, \quad p_w = \partial S/\partial W) + \partial S/\partial t = H^* = 0 \tag{14}$$

Once equation (14) is solved for S, the coordinates (V, W) are obtained in terms of the constants (α_v, α_w) and (β_v, β_w) from the relations

$$\partial S/\partial\alpha_i = \beta_i \quad (i = v, w) \tag{15}$$

With H_2 given as in equation (11), equation (14) becomes

$$\frac{1}{2}\left[\left(\frac{\partial S}{\partial V}\right)^2 + \omega_v{}^2V^2\right] + \frac{1}{2}\left[\left(\frac{\partial S}{\partial W}\right)^2 + \omega_w{}^2W^2\right] + \frac{\partial S}{\partial t} = 0 \tag{16}$$

Since none of the bracketed terms in the above equation is a function of the variables contained in the other bracket, each of these terms is a constant. Choosing these constants to be α_v and α_w, the solution to equation (16) is then obtained as

$$S = -(\alpha_v + \alpha_w)t + \int (2\alpha_v - \omega_v{}^2V^2)^{1/2}dt + \int (2\alpha_w - \omega_w{}^2W^2)^{1/2}dt \tag{17}$$

From equations (15) and (17), the following solutions to the linearized differential equations (i.e., when $H = H_2$) are obtained

$$V(t) = \frac{\sqrt{2\alpha_v}}{\omega_v}\sin\omega_v(t + \beta_v); \quad p_v = \sqrt{2\alpha_v}\cos\omega_v(t + \beta_v) \tag{18a}$$

$$W(t) = \frac{\sqrt{2\alpha_w}}{\omega_w}\sin\omega_w(t + \beta_w); \quad p_w = \sqrt{2\alpha_w}\cos\omega_w(t + \beta_w) \tag{18b}$$

If the presence of the term H_4 in the Hamiltonian H is now taken into account, the quantities (α_v, α_w) and (β_v, β_w) in the solutions for $V(t)$ and $W(t)$ are no longer constants. By applying the method of variation of parameters to equations (13), an approximate solution to the nonlinear differential equations of motion is given as in equations (18a, b) with α_i and β_i satisfying the differential equations

$$\partial H_4/\partial\alpha_i = \dot{\beta}_i; \quad \partial H_4/\partial\beta_i = -\dot{\alpha}_i \tag{19}$$

The expression for H_4 in terms of $(\alpha_v, \alpha_w, \beta_v, \beta_w)$ is readily obtained from equations (11) and (18a, b). It contains terms with frequencies $2\omega_v$, $2\omega_w$, $4\omega_v$, $4\omega_w$, $2(\omega_v + \omega_w)$ and $2|\omega_v - \omega_w|$.

5 Nonlinear Resonant Motion

When the frequency $2|\omega_v - \omega_w|$, present in H_4, is zero or near zero, a resonant phenomenon between the $V(t)$ and $W(t)$ motions occur. This phenomenon is characterized by an energy exchange between these motions, due to the nonlinear terms in the differential equations (19). When ω_v is "not near" ω_w the solution to equations (6a, b) may be reasonably approximated by equations (18a, b) with α_i and β_i ($i = v, w$) constants.

For a nonlinear resonant motion (α_v, α_w) and (β_v, β_w) are slowly varying functions of time that may be obtained by averaging out the high frequency terms (denoted by HFT below) in the expression for H_4. From equations (11) and (18a, b) the following averaged Hamiltonian is obtained:

$$H_4 = [(3\beta_3/\omega_v{}^2 - 2\alpha_4)\alpha_v{}^2/\omega_v{}^2 + (3\alpha_3/\omega_w{}^2 - 2\alpha_4)\alpha_w{}^2/\omega_w{}^2]/8 + [K_1(2 + \cos\psi) - 2\alpha_4\omega_v\omega_w\cos\psi]\alpha_v\alpha_w/(4\omega_v{}^2\omega_w{}^2) + \text{HFT} \tag{20}$$

where $\psi = 2[(\omega_w - \omega_v)t + \omega_w\beta_w - \omega_v\beta_v]$.

The maximum and minimum values of α_v and α_w [and, hence, of the motions $V(t)$ and $W(t)$], and the range of $\omega_v/\omega_w = f(\beta_y, P)$ for which the motion is resonant, may be readily extracted from equations (19). Toward this end it is first noted that, since

$$\partial H_4/\partial\beta_v = -[\alpha_4 - K_1/(2\omega_v\omega_w)](\alpha_v\alpha_w/\omega_w)\sin\psi \equiv -(\omega_v/\omega_w)\partial H_4/\partial\beta_w = -\dot{\alpha}_v = (\omega_v/\omega_w)\dot{\alpha}_w \tag{21}$$

the following integral of the motion is immediately obtained:

$$(\omega_w/\omega_v)\alpha_v + \alpha_w = \text{constant} = C_1 \tag{22a}$$

Also, since $\omega_v\partial H_4/\partial t \equiv (\omega_v - \omega_w)\partial H_4/\partial\beta_v = -(\omega_v - \omega_w)\dot{\alpha}_v$, and $dH_4/dt = \partial H_4/\partial t$, it follows that

$$H_4 + (1 - \omega_w/\omega_v)\alpha_v = \text{constant} = C_2 \tag{22b}$$

The constants C_1 and C_2 are determined from the initial conditions $V(0)$, $W(0)$, $\dot{V}(0)$, and $\dot{W}(0)$.

The determination of the two integrals of motion C_1 and C_2 make it possible to reduce the differential equation for α_v (or α_w) to the form $\dot{\alpha}_v = \dot{\alpha}_v(\alpha_v)$, from which the extremum values for α_v may be obtained with no major difficulty. Considering initial conditions of the type $\alpha_v(0) \ll \alpha_w(0)$ (i.e., the column is given an initial displacement that is nominally in the x_3-direction shown in Fig. 1), the following differential equation is obtained—to the order of approximation considered here—when $\alpha_w(t)$ and $\psi(t)$ are eliminated from equation (21) through the use of equations (22a, b),

$$\dot{\alpha}_v = \pm(2\alpha_5/\omega_w)\alpha_v\{2(\omega_w/\omega_v - 1)[C_1 + \omega_w{}^4(1 - \omega_w/\omega_v)/(2\alpha_5) - \alpha_v]/\alpha_5\}^{1/2} + o[\alpha_v(0)] \tag{23}$$

where $\alpha_5 = \omega_w{}^2\alpha_4/2 - \alpha_3/4$.

With $C_1 = \alpha_w(0) + O[\alpha_v(0)]$, the previous equation indicates that the maximum value of α_v, for a resonant motion, is independent of the initial conditions for the V motion and is obtained as

$$(\alpha_v)_{\max} = \alpha_w(0) + \omega_w{}^4(1 - \omega_w/\omega_v)/(2\alpha_5) + O[\alpha_v(0)] \tag{24}$$

For $(\alpha_v)_{\max}$ to be positive and the right-hand side of equation (23) to be real, the following inequalities must be satisfied:

$$1 - \omega_w/\omega_v \geq -(2\alpha_5/\omega_w{}^4)\alpha_w(0); \quad \omega_v/\omega_w \leq 1 \tag{25}$$

The foregoing inequalities, with $\omega_w = r_1r_2$ [as disclosed by equations (4f)] and ω_v/ω_w obtained in terms of β_y and P as in equation (6h), determine the resonant region for the column, in the parameter space $(\alpha_w(0), \beta_y, P)$. Along the boundaries of the resonant region $(\alpha_v)_{\max}$ is of the same order as $\alpha_v(0)$. From equation (6h) and inequalities (25) these boundaries are found to be

$$\beta_y = 1 \tag{26a}$$

and

$$\beta_y = \{[1 + 2\alpha_5\alpha_w(0)/\omega_w{}^4]^{-2} - P\alpha_p/\omega_w{}^2\}/(1 - P\alpha_p/\omega_w{}^2) \tag{26b}$$

The expression for $\alpha_w(0)$ is immediately obtained from equations (18a, b) as

$$\alpha_w(0) = \frac{1}{2}[(\omega_w W)^2 + \dot{W}^2]_{t=0} \tag{26c}$$

Fig. 3 shows the variation of the coefficients α_5 and α_p as a function of the load parameter P, while Fig. 4 illustrates the effect of the same parameter on the resonant region of the system. This region, which is bounded by the transition curves given by equations (26a, b), lies between the line $\beta_y = 1$ and the line determined by a given value of P, as shown in Fig. 4. For given values of the flexural stiffness ratio $\beta_y = D_3/D_2$, the initial condition parameter $\alpha_w(0) \gg \alpha_v(0)$, and P, such that the point $(\alpha_w(0), \beta_y, P)$ is inside the resonant region of the system, the motion of the column is nonplanar even if it is nominally started (i.e., $\alpha_v(0) \neq 0$ but very small) along the x_3-direction. For a resonant motion, energy is exchanged between the v and w motions in such a way that the v motion slowly grows to a maximum value that is *independent* of its initial conditions. If the v initial conditions are decreased, the v motion just takes longer to reach its same maximum value. As indicated by Fig. 4, increasing the value of P for given values of $\alpha_w(0)$ and β_y (indicated by point C in that figure) eventually eliminates the resonance phenomenon and the motion of the column becomes nominally planar. This is shown in more detail in Fig. 5 for

Downloaded 01 May 2010 to 171.66.16.243. Redistribution subject to ASME license or copyright; see http://www.asme.org/terms/Terms_Use.cfm

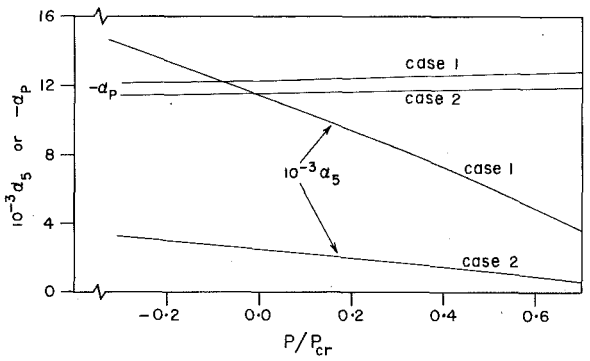

Fig. 3 Coefficients α_5 and α_P as a function of P

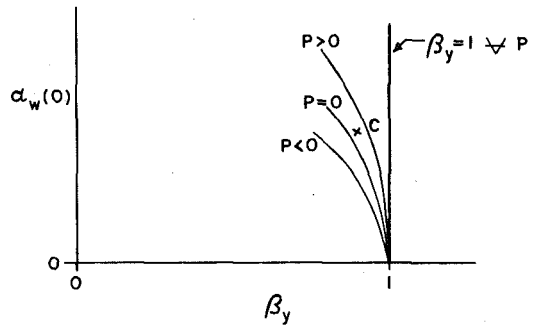

Fig. 4 Effect of the load parameter P on the region of resonance of the column (region bounded by $\beta_y = 1$ and the curved line corresponding to a given value of P)

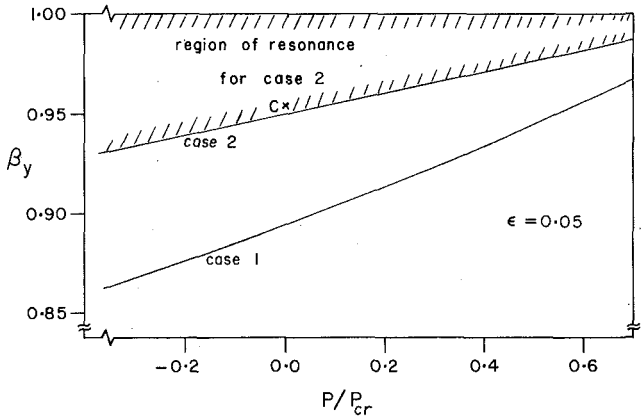

Fig. 5 Region of resonance in the (β_y, P/P_{cr}) space for $\epsilon = 0.05$ (ϵ is the norm of the initial condition of the $W(t)$ motion)

$\epsilon = \sqrt{2\alpha_w(0)}/\omega_w = 0.05$. As indicated by equation (26c), ϵ is the norm of the initial condition of $W(t)$. The $V(t)$ and $W(t)$ motions for Case 2 with $\epsilon = 0.05$ and $\beta_y = 0.955$, which correspond to point C in Fig. 5, are shown in Figs. 6 (C inside the resonant region) and 7 (C outside the resonant region). For a fixed value of ϵ, the maximum value of $V(t)$ in Fig. 6 is independent of the small initial conditions of the V-motion. For the parameters shown in Fig. 7, however, the first of inequalities (25) is not satisfied and, hence, the maximum value of $V(t)$ can be made arbitrarily small by decreasing the magnitude of the initial conditions of the V-motion. Fig. 8 shows a comparison of the maximum value of $V(t)$ for a resonant motion, as determined from equations (24) and (18a, b) (solid lines) and from a numerical integration of equations (6a, b) with $W(0) = \epsilon = 0.05$, $V(0) = \epsilon/10$, and $\epsilon/100$, and $\dot{W}(0) = \dot{V}(0) = 0$.

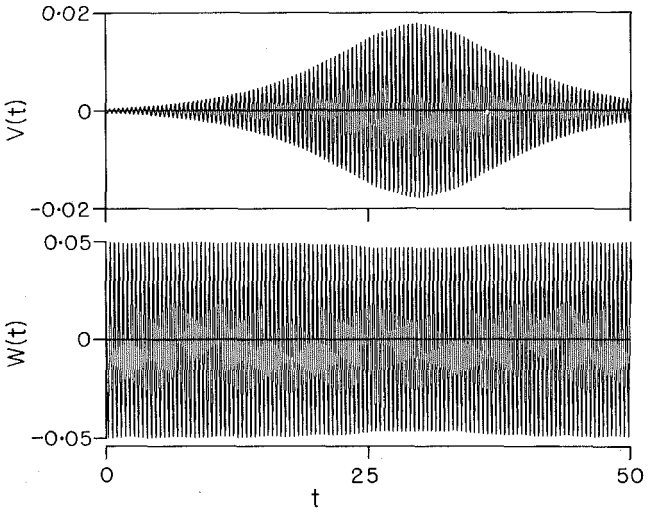

Fig. 6 Resonant $V(t)$ and $W(t)$ motions for Case 2, with $\beta_y = 0.955$, $P = 0$ and $W(0) = \epsilon = 0.05$, $\dot{W}(0) = 0$, $\dot{V}(0) = 0$, $V(0) = \epsilon/100$ (motion corresponding to point C in Fig. 5)

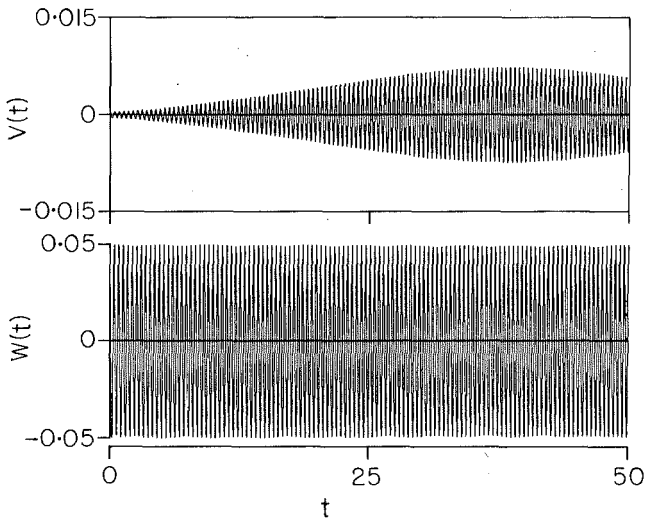

Fig. 7 Nonresonant $V(t)$ and $W(t)$ motions for Case 2; $\beta_y = 0.955$, $P = 0.1P_{cr}$, $W(0) = \epsilon = 0.05$, $\dot{W}(0) = 0$, $\dot{V}(0) = 0$, $V(0) = \epsilon/100$

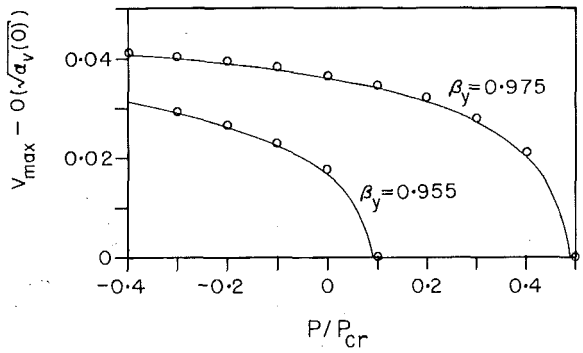

Fig. 8 Maximum value of $V(t)$ versus P/P_{cr} for Case 2; $W(0) = \epsilon = 0.05$, $\dot{W}(0) = 0$, $\dot{V}(0) = 0$, $V(0) = \epsilon/100$ (— analytical results; 0 numerical integration of the nonlinear differential equations)

Downloaded 01 May 2010 to 171.66.16.243. Redistribution subject to ASME license or copyright; see http://www.asme.org/terms/Terms_Use.cfm

6 Concluding Remarks

The problem of nonlinear resonant interactions between the lateral oscillations of a column was analyzed using Galerkin's method together with a perturbation method based on Hamilton-Jacobi theory. The former was used to transform the partial integro-differential equations of motion to ordinary ones, to which the perturbation method used here was employed. To this author's knowledge, this is the first time this method has been applied to an elastic system. The analysis presented here also indicates, as pointed out elsewhere [4], that when β_y is near unity the terms multiplied by $(1 - \beta_y)$ in equations (1*a*, *b*) do not significantly affect the motion. This also includes the term involving the torsional stiffness β_γ.

References

1 Nayfeh, A. H., *Perturbation Methods,* Wiley Interscience, New York, 1973.

2 Nayfeh, A. H., and Mook, D. T., *Nonlinear Oscillations*, Wiley Interscience, New York, 1979.

3 Ho, C. H., Scott, R. A., and Eisley, J. G., "Nonplanar Nonlinear Oscillations of a Beam—II. Free Motions," *Journal of Sound and Vibration,* Vol. 47, No. 3, 1976, pp. 333–339.

4 Crespo da Silva, M. R. M., and Glynn, C. C., "Nonlinear Nonplanar Resonant Oscillations in Fixed Free Beams With Support Asymmetry," *International Journal of Solids and Structures,* Vol. 15, No. 3, 1979, pp. 209–219.

5 Crespo da Silva, M. R. M., and Glynn, C. C., "Nonlinear Flexural-Flexural-Torsional Dynamics of Inextensional Beams—I. Equations of Motion," *Journal of Structural Mechanics,* Vol. 6, No. 4, 1978, pp. 437–448.

6 Breakwell, J. V., and Pringle, R., Jr., "Nonlinear Resonances Affecting Gravity-Gradient Stability," *Astrodynamics,* Gauthier Villars, Paris, 1966.

7 Kane, T. R., and Kahn, M. E., "On a Class of Two-Degree-of-Freedom Oscillations," ASME JOURNAL OF APPLIED MECHANICS, Vol. 35, No. 3, 1968, pp. 547–552.

8 Crespo da Silva, M. R. M., "Nonlinear Resonant Attitude Motions in Gravity-Stabilized Gyrostat Satellites," *International Journal of Nonlinear Mechanics*, Vol. 7, No. 6, 1972, pp. 621–641.

9 Goldstein, H., *Classical Mechanics*, Addison-Wesley, Reading, Mass., 1965.

10 Lanczos, C., *The Variational Principles of Mechanics*, University of Toronto Press, Toronto, 1966.

11 Greenwood, D. T., *Classical Dynamics*, Prentice-Hall, Englewood Cliffs, N. J., 1977.

12 Leipholz, H. H. E., *Stability Theory,* Academic Press, New York, 1970.

13 Crespo da Silva, M. R. M., and Glynn, C. C., "Nonlinear Flexural-Flexural-Torsional Dynamics of Inextensional Beams—II. Forced Motions," *Journal of Structural Mechanics*, Vol. 6, No. 4, 1978, pp. 449–461.

Downloaded 01 May 2010 to 171.66.16.243. Redistribution subject to ASME license or copyright; see http://www.asme.org/terms/Terms_Use.cfm

P. C. Hughes[2]
Visiting Professor.

R. E. Skelton
Associate Professor.

School of Aeronautics and Astronautics,
Purdue University,
West Lafayette, Ind.

Controllability and Observability of Linear Matrix-Second-Order Systems[1]

This paper studies the controllability and observability of the system $\mathbf{M}\ddot{\mathbf{q}} + \mathbf{G}\dot{\mathbf{q}} + \mathbf{K}\mathbf{q} = \mathbf{B}\mathbf{u}$, *where* $\mathbf{M}$ *is symmetric and positive-definite,* $\mathbf{G}$ *is skew-symmetric and* $\mathbf{K}$ *is symmetric. In all cases, the output equation is* $\mathbf{y} = \mathbf{P}\mathbf{q} + \mathbf{R}\dot{\mathbf{q}}$. *This special structure is exploited to derive relatively simple controllability and observability conditions which are shown to provide important insights on the modal behavior of the system and to furnish information on the number and positioning of sensors and actuators.*

Introduction

The behavior of many systems of importance in engineering practice is governed by

$$\mathbf{M}\ddot{\mathbf{q}} + \mathbf{G}\dot{\mathbf{q}} + \mathbf{D}\dot{\mathbf{q}} + \mathbf{K}\mathbf{q} = \mathbf{f} \tag{1}$$

where $\mathbf{q}$ and $\mathbf{f}$ are $N \times 1$, and $\mathbf{M}$, $\mathbf{G}$, $\mathbf{D}$, and $\mathbf{K}$ are $N \times N$ with the following properties:

$$\mathbf{M}^T = \mathbf{M} > 0, \quad \mathbf{G}^T = -\mathbf{G}, \quad \mathbf{D}^T = \mathbf{D}, \quad \mathbf{K}^T = \mathbf{K} \tag{2}$$

To provide a motivation for studying (1), and to illustrate the properties (2) in concrete physical terms, we will regard (1) as a *mechanical* system. By well-known analogies, it can be anticipated that the following results are also applicable to electrical, magnetic, and acoustical systems.

For a mechanical system, $\mathbf{q}$ consists of *configuration variables,* and $\mathbf{f}$ is a matrix of force or torque inputs. $\mathbf{M}$ is called the *system inertia matrix.* On examining the system kinetic energy, given by $T = (\frac{1}{2})\dot{\mathbf{q}}^T\mathbf{M}\dot{\mathbf{q}}$ it is realized that $\mathbf{M}$ is symmetric and positive-definite (provided there are no "massless" members), as stated in (2). *Gyroscopic* forces or torques are represented by $\mathbf{f}_G = -\mathbf{G}\dot{\mathbf{q}}$ and arise, for example, when rotors are present or when $\mathbf{q}$ is defined with respect to a uniformly rotating reference frame. Gyroscopic forces are workless because $\int \mathbf{f}_G{}^T d\mathbf{q} = \int \dot{\mathbf{q}}^T \mathbf{G}\mathbf{q}\, dt \equiv 0$ along the motion. The dissipative (or damping) forces are $\mathbf{f}_D = -\mathbf{D}\dot{\mathbf{q}}$. These forces never add energy to the system; consequently, $\mathbf{D} > 0$ or $\mathbf{D} \geq 0$. Conservative forces, represented by $-\mathbf{K}\mathbf{q}$, are functions only of position. For elastic forces, $\mathbf{K} > 0$ when the system is physically connected to an inertial reference frame. Flight vehicles, on the other hand, provide an important class of systems in which $\mathbf{K} \geq 0$.

Interest centers here on the controllability of (1) when

$$\mathbf{f} = \mathbf{B}\mathbf{u} \tag{3}$$

where $\mathbf{u}$ is an $N_c \times 1$ control vector, and on the observability of $\mathbf{q}$ and $\dot{\mathbf{q}}$ from the $N_0 \times 1$ output vector $\mathbf{y}$ defined by

$$\mathbf{y} = \mathbf{P}\mathbf{q} + \mathbf{R}\dot{\mathbf{q}} \tag{4}$$

Normally $N_c \leq N$, although under some circumstances we may wish to design $N_c > N$ to incorporate redundancy. Similarly, $N_0 > 2N$ corresponds to intentionally redundant outputs. Although there are important exceptions, the output variables often correspond to configuration variables alone and to their rates alone, in which case $\mathbf{P}$ and $\mathbf{R}$ in (4) have the structure

$$\mathbf{P} = \begin{bmatrix} \mathbf{L} \\ \mathbf{0} \end{bmatrix} \begin{matrix} n_p \text{ rows} \\ n_r \text{ rows} \end{matrix} \quad \begin{bmatrix} \mathbf{0} \\ \mathbf{V} \end{bmatrix} = \mathbf{R} \tag{5}$$

where n_p and n_r are the number of configuration-related and rate-related outputs, respectively. Then $N_0 = n_p + n_r$ and, if either $n_p > N$ or $n_r > N$, the outputs are redundant. When (5) is true, we say the outputs are *separated.* In general, however, $\mathbf{y}$ corresponds to either unseparated measurements or outputs. When $\mathbf{y}$ represents measurements, observability properties can be important in sensor location decisions and in measurement-feedback control design. When $\mathbf{y}$ represents outputs one wishes to control (e.g., least-squares control problems), the observability properties are again important in existence and stability theorems.

A straightforward approach is to transform (1) into an equivalent matrix-first-order (i.e., state) form

$$\dot{\mathbf{x}} = \mathbf{A}\mathbf{x} + \mathbf{B}_1\mathbf{u}; \quad \mathbf{y} = \mathbf{C}\mathbf{x} \tag{6}$$

where

---

[1] A condensation of this paper, with some added remarks on stability, was presented at the 1979 JACC Denver, Colo. Reference [10] of that paper is, in fact, the present paper.

[2] Now at the Institute for Aerospace Studies, University of Toronto, Downsview, Ontario, Canada.

Contributed by the Applied Mechanics Division for publication in the JOURNAL OF APPLIED MECHANICS.

Discussion on this paper should be addressed to the Editorial Department, ASME, United Engineering Center, 345 East 47th Street, New York, N.Y. 10017, and will be accepted until September 1, 1980. Readers who need more time to prepare a discussion should request an extension from the Editorial Department. Manuscript received by ASME Applied Mechanics Division, July, 1979; final revision, October, 1979.

Copyright © 1980 by ASME
Downloaded 01 May 2010 to 171.66.16.243. Redistribution subject to ASME license or copyright; see http://www.asme.org/terms/Terms_Use.cfm

$$\mathbf{x} \triangleq \begin{bmatrix}\mathbf{q}\\ \dot{\mathbf{q}}\end{bmatrix}; \quad \mathbf{A} \triangleq \begin{bmatrix}\mathbf{0} & \mathbf{I}\\ -\mathbf{M}^{-1}\mathbf{K} & -\mathbf{M}^{-1}(\mathbf{G}+\mathbf{D})\end{bmatrix}; \quad \mathbf{B}_1 \triangleq \begin{bmatrix}\mathbf{0}\\ \mathbf{B}\end{bmatrix}$$
$$\mathbf{C} \triangleq [\mathbf{P} \quad \mathbf{R}] \tag{7}$$

With the system written in the form (6), the necessary and sufficient conditions for controllability and observability are well known [1]: they are, respectively,

$$rk[\mathbf{B}_1 \; \mathbf{A}\mathbf{B}_1 \cdots \mathbf{A}^{2N-1}\mathbf{B}_1] = 2N \tag{8}$$

$$rk[\mathbf{C}^T \; \mathbf{A}^T\mathbf{C}^T \cdots (\mathbf{A}^T)^{2N-1}\mathbf{C}^T] = 2N \tag{9}$$

Conditions (8) and (9) can be criticized on the grounds that they ignore the special structure of the matrices **M**, **G**, **D**, and **K** exhibited in (2). It can be anticipated that specialized criteria for controllability and observability may be derived by judicious use of the additional information available in (2). This is the central purpose of this paper.

The matrices **G**, **D**, and **K** are not all present in all matrix-second-order systems. We broadly classify these systems as either *nongyroscopic* (**G** = **0**) or *gyroscopic* (**G** ≠ **0**). These are treated in Sections 2 and 3, respectively.

Certain theorems needed in the following development are collected in Appendix *A*, with references cited for their proofs. Notational conventions are listed in Appendix *B*.

2 Nongyroscopic Systems

Consider the nongyroscopic undamped system

$$\mathbf{M}\ddot{\mathbf{q}} + \mathbf{K}\mathbf{q} = \mathbf{B}\mathbf{u}; \quad \mathbf{y} = \mathbf{P}\mathbf{q} + \mathbf{R}\dot{\mathbf{q}} \tag{10}$$

Recall $\mathbf{M}^T = \mathbf{M} > 0$ and $\mathbf{K}^T = \mathbf{K}$. According to Theorem 8 (Appendix *A*), there exists a transformation **T** such that $\mathbf{T}^T\mathbf{M}\mathbf{T} = \mathbf{I}_N$ and $\mathbf{T}^T\mathbf{K}\mathbf{T} = \hat{\mathbf{K}} = \text{diag}\,\{\kappa_1, \ldots, \kappa_N\}$. Let $\mathbf{q} = \mathbf{T}\mathbf{z}$; the transformed system is

$$\ddot{\mathbf{z}} + \hat{\mathbf{K}}\mathbf{z} = \hat{\mathbf{B}}\mathbf{u}; \quad \mathbf{y} = \hat{\mathbf{P}}\mathbf{z} + \hat{\mathbf{R}}\dot{\mathbf{z}} \tag{11}$$

where $\hat{\mathbf{B}} \triangleq \mathbf{T}^T\mathbf{B}$, $\hat{\mathbf{P}} \triangleq \mathbf{P}\mathbf{T}$, and $\hat{\mathbf{R}} \triangleq \mathbf{R}\mathbf{T}$.

The first-order form equivalent to (11) is

$$\dot{\mathbf{x}} = \mathbf{A}\mathbf{x} + \mathbf{B}_1\mathbf{u}; \quad \mathbf{y} = \mathbf{C}\mathbf{x} \tag{12}$$

where

$$\mathbf{x} \triangleq \begin{bmatrix}\mathbf{z}\\ \dot{\mathbf{z}}\end{bmatrix}; \quad \mathbf{A} \triangleq \begin{bmatrix}\mathbf{0}_N & \mathbf{I}_N\\ -\hat{\mathbf{K}} & \mathbf{0}_N\end{bmatrix}; \quad \mathbf{B}_1 \triangleq \begin{bmatrix}\mathbf{0}\\ \hat{\mathbf{B}}\end{bmatrix}$$
$$\mathbf{C} \triangleq [\hat{\mathbf{P}} \quad \hat{\mathbf{R}}] \tag{13}$$

We may now invoke Conditions (8) and (9).

Controllability. The controllability condition (8) becomes

$$rk\begin{bmatrix}\mathbf{0} & \hat{\mathbf{B}} & \mathbf{0} & -\hat{\mathbf{K}}\hat{\mathbf{B}} & \cdots & (-\hat{\mathbf{K}})^{N-1}\hat{\mathbf{B}}\\ \hat{\mathbf{B}} & \mathbf{0} & -\hat{\mathbf{K}}\hat{\mathbf{B}} & \mathbf{0} & \cdots & \mathbf{0}\end{bmatrix} = 2N \tag{14}$$

It is therefore necessary and sufficient that

$$rk[\hat{\mathbf{B}} \; \hat{\mathbf{K}}\hat{\mathbf{B}} \cdots \hat{\mathbf{K}}^{N-1}\hat{\mathbf{B}}] = N \tag{15}$$

According to Theorem 7 (Appendix *A*), we should partition the rows of **B** to correspond with the multiplicities of the κ_n:

$$\hat{\mathbf{B}} \triangleq \begin{bmatrix}\mathbf{B}_1\\ \equiv\\ \mathbf{B}_Q\end{bmatrix} \begin{matrix}\text{N}_1\text{ rows}\\ \\ N_Q\text{ rows}\end{matrix} \tag{16}$$

where $N_1 + \ldots + N_Q = N$ and Q is the number of distinct κ_n. Then (15) is equivalent to $rk\,\mathbf{B}_q = N_q$ $(q = 1, \ldots, Q)$. This proves

Theorem 1. The system (10) is controllable if and only if

$$rk\;\mathbf{B}_q = N_q \quad (q = 1, \ldots, Q) \tag{17}$$

This theorem agrees with the comments made below Theorem 2.2 in [2]. We can also deduce the minimum number of actuators: $N_c \geq \max\{N_1, \ldots, N_Q\}$. Note that the single $2N \times 2NN_c$ matrix in (8) has been replaced by the simpler $N_q \times N_c$ matrices in (17). It is also beneficial to define a *controllability norm*

$$\mathcal{C}_q \triangleq (\det \mathbf{B}_q\mathbf{B}_q^T)^{1/(2N_q)} \tag{18}$$

Then, for controllability, $\mathcal{C}_q > 0$ $(q = 1, \ldots, Q)$ and, more importantly, the magnitude of $\mathcal{C}_q$ provides a relative measure of *how* controllable the modes with a common κ_q are. Occasionally in this paper we will use the notion of "ranking" modes according to the magnitude of their controllability (or observability) norms. Such norms have meaning only with a consistent rule for normalization. Equations (81) and (82) describe the most natural normalization for matrix-second-order systems, and this normalization is used throughout the paper. In [9, 10], norms of observability and controllability for each (Jordan) modal coordinate are discussed for the general state form (6). However, those norms are for distinct roots only and involve the calculation of complex eigenvector norms which will not be needed here.

We have the following two corollaries of Theorem 1.

Corollary 1.1. When the κ_n are distinct, the system (10) is controllable if and only if

$$\mathcal{C}_n \triangleq \|\mathbf{b}_n\| > 0 \quad (n = 1, \ldots, N) \tag{19}$$

where $\mathbf{b}_n$ is the nth row of $\hat{\mathbf{B}}$.

In physical applications, the κ_n are normally distinct. This corollary implies that the N chracteristic modes of (10) can be ranked in terms of their controllability relative to one another according to the size of $\mathcal{C}_n$. Note that (19) might be satisfied using only one actuator.

Corollary 1.2. When $\mathbf{K} = \mathbf{0}$ the system (10) is controllable if and only if $rk\;\mathbf{B} = N$. It follows that $N_c \geq N$.

Observability. The observability conditions (9) becomes

$$rk\begin{bmatrix}\hat{\mathbf{P}} & \hat{\mathbf{R}}\\ -\hat{\mathbf{R}}\hat{\mathbf{K}} & \hat{\mathbf{P}}\\ -\hat{\mathbf{P}}\hat{\mathbf{K}} & -\hat{\mathbf{R}}\hat{\mathbf{K}}\\ \hat{\mathbf{R}}\hat{\mathbf{K}}^2 & -\hat{\mathbf{P}}\hat{\mathbf{K}}\\ \equiv & \equiv\\ \hat{\mathbf{R}}(-\hat{\mathbf{K}})^N & \hat{\mathbf{P}}(-\hat{\mathbf{K}})^{N-1}\end{bmatrix} = 2N \tag{20}$$

Noting that the sign of a row does not affect rank, (20) is equivalent to

$$rk[\mathbf{F}^T\mathbf{\Lambda}\mathbf{F}^T \; \mathbf{\Lambda}^2\mathbf{F}^T \cdots \mathbf{\Lambda}^{N-1}\mathbf{F}^T] = 2N \tag{21}$$

where

$$\mathbf{F} = \begin{bmatrix}\hat{\mathbf{P}} & \hat{\mathbf{R}}\\ -\hat{\mathbf{R}}\hat{\mathbf{K}} & \hat{\mathbf{P}}\end{bmatrix}; \quad \mathbf{\Lambda} \triangleq \begin{bmatrix}\hat{\mathbf{K}} & \mathbf{0}\\ \mathbf{0} & \hat{\mathbf{K}}\end{bmatrix}$$

The aim is to use Theorem 7. Although $\mathbf{\Lambda}$ is diagonal, identical elements are not adjacent (as assumed by Theorem 7). This defect can be remedied by applying an appropriate orthonormal transformation to $\mathbf{\Lambda}$. Define **U** as follows:

$$\mathbf{U} \triangleq [\mathbf{1}_1\mathbf{1}_2 \cdots \mathbf{1}_{N_1}\mathbf{1}_{N+1} \cdots \mathbf{1}_{N+N_1} \cdots \mathbf{1}_f \cdots \mathbf{1}_{2N}]$$

where $\mathbf{1}_i$ is a column of $2N$ zeros except for a 1 in the ith position, and $f = N - N_Q + 1$. Note that $\mathbf{U}^T\mathbf{U} = \mathbf{U}\mathbf{U}^T = \mathbf{I}_{2N}$, and that $\mathbf{U}^T\mathbf{\Lambda}\mathbf{U} = \text{diag}\,\{\kappa_1, \ldots, \kappa_1, \ldots, \kappa_Q, \ldots \kappa_Q\} \triangleq \hat{\mathbf{\Lambda}}$. Repeated elements on the diagonal of $\mathbf{\Lambda}$ are brought into adjacent positions in $\hat{\mathbf{\Lambda}}$. Because $\mathbf{\Lambda} = \mathbf{U}\hat{\mathbf{\Lambda}}\mathbf{U}^T$, (21) is written

$$rk[\hat{\mathbf{F}}^T\hat{\mathbf{\Lambda}}\hat{\mathbf{F}}^T \; \hat{\mathbf{\Lambda}}^2\hat{\mathbf{F}}^T \cdots \hat{\mathbf{\Lambda}}^{N-1}\hat{\mathbf{F}}^T] = 2N \tag{22}$$

where $\hat{\mathbf{F}} = \mathbf{F}\mathbf{U}$

Theorem 7 is now directly applicable. We partition $\hat{\mathbf{F}}$ into columns to match the multiplicity of κ_q in $\hat{\mathbf{\Lambda}}$, observing that if the multiplicity of κ_q in $\hat{\mathbf{K}}$ is N_q, then its multiplicity in $\hat{\mathbf{\Lambda}}$ is $2N_q$:

$$\hat{\mathbf{F}} \triangleq [\mathbf{F}_1 \ldots \mathbf{F}_Q] \tag{23}$$

where $\mathbf{F}_q$ has $2N_q$ columns. In the same manner, we partition $\hat{\mathbf{P}}$ and $\hat{\mathbf{R}}$:

$$\hat{\mathbf{P}} \triangleq [\mathbf{P}_1 \ldots \mathbf{P}_Q]$$
$$\hat{\mathbf{R}} \triangleq [\mathbf{R}_1 \ldots \mathbf{R}_Q] \tag{24}$$

Downloaded 01 May 2010 to 171.66.16.243. Redistribution subject to ASME license or copyright; see http://www.asme.org/terms/Terms_Use.cfm

It may be shown that

$$\mathbf{F}_q = \begin{bmatrix} \mathbf{P}_q & \mathbf{R}_q \\ -\kappa_q \mathbf{R}_q & \mathbf{P}_q \end{bmatrix} \tag{25}$$

According to Theorem 7, the necessary and sufficient conditions for observability are $rk\ \mathbf{F}_q = 2N_q$ $(q = 1, \ldots, Q)$. This proves

Theorem 2. The system (10) is observable if and only if

$$rk\,\mathbf{F}_q = 2N_q \quad (q = 1, \ldots, Q) \tag{26}$$

A rank evaluation for the $2N \times 2NN_0$ matrix in (9) has been replaced by the Q rank evaluations in (26), each of which is $2N_q \times 2N_0$. This represents a substantial simplification in computation. It is also evident that $N_0 \geq \max\{N_1, \ldots, N_Q\}$, and that $\mathcal{O}_q \triangleq (\det \mathbf{F}_q{}^T \mathbf{F}_q)^{1/(4Nq)}$ is a measure of the relative observability of modes associated with different values of κ_q.

Several special cases are of interest. To begin, consider the consequences of distinct κ_n. Denote the nth columns of $\hat{\mathbf{P}}$ and $\hat{\mathbf{R}}$ by $\mathbf{p}_n$ and $\mathbf{r}_n$. From (26) and Theorem 5, we restate (26) thus

$$\det \begin{bmatrix} \mathbf{p}_n^T & -\kappa_n \mathbf{r}_n^T \\ \mathbf{r}_n^T & \mathbf{p}_n^T \end{bmatrix} \begin{bmatrix} \mathbf{p}_n & \mathbf{r}_n \\ -\kappa_n \mathbf{r}_n & \mathbf{p}_n \end{bmatrix} > 0 \quad (n = 1, \ldots, N) \tag{27}$$

Denote $p_n \triangleq \|\mathbf{p}_n\|$, $r_n \triangleq \|\mathbf{r}_n\|$, and $\mathbf{p}_n^T \mathbf{r}_n \triangleq p_n r_n \cos \gamma_n$; and define

$$\mathcal{O}_n^4 \triangleq (p_n^2 + \kappa_n r_n^2)^2 + (1 - \kappa_n)^2 p_n^2 r_n^2 \sin^2 \gamma_n \tag{28}$$

Then we have

Corollary 2.1. *When the κ_n are distinct, the system (10) is observable if and only if*

$$\mathcal{O}_n > 0 \quad (n = 1, \ldots, N) \tag{29}$$

Only one sensor is necessary. It may be either a position sensor or, if none of the κ_n is zero, it may be a rate sensor. Furthermore, the relative observability of the modes may be ranked according to the magnitude of $\mathcal{O}_n$, $n = 1, 2, \ldots N$.

In many important classes of systems, $\mathbf{K} > 0$ (elastic systems, for example). This implies $\kappa_n > 0$ $(n = 1, \ldots, N)$, and Corollary 2.1 reduces to

Corollary 2.2. When $\mathbf{K} > 0$ and the κ_n are distinct, the system (10) is observable if and only if

$$\mathcal{O}_n^2 \triangleq \|\mathbf{p}_n\|^2 + \|\mathbf{r}_n\|^2 > 0 \quad (n = 1, \ldots, N) \tag{30}$$

Only one position sensor or one rate sensor is necessary, provided it is placed so that (30) are satisfied. The contrast in size between (30) and (9) is self-evident. At the opposite extreme are systems with no elasticity.

Corollary 2.3. When $\mathbf{K} = \mathbf{0}$, the system (10) is observable if and only if $rk\,\mathbf{P} = N$.

We return now to permit indistinct κ_n, and consider the conditions that attend outputs that are separated in the sense of (5). We may partition $\hat{\mathbf{P}}$ and $\hat{\mathbf{R}}$ as follows:

$$\mathbf{P}_q \triangleq \begin{bmatrix} \mathbf{L}_q \\ \mathbf{0} \end{bmatrix} \begin{matrix} n_p \text{ rows} \\ n_r \text{ rows} \end{matrix} \begin{bmatrix} \mathbf{0} \\ \mathbf{V}_q \end{bmatrix} \triangleq \mathbf{R}_q \tag{31}$$

Then (26) reduces to

$$rk \begin{bmatrix} \mathbf{L}_q \\ -\kappa_q \mathbf{V}_q \end{bmatrix} = N_q \quad \text{and} \quad rk \begin{bmatrix} \mathbf{L}_q \\ \mathbf{V}_q \end{bmatrix} = N_q \quad (q = 1, \ldots, Q) \tag{32}$$

If none of the κ_q is zero, we may divide out the κ_q in (32a), hence the two conditions are identical. If one of the κ_q is zero (the κ_q, recall, are distinct by definition, unlike the κ_n), let $\kappa_1 = 0$ with no loss in generality; for $q = 1$, (32) becomes $rk\,\mathbf{L}_1 = N_1$. These results are summarized in the following corollary:

Corollary 2.4. When the outputs are separated, the system (10) is observable if and only if

$$rk \begin{bmatrix} \mathbf{L}_q \\ \mathbf{V}_q \end{bmatrix} = N_q \quad (q = 1, \ldots, Q) \tag{33}$$

unless $\kappa_1 = 0$, in which case (33), for $q = 1$, is replaced by $rk\,\mathbf{L}_1 = N_1$.

To discover the equivalent of Corollary 2.2 when the outputs are separated, denote the nth columns of $\hat{\mathbf{P}}$ and $\hat{\mathbf{R}}$ by

$$\mathbf{p}_n \triangleq \begin{bmatrix} \mathbf{l}_n \\ \mathbf{0} \end{bmatrix} \begin{matrix} n_p \text{ elements} \\ n_r \text{ elements} \end{matrix} \begin{bmatrix} \mathbf{0} \\ \mathbf{v}_n \end{bmatrix} \triangleq \mathbf{r}_n \tag{34}$$

Then we have

Corollary 2.5. When $\mathbf{K} > 0$, the κ_n are distinct, and the outputs are separated, the system (10) is observable if and only if

$$\mathcal{O}_n^2 \triangleq \|\mathbf{l}_n\|^2 + \|\mathbf{v}_n\|^2 > 0 \quad (n = 1, \ldots, N) \tag{35}$$

Finally, we examine the special cases where only $\mathbf{q}$ (or only $\dot{\mathbf{q}}$) is measured. The proofs of the following two corollaries are straightforward and follow directly from (26).

Corollary 2.6. When only position outputs are available, $\mathbf{y} = \mathbf{L}\mathbf{x}$, the system (10) is observable if and only if

$$rk\,\mathbf{L}_q = N_q \quad (q = 1, \ldots, Q) \tag{36}$$

This agrees with the comments below Theorem 2.2 of [2], and hence our Theorem 2 can be regarded as a generalization of [2].

Corollary 2.7. When only rate outputs are available, $\mathbf{y} = \mathbf{V}\dot{\mathbf{x}}$, the system (10) is observable if and only if

$$\left.\begin{matrix} (i) & \kappa_q \neq 0 \\ (ii) & rk\,\mathbf{V}_q = N_q \end{matrix}\right\} \quad (q = 1, \ldots, Q) \tag{37}$$

3 Gyroscopic Systems

With some escalation in difficulty, we now consider the gyroscopic system

$$\begin{aligned} &\mathbf{M}\ddot{\mathbf{q}} + \mathbf{G}\dot{\mathbf{q}} + \mathbf{K}\mathbf{q} = \mathbf{B}\mathbf{u}, \qquad \mathbf{y} = \mathbf{P}\mathbf{q} + \mathbf{R}\dot{\mathbf{q}} \\ &\mathbf{M}^T = \mathbf{M} > 0, \quad \mathbf{G}^T = -\mathbf{G}, \quad \mathbf{K}^T = \mathbf{K} > 0 \quad \text{or} \quad \geq \quad 0. \end{aligned} \tag{38}$$

For reasons shortly to become apparent, we have restricted $\mathbf{K}$ to either $\mathbf{K} > 0$ or $\mathbf{K} \geq 0$. As in the last section, we may simultaneously diagonalize $\mathbf{M}$ and $\mathbf{K}$ by the transformation $\mathbf{T}$. Then system (38) is transformed to

$$\ddot{\mathbf{z}} + \hat{\mathbf{G}}\dot{\mathbf{z}} + \hat{\mathbf{K}}\mathbf{z} = \hat{\mathbf{B}}\mathbf{u}; \quad \mathbf{y} = \hat{\mathbf{P}}\mathbf{z} + \hat{\mathbf{R}}\dot{\mathbf{z}} \tag{39}$$

where $\hat{\mathbf{G}} \triangleq \mathbf{T}^T \mathbf{G} \mathbf{T}$. Note that $\hat{\mathbf{G}}^T = -\hat{\mathbf{G}}$.

To obtain an equivalent matrix-first-order form, we look more closely at $\hat{\mathbf{K}}$. When $\mathbf{K} > 0$, $\hat{\mathbf{K}} > 0$, i.e., $\kappa_n > 0$ $(n = 1, \ldots, N)$ and we denote $\kappa_n = \omega_n^2$ and $\text{diag}\{\omega_1, \ldots, \omega_N\} \triangleq \boldsymbol{\omega}$. That is, $\hat{\mathbf{K}} = \boldsymbol{\omega}^2$. When $\mathbf{K} \geq 0$, we denote $\kappa_1 = \kappa_2 = \ldots \kappa_{N-M} = 0$, (where M is the number of positive eigenvalues of $\mathbf{K}$), $\kappa_{N-M+1} = \omega_1^2, \ldots, \kappa_N = \omega_M^2$. Define $\text{diag}\{\omega_1, \ldots, \omega_M\} \triangleq \boldsymbol{\omega}$; then $\hat{\mathbf{K}} = \text{diag}\{\mathbf{0}_{N-M}, \boldsymbol{\omega}^2\}$.

We next partition $\mathbf{z}$, $\hat{\mathbf{G}}$, $\hat{\mathbf{B}}$, $\hat{\mathbf{P}}$, and $\hat{\mathbf{R}}$ to match $\hat{\mathbf{K}}$ (r for "rigid" and e for "elastic"):

$$\mathbf{z} \triangleq \begin{bmatrix} \mathbf{z}_r \\ \mathbf{z}_e \end{bmatrix}; \quad \mathbf{G} = \begin{bmatrix} \mathbf{G}_{rr} & \mathbf{G}_{re} \\ \mathbf{G}_{er} & \mathbf{G}_{ee} \end{bmatrix}; \quad \hat{\mathbf{B}} \triangleq \begin{bmatrix} \mathbf{B}_r \\ \mathbf{B}_e \end{bmatrix};$$

$$\hat{\mathbf{P}} \triangleq [\mathbf{P}_r \quad \mathbf{P}_e]; \quad \hat{\mathbf{R}} \triangleq [\mathbf{R}_r \quad \mathbf{R}_e] \tag{40}$$

$\mathbf{z}_r$ and $\mathbf{z}_e$ are, respectively, $(N - M) \times 1$ and $M \times 1$; $\mathbf{G}_{rr}$, $\mathbf{G}_{re}$, $\mathbf{G}_{er}$, and $\mathbf{G}_{ee}$ are, respectively, $(N - M) \times (N - M)$, $(N - M) \times M$, $M \times (N - M)$, and $M \times M$; $\mathbf{B}_r$ and $\mathbf{B}_e$ are, respectively, $(N - M) \times N_c$ and $M \times N_c$; $\mathbf{P}_r$ and $\mathbf{R}_r$ are $N_0 \times (N - M)$, and $\mathbf{P}_e$ and $\mathbf{R}_e$ are $N_0 \times M$. Because $\hat{\mathbf{G}}^T = -\mathbf{G}$, note that $\mathbf{G}_{rr}^T = -\mathbf{G}_{rr}$, $\mathbf{G}_{ee}^T = -\mathbf{G}_{ee}$, and $\mathbf{G}_{er}^T = -\mathbf{G}_{re}$.

A matrix-first-order form equivalent to (39) is therefore

$$\begin{bmatrix} \boldsymbol{\omega}^2 & \mathbf{0} & \mathbf{0} \\ \mathbf{0} & \mathbf{I}_{N-M} & \mathbf{0} \\ \mathbf{0} & \mathbf{0} & \mathbf{I}_M \end{bmatrix} \begin{bmatrix} \mathbf{z}_e \\ \dot{\mathbf{z}}_r \\ \dot{\mathbf{z}}_e \end{bmatrix}^{\cdot}$$

$$= \begin{bmatrix} \mathbf{0}_M & \mathbf{0} & \boldsymbol{\omega}^2 \\ \mathbf{0} & -\mathbf{G}_{rr} & -\mathbf{G}_{re} \\ -\boldsymbol{\omega}^2 & -\mathbf{G}_{er} & -\mathbf{G}_{ee} \end{bmatrix} \begin{bmatrix} \mathbf{z}_e \\ \dot{\mathbf{z}}_r \\ \dot{\mathbf{z}}_e \end{bmatrix} + \begin{bmatrix} \mathbf{0} \\ \mathbf{B}_r \\ \mathbf{B}_e \end{bmatrix} \mathbf{u}$$

$$(\mathbf{z}_r)^{\cdot} = \dot{\mathbf{z}}_r \tag{41}$$

Downloaded 01 May 2010 to 171.66.16.243. Redistribution subject to ASME license or copyright; see http://www.asme.org/terms/Terms_Use.cfm

$$\mathbf{y} = \mathbf{P}_r \mathbf{z}_r + [\mathbf{P}_e \ \mathbf{R}_r \ \mathbf{R}_e] \begin{bmatrix} \mathbf{z}_e \\ \dot{\mathbf{z}}_r \\ \dot{\mathbf{z}}_e \end{bmatrix} \tag{41}$$

(*Cont.*)

Next, apply the nonsingular transformation

$$\begin{bmatrix} \mathbf{z}_e \\ \dot{\mathbf{z}}_r \\ \dot{\mathbf{z}}_e \end{bmatrix} = \begin{bmatrix} \omega^{-1} & \mathbf{0} & \mathbf{0} \\ \mathbf{0} & \mathbf{I}_{N-M} & \mathbf{0} \\ \mathbf{0} & \mathbf{0} & \mathbf{I}_M \end{bmatrix} \cdot \mathbf{w} \tag{42}$$

whereupon (4) transforms to

$$\left.\begin{aligned} \dot{\mathbf{w}} &= \mathcal{G}\mathbf{w} + \mathcal{B}\mathbf{u} \\ \dot{\mathbf{z}}_r &= [\mathbf{0}\ \mathbf{I}_{N-M}\ \mathbf{0}]\mathbf{w} \\ \mathbf{y} &= \mathbf{P}_r \mathbf{z}_r + \mathcal{R}\mathbf{w} \end{aligned}\right\} \tag{43}$$

where

$$\mathcal{G} \triangleq \begin{bmatrix} \mathbf{0}_M & \mathbf{0} & \omega \\ \mathbf{0} & -\mathbf{G}_{rr} & -\mathbf{G}_{re} \\ -\omega & -\mathbf{G}_{er} & -\mathbf{G}_{ee} \end{bmatrix}; \quad \mathcal{B} \triangleq \begin{bmatrix} \mathbf{0} \\ \mathbf{B}_r \\ \mathbf{B}_e \end{bmatrix}; \quad \mathcal{R} \triangleq [\mathbf{P}_e \omega^{-1} \mathbf{R}_r \ \mathbf{R}_e] \tag{44}$$

Note that the $(N + M) \times (N + M)$ matrix $\mathcal{G}$ is skew symmetric. Therefore, according to Theorem 9, there is an $(N + M) \times (N + M)$ transformation such that $\mathcal{T}^T \mathcal{G} \mathcal{T} \triangleq \hat{\mathcal{G}} = \text{diag}\,\{\mathbf{0}_{N+M-2P}, \mathbf{S}\}$, $\mathcal{T}^T \mathcal{T} = \mathbf{I}_{N+M}$, and $2P$ is the number of nonzero eigenvalues of $\mathcal{G}^2$. As a final transformation then, set $\mathbf{w} = \mathcal{T}\mathbf{v}$, hence (43) transforms to

$$\left.\begin{aligned} \dot{\mathbf{z}}_r &= \mathcal{T}_r \mathbf{v} \\ \dot{\mathbf{v}} &= \hat{\mathcal{G}}\mathbf{v} + \hat{\mathcal{B}}\mathbf{u} \\ \mathbf{y} &= \mathbf{P}_r \mathbf{z}_r + \hat{\mathcal{R}}\mathbf{v} \end{aligned}\right\} \tag{45}$$

where $\hat{\mathcal{B}} = \mathcal{T}^T \mathcal{B}$, $\hat{\mathcal{R}} \triangleq \mathcal{R}\mathcal{T}$, and $\mathcal{T}_r \triangleq [\mathbf{0}\ \mathbf{I}_{N-M}\ \mathbf{0}]\mathcal{T}$.

The state form equivalent to (45) is

$$\dot{\mathbf{x}} = \mathbf{A}\mathbf{x} + \mathbf{B}_1 \mathbf{u}; \quad \mathbf{y} = \mathbf{C}\mathbf{x} \tag{46}$$

where

$$\mathbf{x} \triangleq \begin{bmatrix} \mathbf{z}_r \\ \mathbf{v} \end{bmatrix}; \quad \mathbf{A} \triangleq \begin{bmatrix} \mathbf{0} & \mathcal{T}_r \\ \mathbf{0} & \hat{\mathcal{G}} \end{bmatrix}; \quad \mathbf{B}_1 \triangleq \begin{bmatrix} \mathbf{0} \\ \hat{\mathcal{B}} \end{bmatrix}; \quad \mathbf{C} \triangleq [\mathbf{P}\ \hat{\mathcal{R}}] \tag{47}$$

The controllability and observability properties for (46), given by (8) and (9), are identical to those for (38).

Controllability. The controllability condition (8) is how applied, and the result expressed in the form

$$rk[\mathbf{F} \quad \Lambda\mathbf{F} \quad \Lambda^2\mathbf{F} \cdots \Lambda^{N-1}\mathbf{F}] = 2\mathbf{N} \tag{48}$$

where

$$\mathbf{F} \triangleq \begin{bmatrix} \mathbf{0} & \mathcal{T}_r \hat{\mathcal{B}} \\ \mathcal{B}_z & \mathbf{0} \\ \mathcal{B}_s & \mathbf{S}\mathcal{B}_s \end{bmatrix}; \quad \Lambda \triangleq \begin{bmatrix} \mathbf{0} & \mathbf{0} & \mathcal{T}_{rs}\mathbf{S} \\ \mathbf{0} & \mathbf{0} & \mathbf{0} \\ \mathbf{0} & \mathbf{0} & \mathbf{S}^2 \end{bmatrix} \tag{49}$$

and where $\mathcal{T}_r$ and $\hat{\mathcal{B}}$ have been partitioned to correspond to $\hat{\mathcal{G}}$:

$$\mathcal{T}_r \triangleq [\mathcal{T}_{rz}\ \mathcal{T}_{rs}]; \quad \hat{\mathcal{B}} \triangleq \begin{bmatrix} \mathcal{B}_z \\ \mathcal{B}_s \end{bmatrix} \tag{50}$$

$\mathcal{T}_{rz}$ has $N + M - 2P$ columns; $\mathcal{T}_{rs}$ has $2P$ columns; $\mathcal{B}_z$ has $N + M - 2P$ rows; and $\mathcal{B}_s$ has $2P$ rows. To use Theorem 7, Λ must be diagonal. The offending term, $\mathcal{T}_{rs}\mathbf{S}$, can be eliminated through a transformation $\hat{\Lambda} \triangleq \mathbf{E}^{-1}\Lambda\mathbf{E}$ where $\hat{\Lambda} = \text{diag}\,\{\mathbf{0}_{N-M}, \mathbf{0}_{N+M-2P}, \mathbf{S}^2\}$, and

$$\mathbf{E} \triangleq \begin{bmatrix} \mathbf{I}_{N-M} & \mathbf{0} & \mathcal{T}_{rs}\mathbf{S}^{-1} \\ \mathbf{0} & \mathbf{I}_{N+M-2P} & \mathbf{0} \\ \mathbf{0} & \mathbf{0} & \mathbf{I}_{2P} \end{bmatrix} \tag{51}$$

A display for $\mathbf{E}^{-1}$ would look the same as for $\mathbf{E}$, except for the sign of $\mathcal{T}_{rs}\mathbf{S}^{-1}$. Upon substitution of $\Lambda = \mathbf{E}\hat{\Lambda}\mathbf{E}^{-1}$ into (48), and noting that premultiplication by $\mathbf{E}^{-1}$ does not affect rank, we have the equivalent condition (with $\hat{\mathbf{F}} \triangleq \mathbf{E}^{-1}\mathbf{F}$):

$$rk[\hat{\mathbf{F}}\ \hat{\Lambda}\hat{\mathbf{F}}\ \hat{\Lambda}^2\hat{\mathbf{F}} \cdots \hat{\Lambda}^{N-1}\mathbf{F}] = 2N \tag{52}$$

which is now in a form amenable to treatment via Theorem 7. We must partition $\hat{\mathbf{F}}$, given by

$$\hat{\mathbf{F}} = \begin{bmatrix} -\mathcal{T}_{rs}\mathbf{S}^{-1}\mathcal{B}_s & \mathcal{T}_{rz}\mathcal{B}_z \\ \mathcal{B}_z & \mathbf{0} \\ \mathcal{B}_s & \mathbf{S}\mathcal{B}_s \end{bmatrix} \tag{53}$$

into its first $2(N - P)$ rows, and then into $2N_1$ rows, $2N_2$ rows, . . . , $2N_Q$ rows, corresponding to the multiplicities, respectively, of $-\omega_1^2$, $-\omega_2^2, \ldots, -\omega_Q^2$ on the diagonal of $\mathbf{S}^2$. The rank condition corresponding to the $2(N - P)$-fold zero on the diagonal of $\hat{\Lambda}$ is

$$rk \begin{bmatrix} -\mathcal{T}_{rs}\mathbf{S}^{-1}\mathcal{B}_s & \mathcal{T}_{rz}\mathcal{B}_z \\ \mathcal{B}_z & \mathbf{0} \end{bmatrix} = 2(N - P) \tag{54}$$

To write the remaining conditions, we further partition $\mathcal{B}_s$ into rows as follows:

$$\mathcal{B}_s^T \triangleq [\mathcal{b}_1^\alpha \mathcal{b}_1^\beta \cdots \mathcal{b}_p^\alpha \mathcal{b}_p^\beta] \tag{55}$$

whereupon the remaining conditions are

$$\left.\begin{aligned} rk \begin{bmatrix} \mathcal{b}_1^\alpha & \mathcal{b}_1^\beta & \cdots & \mathcal{b}_{N_1}^\alpha & \mathcal{b}_{N_1}^\beta \\ \mathcal{b}_1^\beta & -\mathcal{b}_1^\alpha & \cdots & \mathcal{b}_{N_1}^\beta & -\mathcal{b}_{N_1}^\alpha \end{bmatrix} &= 2N_1 \\ \vdots & \\ rk \begin{bmatrix} \mathcal{b}_f^\alpha & \mathcal{b}_f^\beta & \cdots & \mathcal{b}_P^\alpha & \mathcal{b}_P^\beta \\ \mathcal{b}_f^\beta & -\mathcal{b}_f^\alpha & \cdots & \mathcal{b}_P^\beta & -\mathcal{b}_P^\alpha \end{bmatrix} &= 2N_Q \end{aligned}\right\} \tag{56}$$

where $f \triangleq P - N_Q + 1$ in $(56)_Q$. The factor $\omega_q \neq 0$ has been divided out of (56).

The preceding development proves:

Theorem 3. The system (38) is controllable if and only if Conditions (54) and (56) are satisfied.

It follows that the number of control actuators cannot be less than max $\{N - P, N_1, N_2, \ldots, N_Q\}$. Controllability norms corresponding to (54) and (56) can also be defined.

Several special cases of this theorem are still quite general and of interest; these are now stated as corollaries.

Corollary 3.1. When $\mathbf{K} > 0$, the system (38) is controllable if and only if Conditions (56) hold. Corollary 3.1 is equivalent to the theorem in [8].

Proof. Recall that M is the number of positive eigenvalues of $\mathbf{K}$. Then by definition, $M = N$. From (44), $\det \mathcal{G} \neq 0$, and therefore $P = N$. Condition (44) vanishes.

Corollary 3.2. When the ω_p are distinct, the system (38) is controllable if and only if

$$\mathcal{C}_p^2 \triangleq \|\mathcal{b}_p^\alpha\|^2 + \|\mathcal{b}_p^\beta\|^2 > 0 \quad (p = 1, \ldots, P) \tag{57}$$

and Condition (54) holds.

Proof Conditions (56) become, with $N_1 = 1, \ldots, N_Q = 1$,

$$rk \begin{bmatrix} \mathcal{b}_p^\alpha & \mathcal{b}_p^\beta \\ \mathcal{b}_p^\beta & -\mathcal{b}_p^\alpha \end{bmatrix} = 2 \quad (p = 1, \ldots, P) \tag{58}$$

Applying Theorem 5 (Appendix *A*) leads to (57).

Corollary 3.3. When $\det \mathcal{G}_{rr} \neq 0$, the system (38) is controllable if and only if

$$rk\mathcal{T}_r\mathbf{S}^{-1}\hat{\mathcal{B}} = N - M \tag{59}$$

and Conditions (56) hold.

Proof. It is relatively straightforward to show from (44) that $\det \mathcal{G} \neq 0$ if and only if $\det \mathcal{G}_{rr} \neq 0$. This is possible only when $N - M$ is even (although $N - M$ being even does not imply that $\det \mathcal{G}_{rr} \neq 0$). Of course, $N + M$ is also even; in fact $N + M = 2P$, since $\det \mathcal{G} \neq 0$. $\mathcal{B}_z$

Downloaded 01 May 2010 to 171.66.16.243. Redistribution subject to ASME license or copyright; see http://www.asme.org/terms/Terms_Use.cfm

disappears in (54) and we are left with (59). The number of actuators must be $\geq \max\{1, N-M\}$.

Corollary 3.4. When $\mathbf{K} > 0$ and the ω_p are distinct, the system (38) is controllable if and only if

$$\mathcal{C}_n^2 \triangleq \|\boldsymbol{\mathcal{C}}_n^\alpha\|^2 + \|\boldsymbol{\mathcal{C}}_n^\beta\|^2 > 0 \quad (n = 1, \ldots, N) \tag{60}$$

Proof. This corollary is a combination of Corollaries 3.1 and 3.2. A single actuator is sufficient, provided (60) are satisfied. The size of $\mathcal{C}_n$ can be interpreted as the relative controllability of mode n.

For some systems, which might be described as "inelastic," $\mathbf{K}$ is absent.

Corollary 3.5. When $\mathbf{K} = \mathbf{0}$, the system (38) is controllable if and only if $rk\ \mathbf{B} = N$.

Proof. Here $M = 0$, quantities with an "e" subscript disappear, and the "r" subscript is no longer required. The rank of the matrix in Condition (54) is not affected if we premultiply by the nonsingular matrix

$$\begin{bmatrix} \mathcal{T}_z^T & \mathbf{0} \\ \mathcal{T}_s^T & \mathbf{0} \\ \mathbf{0} & \mathbf{I}_{N-2P} \end{bmatrix}$$

Noting that $\mathcal{T}_z^T\mathcal{T}_s = \mathbf{0}$, $\mathcal{T}_z^T\mathcal{T}_z = \mathbf{I}_{N-2P}$, $\mathcal{T}_s^T\mathcal{T}_s = \mathbf{I}_{2P}$, (54) reduces to

$$rk \begin{bmatrix} \mathbf{0} & \mathcal{B}_z \\ -\mathbf{S}^{-1} & \mathbf{0} \\ \mathcal{B}_z & \mathbf{0} \end{bmatrix} = 2(N-P) \tag{61}$$

which is satisfied if and only if

$$rk \begin{bmatrix} \mathbf{S}^{-1}\mathcal{B}_s \\ \mathcal{B}_z \end{bmatrix} = N \tag{62}$$

Because $\mathbf{S}$ is nonsingular, (62) is equivalent to $rk\ \mathcal{B} = N$ which, in turn, is equivalent to $rk\ \mathbf{B} = N$. Conditions (56) are automatically satisfied if $rk\ \mathcal{B} = N$.

Observability. Apply the observability condition, (9), to (46) and (47), and express the result as follows:

$$rk[\mathbf{F}^T \quad \boldsymbol{\Lambda}\mathbf{F}^T\ \boldsymbol{\Lambda}^2\mathbf{F}^T \cdots \boldsymbol{\Lambda}^{N-1}\mathbf{F}^T] = 2N \tag{63}$$

where

$$\boldsymbol{\Lambda} = \begin{bmatrix} \mathbf{0}_{N-M} & \mathbf{0} & \mathbf{0} \\ \mathbf{0} & \mathbf{0}_{N+M-2P} & \mathbf{0} \\ -\mathbf{S}\mathcal{T}_{rs}^T & \mathbf{0} & \mathbf{S}^2 \end{bmatrix}; \quad \mathbf{F} \triangleq \begin{bmatrix} \mathbf{P}_r & \mathcal{R}_z & \mathcal{R}_s \\ \mathbf{0} & \mathbf{P}_r\mathcal{T}_{rz} & \mathbf{P}_r\mathcal{T}_{rs} + \mathcal{R}_s\mathbf{S} \end{bmatrix} \tag{64}$$

and we have partitioned

$$\hat{\mathcal{R}} = [\mathcal{R}_z\ \mathcal{R}_s] \tag{65}$$

into $N + M - 2P$ columns and $2P$ columns. As earlier, we can remove the obstacle of a nondiagonal $\boldsymbol{\Lambda}$ by the transformation $\hat{\boldsymbol{\Lambda}} \triangleq \mathbf{E}^{-1}\boldsymbol{\Lambda}\mathbf{E}$ where $\hat{\boldsymbol{\Lambda}} = \text{diag}\,[\mathbf{0}_{N-M}, \mathbf{0}_{N+M-2P}, \mathbf{S}^2]$ and

$$\mathbf{E} \triangleq \begin{bmatrix} \mathbf{I}_{N-M} & \mathbf{0} & \mathbf{0} \\ \mathbf{0} & \mathbf{I}_{N+M-2P} & \mathbf{0} \\ \mathbf{S}^{-1}\mathcal{T}_{rs}^T & \mathbf{0} & \mathbf{I}_{2P} \end{bmatrix} \tag{66}$$

$\mathbf{E}^{-1}$ looks the same as $\mathbf{E}$, except for the sign of $\mathbf{S}^{-1}\mathcal{T}_{rs}{}^T$. Substitute $\boldsymbol{\Lambda} = \mathbf{E}\hat{\boldsymbol{\Lambda}}\mathbf{E}^{-1}$ into (63), and define $\hat{\mathbf{F}} \triangleq \mathbf{F}\mathbf{E}^{-T}$. The necessary and sufficient condition for observability is therefore

$$rk[\hat{\mathbf{F}}^T \quad \hat{\boldsymbol{\Lambda}}\hat{\mathbf{F}}^T \quad \hat{\boldsymbol{\Lambda}}^2\mathcal{F}^T \cdots \hat{\boldsymbol{\Lambda}}^{N-1}\hat{\mathbf{F}}^T] = 2N \tag{67}$$

with

$$\mathbf{F} = \begin{bmatrix} \mathbf{P}_r & \mathcal{R}_z & \mathbf{P}_z\mathcal{T}_{rs}\mathbf{S}^{-1} + \mathcal{R}_s \\ \mathbf{0} & \mathbf{P}_r\mathcal{T}_{rz} & \mathbf{P}_r\mathcal{T}_{rs} + \mathcal{R}_s\mathbf{S} \end{bmatrix} \tag{68}$$

Following Theorem 7, we must partition the rows of $\hat{\mathbf{F}}^T$ (the columns of $\hat{\mathbf{F}}$) first into $2(N-P)$ rows, corresponding to the $2(N-P)$-fold 0 diagonal element in $\hat{\boldsymbol{\Lambda}}$, and thereafter into $2N_1$ columns, $2N_2$ columns, . . , $2N_Q$ columns, corresponding, respectively, to the multiplicities of $-\omega_1^2, -\omega_2^2, \ldots, -\omega_Q^2$. The first rank condition is:

$$rk \begin{bmatrix} \mathbf{P}_r & \mathcal{R}_z \\ \mathbf{0} & \mathbf{P}_r\mathcal{T}_{rz} \end{bmatrix} = 2(N-P) \tag{69}$$

To express the remaining condition, partition as follows:

$$\begin{aligned} \mathbf{P}_r\mathcal{T}_{rs} &\triangleq [\boldsymbol{\rho}_1^\alpha \quad \boldsymbol{\rho}_1^\beta \cdots \boldsymbol{\rho}_P^\alpha \quad \boldsymbol{\rho}_P^\beta] \\ \mathcal{R}_s &\triangleq [\boldsymbol{\pi}_1^\alpha \quad \boldsymbol{\pi}_1^\beta \cdots \boldsymbol{\pi}_P^\alpha \quad \boldsymbol{\pi}_P^\beta] \end{aligned} \tag{70}$$

hence they become

$$rk \begin{bmatrix} \omega_1\boldsymbol{\pi}_1^\alpha - \boldsymbol{\rho}_1^\beta & \omega_1\boldsymbol{\pi}_1^\beta + \boldsymbol{\rho}_1^\alpha \cdots \omega_1\boldsymbol{\pi}_{N_1}^\alpha - \boldsymbol{\rho}_{N_1}^\beta & \omega_1\boldsymbol{\pi}_{N_1}^\beta + \boldsymbol{\rho}_{N_1}^\alpha \\ \boldsymbol{\rho}_1^\alpha + \omega_1\boldsymbol{\pi}_1^\beta & \boldsymbol{\rho}_1^\beta - \omega_1\boldsymbol{\pi}_1^\alpha \cdots \boldsymbol{\rho}_{N_1}^\alpha + \omega_a\boldsymbol{\pi}_{N_1}^\beta, \boldsymbol{\rho}_{N_1}^\beta - \omega_1\boldsymbol{\pi}_{N_1}^\alpha \end{bmatrix} = 2N_1$$

$$\vdots$$

$$rk \begin{bmatrix} \omega_Q\boldsymbol{\pi}_f^\alpha - \boldsymbol{\rho}_f^\beta & \omega_Q\boldsymbol{\pi}_f^\beta + \boldsymbol{\rho}_f^\alpha \cdots \omega_Q\boldsymbol{\pi}_P^\alpha - \boldsymbol{\pi}_P^\beta & \omega_Q\boldsymbol{\pi}_P^\beta + \boldsymbol{\pi}_P^\alpha \\ \boldsymbol{\rho}_f^\alpha + \omega_Q\boldsymbol{\pi}_f^\beta & \boldsymbol{\rho}_f^\beta - \omega_Q\boldsymbol{\pi}_f^\alpha \cdots \boldsymbol{\rho}_P^\alpha + \omega_Q\boldsymbol{\pi}_P^\beta & \boldsymbol{\rho}_P^\beta - \omega_Q\boldsymbol{\rho}_P^\alpha \end{bmatrix} = 2N_Q \tag{71}$$

where the subscript $f \triangleq P - N_Q + 1$. This proves

Theorem 4. The system (38) is observable if and only if Conditions (69) and (71) hold.

One can also deduce that the size of the output vector, N_0, must be at least $\max\{N-P, N_1, N_2, \ldots, N_Q\}$. Several special cases are of interest and are now presented as corollaries.

Corollary 4.1. When $\mathbf{K} > 0$, the system (38) is observable if and only if Conditions (71) hold.

Proof. Here the number of positive eigenvalues of $\mathbf{K}$ is $M = N$. From (44), $\det \mathcal{G} \neq 0$ from which $P = N$. Condition (69) disappears.

Corollary 4.2. When the ω_p are distinct, the system (38) is observable if and only if Condition (69) and the following conditions hold:

$$\mathcal{O}_p^2 \triangleq \|\boldsymbol{\rho}_p^\beta + \omega_p\boldsymbol{\pi}_p^\alpha\|^2 + \|\boldsymbol{\rho}_p^\alpha - \omega_p\boldsymbol{\pi}_p^\beta\|^2 > 0 \quad (p = 1, \ldots, P) \tag{72}$$

Corollary 4.3. When $\det \mathcal{G}_{rr} \neq 0$, the system (38) is observable if and only if

$$rk\,\mathbf{P}_r = N - M \tag{73}$$

and Conditions (71) hold. It follows that $N_0 \geq \max\{N-M, N_1, N_2, \ldots, N_Q\}$.

Corollary 4.4. When $\mathbf{K} > 0$ and the ω_p are distinct, the system (38) is observable if and only if

$$\mathcal{O}_n^2 \triangleq \|\boldsymbol{\rho}_n^\beta + \omega_n\boldsymbol{\pi}_n^\alpha\|^2 + \|\boldsymbol{\rho}_n^\alpha - \omega_n\boldsymbol{\pi}_n^\beta\|^2 > 0 \quad (n = 1, \ldots, N) \tag{74}$$

Proof. This corollary combines Corollaries 4.1 and 4.2. Corollary 4.4 is equivalent to a result in the theorem of [8]. A single sensor is adequate, provided (74) satisfied. If it is a position sensor, the relative observability of the modes may be ordered according to the magnitude $(\|\boldsymbol{\rho}_n^\alpha\|^2 + \|\boldsymbol{\rho}_n^\beta\|^2)$, $n = 1, 2, \ldots N$. If it is a rate sensor, the relative observability can be ordered according to the magnitude of $\omega_n^2[\|\boldsymbol{\pi}_n^\alpha\|^2 + \|\boldsymbol{\pi}_n^\beta\|^2]$.

For inelastic systems, we have

Corollary 4.5. When $\mathbf{K} = \mathbf{0}$, the system (38) is observable if and only if $rk\ \mathbf{P} = N$ and Conditions (71) hold. The proof is similar to the proof of Corollary 3.5.

When the outputs are separated, in the sense of (5), some additional progress can be made, but the required matrix partitioning necessitates much additional notation and so will be omitted here.

4 Effects of Energy Dissipation

Energy dissipation is normally present in physical systems. In the present context, it is represented by the $\mathbf{D}\dot{\mathbf{q}}$ term in (1). In principle, this term could be added to each of the four systems already considered in Sections 2 and 3, and its effects on system properties ascertained. We instead limit our scope to some qualitative remarks.

It is clear that the $\mathbf{D}\dot{\mathbf{q}}$ term provides a new mechanism for coupling between modes. Modes uncontrollable or unobservable with $\mathbf{D} = \mathbf{0}$ may

Downloaded 01 May 2010 to 171.66.16.243. Redistribution subject to ASME license or copyright; see http://www.asme.org/terms/Terms_Use.cfm

become so when $\mathbf{D} \neq \mathbf{0}$. If system damping is sufficiently large to make the coupling quantitatively significant, it should be expected that fewer actuators and sensors will generally be needed to establish controllability and observability.

When the dissipative mechanisms are weak, however, it might be best to establish acceptable controllability and observability characteristics with $\mathbf{D} = \mathbf{0}$, and regard $\mathbf{D}\dot{\mathbf{q}}$ as a secondary influence on these characteristics. We are assured by the principle which states that controllability and observability are preserved under small perturbations [3, Theorem 1.3, p. 43] that sufficiently small $\mathbf{D}\dot{\mathbf{q}}$ will not eliminate these properties if they are established for $\mathbf{D} = \mathbf{0}$. This was pointed out in this context in [2].

5 Concluding Remarks

The special structure of the matrix-second-order representation of linear mechanical systems has been exploited to derive new specialized conditions for the controllability and observability of such systems. These results extend previous work in that $\mathbf{K}$ is no longer assumed to be positive-definite. It can be anticipated that these results will apply also to broad classes of electrical, magnetic, and acoustical systems.

With the aid of appropriate transformations, the basic rank conditions (8) and (9) have been reduced to several simpler subsidiary rank conditions. The investment made in these transformations, which would be of interest in any case since they reveal the natural modes of the system, is more than repaid by the benefits of simplifying the eventual rank conditions. The results obtained lead, in many cases, to simple literal conditions. In other cases, the benefit is computational efficiency. A less measurable but nonetheless real benefit is the insight gained by viewing controllability and observability on a mode-by-mode basis rather than on a total system basis. More precise guidance is given on how many sensors and actuators are needed, and on how they may best be placed to maximize the degree of controllability and observability.

Acknowledgment

This research was sponsored by the Jet Propulsion Laboratory under Contract No. 955369.

References

1 Chen, C. T., *Introduction to Linear System Theory,* Holt, Rinehart and Winston, 1970.

2 Balas, M. J., "Feedback Control of Flexible Systems," *IEEE Trans. Automatic Control,* Vol. AC-23, Aug. 1978, pp. 674–679.

3 Wonham, W., *Linear Multivariable Control,* Springer, 1974.

4 Franklin, J. N., *Matrix Theory,* Prentice-Hall, 1968.

5 Finkbeiner, D. T., *Introduction to Matrices and Linear Transformations,* W. H. Freeman, 1960.

6 Hadley, G., *Linear Algebra,* Addison-Wesley, 1961.

7 Greub, W. H., *Linear Algebra,* Springer-Verlag, 1967.

8 Juang, J. N., and Balas, M., "Dynamics and Control of Large Spinning Spacecraft," *Journal of Astronautical Sciences,* 1979, to appear.

9 Skelton, R. E., "Observability Measures and Performance Sensitivity in the Model Reduction Problem," *International Journal of Control,* Vol. 29, No. 4, 1979, pp. 541–556.

10 Skelton, R. E., and Gregory, C. Z., "Measurement Feedback and Model Reduction by Modal Cost Analysis," *JACC Proceedings,* Denver, 1979.

APPENDIX *A*

Theorems on Rank, and Two Transformations

The following theorems are used repeatedly in the text. All matrices are real.

Theorem 5. Let $\mathbf{A}$ be an $N \times M$ matrix.

$$rk\,\mathbf{A} = rk\,\mathbf{A}^T = rk\,\mathbf{A}\mathbf{A}^T = rk\,\mathbf{A}^T\mathbf{A} \tag{15}$$

For a proof, see [4, p. 43].

Theorem 6. Let $\mathbf{A}$ be an $N \times M$ matrix, and let $\mathbf{B}$ and $\mathbf{C}$ be $N \times N$ and $M \times M$ nonsingular matrices, respectively. Then

$$rk\,\mathbf{A} = rk\,\mathbf{B}\mathbf{A} = rk\,\mathbf{A}\mathbf{C} \tag{76}$$

For a proof, see [5, p. 78].

Theorem 7. Let $\mathbf{B}$ be an $N \times M$ matrix, and $\mathbf{\Lambda}$ an $N \times N$ diagonal matrix with nondistinct elements: $\mathbf{\Lambda} = \text{diag}\,\{\lambda_1$ (multiplicity N_1), λ_2 (multiplicity N_2), . . . , λ_Q (multiplicity N_Q)$\}$ where $N_1 + \ldots + N_Q = N$. Furthermore, let $\mathbf{B}$ be partitioned thus

$$\mathbf{B} \triangleq \begin{bmatrix} \mathbf{B}_1 \\ \vdots \\ \mathbf{B}_Q \end{bmatrix} \begin{matrix} N_1 \text{ rows} \\ \\ N_Q \text{ rows} \end{matrix} \tag{77}$$

then $rk[\mathbf{B}\ \mathbf{\Lambda}\mathbf{B}\ \mathbf{\Lambda}^2\mathbf{B} \ldots \mathbf{\Lambda}^{N-1}\mathbf{B}] = N$ if and only if

$$rk\,\mathbf{B} = N_q \quad (q = 1, \ldots, Q) \tag{78}$$

Proof. This theorem is a special case of the Jordan-form controllability theorem [1, p. 191], which applies when $\mathbf{\Lambda}$ is in Jordan form.

Corollary. When the elements of $\mathbf{\Lambda}$ are distinct, partition $\mathbf{B}$ into rows thus

$$\mathbf{B} \triangleq \begin{bmatrix} \mathbf{b}_1{}^T \\ \vdots \\ \mathbf{b}_N{}^T \end{bmatrix} \tag{79}$$

Then the necessary and sufficient conditions for controllability are

$$\|\mathbf{b}_n\| > 0 \quad (n = 1, \ldots, N) \tag{80}$$

The form used in (80) is chosen to be analogous to conditions found elsewhere in this paper.

Theorem 8. Let $\mathbf{M}$ and $\mathbf{K}$ be $N \times N$ matrices such that $\mathbf{M}^T = \mathbf{M} > 0$, $\mathbf{K}^T = \mathbf{K}$. There exists a transformation $\mathbf{T}$ such that

$$\mathbf{T}^T\mathbf{M}\mathbf{T} = \mathbf{I}_N \tag{81}$$

$$\mathbf{T}^T\mathbf{K}\mathbf{T} \triangleq \hat{\mathbf{K}} = \text{diag}\,\{\kappa_1, \ldots, \kappa_N\} \tag{82}$$

For a proof, see [6, p. 263]. We shall always assume that $\mathbf{T}$ has been chosen such that $\kappa_1 \leq \kappa_2 \leq \cdots \leq \kappa_N$. Note that $\mathbf{T}$ is nonsingular.

Theorem 9. Let $\mathbf{G}$ be an $N \times M$ matrix such that $\mathbf{G}^T = -\mathbf{G}$. There exists a transformation $\mathbf{T}$ such that

$$\mathbf{T}^T\mathbf{G}\mathbf{T} = \text{diag}\,\{0_{N-2P}, \mathbf{S}\} \tag{83}$$

$$\mathbf{T}^T\mathbf{T} = \mathbf{I}_N \tag{84}$$

$$\mathbf{S} \triangleq \text{diag}\,\{\mathbf{S}_1, \ldots, \mathbf{S}_P\} \tag{85}$$

$$\mathbf{S}_p \triangleq \begin{bmatrix} 0 & -\omega_p \\ \omega_p & 0 \end{bmatrix} (\omega_p \neq 0) \quad (p = 1, \ldots, P) \tag{86}$$

where $2P$ is the number of nonzero eigenvalues of $\mathbf{G}^2$. For a proof, see [7, p. 217]. $\mathbf{G}^2$ is negative semidefinite, and has nonzero eigenvalues $-\omega_1^2, -\omega_1^2, -\omega_2^2, -\omega_2^2, \ldots, -\omega_P^2, -\omega_P^2$. The $\omega_P^2 (p = 1, \ldots, P)$ need not be distinct. We note, e.g., from (84), that $\mathbf{T}$ is nonsingular.

APPENDIX *B*

Notational Conventions

$\mathbf{M} > 0$ = the symmetric matrix $\mathbf{M}$ is positive-definite
$\mathbf{K} \geq 0$ = the symmetric matrix $\mathbf{K}$ is positive-semidefinite
$rk\,\mathbf{A}$ = rank of the matrix $\mathbf{A}$
$\mathbf{I}_N$ = the $N \times N$ unit matrix
$\mathbf{0}_N$ = the $N \times N$ zero matrix

Downloaded 01 May 2010 to 171.66.16.243. Redistribution subject to ASME license or copyright; see http://www.asme.org/terms/Terms_Use.cfm

C. S. Hsu

Professor of Applied Mechanics,
Department of Mechanical Engineering,
University of California,
Berkeley, Calif. 94720
Fellow ASME

Theory of Index for Dynamical Systems of Order Higher Than Two

This paper is concerned with the generalization of Poincaré's theory of index to systems of order higher than two. The basic tool used in the generalization is the concept of the degree of a map. *In topology this concept has been used to discuss the index of a vector field. In this paper we shall use the degree of a map concept to present a theory of index for higher-order systems in a form which might make it more accessible to engineers for applications. The theory utilizes the notion of the index of a hypersurface with respect to a given vector field. After presenting the theory, it is applied to dynamical systems governed by ordinary differential equations and also to dynamical systems governed by point mappings. Finally, in order to show how the abstract concept of the degree of a map, hence the index of a surface, may actually be evaluated, illustrative procedures of evaluation for two kinds of hypersurfaces are discussed in detail and an example of application is given.*

1 Introduction

One of the most interesting results in the theory of nonlinear oscillations is the celebrated Poincaré's theory of index for singular points of two-dimensional systems. The theory is a remarkable one because for nonlinear systems global results such as this are rare indeed. The subject is discussed in most of the texts and reference books; see, for instance, Stoker [1], Minorsky [2], Kauderer [3], Coddington and Levinson [4], and Lefschetz [5]. A detailed analytical development of the theory may be found in [4, 5]. While this theory of Poincaré's is now well known and classic, its extension to dynamical systems of orders higher than two is, however, not often discussed in the literature of nonlinear oscillations. One of the places where one can find some discussion of the extension to the multidimensional case is in Arnold [6].

As seen in [6], the ideal tool to use to generalize Poincaré's theory to higher-order systems is the concept of the *degree of a map*. It is a well-known concept in topology and differential geometry valid for manifolds of any dimension; see, for instance, Lefschetz [7], Sternberg [8], Guillemin and Pollack [9]. In that area of mathematics this concept has been used to discuss the index of a vector field. However, the theory does not seem to have been sufficiently developed into a form which will make it readily accessible to engineers for applications to physical problems. In this sense its potential for application has not been fully exploited. In this paper we shall utilize the concept of the degree of a map to present the theory of index for higher-order systems in a form which is a parallel to Poincaré's and in mathematical terms more familiar to engineers. More importantly, we shall present explicit formulas to illustrate how the abstract concept of the degree of a map may actually be evaluated. Inasmuch as the basic idea involved is one concerning mapping, the theory of index based upon the degree of a map could have very wide applications. To dynamical systems governed by ordinary differential equations the application is immediate. It can also be applied to dynamical systems governed by point mappings, leading in fact to a more interesting application of the theory.

As a concept in topology and modern differential geometry, the degree of a map is invariably presented and discussed in topological terms [7–9]. It is probably because of this that its meaning and its possible applications are not widely known outside mathematics. This is unfortunate. Nevertheless, there does not seem to be any elementary way to present this important and yet very general mathematical result. Therefore, in this paper the degree of a map from a manifold to a manifold will be introduced in its mathematical form using the modern terminology. Next we put the degree formula in a more explicit form which is more convenient for further analysis and evaluation. Following this we present a theory of index for a vector field and discuss its applications to dynamical systems. Finally, a numerical example will be given to illustrate how the index formula may be used in application. Any theory of index being a global one, it is not expected that an application of it to a specific problem would yield results in all the details. On the other hand, precisely because of its global nature it could provide us with qualitative predictions and quantitative verifications which would be very difficult to obtain otherwise.

2 Mapping of a Vector Field

As a preliminary, let us first discuss the type of mapping we shall be concerned with. Let $\mathbf{X}$ be an n-dimensional Euclidean space. Let x_i $(i = 1, 2, \ldots, n)$ be the coordinates of a point $\mathbf{x}$ in $\mathbf{X}$. Let $\mathbf{F}$ $(F_i, i = 1, 2, \ldots n)$ be a continuous real-valued vector field defined on $\mathbf{X}$. A point at which $\mathbf{F} = \mathbf{0}$ is called a *singular point* of $\mathbf{F}$. We assume that all the singular points of $\mathbf{F}$ are isolated. Let $\mathbf{S}$ be a compact and ori-

Contributed by the Applied Mechanics Division for publication in the JOURNAL OF APPLIED MECHANICS.

Discussion on this paper should be addressed to the Editorial Department, ASME, United Engineering Center, 345 East 47th Street, New York, N. Y. 10017, and will be accepted until September 1, 1980. Readers who need more time to prepare a discussion should request an extension from the Editorial Department. Manuscript received by ASME Applied Mechanics Division, November, 1979; final revision, January, 1980.

Copyright © 1980 by ASME
Downloaded 01 May 2010 to 171.66.16.243. Redistribution subject to ASME license or copyright; see http://www.asme.org/terms/Terms_Use.cfm

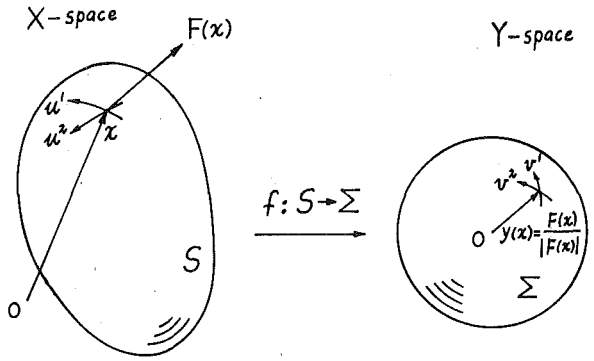

Fig. 1 Mapping of F on S to Σ

ented hypersurface of dimension $(n-1)$ in **X** which divides **X** into two parts, its interior and its exterior, and which passes through no singular points of **F**. At each point **x** on **S**, **F**(**x**) is defined. With this **F**(**x**) we construct a unit vector **y**(**x**) defined as

$$\mathbf{y}(\mathbf{x}) = \frac{1}{|\mathbf{F}(\mathbf{x})|}\mathbf{F}(\mathbf{x}) \tag{1}$$

This vector then lies on the hypersurface Σ of a unit sphere in an n-dimensional Euclidean space with coordinates y_i, $i = 1, 2, \ldots n$. This construction evidently defines a mapping f which maps a point **x** on **S** to a point **y** on Σ, see Fig. 1.

$$f: \quad \mathbf{x}(\mathbf{S}) \rightarrow \mathbf{y}(\Sigma), \quad \text{or} \quad \mathbf{S} \rightarrow \Sigma. \tag{2}$$

It is a mapping from an $(n-1)$-dimensional manifold to an $(n-1)$-dimensional manifold.

3 The Degree of a Map

We state here a result from geometry; see, for instance, [9], Flanders [10], and Choquet-Bruhat, et al. [11]. Let $\mathbf{M}^m$ and $\mathbf{N}^m$ be compact and oriented manifolds of dimension m. Let f be a mapping from $\mathbf{M}^m$ to $\mathbf{N}^m$

$$f: \quad \mathbf{M}^m \rightarrow \mathbf{N}^m. \tag{3}$$

Then there exists an integer called the *degree of f*, given by

$$\int_{\mathbf{M}^m} f^*\omega = [\deg\,(f)] \int_{\mathbf{N}^m} \omega \tag{4}$$

where ω is any m-form on $\mathbf{N}^m$. In (4) f^* is the pull-back (or reciprocal image) induced by f. For a proof of this result the reader is referred to [9, 11]. Geometrically the integer deg (f) may be interpreted as the number of times $\mathbf{N}^m$ is covered by the image $f(\mathbf{M}^m)$. Each covering is counted as a positive or a negative one depending upon whether the mapping is locally orientation-preserving or orientation-reversing.

For the purpose of applications we need to put this abstract form of the result into a more explicit and elementary form. Let u^i $(i = 1, 2, \ldots, m)$ be the local coordinates for $\mathbf{M}^m$ and let v^i $(i = 1, 2, \ldots, m)$ be those of $\mathbf{N}^m$. Let the m-form (volume form) ω of $\mathbf{N}^m$ be given by

$$\omega = \tau(\mathbf{v}) dv^1 \Lambda\, dv^2 \Lambda \ldots \Lambda\, dv^m. \tag{5}$$

(4) may now be written as

$$\deg\,(f) = \frac{A(\mathbf{M}^m)}{B(\mathbf{N}^m)} \tag{6}$$

where

$$A(\mathbf{M}^m) = \int_{\mathbf{M}^m} \tau(f(\mathbf{u})) \frac{\partial(v^1, v^2, \ldots, v^m)}{\partial(u^1, u^2, \ldots, u^m)} du^1 \Lambda\, du^2 \Lambda \ldots \Lambda\, du^m \tag{6a}$$

$$B(\mathbf{N}^m) = \int_{\mathbf{N}^m} \tau(\mathbf{v}) dv^1 \Lambda\, dv^2 \Lambda \ldots \Lambda\, dv^m. \tag{6b}$$

When this result is applied to the mapping f defined in Section 2 we can identify m with $n-1$, $\mathbf{M}^m$ with **S**, and $\mathbf{N}^m$ with Σ. This will be done for the remainder of the paper.

At this point a disgression may be in order with regard to the degree of a map formula. Equation (4) may be called the integral form of the degree formula. The degree of a map may also be expressed in the form

$$\deg \quad (f) = \sum_{\xi = f^{-1}(\eta)} \deg_\xi (f)$$

where η in $\mathbf{N}^m$ is a regular value of f, ξ in $\mathbf{M}^m$ is a preimage of η, $\deg_\xi$ (f) is the degree of f at ξ which is $+1$ or -1 depending upon whether f is locally orientation preserving or orientation reversing. The summation is over all the preimages of η. For a more detailed discussion of this preimage form of the degree formula, the reader is referred to [6, 9]. This preimage form is simple and attractive in appearance. However, to use this form in application will require finding *all* the preimages $f^{-1}(\eta)$ in $\mathbf{M}^m$ for a regular point η in $\mathbf{N}^m$ by solving a set of nonlinear equations. Here lies the superiority of the integral form (4) of the degree formula. In any event, to generalize Poincaré's theory of index the integral form is the more appropriate one to use. However, we do wish to mention the preimage form here because it is an important alternate form which could conceivably be exploited to good advantage under different circumstances.

Another comment on (4) might also be in order here. (4) involves some rather abstract concepts. The degree formula we shall use later in the paper is (6) which is in coordinate form and which is derived from (4) by taking a specific ω. By using different m-forms ω, one could possibly utilize the degree of a map concept in a different manner. For this reason we elect to start our discussion by presenting the general and basic formula (4) of the degree theory rather than starting immediately with (6).

4 A Theory of Index for Vector Fields

Consider a continuous real-valued vector field **F** defined on a Euclidean space **X** of dimension n. A point in **X** at which **F** = **0** is called a singular point of **F**. We assume that all the singular points of **F** are isolated. Let **S** be a compact, connected, and oriented $(n-1)$-dimensional hypersurface in **X** which divides **X** into an interior and an exterior part and which contains no singular points of **F** on it.[1] Next, we construct the mapping f: **S** → Σ according to the rules given in Section 2. In what follows we make use of the idea of the degree of a map to present a theory of index which is a generalization of Poincaré's theory to vector fields of dimensions higher than two. The presentation of the theory will be very much in parallel to what is given in [4] for two-dimensional vector fields.

First, we recall that Σ is an $(n-1)$-dimensional surface of a unit sphere in an n-dimensional Euclidean space and it is identified with $\mathbf{N}^m$ of the degree formula (4). Therefore, if we choose the m-form ω to be the "volume"-form of $\mathbf{N}^m$ in the form of (5), then $B(\mathbf{N}^m)$ is nothing but the total surface area of Σ, which will be designated by $B(\Sigma)$ and is known to be [10],

$$B(\Sigma) = \frac{n\pi^{n/2}}{\Gamma\left(\frac{n}{2}+1\right)} \tag{7}$$

where $\Gamma(k)$ is the Gamma function. In this manner we may rewrite the degree of the mapping f of our study in the form

$$\deg\,(f) = \frac{1}{B(\Sigma)} A(\mathbf{S}) \tag{8}$$

where $A(\mathbf{S})$ is given by (6a) with $\mathbf{M}^m$ identified with **S**.

Definition 1. The index of a compact, connected, and oriented surface **S** with respect to **F**, to be denoted by $I(\mathbf{S}, \mathbf{F})$, is defined as

[1] In the remainder of the paper, we shall use the term "surface" to mean a hypersurface having these properties.

Downloaded 01 May 2010 to 171.66.16.243. Redistribution subject to ASME license or copyright; see http://www.asme.org/terms/Terms_Use.cfm

$$I(\mathbf{S}, \mathbf{F}) = \deg(f) \tag{9}$$

where $\deg(f)$ is the degree of the map $f: \mathbf{S} \to \Sigma$.

Theorem 1. Let $\mathbf{S}_1$ and $\mathbf{S}_2$ be two compact, connected, and oriented surfaces which have disjointed interiors but have a common part $\mathbf{S}_c$. Let $\mathbf{S}$ be $\mathbf{S}_1$ plus $\mathbf{S}_2$ but with $\mathbf{S}_c$ deleted. Then

$$I(\mathbf{S}, \mathbf{F}) = I(\mathbf{S}_1, \mathbf{F}) + I(\mathbf{S}_2, \mathbf{F}) \tag{10}$$

Proof. Let f be the mapping from $\mathbf{S}$ to Σ, f_1 be that from $\mathbf{S}_1$ to Σ, and f_2 be that from $\mathbf{S}_2$ to Σ. The common part $\mathbf{S}_c$ when regarded as a part of $\mathbf{S}_1$ will obviously have an orientation opposite to that of $\mathbf{S}_c$ regarded as a part of $\mathbf{S}_2$. Let us denote it by $\mathbf{S}_{c+}$ and $\mathbf{S}_{c-}$ in the respective cases. Then by Definition 1 and the degree formula (8) we have

$$I(\mathbf{S}_1, \mathbf{F}) + I(\mathbf{S}_2, \mathbf{F}) = \deg(f_1) + \deg(f_2) = \frac{1}{B(\Sigma)}\{A(\mathbf{S}_1 - \mathbf{S}_{c+}) + A(\mathbf{S}_{c+}) + A(\mathbf{S}_2 - \mathbf{S}_{c-}) + A(\mathbf{S}_{c-})\}$$

In this expression the contributions $A(\mathbf{S}_{c+})$ and $A(\mathbf{S}_{c-})$ cancel each other, and the sum of $A(\mathbf{S}_1 - \mathbf{S}_{c+})$ and $A(\mathbf{S}_2 - \mathbf{S}_{c-})$ is merely $A(\mathbf{S})$. Therefore, $I(\mathbf{S}_1, \mathbf{F}) + I(\mathbf{S}_2, \mathbf{F})$ is equal to $\deg(f)$, hence $I(\mathbf{S}, \mathbf{F})$.

Theorem 2. If $\mathbf{S}$ is a compact, connected, and oriented surface containing no singular point of $\mathbf{F}$ on it and in its interior, then $I(\mathbf{S}, \mathbf{F}) = 0$.

Outline of Proof. Intuitively, this result is obvious, particularly if $\mathbf{S}$ is small in extent. $\mathbf{F}$ being continuous, the maximum variation in direction of $\mathbf{F}$ over $\mathbf{S}$ is very limited. Therefore, the image of $\mathbf{S}$ under f can only cover a small part of Σ with an equal number of positive and negative coverings. Consequently, $\deg(f) = 0$. Using this result and Theorem 1 repeatedly, the result can be extended to a surface $\mathbf{S}$ of any size. Analytically, one can prove Theorem 2 by using a theorem given in [9, p. 189] which shows $A(\mathbf{S}) = 0$ if $\mathbf{S}$ contains no singular points. Hence $\deg(f) = I(\mathbf{S}, \mathbf{F}) = 0$. The reader is referred to [9] for detail.

Theorem 3. If $\mathbf{S}_1$ is a compact, connected, and oriented surface which is contained in the interior of another compact, connected, and oriented surface $\mathbf{S}_2$, and if no singular points lie between $\mathbf{S}_1$ and S_2, then $I(\mathbf{S}_1, \mathbf{F}) = I(\mathbf{S}_2, \mathbf{F})$.

Proof. Let f_1 and f_2 be, respectively, the mapping from $\mathbf{S}_1$ to Σ and the mapping from $\mathbf{S}_2$ to Σ. $\mathbf{S}_2$ can obviously be obtained by a continuous deformation from $\mathbf{S}_1$ without passing through any singular points of $\mathbf{F}$. $\mathbf{F}$ being continuous, the change of the mapping from f_1 to f_2 is a continuous one, and so must be the change in the degree of the mapping. However, the degree of a map is necessarily an integer. Therefore, a $\deg(f_2)$ must be equal to $\deg(f_1)$.

Definition 2. The index of an isolated singular point $\mathbf{P}$ with respect to a vector field $\mathbf{F}$ is defined as the index of any compact, connected, and oriented surface $\mathbf{S}$ which contains only $\mathbf{P}$ and no other singular points of $\mathbf{F}$ in its interior and is denoted by $I(\mathbf{P}, \mathbf{F})$, i.e., $I(\mathbf{P}, \mathbf{F}) = I(\mathbf{S}, \mathbf{F})$.

Theorem 4. If $\mathbf{S}$ is a compact, connected, and oriented surface containing a finite number $\mathbf{P}_1, \mathbf{P}_2, \ldots, \mathbf{P}_N$ of singular points of $\mathbf{F}$ in its interior, then

$$I(\mathbf{S}, \mathbf{F}) = \sum_{i=1}^{N} I(\mathbf{P}_i, \mathbf{F}) \tag{11}$$

This result follows immediately from Definition 2 and Theorem 1.

Let $\mathbf{F}$ have an isolated singular point which, without any loss of generality, will be assumed to be located at the origin $\mathbf{0}$. Let $\mathbf{F}$ admit the form

$$\mathbf{F}(\mathbf{x}) = \mathbf{L}\mathbf{x} + \mathbf{Q}(\mathbf{x}) \tag{12}$$

where $\mathbf{L}$ is a $n \times n$ constant matrix and $\mathbf{Q}(\mathbf{x})$ represents the nonlinear part of $\mathbf{F}$ and is assumed to satisfy

$$\lim \frac{\|\mathbf{Q}(\mathbf{x})\|}{\|\mathbf{x}\|} = 0 \quad \text{as} \quad \|\mathbf{x}\| \to 0. \tag{13}$$

We also assume

$$\det(\mathbf{L}) \neq \mathbf{0}. \tag{14}$$

The origin is now an isolated non-degenerate singular point of $\mathbf{F}$. Its index with respect to $\mathbf{F}$ is entirely determined by the linear part $\mathbf{L}(\mathbf{x})$ of $\mathbf{F}$, yielding the following results.

Theorem 5. Let the origin be a nondegenerate singular point of $\mathbf{F}$. Let $\mathbf{L}(\mathbf{x})$ be the linear part of $\mathbf{F}(\mathbf{x})$ and let the nonlinear part $\mathbf{Q}(\mathbf{x})$ of $\mathbf{F}(\mathbf{x})$ satisfy (13), then $I(\mathbf{0}, \mathbf{F}) = I(\mathbf{0}, \mathbf{L})$.

Outline of Proof. For a proof of this result one can adopt the proof given in [4, pp. 400–401] for two-dimensional vector fields. The only changes required are the replacing of the Jordan curve by a compact, connected, and oriented hypersurface $\mathbf{S}$ and some slight rewording of the proof for higher-dimensional vector fields.

Theorem 6. The index of an isolated nondegenerate singular point of $\mathbf{F}$ at the origin is $+1$ or -1, according as $\det(\mathbf{L}) > 0$ or < 0.

The proof of this important and specific result follows from a geometrical theorem that if f is locally a diffeomorphism, i.e., one–one and onto then the degree of f is either $+1$ or -1 depending upon whether f is orientation preserving or not. In the present case the orientation preserving or reversing depends upon the sign of $\det(\mathbf{L})$.

In a more general term the matrix $\mathbf{L}$ associated with a singular point $\mathbf{P}$ of $\mathbf{F}$ may be identified with $(\partial \mathbf{F}/\partial \mathbf{x})_{\mathbf{P}}$, or $\mathbf{DF}(\mathbf{P})$, the Jacobian matrix of $\mathbf{F}$ at $\mathbf{P}$. This leads to the following result:

Theorem 6(*a*). The index of an isolated nondegenerate singular point $\mathbf{P}$ of $\mathbf{F}$ is given by

$$I(\mathbf{P}, \mathbf{F}) = \begin{matrix} +1 \\ -1 \end{matrix} \quad \text{if} \quad \det[\mathbf{DF}(\mathbf{P})] \gtrless 0. \tag{15}$$

5 Application to Differential Dynamical Systems

Consider a dynamical system governed by

$$\dot{\mathbf{x}} = \mathbf{F}(\mathbf{x}) \tag{16}$$

The equilibrium states of the system are obviously singular points of $\mathbf{F}$. Take a surface $\mathbf{S}$ in the state space $\mathbf{X}$. Assume that the required conditions are met so that the theory of index given in Section 4 is applicable. Then the index $I(\mathbf{S}, \mathbf{F})$ is equal to the sum of the indices of all the equilibrium states inside $\mathbf{S}$.

Theorem 7. If the surface $\mathbf{S}$ contains equilibrium states $\mathbf{P}_1, \mathbf{P}_2, \ldots, \mathbf{P}_N$ in its interior, all nondegenerate with respect to $\mathbf{F}$, then

$$I(\mathbf{S}, \mathbf{F}) = \sum_{i=1}^{N} I(\mathbf{P}_i, \mathbf{F}) \tag{17}$$

where $I(\mathbf{P}_i, \mathbf{F})$ are determined by (15).

This is an interesting global result by itself. However, this theory of index could also be of great utility in a practical direction. For a strongly nonlinear system the determination of the solutions of a nonlinear vector equation like

$$\mathbf{F}(\mathbf{x}) = \mathbf{0} \tag{18}$$

is not an easy task even with the aid of a computer. Also unless special care is taken or the equation is reformulated, various numerical procedures often would not yield equilibrium states which are unstable. And yet these unstable equilibrium states also strongly control the trajectories of the system and any information on them is extremely useful in a global study of the problem. Here, the index theory could be used to advantage. One possible use is the following. Consider the surface mentioned in the last paragraph. If we vary $\mathbf{S}$ in a systematical way, we can compute the variation of the index of $\mathbf{S}$ with respect to $\mathbf{F}$ and, hence, ascertain the distribution and their characters of all the equilibrium states (stable as well as unstable ones) located in a region of the state space which is of interest to us. This could aid to clarify the global picture.

6 Application to Point Mapping Dynamical Systems

Consider next a dynamical system governed by a system of difference equations

$$\mathbf{x}(m+1) = \mathbf{G}(\mathbf{x}(m)) \tag{19}$$

Downloaded 01 May 2010 to 171.66.16.243. Redistribution subject to ASME license or copyright; see http://www.asme.org/terms/Terms_Use.cfm

where $\mathbf{x}$ is a state vector of dimension n. Systems of this kind has been sometimes called difference dynamical systems in order to differentiate them from systems governed by differential equations. In this paper we shall use the more descriptive name "point mapping dynamical systems."

Point mapping dynamical systems have been receiving increasing attention in the recent years. The general method dates back to Poincaré [13] and Birkhoff [14]. In the past 20 years or so it has received a great deal of mathematical development, mainly by people working in the field of differentiable dynamics; see for instance the work by Arnol'd [15], Smale [16], Markus [17], Takens [18], Marsden and McCracken [19], Bernussou [20]. Hsu, et al. [21–25], have used this approach to study periodic dynamical systems.

6.1 Periodic Solutions of Point Mappings. Consider now the periodic solutions of (19). Let us denote by $\mathbf{G}^k$ the mapping $\mathbf{G}$ applied k times, with $\mathbf{G}^0$ understood to be an identity mapping. A periodic solution of period K of a mapping $\mathbf{G}$ is a set of K distinct points $\mathbf{x}^*(j)$, $j = 1, 2, \ldots, K$, such that

$$\mathbf{x}^*(m+1) = \mathbf{G}^m(\mathbf{x}^*(1)), \quad m = 1, 2, \ldots, K-1,$$
$$\mathbf{x}^*(1) = \mathbf{G}^K(\mathbf{x}^*(1)). \tag{20}$$

Since we will refer to periodic solutions of this kind time and again, it is convenient to adopt an abbreviated name. We shall call a periodic solution of period K as a $P-K$ *solution* and any of its elements $\mathbf{x}^*(j)$, $j = 1, 2, \ldots, K$, a periodic point of period K, or, in abbreviation, a *P–K point*. The $P-1$ points can, of course, be interpreted as the equilibrium states of the point mapping dynamical systems. However, if the point mapping is in fact obtained from a system of periodic differential equations by integrating over one period, then a $P-1$ point could be either an equilibrium state or a periodic solution of period 1 for the original differential dynamical system and the $P-K$ points will correspond to subharmonic solutions of period K.

6.2 The Index of a $P-1$ Point With Respect to $G-I$. In the next few sections we shall discuss the application of the theory of index of Section 4 to point mapping dynamical systems. In [25] Hsu has applied Poincaré's theory of index to two-dimensional point mapping systems. Therefore, what follows may be regarded as a generalization of [25] to higher order systems. Once we have used the *degree of a map* as the basic tool to define the index of a surface, then with some slight modification in wording, the development given in [25] for the second-order systems is equally valid for higher-order systems. For this reason we shall merely present the results without offering any proofs. The reader is referred to [25] for the analytical arguments used in arriving at the results.

First, in this section we consider the index of a $P-1$ point of $\mathbf{G}$. Here, we identify the vector field $\mathbf{F}$ of Section 4 with $\mathbf{G}-\mathbf{I}$ where $\mathbf{I}$ is the identity mapping.

$$\mathbf{F}(\mathbf{x}) = (\mathbf{G}-\mathbf{I})(\mathbf{x}) = \mathbf{G}(\mathbf{x}) - \mathbf{x} \tag{21}$$

Obviously all the $P-1$ points of $\mathbf{G}$ are the singular points of $\mathbf{F}$ as defined by (21) and all the singular points of $\mathbf{F}$ are the $P-1$ points of $\mathbf{G}$. Then, by Theorem 6(a) we have the following result.

Theorem 8. If $\mathbf{x}^*$ is a $P-1$ point of $\mathbf{G}$ nondegenerate with respect to $(\mathbf{G}-\mathbf{I})$, then its index with respect to $(\mathbf{G}-\mathbf{I})$, to be denoted by $I(\mathbf{x}^*, \mathbf{G}-\mathbf{I})$, is equal to $+1$ or -1, according as $\det(\mathbf{DG}(\mathbf{x}^*)-\mathbf{I}) > 0$ or <0. Here we have adopted the nomenclature that if, for a singular point $\mathbf{P}$ of $\mathbf{F}$, $\det(\mathbf{DF}(\mathbf{P})) \neq 0$, then the point $\mathbf{P}$ is said to be nondegenerate with respect to $\mathbf{F}$.

Combining Theorem 4 and Theorem 8, we obtain the following:

Theorem 9. Given a point mapping $\mathbf{G}$, if a hypersurface $\mathbf{S}$ of dimension $n-1$ contains a finite number $\mathbf{P}_1, \mathbf{P}_2, \ldots, \mathbf{P}_N$ of $P-1$ points of $\mathbf{G}$ in its interior and if p_1 is the number of points having positive $\det(\mathbf{DG}(\mathbf{P}_i)-\mathbf{I})$ and q_1 is the number of points having negative $\det(\mathbf{DG}(\mathbf{P}_i)-\mathbf{I})$, with $p_1 + q_1 = N$, then the index of $\mathbf{S}$ with respect $(\mathbf{G}-\mathbf{I})$, to be denoted by $I(\mathbf{S}, \mathbf{G}-\mathbf{I})$, is $p_1 - q_1$.

6.3 The Index of a $P-1$ Point With Respect to $G^2-\mathbf{I}$. Again consider a $P-1$ point $\mathbf{x}^*$ but now consider a vector field $\mathbf{F}$ defined as

$$\mathbf{F}(\mathbf{x}) = (\mathbf{G}^2-\mathbf{I})(\mathbf{x}) = \mathbf{G}^2(\mathbf{x}) - \mathbf{x}. \tag{22}$$

A $P-1$ point of $\mathbf{G}$ is again a singular point of $\mathbf{F}$.

Theorem 10. If $\mathbf{x}^*$ is a $P-1$ point of $\mathbf{G}$ nondegenerate with respect to $(\mathbf{G}^2-\mathbf{I})$, then its index with respect to $(\mathbf{G}^2-\mathbf{I})$, to be denoted by $I(\mathbf{x}^*, \mathbf{G}^2-\mathbf{I})$, is $+1$ or -1, according as $\det(\mathbf{DG}^2(\mathbf{x}^*)-\mathbf{I}) > 0$ or <0.

It might be noted here that the expression $\det(\mathbf{DG}^2(\mathbf{x}^*)-\mathbf{I}) \gtrless 0$ may also be written as

$$\det(\mathbf{DG}(\mathbf{x}^*)-\mathbf{I}) \cdot \det(\mathbf{DG}(\mathbf{x}^*)+\mathbf{I}) \gtrless 0. \tag{23}$$

6.4 The Index of a $P-1$ Point With Respect to G^k-I. Consider now a vector field $\mathbf{F}$ defined by

$$\mathbf{F}(\mathbf{x}) = (\mathbf{G}^k-\mathbf{I})(\mathbf{x}) = \mathbf{G}^k(\mathbf{x}) - \mathbf{x} \tag{24}$$

where k is a positive integer. A $P-1$ point $\mathbf{x}^*$ of $\mathbf{G}$ is again a singular point of $\mathbf{F}$. Following the analysis given in [25] except to generalize it to higher-order systems, we can arrive at the following results.

Theorem 11. If k is odd and if $\mathbf{x}^*$ is a $P-1$ point of $\mathbf{G}$ nondegenerate with respect to $(\mathbf{G}^k-\mathbf{I})$, then the index of $\mathbf{x}^*$ with respect to $(\mathbf{G}^k-\mathbf{I})$ is equal to its index with respect to $(\mathbf{G}-\mathbf{I})$.

Theorem 12. If k is even and if $\mathbf{x}^*$ is a $P-1$ point of $\mathbf{G}$ nondegenerate with respect to $(\mathbf{G}^k-\mathbf{I})$, then the index of $\mathbf{x}^*$ with respect to $(\mathbf{G}^k-\mathbf{I})$ is equal to its index with respect to $(\mathbf{G}^2-\mathbf{I})$.

6.5 The Index of a $P-K$ Point. Consider now a $P-K$ solution of $\mathbf{G}$. Such a solution satisfies (20) and has K elements $\mathbf{x}^*(j)$, $j = 1, 2, \ldots, K$. Let us take $\mathbf{x}^*(j)$ as a typical $P-K$ point. Moreover, let us take $(\mathbf{G}^K-\mathbf{I})(\mathbf{x})$ to be the vector field $\mathbf{F}(\mathbf{x})$. Evidently, $\mathbf{x}^*(j)$ is a singular point of $\mathbf{F}$. Applying Theorem 6(a) to this case, one finds the following:

Theorem 13. If $\mathbf{x}^*(j)$ is a $P-K$ point of $\mathbf{G}$ nondegenerate with respect to $(\mathbf{G}^K-\mathbf{I})$, then the index of $\mathbf{x}^*(j)$ with respect to $(\mathbf{G}^K-\mathbf{I})$, to be denoted by $I(\mathbf{x}^*(j), \mathbf{G}^K-\mathbf{I})$, is $+1$ or -1, according as $\det(\mathbf{DG}^K(\mathbf{x}^*(j))-\mathbf{I}) > 0$ or <0.

Here one should note that $\mathbf{DG}^K(\mathbf{x}^*(j))$ is given by

$$\mathbf{DG}^K(\mathbf{x}^*(j)) = \mathbf{DG}(\mathbf{x}^*(j-1)) \ldots \mathbf{DG}(\mathbf{x}^*(1))\mathbf{DG}(\mathbf{x}^*(K)) \ldots \mathbf{DG}(\mathbf{x}^*(j)). \tag{25}$$

Similar to Theorems 11 and 12, we may take, instead of $(\mathbf{G}^K-\mathbf{I})$, $(\mathbf{G}^{kK}-\mathbf{I})$ to be the vector field $\mathbf{F}$ with k being a positive integer. Assuming that $\mathbf{x}^*(j)$ is nondegenerate with respect to this $\mathbf{F}$, we have the following results.

Theorem 14. If k is odd and if $\mathbf{x}^*(j)$ is a $P-K$ point of $\mathbf{G}$ nondegenerate with respect to $(\mathbf{G}^{kK}-\mathbf{I})$, then the index of $\mathbf{x}^*(j)$ with respect to $(\mathbf{G}^{kK}-\mathbf{I})$ is $+1$ or -1, according to whether $\det(\mathbf{DG}^K(\mathbf{x}^*(j))-\mathbf{I}) > 0$ or <0.

Theorem 15. If k is even and if $\mathbf{x}^*(j)$ is a $P-K$ point of $\mathbf{G}$ nondegenerate with respect to $(\mathbf{G}^{kK}-\mathbf{I})$, then the index of $\mathbf{x}^*(j)$ with respect to $(\mathbf{G}^{kK}-\mathbf{I})$ is $+1$ or -1, according to whether $\det[(\mathbf{DG}^K(\mathbf{x}^*(j)))^2 - \mathbf{I}] > 0$ or <0.

6.6 The Index of a Hypersurface S With Respect to $(\mathbf{G}^L-\mathbf{I})$. With the development of Sections 6.2–6.5 at hand, we can now establish a global result of the index theory for point mapping dynamical systems. Consider a surface $\mathbf{S}$ and consider a vector field $\mathbf{F}$ defined by

$$\mathbf{F}(\mathbf{x}) = (\mathbf{G}^L-\mathbf{I})(\mathbf{x}) = \mathbf{G}^L(\mathbf{x}) - \mathbf{x} \tag{26}$$

where L is a positive integer. Let $f_1 = 1, f_2, f_3, \ldots, f_Q = L$ be the complete set of positive integer factors of L. Then it is obvious that all $P-1, P-f_2, P-f_3, \ldots, P-L$ points of $\mathbf{G}$ are singular points of $\mathbf{F}$, and vice versa. Let N of these points be contained in the interior of $\mathbf{S}$ and let them be labeled as $\mathbf{P}_i(K_i)$, $i = 1, 2, \ldots, N$, where K_i equal to one of the factors f_q, $q = 1, 2, \ldots, Q$, is used to indicate the periodicity of the point. To each point $\mathbf{P}_i(K_i)$ is associated a number $k_i = L/K_i$. We assume that all the $\mathbf{P}_i(K_i)$ points are nondegenerate with respect to $\mathbf{F}$ in the sense that $\det[(\mathbf{DG}^{K_i}(\mathbf{P}_i))^{k_i} - \mathbf{I}] \neq 0$. The index $I(\mathbf{P}_i(K_i), \mathbf{G}^{k_iK_i}-\mathbf{I})$ of each point $\mathbf{P}_i(K_i)$ with respect to $(\mathbf{G}^L-\mathbf{I})$ can be determined by Theorem 14 if k_i is odd, or by Theorem 15 if k_i is even. Applying now Theorem 4, we obtain the following:

Theorem 16. The index of $\mathbf{S}$ with respect to $(\mathbf{G}^L-\mathbf{I})$ is

Downloaded 01 May 2010 to 171.66.16.243. Redistribution subject to ASME license or copyright; see http://www.asme.org/terms/Terms_Use.cfm

$$I(\mathbf{S}, \mathbf{G}^L - \mathbf{I}) = \sum_{i=1}^{N} I(\mathbf{P}_i(K_i), \mathbf{G}^{k_i K_i} - \mathbf{I}).$$

So far we have presented a general theory of index for vector fields of any dimensions and we have seen how the corresponding theories of index for differential dynamical systems and point mapping dynamical systems are established. In the remaining two sections we discuss methods of implementation and specific procedures of computation necessary if one is to apply the theory to specific problems.

7 Illustrative Procedures of Computing Deg(f) for Two Special Surfaces

Assume that a vector field $\mathbf{F}$ is given. Then, according to Definition 1, for each choice of a surface $\mathbf{S}$ one can determine its index $I(\mathbf{S}, \mathbf{F})$ with respect to $\mathbf{F}$ by (i) constructing the mapping $f: \mathbf{S} \to \boldsymbol{\Sigma}$ according to Section 2, and (ii) computing deg (f) by using (4) or (6). In principle, (6)–(8) give us the necessary mathematical equations for computing deg (f). However, these equations are still too implicit to be of immediate use. In order to make the theory of index readily available for application to concrete physical problems, it would be desirable to indicate how the various expressions involved in (6)–(8) can be evaluated. This we shall do by considering two special cases in detail and present the required explicit formulas of implementation.

The first is the case where $\mathbf{S}$ is a hypersurface of a sphere of radius R. For the local coordinates u^i, $i = 1, 2, \ldots, n-1$, on the spherical surface $\mathbf{S}$ in the $\mathbf{X}$-space we may take the "generalized" spherical coordinates. Thus

$$\begin{aligned} x_1 &= R \cos u^1 \\ x_2 &= R \sin u^1 \cos u^2 \\ x_3 &= R \sin u^1 \sin u^2 \cos u^3 \\ &\cdots\cdots \\ x_n &= R \sin u^1 \sin u^2 \ldots \sin u^{n-1} \end{aligned} \tag{27}$$

where x_i, $i = 1, 2, \ldots, n$, are the Euclidean coordinates of the $\mathbf{X}$-space. The vector field is assumed to be given.

$$F_i = F_i(x_1, x_2, \ldots, x_n), \quad i = 1, 2, \ldots, n. \tag{28}$$

An image point of f on the unit spherical surface $\boldsymbol{\Sigma}$ in the $\mathbf{Y}$-space is given by

$$y_i(\boldsymbol{\Sigma}) = \frac{1}{|\mathbf{F}(\mathbf{x}(\mathbf{S}))|} F_i(\mathbf{x}(\mathbf{S})) \tag{29}$$

For the local coordinates v^i, $i = 1, 2, \ldots, n-1$, on $\boldsymbol{\Sigma}$ we may again take the generalized spherical coordinates. This leads to

$$\begin{aligned} v^1 &= \tan^{-1}\left\{\left[\sum_{i=2}^{n} (y_i)^2\right]^{1/2} \Big/ y_1\right\} \\ v^2 &= \tan^{-1}\left\{\left[\sum_{i=3}^{n} (y_i)^2\right]^{1/2} \Big/ y_2\right\} \\ &\cdots\cdots \\ v^{n-1} &= \tan^{-1}\{y_n / y_{n-1}\} \end{aligned} \tag{30}$$

Next we should find the "volume" form needed in (6a) for the unit spherical surface $\boldsymbol{\Sigma}$ in the $\mathbf{Y}$-space. This can be derived by using the volume form formula for a unit $(n-1)$-sphere in a n-dimensional Euclidaean space; see, for instance, [10, p. 76]. Such a calculation leads to the following coefficient $\tau(\mathbf{v})$ for the volume form of $\boldsymbol{\Sigma}$.

$$\tau(\mathbf{v}) = (\sin v^1)^{n-2} (\sin v^2)^{n-3} \ldots (\sin v^{n-2}). \tag{31}$$

The sequence of transformations of (27)–(30) defines a mapping f from $\mathbf{S}$ to $\boldsymbol{\Sigma}$ or from u^i to v^i, $i = 1, 2, \ldots, n-1$. The Jacobian matrix $\partial\mathbf{v}/\partial\mathbf{u}$ required in (6a) can be evaluated by using the chain rule.

$$\frac{\partial \mathbf{v}}{\partial \mathbf{u}} = \frac{\partial \mathbf{v}}{\partial \mathbf{y}} \frac{\partial \mathbf{y}}{\partial \mathbf{F}} \frac{\partial \mathbf{F}}{\partial \mathbf{x}} \frac{\partial \mathbf{x}}{\partial \mathbf{u}} \tag{32}$$

Explicitly and individually we have

$$\frac{\partial \mathbf{v}}{\partial \mathbf{y}} = \begin{bmatrix} -s_1', & c_1' c_2', & c_1' s_2' c_3', & \ldots, & c_1' s_2' s_3' \ldots c_{n-1}', & c_1' s_2' s_3' \ldots s_{n-1}' \\ 0, & -\dfrac{s_2'}{s_1'}, & \dfrac{c_2' c_3'}{s_1'}, & \ldots, & \dfrac{c_2' s_3' s_4' \ldots c_{n-1}'}{s_1'}, & \dfrac{c_2' s_3' s_4' \ldots s_{n-1}'}{s_1'} \\ 0, & 0, & -\dfrac{s_3'}{s_1' s_2'}, & \ldots, & \dfrac{c_3' s_4' s_5' \ldots c_{n-1}'}{s_1' s_2'}, & \dfrac{c_3' s_4' s_5' \ldots s_{n-1}'}{s_1' s_2'} \\ \cdots & \cdots & \cdots & \cdots & \cdots & \cdots \\ 0, & 0, & 0, & \ldots, & -\dfrac{s_{n-1}'}{s_1' s_2' s_3' \ldots s_{n-2}'}, & \dfrac{c_{n-1}'}{s_1' s_2' s_3' \ldots s_{n-2}'} \end{bmatrix} \tag{33}$$

$$\frac{\partial y_i}{\partial F_j} = F^{-1}\delta_{ij} - F^{-3} F_i F_j \tag{34}$$

$$\frac{\partial \mathbf{x}}{\partial \mathbf{u}} = \begin{bmatrix} -Rs_1, & 0, & \ldots, & 0 \\ Rc_1 c_2, & -Rs_1 s_2, & \ldots, & 0 \\ \cdots & \cdots & \ldots, & \cdots \\ Rc_1 s_2 \ldots s_{n-1}, & Rs_1 c_2 \ldots s_{n-1}, & \ldots, & Rs_1 s_2 \ldots c_{n-1} \end{bmatrix} \tag{35}$$

where

$$\begin{aligned} F &= \left\{\sum_{i=1}^{n} F_i^2\right\}^{1/2} \\ c_i &= \cos u^i, \quad s_i = \sin u^i, \\ c_i' &= \cos v^i, \quad s_i' = \sin v^i. \end{aligned} \tag{36}$$

In (33) some of the elements have denominators which might vanish. Thus (33) as it stands is not a desirable one for the purpose of numerical evaluation. Here, one recognizes however that in (6a) the determinant of the Jacobian $\partial\mathbf{v}/\partial\mathbf{u}$ is to be multiplied by $\tau(\mathbf{v})$ which for the present case is given by (31) and has precisely the factors to cancel those undesirable denominators. We can therefore incorporate $\tau(\mathbf{v})$ with $\partial\mathbf{v}/\partial\mathbf{u}$ and obtain the following expression for the integrand in (6a)

$$\tau(\mathbf{v}) \frac{\partial(v^1, v^2, \ldots, v^m)}{\partial(u^1, u^2, \ldots, u^m)} = \det\left\{\mathbf{C} \frac{\partial \mathbf{y}}{\partial \mathbf{F}} \frac{\partial \mathbf{F}}{\partial \mathbf{x}} \frac{\partial \mathbf{x}}{\partial \mathbf{u}}\right\} \tag{37}$$

where

Downloaded 01 May 2010 to 171.66.16.243. Redistribution subject to ASME license or copyright; see http://www.asme.org/terms/Terms_Use.cfm

$$\mathbf{C} = \begin{bmatrix} -s_1', & c_1'c_2', & c_1's_2'c_3', & \dots, & c_1's_2's_3'\dots c_{n-1}', & c_1's_2's_3'\dots s_{n-1}' \\ 0, & -s_2', & c_2'c_3', & \dots, & c_2's_3's_4'\dots c_{n-1}', & c_2's_3's_4'\dots s_{n-1}' \\ 0, & 0, & -s_3', & \dots, & c_3's_4's_5'\dots c_{n-1}', & c_3's_4's_5'\dots s_{n-1}' \\ \cdot, & \cdot, & \cdot, & \dots, & \cdot, & \cdot \\ 0, & 0, & 0, & \dots, & -s_{n-1}', & c_{n-1}' \end{bmatrix} \quad (38)$$

For a given vector field $\mathbf{F}$ and for a spherical hypersurface $\mathbf{S}$ of chosen radius R, (27)–(38) allow us to compute deg (f) by (6)–(8) and therefore $I(\mathbf{S}, \mathbf{F})$.

The second illustrative example to be given here is for the case where $\mathbf{S}$ is the boundary of a rectangular region defined by

$$a_i < x_i < b_i, \quad i = 1, 2, \dots, n \quad (39)$$

This surface consists of $2n$ "plane" surfaces which will be designated as $\mathbf{S}_{i+}$ and $\mathbf{S}_{i-}$, $i = 1, 2, \dots, n$, with $\mathbf{S}_{i+}$ located at $x_i = b_i$ and $\mathbf{S}_{i-}$ at $x_i = a_i$. For $\mathbf{S}_{i+}$ and $\mathbf{S}_{i-}$ we use the Euclidean coordinates x_j, $j = 1, 2, \dots, i-1, i+1, \dots, n$, as the surface coordinates u^i as follows:

$$\begin{aligned} &x_1 = u^{n-i+1}, \quad x_2 = u^{n-i+2}, \dots \\ &x_{i-1} = u^{n-1}, \quad x_{i+1} = u^1, \dots \\ &x_n = u^{n-i} \end{aligned} \quad (40)$$

In (32) all the factors on the right-hand side remain unchanged except the last one. For $\mathbf{S}_{i+}$, $\partial\mathbf{x}/\partial\mathbf{u}$ now take the form

$$\frac{\partial \mathbf{x}}{\partial \mathbf{u}} = \begin{bmatrix} \mathbf{0}_{(i-1)x(n-i)}, & \mathbf{I}_{(i-1)x(i-1)} \\ \mathbf{0}_{(1)x(n-i)}, & \mathbf{0}_{(1)x(i-1)} \\ \mathbf{I}_{(n-i)x(n-i)}, & \mathbf{0}_{(n-i)x(i-1)} \end{bmatrix} \quad (41)$$

where $\mathbf{I}_{(m)x(m)}$ is a unit matrix of order m and $\mathbf{0}_{(m_1)x(m_2)}$ is a zero matrix of order $m_1 x m_2$.

In applying (32) to evaluate (6a) one needs however to take into account the fact that while the side of $\mathbf{S}_{i+}$ facing the positive direction of x_i has an orientation in agreement with that of $\mathbf{S}$, it is the side of $\mathbf{S}_{i-}$ facing the negative direction of x_i that has an orientation in agreement with that of $\mathbf{S}$. Hence we should modify (6a) as follows:

$$\begin{aligned} A = &\sum_{i=1}^{n} \int_{\mathbf{S}_{i+}} \tau(f(\mathbf{u})) \frac{\partial(v^1, v^2, \dots, v^m)}{\partial(u^1, u^2, \dots, u^m)} du^1 \Lambda\, du^2 \Lambda \dots \Lambda\, du^m \\ &- \sum_{i=1}^{n} \int_{\mathbf{S}_{i-}} \tau(f(\mathbf{u})) \frac{\partial(v^1, v^2, \dots, v^m)}{\partial(u^1, u^2, \dots, u^m)} du^1 \Lambda\, du^2 \Lambda \dots \Lambda\, du^m \end{aligned} \quad (42)$$

8 An Example

To demonstrate how the index theory for higher-order systems may be applied we consider the following simple problem:

$$\begin{aligned} \dot{x}_1 &= F_1(\mathbf{x}) = x_1 \\ \dot{x}_2 &= F_2(\mathbf{x}) = x_3 \\ \dot{x}_3 &= F_3(\mathbf{x}) = -x_2 + x_2^3 \end{aligned} \quad (43)$$

In a sense this is a trivial example because the equilibrium states can be found by inspection and their character can be determined easily. However, it does have the virtue that by working through this problem in a familiar setting of a three-dimensional state space and two-dimensional surfaces one can clearly see how the utilization of the index theory is carried out.

We take $\mathbf{S}$ to be a spherical surface of radius R. The matrix $\partial\mathbf{F}/\partial\mathbf{x}$ is given by

$$\frac{\partial \mathbf{F}}{\partial \mathbf{x}} = \begin{bmatrix} 1 & 0 & 0 \\ 0 & 0 & 1 \\ 0 & -1 + 3x_2^2 & 0 \end{bmatrix} \quad (44)$$

Now using (38) for $\mathbf{C}$, (34) for $\partial\mathbf{y}/\partial\mathbf{F}$, (44) for $\partial\mathbf{F}/\partial\mathbf{x}$, and (35) for $\partial\mathbf{x}/\partial\mathbf{u}$, one can evaluate A in (6a). In this manner one finds

$$I(\mathbf{S}(R), \mathbf{F}) = \frac{1}{4\pi} \int_0^{2\pi} \int_0^{\pi} \times \frac{s_1\{1 - R^2(3s_1^2c_1^2c_2^2 + 3s_1^4s_2^2c_2^2 + s_1^4c_2^4)\}}{\{1 - R^2(2s_1^4c_2^4) + R^4(s_1^6c_2^6)\}^{3/2}} du^1 du^2 \quad (45)$$

The integral in (45) may be evaluated using any convenient numerical procedures. The results show that

$$I(\mathbf{S}(R), \mathbf{F}) = \begin{cases} +1 & \text{for } 0 < R < 1 \\ -1 & \text{for } 1 < R \end{cases} \quad (46)$$

This verifies the knowledge that there are three equilibrium states. One $\mathbf{P}_1$ is located at the origin (0, 0, 0) with det $(\mathbf{DF}(\mathbf{P}_1)) > 0$, hence $I(\mathbf{P}_1, \mathbf{F}) = 1$, and two equilibrium states $\mathbf{P}_{2,3}$ are located at $(0, \pm 1, 0)$ with det $(\mathbf{DF}(\mathbf{P}_{2,3})) < 0$, hence $I(\mathbf{P}_2, \mathbf{F}) = -1$ and $I(\mathbf{P}_3, \mathbf{F}) = -1$.

This simple example is used here merely to lend confidence to the viability of the approach. Other less simple applications will be reported elsewhere.

Acknowledgments

The results presented here were obtained in the course of research supported by a grant from the National Science Foundation. The author also wishes to acknowledge the assistance of Mr. Ramesh S. Guttalu in carrying out some of the computations, and the helpful suggestions and comments by Profs. R. M. Rosenberg and L. A. Month.

References

1 Stoker, J. J., *Nonlinear Vibrations*, Interscience Publishers, New York, 1950.

2 Minorsky, N., *Nonlinear Oscillations*, D. Van Nostrand Co., Princeton, N. J., 1962.

3 Kauderer, H., *Nichtlineare Mechanik*, Springer-Verlag, Berlin/Göttingen/Heidelberg, 1958.

4 Coddington, E. A., and Levinson, N., *Theory of Ordinary Differential Equations*, McGraw-Hill, New York, 1955.

5 Lefschetz, S., *Differential Equations: Geometric Theory*, Interscience Publishers, New York, 1957.

6 Arnold, V. I., *Ordinary Differential Equations*, translated and edited by R. A. Silverman, The M. I. T. Press, Cambridge, Mass., 1973.

7 Lefschetz, S., *Introduction to Topology*, Princeton University Press, Princeton, N. J., 1949.

8 Sternberg, S., *Lectures on Differential Geometry*, Prentice-Hall, Englewood Cliffs, N. J., 1964.

9 Guillemin, V., and Pollack, A., *Differential Topology*, Prentice-Hall, Englewood Cliffs, N. J., 1974.

10 Flanders, H., *Differential Forms*, Academic Press, New York, 1963.

11 Choquet-Bruhat, Y., DeWitt-Morette, C., and Dillard-Bleick, M., *Analysis, Manifolds and Physics*, North-Holland Publishing Company, Amsterdam, 1977.

12 El'sgol'c, L. Ė., *Qualitative Methods in Mathematical Analysis*, American Mathematical Society, Providence, R. I., 1964.

13 Poincaré, H., "Sur les courbes définies par les équations différentielles," *J. Math. Pure Appl.* Series (3), Vol. 7, 1881, pp. 375–422.

14 Birkhoff, G. D., "Surface Transformations and Their Dynamical Applications," *Acta Math.*, Vol. 43, 1920, pp. 1–119.

15 Arnol'd, V. D., "Small Denominators and Problems of Stability of Motion in Classical and Celestial Mechanics," *Russian Mathematical Surveys*, Vol. 18, 1963, pp. 85–191.

16 Smale, S., "Differentiable Dynamical Systems," *Bulletins of the American Mathematical Society*, Vol. 73, 1967, pp. 747–817.

17 Markus, L., *Lectures on Differentiable Dynamics*, Regional Conference Series in Mathematics, No. 3, American Mathematical Society, Providence, R. I., 1971.

18 Takens, F., *Introduction to Global Analysis*, Communications of the Mathematical Institute, Rijksuniversiteit Utrecht, 1973.

Downloaded 01 May 2010 to 171.66.16.243. Redistribution subject to ASME license or copyright; see http://www.asme.org/terms/Terms_Use.cfm

19 Marsden, J. E., and McCracken, M., *The Hopf Bifurcation and Its Applications*, Springer-Verlag, New York, 1976.
20 Bernussou, J., *Point Mapping Stability*, Pergamon Press, New York, 1977.
21 Hsu, C. S., "Impulsive Parametric Excitation: Theory," ASME JOURNAL OF APPLIED MECHANICS, Vol. 39, 1972, pp. 551–558.
22 Hsu, C. S., Yee, H. C., and Cheng, W. H., "Steady-State Response of A Nonlinear System Under Impulsive Periodic Parametric Excitation," *Journal of Sound and Vibration*, Vol. 50, 1977, pp. 95–116.
23 Hsu, C. S., "On Nonlinear Parametric Excitation Problems," *Advances in Applied Mechanics*, Vol. 17, 1977, pp. 245–301.
24 Hsu, C. S., "Nonlinear Behavior of Multibody Systems Under Impulsive Parametric Excitation," *Dynamics of Multibody Systems*, ed., Magnus, K., Springer-Verlag, *Proceedings of the IUTAM Symposium on Dynamics of Multibody Systems*, held in Munich, Germany, August 29–September 3, 1977, pp. 63–74.
25 Hsu, C. S., "A Theory of Index for Point Mapping Dynamical Systems," ASME JOURNAL OF APPLIED MECHANICS, Vol. 47, 1980, pp. 185–190.

Downloaded 01 May 2010 to 171.66.16.243. Redistribution subject to ASME license or copyright; see http://www.asme.org/terms/Terms_Use.cfm

Journal of Applied Mechanics

Brief Notes

A Brief Note is a short paper which presents a specific solution of technical interest in mechanics but which does not necessarily contain new general methods or results. A Brief Note should not exceed 1500 words *or equivalent* (a typical one-column figure or table is equivalent to 250 words; a one line equation to 30 words). Brief Notes will be subject to the usual review procedures prior to publication. After approval such Notes will be published as soon as possible. The Notes should be submitted to the Technical Editor of the JOURNAL OF APPLIED MECHANICS. Discussions on the Brief Notes should be addressed to the Editorial Department, ASME, United Engineering Center, 345 East 47th Street, New York, N. Y. 10017, or to the Technical Editor of the JOURNAL OF APPLIED MECHANICS. Discussions on Brief Notes appearing in this issue will be accepted until two months after publication. Readers who need more time to prepare a Discussion should request an extension of the deadline from the Editorial Department.

Vibrated Pendulum With a Mass Free to Move Radially

B. A. Schmidt[1]

This work concerns a pendulum made up of a mass and a weightless rod attached to a pivot. The mass is constrained to move rotationally with the rod but is free to move along the rod. Horizontal vibration of the pivot causes an inertia force in the negative radial direction which prevents the mass from sliding off the rod. Stability of an equilibrium solution is determined.

Introduction

The vibrated pendulum has been the subject of study for many investigators. Stephenson [1], in several papers, considered the effect of vibration applied to several devices. Included in these was the plane pendulum with a harmonic vertical vibration applied at the pivot. More complex pendulum problems were considered later. Miles [2] considered the stability of a spherical pendulum to which a horizontal harmonic vibration was applied. Sethna and Hemp [3] studied the spherical gyroscopic pendulum with a high frequency vertical vibration. Several authors, including Howe [4] and Bogdanoff and Citron [5] have investigated the effects of random vertical vibrations applied to plane pendulums. Ryland and Meirovitch [6] examined the plane flexible pendulum with a vertical vibration. Their pendulum was made up of a concentrated mass free to move radially under the influence of a spring. The vibration was harmonic at an unrestricted frequency.

This work involves a device similar to the flexible pendulum with the spring removed. The pendulum is made up of a pivoted weightless rod and a mass. The mass is constrained to move with the rod rotationally but is free to move along the rod. There is no spring. The mass is distributed. The pivot point is given a horizontal harmonic vibration at a high frequency and small amplitude. The pendulum is described in Fig. 1.

The Analysis

The pivot is given a horizontal vibration with displacement $A \cos \nu t$. The equations of motion are

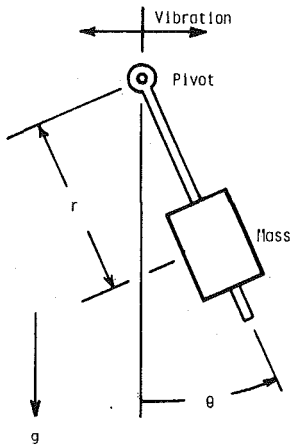

Fig. 1 The pendulum

$$(I + mr^2)\ddot{\theta} + 2mr\dot{r}\dot{\theta} + c_1\dot{\theta} + mrg \sin \theta - mA\nu^2 r \cos \theta \cos \nu t = 0$$

and

$$m\ddot{r} - mr\dot{\theta}^2 + c_2\dot{r} - mg \cos \theta - mA\nu^2 \sin \theta \cos \nu t = 0,$$

where m is the mass, I is the moment of inertia of the mass, r is the radius of the center of mass, θ is the angle of the pendulum measured from downward vertical, g is the gravitational constant, A is the amplitude of the vibration, ν is the frequency of the vibration, c_1 and c_2 are damping coefficients, t is time, and the dot indicates the derivative with respect to time.

An approximate solution is to be found by using the method of averaging [7].

The problem is restricted so that the amplitude of the vibration is small and the frequency is large. To represent the problem in terms of dimensionless parameters and variables, let $x = r/r_e$, $\epsilon = A/r_e$, $\tau = \nu t$, $\epsilon^2\delta = g/r_e\nu^2$, $\epsilon a_1 = c_1/mr_e^2\nu$, $\epsilon a_2 = c_2/m\nu$ and let the prime indicate differentiation with respect to τ. r_e is the radius of gyration of the mass. The equations of motion become

$$(1 + x^2)\theta'' + 2xx'\theta' + \epsilon a_1\theta' + \epsilon^2\delta x \sin \theta - \epsilon x \cos \theta \cos \tau = 0 \quad (1a)$$

and

$$x'' - x\theta'^2 + \epsilon a_2 x' - \epsilon^2\delta \cos \theta - \epsilon \sin \theta \cos \tau = 0. \quad (1b)$$

---

[1] Assistant Professor of Mathematics, Department of Mathematics, Central Michigan University, Mt. Pleasant, Mich. 48859.

Manuscript received by ASME Applied Mechanics Division, September, 1979; final revision, January, 1980.

Copyright © 1980 by ASME

Downloaded 01 May 2010 to 171.66.16.243. Redistribution subject to ASME license or copyright; see http://www.asme.org/terms/Terms_Use.cfm

In this problem, ϵ is positive and near zero and a_1, a_2, and δ are positive and independent of ϵ. It can be noted that representing the problem in this way demands that ϵ, i.e., A/r_e is restricted to have the same order of magnitude as ν^{-1}.

To find a transformation that would express equations (1) in the standard form for the method of averaging, it is useful to make the speculations, (a) that in the absence of the vibration, the motions would be slow and (b) the effect of the vibration would add small fast motions to the slow motions, i.e.,

$$\theta = F(\epsilon\tau) + \epsilon f(\tau)$$

and

$$x = G(\epsilon\tau) + \epsilon g(\tau).$$

This suggests a transformation of the form

$$\theta' = \epsilon\phi + \epsilon f'$$

and

$$x' = \epsilon y + \epsilon g',$$

where ϕ and y are new dependent variables.

Using this in an attempt to express equations (1) as four first-order equations in the standard form (with variables θ, ϕ, x, y, and τ), it is seen that f' and g' must be chosen in a certain form which will cancel some large terms which would otherwise appear in these equations. This leads to the transformation

$$\theta' = \epsilon\phi + \epsilon x(1 + x^2)^{-1} \cos\theta \sin\tau \tag{2a}$$

and

$$x' = \epsilon y + \epsilon \sin\theta \sin\tau. \tag{2b}$$

Differentiation of (2) and substitution of (1) and (2) give two new first-order differential equations involving ϕ' and y'. These equations, along with equations (2), give four equations in the standard form for the method of averaging. They are

$$\theta' = \epsilon\phi + \epsilon x(1 + x^2)^{-1} \cos\theta \sin\tau \tag{3a}$$

$$\begin{aligned}\phi' = {} & -\epsilon 2x(1 + x^2)^{-1}(y + \sin\theta \sin\tau)(\phi + x(1 + x^2)^{-1} \cos\theta \sin\tau) \\ & -\epsilon a_1(1 + x)^{-1}(\phi + x(1 + x^2)^{-1} \cos\theta \sin\tau) \\ & -\epsilon\delta x(1 + x^2)^{-1} \sin\theta \\ & -\epsilon(1 - x^2)(1 + x^2)^{-2}(y + \sin\theta \sin\tau) \cos\theta \sin\tau \\ & +\epsilon x(1 + x^2)^{-1}(\phi + x(1 + x^2)^{-1} \cos\theta \sin\tau) \sin\theta \sin\tau\end{aligned} \tag{3b}$$

$$x' = \epsilon y + \epsilon \sin\theta \sin\tau \tag{3c}$$

$$\begin{aligned}y' = {} & \epsilon x(\phi + x(1 + x^2)^{-1} \cos\theta \sin\tau)^2 \\ & -\epsilon a_2(y + \sin\theta \sin\tau) \\ & +\epsilon\delta \cos\theta \\ & -\epsilon(\phi + x(1 + x^2)^{-1} \cos\theta \sin\tau) \cos\theta \sin\tau.\end{aligned} \tag{3d}$$

These equations are in the standard form for the method of averaging. Averaging equations (3) gives

$$\Theta' = \epsilon\Phi \tag{4a}$$

$$\begin{aligned}\Phi' = {} & -\epsilon 2X(1 + X^2)^{-1} Y\Phi - \epsilon \tfrac{1}{2}(1 + X^2)^{-2} \sin\Theta \cos\Theta \\ & -\epsilon a_1(1 + X^2)^{-1}\Phi - \epsilon\delta X(1 + X^2)^{-1} \sin\Theta\end{aligned} \tag{4b}$$

$$X' = \epsilon Y \tag{4c}$$

$$Y' = \epsilon X\Phi^2 - \epsilon \tfrac{1}{2}X(1 + X^2)^{-2} \cos^2\Theta - \epsilon a_2 Y + \epsilon\delta \cos\Theta, \tag{4d}$$

where Θ, Φ, X, and Y are the averaged variables corresponding to θ, ϕ, x, and y.

Finding the general solution to equations (4) is unlikely but some analysis is possible and finding equilibrium solutions is elementary. In this analysis, equilibrium solutions are to be found. By means of a theorem of Sethna [8], it can be stated that equilibrium solutions of equation (4) represent solutions of (3) in this sense: if an equilibrium solution of (4) exists, then there exists an almost periodic solution of (3) which approaches the equilibrium solution of (4) as $\epsilon \to 0$. Also, by this theorem, it is known that stability properties of the almost periodic solutions of (3) are the same as the stability properties of the zero solution of the variation equation of (4) with respect to the equilibrium solutions of (4). The remainder of this work is devoted to finding the equilibrium solutions of equation (4) and examining stability at these equilibrium solutions. The equilibrium solution obtained will be valid in the sense just mentioned. The variation equations will be examined to determine stability.

Equations (4) indicate that equilibrium occurs only if

$$(\cos\Theta_e + 2\delta X_e(1 + X_e^2)) \sin\Theta_e = 0 \tag{5a}$$

and

$$(-X_e \cos\Theta_e + 2\delta(1 + X_e^2)^2) \cos\Theta_e = 0, \tag{5b}$$

where Θ_e and X_e are equilibrium values of Θ and X.

Equations (5) imply equilibrium only if, (a) $X_e = 0$ and $\Theta_e = \frac{1}{2}\pi$ or $\frac{3}{2}\pi$, or (b) $\Theta_e = 0$ and X_e satisfies

$$-X_e(1 + X_e^2)^{-2} + 2\delta = 0. \tag{6}$$

Equation (6) describes two values of X_e if $\delta < 3\sqrt{3}/32$. One of these values is between zero and $1/\sqrt{3}$ and the other is larger than $1/\sqrt{3}$. If $\delta = 3\sqrt{3}/32$, $X_e = 1/\sqrt{3}$. If $\delta > 3\sqrt{3}/32$, equation (6) cannot be satisfied when X_e is real.

Examination of the variation equation for Case (a) indicates instability. It is not discussed further.

For the equilibrium positions mentioned in Case (b), stability can be determined by considering the variation equation at the two equilibrium points when $\delta < 3\sqrt{3}/32$ ($\delta = 3\sqrt{3}/32$ is not considered. A different analysis is needed.). The variation equations at these points are

$$\Theta'_1 = \epsilon\Phi_1 \tag{7a}$$

$$\begin{aligned}\Phi'_1 = {} & -\epsilon(\tfrac{1}{2}(1 + X_e^2)^{-2} + \delta X_e(1 + X_e^2)^{-1})\Theta_1 \\ & -\epsilon a_1(1 + X_e^2)^{-1}\Phi_1\end{aligned} \tag{7b}$$

$$X'_1 = \epsilon Y_1 \tag{7c}$$

$$Y'_1 = -\epsilon \tfrac{1}{2}(1 + X_e^2)^{-3}(1 - 3X_e^2)X_1 - \epsilon a_2 Y_1, \tag{7d}$$

where Θ_1, Φ_1, X_1, and Y_1 are the deviations of Θ, Φ, X, and Y from the equilibrium values Θ_e, Φ_e, X_e, and Y_e.

Equations (7a) and (7b) involve only the variables Θ_1 and Φ_1. Since the coefficients of Θ_1 and Φ_1 in (7b) are always negative these equations indicate Θ_1 has a decaying oscillation for both equilibrium positions mentioned in Case (b). Equations (7c) and (7d) involve only the variables X_1 and Y_1. For the equilibrium value $X_e < 1/\sqrt{3}$, the coefficients of X_1 and Y_1 in equation (7d) are negative which indicates X_1 has a decaying oscillation and for the equilibrium value $X_e > 1/\sqrt{3}$, the coefficient of X_1 in equation (7d) is positive which indicates instability.

This examination of the variation equations (7) indicates there is one stable equilibrium solution of the averaged equations (4) when $\delta < 3\sqrt{3}/32$. It is $\Theta_e = 0$ and X_e is a number between zero and $1/\sqrt{3}$ described by equation (6). This solution of equations (4) is an approximate solution of equation (3) (or (1)) in the sense previously mentioned.

Conclusion

If this pendulum is vibrated horizontally, it is possible (depending on initial conditions) for the pendulum to hang in a vertically downward position and the mass will remain near a positive constant radius, i.e., the mass will not slide off the rod.

Remarks

It might be helpful to attempt an intuitive explanation of the effects of the vibration. There are two effects:

1 There is an inertia force in the negative radial direction (second term on the right of 4(d)).

2 There is an inertia torque tending to move the pendulum to a

Downloaded 01 May 2010 to 171.66.16.243. Redistribution subject to ASME license or copyright; see http://www.asme.org/terms/Terms_Use.cfm

line perpendicular to the line of the vibration (second term on the right of 4(*b*)). Both effects are dependent only on the vibration (they are independent of gravity). The first effect is easy to understand. The pivot moves horizontally and a point on the rod below the mass will move horizontally but a smaller amount. It is easy to imagine an inertia force, centrifugal in nature, acting in the negative radial direction. The second effect is more difficult. There will be an oscillating inertia force caused by the vibration and there will be an oscillation in the radius at the same frequency. It is possible to imagine that this oscillating force multiplied by the oscillating radius will cause a rectified torque.

References

1 Stephenson, A., "On a New Type of Dynamical Stability," *Memoirs and Proceedings of the Manchester Literary and Philosophical Society,* Vol. 52, 1907, pp. 1–10.

2 Miles, J. W., "Stability of Forced Oscillations of a Spherical Pendulum," *Quarterly of Applied Mathematics,* Vol. 20, No. 1, Apr. 1962, pp. 21–32.

3 Sethna, P. R., and Hemp, G. W., "Nonlinear Oscillations of a Gyroscopic Pendulum With an Oscillating Point of Suspension," *Proceedings Colloq. International du Center National de la Recherche Scientifique,* N-148, Les Vibrations Forcees dans les Systems Non-Lineares, 1964, pp. 375–392.

4 Howe, M. S., "The Mean Square Stability of an Inverted Pendulum Subject to Random Parametric Excitation," *Journal of Sound and Vibration,* Vol. 32(3) 1974, pp. 407–421.

5 Bodganoff, J. L., and Citron, S. J., "Experiments With an Inverted Pendulum Subject to Random Parametric Excitation," *Journal of the Acoustical Society of America,* Vol. 38, 1965, pp. 447–452.

6 Ryland, G., II. and Meirovitch, L., "Stability Boundaries of a Swinging Spring With Oscillatory Support," *Journal of Sound and Vibration,* Vol. 51(4), 1977, pp. 547–560.

7 Bogoliuboff, N. M., and Mitropolskii, Yu. A., *Asymptotic Methods in the Theory of Nonlinear Oscillation,* Chapters 5 and 6, Gordon and Breach, New York, 1962.

8 Sethna, P. R., "An Extension of the Method of Averaging," *Quarterly of Applied Mathematics,* Vol. 25, 1967, pp. 205–211.

On the Effect of a Small Circular Hole on States of Uniform Membrane Shear in Spherical Shells[1]

E. Reissner[2]

Introduction

In extension of a recent analysis of the problem of stress concentration due to a small circular hole in a transversely twisted shallow spherical shell [1], we consider in what follows the problem of stress concentration in the same shell which, without the hole, would be in a state of uniform membrane shear. The method of analysis is similar to the method described in [1]. However, the nature of the results which are obtained in what follows is significantly different from the nature of the results for the problem of transverse twisting. While for the former problem the effect of the parameter a^2/Rh—where a is the radius of the hole, R the radius of the shell, and h the wall thickness of the shell—did not greatly affect the numerical value of the stress-concentration factor, it is found that for the present problem not just the numerical value but the order of magnitude of the stress-concentration factor depends on the value of the parameter a^2/Rh.

Differential Equations and Boundary Conditions

With polar coordinates r, θ in the base plane of the shallow spherical shell with middle surface equation $z = H - r^2/2R$, and with the radius of the small circular hole being at $r = a$, we have that stress resultants and stress couples may be expressed in terms of a transverse deflection function w and an Airy stress function K, where w and K are given in the form

$$w = \phi + \chi, \quad K = \psi - RD\nabla^2\chi. \tag{1}$$

In this ϕ and ψ are harmonic functions and χ satisfies the differential equation $\nabla^4\chi + \lambda^4\chi = 0$, where $\lambda^4 = 1/R^2BD$. For a shell which is uniform in thickness direction, so that $D = Eh^3/12(1-\nu^2)$ and $B = 1/Eh$, the defining relation for λ takes on the form $\lambda^4 = 12(1-\nu^2)/R^2h^2$.

For the determination of the functions ϕ, ψ, and χ use is made of the boundary conditions of the problem. The condition that at an "infinite" distance from the hole the state of stress is a state of uniform membrane shear of magnitude S, means that as r approaches infinity, w must tend to zero, and K must approach $-Sxy = -\frac{1}{2}Sr^2\sin 2\theta$. The stipulation of a traction-free edge of the hole is expressed by means of the four conditions

$$r = a; \quad N_{rr} = N_{r\theta} = M_{rr} = Q_r + r^{-1}M_{r\theta,\theta} = 0. \tag{2}$$

In order to satisfy these conditions, expressions are needed for N_{rr}, $N_{r\theta}$, M_{rr}, Q_r, and $M_{r\theta}$ in terms of ϕ, ψ, and χ. These are [1]

$$\begin{aligned}
N_{rr} &= -\psi_{,rr} - RD\left(\frac{(\nabla^2\chi)_{,r}}{r} + \frac{(\nabla^2\chi)_{,\theta\theta}}{r^2}\right), \quad Q_r = -D(\nabla^2\chi)_{,r}, \\
N_{r\theta} &= -\frac{\psi_{,r\theta}}{r} + \frac{\psi_{,\theta}}{r^2} + RD\left(\frac{(\nabla^2\chi)_{,r\theta}}{r} - \frac{(\nabla^2\chi)_{,\theta}}{r^2}\right), \\
M_{rr} &= -(1-\nu)D\phi_{,rr} - D\left[\nabla^2\chi - (1-\nu)\left(\frac{\chi_{,r}}{r} + \frac{\chi_{,\theta\theta}}{r^2}\right)\right], \\
M_{r\theta} &= -(1-\nu)D\left(\frac{\phi_{,r\theta}}{r} - \frac{\phi_{,\theta}}{r^2}\right) - (1-\nu)D\left(\frac{\chi_{,r\theta}}{r} - \frac{\chi_{,\theta}}{r^2}\right).
\end{aligned} \tag{3}$$

For the determination of stress-concentration factors, the edge values of the resultant $N_{\theta\theta}$ and the couple $M_{\theta\theta}$ are needed. In view of the form of the boundary conditions, it is convenient to take these, for an exact solution, in the form

$$N_{\theta\theta} = \nabla^2K - N_{rr}, \qquad M_{\theta\theta} = -(1+\nu)D\nabla^2w - M_{rr}. \tag{4}$$

For an asymptotic solution, for large values of the dimensionless parameter λa, it is preferable to write $N_{\theta\theta}$ and $M_{\theta\theta}$ in the form

$$\begin{aligned}
N_{\theta\theta} &= \psi_{,rr} + RD\left(\frac{(\nabla^2\chi)_{,r}}{r} + \frac{(\nabla^2\chi)_{,\theta\theta}}{r^2} + \lambda^4\chi\right), \\
M_{\theta\theta} &= (1-\nu)D\phi_{,rr} - D\left[\nu\nabla^2\chi + (1-\nu)\left(\frac{\chi_{,r}}{r} + \frac{\chi_{,\theta\theta}}{r^2}\right)\right].
\end{aligned} \tag{5}$$

Closed-Form Solution

The boundary conditions at infinity indicate that w and K should be products of the form $f(r)\sin 2\theta$. Considering the representation (1) and deleting at the outset terms which are inconsistent with the existence of a uniform membrane stress state at infinity, K and w come out to be

$$\begin{aligned}
K &= -Sa^2\left(\frac{1}{2}\frac{r^2}{a^2} + c_2\frac{a^2}{r^2} - c_3\,\mathrm{kei}_2\,\lambda r + c_4\,\mathrm{ker}_2\,\lambda r\right)\sin 2\theta, \\
w &= \frac{Sa^2}{RD\lambda^2}\left(c_1\frac{a^2}{r^2} + c_3\,\mathrm{ker}_2\,\lambda r + c_4\,\mathrm{kei}_2\,\lambda r\right)\sin 2\theta.
\end{aligned} \tag{6}$$

In this the c_n are four arbitrary constants and ker_2 and kei_2 are Kelvin functions.

Having equations (6), it is possible to obtain as edge values of $N_{\theta\theta}$ and $M_{\theta\theta}$, on the basis of equations (4) and (2) and with $\mu \equiv \lambda a$,

$$\begin{aligned}
N_{\theta\theta}\,(a,\theta) &= S\mu^2\,(c_3\,\mathrm{ker}_2\,\mu + c_4\,\mathrm{kei}_2\,\mu)\sin 2\theta, \\
M_{\theta\theta}\,(a,\theta) &= \sqrt{\frac{1+\nu}{1-\nu}}\frac{S\mu^2h}{\sqrt{12}}\,(c_3\,\mathrm{kei}_2\,\mu - c_4\,\mathrm{ker}_2\,\mu)\sin 2\theta.
\end{aligned} \tag{7}$$

In view of the relative complexity of determining the constants c_n,

[1] Supported by the Office of Naval Research.

[2] Department of Applied Mechanics and Engineering Sciences, University of California, San Diego, La Jolla, Calif. 92093. Fellow ASME.

Manuscript received by ASME Applied Mechanics, July, 1979; final revision, February, 1980.

Downloaded 01 May 2010 to 171.66.16.243. Redistribution subject to ASME license or copyright; see http://www.asme.org/terms/Terms_Use.cfm

line perpendicular to the line of the vibration (second term on the right of 4(*b*)). Both effects are dependent only on the vibration (they are independent of gravity). The first effect is easy to understand. The pivot moves horizontally and a point on the rod below the mass will move horizontally but a smaller amount. It is easy to imagine an inertia force, centrifugal in nature, acting in the negative radial direction. The second effect is more difficult. There will be an oscillating inertia force caused by the vibration and there will be an oscillation in the radius at the same frequency. It is possible to imagine that this oscillating force multiplied by the oscillating radius will cause a rectified torque.

References

1 Stephenson, A., "On a New Type of Dynamical Stability," *Memoirs and Proceedings of the Manchester Literary and Philosophical Society,* Vol. 52, 1907, pp. 1–10.

2 Miles, J. W., "Stability of Forced Oscillations of a Spherical Pendulum," *Quarterly of Applied Mathematics,* Vol. 20, No. 1, Apr. 1962, pp. 21–32.

3 Sethna, P. R., and Hemp, G. W., "Nonlinear Oscillations of a Gyroscopic Pendulum With an Oscillating Point of Suspension," *Proceedings Colloq. International du Center National de la Recherche Scientifique,* N-148, Les Vibrations Forcees dans les Systems Non-Lineares, 1964, pp. 375–392.

4 Howe, M. S., "The Mean Square Stability of an Inverted Pendulum Subject to Random Parametric Excitation," *Journal of Sound and Vibration,* Vol. 32(3) 1974, pp. 407–421.

5 Bodganoff, J. L., and Citron, S. J., "Experiments With an Inverted Pendulum Subject to Random Parametric Excitation," *Journal of the Acoustical Society of America,* Vol. 38, 1965, pp. 447–452.

6 Ryland, G., II. and Meirovitch, L., "Stability Boundaries of a Swinging Spring With Oscillatory Support," *Journal of Sound and Vibration,* Vol. 51(4), 1977, pp. 547–560.

7 Bogoliuboff, N. M., and Mitropolskii, Yu. A., *Asymptotic Methods in the Theory of Nonlinear Oscillation,* Chapters 5 and 6, Gordon and Breach, New York, 1962.

8 Sethna, P. R., "An Extension of the Method of Averaging," *Quarterly of Applied Mathematics,* Vol. 25, 1967, pp. 205–211.

On the Effect of a Small Circular Hole on States of Uniform Membrane Shear in Spherical Shells[1]

E. Reissner[2]

Introduction

In extension of a recent analysis of the problem of stress concentration due to a small circular hole in a transversely twisted shallow spherical shell [1], we consider in what follows the problem of stress concentration in the same shell which, without the hole, would be in a state of uniform membrane shear. The method of analysis is similar to the method described in [1]. However, the nature of the results which are obtained in what follows is significantly different from the nature of the results for the problem of transverse twisting. While for the former problem the effect of the parameter a^2/Rh—where a is the radius of the hole, R the radius of the shell, and h the wall thickness of the shell—did not greatly affect the numerical value of the stress-concentration factor, it is found that for the present problem not just the numerical value but the order of magnitude of the stress-concentration factor depends on the value of the parameter a^2/Rh.

Differential Equations and Boundary Conditions

With polar coordinates r, θ in the base plane of the shallow spherical shell with middle surface equation $z = H - r^2/2R$, and with the radius of the small circular hole being at $r = a$, we have that stress resultants and stress couples may be expressed in terms of a transverse deflection function w and an Airy stress function K, where w and K are given in the form

$$w = \phi + \chi, \quad K = \psi - RD\nabla^2\chi. \tag{1}$$

In this ϕ and ψ are harmonic functions and χ satisfies the differential equation $\nabla^4\chi + \lambda^4\chi = 0$, where $\lambda^4 = 1/R^2BD$. For a shell which is uniform in thickness direction, so that $D = Eh^3/12(1-\nu^2)$ and $B = 1/Eh$, the defining relation for λ takes on the form $\lambda^4 = 12(1-\nu^2)/R^2h^2$.

For the determination of the functions ϕ, ψ, and χ use is made of the boundary conditions of the problem. The condition that at an "infinite" distance from the hole the state of stress is a state of uniform membrane shear of magnitude S, means that as r approaches infinity, w must tend to zero, and K must approach $-Sxy = -\frac{1}{2}Sr^2\sin 2\theta$. The stipulation of a traction-free edge of the hole is expressed by means of the four conditions

$$r = a; \quad N_{rr} = N_{r\theta} = M_{rr} = Q_r + r^{-1}M_{r\theta,\theta} = 0. \tag{2}$$

In order to satisfy these conditions, expressions are needed for N_{rr}, $N_{r\theta}$, M_{rr}, Q_r, and $M_{r\theta}$ in terms of ϕ, ψ, and χ. These are [1]

$$\begin{aligned}
N_{rr} &= -\psi_{,rr} - RD\left(\frac{(\nabla^2\chi)_{,r}}{r} + \frac{(\nabla^2\chi)_{,\theta\theta}}{r^2}\right), \quad Q_r = -D(\nabla^2\chi)_{,r}, \\
N_{r\theta} &= -\frac{\psi_{,r\theta}}{r} + \frac{\psi_{,\theta}}{r^2} + RD\left(\frac{(\nabla^2\chi)_{,r\theta}}{r} - \frac{(\nabla^2\chi)_{,\theta}}{r^2}\right), \\
M_{rr} &= -(1-\nu)D\phi_{,rr} - D\left[\nabla^2\chi - (1-\nu)\left(\frac{\chi_{,r}}{r} + \frac{\chi_{,\theta\theta}}{r^2}\right)\right], \\
M_{r\theta} &= -(1-\nu)D\left(\frac{\phi_{,r\theta}}{r} - \frac{\phi_{,\theta}}{r^2}\right) - (1-\nu)D\left(\frac{\chi_{,r\theta}}{r} - \frac{\chi_{,\theta}}{r^2}\right).
\end{aligned} \tag{3}$$

For the determination of stress-concentration factors, the edge values of the resultant $N_{\theta\theta}$ and the couple $M_{\theta\theta}$ are needed. In view of the form of the boundary conditions, it is convenient to take these, for an exact solution, in the form

$$N_{\theta\theta} = \nabla^2 K - N_{rr}, \qquad M_{\theta\theta} = -(1+\nu)D\nabla^2 w - M_{rr}. \tag{4}$$

For an asymptotic solution, for large values of the dimensionless parameter λa, it is preferable to write $N_{\theta\theta}$ and $M_{\theta\theta}$ in the form

$$\begin{aligned}
N_{\theta\theta} &= \psi_{,rr} + RD\left(\frac{(\nabla^2\chi)_{,r}}{r} + \frac{(\nabla^2\chi)_{,\theta\theta}}{r^2} + \lambda^4\chi\right), \\
M_{\theta\theta} &= (1-\nu)D\phi_{,rr} - D\left[\nu\nabla^2\chi + (1-\nu)\left(\frac{\chi_{,r}}{r} + \frac{\chi_{,\theta\theta}}{r^2}\right)\right].
\end{aligned} \tag{5}$$

Closed-Form Solution

The boundary conditions at infinity indicate that w and K should be products of the form $f(r)\sin 2\theta$. Considering the representation (1) and deleting at the outset terms which are inconsistent with the existence of a uniform membrane stress state at infinity, K and w come out to be

$$\begin{aligned}
K &= -Sa^2\left(\frac{1}{2}\frac{r^2}{a^2} + c_2\frac{a^2}{r^2} - c_3\,\mathrm{kei}_2\,\lambda r + c_4\,\mathrm{ker}_2\,\lambda r\right)\sin 2\theta, \\
w &= \frac{Sa^2}{RD\lambda^2}\left(c_1\frac{a^2}{r^2} + c_3\,\mathrm{ker}_2\,\lambda r + c_4\,\mathrm{kei}_2\,\lambda r\right)\sin 2\theta.
\end{aligned} \tag{6}$$

In this the c_n are four arbitrary constants and ker_2 and kei_2 are Kelvin functions.

Having equations (6), it is possible to obtain as edge values of $N_{\theta\theta}$ and $M_{\theta\theta}$, on the basis of equations (4) and (2) and with $\mu \equiv \lambda a$,

$$\begin{aligned}
N_{\theta\theta}(a,\theta) &= S\mu^2(c_3\,\mathrm{ker}_2\,\mu + c_4\,\mathrm{kei}_2\,\mu)\sin 2\theta, \\
M_{\theta\theta}(a,\theta) &= \sqrt{\frac{1+\nu}{1-\nu}}\frac{S\mu^2h}{\sqrt{12}}(c_3\,\mathrm{kei}_2\,\mu - c_4\,\mathrm{ker}_2\,\mu)\sin 2\theta.
\end{aligned} \tag{7}$$

In view of the relative complexity of determining the constants c_n,

[1] Supported by the Office of Naval Research.

[2] Department of Applied Mechanics and Engineering Sciences, University of California, San Diego, La Jolla, Calif. 92093. Fellow ASME.

Manuscript received by ASME Applied Mechanics, July, 1979; final revision, February, 1980.

Copyright © 1980 by ASME
Downloaded 01 May 2010 to 171.66.16.243. Redistribution subject to ASME license or copyright; see http://www.asme.org/terms/Terms_Use.cfm

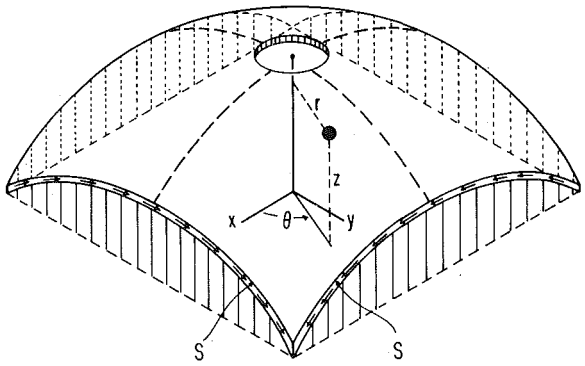

Fig. 1

we limit ourselves here to the observation that the results obtained in this way are consistent with the flat-plate results

$$\mu = 0; \quad N_{\theta\theta}(a, \theta) = -4S \sin 2\theta, \quad M_{\theta\theta}(a, \theta) = 0, \tag{8}$$

and that in the range $1 \ll \mu$, where the form of the solution (6) indicates the distinction between the "interior" solution contribution, involving the constants c_1 and c_2 and an "edge zone" solution contribution involving the constants c_3 and c_4, there is consistency with the more simply derived asymptotic results which follow.

Asymptotic Solution for Large Values of μ

The solution (1) is now written in the form

$$w = w^i + w^e, \quad K = K^i + K^e, \tag{9}$$

where $w^e = \chi$, $K^e = -RD\nabla^2\chi$ and, consistent with (6),

$$w^i = \frac{Sa^2}{RD\lambda^2}\left(c_1 \frac{a^2}{r^2}\right) \sin 2\theta, \quad K^i = -Sa^2\left(\frac{1}{2}\frac{r^2}{a^2} + c_2\frac{a^2}{r^2}\right)\sin 2\theta. \tag{10}$$

In applying the boundary conditions (2) with the help of (3), an asymptotic solution of the problem is obtained by using the fact that when $1 \ll \mu$ then $\chi/a = o(\chi_{,r})$ etc. This allows writing the conditions of vanishing edge values of M_{rr} and $Q_r + r^{-1}M_{r\theta,\theta}$ in the asymptotic form

$$\nabla^2\chi = -(1-\nu)\phi_{,rr}, \quad (\nabla^2\chi)_{,r} = -\frac{1-\nu}{r}\left(\frac{\phi_{,r}}{r} - \frac{\phi}{r^2}\right)_{,\theta\theta}, \tag{11}$$

for $r = a$. A substitution of (11) into the conditions of vanishing N_{rr} and $N_{r\theta}$ for $r = a$ then leads to the relations

$$\begin{aligned} &\psi_{,rr} - RD\frac{1-\nu}{r^2}\left[\frac{\phi_{,r}}{r} - \frac{\phi}{r^2} + \phi_{,rr}\right]_{,\theta\theta} = 0, \\ &\left(\frac{\psi_{,r}}{r} - \psi/r^2\right)_{,\theta} + RD\frac{1-\mu}{r^2}\left[\left(\frac{\phi_{,r}}{r} - \frac{\phi}{r^2}\right)_{,\theta\theta} - \phi_{,rr}\right]_{,\theta} = 0, \end{aligned} \tag{12}$$

for $r = a$. The introduction of (10) into (12) gives

$$12(1-\nu)c_1 = \mu^2, \quad c_2 = 0. \tag{13}$$

Having determined ϕ and ψ it remains to determine the asymptotic form of the edge zone solution contribution χ, with the help of (11). For this purpose we write as asymptotic expression for χ, consistent with (6),

$$\chi = \frac{Sa^2}{RD\lambda^2}\left(C_3 \cos\lambda\frac{r-a}{\sqrt{2}} + C_4 \sin\lambda\frac{r-a}{\sqrt{2}}\right)\exp\left(-\lambda\frac{r-a}{\sqrt{2}}\right)\sin 2\theta, \tag{14}$$

and as asymptotic expression for $\nabla^2\chi$

$$\nabla^2\chi = \frac{Sa^2}{RD}\left(C_3 \sin\lambda\frac{r-a}{\sqrt{2}} - C_4 \cos\lambda\frac{r-a}{\sqrt{2}}\right)\exp\left(-\lambda\frac{r-a}{\sqrt{2}}\right)\sin 2\theta. \tag{15}$$

A use of (15) and of the corresponding formula for $(\nabla^2\chi)_{,r}$ in (11) gives

$$C_4 = 6\frac{1-\nu}{\mu^2}c_1 = \frac{1}{2}, \quad C_3 + C_4 = -12\sqrt{2}\frac{1-\nu}{\mu^3}c_1 \approx 0. \tag{16}$$

Having determined c_1, c_2, C_3, and C_4, we now obtain the relevant values of $N_{\theta\theta}$ and $M_{\theta\theta}$, on the basis of (5). Outside the edge zone these values are

$$N^i_{\theta\theta} = \psi_{,rr} = -S \sin 2\theta, \tag{17a}$$

$$M^i_{\theta\theta} = (1-\nu)D\phi_{,rr} = \frac{Sh\mu^2}{4\sqrt{3(1-\nu^2)}}\frac{a^4}{r^4}\sin 2\theta. \tag{17b}$$

Inside the edge zone we are limiting ourselves here to giving the corresponding values *at* the edge,

$$N_{\theta\theta}(a, \theta) = -\frac{1}{2}S\mu^2 \sin 2\theta, \tag{18a}$$

$$M_{\theta\theta}(a, \theta) = \sqrt{\frac{1+\nu}{1-\nu}}\frac{Sh\mu^2}{4\sqrt{3}}\sin 2\theta. \tag{18b}$$

Equations (18) imply as the asymptotic values of membrane and bending stress-concentration factors

$$k_m = \frac{\mu^2}{2}, \quad k_b = \sqrt{\frac{3+3\nu}{1-\nu}}\frac{\mu^2}{2}. \tag{19}$$

The foregoing results are noteworthy for the following reasons:

1 While the state of stress in the shell is, in the absence of a hole at the apex, a pure membrane state, the existence of the hole changes the "interior" state into a state which is predominantly a state of inextensional bending, in spite of the fact that the loading conditions for the shell involve tangential stress resultants only.

2 The state of stress in the edge zone adjacent to the hole involves membrane and bending stresses of the same order of magnitude. More importantly, as the value of $\mu^2 = \sqrt{12(1-\nu^2)}a^2/Rh$ increases, a more and more pronounced stress concentration occurs, with the stress-concentration factors k_m and k_b becoming large compared to the value "4" of the factor k_m for the limiting case $\mu = 0$ of a flat plate.

Reference

1 Reissner, E., "On the Transverse Twisting of Shallow Spherical Caps," ASME JOURNAL OF APPLIED MECHANICS, Vol. 47, 1980, pp. 101–105.

Closed-Form Inversion of the Axisymmetric Integrated Photoelasticity Equations

J. F. Doyle[1]

The purpose of the present Note is to show how the general axisymmetric photoelastic problem can be solved using only the integrated data. Indeed, the axisymmetric problem is reduced to a quasi-plane problem in that only a fringe photograph plus a plot of the family of isoclinics is sufficient to yield a complete solution. The formulation includes the treatment of thermoelastic and residual stress problems.

The Integrated Optical Effect

When the light ray passes through a plane of symmetry then only

[1] Assistant Professor, School of Aeronautics and Astronautics, Purdue University, West Lafayette, Ind. 47907

Manuscript received by ASME Applied Mechanics, July, 1979; final revision, January, 1980.

Downloaded 01 May 2010 to 171.66.16.243. Redistribution subject to ASME license or copyright; see http://www.asme.org/terms/Terms_Use.cfm

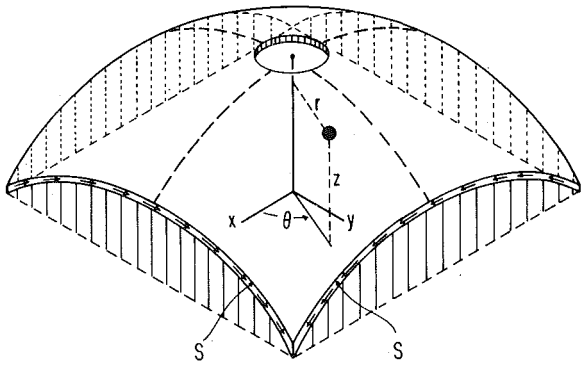

Fig. 1

we limit ourselves here to the observation that the results obtained in this way are consistent with the flat-plate results

$$\mu = 0; \quad N_{\theta\theta}(a, \theta) = -4S \sin 2\theta, \quad M_{\theta\theta}(a, \theta) = 0, \tag{8}$$

and that in the range $1 \ll \mu$, where the form of the solution (6) indicates the distinction between the "interior" solution contribution, involving the constants c_1 and c_2 and an "edge zone" solution contribution involving the constants c_3 and c_4, there is consistency with the more simply derived asymptotic results which follow.

Asymptotic Solution for Large Values of μ

The solution (1) is now written in the form

$$w = w^i + w^e, \quad K = K^i + K^e, \tag{9}$$

where $w^e = \chi$, $K^e = -RD\nabla^2\chi$ and, consistent with (6),

$$w^i = \frac{Sa^2}{RD\lambda^2}\left(c_1 \frac{a^2}{r^2}\right) \sin 2\theta, \quad K^i = -Sa^2\left(\frac{1}{2}\frac{r^2}{a^2} + c_2\frac{a^2}{r^2}\right)\sin 2\theta. \tag{10}$$

In applying the boundary conditions (2) with the help of (3), an asymptotic solution of the problem is obtained by using the fact that when $1 \ll \mu$ then $\chi/a = o(\chi_{,r})$ etc. This allows writing the conditions of vanishing edge values of M_{rr} and $Q_r + r^{-1}M_{r\theta,\theta}$ in the asymptotic form

$$\nabla^2\chi = -(1-\nu)\phi_{,rr}, \quad (\nabla^2\chi)_{,r} = -\frac{1-\nu}{r}\left(\frac{\phi_{,r}}{r} - \frac{\phi}{r^2}\right)_{,\theta\theta}, \tag{11}$$

for $r = a$. A substitution of (11) into the conditions of vanishing N_{rr} and $N_{r\theta}$ for $r = a$ then leads to the relations

$$\begin{aligned} &\psi_{,rr} - RD\frac{1-\nu}{r^2}\left[\frac{\phi_{,r}}{r} - \frac{\phi}{r^2} + \phi_{,rr}\right]_{,\theta\theta} = 0, \\ &\left(\frac{\psi_{,r}}{r} - \psi/r^2\right)_{,\theta} + RD\frac{1-\mu}{r^2}\left[\left(\frac{\phi_{,r}}{r} - \frac{\phi}{r^2}\right)_{,\theta\theta} - \phi_{,rr}\right]_{,\theta} = 0, \end{aligned} \tag{12}$$

for $r = a$. The introduction of (10) into (12) gives

$$12(1-\nu)c_1 = \mu^2, \quad c_2 = 0. \tag{13}$$

Having determined ϕ and ψ it remains to determine the asymptotic form of the edge zone solution contribution χ, with the help of (11). For this purpose we write as asymptotic expression for χ, consistent with (6),

$$\chi = \frac{Sa^2}{RD\lambda^2}\left(C_3 \cos\lambda\frac{r-a}{\sqrt{2}} + C_4 \sin\lambda\frac{r-a}{\sqrt{2}}\right)\exp\left(-\lambda\frac{r-a}{\sqrt{2}}\right)\sin 2\theta, \tag{14}$$

and as asymptotic expression for $\nabla^2\chi$

$$\nabla^2\chi = \frac{Sa^2}{RD}\left(C_3 \sin\lambda\frac{r-a}{\sqrt{2}} - C_4 \cos\lambda\frac{r-a}{\sqrt{2}}\right)\exp\left(-\lambda\frac{r-a}{\sqrt{2}}\right)\sin 2\theta. \tag{15}$$

A use of (15) and of the corresponding formula for $(\nabla^2\chi)_{,r}$ in (11) gives

$$C_4 = 6\frac{1-\nu}{\mu^2}c_1 = \frac{1}{2}, \quad C_3 + C_4 = -12\sqrt{2}\frac{1-\nu}{\mu^3}c_1 \approx 0. \tag{16}$$

Having determined c_1, c_2, C_3, and C_4, we now obtain the relevant values of $N_{\theta\theta}$ and $M_{\theta\theta}$, on the basis of (5). Outside the edge zone these values are

$$N^i_{\theta\theta} = \psi_{,rr} = -S \sin 2\theta, \tag{17a}$$

$$M^i_{\theta\theta} = (1-\nu)D\phi_{,rr} = \frac{Sh\mu^2}{4\sqrt{3(1-\nu^2)}}\frac{a^4}{r^4}\sin 2\theta. \tag{17b}$$

Inside the edge zone we are limiting ourselves here to giving the corresponding values *at* the edge,

$$N_{\theta\theta}(a, \theta) = -\frac{1}{2}S\mu^2 \sin 2\theta, \tag{18a}$$

$$M_{\theta\theta}(a, \theta) = \sqrt{\frac{1+\nu}{1-\nu}}\frac{Sh\mu^2}{4\sqrt{3}}\sin 2\theta. \tag{18b}$$

Equations (18) imply as the asymptotic values of membrane and bending stress-concentration factors

$$k_m = \frac{\mu^2}{2}, \quad k_b = \sqrt{\frac{3+3\nu}{1-\nu}}\frac{\mu^2}{2}. \tag{19}$$

The foregoing results are noteworthy for the following reasons:

1 While the state of stress in the shell is, in the absence of a hole at the apex, a pure membrane state, the existence of the hole changes the "interior" state into a state which is predominantly a state of inextensional bending, in spite of the fact that the loading conditions for the shell involve tangential stress resultants only.

2 The state of stress in the edge zone adjacent to the hole involves membrane and bending stresses of the same order of magnitude. More importantly, as the value of $\mu^2 = \sqrt{12(1-\nu^2)}a^2/Rh$ increases, a more and more pronounced stress concentration occurs, with the stress-concentration factors k_m and k_b becoming large compared to the value "4" of the factor k_m for the limiting case $\mu = 0$ of a flat plate.

Reference

1 Reissner, E., "On the Transverse Twisting of Shallow Spherical Caps," ASME JOURNAL OF APPLIED MECHANICS, Vol. 47, 1980, pp. 101–105.

Closed-Form Inversion of the Axisymmetric Integrated Photoelasticity Equations

J. F. Doyle[1]

The purpose of the present Note is to show how the general axisymmetric photoelastic problem can be solved using only the integrated data. Indeed, the axisymmetric problem is reduced to a quasi-plane problem in that only a fringe photograph plus a plot of the family of isoclinics is sufficient to yield a complete solution. The formulation includes the treatment of thermoelastic and residual stress problems.

The Integrated Optical Effect

When the light ray passes through a plane of symmetry then only

[1] Assistant Professor, School of Aeronautics and Astronautics, Purdue University, West Lafayette, Ind. 47907

Manuscript received by ASME Applied Mechanics, July, 1979; final revision, January, 1980.

Copyright © 1980 by ASME
Downloaded 01 May 2010 to 171.66.16.243. Redistribution subject to ASME license or copyright; see http://www.asme.org/terms/Terms_Use.cfm

two pieces of optical data are obtained, and these are recorded in the identical fashion as for the isochromatics and isoclinics in plane photoelasticity [1,2]. To a first approximation, the fringe order is given as the integral of the difference of the secondary principal stresses along the light path. That is, in terms of the cylindrical coordinate stresses [3]

$$\frac{1}{2}N = \frac{1}{f_\sigma}\int_0^{y_0}(\sigma_1 - \sigma_2)dy = \frac{1}{f_\sigma}\int_0^{y_0}\sqrt{\left[(\sigma_r - \sigma_\theta)\frac{x^2}{y^2} + (\sigma_\theta - \sigma_z)\right]^2 + \left[2\sigma_{rz}\frac{x}{r}\right]^2}\,dy \quad (1)$$

where N is the fringe order and f_σ is the material fringe coefficient. This is highly nonlinear in the stresses, but it can be simplified if it is assumed that the measured isoclinic angle α represents the average orientation of the secondary principal directions. Consistent with this assumption, the optical relations can be written as

$$\frac{1}{2}N\begin{Bmatrix}\cos 2\alpha \\ \sin 2\alpha\end{Bmatrix} f_\sigma = \int_0^{y_0}\begin{Bmatrix}(\sigma_r - \sigma_\theta)\dfrac{x^2}{r^2} + (\sigma_\theta - \sigma_z) \\ 2\sigma_{rz} \qquad \dfrac{x}{r}\end{Bmatrix} dy \quad (2)$$

The assumption about the isoclinic angle has been shown to be good for some cases [3], but it can be expected to be also good in general because the final relations are integrals which effect an averaging process in any event.

If the variable of integration in equation (2) is changed to r, both sides multiplied by $x/\sqrt{x^2 - s^2}$, and integrated with respect to x from s to b. Then after changing the order of integration and simplifying, get

$$(\sigma_r - \sigma_\theta) - \int_r^b \frac{1}{\bar{r}}(\sigma_r - \sigma_\theta)d\bar{r} = -\frac{1}{r}I_{1,r} \equiv -\frac{1}{r}\frac{f_\sigma}{h}\frac{\partial}{\partial r}\int_r^b \frac{N\cos 2\alpha}{\sqrt{\bar{x}^2 - r^2}}\bar{x}\,d\bar{x}$$

$$\sigma_{rz} = -I_{2,r} \equiv -\frac{f_\sigma}{h}\frac{\partial}{\partial r}\int_r^b \frac{N\sin 2\alpha}{\sqrt{\bar{x}^2 - r^2}}\bar{d}x \quad (3)$$

The subscript comma indicates partial differentiation. In comparison to the equivalent 2-D relations, it is seen that the integration essentially provides weighted averages of the optical effect. But, in addition, there is also a contribution by the third component of stress.

From these equations it is apparent that the optical data alone are insufficient to solve for the stresses. Indeed, it will not even give the stress differences, as is so for the equivalent plane case.

Solution

A source of additional information often used in photoelasticity is the equilibrium equations. For the axisymmetric problem, it is possible to substitute for $(\sigma_r - \sigma_\theta)$ in the optical relations, then integrating gives

$$\sigma_z = \sigma_r^b + \frac{1}{r}I_{1,r} + I_{2,z} \quad (4)$$

Thus σ_z is obtainable on the section using only optical data.

It is pointed out that when approximating the derivative with respect to z in equation (4) that the change in cross section of the model must also be considered. This approximation may have larger errors than the corresponding plane case.

Additional data is required if σ_r and σ_θ is to be determined, and a convenient source of this data for axisymmetric problems is through the compatibility equations. Using the strain displacement relations and Hooke's law gives (after eliminating the displacement and integrating)

$$\sigma_r + \sigma_\theta = (1 + 2\nu)\sigma_r^b + (1 + \nu)K_1 + \frac{\nu}{r}I_{1,r} + (1 + 2\nu)I_{2,z} - E\beta T \quad (5)$$

where ν is Poisson's ratio, E is Young's modulus, β is the coefficient of thermal expansion, T is the temperature change, and K_1 is a constant of integration.

Substituting for σ_θ from equation (5) into equation (3) and integrating allows σ_r to be determined. Consequently, all the other components can also be determined, and are given as

$$\sigma_r = \frac{1}{2}K_2 + K_3\frac{a^2}{r^2} + \frac{\nu}{r^2}(I_1 - I_1^a) + I_{2,z} - \frac{(1 - 2\nu)}{r^2}\int_a^r I_{2,z}\,r dr - \frac{E\beta}{r^2}\int_a^r T\,r dr$$

$$\sigma_\theta = \frac{1}{2}K_2 - K_3\frac{a^2}{r^2} + \frac{\nu}{r}I_{1,r} - \frac{\nu}{r^2}(I_1 - I_1^a) + 2\nu I_{2,z} + \frac{(1 - 2\nu)}{r^2}\int_a^r I_{2,z}\,r dr - E\beta T + \frac{E\beta}{r^2}\int_a^r T\,r dr$$

$$\sigma_{rz} = -I_{2,r} \quad (6)$$

where K_2 and K_3 are combined constants.

These equations show that the solution of the axisymmetric photoelastic problem, just as in plane photoelasticity, can be reduced to quadratures of the experimental data. However, these quadratures involve singular integrals and therefore must be given special treatment.

Evaluating the Integrals

Probably the simplest method of evaluating the integrals is to first curve fit the experimental data in the following form:

$$N\cos 2\alpha\, f_\sigma = \sqrt{b^2 - r^2}\sum_0 A_n(b^2 - r^2)^n$$

$$\frac{\partial}{\partial z}(N\sin 2\alpha)\, f_\sigma = \sqrt{b^2 - r^2}\sum_0 B_n r(b^2 - r^2)^n \quad (7)$$

giving, for example,

$$I_1 = \frac{1}{2}\sum_0 A_n\frac{(n + \tfrac{1}{2})!}{n!}(b^2 - r^2)^{n+1}$$

$$I_{2,z} = \sum_0 B_n\frac{(n + \tfrac{1}{2})!}{(n + 1)!}(b^2 - r^2)^{n+1} \quad (8)$$

Once the coefficients A_n and B_n have been obtained (say by a least-squares fit of the data), then these terms can be evaluated for different r and their values entered into columns for later use. The number of terms chosen in the curve fitting will depend on the complexity of the data distribution.

Special Cases

The solution as presented in equations (4) and (6) is quite general, but it is instructive to investigate some of its special cases.

(*a*) **Boundary Values.** At the outer boundary, σ_r^b is generally known and therefore σ_z at the boundary is obtained simply by curve fitting the data near the boundary to get I_1 and taking off the leading term. This has been used by Cheng [4] for determining stress-concentration factors. However, an important point to note: if all the components of stress at one boundary or some of the components at both boundaries are required, then the complete problem on the section must be solved. This is fundamentally different from the plane case where the optical data is sufficient to obtain all the components of stress at any boundary.

(*b*) **Solid Body.** When the radius of the internal cavity goes to zero then K_3 drops out and the solution takes on a simpler form.

(*c*) **Incompressible Materials.** For many materials, especially polymers the approximation $1\text{-}2\nu = 0$ can lead to good engineering solutions. For stress frozen models the approximation is nearly exact. However, this assumption does not cause any significant simplification in the calculation of the stresses. The stress differences, on the other hand, can be written in terms of I_1, K_2, and K_3, and if, further, the body is solid, then $K_3 = 0$ and the stress differences on the transverse section can be obtained simply. This is essentially what Srinath [5] did for the solid sphere in diametral compression.

Downloaded 01 May 2010 to 171.66.16.243. Redistribution subject to ASME license or copyright; see http://www.asme.org/terms/Terms_Use.cfm

(*d*) **Transverse Plane of Symmetry.** In many problems, such as symmetrically notched bars, a transverse plane of symmetry occurs. For these planes, the optical relations (3) are exact since there is no rotation of the secondary principal axes, but otherwise there is no further simplification of the problem.

(*e*) **Quasi-Two-Dimensional.** When the body or the loading conditions are essentially uniform in a section, the rate of change of shear stress is small, leading to the approximation $I_{2,z} = 0$ and thus the problem is reduced to determining only the single function I_1. This is one of the assumptions made by O'Rourke in his study of quenched cylinders [6].

(*f*) **Residual and Quenching Stresses.** When residual and quenching stresses occur, the body will have experienced local volume changes in addition to those caused by the loading. This can be incorporated in the previous equations by replacing T by an equivalent temperature distribution T^*. The big difference from the experimental point of view, however, is that T^* is now an additional unknown which must be determined. Since equilibrium, compatibility, and the optical relations have already been used, then some further approximations and simplifications must be resorted to. For example, O'Rourke [6] in his studies of quenching stresses made the assumptions

$$I_{2,z} = 0, \quad \int_a^b \sigma_z r dr = 0, \quad \sigma_r^a = \sigma_r^b = 0, \quad e_z = 0$$

and obtained the stresses as simple functions of I_1 only.

Conclusion

It has been shown that the general axisymmetric integrated photoelastic problem can be solved using only data collected in a manner analogous to the plane problem. This was achieved because the two measured optical data plus the equilibrium equation and the compatibility equation, constituted four independent sources of information sufficient to solve for the four components of stress.

Since there are classes of axisymmetric problems of practical interest still unsolved then the present integrated method can play an important role. There are problems such as the shrink fitting of collars onto shafts where conventional experimental, as well as numerical, methods give poor results. In these situations, the added computations of the present method is no drawback in comparison to the alternative methods.

References

1 Aben, H. K., *Integrated Photoelasticity,* Akad. Nauk. Estonian SSR, Tallin, 1975 (in Russian, English version to be published by McGraw-Hill in 1979).

2 Aben, H. K., "Optical Phenomena in Photoelastic Models by the Rotation of Principal Axes," *Experimental Mechanics,* Jan. 1966, pp. 13–22.

3 Doyle, J. F., and Danyluk, H. T., "Integrated Photoelasticity for Axisymmetric Problems," *Experimental Mechanics,* June 1978, pp. 215–220.

4 Cheng, Y. F., "Stress at Notch Root of Shafts Under Axially Symmetrically Loading," *Experimental Mechanics,* Vol. 10(12), Dec. 1970, pp. 534–536.

5 Srinath, L., "Principal Stress Differences in Transverse Planes of Symmetry," *Experimental Mechanics,* Vol. 11(3), Mar. 1971, pp. 130–137.

6. O'Rourke, R. C., *Theoretical Studies in Photoelasticity,* PhD Thesis, University of Michigan, 1950.

Performance of the Axisymmetric Linear Shell Element for Vibration of Thin Circular Plates

T. A. I. Akeju[1]

Introduction

The introduction of the isoparametric family of elements into finite-element analysis coupled with the increasing use of numerical integration techniques have led to a rapid growth in the development of complex finite-element schemes with varying degrees of accuracy and performance. The same procedures could well facilitate the formulation of comparatively simple elements. One such case is the generation of axisymmetric shell element family developed by Zienkiewicz, et al. [1].

The derivation of the element involves the introduction of a shear strain energy term to the predominant flexural strain energy term to insure its applicability to thick structures. The solution here can be described as the minimization of a penalty-type energy functional

$$\Pi^* = \Pi_1 + \alpha\Pi_2 \quad \alpha \to \infty \tag{1}$$

in which the second quadratic term

$$\Pi_2 = \int_\Omega C^T C d\Omega \tag{2}$$

is introduced to impose constraints $C = 0$ on the shear deformation.

The ratio of the stiffnesses acts as the penalty parameter α in the discretized equations

$$(K_1 + \alpha K_2)a = f \tag{3}$$

As α becomes very large, the only available solution for the displacement is $a \to 0$ unless K_2 is singular. The use of reduced integration among other functions insures the singularity of constraint matrix K_2 and thereby leads to approximate results for a thin structure.

In what follows here, the simplest version of the element, a two noded straight element is applied to the free-vibration problem of thin circular disks and thin annular plates. Comparison with analytical solutions confirms the same degree of accuracy already demonstrated for static problems. While the selective integration technique appears to give closer estimates of the exact solutions, it is noted that the extra programming efforts may not be justified since overall reduced integration produces near enough results.

Theory

An axisymmetric shell under an axisymmetric load system has been shown [2] to have the following strain displacement relations:

$$\epsilon_s = \begin{Bmatrix} \epsilon_s \\ \epsilon_\theta \\ \chi_s \\ \chi_\theta \\ \gamma \end{Bmatrix} = \begin{bmatrix} \dfrac{du}{ds} + \dfrac{w}{R} \\ (w\cos\phi + u\sin\phi)/r \\ \dfrac{d^2w}{ds^2} + d(u/R)/d_s \\ -\sin\phi\left(\dfrac{dw}{ds} - u/R\right)\Big/ r \\ \dfrac{dw}{ds} - \beta \end{bmatrix} \tag{4}$$

The first two terms represent the membrane deformations, the next two the flexural deformations, while the last term is the shear strain brought in to accommodate thick structures; u and w are the tangential and normal components of displacements, respectively, and β is the rotation. R is the radius of curvature of the meridian while r is the radius of the parallel circle. The model (4) can be applied to a circular plate by means of the approximation $R \to \infty$.

The displacement vector can be defined by means of the familiar finite-element notation [3]

[1] Department of Civil Engineering, University of Lagos, Lagos, Nigeria.

Manuscript received by ASME Applied Mechanics Division, April, 1979; final revision, September, 1979.

Downloaded 01 May 2010 to 171.66.16.243. Redistribution subject to ASME license or copyright; see http://www.asme.org/terms/Terms_Use.cfm

(*d*) **Transverse Plane of Symmetry.** In many problems, such as symmetrically notched bars, a transverse plane of symmetry occurs. For these planes, the optical relations (3) are exact since there is no rotation of the secondary principal axes, but otherwise there is no further simplification of the problem.

(*e*) **Quasi-Two-Dimensional.** When the body or the loading conditions are essentially uniform in a section, the rate of change of shear stress is small, leading to the approximation $I_{2,z} = 0$ and thus the problem is reduced to determining only the single function I_1. This is one of the assumptions made by O'Rourke in his study of quenched cylinders [6].

(*f*) **Residual and Quenching Stresses.** When residual and quenching stresses occur, the body will have experienced local volume changes in addition to those caused by the loading. This can be incorporated in the previous equations by replacing T by an equivalent temperature distribution T^*. The big difference from the experimental point of view, however, is that T^* is now an additional unknown which must be determined. Since equilibrium, compatibility, and the optical relations have already been used, then some further approximations and simplifications must be resorted to. For example, O'Rourke [6] in his studies of quenching stresses made the assumptions

$$I_{2,z} = 0, \quad \int_a^b \sigma_z r dr = 0, \quad \sigma_r^a = \sigma_r^b = 0, \quad e_z = 0$$

and obtained the stresses as simple functions of I_1 only.

Conclusion

It has been shown that the general axisymmetric integrated photoelastic problem can be solved using only data collected in a manner analogous to the plane problem. This was achieved because the two measured optical data plus the equilibrium equation and the compatibility equation, constituted four independent sources of information sufficient to solve for the four components of stress.

Since there are classes of axisymmetric problems of practical interest still unsolved then the present integrated method can play an important role. There are problems such as the shrink fitting of collars onto shafts where conventional experimental, as well as numerical, methods give poor results. In these situations, the added computations of the present method is no drawback in comparison to the alternative methods.

References

1 Aben, H. K., *Integrated Photoelasticity,* Akad. Nauk. Estonian SSR, Tallin, 1975 (in Russian, English version to be published by McGraw-Hill in 1979).

2 Aben, H. K., "Optical Phenomena in Photoelastic Models by the Rotation of Principal Axes," *Experimental Mechanics,* Jan. 1966, pp. 13–22.

3 Doyle, J. F., and Danyluk, H. T., "Integrated Photoelasticity for Axisymmetric Problems," *Experimental Mechanics,* June 1978, pp. 215–220.

4 Cheng, Y. F., "Stress at Notch Root of Shafts Under Axially Symmetrically Loading," *Experimental Mechanics,* Vol. 10(12), Dec. 1970, pp. 534–536.

5 Srinath, L., "Principal Stress Differences in Transverse Planes of Symmetry," *Experimental Mechanics,* Vol. 11(3), Mar. 1971, pp. 130–137.

6. O'Rourke, R. C., *Theoretical Studies in Photoelasticity,* PhD Thesis, University of Michigan, 1950.

Performance of the Axisymmetric Linear Shell Element for Vibration of Thin Circular Plates

T. A. I. Akeju[1]

Introduction

The introduction of the isoparametric family of elements into finite-element analysis coupled with the increasing use of numerical integration techniques have led to a rapid growth in the development of complex finite-element schemes with varying degrees of accuracy and performance. The same procedures could well facilitate the formulation of comparatively simple elements. One such case is the generation of axisymmetric shell element family developed by Zienkiewicz, et al. [1].

The derivation of the element involves the introduction of a shear strain energy term to the predominant flexural strain energy term to insure its applicability to thick structures. The solution here can be described as the minimization of a penalty-type energy functional

$$\Pi^* = \Pi_1 + \alpha\Pi_2 \quad \alpha \to \infty \tag{1}$$

in which the second quadratic term

$$\Pi_2 = \int_\Omega C^T C d\Omega \tag{2}$$

is introduced to impose constraints $C = 0$ on the shear deformation.

The ratio of the stiffnesses acts as the penalty parameter α in the discretized equations

$$(K_1 + \alpha K_2)a = f \tag{3}$$

As α becomes very large, the only available solution for the displacement is $a \to 0$ unless K_2 is singular. The use of reduced integration among other functions insures the singularity of constraint matrix K_2 and thereby leads to approximate results for a thin structure.

In what follows here, the simplest version of the element, a two noded straight element is applied to the free-vibration problem of thin circular disks and thin annular plates. Comparison with analytical solutions confirms the same degree of accuracy already demonstrated for static problems. While the selective integration technique appears to give closer estimates of the exact solutions, it is noted that the extra programming efforts may not be justified since overall reduced integration produces near enough results.

Theory

An axisymmetric shell under an axisymmetric load system has been shown [2] to have the following strain displacement relations:

$$\epsilon_s = \begin{Bmatrix} \epsilon_s \\ \epsilon_\theta \\ \chi_s \\ \chi_\theta \\ \gamma \end{Bmatrix} = \begin{bmatrix} \dfrac{du}{ds} + \dfrac{w}{R} \\ (w\cos\phi + u\sin\phi)/r \\ \dfrac{d^2w}{ds^2} + d(u/R)/d_s \\ -\sin\phi\left(\dfrac{dw}{ds} - u/R\right)\Big/ r \\ \dfrac{dw}{ds} - \beta \end{bmatrix} \tag{4}$$

The first two terms represent the membrane deformations, the next two the flexural deformations, while the last term is the shear strain brought in to accommodate thick structures; u and w are the tangential and normal components of displacements, respectively, and β is the rotation. R is the radius of curvature of the meridian while r is the radius of the parallel circle. The model (4) can be applied to a circular plate by means of the approximation $R \to \infty$.

The displacement vector can be defined by means of the familiar finite-element notation [3]

[1] Department of Civil Engineering, University of Lagos, Lagos, Nigeria.

Manuscript received by ASME Applied Mechanics Division, April, 1979; final revision, September, 1979.

Copyright © 1980 by ASME
Downloaded 01 May 2010 to 171.66.16.243. Redistribution subject to ASME license or copyright; see http://www.asme.org/terms/Terms_Use.cfm

$$\epsilon = Ba \tag{5}$$

where the nodal displacement is given by

$$a_i = \begin{bmatrix} u \\ w \\ \beta \end{bmatrix}_i \tag{6}$$

Isoparametric approximation for a displacement component at any point in terms of the nodal displacements for a two noded element is given by

$$u(\xi) = N_1(\xi)u_1 + N_2(\xi)u_2 \tag{7}$$

where

$$\begin{aligned} N_1(\xi) &= (1 - \xi)/2 \\ N_2(\xi) &= (1 + \xi)/2 \end{aligned} \tag{8}$$

and the element coordinate is given by

$$-1 \le \xi \le 1 \tag{9}$$

The finite-element discretization scheme easily leads to the formulation of the free-vibration problem in the form of a classical eigenvalue equation

$$Ka - \omega^2 Ma = 0 \tag{10}$$

where ω are the free-vibration frequencies, K is the stiffness matrix which is obtained from assembly of the element stiffness matrices. A typical submatrix of the stiffness matrix can be defined in terms of the element stiffness matrices as

$$K_{ij} = \sum K_{ij}^e \tag{11}$$

where

$$K_{ij}^e = \int_{-1}^{1} B_i^T D B_j \, 2\pi r \, d\xi \tag{12}$$

In a similar way, M is the consistent or lumped mass matrix which is obtained from the assembly of the element mass matrix. A typical submatrix of the mass matrix can be defined in terms of the element mass matrices as

$$M_{ij} = \sum M_{ij}^e \tag{13}$$

where

$$M_{ij}^e = \int_{-1}^{1} N_i^T \rho \, N_j \, 2\pi r \, d\xi \tag{14}$$

The only quantity yet to be defined is the elasticity matrix D which in the axisymmetric plate problem is given by

$$D = \frac{Eh}{1-\nu^2} \begin{bmatrix} 1 & \nu & 0 & 0 & 0 \\ & 1 & 0 & 0 & 0 \\ & & h^2/12 & \nu h^2/12 & 0 \\ \text{Symmetry} & & & h^2/12 & 0 \\ & & & & \dfrac{1-\nu}{2k} \end{bmatrix} \tag{15}$$

where E is the Young's modulus of elasticity, ν the Poisson's ratio, h is the thickness of the plate, and $k = 1.2$ is the ratio of the relevant strain energies, $1/k$ being the shear rigidity factor 5/6.

The numerical solution of (10) was accomplished by means of Bathe-Wilson's subspace iteration algorithm [4].

Numerical Examples

The model was tested for thin circular disks and annular plates. Table 1 shows a comparison of the finite-element results with analytical solutions for simply supported and clamped thin circular disks. Results under the column designated as reduced integration were obtained by using the one point Gauss integration rule for (12) and (14) while selective integration implies the one point rule for the shear energy term and two point rule for other terms. Very little difference can be observed from the two methods although the selective integration technique results are closer to the analytical solutions.

In Table 2, the remarkable closeness of the finite-element solution to Rayleigh-Ritz and exact solutions for annular plates with combinations of clamped, simple and free supports is displayed. Here the

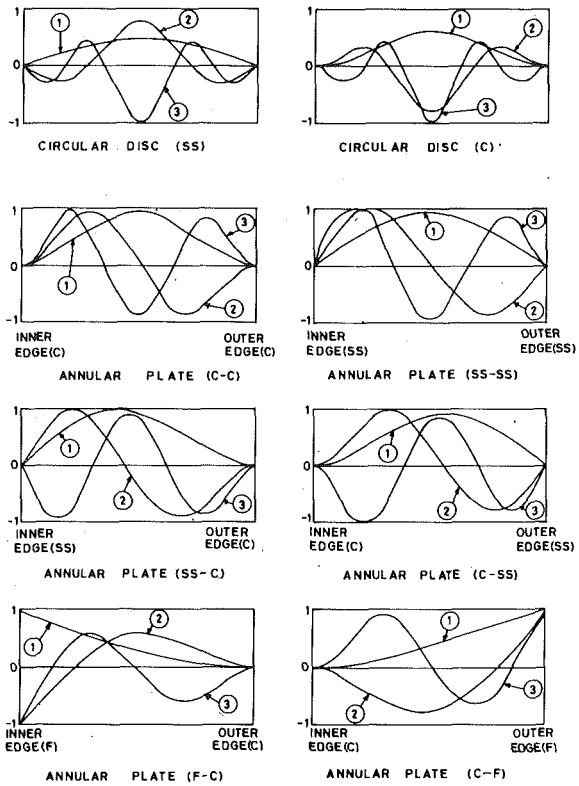

Fig. 1 Axisymmetric (w) modes of circular plates

Table 1 Frequency parameter $\omega a^2\sqrt{\rho/D}$ for thin circular disks

Boundary condition	Finite-element solution (10 elements) Reduced integration	Selective integration	Analytical solution [5]
Simply supported	4.957	4.979	4.977
Clamped	10.1392	10.2160	10.2158

Table 2 Frequency parameter $\omega a^2\sqrt{\rho/D}$ for thin annular plates

Boundary conditions $r = a$	$r = b$	Finite elements (10 elements)	Rayleigh and Ritz [5]	Exact [5] solution
C	C	89.65	89.42	89.03
C	SS	63.99	65.17	64.06
SS	C	60.09	61.81	59.91
SS	SS	40.04	43.19	40.01
C	F	17.58	17.56	17.51
F	C	13.09	13.59	13.05

C = Clamped
SS = Simply supported
F = Free

$a/b = 0.5$
$\nu = 1/3$

Downloaded 01 May 2010 to 171.66.16.243. Redistribution subject to ASME license or copyright; see http://www.asme.org/terms/Terms_Use.cfm

finite-element solutions were obtained by the selective integration technique.

The first three w mode shapes for the circular disks and annular plates of Tables 1 and 2, respectively, are shown in Fig. 1.

Conclusion

The simple two noded version of the linear axisymmetric shell element of Zienkiewicz, et al., has been shown to give very good results for vibration of thin circular disks and annular plates where comparison with such are readily available. While some advantage has been shown to be gained by selectively integrating the terms, the numerical results presented for clamped and simply supported circular disks tend to indicate that the extra effort may not be worthwhile. The direct overall reduced integration technique gives results that are suitable.

Acknowledgment

The initial part of this work was carried out at the Department of Civil Engineering, University College of Wales, Swansea, during a short visit there. The help of colleagues, in particular, Dr. E. Hinton is gratefully acknowledged. Numerical results presented here were produced on the IBM 370/145 of the University of Lagos Computer Centre using funds from the University's Central Research Grant.

References

1 Zienkiewicz, O. C., et al., "An Efficient Element for Axisymmetric Shells," *International Journal for Numerical Methods in Engineering,* Vol. 11, 1977, pp. 1545–1558.

2 Timoshenko, S. P., and Woinowsky-Krieger, S., *Theory of Plates and Shells,* 2nd ed., McGraw-Hill, New York, 1959.

3 Zienkiewicz, O. C., *The Finite-Element Method,* 3rd ed., McGraw-Hill, New York, 1977.

4 Bathe, K. J., and Wilson, E. L., "Large Eigenvalue Problems in Dynamic Analysis," *ASCE Journal of Engineering Mechanics Division,* Vol. 98, 1972, pp. 1471–1485.

5 Leissa, A. W., *Vibration of Plates,* NASA, 1969.

Concerning the Solution of Elastic-Plastic Problems by the Finite-Element Method

E. Zahavi[1]

Introduction

The present Note applies to the *FE* initial-stress and variable-stiffness methods, [1, 2]. It concerns numerical errors that are caused by load discretization in the said methods. For simplification, the work is restricted to monotonically increasing loads. As an additional restriction, the analysis is limited to Mises materials with isotropic hardening.

Consider a body subject to elastic-plastic deformation in the course of monotonically increasing load. According to the uniqueness theorem, there will be at any time t only one stress rate and strain rate distribution that satisfies the equilibrium, compatibility, and boundary conditions. Parameters such as forces, deformations, stresses, and strains are implicitly time-dependent—through the applied load which is a continuous function of time. The equilibrium condition for the stress rates is expressed by the equation

$$\frac{d}{dt}\frac{\partial \dot{\sigma}_{ij}}{\partial x_j} + \frac{d\dot{X}_i}{dt} = 0 \tag{1}$$

In the *FE* formulation the space derivative of the stress equals

$$\frac{\partial \sigma_{ij}}{\partial x_j} = [B]^T \{\sigma\} \tag{2}$$

The stress vector $\{\sigma\}$ is assumed to have a discrete distribution that corresponds to the *FE* division, and the matrix operator $[B]^T$ replaces the derivative, see [3]. The equilibrium equation in integral form then becomes

$$\sum^{E}\left(\int_E [B]^T \{\dot{\sigma}\} dv + \{\dot{F}\}\right) = 0 \tag{3}$$

For discrete time increments Δt, equation (3) obtains the form

$$\sum^{E}\left(\int_E [B]^T \{\Delta\sigma\} dv + \{\Delta F\}\right) = 0 \tag{4}$$

Initial-Stress and Variable-Stiffness Methods

Equation (4) is solved in terms of nodal displacements $\Delta\delta_i$ using the transformations

$$\{\Delta\sigma\} = [D^{ep}]\{\Delta\epsilon\} \tag{5}$$

and

$$\{\Delta\epsilon\} = [B]\{\Delta\delta\} \tag{6}$$

Equation (5) is a difference approximation of the differential equation

$$d\sigma_{ij} = D_{ijkl}{}^{ep} \cdot d\epsilon_{kl} \tag{7}$$

$D_{ijkl}{}^{ep}$ is the elastic-plastic modulus that is a function of yield criteria. For Mises materials it equals

$$D_{ijkl}{}^{ep} = 2G\left(\delta_{ik}\delta_{jl} + \frac{\nu}{1-2\nu}\delta_{ij}\delta_{kl} - \frac{1}{1+\dfrac{H'}{3G}}\cdot\frac{s_{ij}s_{kl}}{s_{pr}s_{pr}}\right) \tag{8}$$

see [4]. It is convenient to divide $D_{ijkl}{}^{ep}$ into the elastic and plastic parts

$$D_{ijkl}{}^{ep} = D_{ijkl}{}^{e} + D_{ijkl}{}^{p} \tag{9}$$

where $D_{ijkl}{}^{e}$ includes the first two terms in brackets of equation (8), while $D_{ijkl}{}^{p}$ corresponds to the last term in the brackets.

The initial-stress approach, [1], introduces a fictitious plastic force defined as

$$\{\Delta F^p\} = \int_E [B]^T [D^p]\{\Delta\epsilon\} dv \tag{10}$$

which brings the equilibrium equation (4) into the form

$$\sum^{E}\left(\int_E [B]^T [D^e][B]\{\Delta\delta\} dv + \{\Delta F\} + \{\Delta F^p\}\right) = 0 \tag{11}$$

With the elastic stiffness matrix defined as

$$[K] = \sum^{E}\int_E [B]^T[D^e][B] dv \tag{12}$$

the equilibrium equation becomes

$$[K]\{\Delta\delta\} + \sum^{E}(\{\Delta F\} + \{\Delta F^p\}) = 0 \tag{13}$$

which is solved for $\Delta\delta$ by an iterative procedure.

In the variable-stiffness approach [2], one uses the corrective stiffness

$$[K^p] = \sum^{E}\int_E [B]^T [D^p][B] dv \tag{14}$$

whereby the equilibrium equations obtains the form

$$([K] + [K^p])\{\Delta\delta\} + \sum^{E}\{\Delta F\} = 0 \tag{15}$$

which again is solved iteratively.

[1] Department of Mechanical Engineering, Ben-Gurion University of the Negev, Beer Sheva, Israel.

Manuscript received by ASME Applied Mechanics Division, May, 1979; final revision, August, 1979.

Downloaded 01 May 2010 to 171.66.16.243. Redistribution subject to ASME license or copyright; see http://www.asme.org/terms/Terms_Use.cfm

finite-element solutions were obtained by the selective integration technique.

The first three w mode shapes for the circular disks and annular plates of Tables 1 and 2, respectively, are shown in Fig. 1.

Conclusion

The simple two noded version of the linear axisymmetric shell element of Zienkiewicz, et al., has been shown to give very good results for vibration of thin circular disks and annular plates where comparison with such are readily available. While some advantage has been shown to be gained by selectively integrating the terms, the numerical results presented for clamped and simply supported circular disks tend to indicate that the extra effort may not be worthwhile. The direct overall reduced integration technique gives results that are suitable.

Acknowledgment

The initial part of this work was carried out at the Department of Civil Engineering, University College of Wales, Swansea, during a short visit there. The help of colleagues, in particular, Dr. E. Hinton is gratefully acknowledged. Numerical results presented here were produced on the IBM 370/145 of the University of Lagos Computer Centre using funds from the University's Central Research Grant.

References

1 Zienkiewicz, O. C., et al., "An Efficient Element for Axisymmetric Shells," *International Journal for Numerical Methods in Engineering,* Vol. 11, 1977, pp. 1545–1558.

2 Timoshenko, S. P., and Woinowsky-Krieger, S., *Theory of Plates and Shells,* 2nd ed., McGraw-Hill, New York, 1959.

3 Zienkiewicz, O. C., *The Finite-Element Method,* 3rd ed., McGraw-Hill, New York, 1977.

4 Bathe, K. J., and Wilson, E. L., "Large Eigenvalue Problems in Dynamic Analysis," *ASCE Journal of Engineering Mechanics Division,* Vol. 98, 1972, pp. 1471–1485.

5 Leissa, A. W., *Vibration of Plates,* NASA, 1969.

Concerning the Solution of Elastic-Plastic Problems by the Finite-Element Method

E. Zahavi[1]

Introduction

The present Note applies to the *FE* initial-stress and variable-stiffness methods, [1, 2]. It concerns numerical errors that are caused by load discretization in the said methods. For simplification, the work is restricted to monotonically increasing loads. As an additional restriction, the analysis is limited to Mises materials with isotropic hardening.

Consider a body subject to elastic-plastic deformation in the course of monotonically increasing load. According to the uniqueness theorem, there will be at any time t only one stress rate and strain rate distribution that satisfies the equilibrium, compatibility, and boundary conditions. Parameters such as forces, deformations, stresses, and strains are implicitly time-dependent—through the applied load which is a continuous function of time. The equilibrium condition for the stress rates is expressed by the equation

$$\frac{d}{dt}\frac{\partial \dot{\sigma}_{ij}}{\partial x_j} + \frac{d\dot{X}_i}{dt} = 0 \tag{1}$$

In the *FE* formulation the space derivative of the stress equals

$$\frac{\partial \sigma_{ij}}{\partial x_j} = [B]^T \{\sigma\} \tag{2}$$

The stress vector $\{\sigma\}$ is assumed to have a discrete distribution that corresponds to the *FE* division, and the matrix operator $[B]^T$ replaces the derivative, see [3]. The equilibrium equation in integral form then becomes

$$\sum^{E}\left(\int_E [B]^T \{\dot{\sigma}\} dv + \{\dot{F}\}\right) = 0 \tag{3}$$

For discrete time increments Δt, equation (3) obtains the form

$$\sum^{E}\left(\int_E [B]^T \{\Delta\sigma\} dv + \{\Delta F\}\right) = 0 \tag{4}$$

Initial-Stress and Variable-Stiffness Methods

Equation (4) is solved in terms of nodal displacements $\Delta\delta_i$ using the transformations

$$\{\Delta\sigma\} = [D^{ep}]\{\Delta\epsilon\} \tag{5}$$

and

$$\{\Delta\epsilon\} = [B]\{\Delta\delta\} \tag{6}$$

Equation (5) is a difference approximation of the differential equation

$$d\sigma_{ij} = D_{ijkl}{}^{ep} \cdot d\epsilon_{kl} \tag{7}$$

$D_{ijkl}{}^{ep}$ is the elastic-plastic modulus that is a function of yield criteria. For Mises materials it equals

$$D_{ijkl}{}^{ep} = 2G\left(\delta_{ik}\delta_{jl} + \frac{\nu}{1-2\nu}\delta_{ij}\delta_{kl} - \frac{1}{1+\dfrac{H'}{3G}}\cdot\frac{s_{ij}s_{kl}}{s_{pr}s_{pr}}\right) \tag{8}$$

see [4]. It is convenient to divide $D_{ijkl}{}^{ep}$ into the elastic and plastic parts

$$D_{ijkl}{}^{ep} = D_{ijkl}{}^{e} + D_{ijkl}{}^{p} \tag{9}$$

where $D_{ijkl}{}^{e}$ includes the first two terms in brackets of equation (8), while $D_{ijkl}{}^{p}$ corresponds to the last term in the brackets.

The initial-stress approach, [1], introduces a fictitious plastic force defined as

$$\{\Delta F^p\} = \int_E [B]^T [D^p]\{\Delta\epsilon\} dv \tag{10}$$

which brings the equilibrium equation (4) into the form

$$\sum^{E}\left(\int_E [B]^T [D^e][B]\{\Delta\delta\} dv + \{\Delta F\} + \{\Delta F^p\}\right) = 0 \tag{11}$$

With the elastic stiffness matrix defined as

$$[K] = \sum^{E}\int_E [B]^T[D^e][B] dv \tag{12}$$

the equilibrium equation becomes

$$[K]\{\Delta\delta\} + \sum^{E}(\{\Delta F\} + \{\Delta F^p\}) = 0 \tag{13}$$

which is solved for $\Delta\delta$ by an iterative procedure.

In the variable-stiffness approach [2], one uses the corrective stiffness

$$[K^p] = \sum^{E}\int_E [B]^T [D^p][B] dv \tag{14}$$

whereby the equilibrium equations obtains the form

$$([K] + [K^p])\{\Delta\delta\} + \sum^{E}\{\Delta F\} = 0 \tag{15}$$

which again is solved iteratively.

[1] Department of Mechanical Engineering, Ben-Gurion University of the Negev, Beer Sheva, Israel.

Manuscript received by ASME Applied Mechanics Division, May, 1979; final revision, August, 1979.

Copyright © 1980 by ASME
Downloaded 01 May 2010 to 171.66.16.243. Redistribution subject to ASME license or copyright; see http://www.asme.org/terms/Terms_Use.cfm

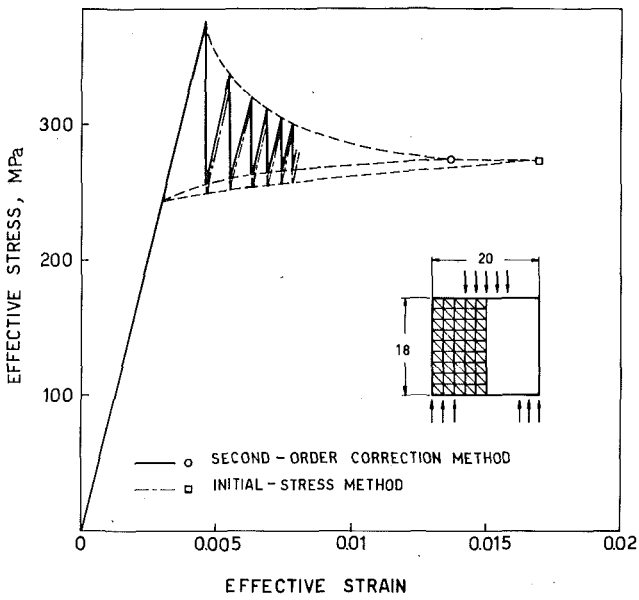

Fig. 1 Computed data of iterative steps for a critical element in a short aluminum beam; applied load distribution 274 MPa; yield point 238 MPa; $E = 6.86 \times 10^4$ MPa; $H' = 2205$ MPa; $\nu = 0.2$

Second-Order Correction

The discretization error of the initial-stress and variable-stiffness methods stems from replacing the differential equation (7) by the approximate expression (5). Consider the function

$$\sigma_{ij} = f(\epsilon_{kl}) \tag{16}$$

Assume the external loads F_i to be continuously differentiable functions of time, in addition to being monotonic. Then one can replace function (16) by its Taylor expansion

$$\sigma_{ij} = (\sigma_{ij})_o + \left(\frac{\partial \sigma_{ij}}{\partial \epsilon_{kl}}\right)_o \Delta\epsilon_{kl} + \frac{1}{2}\left(\frac{\partial^2 \sigma_{ij}}{\partial \epsilon_{kl}\partial \epsilon_{mn}}\right)_o \Delta\epsilon_{kl}\Delta\epsilon_{mn} + \ldots \tag{17}$$

where index o denotes a known point in the stress-strain space. It is evident that equation (5) is a Taylor series truncated to the first-order with

$$\left(\frac{\partial \sigma_{ij}}{\partial \epsilon_{kl}}\right)_o = D_{ijkl}{}^{ep} \tag{18}$$

and index o denotes the known point at the start of each iteration.

A more accurate expression in lieu of equation (5) will be a truncated Taylor series up to the second-order term

$$\Delta\sigma_{ij} = D'_{ijkl} \cdot \Delta\epsilon_{kl} + \tfrac{1}{2} D''_{ijklmn} \cdot \Delta\epsilon_{kl} \cdot \Delta\epsilon_{mn} \tag{19}$$

where D' equals D^{ep} and D'' is a second-order derivative of σ_{ij} with respect to ϵ_{kl}. For Mises materials D'' equals

$$D''_{ijklmn} = \frac{1}{1 + \dfrac{H'}{3G}}\left[\frac{2}{(s_{pr}s_{pr})^2} A_{prmn}s_{pr}s_{ij}s_{kl} - \frac{1}{s_{pr}s_{pr}}(A_{klmn}s_{ij} + A_{ijmn}s_{kl})\right] \tag{20}$$

with

$$A_{ijkl} = \delta_{ik}\delta_{jl} - \frac{1}{3}\delta_{ij}\delta_{kl} \tag{21}$$

as can be easily verified by differentiation of equation (8) with respect to ϵ_{mm}.

The application of the corrected method is executed best by using the initial-stress procedure in which equation (5) is replaced by equation (10). The difference between the numerical results of the original initial-stress method and the second-order correction method may be negligible where the loading mode is close to proportional loading. However, the difference becomes considerable for loading cases with large rotation and shear stresses. Fig. 1 shows the numerical results of a comparison study involving a two-dimensional plane-strain beam of short dimensions, where the computation involved one large load increment. The figure shows the values of the effective stress and strain in a critical element at the consecutive iterations. Similar diagrams can be drawn for the components of the stress and strain tensors. As seen in the figure, the difference between the plastic deformation values reaches about 33 percent.

References

1 Nayak, G. C., and Zienkiewicz, O. C., "Elasto-Plastic Stress Analysis," *International Journal for Num. Meth. Engng.*, Vol. 5, 1972, pp. 113–135.

2 Marcal, P. V., and King, I. P., "Elastic-Plastic Analysis of Two-Dimensional Stress Systems by the Finite-Element Method," *International Journal of Mechanical Sciences*, Vol. 9, 1967, pp. 143–155.

3 Zienkiewicz, O. C., *The Finite-Element Method*, 3rd ed., McGraw-Hill, London, 1977.

4 Yamada, Y., Yoshimura, N., and Sakurai, T., "Plastic Stress-Strain Matrix and Its Application for the Solution of Elastic-Plastic Problems by the Finite-Element Method," *International Journal of Mechanical Sciences*, Vol. 10, 1968, pp. 343–354.

Thermal-Stress Singularities at the Ends of a Thin Elastic Stiffener Bonded to a Semi-Infinite Medium

O. Tamate,[1] H. Sekine,[2] and T. Hanazawa[3]

Introduction

The first analytical study of the problem of a thin stiffener of finite length bonded to a half plane was made by Bufler [1]. Although he discussed the diffusion of load from the stiffener to the half plane, the stress singularities at the ends of the stiffener were not studied.

With the progress of linear fracture mechanics, the stress singularities at the ends of an elastic stiffener bonded to a half plane have received considerable attention. In this field, Arutiunian [2] discussed the contact stresses between an elastic stiffener of finite length and a half plane, and showed that the stress singularity at the end of the stiffener is of the order $r^{-1/2}$, where r is radial distance from the end of the stiffener. In recent years, Erdogan and Gupta [3] have reconsidered the same problem by using the rather simple Erdogan's method [4], and the numerical examples have been given for the strength of the stress singularity and the contact stresses.

When a heat flow transferred in a semi-infinite medium is disturbed by the presence of a thin elastic stiffener of finite length bonded to a semi-infinite medium, large thermal stresses arise in the neighborhood of the ends of the stiffener. Thermal stresses of this kind may in some cases cause serious damage to structures. Consequently, the study of the thermal stresses in the vicinity of the ends of the stiffener is of great practical importance. In this Note, the thermal-stress singularities at the ends of a thin elastic stiffener are considered by using the steady-state two-dimensional theory of linear thermoelasticity. The analysis is based on the singular point method extended to the thermoelastic stiffener problem. Some numerical calculations

[1] Professor, Department of Mechanical Engineering, Tohoku University, Sendai, Japan.

[2] Instructor, Department of Mechanical Engineering, Tohoku University, Sendai, Japan.

[3] Graduate Student, Department of Mechanical Engineering, Tohoku University, Sendai, Japan. Presently, Kawasaki Steel Corp., Kobe, Japan.

Manuscript received by ASME Applied Mechanics Division, July, 1979; final revision, October, 1979.

Downloaded 01 May 2010 to 171.66.16.243. Redistribution subject to ASME license or copyright; see http://www.asme.org/terms/Terms_Use.cfm

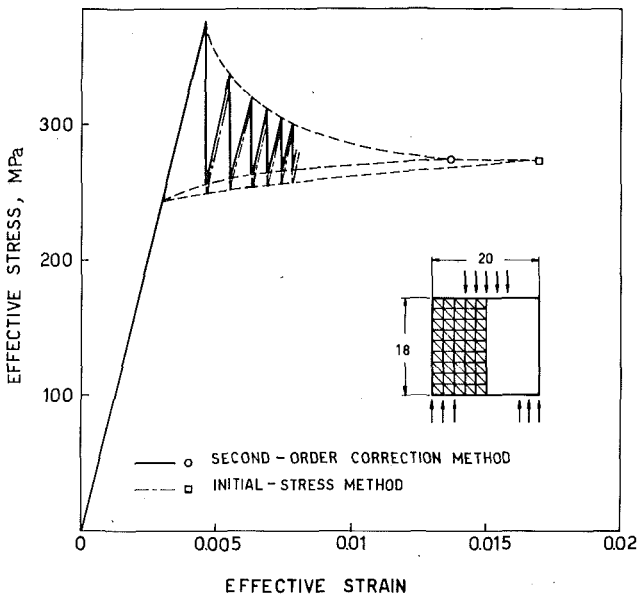

Fig. 1 Computed data of iterative steps for a critical element in a short aluminum beam; applied load distribution 274 MPa; yield point 238 MPa; $E = 6.86 \times 10^4$ MPa; $H' = 2205$ MPa; $\nu = 0.2$

Second-Order Correction

The discretization error of the initial-stress and variable-stiffness methods stems from replacing the differential equation (7) by the approximate expression (5). Consider the function

$$\sigma_{ij} = f(\epsilon_{kl}) \tag{16}$$

Assume the external loads F_i to be continuously differentiable functions of time, in addition to being monotonic. Then one can replace function (16) by its Taylor expansion

$$\sigma_{ij} = (\sigma_{ij})_o + \left(\frac{\partial \sigma_{ij}}{\partial \epsilon_{kl}}\right)_o \Delta\epsilon_{kl} + \frac{1}{2}\left(\frac{\partial^2 \sigma_{ij}}{\partial \epsilon_{kl}\partial \epsilon_{mn}}\right)_o \Delta\epsilon_{kl}\Delta\epsilon_{mn} + \ldots \tag{17}$$

where index o denotes a known point in the stress-strain space. It is evident that equation (5) is a Taylor series truncated to the first-order with

$$\left(\frac{\partial \sigma_{ij}}{\partial \epsilon_{kl}}\right)_o = D_{ijkl}{}^{ep} \tag{18}$$

and index o denotes the known point at the start of each iteration.

A more accurate expression in lieu of equation (5) will be a truncated Taylor series up to the second-order term

$$\Delta\sigma_{ij} = D'_{ijkl} \cdot \Delta\epsilon_{kl} + \tfrac{1}{2} D''_{ijklmn} \cdot \Delta\epsilon_{kl} \cdot \Delta\epsilon_{mn} \tag{19}$$

where D' equals D^{ep} and D'' is a second-order derivative of σ_{ij} with respect to ϵ_{kl}. For Mises materials D'' equals

$$D''_{ijklmn} = \frac{1}{1 + \dfrac{H'}{3G}}\left[\frac{2}{(s_{pr}s_{pr})^2} A_{prmn}s_{pr}s_{ij}s_{kl} - \frac{1}{s_{pr}s_{pr}}(A_{klmn}s_{ij} + A_{ijmn}s_{kl})\right] \tag{20}$$

with

$$A_{ijkl} = \delta_{ik}\delta_{jl} - \frac{1}{3}\delta_{ij}\delta_{kl} \tag{21}$$

as can be easily verified by differentiation of equation (8) with respect to ϵ_{mm}.

The application of the corrected method is executed best by using the initial-stress procedure in which equation (5) is replaced by equation (10). The difference between the numerical results of the original initial-stress method and the second-order correction method may be negligible where the loading mode is close to proportional loading. However, the difference becomes considerable for loading cases with large rotation and shear stresses. Fig. 1 shows the numerical results of a comparison study involving a two-dimensional plane-strain beam of short dimensions, where the computation involved one large load increment. The figure shows the values of the effective stress and strain in a critical element at the consecutive iterations. Similar diagrams can be drawn for the components of the stress and strain tensors. As seen in the figure, the difference between the plastic deformation values reaches about 33 percent.

References

1 Nayak, G. C., and Zienkiewicz, O. C., "Elasto-Plastic Stress Analysis," *International Journal for Num. Meth. Engng.*, Vol. 5, 1972, pp. 113–135.

2 Marcal, P. V., and King, I. P., "Elastic-Plastic Analysis of Two-Dimensional Stress Systems by the Finite-Element Method," *International Journal of Mechanical Sciences*, Vol. 9, 1967, pp. 143–155.

3 Zienkiewicz, O. C., *The Finite-Element Method*, 3rd ed., McGraw-Hill, London, 1977.

4 Yamada, Y., Yoshimura, N., and Sakurai, T., "Plastic Stress-Strain Matrix and Its Application for the Solution of Elastic-Plastic Problems by the Finite-Element Method," *International Journal of Mechanical Sciences*, Vol. 10, 1968, pp. 343–354.

Thermal-Stress Singularities at the Ends of a Thin Elastic Stiffener Bonded to a Semi-Infinite Medium

O. Tamate,[1] H. Sekine,[2] and T. Hanazawa[3]

Introduction

The first analytical study of the problem of a thin stiffener of finite length bonded to a half plane was made by Bufler [1]. Although he discussed the diffusion of load from the stiffener to the half plane, the stress singularities at the ends of the stiffener were not studied.

With the progress of linear fracture mechanics, the stress singularities at the ends of an elastic stiffener bonded to a half plane have received considerable attention. In this field, Arutiunian [2] discussed the contact stresses between an elastic stiffener of finite length and a half plane, and showed that the stress singularity at the end of the stiffener is of the order $r^{-1/2}$, where r is radial distance from the end of the stiffener. In recent years, Erdogan and Gupta [3] have reconsidered the same problem by using the rather simple Erdogan's method [4], and the numerical examples have been given for the strength of the stress singularity and the contact stresses.

When a heat flow transferred in a semi-infinite medium is disturbed by the presence of a thin elastic stiffener of finite length bonded to a semi-infinite medium, large thermal stresses arise in the neighborhood of the ends of the stiffener. Thermal stresses of this kind may in some cases cause serious damage to structures. Consequently, the study of the thermal stresses in the vicinity of the ends of the stiffener is of great practical importance. In this Note, the thermal-stress singularities at the ends of a thin elastic stiffener are considered by using the steady-state two-dimensional theory of linear thermoelasticity. The analysis is based on the singular point method extended to the thermoelastic stiffener problem. Some numerical calculations

[1] Professor, Department of Mechanical Engineering, Tohoku University, Sendai, Japan.

[2] Instructor, Department of Mechanical Engineering, Tohoku University, Sendai, Japan.

[3] Graduate Student, Department of Mechanical Engineering, Tohoku University, Sendai, Japan. Presently, Kawasaki Steel Corp., Kobe, Japan.

Manuscript received by ASME Applied Mechanics Division, July, 1979; final revision, October, 1979.

Copyright © 1980 by ASME
Downloaded 01 May 2010 to 171.66.16.243. Redistribution subject to ASME license or copyright; see http://www.asme.org/terms/Terms_Use.cfm

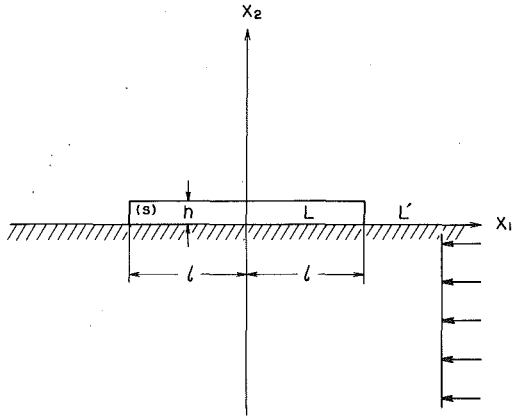

Fig. 1 Configuration and coordinate system

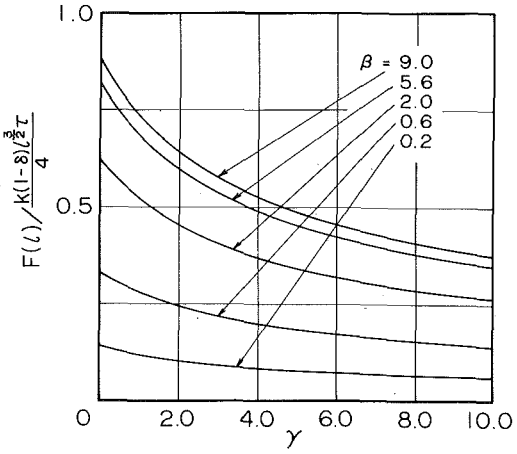

Fig. 2 Strength $F(l)$ of the thermal-stress singularity against β and γ for $c = 0$

are carried out for the strength of the thermal-stress singularity and the results are shown in graphs.

Mathematical Formulation of the Problem

Consider a thin elastic stiffener of uniform thickness h bonded to a semi-infinite elastic medium, homogeneous and isotropic, under uniform heat flow (Fig. 1). The bonding region is denoted by L ($|x_1| \leqq l, x_2 = 0$). The surface of the stiffener and the remaining surface L' ($|x_1| > l, x_2 = 0$) are thermally insulated and free from tractions. The semi-infinite medium is assumed to obey Fourier's law of heat conduction and the Duhamel-Neumann relation. For plane deformation, the material constants are

$$\mu = E/2(1+\nu), \quad \kappa = 3 - 4\nu, \quad \lambda, \quad k = E\alpha/(1-\nu). \tag{1}$$

where E is Young's modulus, ν Poisson's ratio, λ the thermal conductivity, and α the thermal expansion coefficient.

The elastic stiffener is thin and the bending stiffness of the stiffener is assumed to be negligible. Since the surface of the stiffener is thermally insulated and free from tractions, the heat flux $q_2^{(s)}$ and the stress component $t_{22}^{(s)}$ are supposed to be zero everywhere in the stiffener. In what follows, the superscript (s) will refer to quantities associated with the stiffener.

On the bonding region L, the continuity conditions for temperature T and displacement component u_1 give

$$T_{,1} = T^{(s)}{}_{,1}, \quad u_{1,1} = u_1{}^{(s)}{}_{,1}. \tag{2}$$

It should be noted that the equilibrium equation of the stress component $t_{11}{}^{(s)}$ and the tangential force acting on the surface of the stiffener is used instead of the continuity condition for the shear stress component, because the elastic stiffener is thin. On the surface L', $q_2 = 0$ and $t_{22} = t_{12} = 0$:

$$\theta'(x_1) - \overline{\theta'(x_1)} = 0, \quad \Phi(x_1) + \overline{\Phi(x_1)} + x_1\overline{\Phi'(x_1)} + \overline{\Psi(x_1)} = 0 \tag{3}$$

where $\theta(z)$ is the temperature potential function and $\Phi(z)$ and $\Psi(z)$ are the elastic potential functions [5]. At infinity in the semi-infinite medium, $T_{,1} = \tau$, $T_{,2} = 0$, and $t_{11} = t_{22} = t_{12} = 0$:

$$\theta(z) = \tau z + c + O(z^{-1}) \quad \text{and}$$
$$\Phi(z), \Psi(z) = O(z^{-1}) \quad \text{as} \quad |z| \to \infty \tag{4}$$

where τ is the temperature gradient of the uniform heat flow and c is the constant temperature increment from the temperature corresponding to the stress-free state of the medium.

To solve this problem, the singular point method is extended to be applicable to the thermoelastic stiffener problem. Simulating the heat flux and contact stress between the stiffener and the semi-infinite medium by the continuous distributions of line heat sources and concentrated forces, we obtain a system of singular integral equations for density functions. The solution is assumed in the form of the product of a series of Chebyshev polynomials of the first kind and their weight function and is determined by transforming the singular integral equations into linear algebraic equations.

Strength of Thermal-Stress Singularity

With the local coordinate system

$$z = l + re^{i\omega} \quad (r > 0, \pi \leqq \omega < 2\pi), \tag{5}$$

the singular behavior of the thermal stresses at the end $z = l$ of the thin elastic stiffener is given by

$$t_{11} = \frac{F}{(2r)^{1/2}} \cos\frac{\omega}{2}\left(2 - \sin\frac{\omega}{2}\sin\frac{3}{2}\omega\right),$$
$$t_{22} = \frac{F}{(2r)^{1/2}} \cos\frac{\omega}{2}\sin\frac{\omega}{2}\sin\frac{3}{2}\omega, \tag{6}$$
$$t_{12} = \frac{F}{(2r)^{1/2}} \sin\frac{\omega}{2}\left(1 + \cos\frac{\omega}{2}\cos\frac{3}{2}\omega\right)$$

where F is the strength of the thermal-stress singularity. On the other hand, by using the coordinate system

$$z = -l + re^{i(\pi+\omega)} \quad (r > 0, 0 < \omega \leqq \pi), \tag{7}$$

the singular behavior of the thermal stresses at the other end $z = -l$ can be also written in the same form of (6).

Numerical Results and Discussion

Numerical calculations were carried out for the strength of the thermal-stress singularity. The results are plotted in terms of nondimensional parameters, consisting of the dimensions of the stiffener and the material constants of the stiffener and semi-infinite medium, as follows:

$$\beta = \frac{2\lambda l}{\lambda^{(s)}h}, \quad \gamma = \frac{\mu(1+\kappa^{(s)})l}{2\mu^{(s)}(1+\kappa)h}. \tag{8}$$

The infinite system of linear algebraic equations can be solved by the method of reduction, since the system is regular. The computation reveals that the convergence becomes slower with increasing β and γ. With $\tau \neq 0$ and $c = 0$, an example is shown in Table 1, which gives the values of

$$F(l) \Big/ \frac{k(1-\delta)\tau l^{3/2}}{4} \quad \left(\text{where} \quad \delta = \frac{\mu(1+\kappa^{(s)})k^{(s)}}{\mu^{(s)}(1+\kappa)k}\right)$$

against the number of unknowns N for the combination of two values 0.2 and 1.2 of β and γ.

Fig. 2 shows the variation of the strength $F(l)$ of the thermal-stress singularity against the parameters β and γ for the case of $\tau \neq 0$ and $c = 0$. As can be seen, the strength $F(l)$ decreases monotonically as

Downloaded 01 May 2010 to 171.66.16.243. Redistribution subject to ASME license or copyright; see http://www.asme.org/terms/Terms_Use.cfm

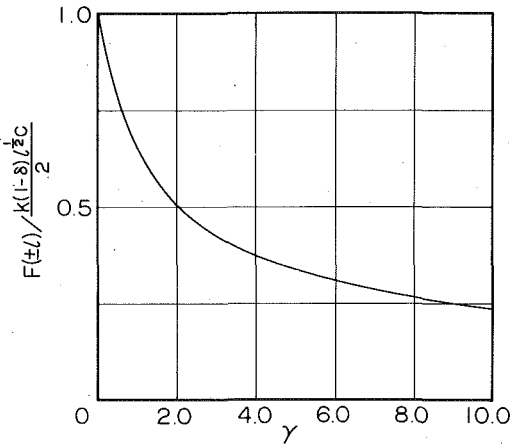

Fig. 3 Strength $F(\pm l)$ of the thermal-stress singularity against γ for $\tau = 0$

the parameter γ increases, and the tendency is marked as β is larger. The strength $F(l)$ is zero for $\gamma = \infty$, because there is no effect of the stiffener on the thermal stresses in the semi-infinite medium. When $\beta = 0$, $F(l)$ is zero. This may be understood from the fact that if $c = 0$ and $\beta = 0$, the temperature increment is zero along the length of the stiffener. It is really seen that we have $F(l) = -F(-l)$ when $\tau \neq 0$, $c = 0$.

Table 1 Dependence of the speed of convergence on β and γ for $c = 0$

N	β = 0.2 γ = 0.2	β = 1.2 γ = 0.2	β = 0.2 γ = 1.2	β = 1.2 γ = 1.2
6	0.138 396	0.479 603	0.114 684	0.397 942
10	0.138 627	0.480 401	0.115 914	0.402 211
20	0.138 737	0.480 780	0.116 483	0.404 187
30	0.138 759	0.480 856	0.116 595	0.404 576

Fig. 3 corresponds to the case of $\tau = 0$ and $c \neq 0$. In this case, the strength is independent of the parameter β, since heat is not transferred within the stiffener. It can be recognized from Fig. 3 that the strength $F(\pm l)$ tends to zero monotonically with increasing γ. When $\gamma = 0$, we have $F(\pm l) = k(1 - \delta)l^{1/2}c/2$.

References

1 Bufler, H., "Scheibe mit endlicher, elastischer Versteifung," *VDI-Forschungsheft*, Vol. 485, 1961.

2 Arutiunian, N. Kh., "Contact Problem for a Half Plane With Elastic Reinforcement," *Journal of Applied Mathematics and Mechanics*, Vol. 32, 1968, pp. 652–665.

3 Erdogan, F., and Gupta, G. D., "The Problem of an Elastic Stiffener Bonded to a Half Plane," ASME JOURNAL OF APPLIED MECHANICS, Vol. 38, 1971, pp. 937–941.

4 Erdogan, F., "Approximate Solutions of Systems of Singular Integral Equations," *SIAM Journal of Applied Mathematics*, Vol. 17, 1969, pp. 1041–1059.

5 Bogdanoff, J. L., "Note on Thermal Stresses," ASME JOURNAL OF APPLIED MECHANICS, Vol. 21, 1954, p. 88.

On Optimal Imperfect Columns Subjected to Linear Creep Buckling

R. Wojdanowska[1] and M. Życzkowski[2]

There exist various approaches to theoretical description of creep buckling phenomenon. The first theories (Freudenthal, Rzhanitsyn, Kempner, Hoff) considered imperfect columns and analyzed the increase of deflections in time; the Rabotnov-Shesterikov theory and some related approaches discussed the stability of perfectly straight columns.

The present authors determined in [1] the optimal shape of a perfectly straight column subject to creep buckling as described by the Rabotnov-Shesterikov theory. Moreover, Wojdanowska analyzed in [2] optimal imperfect columns subject to linear creep of Maxwell's type. According to the classification given in [3], this optimization pertains rather to a stiffness constraint than to stability (minimal volume for a given logarithmic velocity of buckling). A certain analogy with elastic optimization was established: it is valid for imperfect columns with such initial deflection lines which preserve their shape in the course of creep buckling (proportional increase, modal creep buckling). The present Note generalizes that analogy for arbitrary linear creep law with time-dependent coefficients.

Assume the following uniaxial creep law:

$$f_1(t)\dot{\epsilon} + f_2(t)\epsilon = f_3(t)\dot{\sigma} + f_4(t)\sigma, \tag{1}$$

where ϵ and σ denote normal strain and normal stress, respectively, $f_j(t)$ are non-negative functions of time t and dots denote differentiation with respect to t. If all $f_j(t)$ are constant, then (1) turns into the standard material (Prager-Hohenemser); time-dependence of coefficients takes possible aging effects into account.

The Bernoulli hypothesis of plane sections results in the following linear strain distribution in a cross section of a slightly curved bar:

$$\epsilon = \kappa(z - z_0), \tag{2}$$

where the coordinate z is measured from the centroidal axis, κ denotes the curvature increment and in a linearized treatment amounts

$$\kappa = -(w'' - w_-''), \tag{3}$$

$w_- = w_-(x)$ determines the initial deflection line, before loading (column imperfection), and dashes denote differentation with respect to the spatial variable x. Substitute (2) into (1), multiply the whole equation by z and integrate over the cross-sectional area; one obtains then

$$f_1(t)I\dot{\kappa} + f_2(t)I\kappa = f_3(t)\dot{M} + f_4(t)M, \tag{4}$$

where $I = I(x)$ denotes the moment of inertia of the cross section, and $M = M(x,t)$—the bending moment.

Consider a column compressed by a concentrated force $P(t) = PH(t)$, where H denotes Heaviside's function, and assume the system of coordinates in such a way as to obtain

$$M = Pw. \tag{5}$$

Equation (5) holds not only in the simplest case of a column clamped at one end and compressed by a force preserving fixed direction, but it comprises also more complicated cases (cf. Gajewski and Życzkowski [4]). Of course, some kinds of support do not allow to use (5), e.g., those who lead to bimodal optimization (Olhoff and Rasmussen [5]), and such problems will not be considered here. Substitution of (5) and (3) into (4) leads to the following governing equation, valid for $t > 0$:

$$f_1(t)I\dot{w}'' + f_2(t)I(w'' - w_-'') + f_3(t)P\dot{w} + f_4(t)Pw = 0. \tag{6}$$

Now we confine our consideration to such initial deflection lines w_-

[1] Adjunct, Institute of Mechanics and Machine Design, Politechnika Krakowska, Kraków, Poland.

[2] Professor, Institute of Mechanics and Machine Design, Politechnika Krakowska, Kraków, Poland.

Manuscript received by ASME Applied Mechanics Division, April, 1979; final revision, October, 1979.

Downloaded 01 May 2010 to 171.66.16.243. Redistribution subject to ASME license or copyright; see http://www.asme.org/terms/Terms_Use.cfm

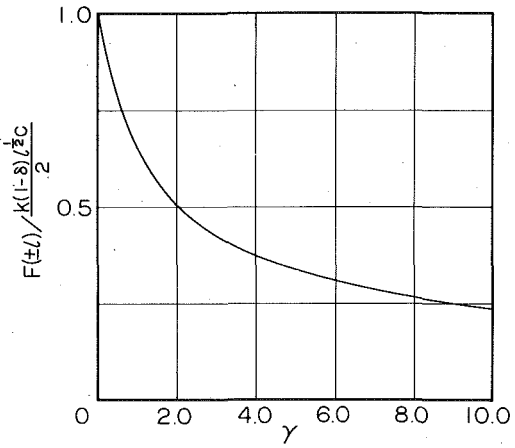

Fig. 3 Strength $F(\pm l)$ of the thermal-stress singularity against γ for $\tau = 0$

the parameter γ increases, and the tendency is marked as β is larger. The strength $F(l)$ is zero for $\gamma = \infty$, because there is no effect of the stiffener on the thermal stresses in the semi-infinite medium. When $\beta = 0$, $F(l)$ is zero. This may be understood from the fact that if $c = 0$ and $\beta = 0$, the temperature increment is zero along the length of the stiffener. It is really seen that we have $F(l) = -F(-l)$ when $\tau \neq 0$, $c = 0$.

Table 1 Dependence of the speed of convergence on β and γ for $c = 0$

N	β = 0.2 γ = 0.2	β = 1.2 γ = 0.2	β = 0.2 γ = 1.2	β = 1.2 γ = 1.2
6	0.138 396	0.479 603	0.114 684	0.397 942
10	0.138 627	0.480 401	0.115 914	0.402 211
20	0.138 737	0.480 780	0.116 483	0.404 187
30	0.138 759	0.480 856	0.116 595	0.404 576

Fig. 3 corresponds to the case of $\tau = 0$ and $c \neq 0$. In this case, the strength is independent of the parameter β, since heat is not transferred within the stiffener. It can be recognized from Fig. 3 that the strength $F(\pm l)$ tends to zero monotonically with increasing γ. When $\gamma = 0$, we have $F(\pm l) = k(1 - \delta)l^{1/2}c/2$.

References

1 Bufler, H., "Scheibe mit endlicher, elastischer Versteifung," *VDI-Forschungsheft*, Vol. 485, 1961.

2 Arutiunian, N. Kh., "Contact Problem for a Half Plane With Elastic Reinforcement," *Journal of Applied Mathematics and Mechanics*, Vol. 32, 1968, pp. 652–665.

3 Erdogan, F., and Gupta, G. D., "The Problem of an Elastic Stiffener Bonded to a Half Plane," ASME JOURNAL OF APPLIED MECHANICS, Vol. 38, 1971, pp. 937–941.

4 Erdogan, F., "Approximate Solutions of Systems of Singular Integral Equations," *SIAM Journal of Applied Mathematics*, Vol. 17, 1969, pp. 1041–1059.

5 Bogdanoff, J. L., "Note on Thermal Stresses," ASME JOURNAL OF APPLIED MECHANICS, Vol. 21, 1954, p. 88.

On Optimal Imperfect Columns Subjected to Linear Creep Buckling

R. Wojdanowska[1] and M. Życzkowski[2]

There exist various approaches to theoretical description of creep buckling phenomenon. The first theories (Freudenthal, Rzhanitsyn, Kempner, Hoff) considered imperfect columns and analyzed the increase of deflections in time; the Rabotnov-Shesterikov theory and some related approaches discussed the stability of perfectly straight columns.

The present authors determined in [1] the optimal shape of a perfectly straight column subject to creep buckling as described by the Rabotnov-Shesterikov theory. Moreover, Wojdanowska analyzed in [2] optimal imperfect columns subject to linear creep of Maxwell's type. According to the classification given in [3], this optimization pertains rather to a stiffness constraint than to stability (minimal volume for a given logarithmic velocity of buckling). A certain analogy with elastic optimization was established: it is valid for imperfect columns with such initial deflection lines which preserve their shape in the course of creep buckling (proportional increase, modal creep buckling). The present Note generalizes that analogy for arbitrary linear creep law with time-dependent coefficients.

Assume the following uniaxial creep law:

$$f_1(t)\dot{\epsilon} + f_2(t)\epsilon = f_3(t)\dot{\sigma} + f_4(t)\sigma, \tag{1}$$

where ϵ and σ denote normal strain and normal stress, respectively, $f_j(t)$ are non-negative functions of time t and dots denote differentiation with respect to t. If all $f_j(t)$ are constant, then (1) turns into the standard material (Prager-Hohenemser); time-dependence of coefficients takes possible aging effects into account.

The Bernoulli hypothesis of plane sections results in the following linear strain distribution in a cross section of a slightly curved bar:

$$\epsilon = \kappa(z - z_0), \tag{2}$$

where the coordinate z is measured from the centroidal axis, κ denotes the curvature increment and in a linearized treatment amounts

$$\kappa = -(w'' - w_-''), \tag{3}$$

$w_- = w_-(x)$ determines the initial deflection line, before loading (column imperfection), and dashes denote differentation with respect to the spatial variable x. Substitute (2) into (1), multiply the whole equation by z and integrate over the cross-sectional area; one obtains then

$$f_1(t)I\dot{\kappa} + f_2(t)I\kappa = f_3(t)\dot{M} + f_4(t)M, \tag{4}$$

where $I = I(x)$ denotes the moment of inertia of the cross section, and $M = M(x,t)$—the bending moment.

Consider a column compressed by a concentrated force $P(t) = PH(t)$, where H denotes Heaviside's function, and assume the system of coordinates in such a way as to obtain

$$M = Pw. \tag{5}$$

Equation (5) holds not only in the simplest case of a column clamped at one end and compressed by a force preserving fixed direction, but it comprises also more complicated cases (cf. Gajewski and Życzkowski [4]). Of course, some kinds of support do not allow to use (5), e.g., those who lead to bimodal optimization (Olhoff and Rasmussen [5]), and such problems will not be considered here. Substitution of (5) and (3) into (4) leads to the following governing equation, valid for $t > 0$:

$$f_1(t)I\dot{w}'' + f_2(t)I(w'' - w_-'') + f_3(t)P\dot{w} + f_4(t)Pw = 0. \tag{6}$$

Now we confine our consideration to such initial deflection lines w_-

[1] Adjunct, Institute of Mechanics and Machine Design, Politechnika Krakowska, Kraków, Poland.

[2] Professor, Institute of Mechanics and Machine Design, Politechnika Krakowska, Kraków, Poland.

Manuscript received by ASME Applied Mechanics Division, April, 1979; final revision, October, 1979.

Copyright © 1980 by ASME
Downloaded 01 May 2010 to 171.66.16.243. Redistribution subject to ASME license or copyright; see http://www.asme.org/terms/Terms_Use.cfm

$= w_-(x)$ which preserve their shape during buckling; the effective shape of such deflection lines will be determined later. Thus we substitute

$$w(x,t) = w_-(x)T(t) \tag{7}$$

and separate the variables in (6) as follows:

$$-\frac{I(x)w_-''(x)}{w_-(x)} = \frac{Pf_3(t)\dot{T}(t) + Pf_4(t)T(t)}{f_1(t)\dot{T}(t) + f_2(t)[T(t) - 1]} = k^2 > 0. \tag{8}$$

The second part of this equation may be written in the form

$$\frac{\dot{T}}{T} = \frac{Pf_4(t) - k^2 f_2(t)}{k^2 f_1(t) - Pf_3(t)} + \frac{f_2(t)}{\left[f_1(t) - \dfrac{Pf_3(t)}{k^2}\right]T}. \tag{9}$$

To avoid instanteneous buckling at any time t we impose the following constraint on the force P:

$$P < \frac{k^2 f_1(t)}{f_3(t)} \text{ for any } t \geq 0. \tag{10}$$

Under this constraint it is seen that $\dot{T}/T$ (logarithmic velocity of buckling) is a monotonically decreasing function of k^2, hence k^2 may be regarded as a parameter responsible for the column stiffness.

The problem of optimal design is now formulated as follows. For a given stiffness parameter k^2 and for a given force P determine the shape of the column furnishing the minimal volume

$$V = \int_0^L A(x)dx \to \min. \tag{11}$$

In most practical cases of variable cross section we can express the cross-sectional area $A(x)$ in terms of the moment of inerita $I(x)$ as follows:

$$A = cI^q, \tag{12}$$

where the exponent q equals $q = \frac{1}{2}$ for spatially uniformly tapered bars (e.g., rotationally symmetric shapes, pyramides, etc.), $q = 1$ or $q = \frac{1}{3}$ for plane-tapered bars, depending on the direction of buckling. The moment of inertia may be determined from the first part of equation (8):

$$I(x) = -k^2 \frac{w_-(x)}{w_-''(x)}. \tag{13}$$

Substituting (13) into (12) and then into (11) we arrive at unconstrained minimization of the functional

$$V = ck^{2q} \int_0^L \left[-\frac{w_-(x)}{w_-''(x)}\right]^q dx, \tag{14}$$

which is equivalent to optimization of elastic columns. Particular solutions to that problem for a general conservative behaviour of loading were given in [4]. Having determined the function w_- minimizing (14), we find the optimal shape of the column from (13).

Now we have to show that the deflection line after the application of the force $w_+ = w_+(x)$, which furnishes the initial condition for the equation (6), is also proportional to $w_-(x)$ before application of the loading. These two deflection lines are interrelated by Hooke's law, and for slightly curved bars it results in the equation

$$EI(w_+'' - w_-'') + Pw_+ = 0, \tag{15}$$

where E is the instanteneous elastic modulus, $E = f_1(0)/f_3(0)$. Indeed, substituting (13) into (15) we obtain

$$-Ek^2 w_-(w_+'' - w_-'') + Pw_-'' w_+ = 0 \tag{16}$$

and it is seen that these equation is satisfied by the function $w_+(x) = Cw_-(x)$, where

$$C = \frac{Ek^2}{Ek^2 - P}. \tag{17}$$

This constant is positive by virtue of (10) and hence the required proportionality of w_- and w_+ is proved.

It should be emphasized, however, that these simple solutions hold only for the initial deflection lines $w_-(x)$ determined by the variational problem (14), since they insure the modal creep buckling. For other initial deflection lines the optimization problem may be much more difficult.

References

1 Życzkowski, M., and Wojdanowska-Zajac R., "Optimal Structural Design With Respect to Creep Buckling," IUTAM Symposium Creep in Structures II, 1970, Springer, 1972, pp. 371–387.

2 Wojdanowska R., "Optimal Design of Weakly Curved Compressed Bars With Maxwell-Type Creep Effects," *Arch. Mech. Stos.*, Vol. 30, No. 6, 1978, pp. 845–851.

3 Życzkowski, M., "Optimal Structural Design in Rheology," ASME JOURNAL OF APPLIED MECHANICS, Vol. 38, 1971, pp. 39–45.

4 Gajewski, A., and Życzkowski, M. "Optimal Design of Elastic Columns Subject to the General Conservative Behavior of Loading," *Zeitschrift für angewandte Mathematik und Physik*, Vol. 21, No. 5, 1970, pp. 806–818.

5 Olhoff, N., and Rasmussen, S. H., "On Single and Bimodal Optimum Buckling Loads of Clamped Columns, "*International Journal of Solids and Structures*, Vol. 13, 1977. pp. 605–614.

Constitutive Equations for Rate-Independent, Isotropic, Elastic-Plastic Solids Exhibiting Pressure-Sensitive Yielding and Plastic Dilatancy

L. Anand[1]

The purpose of this Note is to propose a set of special, approximate constitutive equations for large deformations of rate-independent, isotropic, elastic-plastic solids which may exhibit pressure-sensitive yielding and plastic dilatancy.

We limit ourselves to mechanical considerations and assume that the Cauchy stress $\mathbf{T}$ is determined by the deformation gradient $\mathbf{F}$, $\det \mathbf{F} > 0$, and a list $\mathbf{I}_n$ of n plastic variables:

$$\mathbf{T} = \bar{\mathbf{T}}(\mathbf{F}, \mathbf{I}_n). \tag{1}$$

For the simple phenomenological theory to be formulated, we choose the list of these plastic variables to be the pair

$$(\mathbf{F}^p, \gamma) \quad \text{with} \quad \det \mathbf{F}^p > 0 \quad \text{and} \quad \gamma \geq 0. \tag{2}$$

As usual [1], $\mathbf{F}^p$ is the plastic deformation gradient and it is assumed that the local configuration determined by $\mathbf{F}^p$ is stress-free. The scalar γ represents a scalar memory of prior plastic flow.

We define the elastic deformation gradient by [1]

$$\mathbf{F}^e := \mathbf{F}(\mathbf{F}^p)^{-1}, \quad \det \mathbf{F}^e > 0. \tag{3}$$

Further, we write

$$\delta := \det \mathbf{F}^p > 0 \tag{4}$$

for the plastic dilation, and assume henceforth that the constitutive equations considered here depend on the list

$$(\mathbf{F}^e, \delta, \gamma), \tag{5}$$

or any suitable variables which might be determined by this list.[2]

Equation (1) may now be written in the special form

$$\mathbf{T} = \hat{\mathbf{T}}(\mathbf{F}^e, \delta, \gamma), \quad \text{with} \quad \hat{\mathbf{T}}(\mathbf{I}, \delta, \gamma) = \mathbf{0}. \tag{6}$$

[1] United States Steel Corporation, Research Laboratory, Monroeville, Pa. 15146.

[2] For example, the stress measure $\bar{\mathbf{T}}$ to be defined in (8).

Manuscript received by ASME Applied Mechanics Division, April, 1979; final revision, February , 1980.

Downloaded 01 May 2010 to 171.66.16.243. Redistribution subject to ASME license or copyright; see http://www.asme.org/terms/Terms_Use.cfm

$= w_-(x)$ which preserve their shape during buckling; the effective shape of such deflection lines will be determined later. Thus we substitute

$$w(x,t) = w_-(x)T(t) \tag{7}$$

and separate the variables in (6) as follows:

$$-\frac{I(x)w_-''(x)}{w_-(x)} = \frac{Pf_3(t)\dot{T}(t) + Pf_4(t)T(t)}{f_1(t)\dot{T}(t) + f_2(t)[T(t) - 1]} = k^2 > 0. \tag{8}$$

The second part of this equation may be written in the form

$$\frac{\dot{T}}{T} = \frac{Pf_4(t) - k^2 f_2(t)}{k^2 f_1(t) - Pf_3(t)} + \frac{f_2(t)}{\left[f_1(t) - \dfrac{Pf_3(t)}{k^2}\right]T}. \tag{9}$$

To avoid instanteneous buckling at any time t we impose the following constraint on the force P:

$$P < \frac{k^2 f_1(t)}{f_3(t)} \text{ for any } t \geq 0. \tag{10}$$

Under this constraint it is seen that $\dot{T}/T$ (logarithmic velocity of buckling) is a monotonically decreasing function of k^2, hence k^2 may be regarded as a parameter responsible for the column stiffness.

The problem of optimal design is now formulated as follows. For a given stiffness parameter k^2 and for a given force P determine the shape of the column furnishing the minimal volume

$$V = \int_0^L A(x)dx \to \min. \tag{11}$$

In most practical cases of variable cross section we can express the cross-sectional area $A(x)$ in terms of the moment of inerita $I(x)$ as follows:

$$A = cI^q, \tag{12}$$

where the exponent q equals $q = \frac{1}{2}$ for spatially uniformly tapered bars (e.g., rotationally symmetric shapes, pyramides, etc.), $q = 1$ or $q = \frac{1}{3}$ for plane-tapered bars, depending on the direction of buckling. The moment of inertia may be determined from the first part of equation (8):

$$I(x) = -k^2 \frac{w_-(x)}{w_-''(x)}. \tag{13}$$

Substituting (13) into (12) and then into (11) we arrive at unconstrained minimization of the functional

$$V = ck^{2q} \int_0^L \left[-\frac{w_-(x)}{w_-''(x)}\right]^q dx, \tag{14}$$

which is equivalent to optimization of elastic columns. Particular solutions to that problem for a general conservative behaviour of loading were given in [4]. Having determined the function w_- minimizing (14), we find the optimal shape of the column from (13).

Now we have to show that the deflection line after the application of the force $w_+ = w_+(x)$, which furnishes the initial condition for the equation (6), is also proportional to $w_-(x)$ before application of the loading. These two deflection lines are interrelated by Hooke's law, and for slightly curved bars it results in the equation

$$EI(w_+'' - w_-'') + Pw_+ = 0, \tag{15}$$

where E is the instanteneous elastic modulus, $E = f_1(0)/f_3(0)$. Indeed, substituting (13) into (15) we obtain

$$-Ek^2 w_-(w_+'' - w_-'') + Pw_-'' w_+ = 0 \tag{16}$$

and it is seen that these equation is satisfied by the function $w_+(x) = Cw_-(x)$, where

$$C = \frac{Ek^2}{Ek^2 - P}. \tag{17}$$

This constant is positive by virtue of (10) and hence the required proportionality of w_- and w_+ is proved.

It should be emphasized, however, that these simple solutions hold only for the initial deflection lines $w_-(x)$ determined by the variational problem (14), since they insure the modal creep buckling. For other initial deflection lines the optimization problem may be much more difficult.

References

1 Życzkowski, M., and Wojdanowska-Zajac R., "Optimal Structural Design With Respect to Creep Buckling," IUTAM Symposium Creep in Structures II, 1970, Springer, 1972, pp. 371–387.

2 Wojdanowska R., "Optimal Design of Weakly Curved Compressed Bars With Maxwell-Type Creep Effects," *Arch. Mech. Stos.*, Vol. 30, No. 6, 1978, pp. 845–851.

3 Życzkowski, M., "Optimal Structural Design in Rheology," ASME JOURNAL OF APPLIED MECHANICS, Vol. 38, 1971, pp. 39–45.

4 Gajewski, A., and Życzkowski, M. "Optimal Design of Elastic Columns Subject to the General Conservative Behavior of Loading," *Zeitschrift für angewandte Mathematik und Physik*, Vol. 21, No. 5, 1970, pp. 806–818.

5 Olhoff, N., and Rasmussen, S. H., "On Single and Bimodal Optimum Buckling Loads of Clamped Columns, "*International Journal of Solids and Structures*, Vol. 13, 1977. pp. 605–614.

Constitutive Equations for Rate-Independent, Isotropic, Elastic-Plastic Solids Exhibiting Pressure-Sensitive Yielding and Plastic Dilatancy

L. Anand[1]

The purpose of this Note is to propose a set of special, approximate constitutive equations for large deformations of rate-independent, isotropic, elastic-plastic solids which may exhibit pressure-sensitive yielding and plastic dilatancy.

We limit ourselves to mechanical considerations and assume that the Cauchy stress $\mathbf{T}$ is determined by the deformation gradient $\mathbf{F}$, $\det \mathbf{F} > 0$, and a list $\mathbf{I}_n$ of n plastic variables:

$$\mathbf{T} = \bar{\mathbf{T}}(\mathbf{F}, \mathbf{I}_n). \tag{1}$$

For the simple phenomenological theory to be formulated, we choose the list of these plastic variables to be the pair

$$(\mathbf{F}^p, \gamma) \quad \text{with} \quad \det \mathbf{F}^p > 0 \quad \text{and} \quad \gamma \geq 0. \tag{2}$$

As usual [1], $\mathbf{F}^p$ is the plastic deformation gradient and it is assumed that the local configuration determined by $\mathbf{F}^p$ is stress-free. The scalar γ represents a scalar memory of prior plastic flow.

We define the elastic deformation gradient by [1]

$$\mathbf{F}^e := \mathbf{F}(\mathbf{F}^p)^{-1}, \quad \det \mathbf{F}^e > 0. \tag{3}$$

Further, we write

$$\delta := \det \mathbf{F}^p > 0 \tag{4}$$

for the plastic dilation, and assume henceforth that the constitutive equations considered here depend on the list

$$(\mathbf{F}^e, \delta, \gamma), \tag{5}$$

or any suitable variables which might be determined by this list.[2]

Equation (1) may now be written in the special form

$$\mathbf{T} = \hat{\mathbf{T}}(\mathbf{F}^e, \delta, \gamma), \quad \text{with} \quad \hat{\mathbf{T}}(\mathbf{I}, \delta, \gamma) = \mathbf{0}. \tag{6}$$

[1] United States Steel Corporation, Research Laboratory, Monroeville, Pa. 15146.

[2] For example, the stress measure $\bar{\mathbf{T}}$ to be defined in (8).

Manuscript received by ASME Applied Mechanics Division, April, 1979; final revision, February , 1980.

Copyright © 1980 by ASME

Downloaded 01 May 2010 to 171.66.16.243. Redistribution subject to ASME license or copyright; see http://www.asme.org/terms/Terms_Use.cfm

Let $\mathbf{Q}$ be a time-dependent rotation in a change in frame. The transformation rules for $\mathbf{T}$, $\mathbf{F}$, $\mathbf{F}^p$, $\mathbf{F}^e$, and γ under a change in frame are here taken to be

$$\mathbf{T} \to \mathbf{QTQ}^T, \mathbf{F} \to \mathbf{QF}, \mathbf{F}^p \to \mathbf{F}^p, \mathbf{F}^e \to \mathbf{QF}^e, \gamma \to \gamma. \tag{7}$$

The transformation rule for γ is immediate, and the rules for $\mathbf{T}$ and $\mathbf{F}$ are standard [2]. The transformation rule for $\mathbf{F}^p$ has been recently suggested by Silhavy [3][3] and the rule for $\mathbf{F}^e$ follows from its definition (3) and the rules $(7)_{2,3}$.

By using the foregoing transformation rules, we may obtain various reduced forms for (6). One such form is

$$\bar{\mathbf{T}} = \hat{\bar{\mathbf{T}}}(\mathbf{E}^e, \delta, \gamma), \quad \hat{\bar{\mathbf{T}}}(\mathbf{0}, \delta, \gamma) = \mathbf{0}, \tag{8}$$

with

$$\bar{\mathbf{T}} := (\mathbf{R}^e)^T \mathbf{T}\mathbf{R}^e \quad \text{and} \quad \mathbf{E}^e := \ln \mathbf{U}^e.$$

Here $\mathbf{R}^e$ and $\mathbf{U}^e$ are the rotation and the stretch in the right polar decomposition of $\mathbf{F}^e$.

We now assume that there exists a smooth scalar-valued yield function f such that

$$y = f(\bar{\mathbf{T}}, \delta, \gamma) \leqq 0, \tag{9}$$

and assume further that the evolution of the plastic variables is governed by the rate equations

$$\mathbf{L}^p (:= \dot{\mathbf{F}}^p (\mathbf{F}^p)^{-1}) = \mathbf{A}(\bar{\mathbf{T}}, \delta, \gamma) \overset{*}{y} \mathrm{H}(y) \mathrm{H}(\overset{*}{y}), \tag{$10)_1$}$$

and

$$\dot{\gamma} = \alpha(\bar{\mathbf{T}}, \delta, \gamma) \overset{*}{y} \mathrm{H}(y) \mathrm{H}(\overset{*}{y}). \tag{$10)_2$}$$

Here $\mathrm{H}(\cdot)$ is the Heaviside unit step function, and $\overset{*}{y}$ is the loading rate defined by

$$\overset{*}{y} := \partial_{\bar{\mathbf{T}}} f \cdot \dot{\bar{\mathbf{T}}}. \tag{$10)_3$}$$

A triplet $(\bar{\mathbf{T}}, \delta, \gamma)$ giving a value $y = 0$ in (9) is called an elastic-plastic state. For an elastic-plastic state to remain elastic-plastic during loading the condition

$$\dot{y} = \overset{*}{y} + \dot{\delta} \partial_\delta f + \dot{\gamma} \partial_\gamma f = 0 \tag{11}$$

must hold. Then (11) with the use of (4) and (10) gives the following consistency condition:

$$1 + \delta \operatorname{tr} \mathbf{A} \partial_\delta f + \alpha \partial_\gamma f = 0 \tag{12}$$

between the yield function f and functions $\mathbf{A}$ and α in the evolution equations (10).

Following Hahn [5] we define the local instantaneous symmetry group $\mathcal{S}(\delta, \gamma)$ of an elastic-plastic solid relative to the local (undistorted) configuration determined by $\mathbf{F}^p$ to be the group of all time-independent rotations such that if $\mathbf{Q}_0 \in \mathcal{S}(\delta, \gamma)$ then $\mathbf{F}^p$, $\mathbf{F}^e$, $\mathbf{E}^e$, $\bar{\mathbf{T}}$, and γ transform as

$$\mathbf{F}^p \to \mathbf{Q}_0{}^T \mathbf{F}^p, \mathbf{F}^e \to \mathbf{F}^e \mathbf{Q}_0, \mathbf{E}^e \to \mathbf{Q}_0{}^T \mathbf{E}^e \mathbf{Q}_0, \bar{\mathbf{T}} \to \mathbf{Q}_0{}^T \bar{\mathbf{T}} \mathbf{Q}_0, \gamma \to \gamma. \tag{13}$$

We restrict our attention to solids for which $\mathcal{S}(\delta, \gamma)$ is the full proper orthogonal group for every (δ, γ). Under this assumption the response functions $\hat{\bar{\mathbf{T}}}$, f, $\mathbf{A}$, and α will be isotropic functions.

Hence, upon using a standard representation theorem [2], we find that $(10)_1$ reduces to

$$\left.\begin{aligned} \mathbf{D}^p &= \operatorname{sym} \mathbf{L}^p = \{\phi_0 \mathbf{I} + \phi_1 \bar{\mathbf{T}} + \phi_2 \bar{\mathbf{T}}^2\} \overset{*}{y} \mathrm{H}(y) \mathrm{H}(\overset{*}{y}), \\ \mathbf{W}^p &= \operatorname{skw} \mathbf{L}^p = \mathbf{0}, \end{aligned}\right\} \tag{14}$$

where ϕ_0, ϕ_1, and ϕ_2 are scalar functions of the list

$$l = (\operatorname{tr} \mathbf{T}, \operatorname{tr} \mathbf{T}^2, \operatorname{tr} \mathbf{T}^3, \delta, \gamma). \tag{15}$$

Here we consider the special case $\phi_1 > 0$, $\phi_2 = 0$, and to (14) we add the constitutive assumption[4]

$$\operatorname{tr} \mathbf{D}^p (\equiv \dot{\delta} \delta^{-1}) = \beta \{\sqrt{2} |\mathbf{D}^{p\prime}|\}, \quad \beta = \hat{\beta}(l), \tag{16}$$

where β is called the plastic dilatancy factor [6]. Thus the evolution equation for $\mathbf{F}^p$ (the "flow rule") reduces to

$$\mathbf{D}^p = 2\bar{\tau} \phi_1 \left\{ \frac{\bar{\mathbf{T}}'}{2\bar{\tau}} + \frac{\beta}{3} \mathbf{I} \right\} \overset{*}{y} \mathrm{H}(y) \mathrm{H}(\overset{*}{y}), \tag{17}$$

where

$$\bar{\tau} := \sqrt{(1/2) \bar{\mathbf{T}}' \cdot \bar{\mathbf{T}}'} \tag{18}$$

is the equivalent shear stress.

For the evolution of γ we adopt the common definition

$$\dot{\gamma} := \{\sqrt{2} |\mathbf{D}^{p\prime}|\} \equiv 2\bar{\tau} \phi_1 \overset{*}{y} \mathrm{H}(y) \mathrm{H}(\overset{*}{y}). \tag{19}$$

That is, we take the plastic history parameter γ to be the equivalent plastic shear strain.

From a representation theorem for isotropic scalar functions [2] the yield function f has the representation $f(\bar{\mathbf{T}}, \delta, \gamma) = \bar{f}(l)$. We adopt the following particular form for $\bar{f}$:

$$\bar{f} = \{\bar{\tau} - s(\bar{p}, \delta, \gamma)\}, \quad \bar{p} := -\frac{1}{3} (\operatorname{tr} \bar{\mathbf{T}}). \tag{20}$$

The scalar $\bar{p}$ is called the mean normal pressure, and s is a nonzero, positive-valued smooth function with

$$\left.\begin{aligned} \pi &= \partial_{\bar{p}} s(\bar{p}, \delta, \gamma) =: \hat{\pi}(\bar{p}, \delta, \gamma) \geqq 0, \\ h_1 &= \partial_\delta s(\bar{p}, \delta, \gamma) =: \hat{h}_1(\bar{p}, \delta, \gamma), \\ h_2 &= \partial_\gamma s(\bar{p}, \delta, \gamma) =: \hat{h}_2(\bar{p}, \delta, \gamma). \end{aligned}\right\} \tag{$20)_2$}$$

The parameter π is called the internal friction coefficient, and the parameters h_1 and h_2 are called the plastic volumetric hardening (softening) and the plastic distortional hardening moduli, respectively.

From the assumed yield function (20) and the consistency equation (12) we may solve for ϕ_1 to obtain

$$\phi_1 = (2\bar{\tau} h)^{-1} \quad \text{where} \quad h := (\delta \beta h_1 + h_2). \tag{21}$$

For most applications it suffices to limit ourselves to positive nonzero values of the effective hardening modulus h; that is, to strain-hardening materials.

Upon substituting (21) into (17) and (19) we obtain

$$\mathbf{D}^p = h^{-1} \left\{ \frac{\bar{\mathbf{T}}'}{2\bar{\tau}} + \frac{\beta}{3} \mathbf{I} \right\} \overset{*}{y} \mathrm{H}(y) \mathrm{H}(\overset{*}{y}), \tag{$22)_1$}$$

and

$$\dot{\gamma} = h^{-1} \overset{*}{y} \mathrm{H}(y) \mathrm{H}(\overset{*}{y}), \tag{$22)_2$}$$

where for the yield function (20) the loading rate $\overset{*}{y}$ defined in $(10)_3$ is

$$\overset{*}{y} = \left\{ \frac{\bar{\mathbf{T}}'}{2\bar{\tau}} + \frac{\pi}{3} \mathbf{I} \right\} \cdot \dot{\bar{\mathbf{T}}}. \tag{$22)_3$}$$

It is important to note that the normality flow rule of classical plasticity would correspond to $\beta = \pi$ in (22). It is emphasized that we do not make this assumption.

Henceforth we assume that at each instant the elastic rotation $\mathbf{R}^e$ is arbitrary, while the elastic stretch $\mathbf{U}^e$ is infinitesimal. That is $|\mathbf{U}^e - \mathbf{I}| < \epsilon$, with $0 < \epsilon < 1$.

Then, upon assuming that the stress response function is sufficiently smooth and expanding $\hat{\bar{\mathbf{T}}}(\cdot, \delta, \gamma)$ about $\mathbf{E}^e = \mathbf{0}$ we obtain

[3] Green and Naghdi [4] have proposed the transformation rule $\mathbf{F}^p \to \bar{\mathbf{Q}} \mathbf{F}^p$ where $\bar{\mathbf{Q}}$ is an *arbitrary time-dependent* rotation. However, if we assume this transformation rule then it is easy to show that the plastic power is not invariant under a change in frame.

[4] For any tensor $\mathbf{P}$, $\mathbf{P}' := \{\mathbf{P} - \frac{1}{3} (\operatorname{tr} \mathbf{P}) \mathbf{I}\}$ defines its deviatoric part.

Downloaded 01 May 2010 to 171.66.16.243. Redistribution subject to ASME license or copyright; see http://www.asme.org/terms/Terms_Use.cfm

$$\hat{\bar{\mathbf{T}}} \doteq \mathcal{L}(\delta, \gamma)[\mathbf{E}^e] = 2\mu\mathbf{E}^e + \lambda(\mathrm{tr}\,\mathbf{E}^e)\mathbf{I} \tag{23}$$

to within $\mathbf{o}(\epsilon)$. In writing (23) we have used $(8)_2$, the isotropy of $\bar{\mathbf{T}}$, and a well-known representation theorem [2]. The scalars $\mu = \hat{\mu}(\delta, \gamma)$ and $\lambda = \hat{\lambda}(\delta, \gamma)$ are the Lamé moduli. Taking the material time derivative of (23) we obtain

$$\dot{\bar{\mathbf{T}}} = \mathcal{L}(\delta, \gamma)[\dot{\mathbf{E}}^e] + \dot{\mathcal{L}}(\delta, \gamma)[\mathbf{E}^e]. \tag{24}$$

Under the assumption of small elastic stretches it may be shown that

$$\begin{gathered}\mathbf{E}^e = \mathbf{O}(\epsilon),\\ \dot{\mathbf{E}}^e = (\mathbf{R}^e)^T\mathbf{D}\mathbf{R}^e - \mathbf{D}^p + \mathbf{O}(\epsilon),\\ \Omega := \dot{\mathbf{R}}^e(\mathbf{R}^e)^T = \mathbf{W} - \mathbf{R}^e\mathbf{W}^p(\mathbf{R}^e)^T + \mathbf{O}(\epsilon),\end{gathered} \tag{25}$$

and

$$\begin{aligned}\dot{\bar{\mathbf{T}}} &= (\mathbf{R}^e)^T(\dot{\mathbf{T}} - \Omega\mathbf{T} + \mathbf{T}\Omega)\mathbf{R}^e\\ &= (\mathbf{R}^e)^T\,\mathring{\mathbf{T}}\mathbf{R}^e + \mathbf{O}(\epsilon),\end{aligned}$$

with

$$\mathring{\mathbf{T}} := \dot{\mathbf{T}} - \mathbf{W}\mathbf{T} + \mathbf{T}\mathbf{W}.$$

Here $\mathbf{D} := \mathrm{sym}\,\mathbf{L}$, $\mathbf{W} := \mathrm{skw}\,\mathbf{L}$ and $\mathring{\mathbf{T}}$ are the stretching, the spin and the corotational rate of the Cauchy stress, respectively. In writing the second of $(25)_4$ we have used the important fact that the plastic spin vanishes for isotropic materials, $(14)_2$.

Hence upon using (25) in (24) and $(22)_3$ and neglecting terms of $\mathbf{O}(\epsilon)$ we obtain

$$\mathring{\mathbf{T}} = 2\mu(\mathbf{D} - \mathbf{R}^e\mathbf{D}^p(\mathbf{R}^e)^T) + \lambda(\mathrm{tr}\,\mathbf{D} - \mathrm{tr}\,\mathbf{D}^p)\mathbf{I}, \tag{26}$$

and

$$\mathring{y} = \left\{\frac{\mathbf{T}'}{2\bar{\tau}} + \frac{\pi}{3}\mathbf{I}\right\} \cdot \mathring{\mathbf{T}}. \tag{27}$$

Finally, using $(22)_{1,2}$, (26), and (27), and after some standard manipulations, we may write the particular approximate set of rate constitutive equations proposed here as

$$\left.\begin{aligned}\mathring{\mathbf{T}} &= 2\mu\mathbf{D} + (\kappa - (2/3)\mu)(\mathrm{tr}\,\mathbf{D})\mathbf{I} - g^{-1}\bar{\mathbf{M}}\,\langle \mathbf{M}\cdot\mathbf{D}\rangle\,\mathrm{H}(y),\\ \dot{\gamma} &= g^{-1}\,\langle \mathbf{M}\cdot\mathbf{D}\rangle\,\mathrm{H}(y) \quad \text{and} \quad \dot{\delta} = \delta\beta\dot{\gamma},\end{aligned}\right\} \tag{28}_1$$

where

$$\kappa := (\lambda + (2/3)\mu), \quad g := (h + \mu + \kappa\pi\beta) > 0,$$

$$\bar{\mathbf{M}} := \left(\mu\frac{\mathbf{T}'}{\bar{\tau}} + \kappa\beta\mathbf{I}\right), \quad \mathbf{M} := \left(\mu\frac{\mathbf{T}'}{\bar{\tau}} + \kappa\pi\mathbf{I}\right), \tag{28}_2$$

and $x \mapsto \langle x\rangle$ and $x \mapsto \mathrm{H}(x)$ are *singularity maps* defined by

$$\langle x\rangle = \begin{cases}0 \text{ for } x \leqq 0\\ x \text{ for } x > 0\end{cases} \quad \text{and} \quad \mathrm{H}(x) = \begin{cases}1 \text{ for } x \geqq 0\\ 0 \text{ for } x < 0\end{cases}, \text{ respectively.} \tag{28}_3$$

These constitutive equations, although differing in detail, are of a final form identical to those proposed by Rudnicki and Rice [6] for geological materials.

For the special case of pressure-insensitive yielding and plastic incompressibility ($\pi = \beta = 0$) the constitutive equations reduce to a finite deformation generalization of the classical Prandtl-Reuss constitutive equations. The appropriateness of these special constitutive equations has been amply demonstrated by Richmond, et al. [7], in their comparisons between some experimental observations and the corresponding theoretical (finite-element) predictions. Further, a simple special case[5] of the present set of constitutive equations can take into account the experimental observations of a slight pressure-sensitivity of yielding, and near plastic incompressibility of certain metallic materials [8, 9]. For the general pressure-sensitive and plastically dilatant case, however, the usefulness of these constitutive equations remains to be demonstrated.

Acknowledgments

The author is grateful to Dr. Owen Richmond and Prof. David R. Owen for some extremely valuable discussions.

References

1 Lee, E. H., "Elastic-Plastic Deformation at Finite Strains," ASME JOURNAL OF APPLIED MEHANICS, 1969, Vol. 36, pp. 1–6.

2 Truesdell, C., and Noll, W., "The Nonlinear Field Theories of Mechanics," *Handbuch der Physik*, Vol. III/3, ed., Truesdell, C., Springer-Verlag, Berlin, 1965.

3 Silhavy, M., "On Transformation Laws for Plastic Deformations of Materials With Elastic Range," *Archive for Rational Mechanics and Analysis*, 1977, Vol. 63, n2, pp. 169–182.

4 Green, A. E., and Naghdi, P. M., "Some Remarks on Elastic-Plastic Deformation at Finite Strain," *International Journal of Engineering Science*, 1971, Vol. 9, pp. 1219–1229.

5 Hahn, H. T., "A Finite Deformation Theory of Plasticity," *International Journal of Solids and Structures*, 1974, Vol. 10, pp. 111–121.

6 Rudnicki, J. W., and Rice, J. R., "Conditions for the Localization of Deformation in Pressure Sensitive Dilatant Materials," *Journal of the Mechanics and Physics of Solids*," 1975, Vol. 23, pp. 371–394.

7 Richmond, O., Devenpeck, M. L., and Appleby, E. J., "Large Tensile Deformation of Sheets and Rods: A Comparison of Observations and Predictions," *Proceedings of the Symposium on Formability: Analysis Modeling and Experimentation*, AIME/ASM Fall Meeting, Chicago, October 24–27, 1977.

8 Spitzig, W. A., Sober, R. J., and Richmond, O., "Pressure Dependence of Yielding and Associated Volume Expansion in Tempered Martensite," *Acta Metallurgica*, 1975, Vol. 23, pp. 885–893.

9 Spitzig, W. A., Sober, R. J., and Richmond, O., "The Effect of Hydrostatic Pressure on the Deformation Behavior of Maraging and HY-80 Steels and Its Implications for Plasticity Theory," *Metallurgical Transactions*, 1976, Vol. 7A, pp. 1703–1710.

On Stress-Intensity Factors for Circumferentially Cracked Circular Cylinders

Tsu-Tao Loo[1]

A long circular cylinder with circumferential notch as shown in Fig. 1 is one of the preferable geometries for test specimens used in the material fracture-toughness testing. In the presence of a circumferential notch, the crack tip of the specimen is in a triaxial state of stress, so that it is more apt to develop brittle fracture. However, even if the cylinder is under simple tension, an exact solution for such cylinder remains very difficult to obtain. Consequently, the prevailing expressions of the stress-intensity factors for these specimens are formulated approximately by an asymptotic interpolation approach, based on the results of two limiting cases [1, 2]. They lack rigorous theoretical bases. More recently, the problem has been treated again by approximate numerical analysis [3]. Differing from all the previous works, the present paper treats the problem by using some physical approximation. An explicit formula of stress-intensity factor for such a cylinder is thus derived for the first time. In this paper, instead of free boundary conditions on the lateral surface of the cylinder, some self-equilibrated residual stresses are allowed to be present. Such an approximation is justified as far as the calculation of stress-intensity factors is concerned. This is so because the self-equilibrated stresses are extremely small indeed in the case of shallow notch, while in the

[5] This special case corresponds to the plastic dilatancy factor β taking the value $\beta = 0$ and the function s in the yield function $(20)_1$ taking the form $s(\bar{p}, \delta, \gamma) = \pi\bar{p} + \bar{s}(\gamma)$ where π is a constant internal friction coefficient and $\bar{s}$ is a function of the equivalent plastic shear strain γ alone.

[1] Shanghai Chiao-Tung University, Department of Engineering Mechanics, Shanghai 200030, The People's Republic of China.

Manuscript received by ASME Applied Mechanics Division, September, 1979; final revision, February, 1980.

Downloaded 01 May 2010 to 171.66.16.243. Redistribution subject to ASME license or copyright; see http://www.asme.org/terms/Terms_Use.cfm

$$\hat{\bar{\mathbf{T}}} \doteq \mathcal{L}(\delta, \gamma)[\mathbf{E}^e] = 2\mu\mathbf{E}^e + \lambda(\mathrm{tr}\,\mathbf{E}^e)\mathbf{I} \tag{23}$$

to within $\mathbf{o}(\epsilon)$. In writing (23) we have used $(8)_2$, the isotropy of $\bar{\mathbf{T}}$, and a well-known representation theorem [2]. The scalars $\mu = \hat{\mu}(\delta, \gamma)$ and $\lambda = \hat{\lambda}(\delta, \gamma)$ are the Lamé moduli. Taking the material time derivative of (23) we obtain

$$\dot{\bar{\mathbf{T}}} = \mathcal{L}(\delta, \gamma)[\dot{\mathbf{E}}^e] + \dot{\mathcal{L}}(\delta, \gamma)[\mathbf{E}^e]. \tag{24}$$

Under the assumption of small elastic stretches it may be shown that

$$\begin{gathered}\mathbf{E}^e = \mathbf{O}(\epsilon),\\ \dot{\mathbf{E}}^e = (\mathbf{R}^e)^T\mathbf{D}\mathbf{R}^e - \mathbf{D}^p + \mathbf{O}(\epsilon),\\ \Omega := \dot{\mathbf{R}}^e(\mathbf{R}^e)^T = \mathbf{W} - \mathbf{R}^e\mathbf{W}^p(\mathbf{R}^e)^T + \mathbf{O}(\epsilon),\end{gathered} \tag{25}$$

and

$$\begin{aligned}\dot{\bar{\mathbf{T}}} &= (\mathbf{R}^e)^T(\dot{\mathbf{T}} - \Omega\mathbf{T} + \mathbf{T}\Omega)\mathbf{R}^e\\ &= (\mathbf{R}^e)^T\,\mathring{\mathbf{T}}\mathbf{R}^e + \mathbf{O}(\epsilon),\end{aligned}$$

with

$$\mathring{\mathbf{T}} := \dot{\mathbf{T}} - \mathbf{W}\mathbf{T} + \mathbf{T}\mathbf{W}.$$

Here $\mathbf{D} := \mathrm{sym}\,\mathbf{L}$, $\mathbf{W} := \mathrm{skw}\,\mathbf{L}$ and $\mathring{\mathbf{T}}$ are the stretching, the spin and the corotational rate of the Cauchy stress, respectively. In writing the second of $(25)_4$ we have used the important fact that the plastic spin vanishes for isotropic materials, $(14)_2$.

Hence upon using (25) in (24) and $(22)_3$ and neglecting terms of $\mathbf{O}(\epsilon)$ we obtain

$$\mathring{\mathbf{T}} = 2\mu(\mathbf{D} - \mathbf{R}^e\mathbf{D}^p(\mathbf{R}^e)^T) + \lambda(\mathrm{tr}\,\mathbf{D} - \mathrm{tr}\,\mathbf{D}^p)\mathbf{I}, \tag{26}$$

and

$$\mathring{y} = \left\{\frac{\mathbf{T}'}{2\bar{\tau}} + \frac{\pi}{3}\mathbf{I}\right\} \cdot \mathring{\mathbf{T}}. \tag{27}$$

Finally, using $(22)_{1,2}$, (26), and (27), and after some standard manipulations, we may write the particular approximate set of rate constitutive equations proposed here as

$$\left.\begin{aligned}\mathring{\mathbf{T}} &= 2\mu\mathbf{D} + (\kappa - (2/3)\mu)(\mathrm{tr}\,\mathbf{D})\mathbf{I} - g^{-1}\bar{\mathbf{M}}\,\langle \mathbf{M}\cdot\mathbf{D}\rangle\,\mathrm{H}(y),\\ \dot{\gamma} &= g^{-1}\,\langle \mathbf{M}\cdot\mathbf{D}\rangle\,\mathrm{H}(y) \quad \text{and} \quad \dot{\delta} = \delta\beta\dot{\gamma},\end{aligned}\right\} \tag{28}_1$$

where

$$\kappa := (\lambda + (2/3)\mu), \quad g := (h + \mu + \kappa\pi\beta) > 0,$$

$$\bar{\mathbf{M}} := \left(\mu\frac{\mathbf{T}'}{\bar{\tau}} + \kappa\beta\mathbf{I}\right), \quad \mathbf{M} := \left(\mu\frac{\mathbf{T}'}{\bar{\tau}} + \kappa\pi\mathbf{I}\right), \tag{28}_2$$

and $x \mapsto \langle x\rangle$ and $x \mapsto \mathrm{H}(x)$ are *singularity maps* defined by

$$\langle x\rangle = \begin{Bmatrix}0 \text{ for } x \leqq 0\\ x \text{ for } x > 0\end{Bmatrix} \quad \text{and} \quad \mathrm{H}(x) = \begin{Bmatrix}1 \text{ for } x \geqq 0\\ 0 \text{ for } x < 0\end{Bmatrix}, \text{ respectively.} \tag{28}_3$$

These constitutive equations, although differing in detail, are of a final form identical to those proposed by Rudnicki and Rice [6] for geological materials.

For the special case of pressure-insensitive yielding and plastic incompressibility ($\pi = \beta = 0$) the constitutive equations reduce to a finite deformation generalization of the classical Prandtl-Reuss constitutive equations. The appropriateness of these special constitutive equations has been amply demonstrated by Richmond, et al. [7], in their comparisons between some experimental observations and the corresponding theoretical (finite-element) predictions. Further, a simple special case[5] of the present set of constitutive equations can take into account the experimental observations of a slight pressure-sensitivity of yielding, and near plastic incompressibility of certain metallic materials [8, 9]. For the general pressure-sensitive and plastically dilatant case, however, the usefulness of these constitutive equations remains to be demonstrated.

Acknowledgments

The author is grateful to Dr. Owen Richmond and Prof. David R. Owen for some extremely valuable discussions.

References

1 Lee, E. H., "Elastic-Plastic Deformation at Finite Strains," ASME JOURNAL OF APPLIED MEHANICS, 1969, Vol. 36, pp. 1–6.

2 Truesdell, C., and Noll, W., "The Nonlinear Field Theories of Mechanics," *Handbuch der Physik*, Vol. III/3, ed., Truesdell, C., Springer-Verlag, Berlin, 1965.

3 Silhavy, M., "On Transformation Laws for Plastic Deformations of Materials With Elastic Range," *Archive for Rational Mechanics and Analysis*, 1977, Vol. 63, n2, pp. 169–182.

4 Green, A. E., and Naghdi, P. M., "Some Remarks on Elastic-Plastic Deformation at Finite Strain," *International Journal of Engineering Science*, 1971, Vol. 9, pp. 1219–1229.

5 Hahn, H. T., "A Finite Deformation Theory of Plasticity," *International Journal of Solids and Structures*, 1974, Vol. 10, pp. 111–121.

6 Rudnicki, J. W., and Rice, J. R., "Conditions for the Localization of Deformation in Pressure Sensitive Dilatant Materials," *Journal of the Mechanics and Physics of Solids*," 1975, Vol. 23, pp. 371–394.

7 Richmond, O., Devenpeck, M. L., and Appleby, E. J., "Large Tensile Deformation of Sheets and Rods: A Comparison of Observations and Predictions," *Proceedings of the Symposium on Formability: Analysis Modeling and Experimentation*, AIME/ASM Fall Meeting, Chicago, October 24–27, 1977.

8 Spitzig, W. A., Sober, R. J., and Richmond, O., "Pressure Dependence of Yielding and Associated Volume Expansion in Tempered Martensite," *Acta Metallurgica*, 1975, Vol. 23, pp. 885–893.

9 Spitzig, W. A., Sober, R. J., and Richmond, O., "The Effect of Hydrostatic Pressure on the Deformation Behavior of Maraging and HY-80 Steels and Its Implications for Plasticity Theory," *Metallurgical Transactions*, 1976, Vol. 7A, pp. 1703–1710.

On Stress-Intensity Factors for Circumferentially Cracked Circular Cylinders

Tsu-Tao Loo[1]

A long circular cylinder with circumferential notch as shown in Fig. 1 is one of the preferable geometries for test specimens used in the material fracture-toughness testing. In the presence of a circumferential notch, the crack tip of the specimen is in a triaxial state of stress, so that it is more apt to develop brittle fracture. However, even if the cylinder is under simple tension, an exact solution for such cylinder remains very difficult to obtain. Consequently, the prevailing expressions of the stress-intensity factors for these specimens are formulated approximately by an asymptotic interpolation approach, based on the results of two limiting cases [1, 2]. They lack rigorous theoretical bases. More recently, the problem has been treated again by approximate numerical analysis [3]. Differing from all the previous works, the present paper treats the problem by using some physical approximation. An explicit formula of stress-intensity factor for such a cylinder is thus derived for the first time. In this paper, instead of free boundary conditions on the lateral surface of the cylinder, some self-equilibrated residual stresses are allowed to be present. Such an approximation is justified as far as the calculation of stress-intensity factors is concerned. This is so because the self-equilibrated stresses are extremely small indeed in the case of shallow notch, while in the

[5] This special case corresponds to the plastic dilatancy factor β taking the value $\beta = 0$ and the function s in the yield function $(20)_1$ taking the form $s(\bar{p}, \delta, \gamma) = \pi\bar{p} + \bar{s}(\gamma)$ where π is a constant internal friction coefficient and $\bar{s}$ is a function of the equivalent plastic shear strain γ alone.

[1] Shanghai Chiao-Tung University, Department of Engineering Mechanics, Shanghai 200030, The People's Republic of China.

Manuscript received by ASME Applied Mechanics Division, September, 1979; final revision, February, 1980.

Copyright © 1980 by ASME
Downloaded 01 May 2010 to 171.66.16.243. Redistribution subject to ASME license or copyright; see http://www.asme.org/terms/Terms_Use.cfm

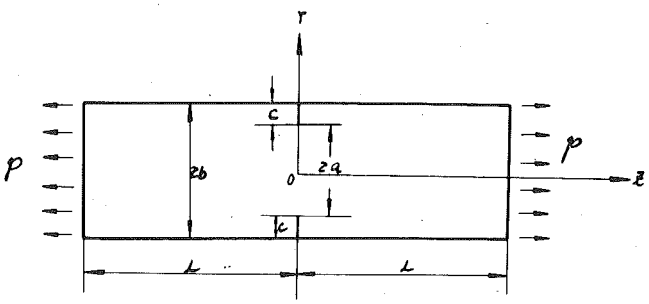

Fig. 1

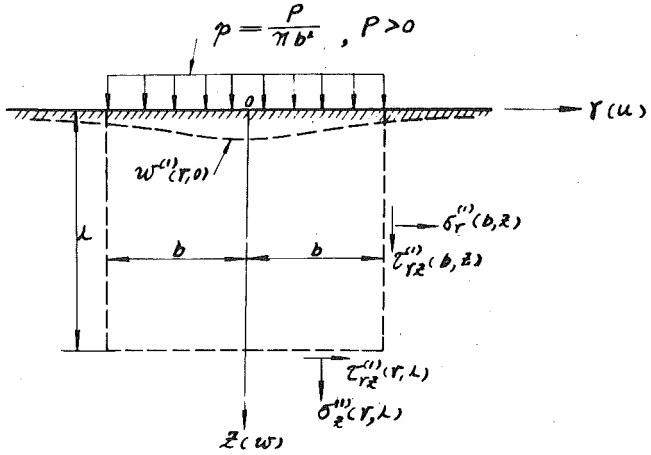

Fig. 3

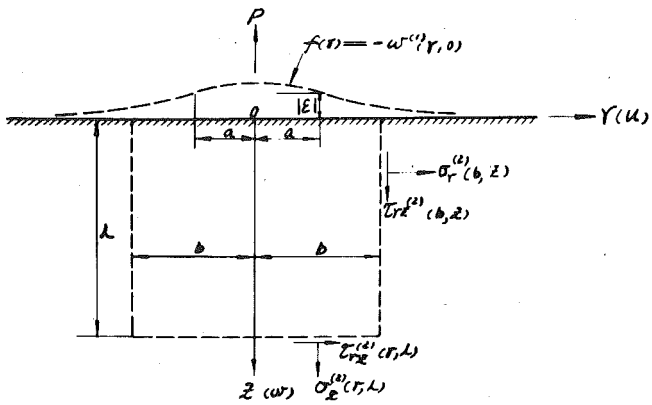

Fig. 2

case of deep notch, the surface boundary is sufficiently far apart from the crack tip and the boundary effect becomes very small. The problem of stress-intensity factors for a notched cylinder under simple tension may thus be reduced to the solutions of two classical half-space problems superimposed together. The first one is the problem of uniformly distributed pressure acting on the plane boundary within a circular region of the same size as the gross cross section of the circular cylinder. The second is the Boussinesq's problem of circular rigid punch with a radius equal to that of the notched cross section of the cylinder. The normal displacements on the plane boundary obtained in the first problem is taken as the rigid punch shape. Furthermore, we make the tensile force applied on the rigid punch equal to the total pressure loaded in the first problem. The circular cylinder cut out from the semi-infinite medium as shown in Fig. 2 then agrees with the problem of a circumferentially cracked circular cylinder specimen under simple tension, except that there remains a system of small self-equilibrated residual stresses on its lateral surface.

Problem 1 Half-Space Problem With Uniform Pressure Acting on the Plane Boundary Within a Circular Area

As shown in Fig. 2, an semi-infinite medium is bounded by the infinite plane $Z = 0$, with Z-axis normal to the plane boundary. On the boundary, a uniform normal pressure p is applying over the area of a circle of radius b. Such problem has been solved by several investigators. According to Love's solution [4], the normal displacement of a point on the boundary plane due to a distributive load $p(x', y', 0)$ over the area Σ will be

$$w(x, y, 0) = \frac{1-\mu^2}{\pi E} \iint_{\Sigma} \frac{p\,(x'\,y')\,dx'\,dy'}{\sqrt{(x-x')^2+(y-y')^2}} = \frac{1-\mu^2}{\pi E} V(x, y) \tag{1}$$

In case of uniform pressure, and for the point within the loaded area, the displacement expressed in cylindrical polar coordinates are found to be

$$[w^{(1)}(r, z)]_{z=0} = \frac{4(1-\mu^2)}{\pi E} bpE(k) \tag{2}$$

where

$$k = r/b \qquad (0 \leqslant k \leqslant 1)$$

and the complete elliptical integral of second kind is

$$E(k) = \frac{\pi}{2}\left\{1 - \frac{1}{2^2}k^2 - \frac{1^2\cdot 3}{2^2\cdot 4^2}k^4 - \frac{1^2\cdot 3^2\cdot 5}{2^2\cdot 4^2\cdot 6^2}k^6 - \ldots\right\} \tag{3}$$

In nondimensional form

$$[w^{(1)}(\rho)]_{z=0} = \frac{2(1-\mu^2)}{\pi E}\frac{P}{b}\left\{1 - \frac{1}{4}(\alpha\rho)^2 - \frac{3}{64}(\alpha\rho)^4 - \frac{5}{256}(\alpha\rho)^6 - \ldots\right\} \tag{2a}$$

with

$$\alpha = a/b, \quad \rho = r/a, \quad P = \pi b^2 p \tag{4}$$

Problem 2 Identation Problem of a Circular Rigid Punch With Prescribed End-Shape (Fig. 3)

Here, the circular punch of the radius a has an end-shape

$$f(r) = -w^{(1)}(r, 0), \quad 0 \leqslant r \leqslant a \tag{5}$$

with $w^{(1)}(r, 0)$, the normal displacement on the plane boundary of Problem 1. Hence, the boundary conditions in this case will be

$$\begin{aligned} Z = 0: \quad & w^{(2)} = \text{constant } \epsilon + f(r) = f^*(r), \quad 0 \leqslant r \leqslant a \\ & \sigma_z{}^{(2)} = 0, \quad r > a \\ & \tau_{rz}{}^{(2)} = 0, \quad 0 \leqslant r < \infty \end{aligned} \tag{6}$$

Using Hankel transformation in the half-space problems of axisymmetry, we have the displacement field [5]

$$u^{(2)} = \frac{\lambda+G}{G}\int_0^{\infty} \xi^2 \frac{dH}{dz} J_1(\xi r)\,d\xi$$

$$w^{(2)} = \int_0^{\infty} \xi\left[\frac{d^2H}{dz^2} - \frac{\lambda+2G}{G}\xi^2 H\right] J_0(\xi r)d\xi \tag{7}$$

in which the function

$$H(\xi, z) = (C + Dz)\,e^{-\xi z} \tag{8}$$

Thus the stresses

$$\sigma_z{}^{(2)} = \int_0^{\infty} \xi\left[(\lambda+2G)\frac{d^3H}{dz^3} - (3\lambda+4G)\,\xi^2\frac{dH}{dz}\right] J_0(\xi r)d\xi$$

$$\tau_{rz}{}^{(2)} = \int_0^{\infty} \xi^2\left[\lambda\frac{d^2H}{dz^2} + (\lambda+2G)\xi^2 H\right] J_1(\xi r)\,d\xi \tag{9}$$

Downloaded 01 May 2010 to 171.66.16.243. Redistribution subject to ASME license or copyright; see http://www.asme.org/terms/Terms_Use.cfm

Table 1 Coefficient k_1

$$k_1 = K_I/\sigma_{net}\sqrt{\frac{ac}{b}}$$

$\alpha = a/b$	0.1	0.3	0.5	0.6	0.7	0.8	0.9	0.95
Paris-Sih [1]	—	—	0.642	0.687	0.746	0.824	0.966	—
Bueckner [7]	—	—	0.680	0.735	0.800	0.885	0.985	—
Benthem-Koiter [2]	0.527	0.590	0.672	0.726	0.793	0.877	0.985	1.047
Keer, et al. [3]	0.520	0.591	0.683	0.742	0.814	0.902	1.008	1.066
Present paper	0.524	0.589	0.667	0.709	0.752	0.810	0.921	1.084

From third boundary condition, we get

$$C = \frac{\lambda}{\lambda + G}\frac{1}{\xi}D$$

and the first and second boundary conditions give dual integral equations

$$\int_0^\infty \xi^2 DJ_0(\xi r)\, d\xi = -\frac{G}{\lambda + 2G} f^*(r), \quad 0 \leqslant r \leqslant a$$

$$\int_0^\infty \xi^3 DJ_0(\xi r)\, d\xi = 0 \quad r > a \tag{10}$$

or in dimensionless form

$$\int_0^\infty h(\beta) J_0(\beta\rho)\, d\beta = g(\rho) \quad 0 \leqslant \rho \leqslant 1$$

$$\int_0^\infty \beta h(\beta) J_0(\beta\rho)\, d\beta = 0 \quad \rho > 1 \tag{11}$$

where

$$\rho = r/a, \quad \beta = \xi a, \quad h(\beta) = \beta^2 Da$$

$$g(\rho) = -\frac{G}{\lambda + 2G} a^4 f^*(\rho) \tag{12}$$

Solving for $h(\beta)$ and substituting it into equation (9), we obtain the normal stress on the plane boundary

$$[\sigma_z{}^{(2)}]_{z=0} = \frac{2(\lambda + G)}{a^5}\int_0^\infty \beta h(\beta) J_0(\beta\rho)\, d\beta \tag{13}$$

Taking the applied force on the rigid punch equal to the total pressure in Problem 1, we have

$$P = 2\pi a^2 \int_0^1 [\sigma_z{}^{(2)}]_{z=0}\, \rho d\rho \tag{14}$$

By superimposing these two problems, and cutting the cylinder out from the semi-infinite medium, we then have a cylinder of which boundary conditions for $L \gg b$ (say, $L > 3b$) will be

$$\begin{array}{lll} Z = 0: & w = \epsilon = \text{constant}, & 0 \leqslant r \leqslant a \\ & \sigma_z = -p = \text{constant}, & a < r \leqslant b \\ & \tau_{rz} = 0 & 0 \leqslant r \leqslant b \\ Z = L: & \sigma_z \to 0, \quad \tau_{rz} \to 0 & \\ r = b: & \text{Self-equilibrated stresses} & \end{array} \tag{15}$$

If we take two-terms approximation of the series in equation (2a) for $w^{(1)}$, we find the corresponding stress-intensity factor

$$K_I = \lim_{\rho \to 1^-} \sqrt{2\pi a(1-\rho)}\, [(\sigma_z{}^{(1)}) + (\sigma_z{}^{(2)})]_{z=0}$$

$$= \frac{P}{2a\sqrt{\pi a}}\left(1 - \frac{4}{3\pi}\alpha^3\right) \tag{16}$$

When more terms of the series in equation (2a) are taken in order to improve the accuracy, particularly for the value $\alpha = a/b$ close to unity, Henkel transformation method fails to yield a solution because of the divergence of the integrals. However, from the result obtained in the two-terms approximation, it is logical to express the distribution of the normal stresses under the punch in a form as follows:

$$[\sigma_z{}^{(2)}]_{z=0} = \sum_{m=0}^{s} C_m (1 - \rho^2)^{m-1/2}, \quad 0 \leqslant \rho \leqslant 1 \tag{17}$$

with the constant coefficients C_m yet to be determined. Thus the integral in equation (1) will be

$$V^{(2)}(x, y) = \iint_\Sigma \frac{[\sigma_z{}^{(2)}]_{z=0}\, dx'dy'}{\sqrt{(x - x')^2 + (y - y')^2}} \tag{18}$$

By using Steuermann's method of integration for the point within the loaded area, we have [6]

$$V^{(2)}(\rho) = \pi a \int_0^\pi \left\{C_0 + \sum_{m=1}^{s} \frac{1\cdot 3\cdot 5 \ldots (2m-1)}{2\cdot 4\cdot 6 \ldots 2m} \times C_m (1 - \rho^2 \sin^2\phi)^m\right\} d\phi \tag{19}$$

Now, from the equation of the punch shape

$$[w^{(2)}(\rho)]_{z=0} = f^*(\rho) = \epsilon - [w^{(1)}(\rho)]_{z=0}$$

or

$$\frac{1 - \mu^2}{\pi E}[V^{(2)}(\rho)] = \epsilon - [w^{(1)}(\rho)]_{z=0}, \quad 0 \leqslant \rho \leqslant 1 \tag{20}$$

together with the total load equation

$$P = \iint_\Sigma [\sigma_z{}^{(2)}]_{z=0}\, dA = 2\pi a^2 \sum_{m=0}^{s} C_m \int_0^1 (1 - \rho^2)^{m-1/2}\, \rho d\rho \tag{21}$$

we can determine the coefficients $C_0, C_1 \ldots C_s$, and ϵ, and then the stress-intensity factor

$$K_I = \lim_{\rho \to 1^-} \sqrt{2\pi a\,(1-\rho)}\, [\sigma_z{}^{(2)}]_{Z=0} = C_0\sqrt{\pi a} \tag{22}$$

Take $s = 3$, we then obtain

$$K_I = C_0\sqrt{\pi a} = \frac{P}{2a\sqrt{\pi a}}\left\{1 - \frac{4}{3\pi}\alpha^3 - \frac{2}{5\pi}\alpha^5 - \frac{3}{14\pi}\alpha^7\right\} \tag{23}$$

This is the explicit formula of stress-intensity factor, obtained through an analytical approach, for a circumferentially cracked cylinder under simple tension. Table 1 shows the comparison with the results from others.

References

1 Paris, P. C., and Sih, G. C., "Stress Analysis of Cracks. Fracture Toughness Testing and Its Applications," ASTM STP No. 381, 1965, pp. 30–81.

2 Benthem, J. P., and Koiter, W. T., "Asymptotic Approximations to Crack Problems," *Mechanics of Fracture*, Vol. 1, Noordhoff International Publishing, Leyden, The Netherlands, 1973, pp. 131–178.

3 Keer, L. M., et al., "Infinite Tensile Cylinder With Circumferential Edge Crack," *Letters in Applied and Engineering Sciences*, Vol. 5, 1977, pp. 129–139.

4 Love, A. E. H., "The Stress Produced in a Semi-Infinite Solid by Pressure on Part of the Boundary," *Philosophical Transactions of the Royal Society*, London, Series A, Vol. 228, 1929.

5 Snedden, I. N., *Fourier Transforms*, McGraw-Hill, New York, 1951.

6 Steuermann, I. Ya., *Contact Problems of the Theory of Elasticity*, National Technical Publisher, Moscow, USSR, 1949.

7 Bueckner, H. F., Discussion, *ASTM STP No. 381, 1965, pp. 82–83.*

Downloaded 01 May 2010 to 171.66.16.243. Redistribution subject to ASME license or copyright; see http://www.asme.org/terms/Terms_Use.cfm

The Response of Cracked Cylindrical Shells[1]

H. J. Petroski[2] and J. L. Glazik, Jr.[3]

A flawless cylindrical shell will deform in an axisymmetric mode when subjected to a uniform pressure, but the presence of material and geometric irregularities will cause other deformation modes to appear also. These additional modes induce bending deformations which are superimposed upon the basic breathing mode response, and when such additional modes are due to the presence of a crack they can have a significant effect on the overall response of the shell.

To examine such effects, the linear elastic plane-strain problem of a thin cylindrical shell with any number of cracks equally spaced around the circumference of the shell has been considered. The weakening effects of the cracks have been modeled to induce the bending modes of deformation, and it is possible to draw qualitative and quantitative conclusions about the nature of the bending. The results obtained via Fourier series techniques compare favorably with finite-element analyses of the cracked geometry and provide an economical means of interpolating between and extrapolating from a limited number of finite-element solutions.

The geometry of the problem is shown in Fig. 1. The mean radius of the cylinder is a, the thickness h, and the tangential and radial physical displacement components of a generic point on the midsurface are v and w, respectively. Polar coordinate θ is measured from a typical crack, and it is assumed that there are N such cracks spaced equally around the circumference at intervals of $2\pi/N$. It is convenient to work with the dimensionless displacements

$$\psi = v/a, \qquad \zeta = w/a, \tag{1}$$

and the dimensionless time

$$\tau = \frac{t}{a}\sqrt{\frac{H}{\rho}}, \tag{2}$$

where t is physical time, ρ is the mass density and, for the plane-strain conditions we consider, $H = E/(1-\nu^2)$ in terms of Young's modulus E and Poisson's ratio ν. It is also convenient to introduce the shell parameter

$$\alpha^2 = h^2/12a^2. \tag{3}$$

Since the loadings we consider are symmetric about the crack plane $\theta = 0$, and since we will model the cracked shell by a uniform one, it is reasonable to assume that the displacements can be represented by the Fourier series

$$\zeta = \zeta_0 + \sum_{n=1}^{\infty} \zeta_n \cos Nn\theta, \tag{4}$$

$$\psi = \sum_{n=1}^{\infty} \zeta_n \sin Nn\theta, \tag{5}$$

in which only terms consistent with the symmetry of the cracked shell are present. When flexural wavelengths are long compared with the wall thickness, the inextensionality condition $\zeta + \psi' = \zeta_0$ may be imposed. This implies $\psi_n = -\zeta_n/Nn$, and this also implies that $Nn = 1$ corresponds to a rigid body displacement, so that we may take $\zeta_1 \equiv 0$ when $N = 1$.

Hetényi [1] has shown how the deflection of beams whose cross sections vary by steps may be determined by loading a uniform beam

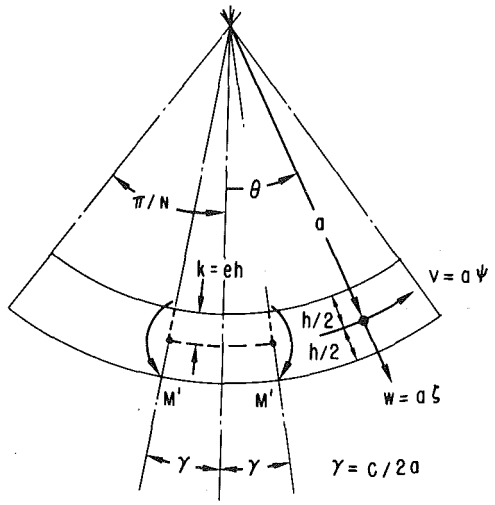

Fig. 1 Cylindrical segment with a pair of couples M' which represent the effects of a notch of depth k subtended by the angle c/a

with a properly chosen force system. The application of Hetényi's technique to straight beams with narrow grooves or cracks was subsequently made by Thompson [2]. The technique mutatis mutandis may be applied to curved beams or shells, and we shall outline it here for those geometries.

The circumferential bending moment resultant M per unit axial length is given in terms of the radial displacement by

$$M = Hha\alpha^2(\zeta'' + \zeta). \tag{6}$$

This may be rearranged, using the definition of α, equation (3), to give

$$\zeta'' + \zeta = \frac{12}{H}\frac{aM}{h^3}. \tag{7}$$

If the cylindrical geometry has a step discontinuity such as a notch, equation (7) must be integrated piecewise. However, a simple rearrangement of the right side of equation (7) shows how the problem may be reduced to integration around a uniform cylindrical shell. If $\bar{a}$ and $\bar{h}$ are the mean radius and thickness of the local section, then equation (7) may be written

$$\zeta'' + \zeta = \frac{12}{H}\frac{a}{h^3}\frac{(\bar{a}/a)M}{(\bar{h}/h)^3} \equiv \frac{12a}{Hh^3}\overline{M}. \tag{8}$$

Thus, if a uniform shell is loaded by a new, related moment distribution $\overline{M}$, the same deflection curve as for the notched shell may be determined from the differential equation.

For thin shells with $h/a \ll 1$, the term $\bar{a}/a$ may be taken as unity. Then $\overline{M}$ is related to M in the same way for curved and straight beams, and Hetényi's results apply. These are that the section of the uniform beam that replaces the notch must be subject to a self-equilibrating complementary loading that alters the bending moment distribution in the appropriate way, which follows from considerations of statics. Generally, this loading comprises couples and distributed and concentrated force systems, but for narrow notches with $c/a \ll 1$, it can be shown that the addition of couples alone to the notch ends, as done by Thompson [2], suffices to model the effect of a crack. These couples are given by

$$M' = \left[\frac{1}{(1-e)^3} - 1\right] M_0 \equiv E'M_0, \tag{9}$$

where $e = k/h$ is the dimensionless crack depth and M_0 is the moment transmitted across the uncracked ligament when the notched structure is subject to the physical load of interest. For the closed cylindrical shell the moment M_0 is statically indeterminate and depends on the deflection of the shell, but the straight-beam formula (9) may

[1] This work is part of the Engineering Mechanics Program of the Reactor Analysis and Safety Division of Argonne National Laboratory, and it was supported by the U.S. Department of Energy.

[2] Engineering Mechanics Program, Reactor Analysis and Safety Division, Argonne National Laboratory, Argonne, Ill. 60439. Mem. ASME

[3] Present address: Bell Telephone Laboratories, Naperville, Ill. 60540.

Manuscript received by ASME Applied Mechanics Division, March, 1979; final revision, January, 1980.

Copyright © 1980 by ASME
Downloaded 01 May 2010 to 171.66.16.243. Redistribution subject to ASME license or copyright; see http://www.asme.org/terms/Terms_Use.cfm

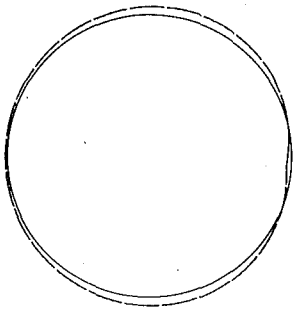

Fig. 2 Simple model (dot-dash line) and finite-element (dash line) predictions for the deformation of a uniformly pressurized cylinder with one internal crack halfway through the wall virtually coincide

Table 1 Calibration parameters for the cracked cylinder ($a/h = 25$)

Crack depth	$\zeta_C + \zeta_A$ (SAP-IV)	Normalized $M'\gamma$	
		equation (11)	equation (9)
0.25	0.001320	0.155	0.196
0.50	−0.000542	1	1
0.75	−0.011228	5.85	9.00

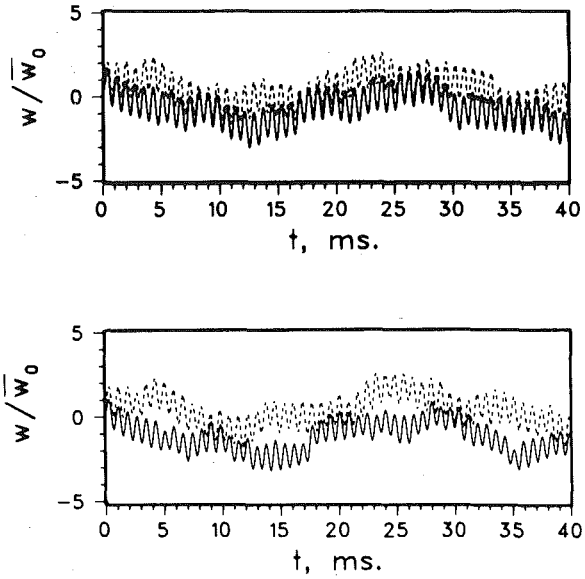

Fig. 3 Response of crack plane (solid curves) and diametrically opposite plane (dashed curves) of a cylinder with one internal crack subjected to a suddenly applied uniform internal pressure; top curves are the predictions of the simple model; bottom curves are finite-element results

be taken to represent the behavior of a cracked shell and M_0 may be assumed independent of e as a first approximation.

For a uniformly pressurized cylinder with N internal cracks (represented by N pairs of couples M' centered about the crack planes), the Fourier coefficients may be determined by familiar energy methods (see, e.g., Langhaar's text [3]) to be

$$\zeta_0 = \frac{ap}{Hh},$$

$$\zeta_n = \frac{-2M'}{\pi Hha\alpha^2} \frac{\sin Nn\gamma}{n(N^2n^2-1)}, \quad (Nn \neq 1), \tag{10}$$

where $\gamma = c/2a$ is the dimensionless notch width, which Thompson [2] has observed may have to be a function of crack size in order to model the effects of cracks properly. We shall see that in application our model obviates this complication by only involving the product $M'\gamma$. Since the amplitude ζ_n decays rapidly with increasing n, the deformation of the cracked cylinder may be approximated by the first few terms of the Fourier series.

Furthermore, for the one-crack case and $\gamma < \pi$ the infinite series may be summed in closed form to give an alternative for calibrating the model for small γ

$$M'\gamma = \pi Hha\alpha^2\left[\zeta_0 - \frac{1}{2}(\zeta_A + \zeta_C)\right], \quad (N = 1), \tag{11}$$

and this formula may be employed to get an improved estimate over equation (9) for M' as a function of crack depth, and it eliminates the ambiguous role of the notch width γ.

The finite-element program SAP-IV [4] has been employed to analyze the cracked cylinder. This program was used with $Q6$ elements, which give improved bending response over the parametric quadrilateral elements designated $Q4$. Since singular elements have been shown [5] to be unnecessary to model the vibrational response of thin elastic structures containing cracks, ordinary elements were used throughout our analysis. The specific geometry chosen for our studies was a 1 in. thick ($h = 2.54$ cm) shell with $a/h = 25$. The material's properties used were $E = 193$ GPa (28×10^6 psi), $\nu = 0.266$, and $\rho = 0.0298$ g/cm^3 (0.00075 lb/in.^{3}), and the cylinder was loaded with a uniform internal pressure of 6.89 MPa (1000 psi).

Table 1 gives the finite-element results for the quasi-static net outward radial displacement of the crack plane for the single-internal-crack case. These are the only results necessary to calibrate our simple model. Also shown in this table are normalized values of M' given by equation (11), with ζ_0 given by (10), and by equation (9). We see that equation (9) will overpredict the crack-plane displacement of the shell for cracks both shallower and deeper than the half-deep crack, but it could be used as a first approximation, thus allowing the simple model to be calibrated from only one finite-element result. This has been done elsewhere [6].

Fig. 2 compares the deformed shape of a cracked cylinder predicted by the finite-element analysis with a 25 term Fourier series representation given by the simple model. This figure, in which deformations are amplified 40 times to exaggerate any differences in the two predictions, demonstrates that the series representation and finite-element results virtually coincide. The crack plane is seen actually to move inward when the cylinder is pressurized uniformly, and for a crack three-quarters through the wall the nonuniform bending dominates the response. We need only change the value of N to treat different numbers of cracks, and to change the sign of M' to represent an external, rather than an internal, crack. Cases of external loading, of course, may be treated by reversing the sign of p_0. Generalization of the simple model to different a/h ratios and nonuniform loading is also easily made without recalibration [7].

Our simple model may also be employed to predict the dynamic response of cracked cylindrical shells to a suddenly applied uniform pressure. In this case,

$$p_0 = p_0H(\tau) \quad \text{and} \quad M' = M'H(\tau), \tag{12}$$

where $H(\tau)$ is the Heaviside step function, and the dynamic response of the cracked cylinder is made up of a number of modes, each representing a free vibration about the static value of the respective mode. Thus the total dynamic response is given by

$$\zeta(\tau,\theta) = \bar{\zeta}_0(1 - \cos\tau) + \sum_{n=1}^{\infty} \bar{\zeta}_n(1 - \cos\omega_n\tau)\cos Nn\theta, \tag{13}$$

where $\bar{\zeta}_0$ and $\bar{\zeta}_n$ are the static values given above in equation (10), and where

$$\omega_n = \frac{\alpha Nn(N^2n^2-1)}{\sqrt{N^2n^2+1}}, \tag{14}$$

are the familiar natural frequencies for bending vibrations of uniform rings. Real cracks will have an effect on the natural frequencies, and this effect will increase with crack depth. Our model does not exhibit this effect and thus will misrepresent the frequency response for

Downloaded 01 May 2010 to 171.66.16.243. Redistribution subject to ASME license or copyright; see http://www.asme.org/terms/Terms_Use.cfm

deeper cracks. However, despite these shortcomings, the simple model is adequate to represent the quality of the dynamic response and to predict reasonably well the maximum amplitudes of vibration of cracked cylinders from only the static calibrations previously described.

Fig. 3 shows the radial displacements of the crack plane and the plane diametrically opposite the crack resulting from a uniform pressure suddenly applied to a cylinder with one internal crack half way through the wall. In this figure, displacements have been normalized with respect to the quasi-static displacement of the uncracked shell, i.e., the magnitude $\bar{w}_0$ of the breathing mode. The top set of curves in Fig. 3 results from employing the breathing mode and the first nine bending modes of the simple model, while the bottom row of curves represents finite-element solutions using the first 10 modes of response.

If the cylinder were flawless, all sections would, of course, vibrate in the breathing mode alone, and the dashed and solid curves would coincide at all times with the curve $1 - \cos \tau$, whose amplitude is two. An internal crack $h/4$ deep does not appreciably change the dynamic response of the cylinder, but the presence of deeper cracks does alter the overall response and this effect increases nonlinearly with crack depth. The deeper the crack the greater the importance of the bending modes of vibration relative to the breathing mode, and for a crack three-quarters through the wall the bending dominates the response and amplitudes an order of magnitude greater than those of an uncracked shell result.

The slight differences in the responses of the two models can be attributed largely to the fact that only the finite-element results show the effects of crack depth on frequency. While the simple model could be calibrated to reflect a frequency dependence on crack depth, this does not appear to be necessary to obtain an adequate qualitative representation of the response. Some of the differences in quality of response can be attributed further to the artificial constraint imposed on the finite-element model to prevent rigid body motion. Such constraint is, of course, not necessary in the simple model. Nevertheless, the maximum dynamic displacements are in good agreement for both solutions, and the simpler model appears adequate for use in dynamic scoping analyses and parametric studies.

Thus we have demonstrated the efficacy of a very simple model for predicting the static and dynamic deformation of cracked cylindrical shells. From a single quasi-static calibration one may study an unlimited number of cases with convenience and economy [7]. Those cases identified as warranting closer attention may be carefully analyzed with finite-element techniques. Even here the simpler model provides a language and context within which the finite-element results may be interpreted.

References

1 Hetényi, M., "Deflection of Beams of Varying Cross Section," ASME JOURNAL OF APPLIED MECHANICS, Vol. 4, 1937, pp. A-49–A-52.

2 Thompson, W. T., "Vibration of Slender Bars With Discontinuities in Stiffness," ASME JOURNAL OF APPLIED MECHANICS, Vol. 16, 1949, pp. 203–207.

3 Langhaar, H. L., *Energy Methods in Applied Mechanics*, Wiley, New York, 1962.

4 Bathe, K.-J., Wilson, E. L., and Peterson, F. E., "SAP-IV—A Structural Analysis Program for Static and Dynamic Response of Linear Systems," EERC Report No. 73-11, College of Engineering, University of California, Berkeley, Calif., June 1979; revised Apr. 1974.

5 Glazik, J. L., "Dynamic Finite-Element Analysis of Cracked Bodies," ASME *Journal of Pressure Vessel Technology*, Vol. 102, 1980, pp. 2–7.

6 Petroski, H. J., and Glazik, J. L., "The Response of Cracked Cylindrical Vessels," ASCE Preprint 3296, presented at the ASCE Convention and Exposition, Chicago, Oct. 1978.

7 Petroski, H. J., and Glazik, J. L., "Effects of Cracks on the Response of Cracked Cylindrical Shells," *Nuclear Technology*, to appear.

Analysis of a Cemented Tubular Joint

R. P. Nordgren[1]

We consider the axisymmetric joint formed by cementing the annulus between a tubular pin and two abutting sections of a tubular sleeve as shown in Fig. 1. Axial tension is applied at a large distance from the joint. Such tubular joints have been used recently to join the sections of a three-part offshore platform [1]. Similar joints are commonly used to join offshore platforms to their foundation piles [2]. Axial tension across these grouted joints may arise from the overturning moment generated by storm waves.

The plane problem of a cemented lap joint has been studied by a number of authors including Goland and Reissner [3] and Renton and Vinson [4]. Their analyses employ special theories of elasticity similar to plate theory.

The present analysis of an axisymmetric tubular joint also uses an approximate special theory. The equations include the axial elasticity of the pin and sleeve as well as the shear elasticity of the cement annulus. In addition, we introduce a limit interfacial shear stress at which slip occurs between the cement and the pin or sleeve. Stress couples and radial stress are neglected in the present analysis.

First, we obtain an elastic slip-free solution which exhibits the usual exponential decay of shear stress with distance from the joint. The axial tension for initiation of slip is determined. Slip initiates at the joint on the pin-cement interface for the assumed case of equal limit stress at the two interfaces. Next, we obtain a solution which accounts for slip between the cement and pin. The length of the slipped zone is related to the axial tension.

The determination of the limit interfacial shear stress can be left as an experimental problem. However, for some joints, further analytical considerations are possible. In particular, the pin and sleeve of grouted joints on offshore platforms often are fitted with circumferential shear keys (bars or weld beads) in order to increase the interfacial shear strength [1, 2]. For such keyed joints, the limit shear stress can be related to the crushing strength of the cement grout on the shear keys. Cracking across the cement annulus also may be a limiting factor. Experimental results for grouted tubular joints have been presented by Billington and Lewis [2] who also discuss design considerations.

The solutions obtained in the present Note lend confidence to the usual design procedure based on the concept of limit shear transfer. The solutions also may be useful in interpreting experimental results.

Analysis

The sleeve and pin are assumed to displace axially without radial restraint, hence

$$\sigma_\alpha = Ee_\alpha = E\frac{\partial u_\alpha}{\partial z}, \qquad (\alpha = 1, 2) \tag{1}$$

where

σ_1, σ_2 = axial stresses in the pin and sleeve, respectively
e_1, e_2 = axial strains
u_1, u_2 = axial displacements (Fig. 1)
E = Young's modulus

The cement annulus is assumed to deform elastically in shear according to

$$\bar{q} = \frac{1}{2}(q_1 + q_2) = G\frac{(u_{2c} - u_{1c})}{(r_2 - r_1)}, \tag{2}$$

where

[1] Shell Development Company, Bellaire Research Center, P.O. Box 481, Houston, Texas. Mem. ASME.

Manuscript received by ASME Applied Mechanics Division, November, 1979; final revision, March, 1980.

Downloaded 01 May 2010 to 171.66.16.243. Redistribution subject to ASME license or copyright; see http://www.asme.org/terms/Terms_Use.cfm

deeper cracks. However, despite these shortcomings, the simple model is adequate to represent the quality of the dynamic response and to predict reasonably well the maximum amplitudes of vibration of cracked cylinders from only the static calibrations previously described.

Fig. 3 shows the radial displacements of the crack plane and the plane diametrically opposite the crack resulting from a uniform pressure suddenly applied to a cylinder with one internal crack half way through the wall. In this figure, displacements have been normalized with respect to the quasi-static displacement of the uncracked shell, i.e., the magnitude $\bar{w}_0$ of the breathing mode. The top set of curves in Fig. 3 results from employing the breathing mode and the first nine bending modes of the simple model, while the bottom row of curves represents finite-element solutions using the first 10 modes of response.

If the cylinder were flawless, all sections would, of course, vibrate in the breathing mode alone, and the dashed and solid curves would coincide at all times with the curve $1 - \cos \tau$, whose amplitude is two. An internal crack $h/4$ deep does not appreciably change the dynamic response of the cylinder, but the presence of deeper cracks does alter the overall response and this effect increases nonlinearly with crack depth. The deeper the crack the greater the importance of the bending modes of vibration relative to the breathing mode, and for a crack three-quarters through the wall the bending dominates the response and amplitudes an order of magnitude greater than those of an uncracked shell result.

The slight differences in the responses of the two models can be attributed largely to the fact that only the finite-element results show the effects of crack depth on frequency. While the simple model could be calibrated to reflect a frequency dependence on crack depth, this does not appear to be necessary to obtain an adequate qualitative representation of the response. Some of the differences in quality of response can be attributed further to the artificial constraint imposed on the finite-element model to prevent rigid body motion. Such constraint is, of course, not necessary in the simple model. Nevertheless, the maximum dynamic displacements are in good agreement for both solutions, and the simpler model appears adequate for use in dynamic scoping analyses and parametric studies.

Thus we have demonstrated the efficacy of a very simple model for predicting the static and dynamic deformation of cracked cylindrical shells. From a single quasi-static calibration one may study an unlimited number of cases with convenience and economy [7]. Those cases identified as warranting closer attention may be carefully analyzed with finite-element techniques. Even here the simpler model provides a language and context within which the finite-element results may be interpreted.

References

1 Hetényi, M., "Deflection of Beams of Varying Cross Section," ASME JOURNAL OF APPLIED MECHANICS, Vol. 4, 1937, pp. A-49–A-52.

2 Thompson, W. T., "Vibration of Slender Bars With Discontinuities in Stiffness," ASME JOURNAL OF APPLIED MECHANICS, Vol. 16, 1949, pp. 203–207.

3 Langhaar, H. L., *Energy Methods in Applied Mechanics*, Wiley, New York, 1962.

4 Bathe, K.-J., Wilson, E. L., and Peterson, F. E., "SAP-IV—A Structural Analysis Program for Static and Dynamic Response of Linear Systems," EERC Report No. 73-11, College of Engineering, University of California, Berkeley, Calif., June 1979; revised Apr. 1974.

5 Glazik, J. L., "Dynamic Finite-Element Analysis of Cracked Bodies," ASME *Journal of Pressure Vessel Technology*, Vol. 102, 1980, pp. 2–7.

6 Petroski, H. J., and Glazik, J. L., "The Response of Cracked Cylindrical Vessels," ASCE Preprint 3296, presented at the ASCE Convention and Exposition, Chicago, Oct. 1978.

7 Petroski, H. J., and Glazik, J. L., "Effects of Cracks on the Response of Cracked Cylindrical Shells," *Nuclear Technology*, to appear.

Analysis of a Cemented Tubular Joint

R. P. Nordgren[1]

We consider the axisymmetric joint formed by cementing the annulus between a tubular pin and two abutting sections of a tubular sleeve as shown in Fig. 1. Axial tension is applied at a large distance from the joint. Such tubular joints have been used recently to join the sections of a three-part offshore platform [1]. Similar joints are commonly used to join offshore platforms to their foundation piles [2]. Axial tension across these grouted joints may arise from the overturning moment generated by storm waves.

The plane problem of a cemented lap joint has been studied by a number of authors including Goland and Reissner [3] and Renton and Vinson [4]. Their analyses employ special theories of elasticity similar to plate theory.

The present analysis of an axisymmetric tubular joint also uses an approximate special theory. The equations include the axial elasticity of the pin and sleeve as well as the shear elasticity of the cement annulus. In addition, we introduce a limit interfacial shear stress at which slip occurs between the cement and the pin or sleeve. Stress couples and radial stress are neglected in the present analysis.

First, we obtain an elastic slip-free solution which exhibits the usual exponential decay of shear stress with distance from the joint. The axial tension for initiation of slip is determined. Slip initiates at the joint on the pin-cement interface for the assumed case of equal limit stress at the two interfaces. Next, we obtain a solution which accounts for slip between the cement and pin. The length of the slipped zone is related to the axial tension.

The determination of the limit interfacial shear stress can be left as an experimental problem. However, for some joints, further analytical considerations are possible. In particular, the pin and sleeve of grouted joints on offshore platforms often are fitted with circumferential shear keys (bars or weld beads) in order to increase the interfacial shear strength [1, 2]. For such keyed joints, the limit shear stress can be related to the crushing strength of the cement grout on the shear keys. Cracking across the cement annulus also may be a limiting factor. Experimental results for grouted tubular joints have been presented by Billington and Lewis [2] who also discuss design considerations.

The solutions obtained in the present Note lend confidence to the usual design procedure based on the concept of limit shear transfer. The solutions also may be useful in interpreting experimental results.

Analysis

The sleeve and pin are assumed to displace axially without radial restraint, hence

$$\sigma_\alpha = Ee_\alpha = E\frac{\partial u_\alpha}{\partial z}, \qquad (\alpha = 1, 2) \tag{1}$$

where

σ_1, σ_2 = axial stresses in the pin and sleeve, respectively
e_1, e_2 = axial strains
u_1, u_2 = axial displacements (Fig. 1)
E = Young's modulus

The cement annulus is assumed to deform elastically in shear according to

$$\bar{q} = \frac{1}{2}(q_1 + q_2) = G\frac{(u_{2c} - u_{1c})}{(r_2 - r_1)}, \tag{2}$$

where

[1] Shell Development Company, Bellaire Research Center, P.O. Box 481, Houston, Texas. Mem. ASME.

Manuscript received by ASME Applied Mechanics Division, November, 1979; final revision, March, 1980.

Copyright © 1980 by ASME
Downloaded 01 May 2010 to 171.66.16.243. Redistribution subject to ASME license or copyright; see http://www.asme.org/terms/Terms_Use.cfm

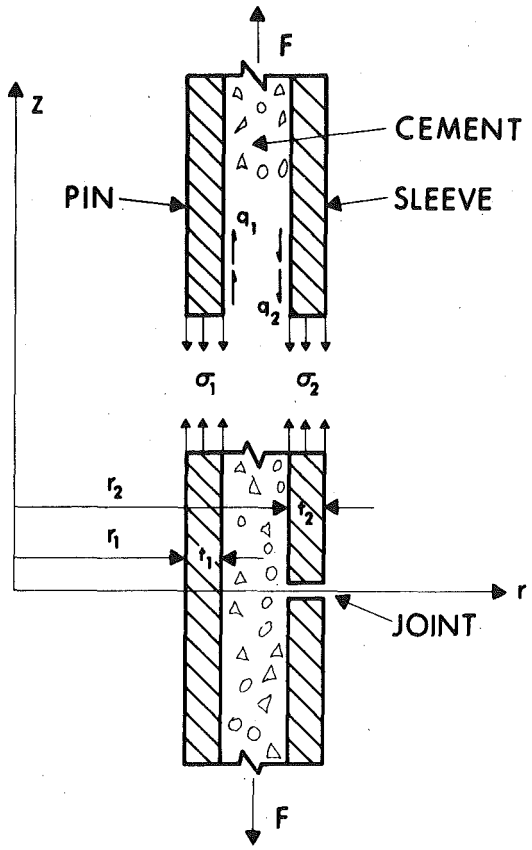

Fig. 1 Cemented tubular joint

$\bar{q}$ = the mean shear stress
q_1, q_2 = shear stresses across the pin-cement and sleeve-cement interfaces, respectively
u_{1c}, u_{2c} = displacements of the cement at these interfaces
r_1, r_2 = interface radii
G = the shear modulus of the cement

If there is no slip at the interfaces, then

$$u_{1c} = u_1, \qquad u_{2c} = u_2. \tag{3}$$

Axial stress in the cement is neglected for analytical simplicity, although there is no essential difficulty in including it.

The equations of axial equilibrium for the pin, sleeve, and cement read

$$t_1' \frac{\partial \sigma_1}{\partial z} + q_1 = 0, \quad t_2' \frac{\partial \sigma_2}{\partial z} - q_2 = 0, \quad r_2 q_2 - r_1 q_1 = 0, \tag{4}$$

where

$$t_1' = t_1 (1 - \tfrac{1}{2} t_1/r_1), \quad t_2' = t_2 (1 + \tfrac{1}{2} t_2/r_2),$$

t_1 and t_2 being the thicknesses of the pin and sleeve, respectively.

For the joint under consideration (Fig. 1), the sleeve is stress-free at the joint and the pin can be taken fixed there; i.e.,

$$\sigma_2 = u_1 = 0 \quad \text{at} \quad z = 0. \tag{5}$$

Then only $z \geq 0$ needs to be considered. At a large distance from the joint, a condition of generalized plane strain exists with total axial force F, i.e.,

$$e_1 = e_2, \quad F = 2\pi(t_1' r_1 \sigma_1 + t_2' r_2 \sigma_2) \quad \text{as} \quad z \to \infty. \tag{6}$$

For the case of no slip at the interfaces (3), the solution of equations (1)–(6) is

$$u_1 = \frac{F}{2\pi\lambda E\,(t_1' r_1 + t_2' r_2)} \left[\frac{r_2 t_2'}{r_1 t_1'}(1 - e^{-\lambda z}) + \lambda z\right],$$

$$u_2 = \frac{F}{2\pi\lambda E\,(t_1' r_1 + t_2' r_2)} \left[\frac{r_2 t_2'}{r_1 t_1'} + e^{-\lambda z} + \lambda z\right] \tag{7}$$

where

$$\lambda = \left[\frac{2G\,(r_1 t_1' + r_2 t_2')}{E\,(r_2^2 - r_1^2) t_1' t_2'}\right]^{1/2}.$$

The solution exhibits exponential decay with increasing z. The interface shear stresses are

$$q_1 = \frac{r_2}{r_1} q_2 = \frac{F\lambda r_2 t_2'}{2\pi(t_1' r_1 + t_2' r_2) r_1} e^{-\lambda z}, \tag{8}$$

which have a maximum at $z = 0$. Of course, the solution (8) is only a crude approximation to the three-dimensional stress state near $z = 0$.

We assume that slip initiates at the pin-cement or sleeve-cement interface when the shear stress q_1 or q_2 equals the limit shear stress q^*. Only the case of equal shear strength at both interfaces is considered here. By (8), $q_1 > q_2$; thus slip initiates on the pin-cement interface at the joint ($z = 0$) when the axial load F reaches

$$F^* = 2\pi q^* (t_1' r_1 + t_2' r_2)\, r_1/\lambda r_2 t_2'. \tag{9}$$

For axial load, $F > F^*$, we postulate that slip occurs on the pin-cement interface over a distance ℓ from the joint with

$$\begin{aligned} &q_1 = q^*, \quad u_1 \leq u_{1c}, \quad 0 \leq z \leq \ell, \\ &q_1 \leq q^*, \quad u_1 = u_{1c}, \quad z \geq \ell, \end{aligned} \tag{10}$$

and

$$q_2 < q^*, \quad u_2 = u_{2c}, \quad z \geq 0. \tag{11}$$

The condition (11) will be verified later. Integration of (4) with (1), (2), (5), and (10) gives

$$\left.\begin{aligned} u_1 &= B_1 z - q^* z^2/2t'E \\ u_{1c} &= u_2 - (r_2^2 - r_1^2) q^*/2r_2 G \\ u_2 &= u_{2c} = B_2 + q^* r_1 z^2/2r_2 t_2' E \end{aligned}\right\} \quad 0 \leq z \leq \ell. \tag{12}$$

Outside the slip zone, the elastic solution of (1), (2), and (4) has the form

$$\left.\begin{aligned} u_1 &= u_{1c} = A_1 + A_2 z + A_3 e^{-\lambda z} \\ u_2 &= u_{2c} = A_1 + A_2 z + A_4 e^{-\lambda z} \end{aligned}\right\} \quad z \geq \ell. \tag{13}$$

Continuity of displacements and stresses at $z = \ell$, together with (6) determine the constants in (12) and (13) and the length ℓ of the slipped zone as

$$A_1 = \frac{q^*}{\lambda^2 t_1' E}\left(1 + \lambda\ell + \frac{1}{2}\lambda^2\ell^2\right), \quad A_2 = \frac{F}{2\pi E\,(t_1' r_1 + t_2' r_2)}$$

$$A_3 = -\frac{q^*}{\lambda^2 E t_1'} e^{\lambda\ell}, \quad A_4 = \frac{r_1 q^*}{r_2 \lambda^2 E t_2'} e^{\lambda\ell}$$

$$B_1 = F/2\pi E r_1 t_1, \qquad B_2 = \frac{F}{2\pi E r_1 t_1' \lambda}\left[1 + \frac{1}{2}\lambda^2\ell^2/(1 + \lambda\ell)\right] \tag{14}$$

$$\ell = \frac{r_2 t_2' F}{2\pi r_1\,(t_1' r_1 + t_2' r_2) q^*} - \frac{1}{\lambda} = (q_{E1}(0)/q^* - 1)/\lambda, \tag{15}$$

where $q_{E1}(0)$ is given by the elastic solution (8) and λ is defined by (7). The maximum slip between pin and cement occurs at $z = 0$ and is equal to the sleeve displacement there as given by

$$u_{1c}(0) - u_1(0) = u_2(0) = B_2.$$

The interface shear stress between sleeve and cement, by (1), (4), (12), and (14) is

$$q_2 = \frac{r_1}{r_2} q^*, \qquad 0 \leq z \leq \ell$$

Downloaded 01 May 2010 to 171.66.16.243. Redistribution subject to ASME license or copyright; see http://www.asme.org/terms/Terms_Use.cfm

$$q_2 = \frac{r_1}{r_2} q^* e^{-\lambda(z-\ell)}, \qquad z \geq \ell.$$

Thus $q_2 < q^*$, slip does not occur at the sleeve-cement interface, and our assumption (11) is confirmed.

The formula (15) for length of cement-pin slip zone may be useful in design practice. The first term in (15) can be obtained by limit analysis considerations together with the generalized plane strain condition (6). The $1/\lambda$ term represents elastic stress transfer outside the slip zone. In most practical cases, the first term dominates and neglect of the $1/\lambda$ term is conservative for considerations of shear key placement.

Extensions of the foregoing analysis are possible. In particular, the effect of radial stress on interfacial bond strength may be important when shear keys are absent. Also, cracking and crushing of the cement could be studied with a finite-element computer program. Limited finite-element studies have tended to confirm the validity of the approximate solution presented here.

References

1 Sterling, G. H., Cox, B. E., and Warrington, R. M., "Design of the Cognac Plaform for 1025-Foot Water Depth, Gulf of Mexico," Offshore Technology Conference Paper 3494, Houston, May 1979.

2 Billington, C. J., and Lewis, G. H. G., "The Strength of Large Diameter Grouted Connections," Offshore Technology Conference Paper 3083, Houston, May 1978.

3 Goland, M., and Reissner, E., (1944), "The Stresses in Cemented Joints," ASME JOURNAL OF APPLIED MECHANICS, Vol. 11, Mar. 1944, pp. A-17–A-27.

4 Renton, W. J., and Vinson, J. R., "Analysis of Adhesively Bonded Joints Between Panels of Composite Materials," ASME JOURNAL OF APPLIED MECHANICS, Vol. 44, 1977, pp. 101–106.

Downloaded 01 May 2010 to 171.66.16.243. Redistribution subject to ASME license or copyright; see http://www.asme.org/terms/Terms_Use.cfm

Journal of Applied Mechanics

Discussion

Distributed Damage Theory of Beams in Pure Bending[1]

C. W. Bert[2] and M. Kumar.[3] The author is commended for his novel approach to the prediction of failure in brittle materials in bending.

Using a different approach than that used by the author, the present discussers have obtained simpler but analogous results up through the author's equation (24). This analysis, which uses the methodology presented by Marin [1] for flexure of materials with different stress-strain relations in tension and compression, is outlined here briefly.

The stress-strain (σ versus ϵ) relation is, in compression

$$\sigma_c = E\epsilon \tag{1a}$$

and in tension

$$\sigma_t = E\epsilon - (E^2/D)\epsilon^2 \tag{1b}$$

Here $E \equiv$ Young's modulus and $D \equiv$ damage modulus.

The Bernoulli-Euler hypothesis is

$$\epsilon = \kappa z \tag{2}$$

where $\kappa \equiv$ bending curvature and $z \equiv$ distance from neutral surface.

For pure bending, equilibrium of forces and moments requires

$$\int_{-C_c}^{0} \sigma_c\, b\, dz + \int_{0}^{C_t} \sigma_t\, b\, dz = 0 \tag{3}$$

$$\int_{-C_c}^{0} z\sigma_c\, b\, dz + \int_{0}^{C_t} z\sigma_t\, b\, dz = M \tag{4}$$

Here $b\, dz \equiv$ differential cross-sectional area, C_c and C_t are the respective distances to the compressive and tensile outer fibers, measured from the neutral surface, and $M \equiv$ applied bending moment.

Geometrically, it is necessary that

$$C_c + C_t = H \tag{5}$$

where $H \equiv$ total depth of the cross section.

The foregoing analysis leads to the following relatively simple expression for the dimensionless bending moment m, as defined in the paper ($= 6M/DbH^2$ in terms of the present symbols):

$$m = 6[1 - (15/8)K_t + (3/4)K_t^2][K_t^{-2} - (1/2)K_t^{-3}] \tag{6}$$

where $K_t \equiv C_t/H$.

However, there is one point on which we beg to differ with the author. This is on the appropriate criterion for determining the ultimate bending moment. The author used one proposed by Janson and Hult for failure under *simple tension* loading:

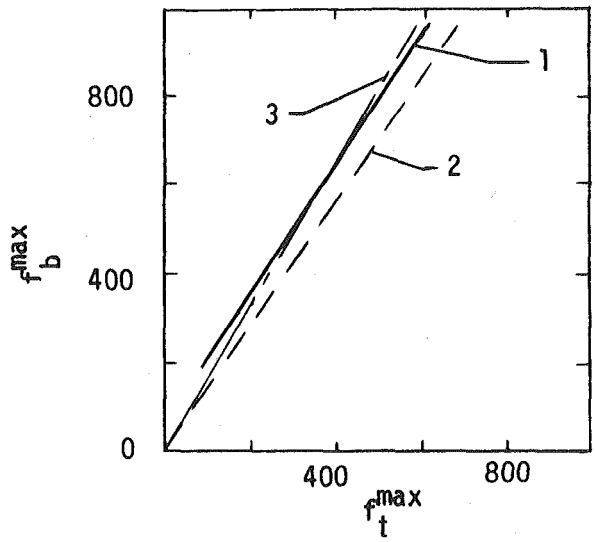

Fig. 1 Rupture tensile stress in bending versus rupture stress in tension; Curve 1—experimental results of Gonnerman and Shuman; Curve 2—prediction of Krajcinovic; Curve 3—present prediction

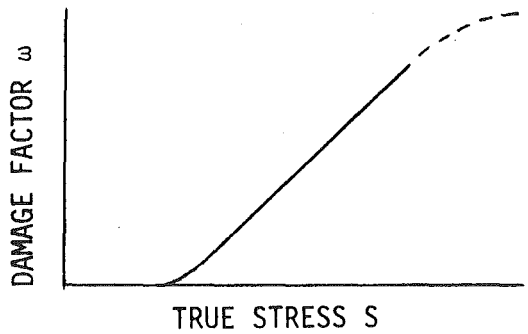

Fig. 2 Proposed relation between damage factor and true stress

$$d\sigma/d\epsilon = 0 \tag{7}$$

The discussers believe that equation (7) is unduly conservative for the present bending case in that it does not represent the maximum value of m as determined by application of differential calculus to the discussers' equation (6). This latter approach shows that at a value of $K_t = 0.5875$, m reaches its maximum value of 0.407. These values are to be compared with $K_t = (1/2)[1 + (y_0/h)] = (1/2)(1 + 0.101) = 0.5505$ and $m = 0.354$ obtained by the author.

Clearly, it is predicted that the dimensionless moment reaches the author's value of 0.354 before it reaches its peak value of 0.407. This means that physically when m reaches 0.354, the tensile outer fiber starts to "dump" load to other fibers which have not yet failed. This process continues until finally the ultimate bending moment ($m = 0.407$) is reached.

The criterion presented here corresponds to a ratio of maximum

[1] By D. Krajcinovic, and published in the September, 1979, issue of the ASME JOURNAL OF APPLIED MECHANICS, Vol. 46, pp. 592–596.

[2] Benjamin H. Perkinson Professor of Engineering, School of Aerospace, Mechanical and Nuclear Engineering, The University of Oklahoma, Norman, Okla. 73019. Mem. ASME

[3] Graduate Research Assistant, Mechanical Engineering, The University of Oklahoma, Norman, Okla. 73019.

Copyright © 1980 by ASME
Downloaded 01 May 2010 to 171.66.16.243. Redistribution subject to ASME license or copyright; see http://www.asme.org/terms/Terms_Use.cfm

tensile stress at rupture in bending to that in tension (f_b^{max}/f_t^{max}) of 1.63, instead of the value of 1.42 obtained by the author. A comparison of the present prediction with the author's prediction and the experimental results of Gonnerman and Shuman [2 in the paper] is shown in Fig. 1. It can be seen that the *slope* of the author's prediction is in good agreement with the slope of the experimental data. However, the present prediction gives actual values which fall much closer to the experimental data, although the slopes are slightly different.

Finally, we would like to propose a damage function, $\omega(S)$, which may be more plausible physically than the linear relation with stress used by the author and by the discussers. We believe that this function should be an S-shaped curve as shown in Fig. 2. There is probably some threshold value of tensile stress below which there would be negligible damage. This would be followed by a transition region of rapid increase in damage with stress, and finally perhaps a plateau or saturation effect. Hopefully, future research will shed light on this question.

The authors are presently applying the philosophy used here for predicting bending strength of materials weak in tension to similar predictions for materials weak in compression (so-called bimodulus materials, such as tire-cord/rubber, wire-reinforced solid propellant grains, and certain biological materials [2]).

References

1 Marin, J., *Mechanical Behavior of Engineering Materials,* Prentice-Hall, Englewood, Cliffs, N.J., 1962, Section 2-7.

2 Bert, C. W., "Micromechanics of the Different Elastic Behavior of Filamentary Composites in Tension and Compression," *Mechanics of Bimodulus Materials,* ASME, New York, 1979, pp. 17–28.

Author's Closure

The author appreciates the discussion by Bert and Kumar and welcomes the opportunity to elaborate on some of the details left obscure in the original paper. The main idea of the paper is an introduction of a new internal (hidden) variable defining gradual cracking as the only irreversible mechanical process (see, for example, Perzyna [3], or Kratochvil and Dillon [4, 5]). While it is quite possible that in case of a monotonic loading a similar result can be obtained by a clever combination of state variables (defining reversible processes) the equivalency quite obviously ceases to exist in a general loading case.

It was further the author's intention to present a viable approach to a decidedly complex problem. The fact that the simplest damage law lead to a fine (if not perfect) agreement with experimental data is either a pure coincidence or a further proof that the nature favors simple relationships. While the author would prefer to discount the first alternative the intent was to discern the trends rather than to match data.

The discussers' belief that the damage law should be an S curve with a certain threshold value might be true for certain materials. However, if the damage variable is conceived in sense of the Vakulenko and Kachanov [6] (i.e., in terms of crack opening) the existence of the threshold value will be contingent on the total absence of decohesions and voids in the "virgin" material. If those voids exist even a minute tension will result in damage evolution. The only restriction on the selection of the damage law will be associated with the Clausius-Duhem inequality, i.e., the internal entropy production rate.

As already indicated by the last sentence of the original paper the author agrees with discussers in relation to the application of the Janson-Hult criterion in case of the bending. The real problem, incidentally, is to define the fracture criterion in a very general case. Quite obviously, this problem will necessitate investigation of the problem in the general, thermomechanical, context.

Additional References

3 Perzyna P., "Thermodynamics of Rheological Materials With Internal Changes," *Journal de Mecanique,* Vol. 10, 1971, pp. 391–408.

4 Kratochvil J., and Dillon O. W., Jr., "Thermodynamics of Elastic-Plastic Materials as a Theory With Internal State Variables," *Journal of Applied Physics,* Vol. 40 1969, pp. 3207–3218.

5 Kratochvil J., and Dillon O. W., Jr., "Thermodynamics of Crystalline Elastic-Viscoplastic Materials," *Journal of Applied Physics,* Vol. 44, 1970, pp. 1470–1478.

6 Vakulenko A. A., and Kachanov, M. L., "Continuum Theory of Cracked Media," *Mekhanika Tverdogo Tela,* Vol. 6, 1971, pp. 159–166 (in Russian).

A Physically Consistent Method for the Prediction of Creep Behavior of Metals[1]

W. N. Findley.[2] I was pleased that Mr. Weng found our data on creep of 2618 aluminum under combined stress useful in evaluating his theory. It was very disappointing therefore to find on reading his preprint that our data had not been accurately transcribed so that the actual agreement with the theory was not as close as reported.

It seems necessary, to avoid future misinterpretation by other investigators, to present the following clarifications. As reported in [1] two lots of material were used. Our tests A, B, C were from swaged material, tests D–H from extruded material. Unfortunately, Mr. Weng's primary input Fig. 1 was taken from one test from each material, (our tests $A1$ and $F1$). Another problem arises from the fact that creep strain cannot be measured with any precision directly. Creep occurs so rapidly at the start of a test that large errors may arise from measuring creep strain from the first observed strain reading, as employed in the subject paper. In [1] total strain was reported. Creep strain could be obtained by: (A) Fitting an equation to the strain-time data and then extrapolating back to zero or (B) Subtracting the elastic strain from the total strain, providing there was no plastic strains as happened to be true in our tests. Method (B) was employed in our recent papers on this subject [2, 3].

Concerning the plotting of the experimental data, the lowest curve (our test $A1$) in Fig. 1 is correct. However, the highest curve (our test $F1$) is too high and there are too many points shown in the early part. The original data of our tests $A1$ and $F1$ are replotted in Fig. D1, where total strains are shown as ordinates. The corresponding elastic strain, which would be the correct origin for creep strains, was 0.2651 percent for our test $F1$, for example.

In Fig. 2 the shape of the early part of the curve is considerably distorted. A replot of our test $B1$ is shown in Fig. D2, which shows that the test data lies between the two theories shown by the author.

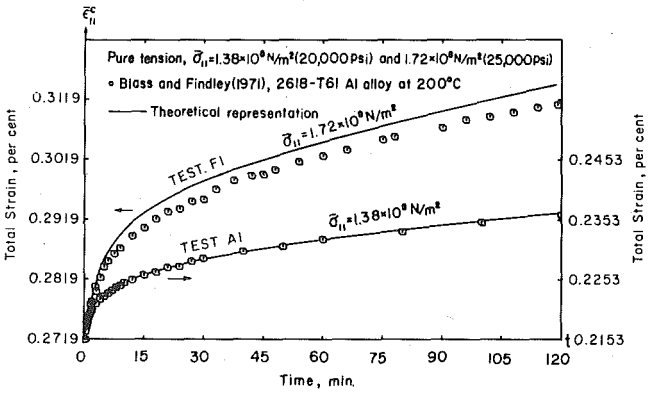

Fig. D1 Tensile creep strains of an aluminum alloy

[1] By G. J. Weng, and published in the December, 1979, issue of the ASME JOURNAL OF APPLIED MECHANICS, Vol. 46, pp. 800–804.

[2] Professor of Engineering, Brown University, Providence, R.I. 02912.

Downloaded 01 May 2010 to 171.66.16.243. Redistribution subject to ASME license or copyright; see http://www.asme.org/terms/Terms_Use.cfm

tensile stress at rupture in bending to that in tension (f_b^{max}/f_t^{max}) of 1.63, instead of the value of 1.42 obtained by the author. A comparison of the present prediction with the author's prediction and the experimental results of Gonnerman and Shuman [2 in the paper] is shown in Fig. 1. It can be seen that the *slope* of the author's prediction is in good agreement with the slope of the experimental data. However, the present prediction gives actual values which fall much closer to the experimental data, although the slopes are slightly different.

Finally, we would like to propose a damage function, $\omega(S)$, which may be more plausible physically than the linear relation with stress used by the author and by the discussers. We believe that this function should be an S-shaped curve as shown in Fig. 2. There is probably some threshold value of tensile stress below which there would be negligible damage. This would be followed by a transition region of rapid increase in damage with stress, and finally perhaps a plateau or saturation effect. Hopefully, future research will shed light on this question.

The authors are presently applying the philosophy used here for predicting bending strength of materials weak in tension to similar predictions for materials weak in compression (so-called bimodulus materials, such as tire-cord/rubber, wire-reinforced solid propellant grains, and certain biological materials [2]).

References

1 Marin, J., *Mechanical Behavior of Engineering Materials,* Prentice-Hall, Englewood, Cliffs, N.J., 1962, Section 2-7.

2 Bert, C. W., "Micromechanics of the Different Elastic Behavior of Filamentary Composites in Tension and Compression," *Mechanics of Bimodulus Materials,* ASME, New York, 1979, pp. 17–28.

Author's Closure

The author appreciates the discussion by Bert and Kumar and welcomes the opportunity to elaborate on some of the details left obscure in the original paper. The main idea of the paper is an introduction of a new internal (hidden) variable defining gradual cracking as the only irreversible mechanical process (see, for example, Perzyna [3], or Kratochvil and Dillon [4, 5]). While it is quite possible that in case of a monotonic loading a similar result can be obtained by a clever combination of state variables (defining reversible processes) the equivalency quite obviously ceases to exist in a general loading case.

It was further the author's intention to present a viable approach to a decidedly complex problem. The fact that the simplest damage law lead to a fine (if not perfect) agreement with experimental data is either a pure coincidence or a further proof that the nature favors simple relationships. While the author would prefer to discount the first alternative the intent was to discern the trends rather than to match data.

The discussers' belief that the damage law should be an S curve with a certain threshold value might be true for certain materials. However, if the damage variable is conceived in sense of the Vakulenko and Kachanov [6] (i.e., in terms of crack opening) the existence of the threshold value will be contingent on the total absence of decohesions and voids in the "virgin" material. If those voids exist even a minute tension will result in damage evolution. The only restriction on the selection of the damage law will be associated with the Clausius-Duhem inequality, i.e., the internal entropy production rate.

As already indicated by the last sentence of the original paper the author agrees with discussers in relation to the application of the Janson-Hult criterion in case of the bending. The real problem, incidentally, is to define the fracture criterion in a very general case. Quite obviously, this problem will necessitate investigation of the problem in the general, thermomechanical, context.

Additional References

3 Perzyna P., "Thermodynamics of Rheological Materials With Internal Changes," *Journal de Mecanique,* Vol. 10, 1971, pp. 391–408.

4 Kratochvil J., and Dillon O. W., Jr., "Thermodynamics of Elastic-Plastic Materials as a Theory With Internal State Variables," *Journal of Applied Physics,* Vol. 40 1969, pp. 3207–3218.

5 Kratochvil J., and Dillon O. W., Jr., "Thermodynamics of Crystalline Elastic-Viscoplastic Materials," *Journal of Applied Physics,* Vol. 44, 1970, pp. 1470–1478.

6 Vakulenko A. A., and Kachanov, M. L., "Continuum Theory of Cracked Media," *Mekhanika Tverdogo Tela,* Vol. 6, 1971, pp. 159–166 (in Russian).

A Physically Consistent Method for the Prediction of Creep Behavior of Metals[1]

W. N. Findley.[2] I was pleased that Mr. Weng found our data on creep of 2618 aluminum under combined stress useful in evaluating his theory. It was very disappointing therefore to find on reading his preprint that our data had not been accurately transcribed so that the actual agreement with the theory was not as close as reported.

It seems necessary, to avoid future misinterpretation by other investigators, to present the following clarifications. As reported in [1] two lots of material were used. Our tests *A, B, C* were from swaged material, tests *D–H* from extruded material. Unfortunately, Mr. Weng's primary input Fig. 1 was taken from one test from each material, (our tests *A*1 and *F*1). Another problem arises from the fact that creep strain cannot be measured with any precision directly. Creep occurs so rapidly at the start of a test that large errors may arise from measuring creep strain from the first observed strain reading, as employed in the subject paper. In [1] total strain was reported. Creep strain could be obtained by: (*A*) Fitting an equation to the strain-time data and then extrapolating back to zero or (*B*) Subtracting the elastic strain from the total strain, providing there was no plastic strains as happened to be true in our tests. Method (*B*) was employed in our recent papers on this subject [2, 3].

Concerning the plotting of the experimental data, the lowest curve (our test *A*1) in Fig. 1 is correct. However, the highest curve (our test *F*1) is too high and there are too many points shown in the early part. The original data of our tests *A*1 and *F*1 are replotted in Fig. D1, where total strains are shown as ordinates. The corresponding elastic strain, which would be the correct origin for creep strains, was 0.2651 percent for our test *F*1, for example.

In Fig. 2 the shape of the early part of the curve is considerably distorted. A replot of our test *B*1 is shown in Fig. D2, which shows that the test data lies between the two theories shown by the author.

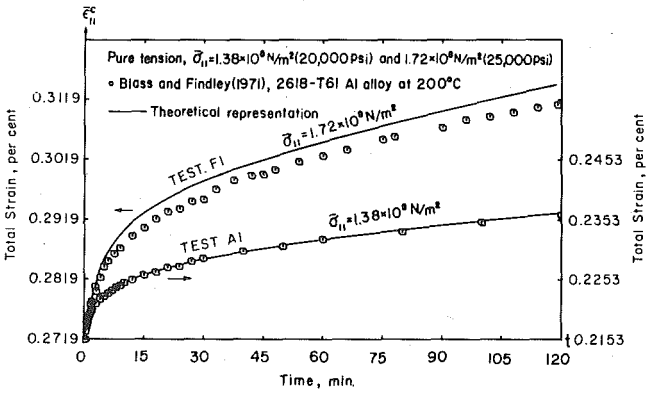

Fig. D1 Tensile creep strains of an aluminum alloy

[1] By G. J. Weng, and published in the December, 1979, issue of the ASME JOURNAL OF APPLIED MECHANICS, Vol. 46, pp. 800–804.

[2] Professor of Engineering, Brown University, Providence, R.I. 02912.

Copyright © 1980 by ASME

Downloaded 01 May 2010 to 171.66.16.243. Redistribution subject to ASME license or copyright; see http://www.asme.org/terms/Terms_Use.cfm

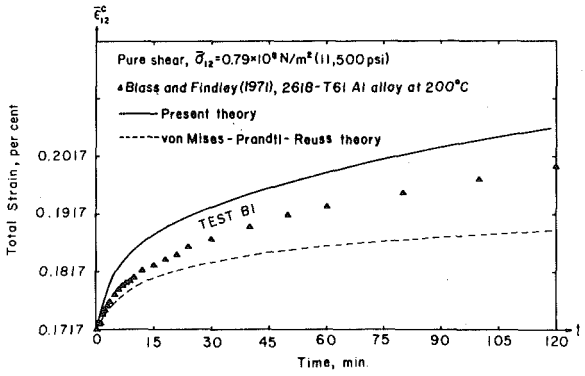

Fig. D2 Shear Creep strain of an aluminum alloy

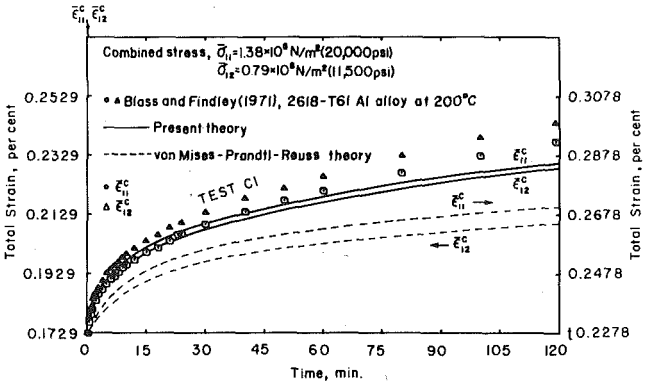

Fig. D3 Creep strains under combined stress

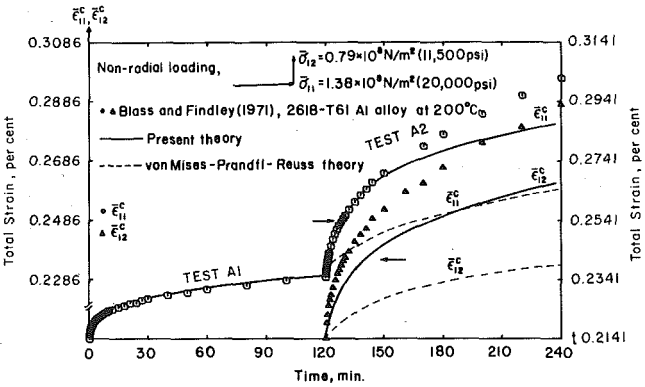

Fig. D4 Creep strains under nonradial loading

As shown in Fig. D3 the data for our test $C1$ lies above the author's curves and has a somewhat steeper slope than shown in Fig. 3.

In Fig. 4 the shapes of the plotted curves for the combined stress portion are considerably in error and the slopes of both curves are too low, as shown by Fig. D4 in which our test $A1$-$A2$ is replotted.

References

1 Blass, J. J., and Findley, W. N., "Short-Time Biaxial Creep of an Aluminum Alloy With Abrupt Changes of Temperature and State of Stress," ASME JOURNAL OF APPLIED MECHANICS, Vol. 38, 1971, pp. 489–501; (same as Author's [20]).

2 Findley, W. N., and Lai, J. S., "Creep and Recovery of 2618 Aluminum Alloy Under Combined Stress With a Representation by a Viscous-Viscoelastic Model," ASME JOURNAL OF APPLIED MECHANICS, Vol. 45, 1978, pp. 507–514.

3 Lai, J. S., and Findley, W. N., "Creep of 2618 Aluminum Under Step Stress Changes Predicted by a Viscous-Viscoelastic Model," ASME JOURNAL OF APPLIED MECHANICS, Vol. 47, Mar. 1980, pp. 21–26.

Author's Closure

The author wishes to thank Professor Findley and Dr. Blass for bringing to his attention some problems concerning his reproduced data from their experiment. Certain points need to be clarified, however:

1 The original paper by Blass and Findley (reference [1], Discussion) states that "The material used in these experiments was an aluminum forging alloy designated by the Aluminum Association as 2618-T61." "The rod used for specimens A, B, and C was from a different lot from that used for specimens D–H." Unfortunately, these were then interpreted as that these two lots of alloy were identical alloys, but perhaps received at different times. Had they stated clearly, as Professor Findley does here, that lot one was swaged while lot two extruded, indicating two different types of mechanical processing, such a misunderstanding surely would have been avoided.

2 Although Professor Findley and Dr. Blass prefer presenting their data in terms of total strains, the author considers presentation in terms of creep strains more revealing and useful to the study of "creep" behavior of materials. In reproducing curve $F1$ (Fig. 1), the origin of axial creep strain was originally taken at 0.2691 percent of the total strain and the end creep strain at 0.3116 percent of the total strain, and this resulted in 0.0425 percent for creep strain at the end of 2 hrs, as originally plotted in Fig. 1 with creep strain as ordinate. If now we use Findley's suggested method (B), with $E = 6.50 \times 10^{10}$ Pa (9.43×10^6 psi) (see reference [2], Discussion), the origin of creep strain should be at 0.2651 percent (not 0.2719 percent as shown in Fig. D1, Discussion) and this would lead to a creep strain of 0.0465 percent at the end of 2 hrs. Thus, following Findley's suggestion and using creep strain as ordinate, the creep curve for $F1$ not only is not "too high," but in fact not high enough.

3 The origin of shear creep strain for $B1$ (Fig. 2) was originally taken at 0.1652 percent of the total strain and the end creep strain at 0.1994 percent of the total strain, and this resulted in a creep strain of 0.0342 percent at the end of 2 hrs, as originally plotted in Fig. 2 with creep strain as ordinate. If we again use Findley's suggested method (B) and take $G = 2.46 \times 10^{10}$ Pa (3.57×10^6 psi) (see reference [2], Discussion), the origin of creep strain should be at 0.1611 percent of the total strain (not 0.1717 percent as shown in Fig. D2, Discussion), and the creep strain at the end of 2 hrs would be 0.0383 percent. Thus the reproduced creep strain again not only is not too high (as it appears by comparing the data in Figs. 2 and D2), but not high enough. Indeed, if Fig. D2 was plotted with 0.1611 percent strain as the origin, it would become evident that, *starting from the origin,* the trend of the creep data, except the first three data points, would bend in a manner as shown in Fig. 2.

4 The foregoing explanations indicate how sensitive the creep curves could be to the "onset" point of creep deformation. The discrepancies between the author's reproduced data and Findley's for Figs. 3 and 4 (except $\bar{\epsilon}_{11}{}^c$ for $A2$, see below) are again due to the differences in identifying the onset points of creep deformation and in presenting the data points in terms of total strains or of creep strains. It should be pointed out though, that in studying the experimental data of Blass and Findley, the author encountered some difficulty. Since there was no plastic strain in these tests, as Professor Findley pointed out, the instantaneous response was always elastic. But the initial strains under the same stress, or strain components under abrupt change of unrelated stress, are usually not identical, and the differences are often of the same order of magnitude and in some cases even greater than the differences between the author's reproduced data and Findley's. For instance their original data indicates that the initial axial strain for $A1$ is about 0.2153 percent and for $B2$ about 0.2333 percent, while both under the same tensile stress of 13.79×10^7 Pa (20 ksi). Some other such discrepancies were also observed, as

Downloaded 01 May 2010 to 171.66.16.243. Redistribution subject to ASME license or copyright; see http://www.asme.org/terms/Terms_Use.cfm

listed in Table 1. Indeed it was primarily due to this type of problems that the author frequently could not simply take the first data point as the onset point of creep deformation, and instead, had to consider the nature of these discrepancies during his identification of these onset points, and this inevitably could lead to disagreement.

5 A reexamination of the reproduced data $\bar{\epsilon}_{11}{}^c$ for $A2$ showed that this portion of curve was misrepresented. The original calculation of $\bar{\epsilon}_{11}{}^c$ at the end of 2 hrs gave a creep strain of 0.0665 percent and this was inadvertently taken as the total creep strain at the end of the nonradial loading, while in fact the end creep strain for $A1$, 0.0212 percent should be superimposed to give a final creep strain of 0.0877 percent. Thus, unlike the original drawing, this portion of experimental data, like that of $\bar{\epsilon}_{12}{}^c$, should lie above, not below, the theoretical curve.

6 In light of the misunderstanding on these two different materials the offered quantitative comparison between the theory and experiment should be viewed from a new ground. Fortunately, the tensile creep property of the swaged aluminum is fairly close to that of the extruded one; comparison of the creep strains between $A1$ and $H1$ indicates that at the end of 2 hrs the creep strain of the swaged specimen is about 9 percent higher than that of the extruded one. It is conceivable, then, that if a swaged specimen were tested under the condition of $F1$ to yield a tensile creep curve in place of the top curve in Fig. 1, a higher creep curve would result. Then the value of β, the exponent of the resolved shear stress in the constitutive equation, would correspondingly increase from its original value 3.50. This would lead to relatively higher theoretical creep strains for both combined stress (Fig. 3) and nonradial loading (Fig. 4), both offering much higher resolved shear stress compared to the two pure tensions. Since the resolved shear stress offered by the pure shear (Fig. 2) lies between the two pure tensions, its recomputed creep strain would only be increased slightly. With the origin of creep strain determined by Findley's suggested method (B) reasonably good agreement between the theory and experiment, except for the first few data points, therefore, could still be expected for these three loading conditions.

Table 1 Some inconsistent data points in reference [1] of the Discussion

			Total Strains	Differences
i)	Initial ϵ_{11} for	A1	ϵ_{11} = 0.2153%	0.0180%
		C1	ϵ_{11} = 0.2278%	
		B2	ϵ_{11} = 0.2333%	
ii)	Initial ϵ_{12} for	B1	ϵ_{12} = 0.1717%	0.0528%
		C1	ϵ_{12} = 0.1729%	
		A2	ϵ_{12} = 0.2141%	
		F1	ϵ_{12} = 0.1613%*	
iii)	End ϵ_{11} for	A1	ϵ_{11} = 0.2366%	0.0066%
	Beginning ϵ_{11} for	A2	ϵ_{11} = 0.2300%	
iv)	End ϵ_{12} for	B1	ϵ_{12} = 0.2000%	0.0133%
	Beginning ϵ_{12} for	B2	ϵ_{12} = 0.2133%	
v)	End ϵ_{11} for	B4	ϵ_{11} = 0.7261%	0.0210%
	Beginning ϵ_{11} for	B5	ϵ_{11} = 0.7471%	

*Different mechanical processing could change the microstructure of the material, but not its elastic property to a noticeable degree.

On the Determination of Stresses, Displacements, and Stress-Intensity Factors in Edge-Cracked Sheets With Mixed Boundary Conditions[1]

J. L. Swedlow.[2] The author is to be congratulated for his insightful use of Williams's series solution for crack problems [1] to evaluate experimental data in terms of stress intensity. With the method he describes, one may hope to utilize *in situ* displacement measurements via holographic techniques, for example, to assess the severity of a crack found in a structure. Such utility goes beyond the fatigue gage he describes and could eventually prove to be a valuable adjunct to NDE (nondestructive evaluation) of structures.

To achieve this capacity, the formulation given in the paper should be moderately extended. Even if a structure or, for that matter, a laboratory specimen is loaded to produce purely Mode-I response, the displacement data may contain rigid-body motions beyond those considered. The author does observe one of these components in his equation (25) but excludes it from further consideration. Thus the procedure will treat rigid translation parallel to the line of the crack only; it omits rigid rotation and rigid translation normal to the crack.

In an earlier analysis [2] aimed at the same objectives as the present paper, we considered these components of rigid motion. Our treatment lacked some of the elegance of the present paper so that we were obliged to approximate the calculation of total rigid motion. The technique seemed to work well nonetheless, for a sequence of test cases. Our formulation was not limited to the "even" or symmetric series reported by Williams [1], but carried the full solution. In that representation, the term represented by the author's equation (25) was retained; rigid rotation is built into the linear term of the "odd" or antisymmetric series. It is thus suggested that the author extend his formulation to carry such terms and, thereby, to increase its range of utility.

References

1 Williams, M. L., "On the Stress Distribution at the Base of a Stationary Crack," ASME JOURNAL OF APPLIED MECHANICS, Vol. 24, 1957, pp. 109–114.

2. Swedlow, J. L., Karabin, M. E., Jr., and Maddux, G. E., "Crack-Tip Stress Analysis From Field Values of the Displacements Using Complementary Energy," in *Fracture 1977*, University of Waterloo, Vol. 3, 1977, pp. 103–109.

Author's Closure

Professor Swedlow's kind words concerning my method of using the Williams' functions as elements of an expansion are appreciated. It is regretted that his use of the Williams' functions was not mentioned in my survey of prior applications.

He is perfectly correct, of course, in observing that while all components of rigid-body motion were discussed in my original formulation, only one remains after the restriction to the class of problems symmetric about the crack. This restriction was made only because

[1] By P. J. Torvik, and published in the September, 1979, issue of the ASME JOURNAL OF APPLIED MECHANICS, Vol. 46, pp. 611–617.

[2] Professor, Department of Mechanical Engineering, Carnegie-Mellom University, Pittsburgh, Pa. 15213.

Downloaded 01 May 2010 to 171.66.16.243. Redistribution subject to ASME license or copyright; see http://www.asme.org/terms/Terms_Use.cfm

listed in Table 1. Indeed it was primarily due to this type of problems that the author frequently could not simply take the first data point as the onset point of creep deformation, and instead, had to consider the nature of these discrepancies during his identification of these onset points, and this inevitably could lead to disagreement.

5 A reexamination of the reproduced data $\bar{\epsilon}_{11}{}^c$ for $A2$ showed that this portion of curve was misrepresented. The original calculation of $\bar{\epsilon}_{11}{}^c$ at the end of 2 hrs gave a creep strain of 0.0665 percent and this was inadvertently taken as the total creep strain at the end of the nonradial loading, while in fact the end creep strain for $A1$, 0.0212 percent should be superimposed to give a final creep strain of 0.0877 percent. Thus, unlike the original drawing, this portion of experimental data, like that of $\bar{\epsilon}_{12}{}^c$, should lie above, not below, the theoretical curve.

6 In light of the misunderstanding on these two different materials the offered quantitative comparison between the theory and experiment should be viewed from a new ground. Fortunately, the tensile creep property of the swaged aluminum is fairly close to that of the extruded one; comparison of the creep strains between $A1$ and $H1$ indicates that at the end of 2 hrs the creep strain of the swaged specimen is about 9 percent higher than that of the extruded one. It is conceivable, then, that if a swaged specimen were tested under the condition of $F1$ to yield a tensile creep curve in place of the top curve in Fig. 1, a higher creep curve would result. Then the value of β, the exponent of the resolved shear stress in the constitutive equation, would correspondingly increase from its original value 3.50. This would lead to relatively higher theoretical creep strains for both combined stress (Fig. 3) and nonradial loading (Fig. 4), both offering much higher resolved shear stress compared to the two pure tensions. Since the resolved shear stress offered by the pure shear (Fig. 2) lies between the two pure tensions, its recomputed creep strain would only be increased slightly. With the origin of creep strain determined by Findley's suggested method (B) reasonably good agreement between the theory and experiment, except for the first few data points, therefore, could still be expected for these three loading conditions.

Table 1 Some inconsistent data points in reference [1] of the Discussion

			Total Strains	Differences
i)	Initial ϵ_{11} for	A1	ϵ_{11} = 0.2153%	0.0180%
		C1	ϵ_{11} = 0.2278%	
		B2	ϵ_{11} = 0.2333%	
ii)	Initial ϵ_{12} for	B1	ϵ_{12} = 0.1717%	0.0528%
		C1	ϵ_{12} = 0.1729%	
		A2	ϵ_{12} = 0.2141%	
		F1	ϵ_{12} = 0.1613%*	
iii)	End ϵ_{11} for	A1	ϵ_{11} = 0.2366%	0.0066%
	Beginning ϵ_{11} for	A2	ϵ_{11} = 0.2300%	
iv)	End ϵ_{12} for	B1	ϵ_{12} = 0.2000%	0.0133%
	Beginning ϵ_{12} for	B2	ϵ_{12} = 0.2133%	
v)	End ϵ_{11} for	B4	ϵ_{11} = 0.7261%	0.0210%
	Beginning ϵ_{11} for	B5	ϵ_{11} = 0.7471%	

*Different mechanical processing could change the microstructure of the material, but not its elastic property to a noticeable degree.

On the Determination of Stresses, Displacements, and Stress-Intensity Factors in Edge-Cracked Sheets With Mixed Boundary Conditions[1]

J. L. Swedlow.[2] The author is to be congratulated for his insightful use of Williams's series solution for crack problems [1] to evaluate experimental data in terms of stress intensity. With the method he describes, one may hope to utilize *in situ* displacement measurements via holographic techniques, for example, to assess the severity of a crack found in a structure. Such utility goes beyond the fatigue gage he describes and could eventually prove to be a valuable adjunct to NDE (nondestructive evaluation) of structures.

To achieve this capacity, the formulation given in the paper should be moderately extended. Even if a structure or, for that matter, a laboratory specimen is loaded to produce purely Mode-I response, the displacement data may contain rigid-body motions beyond those considered. The author does observe one of these components in his equation (25) but excludes it from further consideration. Thus the procedure will treat rigid translation parallel to the line of the crack only; it omits rigid rotation and rigid translation normal to the crack.

In an earlier analysis [2] aimed at the same objectives as the present paper, we considered these components of rigid motion. Our treatment lacked some of the elegance of the present paper so that we were obliged to approximate the calculation of total rigid motion. The technique seemed to work well nonetheless, for a sequence of test cases. Our formulation was not limited to the "even" or symmetric series reported by Williams [1], but carried the full solution. In that representation, the term represented by the author's equation (25) was retained; rigid rotation is built into the linear term of the "odd" or antisymmetric series. It is thus suggested that the author extend his formulation to carry such terms and, thereby, to increase its range of utility.

References

1 Williams, M. L., "On the Stress Distribution at the Base of a Stationary Crack," ASME JOURNAL OF APPLIED MECHANICS, Vol. 24, 1957, pp. 109–114.

2. Swedlow, J. L., Karabin, M. E., Jr., and Maddux, G. E., "Crack-Tip Stress Analysis From Field Values of the Displacements Using Complementary Energy," in *Fracture 1977*, University of Waterloo, Vol. 3, 1977, pp. 103–109.

Author's Closure

Professor Swedlow's kind words concerning my method of using the Williams' functions as elements of an expansion are appreciated. It is regretted that his use of the Williams' functions was not mentioned in my survey of prior applications.

He is perfectly correct, of course, in observing that while all components of rigid-body motion were discussed in my original formulation, only one remains after the restriction to the class of problems symmetric about the crack. This restriction was made only because

[1] By P. J. Torvik, and published in the September, 1979, issue of the ASME JOURNAL OF APPLIED MECHANICS, Vol. 46, pp. 611–617.

[2] Professor, Department of Mechanical Engineering, Carnegie-Mellom University, Pittsburgh, Pa. 15213.

Copyright © 1980 by ASME

Downloaded 01 May 2010 to 171.66.16.243. Redistribution subject to ASME license or copyright; see http://www.asme.org/terms/Terms_Use.cfm

the particular example chosen was of such symmetry. The same procedure should work if antisymmetric terms (and the additional rigid-body displacements) are included, although I have not so demonstrated with an example problem.

Vortex-Induced Oscillations
A Selective Review[1]

G. V. Parkinson.[2] I congratulate Professor Sarpkaya on his lucid and up-to-date review of research on the complex and absorbing phenomena of vortex-induced oscillations. It will prove a most helpful reference paper to workers in the field. For example, he has performed a useful service by devoting several paragraphs to the importance of distinguishing the system damping ζ_s from any damping arising directly from the fluid forces.

However, some comments in the paper relating to ζ_s and arising from work in my laboratory by Feng [1] and by Wood [2] require clarification. In his footnote 18 on Page 251, Professor Sarpkaya implies that Feng's values of $\overline{C}_L$ for an oscillating circular cylinder are too high, possibly due to large tunnel blockage effects, and that his data including $\overline{C}_L$ do not satisfy equation (9) (or its equivalent, equation (37)) of the present paper, as they should. In fact, as I pointed out previously in [3] for these same data, the reason equation (9) is not satisfied is that ζ_s as measured by Feng (using a streamlined bar of the same mass as the circular cylinder oscillated in still air) is too low, since it doesn't account for the effects of the wind-on drag load transmitted to the external cylindrical air-bearing mounting system or of the wind-on vibration of the tunnel structure to which the system was attached. The unbalance of equation (9) has nothing to do with Feng's $\overline{C}_L$-values. They will indeed be somewhat high compared to free-air values due to tunnel blockage effects, as I suggested to Professor Sarpkaya in a telephone conversation when he was writing the paper, but not enough to explain the difference from Sarpkaya's computed values. It is of interest that a recent paper by Bearman and Currie [4] presents fluctuating pressure data for an oscillating circular cylinder that are in good agreement with Feng's, and would correspond to $\overline{C}_L$-values as high as his for the same reduced velocity and cylinder amplitude. Elsewhere in the present paper, in equation (17) on Page 248, Professor Sarpkaya refers to Wood's empirical approximation to the effective ζ_s deduced from Feng's data, and used by Wood in nonlinear oscillator modeling. Sarpkaya also used equation (17) for ζ_s in his discrete-vortex model and, like Wood, found that it caused the prediction of double-amplitude responses. This led him to conclude tentatively that double-amplitude responses are primarily a consequence of variable structural damping. I am reluctant to share that conclusion, despite Wood's results from my laboratory, because of the considerable evidence that double-amplitude effects originate in the flow rather than in the elastic system. It seems probable to me that a sudden change in the vortex correlation length plays an important role in the jump from one $\overline{C}_L$-value to another.

References

1 Feng, C. C., "The Measurement of Vortex Induced Effects in Flow Past Stationary and Oscillating Circular and D-Section Cylinders," MASc Thesis, University of British Columbia, 1968.

2 Wood, K. N. "Coupled-Oscillator Models for Vortex-Induced Oscillation of a Circular Cylinder," MASc Thesis, University of British Columbia, 1976.

3 Parkinson, G. V. "Mathematical Models of Flow-Induced Vibrations of Bluff Bodies," *Flow-Induced Structural Vibrations*, ed., Naudascher, E., Springer-Verlag, Berlin, 1974, pp. 81–127.

4 Bearman, P. W., and Currie, I. G., "Pressure-Fluctuation Measurements on an Oscillating Circular Cylinder," *Journal of Fluid Mechanics*, Vol. 91, Part 4, 1979, pp. 661–677.

[1] By T. Sarpkaya and published in the June, 1979, issue of ASME JOURNAL OF APPLIED MECHANICS, Vol. 46, pp. 241–258.

[2] Professor of Mechanical Engineering, The University of British Columbia. Currently on leave in the Department of Aeronautics, Imperial College, London SW7 2BY, England.

Author's Closure

Professor Parkinson's comments are very much appreciated. Clearly, there is need for additional data on all aspects of vortex-induced oscillations. The measurement of the sectional lift coefficients, chordwise and spanwise correlation, and the material damping will help to resolve some of the outstanding issues. A sudden change in the vortex correlation length may play an important role in the jump from one lift coefficient to another. Such a change may be due to mechanical reasons (end effects, etc.) or due to fluid-mechanical reasons (Reynolds number effect, instabilities associated with the large excursions of the separation points, etc.). The discrete vortex model cannot, out of necessity, take into consideration the changes in the correlation length. The fact that the nonlinear variation of the material damping resulted in a double-amplitude response led this writer to conclude tentatively that double-amplitude responses are primarily a consequence of variable structural damping. Experiments with cylinders with controlled nonlinear material damping may shed some light on the problem and show whether a sudden jump in the correlation length or the nonlinear damping or some other important parameter or phenomenon which has not yet been incorporated into the analysis is responsible for the double-amplitude response.

The author wishes to point out some typographical errors which appeared in the paper. The equation number in the last paragraph of the left column of Page 246 and in line 3 of the right column of Page 246 should be changed to 3. Also, the exponents in equations (13) and (14) should be changed to read $+3.35$ and $+\frac{1}{2}$. The reference [10] has now been published and should read as follows:

10 Sarpkaya, T., and Shoaff, R. L., "Inviscid Model of Two-Dimensional Vortex Shedding by a Circular Cylinder," *AIAA Journal*, Vol. 17, No. 11, 1979, pp. 1193–1200.

Comparative Analysis by the Displacement-Discontinuity Method of Two Energy Criteria of Fracture[1]

E. T. Moyer, Jr.[2] In his paper, the author attempted to compare two, well-established, crack growth prediction theories; the maximum strain-energy release-rate theory (G theory),[3] and the minimum strain-energy-density theory (S theory). An underemphasized point of comparison is that to calculate G, the stress state in the body must be known before and after the crack grows while S theory requires only a knowledge of stress state before growth takes place. Thus, for many known crack configurations, S can be calculated with a high degree of accuracy where the results for G must be questioned.

Since numerically, G cannot be calculated in the exact limit as da (amount of crack growth) tends to zero, the author proposes a numerical convergence criterion (equation (10) of [1]).

$$|G(\theta,a + da) - G(\theta,a + da/2)| < \epsilon \qquad (1)$$

where θ is the angle of crack propagation and a is the original crack length. The choice of $da/2$ seems a bit arbitrary and unmotivated (ϵ would vary significantly as a function of n is da/n were used instead

[1] By F. H. Cornet, and published in the June, 1979, issue of the ASME JOURNAL OF APPLIED MECHANICS, Vol. 46, pp. 349–355.

[2] Research Assistant, Department of Mechanical Engineering and Mechanics, Lehigh University, Bethlehem, Pa. 18015.

[3] It should be pointed out that for mixed mode problems the maximum energy release rate theory is not a "derived" theory but a heuristic criterion as are all the existing continuum fracture theories. At present, there is no established law which governs the direction of crack initiation.

Downloaded 01 May 2010 to 171.66.16.243. Redistribution subject to ASME license or copyright; see http://www.asme.org/terms/Terms_Use.cfm

the particular example chosen was of such symmetry. The same procedure should work if antisymmetric terms (and the additional rigid-body displacements) are included, although I have not so demonstrated with an example problem.

Vortex-Induced Oscillations
A Selective Review[1]

G. V. Parkinson.[2] I congratulate Professor Sarpkaya on his lucid and up-to-date review of research on the complex and absorbing phenomena of vortex-induced oscillations. It will prove a most helpful reference paper to workers in the field. For example, he has performed a useful service by devoting several paragraphs to the importance of distinguishing the system damping ζ_s from any damping arising directly from the fluid forces.

However, some comments in the paper relating to ζ_s and arising from work in my laboratory by Feng [1] and by Wood [2] require clarification. In his footnote 18 on Page 251, Professor Sarpkaya implies that Feng's values of $\overline{C}_L$ for an oscillating circular cylinder are too high, possibly due to large tunnel blockage effects, and that his data including $\overline{C}_L$ do not satisfy equation (9) (or its equivalent, equation (37)) of the present paper, as they should. In fact, as I pointed out previously in [3] for these same data, the reason equation (9) is not satisfied is that ζ_s as measured by Feng (using a streamlined bar of the same mass as the circular cylinder oscillated in still air) is too low, since it doesn't account for the effects of the wind-on drag load transmitted to the external cylindrical air-bearing mounting system or of the wind-on vibration of the tunnel structure to which the system was attached. The unbalance of equation (9) has nothing to do with Feng's $\overline{C}_L$-values. They will indeed be somewhat high compared to free-air values due to tunnel blockage effects, as I suggested to Professor Sarpkaya in a telephone conversation when he was writing the paper, but not enough to explain the difference from Sarpkaya's computed values. It is of interest that a recent paper by Bearman and Currie [4] presents fluctuating pressure data for an oscillating circular cylinder that are in good agreement with Feng's, and would correspond to $\overline{C}_L$-values as high as his for the same reduced velocity and cylinder amplitude. Elsewhere in the present paper, in equation (17) on Page 248, Professor Sarpkaya refers to Wood's empirical approximation to the effective ζ_s deduced from Feng's data, and used by Wood in nonlinear oscillator modeling. Sarpkaya also used equation (17) for ζ_s in his discrete-vortex model and, like Wood, found that it caused the prediction of double-amplitude responses. This led him to conclude tentatively that double-amplitude responses are primarily a consequence of variable structural damping. I am reluctant to share that conclusion, despite Wood's results from my laboratory, because of the considerable evidence that double-amplitude effects originate in the flow rather than in the elastic system. It seems probable to me that a sudden change in the vortex correlation length plays an important role in the jump from one $\overline{C}_L$-value to another.

References

1 Feng, C. C., "The Measurement of Vortex Induced Effects in Flow Past Stationary and Oscillating Circular and D-Section Cylinders," MASc Thesis, University of British Columbia, 1968.

2 Wood, K. N. "Coupled-Oscillator Models for Vortex-Induced Oscillation of a Circular Cylinder," MASc Thesis, University of British Columbia, 1976.

3 Parkinson, G. V. "Mathematical Models of Flow-Induced Vibrations of Bluff Bodies," *Flow-Induced Structural Vibrations*, ed., Naudascher, E., Springer-Verlag, Berlin, 1974, pp. 81–127.

4 Bearman, P. W., and Currie, I. G., "Pressure-Fluctuation Measurements on an Oscillating Circular Cylinder," *Journal of Fluid Mechanics*, Vol. 91, Part 4, 1979, pp. 661–677.

[1] By T. Sarpkaya and published in the June, 1979, issue of ASME JOURNAL OF APPLIED MECHANICS, Vol. 46, pp. 241–258.

[2] Professor of Mechanical Engineering, The University of British Columbia. Currently on leave in the Department of Aeronautics, Imperial College, London SW7 2BY, England.

Author's Closure

Professor Parkinson's comments are very much appreciated. Clearly, there is need for additional data on all aspects of vortex-induced oscillations. The measurement of the sectional lift coefficients, chordwise and spanwise correlation, and the material damping will help to resolve some of the outstanding issues. A sudden change in the vortex correlation length may play an important role in the jump from one lift coefficient to another. Such a change may be due to mechanical reasons (end effects, etc.) or due to fluid-mechanical reasons (Reynolds number effect, instabilities associated with the large excursions of the separation points, etc.). The discrete vortex model cannot, out of necessity, take into consideration the changes in the correlation length. The fact that the nonlinear variation of the material damping resulted in a double-amplitude response led this writer to conclude tentatively that double-amplitude responses are primarily a consequence of variable structural damping. Experiments with cylinders with controlled nonlinear material damping may shed some light on the problem and show whether a sudden jump in the correlation length or the nonlinear damping or some other important parameter or phenomenon which has not yet been incorporated into the analysis is responsible for the double-amplitude response.

The author wishes to point out some typographical errors which appeared in the paper. The equation number in the last paragraph of the left column of Page 246 and in line 3 of the right column of Page 246 should be changed to 3. Also, the exponents in equations (13) and (14) should be changed to read $+3.35$ and $+\frac{1}{2}$. The reference [10] has now been published and should read as follows:

10 Sarpkaya, T., and Shoaff, R. L., "Inviscid Model of Two-Dimensional Vortex Shedding by a Circular Cylinder," *AIAA Journal*, Vol. 17, No. 11, 1979, pp. 1193–1200.

Comparative Analysis by the Displacement-Discontinuity Method of Two Energy Criteria of Fracture[1]

E. T. Moyer, Jr.[2] In his paper, the author attempted to compare two, well-established, crack growth prediction theories; the maximum strain-energy release-rate theory (G theory),[3] and the minimum strain-energy-density theory (S theory). An underemphasized point of comparison is that to calculate G, the stress state in the body must be known before and after the crack grows while S theory requires only a knowledge of stress state before growth takes place. Thus, for many known crack configurations, S can be calculated with a high degree of accuracy where the results for G must be questioned.

Since numerically, G cannot be calculated in the exact limit as da (amount of crack growth) tends to zero, the author proposes a numerical convergence criterion (equation (10) of [1]).

$$|G(\theta,a + da) - G(\theta,a + da/2)| < \epsilon \qquad (1)$$

where θ is the angle of crack propagation and a is the original crack length. The choice of $da/2$ seems a bit arbitrary and unmotivated (ϵ would vary significantly as a function of n is da/n were used instead

[1] By F. H. Cornet, and published in the June, 1979, issue of the ASME JOURNAL OF APPLIED MECHANICS, Vol. 46, pp. 349–355.

[2] Research Assistant, Department of Mechanical Engineering and Mechanics, Lehigh University, Bethlehem, Pa. 18015.

[3] It should be pointed out that for mixed mode problems the maximum energy release rate theory is not a "derived" theory but a heuristic criterion as are all the existing continuum fracture theories. At present, there is no established law which governs the direction of crack initiation.

Copyright © 1980 by ASME

Downloaded 01 May 2010 to 171.66.16.243. Redistribution subject to ASME license or copyright; see http://www.asme.org/terms/Terms_Use.cfm

is led to erroneous conclusions with respect to the inconsistencies between my results for uniaxial and triaxial compressions: negative θ values for G maximum imply that the crack propagates in the compressive uniaxial stress direction. This result is in qualitative agreement with Hoek and Bieniawski's Fig. 8 [9] but result obtained with Sih's strain-energy density factor theory [10] is not (if one considers results of Fig. 3(b) as valid).

8 A crack inclined 45° with respect to a uniaxial *tensile* stress field direction propagates in mixed mode 1 and 2. For this case it is shown that, with the proposed numerical model, both S and G criteria yield identical path and that computed value for S is within 5 percent of that of Sih's solution [6].

9 I would like to express my sincere thanks to Mr. Moyer for allowing me to clarify some of the apparent inconsistencies of my paper. I would like to add three major corrections. At the bottom of Page 352, "orientation changing form −15° to +75°" should read "orientations changing from +15° to −75°"; same page, 17 lines above "equation (12)" should read "equation (10)"; caption of Fig. 4 "σ = 100 mPa" should read "σ_1 = 100 mPa."

Additional References

5 Griffith A. A., *Philosophical Transactions of the Royal Society*, London, Series A, Vol. 221, 1921, p. 163.

6 Brace W. F., and Walsh J. B., *Am. Miner.*, Vol. 47, 1962, p. 1111.

7 *The American Heritage Dictionary of the English Language*, Morris, W., editor; American Heritage Publishing Co., N.Y., Boston.

8 McClintock, F. A., and Walsh, J. B., *Proceedings of the 4th U.S. National Congress of Applied Mechanics*, 1962, p. 1015.

9 Hoek E., and Bieniawski, Z. T., *International Journal of Fracture Mechanics*, Vol. 1, 1965, p. 137.

10 Sih G. C., *Mechanics of Fracture*, Vol. 1, Noordhoff International Publishing, Leyden, The Netherlands, 1973, p. XXI.

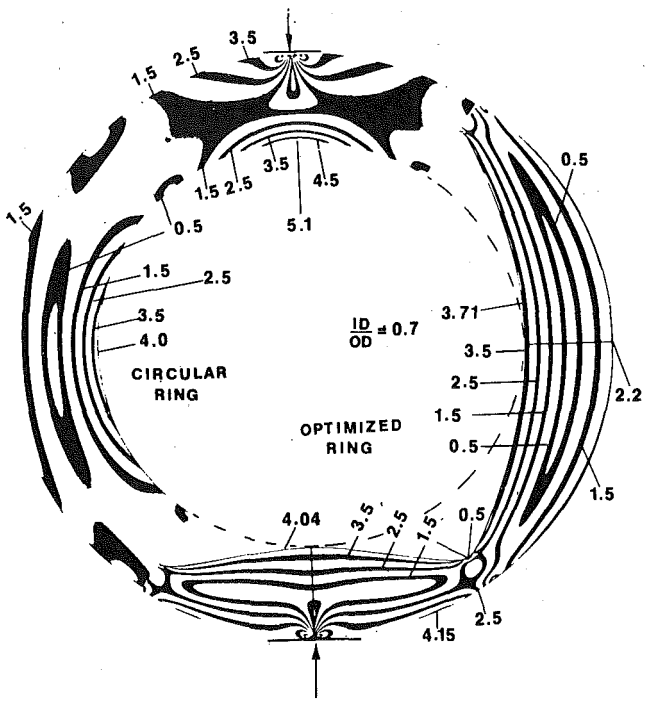

Fig. 1 Light field isochromatics in circular and optimized rings, subjected to the same load

Harmonic Holes for Nonconstant Fields[1]

A. J. Durelli.[2] The usual design procedure consists in the determination of displacements, strains, and stresses by analysis of a given loaded geometry of a structural component. If the analysis shows that the displacements, strains or stresses are not acceptable, changes have to be introduced in the geometry or in the loading, and the analysis be repeated. This may be today a necessary procedure, but obviously it would be much better if the procedure could be reversed and the geometry obtained from the prescribed loads and design requirements. Therefore, the attempt, by the authors, to invert the standard problems of classic elasticity to solve for the geometry of a hole, which has no stress concentration in a stress field, should be welcome.

The method proposed by the authors requires an analytic representation of the boundary, and although this is always useful because of the generality of the approach and because it stimulates the imagination, it becomes very complicated very fast and it does not seem fruitful. Other approaches have been followed recently which permit a much easier determination of optimum configurations. References can be found in one of the discusser's papers [1]. In particular, the use of finite elements and photoelasticity should be mentioned. As a sample of the kind of work that can be conducted, and of the results obtained, Fig. 1 may be useful. It represents the isochromatics in a circular ring, subjected to diametral compression. In the top left half, the inside (ID) and outside (OD) boundaries of the ring are concentric and the well-known stress concentrations at the vertical and horizontal axes are shown. It is a classic case of stress

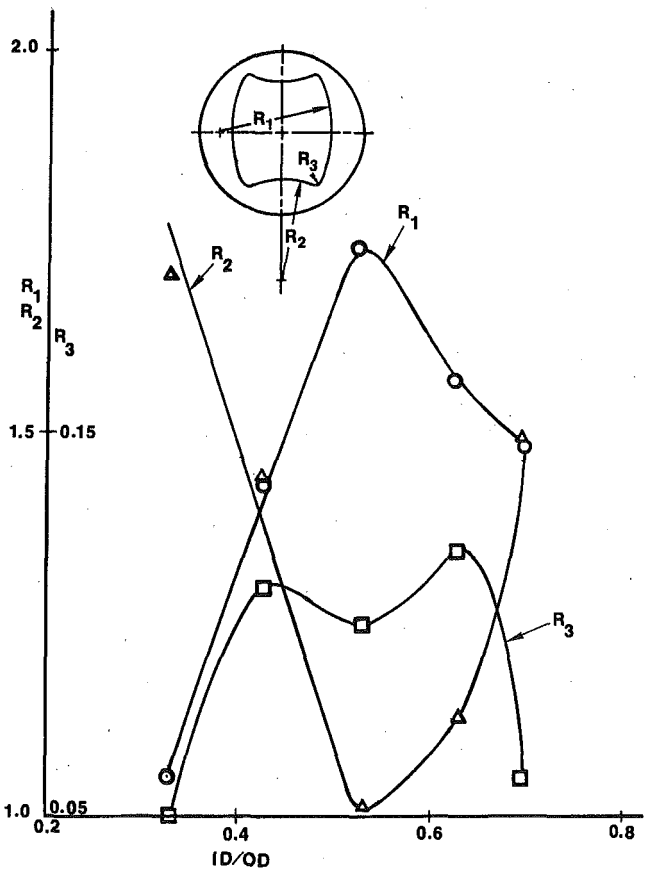

Fig. 2 Radii of the elements of holes producing optimum distribution of stress in circular rings under diametral compression

[1] By G. S. Bjorkman, Jr., and R. Richards, Jr., and published in September, 1979, issue of ASME JOURNAL OF APPLIED MECHANICS, Vol. 46, pp. 573–576.

[2] John F. Dodge Professor, Oakland University, Rochester, Mich. 48063.

Copyright © 1980 by ASME

Downloaded 01 May 2010 to 171.66.16.243. Redistribution subject to ASME license or copyright; see http://www.asme.org/terms/Terms_Use.cfm

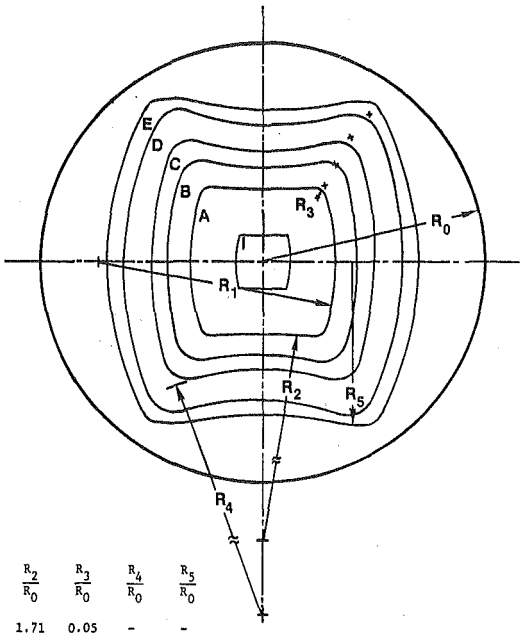

	ID/OD	R1/R0	R2/R0	R3/R0	R4/R0	R5/R0	
A	0.33	1.06	1.71	0.05	-	-	
B	0.43	1.43	1.44	0.11	-	-	
C	0.53	1.73	1.01	0.10	1.25	-	
D	0.63	1.51	1.13	0.12	-	-	
E	0.70	1.49	1.49	0.06	-	0.73	
I	0.14	0.35	∞	0.05	-	-	(Estimated)

Fig. 3 Optimum shape of the inner boundary of circular rings subjected to diametral compression

concentrations at the edge of a hole, and gradient of stresses along the hole.

The bottom right part of the figure shows the isochromatics for the ring, subjected to the same amount of load, after an appreciable amount of material has been removed, and respecting the design constrains: (*a*) the outside boundary must remain circular; (*b*) the inside boundary has to clear the same space as the inside boundary of the concentric ring.

In the optimized ring: (1) the gradients of stresses along the inside boundary, where the stresses are maxima, have practically disappeared both at the vertical and horizontal portions of that boundary; (2) there is a gradient of stress along a very small portion of the inside boundary at the corner, down to zero; (3) the stress-concentration factor has decreased by 27 percent; (4) the size of the hole has increased, decreasing the amount of material used to build the ring, by as much as 13 percent; (5) the outside diameter has been maintained circular as prescribed; (6) the clearance about the original inside diameter has also been maintained as prescribed; (7) the coefficient of efficiency [1] has increased from 60 percent for the circular ring to 96 percent for the optimized ring; (8) in the process of optimizing the inside boundary, the outside boundary became practically optimized; (9) the optimized hole has sharp corners with zero stress occurring at the sharp corners.

After this operation is performed, the geometry of the inside of the boundary is very closely approximated by a series of circles with common tangents at the point of contact, as shown in Fig. 2. If this procedure is followed parametrically, for rings of different widths, very interesting results are obtained. Fig. 3 shows optimized shapes for all ID/OD.

Obviously this experimental approach requires a different definition of optimum shape. The discusser introduced the concept of a coefficient of efficiency, the value of which is one for an ideal optimized shape. The discusser wonders whether the definition the authors use, of optimum shape, would permit, at all, the optimization of boundaries along which the sign of the stress changes.

Reference

1 Durelli, A. J., Brown, K., and Yee, P., "Optimization of Geometric Discontinuities in Stress Fields," *Experimental Mechanics*, Vol. 18, No. 8, Aug. 1978, pp. 303–308.

Authors' Closure

The authors wish to express their appreciation to Professor Durelli for his comments, and welcome his most recent contribution to the development of techniques to reduce stress concentrations. The particular technique described by Durelli in his discussion is a trial and error photoelastic procedure which relies upon achieving a condition of constant tensile and/or compressive stress along the boundary which is to be "optimized." A coefficient of efficiency, subject to a constraint on the value of the maximum boundary stress, is a measure of the extent to which the boundary has achieved this optimum condition (i.e., satisfied the constant stress design criteria). It is reasonable to conclude therefore, that this technique is limited to combinations of initial stress fields and region connectivity for which it is possible to achieve a condition of constant stress along part or all of the boundary being optimized.

The case considered in the authors' paper is an example of a specific combination of initial stress field and region connectivity to which Durelli's technique cannot be applied. In this case, where an infinite sheet with a single hole is subjected to a nonconstant stress field, it can be proved that it is impossible to achieve a constant stress along *any* portion of the hole boundary. Thus the shape of an initially circular hole in this stress field could not be "optimized" using Durelli's procedure since the constant stress design criteria is itself absolutely unattainable.

It should be emphasized that the harmonic field condition and the methods used by the authors are quite general and can be applied, not only to loaded and unloaded holes but also to inclusions. A recent paper [2] by the authors gives a simple application of the harmonic field condition to the optimization of an inclusion. The authors solve the inverse problem of determining the geometry of a rigid inclusion which satisfies the harmonic field condition for a constant stress field. As illustrated in Fig. 1 of the Closure, the solution is an ellipse where the ratio of the principal axes are in proportion to the ratio of the principal strains, i.e.,

$$\frac{a}{b} = \frac{\epsilon_2}{\epsilon_1}$$

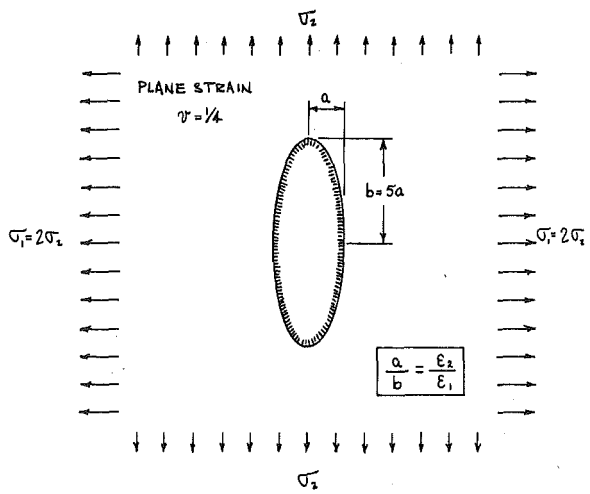

Fig. 1 The rigid harmonic inclusion

Downloaded 01 May 2010 to 171.66.16.243. Redistribution subject to ASME license or copyright; see http://www.asme.org/terms/Terms_Use.cfm

In addition the authors prove that this rigid harmonic inclusion produces the absolute minimum stress concentration.

Using the harmonic field condition the authors have been able to prove for the first time that in constant fields specific hole and inclusion geometries produce the absolute minimum stress concentration. Since these solutions are not approximate, but exact closed-form solutions, it is therefore possible to precisely determine the characteristics of the perturbed stress field for which a hole produces minimum stress concentration [3]. Knowledge of these characteristics may well lead to general theorems for the minimization of stress concentrations.

Additional References

2 Bjorkman, Jr., G. S., and Richards, Jr., R., "The Rigid Harmonic Inclusion," *Proceedings of the Third ASCE Engineering Mechanics Division Specialty Conference,* University of Texas, Austin, Texas, Sept. 1979.

3 Richards, Jr., R. and Bjorkman, Jr., G. S., "Harmonic Shapes and Optimum Design," submitted for publication to the *ASCE Journal of the Engineering Mechanics Division.*

On the Barber Boundary Conditions for Thermoelastic Contact[1]

J. R. Barber.[2] The authors give a gratifyingly convincing demonstration of the self-consistency of the concept of imperfect contact with regard to conditions local to the transitions and their paper represents a significant step toward the establishment of existence theorems for thermoelastic contact.

The argument from particular cases and the general trends of the asymptotic analysis strongly suggest that, for smooth contact problems, imperfect contact regions will occur *if and only if* the heat flows into the material of smaller distortivity. However, there appear to be two possible exceptions which the authors may be able to eliminate:

1 For heat flow into the material of larger distortivity, imperfect contact regions are still allowable if they are completely surrounded by separation. This requires that the imperfect contact region in question was concave in the undisturbed state and such a solution will almost certainly be unstable, but it does not seem to be ruled out on a steady-state basis.

2 As the authors remark at the end of Section 3, a transition from perfect contact to separation is possible even with heat flow into the material of smaller distortivity "if, for one reason or another, no square root singularity occurs in the heat flux." I should be interested to know under what conditions this might arise. In the particular case in which the contacting solids can be represented as half spaces, the perfect contact regions will constitute an isothermal surface which passes between the solids in the separation regions. The heat-conduction problem is then a classical mixed boundary-value problem analogous to the identation of an elastic solid by a flat rigid punch and a square root singularity must arise on the boundary.

Finally, I consider that the authors have overstated the case in excluding the logarithmic terms in temperature at the transition from imperfect contact to separation. The basic principle of the asymptotic method is that analytically smooth functions cannot interact with the discontinuities which arise at the transitions and hence only the latter need to be considered. However, the inequality (69) involves the product of a temperature difference and a heat flux so that, if the latter is discontinuous, the magnitude *and sign* of the discontinuity in the left-hand side of (69) will be affected by analytically smooth components of the temperature difference. This inequality can therefore only be assessed in the context of the contact problem as a whole.

Perhaps the authors could be persuaded to provide us with a more complete discription of this transition. It would appear that the logarithmic terms give a discontinuity in heat flux at the transition, which implies a discontinuity in curvature (authors' reference [14]). This in turn will violate inequality (18) in the separation zone if heat flows into the material of larger distortivity. Hence, the logarithmic terms are only allowable for the reverse direction of heat flow.

[1] By Maria Comninou and J. Dundurs, and published in the December, 1979, issue of ASME JOURNAL OF APPLIED MECHANICS, Vol. 46, pp. 849–853.

[2] Department of Mechanical Engineering, University of Newcastle upon Tyne, Newcastle upon Tyne NE1 7RU, England.

Authors' Closure

We reply to the points raised by Dr. Barber by referring to the pertinent paragraphs in his discussion.

We must say with regard to the second paragraph that our results say nothing about the existence of specific regions as such, but pertain only to the various transitions in the boundary conditions and the *local* directions of heat flow. They do not restrict the *global* features of thermoelastic contact to the extent that one could arrive at an *if and only if* statement even for heat flow that is in the same direction everywhere. Thus, for instance as suggested in the discussion, it is entirely possible to have a central zone of imperfect contact bordered by zones of separation. Moreover, these zones of separation could be surrounded on the outside by zones of perfect contact, transmitting a net force, and subsequent zones of separation. In such a case heat could flow through both types of contact zones into the material with the larger distortivity without violating any of the conditions imposed in our article. This could happen by coincidence in a given situation, or a problem could be tailored to illustrate such a possibility by adjusting the surface profiles of the bodies, the distribution of the applied forces and the imposed thermal conditions. It is also not difficult to envision situations, such that in different places heat flows in opposite directions from one body to the other and more complicated arrangement of the zones is encountered. The point is that one should not read more into our results than there is: They simply indicate that it is generally not possible to have a direct transition from perfect contact to separation unless heat flows *locally* into the material with the larger distortivity, and the difficulty with heat flow in the opposite direction may consistently be overcome by introducing the Barber boundary conditions of imperfect contact.

An asymptotic analysis by its very nature cannot establish the existence of a singularity in a specific problem. That is, it can predict only the type of singularity that is possible at a given transition in the boundary conditions. Thus one can imagine two different sets of imposed thermal and mechanical conditions giving square-root singularities of the same strength but of opposite signs, so that they cancel upon superposition. The disappearance of a singularity in heat flux at the transition from perfect contact to separation is possible, but it is likely to be an exception.

The point raised in the third paragraph is well taken. In fact, a constant in the temperature difference is the dominant term in the asymptotic expansion, and the inequality (69) is not violated by the logarithmic terms. Then the coefficients M_1 and M_2 need not vanish and are related by

$$M_2 = -\frac{k_1}{k_2} M_1.$$

Equation (71) in the paper is replaced with

$$\frac{\kappa_2 + 1}{2\mu_2} B_2 = \frac{\kappa_1 + 1}{2\mu_1} B_1 + \frac{\pi k_1}{1 - \lambda} (\delta_1 - \delta_2) M_1.$$

The dominant part of the heat flux corresponding to $\lambda = -1$ is

$$q_\theta^{(1)}(r, \pi) = q_\theta^{(2)}(r, -\pi) = -\pi k_1 M_1$$

Downloaded 01 May 2010 to 171.66.16.243. Redistribution subject to ASME license or copyright; see http://www.asme.org/terms/Terms_Use.cfm

In addition the authors prove that this rigid harmonic inclusion produces the absolute minimum stress concentration.

Using the harmonic field condition the authors have been able to prove for the first time that in constant fields specific hole and inclusion geometries produce the absolute minimum stress concentration. Since these solutions are not approximate, but exact closed-form solutions, it is therefore possible to precisely determine the characteristics of the perturbed stress field for which a hole produces minimum stress concentration [3]. Knowledge of these characteristics may well lead to general theorems for the minimization of stress concentrations.

Additional References

2 Bjorkman, Jr., G. S., and Richards, Jr., R., "The Rigid Harmonic Inclusion," *Proceedings of the Third ASCE Engineering Mechanics Division Specialty Conference,* University of Texas, Austin, Texas, Sept. 1979.

3 Richards, Jr., R. and Bjorkman, Jr., G. S., "Harmonic Shapes and Optimum Design," submitted for publication to the *ASCE Journal of the Engineering Mechanics Division.*

On the Barber Boundary Conditions for Thermoelastic Contact[1]

J. R. Barber.[2] The authors give a gratifyingly convincing demonstration of the self-consistency of the concept of imperfect contact with regard to conditions local to the transitions and their paper represents a significant step toward the establishment of existence theorems for thermoelastic contact.

The argument from particular cases and the general trends of the asymptotic analysis strongly suggest that, for smooth contact problems, imperfect contact regions will occur *if and only if* the heat flows into the material of smaller distortivity. However, there appear to be two possible exceptions which the authors may be able to eliminate:

1 For heat flow into the material of larger distortivity, imperfect contact regions are still allowable if they are completely surrounded by separation. This requires that the imperfect contact region in question was concave in the undisturbed state and such a solution will almost certainly be unstable, but it does not seem to be ruled out on a steady-state basis.

2 As the authors remark at the end of Section 3, a transition from perfect contact to separation is possible even with heat flow into the material of smaller distortivity "if, for one reason or another, no square root singularity occurs in the heat flux." I should be interested to know under what conditions this might arise. In the particular case in which the contacting solids can be represented as half spaces, the perfect contact regions will constitute an isothermal surface which passes between the solids in the separation regions. The heat-conduction problem is then a classical mixed boundary-value problem analogous to the identation of an elastic solid by a flat rigid punch and a square root singularity must arise on the boundary.

Finally, I consider that the authors have overstated the case in excluding the logarithmic terms in temperature at the transition from imperfect contact to separation. The basic principle of the asymptotic method is that analytically smooth functions cannot interact with the discontinuities which arise at the transitions and hence only the latter need to be considered. However, the inequality (69) involves the product of a temperature difference and a heat flux so that, if the latter is discontinuous, the magnitude *and sign* of the discontinuity in the left-hand side of (69) will be affected by analytically smooth components of the temperature difference. This inequality can therefore only be assessed in the context of the contact problem as a whole.

Perhaps the authors could be persuaded to provide us with a more complete discription of this transition. It would appear that the logarithmic terms give a discontinuity in heat flux at the transition, which implies a discontinuity in curvature (authors' reference [14]). This in turn will violate inequality (18) in the separation zone if heat flows into the material of larger distortivity. Hence, the logarithmic terms are only allowable for the reverse direction of heat flow.

[1] By Maria Comninou and J. Dundurs, and published in the December, 1979, issue of ASME JOURNAL OF APPLIED MECHANICS, Vol. 46, pp. 849–853.

[2] Department of Mechanical Engineering, University of Newcastle upon Tyne, Newcastle upon Tyne NE1 7RU, England.

Authors' Closure

We reply to the points raised by Dr. Barber by referring to the pertinent paragraphs in his discussion.

We must say with regard to the second paragraph that our results say nothing about the existence of specific regions as such, but pertain only to the various transitions in the boundary conditions and the *local* directions of heat flow. They do not restrict the *global* features of thermoelastic contact to the extent that one could arrive at an *if and only if* statement even for heat flow that is in the same direction everywhere. Thus, for instance as suggested in the discussion, it is entirely possible to have a central zone of imperfect contact bordered by zones of separation. Moreover, these zones of separation could be surrounded on the outside by zones of perfect contact, transmitting a net force, and subsequent zones of separation. In such a case heat could flow through both types of contact zones into the material with the larger distortivity without violating any of the conditions imposed in our article. This could happen by coincidence in a given situation, or a problem could be tailored to illustrate such a possibility by adjusting the surface profiles of the bodies, the distribution of the applied forces and the imposed thermal conditions. It is also not difficult to envision situations, such that in different places heat flows in opposite directions from one body to the other and more complicated arrangement of the zones is encountered. The point is that one should not read more into our results than there is: They simply indicate that it is generally not possible to have a direct transition from perfect contact to separation unless heat flows *locally* into the material with the larger distortivity, and the difficulty with heat flow in the opposite direction may consistently be overcome by introducing the Barber boundary conditions of imperfect contact.

An asymptotic analysis by its very nature cannot establish the existence of a singularity in a specific problem. That is, it can predict only the type of singularity that is possible at a given transition in the boundary conditions. Thus one can imagine two different sets of imposed thermal and mechanical conditions giving square-root singularities of the same strength but of opposite signs, so that they cancel upon superposition. The disappearance of a singularity in heat flux at the transition from perfect contact to separation is possible, but it is likely to be an exception.

The point raised in the third paragraph is well taken. In fact, a constant in the temperature difference is the dominant term in the asymptotic expansion, and the inequality (69) is not violated by the logarithmic terms. Then the coefficients M_1 and M_2 need not vanish and are related by

$$M_2 = -\frac{k_1}{k_2} M_1.$$

Equation (71) in the paper is replaced with

$$\frac{\kappa_2 + 1}{2\mu_2} B_2 = \frac{\kappa_1 + 1}{2\mu_1} B_1 + \frac{\pi k_1}{1 - \lambda} (\delta_1 - \delta_2) M_1.$$

The dominant part of the heat flux corresponding to $\lambda = -1$ is

$$q_\theta^{(1)}(r, \pi) = q_\theta^{(2)}(r, -\pi) = -\pi k_1 M_1$$

Copyright © 1980 by ASME

Downloaded 01 May 2010 to 171.66.16.243. Redistribution subject to ASME license or copyright; see http://www.asme.org/terms/Terms_Use.cfm

through the zone of imperfect contact. Since no heat flows through the separation zone, the heat flux has a jump discontinuity at the transition. For $\lambda = -1$, the gap in the separation zone is

$$g(r) = \frac{1}{2}\pi k_1 (\delta_2 - \delta_1) M_1 r^2.$$

The last two expressions support the last statement made by Dr. Barber.

Downloaded 01 May 2010 to 171.66.16.243. Redistribution subject to ASME license or copyright; see http://www.asme.org/terms/Terms_Use.cfm

Journal of Applied Mechanics

Book Reviews

Theory of Thermoelasticity With Applications. By J. L. Nowinski. Sijthoff & Noordhoff, The Netherlands. 1978. Pages 852. Price $93.

REVIEWED BY B. BOLEY[1]

The Table of Contents of this book presents to the prospective reader an ambitious program, covering in effect all aspects of linear thermoelasticity. This of course includes basic material which has been treated in other books on the subject, but extends widely into newer topics which have gained increased prominence in recent years. On the former category, the book does an adequate job of presentation, although I suspect that during the author's lectures on these subjects (from which, as he states in the Preface, the book originated) he was able to add a great deal orally to enhance both clarity and completeness.

On the more advanced subjects, I must confess a certain feeling of disappointment. The treatment tends to be a little too episodic, relying on detailed solutions of a few examples, often without any real attempt to the kind of synthesis (or at least summary) that a textbook reader might expect. For example, in the case of electromagnetic effects, a commendably detailed derivation of the basic equations some 50 pages long is followed by 8 pages containing two examples but little discussion. I would not be surprised if this leaves the student with little guidance on the role of this particular physical effect in actual problems. In addition, the author has regrettably endeavored to supply only a representative bibliography rather than a reasonably exhaustive listing. The latter is of course a tremendous task, because of the very extensive number of publications in the subject; nevertheless a more complete reference to the literature might have provided (particularly if critical comments were added) some of the needed guidance to the reader in this notoriously broad field. That very breadth presents anyone who proposes to write a text on thermoelasticity with very difficult problems of choice and emphasis. The same problems must of course be faced by anyone attempting to teach a course on the subject, and in this regard the book's comprehensive program may provide a useful framework, even if not all will find the treatment to their complete satisfaction.

Kinematics and Dynamics of Planar Machinery. By Burton Paul. Prentice-Hall, Inc., Englewood Cliffs, N.J. 1979. Pages xviii-670. Price $29.95.

REVIEWED BY R. L. HUSTON[2]

This is a textbook providing a novel and modern approach to an old subject. Its lucid style together with its incorporation of recent advances make it a welcome addition to the literature.

The title subject is covered in three parts: Geometrical Kinematics, Analytical Kinematics, and Analytical Dynamics. The approach throughout is analytical as opposed to graphical with the emphasis upon solution procedures and techniques as opposed to design and synthesis. Indeed, the book is oriented toward computer solutions and it includes extensive discussion and listing of computer codes for the solution of various problems encountered in planar machinery.

The first part of the text containing six chapters, covers classical or geometrical kinematics: gears, cams, four-bar linkages, cranks, and graphical kinematics. The second part on analytical kinematics, stresses the algebraic approach for determining displacement, velocity, and acceleration. It contains four chapters and discusses single loop mechanisms, constraints, position analysis, and velocity and acceleration analysis. The third part on dynamics, builds directly upon the results of the second part with an analytical approach to machinery dynamics. In four chapters the principle of virtual work, single-degree-of-freedom systems are established. A strong emphasis is placed on the use of Lagrange's form of d'Alembert's principle for the automated analysis of multibody systems. The book concludes with an Appendix containing nearly 80 pages summarizing numerical methods, geometrical methods, graph theory, matrices and linear algebra, complex numbers, and computational procedures.

The reviewer would like to have seen three-dimensional analyses included in the work but page constraints apparently have made this impractical in the volume. (The book has approximately 700 pages.) Also, there is probably a transient nature to some of the computer codes cited because of the current rapid advances in this field. However, this can be updated in subsequent editions.

Although the book is written for students with many examples and problems (with answers), it should also be a very useful aid for practicing engineers and researchers working with kinematics and mechanical systems.

Introduction to the Mechanics of Plastic Forming of Metals. By W. Szczepinski. Sijthoff & Noordhoff. 1979. Pages 368. Price $60.

REVIEWED BY S. KOBAYASHI[3]

The book begins with usual introductory subjects of plastic forming of metals, namely, mechanical properties of metals, stresses and strains, yield conditions, and flow rules. The concept is classical and based on the incremental strain theory. The book then emphasizes the theory and application for two-dimensional problems of plane strain and plane stress, with some considerations for axisymmetric problems. The theories are described in detail on the method of

[1] Dean, The Technological Institute, Northwestern University, Evanston, Ill. 60201.

[2] Professor, Department of Engineering Science, University of Cincinnati, Cincinnati, Ohio 45221.

[3] Professor of Mechanical Engineering, University of California, Berkeley, Calif. 94720.

Copyright © 1980 by ASME

Downloaded 01 May 2010 to 171.66.16.243. Redistribution subject to ASME license or copyright; see http://www.asme.org/terms/Terms_Use.cfm

characteristics for plane strain and plane stress. The applications of the theories to metal-forming problems are limited, but the treatment of some of the problems is unique. An example is the analysis of plastic deformation of flat rings using the method of characteristics under the plane stress condition. Also, Chapter 11, dealing with drawing and stretch forming of thin-walled shells of arbitrary double curvature, is new in demonstrating rigorous analysis using the method of characteristics. It is a little disappointing, however, to find that recent references from the 1970's are not quoted.

A Mathematical Introduction to Fluid Mechanics. By A. J. Chorin and J. E. Marsden. 1979. Springer-Verlag, New York Inc. Pages v-205. Price $14.50.

REVIEWED BY A. LEONARD[4]

The book is based on notes for a short course in fluid mechanics in the Department of Mathematics at the University of California at Berkeley. The contents include the derivation of the equations of fluid motion and theorems concerning the motion of vorticity in Chapter I. In Chapter II potential flow, boundary layers, and flow separation are discussed along with a random vortex sheet algorithm for the simulation of boundary-layer flows. In Chapter III compressible flow in one dimension is covered including a computational algorithm based on Glimm's existence proof. In addition the mathematics of combustion waves is presented. The goals of the course were: "(*i*) to present some of the basic ideas of fluid mechanics in a mathematically attractive manner (which does not mean 'fully rigorous'); (*ii*) to present the physical background and motivation for some constructions which have been used in recent mathematical and numerical work on the Navier-Stokes equations and on hyperbolic systems; (*iii*) to interest some of the students in this beautiful and difficult subject."

Even though the book is written for mathematics students it should be palatable even enjoyable to a broad group of engineers and scientists. Several mathematical concepts not usually encountered in the traditional fluid mechanics text are inserted in various parts of the development. To this reviewer the extra mathematics is worthwhile and usually provides substantial clarification of some of the physical concepts. One example is the use of a flow map in the developments of the law of mass conservation and the vorticity theorems for inviscid flow. Another example is the introduction of a projection operator to clarify the meaning of pressure and the boundary conditions for the incompressible Navier-Stokes equations.

As with nearly every book there are a few rough spots, one in this case being the rather obscure derivation of the equations for isentropic flow. On the whole, however, the book is highly recommended to those who want a refreshing look at what is known about fluid mechanics and some insights on outstanding problems.

Mechanics of Composite Materials. By R. M. Christensen. John Wiley & Sons, Inc., 1979. Pages xiv–348. Price, $29.95.

REVIEWED BY J. J. McCOY[5]

It is convenient to classify the literature treating the mechanics of composite materials according to the attention given to the microstructure. The "phenomenologist," for the most part, ignores it in the formulation of response models, and resorts to empiricism to determine model parameters. The "rationalist" also formulates response models on a macroscale, but looks down toward the microscale to set constraints on the nature of these models and to introduce prediction models for the parameters contained in them. The "fundamentalist" does his response modeling on the microscale and seeks to integrate up, or project out, in order to obtain a macroscale formulation. Prediction models for the parameters of the macroscale formulation are a byproduct of the integration, or projection, process. Finally, the "purist" has difficulty accepting a continuum model on the microscale.

R. M. Christensen is clearly a "rationalist" and his book is written from this perspective. It is my opinion that it is one of the finest texts available which takes this approach and is a very welcome addition to the literature. My satisfaction with the book is not complete; but any perceived shortcoming is in details, or arises because of my different perspective. On balance the treatment is well reasoned and readable. The book is ideal for a graduate level course for engineers and materials scientists.

The book is some 340 pages long and is divided into nine chapters, all of roughly the same length. The first chapter presents some basic mechanics and is distinguished from similar treatments in the derivation of a formula, due to Eshelby, which reduces the calculation of the strain energy of a suspension to evaluating surface integrals taken over the inclusions. This formula is referred to several times during the next three chapters, which treat prediction models for the effective moduli of elasticity of suspensions. Chapter three considers suspensions of spherical inclusions; Chapter four discusses cylindrical and lamellar systems; and Chapter five treats bounds on effective moduli and some additional results.

Christensen is a strong advocate of the efficacy of the composite sphere assemblage, introduced by Hashin, and of its two-dimensional equivalent, the composite cyclinder assemblage, as models for predicting the effective moduli of composites. Because the two models lead to similar calculations, we need only discuss one. A composite sphere assemblage is a suspension constructed by filling three-dimension space with composite spheres, comprised of a spherical inclusion of one phase surrounded by a spherical shell of a second phase. The relative size of the inclusion to the shell is fixed by a requirement that the volume fraction of all composite spheres are the same. In order to fill space completely, it is necessary to allow a gradation in the absolute sizes of the composite spheres, down to an infinitesimal. The importance of the assemblage models is that they represent real physical suspensions for which we can exactly calculate some effective moduli. We can, for example, obtain an exact expression for the effective bulk modulus of a composite sphere assemblage; although we cannot similarly obtain an exact expression for the effective shear modulus. To obtain an expression for the shear modulus, the author makes use of a model that places a single composite sphere in an equivalent homogeneous specimen. As noted in the text, the calculation based on this three-phase model is sometimes viewed as a self-consistent calculation; I would so view it. This reviewer is also an advocate, but a less strong one, of the efficacy of the composite sphere and composite cylinder assemblages. The difficulty, of course, is that while they do represent physically real suspensions, we seem to have no way of ascertaining whether a given suspension is properly modeled by one of them. One might argue that this criticism is the same as one leveled at self-consistent calculation, an argument that Christensen quite rightly rejects. Self-consistent calculations are not based on a physically realizable suspension. Hence, prediction models for effective property measures based on them are not rational in the sense of exact calculations based on the composite sphere (cylinder) assemblage.

Bounds of the Hashin-Shtrikman type are central to Christensen's discussion of this topic, which the reviewer thought illuminating. A small criticism, prompted by my different perspective of the problem, is a failure to emphasize that the separation of the bounds is not due to a weakness in analysis but to a lack of information of the microstructure. In my view the separation of the bounds is not to be decried but actually represents an opportunity for possibly controlling the

[4] AMES Laboratory, NASA, Moffett Field, Calif. 94035.

[5] Professor, Department of Civil Engineering, The Catholic University of America, Washington, D. C. 20064.

Copyright © 1980 by ASME
Downloaded 01 May 2010 to 171.66.16.243. Redistribution subject to ASME license or copyright; see http://www.asme.org/terms/Terms_Use.cfm

effective property of composites by controlling the shapes, size distributions, and maybe the positioning of inclusions.

Chapter five treats the important topic of the mechanics of laminates. The two main topics are a classical theory of laminated plates; i.e., a thin-plate theory, based on a Kirchhoff-Love hypothesis, in which extension and flexure are coupled as a consequence of the layering; and a higher-order theory in which some restrained warping of a cross-sectional plane is allowed. The derivation of the higher-order theory appears to parallel derivations of dynamical thick-plate theories, by Mindlin and his students. This reviewer has a bit of a difficulty with this approach in the present application since the wish is to predict the stress variation across the plate thickness, a variation that is severely restrained by the assumed form for the warping.

Chapter six considers a collection of topics involving analysis, strength, and design; Chapter seven introduces some topics in wave propagation; Chapter eight some inelastic and nonlinear effects; and Chapter nine returns to predicting effective properties, this time thermal properties. This reviewer is less familiar with the subject matter of Chapters six and eight and cannot review these chapters critically. They are clearly written and would appear to be state of the art. The chapter on wave propagation was introduced for completeness. It provides a broad overview treating the effects of a layering on both CW and pulse propagation. Interest in such studies clearly pertain to propagation in laminates. Effects of the microstructure, on which inclusions can be observed, are largely ignored; although a source of attenuation due to a random positioning of inclusions is demonstrated. The chapter treating effective thermal properties mirrors those treating effective mechanical properties.

Energy Methods in Finite-Element Analysis. Edited by R. Glowinski, E. Y. Rodin, and O. C. Zienkiewcz. John Wiley & Sons, 1979. Pages xviii-361. Price $43.95.

REVIEWED BY T. H. H. PIAN[6]

This volume is dedicated to the memory of Prof. B. Fraeijs de Veubeke, who was well recognized in his contributions to the theory of energy (variational) methods in finite-element analysis. The papers in this volume may be divided into three categories:

1 Mathematical theories of variational principles.
2 Mechanics aspect of finite-element methods.
3 Problems in numerical analysis.

The first group includes a presentation of the modern theory of variational boundary-value problems and their applications to elastostatics, a derivation of the classical plate theory from the standard three-dimensional elasticity theory, a new mixed finite-element formulation for the solution of Stokes problem and a theoretical analysis of the duality between the static and kinematic theories of limit analysis in perfect plasticity. Three other papers are devoted to the mathematical analysis of the so-called "nonstandard" or "nonconventional" finite elements in solid mechanics, i.e., the equilibrium mixed and hybrid models.

Papers under the second category include the following topics:

1 A derivation of sufficient conditions for convergence of noncompatible elements for bending.
2 A review of finite-element methods in structural dynamics.
3 The coupling of standard finite-element method and boundary integral method.
4 The derivation of a linear-stress equilibrium element for plate stretching that can avoid spurious kinematic modes.
5 The use of a mutually supplementing displacement and equilibrium fields and a hybrid approach for finite-element stiffness formulation for thin shells.
6 The use of penalty function method for assumed stress finite-element formulation.
7 The formulation of incompressible material using low-order displacement elements.
8 The optimization of incremental finite-element solutions by monitoring the change in incremental stiffness.
9 A unified presentation of total and updated Lagrangian descriptions in nonlinear structural analysis.
10 Finite-element solutions for deformations of creeping structures under cyclic loading.

Finally, under the category of numerical analysis one paper is a discussion of some difficulties related to generalized splines and the other, an application of Lanczos algorithm for large eigenvalue problems.

It is seen that not all the 19 papers in this volume have stuck to the subject indicated by the title of the book. Some of the papers are extensions of the individual authors' previously published works. The book should attract readers who are doing research in different aspects of finite-element methods.

The volume includes a list of main publications of Professor Fraeijs de Veubeke, but it does not point out specifically the extent and impact of his contributions to the development of finite-element methods in structural mechanics. Also there is an apparent absence of a paper that discusses or extends Fraeijs de Veubeke's unfinished work on a new variational principle for finite displacements.

Formulas for Natural Frequency and Mode Shape. By Robert D. Blevins. Van Nostrand Reinhold. 1979. Pages 512, 107 Illustrations; $6\frac{7}{8} \times 10$. Price $29.95.

REVIEWED BY R. PLUNKETT[7]

Blevins is once more generously sharing the contents of his extensive library with his colleagues. The author of the widely used and cited "Flow Induced Vibration" has compiled an extensive and useful set of formulas and tables which cover the title topics. He also includes solid-fluid interaction and sloshing. The book is addressed to the person with a firm grasp of dynamics and deformable body mechanics and is not intended as a quick answer handbook. Each chapter starts with a very brief, clearly written introduction which serves primarily to define the conventions used and list the assumptions and limitations. The author then gives extensive tables of mode shapes and frequencies for specific cases with the presentation similar to that in Roark's tables. He includes some worked out examples using numbers of practical interest to illustrate the effect of various assumptions. Each chapter ends with an up-to-date bibliography which includes both general references and applications papers; these lists are meant to be informative rather than exhaustive. The author anticipates that the user will have access to a computer; as a result, he only gives representative tables for specific cases and formulas for calculator use for the rest. The one case covered exhaustively is that of the uniform beam where he gives the Felgar and Young beam tables with coefficients for the transcendental equations and graphs of mode shapes. He also includes 30 pages of Felgar's integral relationships among the beam modes and their derivatives which are extremely useful for modal expansion. The important chapter headings are: 6. Spring and Pendulum Systems (lumped masses), 19 references, mainly text books; 7. Cables and Cable Trusses, 8 references; 8. Straight beams (discussed previously), 41 references; 9. Curved beams and frames, 17 references; 10. Membranes, 8 references; 11. Plates, 89 references; 12. Shells, 55 references; 13. Fluid Systems, 29 references; 14. Structural Vibrations in a Fluid, 61 references. There is an eight page chapter on finite-element methods, expository rather

---

[6] Professor, Department of Aeronautics and Astronautics, Massachusetts Institute of Technology, Cambridge, Mass. 02139.

[7] Professor, Department of Aero Engineering and Mechanics, 107 Aero Engineering, University of Minnesota, Minneapolis, Minn. 55455.

Copyright © 1980 by ASME
Downloaded 01 May 2010 to 171.66.16.243. Redistribution subject to ASME license or copyright; see http://www.asme.org/terms/Terms_Use.cfm

ERRATUM

Erratum on "On the Stability of Steady Motions in Free and Restrained Dynamical Systems," by P. Hagedorn, and published in the June, 1979, issue of the ASME JOURNAL OF APPLIED MECHANICS, Vol. 46, No. 2, pp. 427–432.

1 The example on the top of page 430 (first three phrases) is inappropriate, since the equilibrium $\mathbf{q} = \mathbf{0}, \dot{\mathbf{q}} = \mathbf{0}$ is not mapped into $\mathbf{q} = \mathbf{0}, \mathbf{p} = \mathbf{0}$ in this example.

2 Replace the expression in the second bracket in (46) and in the left side of the second inequality (47) with

$$Px_0 - (A - B)\omega^2 - k\omega - [k + (A - B)\omega]^2/B.$$

Copyright © 1980 by ASME
Downloaded 01 May 2010 to 171.66.16.243. Redistribution subject to ASME license or copyright; see http://www.asme.org/terms/Terms_Use.cfm